

Environmental Science and Engineering

Phu Le Vo · Dang An Tran ·
Lan Pham Thi · Ha Le Thi Thu ·
Nghia Nguyen Viet *Editors*

Advances in Research on Water Resources and Environmental Systems

Selected papers of the 2nd International
Conference on Geo-Spatial Technologies
and Earth Resources 2022

 Springer

Environmental Science and Engineering

Series Editors

Ulrich Förstner, Buchholz, Germany

Wim H. Rulkens, Department of Environmental Technology, Wageningen,
The Netherlands

The ultimate goal of this series is to contribute to the protection of our environment, which calls for both profound research and the ongoing development of solutions and measurements by experts in the field. Accordingly, the series promotes not only a deeper understanding of environmental processes and the evaluation of management strategies, but also design and technology aimed at improving environmental quality. Books focusing on the former are published in the subseries Environmental Science, those focusing on the latter in the subseries Environmental Engineering.


Phu Le Vo · Dang An Tran · Thi Lan Pham ·
Ha Le Thi Thu · Nghia Nguyen Viet
Editors

Advances in Research on Water Resources and Environmental Systems

Selected papers of the 2nd International
Conference on Geo-Spatial Technologies
and Earth Resources 2022

 Springer

Editors

Phu Le Vo 
Faculty of Environment and Natural
Resources
Ho Chi Minh City University of Technology
(HCMUT), Vietnam National University
Ho Chi Minh (VNU-HCM)
Ho Chi Minh City, Vietnam

Thi Lan Pham 
Hanoi University of Mining and Geology
Hanoi, Vietnam

Nghia Nguyen Viet 
Hanoi University of Mining and Geology
Hanoi, Vietnam

Dang An Tran 
Faculty of Water Resources Engineering
Thuyloi University
Hanoi, Vietnam

Ha Le Thi Thu
Department of Mine Surveying Faculty
of Geomatics and Land Administration
Hanoi University of Mining and Geology
Hanoi, Vietnam

ISSN 1863-5520 ISSN 1863-5539 (electronic)
Environmental Science and Engineering
ISBN 978-3-031-17807-8 ISBN 978-3-031-17808-5 (eBook)
<https://doi.org/10.1007/978-3-031-17808-5>

© The Editor(s) (if applicable) and The Author(s), under exclusive license to Springer Nature Switzerland AG 2023, corrected publication 2023

This work is subject to copyright. All rights are solely and exclusively licensed by the Publisher, whether the whole or part of the material is concerned, specifically the rights of translation, reprinting, reuse of illustrations, recitation, broadcasting, reproduction on microfilms or in any other physical way, and transmission or information storage and retrieval, electronic adaptation, computer software, or by similar or dissimilar methodology now known or hereafter developed.

The use of general descriptive names, registered names, trademarks, service marks, etc. in this publication does not imply, even in the absence of a specific statement, that such names are exempt from the relevant protective laws and regulations and therefore free for general use.

The publisher, the authors, and the editors are safe to assume that the advice and information in this book are believed to be true and accurate at the date of publication. Neither the publisher nor the authors or the editors give a warranty, expressed or implied, with respect to the material contained herein or for any errors or omissions that may have been made. The publisher remains neutral with regard to jurisdictional claims in published maps and institutional affiliations.

This Springer imprint is published by the registered company Springer Nature Switzerland AG
The registered company address is: Gewerbestrasse 11, 6330 Cham, Switzerland

Preface

In parallel with a remarkable economic growth over the past several decades, the consequences of environmental degradation and resources depletion have placed a paramount challenge on the sustainable development track in Vietnam. Accordingly, in the course of the national rapid socio-economic development, issues of environmental pollution, natural resources management coupled with stresses in the age of global change have increasingly becoming a vital of concern. Therefore, both engineering and management techniques are necessary for environmental pollution control, resources management, and resilience that draw much attention from various stakeholders, including government managers, academia, and industry.

Given this context, we would like to welcome you to the 2nd International Conference on Geo-spatial Technologies and Earth Resources 2022 (GTER 2022), which will be held during October 14–15, 2022, at Hanoi University of Mining and Geology (HUMG), Hanoi, Vietnam. The event is co-organized by HUMG and the International Society for Mine Surveying (ISM) to celebrate the 55th anniversary of the Department of Mine Surveying (HUMG). The conference is financially supported by the Vietnam Mining Science and Technology Association (VMSTA), the Vietnam Association of Geodesy, Cartography and Remote Sensing (VGCR), Vietnam National Coal-Mineral Industries Holding Corporation Limited (VINACOMIN), and Dong Bac Corporation (NECO).

This Volume 2 comprises a series of selected high-quality peer-reviewed papers delivered at the GTER 2022. It provides an in-depth coverage of advanced research in water resources and environmental systems that cover a wide range of topics in recent advanced research in water resources engineering (i.e., surface and subsurface water flow systems, water resources management), advanced techniques and solutions for water and wastewater treatment, water supply and suitable drainage systems, flood modeling and risk assessment, environmental earth systems (i.e., air, coastal, and marine pollution, sustainability and circular economy), applying advanced RS&GIS technologies in natural hazards, monitoring and management for environmental systems such as vulnerability and risk assessment, natural resources, and environmental changes. This critical Volume 2 will bring together, from a global perspective, scientists, researchers, end-users, industry, policymakers from several

countries and professional backgrounds to exchange ideas, advance knowledge, and discuss critical issues for Geospatial Technologies and Earth Resources. It also serves as a valuable reference work for advanced undergraduate and graduate students, designers of water resources systems, and scientists and researchers. The goals of the Volume 2 are: (1) to cover entire water and environmental fields, including hydrogeology, environmental systems, RS&GIS technologies in natural hazard, disaster risks, monitoring and management for environmental systems and geological system; and (2) to employ a multimedia approach to environmental conservation and protection since air, water, soil, and energy are all interrelated.

Totally, 89 abstracts and 50 full manuscripts have been received by the organizing committee. Subsequently, after screening by the scientific committee and reviewing by at least two blind reviewers, 42 research and review papers have been selected to be presented at the conference. The selected papers will be delivered over four planned sessions covering different topics of *Geospatial Technologies*, *Earth Sciences*, *Water Resources*, and *Environmental Systems and Sustainability*. These 42 papers were also selected for publication in this book with Digital Object Identifier (DOI) references. We believe that this book will provide the readers with an overview of recent advances in the fields of Geospatial Technologies and Earth Resources.

We would like to express our sincere thanks to all members of the organizing and selection committees, all blind peer reviewers, all chairpersons, and invited speakers for their invaluable contributions. We are also thankful to Mr. Phuong Kim Minh, President of Dong Bac Corporation; Prof. Tran Thanh Hai, President of the HUMG University Council; Assoc. Prof. Trieu Hung Truong, Vice-rector of HUMG for their administrative work and financial supports. Special thanks are also to Doris Bleier and Viradasarani Natarajan at Springer Nature for their helpful assistance and support throughout the procedures of this book production. Finally, all authors are thankful for their manuscript submissions regardless of whether or not their manuscripts were selected.

Hanoi, Vietnam
June 2022

Phu Le Vo
Dang An Tran
Thi Lan Pham
Ha Le Thi Thu
Nghia Nguyen Viet

Contents

1	Application of Modflow-Based Seawat Code for Seawater Intrusion Forecasting into the Upper Pliocene Coastal Aquifer in the Ca Mau Peninsula, Southern Vietnam	1
	Thi Thuy Van Le, Rungruang Lertsirivorakul, Hong Thang Chau, and Phi Hieu Le	
2	Seawater Intrusion Processes Along the Tien River Mouth in the Period 2000–2020	19
	Thuc Thi Bich Pham, Vu Truong Nguyen, Binh Thanh Pham, Hieu Duc Tran, Man Ba Duong, Thu Thi Mong Ngo, Tran Duc Mai, and Quan Minh Pham	
3	Developing Software Package for 2D Modeling Hydrodynamics and Salinity Transport in Cu Lao Dung, Mekong Delta	35
	Xuan Dung Tran and Anh-Ha Le	
4	An Assessment of Some Algorithms for Modeling and Forecasting Horizontal Displacement of Ialy Dam, Vietnam	51
	Kien-Trinh Thi Bui and Cuong Manh Nguyen	
5	Simulation of the Hydrodynamic Regime of Aquaculture Development Zones Within Binh Dinh, Vietnam	65
	Duy Vu Luu, Thi Ngoc Canh Doan, Khanh Le Nguyen, Ngoc Duong Vo, and Chau Van Truong	
6	Prediction of Suspended Sediment Concentration by Artificial Neural Networks at the Vu Gia-Thu Bon Catchment, Vietnam	77
	Duy Vu Luu	
7	Criteria Affecting Groundwater Potential: A Systematic Review of Literature	85
	Dang Tuyet Minh	

8	Pumped Storage Power Plant, Solutions to Ensure Water Sustainability and Environmental Protection	111
	Trung Son Pham	
9	Modelling the Influences of River Water Level on the Flooding Situation of Urban Areas: A Case Study in Hanoi, Vietnam	121
	Van Minh Nguyen, Kim Chau Tran, and Thanh Thuy Nguyen	
10	Assessing the Current Characteristics of Concrete in Some Parts Hoa Binh Hydropower Plant	133
	Duong Thi Toan and Nguyen Thi Mai Phuong	
11	Hydraulic Performance of a Sand Trap in the Flushing Period to Support the Maintenance of the Pengasih Irrigation Network, Indonesia	145
	Ansita Gupitakingkin Pradipta, Ho Huu Loc, S. Mohana Sundaram, Sangam Shrestha, Murtiningrum, and Sigit Supadmo Arif	
12	Identification of Hydrogeochemical Processes and Controlling Factors in Groundwater and Surface Water Using Integrated Approaches, Tuul River Basin (Ulaanbaatar, Mongolia)	167
	Odsuren Batdelger, Maki Tsujimura, Dang An Tran, Byambasuren Zorigt, and Pham Thi Bich Thuc	
13	Application of Plant Endophytic Microorganisms (<i>Endophytes</i>) in the Treatment of Heavy Metal Pollution in Soils ...	199
	Kieu Bang Tam Nguyen and Thi Hong Thao Phan	
14	Evaluation of Density Characterization of Municipal Solid Waste in Southern Part of Vietnam	223
	Hung-T. Vo, Thong-H. Nguyen, Vinh-T. Bui, Ngoc-L. Dang, Phong-T. Le, Hau-T. Le, Linh-T. D. Le, and Thong-V. Pham	
15	Assessment of Lead (Pb) Accumulation in Native Plants Growing on Coal Mine Site in Northeastern Vietnam	237
	Bui Xuan Dung, Truong Ngoc Anh, and Nguyen Thi My Linh	
16	Assessment and Risk Management of Malicious Acts Aimed at Potentially Hazrdous Hydrotechnical Constructions	253
	Valery Mitkov	
17	3D Numerical Modelling for Hydraulic Characteristics of a Hollow Triangle Breakwater	265
	Tu Le Xuan, Hung Le Manh, Hoang Tran Ba, Thanh Dang Quang, Vo Quoc Thanh, and Duong Tran Anh	

18	The Role of Hydrodynamics in the Development of Mangrove Forests in Can Gio Mangrove Biosphere Reserve (Ho Chi Minh, Vietnam)	285
	Hoa Tien Le Nguyen, Xuan Dung Tran, Tien Thanh Nguyen, and Hong Phuoc Vo Luong	
19	The Method for Delimiting the Maritime Boundary in the Internal Waters of Coastal Provinces of Vietnam (From Binh Thuan Province to Ca Mau Province)	297
	Thi Nguyet Que Phan, Ngoc Lam Hoang, Thi Bao Hoa Dinh, and Van Soat Hoang	
20	Assessment of the Status of Supervision and Social Criticism of the Majority of People in the Fields of Land at Quy Nhon City, Binh Dinh Province	313
	Hang Thi Pham, Thuy Le Thi Phan, and Hien Dieu Thi Bui	
21	Assessment of Sustainable Development for Ly Son and Phu Quy Islands Using Sustainable Development Index	329
	Pham Viet Hai, Nguyen Thi Diem Thuy, Phan Thi Thanh Hang, and Dao Nguyen Khoi	
22	Multi Criteria Decision Analysis (MCDA) Approach to Evaluate the Applicability of Nature Based Solutions (NBS) in Tropical Region: A Field Note from the Asian Institute of Technology (AIT), Thailand	345
	Fahad Ahmed, Ho Huu Loc, Sangam Shrestha, Sutat Weesakul, and Nguyen Hoai Thanh	
23	Decision Support Tool for Integrated Water Resources Management Based on GIS, Remote Sensing and SWAT Model: A Case Study in the Upper Part of Dong Nai River Basin, Vietnam	361
	Pham Hung, Le Van Trung, and Phu Le Vo	
24	Spatial–Temporal Changes in Land Surface Temperature Pattern in the Western Edge of the Inner Hanoi City, Vietnam During the 2005–2019 Period	389
	Duc-Loc Nguyen, Tien-Yin Chou, Thanh-Van Hoang, Mei-Hsin Chen, Chun-Tse Wang, and Van-Khue Phan	
25	Salinity Prediction in Coastal Aquifers of the Vietnamese Mekong River Delta Using Innovative Machine Learning Algorithms	403
	Dang An Tran, Ha Nam Thang, Dieu Tien Bui, and Vuong Trong Kha	

26	Application of Convolution Neural Network for Rapid Flood Mapping Using Sentinel-1 Imagery—A Case Study in Central Region of Vietnam	431
	Hien Phu La and Quan Van Ngo	
27	WebGIS and Random Forest Model for Assessing the Impact of Landslides in Van Yen District, Yen Bai Province, Vietnam	445
	Xuan Quang Truong, Nhat Duong Tran, Nguyen Hien Duong Dang, Thi Hang Do, Quoc Dinh Nguyen, Vasil Yordanov, Maria Antonia Brovelli, Anh Quan Duong, and Thanh Dong Khuc	
28	Analysis of Riverbank Changes of Go Gia River in Can Gio District in the Period of 2013–2021	465
	Nguyen Phuong Uyen, Pham Thi Loi, Nguyen Thi Diem Thuy, Nguyen Thi Bay, and Dao Nguyen Khoi	
29	Estimate Petrophysical Properties by Using Machine Learning Methods	475
	Tran Nguyen Thien Tam and Dinh Hoang Truong Thanh	
30	Mapping Wetland Ecosystems Protection and Restoration Priority Using GIS, Remote Sensing, Landscape Ecology, and Multi-criteria Analysis (Case Study in Dong Thap Muoi)	487
	Phi Son Nguyen, Thanh Thuy Nguyen, Thi Thanh Dinh, Thi Hang Vu, Thi Thanh Huong Nguyen, and Lam Le	
31	The Study of Extraction Soil Salinity Information from High Resolution Multispectral Remote Sensing Data, Pilot Area in DongNai Province, Vietnam	515
	Xuan Huy Chu, Minh Ngoc Nguyen, Ngoc Dat Dinh, Thu Thuy Le, Quang Huy Bui, Thi Lan Pham, Thi Huyen Ai Tong, Van Tiep Trinh, and Van Lap Nguyen	
32	Dynamics and Determinants of Forest Changes Across Mainland Vietnam in the Recent Three Decades	527
	Duong Cao Phan, Ba Thao Vu, Dang An Tran, Vuong Trong Kha, and Kenlo Nishida Nasahara	
33	Monitoring Mangrove Forest Changes in Vietnam Using Cloud-Based Geospatial Analysis and Multi-temporal Satellite Images	543
	Quang Thang Le and Si Son Tong	
34	Analysis and Assessment of the Relationship Between Chlorophyll and Hydrodynamic Factors in Cu Lao Dung (Soc Trang)	561
	Pham Vu Phuong Trang and Vo Luong Hong Phuoc	

35 Flash Flood Hazard Mapping Based on Analytic Hierarchy Process for a Complex Terrain: A Case Study of Chu Lai Peninsula, Vietnam 573
 Thi Lan Pham, Si Son Tong, and Nghia Nguyen Viet

36 A Comparative Flood Susceptibility Assessment in a Norwegian Coastal City Using Feature Selection Methods and Machine Learning Algorithms 591
 Lam Van Nguyen, Dieu Tien Bui, and Razak Seidu

37 Application of Fuzzy and Geospatial Analysis for Identifying Water Pollution Zone in the Can Gio Coastal Mangrove Biosphere Reserve Area 619
 Son V. Lam, Phong V. Nguyen, Kien T. Ta, Chau P. T. Nguyen, Hoa T. Le, and Phu L. Vo

38 Closed Chain System for Plastic Wastes Model Toward Circular Economy, Case Study in Co to, Quang Ninh, Vietnam 641
 Hung Son Pham, Thi Minh Hang Tran, Manh Dat Ngo, Thi Hoang Hao Phan, Anh Hung Pham, Dinh Tuan Vu, Le Anh Tuan, Thien Cuong Tran, and Thi Thuy Pham

39 Evaluation of the Possibility of Application of Porous Asphalt Concrete Containing Steel Slag to Road Construction 661
 Van Long Nguyen, Duc Sy Nguyen, Thi Hanh Nguyen, and Thuy-Linh Le

Correction to: Mapping Wetland Ecosystems Protection and Restoration Priority Using GIS, Remote Sensing, Landscape Ecology, and Multi-criteria Analysis (Case Study in Dong Thap Muoi) C1
 Phi Son Nguyen, Thanh Thuy Nguyen, Thi Thanh Dinh, Thi Hang Vu, Thi Thanh Huong Nguyen, and Lam Le

About the Editors

Dr. Phu Le Vo is currently Associate Professor and Dean of the Faculty of Environment and Natural Resources (FENR), Ho Chi Minh City University of Technology (HCMUT). He obtained his Bachelor degree in Biochemistry, Hue University, Vietnam, in 1994, and received Master and Ph.D. degrees in Environmental Studies at the University of Adelaide, South Australia, in 2000 and 2008, respectively. He started his academic career at HCMUT since September 2000. He was Research Fellow at Sanford School of Public Policy and Nicholas School of Environmental Science (NSOE), Duke University, North Carolina, USA, in 2010 and 2011. He was also Visiting Professor at Faculty of Life and Environmental Sciences, Tsukuba University, Japan, in 2012. He was Visiting Scholar at Faculty of Environmental Sciences, Wageningen UR, and UNESCO-IHE (Delft), The Netherlands, in 2013, and was a key member of the Consultancy Board for developing a master curriculum program on Water Management and Climate Change Adaptation which was run by the Center for Water Management and Climate Change, VNU-HCM. His professional experience in teaching, research, and consultancy spans over 22 years in Vietnam. He teaches several undergraduate subjects, including water resources management, coastal zone management, clean technology and graduate courses on water governance, integrated urban water management, climate change, and adaptation measures. His field of expertise is water resources management and policy, IWRM, groundwater chemistry, climate change, and water management. Since 2015, he became national Short-term Consultant (STC) on Environmental Safeguards for various world bank-financed projects in Vietnam in the Water and Transport Sectors. He is the author and co-author of more than 40 articles published in SCI, SCIE, Scopus and international journals, 36 international conference papers, 23 national journal papers, and three international book chapters. He is currently Editorial Member of the *Science and Technology Development Journal (STDJ)* of Vietnam National University Ho Chi Minh City (since 2014) and Member of Vietnam Association of Conservation for Nature and Environment (VACNE). e-mail: volephu@hcmut.edu.vn

Dang An Tran is currently Lecturer of Water Resources Engineering and Environment, Faculty of Water Resources Engineering, Thuyloi University (TLU), Vietnam. He received M.Sc. degree in Environmental Sciences in 2014 and Ph.D. degree in Sustainable Environmental Studies in 2020, both from the University of Tsukuba, Japan. He has been working for more than 15 years on water supply and sewage system, water resources engineering, groundwater hydrology, applied isotopes, environmental sciences, and water-related risks in Vietnam and other parts of the world. He is the author and co-author of over 20 high-qualified papers and the speaker of more than 10 international presentations relating to his scientific interests. He is also a reviewer of peer-reviewed journals, a guest editor of *Remove Sensing Journal*, and a member of Editorial Board of *Tropical Forests*. e-mail: antd@tlu.edu.vn

Dr. Thi Lan Pham is Lecturer at the Faculty of Geomatics and Land Administration, Hanoi University of Mining and Geology (HUMG), Vietnam. Her current research interests have been focused on the use of new technology equipment for mapping; the application of remote sensing and geographical information system for the management practices of environmental issues. She has joined many projects financed by the Ministry of Education and Training (MOET) and the Ministry of Natural Resources and Environment (MONRE). Further, she has also been a coordinator of many projects funded by HUMG. She has published two books and more than 40 articles in national and international reputation journals including more than 10 articles in various SCIE and Scopus-indexed journals, including *Journal of Korean Society of Surveying, Geodesy, Photogrammetry and Cartography*, *Estuarine, Coastal and Shelf Science*, *Journal of Southwest Jiaotong University*, *Environment Development and Sustainability*, and *Inzynieria Mineralna*. e-mail: phamthilan@humg.edu.vn

Dr. Ha Le Thi Thu is Lecturer at the Faculty of Geomatics and Land Administration, Hanoi University of Mining and Geology (HUMG), Vietnam. She received her Bachelor of Science in 2001, Master of Science in 2006, and Ph.D. degrees in 2017 in Engineering in Geodesy from Hanoi University of Mining and Geology, Vietnam. Her expertise focuses on remote sensing, modeling and GIS of land-use/land-cover change, climate change, and smart city management. She has published three books and more than 60 articles in national and international reputation journals. Besides that, she is an active member of various projects financed by the Ministry of Natural Resources and Environment (MONRE). e-mail: lethithuha@humg.edu.vn

Dr. Nghia Nguyen Viet is currently Managing Editor of the *Journal of Mining and Earth Sciences* and Deputy Dean of the Mine Surveying Department, Geomatics and Land Administration, Hanoi University of Mining and Geology (HUMG). He received Ph.D. about Geodesy, Surveying, and Cartography at the AGH University of Science and Technology (Poland) in 2016. His expertise focuses on the application of geomatics methods in resources and environment research to forecasting and warning impacts of environmental pollution, degradation, and catastrophes. Besides that, he researches applying new technologies on

mine surveying to improve the efficiency of the management and administration of mine production (both open-pit and underground mines). He is the author and co-author of over six high-qualified papers and more than 50 articles in national as well as *Journals of the WoS*. He has been taking on some national and provincial projects. He is also Member of the Association of Mining Science and Technology, Vietnam. e-mail: nguyenvietnghia@humg.edu.vn

Chapter 1

Application of Modflow-Based Seawat Code for Seawater Intrusion Forecasting into the Upper Pliocene Coastal Aquifer in the Ca Mau Peninsula, Southern Vietnam



Thi Thuy Van Le , Rungruang Lertsirivorakul, Hong Thang Chau, and Phi Hieu Le

Abstract To identify the extent of seawater intrusion into the Upper Pliocene aquifer on the Ca Mau Peninsula, southern Vietnam, the groundwater flow and solute transport model are applied. A total of five observation wells evenly distributed throughout the study area are applied to build a groundwater flow model using the MODFLOW-based SEAWAT code from 2000 to 2015. The groundwater flow model calibrates by a trial and error approach of two parameters: hydraulic conductivity and sink/source rate. Then, the seawater intrusion simulation model for the next 16 years runs with the same initial conditions as 2015. The groundwater flow model result showed that the freshwater area with the Chloride concentration of 250 mg/L only existed from 2000 to 2003 with a displacement range of 400 m/year in the study area. After 2003, this freshwater area no longer existed and was replaced by a 500 mg/L value with a displacement range of 410 m/year. The simulation model of seawater prediction shows that, by 2031, the lowest Chloride concentration might be 2000 mg/L. An average displacement range of this value from 2016 to 2031 reaches an average level of 439 m/year.

Keywords MODFLOW-based SEAWAT · Seawater intrusion · Coastal aquifer · Southern Vietnam

T. T. V. Le (✉) · P. H. Le
Faculty of Geology, University of Science–Vietnam National University Ho Chi Minh City (VNU-HCMC), Ho Chi Minh City, Vietnam
e-mail: lttvan@hcmus.edu.vn

T. T. V. Le · R. Lertsirivorakul
Faculty of Technology, Department of Geotechnology, Khon Kaen University, Khon Kaen, Thailand

H. T. Chau
Department of Geography, University of Education Ho Chi Minh City, Ho Chi Minh City, Vietnam

1.1 Introduction

In recent years, the Mekong Delta region of Vietnam, which is sensitive to sea-level rise due to climate change, has received much research attention. A study in 2019 of Climate Central even warned that in the next 30 years, almost the entire area will be submerged in seawater at high tide (Climate Central, <https://coastal.climatecentral.org/map> 2019). The concern of the local government is not only the submerged land but also the reduction of freshwater groundwater resources in this area. The reason is that groundwater has become an important source for local agricultural economic development. Of the eight aquifers of the Mekong River Delta, two are much exploited due to their good quality. These are the Upper Pleistocene (qp_{2-3}) and the Upper Pliocene (n_2^2) aquifers. While the qp_{2-3} aquifer is mainly withdrawn on the scale of the households, the n_2^2 aquifer with deeper depth is on the industrial scale. According to previous research results, the trend of saline intrusion into the qp_{2-3} aquifers has appeared (Le et al. 2020). The remaining n_2^2 aquifer will be the focus of this research. The expected result from this study is to determine the future trend of changing the freshwater area of the n_2^2 aquifer using the groundwater flow model.

1.2 Materials and Methods

1.2.1 Site Location

The study area, a part of the Mekong River Delta, has a peninsular pattern. The Ca Mau Peninsula covers the provinces of Ca Mau, Soc Trang, Bac Lieu, Hau Giang, Can Tho, and part of the Kien Giang and An Giang provinces (Fig. 1.1). The research area covers an area of more than 18,160 km², the length of the coastline stretching from the West Sea to the East Sea with more than 540 km. The topography is flat with an average elevation of 0.7–1.2 m. The elevation of 1.0–1.5 m in the central gradually decreases to 0.3–0.7 m in the coastal area. The study area covers the provinces of Soc Trang, Bac Lieu, Ca Mau, and the coastal part of Kien Giang in the coastal zone, while the rest further inland belongs to part of An Giang, Can Tho, and Soc Trang provinces. Coastal areas often suffer from surface saline intrusion into the Hau River in the dry season. Sediments in the study area were deposited from the transgression and regression periods in the Quaternary period (Ho et al. 1991; Nguyen and Do 2007). Over geological time, these sedimentary strata become the coastal aquifers in the study area. The study area has a tropical monsoon climate with two distinct rainy and dry seasons (Tran et al. 2019). While the rainy season is from May to October, the dry season lasts from November to April next year. In rainy season, the hourly rainfall ranges from 19.7 to 47.6 mm and the daily rainfall varies from 60.9 to

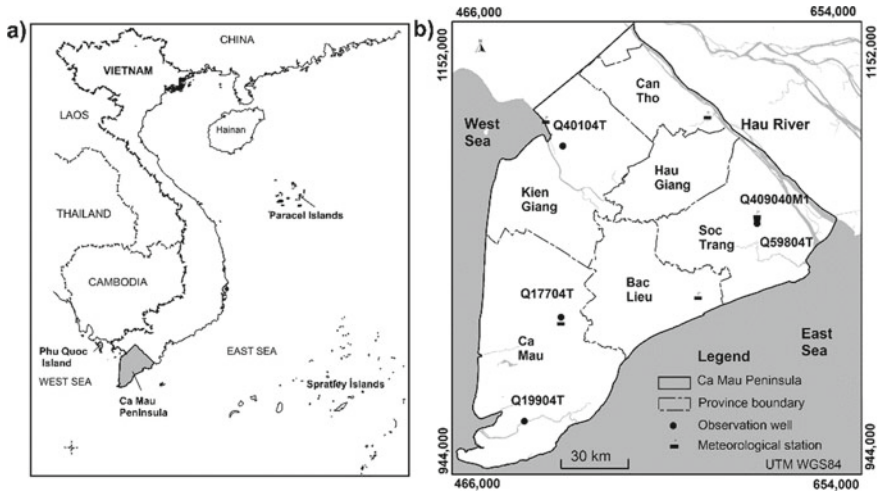


Fig. 1.1 Location of Ca Mau Peninsula (a), province locations of the study area (b)

189.2 mm (Dang 2020). The coastal lands of Ca Mau, Soc Trang, and Bac Lieu have been affected by the tidal regime of the East Sea and West Sea, which are bi-diurnal and diurnal regimes, respectively. The surface water system has faced severe saline contamination risks in the dry season (Vu et al. 2018).

1.2.2 Hydrogeological Units

According to the Division of Water Resources Planning and Investigation Southern Vietnam, in the Mekong River Delta, there are 8 aquifers in porous sediments. These are the Holocene (qh), Upper Pleistocene (qp₃), Upper Middle Pleistocene (qp₂₋₃), Lower Pleistocene (qp₁), Upper Pliocene (n₂²), Lower Pliocene (n₂¹), and Upper Miocene (n₁³), and Upper Middle Miocene (n₁²⁻³) aquifers. While the upper seven aquifers have been properly studied, the Upper Middle Miocene aquifer (n₁²⁻³) has not been investigated due to its deep depth. Interspersed between the aforementioned porous aquifers are impermeable layers or aquitards. They have corresponding geological ages of Holocene (Q₂), Upper Pleistocene (Q₁³), Upper-middle Pleistocene (Q₁²⁻³), Lower Pleistocene (Q₁¹), Upper Pliocene (N₂²), Lower Pliocene (N₂¹), Upper Miocene (N₁³), and Upper-middle Miocene (N₁²⁻³) (Fig. 1.2).

The materials of the n₂² aquifer have alluvial and marine origins (Pham et al. 2019; Bui et al. 2014). Aquifer roof from 42.60 to 328.90 m, average 206.47 m. Aquifer depth from 125.00 to 415.40 m, with an average of 258.92 m, and aquifer thickness from 4.00 to 147.00 m, with an average of 51.33 m. The hydraulic conductivity ranges from 0.17 to 67.20 m/d. The piezometric head is below the mean sea level, from -7.00 to -20.14 m. They have tended to decline from north to south and formed a

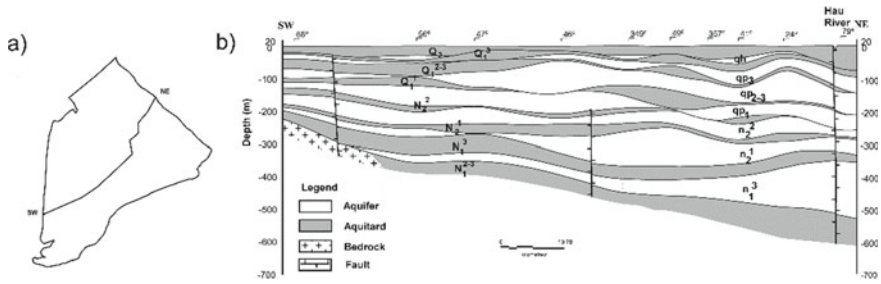


Fig. 1.2 Cross-section line (a), hydrogeological units (b) (*Source* Division of Water Resources Planning and Investigation Southern Vietnam, 2014)

depression zone in the center of Ca Mau province (Bui et al. 2014). Research by Bui et al. 2014 shows that the freshwater area of the Upper Pliocene aquifer has an area of 8507 km² and the saltwater area has an area of 7625 km². The groundwater withdrawals of this aquifer were 169,521 m³/d in 2010 (Bui et al. 2014). With deep depth, far from the recharge zones, and high groundwater withdrawals, the Upper Pliocene aquifer has a high potential for saline intrusion.

1.2.3 Data

The data used for the study are five observation wells for monitoring water level and water quality from 2000 to 2015. They were sampled by the Division of Water Resources Planning and Investigation Southern Vietnam (DWRPIS). Samples were gathered in polyethylene bottles, which had been cleaned by distilled water and rinsed with sample water before storage, and refrigerated at 4 °C for later laboratory analysis. The water quality was analyzed at the Center for Analysis and Test and Materials of DWRPIS, using APHA standard methods (Eaton et al. 2005). The Chloride concentration was identified by Mohr titration.

1.2.4 Numerical Model

There are many methods to predict seawater intrusion in coastal aquifers. The methods are widely applied such as groundwater flow modeling, hydrogeochemical facies, isotopes, trace elements, etc. Many studies on groundwater in the Mekong River Delta applied these methods such as the impact of groundwater extraction in Mekong River Delta under climate change scenarios by using groundwater flow modeling (Bui et al. 2014); saline intrusion at Cu Lao Dung in Soc Trang province by using geochemical and isotopic methods (Tran et al. 2014); saline intrusion trend for

Holocene and Pleistocene aquifers at Long Xuyen Quadrangle and Ca Mau Peninsula by using hydrochemical facies diagram (HFE-D) (Le et al. 2020). In this study, the groundwater flow model, MODFLOW-based SEAWAT code method, is applied for the local important n_2^2 aquifer to predict the extent of seawater intrusion.

MODFLOW-based SEAWAT code is a three-dimensional variable-density flow developed by the United States Geological Survey based on a combination of MODFLOW and MT3DMS (a three-dimensional multi-species solute). The SEAWAT code is combined with MODFLOW and MT3DMS to solve the flow and solute transport equations (Guo and Langevin 2002). First, the flow Eq. (1.1) solves the fluid velocity.

$$\begin{aligned} \frac{\partial}{\partial \alpha} \left\{ \rho K_{f\alpha} \left[\frac{\partial h_f}{\partial \alpha} + \frac{\rho - \rho_f}{\rho_f} \frac{\partial Z}{\partial \alpha} \right] \right\} + \frac{\partial}{\partial \beta} \left\{ \rho K_{f\beta} \left[\frac{\partial h_f}{\partial \beta} + \frac{\rho - \rho_f}{\rho_f} \frac{\partial Z}{\partial \beta} \right] \right\} \\ + \frac{\partial}{\partial \gamma} \left\{ \rho K_{f\gamma} \left[\frac{\partial h_f}{\partial \gamma} + \frac{\rho - \rho_f}{\rho_f} \frac{\partial Z}{\partial \gamma} \right] \right\} = \rho S_f \frac{\partial h_f}{\partial t} + \theta \frac{\partial \rho}{\partial C} \frac{\partial C}{\partial t} - \bar{\rho} q_s. \end{aligned} \quad (1.1)$$

where: α, β, γ are orthogonal coordinate axes, aligned with the principal directions of permeability; $K_{f\alpha}, K_{f\beta}, K_{f\gamma}$ are equivalent freshwater hydraulic conductivity in the three coordinate directions [LT⁻¹]; ρ is the fluid density [ML⁻¹]; ρ_f is the density of freshwater [ML⁻¹]; h_f is the equivalent freshwater head [L]; Z is the elevation above datum of center of model cell [L]; S_f is the equivalent freshwater specific storage [L⁻¹]; θ is effective porosity [dimensionless]; C is solute concentration [ML⁻³]; $\bar{\rho}$ is the density of water entering from a source or leaving through a sink [ML⁻³]; q_s is the volumetric flow rate of sources or sinks per unit volume of aquifer [LT⁻¹]; t is time [T].

Next, they are used in the advection term to solve the solute transport Eq. (1.2).

$$\frac{\partial C}{\partial t} = \nabla \cdot (D \nabla C) - \nabla \cdot (\bar{v} C) - \frac{q_s}{\theta} C_s + \sum_{k=1}^N R_k. \quad (1.2)$$

where: D is the hydrodynamic dispersion coefficient [L²T⁻¹]; v is fluid velocity [LT⁻¹]; C_s is the solute concentration of water entering from sources or leaving through sinks [ML⁻³]; R_k ($k = 1, \dots, N$) is the rate of solute production or decay in reaction k of N different reactions [ML⁻³T⁻¹]; θ is the effective porosity [dimensionless].

The SEAWAT code used a linear Eq. (1.3) to convert the solute concentration to the density of the liquid after ignoring the effects of pressure and temperature on the liquid density and assuming that liquid density is just a function of solute concentration.

$$\rho = \rho_f + \frac{\partial \rho}{\partial C} C. \quad (1.3)$$

where:

$\frac{\partial \rho}{\partial C} = 0.7143$ is the slope of equation.

The flow and solute transport is solved synchronously through the time-step loop method. The more detailed content of SEAWAT is indicated in the manual (Guo and Langevin 2002).

Before discretizing the model, the conceptual model is fully sketched based on geological and hydrogeological units. In the plane view, the study area with an area of 18,160 km², divided into 190 rows and 270 columns with a uniform grid area of 1 km². In the vertical direction, from the ground down to the position of the Upper Pliocene aquifer, the conceptual model is divided into 14 layers corresponding to seven aquifers and seven aquitards. In the conceptual model, the upper and lower boundaries of the Upper Pliocene aquifer (n_2^2) are the Lower Pleistocene aquitard (Q_1^1) and the Lower Pliocene aquitard (N_2^1), respectively.

1.2.5 Hydrogeological Inputs

The hydraulic conductivity K is a key parameter in the flow equation. They are estimated from the pumping test data conducted by the DWRPIS. The K values ranged from 1.29 to 60.66 m/d (Table 1.1). The vertical K equals 1/10 of the horizontal K. The specific yield and specific storage have values ranging from 0.12 to 0.20 and 0.00005 to 0.0032, respectively (Table 1.2). For the impermeable layer, these values are in Table 1.3.

Table 1.1 Hydraulic conductivity K of the n_2^2 aquifer

Boreholes	Coordinate (X)	Coordinate (Y)	(K _x)	(K _y)	(K _z)
82	530,877	1,009,534	35.52	35.52	3.552
83	511,600	1,008,042	17.96	17.96	1.796
215-II-NB	515,939	1,014,664	25.69	25.69	2.569
87	508,833	1,015,301	59.38	59.38	5.938
80	507,304	1,021,753	16.89	16.89	1.689
85	522,277	1,025,559	32.68	32.68	3.268
841a	570,638	1,021,911	1.29	1.29	0.129
847a	568,954	1,026,180	7.24	7.24	0.724
845a	573,651	1,029,133	32.12	32.12	3.212
S234	580,165	1,027,685	8.52	8.52	0.852
843a	583,217	1,027,968	19.33	19.33	1.933
843b	583,216	1,027,967	27.14	27.14	2.714
807-RG	515,933	1,102,812	60.66	60.66	6.066
09-TH	531,741	1,118,367	9.80	9.80	0.980
671-LX	550,123	1,144,035	18.35	18.35	1.835
673-LX	546,907	1,147,010	12.30	12.30	1.230

Table 1.2 Specific yield (S_y) and specific storage (S_s) of the local aquifers

Layers	2	4	6	8	10	12	14
Aquifers	qh	qp3	qp2-3	qp1	n_2^2	n_2^1	n_1^3
S_y	0.12	0.20	0.19	0.18	0.18	0.17	0.15
S_s	0.00075	0.00047	0.00320	0.00030	0.00030	0.00005	0.00005

Table 1.3 Specific yield (S_y) and specific storage (S_s) of the local aquitards

Layers	Aquitars	K_x	K_y	K_z	S_s	S_y
1	Q_2	0.5	0.05	0.05	0.005	0.106
3	Q_1^3	$1.0e-04$	$1.0e-05$	$1.0e-05$	$1.0e-05$	0.031
5	Q_1^{2-3}	$1.0e-04$	$1.0e-05$	$1.0e-05$	$1.0e-05$	0.031
7	Q_1^1	$1.0e-06$	$1.0e-07$	$1.0e-07$	$1.0e-05$	0.016
9	N_2^2	$1.0e-07$	$1.0e-08$	$1.0e-08$	$5.0e-04$	0.012
11	N_2^1	$1.0e-07$	$1.0e-08$	$1.0e-08$	$5.0e-04$	0.012
13	N_1^3	$1.0e-07$	$1.0e-08$	$1.0e-08$	$5.0e-04$	0.012

Based on the lithology characteristics of the aquifer consisting of mainly fine to medium-grained sand, the aquifer porosity is assigned from 0.15 to 0.45 (Dieulin et al. 1981), the aquifer dispersion is set at 10 m (Schulze-Makuch 2005), meanwhile, and the aquitard dispersion is assigned at 0.001. These input parameter values will be calibrated during model calibration.

1.2.6 Boundaries and Initial Conditions

Constant Head and Concentration Boundaries

The horizontal boundary of the study area is considered as the specified boundary. The upper and lower layers which are impermeable aquifers were set as no flow boundary. Based on the piezometric head of the five observation wells (Q40104T, Q409040M1, Q59804T, Q19904T, Q17704T), the head and concentration contours from 2000 to 2015 are mapped. Then, the head and concentration boundary conditions in time series are determined.

River Boundaries

The in-site surface water system has almost no direct connection to the Upper Pliocene (n_2^2) aquifer (Bui et al. 2014). The surface water only directly influences the unconfined Holocene aquifer (Bui et al. 2014). Although the vertical hydraulic conductivity values are very small, the shallow groundwater could penetrate through the aquitards that are quite thin elsewhere to the below-confined aquifers. Therefore, river boundary conditions should be assigned to simulate the most realistic natural

Table 1.4 River boundaries (DWRPIS, 2014)

No.	Parameters	Units	Layer 1
1	River stage elevation ^a	m	1.36–0.01
2	River bottom elevation ^b	m	28–2
3	River width	m	400–4000
4	Riverbed thickness	m	2–4
5	Conductance of river bed ^c	m ² /d	e ⁻⁵ –e ⁻⁴

^aabove mean sea level, ^bbelow mean sea level, ^cestimated by model

conditions in the study area. In addition, the Chloride concentration of 19,400 mg/L is assigned to the shoreline. The seawater might intrude on the n₂² aquifer by the recirculating flow mechanism near the coast (LaMoreaux et al. 2008). Values of river water level, bottom depth, river width have the same value as Table 1.4.

Recharge Boundaries

Although the in-situ recharge does not directly affect the n₂² aquifer, they are still assigned in the model to simulate the most realistic natural conditions in the study area. From 2000 to 2010, the recharge rates were inherited from the report of Assessment of the impact of groundwater abstraction and climate change on groundwater resources in Mekong Delta, Vietnam (Bui et al. 2014). They were estimated from 1999 to 2010 by using the Water and Energy Transfer between Soil, Plants, and Atmosphere under Quasi Steady State model (WETSPASS), in which groundwater recharge rate is a function of hydrometeorological data, including precipitation, potential evaporation, wind speed, temperature, groundwater depth, land use, slope, and topography and integrated into a single study on a regional scale. From 2011 to 2015, they are calculated as 15% of the average annual rainfall in each locality in the study area (Nguyen et al. 2015). The recharge rates are shown in Table 1.5.

Initial Conditions

The initial conditions are the head and concentration values of the first time step of the simulation model. The piezometric heads and Chloride concentrations of the observation wells in 2000 are used as the initial conditions for the groundwater flow model.

Table 1.5 Recharge rate (mm/year) at study area in 16 years (from 2000 to 2015)

n = 32	Provinces						
	Ca Mau	Bac Lieu	Soc Trang	Kien Giang	Can Tho	An Giang	Hau Giang
Min	2.70	2.60	3.00	1.50	0.40	0.50	0.40
Max	40.60	37.00	45.00	20.80	15.50	12.20	15.50
Average	16.71	15.68	18.19	9.12	5.78	4.01	5.78
SD	12.87	10.21	12.01	6.32	5.29	3.18	5.29

Table 1.6 Simulated Chloride concentrations at the wells by the steady state solute model

Number of wells	Residual mean (mg/L)	Standard error (mg/L)	Normalized root mean square (%)	Correlation coefficient
5	- 7.55	203.97	5.446	0.992

To simulate the groundwater flow model from 2000 to 2015, a total of 32 stress periods was used. Each season in a year corresponds to 1 time step.

1.2.7 Model Calibration

The model is calibrated using a trial and error method by adjusting the input hydrological parameters, mainly the hydraulic conductivity K and the sink/source rate before the re-run model. The sink/source rate was adjusted through the pumping package including pumping wells and injection wells. The location of these wells were located next to the observation wells for adjusting the calculated heads to fit the observed heads. This process is repeated until the calculated heads are fixed to observation heads. The model is calibrated for 5840 days (from 2000 to 2015) consisting of 32 stress periods and 182.5 days for each time step. The transient solute transport model calibration, however, could not be performed since the spatio-temporal Chloride data was not available. To validate the solute model, the steady solute transport model calibration was done before the fully-transient modelling. The results of Chloride concentrations at the wells by the steady state solute model showed in Table 1.6.

The flow model calibration results show that the Normalized Root Mean Square ranges from 1.426 to 3.550% at one time step, the Standard Error from 0.041 to 0.328 m, and the residual from - 0.580 to 0.244 m, and the correlation coefficient from 0.994 to 0.999 from 2000 to 2015 (Table 1.7). They indicated a good fit between the observed heads and calculated heads in the time steps. Figure 1.3 shows the observed and calculated heads versus time series and the calibrated model results of the dry season in 2015, which is the year to be used as the initial condition for the seawater intrusion simulation model for the next 16 years. For this study, due to the limitation of observation data, the model calibration was only performed in preliminary nature. Therefore, the model calibration should be rerun when the additional observed data are available in the future.

1.2.8 Sensitivity Analysis

To analyze the model sensitivity, the input parameters such as the hydraulic conductivity K , recharge rate, the head boundary were plus and minus 20% and 50% of

Table 1.7 Statistical index of flow model calibration

No.	Time steps (days)	Residual mean (m)	Standard error (m)	Normalized root mean square (%)	Correlation coefficient
1	182.5	- 0.580	0.041	1.916	0.999
2	365	- 0.530	0.096	3.758	0.997
3	547.5	0.043	0.101	3.550	0.996
4	730	0.090	0.067	2.639	0.999
5	912.5	- 0.032	0.090	2.708	0.997
6	1095	- 0.066	0.097	2.771	0.999
7	1277.5	0.155	0.139	4.033	0.994
8	1460	0.011	0.131	3.356	0.995
9	1642.5	- 0.126	0.092	2.652	0.998
10	1825	- 0.058	0.291	3.300	0.995
11	2007.5	- 0.105	0.328	3.537	0.995
12	2190	0.007	0.172	3.595	0.994
13	2372.5	- 0.001	0.168	3.445	0.995
14	2555	- 0.040	0.139	2.710	0.997
15	2737.5	- 0.007	0.172	3.337	0.995
16	2920	- 0.083	0.160	2.985	0.997
17	3102.5	- 0.055	0.184	2.792	0.997
18	3285	- 0.155	0.157	2.572	0.998
19	3467.5	- 0.156	0.170	2.901	0.997
20	3650	- 0.244	0.113	2.823	0.999
21	3832.5	- 0.145	0.167	3.103	0.996
22	4015	- 0.096	0.146	2.623	0.997
23	4197.5	- 0.082	0.163	2,653	0.997
24	4380	- 0.054	0.182	2.830	0.997
25	4562.5	- 0.071	0.171	2.863	0.996
26	4745	- 0.155	0.154	2.996	0.997
27	4927.5	- 0.127	0.158	2.656	0.998
28	5110	- 0.250	0.108	2.497	0.999
29	5292.5	- 0.174	0.173	2.859	0.997
30	5475	- 0.031	0.196	2.783	0.997
31	5657.5	- 0.110	0.198	2.852	0.997
32	5840	- 0.123	0.084	1.426	0.999

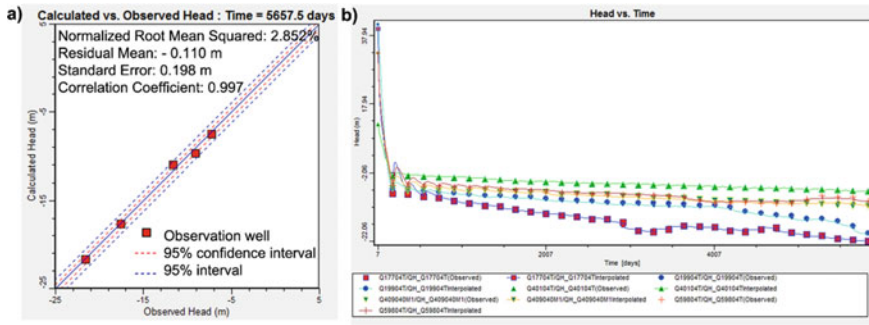


Fig. 1.3 Calibrated model results of dry season in 2015 (a) and observed and calculated heads versus time series (b)

the original value. Then, the model is re-run to analyze the head changes. They are shown in Table 1.8.

The results show that the hydraulic conductivity K and the head boundary have affected the calculated heads. Meanwhile, the recharge rate changed insignificantly to the calculated heads. This is reasonable because of a deep depth from -210 to -230 m of the n_2^2 aquifer. Hence, the sensitive inputs of the model are the hydraulic

Table 1.8 Changes of calculated head (m) of 2015 in sensitivity analysis processes

Observation well	Observed head (m)	- 50%	- 20%	20%	50%
		<i>Head boundary</i>			
Q17704T	- 21.60	- 13.90	- 18.57	- 24.81	- 29.48
Q19904T	- 17.55	- 9.38	- 14.36	- 20.99	- 25.97
Q40104T	- 7.21	- 1.91	- 5.34	- 9.90	- 13.33
Q409040M1	- 11.62	- 4.60	- 8.48	- 13.66	- 17.55
Q59804T	- 9.07	- 3.16	- 7.09	- 12.33	- 16.26
<i>Hydraulic conductivity</i>					
Q17704T	- 21.60	- 30.31	- 23.82	- 20.29	- 18.92
Q19904T	- 17.55	- 19.47	- 18.12	- 17.38	- 17.09
Q40104T	- 7.21	- 6.92	- 7.37	- 7.84	- 8.14
Q409040M1	- 11.62	- 13.03	- 11.54	- 10.80	- 10.59
Q59804T	- 9.07	- 9.81	- 9.71	- 9.75	- 9.85
<i>Recharge rate</i>					
Q17704T	- 21.60	- 21.69	- 21.69	- 21.69	- 21.69
Q19904T	- 17.55	- 17.68	- 17.68	- 17.68	- 17.68
Q40104T	- 7.21	- 7.62	- 7.62	- 7.62	- 7.62
Q409040M1	- 11.62	- 11.07	- 11.07	- 11.07	- 11.07
Q59804T	- 9.07	- 9.71	- 9.71	- 9.71	- 9.71

conductivity K and head boundary. It shows that future changes of these two factors will impact the flow pattern of this aquifer.

1.3 Results and Discussions

1.3.1 Results of Groundwater Flow Model

The groundwater flow model results are shown in Fig. 1.4. The results show that the Ca Mau Province had a low equipotential head (approximately 25 m below mean sea level). It tended to change insignificantly over time. In contrast, a part of Kien Giang, Can Tho, and Bac Lieu Provinces had a sharp decline in the equipotential head from above mean sea level in 2000 to 15 m below mean sea level in 2015 (Fig. 1.4).

Lines of 250 and 10,000 mg/L Chloride concentration are transferred to the map by the GIS (Geographic Information System) method. These lines were overlapped on one map to observe whether the displacement tends to narrow or widen over time. The Chloride value of 250 mg/L was chosen because this is the Vietnamese standard of freshwater. The value of 10,000 mg/L, which was shifted significantly in sixteen years, was chosen to show the converse trend in comparison to 250 mg/L-line.

The results show that the extent of seawater intrusion occurred very quickly. The iso-concentration line for Chloride 10,000 mg/L tends to gradually widen (Fig. 1.5) with a displacement of about 200 m/year. Particularly in Ca Mau Province, the freshwater area existed in 2000 but tended to narrow over time. According to Bui et al., 2014, in Ca Mau Province, the groundwater exploitation rate was higher than in other provinces. This explains the tendency to narrow the freshwater area in this area. By 2003, this freshwater area no longer existed. From 2003 onward, the 500 mg/L-line was shown instead in order to continue to observe the evolution of this brackish water zone. From 2000 to 2003, the iso-concentration line of Chloride 250 mg/L narrows about 400 m/year. In the following period from 2003 to 2015, the shift of the 500 mg/L-line is about 410 m/year.

1.3.2 Results of Simulation Model

The total groundwater withdrawals in 2015 are calculated based on the demand for water use for domestic, agricultural, and industrial purposes, from the report of Assessment of the impact of groundwater abstraction and climate change on groundwater resources in Mekong Delta, Vietnam (Bui et al. 2014). Specifically, the percentage increase due to water demand in the Upper Pliocene aquifer from 2010 to 2015 increased by about 52% in Bac Lieu, 83% in Can Tho, 39% in Kien Giang, 38% in Ca Mau, and 34% in An Giang Provinces (Table 1.9). Groundwater withdrawals in 2015 are updated in the model to forecast the extent of seawater intrusion for the next

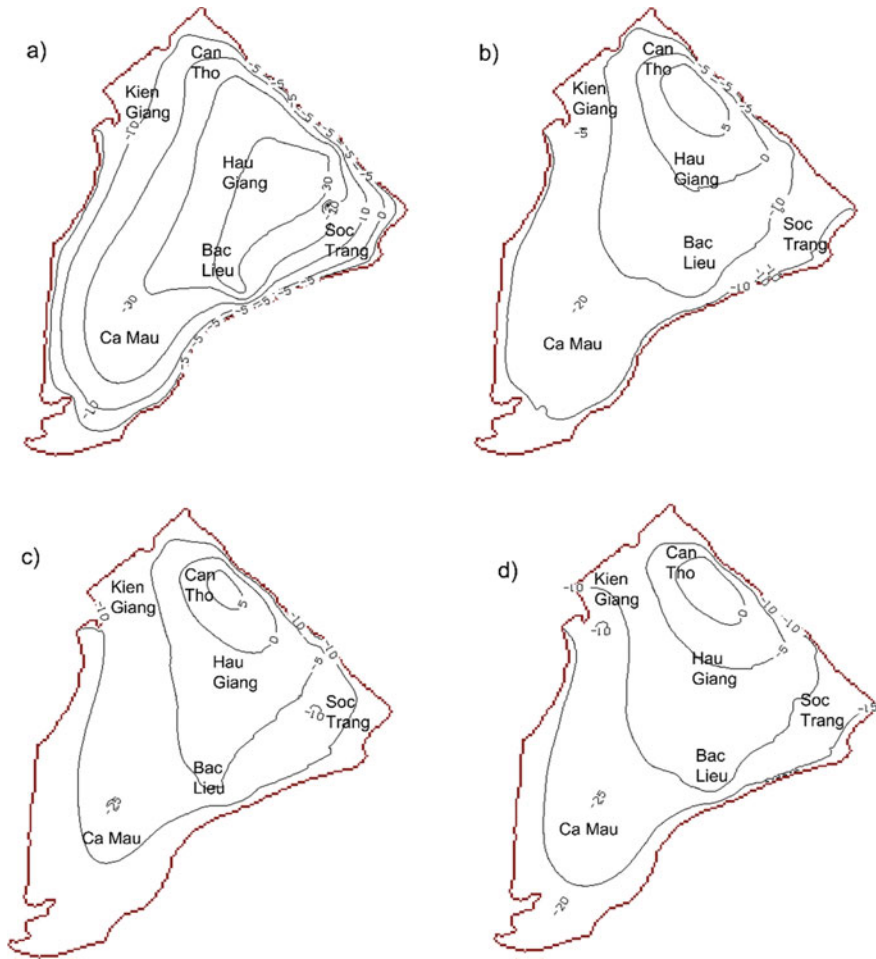


Fig. 1.4 Head equipotentials of the groundwater flow model in **a** 2000, **b** 2005, **c** 2010, and **d** 2015

16 years. For running the simulation model, all inputs presumed as the calibration model except for the initial conditions as the same as those in 2015. To follow the process of seawater intrusion over time, the forecast results for the time steps of the dry season in 2016, 2021, 2026, and 2031 are chosen to represent (Fig. 1.5).

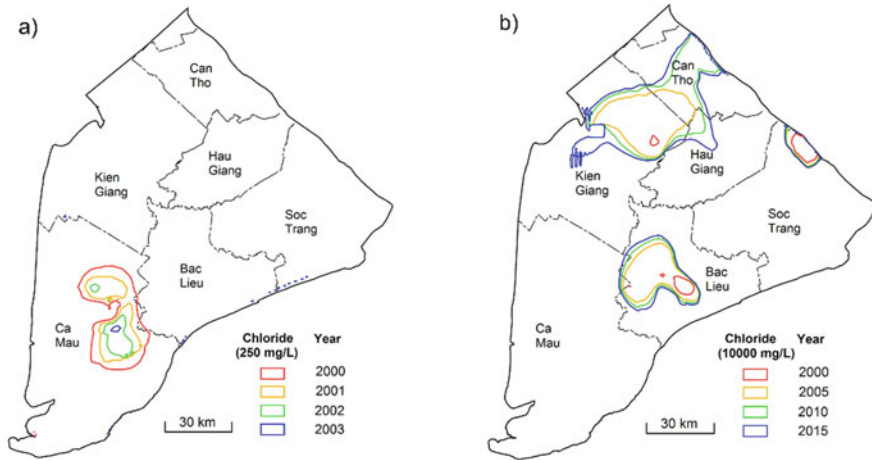


Fig. 1.5 Iso-concentration of Chloride of groundwater flow model

Table 1.9 Groundwater withdrawals in the Upper Pliocene aquifer (DWRPIS 2014)

No.	Province	Groundwater withdrawals		Increase (%)
		2010 ^a	2015 ^b	
1	Bac Lieu	12,397.73	18,967.81	52
2	Ca Mau	103,442.12	143,784.41	38
3	Can Tho	43,895.93	80,329.56	83
4	Kien Giang	7,835.32	10,890.54	38
5	An Giang	1,950.21	2,613.43	34
6	Soc Trang	0	–	–

^aFrom the report of assessment of the impact of groundwater abstraction and climate change on groundwater resources in Mekong Delta, Vietnam, ^bData estimated based on groundwater demand for domestic, agriculture, and industry

The forecast results show that freshwater (250 mg/L Chloride) might no longer exist by 2021. The line of 500 mg/L Chloride might also disappear and be replaced by the line of 2000 mg/L in 2031 (Fig. 1.5). Therefore, the 2000 mg/L-line was chosen to display the trend of seawater intrusion over time.

The seawater intrusion simulation model based only on the exploitation demand of 2015 has shown the narrowing of the freshwater area and extending the brackish water area. By 2031, only the line of 2000 mg/L will remain. Figure 1.6 shows the 2000 mg/L-line exported from the simulation model and overlapped in one map. From 2016 to 2031, the results show that an average displacement speed of 2000 mg/L-lines is 439 m/year. It can be predicted that the narrowing of the freshwater zone of the Upper Pliocene aquifer might be more quickly because of the increasing demand for water for economic and urban development (Fig. 1.7).

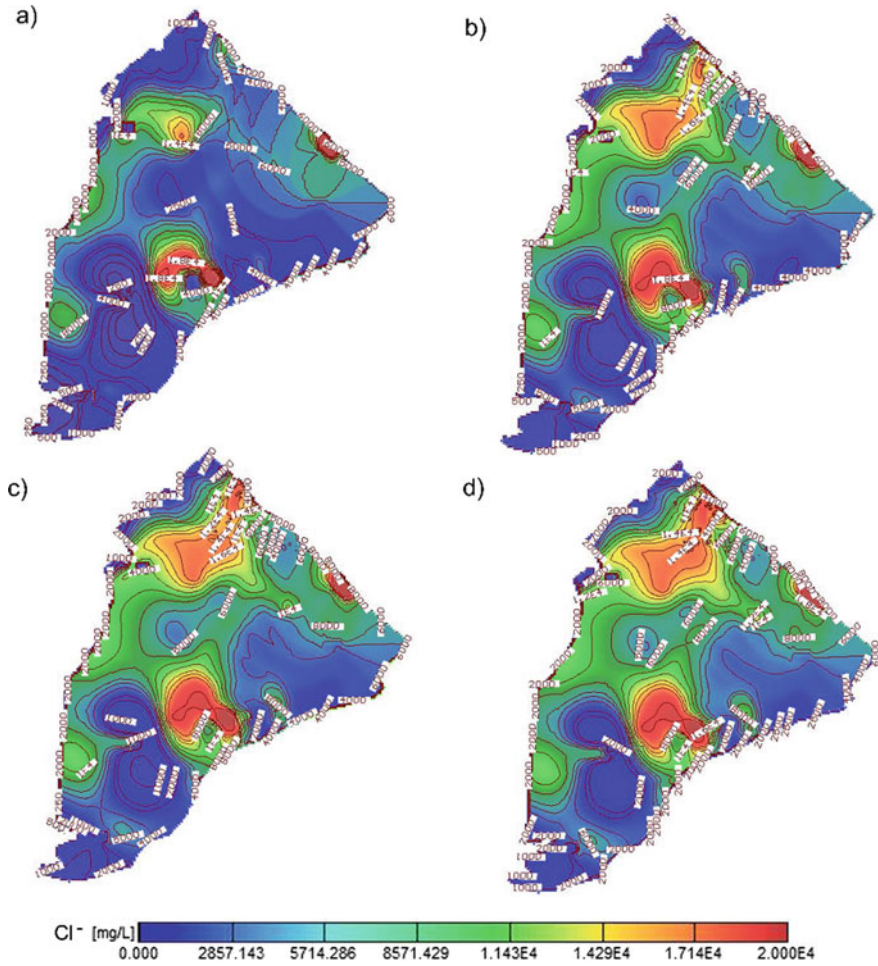


Fig. 1.6 Simulation model results of 2016 (a) 2021 (b) 2026 (c) and 2031 (d)

The results show that most of the Upper Pliocene aquifer in the study area might be saline. While the brackish water zone is expanding, the freshwater is narrowing from 2016 to 2031 in Bac Lieu, Can Tho, and Ca Mau Provinces where groundwater withdrawals are high (Table 1.7). In contrast, in the Soc Trang Province where groundwater withdrawals have concentrated mainly on the Middle Pleistocene aquifer (Bui et al. 2014), the situation salinity in the Upper Pliocene aquifer is better. Hence, this result is consistent with the demand and level of groundwater withdrawals in these areas (Table 1.9, Fig. 1.4).

This simulation model might change if groundwater withdrawals are updated. Therefore, in the future, when hydrogeological or groundwater extraction data are more detailed and accurate, this simulation result will also be updated.

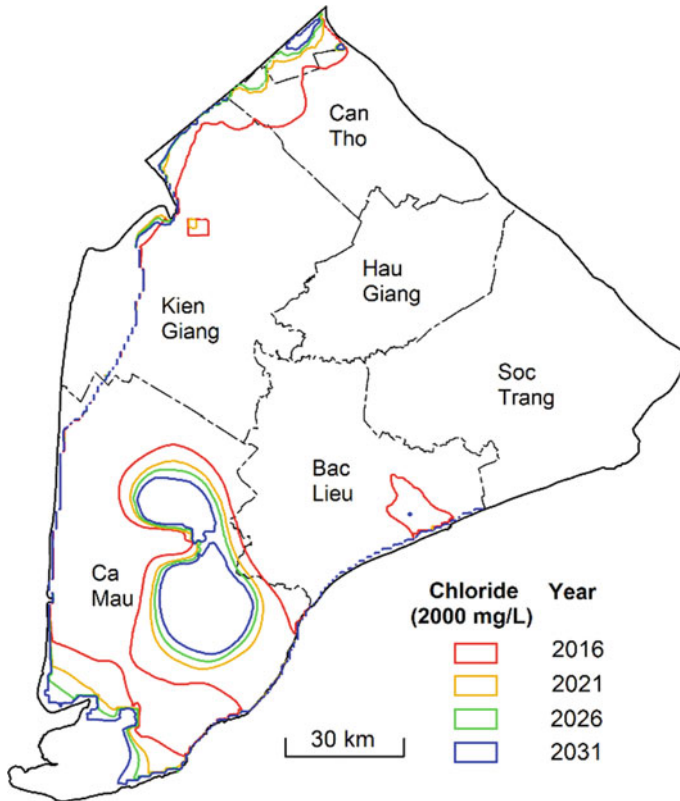


Fig. 1.7 Iso-concentration of Chloride of simulation model

Although the flow model was calibrated, there are still limitations such as the large grid size, the beach slope that has not been considered in the conceptual model, the influence of tides, etc. If groundwater level and Chloride data for the years from 2016 to 2021 have been available, it might verify the simulation model for these years. These issues are expected to be updated in future studies.

1.4 Conclusions

The results show that the extent of seawater intrusion in the Upper Pliocene aquifer takes place at a very fast rate. The simulation model shows that by 2021, the fresh-water area (250 mg/L of Chloride) no longer appears, the zone of 500 mg/l Chloride concentration will move towards the high groundwater withdrawals sites at the rate of 420 m/year. By the year 2031, the area with the 500 mg/L Chloride concentration will disappear, and instead, the area with the smallest Chloride concentration will

be 2000 mg/L. The area of freshwater areas is gradually shrinking. This situation is strongest in Ca Mau, Can Tho, and Bac Lieu province. With this situation, in the future, the level of seawater intrusion will become more and more serious if local authorities do not have effective management solutions. This research result is expected to contribute more valuable information for the local government in groundwater resources management.

Acknowledgements This research was supported by the KKU Scholarship for ASEAN and GMS Countries' Personnel for the academic year 2016, the Faculty of Technology Scholarship for the academic year 2016, and the Department of Geotechnology. The authors would like to thank the Division of Water Resources Planning and Investigation for the South of Vietnam (DWRPIS) staff for providing the observation data. The authors also would like to give a special thanks to the valuable comments and suggestions of editors, Dr. Dang An Tran, Dr. Phu Le Vo, and other reviewers for enhancing the research quality.

References

- Bui TV, Ngo DC, Le HN, Tran VB, Pham NL, Pham VH (2014) Assessment of impacts of groundwater abstraction and climate change on groundwater resources in Mekong delta, Vietnam. Division of Water Resources Planning and Investigation for the South of Vietnam, Vietnam, pp 13–22
- Climate central (2019). <https://coastal.climatecentral.org/map/>
- Dang TA (2020) Simulating rainfall IDF curve for flood warnings in the Ca Mau coastal area under the impacts of climate change. *Int J Clim Change Strat Manage* 12:705–715
- Dieulin A, Matheron G, de Marsily G (1981) Growth of the dispersion coefficient with the mean travelled distance in porous media. *Sci Total Environ* 21:319–328
- Eaton AD, Clesceri LS, Rice EW, Greenberg AE, Franson M (2005) Standard methods for the examination of water and wastewater. American Public Health Association, American Water Works Association, Water Environment Federation. Port City, Baltimore
- Guo W, Langevin CD (2002) User's guide to SEAWAT: a computer program for simulation of three-dimensional variable-density ground-water flow. In: *Techniques of water-resources investigations* 6-A7. U.S. Geological Survey, Tallahassee, Florida, pp 19–34
- Ho HD, Aranyossy JF, Louvat D, Hua MQ, Nguyen TV, Nguyen KC (1991) Environmental isotope study related to the origin, salinization and movement of groundwater in the Mekong Delta (Viet Nam). In: *Proceedings of a symposium, Vienna: isotope techniques in water resources development 1991*. IAEA in co-operation with UNESCO, pp 415–428
- LaMoreaux PE, LaMoreaux JW, Soliman MM, Memon BA, Assaad FA (2008) *Environmental hydrogeology*. CRC Press, New York, pp 109–114
- Le TTV, Lertsirivorakul R, Bui TV, Schulmeister MK (2020) An application of HFE-D for evaluating sea water intrusion in coastal aquifers of Southern Vietnam. *Groundwater* 58:1012–1022
- Nguyen CN, Ho VT, Trieu DH, Dang OH (2015) Using groundwater monitoring data to determine groundwater recharge of the Holocene aquifer in Hanoi city. *Vietnam Geotech J* 19:40–50
- Nguyen VK, Do TH (2008) Influence of paleogeographical conditions on chemical components of ground water in the Southern plain, Vietnam. In: *Annual Report of FY 2007, The Core University Program between Japan Society for the Promotion of Science (JSPS) and Vietnamese Academy of Science and Technology (VAST)*, pp 28–32
- Pham VH, Van Geer FC, Bui TV, Dubelaar W, Essink GHO (2019) Paleo-hydrogeological reconstruction of the fresh-saline groundwater distribution in the Vietnamese Mekong Delta since the late Pleistocene. *J Hydrol Reg Stud* 23:100594

- Schulze-Makuch D (2005) Longitudinal dispersivity data and implications for scaling behavior. *Ground Water* 43:443–456
- Tran DA, Maki T, Vo LP, Atsushi K, Doan TH (2014) Chemical characteristics of surface water and groundwater in coastal watershed, Mekong Delta, Vietnam. *Procedia Environ Sci* 20:712–721
- Tran TN, Vo LP, Vu VN, Ho HB (2019) Salt intrusion adaptation measures for sustainable agricultural development under climate change effects: a case of Ca Mau Peninsula, Vietnam. *Clim Risk Manage* 23:88–100
- Vu D, Yamada T, Ishidaira H (2018) Assessing the impact of sea level rise due to climate change on seawater intrusion in Mekong Delta, Vietnam. *Water Sci Technol* 77:1632–1639

Chapter 2

Seawater Intrusion Processes Along the Tien River Mouth in the Period 2000–2020



Thuc Thi Bich Pham, Vu Truong Nguyen, Binh Thanh Pham, Hieu Duc Tran, Man Ba Duong, Thu Thi Mong Ngo, Tran Duc Mai, and Quan Minh Pham

Abstract Seawater intrusion is a severe issue and is a main cause of serious fresh-water scarcity during the dry season in the Mekong Delta. Insights into seawater intrusion processes and its controlling factors are needed to adaptation strategies. In this paper, we use long-term salinity observation data and hydraulic modelling to simulate the salinization processes (spatial–temporal salinity distribution and concentration) in the context of changes in upstream discharge and tidal regimes over 20 years. The seawater intrusion model is based on DHI MIKE 11 software which is an one-dimensional equations of continuity, momentum conservation and transport in natural waters. In addition, longitudinal simulations along the Tien River mouth illustrate different hydrodynamic conditions of the river, help reproduce the observable salinity trends and contribute to a better understanding of this natural phenomenon. The Mike 11 model allows a quick assessment of saline intrusion in the Tien River mouth to predict a 4‰ salty border for agricultural production and a 0.3‰ salty border for domestic water exploitation for irrigation systems in Ben Tre to help ensure the plan to use water for production and daily life in the dry season 10 days in advance.

Keywords Tien River mouth · Saline intrusion · Mike 11 model

T. T. B. Pham (✉) · V. T. Nguyen · B. T. Pham · H. D. Tran · Q. M. Pham
Institute of Mechanics and Applied Informatics, Vietnam Academy of Science and Technology (VAST), Ho Chi Minh City, Vietnam
e-mail: ptbthuc@iami.vast.vn

M. B. Duong
Ho Chi Minh City Institute of Resources Geography, Vietnam Academy of Science and Technology (VAST), Ho Chi Minh City, Vietnam

T. T. M. Ngo
Nguyen Huu Huan High School, 11 Doan Ket Street, Binh Tho Ward, Thu Duc, Ho Chi Minh City, Vietnam

T. D. Mai
Dai Phat Construction Design and Design Company Limited, 268 Apartment, Linh Trung Ward, Thu Duc, Ho Chi Minh City, Vietnam

2.1 Introduction

Water resources are essential for the development of human society. This development, mainly in the industrial and agricultural sectors, increasingly affects other resources on multiple levels. Water shortage is considered as a limiting factor for the socio-economic development of an area. The main objective is to make companies to establish sustainable management policies and rules for managing water resources to ensure their permanence (Sam et al. 2006). The water source of Tien River mouth in the dry season is very unstable, causing random import along the river depends on each year and the amount of fresh water from Mekong River. The result of the process of river-sea interaction is that it provides low salinity, high salinity and affects the process of exploiting fresh water in the river mouth for agriculture and daily life. Typically, in the dry season of 2020, the salinity limit of 4 g/l in February 2020 on Ham Luong River is 75 km, Tieu Estuary and Dai Estuary rivers are 55 km, Co Chien is 68 km, Hau River is 66 km (Southern Institute of Irrigation Science). Also in February, the salinity measured at My Hoa on the Ham Luong River, 48 km from the river mouth, reached 14.5 g/l (February 14, 2020). Early and deep salinity intrusion has caused the largest freshwater reservoir in the West at Ba Tri-Ben Tre to be contaminated with 2 g/l of salinity. As a result of this drought, millions of people in Ben Tre lack fresh water for daily life and production.

Tien River mouth is a shallow estuary with many creeks flowing into the East Sea, including Tieu, Dai, Ba Lai, Ham Luong, Co Chien, Cung Hau estuaries, in which Ba Lai estuary has been degraded and prevented by saline sluices to remove salinity. The boundary of Tien River mouth is determined from My Thuan station 87 km from the sea (Legates and McCabe 1999; Perillo 1995). The salinity of the Tien River mouth varies from 0 to 31.5‰, along the length of the estuary. Salinity varies from year to year, depending on the freshwater flow in the main river. The typical tidal regime is an irregular semi-diurnal tide, with two peaks and two low tides in a day. Tidal amplitude ranges from 2 to 4 m. The low tide season can affect Tan Chau, which is 197 km from the sea.

The monitoring of salinity distribution along the main river in the Mekong estuary has been started since 1994. All salinity measuring stations are set up on the salinity evolution along the river according to their own installation criteria and not based on the calculation of the salinity dispersion along the river by hydrodynamics and river morphology. However, the monitoring process is in batches during the dry season, and there are limitations in terms of salinity measurement locations. In the current context that managers want to quickly estimate the evolution of salinity distribution along the estuary, one-dimensional mathematical models are suitable tools because they are easy to use and suitable for the management context. In addition, it is also a simple methodology to start approaching the approximate assessment of saline intrusion in the study area.

In this paper, we study the spatial and temporal variation of salinity distribution in the Tien estuary based on monitoring data of stations along the estuaries and detailed calculations according to cross-sections on the Mike 11 model calculation network. Firstly, simulation of the hydrodynamic regime of the river has been performed. Vital databases were used, including river morphology, friction factors, river flow and river level. These data were used to calibrate the hydrodynamic model, which was later linked to the AD modulus. The output of the AD modulus is the evolution of salts from upstream to downstream of the estuary under different hydrodynamic conditions. The model allows to estimate salinity changes even in areas where we do not need to measure in actual area. It also allows to plot isoline chart (areas of equal salinity) for a typical salinity.

2.2 Data and Research Methods

2.2.1 *Measuring Station Data*

Tien river mouth area and measuring stations along the river mouth Fig. 2.1. Ben Tre province is located entirely in the Tien River mouth, so the fluctuation of salinity along the estuary directly affects the exploitation of water resources for domestic service, agriculture and industry of the province. Irrigation system is divided into two, North Ben Tre sub-region (Thuong Ba Lai, Giong Trom-Ba Tri Irrigation system, Ba Tri coastal area, Binh Dai coastal area, Binh Dai), South Ben Tre sub-region (Irrigation Zone Tay Cho Lach, Cho Lach-Mo Cay, Mo Cay-Thanh Phu, coastal area of Thanh Phu). These irrigation systems ensure 75% of the cultivated area, 82% of domestic water for rural areas, and improve logistics for fishing, and effectively prevent natural disasters in coastal areas. The production model of these irrigation zones includes the model of aquaculture, giant tiger prawn, *litopenaeus vannamei*, wild shrimp, shuchhi catfish, water rotation model of Shrimp-Rice (Binh Dai and Thanh Phu), Crayfish model on rice field (Thuong Binh Dai, Ba Tri, Thanh Phu in tidal and river dynamical transition zones), 3-Crop rice model (Winter-Spring I-IV, Summer-Autumn V-IX, Autumn-Winter IX-XII), two rice crops and one crop located in the freshwater area, raising shrimp and fish in garden ditches (Tay Cho Lach, Cho Lach-Mo Cay, Thuong Ba Lai, Thuong Mo Cay-Thanh Phu, river water predominates). However, freshwater systems have not been closed, so the years of deep and prolonged intrusion caused damage to production and people's lives. In the dry season 2015–2016, saltwater intrusion covered 162/164 communes and wards of Ben Tre province, causing damage to agricultural production about 1794 billion VND.

The stations are made to measure the water level, salinity along the river. Measuring the water level 24 times a year all year round, measuring salinity in batches in the dry season from February to July, recently measured in January-VI, measuring level 12 times/day, 3–4 times/month, each 3 days. Manual method of

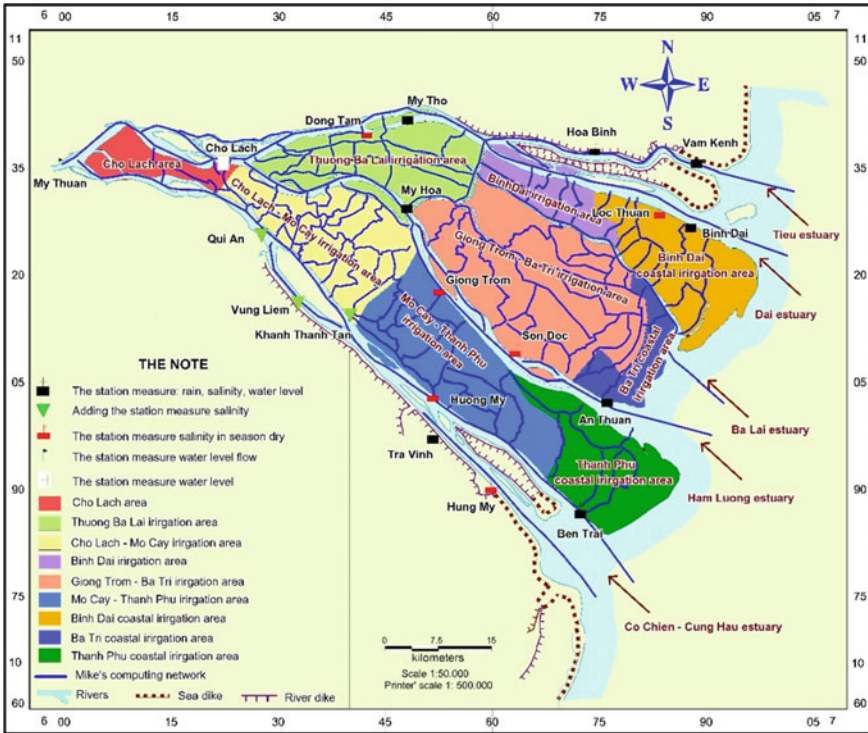


Fig. 2.1 Calculation diagram of Tien River mouth study area—Mekong Delta

measuring salinity was taken at 03 layers, the surface layer is 0.2 h, the middle layer is 0.5 h, the bottom layer is 0.8 h.

- The most recent model used for river systems in the Mekong Delta is MIKE 11 (DHI, 2007) which has been developed and updated over the decades by various organizations based on previous models and data. Organizations involved in model development, tributary updates and the cross-sections and model corrections include the Mekong River Commission (MRC), Southern Institute of Water Resources Science (SIWRR) and Thuyloi University (TLU). To simulate the problem of saline intrusion in the Mekong Delta, the model uses the MIKE 11 HD hydrodynamic module to calculate the water level and flow and the MIKE 11 AD convection diffusion module to calculate the salinity level in the river system.
- The MIKE 11 HD hydrodynamics module solves the Saint Venant equations including the equation of continuity (2.1) and the equation of momentum (2.2) (DHI, 2007):

$$\frac{\partial A}{\partial t} + \frac{\partial Q}{\partial x} = q \tag{2.1}$$

$$\frac{\partial Q}{\partial t} + \frac{\partial}{\partial x} \left(\varphi \frac{Q^2}{A} \right) + gA \frac{\partial Z}{\partial x} + g \frac{Q|Q|}{C^2 AR} = 0 \quad (2.2)$$

where t is the time, x is the distance along the river, Q is the flow, Z is the water level, A is the cross-sectional area, R is the hydraulic radius, C is the Chezy roughness coefficient, q is the flow mass per unit length, g is the acceleration due to gravity, and α is the kinetic energy correction factor.

The MIKE 11 AD convection diffusion module solves the conservation of mass Eq. (2.3) to estimate the salt concentration (DHI, 2007)

$$\frac{\partial AC}{\partial t} + \frac{\partial QC}{\partial x} - \frac{\partial}{\partial x} \left(AD \frac{\partial C}{\partial x} \right) = -AKC + C_s q \quad (2.3)$$

where C is the salt concentration, C_s is the source/sink amount of the salt concentration, K is the zero possible linear decay coefficient for salinity, and D is the diffusion coefficient.

Calculation diagram for simulation of salinity in the Tien estuary model calibration and verification are as follows: The upstream boundary is calculated from My Thuan station in Vinh Long province, the downstream boundary uses saline and water level stations to serve simulations of Vam Kenh, Loc Thuan, An Thuan, and Ben Trai. The stations used to calibrate and inspect models Son Doc, Hoa Binh, My Tho, Dong Tam, My Hoa, Giong Trom, Huong My, Khanh Thanh Tan, Vung Liem.

The calibration parameter is the roughness of the Manning coefficient. Initial values of the Manning roughness varied according to the approach studied, with mean values of 0.02–0.027. In the calibration procedure, the Manning coefficient is modified to the same extent along the study range because we assume that the sources of error associated with its evaluation are the same for all grids. Calibration and validation were performed using water level data at Cho Lach station, My Hoa, My Tho Hoa Binh. The time period selected for calibration is from January 1, 2016 to June 30, 2016. Figures 2.2 and 2.3 show the results of the calibration. This figure shows a good correspondence between the calculated water level and the observed water level at the station.

In addition, the model performance was checked by statistical indicators: root mean square error (RMSE), Nash–Sutcliffe model efficiency index (NSC) and correlation coefficient (R2). The equations used to determine these indices are available in Sanchez (1992). RMSE indicates a perfect combination between observed and predicted values when it is zero. NSC ranges from $-\infty$ to 1. It indicates a perfect combination between observed and predicted values when it equals 1. Values between 0 and 1 are generally considered to be an acceptable level of performance (Zhang et al. 2015).

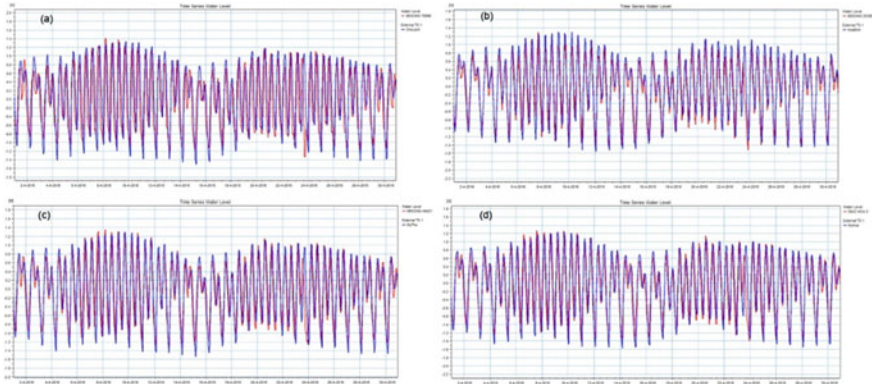


Fig. 2.2 Test results of water level between calculation and actual measurement in which **a** Cho Lach, **b** Hoa Binh, **c** My Tho, **d** My Hoa

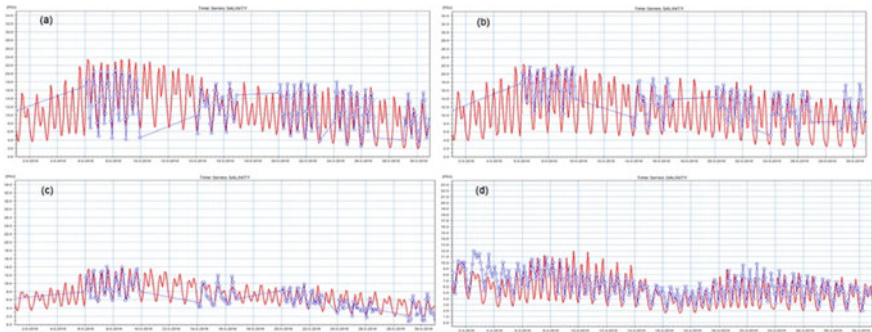


Fig. 2.3 Salinity simulation results and actual measurements in which **a** Vam Kenh, **b** Binh Dai, **c** Son Doc, **d** Hoa Binh

2.3 Results and Discussion

(a) Maximum Salinity in Dry Season

Figure 2.4 shows the maximum salinity at the measuring stations in the period 1994–2020 according to the distance from the sea estuary to the river estuary. The lowest salinity is in 2014 and the highest is in 2020. The station area which is 4–7.8 km from the sea, the salinity is always high from 20 to 32‰, the stations along the river which are 10–28 km from the sea, the salinity fluctuates greatly from 3 to 27‰. The area which is 45–63 km from the sea, the level ranges from 1 to 14‰. The change of salinity peaks in areas along the main river ranges from 10 to 28 km each year depending on the freshwater flow in the main river. However, according to the salinity data of stations along the river, we divide the Tien River mouth by region based on salinity according to the Venice system (Ippen and Harleman 1961;

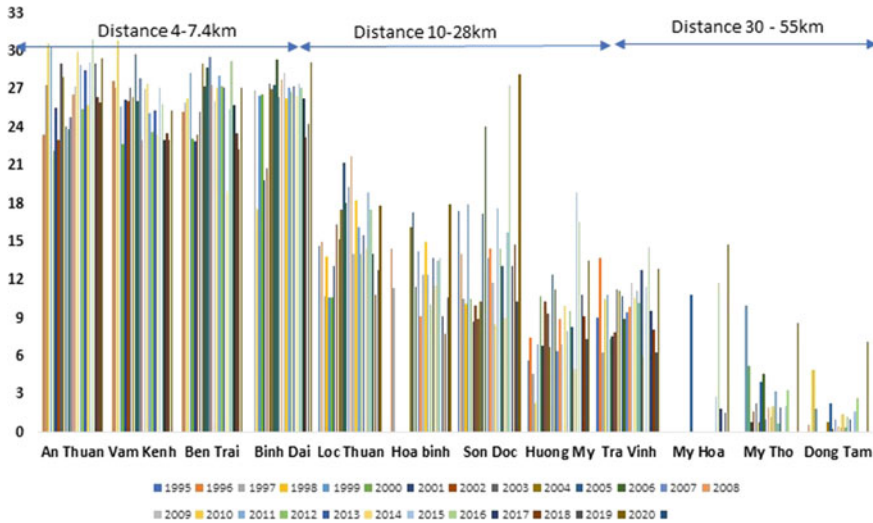


Fig. 2.4 Highest salinity value at measuring stations along the river in the period 1994–2020

Venice System 1958) as follows: the station area which is less than 10 km-distance-from-the-sea is the saltwater tidal area, stations which are 10–20 km from the sea is brackish tide area (tidal dynamics always prevail), distance from 20 to 28 km is brackish tide, 28–37 km is brackish tidal area (tidal and river dynamics transition zone, tidal predominates), 37–45 km is brackish tidal zone (transition zone between tidal dynamics and river flow but river flow predominates), 45–63 km is freshwater tide (dominant river dynamics region).

(b) Evaluation of Salinity Along the River in the Dry Season

Evaluation of salinity changes over time from measuring stations along the river showed that there were years of high salinity going deep into the estuary, and low salinity for the transitional area between the tide and the headspring flow. For general purposes, we choose 03 years for analysis 2005, 2016, 2017. The year 2005 is the highest salinity year in the period when there have not been much changes according to the freshwater flow from the Mekong River to the Mekong Delta., in 2016 the highest salinity in the period (2006–2016), 2017 in low salinity represents significant changes in hydropower dams upstream of Mekong coming into operation. The process of salinity evolution in the dry season from January to June is presented in Fig. 2.5a–c. In 2005, 2016–2017 in the dominant tidal area, the salinity did not change, the dominant tidal dynamic transition zone had a great change in salinity, specifically at Son station, the highest salinity in 2005 was 24.0‰, 2016 is 27.4‰, in 2017 it is 13.7‰, Hoa Binh 18‰, 15‰, 9‰, Tra Vinh 10.8‰, 14‰, 9.6‰. The area of fresh tide and river flow dominates at My Hoa station 10.9‰, 11.8‰, 1.6‰, My Tho 4.6‰, 3.4‰, 0‰, Khanh Thanh Tan 8.7‰, 2.6‰. The salinity variation at the stations changes due to the interaction between river currents and tides. In terms

of flow amplitude upstream of Tien station My Thuan estuary, Fig. 2.6a, b show the flow amplitude tends to increase. In three years, choose to analyze and arrange in ascending order 2005, 2016, 2017, however, in terms of average day there is a change in the order of 2016, 2005, 2017 which explains why in 2016 salinity is larger than in 2005 and 2017.

The flow with a positive value indicates the upstream current flowing towards the sea at low tide and vice versa at high tide. Figure 2.6a show the flow amplitude gradually increases for the time it shows signs of tidal action which tends to increase in the Tien River estuary. Therefore, according to the salinity monitoring data of stations along the river mouth, Ham Luong estuary has a stronger interaction than other estuaries based on the salinity of My Hoa and Son Doc stations, in 2016 the highest salinity at My Hoa station was 11.8‰, Son Doc 27.4‰, in 2017 My Hoa decreased by 86–1.6‰, Son Doc decreased by 50–13.7‰. Stations at Co Chien and Estuary Tieu decrease by 30–70% depending on the location away from the sea. Thus, for Ham Luong estuary, when the headspring water is reduced in salinity, it will be pushed up higher than that of other estuaries, causing difficulties in water resource management in the dry season for the year when the salinity is high.

(c) Salinity Along Hydrologic Depths

Saline intrusion is generally divided into three categories according to the degree of stratification (Nguyen Sinh Huy 2010; Cameron and Pritchard 1963) including saline wedge, partial disturbance and total disturbance. Saline wedges form when the amount of fresh water flowing into the estuary is greater than the tidal flow. Partial turbulence is a strong freshwater current that lies above the salty tidal current. When the high tide forces the upper freshwater current, the salinity layer increases with the water flow to the sea. Estuary total disturbance occurs when the flow in the river is small, tidal flow plays a major role in the water cycle in the estuary. The result of this process is uniform salinity at all depths in the river. This classification is determined through the classification of *Ne* (Kettab 2014). Considering the salinity monitoring data according to the depth along the Tien River estuary, the results of salinity layers measurement data collected are very few, mainly collected at Ham Luong estuary, the other estuaries are only available in 2015. Therefore, 2015 was used to analyze and evaluate the distribution of salinity according to the depth of the Tien River mouth. Figure 2.7a–c show the salinity along the depth of the measuring stations Tieu, Ham Luong and Co Chien estuaries, symbols D: bottom salinity 0.8 h, G: salinity depth 0.5 h, M: salinity salinity on the water surface at a depth of 0.2 h.

Tieu Estuary has the uniform disturbance in the area 4–18 km from the sea, My Tho has a difference in salinity between layers, but it is not significant, ranging from 0.2 to 0.6‰.

Ham Luong estuary has a difference in salinity between layers, but it is not significant, ranging from 0.3 to 1‰, in the area 20–37 km from the sea, there is almost no difference in salinity between layers, My Hoa station which is far from the sea 45km has the difference between layers 0.5‰.

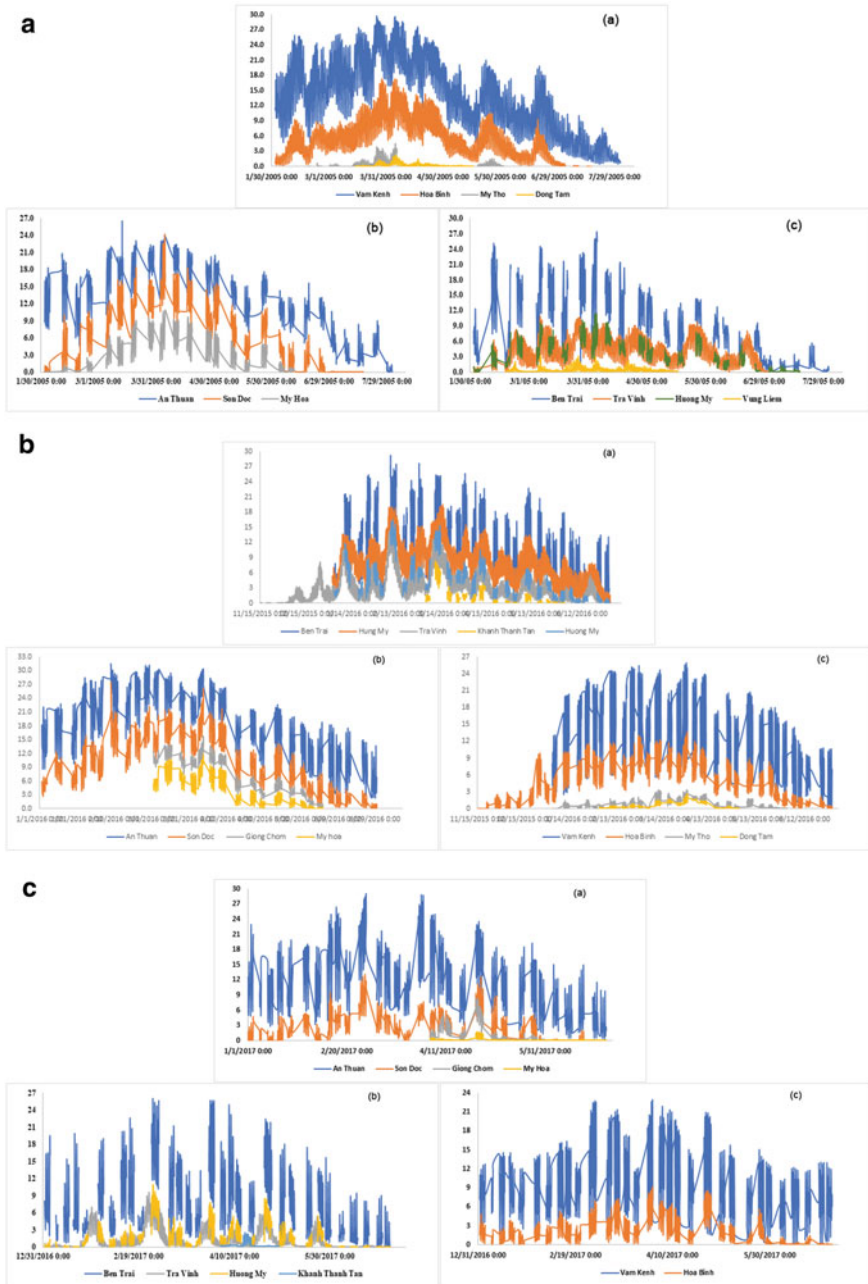


Fig. 2.5 a Salinity evolution along the Tien River estuary in 2005 in which (a) Cua Tieu, (b) Ham Luong, (c) Co Chien. b Salinity evolution along the Tien River in 2016 in which (a) Co Chien, (b) Ham Luong, (c) Cua Tieu. c Salinity evolution along the Tien River estuary in 2017 in which (a) Ham Luong, (b) Co Chien, (c) Cua Tieu

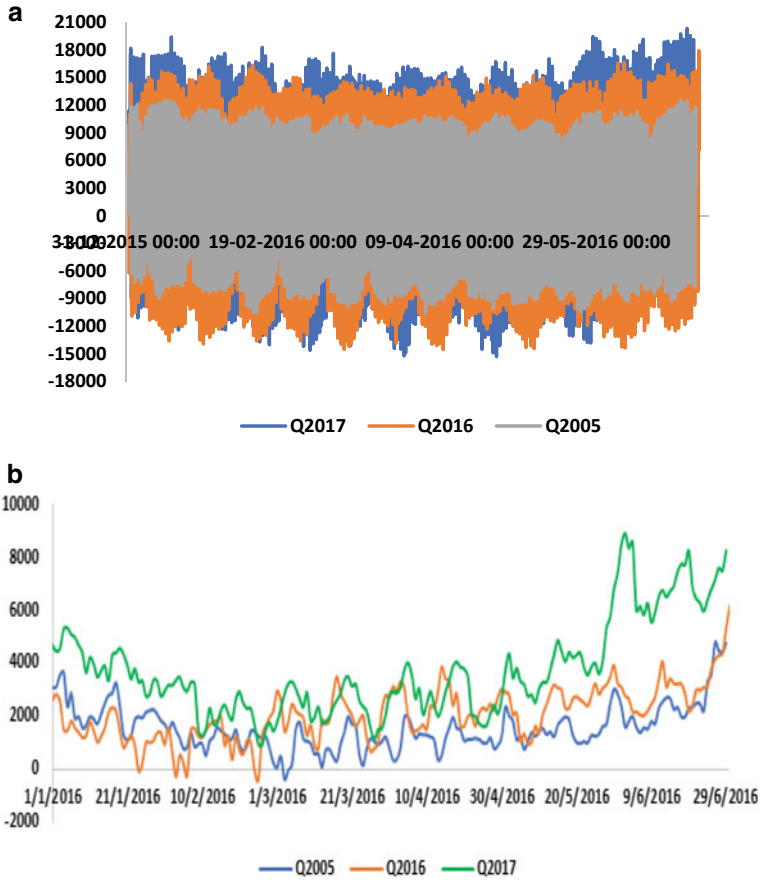


Fig. 2.6 a Flow volume in dry season at My Thuan in dry season 2005, 2016, 2017, b average daily flow in dry season of My Thuan station

The difference between layers of Co Chien estuary is 0.4‰ at Ben Trai, Huong My, and Khanh Thanh Tan stations at 0.2‰.

Because the salinity difference between layers according to the depth from 0.2 to 1‰ is small, if only based on the salinity measured value according to the depth, it is possible to classify the Tien River mouth in the estuary area with uniform disturbance and dominant tidal flow. However, the distribution of salinity in the estuary depends on the hydrodynamic regime of the estuary, where the estuary morphology plays a decisive role. Therefore, to evaluate more accurately the 2D-3D model because the 1D model cannot simulate the stratified salinity by degrees.

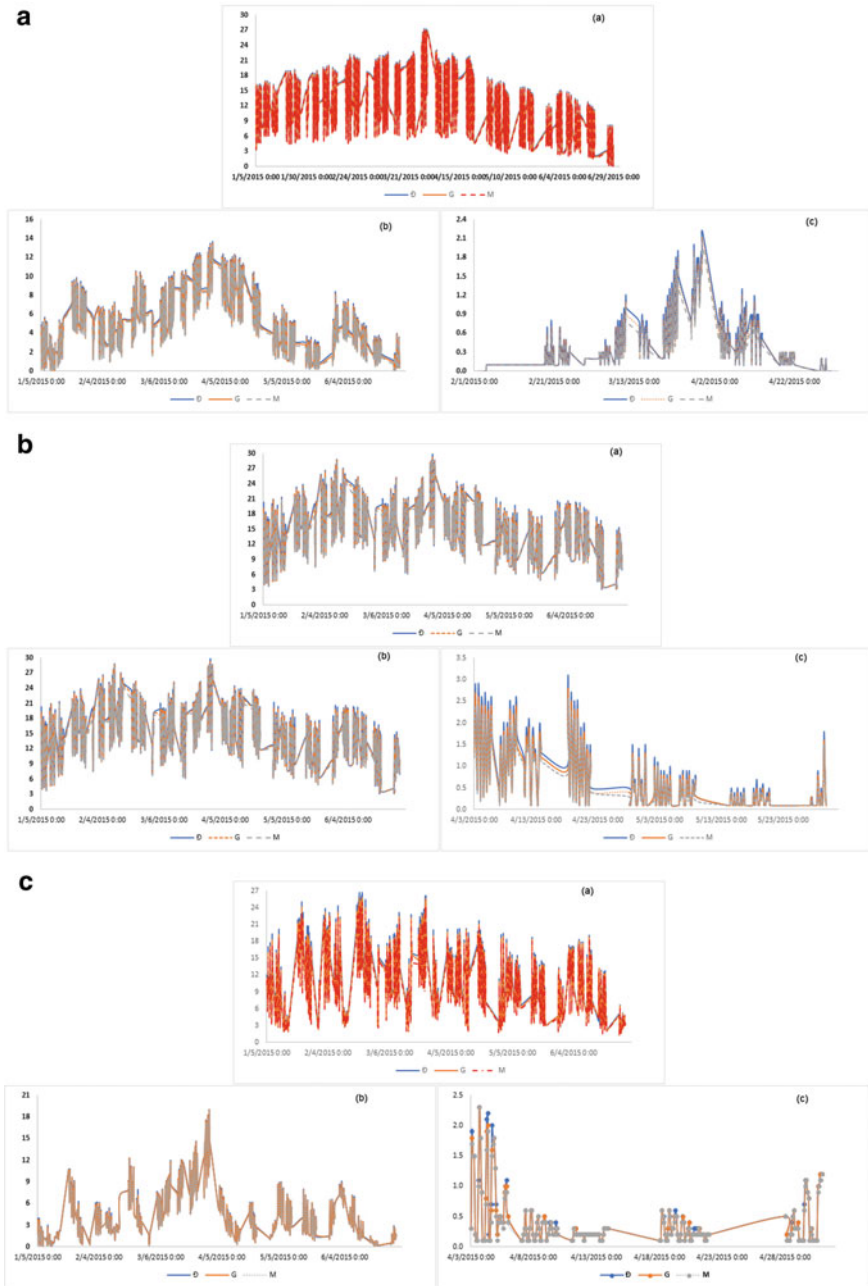


Fig. 2.7 a Distribution of salinity by depth of stations along Estuary Tieu River 2015 in which (a) Vam Kenh, (b) Hoa Binh, (c) My Tho. **b** Salinity evolution along Ham Luong River in 2015 in which (a) An Thuan, (b) Son Doc, (c) My Hoa. **c** Salinity evolution by depth along the Co Chien River in 2015 in which (a) Ben Trai, (b) Huang My, (c) Khanh Thanh Tan

2.4 Evolution of Water Level and Salinity

To study the variation of salinity over a 24-h period, March 28, 2016 was selected as the date of the highest salinity at measuring stations along Tieu estuary and Ham Luong estuary. Measuring mode 12 op/day Fig. 2.8. The blue line represents the water fluctuation at stations along the river, the orange line the salinity variation along the river as determined by the measuring stations. Salinity varies with the rhythm of the sinusoidal tidal water level. Salinity fluctuates in Ben Trai with the highest 24‰, the smallest 10.7‰ falling at highest tide and lowest tide.

Considering the fluctuation of water level at stations along the river, the Tieu estuary branch, the water level and salinity at the measuring stations show that the higher the upstream, the higher the peak and the low tide are compared to the downstream stations due to the participation of currents in the river. River. Salinity changes at stations along the river are opposite, salinity decreases sharply when moving upstream. Thus, the water level of measuring stations along the estuary which is influenced by tide is directive by astronomical factors, while the distribution of salinity along the main river upstream is determined by the flow of freshwater and velocity. Evaluation of salinity change on the day when the salinity peaked in the dry season in 2016 showed that: Co Chien estuary used salinity at Ben Trai as a landmark; at Hung My station 12 km away, the salinity decreased by 34; and Huong My at 20 km away, the salinity decreased by 69%; Tra Vinh 23 km away decreased

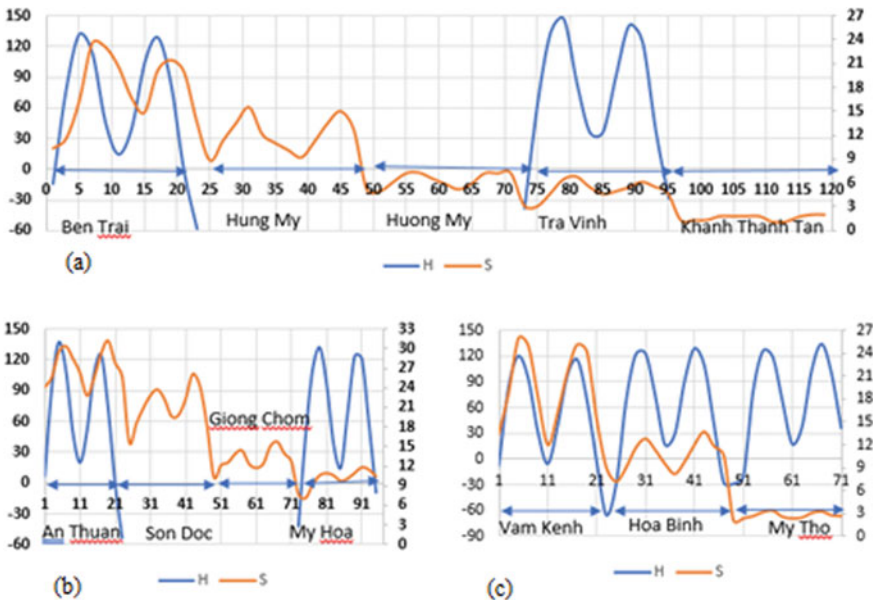


Fig. 2.8 Salinity evolution along Tien River mouths on March 28, 2016 in which **a** Co Chien, **b** Ham Luong, **c** Cua Tieu

71%; Khanh Thanh Tan 34.5 km away, salinity decreased 91.2%. Ham Luong branch takes An Thuan station as a landmark, 5.29 km from the sea, the highest salinity of the day is 31.2‰, Son Doc station 15 km away, the salinity decreases by 16%, Giong Trom station 31.7 km away, the salinity decreases by 49%, the My Hoa station 42 km away salinity decreased by 62%. Tieu Estuary and Vam Kenh branches 4.1 km from the sea, the highest salinity of the day is 25.9‰, at Hoa Binh station 17.8 km away salinity reduced by 47%, My Tho station 50 km away salinity decreased by 87%. Based on the salinity reduction process along the main river, it can be seen that the flow determines the salinity along the river. Co Chien receives more fresh water, 2‰ is the highest salty border of the day, located 40 km from the sea, Tieu estuary receives the smallest 3.4‰ at 55 km away. Particularly in Ham Luong, the amount of fresh water accounting for 16% is larger than that of Tieu estuary, but in My Hoa, 47 km from the sea, the maximum salinity reaches 11.8‰, 3.47 times higher than My Tho station, 5.9 times higher than Khanh Thanh Tan station. On the other hand, at the inlet of An Thuan, the salinity is 31.2‰, higher than the other two estuaries 5.9–7.6‰, so the salinity is pushed higher and deeper than these. Thus, the saline tide at Ham Luong River is stronger than the other one due to the different morphology of this estuary. Therefore, the Ham Luong estuary is very sensitive to the amount of fresh water flowing from upstream. In years with smaller amount of fresh water, the higher the salinity, the deeper the saltwater intrusion. In years with larger amount of fresh water, the salinity decrease more sharply than other rivers belong to Tien River mouth.

2.5 Simulation Results from Model Number 1D

The year 2016 was chosen to simulate in mile 11 because this is a year of high salinity, the flow at the beginning of the dry season has decreased sharply due to the operation of the upstream reservoirs of the Mekong. Figure 2.9 shows the results of the highest salinity intrusion in the dry season 2016. The salinity limit for agriculture is 4‰ (Legates and McCabe 1999) from Ham Luong estuary to Cho Lach. Co Chien estuary climb 4‰ salty border beyond Vung Liem-Vinh Long, and Tieu estuary climb about 50 km from the sea. The saline boundary exploits domestic water when the salinity in rivers and canals is less than 0.3‰, beyond Cho Lach, Cuu Tieu River, Quoi An river, Co Chien River. 2016 is the year causing great damage to water supply for the winter-spring crop of people in the Tien river mouth because the winter-spring crop lasts from January to April. Model of Dong Xuan Rice, Shrimp Rice belong to Mo Cay-Thanh Phu, Giong Trom-Ba Tri, Binh Dai irrigation zones in the transition zone between tidal dynamics and river flow. When tidal currents dominate, high saline water at the time of sowing will not be enough for agricultural production because these irrigation systems have not been closed. Therefore, when the salinity in the main river increases, it will go into the canal system of Ben Tre province, causing damage to agricultural production or daily life. Irrigation systems in brackish and fresh brackish water in the Ham Luong estuary are at higher risk of

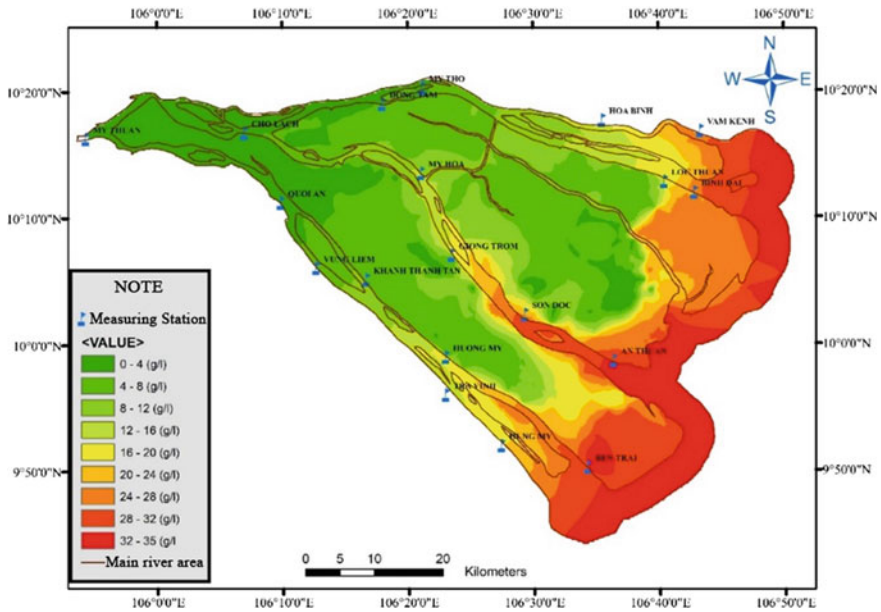


Fig. 2.9 Simulation results of saline intrusion along Tien estuary in dry season 2016

saline intrusion than in Giong Trom-Ba Tri, the downstream of Thuong Ba Lai, Mo Cay-Thanh Phu. Currently, the ability to predict the salinity of the model is done in a short time of 10 days. Actively storing water or operating irrigation works in agricultural production areas can be done soon, but the water demand for agriculture is great, so when there is saline intrusion in the river during the prolonged time cannot avoid damage. Freshwater areas such as Thuong Ba Lai, Nam Cho Lach, Cho Lach will be affected by saline intrusion when the salinity in the main river increases and penetrates deep upstream. Predicting the salinity in advance in the river is a necessity to prepare water sources for production and daily life. Therefore, the fastest way to know changes in salinity in the main river in the dry season is to use a one-dimensional model like Mike 11.

2.6 Conclusion

The purpose of this study is to learn about the mechanism of saltwater intrusion in the Tien estuary in space and time, its dependence on the hydrodynamic regime of the estuary using the Mike 11 model and actual measured data along the estuary stations of the Tien River. Measuring stations are carried out for many years during the dry season from January to June every year. However, the salinity measurement in the dry season is not continuous for a month, only 3–4 times at high tide and low

tide. Through the analysis, it was found that the tides and the amount of fresh water in the river dominated the distribution of salinity in the main river. The monitoring values of salinity combined with the basic data of the model such as river cross-section, estuary morphology, water level boundary conditions, salinity, flow are used to simulate in one-dimensional model.

This model includes hydrodynamic module combined with new diffusive transport module. Mike 11 model has been calibrated with actual values of water level and salinity measurements at main river stations with values calculated from the model is suitable. Model can be used to forecast the evolution of salinity distribution along the estuary during the dry season 10 days in advance, in order to ensure production or daily activities with salty border 4‰, 0.3‰. This forecast is the most effective and practical for the transitional area between tidal and river flow dynamics because this is a sensitive area of the 4‰ salty border pushing upstream deeply when the tidal current is dominant and 0.3‰ salty border pushing down very close to the mouth of the sea when river currents prevail. For the Tien River mouth, these sensitive areas are the Ba Tri-Giong Trom, Binh Dai, Mo Cay-Thanh Phu and Binh Dai irrigation zones.

Finally, based on the actual salinity values measured at stations along the river, we analyze the salinity reduction along the main river, distinguishing the typical areas of the Tien River mouth. Temporarily assessing the distribution of salinity by depth. However, the one-dimensional model does not evaluate the salinity stratification according to the cross-sectional depth, so the study has not concluded the salinity stratification in the Tien estuary. The actual measured values are to verify the calculated results of the one-dimensional model.

References

- Cameron WM, Pritchard DW (1963) Estuaries in the sea. In: Hill MN (ed.), vol 2. Wiley, New York, pp 306–324
- Ippen AT, Harleman DRF (1961) One-dimensional analysis of salinity intrusion in estuaries. Technical bulletin no. 5. Committee on Tidal Hydraulics, Water ways Exp. Station, Corps of Engineers, United States Army
- Kettab A (2014) Water for all with quality and quantity: it is the concern of all! *Desalin Water Treat* 52:1965–1966
- Legates DR, McCabe GJ Jr (1999) Evaluating the use of “goodness-of-fit” measures in hydrologic and hydroclimatic model validation. *Water Resour Res* 35(1):233–241
- Nguyen SH (2010) Study on scientific basis and propose response measures for the Mekong Delta to ensure sustainable development in the context of climate change-sea level rise. Ministry of Agriculture project and PTNN
- Perillo GME (1995) *Geomorphology and sedimentology of estuaries, developments in sedimentology* 53. Elsevier Science, Amsterdam
- Sam L et al (2006) *Saline intrusion in the Mekong Delta*. Agricultural Publishing House, Ho Chi Minh City
- Sanchez AM (1992) Modeling in a tidal estuary: marine soils behavior in the high turbidity zones. Ph.D. thesis, Universite´ de Nantes, Ecole Centrale de Nantes

- Venice System (1958) Symposium on the classification of brackish waters, Venice, 8–14 Apr 1958. Archives for Oceanography and Limnology (Supple.), vol 11, pp 1–248
- Zhang P, Lu J, Feng L, Chen X, Zhang L, Xiao X, Liu H (2015) Hydrodynamic and inundation modeling of China's largest freshwater lake aided by remote sensing data. Remote Sens 7(4):4858–4879

Chapter 3

Developing Software Package for 2D Modeling Hydrodynamics and Salinity Transport in Cu Lao Dung, Mekong Delta



Xuan Dung Tran and Anh-Ha Le

Abstract In this study, we simulate the flow and salinity transport in Cu Lao Dung, the Mekong Delta. The kinetic–finite volume scheme is used to discretize the shallow water and salinity transport equations on two dimensions. The scheme is stable and positivity preserve water depth when dealing with wet-dry interfaces and a well-balanced scheme satisfying the steady-state condition of still water. Moreover, the salinity computation ensures the conservation of salinity mass, non-negativity property and a maximum principle for salinity and the preservation of discrete steady states associated with the lake at rest equilibrium. The simulated data are compared with simulated data from MIKE 21FM to verify and be applicable to our method to simulate the salinity transport in rivers.

Keywords Hydrodynamic model · Salinity transport · Finite volume scheme · Well-balanced scheme · Cu Lao Dung

3.1 Introduction

The estuary and coastal areas are places where a strong interaction occurs between hydrodynamic factors from the outflow of the river to the tide, current, and wave regime from the sea. In recent years, under the influence of climate change and sea level rise, along with impacts from socio-economic activities of humans, the current status in coastal areas has changed strongly, saline intrusion also has more serious

X. D. Tran (✉)

Faculty of Physics and Engineering Physics, University of Science, Ho Chi Minh City, Vietnam
e-mail: txdung@hcmus.edu.vn

A.-H. Le

Faculty of Mathematics and Computer Science, University of Science, Ho Chi Minh City, Vietnam

e-mail: laha@hcmus.edu.vn

X. D. Tran · A.-H. Le

Vietnam National University, Ho Chi Minh City, Vietnam

changes and effects. The Mekong Delta, with its gentle terrain and long coastline, is one of the most affected areas. With the above situation, scientific research activities on coastal areas are very necessary. Today, with the strong development of technology, the computing power of computers is enhanced, so the numerical method is also widely used. There are many models used to simulate hydrodynamic regimes such as MIKE, TELEMAC, Delft, SMS, CCHE2D, TABS-MD... Some have been applied in the Mekong Delta such as Doan et al. (2014) used MIKE model to evaluate the effect of dredging on salinity intrusion in the estuary of the Mekong River, Vu et al. (2015) used the Delft3D model to study the morphological change in the coastal region of the Mekong River under the influences of sea water level rise, or Xing et al. (2017) used two- and three-dimensional Delft3D Flow and Morphology models to simulate the hydrodynamics and sand transport in Hau river estuary. The models used in these studies are either fully software packages or commercial models with good applicability, but users can only use software that cannot change the algorithm or program to study in some specific cases.

In the direction of open research, in Vietnam, there are now several authors building and developing an open source 2D hydrodynamic model such as Nguyen and Nguyen (2003) in developed Twodimensional River bed Evolution Model (TREM) applied to rivers in Vietnam, Luong and Nguyen (2006) in used Third order Runge Kutta method and linear interpolation method to solve the 2D shallow water equations. Although there are some results, the research direction to build an open source code for the hydrodynamics model combine with saline intrusion in Vietnam is still not popular, so we have developed a software package for this problem to apply and develop for further research directions.

Most flows in rivers have their hydraulic characteristics varying in all three spatial dimensions. However, when the width of the stream is much larger than the depth, a two-dimensional (2D) flow model using the shallow water equations or the depth-averaged equations is considered sufficient to describe flow characteristics. In the scope of this paper, we focus on developing an open source solution of shallow water equations and diffusion equations by finite volume method on an unstructured mesh to simulate hydrodynamics and saline intrusion in two spatial dimensions.

We consider the two dimensions Saint-Venant system and salinity transport, written in conservative form

$$\frac{\partial \mathbf{U}}{\partial t} + \nabla \cdot \mathbf{F}(\mathbf{U}) = \mathbf{S}(\mathbf{U}) \quad (3.1)$$

where $\mathbf{U} = (h, q_x, q_y, e)^T$ and

$$\mathbf{F}(\mathbf{U}) = \begin{pmatrix} q_x & q_y \\ \frac{q_x^2}{h} + \frac{g}{2}h^2 & \frac{q_x q_y}{h} \\ \frac{q_x q_y}{h} & \frac{q_y^2}{h} + \frac{g}{2}h^2 \\ q_x & q_y \end{pmatrix}, \quad \mathbf{S}(\mathbf{U}) = \begin{pmatrix} 0 \\ gh(S_{0x} - S_{fx}) \\ gh(S_{0y} - S_{fy}) \\ 0 \end{pmatrix}$$

where $h = h(x, y, t) \geq 0$ is water depth, $\eta = h + z$ is the water surface level, $\mathbf{u} = (u, v)^T$ is velocity respect x and y , $q_x = hu$, $q_y = hv$, $\mathbf{q} = (q_x, q_y)^T$, s is salinity and $e = hs$, $g = 9.8 \text{ m}^2/\text{s}$ is gravity constant, $S_{0x} = -\frac{\partial z}{\partial x}$, $S_{0y} = -\frac{\partial z}{\partial y}$, z is topography, S_{fx} (S_{fy}) is friction force respect x (respectively y). In hydrological models, based on empirical considerations, Manning–Strickler law can be used.

We mention now some important properties of the system (Eq. 3.1) that have to be taken into account to construct a well-adapted numerical solver.

3.2 The Kinetic Solver

3.2.1 2D Finite Volume Formalism

Let Ω denote the computational domain with boundary Γ , we assume Ω is polygonal. Let Ω be covered by a triangulation mesh \mathcal{T}_h which includes T_i , $i \in [1, I]$ (I is the triangular number). We associate with each T_i , a point G_i located in the interior of T_i be called a centroid point. Let I^Γ be the number of boundary edge, each boundary edge is considered like a ghost element. For $i \in [1, I]$, we denote by $V(i) \subset [1; I + I^\Gamma]$ the set of the neighboring indexes of the element T_i , let $|T_i|$ be the area of T_i . We will denote by e_{ij} the common edge of two elements T_i and T_j with $i \in [1, I]$, $j \in [1; I + I^\Gamma]$. Let l_{ij} be the length of edge e_{ij} ($l_{ij} = l_{ji}$) and \mathbf{n}_{ij} be the unit vector orthogonal to e_{ij} pointing from T_i to T_j ($\mathbf{n}_{ij} = -\mathbf{n}_{ji}$).

Let Δt be the time-step, we set $t_n = n\Delta t$. We denote by \mathbf{U}_i^n the approximation of the cell average of the exact solution at time t_n

$$\mathbf{U}_i^n = \frac{1}{|T_i|} \int_{T_i} \mathbf{U}(\mathbf{x}, t_n) d\mathbf{x} \quad (3.2)$$

We integrate in space and time the Eq. (3.1) on the set $T_i \times (t_n, t_{n+1})$, we obtain

$$\mathbf{U}_i^{n+1} = \mathbf{U}_i^n - \sum_{j \in V(i)} \sigma_{i,j} F(\mathbf{U}_i^n, \mathbf{U}_j^n, \mathbf{n}_{ij}), \quad \text{where } \sigma_{i,j} = \frac{\Delta t l_{i,j}}{|T_i|} \quad (3.3)$$

3.2.2 Kinetic Solver

For an interface with unit normal $\mathbf{n}_{ij} = (n_x, n_y)^T$. We define a local basis (n, τ) which associate to the normal direction and to the tangential one. We can write the flux at Eq. (3.3) with

$$F(\mathbf{U}_i^n, \mathbf{U}_j^n, \mathbf{n}_{ij}) = \mathbf{F}^+(\mathbf{U}_i^n, \mathbf{U}_j^n, \mathbf{n}_{ij}) + \mathbf{F}^-(\mathbf{U}_i^n, \mathbf{U}_j^n, \mathbf{n}_{ij}) \quad (3.4)$$

The positive and negative fluxes are defined following

$$\begin{aligned} \mathbf{F}^+(\mathbf{U}_i, \mathbf{U}_j, \mathbf{n}_{ij}) &= \frac{\tilde{c}_i \mathbf{R}_n}{6g\sqrt{3}} \begin{pmatrix} 3(M_+^2 - M_-^2) \\ 2(M_+^3 - M_-^3) \\ 3u_{\tau,i}(M_+^2 - M_-^2) \\ 3s_i(M_+^2 - M_-^2) \end{pmatrix}, \\ \mathbf{F}^-(\mathbf{U}_i, \mathbf{U}_j, \mathbf{n}_{ij}) &= \frac{\tilde{c}_i \mathbf{R}_n}{6g\sqrt{3}} \begin{pmatrix} 3(N_+^2 - N_-^2) \\ 2(N_+^3 - N_-^3) \\ 3u_{\tau,i}(N_+^2 - N_-^2) \\ 3s_i(N_+^2 - N_-^2) \end{pmatrix} \end{aligned} \quad (3.5)$$

where $\mathbf{R}_n = [1, 0, 0, 0; 0, n_x, -n_y, 0; 0, n_y, n_x, 0; 0, 0, 0, 1]$, $M_{\pm} = \max(u_{n,i} \pm \sqrt{3}\tilde{c}_i, 0)$, $N_{\pm} = \min(u_{n,j} \pm \sqrt{3}\tilde{c}_i, 0)$ and $\tilde{c}^2 = \frac{gh}{2}$.

In order to reduce the diffusion of the scheme, we slightly modify the computation of the following fluxes:

$$\begin{pmatrix} F_{q_y}(\mathbf{U}_i, \mathbf{U}_j, \mathbf{n}_{ij}) \\ F_e(\mathbf{U}_i, \mathbf{U}_j, \mathbf{n}_{ij}) \end{pmatrix} = \begin{pmatrix} u_{ij,\tau} \\ s_{ij} \end{pmatrix} F_h(\mathbf{U}_i, \mathbf{U}_j, \mathbf{n}_{ij}) \quad (3.6)$$

with $\begin{pmatrix} u_{ij,\tau} \\ s_{ij} \end{pmatrix} = \begin{cases} (u_{i,\tau}, s_i)^T & \text{if } F_h \geq 0 \\ (u_{j,\tau}, s_j)^T & \text{elsewhere} \end{cases}$

From definition term s_{ij} , we can prove that the salinity is positive and satisfy maximum principle (see more details in Audusse and Bristeau 2003; Audusse and Bristeau 2005).

3.2.3 Second-Order Reconstructions

In order to improve the accuracy of the results the first-order scheme defined in Eq. (3.3) can be extended to a formally second-order one using a MUSCL like in Hou et al. (2013). In Sect. 2.3, we define limited reconstructed variables and in Sect. 2.4, we introduce the hydrostatic reconstruction that preserves the positivity and equilibrium properties of the first-order scheme.

In the definition of the flux Eq. (3.4), we replace the piecewise constant values \mathbf{U}_i , \mathbf{U}_j by more accurate reconstructions deduced from piecewise linear approximations, namely the values \mathbf{U}_{ij} , \mathbf{U}_{ji} reconstructed on both sides of the interface.

Like Hou et al. (2013), For the variable vector $\mathbf{U} = (\eta, h, q_x, q_y)^T$, we define the gradient $\nabla \mathbf{U}_i$ at triangular cell T_i is illustrated on unlimited gradient $\bar{\nabla} \mathbf{U}_i$ and min-mod function. The values at midpoint M_{ijk} of common edge e_{ijk} can be extrapolated

by

$$\mathbf{U}_{ijk} = \mathbf{U}_i + \nabla \mathbf{U}_i \cdot \mathbf{r}_{ijk} \quad (3.7)$$

The variables η , h , q_x and q_y are be extrapolated to $\eta_{ijk}, h_{ijk}, q_{x,ijk}$ and $q_{y,ijk}$ respectively at the midpoint M_{ijk} . The bed elevations z_{ijk} is computed from

$$z_{ijk} = \eta_{ijk} - h_{ijk} \quad (3.8)$$

Additionally, the velocities at M_{ijk} are calculated by $\mathbf{u}_{ijk} = \mathbf{q}_{ijk} / h_{ijk}$.

3.2.4 The Hydrostatic Reconstruction

We consider also piecewise linear approximation of the variable z and we reconstruct the values z_{ij} , z_{ji} on both sides of the interface. To preserve the well-balanced property, it is necessary that the formally second-order reconstruction preserves an interface equilibrium. It means that if.

$$h_{ij} + z_{ij} = h_{ji} + z_{ji} = H, \mathbf{u}_{ij} = \mathbf{u}_{ji} = 0 \quad (3.9)$$

Given the solution \mathbf{U}^n at time t_n for each cell, we thus compute \mathbf{U}^{n+1} by the following algorithm with five steps:

- “*Second-order*” reconstruction. We define “second-order” reconstructions of primitive variables as it is described in the previous subsection.
- *Interface topography*. We first construct a piecewise constant approximation of the bottom topography $z(x)$.

$$z_i = \frac{1}{|T_i|} \int_{T_i} z(x) dx \quad (3.10)$$

From these “second-order” reconstructed values we derive “second-order” reconstructed values z_{ij} for the topography. Then, we define an interface topography

$$z_{ij}^* = z_{ji}^* = \max(z_{ij}, z_{ji}) \quad (3.11)$$

- *Interface water depth*. We define new hydrostatic reconstructed interface values $\mathbf{U}_{ij}^* = \left(h_{ij}^*, h_{ij}^* \mathbf{u}_{ij}^T, h_{ij}^* s_{ij} \right)^T$

$$h_{ij}^* = \max(h_{ij} + z_{ij} - z_{ij}^*, 0) \quad (3.12)$$

With wet-dry interface, we redefine interface topography:

$$z_{ij}^* = \max(z_{ij}^*, h_{ij} + z_{ij}) \quad (3.13)$$

and we can rewrite h_{ij}^* like Eq. (3.12).

- *Source term.* We define an interface source term

$$S(\mathbf{U}_{ij}, \mathbf{U}_{ij}^*, \mathbf{n}_{ij}) = \begin{pmatrix} 0 \\ \frac{g}{2} \left((h_{ij}^*)^2 - h_{ij}^2 \right) \mathbf{n}_{ij}^T \end{pmatrix} \quad (3.14)$$

For “second order” reconstruction, we add a centered source term to satisfy the consistency of the numerical scheme

$$S^c(\mathbf{U}_i^n, \mathbf{U}_{ij}^n, z_i, z_{ij}, \mathbf{n}_{ij}) = \begin{pmatrix} 0 \\ -\frac{g}{2} (h_{ij} + h_i) (z_{ij} - z_i) \mathbf{n}_{ij}^T \end{pmatrix} \quad (3.15)$$

- *Computation of the solution.* Finally, we write the formally second-order well-balanced scheme by introducing the new interface values Eq. (3.12) in the fluxes Eq. (3.5).

$$\begin{aligned} \mathbf{U}_i^{n+1} &= \mathbf{U}_i^n - \sum_{j \in V(i)} \sigma_{ij} F(\mathbf{U}_{ij}^{*,n}, \mathbf{U}_{ji}^{*,n}, \mathbf{n}_{ij}) \\ &+ \sum_{j \in V(i)} \sigma_{ij} [S(\mathbf{U}_{ij}, \mathbf{U}_{ij}^*, \mathbf{n}_{ij}) + S^c(\mathbf{U}_i^n, \mathbf{U}_{ij}^n, z_i, z_{ij}, \mathbf{n}_{ij})] \end{aligned} \quad (3.16)$$

We can now prove that the hydrostatic reconstruction strategy allows us to preserve the still water steady-state while preserving the positivity property (see Audusse and Bristeau 2005 and Bristeau 2001).

3.2.5 Properties of Scheme

The scheme in Eq. (3.16) is conservative, positive depth water and preserves the well-balanced property. The salinity is positive and satisfies maximum principle property. Now the CFL condition writes that the scheme is consistent:

$$\Delta t \leq \min \frac{|T_i|}{\left(|\mathbf{u}_i| + \sqrt{3} \bar{c}_i^n \right) \sum_{j \in V(i)} l_{ij}} \quad (3.17)$$

3.2.6 Friction Terms

The friction terms only appear in momentum equations, the semi-implicit scheme is implemented to treat these terms. From Eq. (3.16), we have

$$\begin{aligned} \mathbf{q}_i^{n+1} + c_f g \Delta t \frac{|\mathbf{q}_i|^n \mathbf{q}_i^{n+1}}{h_i^n (h_i^{n+1})^{4/3}} &= \mathbf{q}_i^n - \sum_{j \in V(i)} \sigma_{i,j} F_{\mathbf{q}}(\mathbf{U}_i^n, \mathbf{U}_j^n, \mathbf{n}_{ij}) \\ &+ \sum_{j \in V(i)} \sigma_{ij} \left[S_{\mathbf{q}}(\mathbf{U}_{ij}, \mathbf{U}_{ij}^{*,n}, \mathbf{n}_{ij}) + S_{\mathbf{q}}^c(\mathbf{U}_{ij}^n, \mathbf{U}_{ij}^n, z_i, z_{ij}, \mathbf{n}_{ij}) \right] \end{aligned} \quad (3.18)$$

If we donate $\tilde{\mathbf{q}}^{n+1}$ the right hand side of previous formula, we have

$$\mathbf{q}^{n+1} = \frac{\tilde{\mathbf{q}}^{n+1}}{1 + c_f g \Delta t \frac{|\mathbf{q}_i^n|}{h_i^n (h_i^{n+1})^{4/3}}} \quad (3.19)$$

3.2.7 Boundary Condition

Herein, the boundary conditions are implemented to computation of the boundary flux $F(\mathbf{U}_i^n, \mathbf{U}_j^n, \mathbf{n}_{ij})_{j \in [I+1, I^\Gamma]}$ which appear in Eq. (3.3). The variable \mathbf{U}_j^n , can be interpreted as an approximation of the solution in a ghost cell adjacent to the boundary.

3.2.7.1 Solid Boundary

On the solid wall we prescribe a continuous slip condition. It follows that finally

$$F(\mathbf{U}_i^n, \mathbf{U}_j^n, \mathbf{n}_i) = \left(0, \frac{g(h_i^n)^2}{2} \mathbf{n}_i^T, 0 \right)^T \quad (3.20)$$

3.2.7.2 Open Boundary

On the open boundary, the type of flow and then the number of boundary conditions depend on the Froude number. Here, we consider a local Froude number associated to the normal component of the velocity. We have two types.

- Subcritical flow: For the subcritical flow, the value U_j is defined by adding to the given boundary condition and using the assumption that the Riemann invariant is constant along the characteristic.
- Supercritical flow: In the case of supercritical flow, the values h_j, \mathbf{u}_j which are prescribed at the inflow boundary, are equal to h_i, \mathbf{u}_i respectively, at the outflow boundary.

For salinity transport, s_j will take s_i in the outflow and given salinity at the boundary in the inflow.

3.3 Numerical Experiments

3.3.1 Model Setup

The computational domain includes the area of the river and the estuaries of the Mekong River extending from Can Tho to the area outside the mouth of the Hau River. The domain has variations in the width of the river as well as the coastal areas, so an unstructured triangular grid is used to discretize the domain along with the topographic information. The grid has a spatially variable to suit different interest areas, thick in narrow river branches and the estuaries, thinner in areas far out to sea (Fig. 3.1). This approach can help improve computational performance and reduce computation time. The bathymetry was digitized from topography maps which were published by the Department of Survey, Mapping and Geographic Information Vietnam, and from the dataset of Mekong River Commission. Additionally, the bathymetry in the coastal area near the river mouths was updated by measured data from the Department of Oceanology, Meteorology and Hydrology, University of Science—VNU-HCM.

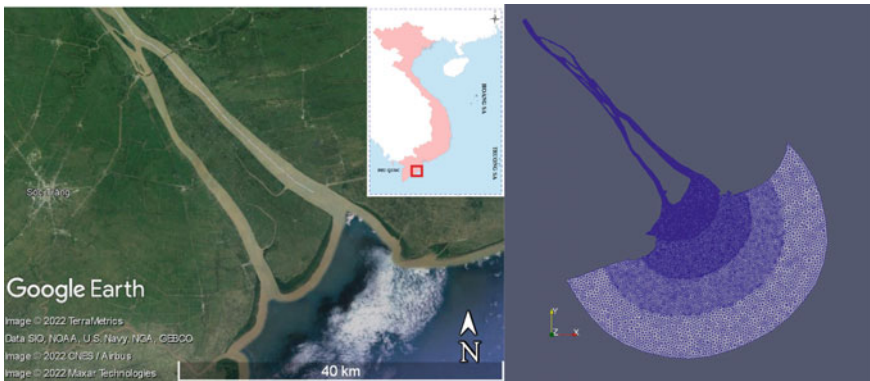


Fig. 3.1 The study area at Cu Lao Dung and the computational grid

The upstream boundary of the model at Can Tho is defined by the water discharge collected from the data of the national hydro-meteorological station. The open sea boundary condition is the predicted tidal level fluctuations according to the tidal harmonics constants imposed offshore which were extracted from FES2004 (Lyard et al. 2006). For the salinity boundary conditions, the salinity is set to 32 psu at the open sea boundary and 0 at the upstream boundary at Can Tho.

The initial condition for the model is set by the hoststart method with a certain buffer running time so that the model automatically detects the appropriate initial conditions to stabilize the model. The model is set up and run for a period from January 1st to March 31st in 2017, with the minimum time steps of 0.01 s.

3.3.2 Results and Discussion

Using the computational model gave results on hydrodynamics and salinity distribution in space and time. To evaluate the computational ability and efficiency of the built model, these results are compared with the calculated results by the MIKE 21FM model. MIKE 21FM is a module in the commercial model MIKE of DHI company, which has been tested and applied well in many practical studies in the world as well as in Vietnam.

The comparison results in Figs. 3.2, 3.3, 3.4 and 3.5 show similar spatial distributions of water levels simulated by the built model and the MIKE 21FM model. The spatial distribution of water level changes according to the tidal cycle from low tide (Fig. 3.2) to high tide (Fig. 3.4) and low tide again (Fig. 3.5) indicating the propagation of tides from outside into the estuary and river area. This similarity can be seen more clearly through the comparison of the change of water levels in time at some locations in the calculation domain. As shown in Fig. 3.6, the difference between simulation results by the built model and by MIKE is not much, especially in the sea area. The correlation coefficient between the two results is higher than 0.97.

The calculated results of the propagation of salinity are also quite consistent with the trend of saline intrusion in the study area. In Figs. 3.7, 3.8, 3.9 and 3.10, it can be seen that the similarity of the salinity distribution of the results by the built model compared with the results by the MIKE 21FM model. Both calculation results show that when the tide is high (Fig. 3.9), the saltwater will be gradually spread into the river, then when the tide goes down (Figs. 3.7 and 3.10), it will be gradually pushed out of the river's mouth. This process leads to changes in salinity in the areas. Figure 3.11 gives a clearer depiction of the changes in salinity along with tidal fluctuations.

Thus, through comparison, it can be seen that the built model gives relatively stable calculation results similar to the commercial MIKE 21FM model. The methods and algorithms used are suitable for building a computational model for the problem of shallow water hydrodynamics and 2D salt propagation.

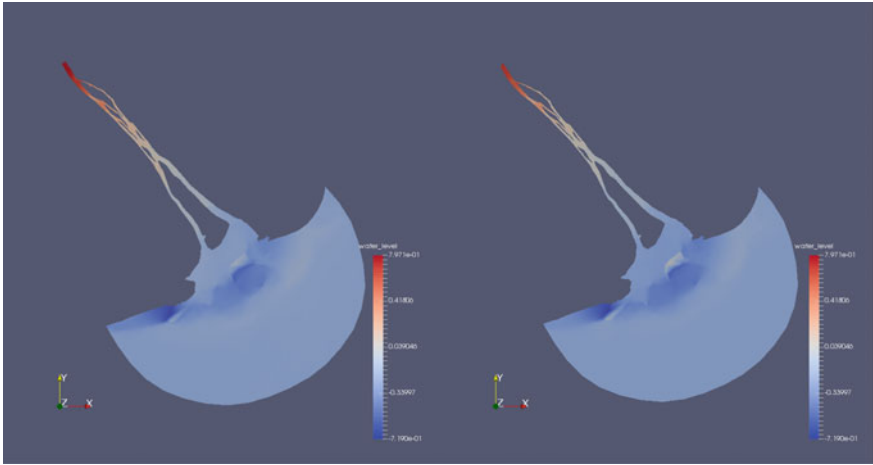


Fig. 3.2 Water levels (left: our model, right: MIKE) at 0:00 02/15/2017

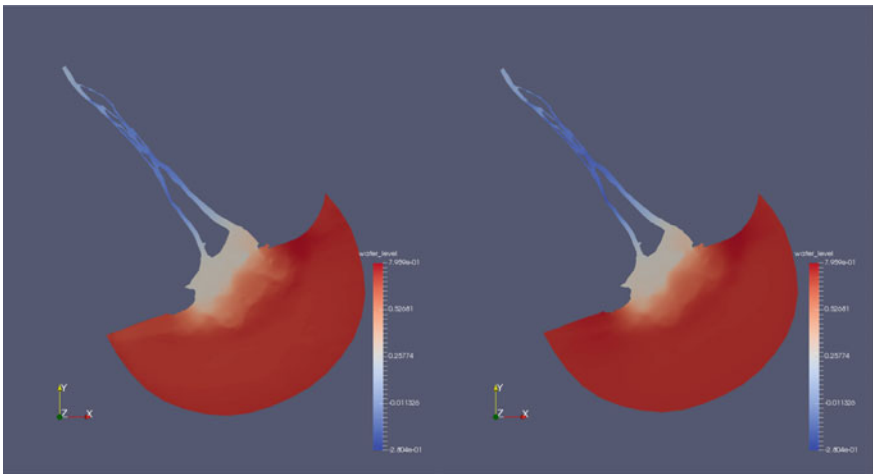


Fig. 3.3 Water levels (left: our model, right: MIKE) at 3:00 02/15/2017

The study is in the process of building and evaluating the computational model, so it has not been possible to run many cases with different conditions in reality. In the future, if it is possible to expand research and develop deeper, with the advantage of the ability to modify the source code, it will help support calculations for specific application cases, and also help cost savings in studying problems related to hydrodynamics in the estuary and coastal zone compared to using commercial models.

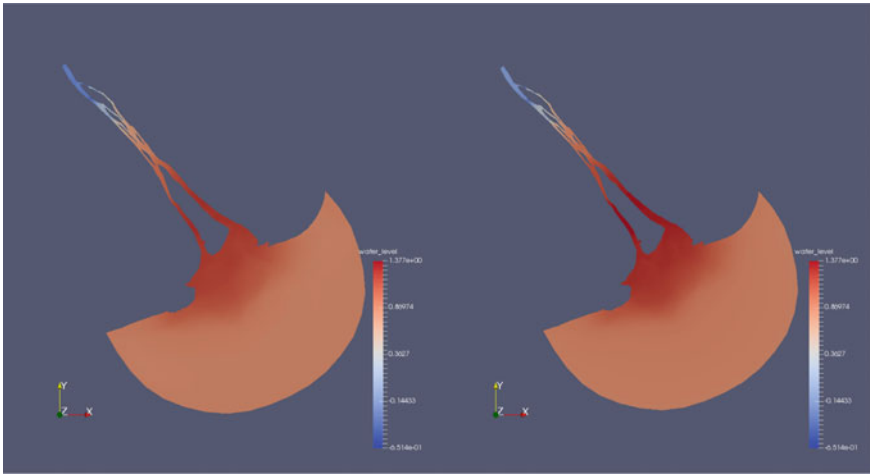


Fig. 3.4 Water levels (left: our model, right: MIKE) at 6:00 02/15/2017

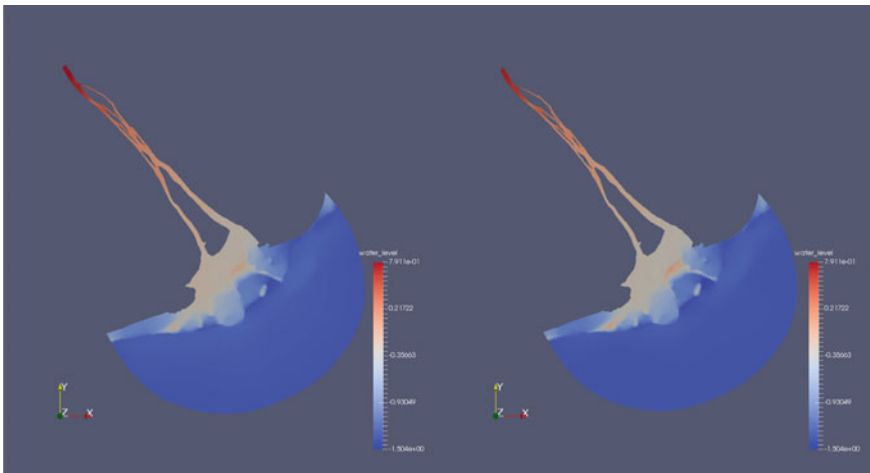


Fig. 3.5 Water levels (left: our model, right: MIKE) at 12:00 02/15/2017

3.4 Conclusion

Studying flow simulation using a hydrodynamic model combined with saline intrusion is a complicated problem that cannot be solved by an analytical method. Therefore, it is very necessary to conduct research on numerical solutions and build a calculation program with stable, effective, and suitable solutions to reality. The study used the finite volume method with a kinetic scheme to discretize the shallow water and salinity transport equations in two dimensions. The scheme is stable and positively

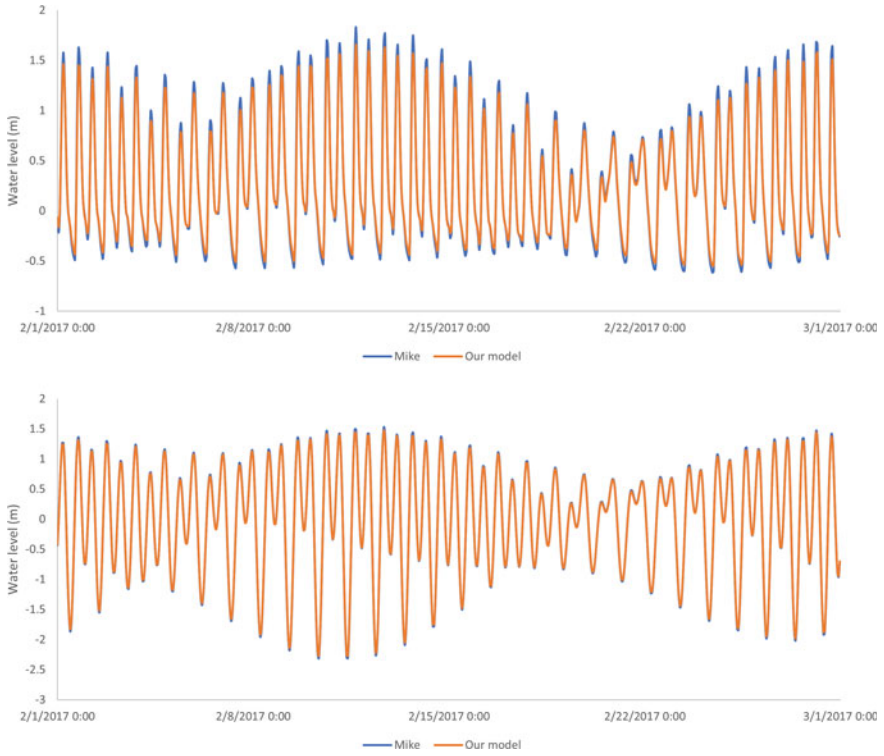


Fig. 3.6 The comparison of water levels at the estuary and the outside

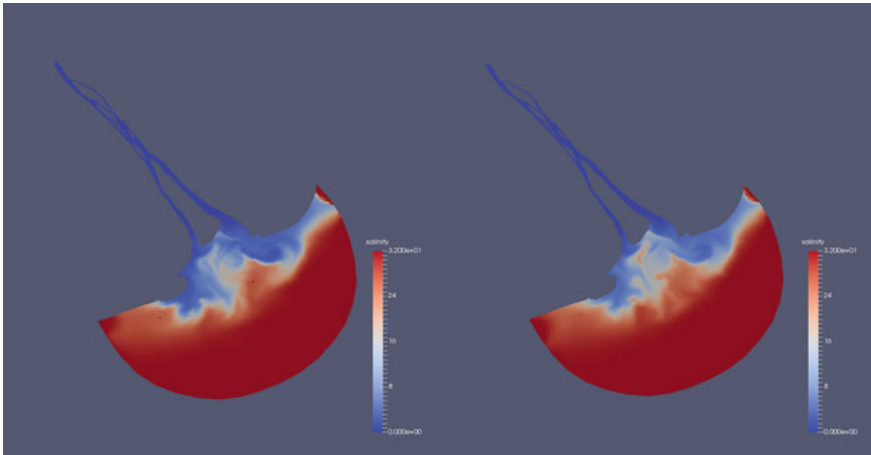


Fig. 3.7 Salinity (left: our model, right: MIKE) at 0:00 03/02/2017

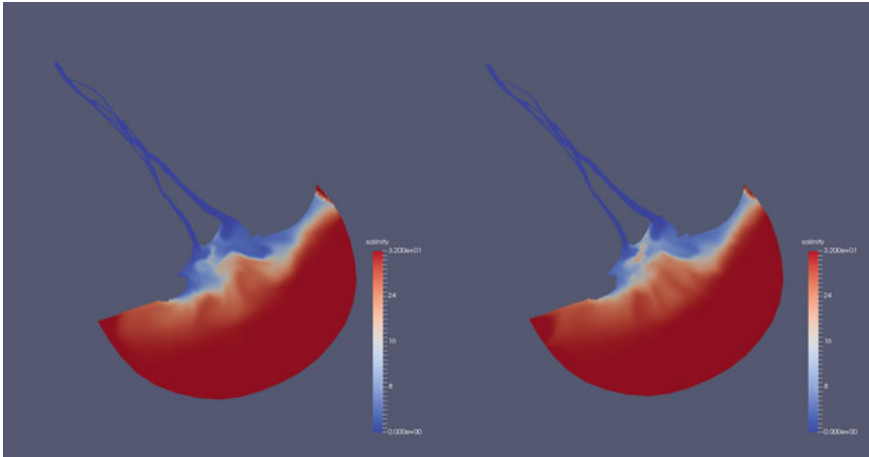


Fig. 3.8 Salinity (left: our model, right: MIKE) at 3:00 03/02/2017

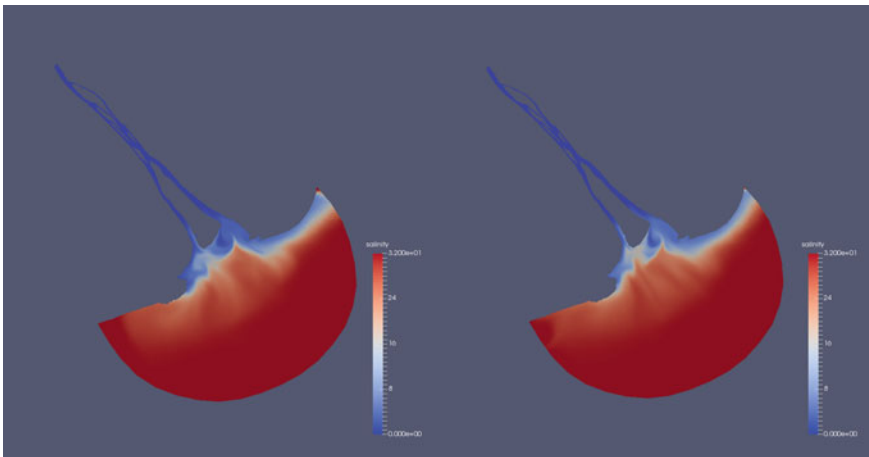


Fig. 3.9 Salinity (left: our model, right: MIKE) at 6:00 03/02/2017

preserves water depth when dealing with wet-dry interfaces and a well-balanced scheme satisfies the steady-state condition of still water. Moreover, the salinity is positive and satisfies the maximum principle. This is also the difference of the built model compared to the MIKE 21FM model.

Based on these numerical methods, the research has built an open source program and applied it to calculate conditions in Cu Lao Dung area, the Mekong Delta. The calculated results by the built model are compared with the calculated results by MIKE 21FM model, showing that the model has relatively well solved the problem

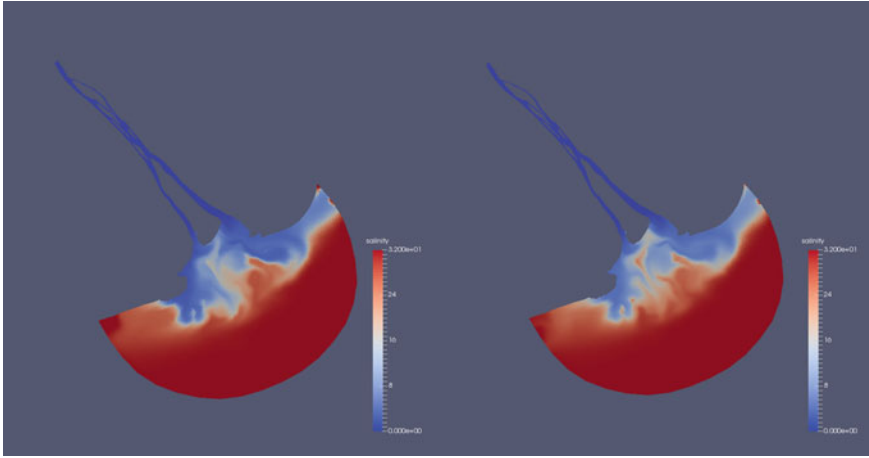


Fig. 3.10 Salinity (left: our model, right: MIKE) at 12:00 03/02/2017

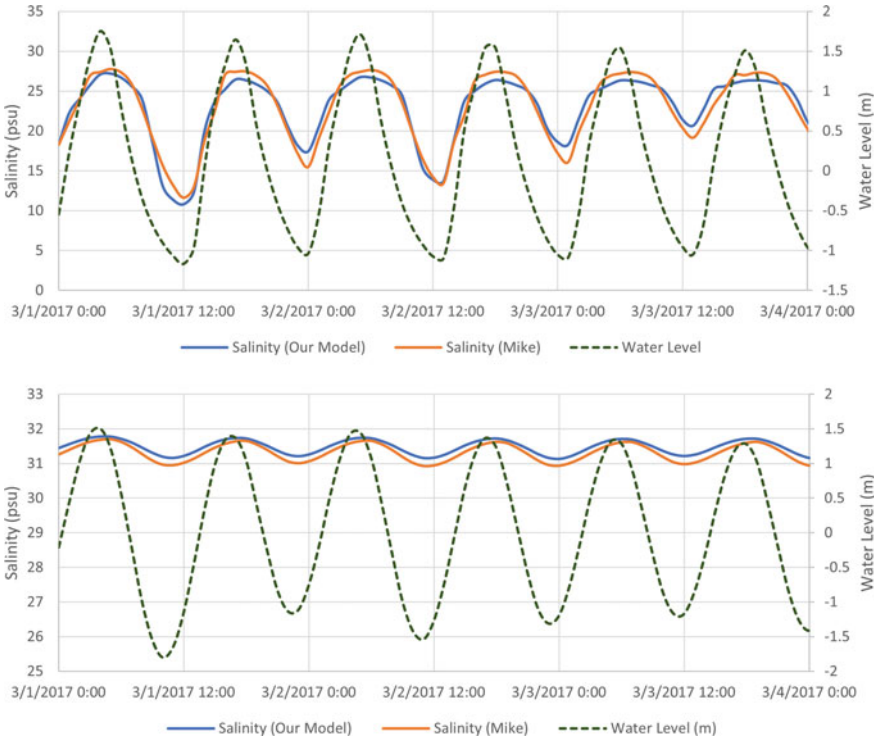


Fig. 3.11 Salinity and water levels at the estuary and the outside

of two-dimensional hydrodynamic and salinity transport problem, which is suitable for application in real river conditions.

Acknowledgements This research is funded by University of Science, VNU-HCM under grant number T2022-01.

References

- Audusse E, Bristeau MO (2003) Transport of pollutant in shallow water: a two time steps kinetic method. *M2AN* 37(2):389–416
- Audusse E, Bristeau M-O (2005) A well-balanced positivity preserving “second-order” scheme for shallow water flows on unstructured meshes. *J Comput Phys* 206:311–333
- Bristeau MO, Coussin B (2001) Boundary conditions for the shallow water equations solved by kinetic schemes. *Rapport de Recherche* 4248
- Doan QT, Nguyen CD, Chen YC, Mishra PK (2014) Modeling the influence of river flow and salinity intrusion in the Mekong river estuary, Vietnam. *Lowland Technol Int* 16(1):14–25
- Hou J, Simons F, Mahgoub M, Hinkelmann R (2013) A robust well-balanced model on unstructured grids for shallow water flows with wetting and drying over complex topography. *Comput Methods Appl Mech Eng* 257:126–149
- Luong TA, Nguyen HM (2006) An efficient algorithm to solve the system of two-dimensional wave equations. *J Agric Food Ind* 3
- Lyard F, Lefevre F, Letellier T, Francis O (2006) Modelling the global ocean tides: modern insights from FES2004. *Ocean Dyn* 56:394–415
- Nguyen HK, Nguyen TG (2003) Research and application of 2-D model to calculate the deformation of the conducting channel. *J Hydrometeorol* 512:8–15
- Vu DV, Tran DL, Tran AT, Nguyen TKA (2015) Simulation of the impact of sea level rise on morphological change in the coastal region of Mekong River. *Vietnam J Mar Sci Technol* 15(2):14–25
- Xing F, Meselhe EA, Allison MA, Weathers HD (2017) Analysis and numerical modeling of the flow and sand dynamics in the lower Song Hau channel, Mekong Delta. *Cont Shelf Res* 147:62–77

Chapter 4

An Assessment of Some Algorithms for Modeling and Forecasting Horizontal Displacement of Ialy Dam, Vietnam



Kien-Trinh Thi Bui  and Cuong Manh Nguyen 

Abstract In order to simulate and reproduce the operational characteristics of a dam visually, it is necessary to capture the displacement at different measurement points and analyze the observed movement data promptly to forecast the dam safety. The accuracy of forecasts is further improved by applying machine learning methods to data analysis progress. In this study, the horizontal displacement monitoring data of the Ialy hydropower dam was applied with machine learning algorithms: Gaussian processes (GP), Multi-layer Perceptron Neural Networks (MLPs), and the M5-Rules algorithm for modelling and forecasting of horizontal displacement of the Ialy hydropower dam (Vietnam), respectively for the analysis. The database used in this research was developed by collecting time series of data from 2006 to 2021 and divided into two parts: training dataset and validating dataset. The final results show all three algorithms have high performance for both training and model validation, in which the MLPs is the best model. The usability of them is further investigated by comparison with benchmark models created by Multi-linear Regression (MLR). The result shows among the performance which obtained from all the GP model, the MLPs model and the M5-Rules model are superior. Therefore, these three models should be used to analyze and predict horizontal displacement of the dam.

Keywords Gaussian processes · Horizontal displacement · Hydropower dam · M5-rules · Multi-layer perceptron neural networks

K.-T. T. Bui (✉)
Thuyloi University, Hanoi, Vietnam
e-mail: bktrinh@tlu.edu.vn

C. M. Nguyen
Royal HaskoningDHV, Hanoi, Vietnam

4.1 Introduction

Monitoring and predicting deformations on hydropower dams are important tasks contributing to damage prevention, structural integrity and public safety (Bagher-Ebadian et al. 2011). However, the deformation and displacement of the dam is a non-linear and highly complicated process. It is greatly influenced by surrounding factors such as hydraulic pressure, material deformation, seismic load and air temperature (Chai and Draxler 2014; Bayrak 2007).

There are many approaches and methods to model and predict the deformation and displacement of hydropower dams that have been proposed in the past decade. In summary, they can be divided into three main groups: deterministic methods, statistical, and combined methods (Kao and Loh 2013; Sortis and Paoliani 2007). One of the most widely used methods is the deterministic method. However, its disadvantage is: it requires elusive and high accuracy indicators such as uplift pressure and leakage flow (Kuremoto et al. 2014). Therefore, the combined method and the statistical method are proposed as an alternative to the deterministic method. Nevertheless, these methods still require an abundance of data to be collected and analyzed to ensure the accuracy of the results (Lombardi et al. 2008; Massinaei et al. 2014).

As an important issue of concern, machine learning methods and artificial intelligence techniques have been proposed to analyze and predict dam deformation including vector regression (Chai and Draxler 2014; Mata 2011), artificial neural networks (Nguyen et al. 2013), and neural fuzzy (Pytharouli and Stiros 2005). In general, the new predictive models have improved the performance and the artificial neural network has become an effective tool for modelling and analyzing the displacement of hydropower dams.

Along with the development of artificial intelligence, new algorithms and data training techniques are also introduced such as Gaussian Processes (GP), Multi-layer Perceptron Neural Networks (MLPs) and M5-Rules algorithm (Quinlan 1992). Regarding these three models, the methods have been recently reported to be a powerful regression tool for the dam displacement analysis (Quinlan 1992; Ranković et al. 2012) as of their performance and potential. Unfortunately, in Vietnam, the application of displacement modelling techniques of hydropower dams has only been applied to Hoa Binh dam. The Ialy hydropower dam—one of the oldest, largest and most important hydropower dams in Vietnam—has a wide range of social applications. Therefore, in this study, we decided to investigate and compare the potential application of the Gaussian Processes, the Multi-layer Perceptron Neural Networks and M5-Rules algorithms to model and predict the horizontal displacement of the Ialy dam.

The modeling process used GP, MLP, M5-Rules, Multi-linear Regression (MLR) and Additive Regression (AR) with the support of WEKA 3.8.5 software (Frank et al. 2016).

The structure of this paper is organized as follows: the second part provides description of study area and the database collected; the third part gives a brief description of the applied theory of the selected algorithms used in this study and the model performance evaluation indicators; the final parts are results, discussion and conclusions.

4.2 Study Area and Data Used

4.2.1 Study Area

The Ialy hydropower project construction was started on November 4, 1993 and inaugurated on April 27, 2003. The Ialy Dam was designed by Vietnamese engineers and constructed by Vietnamese construction companies. It was completed in 1998, and it is the third largest hydropower dam in Vietnam which is located two districts of two different provinces: Chu Pah district-Gia Lai province and Sa Thay district-Kon Tum province. It is the third project of the dam cascade system on the Sesan River-a tributary of the Mekong River, formed from the tributaries of the Dakbla and KrongPok rivers (Fig. 4.1). Its hydropower plant is also the biggest one of six plants on Sesan River within Vietnam with three other hydropower plants located in Cambodia.

Ialy Hydropower plants and other underground structures were designed by Hydroprojekt of Russia. The first unit started operating on 02/05/2000. The last unit started generating electricity on 12/12/2001. Some specifications of Ialy dams are given in Table 4.1.



Fig. 4.1 Location of the study area

Table 4.1 Specifications of the Ialy hydropower dam

No.	Specifications	Value
1	Total reservoir storage	$1037.09 \times 10^6 \text{ m}^3$
2	Total reservoir area	64.5 km^2
3	Live storage	$779 \times 10^6 \text{ m}^3$
4	Normal water level	515 m
5	Maximum water level	518 m
6	Minimum water level	490 m
7	Number of units	4 units
8	Design capacity	720 MW
9	Average amount of electricity	$3680 \times 10^6 \text{ kWh/year}$

4.2.2 Data Used

There are 3 main displacement monitoring routes that exist at Ialy dam: (i) 4 points at 4795 m and 15 points mounted on components at different heights on the dam surface; (ii) 4 points at 500 m and (iii) 17 points at 522 m on spillways. The horizontal displacement and settlement of specific points on these three routes are measured by high-precision total station and leveling machines.

Of the 40 monitoring points, only 4 points are measured twice a month to detect the three-dimensional displacement of the dam. In this research, the point M17 was selected and its time series data from January 2004 to December 2016 of horizontal displacement was collected for analyzing (Fig. 4.2).

According to Chai and Draxler (2014), the factors that co-influence to the horizontal displacement of hydropower dams include: air temperature data, ageing factors, hydraulic data (Table 4.2). In this research, we used: (i) the reservoir water level (H) with three exponential components H^1, H^2, H^3 ; (ii) the air temperature (T) consists of five components $T_0, T_{14}, T_{28}, T_{42}, T_{56}$ where indexes 0, 14, 28, 42 and 56 are number of days prior to the measurement; (iii) the age of the dam (t) includes two components t and $\ln(t)$. A total of ten input variables were taken into account ($H^1, H^2, H^3, T_0, T_{14}, T_{28}, T_{42}, T_{56}, t, \ln t$) and the dependent variable—the measured horizontal displacement (HD). These 10 input variables are encoded in the matrix V_i where index $i = 1, \dots, 10$.

To analyze the horizontal displacement of Ialy dam, the collected data including 339 samples was divided into two subsets: the first subset was used to build a regression model (time-series data from 09/01/2004 to 24/02/2014 including 270 samples) whereas the second subset is used to validate the performance of the used algorithm (time-series data from 10/03/2014 to 19/12/2016 including 69 samples).

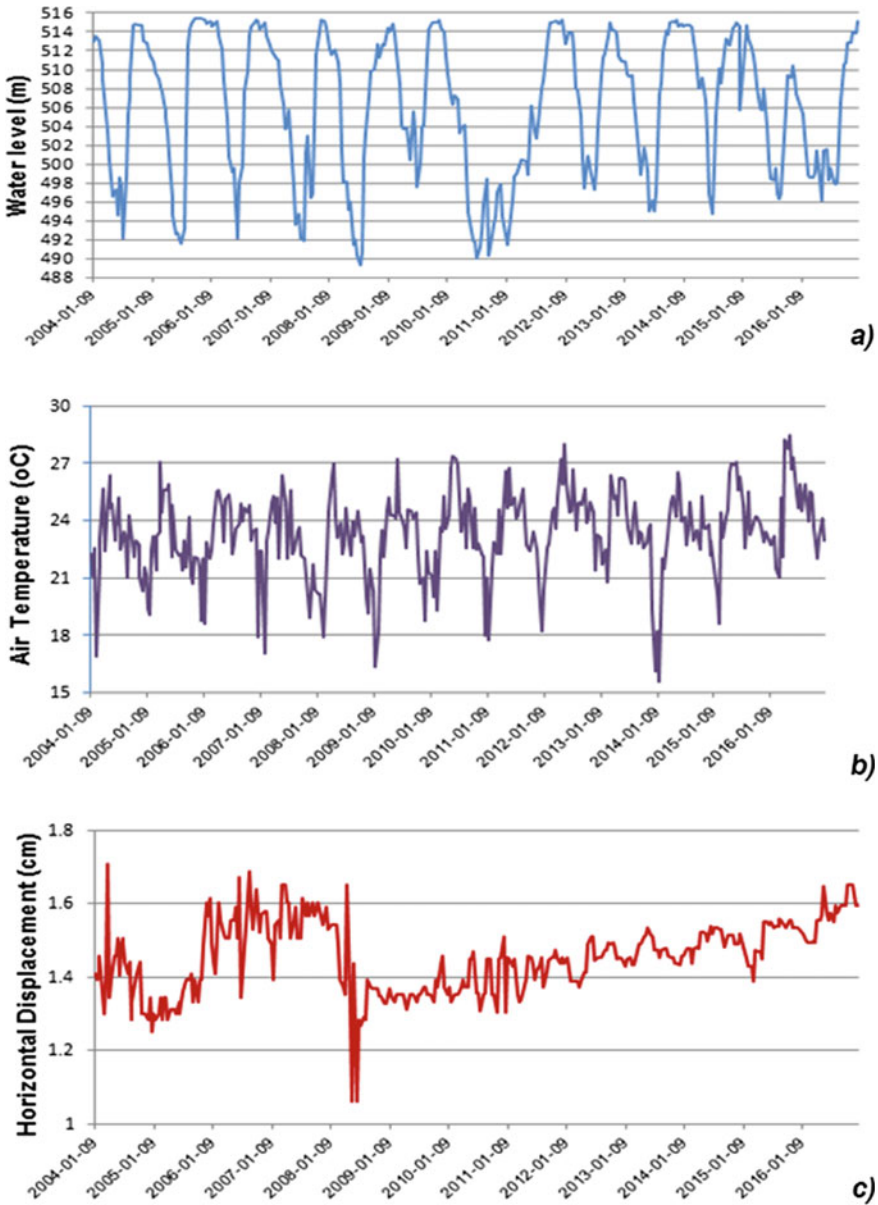


Fig. 4.2 Time-series data for horizontal displacement at the M17 point of Italy dam **a** water level, **b** air temperature, **c** horizontal displacement

Table 4.2 Overview of the data used

No.	Data type	Unit	Max	Min
1	Horizontal displacement (HD)	Meter	0.1707	0.0640
2	Reservoir water level (H)	Meter	515.44	489.30
3	Air temperature (T)	Degree	28.5	15.6
4	Dam age (t)	Month	215.7	58.4

4.3 Method

Since there are many well-documented with detailed explanations of Gaussian Processes, Multilayer Perceptron Neural Networks and M5-Rules algorithms for dam displacement models, we only briefly summarize how these methods worked in this study.

4.3.1 Gaussian Process

Displayed equations or formulas are centered and set on a separate line (with an extra line or halfline space above and below). Displayed expressions should be numbered for reference. The numbers should be consecutive within each section or within the contribution, with numbers enclosed in parentheses and set on the right margin.

A Gaussian process (GP) is also known as a normal stochastic process. From a function space point of view, a GP is a set of random variables, where any finite subset of which has a common Gaussian distribution, i.e. common probability distribution of any set of random variables $\{x_i \in X; i = 1, \dots, n\}$ and processes with corresponding state $\{f(x_1), \dots, f(x_n)\}$ follows the n -dimensional Gaussian distribution (Salazar et al. 2017). The characteristics of the GP can be fully determined using the corresponding mean function $m(x)$ and the covariance function (kernel) function $k(x, x')$:

$$\begin{cases} m(x) = E[f(x)] \\ k(x, x') = E[(f(x) - m(x)) * (f(x') - m(x'))^T] \end{cases} \quad (4.1)$$

where $x, x' \in X$ are d -dimensional input vectors and E represents the mathematical expectation. The average function $m(x)$ represents the expected value of the function $f(x)$ at the input point x . The covariance function $k(x, x')$ can be understood as a measure of the confidence level for $m(x)$. The GP can be expressed as follows:

$$f(x) \sim GP(m(x), k(x, x')) \quad (4.2)$$

The covariance function in GP is often chosen by the user's experience. Many previous studies have demonstrated that different covariance functions have their

own characteristics (Salazar et al. 2015; Su et al. 2015). Thus, the performance of different covariance functions needs to be compared to choose the function that best fits the training model of the dam.

4.3.2 Multilayer Perceptron Neural Networks

One of the most popular methods for time series modelling and forecasting with high accuracy is using Multilayer Perceptron Neural Networks (MLP) (Bui et al. 2012). In principle, MLP supplement forward networks that use back-propagation algorithms to update weights through each training phase (Quinlan 1992). The used MLP model in this study is formed by three layers: an input layer consisting of ten input neurons, V_i with $i = 1, \dots, 10$; a hidden layer; and one output layer. The number of neurons in the hidden layer is determined in the training phase, while there is only one neuron in the output layer. The logistic sigmoid is selected as the activation function:

$$f(x) = \frac{1}{1 - e^V} \quad (4.3)$$

where V is the input variable.

The weight of the interconnected neurons across the three layers directly affects the performance of the MLP. By using a two-stage back-propagation algorithm: forward and backward (Bui et al. 2015) the weights are always modified and updated during the different training phases. It is an iterative process. In the transition phase, the input values are brought forward from the input layer to the output layer, and then the output values are calculated. Next is the process of estimating the error value by comparing the output values with the monitored displacement values. The weights are then updated in the rollback to minimize errors as follows:

$$Error = \sum_{i=1}^n (pr_i - y_i)^2 \quad (4.4)$$

where pr_i and y_i are predicted and measure values of HD , n is the total number of samples.

4.3.3 M5-Rules

The M5-Rules algorithm is a machine learning algorithm for regression problems. Based on the separate and conquer theory, it generates a decision list from the M5 Model Tree (Vladimirov et al. 2003).

Training data set D which containing 10 input variables, the M5 Model Tree (Wang and Witten 1996) built a tree-like model with each node of the model was generated by the information reduction of the standard deviation estimated by the following equation:

$$Reduction = Std(D) - \sum \frac{|D_i|}{|D|} * Std(D) \quad (4.5)$$

where D_i is a subset of D , Std is the standard deviation.

The tree model when reached the maximum level will be punched to prevent overfitting. Meanwhile, a smoothing process is performed to deal with discontinuities of the model tree shape (Were et al. 2015). One important thing to keep in mind: the branches of the M5 model tree are formed using linear regression.

The decision lists will be generated in parallel with the construction of the M5 model tree. Detailed explanations of the M5 algorithm can be found in the publication of Witten et al. (2011).

4.4 Performance Assessment

By using parameters such as the original Root mean square error (RMSE), Mean absolute error (MAE), and Correlation coefficient (R^2) it is possible to evaluate the accuracy and performance of the forecasting model. The higher the R^2 is, and the lower the RMSE and the MAE are, the better performance of the models is. Detailed explanations of model verification can be found in Bayrak (2007) and Zhao and Jin (2008):

$$RMSE = Sqrt \sum_{i=1}^n \frac{(pr_i - y_i)^2}{n} \quad (4.6)$$

$$MAE = \sum_{i=1}^n \frac{|pr_i - y_i|}{n} \quad (4.7)$$

$$R^2 = \frac{\sum_{i=1}^n (pr_i - \overline{pr_i})(y_i - \overline{y_i})}{\sqrt{\sum_{i=1}^n (pr_i - \overline{pr_i})^2 * \sum_{i=1}^n (y_i - \overline{y_i})^2}} \quad (4.8)$$

where $\overline{pr_i}$ and $\overline{y_i}$ are mean measured values and mean predicted values of horizontal movement, respectively.

4.5 Results and Discussions

Together with the Gaussian process, the kernel function is chosen based on the Gaussian kernel (RBF function), and the value of the kernel parameter is chosen in the range [0.001, 1] with a minimum step of 0.001. The optimum values of the kernel parameter and the regulation constant obtained by searching are 53 and 0.0056, respectively.

Setting values 0.3, 0.2 and 1000 respectively for learning rate, momentum and epoch to train Neural Nets MLPs respectively. It is noted that the activation function is the logistics sigmoid. The number of neurons in the hidden layers affects the performance of the MLP model. Therefore, Bui et al. (2017a) proposed an experiment with two selected neurons. Figure 4.3 shows the structure of the MLP model.

The minimum number of permissive samples at a selected leaf note is 4 for the case of the M5-Rules model. A total of four rules were generated:

Rule 1: If $V_9 > 0.356$ then

$$HD = 0.0092 * V_1 + 0.0384 * V_8 + 0.2944 * V_9 + 1.196 \quad (4.9)$$

Rule 2: If ($V_7 > 0.282$; $V_9 > 0.141$) then

$$HD = 0.0092 * V_1 + 0.0314 * V_4 + 0.0447 * V_5 + 1.1924 \quad (4.10)$$

Rule 3: If ($V_7 > 0.282$; $V_9 \leq 0.356$; $V_9 > 0.141$) then

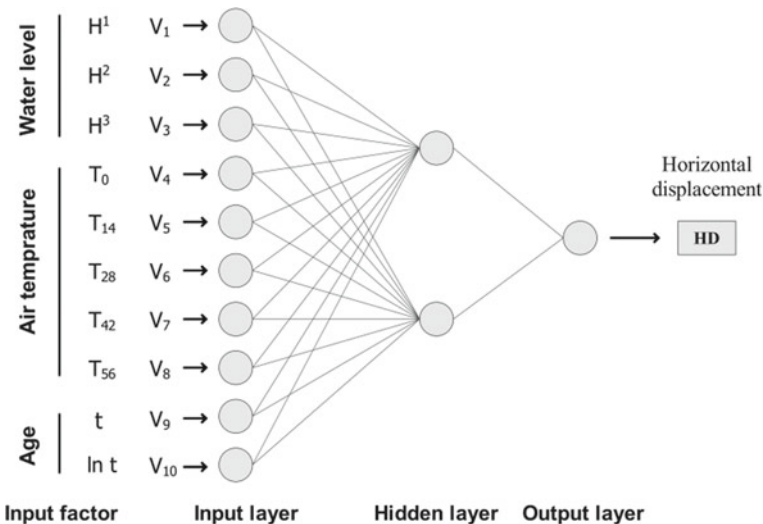


Fig. 4.3 Structure of the MLP model in this study

$$HD = 0.0092 * V_1 + 0.0447 * V_5 + 0.0384 * V_8 + 1.0204 \quad (4.11)$$

Rule 4:

$$HD = 0.1986 * V_1 + 0.1803 * V_4 + 0.4033 * V_9 + 1.1379 \quad (4.12)$$

The GP, MLP and M5-Rules model were developed using the training dataset for each training phase and the results are shown in Fig. 4.4 and Table 4.3.

The result shows that all of three models have higher performance than the benchmark model, and the MLP has the highest performance. Validating the model with standard deviation (11.6 mm) of measured displacement estimated from the training dataset, Gaussian Process RMSE (2808 mm), MLP model (2527 mm) and the model M5-Rules (2792 mm), it is clear that the goodness of fit of the three models is high.

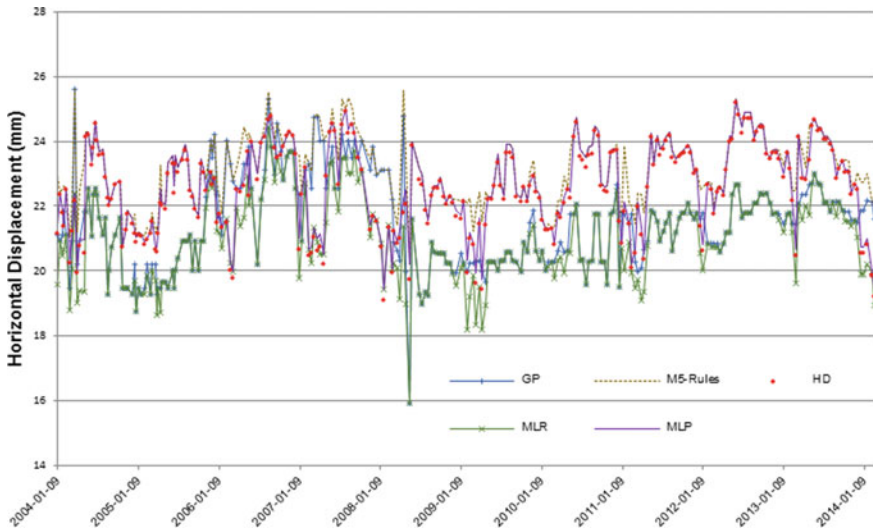


Fig. 4.4 The output values of training dataset derived from the GP, the MLP, the M5R and the MLR model

Table 4.3 Performance of the models, and the benchmark models using the training dataset

Characteristics	Training dataset		
	RMSE (mm)	MAE (mm)	R ²
GP	2.808	2.192	0.8934
MLP	2.527	1.921	0.9303
M5-rules	2.792	2.092	0.9155
Multi-linear regression	3.103	2.413	0.8214
Additive regression	3.032	2.628	0.8356

The picture of the error distribution is formed based on the RMSE quadratic scoring rule. However, these coefficients are sensitive to large outliers and values (Zheng et al. 2013). Therefore, we have additionally used MAE.

To diagnose the variability of the errors that need to compare the differences between RMSE and MAE.

The results in Table 4.3 show that the difference between GP, MLP model and M5-Rules model is 0.616 mm, 0.606 mm and 0.7 mm for RMSE and MAE respectively. The above results and $R^2 = 0.9303$ showed the better fit of the MLP Neural Nets model compared with the remaining trained models.

The forecasting ability of the three models were evaluated using a validation dataset that was not used during the training phase. The results show that the MLP model has the lowest RMSE and MAE. The MLP model performs better than the GP and the M5-Rules model (Table 4.4). The difference between RMSE and MAE for GP, MLP model and M5-Rules model is 0.609 mm, 0.528 mm and 0.547 mm respectively. And the MLP model has the lowest variation of the errors.

The performance of the three models is further compared with two popular models, Multi-linear Regression model (MLR) and Additive Regression model (AR). These two methods were selected as benchmark methods as of having been proven outperforming conventional methods in dam behavior modeling (Kao and Loh 2013; Mata 2011; Pytharouli and Stiros 2005; Salazar et al. 2017; Bui et al. 2018; Bui 2022; Lin et al. 2019; Bui, et al. 2017a, 2017b). The Multi-linear Regression model was built using sequential minimal optimization (Were et al. 2015). The results are shown in Tables 4.3 and 4.4. It shows that the overall performance of the three models is better than the performance of the benchmark models and that MLP is the best model.

The efficiency of three models for forecasting the deformation of Ialy dam were also compared to the results of the same types of models in Bui et al. (2018), Bui (2022), Lin et al. (2019), Bui et al. (2017a), Bui et al. (2017b) (Tables 4.5, 4.6 and 4.7).

Although the values of RMSE and MAE in this study is considerably large, the R^2 value is similar to the values from comparison studies. This indicates that the forecasting precision of three models used in this study is equivalent to the same types of models used in those studies. Due to the difference in the monitoring methods, observed values at the Ialy dam which was obtained from different instruments with completely different accuracy, further studies are needed to optimize the models

Table 4.4 Performance of the models, and the benchmark models using the validating dataset

Characteristics	Validating dataset		
	RMSE (mm)	MAE (mm)	R^2
GP	4.017	3.408	0.7855
MLP	3.803	3.275	0.7903
M5-rules	3.939	3.392	0.7834
Multi-linear regression	4.502	3.816	0.7252
Additive regression	4.719	4.064	0.6889

Table 4.5 Performance of the MLPs model using training and validating dataset

	Criteria	This study	Bui et al. (2018)	Bui (2022)	Bui et al. (2017a)	Bui et al. (2017b)
Training	RMSE (mm)	2.527	0.596	0.750	0.343	0.480
	MAE (mm)	1.921	0.516	0.570	0.284	0.382
	R ²	0.930	0.925	0.882	0.963	0.952
Validating	RMSE (mm)	3.803	0.616	1.060	0.445	0.420
	MAE (mm)	3.275	0.563	0.990	0.364	0.344
	R ²	0.790	0.888	0.759	0.781	0.781

Table 4.6 Performance of the GP model using training and validating dataset

Criteria	Training				Validating			
	This study	Bui et al. (2018)	Bui (2022)	Lin et al. (2019)	This study	Bui et al. (2018)	Bui (2022)	Lin et al. (2019)
RMSE	2.808	0.419	0.900	0.214	4.017	0.365	0.470	0.168
MAE	2.192	0.328	0.630	0.153	3.408	0.302	0.410	0.132
R ²	0.893	0.927	0.865	0.978	0.7855	0.883	0.764	0.979

Table 4.7 Performance of the M5-rules model using training and validating dataset

Criteria	Training			Validating		
	This study	Bui (2022)	Bui, et al. (2017b)	This study	Bui (2022)	Bui, et al. (2017b)
RMSE	2.792	0.610	0.270	3.939	0.710	0.351
MAE	2.092	0.470	0.210	3.392	0.630	0.291
R ²	0.916	0.922	0.977	0.7834	0.781	0.744

and reduce the RMSE, MAE values, thereby further improving the performance of predictive models.

4.6 Conclusion

In this study, the potential application of GP, MLP and M5-Rules algorithm in modelling and forecasting of horizontal displacement of the Ialy hydropower dam is evaluated and compared. According to current literature, M5-Rules is a relatively new, modern soft computational algorithm that has not been used for modelling and forecasting the horizontal displacement of the Ialy hydropower dam.

The dam database was built, collected, and processed from the dam ageing and air temperature data along with 10 input variables derived from the upstream reservoir water level and the transition data and the horizontal position measured by the geodetic method. The time-series data covers the period of 13 years (2004–2016). The degree-of-fit and predictive potential of the trained models were evaluated using RMSE, MAE and R^2 . Additionally, the results from Multilinear Regression were also included to make the comparison.

In general, the process of building an MLP model is more complex because it requires many parameters that are determined through a trial-and-error process while developing an M5-Rules model is simpler when just a minimum number of samples at a leaf node. In addition, the M5-Rules model has an advantage as it generates a list of decision rules that can serve in decision-making for hydropower dam maintenance.

The results shown that the MLP model has better performance than the M5-Rules model and the GP model on both training and validation datasets. In addition, the variation of errors of the MLP model is lower than that of the M5-Rules model and GP model.

Although the MLP model has better performance than the other models in this study, it can be concluded that the M5-Rules is still a promising tool that should be used for modelling and forecasting movements of hydropower dam.

Acknowledgements This research is funded by Vietnam National Foundation for Science and Technology Development (NAFOSTED) under grant number 105.08-2018.06.

The authors also would like to thank Ialy Hydropower Company for providing the periodically monitoring data and supporting us in collecting anomaly observations.

References

- Bagher-Ebadian H et al (2011) Predicting final extent of ischemic infarction using artificial neural network analysis of multi-parametric mri in patients with stroke. *PLoS ONE* 6:1–9
- Bayrak T (2007) Modelling the relationship between water level and vertical displacements on the Yamula dam, Turkey. *Nat Hazards Earth Syst Sci* 7:289–297
- Bui DT et al (2015) Spatial prediction models for shallow landslide hazards: a comparative assessment of the efficacy of support vector machines, artificial neural networks, kernel logistic regression, and logistic model tree. *Landslides* 13:361–378
- Bui KTT et al. (2022) Deformation forecasting of a hydropower dam by hybridizing a long short-term memory deep learning network with the coronavirus optimization algorithm. *Comput Aided Civ Infrastruct Eng*
- Bui DT et al. (2012) Landslide susceptibility assessment in Vietnam using support vector machines, decision tree and naïve bayes models. *Math Prob Eng*
- Bui D et al. (2017a) Hybrid intelligent model based on least squares support vector regression and artificial bee colony optimization for time-series modeling and forecasting horizontal displacement of hydropower dam. In: *Handbook of neural computation*. Elsevier, pp 279–293
- Bui DT et al. (2017b) A comparative assessment of multi-layer perceptron neural networks and M5-rules algorithm for modeling and forecasting of horizontal displacement of the Hoa Binh hydropower dam (Vietnam). In: *The international symposium on geo-spatial and mobile mapping technology (GMMT2016)*. Hanoi

- Chai T, Draxler RR (2014) Root mean square error (RMSE) or mean absolute error (MAE)?—arguments against avoiding RMSE in the literature. *Geosci Model Dev* 7:1247–1250
- Frank E, Hall MA, Witten IH (2016) The WEKA workbench. Online appendix for “data mining: practical machine learning tools and techniques. https://waikato.github.io/weka-wiki/citing_weka/
- Kao CY, Loh CH (2013) Monitoring of long-term static deformation data of fei-tsu arch dam using artificial neural network-based approaches. *Struct Control Health Monit* 20:282–303
- Kuremoto T et al (2014) Time series forecasting using a deep belief network with. *Neurocomputing* 137:47–56
- Lin C et al (2019) Gaussian process regression-based forecasting model of dam deformation. *Neural Comput Appl* 31:8503–8518
- Lombardi G, Amberg F, Darbre G (2008) Algorithm for the prediction of functional delays in the behaviour of concrete dams. *Int J Hydropower Dams* 15(3):111–130
- Massinaei M et al (2014) Using data mining to assess and model the metallurgical efficiency of a copper concentrator. *Chem Eng Commun* 201:1314–1326
- Mata J (2011) Interpretation of concrete dam behaviour with artificial neural network and multiple linear regression models. *Eng Struct* 33(3):903–910
- Nguyen TT, Pham VD, Tenhunen J (2013) Linking regional land use and payments for forest hydrological services: a case study of Hoa Binh reservoir in Vietnam. *Land Use Policy* 33:130–140
- Pytharouli SI, Stiros SC (2005) Ladon dam (Greece) deformation and reservoir level fluctuations: evidence for a causative relationship from the spectral analysis of a geodetic monitoring record. *Eng Struct* 27(3):361–370
- Quinlan JR (1992) Learning with continuous classes. In: 5th Australian joint conference on artificial intelligence. Singapore
- Ranković V et al (2012) Modelling of dam behaviour based on neuro-fuzzy identification. *Eng Struct* 35:107–113
- Salazar F et al (2015) An empirical comparison of machine learning techniques for dam behaviour modelling. *Struct Saf* 56:9–17
- Salazar F et al (2017) Data-based models for the prediction of dam behaviour: a review and some methodological considerations. *Arch Comput Methods Eng* 24:1–21
- Sortis AD, Paoliani P (2007) Statistical analysis and structural identification in concrete dam monitoring. *Eng Struct* 29(1):110–120
- Su H et al (2015) Rough set-support vector machine-based real-time monitoring model of safety status during dangerous dam reinforcement. *Int J Damage Mech* 26(4):501–522
- Bui KTT et al (2018) A novel hybrid artificial intelligent approach based on neural fuzzy inference model and particle swarm optimization for horizontal displacement modeling of hydropower dam. *Neural Comput Appl* 29(12):1495–1506
- Vladimirov VB, Zaretskii YK, Orekhov VB (2003) A mathematical model for monitoring the rock-earthen dam of the Hoa Binh hydraulic power system. *Power Technol Eng* 37:161–166
- Wang Y, Witten I (1996) Induction of model trees for predicting continuous classes. Computer science working paper. University of Waikato, pp 13
- Were K et al (2015) A comparative assessment of support vector regression, artificial neural networks, and random forests for predicting and mapping soil organic carbon stocks across an afro-montane landscape. *Ecol Ind* 52:394–403
- Witten IH, Frank E, Hall MA (2011) Data mining: practical machine learning tools and techniques, 3rd edn. Morgan Kaufmann, Burlington
- Zhao E, Jin Y (2008) Dam deformation monitoring model and forecast based on hierarchical diagonal neural network. In: 4th International conference on wireless communications, networking and mobile computing
- Zheng D et al (2013) Integrated parameter inversion analysis method of a CFRD based on multi-output support vector machines and the clonal selection algorithm. *Comput Geotech* 47:68–77

Chapter 5

Simulation of the Hydrodynamic Regime of Aquaculture Development Zones Within Binh Dinh, Vietnam



Duy Vu Luu , Thi Ngoc Canh Doan , Khanh Le Nguyen ,
Ngoc Duong Vo , and Chau Van Truong 

Abstract Binh Dinh province is suitable for fishery, such as brackish seafood, because the province has a long coastline and many lagoons. However, its brackish seafood farming has been impacted by sea level rise, drought and salinization caused by climate change. For example, both low and high salinity negatively affect the growth of many brackish populations. In this research, the hydrodynamic regime and salinity spreading in the coastal areas are estimated based on the MIKE 21 model, a numerical model. The model is calibrated against tide levels and salinity records from 1st June 2010 to 11th June 2010. The validation period is from 1st June 2016 to 11th June 2016. The modelled output shows good agreement with the observed data at Quy Nhon station, Binh Dinh. The values of the Nash–Sutcliffe efficiency coefficient and correlation coefficient are very good, over 0.87. The verified model parameters are important data for the future salinity forecasting projects under climate change.

Keywords Hydrodynamic · Salinity · MIKE 21 · Binh Dinh

5.1 Introduction

Binh Dinh is a coastal province in South Central Vietnam. The province is in a very important strategic position in the socio-economic development of the Central region. It is also an important gateway to the Central Highlands, Southern Laos and Northeastern Cambodia, Thailand, and into the East Sea. The province has a

D. V. Luu (✉)

The University of Danang—University of Technology and Education, 48 Cao Thang, Danang, Vietnam

e-mail: ldvu@ute.udn.vn

T. N. C. Doan · K. Le Nguyen

The University of Danang—University of Economics, Danang, Vietnam

N. D. Vo · C. Van Truong

The University of Danang—University of Science and Technology, Danang, Vietnam

134 km long coastline interspersed with many lagoons and bays. There is a wide range of aquatic resources in Binh Dinh. Its waters have biodiversity and are rich in aquatic resources with hundreds of species. For example, there are 500 species of fish. Marine shrimp has 20 species. Therefore, in recent years, Binh Dinh has focused on the ocean economy and fisheries (Development, B.D.D.o.A.a.R.: Binh Dinh Fisheries Development Master Plan To2020 2020).

Binh Dinh has promoted the development of freshwater and brackish-water aquaculture Producers (Producers, V.A.o.S.E.a.: Binh Dinh: the sustainable development of brackish shrimp farming (in Vietnamese) xxxx). The environmental conditions, such as salinity, play a very important role in the growth of brackish-water and salt-water aquaculture (Tibblin et al. 2012). If the salt concentration in the water exceeds the allowable threshold, it will negatively impact on aquaculture. In many fish farms, the change in salinity has killed a large number of aquatic animals (Boamah et al. 2020). In addition, climate change in Vietnam has made salinity spread stronger in recent years. It directly impacts aquatic ecosystems as well as fish farming. Therefore, a hydrodynamic model and a salinity map for the aquaculture environment are necessary for planning for aquaculture development in Binh Dinh.

There are two main kinds of models for hydrodynamic processes, such as physical models and numerical models. In terms of the physical models, they can represent the phenomenon because they use laboratories with precise measuring instruments. Therefore, this method can represent mechanisms and phenomena that are difficult to observe in real conditions. However, it is very expensive to install and maintain the physical model. Numerical models refer to the use of computer codes based on the theoretical foundations and the most reliable conditions and scenarios. In recent decades, computing technologies have been developed significantly, which allows the numerical models to correctly simulate hydrodynamic problems. The numerical models usually use the finite element method, boundary element method, finite difference method, and finite volume method. They can be classified into different spatial dimensions, such as one-dimensional (1D) models and two-dimensional (2D) models.

This study uses a 2D numerical model because the model has been widely popular in simulating the hydrology and water quality processes of rivers, estuaries, and oceans. One example of a 2D numerical model is MIKE21. Danish MIKE 21 is developed and maintained by the Danish Hydraulic Institute. It is a two-dimensional model to simulate the hydrodynamics, transport of pollutants, thermal plumes, and water quality parameters of rivers, estuaries, and oceans (Gao et al. 2018; Zhang et al. 2020; Kim et al. 2017; Remya et al. 2012).

5.2 The Study Area

Binh Dinh province, shown on Fig. 5.1, located in Vietnam South Central Coast, has diverse types of terrain and a dense system of streams and rivers. The province is influenced by the tropical monsoon climate. Climate in Binh Dinh is typified by the humid

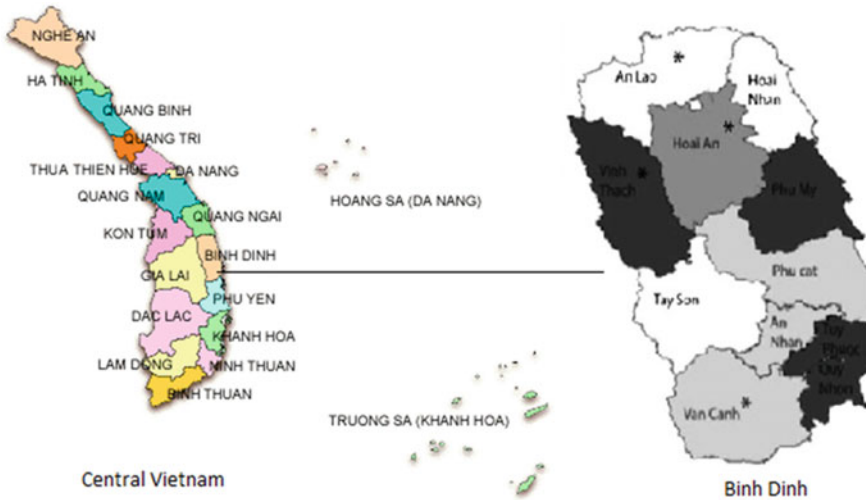


Fig. 5.1 Binh Dinh province

tropical monsoon. Due to the complexity of the terrain, the monsoon winds change direction and intensity when reaching the province. The rainy season runs from September to December. In mountainous regions, there is an additional rainy season lasting from May to August under the influence of the rainy season in the Central Highlands. The dry season in Binh Dinh lasts from January to August. The annual average rainfall in mountainous districts is 2000–2400 mm, and in coastal regions it is 1751 mm. The rainfall tends to decrease gradually from mountainous regions to coastal areas and from the northwest to the southeast. Rivers in the Binh Dinh province are derived from the high mountains of the eastern slope of the Annamite Mountains. Rivers are small and short, having steep slopes and low silt concentration.

Binh Dinh has a 134 km coastline, a 2500 km² territorial sea and a 40,000 km² exclusive economic zone. Along the coast of Binh Dinh, there are some estuaries, such as Tam Quan, De Gi and Quy Nhon. Moreover, it has many lagoons, such as Tra O lagoon, covering an area of about 1200–1400 ha, Thi Nai lagoon (5060 ha), De Gi lagoon (1600 ha) and the Tam Quan estuary, covering an area of about 300 ha. The Thi Nai lagoon is known as a nursery for endangered aquatic species. The Tam Quan estuary is suitable for brackish water aquaculture such as shrimp and crab farming, fish and oysters. In addition, there are about 2283 ha for brackish water aquaculture, such as white leg shrimp and black tiger shrimp.

In recent years, salinity intrusion has negatively affected aquaculture activities in Binh Dinh province. Salinity intrusion is one of the main reasons for the tons of dead fish in the Tuy Phuoc district, Binh Dinh province.

Salinity intrusion is observed in estuaries, land and sea in Binh Dinh. It is affected by river flows, tidal regimes, river bed slopes and topography. Because tidal dynamics can lead to turbulent mixing based on saltwater transportation, tides are considered one of the most powerful sources of mixed fresh and saltwater. Therefore, it is the

main source of saltwater intrusion. The tidal regime is unequal at the study site. At Quy Nhon station, the number of tidal days lasts from 18 to 22 days. The high tides last longer than the low tide. The variation in high and low tidal amplitudes is negligible. During May and June, the tidal regime at Thi Nai lagoon is similar to that in Quy Nhon. The heights of the tidal peaks in both locations do not change significantly.

5.3 Methodology

MIKE 21 is a proven computer program available worldwide to estimate flows, waves, sediments and ecology in rivers oceans, coasts and estuaries in two dimensions. The spectral wave (SW) module, the hydrodynamic (HD) module and the Advection–Dispersion (AC) module of MIKE 21 are adopted in this study. The SW module can be used to simulate wind generated waves (Xiang et al. 2019). The HD module is the foundation part of the MIKE 21 model, and generates the hydrodynamic input for other modules of MIKE 21, such as the AD and Water Quality modules (Warren and Bach 1992). The AD module can simulate suspended substances, including salinity and temperature, in an aquatic environment (Warren and Bach 1992).

5.3.1 The Spectral Wave (SW) Module

The SW module is developed to estimate the growth, decay and transformation of wind based on waves in offshore and coastal areas. The SW module has a wide range of formulations and parameters. Two formulations are available: a directional decoupled parametric formulation (Holthuijsen et al. 1989) and a fully spectral formulation (Young 1999). The first is also suitable for the nearshore zones, while the second one is used for the offshore areas. In this study, the SW module is used to analyse the growth of waves under wind action. The wave boundary condition set includes wave height, wave crest and wave direction.

5.3.2 The Hydrodynamic (HD) Module

The HD module can calculate flows and distributions of temperature and salt, which are influenced by different functions and boundary conditions. The module is a 2-dimensional model and based on the numerical solution of the two-dimensional incompressible Reynolds averaged Navier–Stokes equations with the assumptions of Boussinesq and hydrostatic pressure. It uses a cell-centred finite volume method to model the spatial discretisation of the primitive equations.

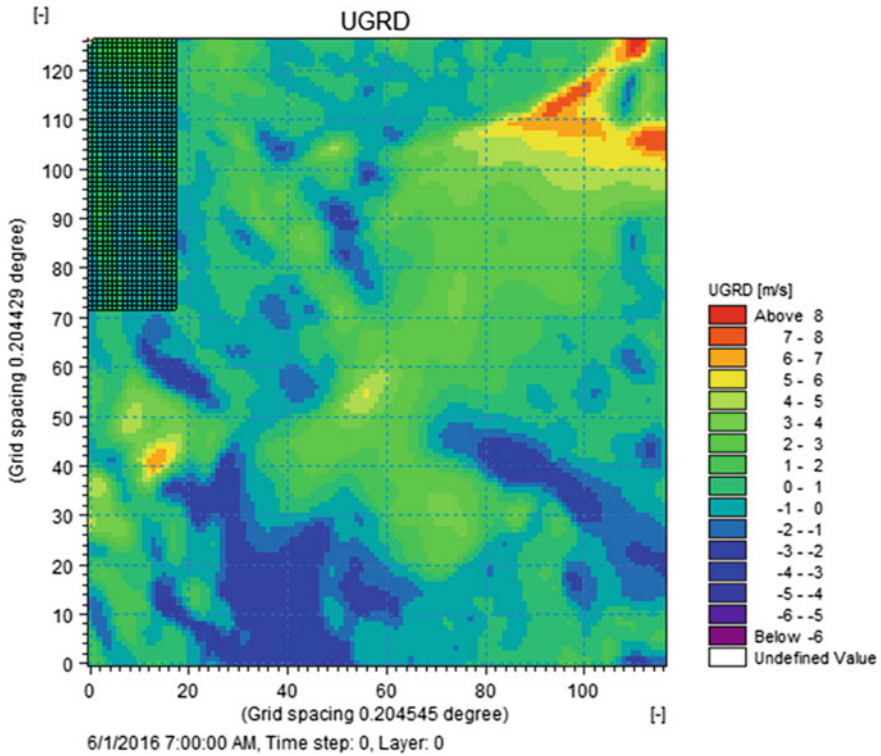


Fig. 5.2 Wind data

5.3.3 The Advection–Dispersion (AD) Module

The AD module can simulate suspended substances, including salinity and temperature based on a two-dimensional form of the QUICKEST finite difference scheme (Warren and Bach 1992). The module uses points of the grid covering the study site to estimate the concentration of the substance. Currents and water depths at the points are generated by the HD module. Other input data are substance concentrations at outfalls and boundaries as well as discharge quantities at outfalls.

5.3.4 The Detailed Bathymetry

Bathymetry plays an important role in hydrodynamic estimation based on Mike 21. Bathymetric data is obtained and processed in an XYZ format from old bathymetric maps before it is added to the Mesh Generator tool in MIKE Zero. The unstructured finite-element model domain has 29,607 elements and 17,397 nodes. The study

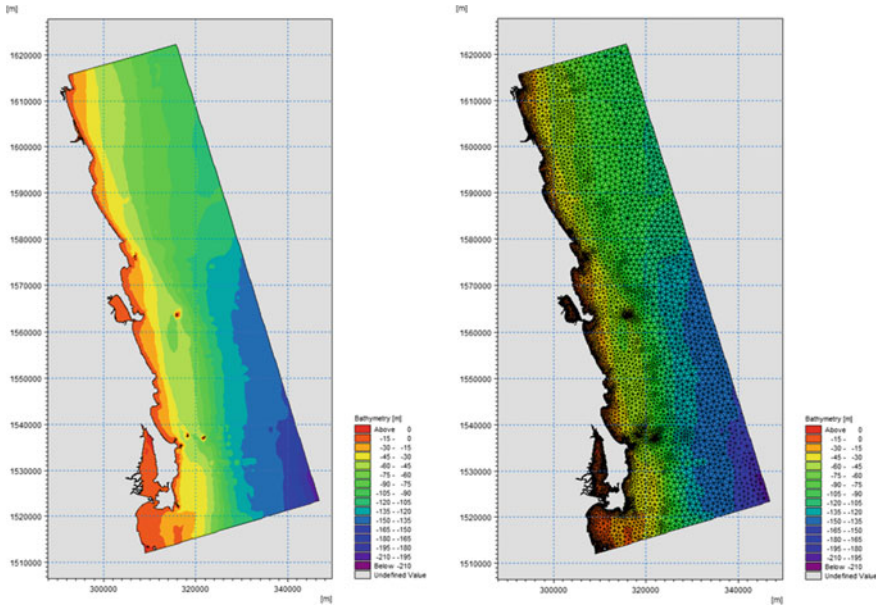


Fig. 5.3 The bathymetry (left) and computational mesh scheme (right) of the study area

carefully considers the trade-off between computational time and numerical stability. When the number of elements increases, the model reduces the simulation time step but requires more numerical effort. The bathymetry and grid resolution are shown on Fig. 5.3.

5.3.5 *Input Data*

The input data for the SW module has wind data and boundary conditions provided by the Southern Institute of Water Resources Research, Vietnam. The boundary conditions include average wave height, wave period and wave direction.

For the AD module, the input data includes the salinity value and temperature. The salinity value is 0 PSU for flows from rivers in the area. Salinity in the coastal waters is divided into 3 regions with different salinities: offshore (35 PSU); inshore (32 PSU) and near shore, lagoon, bay (30 PSU). The temperature over the study site is settled at 30 °C.

In terms of the HD module, the input data consists of wind speed, wave height, boundary condition, viscosity coefficient and roughness coefficient. Wind data is observed in the coastal area and the offshore areas in Binh Dinh. The wind data is shown on Fig. 5.2. Wave data is calculated by the SW module. Boundary conditions include sea-level conditions and river discharges. Sea-level conditions are

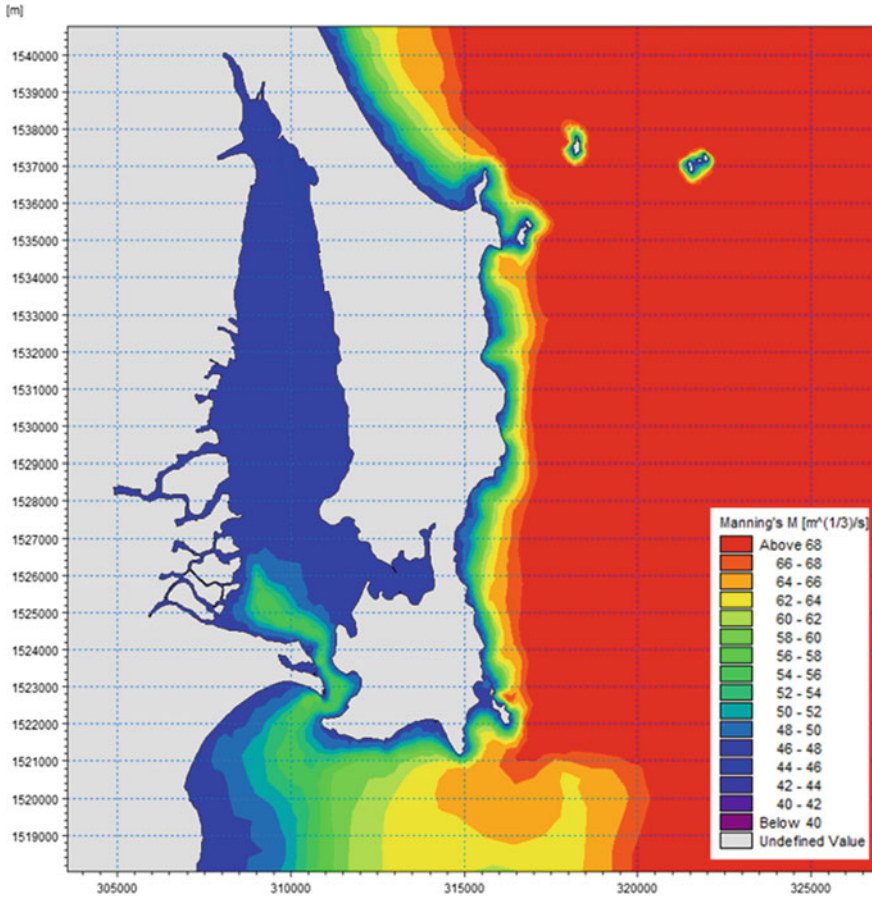


Fig. 5.4 The Manning's roughness coefficients at the study site

provided by the Southern Institute of Water Resources Research, Vietnam and hourly discharge, shown on Fig. 5.5, is recorded at the Con River, Ha Thanh River, Lai Giang River and La Tinh River. The Manning's roughness coefficients built into the whole grid domain represent each seabed topography and region (Fig. 5.4).

5.4 Model Evaluation Criteria

The model parameters are determined by the trial-error method. The selected parameters allow the model calculated results being close to the observed data. The simulation results will be evaluated through the Nash-Sutcliffe efficiency coefficient (E) and correlation coefficient (R).

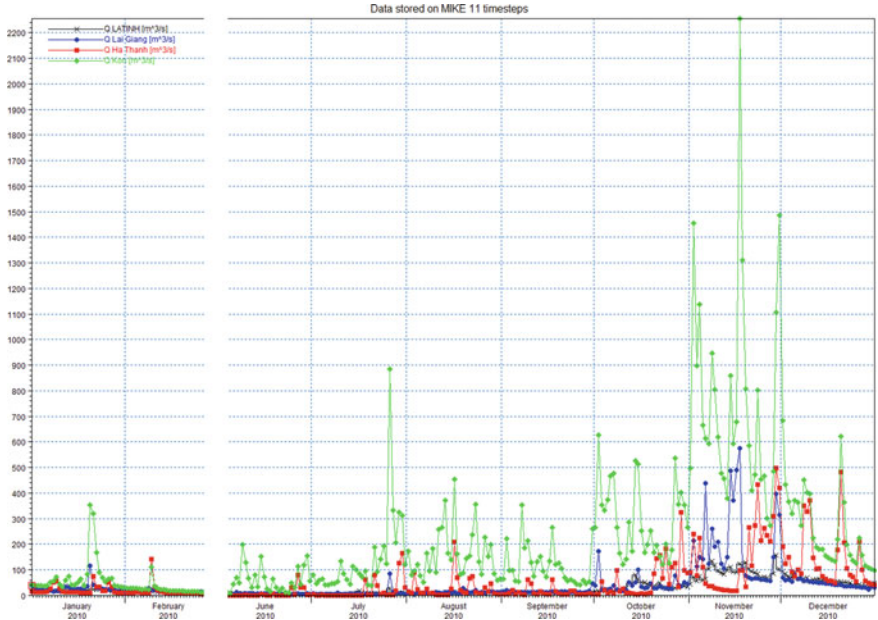


Fig. 5.5 Hourly discharge recorded at Con River, Ha Thanh River, Lai Giang River and La Tinh River

$$E = 1 - \frac{\sum_{i=1}^n (X_{obs,i} - X_{model,i})^2}{\sum_{i=1}^n (X_{obs,i} - \bar{X}_{obs})^2} \tag{5.1}$$

$$R = \frac{\sum_{i=1}^n (X_{obs,i} - \bar{X}_{obs}) \cdot (X_{model,i} - \bar{X}_{model})}{\sqrt{\sum_{i=1}^n (X_{obs,i} - \bar{X}_{obs})^2 \cdot (X_{model,i} - \bar{X}_{model})^2}} \tag{5.2}$$

5.5 Model Calibration and Validation

5.5.1 Model Calibration

The HD and AD modules are calibrated against the observed tide levels and salinity concentration at Quy Nhon station. The calibration period was from 1st June 2010 to 11th June 2010. The calibration process aims to adjust and select parameters of the HD and AD modules (Table 5.1).

Table 5.1 Model evaluation criteria

Evaluation criteria	Very good	Good	Satisfactory	Unsatisfactory
Nash	> 0.85	0.65–0.85	0.5–0.65	< 0.5
R	> 0.95	0.85–0.95	0.75–0.85	< 0.75

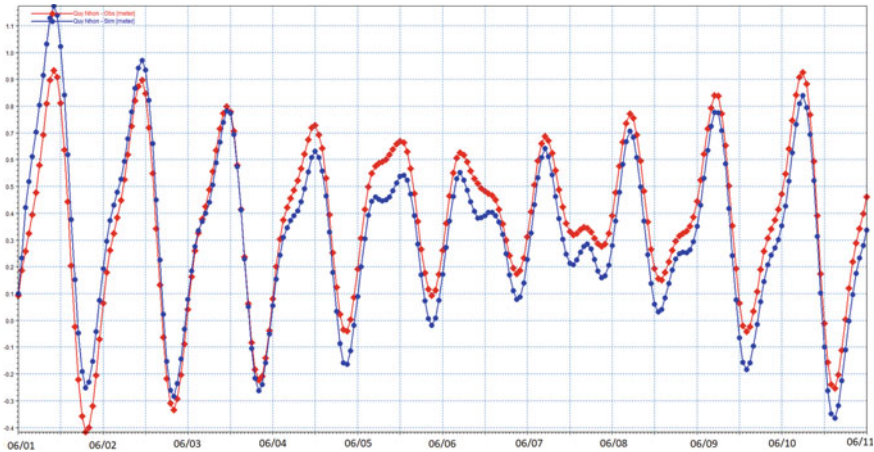


Fig. 5.6 Calibration results for tide levels from 1st June 2010 to 11th June 2010

The results show a good agreement between the modelled data and the observations shown on Figs. 5.6 and 5.7 and Table 5.2. The highest amplitude difference between the modelled and observed tidal levels is about 0.25 m. The highest observed tide level is 1.16 m, while its counterpart is 0.92 m. Similarly, the modelled and observed salinity concentration values share the same trend in this station, as shown on Fig. 5.7. In addition, the evaluation criteria shown in Table 5.2 indicate that the model performance is very good. These indicate that the calibrated parameters are reasonable. However, the model usually underestimates the tide levels.

5.5.2 Model Validation

The model is validated by another set of data on the tide levels and salinity concentration collected in June 2016 for Quy Nhon station.

Figures 5.8 and 5.9 and Table 5.3 compare the modelled values and observations from 1st June 2016 to 11th June 2016. The modelled tide levels and the observed data show a very good fit. The comparison demonstrates the model has the ability to estimate the tide levels on this study side. Therefore, the selected model parameters are useful for future research. In terms of salinity concentration, there are just a few

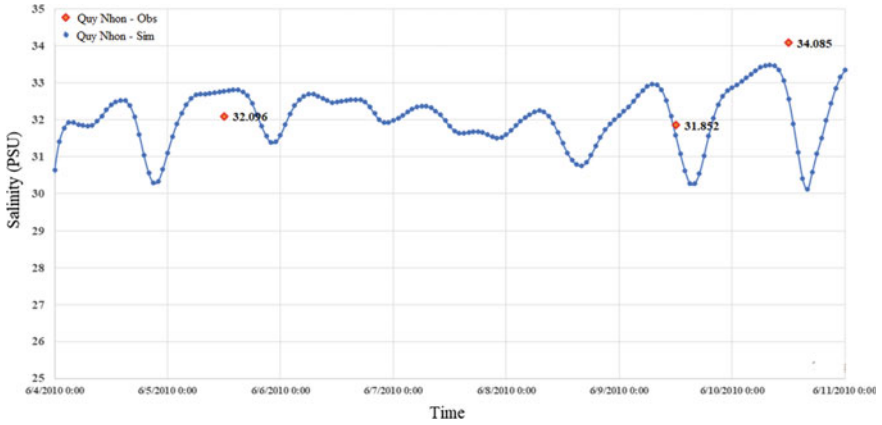


Fig. 5.7 Calibration results for salinity concentration from 1st June 2010 to 11th June 2010

Table 5.2 The calibration performances

Evaluation criteria	Nash	R
Results	0.875	0.950
	Very good	Very good

measured data points, but it is clear that the model can predict the trend in changes of salinity concentration in this station.

In the following, the validated model has the ability to model the impacts of future climatic changes on the hydrodynamic and salinity characteristics of Binh

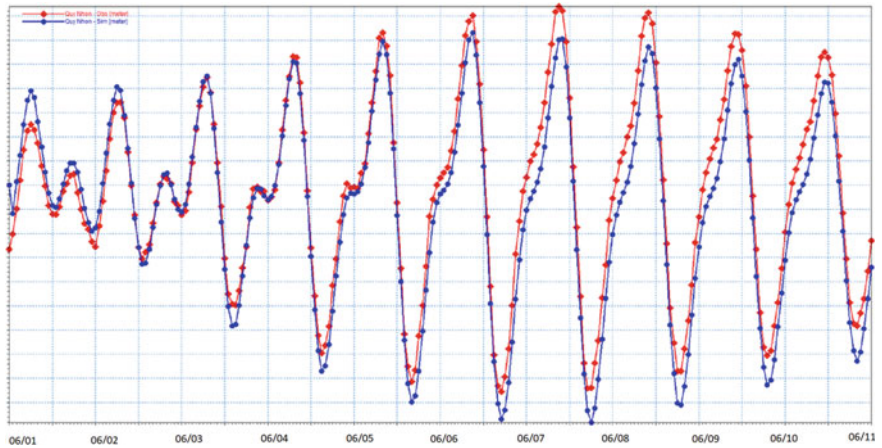


Fig. 5.8 Validation results for tide levels from 1st June 2016 to 11th June 2016

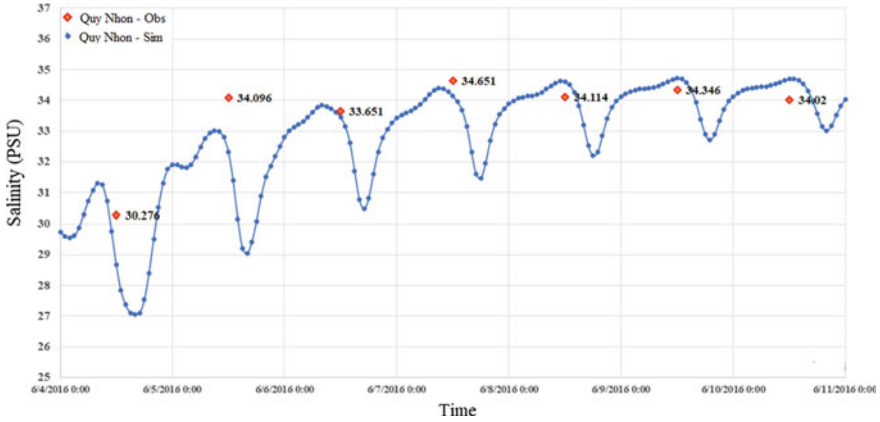


Fig. 5.9 Validation results for salinity concentration from 1st June 2016 to 11th June 2016

Table 5.3 The validation performances

Evaluation criteria	Nash	R
Results	0.931	0.980
	Very good	Very good

Dinh. Moreover, this proposed model can be adopted to estimate different quality prediction scenarios for Binh Dinh.

5.6 Conclusion

Changes in hydrodynamics and salinization caused by climate change have led to significant damage to freshwater aquaculture brackish, threatening the lives of people in the periphery. It is crucial to develop an accurate model to predict the disaster and allow the Government to give necessary response solutions. The study very well evaluates the hydrodynamic regime and the salt propagation based on the Mike 21 model in Binh Dinh province. The model is calibrated and tested in 2010 and 2016. The verified model parameters are important information in developing saline zoning maps, forecasting warnings under the impacts of natural disasters and climate change.

References

- Boamah GA, Wang T, Chowdhury IA, Luo X, Huang M, Xu C, Ke C, You W (2020) Sub-low salinity impact on survival, growth and meat quality of the Pacific abalone (*Haliotis discus hannai*) and hybrids. *Aquac Res* 51:5184–5193
- Development, B.D.D.o.A.a.R. (2020) Binh Dinh fisheries development master plan to 2020
- Gao Q, He G, Fang H, Bai S, Huang L (2018) Numerical simulation of water age and its potential effects on the water quality in Xiangxi Bay of Three Gorges Reservoir. *J Hydrol* 566:484–499
- Holthuijsen L, Booij N, Herbers T (1989) A prediction model for stationary, short-crested waves in shallow water with ambient currents. *Coast Eng* 13:23–54
- Kim J, Lee T, Seo D (2017) Algal bloom prediction of the lower Han River, Korea using the EFDC hydrodynamic and water quality model. *Ecol Model* 366:27–36
- Producers, V.A.o.S.E.a.: Binh Dinh: the sustainable development of brackish shrimp farming (in Vietnamese)
- Remya P, Kumar R, Basu S, Sarkar A (2012) Wave hindcast experiments in the Indian Ocean using MIKE 21 SW model. *J Earth Syst Sci* 121:385–392
- Tibblin P, Koch-Schmidt P, Larsson P, Stenroth P (2012) Effects of salinity on growth and mortality of migratory and resident forms of Eurasian perch in the Baltic Sea. *Ecol Freshw Fish* 21:200–206
- Warren I, Bach HK (1992) MIKE 21: a modelling system for estuaries, coastal waters and seas. *Environ Softw* 7:229–240
- Xiang Y, Fu ZM, Meng Y, Zhang K, Cheng ZF (2019) Analysis of wave clipping effects of plain reservoir artificial islands based on MIKE21 SW model. *Water Sci Eng* 12:179–187
- Young IR (1999) Wind generated ocean waves. Elsevier
- Zhang D, Han D, Song X (2020) Impacts of the Sanmenxia dam on the interaction between surface water and groundwater in the lower Weihe River of Yellow River watershed. *Water* 12:1671

Chapter 6

Prediction of Suspended Sediment Concentration by Artificial Neural Networks at the Vu Gia–Thu Bon Catchment, Vietnam



Duy Vu Luu 

Abstract Suspended sediment concentration (SSC) is a key hydrological phenomenon that influences river engineering sustainability. Sediment has a significant impact on many water resources engineering problems, such as reservoir design and water quality. The approaches for estimating sediment based on the characteristics flow and sediment have some limitations due to lack of multiple observed factors. Therefore, an artificial neural network (ANN) model is used in this study to estimate monthly SSC at the catchment. The model adopts monthly observed time series of river discharge (Q) and SSC at the Vu Gia–Thu Bon catchment in Vietnam. The effectiveness of the model was evaluated using the Nash–Sutcliffe model efficiency coefficient (NSE), Root Mean Squared Error (RMSE) and Mean Absolute Error (MAE). The results show that ANN may be used as a competent tool to forecast SSC.

Keywords ANN · SSC · Vu Gia–Thu Bon

6.1 Introduction

Changes of the sediment dynamics in the world’s major river basins can have serious impact on humans and aquatic biota. For example, reservoir sedimentation has negative impact on dam efficiency. It can reduce the ability of reservoirs to produce energy and control downstream flood (Schmitt et al. 2016). Therefore, sediment is a key issue that impacts many water resource engineering projects, such as reducing reservoir capacity (Buyukyildiz and Kumcu 2017). There are many methods proposed to estimate sediment in rivers.

D. V. Luu (✉)

The University of Danang—University of Technology and Education, 48 Cao Thang, Danang, Vietnam

e-mail: ldvu@ute.udn.vn

Several models have been developed for predicting SSC, such as direct measurements, physical-based, empirical and machine learning (ML) models. First, the direct measurements seem to be the most reliable method for estimating suspended sediment load, however it is difficult to sample sediment. Moreover, sophisticated and pricey measurement instruments are required because of the large variability in the river system (Fan and Morris 1998). Due to these restrictions, the Vu Gia–Thu Bon catchment has a low quality of sediment observation. Second, the physics-based models use equations of conservation of mass for water and sediment and momentum for flow, but these equations must be solved numerically and require more detailed field data for reliable forecasts (Kavvas et al. 2006). The data are seldom accessible, particularly in rivers where there is less gauging stations, such as the Vu Gia–Thu Bon. In addition, because of errors in measuring the input parameters, using empirical techniques can result in uncertainties in the final findings (Aytek and Kişi 2008). Finally, machine learning (ML) models have been effectively used in sedimentation research in many areas over the world (Bhattacharya et al. 2007; Azamathulla et al. 2010). The ML models have many advantages. For example, they require less data. They are adaptable in capturing the nonlinearity of sediment processes. Lafdani et al. adopted artificial neural networks (ANN) and support vector machine (SVM) models to forecast daily SSL in the Doiraj River, Iran (Lafdani et al. 2013). Kumar et al. employed an ANN model for rainfall-runoff-sediment modelling (Bhattacharya et al. 2007). Khosravi et al. used stand-alone and hybrid ML models to assessed hourly sediment load influx at the Adean catchment in Chile (Khosravi et al. 2018). The ANN methodology performs better than other previous methods in many cases since it does not require an explicit mathematical explanation of the underlying natural process in rivers. Therefore, ANN models are used in this study.

6.2 Theoretical Review

The ANN model has a great potential for estimation of many problems, such as hydrological predictions (Seckin et al. 2013). The model consists of an input layer, one or more hidden layers, and an output layer. It does not require any direct data-flow loop. In the layers, there are the nodes which are fully or partially connected to each other by linking weights. The input layer gets the input data from the outside. Then information is transferred into the hidden layers. In which, data at each node is multiplied by the weight and added with a bias value before going through an activation function. The data is continuously forwarded until it reaches the output layer.

An ANN model can adopt one and more hidden layers. However, some research indicate that one hidden layer is sufficient for ANNs to model complex nonlinear processes (Cybenko 1989; Hornik et al. 1989). Therefore, an ANN model with a one or two-hidden-layer was used in this study. There is no rule universally accepted for selecting the number of nodes in the hidden layer (Kavzoglu 2001).

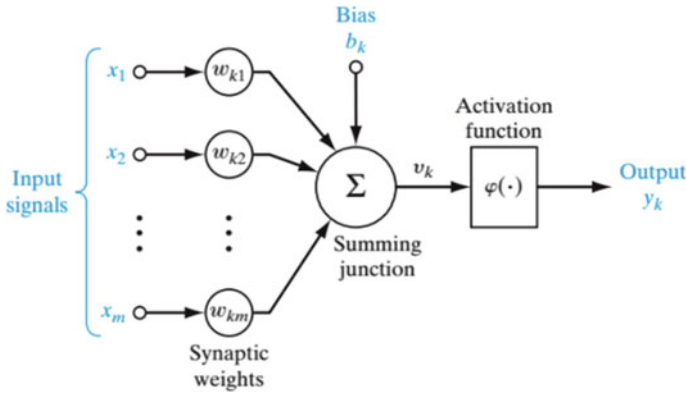


Fig. 6.1 An ANN with one hidden layer (https://www.kaggle.com/mirichoi0218/ann-making-model-for-binary-classification.xxxx)

There are some kinds of the activation function, such as Log-sigmoid transfer function, Hyperbolic tangent transfer function, ReLU (Rectified Linear Unit) activation function, and Purelin Transfer function. The Purelin Transfer function is a simply a linear function. The most common nonlinear functional forms are the Log-sigmoid transfer function and ReLU (Dawson and Wilby 1998). After comparing the ANN models with different activation function, the ReLU and Purelin Transfer function are adopted in nodes in the hidden and output layer respectively (Fig. 6.1).

The operation of a node k at the hidden layer is calculated as:

$$I_k = \sum w_{ki}x_i + b_k \tag{6.1}$$

$$y_k = \varphi(I_k) \tag{6.2}$$

in which y_k is the output of the node k , φ is an activation function, x_i is an input i of the node k , w_{ki} is the weight, b_k is the bias.

The weights are the most important factor in converting an input to affect the output. A training algorithm allows the model to adjust the weights in order to find the optimal weight value which can minimize the error of the network outputs.

6.3 Study Area

The Vu Gia-Thu Bon catchment is one of the biggest catchments in the center of Vietnam, with a drainage basin of nearly 10,000 km². The climate type in the region is tropical monsoon. The flood season lasts three months and accounts for 80% of yearly flow. The dry season lasts nine months but only accounts for 20% of the yearly flow.

Da Nang, Hoi An and Tam Ky are the three major cities in the area. The area has been industrialized as well as agriculturalized. The changes in land use included a decline in forests land and a rise in agricultural land and residential land. The catchment is characterized by rough topography, frequent floods, and mountainous features, with minimal plant cover in the headwaters. When major floods occur in the area protective plant cover is mostly missing.

6.4 Model Development

The proposed model uses continuous time series data from the Thanh My station, comprising monthly discharge data (Q) and monthly suspended sediment concentration (SSC). The data is divided into three time series datasets for the training, verifying, and testing states. Monthly data from 1978 to 2002 (24 years) and data from 2003 to 2011 (8 years) are utilized in the training and verifying sets respectively. The network weights and biases are updated using the training subset. An early stopping strategy is adopted using the validation subset to avoid overtraining or overfitting. The strategy allows users to specify an large number of training epochs, also stop training when the model performance stops. Finally, the testing subset is used to assess model performance (Fig. 6.2).

It is necessary for assess lag times for the forecasting procedure. The input combinations are shown in Table 6.1. They enable the research to forecast the SSC value one month ahead at time t .

The ANN models use one input layer, one output layer and one and more hidden layers to forecast SSC. The models also adopt the Relu activation and the linear activation in the hidden layers.

The selection of hyperparameters, such as number of nodes in the hidden layer, the number of batch-size, epoches and hidden layers, are crucial to select the best model. The grid search (GS) method is a solution to optimize parameters. GS develops a model for each combination of hyperparameters in order to determine the best hyperparameters.

The optimization algorithm, Adam, is used to turn the weights in the training stage. This algorithm is widely popular in much research (Table 6.2).

The model evaluation criteria include the Nash–Sutcliffe model efficiency coefficient (NSE), Root Mean Squared Error (RMSE) and Mean Absolute Error (MAE). NSE ranges from minus infinity to one. When NSE equals one, there is a perfect match. The value of the RMSE is never negative. Theoretically, when the RMSE value is 0, there are no errors. The lower the MAE number means the better the model.

$$NSE = 1 - \frac{\sum_{i=1}^n (\hat{y}_t - y_t)}{\sum_{i=1}^n (\hat{y}_t - \bar{y})} \quad (6.3)$$

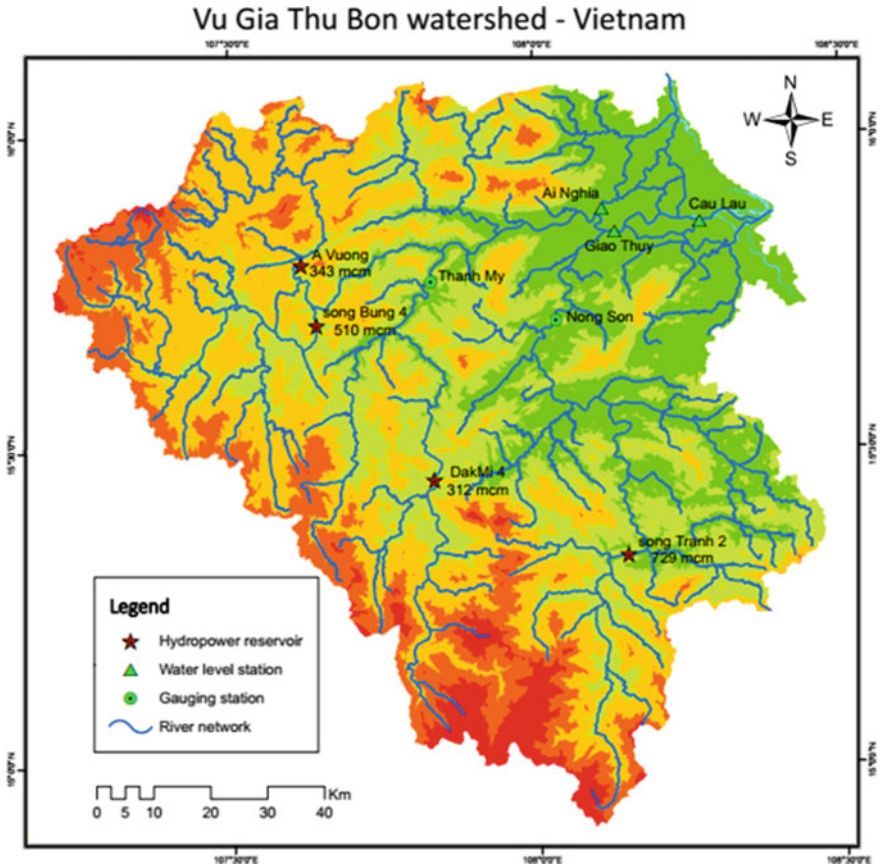


Fig. 6.2 Vu Gia Thu Bon catchment

Table 6.1 The input combinations

Model	The input combinations
S ₁	SSC _{t-1}
SQ ₁	SSC _{t-1} , Q _{t-1}
S ₂	SSC _{t-1} , SSC _{t-2}
SQ ₂	SSC _{t-1} , SSC _{t-2} , Q _{t-1} , Q _{t-2}
S ₃	SSC _{t-1} , SSC _{t-2} , SSC _{t-3}
SQ ₃	SSC _{t-1} , SSC _{t-2} , SSC _{t-3} , Q _{t-1} , Q _{t-2} , Q _{t-3}

$$RMSE = \sqrt{\frac{1}{n} \sum_{i=1}^n \hat{y}_i - y} \tag{6.4}$$

$$MAE = \frac{\sum_{i=1}^n |y_i - \hat{y}_i|}{n} \tag{6.5}$$

Table 6.2 The proposed ANN models

Items	Details
Input variables	Monthly SSC and Q in Thanh My station
Output variable	Monthly SSC in Thanh My station
Training parameters	Number of input neurons: from 1 to 6 Number of hidden neurons: variety Number of hidden layers: 1 or 2 Learning rate: 0.01 Transfer function of hidden layer: Relu Transfer function of output layer: Purelin Transfer Training algorithm: Adam The number of epochs: variety Early stopping: yes

where \hat{y}_t is the observed discharge, y_t is the modeled discharge, and \bar{y}_t is the mean of observed discharge.

6.5 Model Results

Time series comparison of measured data and ANN predicted data for calibration period shown in Fig. 6.3. The values of MAE, RMSE, NSE are from Table 6.3.

Table 6.3 illustrates how the ANN models with different architecture perform. The performance of the models changes when hyperparameters change. The SQ₂ model offers the best MAE, RMSE, NSE value. According to the comparison between the

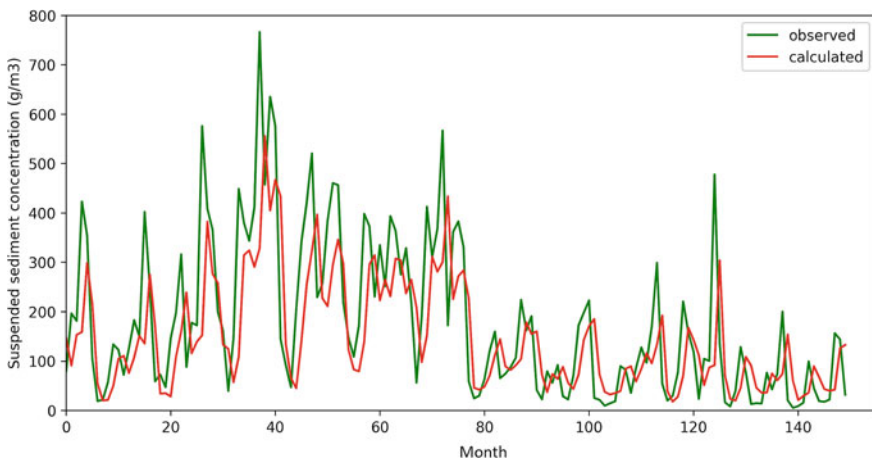


Fig. 6.3 Comparison between the modelled and observed SSC for testing period (the SQ₂ model)

Table 6.3 Performance of the ANN models

Station	Model	Model parameters	Training			Testing		
			MAE (g/m ³)	RMSE (g/m ³)	NSE	MAE (g/m ³)	RMSE (g/m ³)	NSE
Thanh My	S ₁	Structure: 1-7-1 Epoch: 55 Batch_size: 11	31.335	52.195	0.317	86.29	128.566	0.305
	SQ ₁	Structure: 2-5-1 Epoch: 50 Batch_size: 10	29.359	50.051	0.372	85.919	121.808	0.358
	S ₂	Structure: 2-3-1 Epoch: 62 Batch_size: 6	31.178	51.263	0.345	92.565	133.613	0.280
	SQ ₂	Structure: 4-4-1 Epoch: 67 Batch_size: 8	28.119	48.111	0.427	85.007	119.133	0.422
	S ₃	Structure: 3-3-1 Epoch: 66 Batch_size: 10	31.139	52.271	0.318	93.620	134.343	0.275
	SQ ₃	Structure: 6-9-1 Epoch: 60 Batch_size: 10	29.233	49.273	0.395	86.462	122.687	0.375

measured and ANN predicted data on Fig. 6.3. Therefore, the SQ₂ model is the best for Thanh My.

Figure 6.3 illustrates the comparison between the observed data and the predicted SSC based on the SQ₂ model from 1978 to 2007. The observed data and the predicted data follow a similar pattern. However, the ANN model sometimes undervalues the SSC values.

6.6 Conclusion

The ANN model is developed in this study to create SSC. The six ANN models are built and compared to determine which one is best for the catchment. MEA, RMSE, and NSE are the model evaluation criteria. All the scenarios execute admirably, and there are no notable disparities in the outcomes among them. The scenario SQ₂ is slightly better than the others, and it was chosen to test the model in the testing dataset with assurance.

To obtain reliable results, the ANN model just needs two input variables: SSC and discharge. This is a benefit since there isn't enough precise data in this catchment, such as topographical and hydrological data. Despite differences between the

predicted data and observation, the model is capable to producing SSC that is relatively precise. As a result, the ANN model is a valuable tool for understanding the trends of SSC at the Vu Gia-Thu Bon catchment.

References

- Aytek A, Kişi Ö (2008) A genetic programming approach to suspended sediment modelling. *J Hydrol* 351:288–298
- Azamathulla HM, Ghani AA, Chang CK, Hasan ZA, Zakaria NA (2010) Machine learning approach to predict sediment load—a case study. *Clean: Soil, Air, Water* 38:969–976
- Bhattacharya B, Price R, Solomatine D (2007) Machine learning approach to modeling sediment transport. *J Hydraul Eng* 133:440–450
- Buyukyildiz M, Kumcu SY (2017) An estimation of the suspended sediment load using adaptive network based fuzzy inference system, support vector machine and artificial neural network models. *Water Resour Manage* 31:1343–1359
- Cybenko G (1989) Approximation by superpositions of a sigmoidal function. *Math Control Signals Syst* 2:303–314
- Dawson CW, Wilby R (1998) An artificial neural network approach to rainfall-runoff modelling. *Hydrol Sci J* 43:47–66
- Fan J, Morris GL (1998) *Reservoir sedimentation handbook: design and management of dams, reservoirs, and watersheds for sustainable use*. McGraw-Hill
- Hornik K, Stinchcombe M, White H (1989) Multilayer feedforward networks are universal approximators. *Neural Netw* 2:359–366
- <https://www.kaggle.com/mirichoi0218/ann-making-model-for-binary-classification>
- Kavvas M, Yoon J, Chen Z, Liang L, Dogrul E, Ohara N, Aksoy H, Anderson M, Reuter J, Hackley S (2006) Watershed environmental hydrology model: environmental module and its application to a California watershed. *J Hydrol Eng* 11:261–272
- Kavzoglu T (2001) An investigation of the design and use of feed forward artificial neural networks in the classification of remotely sensed images. University of Nottingham, Nottingham
- Khosravi K, Mao L, Kisi O, Yaseen ZM, Shahid S (2018) Quantifying hourly suspended sediment load using data mining models: case study of a glacierized Andean catchment in Chile. *J Hydrol* 567:165–179
- Lafdani EK, Nia AM, Ahmadi A (2013) Daily suspended sediment load prediction using artificial neural networks and support vector machines. *J Hydrol* 478:50–62
- Schmitt RJ, Bizzi S, Castelletti A (2016) Tracking multiple sediment cascades at the river network scale identifies controls and emerging patterns of sediment connectivity. *Water Resour Res* 52:3941–3965
- Seckin N, Cobaner M, Yurtal R, Haktanir T (2013) Comparison of artificial neural network methods with L-moments for estimating flood flow at ungauged sites: the case of East Mediterranean River Basin, Turkey. *Water Resour Manage* 27:2103–2124

Chapter 7

Criteria Affecting Groundwater Potential: A Systematic Review of Literature



Dang Tuyet Minh 

Abstract Groundwater is an indispensable source of freshwater that contributes significantly to the total annual water supply. Therefore It is necessary to maintain, develop and utilize groundwater in a region. This paper has discussed the literature review in groundwater potential zone studies using Multicriteria decision analysis techniques and Geographic Information System (GIS). A systematic review of directly relevant research is presented. From the review of research papers, it is evident that 63 factors were used in the past years for exploring the groundwater potential, of which eight almost always present including geology, lineaments, geomorphology, soil, land use/land cover, rainfall, drainage density, and slope. This paper can be used to choose the criteria affecting groundwater formation in groundwater potential zoning studies using GIS, and Multicriteria Decision Making (MCDM) technique.

Keywords Multicriteria decision making (MCDM) · AHP · Groundwater potential zone · Groundwater

7.1 Introduction

Groundwater is one of the most essential natural resources supporting human health and economic development. Because of its continuous availability and excellent natural quality, it becomes an important source of water supply in both urban and rural areas of any country (Todd and Mays 2004). The quantitatively and qualitatively practical development of groundwater resources will have a significant effect on the improvement of the community's livelihood. Generating a groundwater potential map plays an important role to enhance the sustainable management of groundwater resources. Thus, it is critical to be able to quickly identify of groundwater potential

D. T. Minh (✉)
Thuyloi University, 175 Tay Son Street, Hanoi, Vietnam
e-mail: dtminh@tlu.edu.vn

to overcome water scarcity or overexploitation in the study areas. In the past, most of the hydrogeological investigations and groundwater potential assessments have been done traditionally, using in situ measurement which is not feasible.

Recently, numerous studies have been conducted using index-based models and quantitative approaches for evaluating groundwater prospect regions (Ahmad et al. 2020; Gyeltshen et al. 2020; Thomas and Duraisamy 2018). Besides, Aggarwal et al. and Pani et al. found remote sensing and GIS as promising tools for groundwater exploration (Aggarwal et al. 2013; Pani et al. 2016). However, several scientists insisted that the Analytic Hierarchy Process (AHP) is the most popular and widely used of Multi-Criteria Decision Analysis technique to identify groundwater prospecting areas (Al-Abadi et al. 2017; Razandi et al. 2015). According to Saaty, the AHP is a method of “measurement through pairwise comparisons and depends on the judgments of experts to acquire priority scales” (Saaty 2008). The AHP technique was used to assign the relative importance of each factor for zoning groundwater potential recharging areas. The definition of criteria and the calculation of their weight are central in this approach to evaluating the alternatives. Recently, there are a few studies that mention them. Various publications were referred in order to select the parameters that influence the groundwater potentiality (Arulbalaji et al. 2019; Das and Pal 2020; Murmu et al. 2019). Accordingly, some parameters are the prime factors considered to support the process of potential zone identification. These criteria show the geological formation, and hydrological properties of the groundwater. In addition to the research that adopts the groundwater causative parameters in line with the physical conditions of the study area (Ahmadi et al. 2020; Allafta et al. 2020; Doke et al. 2021; Melese and Belay 2022), some studies divided the influence criteria into two groups including climate change and human activities (Li et al. 2014; Chen et al. 2010; Hsu et al. 2012). Several studies tend to choose influence criteria to focus on some critical features such as geology, topography, or hydrology while ignoring other factors that also have a significant impact on groundwater potentials such as land use/ land cover or rainfall. Typically, Hamdani and Baali chose 3/4 alternatives that are geology-related criteria (Hamdani and Baali 2020), and Jha et al. selected 3/6 variables that are hydrological factors while excluding land use/ land cover and rainfall (Jha et al. 2010). Similarly, although choosing half of the geology-related parameters, Naidu et al. (2015) did not include rainfall to evaluate groundwater potential in their research (Naidu et al. 2015). Likewise, Das and Pal have confirmed that monsoon rainfall is the main source of recharge, yet this variable was not included in their study (Das and Pal 2020). Also, Ajay Kumar et al. insisted that the impact of climate change affects groundwater resources (Ajay Kumar et al. 2020). However, they did not use data related to such features in their study such as rainfall, temperature, etc. According to Singh et al., both domestic and irrigation sectors suffer from water scarcity problems during non-monsoon seasons because of the short rainy season, large Spatio-temporal variability of rainfall, and capricious nature of the monsoon in the study area (Singh et al. 2018). Yet, the authors did not assess the rainfall as the main criterion contributing to groundwater formation, but only adopted 3/5 criteria that are hydrological factors.

Besides choosing elements affecting groundwater potential, deciding on the number of parameters should also be considered in calculating the model. According to Pawel, we can generally deal with seven parameters at once, plus or minus two (Cabala 2010). Thus, it is not recommended to use too many criteria to assess, only a maximum of 9 criteria is sufficient because psychologists conclude that, nine objects are the most that an individual can simultaneously compare and consistently rank. A greater number of criteria causes an individual to lose the thread, which means that they are unable to make a reliable evaluation. However, some studies do not choose the number of influencing criteria in this range. While Alaa and Ayser, Hamdani and Baali only utilized four parameters to establish the groundwater potential map (Hamdani and Baali 2020; Al-Abadi and Al-Shamma'a 2014), Arabameri et al. used 15 variables (Arabameri et al. 2019), Arulbalaji et al. chose 12 elements (Arulbalaji et al. 2019), Halder et al. employed 11 factors (Halder et al. 2020) to delineate the groundwater prospect zone. Although the above studies focus on different parameters and their impact on groundwater occurrence, the literature revealed that there is no specific guideline for choosing criteria affecting groundwater prospecting. Dung et al. reviewed the role of factors affecting flood hazard zoning using AHP (Dung et al. 2021). Darko et al. conducted the review to summarize the existing literature related to AHP applications in construction (Darko et al. 2019). Thungngern et al. presented a review of the AHP approach in water resource management in Thailand (Thungngern et al. 2015). At present, no review has specifically focused on AHP applications in groundwater potential zone. The paper aims to fill this void and develop a systematic review of literature on the real cases that applied AHP to assess criteria influencing groundwater recharge as well as their impact level into a coherent piece. Moreover, this study also provides a deeper understanding of the selection of parameters affecting groundwater potentiality in accordance with the geographical and socioeconomic characteristics of each study area. Though our review is not exhaustive, we seek to give a comprehensive overview of research on the subject. This article provides a useful reference for researchers and practitioners interested in the application of AHP to analyze and model groundwater-related decisions.

7.2 Method

The present study uses a descriptive approach to increase knowledge and making clear how criteria affect groundwater occurrence. This paper reviewed primarily peer-studied related to assessment of groundwater potential zones using GIS and AHP techniques and formulated the following research questions:

- How many parameters affect groundwater potential?
- What are the different groups of factors affecting groundwater potential?
- How likely are the criteria to influence groundwater potential?

A systematic literature review was used as a research strategy because it is an evidence-based practice that obtains different answers to the research question. The peer-reviewed publications in the period from 2010 to 2022 were detected by searching via major search engines such as ASCE Library, ScienceDirect, Google-Scholar, SpringerLink, Taylor and Francis. Some of the journals cited in this review are Sustainability, International Journal of Scientific and Engineering Research, Water, International Journal of Remote Sensing, Geology, Ecology, and Landscapes, Journal flood risk management, Groundwater Sustainable Development, Ecological Indicators, Research Journal of Recent Sciences, Remote Sensing, Hydrogeology, etc. Articles were searched with the keywords “Groundwater potential/prospect zone/map; AHP/ MCDA/ Analytic Hierarchy Process/ Multi-Criteria Decision Analysis”. The titles, abstracts, keywords, and conclusions of the selected research were reviewed. However, not all of the papers searched used AHP as a key or secondary decision-making tool in the assessment of groundwater possibility. A review of each paper’s contents was then performed to filter out unrelated publications; 70 papers were eventually considered valid for further analysis.

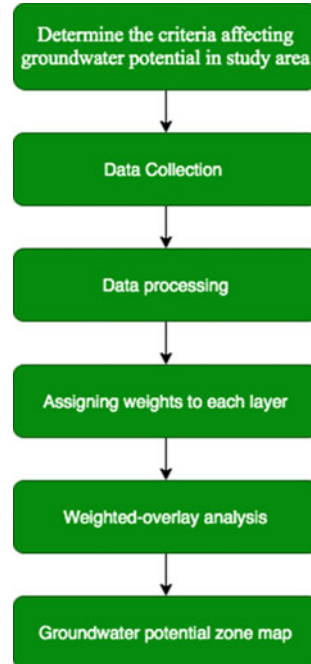
The study analyzed preceding studies related to groundwater potentiality by the AHP approach in nations where freshwater resources are scarce such as China, Iran, Ethiopia, Iraq, Morocco, Turkey, India, Indonesia, Nigeria, and Bangladesh. According to the literature, the classification of influencing alternatives can not cover all factors that cause groundwater scarcity because it is challenging to arrange them in the appropriate groups. Therefore, in this research, there are six groups of factors that contribute to groundwater formation, namely (1) factors related to hydrological and orographic characters; (2) factors related to topographic geomorphologic characters; (3) factors related to geological and hydrogeological characters; (4) factors related to the meteorological character; (5) factors related to cover characters; (6) factors related to soil characteristics.

In the third paragraph, the analysis of the impact level of the factors affecting groundwater prospects needs to be considered during the assessment process. The findings can be suggestions for researchers when deciding on the choice of criteria affecting groundwater generation for their study.

7.3 Results and Discussion

The methodology in all studies to delineate suitable sites for groundwater recharging has been illustrated in Fig. 7.1. So under that basis, the groundwater potential of the area is delineated using thematic layer parameters. However, it is more important to determine the criteria contributing to groundwater potential formation. Based on the type of influence factors, data can be extracted from DEM, satellite images, or acquired in the field. Identification of suitable sites for groundwater recharge was conducted through knowledge-based factor analysis. Based on the physical conditions of the study regions, it is possible to choose the appropriate parameters affecting groundwater potential.

Fig. 7.1 Flow chart of the methodology employed in the studies to delineate groundwater potential



The review indicates that the influencing variables are not the same for different regions. In general, most of the publications are interested in the factors that play a relevant role in the distribution of groundwater occurrences in space including Drainage density, Geomorphology, Slope, Geology (Lithology), Lineament density, Rainfall, Land use/ Land cover, and Soil. In addition to popular criteria mentioned in the past decade, recently scientists have tended to pay attention to other uncommon criteria. It will be difficult for data collection, but these factors have a great influence on groundwater potential such as Runoff coefficient, Node density, Distance to Palaeochannels, and Terrain ruggedness index. Besides, because the degree of impact is not much and there is no data available, some parameters are rarely used in research on groundwater potential, typically the factors of Potentiality around the major streams, Distance to the road, Profile curvature, Slope aspect, Slope angle, Topographic position index, Clay fraction, Lineament frequency, Lineament intersection, Water level fluctuation, Land surface temperature, Soil depth, etc.

The obtained results show that there are 61 criteria affecting groundwater formation classified into six groups. In which, the number of factors belonging to the group of geological and hydrogeological characters accounts for the most with 34%, followed by a group of topographic and geomorphologic characters with 31%, a group of hydrological and orographic characters with 21%. The remaining three groups have a limited number of variables from only 3 to 5%. Figure 7.2 shows the number of criteria affecting groundwater potential in six groups.

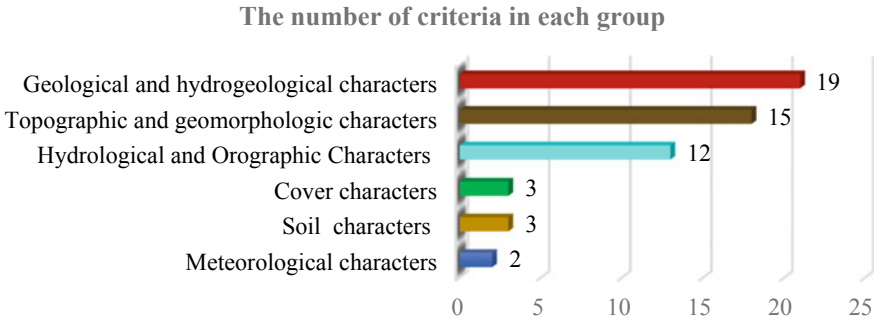


Fig. 7.2 The number of criteria affecting groundwater potential in each group

7.3.1 Factors Related to Hydrological and Orographic Characters

From the literature review, it is found that the factors affecting groundwater prospects related to hydrological and orographic characteristics include 12 factors as shown in Table 7.1. Among the 12 criteria, drainage density was the prevalent criterion for evaluating groundwater occurrence with 57 studies. Drainage density is an inverse function of permeability, and therefore it is an important parameter in assessing the groundwater zone. High drainage density values are favorable for run-off, and hence indicate a low groundwater potential zone (Agarwal et al. 2013). Although used by many authors, the influence of this factor is only accounted for at the moderate (27 studies) and low (23 studies) levels. There are even research areas, the level of influence of this factor ranks the last in the evaluation table (Atmaja et al. 2019; Mohammadi-Behzad et al. 2019; Rajasekhar et al. 2019).

Same as drainage density, to generate Distance to Stream, Distance from the river, authors initially extracted the drainage network from DEM and the criteria were then computed as the Euclidean distance from every pixel to the nearest stream (Arabameri et al. 2019). Though they are created easily, most publications have not taken into account these factors when analyzing groundwater prospects due to their insignificant influence. In addition, other parameters in this group also affect the groundwater occurrence at medium and low levels such as Flow direction, Height above the nearest drainage, Hydraulic conductivity, Normalized difference water index, Surface water body, Pond frequency, Proximity to surface water bodies, Potentiality around the major streams. These factors rarely appear in studies related to groundwater potential. For the remaining criteria in the group, there are not many studies mentioned, but some of them are assigned higher weight, even the highest such as recharge (Jha et al. 2010; Machiwal et al. 2011) and runoff coefficient (Singh et al. 2018). These factors are less commonly used in studies because of the challenges in processing the data or the difficulty of data availability. From the above analysis, the influence level of hydrological and orographic criteria is summarized in Table 7.2.

Table 7.1 Criteria related to hydrological and orographic characters in studies of groundwater potential zoning

No.	Factors	References	Total	High	Medium	Low
1	Distance from river, distance to stream	Razandi et al. (2015), Doke et al. (2021), Arabameri et al. (2019), Halder et al. (2020), Benjmel et al. (2020), Mahato et al. (2022)	6	1	2	3
2	Drainage density	Agarwal et al. (2013), Pani et al. (2016), Razandi et al. (2015), Arulbalaji et al. (2019), Murreu et al. (2019), Ahmadi et al. (2020), Allafia et al. (2020), Doke et al. (2021), Melese and Belay (2022), Jha et al. (2010), Naidu et al. (2015), Ajay Kumar et al. (2020), Singh et al. (2018), Arabameri et al. (2019), Halder et al. (2020), Atmaja et al. (2019), Mohammadi-Behzad et al. (2019), Rajasekhar et al. (2019), Benjmel et al. (2020), Mahato et al. (2022), Santhosh et al. (2018), Wudad et al. (2021), Akbari et al. (2021), Andualem and Demeke (2019), Argaz et al. (2019), Hatefi and Ekhtesasi (2016), Aryanto and Hardiman (2018), Aslan and Çelik (2021), Bashe et al. (2017), Bourjila et al. (2020), Chowdhury et al. (2009), Dar et al. (2020), Das and Mukhopadhyay (2020), Hachem et al. (2015), Ifiediegwu (2022), Jenifer and Jha (2017), Jhariya et al. (2021), Niithya et al. (2019), Owolabi et al. (2020), Panahi et al. (2017), Patil and Mohite (2014), Rajesh et al. (2021), Ramachandra et al. (2019), Roy et al. (2019), Saranya and Saravanan (2020), Shekhar and Pandey (2015), Singh et al. 2017, Siva et al. (2017), Erhan et al. (2018), Sonwane and Usmani (2021), Sresto et al. (2021), Saranya and Saravanan (2019), Yıldırım (2021), Gebru et al. (2020), Zghibi et al. (2020), Das (2019), Maity and Mandal (2019)	57	7	27	23
3	Flow direction	Pande et al. (2021)	1			1
4	Height above the nearest drainage	Hamdani and Baali (2020)	1			1

(continued)

Table 7.1 (continued)

No.	Factors	References	Total	High	Medium	Low
5	Hydraulic conductivity	Sener and Davraz (2018)	1		1	
6	Normalized difference water index	Halder et al. (2020)	1			1
7	Recharge, net recharge	Jha et al. (2010), Chowdhury et al. (2009), Sener and Davraz (2018), Machiwal et al. (2011)	4	2	2	
8	Runoff coefficient	Singh et al. (2018)	1	1		
9	Surface water body	Jha et al. (2010), Chowdhury et al. (2009)	2			2
10	Pond frequency	Das and Pal (2020), Das and Mukhopadhyay (2020)	2		1	1
11	Proximity to surface water bodies	Singh et al. (2018), Jennifer and Jha (2017), Machiwal et al. (2011)	3			3
12	Potentiality around the major streams	Pani et al. (2016)	1			1

Table 7.2 The influence level of criteria related to hydrological and orographic characters

No.	Criteria	Used frequency	Influence level
1	Distance to stream, distance from river	Low	Medium–low
2	Drainage density	High	Medium–low
3	Flow direction	Low	Low
4	Height above the nearest drainage	Low	Low
5	Hydraulic conductivity	Low	Low
6	Normalized difference water index	Low	Low
7	Recharge, net recharge	Medium	High–medium
8	Runoff coefficient	Low	High–medium
9	Surface water body	Low	Low
10	Pond frequency	Low	Low
11	Proximity to surface water bodies	Low	Low
12	Potentiality around the major streams	Low	Low

7.3.2 *Factors Related to Topographic and Geomorphologic Characters*

From the review literature papers, 15 factors related to topographic and geomorphologic characters were detected when studying groundwater recharge. The number of the criteria and their impact degrees are presented in Table 7.3. The results indicate that the slope criterion was used in most studies (61 times), 69% of which assessed that this criterion has a significant role in groundwater formation. In addition to slope, geomorphology represents the landform and topography of an area and is one of the main factors used widely for the delineation of groundwater potential zones. Among the review papers, a total of 40 publications have used geomorphology data to study the groundwater prospect. Notably, geomorphology is considered the most important parameter in the 28 studies and only 2 studies appreciated that this factor is the least important.

The elevation is also one of the topographic factors and is considered a surface indicator to explore groundwater potential. According to the literature review, this criterion has been used for 12 research and has less influence on groundwater occurrence. In addition, the curvature is a significant terrain characteristic that expresses the amount by which a curve deviates from being a straight line, or a surface deviates from being a plane. Water tends to decelerate and tends to accumulate in convex and concave profiles respectively. High weight is assigned for high curvature value and vice versa (Arulbalaji et al. 2019). The curvature map can be easily generated from DEM however only seven authors mentioned this factor due to its negligible influence on groundwater formation. Moreover, the aspect is an essential input data for modeling groundwater occurrence. The aspect replicates the moisture retention, vegetation, moisture air, and attitude of rock bedding, which influenced soil structure's physical assets, sloped materials, and potential groundwater zones (Pande et al.

Table 7.3 Criteria related to topographic and geomorphologic characters in studies of groundwater potential zoning

No.	Factors	References	Total	High	Medium	Low
1	Aspect	Akbari et al. (2021), Singh et al. (2017), Pande et al. (2021), Lakshmi and Reddy (2018)	4			4
2	DEM	Pande et al. (2021)	1			1
3	Distance to road	Arabameri et al. (2019)	1			1
4	Elevation, altitude	Razandi et al. (2015), Melese and Belay (2022), Arabameri et al. (2019), Wudad et al. (2021), Akbari et al. (2021), Argaz et al. (2019), Bourjila et al. (2020), Jenifer and Jha (2017), Saranya and Saravanan (2020), Saranya and Saravanan (2019), Yildirim (2021), Mohamed and Elmahdy (2017)	12	5		7
5	Geomorphology	Agarwal et al. (2013), Pani et al. (2016), Arulbalaji et al. (2019), Das and Pal (2020), Murnu et al. (2019), Doke et al. (2021), Jha et al. (2010), Ajay Kumar et al. (2020), Al-Abadi and Al-Shamma'a (2014), Halder et al. (2020), Rajasekhar et al. (2019), Mahato et al. (2022), Santhosh et al. (2018), Wudad et al. (2021), Andialem and Demeke (2019), Aslan and Çelik (2021), Bashe et al. (2017), Chowdhury et al. (2009), Dar et al. (2020), Ifedigwu (2022), Jhariya et al. (2021), Nithya et al. (2019), Patil and Mohite (2014), Rajesh et al. (2021), Ramachandra et al. (2019), Roy et al. (2019), Saranya and Saravanan (2020), Shekhar and Pandey (2015), Singh et al. (2017), Siva et al. (2017), Sresto et al. (2021), Saranya and Saravanan (2019), Gebru et al. (2020), Zghibi et al. (2020), Das (2019), Pande et al. (2021), Machiwal et al. (2011), Lakshmi and Reddy (2018)	40	28	10	2
6	Hillshade	Pande et al. (2021)	1		1	
7	Plan curvature	Arulbalaji et al. (2019), Melese and Belay (2022), Arabameri et al. (2019), Benjmel et al. (2020), Akbari et al. (2021), Bourjila et al. (2020), Yildirim (2021)	7	3		4

(continued)

Table 7.3 (continued)

No.	Factors	References	Total	High	Medium	Low
0.8	Profile curvature	Benjmel et al. (2020)	1			1
9	Relative relief	Halder et al. (2020)	1			1
10	Relative slope position	Akbari et al. (2021)	1			1
11	Roughness, terrain ruggedness index, terrain class, topography	Arulbalaji et al. (2019), Akbari et al. (2021), Hatefi and Ekhtesasi (2016), Aslan and Çelik (2021), Bashe et al. (2017), Bourjila et al. (2020)	6		2	4
12	Slope	Agarwal et al. (2013), Puni et al. (2016), Arulbalaji et al. (2019), Das and Pal (2020), Murmu et al. (2019), Ahmadi et al. (2020), Allafita et al. (2020), Doke et al. (2021), Melese and Belay (2022), Jha et al. (2010), Ajay Kumar et al. (2020), Singh et al. (2018), Arabameri et al. (2019), Halder et al. (2020), Atmaja et al. (2019), Mohammadi-Behzad et al. (2019), Rajasekhar et al. (2019), Benjmel et al. (2020), Mahato et al. (2022), Santhosh et al. (2018), Argaz et al. (2021), Akbari et al. (2021), Andualtem and Demeke (2019), Wudat et al. (2019), Hatefi and Ekhtesasi (2016), Aryanto and Hardiman (2018), Aslan and Çelik (2021), Bashe et al. (2017), Bourjila et al. (2020), Chowdhury et al. (2009), Dar et al. (2020), Das and Mukhopadhyay (2020), Hachem et al. (2015), Ifedigvu (2022), Jenifer and Jha (2017), Jhariya et al. (2021), Nithya et al. (2019), Owolabi et al. (2020), Panahi et al. (2017), Patil and Mohite (2014), Rajesh et al. (2021), Ramachandra et al. (2019), Roy et al. (2019), Saranya and Saravanan (2020), Shekhar and Pandey (2015), Singh et al. (2017), Siva et al. (2017), Erhan et al. (2018), Sonwane and Usmani (2021), Sresto et al. (2021), Saranya and Saravanan (2019), Yıldırım (2021), Gebru et al. (2020), Zēhibi et al. (2020), Das (2019), Maity and Mandal (2019), Pande et al. (2021), Machiwal et al. (2011), Lakshmi and Reddy (2018), Mohamed and Elmahdy (2017), Khodaei and Nassery (2013)	61	14	28	19
13	Slope aspect	Razandi et al. (2015), Arabameri et al. (2019)	2			2
14	Slope angle	Razandi et al. (2015)	1			1
15	Topographic position index	Arulbalaji et al. (2019), Bourjila et al. (2020)	2			2

Table 7.4 The influence level of factors related to topographic and geomorphologic characters

No.	Criteria	Used frequency	Influence level
1	Aspect	Medium	Low
2	DEM	Low	Low
3	Distance to road	Low	Low
4	Elevation, altitude	Medium	Medium–low
5	Geomorphology	High	High–medium
6	Hillshade	Low	Low
7	Plan curvature	Medium	Medium–low
8	Profile curvature	Low	Low
9	Relative relief	Low	Low
10	Relative slope position	Low	Low
11	Roughness, terrain ruggedness index, terrain class, topography	Low	Low
12	Slope	High	High–medium
13	Slope aspect	Low	Low
14	Slope angle	Low	Low
15	Topographic position index	Low	Low

2021). However, only four researchers choose this alternative because they believed that this criterion has the last important impact on groundwater scarcity hazard and therefore it is evaluated with the lowest weight.

Similarly, slope aspects can influence the main direction of precipitation, but only two studies consider this variable. The obtained results indicated that its impact on groundwater formation is the lowest. Surprisingly, some factors related to topographical features do not seem to be of much interest to scientists, if any, they can only be assessed at the lowest level of influence, such as DEM, distance to road, hillside, profile curvature, relative relief, relative slope position, slope angle, terrain ruggedness index, terrain class (each factor mentioned by only one study), roughness and topographic position index (two studies), and topography (three studies). From the above analysis and used frequency, the influence level of topographic and geomorphologic criteria is summarized in Table 7.4.

7.3.3 Factors Related to Geological, Hydrogeological and Soil Characters

In connection to the geological and hydrogeological characteristics, 19 relevant evaluation criteria were identified and listed in this study in Table 7.5. Geological factors control the porosity and permeability of aquifer materials and are, therefore, considered indicators of hydrological characteristics (Benjmel et al. 2020). The geology of

regions without a local aquifer is a critical parameter as it can amplify or mitigate the extent of surface water percolation to aquifer rocks. Therefore, up to 59 scientists have used this factor to study groundwater potential delineation. The obtained results indicated that geology (lithology) has a considerable impact on groundwater scarcity hazards.

It is worth mentioning that more than half of the aforementioned studies assigned the highest weight to the geological factor. In addition to geology, lineament density also plays a dominant role in groundwater susceptibility studies due to the different susceptibilities of lithological units to active hydrological processes. A lineament is a linear feature in a geographical landscape that is a manifestation of fundamental geological structure (Melese and Belay 2022). Thus, the number of publications that consider that lineament density to be a necessary factor for the analysis of groundwater status accounts for 70% (52 papers). The highest rating was assigned to this criterion in various research (Atmaja et al. 2019; Mohammadi-Behzad et al. 2019; Benjmel et al. 2020; Bourjila et al. 2020; Singh et al. 2017; Erhan et al. 2018).

Besides the above two criteria that appear in many studies, others in this group are rarely concerned by scientists because they have a low and medium effect on groundwater generation. While clay fraction, distance from lineament, geology unconsolidated, lineament frequency, lineament intersection, and water level fluctuation are the least important causes of groundwater scarcity, distance to fault, groundwater depth, karstic domains, and lineament buffer are often assigned by the medium influence weight. On the contrary, although the number of interested authors is limited, distance to Palaeochannels (Mohamed and Elmahdy 2017), node density (Benjmel et al. 2020), vadose zone (Rajasekhar et al. 2019; Sener and Davraz 2018), and weathered zone thickness (Shekhar and Pandey 2015) have the greatest impact on zoning groundwater potential. In particular, this result has only been discovered by a few scientists in the last five years. Table 7.6 shows the used frequency as well as criteria ranking at three levels high, medium, and low.

7.3.4 Factors Related to Soil Characters

Criteria that contribute to occur groundwater connected with soil characteristics include soil, soil depth, and soil texture. Table 7.7 displays the number of criteria that are relevant to soil features and references. While there are only three papers that analyzed the soil depth factor and six publications applied the soil texture criterion to study groundwater potential, soil type was used by 44 authors in their research. Information on the type of soil is often needed as a basic input in hydrologic evaluation. The rank of soil has been assigned on the premise of its infiltration rate. Moreover, the factors related to soil characteristics are of great use in assessing the runoff for any given watershed as soil influences the process of generating runoff from rainfall. Almost all scientists insisted that soil types play an important role in determining the amount of water that can infiltrate into the subsurface formations and hence influence

Table 7.5 Criteria related to geological and hydrogeological characters in studies of groundwater potential zoning

No.	Factors	References	Total	High	Medium	Low
1	Aquifer, aquifer thickness	Razandi et al. (2015), Aslan and Çelik (2021), Das and Mukhopadhyay (2020), Sener and Davraz (2018)	4	1	1	2
2	Clay fraction	Bashe et al. (2017)	1			1
3	Distance to fault	Arabameri et al. (2019), Mohamed and Elmahdy (2017)	2		1	1
4	Distance from lineament	Benjmel et al. (2020), Aryanto and Hardiman (2018)	2		1	1
5	Distance to palaeochannels	Mohamed and Elmahdy (2017)	1	1		
6	Fault density	Arabameri et al. (2019), Benjmel et al. (2020), Khodaei and Nassery (2013)	3		2	1
7	Geology (lithology)	Agarwal et al. (2013), Pani et al. (2016), Razandi et al. (2015), Arulbalaji et al. (2019), Das and Pal (2020), Murnu et al. (2019), Ahmadi et al. (2020), Allafia et al. (2020), Doko et al. (2021), Melese and Belay (2022), Hamdani and Baali (2020), Naidu et al. (2015), Ajay Kumar et al. (2020), Singh et al. (2018), Al-Abadi and Al-Shamma'a (2014), Arabameri et al. (2019), Halder et al. (2020), Aimaaja et al. (2019), Mohammadi-Behzad et al. (2019), Rajasekhar et al. (2019), Benjmel et al. (2020), Mahato et al. (2022), Santhosh et al. (2018), Wudad et al. (2021), Akbari et al. (2021), Andaleem and Demeke (2019), Argaz et al. (2019), Hatefi and Ekhtesasi (2016), Aryanto and Hardiman (2018), Aslan and Çelik (2021), Bashe et al. (2017), Boujila et al. (2020), Chowdhury et al. (2009), Dar et al. (2020), Das and Mukhopadhyay (2020), Hachem et al. (2015), Ifiediegwu (2022), Jennifer and Jha (2017), Jhariya et al. (2021), Nithya et al. (2019), Panahi et al. (2017), Rajesh et al. (2021), Ramachandra et al. (2019), Roy et al. (2019), Shekhar and Pandey (2015), Singh et al. (2017), Siva et al. (2017), Erhan et al. (2018), Sonwane and Usmani (2021), Sresto et al. (2021), Yildirim (2021), Gebru et al. (2020), Zghibi et al. (2020), Das (2019), Maity and Mandal (2019), Machiwal et al. (2011), Lakshmi and Reddy (2018), Mohamed and Elmahdy (2017), Khodaei and Nassery (2013)	59	37	12	10
8	Geology unconsolidated	Saranya and Saravanan (2020), Saranya and Saravanan (2019)	2		2	
9	Groundwater depth below surface	Jhariya et al. (2021), Pande et al. (2021), Machiwal et al. (2011)	3		3	

(continued)

Table 7.5 (continued)

No.	Factors	References	Total	High	Medium	Low
10	Karstic domains, Karst	Hamdani and Baali (2020), Hachem et al. (2015)	2	13	20	16
11	Lineament density	Pani et al. (2016), Arulbalaji et al. (2019), Murnu et al. (2019), Ahmadi et al. (2020), Allafita et al. (2020), Doko et al. (2021), Melese and Belay (2022), Hamdani and Baali (2020), Naidu et al. (2015), Ajay Kumar et al. (2020), Al-Abadi and Al-Shamma'a (2014), Halder et al. (2020), Airmaja et al. (2019), Mohammadi-Behzad et al. (2019), Benjmel et al. (2020), Mahato et al. (2022), Santhosh et al. (2018), Wudad et al. (2021), Andualam and Demeke (2019), Argaz et al. (2019), Hatifi and Ekhtessasi (2016), Aslan and Çelik (2021), Bashe et al. (2017), Bourjila et al. (2020), Dar et al. (2020), Das and Mukhopadhyay (2020), Hachem et al. (2015), Ifedigwu (2022), Jenifer and Jha (2017), Niithya et al. (2019), Owolabi et al. (2020), Panahi et al. (2017), Patil and Mohite (2014), Rajesh et al. (2021), Ramachandra et al. (2019), Roy et al. (2019), Saranya and Saravanan (2020), Shekhar and Pandey (2015), Singh et al. (2017), Erhan et al. (2018), Sonwane and Usmani (2021), Sresto et al. (2021), Saranya and Sarvaman (2019), Yildirim (2021), Gebru et al. (2020), Zghibr et al. (2020), Das (2019), Maity and Mandal (2019), Sener and Davraz (2018)	49	4	1	1
12	Lineament frequency	Naidu et al. (2015)	1			1
13	Lineament intersection	Naidu et al. (2015)	1			1
14	Lineaments buffer	Agarwal et al. (2013), Jhariya et al. (2021)	2		2	
15	Mean post-monsoon groundwater depth, water table level, groundwater depth below surface	Agarwal et al. (2013), Razandi et al. (2015), Jhariya et al. (2021), Pandey et al. (2021), Sener and Davraz (2018), Machiwal et al. (2011)	7	4	1	2
16	Node density	Benjmel et al. (2020)	1	1		
17	Topographic wetness index	Razandi et al. (2015), Arulbalaji et al. (2019), Melese and Belay (2022), Arabameri et al. (2019), Benjmel et al. (2020), Mahato et al. (2022), Akbari et al. (2021), Bourjila et al. (2020), Owolabi et al. (2020), Sresto et al. (2021), Yildirim (2021), Gebru et al. (2020), Mohamed and Elmahdy (2017)	13		10	3
18	Vadose zone	Rajasekhar et al. (2019), Sener and Davraz (2018)	2	1		
19	Weathered zone thickness	Shekhar and Pandey (2015)	1	1		

Table 7.6 The influence level of factors related to geological and hydrogeological characters

No.	Factors	Used frequency	Influence level
1	Aquifer, aquifer thickness	Medium	Medium–low
2	Clay fraction	Low	Low
3	Distance to fault	Low	Low
4	Distance from lineament	Low	Low
5	Distance to palaeochannels	Low	High
6	Fault density	Low	Medium–low
7	Geology (lithology)	High	High–medium
8	Geology unconsolidated	Low	Low
9	Groundwater depth below surface	Low	Medium
10	Groundwater fluctuation, water level fluctuations	Low	Medium–low
11	Karstic domains, Karst	Low	Medium
12	Lineament density	High	High–medium
13	Lineament frequency	Low	Low
14	Lineament intersection	Low	Low
15	Lineaments buffer	Low	Medium
16	Groundwater depth, water table level, groundwater depth below surface	Low	High
17	Node density	Low	High
18	Vadose zone	Low	High
19	Weathered zone thickness	Low	High

groundwater recharge. However, 89% of them indicated that the impact of soil type is only medium and low when categorizing in the above-mentioned research.

Not as popular as soil, soil depth and soil texture have only recently been paid attention to. Pande et al. insisted that soil texture is a crucial controller of infiltration of land water using voids and infiltrates into the subsurface to reach the aquifer (Pande et al. 2021). Therefore, soil texture is also an important component and characteristic of soils. This criterion has a great impact on creating groundwater because sandy soil absorbs water soon and few runoffs occur. There are not many experts including this parameter in the research on groundwater recharge zone. Yet, in some articles, soil texture is assigned to the highest rank of groundwater decline and depletion (Wudad et al. 2021; Das and Mukhopadhyay 2020; Pande et al. 2021).

In addition, some experts found that soil depth is another important control on the groundwater potential as an area with a higher depth of soil is a place for developing a higher prospect of groundwater (Ahmadi et al. 2020). This factor not only has not been used by many studies but is also considered to have an insignificant influence on groundwater recharge. Thus, the impact of soil depth is only low with ranking order always ranked in the last place of the criteria. The used frequency as well as

Table 7.7 Criteria related to soil characters in studies of groundwater potential zoning

No.	Factors	References	Total	High	Medium	Low
1	Soil	Agarwal et al. (2013), Pani et al. (2016), Arulbalaji et al. (2019), Ahmadi et al. (2020), Allafta et al. (2020), Doke et al. (2021), Melese and Belay (2022), Jha et al. (2010), Naidu et al. (2015), Ajay Kumar et al. (2020), Al-Abadi and Al-Shamma'a (2014), Arabameri et al. (2019), Halder et al. (2020), Rajasekhar et al. (2019), Mahato et al. (2022), Santhosh et al. (2018), Andualem and Demeke (2019), Argaz et al. (2019), Aryanto and Hardiman (2018), Aslan and Çelik (2021), Chowdhury et al. (2009), Dar et al. (2020), Ifediegwu (2022), Jenifer and Jha (2017), Jhariya et al. (2021), Nithya et al. (2019), Panahi et al. (2017), Patil and Mohite (2014), Rajesh et al. (2021), Ramachandra et al. (2019), Roy et al. (2019), Saranya and Saravanan (2020), Shekhar and Pandey (2015), Erhan et al. (2018), Sonwane and Usmani (2021), Sresto et al. (2021), Saranya and Sravanan (2019), Yıldırım (2021), Gebru et al. (2020), Zghibi et al. (2020), Maity and Mandal (2019), Sener and Davraz (2018), Machiwal et al. (2011), Lakshmi and Reddy (2018)	44	5	21	18
2	Soil depth	Ahmadi et al. (2020), Arabameri et al. (2019), Das (2019)	3		1	2
3	Soil texture	Das and Pal (2020), Wudad et al. (2021), Das and Mukhopadhyay (2020), Das (2019), Pande et al. (2021), Mohamed and Elmahdy (2017)	6	3	2	1

criteria ranking at three levels including high, medium, and low are shown in Table 7.8.

Table 7.8 The influence level of factors related to soil characters

No.	Factors	Used frequency	Influence level
1	Soil	High	High–medium
2	Soil depth	Low	Low
3	Soil texture	Low	Medium–low

7.3.5 Factors Related to Cover Characters

The literature reviews indicated factors concerning the cover characteristics including green vegetation, land use/ land cover, and NDVI index. Table 7.9 shows the criteria in this group and the total numbers of research used to study groundwater potential. Of the 81 studies, 52 publications have revealed that land use/ land cover plays a very critical part in recharging groundwater. The water addition from the unsaturated zone to the saturated zone of the water-bearing formation is influenced by land use land cover (Gebru et al. 2020). For areas with diversified land cover/ land use patterns, variation in this cover will have an impact on groundwater recharge, evaporation, and surface runoff. Land use describes human operations such as land-related agriculture, settlement, and industry, while the land cover relates to features such as lakes, mountains, vegetation, and rocks on the surface of the earth (Dar et al. 2020). Besides, land use type gives the necessary information on infiltration. Despite the high frequency of use, the number of experts assigning low and medium weight to this criterion accounts for 77% of 40 studies.

Green Vegetation in the dry season and arid and Semi-arid areas is a good indicator of shallow groundwater (Khodaei and Nassery 2013). The vegetation layer can be obtained from satellite images easily and used to detect groundwater resources having different potentials. However, there are only two studies that mentioned this variable due to its negligible influence on this water resources. Similar to Green vegetation, the normalized difference vegetation index (NDVI) shows the canopy density also determined by satellite data, which is helpful as a criterion considering the high canopy bulk increase the probability of groundwater harvesting in poor aquifer zone (Pande et al. 2021). Thus, NDVI is another important factor that plays a crucial role in the delineation of groundwater potential zones. The obtained results revealed that this parameter is assigned a low weight according to its importance for recharge in most of the publications. Although it is easy to compute NDVI from satellite data, there are three authors who used NDVI in their research. From the above analysis and frequency used these criteria, the influence level of cover factors is summarized in Table 7.10.

7.3.6 Factors Related to Meteorological Characters

From 81 reviewed literature publications, it is possible to recognize two criteria contributing to the formation of groundwater that is related to meteorological characteristics including rainfall and land surface temperature. The rainfall is considered one of the most considerable hydrologic factors that crucially control the groundwater recharge of a region. It cannot be denied that many scientists have taken into account this factor when assessing groundwater potential because rainfall is a major hydrological source of groundwater storage. The results of the literature review exposed that the majority of analyzed cases utilized this factor indicating that rainfall has

Table 7.9 Criteria related to cover characters in studies of groundwater potential zoning

No.	Factors	References	Total	High	Medium	Low
1	Green vegetation	Hatefi and Ekhtesasi (2016), Khodaei and Nassery (2013)	2		1	1
2	Land use/ Land cover	Agarwal et al. (2013), Pani et al. (2016), Arulbalaji et al. (2019), Das and Pal (2020), Murrnu et al. (2019), Ahmadi et al. (2020), Allafra et al. (2020), Doke et al. (2021), Melese and Belay (2022), Naidu et al. (2015), Ajay Kumar et al. (2020), Arabameri et al. (2019), Halder et al. (2020), Rajasekhar et al. (2019), Mahato et al. (2022), Santhosh et al. (2018), Wudad et al. (2021), Akbari et al. (2021), Andualem and Demeke (2019), Argaz et al. (2019), Aryanto and Hardiman (2018), Aslan and Çelik (2021), Bashe et al. (2017), Bourjila et al. (2020), Dar et al. (2020), Das and Mukhopadhyay (2020), Hachem et al. (2015), Ifedigwu (2022), Jhariya et al. (2021), Nithya et al. (2019), Owolabi et al. (2020), Panahi et al. (2017), Patil and Mohite (2014), Rajesh et al. (2021), Roy et al. (2019), Saranya and Saravanan (2020), Singh et al. (2017), Siva et al. (2017), Erhan et al. (2018), Sonwane and Usmani (2021), Sresto et al. (2021), Saranya and Saravanan (2019), Yildirim (2021), Gebru et al. (2020), Zehibi et al. (2020), Das (2019), Maity and Mandal (2019), Pande et al. (2021), Sener and Davraz (2018), Mohamed and Elmahdy (2017), Zeinolabedinia and Esmailyb (2015)	51	12	16	23
3	NDVI	Sresto et al. (2021), Gebru et al. (2020), Pande et al. (2021)	3		1	2

Table 7.10 The influence level of factors related to cover characters

No.	Factors	Used frequency	Influence level
1	Green vegetation	Low	Low
2	Land use/ Land cover	High	Medium–low
3	NDVI	Low	Low

a low and medium effect on groundwater occurrence. Among 38 studies reviewed, there are only nine articles that adopted this criterion with high weight (Table 7.11).

In contrast to the rainfall factor that has been paid attention to by many scientists, only one publication mentioned the Land surface temperature (LST) in the study of groundwater potential zone. The authors assessed LST as an indicator of the unsaturated zone thickness. This criterion is related to the temperature of shallow aquifers and shows areas of poor saturation thickness, high evaporation, and evapotranspiration considering the severity of semi-aridity in the study regions (Urqueta et al. 2018). Hence, its spatial information is considered significant to groundwater exploration in the study environment. LTS is deduced from the integration of brightness temperature and emissivity which are extracted from satellite images. The used frequency and influence level of meteorological factors are summarized in Table 7.12.

The review results show the influence level of the factors on the groundwater potential in Tables 7.2, 7.4, 7.6, 7.8, 7.10, and 7.12. This level is evaluated based on the use frequency and priority ranking of the criteria based on the weights calculated by the AHP method in the studies. The obtained results revealed that there is at least one criterion in each group utilized for delineating groundwater prospect zone due to their significant influence as well as the ability to collect data. However, the group of geological and hydrogeological factors has many criteria assigned high and highest weight although some of them have not been used much in research studies. It should also be added that there are not many influencing factors belonging to the group related to meteorological and cover characters and the degree of their influence is also not appreciated remarkably, but these criteria are indispensable when studying groundwater potential, in particular for areas with complex meteorological conditions, and land cover changes. One thing worth noting in this review is that there have been no studies mentioning population density, a factor that directly and significantly affects groundwater recharge. It may be difficult to collect data, but this factor is also a suggestion for scientists interested in groundwater zoning in the future. Thus, it is necessary to add population distribution as a new variable in groundwater potential assessment. Moreover, the literature review revealed that when studying the parameters contributing to groundwater occurrence, it is necessary to consider the characteristics of the physical conditions of the research zone to choose the number of factors as well as the appropriate influencing criteria.

Table 7.11 Criteria related to meteorological characters in studies of groundwater potential zoning

No.	Factors	References	Total	High	Medium	Low
1	Rainfall, Precipitation	Agarwal et al. (2013), Razandi et al. (2015), Arulbalaji et al. (2019), Murmu et al. (2019), Allafia et al. (2020), Doke et al. (2021), Melese and Belay (2022), Arabameri et al. (2019), Atmaja et al. (2019), Mohammadi-Behzad et al. (2019), Mahato et al. (2022), Santhosh et al. (2018), Wudad et al. (2021), Hatefi and Ekhtesasi (2016), Aryanto and Hardiman (2018), Aslan and Çelik (2021), Bashe et al. (2017), Bourjila et al. (2020), Dar et al. (2020), Das and Mukhopadhyay (2020), Ifediegwu (2022), Jenifer and Jha (2017), Jhariya et al. (2021), Nithya et al. (2019), Owolabi et al. (2020), Panahi et al. (2017), Roy et al. (2019), Saranya and Saravanan (2020), Shekhar and Pandey (2015), Erhan et al. (2018), Sresto et al. (2021), Saranya and Saravanan (2019), Yıldırım (2021), Gebru et al. (2020), Zghibi et al. (2020), Das (2019), Lakshmi and Reddy (2018), Zeinolabedinia and Esmailyb (2015)	38	9	10	19
2	Land surface temperature	Owolabi et al. (2020)	1			1

Table 7.12 The influence level of factors related to meteorological characters

No.	Factors	Used frequency	Influence level
1	Rainfall	High	Medium–low
2	Land surface temperature	Low	Low

7.4 Conclusions

This paper reviewed the application of the Analytical Hierarchy Process for groundwater occurrence in 81 peer-reviewed journal articles from 2010 to 2022. The objective of this paper is to (1) review and analyze publications depicting the usage of AHP in groundwater potential zone from 2010 to 2022; (2) From the 81 studies, it was found that AHP, one of the best known and most popular used in MCDA, can be used to assess groundwater potentiality of the study area. The obtained results also indicated that there are 54 factors affecting groundwater occurrence categorized into six groups including factors related to the characteristics of hydrology and orography, topography and geomorphology, geology and hydrogeology, soil, cover, and meteorology. Of which, eight criteria are mentioned by many studies including geology, lineaments, geomorphology, soil, land use/land cover, rainfall, drainage density, and slope. In addition, the criteria evaluated that have a great influence on the groundwater potential are scattered in groups including the following factors: drainage density, geomorphology, slope, geology, Lineament Density, soil, land use/land cover, rainfall. Some factors are not interested in many scientists but are considered to have a significant influence on groundwater potential such as node density, weathered zone thickness, distance to palaeochannels, runoff coefficient. Furthermore, to help minimize researchers' bias regarding goals and factors as well as improve the effectiveness of evaluating groundwater prospect zone, the AHP has been used in combination with other techniques such as the Delphi technique in determining key criteria.

References

- Agarwal E, Agarwal R, Garg RD, Garg PK (2013) Delineation of groundwater potential zone: an AHP/ANP approach. *J Earth Syst Sci* 122:887–898
- Ahmad I, Dar MA, Andualem TG, Teka AH (2020) Groundwater development using geographic information system. *Appl Geomatics* 12:73–82
- Ahmadi H, Kaya OA, Babadagi E, Savas T, Pekkan E (2020) GIS-based groundwater potentiality mapping using AHP and FR models in central antalya, Turkey. *Environ Sci Proc* 11. Multidisciplinary Digital Publishing Institute
- Ajay Kumar V, Mondal N, Ahmed S (2020) Identification of groundwater potential zones using RS, GIS and AHP techniques: a case study in a part of Deccan volcanic province (DVP), Maharashtra, India. *J Indian Soc Remote Sens* 48:497–511
- Akbari M, Meshram SG, Krishna R, Pradhan B, Shadeed S, Khedher KM, Sepehri M, Ildoromi AR, Alimerzaei F, Darabi F (2021) Identification of the groundwater potential recharge zones using

- MCDM models: full consistency method (FUCOM), best worst method (BWM) and analytic hierarchy process (AHP). *Water Resour Manage* 35:4727–4745
- Al-Abadi A, Al-Shamma'a A, (2014) Groundwater potential mapping of the major aquifer in Northeastern Missan Governorate, South of Iraq by using analytical hierarchy process and GIS. *J Environ Earth Sci* 10:125–149
- Al-Abadi AM, Al-Shamma'a AM, Aljabbari MH, (2017) A GIS-based DRASTIC model for assessing intrinsic groundwater vulnerability in northeastern Missan governorate, southern Iraq. *Appl Water Sci* 7:89–101
- Allafta H, Opp C, Patra S (2020) Identification of groundwater potential zones using remote sensing and GIS techniques: a case study of the Shatt Al-Arab Basin. *Remote Sens* 13:112
- Andualem TG, Demeke GG (2019) Groundwater potential assessment using GIS and remote sensing: a case study of Guna tana landscape, upper blue Nile Basin, Ethiopia. *J Hydrol Reg Stud* 24:100610
- Arabameri A, Rezaei K, Cerda A, Lombardo L, Rodrigo-Comino J (2019) GIS-based groundwater potential mapping in Shahroud plain, Iran. A comparison among statistical (bivariate and multivariate), data mining and MCDM approaches. *Sci Total Environ* 658:160–177
- Argaz A, Ouahman B, Darkaoui A, Bikhtar H, Yabsa K, Laghzal A (2019) Application of remote sensing techniques and GIS-multicriteria decision analysis for groundwater potential mapping in souss watershed, Morocco. *J Mater Environ Sci* 10:411–421
- Arulbalaji P, Padmalal D, Sreelash K (2019) GIS and AHP techniques based delineation of groundwater potential zones: a case study from southern Western Ghats, India. *Scientific Rep* 9:1–17
- Aryanto DE, Hardiman G (2018) Assessment of groundwater recharge potential zone using GIS approach in Purworejo regency, Central Java province, Indonesia. In: E3S web of conferences. EDP Sciences, pp 12002
- Aslan V, Çelik R (2021) Integrated gis-based multi-criteria analysis for groundwater potential mapping in the euphrates's sub-basin, Harran basin, turkey. *Sustainability* 13:7375
- Atmaja RRS, Putra DPE, Setijadji LD (2019) Delineation of groundwater potential zones using remote sensing, GIS, and AHP techniques in southern region of Banjarnegara, Central Java, Indonesia. In: Sixth geoinformation science symposium, vol 11311. International Society for Optics and Photonics
- Bashe BB, Bezabih Bashe B, Bashe B (2017) Groundwater potential mapping using remote sensing and GIS in rift valley lakes basin, Weito Sub Basin, Ethiopia. *Int J Sci Eng Res* 8:43–50
- Benjmel K, Amraoui F, Boutaleb S, Ouchchen M, Tahiri A, Touab A (2020) Mapping of groundwater potential zones in crystalline terrain using remote sensing, GIS techniques, and multicriteria data analysis (Case of the Ighrem Region, Western Anti-Atlas, Morocco). *Water* 12:471
- Bourjila A, Dimane F, Nouayti N, Taher M, El Ouarghi H (2020) Use of GIS, remote sensing and AHP techniques to delineate groundwater potential zones in the Nekor Basin, Central Rif of Morocco. In: Proceedings of the 4th edition of international conference on Geo-IT and water resources 2020, Geo-IT and water resources 2020, pp 1–7
- Cabała P (2010) Using the analytic hierarchy process in evaluating decision alternatives. *Oper Res Decis* 20:5–23
- Chen H, Wang S, Gao Z, Hu Y (2010) Artificial neural network approach for quantifying climate change and human activities impacts on shallow groundwater level—a case study of Wuqiao in North China Plain. *IEEE*, New York
- Chowdhury A, Jha M, Chowdary V, Mal B (2009) Integrated remote sensing and GIS-based approach for assessing groundwater potential in West Medinipur district, West Bengal, India. *Int J Remote Sens* 30:231–250
- Dar T, Rai N, Bhat A (2020) Delineation of potential groundwater recharge zones using analytical hierarchy process (AHP) *Geol Ecol Landscapes*
- Darko A, Chan APC, Ameyaw EE, Owusu EK, Pärn E, Edwards DJ (2019) Review of application of analytic hierarchy process (AHP) in construction. *Int J Constr Manag* 19:436–452

- Das S (2019) Comparison among influencing factor, frequency ratio, and analytical hierarchy process techniques for groundwater potential zonation in Vaitarna basin, Maharashtra, India. *Groundwater Sustain Dev* 8:617–629
- Das N, Mukhopadhyay S (2020) Application of multi-criteria decision making technique for the assessment of groundwater potential zones: a study on Birbhum district, West Bengal, India. *Environ Dev Sustain* 22:931–955
- Das B, Pal SC (2020) Assessment of groundwater recharge and its potential zone identification in groundwater-stressed Goghat-I block of Hugli District, West Bengal, India. *Environ Dev Sustain* 22:5905–5923
- Doke AB, Zolekar RB, Patel H, Das S (2021) Geospatial mapping of groundwater potential zones using multi-criteria decision-making AHP approach in a hardrock basaltic terrain in India. *Ecol Ind* 127:107685
- Dung NB, Long NQ, Goyal R, An DT, Minh DT (2021) The role of factors affecting flood hazard zoning using analytical hierarchy process: a review. *Earth Syst Environ* 1–17
- Erhan S, Sehnaz S, Aysen D (2018) Groundwater potential mapping by combining fuzzy-analytic hierarchy process and GIS in Beysehir Lake Basin, Turkey. *Arab J Geosci* 11:187–208
- Gebru H, Gebreyohannes T, Hagos E (2020) Identification of groundwater potential zones using analytical hierarchy process (AHP) and GIS-remote sensing integration, the Case of Golina River Basin, Northern Ethiopia. *Int J Adv Remote Sens GIS* 9:3289–3311
- Gyeltshen S, Tran TV, Teja Gunda GK, Kannaujiya S, Chatterjee RS, Champatiray P (2020) Groundwater potential zones using a combination of geospatial technology and geophysical approach: case study in Dehradun, India. *Hydrol Sci J* 65:169–182
- Hachem AM, Ali E, El Ouali Abdelhadi EHA, Said K (2015) Using remote sensing and GIS-multicriteria decision analysis for groundwater potential mapping in the middle atlas plateaus, Morocco. *Res J Recent Sci*. ISSN: 2277, 2502
- Halder S, Roy MB, Roy PK (2020) Fuzzy logic algorithm based analytic hierarchy process for delineation of groundwater potential zones in complex topography. *Arab J Geosci* 13:1–22
- Hamdani N, Baali A (2020) Characterization of groundwater potential zones using analytic hierarchy process and integrated geomatic techniques in Central Middle Atlas (Morocco). *Appl Geomatics* 12:323–335
- Hatefi AAH, Ekhtesasi MR (2016) Groundwater potentiality through analytic hierarchy process (AHP) using remote sensing and geographic information system (GIS)
- Hsu K-C, Yeh H-F, Chen Y-C, Lee C-H, Wang C-H, Chiu F-S (2012) Basin-scale groundwater response to precipitation variation and anthropogenic pumping in Chih-Ben watershed, Taiwan. *Hydrogeol J* 20:499–517
- Ifediegwu SI (2022) Assessment of groundwater potential zones using GIS and AHP techniques: a case study of the Lafia district, Nasarawa State, Nigeria. *Appl Water Sci*
- Jenifer MA, Jha MK (2017) Comparison of analytic hierarchy process, catastrophe and entropy techniques for evaluating groundwater prospect of hard-rock aquifer systems. *J Hydrol* 548:605–624
- Jha MK, Chowdary V, Chowdhury A (2010) Groundwater assessment in Salboni Block, West Bengal (India) using remote sensing, geographical information system and multi-criteria decision analysis techniques. *Hydrogeol J* 18:1713–1728
- Jhariya D, Khan R, Mondal K, Kumar T, Singh VK (2021) Assessment of groundwater potential zone using GIS-based multi-influencing factor (MIF), multi-criteria decision analysis (MCDA) and electrical resistivity survey techniques in Raipur city, Chhattisgarh, India. *J Water Supply Res Technol Aqua* 70:375–400. *Water Infrastructure, Ecosystems and Society*
- Khodaei K, Nassery HR (2013) Groundwater exploration using remote sensing and geographic information systems in a semi-arid area (Southwest of Urmieh, Northwest of Iran). *Arab J Geosci* 6:1229–1240
- Lakshmi SV, Reddy YV (2018) Multicriteria decision making ahp based groundwater potential mapping for Gummidiipoondi district. *Int J Pure Appl Math* 119:41–58

- Li X, Li G, Zhang Y (2014) Identifying major factors affecting groundwater change in the North China plain with Grey relational analysis. *Water* 6:1581–1600
- Machiwal D, Jha MK, Mal BC (2011) Assessment of groundwater potential in a semi-arid region of India using remote sensing, GIS and MCDM techniques. *Water Resour Manage* 25:1359–1386
- Mahato R, Bushi D, Nimasow G, Nimasow OD, Joshi RC (2022) AHP and GIS-based delineation of groundwater potential of Papum Pare District of Arunachal Pradesh, India. *J Geol Soc India* 98:102–112
- Maity DK, Mandal S (2019) Identification of groundwater potential zones of the Kumari river basin, India: an RS & GIS based semi-quantitative approach. *Environ Dev Sustain* 21:1013–1034
- Melese T, Belay T (2022) Groundwater potential zone mapping using analytical hierarchy process and GIS in Muga Watershed, Abay Basin, Ethiopia. *Global Challenges* 6:2100068
- Mohamed MM, Elmahdy SI (2017) Fuzzy logic and multi-criteria methods for groundwater potentiality mapping at Al Fo'ah area, the United Arab Emirates (UAE): an integrated approach. *Geocarto Int* 32:1120–1138
- Mohammadi-Behzad H, Charchi A, Kalantari N, Nejad AM, Vardanjani HK (2019) Delineation of groundwater potential zones using remote sensing (RS), geographical information system (GIS) and analytic hierarchy process (AHP) techniques: a case study in the Leylia-Keynow watershed, southwest of Iran. *Carbonates Evaporites* 34:1307–1319
- Murmu P, Kumar M, Lal D, Sonker I, Singh SK (2019) Delineation of groundwater potential zones using geospatial techniques and analytical hierarchy process in Dumka district, Jharkhand, India. *Groundwater Sustain Dev* 9:100239
- Naidu CK, Reddy BV, Mouli CC (2015) Delineation of groundwater potential zones using remote sensing and GIS techniques: a case study of Sarada Gedda sub watershed. *Int J Eng Res* 4
- Nithya CN, Srinivas Y, Magesh N, Kaliraj S (2019) Assessment of groundwater potential zones in Chittar basin, Southern India using GIS based AHP technique. *Remote Sens Appl Soc Environ* 15:100248
- Owolabi ST, Madi K, Kalumba AM, Orimoloye IR (2020) A groundwater potential zone mapping approach for semi-arid environments using remote sensing (RS), geographic information system (GIS), and analytical hierarchical process (AHP) techniques: a case study of Buffalo catchment, Eastern Cape, South Africa. *Arab J Geosci* 13:1–17
- Panahi MR, Mousavi SM, Rahimzadegan M (2017) Delineation of groundwater potential zones using remote sensing, GIS, and AHP technique in Tehran-Karaj plain, Iran. *Environ Earth Sci* 76:1–15
- Pande CB, Moharir KN, Panneerselvam B, Singh SK, Elbeltagi A, Pham QB, Varade AM, Rajesh J (2021) Delineation of groundwater potential zones for sustainable development and planning using analytical hierarchy process (AHP), and MIF techniques. *Appl Water Sci* 11:1–20
- Pani S, Chakrabarty A, Bhadur S (2016) Groundwater potential zone Identification by analytical hierarchy process (AHP) weighted overlay in GIS Environment—a case study of Jhargram Block, Paschim Medinipur. *Int J Remote Sens Geosci (IJRSG)* 5:1–10
- Patil SG, Mohite NM (2014) Identification of groundwater recharge potential zones for a watershed using remote sensing and GIS. *Int J Geomatics Geosci* 4:485
- Rajasekhar M, Raju GS, Sreenivasulu Y, Raju RS (2019) Delineation of groundwater potential zones in semi-arid region of Jilledubanderu river basin, Anantapur District, Andhra Pradesh, India using fuzzy logic AHP and integrated fuzzy-AHP approaches. *HydroResearch* 2:97–108
- Rajesh J, Pande CB, Kadam SA, Gorantiwar SD, Shinde MG (2021) Exploration of groundwater potential zones using analytical hierarchical process (AHP) approach in the Godavari river basin of Maharashtra in India. *Appl Water Sci* 11
- Ramachandra M, Raghu Babu K, Rajasekhar M, Pradeep Kumar B (2019) Identification of groundwater potential zones using AHP and geospatial techniques in western part of Cuddapah Basin, Andhra Pradesh, India. *Hydrospatial Anal* 3:60–71
- Razandi Y, Pourghasemi HR, Neisani NS, Rahmati O (2015) Application of analytical hierarchy process, frequency ratio, and certainty factor models for groundwater potential mapping using GIS. *Earth Sci Inf* 8:867–883

- Roy A, Keesari T, Sinha UK, Sabarathinam C (2019) Delineating groundwater prospect zones in a region with extreme climatic conditions using GIS and remote sensing techniques: a case study from central India. *J Earth Syst Sci* 128:1–19
- Saaty TL (2008) Decision making with the analytic hierarchy process. *Int J Serv Sci* 1:83–98
- Santhosh A, Varma D, Gayathry TJ, Nimisha KJ, Johnson AA (2018) Identification of ground water potential zones using gis and remote sensing. *Int J Curr Eng Sci Res* 5
- Saranya T, Saravanan S (2019) Groundwater potential zone mapping using analytical hierarchy process (AHP) and GIS for Kancheepuram District, Tamilnadu, India. *Model Earth Syst Environ*
- Saranya T, Saravanan S (2020) Groundwater potential zone mapping using analytical hierarchy process (AHP) and GIS for Kancheepuram District, Tamilnadu, India. *Model Earth Syst Environ* 6:1105–1122
- Sener E, Davraz A (2018) Assessment of groundwater vulnerability based on a modified DRASTIC model, GIS and an analytic hierarchy process (AHP) method: The case of Egridir Lake basin (Isparta, Turkey). *Hydrogeol J* 21:701–714
- Shekhar S, Pandey AC (2015) Delineation of groundwater potential zone in hard rock terrain of India using remote sensing, geographical information system (GIS) and analytic hierarchy process (AHP) techniques. *Geocarto Int* 30:402–421
- Singh S, Mishra S, Kanga S (2017) Delineation of groundwater potential zone using geospatial techniques for Shimla city, Himachal Pradesh (India). *Int J Sci Res Dev* 5:225–234
- Singh LK, Jha MK, Chowdary V (2018) Assessing the accuracy of GIS-based multi-criteria decision analysis approaches for mapping groundwater potential. *Ecol Ind* 91:24–37
- Siva G, Nasir N, Selvakumar R (2017) Delineation of groundwater potential zone in Sengipatti for Thanjavur district using analytical hierarchy process. In: *IOP conference series: Earth and environmental science*,. IOP Publishing, pp 012063
- Sonwane K, Usmani HU (2021) Assessment of groundwater potential zones using geographic information system and analytic hierarchy process (AHP) techniques in Chhoti Kali Sindh Watershed in Ujjain district, Madhya Pradesh, India. *J Sci Technol* 6:122–131
- Sresto MA, Siddika S, Haque MN, Saroar M (2021) Application of fuzzy analytic hierarchy process and geospatial technology to identify groundwater potential zones in north-west region of Bangladesh. *Environ Challenges* 5:100214
- Thomas R, Duraisamy V (2018) Hydrogeological delineation of groundwater vulnerability to droughts in semi-arid areas of western Ahmednagar district. *Egypt J Remote Sens Space Sci* 21:121–137
- Thungngern J, Wijitkosum S, Sriburi T, Sukhsri C (2015) A review of the analytical hierarchy process (AHP): an approach to water resource management in Thailand. *Appl Environ Res* 37:13–32
- Todd DK, Mays LW (2004) *Groundwater hydrology*. Wiley
- Urqueta H, Jódar J, Herrera C, Wilke H-G, Medina A, Urrutia J, Custodio E, Rodríguez J (2018) Land surface temperature as an indicator of the unsaturated zone thickness: a remote sensing approach in the Atacama Desert. *Sci Total Environ* 612:1234–1248
- Wudad A, Biru D, Darcho A, Mohammed E, Bazie F (2021) Delineation of ground water potential zones using GIS and remote sensing techniques in the case of Korahe zone, Somali regional state, Ethiopia. *Int J Sci Res Publ* 11
- Yıldırım Ü (2021) Identification of groundwater potential zones using GIS and multi-criteria decision-making techniques: a case study upper Coruh River basin (NE Turkey). *ISPRS Int J Geo Inf* 10:396
- Zeinolabedinia M, Esmailyb A (2015) Groundwater Potential Assessment Using Geographic Information. In: *International archives of the photogrammetry, remote sensing and spatial information sciences* 1, W5
- Zghibi A, Mirchi A, Msaddek MH, Merzougui A, Zouhri L, Taupin J-D, Chekirbane A, Chenini I, Tarhouni J (2020) Using analytical hierarchy process and multi-influencing factors to map groundwater recharge zones in a semi-arid Mediterranean coastal aquifer. *Water* 12:2525

Chapter 8

Pumped Storage Power Plant, Solutions to Ensure Water Sustainability and Environmental Protection



Trung Son Pham

Abstract Demand for electricity in recent years has been steadily increasing at an average of 14% per year. Therefore, the construction of a stable power source meets the demands of production and daily life of the people is extremely important and urgent. However, the increasing in energy use has an adverse impact on the ecological environment. Currently, to ensure energy security, environmental safety, and efficient and sustainable use of water resources, the best and almost unique solution is to build pumped storage power plants. The paper focuses on detailed analysis of advantages, disadvantages as well as the efficiency and prospects of using pumped storage power plant technology in Vietnam's power system.

Keywords Pumped storage power plant · Sustainable · Environment · Water resources

8.1 Introduction

According to the Vietnam National Electricity Development Plan during the period 2011–2020, with a vision to 2030 (also called Electricity Plan VII adjustment (The Prime Minister of the Socialist Republic of Vietnam 2030)) with forecast growth of average annual electricity demand of Vietnam at the average of about 14% per year¹. To meet the forecasted demand, the system's generation capacity is planned to increase by 60,000 MW in 2020 and 129,500 MW in 2030.²

¹ Information for forecast growth of average annual electricity demand. <https://tuoitre.vn/thuy-dien-tich-nang---giai-phap-moi-cho-nguon-dien-vn-2808.html>.

² Vietnam coal power development information. <http://thoibaotaichinhvietnam.vn/pages/kinh-doanh/2020-02-27/phat-trien-nang-luong-tai-tao-de-tao-ra-mot-he-thong-nang-luong-ben-vung-83068.aspx>.

T. S. Pham (✉)
Hanoi University of Mining and Geology, Hanoi, Vietnam
e-mail: phamtrungson@humg.edu.vn

As generation capacity increases, the structure of the energy sources in the system is expected to change significantly. Accordingly, the percentage of hydropower in the energy system is expected to decrease from 38% (in 2015) to 17% (in 2030) and natural gas from 21% (in 2015) to 15% (in 2030) ... Meanwhile, coal production capacity is expected to increase from 33% (2015) to 43% (2030), equivalent to the increase of 40 coal thermal power plants. The total capital needs for these investments are estimated at US \$ 9.8 billion per year, most of which focuses on coal power development.³

According to experts from the Electricity and Energy Working Group at the annual Vietnam Business Forum, if the Electricity Plan VII adjustment is continued, the energy development will be based mainly on coal sources. Coal-powered thermo-electricity plants can cause a lot of financial expense, energy security, environmental and public health risks, which related to poor air quality, emissions through factory chimneys, fly ash emissions, coal sludge reservoir and the location of power plants.

On the other hand, the future of coal thermal power plants globally is seriously threatened due to concerns related to limiting greenhouse gas emissions and the risk of asset depreciation⁴. For both reasons, the number of financial institutions is willing to invest in coal thermal power plants will decrease. In addition, the development of energy based mainly on coal does not go along with the trend of developing low carbon economies of the world, contrary to Vietnam's national commitment to reduce carbon emissions, as well as the need to complete the sustainable development goals of the electricity industry.

In the face of food and water security challenges, the environmental challenges, the challenges of rising energy prices, it is necessary to create alternative energy sources for coal thermal power plants. The selection of alternative power sources has been studied based on both socio-economic and environmental calculations to select the appropriate type of energy. Considering the impact of overall socio-economic and from the results of the research, analysts said that replacing coal thermal power plants with renewable energy is necessary. However, a common limitation for all renewable energy sources is that it is difficult to produce a large amount of electricity, depending on the weather, wind and unreliable sunlight, low electricity production efficiency, and new technology with a huge initial investment cost. Therefore, the construction of a stable power supply, meet the needs of production and daily life of the citizens is extremely important and urgent. Besides, the task of ensuring the sustainable use of water resources and ensuring environmental safety cannot be forgotten. At present, the best and almost unique solution is to build pumped storage power plants. The detailed content will be fully analyzed in the following sections.

³ See Footnote 2.

⁴ World energy information. <http://peakoilbarrel.com/world-energy-2016-2050-annual-report/>.

8.2 Analyze and Assess the Pumped Storage Power Plants and Its Current Status in Vietnam

8.2.1 Analyze and Assess the Pumped Storage Power Plants

Pumped storage power plants are a form of energy storage hydropower, with the main purpose of accumulating electricity to supply the system in need. Intuitively, one can imagine the pumped storage power plants as the “battery” of the power system, being “fully charged” in free time and brought out when needed. The model of pumped storage power plants is two reservoirs at two different levels, and a hydroelectric plant with reversible turbines located near the lower reservoir, connected to the upper reservoir by a pressure pipe. Pumped storage power plant works on the principle of balancing the load demand of the electricity system. During peak hours, when the demand for electricity is high, water is discharged through pressure pipes from the reservoir above, turn turbines to generate electricity on the system, the water is stored in the reservoir below. During off-peak hours, when the demand for electricity is low, the plant takes electricity from the system to pump water back from the lower reservoir to the upper reservoir via a two-way turbine, now acting as a pump. Therefore, the pumped storage power plant is both a power generating unit and a power consuming unit, and the practical basis for this mode of operation is the difference in electricity prices between peak and off-peak hour. Statistically, most pumped storage power plants consume more electricity than they can produce, but the economic benefits of the plant are still ensured because electricity prices during off-peak hours are much smaller than peak hours, even, in some power supply systems, at some point, the price of electricity can be zero. Based on technology, pumped storage power plants can reuse water sources, ensure sustainable and safe water energy source with the environment by using green technology. In addition, the pumped storage power plants can ensure the safety of dams and floods downstream in the rainy season by regulating the reservoir system appropriately (Fig. 8.1).⁵

(1) Advantages and Disadvantages of Pumped-Storage Power Plants

Vietnam starts a study on several pumped-storage power plants projects so it will take time to fully evaluate the effectiveness after the operation of some projects. According to the evaluation and experience of operation, pumped-storage power plants have the following advantages and disadvantages:

Pumped-storage power plant has many advantages. The biggest advantage is that it increases the efficiency of the system, when it takes advantage of excess electricity from thermal power plants (coal, gas, nuclear ...) during off-peak hours, plants that have to run idle. The continuous opening and closing will no longer exist (due to excess electricity has been used to pump water up), which helps to increase operational efficiency and operational stability for these plants. As well as

⁵ Pumped storage hydro power plant information. <http://www.electricalpowerenergy.com/2017/01/pumped-storage-hydro-power-plant/>.

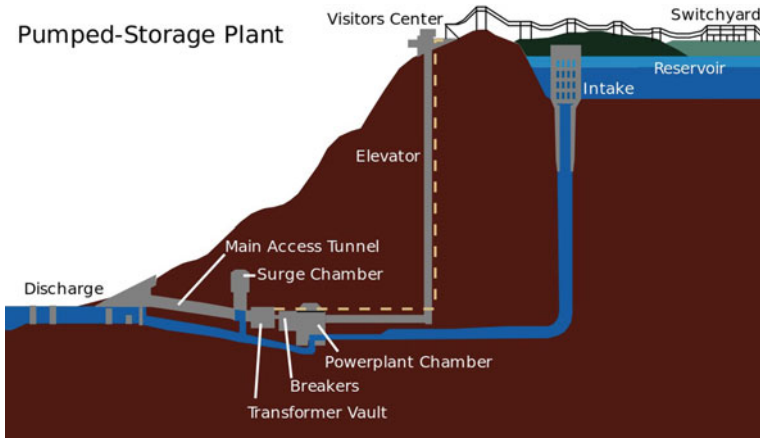


Fig. 8.1 Operating model of pumped-storage power plants. Source <http://www.electricalpowerenergy.com/2017/01/pumped-storage-hydro-power-plant/>

traditional hydroelectric power plants, pumped-storage power plant can also respond very quickly when electricity demand increases abruptly. If one of the power sources is in trouble, it only takes three minutes after pressing the start button to synchronize to the grid; while with other types of sources such as thermal power plant it takes hours or days to start a plant. This initiative helps to ensure the safety of electricity supply, to stabilize the frequency of the power system, and it is very friendly to the environment when it does not generate greenhouse gas emissions. But unlike traditional hydroelectric power plants, pumped-storage power plant does not need a lot of land for reservoirs, because it only needs to store a sufficient amount of water for design hours (usually from 6 to 20 h), minimizes impacts on the natural and ecological environment in the plant construction, with little impact on the surrounding landscape. Moreover, after containing enough water, the amount of water goes up and down between the two reservoirs, the flow of the rivers is as the same before the plant was constructed. Also due to the initiative in the reserved water source, the operation of the pumped-storage power plant does not depend much on the annual hydrological regime, which can flexibly adjust the operating capacity according to the load demand (DOE, EPRI 2013; Prasad et al. 2013; Botterud et al. 2014).^{6,7}

Pumped-storage power plant is the safest and most economical way to store energy, just investing in initial construction without spending money on fuels like other energy sources. Ensure sustainable use of water energy and safe for the environment (DOE, EPRI 2013; Prasad et al. 2013; Botterud et al. 2014).^{8,9}

⁶ See Footnote 5.

⁷ National renewable energy laboratory (2010) The role of energy storage with renewable energy generation. <http://www.nrel.gov/docs/fy10osti/47187.pdf>.

⁸ See Footnote 5.

⁹ See Footnote 7.

Stimulate the development of renewable energy sources. Diversify the types of sources in the system. Establishment of combined synergy between hydroelectric dams, solar and wind power creates more power. The hybrid allows solar panels to produce solar energy during the day, wind power can produce electricity day and night. Another major advantage of installing solar power on dams is the benefit of using existing electrical infrastructure, including high-voltage switchgear and grid access. This significantly reduces overall costs and makes projects happen faster. Because solar power, wind power and hydropower are connected intelligently and the production of electricity from solar power, wind power or hydropower by the hour of the day, so it is not necessary to increase conversion or improve transport capacity if the maximum output of the solar power, wind power does not exceed the maximum capacity of hydropower. In some localities, the combination of three types of electricity generation, solar, wind and hydropower can create a beautiful landscape for eco-tourism, bringing economic benefits to the locality (Figs. 8.2 and 8.3).



Fig. 8.2 Geesthacht pumped storage power plant, near Hamburg, has been operating since 1958.
Source <https://powerplants.vattenfall.com/geesthacht>



Fig. 8.3 Photovoltaic power plant floats on water at the reservoir of Yamakura Dam, Chiba Province, Japan. *Source* <https://www.pv-magazine.com/2018/03/27/kyocera-jv-inaugurates-13-7-mw-floating-pv-plant-in-japan/>

Because the terrain of Vietnam is quite special, the western border, especially the southern central region, has a steep slope, so floods often occur when rain and flood¹⁰. If reservoirs for pumped-storage power plant can be built in such terrain conditions, then can regulate flood flows to ensure safety downstream and deal with climate change.

(2) *Disadvantages*

The main disadvantage of pumped-storage power plants is that they do not have a high operating efficiency (about 70–85%). This lack of efficiency is caused by unavoidable energy losses during the pumping of water from the lower reservoir to the upper reservoir. Another fundamental drawback is that a pumped-storage power plants cannot function independently as a power generating facility. It only can function as a “battery” within a relatively large capacity electrical system. This means that pumped-storage power plants can only be considered, when a relatively extensive system of power plants has been built. They are not feasible in areas far from power load centers with severe electricity shortages. Other electricity generation is not feasible to build up pumped-storage power plants. This also leads to another limitation of pumped-storage power plants, in that it is difficult to choose the construction

¹⁰ Vietnam renewable energy information, <http://socongthuong.tuyenquang.gov.vn/tin-tuc-su-kien/nang-luong-moi-truong/tiem-nang-va-thach-thuc-phat-trien-nang-luong-tai-tao-o-viet-nam-ky-1-110.html>.

site. Pumped-storage power plants require special terrain. There need to be drastic differences in height up to hundreds of meters. It must also be built near a water source with enough space to arrange two reservoirs. An ideal location would be in a mountainous area with wide peaks next to large rivers and streams. Such locations are often wilderness- in protected areas, with stunning scenery and high conservation needs. These areas are rarely near any major power generation facilities- taking into consideration economic factors when building the power transmission lines (DOE, EPRI 2013; Prasad et al. 2013; Botterud et al. 2014).^{11,12}

8.2.2 Assess the Current Situation of the Development of Pumped-Storage Power Plant in Vietnam

During the energetic development of the hydropower industry in Vietnam in the past few decades, pumped-storage power plant has been included in the study as a new power development plan. The planning for the development of pumped-storage power plants nationwide has been approved by the Ministry of Industry in Decision №. 3837/QD-BCN of November 22, 2005. In consultation with Japanese experts (JICA), Vietnam Electricity (EVN) has also conducted research on the potential of pumped-storage power plant projects and are included in the national electricity development plan to be submitted to the Prime Minister for approval. Currently, EVN has started the construction of the discharge gate of the Bac Ai project. The Bac Ai pumped-storage power plant project-invested in by EVN, is one of the first hydroelectricity projects to be built in Vietnam¹³. The project consists of 4 units, total capacity of 1200 MW, with a total investment of about VND 21,100 billion. The plant uses the world's modern technology that integrated with pump-turbine reversing and engine-generator reversing. Multiple projects proposed by JICA have also been approved by the Government and are in the process of being implemented, such as the Dong Phu Yen pumped-storage power plant project. The Dong Phu Yen pumped-storage power plant project (Son La) has a generating capacity of 1500 MW, this is the first pumped-storage power plant project to be applied and built in Vietnam and it is expected to operate in 2026–2030. Until recently, EVN has also completed a pre-feasibility study report for three pumped-storage power plant projects in Moc Chau, Don Duong and Ham Thuan Bac, these projects are scheduled to be implemented step by step. With a well-established reputation and huge store of experience after the successful of Son La and Lai Chau hydroelectric projects; Moc Chau hydroelectric

¹¹ See Footnote 5.

¹² See Footnote 7.

¹³ Bac Ai pumped storage power plants information, <https://thanhvien.vn/khoi-cong-thuy-dien-tich-nang-dau-tien-o-viet-nam-post915227.html>.

project has been trusted by Vietnam Electricity to be assigned to Son La Hydropower PMU. In the next few years, the picture of pumped-storage power plants in Vietnam will be embellished with more projects than now, because with a lot of potential (at least 10 highly feasible projects), pumped-storage power plants will be the future of hydropower in Vietnam.¹⁴

Thus, on the basis of analysis of the advantages and disadvantages of pumped-storage power plant and the assessment of the current status and development potential of this power source. The Ministry of Industry and Trade needs a drastic strategy and solution to realize more construction of the pumped storage power plant to ensure energy security, to ensure water sustainability and environmental protection.

8.3 Discussion

Pumped-storage power plants have been widely used in electrical systems in numerous countries around the world. This type of energy storage technology has many advantages when compared to other types of energy storage technology such as the capacity of large plants as well as the flexible operation...

Pumped-storage power plants are similar in structure to traditional hydroelectric plants, simple to operate and with high efficiency.

When pumped-storage power plants work in the system, the economic efficiency of the whole system will be raised by the following reasons:

- Replace thermal power plants, cover the peak system load at maximum power operation regime.
- Improve the working efficiency of thermal power plants because now the units of thermal power plants will be mobilized with active power optimization and the electricity production cost of thermal power plants will be more optimal.
- Maximum mobilization of hydroelectric plants in flood season to avoid overflow.
- Contribute to stabilizing the system because it can adjust the voltage and frequency of the system as well as the auxiliary services that pumped-storage power plants can bring.

When pumped-storage power plants are integrated into the system, the economic efficiency of the plant itself is also enhanced by using inexpensive electricity at the minimum load regime to operate in the storage mode and will generate electricity to cover peak-load power at maximum load regime with higher costs. These two electricity prices differ greatly, and this has increased the economic efficiency for the pumped-storage power plants itself.

Contribute to ensuring sustainable use of water resources, economical and efficient use of water sources, balance irrigation plans in service of agriculture, ensure dam safety as well as flood safety during rainy and stormy seasons.

¹⁴ Vietnam pumped storage power plants information. <http://nangluongvietnam.vn/news/en/home>.

8.4 Conclusion

Vietnam is facing the challenge of rising energy demands, complicated by increasing environmental constraints. This places pressure upon those entrusted with ensuring national energy security, and it calls upon the economic sector to mobilize enough investment capital for the energy sector.

Overall, Vietnam's energy supply has historically met the basic needs of the country's socio-economic development. However, to solve the energy problems caused by the rapid upturn in economic development, it is necessary to use energy economically while utilizing environmentally friendly technologies for energy production. The move towards a low carbon economy in Vietnam necessitates changes to production patterns- from the inefficient use of fossil fuels to the use of clean, renewable energy sources.

In this paper, a proposed solution is to build a pumped-storage hydropower plant. The results of the analysis have shown that this is the best solution for both the present and the future. The benefits of a pumped-storage hydropower plant are as follows: energy security, energy quality in line with the development of the country's economy, environmental safety and sustainability of water resources. The paper has evaluated the advantages and disadvantages of this type of plant in a comprehensive manner with a long-term perspective for the overall development of Vietnam's electrical system- positing solutions that can guarantee sustainable development of water resources.

References

- Botterud A, Levin T, Koritarov V (2014) Pumped storage hydropower: benefits for grid reliability and integration of variable renewable energy. Argonne National Laboratory
- DOE/EPRI (2013) Electricity storage handbook in collaboration with NRECA. <http://www.sandia.gov/ess/publications/SAND2013-5131.pdf>
- Prasad AD, Jain K, Gairola A (2013) Pumped storage hydropower plants environmental impacts using geomatics techniques: an overview. *Int J Comput Appl* (0975–8887) 81(14)
- Decision number: 428/QĐ-TTg (2016) Approve the adjustment of the national electricity development planning for the 2011–2020 period, with a vision to 2030. The Prime Minister of the Socialist Republic of Vietnam

Chapter 9

Modelling the Influences of River Water Level on the Flooding Situation of Urban Areas: A Case Study in Hanoi, Vietnam



Van Minh Nguyen, Kim Chau Tran, and Thanh Thuy Nguyen

Abstract Urban flooding is one of the typical disasters in many cities, especially in riverside cities. This study has developed an integrated model to assess flooding in Hanoi, Vietnam, taking the water level impact of surrounding rivers into account. In the integrated model, the Mike Urban model is used to simulate the flow in the sewer system, the Mike 21 model is used to present the overland flow on the surface, while the Mike 11 model is used to simulate the flow in the river. The result of the study shows that the river water level has a significant influence on the drainage capacity of the system. When considering the effects of the river water level, the flooding depth becomes more serious as well as the flooding period. This result shows that, by operating the system of works to maintain the low water level of the surrounding rivers, the flood level of Hanoi city will be significantly reduced.

Keywords Urban flooding · Mike · Sewer system · Drainage · River water level

9.1 Introduction

In recent years, urban flooding in Hanoi has become more and more common. Although the city's drainage system has improved significantly over time, it can be seen that the urban drainage requirements are still unmet. According to the current regulations, urban drainage standards in Vietnam in general (VIWASE 2008) or in Hanoi city in particular (The Vietnamese Prime Minister 2013), the drainage system of Hanoi must drain the 10 year return period rainfall event. However, flooding still occurs in annual rainfall season. According to statistics of Hanoi drainage company,

V. M. Nguyen

Power Engineering Consulting Joint Stock Company 1, Km9+200 Nguyen Trai, Thanh Xuan, Hanoi, Vietnam

K. C. Tran · T. T. Nguyen (✉)

Thuyloi University, 175 Tay Son, Dong Da, Ha Noi, Vietnam

e-mail: thanhtthuy_rt@tlu.edu.vn

during the heavy rainfall event on August 18, 2016, there were 45 flooded points in the whole inner city. This number of flooded points decreased to 28 in the rainfall event of April 2019. These heavy rains had not reached the design value. However, the flood situation made the daily life of the people in the city difficult.

Urban flooding is a complex process that includes flow in the sewer system combine with overland flow. Flood simulation using mathematical models is an effective approach to this complex issue. Le et al. (2021) applied 1-D/2-D coupled urban-drainage/flooding model to simulate flooding for Ha Tinh city. Huynh and Pathirana applied similar approach to assess climate change impact on urban flooding for Can Tho city (Huong and Pathirana 2013). These two cities are surrounded by rivers, i.e. Nghen and Rao Cai; Rach Cam, Hau and Can Tho corresponding to Ha Tinh and Can Tho. However, these rivers were not set up in the model to analyse the interaction between river water level and flow from city inner drainage systems.

The interaction between the drainage system and surface runoff in the urban flood simulation problem was considered in many research (GebreEgziabher and Demissie 2020; Seyoum et al. 2012; Jang et al. 2018; Chang et al. 2018; Son et al. 2016; Leandro and Martins 2016). However, the influences of surrounding river has not mentioned specifically in any research. In these studies, the water flow from sewer systems to rivers freely or with known river water level. These assumptions are not suitable for the case the river water level higher than the outlets' invert level or strongly dependent on the flow from sewer system and lateral flow.

This paper, therefore, focuses on the riverside urban. The aim of our work is to develop integrated model to assess impact of water level of surrounding river to drainage capacity of sewer system. This integrated model is linked Mike Urban, Mike 11 HD, and Mike 21 FM together. The study will conduct in 2 cases with and without considering the influence of river water level.

9.2 Materials and Methods

9.2.1 Study Area

Hanoi is the capital of Vietnam. Hanoi is located to the northwest of the center of the Red River Delta. The total area of Hanoi city is 3358.6 km² and the population is 8.25 million people (General Statistics Office of Vietnam 2020). The study area is part of this city where is bounded by the Red river, Nhue river and To Lich river (Fig. 9.1). This is an area with flat terrain with elevations mainly from 4 to 5 m. This elevation is lower than the water level of the Red River in flood season. To protect the city, a dike system along the Red river was built to prevent flooding from the Red River.

The drainage network in the study area is shown in Fig. 9.1. The areas tend to drain the water to the To Lich River on the left, and Nhue River on the right. There are several outlet is presented in Fig. 9.1 along both rivers. In case, water level in Nhue

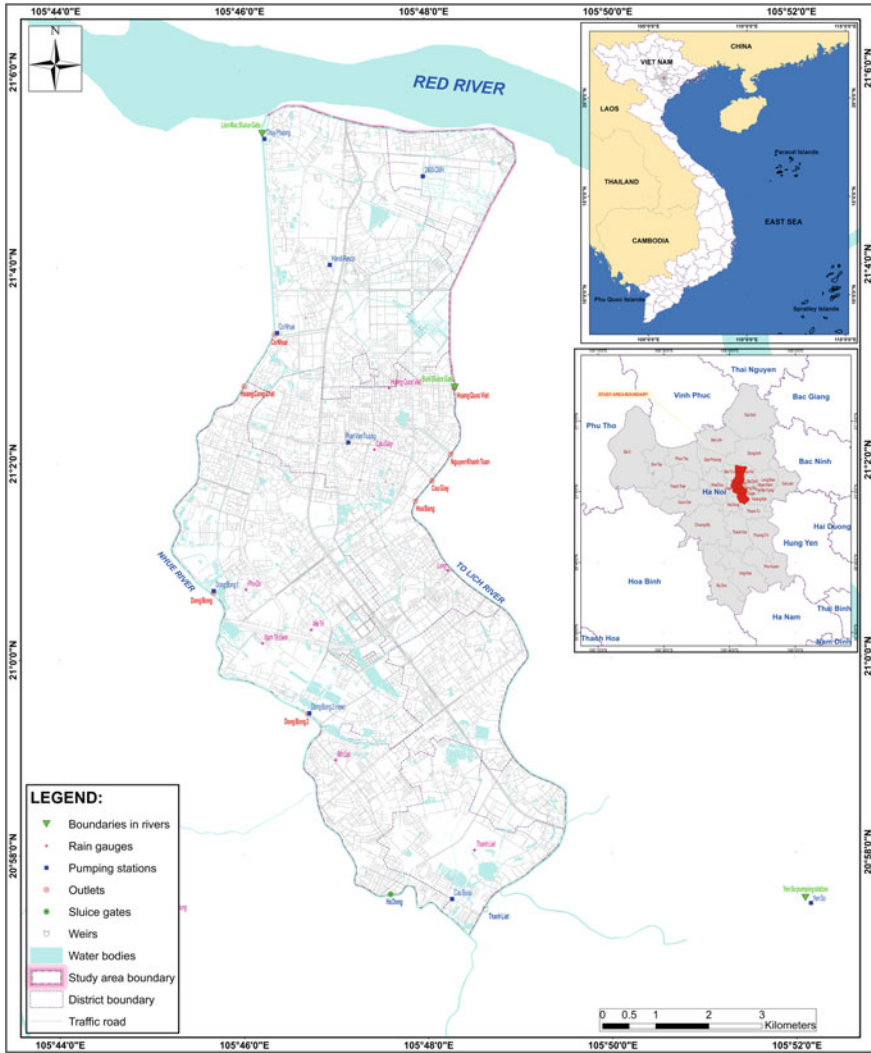


Fig. 9.1 The location of study area

River is high, water is forced to release to river through pumping stations. There are 4 pumping stations setup along the Nhue River. In the To Lich river side, there is no pumping station. So water only drain to river via gravity sewer systems. In addition, the Thanh Liet weir was built in To Lich River. This weir plays an important role to regulate water level in Nhue and To Lich River. It prevents water from the Nhue river flow into the To Lich river when the water level in Nhue River is higher than the water level in To Lich river.

9.2.2 Method

To simulate flooding in the study area, the methodology was described in Fig. 9.2. The integrated model was calibrated and validated for two heavy rainfall events on 29–30/04/2019 and 03/08/2019. These was 2 heavy rainfall event that occurred on the area corresponding to the current state of the drainage system. The calculated results were compared with surveyed flood marks. In this process, the observer rainfall data of 8 stations on the study area was used as the input of rainfall runoff model. For simulation scenarios, the designed rainstorm was derived from Intensity–Duration–Frequency (IDF) curves. IDF curves were constructed from historical data on short-term rainfall observed at Lang station since 1985–2008. From these curves, the alternating block method was applied to develop the design hyetograph (Ghazavi et al. 2016).

In this study, the study area was divided into 365 sub-basins. The division was based on the spatial distribution of manholes in the area. The amount of rainfall per sub-basin was collected into the sewer system. In this study, the time-area curve method was used to convert rain to runoff (DHI 2016b). Besides, the lateral flow contributing to the Tolich and Nhue River was delineated to 15 sub-basins from 1:2000 topography map are shown in Fig. 9.3.

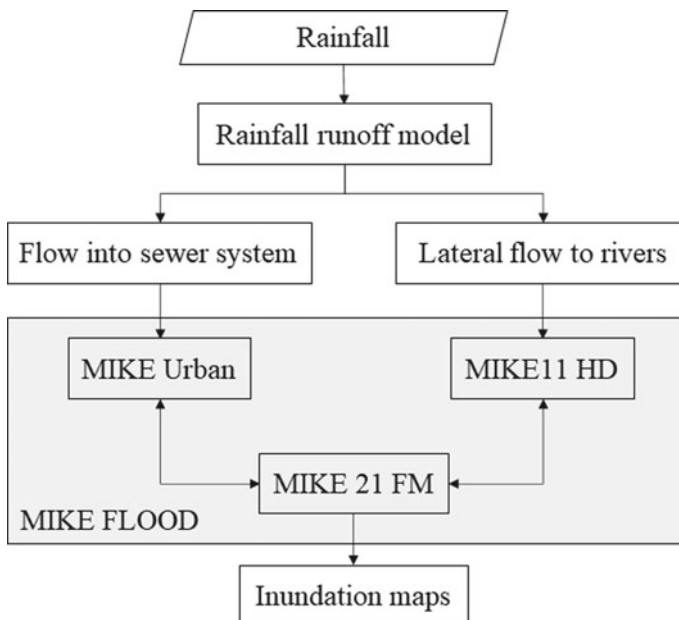


Fig. 9.2 The methodology flowchart

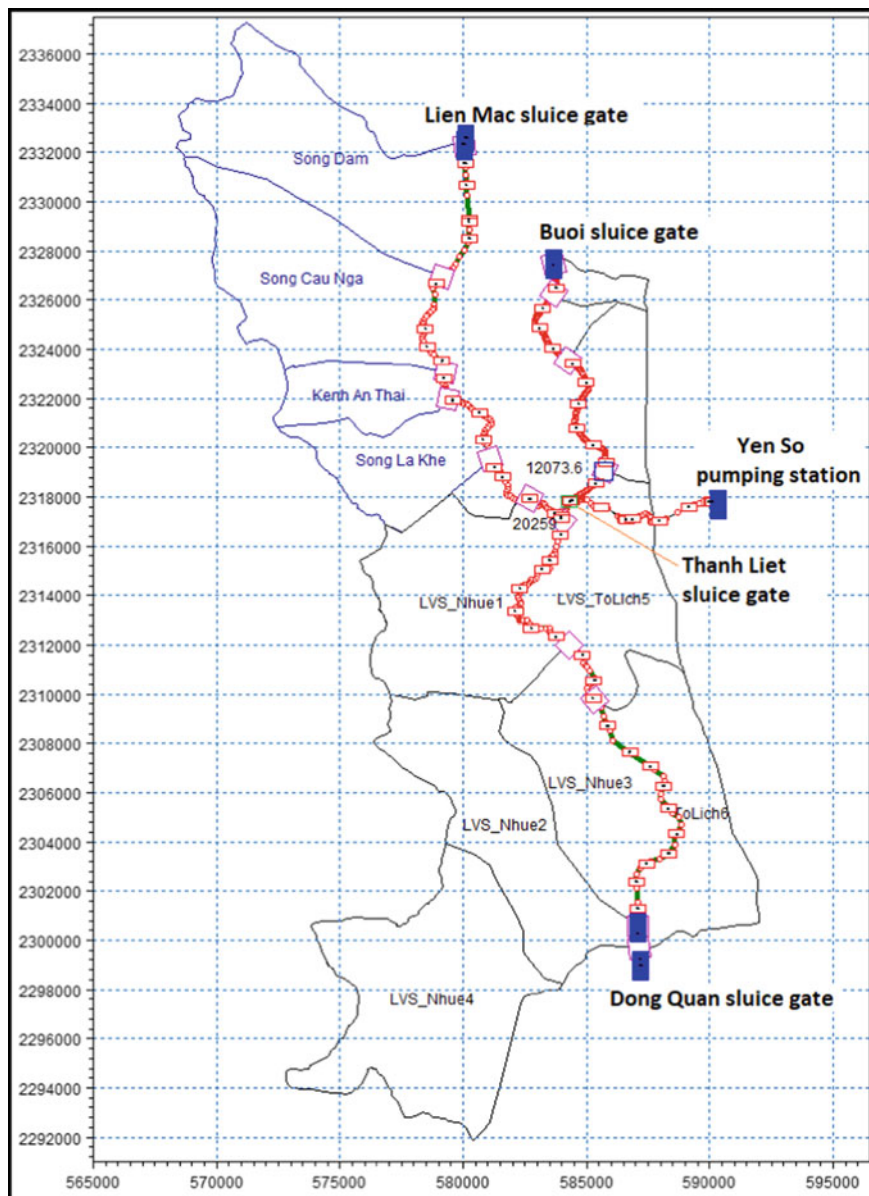


Fig. 9.3 The sub-basins and river network were built in MIKE 11

The study simulated the overland flow via Mike 21 FM model (DHI 2016a). For the study area, because the flooded area is only roads and open spaces. Water cannot enter residential households as well as buildings. According to Syme (2008), the most suitable method to simulate the building in 2D area in this case is blocking out of elements. It leads that, only 2-dimensional grid was setup for roads and open spaces. Besides, the roads have narrow width from 10 to 60 m. In this study, the mesh size was 5–15 m. This approach both saves calculation time as well as ensures the accuracy of the model. The study collected 1/2000 topography data to create 2D simulation mesh. The Mike 21 FM model will be linked to the urban model through connections at manholes. When the drainage capacity of the sewer system could not afford the amount of water, the water was overflowed onto the roads causing flooding. The results of inundation depth and inundation duration from the Mike 21 FM model was used to create inundation maps.

After validation process, the study will calculate 2 cases with and without the influence of water level in river. In case the water level in river was not taken into account. The Mike 11 HD model was not considered. The amount of water was released freely through the outlet of the Mike Urban model, which are the connected nodes with Mike 11 HD model. The calculation results of the two cases are compared to show the importance of the river system's water level problem in the simulation of urban drainage.

9.3 Results and Discussion

9.3.1 Model Calibration and Validation

The model's parameters calibration was conducted by least square error. The main parameters in the model include the roughness of objects in the 1D, 2D and urban models. The calculated results were compared with the observer data. These data are collected from Hanoi Sewerage One Member Limited Liability Company. The model parameter was well calibrated with data of rainstorm event on 29–30th of April, 2019 with the mean error of 0 m and max error of 0.05 m (Fig. 9.4a). The errors were higher at the range water depth of 0.2–0.3 m, correlation coefficient (R) is 0.71.

The 03/08/2019 storm event was simulated for validating parameters. The validation results are shown in (Fig. 9.4b). The difference between the simulated and observed water depths reaches the maximum value of 0.05 m, correlation coefficient (R) is 0.88. The simulated values are overestimated with more points lying above the bio-sector. However, the discrepancies between simulated results and observed values are small with the points lying close to the bio-sector and the mean error of 0.017 m.

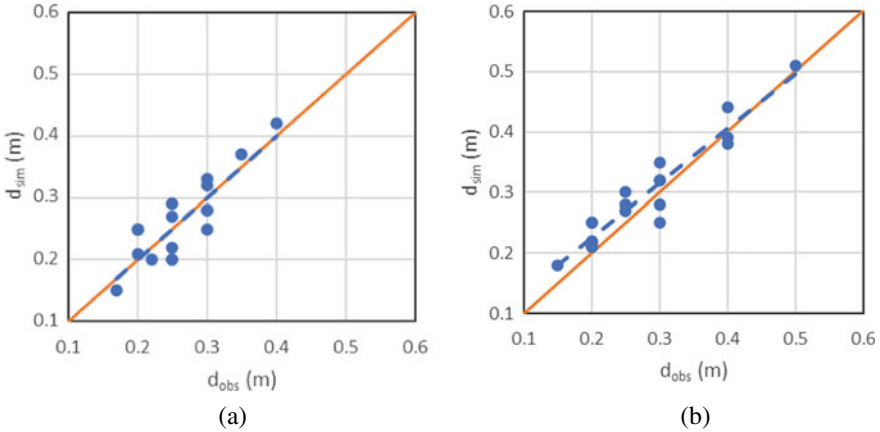


Fig. 9.4 Comparison between simulated and observed inundated depth in **a** calibration and **b** validation

9.3.2 Inundation Map for 10% Design Storm Event

The calibration and validation results in Sect. 9.3.1 indicates that the model parameter can be used to model the flood scenarios. The Figure 9.5a presents the inundation map for 10% design storm event, while Fig. 9.6a presents the inundation period map. There is 71.12 ha with water depth of higher than 1 m, contributing to 19.2% total flooded area. 55% of inundated area is covered with water from 0.5 to 1 m. The spatial distribution of inundation area is ununiform. The Western part of the study area, the water drains towards Nhue River through dynamic pumping stations. Therefore, the flooded area is small. In contrast, the gravity sewer system In the Eastern part of the study area leads to more severe flooding. From North to South, flooding levels is also uneven. At the northern and southern part, under the influence of lakes and ponds, the flood level is much less than in the central area. Topography is also a factor affecting inundation distribution. Along the streets, water will concentrate to low-lying areas.

9.3.3 Asset the Influences of Surrounding River Water Level

To evaluate the influence of the surrounding river water level on the flood drainage capacity, 2 cases with and without rivers were simulated for comparison. Figures 9.5b and 9.6b show the inundation map and inundation period map incase without surrounding river flow modelling. It shows that the inundation in the Western part of study area is similar in both simulations. This is because this area is drained through pumping stations, so it is independent on Nhue River water level. On the opposite side, the water level of To Lich River plays important role to the drainage capacity. In both simulations, the inundated area with water depth in the range of 0.5–1.0 m

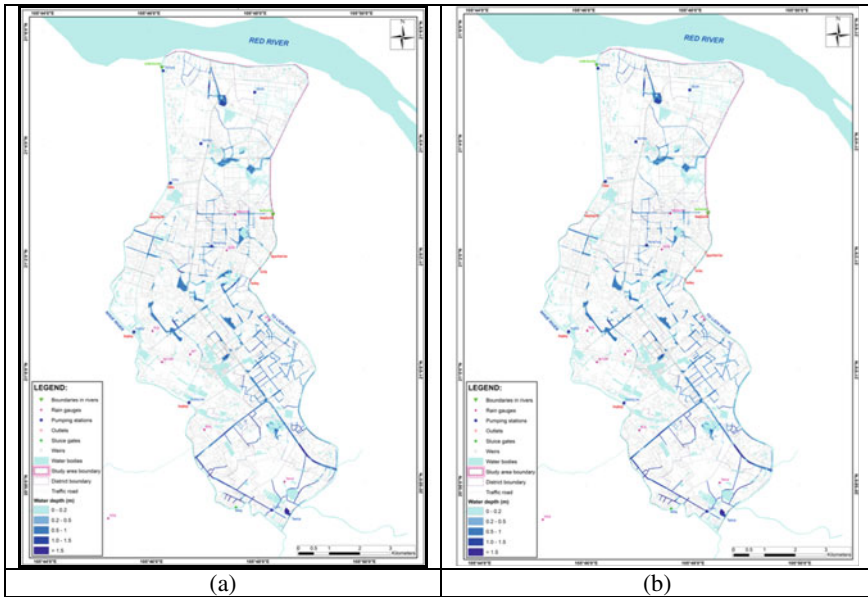


Fig. 9.5 Inundation map for 10% design storm event **a** with and **b** without surrounding river flow modelling

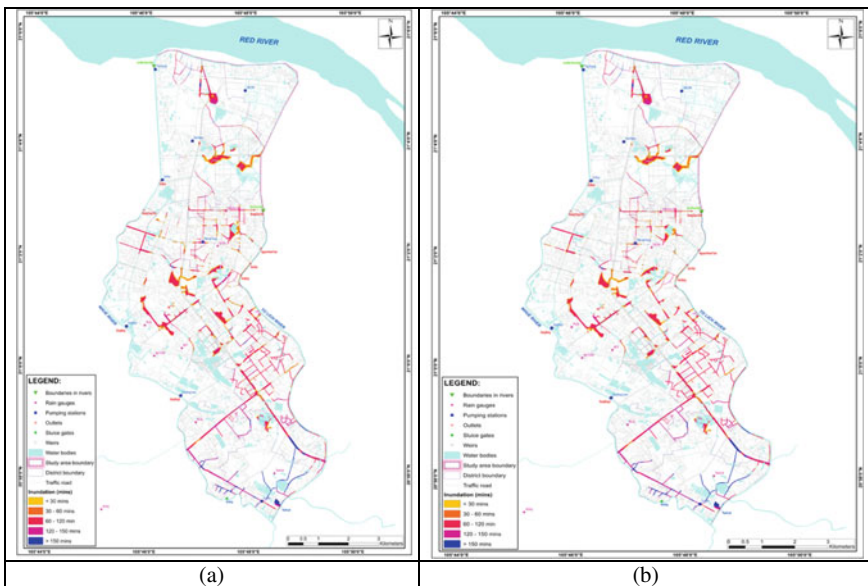
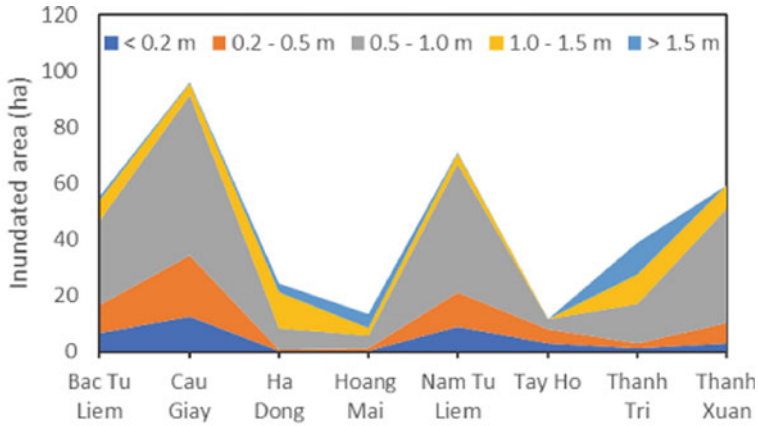
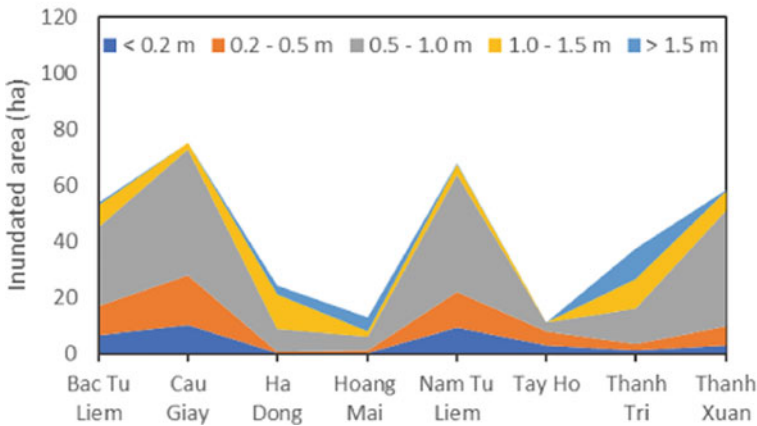


Fig. 9.6 Inundation time map for 10% design storm event **a** with and **b** without surrounding river flow modelling

(Fig. 9.7). Additionally, the highest value of inundated area is observed in Cau Giay district and lowest values in Tay Ho district. The biggest difference in inundated area between the 2 simulation is observed in Cau Giay district, i.e. in the areas of Nguyen Khanh Toan, Cau Giay and Hoa Bang. These areas are near the drainage system outlets, so they are greatly influenced by the river water level. The total affected area when taking into account the influence of surrounding river water level is 106.31 ha, it takes into account for 28.76% of the total flooded area. Although the total affected area is not large, however the percentage is significant.



(a)



(b)

Fig. 9.7 Inundated area corresponding to 5 water depth levels in 8 districts **a** with and **b** without surrounding river flow modelling

Figure 9.6 shows that the inundation period in most areas in both cases is from 1 to 2 h. However, according to the calculation results, when the river water level is taken into account, the inundation period will be longer than about 42 min in almost locations. This is almost never mentioned in previous studies.

9.4 Conclusion

The study had established an integrated hydro-hydraulic model to simulate the flooding level in Hanoi city. The model parameters were well calibrated and validated with 2 huge rainstorm events in 2019. Based on the validated model, a storm event correspond with 10% frequency was simulated. The result showed that the drainage capacity of the sewer system cannot meet the requirements. The degree of flooding is still large in the whole study area with a total flooded area of 369.64 ha. The study also showed that the influence of river water level on the drainage capacity of the sewer system cannot be ignored, i.e. the inundated area can increase more than 20%. This is an important finding in the understanding of the drainage issue.

Acknowledgements This research was supported by “Assessment of urban flood hazard in Hanoi under current and future climate conditions” project funded by VLIR-UOS (VN2019SIN267A101). We would like to show our gratitude to the Ha Noi Sewage and Drainage limited company for sharing the data during this research.

References

- Chang TJ, Wang CH, Chen AS, Djordjević S (2018) The effect of inclusion of inlets in dual drainage modelling. *J Hydrol* 559:541–555. <https://doi.org/10.1016/j.jhydrol.2018.01.066>
- DHI (2016a) Mike 21 flow model user manual
- DHI (2016b) Mike Urban+Collection system user guide
- GebreEgziabher M, Demissie Y (2020) Modeling urban flood inundation and recession impacted by manholes. *Water* 12(4):15–20. <https://doi.org/10.3390/W12041160>
- General Statistics Office of Viet Nam (2020) Statistical Yearbook of Vietnam 2020. Statistical Publishing House
- Ghazavi R, Moafi Rabori A, Ahadnejad Reveshty M (2016) Modelling and assessment of urban flood hazards based on rainfall intensity-duration-frequency curves reformation. *Nat. Hazards Earth Syst Sci Discuss* 1–19. <https://doi.org/10.5194/nhess-2016-304>
- Huong HTL, Pathirana A (2013) Urbanization and climate change impacts on future urban flooding in Can Tho city, Vietnam. *Hydrol Earth Syst Sci* 17(1):379–394. <https://doi.org/10.5194/hess-17-379-2013>
- Jang JH, Chang TH, Chen WB (2018) Effect of inlet modelling on surface drainage in coupled urban flood simulation. *J Hydrol* 562(March):168–180. <https://doi.org/10.1016/j.jhydrol.2018.05.010>
- Le TTA et al (2021) Urban flood hazard analysis in present and future climate after statistical downscaling: a case study in Ha Tinh city, Vietnam. *Urban Water J* 18(4):257–274. <https://doi.org/10.1080/1573062X.2021.1877744>

- Leandro J, Martins R (2016) A methodology for linking 2D overland flow models with the sewer network model SWMM 5.1 based on dynamic link libraries. *Water Sci Technol* 73(12):3017–3026. <https://doi.org/10.2166/wst.2016.171>
- Seyoum SD, Vojinovic Z, Price RK, Weesakul S (2012) Coupled 1D and Noninertia 2D Flood Inundation Model for Simulation of Urban Flooding. *J Hydraul Eng* 138(1):23–34. [https://doi.org/10.1061/\(asce\)hy.1943-7900.0000485](https://doi.org/10.1061/(asce)hy.1943-7900.0000485)
- Son AL, Kim B, Han KY (2016) A simple and robust method for simultaneous consideration of overland and underground space in urban flood modeling. *Water* 8(11):1–16. <https://doi.org/10.3390/w8110494>
- Syme WJ (2008) Flooding in urban areas-2D modelling approaches for buildings and fences. In: 9th National conference on hydraulics in water engineering 2008
- The Vietnamese Prime Minister (2013) Decision approving the master plan on Hanoi capital's drainage through 2030 with a vision toward 2050
- VIWASE (2008) Drainage and sewerage-external networks and facilities-design standard

Chapter 10

Assessing the Current Characteristics of Concrete in Some Parts Hoa Binh Hydropower Plant



Duong Thi Toan  and Nguyen Thi Mai Phuong 

Abstract Hoa Binh Hydropower plant was built in Song Da, Hoa Binh province, is one of the large hydroelectric plant, and very important to Vietnam's electricity industry. Stability assessment of the components of the construction is necessary and require carried out regularly. This paper has the objective to assess the current state characteristics of concrete in the water intake gate and power station system of Hoa Binh hydropower plant. The main evaluated properties include the compressive strength, ultrasonic pulse velocity, pH value, water absorption and the density of the concrete. These properties are performed on core samples and test methods according to current standards. The results show that the compressive strength is in the range of 21.4–33.4 MPa, the ultrasonic pulse velocity is from about 3102 to 3792 m/s; density from 2324 to 2470 kg/m³, pH from 9.98 to 10.69, and the water absorption from 3.6 to 5.2%. These results show that the construction concrete still meets the standard requirements for the heavy concrete in the grade of compressive strength as M300. However, as a result, the pH in some locations dropped below 10, and the carbonation process may be starting. This problem needs to be handled to ensure the safety of the construction.

Keywords Hoa Binh hydropower's concrete · Concrete properties · Concrete quality and problems

10.1 Introduction

Hoa Binh hydropower plant (Fig. 10.1) was kicked off to build in 1979 in the Song Da River, which flows through the Hoa Binh province. From completing the building in 1994–2012, that was the biggest hydropower plant in Vietnam and in Southeast Asia.

D. T. Toan (✉)
University of Science, Vietnam National University, Hanoi, Vietnam
e-mail: duongtoan@hus.edu.vn

N. T. M. Phuong
Hydraulic Construction Institute, Vietnam Academy for Water Resources, Hanoi, Vietnam

Hoa Binh hydropower plant has 8 power generator stations producing a capacity of 1920 MW of electricity, which is the main source of electricity supply for the entire electricity system of Vietnam. Besides, hydropower participates actively and effectively in flood control, ensuring safety for the Northern Delta and Hanoi capital. Hoa Binh hydropower reservoir dam was built by soil, rock, and concrete material with 128 m in high, 743 m in length. The elevation of the reservoir dam's top is 123 m high, the reservoir has a capacity of about 10 billion m^3 , with length of more than 200 km, the average width is about 1 km. The normal water level is 117 m, the highest water level is 122 m, the lowest water level is 80 m. The plant construction consists of main parts: Dam to remain reservoir water; reservoir after dam; intake water gates; power station system (penstock, hydraulic turbine, generator), drainage water line, and gates. In this research, the concrete in the intake gate and power station system (Fig. 10.2) will be investigated and assessed.

In the intake water gate area, the water flow inside of 8 power stations through the 16 intake gates, which are between the concrete pillars. Then every 2 intake gates supply water for one power generator at the power station. Each power station system has a penstock to take water with a diameter of 8 m, through the turbine with the flow rate of $300 \text{ m}^3/\text{s}$, and then through the pressure pipe (12 m in diameter). The pillars in the water intake gate were built by concrete with a height of 17 m, and 190 m in length. Across of intake pillars, there are 16 garbage screens to stop waste and 16 repair valves respectively for 8 power station systems. These valves are controlled by 4 hydraulic actuators located at an altitude of 119 m, for 4 hydraulic cylinders.

The water intake gate and power station system are the most important parts of the hydropower plant. In the intake gate area, the construction is greatly influenced by a number of factors such as the impact high velocity flow, the high hydraulic pressure along with the hard and heavy waste. Issue such as the construction is attacked, the



Fig. 10.1 Hoa Binh hydropower plant area

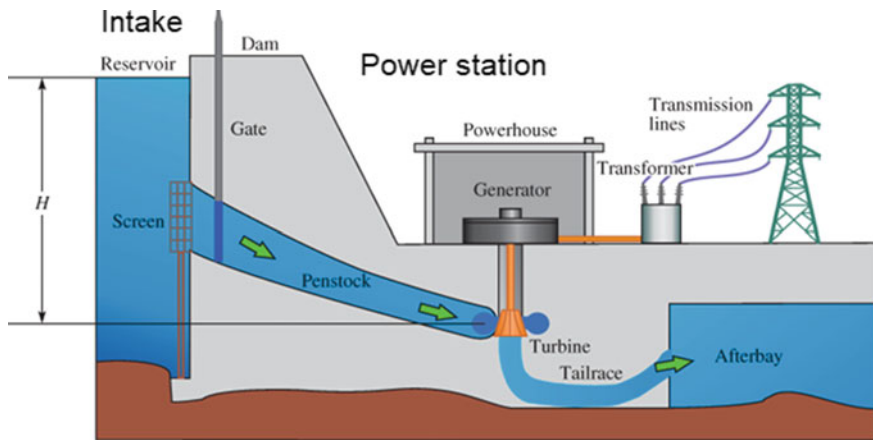


Fig. 10.2 General configuration of hydropower generator system (Electrical academia: How hydropower plants work/Types of hydropower plants. <https://electricalacademia.com/renewable-energy/hydroelectric-power-plant-working-types-hydroelectric-power-plants/>)

materials are eroded and destroyed may happen. In addition, the fluctuation of water level changes in high intensity, going up and down in a short time, making the dry and wet process happen regularly and continuously overtime on the concrete surface, rapidly increasing the degree of penetration of concrete. The power station system is located underground. To prevent earthquakes and seepage, concrete in this area is used by cement injection and blast-drilling techniques. Clay mortars are sprayed into the sand and gravel bed lying in the river bed, then drilled into the rock bed and sprayed cement into all the holes drilled in the rock to create adhesion.

To ensure the materials working in good condition as well as ensuring the durability of the hydropower plant, the assessment of the current state of the material is carried out regularly (Tan et al. 2018; Phuong 2011; Ton et al. 2018). Here the concrete of the intake pillars and power station system are investigated to ensure that the structure continuously keeps its working function and in order to promptly handle important works of national and century level.

The purpose of this study is to assess the status of reinforced concrete in the water intake pillars from + 87.5 to + 123.0 m and in some locations in the power station system. The factors include the quality of concrete (the compressive strength); concrete structure (the magnetic ultrasonic velocity), the quality of concrete reinforcement through measuring the rust of the reinforcement, and the working environment (the pH value), and the properties of concrete density and water absorption capacity.

10.2 Methods

The processing of inspecting and evaluating the condition of concrete and steel reinforcement including: (1) Selecting of position for drilling samples and clean the drilled area; (2) Determining the magnetic ultrasonic velocity at the drilled locations and around area; (3) Drilling samples, packing and transferring samples to the laboratory. Samples were drilled at 17 representative locations with 9 locations at the intake concrete pillar (elevation of + 117.5 m height) and 8 locations at the power station system (elevation of + 1205 m); (4) Preparing and cutting samples in standard size; (5) Doing tests for building the results of the compress strength, ultrasonic pulse velocity, pH, water absorption and the volumetric weight of the concrete. The method and standard to determine these properties are listed in Table 10.1.

Compressive strength is an important parameter that determines the quality of concrete, is also one of the important parameters to classify concrete strength and evaluate the durability of the building (Akorli et al. 2021). The compressive strength of concrete is defined as the compressive stress, calculated in force per unit area, as kG/cm^2 or MPa. Compressive strength is the basic characteristic of concrete to reflect the bearing capacity for construction. The results of the compressive strength will be compared with the strength requirements according to the standard TCXDVN 239:2006 with the grade by compressive strength as M300 (the value of standard compressive strength of Mix concrete is 30 MPa). Accordingly, the determination of concrete strength on a construction structure is a measured value of the actual strength of the structure, which serves as a basis for assessing the safety of the construction under the influence of current loads or for design, renovation, and repair of existing construction.

Compressive strength is usually measured by many different methods but can be divided into two groups: the destructive method and the non-destructive method group (ultrasonic pulse velocity) (Tan et al. 2018). The group of non-destructive methods has the advantage of giving quick results, without affecting the structure, but often does not guarantee the required accuracy. The group of destructive methods (drilled samples) gives the true value of the material properties, but requires a lot of work and is likely to affect the existing structure, so the number of test samples tends

Table 10.1 The methods and standard to determine the concrete characteristic

No.	Processing and proper	Methods and standard
1	Drilling and collecting concrete core sample	TCVN 3105:1993 TCVN 3118:1993
2	Compressive strength	TCVN 3118: 1993 TCVN 9335:2012
3	Ultrasonic pulse velocity	TCVN 9357:2012
4	pH value	TCVN 9339:2012
5	Water absorption	TCVN 3113:1993
6	Desity	TCVN 3115:1993

to decrease to a minimum. Currently, when inspecting old construction, only a small number of drilled samples was collected and determining concrete properties in the laboratory. The results in the laboratory are used to build a correlation curve. A large remaining area of construction will be checked in the field by using non-destructive methods. The field result is corrected based on the determined in the laboratory (Tran and Dang 2015). In addition, other works evaluated in the field include checking for visual defects such as concrete cracking, peeling concrete surface, concrete erosion, damaged concrete areas, concrete steel carbonation... This paper will present only the results of determining strength from drilled samples in the plant construction. The process to cut a concrete sample and testing according to the regulations stated in TCVN 3105:1993, TCVN 3118:1993, and related instructions are given in TCXDVN 239:2006.

The experiment to determine the pH index of concrete is to evaluate the quality of reinforced concrete by measuring the rust of the steel reinforcement and the working environment of the reinforcement (Pu et al. 2012). The determination of pH is carried out with a mortar sample of drilled concrete by measuring the potential difference of the electrode when immersed in the sample solution using a pH meter according to the sampling standards TCVN 7572-15:2006 and measuring by TCVN 9339:2012. Studying the change of pH value in concrete can evaluate possible chemical reactions in concrete with the participation of ions or CO₂ penetration when concrete has cracks or small openings, and evaluate the corrosion of the environment to steel reinforced materials in concrete.

The water absorption of concrete is carried out in the laboratory according to the standard TCVN 3113:1993. The concrete drill specimen is placed in an immersion tank one-third of the specimen height and immersed for one hour. Then add water up to two-thirds of the specimen height and soak for a more hour. Finally, fill water above 5 cm the top of the sample and keep the water level until the sample is saturated with water. After every 24 h of immersion, the sample was taken out, wiped dry samples, and weighed with an accuracy of 0.5%. The sample is considered to be saturated when the difference in weight of the sample in two continue times is not more than 0.2%. After saturated, the samples were placed in an oven with a temperature of 105–110 °C to dry to constant weight. The water absorption is the percent of the water mass absorbed into the sample during the test.

Density is one of the physical parameters that represents the arrangement of components and void in the concrete, which is the ratio of mass to volume. The density of concrete is determined on 3 samples according to the standard TCVN 3115:1993.

10.3 The Results and Discussion

10.3.1 *The Concrete Compressive Strength and the Magnetic Ultrasonic Velocity*

According to Vietnam standard TCXDVN 239:2006, which is used to assess the concrete compressive strength of parts in the constructions, the measured compressive strength at the construction field (R_f) must respond to the critical compressive strength (R_c). The measured compressive strength (R_f) has to be higher than $0.9 R_c$, and the minimum compressive strength of concrete in the field (R_{fmin}) has to be higher than $0.75R_c$. Where the critical compressive strength (R_c) is determined by the equation: $R_c = 0.778 M$, where M is the standard compressive strength value. For the hydroelectric plant, the built concrete requires the value $M = 30$ MPa. Apply this value, the calculation for $R_c = 23.34$ MPa, then $R_f > 0.9 R_c = 21.01$ MPa, and $R_{fmin} > 0.75R_c = 17.51$ MPa.

The compressive strength at the Hoa Binh hydroelectric plant ranges from 25.2 to 33.4 MPa at the intake pillars, and $21.4 \div 28.9$ MPa at the power station. Comparing these values (R_f and R_{fmin}) with the critical value ($0.9 R_c$ and $0.75 R_c$), all value of the field compressive strength are higher than 21.01 MPa and 17.51 MPa. These values are higher than the critical compressive as 1.2–1.6 times at the intake pillars and as 1–1.3 times at the power station. Based on this comparison, it can be seen that the current concrete in the field of the Hoa Binh hydroelectric plant still has good quality and responds to the requirement of the standard compressive strength at grade M300.

To find out any other issues in the structure of concrete construction, the ultrasonic velocity test was done in the locations of drilled samples. The results on the ultrasonic velocity (V_p) are $3328 \div 3792$ m/s at the intake pillars; $3102 \div 3552$ m/s at the power station. Figure 10.3 shows the relationship between the ultrasonic pulse velocity values and the compressive strength. Two of these properties also have quite close consistence with R^2 being 0.77 at the power station and is 0.88 at the intake pillars. The higher the compressive strength, the higher the ultrasonic pulse velocity (Fig. 10.3).

In the standard TCVN 9357:2012, the ultrasonic pulse velocity value range is about 4000–4500 m/s for the precast concrete sample at grade M300 in the laboratory. For the construction, the concrete at grade of M300-M350 (the standard compressive strength of 30–35 MPa), the ultrasonic pulse velocity value range $3810 \div 3993$ m/s (Tran and Dang 2015). And according to that overiewing (Tran and Dang 2015), concrete with good quality should have a V_p of about 3700 m/s. An area with V_p in $2750 \div 3660$ m/s need to make a questionable and thoughtful investigation. However, in the research in Vietnam, the ultrasonic pulse velocity still is used narrowly and depends on the compressive strength. According to the standard TCVN 9396:2012, the ultrasonic pulse velocity values have meaningfull when the concretes obtain the required compressive strength. All investigated location concrete on the compressive strength has responded to the requirement M300, then the results on

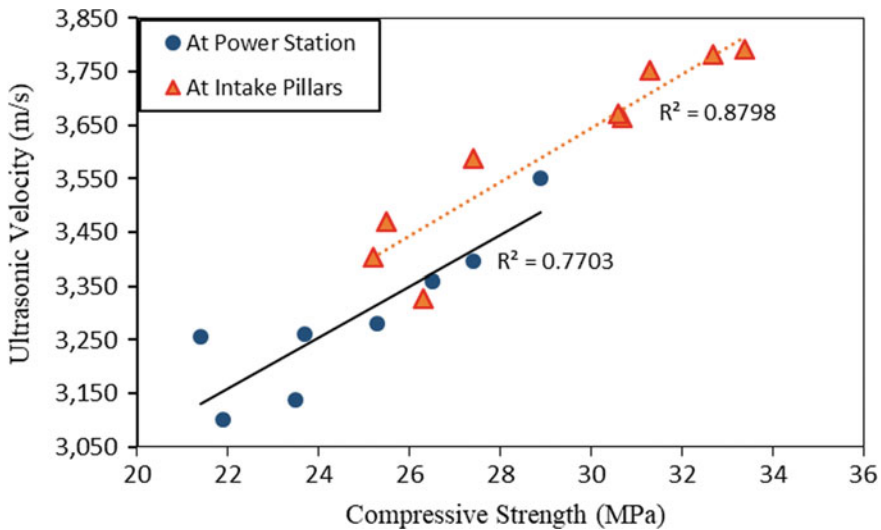


Fig. 10.3 The compressive strength versus the ultrasonic velocity

magnetic ultrasonic velocity values should be considered as the reference results for further testing.

10.3.2 Characteris of pH Value, the Water Absorption and Density

Table 10.2 shows the results of the pH, water absorption, and density determined by the concrete samples in the laboratory. The pH value was measured at the surface, center, and bottom of the sample. In almost locations, the pH value increases from the surface to the bottom of samples and is the smallest at the surface where the construction suffers the effects of the outside environment. The pH value range from 10 to 10.64 on the sample surface at the power station, and from 9.98 to 10.58 at the intake pillars.

Usually, the pore solution of concrete is saturated with calcium hydroxide and also contains sodium and potassium hydroxide, pH is usually 13–14 and can even be higher. When steel reinforcement is embedded in concrete, a passivation layer is formed around the steel from being exposed to the high alkaline environment (Zhiguo et al. 2021). This passivation layer formed on the steel is an oxide layer that protects the embedded rebar from corrosion. Concrete with a pore solution of pH 10–12 is less alkaline than concrete which is still in good condition. When the passivation layer is broken the concrete has pore cracks, the concrete reinforcement is exposed to the atmosphere, the carbon dioxide in the atmosphere will react with the concrete to reduce the pH of the concrete.

Table 10.2 The testing result of pH value, water absorption, and density

Location	pH value			Water absorption	Density
	Bottom	Center	Surface	%	kg/m ³
Power station 1	10.67	10.69	10.64	3.8	2347
Power station 2	10.47	10.52	10.51	3.7	2324
Power station 3	10.23	10.36	10.22	4	2326
Power station 4	10.57	10.6	10.5	4	2383
Power station 5	10.15	10.44	10.32	3.9	2355
Power station 6	10.65	10.62	10.6	3.8	2370
Power station 7	10.59	10.51	10.48	3.7	2406
Power station 8	10.23	10.16	10.18	4.1	2368
<i>Min value</i>	<i>10.15</i>	<i>10.16</i>	<i>10.18</i>	<i>3.7</i>	<i>2324</i>
<i>Max value</i>	<i>10.67</i>	<i>10.69</i>	<i>10.64</i>	<i>4.1</i>	<i>2406</i>
Intake Pillar 1,1	10.58	10.55	10.56	3.6	2412
Intake Pillar 1,2	10.49	10.41	10.39	3.9	2461
Intake Pillar 2,1	10.26	10.23	10.25	4	2424
Intake Pillar 2,2	10.32	10.33	10.27	3.6	2372
Intake Pillar 3,1	10.3	10.26	10.23	4.6	2426
Intake Pillar 5,1	10.34	10.43	10.36	5.2	2380
Intake Pillar 7,3	10.55	10.51	10.58	4.7	2395
Intake Pillar 8,2	10.26	10.21	10.18	4.5	2403
Intake Pillar 8,3	10.05	10.02	9.98	4.3	2413
<i>Min value</i>	<i>10.05</i>	<i>10.02</i>	<i>9.98</i>	<i>3.6</i>	<i>2372</i>
<i>Max value</i>	<i>10.58</i>	<i>10.55</i>	<i>10.58</i>	<i>5.2</i>	<i>2461</i>

When the pH of the concrete decrease below 10, the reinforcement steel in the concrete may begins to corrode. There are two main causes of reinforcement corrosion in reinforced concrete structures, which are: (i) Carbonation of concrete due to CO₂ penetration; (ii) the passivation layer does not protect embedded steel from corrosion when the chloride concentration is above 0.02% by mass of concrete. In the first case, CO₂ in the air penetrates the concrete through a network of pores and cracks. In the presence of the liquid phase present in the concrete and the hydration products of the cement, especially Ca(OH)₂, the carbonate reactions occur to form CaCO₃ (limestone). The pH of the medium decreased from about 12.5 to 13.5 to approximately 9, leading to the breakdown of the passive film protecting the reinforcement (Tan et al. 2018; Pu et al. 2012). Crack damage and corrosion in concrete will continue. When the steel reinforcement is corroded, there is also a loss of mass, a reduction of the working section compared to the calculation, and a danger to people and the process of using and operating. One of the degradations in bearing capacity is the decrease in the adhesion stress between concrete and reinforcement due to corrosion.

In all tested locations, the pH value is quite low, less than 11, even is 9.98 at the intake pillar No. 8.3. Infield investigation, some small broken sides can be found. The concrete surface from the height of + 109 m to the elevation of + 117 m at the intake pillars was slightly eroded, the mortar layer was washed away, exposing the rock due to the impact of water levels up and down. In particular, some major defects in the concrete need to consider thoroughly investigated.

Water absorption indicates the ability of water to penetrate and store in the concrete. Because concrete has a capillary structure, it can be humidified by absorbing a certain amount of water vapor from the surrounding air or can absorb water to saturation when in direct contact with water. The maximum water absorption of cement concrete, solid aggregates often in the state of water saturation can reach 4–8% by weight (10–20% by volume) (Alsayed and Amjad 1996). The measured water absorption in the Hoa Binh ranges from 3.7 to 4.1% at the power station and from 3.6 to 5.2% at the intake pillar. These results are still in the permission value for quality concrete. Through water absorption, it is possible to assess the structure and degree of compaction of concrete. The higher the moisture absorption, the more porosity of the concrete or the appearance of cracks in the structure. Water absorption is one of the parameters to evaluate the strength and durability of concrete (Zhang and Zong 2014; Kumar et al. 2021).

The result of density ranges $2324 \div 2406 \text{ kg/m}^3$ at the power station, and $2372 \div 2461 \text{ kg/m}^3$ at the intake pillars. For hydraulic construction, the density ranges $1800 \div 2200 \text{ kg/m}^3$ with medium-heavy concrete; $2200 \div 2500 \text{ kg/m}^3$ with heavy concrete used for load-bearing structures. The measured results adapt to the standard value. The change of volumetric mass will affect other important mechanical properties of concrete such as compressive strength, shear strength, elastic modulus. Iffat (Iffat 2015) have done a series of testing of the concrete density and compressive strength. Those results show the linear relationship and indicate a simple equation for an estimate of the density from the compressive strength.

To find out the relationship between the concrete properties (compressive strength, water absorption, and density), the coefficient of determination (R^2) were built in Figs. 10.4 and 10.5. However, most of the relationships are quite loose dependences, with a small coefficient of determination (R^2). Anyway, it can be seen that the water absorption has a certain influence on the compressive strength. With higher water absorption, the compressive strength decreases (Fig. 10.4). The correlation of the density and water absorption was shown in Fig. 10.5, the water absorption decrease clearly with higher density at the intake pillars, but decreases only lightly at the power station.

Based on the above present, the concrete samples drilled in the Hoa Binh hydroelectric plant still have good quality. The properties of the compressive strength, density, and water construction adapt the required standard for the concrete in the hydraulic construction with the compressive strength of $M = 30 \text{ MPa}$. There are two properties as the pH value and the magnetic ultrasonic velocity are quite low comparing the standard requirement. The Hoa Binh hydroelectric was kicked off in 1979, and the intake pillars and power station were constructed from 1983 to 1986. It is nearly 40 years since the concreted of this construction was built. Moreover, the

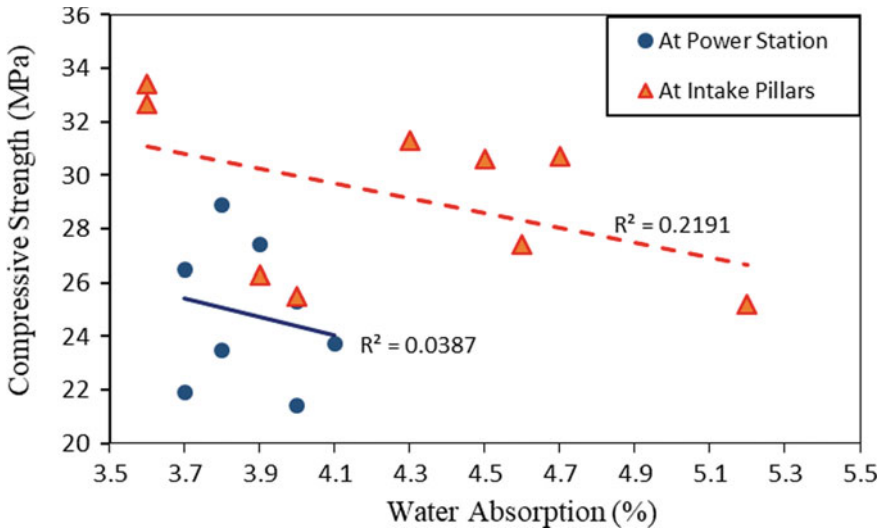


Fig. 10.4 The water absorption versus the compressive strength

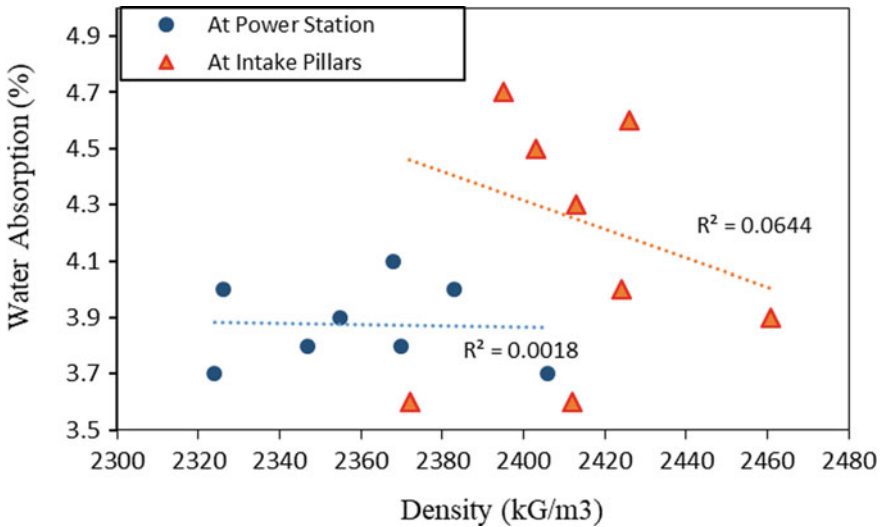


Fig. 10.5 The density versus water absorption

concrete at the intake pillar often is affected by the fluctuation of water level, the hydraulic gradient, and other factors in the way attached to the construction. In the field, some cracks and eroded positions can be found on the surface of both the intake pillars and the power station. Because of these issues, the concrete of this construction is continually investigated and urgent treatment in any area having the problem.

Solving the problem of the low value of pH requires monitoring and assessment in real-time to see the trend of these values changing. Relating to low pH value and areas having cracks on the surface of concrete pillars, further research should focus on clarifying the mechanism and interaction to decrease the pH and their effects on the evolution of crack development. To protect concrete, the treatment methods such as infiltration chemical mortar to fill in the crack, prevent the permeability, and erosion process will be designed in the near future.

10.4 Conclusion

This paper presents the testing results on some main properties of concrete collected in the Hoa Binh hydropower plant, in Vietnam. The obtained results are fundamental for assessing the current concrete condition at the intake water gates and in the power generator system. Comparing with the requirement of standard for the heavy concrete of hydraulic construction with the grade compressive strength of M300, the concrete at both the intake gates and the power generator system have good quality. The measured compressive strength at all drilled location range from 21.4 to 33.4 MPa, which are higher 1–1.6 times than the critical value calculated by the standard. The density and water absorption also range in the acceptable for concrete M300. The density is from 2324 to 2470 kg/m³, and the water absorption is from 3.6 to 5.2%. There are two properties as the pH value and ultrasonic pulse velocity are quite lower for high-quality concrete. The pH value is from 9.98 to 10.69, the ultrasonic pulse velocity is from 3102 to 3792 m/s. The range value of two these factors may indicate that some checked areas do not have really good quality. Also, some are with small crack shadow cracks or erosion on the surface. Then these issues are should be made questionable, and need more careful investigation to find out an effective solution to protect the concrete as well as keep the durability of the Hoa Binh hydropower plant.

Acknowledgements The authors express sincere gratitude to the support of the project Code QMT.22.01, which was sponsored by Vietnam National University.

References

- Akorli KS, Danso K, Ayarkwa J, Acheampong A (2021) Investigating the compressive strength properties of concrete using some common ghanaiian ordinary portland cements. *Int J Technol Manage Res* 6(2):154–166
- Alsayed SH, Amjad MA (1996) Strength, water absorption and porosity of concrete incorporating natural and crushed aggregate. *J King Saud Univ Eng Sci* 8(1):109–119
- Electrical academia: how hydropower plants work | types of hydropower plants. <https://electricalacademia.com/renewable-energy/hydroelectric-power-plant-working-types-hydroelectric-power-plants/>

- Iffat S (2015) Relation between density and compressive strength of hardened concrete. *Concr Res Lett* 6(4):182–189
- Kumar MH, Macharyulu IS, Ray T, Mohanta NR, Jain M, Samantaray S, Sahoo A (2021) Effect of water absorption and curing period on strength and porosity of triple blended concrete. *Mater Today Proc* 43:2162–2169
- Phuong TNM (2011) Some modes of deterioration in marine constructions and structural condition assessments. *J Mar Sci Technol* 27:58–62
- Pu Q, Jiang L, Xu J, Chu H, Xu Y, Zhang Y (2012) Evolution of pH and chemical composition of pore solution in carbonated concrete. *Constr Build Mater* 28(1):519–524
- Tan NN, Dung TA, The NC, Tuan TB, Anh LT (2018) An experimental study to identify the influence of reinforcement corrosion on steel-concrete bond stress. *J Sci Technol Civ Eng* 12(6):29–38
- Thanh N (2019) Hoa Binh hydroelectricity-a magnificent project of the 20th century. <https://vnetexpress.net/thuy-dien-hoa-binh-cong-trinh-ky-vi-cua-the-ky-204007609.html>
- Ton CN, Hung PT, Cuong NV (2018) Studying the influence of large aggregate on the elastic modulus of concrete. *Sci J Architect Constr* 28:10–14
- Tran HQ, Dang MQ (2015) Identification and assessment of construction defects foundation bored pile by using Cross Hole Sonic Logging. <https://www.researchgate.net/publication/283320896>
- Zhang SP, Zong L (2014) Evaluation of relationship between water absorption and durability of concrete materials. *Adv Mater Sci Eng*. <https://doi.org/10.1155/2014/650373>
- Zhiguo N, Yuan L, Ri Y (2021) Carbonation and mechanical property of the concrete core samples from a concrete dam after long-term operation. *IOP Conf Ser Earth Environ Sci* 643(1)

Chapter 11

Hydraulic Performance of a Sand Trap in the Flushing Period to Support the Maintenance of the Pengasih Irrigation Network, Indonesia



Ansita Gupitakingkin Pradipta , Ho Huu Loc , S. Mohana Sundaram , Sangam Shrestha , Murtiningrum , and Sigit Supadmo Arif 

Abstract Sand traps, as the first barrier against sedimentation in irrigation networks, have an essential role in minimizing the sediments in the irrigation channels. A large number of deposits upstream of the weir triggered a decrease in the sand trap performance. Pengasih is one of the irrigation schemes included in the Progo-Opak-Serang River Basin (WS POS) and gets water supply from the Serang River through the Pengasih Weir. 38.17% of the WS POS area is included in critical land, with an erosion rate of 234.83 tons/ha/year. It is necessary to evaluate the performance of the Pengasih Weir sand trap during the flushing period. The study's objectives were to construct a hydraulic model, develop an optimum modeling approach for sediment transport in the flushing period, and identify the performance regarding the discharge and duration of flushing in the sand trap. This study used 1-D mathematical modeling software, HEC-RAS 4.1.0. The primary data were the channel's cross-section, observed water surface, measured discharge, sediment properties, and flushing duration. The hydraulic model was developed by calibration and validation, providing the validated Manning's coefficient of 0.025. The modeling approach for the sediment transport in the flushing period was Laursen for transport function, Exner 5 for sorting method, and Ruby for falling velocity method. The optimum discharge and sand trap flushing duration were 2 m³/s and 315 minutes. The flushing mechanism is optimal, and the duration adjustment is required to achieve a more effective and efficient sand trap operation in the irrigation maintenance period.

Keywords Sedimentation · Irrigation · Sand trap · Flushing · HEC-RAS

A. G. Pradipta · H. H. Loc (✉) · S. M. Sundaram · S. Shrestha
Water Engineering and Management, Department of Civil and Infrastructure Engineering, School of Engineering and Technology, Asian Institute of Technology, 58 Moo 9, Km. 42, Paholyothin Highway, Klong Luang, Pathum Thani 12120, Thailand
e-mail: hohuuloc@ait.asia

A. G. Pradipta · Murtiningrum · S. S. Arif
Department of Agricultural and Biosystems Engineering, Faculty of Agricultural Technology, Universitas Gadjah Mada, Flora Bulaksumur Street No. 1, Yogyakarta 55281, Indonesia

11.1 Introduction

Irrigation is a critical component of Indonesia's agricultural development. A well-functioning irrigation system can help strengthen the agricultural industry and provide food security. However, irrigation performance has deteriorated after less than a century of development and management in Indonesia. The inadequacy of irrigation infrastructure maintenance, the poor management system, the inappropriate rehabilitation system, and poor financing systems are all factors that contribute to this drop. In the case of irrigation infrastructure, the current state of degradation is due to current environmental conditions that are significantly different from the requirements as designed. Sedimentation is now one of the most serious infrastructure issues, affecting everything from weirs to tertiary irrigation channels. The main source of sedimentation in irrigation infrastructure is excessive erosion in the weir upstream, which is caused by poor river basin conservation in the upper weir. Sedimentation can reduce the overall efficiency of an irrigation system (Pradipta et al. 2022; Revel et al. 2015).

In this case, Sand traps play a critical function in preventing or reducing sedimentation in irrigation channels. However, the high amount of sediments coming from upstream of the weir caused the sand trap, the first sediment barrier to enter an irrigation channel, to perform poorly. The incoming water discharge, surrounding soil conditions, and flushing mechanism all have an impact on the sediment suspended in a sand trap. The sediment in the sand trap is removed on a regular basis, either manually or by flushing (Mustafa et al. 2013). Due to farmer requests to meet their irrigation water needs, the flushing period often deviates from its intended schedule. Unsuitable flushing periods also have an impact on sand trap performance (Widaryanto 2018). As a result, reviewing the operation and maintenance of the sand trap is necessary, especially during the flushing period. If the sand trap fails, a large amount of sediment will be carried into the irrigation channel. This can result in an increase in the volume of sediment entering the irrigation channel, reducing the irrigation channel's capacity. If this capacity decline is not addressed promptly, it may become a severe issue. Water availability will decrease, potentially leading to a fall in agricultural production.

One of the irrigation schemes in the Progo-Opak-Serang (POS) River Basin is the Pengasih Irrigation Scheme, which has a service area of 2,291 hectares. Through the Pengasih Weir, it receives water from the Serang River. Progo, Opak, and Serang are the three primary watersheds in the POS River Basin, with 2,421 km², 1,376.34 km², and 280 km², respectively. It was discovered that 38.17% of its land area is classified as critical land, with an erosion rate of 234.83 tons/hectare/year (Anonym 2016). Critical land is indicated by a very high erosion rate and requires prompt conservation activities to restore land functions (Anonym 2016). The Serang Watershed is dominated by clay-textured soils and is sustained by heavy rainfall and topographic variations, which increases the risk of land erosion (Ayuningtyas et al. 2018). This is worsened further by poor land management (Anonym 2016). The high level of erosion in the Serang Watershed causes sedimentation in Pengasih Irrigation Scheme.

It will reduce the irrigation channel's capacity, resulting in inefficient irrigation water allocation. The characteristics and quantity of sediment that enters the Pengasih Weir Sand Trap are affected by land-use change in the upstream Serang Watershed and global climate change. As a result, it's critical to evaluate the present state of the sand trap, particularly during the maintenance period, commonly known as the flushing period. The purpose of this research is to assess the hydraulic performance of the Pengasih Weir sand trap during the flushing period in order to support irrigation network maintenance. The particular goals are to construct a hydraulic model of the sand trap, determine the appropriate modeling approach for sediment transport in the sand trap during the flushing period, and identify the sand trap's performance in terms of discharge and flushing period to empower the irrigation network maintenance. It can assist with the efficient use of irrigation water, which is one of the indicators in the Indonesian irrigation modernization program.

11.2 Methodology

11.2.1 Study Area

The Pengasih Irrigation Scheme, located in Kulon Progo Regency, Special Region of Yogyakarta, Indonesia, was the subject of this research. The Pengasih Irrigation Scheme covers 2,077 hectares of paddy field and has a primary as well as nine secondary channels. The Pengasih Weir, located at $7^{\circ} 50' 08.88''$ S and $110^{\circ} 10' 16.73''$ E, receives water from the Serang River. It occupies an area of 280 km² and has a main river that runs for 28 km. The Serang River in Durungan Station has a monthly average discharge of 10.83 m³/s, with a maximum discharge of 61.10 m³/s and a minimum discharge of 0.28 m³/s. In Kulon Progo Regency, Sermo Reservoir dams the Ngrancah River (a tributary of the Serang River) and serves as a primary source of irrigation and drinking water (Anonym 2016). It provides additional water to the Pengasih Irrigation Scheme during the dry season. Figure 11.1 depicts the research location.

11.2.2 Overall Framework

The study's overall framework is represented in Fig. 11.2. This study conducts three primary analyses. Hydraulic calibration and validation are used to determine the optimal hydraulic parameter, in this case, Manning's coefficient, by comparing simulated and observed water levels. Calibration of sediment aims to establish a modeling approach for the sand trap's sediment transport throughout the flushing period, while simulation and optimization of flushing intend to identify the sand trap's performance in terms of discharge and flushing period.

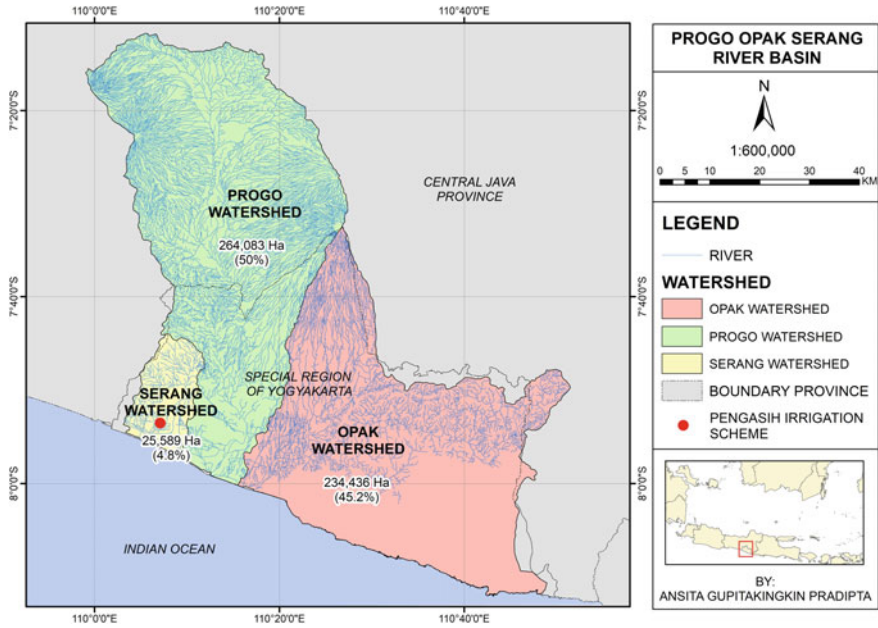


Fig. 11.1 Research location

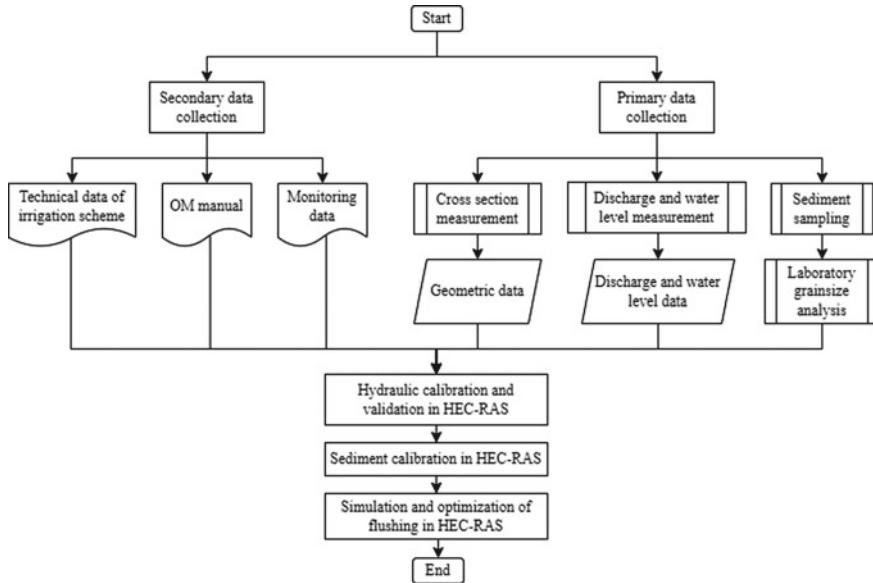


Fig. 11.2 Overall framework

11.2.3 Data Collection

Secondary Data Collection Secondary data required includes irrigation scheme technical specifications, operation and maintenance manuals, and monitoring data. The data came from the Serayu Opak River Basin Organization, the Kulon Progo Regency Public Works Service, and the field observer office.

Primary Data Collection The primary data collection involves cross-sectional measurements, discharge measurements, water surface elevation measurements, and sediment investigations in the Pengasih Weir sand trap. Each data collection is described in the following manner.

Cross Section Measurement Cross-sections were taken along the channel from the sand trap to the beginning of the primary channel. Terrestrial measurements were done with the aid of a total station and its supporting accessories. Figure 11.3 illustrates the configuration for cross-section measurement. From CS_{intake} to CS₁₃, 14 cross-sections must be measured.

Discharge Measurement The velocity was determined using a cup-type current meter. The cup rotates in response to the flow velocity, and the amount of rotation is converted to the flow velocity. Due to the fact that velocity varies with the depth and width of the flow, the measurement was made at a variety of depths (*H*) and was separated into three width segments. As demonstrated in Fig. 11.4, the discharge was computed using the velocity area method, as given in Eqs. (11.1) and (11.2). As illustrated in Fig. 11.4, there are three depth variations, namely 0.2*H*, 0.6*H*, and 0.8*H*, as well as three width segments. Figure 11.5 illustrates the configuration of the velocity measurement system. As can be seen, the measurement location consists of nine points. Three cross-sections in measuring the discharge represent the flow upstream, midstream, and downstream.

Total discharge as calculated by the velocity area method:

$$\bar{V}_I, \bar{V}_{II}, \bar{V}_{III} = \frac{V_{0.2H} + V_{0.6H} + V_{0.8H}}{3} \tag{11.1}$$

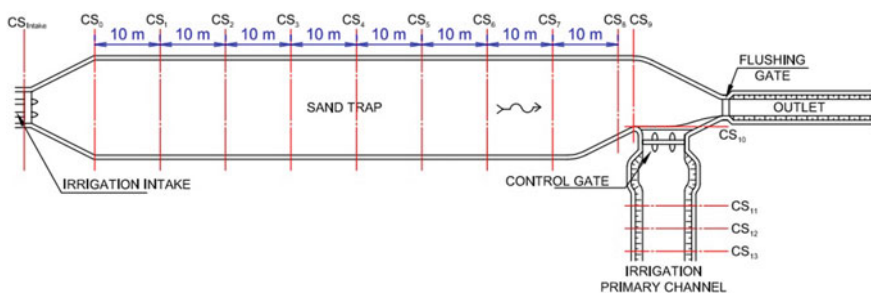


Fig. 11.3 Layout for measuring cross-sections

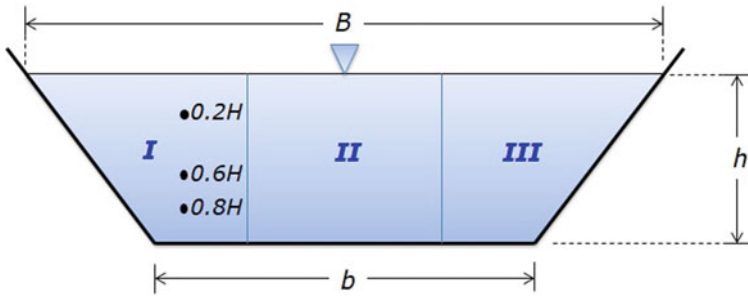


Fig. 11.4 Discharge measurement illustration

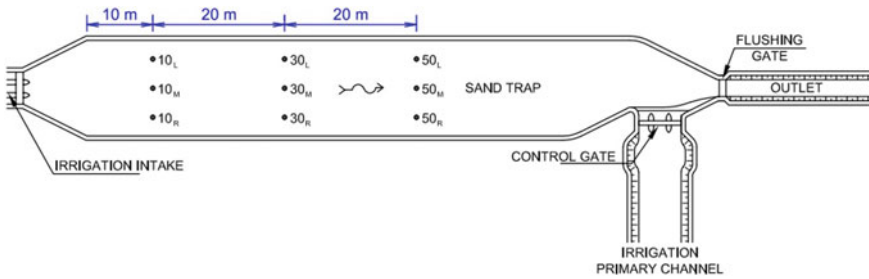


Fig. 11.5 Layout for velocity measurement

$$Q_{tot} = \bar{V}_I A_I + \bar{V}_{II} A_{II} + \bar{V}_{III} A_{III} \tag{11.2}$$

where,

Q_{tot} = total discharge.

A_I = cross-sectional area of segment I

A_{II} = cross-sectional area of segment II

A_{III} = cross-sectional area of segment III

\bar{V}_I = average flow velocity of segment I

\bar{V}_{II} = average flow velocity of segment II

\bar{V}_{III} = average flow velocity of segment III

$V_{0.2H}$ = flow velocity at a depth of $0.2H$ from the water surface

$V_{0.6H}$ = flow velocity at a depth of $0.6H$ from the water surface

$V_{0.8H}$ = flow velocity at a depth of $0.8H$ from the water surface

B = channel top width

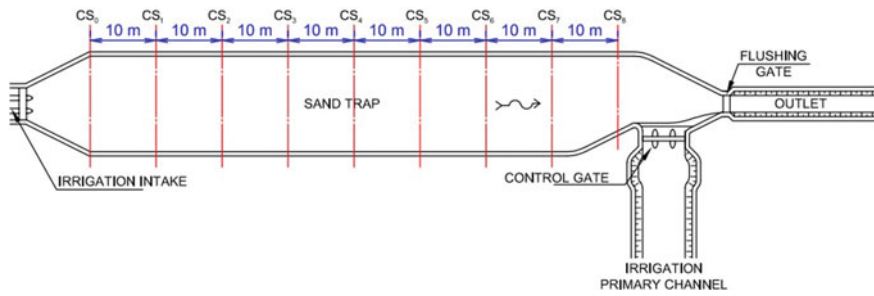


Fig. 11.6 Layout for water surface measurement

b = channel bottom width

h = flow depth.

Water Surface Elevation Measurement Hydraulic calibration and validation in HEC-RAS were performed using the water surface. The measurement was carried out using an automatic level and its associated equipment. Figure 11.6 illustrates the measurement’s layout. As can be seen, there are nine cross-sections to measure, starting with CS₀ and ending with CS₈. The distance between the two cross-sections is ten meters.

Sediment Investigation Sediment properties were utilized for sediment modeling, and it contains information about the current bed sediment in the Pengasih Weir sand trap. Sampling was conducted using a sediment grab sampler. The bed sediment sampling layout is identical to that of the velocity measurement, as illustrated in Fig. 11.5; thus, there are nine sampling points. The sieve and hydrometer methods were conducted to figure out the sample’s specific gravity and particle size distribution.

11.2.4 Mathematical Modeling in Irrigation System Using HEC-RAS

By analyzing the flow characteristics in a large and complex irrigation network under various design and management scenarios, the hydraulic simulation model enables the improvement of irrigation system performance (Van et al. 2020) (Islam et al. 2008). A mathematical model can be used to investigate the hydraulic characteristics and behavior of a large irrigation network, directly evaluating and improving system performance (Serede et al. 2015). Nowadays, technological advancements enable researchers to do mathematical modeling for various purposes. Numerous mathematical models are available for hydraulic modeling tasks, including HEC-RAS, MIKE 11, CCHE1D Model, Fluvial-12, and BRI-Stars (Mohammed et al. 2018). These models can be used to predict how a river or stream will look after a flood,

how sediment will move, and how reservoirs and stream channels will get clogged up (Loc et al. 2015, 2020).

This work simulates both flow and sedimentation models in a sand trap using a one-dimensional flow mathematical model and HEC-RAS version 4.1.0. HEC-RAS (Hydrologic Engineering Center River Analysis System) was established in 1995 by the United States Army Corps of Engineers (a division of the Institute for Water Resources/IWR). HEC-RAS is a piece of software that enables users to perform one-dimensional steady and unsteady flow river hydraulics calculations, sediment transport capacity calculations, uniform flow calculations, and water temperature analyses. The most recent version of HEC-RAS is accessible for free under a public domain license from the US Army Corps of Engineers website (Mehta et al. 2014). HEC-RAS enables the simulation of the one-dimensional water surface profile in stable rivers, the unsteady river flows, delivered sediment load, and water quality in rivers (Ahmad et al. 2021). HEC-RAS 1D model is considerably applied to simulate sediment transport (Joshi et al. 2019). The HEC-RAS one-dimensional model is frequently used to simulate sediment transport (Ahmad et al. 2021). In version 4.0 of HEC-RAS, 1D sediment transport numeration was introduced (Brunner and Gibson 2005). HEC-RAS can be utilized as a decision support system to ensure the optimal operation and maintenance of irrigation systems (Serede et al. 2015). Hydraulic modeling was used to simulate flow and sediment movement along the principal channel in this investigation. The discharge data, geometry data, and sediment characteristic data were all employed in this modeling.

11.2.5 Approach for Sediment Transport Modeling Using HEC-RAS

It is essential to comprehend the approaches used to build sediment transport models in order to ensure that they are applicable to a given stream (Sisinggih et al. 2020). Three ways are provided in HEC-RAS sediment modeling to do this, including a sediment transport function, a sorting mechanism, and a fall velocity method. This model considered both the bed and suspended sediment transports.

Sediment Transport Function Sediment transport functions generally estimate sediment transport rates given a set of steady-state hydraulic parameters and sediment properties. HEC-RAS 4.1.0 includes the following sediment transport functions: Yang, Toffaleti, Ackers and White, Engelund and Hansen, Laursen-Copeland, Meyer-Peter and Müller, and Toffaleti (USACE 2010).

Sorting Method The bed sorting method (sometimes referred to as the mixing or armoring method) records the bed gradation that HEC-RAS utilizes to compute

grain-class-specific transport capacity and simulate supply-side armoring procedures. Armoring is the most prevalent effect of bed sorting, in which a coarse cover layer accumulates atop a more representative subsurface layer of river bed material (USACE 2010). HEC-RAS 4.1.0 supports the following sorting methods: Exner 5 and active layer.

Fall Velocity Method Shear velocity u^* is a well-known fundamental velocity scale of the wall turbulence, widely used for scaling various flow quantities such as mean velocity and turbulent intensities (Pokrajac et al. 2006). It can be referred to as the representation of the intensity of turbulent fluctuations in the boundary layer (USACE 2010). It is also commonly defined as the velocity scale of the momentum absorbed by the bed. It can be evaluated at the roughness crests, where the bed starts extracting momentum from the flow (Pokrajac et al. 2006). Suspension of a sediment particle occurs when the bed-level shear velocity approaches the magnitude of the particle's fall velocity. The particles will remain suspended as long as the bed-level turbulence's velocity components exceed the fall velocity. As a result, determining suspended sediment transport is highly dependent on particle fall velocity (USACE 2010). The user can select the method for computing fall velocity within HEC-RAS. There are four methods: Toffaleti, Van Rijn, Ruby, and Report 12 (USACE 2010).

11.2.6 Performance Indicator

Performance indicators are necessary to evaluate several scenarios employed in this study in order to identify the best alternative. Each scenario involves a comparison of simulated and observed data. We must assess the accuracy of a scenario in light of observable data. The Root Mean Square Error (RMSE) and Mean Absolute Error (MAE) are the two evaluation metrics used in this study (MAE). The root means square error (RMSE) and the mean absolute error (MAE) are frequently employed to determine the accuracy of a recommender system (Wang and Lu 2018). The lower the RMSE and MAE, the better the model or the more precise the forecasts (Ratner Jun. 2009). These formulas are illustrated in Eqs. (11.3) and (11.4) (Wang and Lu 2018).

$$RMSE = \sqrt{\frac{\sum_{n=1}^N (\hat{r}_n - r_n)^2}{N}} \quad (11.3)$$

$$MAE = \frac{\sum_{n=1}^N |\hat{r}_n - r_n|}{N} \quad (11.4)$$

where,

\hat{r}_n = the prediction rating

r_n = the actual rating in the testing data set

N = the number of rating prediction pairs between the testing data and prediction results.

Furthermore, this study evaluated the system using the coefficient of determination (R^2) and the Nash–Sutcliffe efficiency index (NSE). The correlation coefficient, represented as R , quantifies the strength of the relationship between two variables that are either straight-line or linear. Correlation coefficients are frequently misused because their linearity assumption is not checked (Ratner Jun. 2009). The coefficient of determination (R^2) runs typically between 0 and 1; a value of 0 implies no linear relationship, whilst a value of 1 shows a perfect linear relationship (Ratner Jun. 2009). The coefficient of determination is defined in Eqs. (11.5) and (11.6).

$$\text{coefficient of determination} = (\text{coefficient of correlation})^2 \quad (11.5)$$

$$\text{coefficient of correlation, } R = \frac{n(\sum xy) - (\sum x)(\sum y)}{\sqrt{[n \sum x^2 - (\sum x)^2][n \sum y^2 - (\sum y)^2]}} \quad (11.6)$$

where,

R = coefficient of correlation

x = values in the first set of data

y = values in the second set of data

n = total number of values.

Recognizing the correlation coefficient's shortcomings, Nash and Sutcliffe (1971) presented an alternative goodness-of-fit metric, termed the efficiency index. The NSE statistic is a widely used and potentially valid measure of the quality of fit of hydrologic models (Mccuen et al. 2006). If a linear model's predictions are unbiased, its efficiency index will be between 0 and 1. The efficiency index may be algebraically negative in the case of biased models. Even if the model is unbiased, negative efficiencies can occur for nonlinear models, which most hydrologic models are. The NSE is equal to R^2 under the assumption of a linear model (Mccuen et al. 2006). Equation (11.7) illustrates the formula for NSE.

$$NSE = 1 - \frac{\sum_i^n (\hat{Y}_i - Y_i)^2}{\sum_i^n (Y_i - \bar{Y})^2} \quad (11.7)$$

where,

\hat{Y}_i = predicted values of the criterion (dependent) variable Y

Y_i = measured values of the criterion (dependent) variable Y

\bar{Y} = mean of the measured values of Y

n = sample size.

11.3 Results and Discussion

11.3.1 Preparation of Model

The author of this work developed a model of the Pengasih Weir sand trap's hydraulic performance, particularly during the flushing period. The discharge rate and flushing duration can evaluate performance. Prior to simulating the flushing phase, the authors modeled the sand trap's geometry and flow during the operational period in order to calibrate the Manning coefficient at the sand trap's bottom. Water surface elevation is utilized as a reference parameter in calibration, allowing for comparisons between observed data and simulation findings. After calibrating the Manning coefficient, the second measurement results were used to validate it. Sediment modeling is then used to calibrate sediment transport parameters in the sand trap using the sediment properties determined from field data. After flushing the sand trap, the channel's bed configuration changes. Calibration of the sediment model can be accomplished using that bed change.

The author utilized a one-dimensional mathematical modeling program, HEC-RAS version 4.1.0. The technique for doing flow simulations in HEC-RAS is split into five parts (Mehta et al. 2014): model preparation, geometry modeling, flow modeling, hydraulic calculation, and presentation and interpretation of simulation results. This study modeled the operational and flushing periods using two geometry and flow data sets. Figure 11.7 depicts the geometry during the operational period used for hydraulic calibration and validation purposes. The flow moves from the irrigation intake, through the sand trap body, and then enters the primary irrigation canal. In comparison, Fig. 11.8 illustrates the geometry during the flushing period; this geometry was utilized to calibrate the sediment. The flow moves from the irrigation intake, through the sand trap body, and then exits through the natural channel, which is located downstream of the flushing gate. The user should always simulate the river reach using HEC-RAS in the upstream–downstream direction. As a result, the reach's most downstream section is designated as river station 0.

11.3.2 Hydraulic Calibration and Validation

Hydraulic calibration and validation follow a similar procedure, involving the use of flow and water surface elevation data from two independent measurements taken at different times. The flow was modeled as a steady flow because it occurs in a channel with uniform geometry, and the discharge is constant throughout time. Calibration

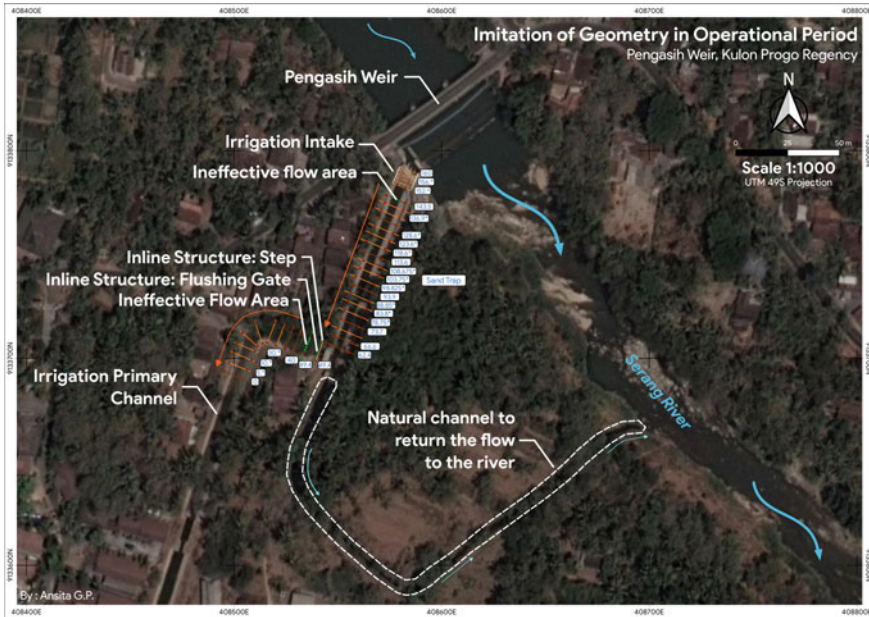


Fig. 11.7 Geometry in the operational period

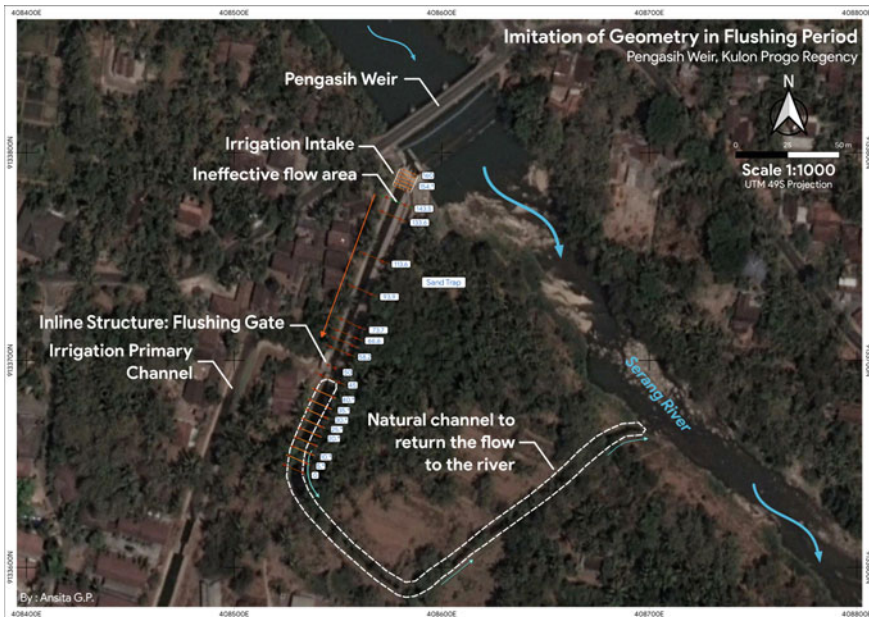


Fig. 11.8 Geometry in the flushing period

and validation used the same geometry data, namely the geometry from the operational period. Figure 11.7 illustrates geometric modeling throughout the operational phase. A normal discharge of $2.03 \text{ m}^3/\text{s}$ was used as the input in steady flow data in the calibration process. The downstream boundary condition is normal depth. Additionally, the observed water surface elevation is fed into the flow modeling, where it is compared to the predicted one. There are eight data points for water surface elevation, with values ranging from $+ 96.382$ to $+ 96.436 \text{ m}$.

The calibration process began by obtaining the Manning’s bed roughness coefficient that will be employed in the simulation. According to field observations, the Pengasih Weir sand trap channel’s walls and bottom are made of stone set in mortar. This type was not completely covered by Manning’s coefficient table, which is available in HEC-RAS’s hydraulic reference. As an approach, a concrete bottom float with random stone on the mortar sides was chosen, with the minimum, normal, and maximum values of 0.017, 0.020, and 0.024, respectively. As a result, the Manning coefficient is set to 0.015 for the first simulation. Figure 11.9 illustrates the hydraulic calibration findings. It compares observed and simulated water surfaces using a variety of Manning’s coefficients. It shows the sand trap’s upstream and downstream parts on the right and left sides of the figure.

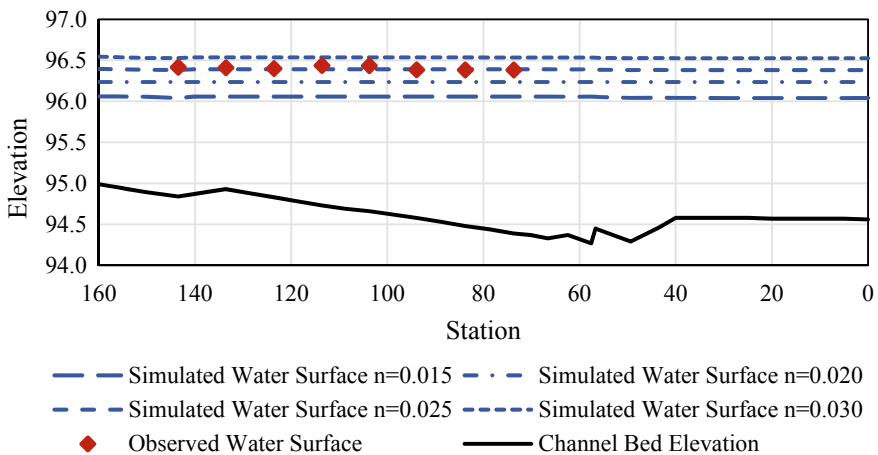


Fig. 11.9 Comparison between observed and simulated water surface with several Manning’s coefficient values

Table 11.1 Performance Indicators of the calibrated Manning's coefficient

No.	Performance indicator	Value, n = 0.025
1	Coefficient of determination (R^2)	0.9522
2	Nash–sutcliffe efficiency index (NSE)	– 0.6402
2	Root mean square error (RMSE)	0.0266
4	Mean absolute error (MAE)	0.0216

As illustrated in Fig. 11.9, the water surface elevation calculated using the input Manning's coefficient of 0.015 is underestimated, with the overall trend being lower than the measured water level. Manning's coefficient was set to 0.020 in the following simulation; as can be seen, the water level elevation obtained by the simulation was still underestimated. The simulation was then repeated using Manning's coefficient of 0.025, and it can be seen that the simulation's water level elevation corresponds to the observed water surface. The simulation was then run with a Manning's coefficient of 0.030 to see whether the 0.025 Manning's coefficient is the suitable value. As can be seen, the results are inflated. It may be concluded that Manning's coefficient is most appropriate at 0.025 for the channel condition of the Pengasih Weir sand trap. This is referred to as a calibrated Manning's coefficient.

The calibrated Manning's coefficient was then evaluated with performance indicators, namely R^2 , NSE, RMSE, and MAE, as indicated in Table 11.1. It can be seen that the results perform well in all indicators. Particularly for NSE, an efficiency less than zero occurs when the observed data is a better predictor than the model. Negative efficiencies can occur with nonlinear models, which the majority of hydrologic models are (McCuen et al. 2006). As a result, a negative NSE value is permissible.

After calibrating Manning's coefficient and resulting in the appropriate value of 0.025, the data set from the second measurement was used to validate it. In steady flow data, the input is a normal discharge of $0.53 \text{ m}^3/\text{s}$. The downstream boundary condition is normal depth. Additionally, the observed water surface was included in the flow modeling process, which will be compared to the simulated one. There are eight data points for water surface elevation, with values ranging from + 95.702 to + 95.741 m. Figure 11.10 illustrates the hydraulic validation results. It demonstrates the comparison between the observed and simulated water surfaces at $n = 0.025$. As can be seen, the validated Manning's coefficient produces a water surface that is consistent with the observed data. As with the calibrated Manning's coefficient, the verified one was evaluated using performance measures, including R^2 , NSE, RMSE, and MAE (see Table 11.2). As can be observed, the results perform admirably across the board. Specifically for NSE, an efficiency smaller than zero arises when observed data outperforms the model as a prediction. As a result, 0.025 was subsequently designated as the validated Manning's coefficient, and it can be used in sediment model simulation.

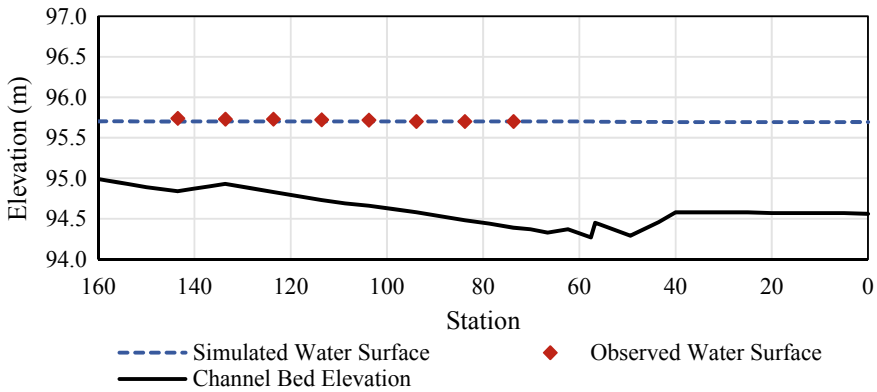


Fig. 11.10 Comparison between observed and simulated water surface with $n = 0.025$

Table 11.2 Performance indicators of the validated Manning’s coefficient

No.	Performance indicator	Value, $n = 0.025$
1	Coefficient of determination (R^2)	0.8479
2	Nash–sutcliffe efficiency index (NSE)	- 0.9833
2	Root mean square error (RMSE)	0.0221
4	Mean absolute error (MAE)	0.0168

11.3.3 Sediment Calibration

Sediment flushing in the sand trap is modeled using the sediment transport concept. Sediment transport modeling is well-known for its complexity. The data used to anticipate bed changes is unclear, and the underlying hypothesis is empirical and highly sensitive to a wide variety of physical variables (USACE 2010). However, with adequate data, it is possible to calibrate regional sedimentation models in order to develop decision plans and assess sedimentation problems. The sand trap hydraulics parameter must be determined before HEC-RAS calculates sediment transport. HEC-RAS uses hydrodynamic simplification, which many sediment transport models use. The quasi-unsteady flow assumption comes close to a continuous hydrograph with a series of separate steady flow profiles.

The maximum amount of sediment that can exit the control volume is dependent on the amount of sediment that the water can move. This is referred to as the sediment transport capacity. A factor that must be obtained for computing sediment transport capacity is sediment transport potential, which is the measure of how much material of a particular grain class a hydrodynamic condition can transport. There are seven equations of sediment transport potential function available in HEC-RAS

4.1.0, including Ackers and White (1973), Engelund and Hansen (1967), Laursen-Copeland (1968, 1989), Meyer-Petter and Müller (1948), Toffaleti (1968), and Yang (1973, 1984) (USACE 2010).

The sediment transport potential is computed by grain size fraction, thereby allowing the simulation of hydraulic sorting and armoring. There are two sorting methods available in HEC-RAS 4.1.0, including active layer and Exner 5. The fall velocity method is also considered to remain consistent with the development of the sediment transport function. Four modes are available: Ruby, Toffaleti, Van Rijn, and Report 12. The researcher must determine the most appropriate approach of sediment transport model, including sorting and velocity methods, for a particular case, location, and condition. Additionally, it is critical to establish the proper transport potential function to improve sediment transport capacity prediction. Calibration is required to address this issue of determining the sediment transport modeling approach. The bed changes after the sediment flushing can be used to figure out the calibration parameter.

The bed alterations following the sand trap flushing operation were measured in this study. For calibration reasons, a comparison was made between the simulated and observed bed changes. The sediment transport simulation includes eight scenarios that consist of two sorting and four fall velocity algorithms listed in Table 11.3. Each scenario is indicated by a graph of seven transport potential functions. A plan in HEC-RAS represented the scenario, and hence eight sediment transport plans were calculated. The results that were considered from HEC-RAS was sediment spatial plot. It displayed the bed elevation after flushing for a particular duration. The actual flushing of the Pengasih Weir sand trap took 90 min and produced a discharge of $2.08 \text{ m}^3/\text{s}$. As a result, the simulations lasted 90 min.

A graph was created to compare the simulated channel bed elevation after 90 minutes of flushing with the measured using multiple transport functions. Each curve corresponds to a particular scenario. They were analyzed to see which one was the closest match to the observed bed elevation following flushing. And scenario 5 demonstrated the most optimal bed elevation comparison, notably using Laursen's

Table 11.3 Scenarios for sediment calibration

Scenario	Sediment transport parameter	
	Sorting method	Fall velocity method
1	Active layer	Ruby
2	Active layer	Toffaleti
3	Active layer	Van Rijn
4	Active layer	Report 12
5	Exner 5	Ruby
6	Exner 5	Toffaleti
7	Exner 5	Van Rijn
8	Exner 5	Report 12

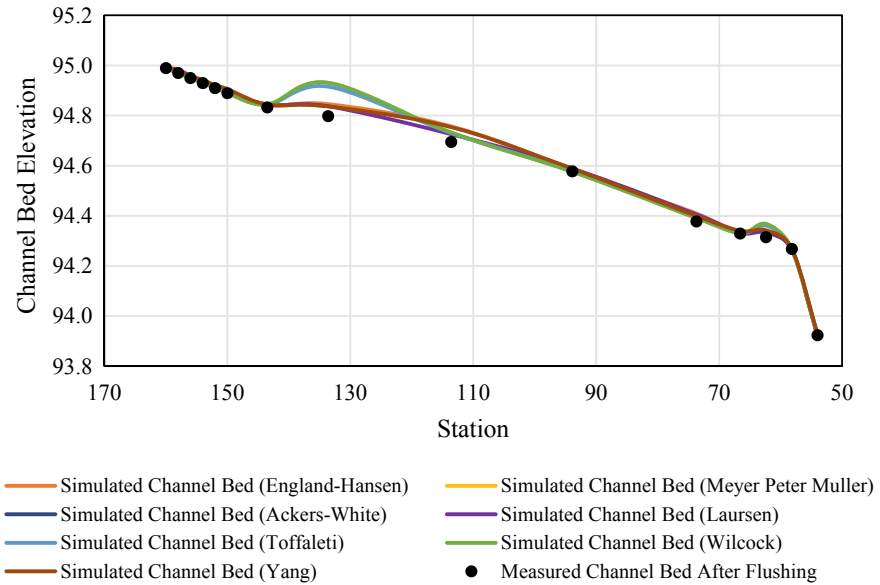


Fig. 11.11 Comparison between simulated channel bed elevation after 90 min flushing from several transport functions with the measured one in scenario 5

transport potential function. The comparison of bed elevation from scenario 5 can be seen in Fig. 11.11. The graph’s left side depicts the upstream region, while the right side depicts the downstream area.

According to Fig. 11.11, the measured channel bed after flushing is depicted by dots, while a purple line indicates the Laursen-simulated channel bed. The purple line is the one that is closest to the dots. It was then evaluated using the performance indicators shown in Table 11.4, namely R2, NSE, RMSE, and MAE. As seen in Table 11.3, all values are satisfactory. As a result, the optimal approaches for modeling sediment transport in this scenario are Laursen for the potential function, Exner 5 for the sorting method, and Ruby for the fall velocity method.

When the actual condition is considered, Laursen-Copeland as a transport function makes sense in this case. Laursen-Copeland equation was developed for gravel transport and extended down into the silt range. None of the other functions currently

Table 11.4 Performance indicators of the sediment calibration

No.	Performance indicator	Value
1	Coefficient of determination (R^2)	0.9986
2	Nash–sutcliffe efficiency index (NSE)	0.9974
2	Root mean square error (RMSE)	0.0163
4	Mean absolute error (MAE)	0.0114

included in HEC-RAS were explicitly designed for silt-sized particles (USACE 2010). This investigation determined the bed gradation, ranging from fine gravel to fine silt. It is consistent with the Laursen-Copeland equation of transport function's identification. In terms of sorting, Exner 5 armoring techniques have been successfully applied to various river systems. As a result, it is also appropriate for this investigation. Additionally, Ruby's calculating fall velocity is suitable for silt, sand, and gravel grains. Further, Ruby recommended that particles with a specific gravity of 2.65 are optimal for the equation (USACE 2010). From the laboratory test result, the specific gravity of the sediment for this study is 2.66.

11.3.4 Flushing Simulation and Optimization

The approach for modeling sediment transport has been determined in the preceding step. The following analysis is a flushing simulation. It evaluates the performance of a variety of discharges used in sand tap flushing over a 90-min time frame. The bed elevation after flushing was then compared with the observed data set. The flushing was simulated for 90 min into five different discharges with an interval of 0.5 m³/s. The discharges were 1.5, 2.0, 2.5, 3.0, and 3.5 m³/s. Figure 11.12 illustrates the results.

According to Fig. 11.12, the left portion represents the upstream zone, while the right leg indicates the downstream region. Each scenario's line is limited to station 66.6, the last part, before going through the flushing gate. The reason for this is that the assessment emphasizes the inside of the sand trap, neglecting its downstream. The black straight line indicates the channel bed before flushing. As can be seen,

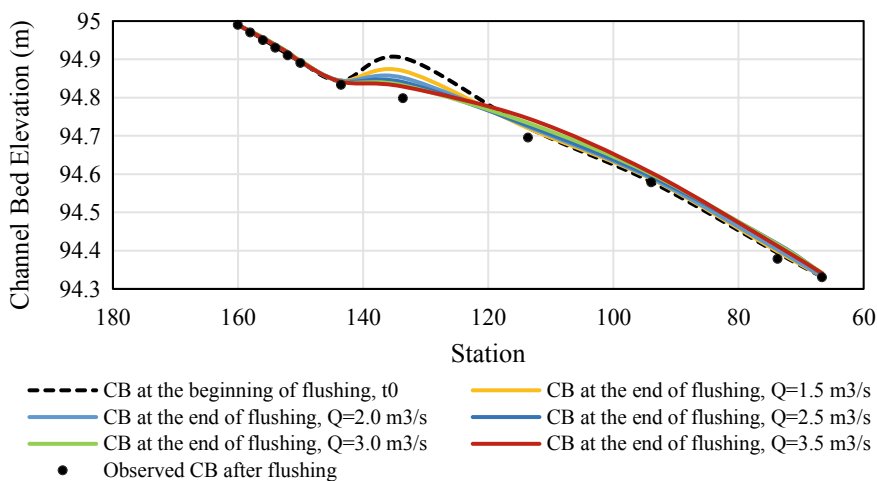


Fig. 11.12 Flushing simulation results (discharge interval = 0.5 m³/s)

Table 11.5 Performance indicators of the sediment simulation results

Performance indicators	Values from the discharge of				
	1.5 m ³ /s	2.0 m ³ /s	2.5 m ³ /s	3.0 m ³ /s	3.5 m ³ /s
R ²	0.9972	0.9981	0.9975	0.9973	0.9968
NSE	0.9956	0.9968	0.9954	0.9950	0.9943
RMSE	0.0212	0.0181	0.0217	0.0226	0.0241
MAE	0.0127	0.0117	0.0149	0.0156	0.0161

significant sediment was deposited at Sta. 133.6, where the bed slope bends, resulting in a sediment thickness of 10.57 cm.

As illustrated in Fig. 11.12, all discharges resulted in a similar trend of decreasing deposited material near Sta. 133.6 and increasing deposited sediment downstream of Sta. 133.6. Each simulated channel bed (after flushing) was compared to the observed channel bed using performance measures such as R², NSE, RMSE, and MAE. Table 11.5 summarizes the performance indicators for the sediment simulation findings. As can be observed, the results from the 2.0 m³/s discharge have the best performance, followed by the 1.5 m³/s discharge. All of the values are acceptable.

The process was then continued to optimization based on the simulation results. The flushing was simulated for 90 min into six different discharges ranging from 1.5 to 2.0 m³/s. The interval was compressed from 0.5 to 0.1 m³/s. The discharges were 1.5, 1.6, 1.7, 1.8, 1.9, and 2.0 m³/s. Figure 11.13 illustrates the results. As can be seen, the graphs produce nearly identical results. The difference in the discharge of 0.1 m³/s is insignificant in comparison to the bed change that occurs after 90 min of flushing. The red line indicated that the channel bed resulting from a 2.0 m³/s discharge was the most similar to the observed data, as indicated by the performance indicators in Table 11.6.

The results indicate that a discharge rate of 2.0 m³/s is optimal for flushing the Pengasih Weir sand trap. According to field measurements, the average actual flushing discharge was 2.083 m³/s. It could argue that the existing discharge and flushing procedures were already suitable and practical. Another factor to consider is the flushing duration. The shorter the time of the flushing operation, the more efficient it is. However, the sediment was not totally flushed during the actual duration (90 min), particularly at Sta. 133.6. That station is the main cross-section where the most sediment was deposited in the Pengasih sand trap since there is a bend of bed slope. We might use the station to ascertain the timeframe of flushing till the entire volume of sediment has been removed.

Figure 11.14 depicts the time series for flushing the sediment, notably that accumulated in Sta.133.6. The curve's straight line implies that all sediment has been removed. As a result, the optimal flushing duration is 315 min or 5.25 h. To manage the flushing process, we must take into account the amount of water available in the source river. If the river's minimum discharge is greater than 2.0 m³/s, the flushing operation can be performed. Currently, the government entity responsible for irrigation in Kulon Progo Regency, which includes the Pengasih Weir, has installed several

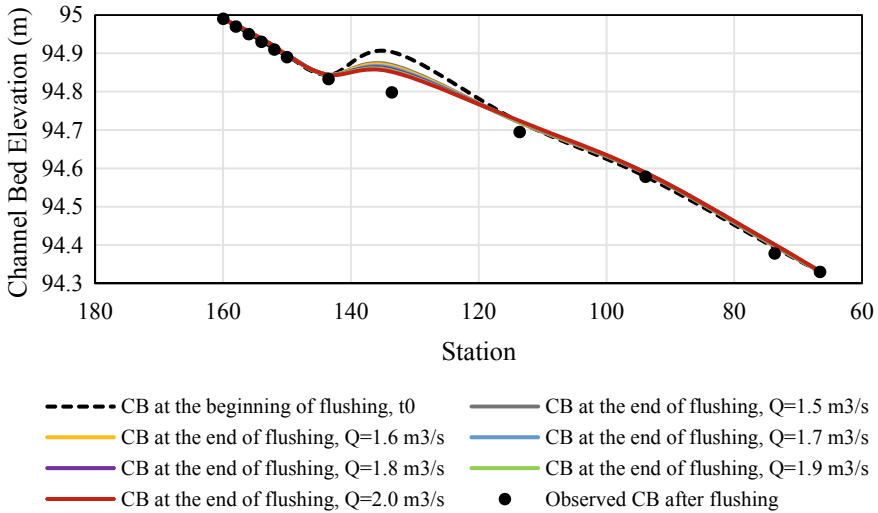


Fig. 11.13 Flushing optimization results (discharge interval = 0.1 m³/s)

Table 11.6 Performance indicators of the sediment optimization results

Performance indicators	Value, Q = 2.0 m ³ /s
R ²	0.9981
NSE	0.9968
RMSE	0.0181
MAE	0.0117

automatic water level recorders (AWLR). They were constructed in numerous sites throughout the Pengasih Irrigation Schemes, including one on the weir’s side. It can assist the operator in flushing the sand trap.

Apart from the water availability in the source river, we should consider the water requirements of the paddy crop, which demands irrigation. Water usage is a priority if they are in the tillage and growth stages. Sedimentation issues occur in the irrigation scheme’s upstream portion and continue through the network to the downstream part. If efforts to prevent sedimentation carried out upstream are still optimal, it is necessary to study the causes and solutions to sedimentation problems that occur along with the network. This is critical to ensuring the irrigation system’s sustainability in order to enable more outstanding agricultural production, which is a national strategic goal. Good agricultural products can contribute to food self-sufficiency, which contributes to the attainment of Sustainable Development Goal 2: end hunger, achieve food security, improve nutrition, and promote sustainable agriculture.

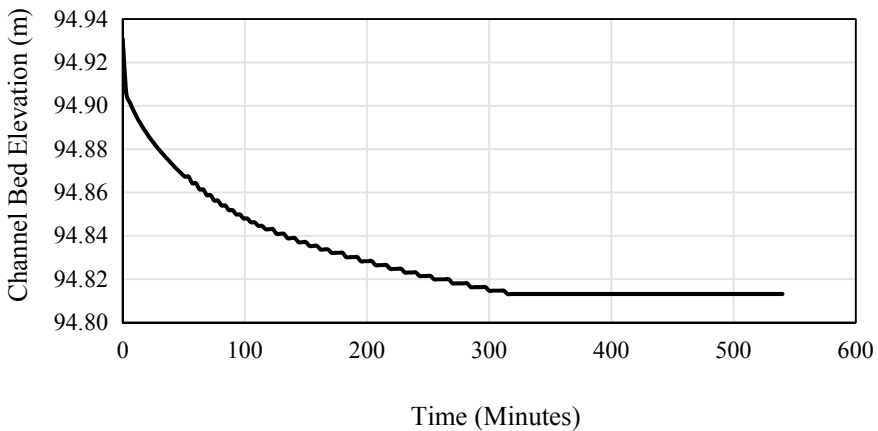


Fig. 11.14 The sediment time series to flush the sediment deposited in Sta. 133.6

11.4 Conclusion

On the basis of the study's findings and discussion, it can be concluded that the hydraulic model of the Pengasih Weir sand trap was developed through a calibration and validation process, generating a validated Manning's bed roughness coefficient of 0.025, which applies to the channel bed type of stone set in mortar. The optimal modeling approach for sediment transport during the flushing period was Laursen-Copeland for the transport function, Exner 5 for the sorting method, and Ruby for the fall velocity method. The discharge and duration that were optimal were 2 m³/s and 315 minutes, respectively. The existing flushing mechanism is reasonable; however, adjusting the length will result in a more effective and efficient sand trap functioning during the irrigation maintenance period.

References

- Ahmad F, Ansari MA, Hussain A, Jahangeer J (2021) Model development for estimation of sediment removal efficiency of settling basins using group methods of data handling. *J Irrig Drain Eng* 147(2):04020043. [https://doi.org/10.1061/\(ASCE\)ir.1943-4774.0001532](https://doi.org/10.1061/(ASCE)ir.1943-4774.0001532)
- Anonym (2016) Rencana Pola Pengelolaan Sumber Daya Air Wilayah Sungai Progo Opak Serang Ayuningtyas EA, Fahmi A, Ilma N, Yudha RB (2018) Pemetaan Erodibilitas Tanah dan Korelasinya Terhadap Karakteristik Tanah di DAS Serang, Kulon Progo. *Jurnal Nasional Teknologi Terapan* 1(2):136–146. <https://doi.org/10.22146/jntt.39194>
- Brunner GW, Gibson S (2005) Sediment transport modeling in HEC RAS. In: *Impacts of global climate change*, pp 1–12
- Islam A, Raghuwanshi NS, Singh R (2008) Development and application of hydraulic simulation model for irrigation canal network. *J Irrig Drain Eng* 134(1):49–59. [https://doi.org/10.1061/\(ASCE\)0733-9437\(2008\)134:1\(49\)](https://doi.org/10.1061/(ASCE)0733-9437(2008)134:1(49))

- Joshi N, Lamichhane GR, Rahaman MM, Kalra A, Ahmad S (2019) Application of HEC-RAS to study the sediment transport characteristics of Maumee River in Ohio. In: World Environmental and Water Resources Congress 2019: Hydraulics, Waterways, and Water Distribution Systems Analysis, pp 257–267. <https://doi.org/10.1061/9780784482353.024>
- Loc HH, Babel MS, Weesakul S, Irvine KN, Duyen PM (2015) Exploratory assessment of SUDS feasibility in Nhieu Loc-Thi Nghe Basin, Ho Chi Minh City, Vietnam. *Br J Environ Clim Change* 5(2):91–103
- Loc HH, Do QH, Cokro AA, Irvine KN (2020) Deep neural network analyses of water quality time series associated with water sensitive urban design (WSUD) features. *J Appl Water Eng Res* 8(4):313–332
- Mccuen RH, Knight Z, Cutter AG (2006) Evaluation of the nash-sutcliffe efficiency index. *J Hydrol Eng* 11(6):597–602. <https://doi.org/10.1061/ASCE1084-0699200611:6597>
- Mehta DJ, Ramani M, Joshi M (2014) Application of 1-D Hec-Ras model in design of channels. *Int J Innovative Res Adv Eng (IJIRAE)* 1(7):1883
- Mohammed HS, Alturfi UAM, Shlash MA (2018) Sediment transport capacity in Euphrates River at Al-Abbasia Reach using HEC-RAS Model. *Int J Civ Eng Technol (IJCIET)* 9(5):919–929. Available: <http://www.iaeme.com/ijciet/issues.asp?JType=IJCIET&VType=9&IType=5>
- Mustafa MR, Tariq AR, Rezaur RB, Javed M (2013) Investigation on dynamics of sediment and water flow in a sand trap. In: International conference on mechanics, fluids, heat, elasticity, and electromagnetic fields, vol 14, pp 31–36. <https://doi.org/10.46300/9105.2020.14.3>
- Pokrajac D, Finnigan JJ, Manes C, McEwan I, Nikora V (2006) On the definition of the shear velocity in rough bed open channel flows. In: Proceedings of the international conference on fluvial hydraulics-river flow 2006, vol 1, pp 89–98. <https://doi.org/10.1201/9781439833865.ch7>
- Pradipta AG, Loc HH, Nurhady S, Mohanasundaram S, Park E, Shrestha S, & Arif SS (2022). Mathematical Modeling-Based Management of a Sand Trap throughout Operational and Maintenance Periods (Case Study: Pengasih Irrigation Network, Indonesia). *Water*, 14(19): 3081.
- Ratner B (2009) The correlation coefficient: its values range between 1/1, or do they. *J Target Meas Anal Mark* 17(2):139–142. <https://doi.org/10.1057/jt.2009.5>
- Revel NMTK, Ranasiri LPGR, Rathnayake RMCRK, Pathirana KPP (2015) Estimation of sediment trap efficiency in reservoirs—an experimental study. *Eng J Inst Eng Sri Lanka* 48(2):43. <https://doi.org/10.4038/engineer.v48i2.6833>
- Serede IJ, Mutua BM, Raude JM (2015) Hydraulic analysis of irrigation canals using HEC-RAS model: a case study of Mwea irrigation scheme, Kenya. *Int J Eng Res Technol (IJERT)* 4(9):1. <https://doi.org/10.11648/j.hyd.20140201.11>
- Sisinggih D, Wahyuni S, Nugroho R, Hidayat F, Idi Rahman K (2020) Sediment transport functions in HEC-RAS 4.0 and their evaluation using data from sediment flushing of Wlingi reservoir–Indonesia. *IOP Conf Ser Earth Environ Sci* 437(1). <https://doi.org/10.1088/1755-1315/437/1/012014>
- USACE (2010) HEC-RAS river analysis systems: hydraulic reference manual, version 4.1. Davis, California
- Van SP, Le HM, Thanh DV, Dang TD, Loc HH, Anh DT (2020) Deep learning convolutional neural network in rainfall–runoff modelling. *J Hydroinf* 22(3):541–561
- Wang W, Lu Y (2018) Analysis of the mean absolute error (MAE) and the root mean square error (RMSE) in assessing rounding model. *IOP Conf Ser Mater Sci Eng* 324(1). <https://doi.org/10.1088/1757-899X/324/1/012049>
- Widaryanto LH (2018) Evaluation on flushing operation frequency of sand trap of Pendowo and Pijenan Weirs. *J Civ Eng Forum* 4(3):233. <https://doi.org/10.22146/jcef.37444>

Chapter 12

Identification of Hydrogeochemical Processes and Controlling Factors in Groundwater and Surface Water Using Integrated Approaches, Tuul River Basin (Ulaanbaatar, Mongolia)



Odsuren Batdelger , Maki Tsujimura, Dang An Tran, Byambasuren Zorigt, and Pham Thi Bich Thuc

Abstract Insights into hydrogeochemical evolution and its controlling factors are crucial for sustainable water resources management in many countries worldwide, especially in arid and semi-arid regions. Here we present the hydrogeochemical characteristics of surface and subsurface water resources in a semi-arid region of Mongolia using stable isotopes, hydrochemistry, and multivariate statistics. A total of 42 surface water and 87 groundwater samples were collected during the 2016 summer and winter seasons, and major ions and stable isotopes ($\delta^2\text{H}$, $\delta^{18}\text{O}$) were analyzed. Hierarchical Cluster Analysis (HCA) classified water samples into 4 clusters (C1–C4) according to hydrochemical facies. Four principal components in summer and three principal components (PC1 through PC4) in winter were identified which explained 86.9 and 83.8% of geochemistry variance. In summer, PC1 represents the pollution related to domestic and industrial waste, and mineral weathering processes and rock-water interactions, PC2 indicates the regional flow system with strong

O. Batdelger (✉) · B. Zorigt
Institute of Geography and Geo-Ecology, Mongolian Academy of Sciences, Ulaanbaatar,
Mongolia
e-mail: odsurenbat@gmail.com

M. Tsujimura
Graduate School of Life and Environmental Sciences, University of Tsukuba, Tsukuba, Japan
e-mail: mktsuji@geoenv.tsukuba.ac.jp

D. A. Tran
Faculty of Water Resources Engineering, Thuyloi University, 175 Tay Son, Dong Da, Hanoi,
Vietnam
e-mail: antd@tlu.edu.vn

P. T. B. Thuc
Institute of Applied Mechanics and Informatics—Vietnam, Academy of Science and Technology,
291 Dien Bien Phu street, Vo Thi Sau ward, district 3, Ho Chi Minh City, Vietnam
e-mail: ptbthuc@iami.vast.vn

loading of stable isotopes and mineral weathering, PC3 represents silicate weathering and pollution, and PC4 indicates physical processes in surface water samples, showing high positive loading for pH and temperature. In the winter, the number of factors decreased, indicating the minor variation in the chemical composition of water samples due to the freezing of the river and solid-state precipitation, and natural processes more influenced the behavior than the summer season. In winter, PC1 and PC2 represent mineral dissolution and anthropogenic inputs, whereas PC3 has positive loading of pH, negative loading of temperature indicates physical processes. The scatter diagrams show that carbonate and silicate weathering, and ion exchange are the dominant processes controlling the mineral water quality. For this study area, the correlations indicate that water mineralization increases from the groundwater recharge area to the discharge area; and mineral weathering processes resulting in dissolution dominated, followed by human impacts associated with municipal waste discharges that also elevated the mineral concentrations of the groundwater.

Keywords Hydrogeochemistry · Hydrochemical processes · Hierarchical cluster analysis · Principal components analysis · Mineral weathering

12.1 Introduction

Water availability is one of the main factors influencing socio-economic development. However, deterioration of water resources has become a global issue, posing a significant challenge to sustainable water resources management (Taylor et al. 2013; Tran et al. 2020). Common sources of water pollution include municipal sewage, industrial wastewater, agricultural runoff, and stormwater and urban runoff (Ahmad et al. 2020; Cao et al. 2018; Stefania et al. 2019). Many pollutants originating from treated and untreated municipal and industrial wastewater can influence receptor water bodies, especially riverine systems. Nonpoint pollutant sources from agricultural and urban areas can also significantly affect water quality, but these effects on water quality are difficult to identify and quantify (Jain and Singh 2019; Yang et al. 2020; Kourakos et al. 2012).

Surface water and groundwater are a part of the water resource system, and their interconnection plays a crucial role in sustainable water resources development (Winter et al. 1139). This interconnection means that changes in the surface water system may directly or indirectly impact the groundwater system. Additionally, seasonal variations significantly influence water availability in arid and semi-arid regions, particularly in Mongolia (Sakakibara et al. 2017; Gao et al. 2018; Verhoeven et al. 2018; Liu et al. 2010). Almost all surface water and subsurface soil in colder regions like Mongolia is frozen in the winter, affecting the recharge processes and water uses. To evaluate complex data sets a multi-disciplinary approach is needed to better understand the influence of agricultural, municipal, recreational, and industrial development on both surface water and groundwater resources. In recent decades, multivariate statistical analysis (MSA), such as correlation analysis, Hierarchical

Cluster Analysis (HCA), and Principal Component Analysis (PCA) have become indispensable methods in hydrological studies (Stefania et al. 2019; Cloutier et al. 2008; Menció et al. 2012; Raiber et al. 2012; Salifu et al. 2012; Matiatos et al. 2014; Machiwal and Jha 2015; Voutsis et al. 2015; Cerar and Mali 2016; Singh et al. 2017; Busico et al. 2018; Roy et al. 2020). Notably, the MSA method coupled with analysis of the isotope composition and chemical concentration has widely been used to understand groundwater origin and recharge processes (Sakakibara et al. 2017; Cloutier et al. 2008; Cortes et al. 2016), groundwater and surface water interaction (Trásy et al. 2018; Keefe et al. 2019), geochemical processes (Salifu et al. 2012; Singh et al. 2017; Roy et al. 2020; Wang et al. 2013; Yidana et al. 2018; Magesh et al. 2020), and inputs from pollution sources (Stefania et al. 2019; Machiwal and Jha 2015; Busico et al. 2018; Matiatos 2016; Wang et al. 2018).

The Tuul River Basin in central Mongolia is the primary water source of Ulaanbaatar, the capital city with a population of 1.3 million. However, rapid population growth, fast industrial development, and unplanned urbanization have resulted in severe water degradation (Batdelger and Julien 2012). In addition, surface water is unavailable in the winter, straining groundwater resources to meet the increasing demand (Javzan et al. 2013). For the last several decades, various studies have been done to understand groundwater characteristics and their relation to the surface water system in the Tuul river basin (Tsujimura et al. 2007, 2013; Guo et al. 2008; Nriagu et al. 2012; Dalai and Ishiga 2013; Batsaikhan et al. 2018). For instance, groundwater resources in eastern Mongolia have a heterogeneous spatial variation in hydrogeochemistry because of geological strata, and wastewater and refuse discharge from residential areas (Tsujimura et al. 2007; Dalai and Ishiga 2013). Tsujimura et al. (2013) showed that Tuul River water, via infiltration processes, is a primary source for recharge of alluvial aquifers used for water supply to Ulaanbaatar. These studies raise the fact that change in Tuul River may directly influence groundwater resources. Recently, Batsaikhan et al. (2018) provided additional evidence showing surface water pollution caused high concentrations of nitrate contamination in groundwater. However, impacts of excessive groundwater pumping practices, surface water degradation, and seasonal climatic variation on groundwater resources are still poorly known for the Tuul River (Batdelger and Julien 2012). Therefore, insights into geochemical processes, dominant factors, and rock-water interactions controlling the water system and its spatiotemporal variability are necessary for sustainable groundwater resources management, not only in Mongolia but in similar arid and semi-arid regions.

Accordingly, the main objectives of the study are (1) to identify associations among water bodies using hierarchical cluster analysis (HCA) of their chemical and stable isotopes, (2) to determine the dominant factors by using PCA, (3) to determine main geochemical processes based on Gibbs diagram, ionic ratio and geochemical equilibrium modeling (using the PHREEQC model), and (4) to evaluate the water system using PCA and HCA. The results will provide insights into spatiotemporal geochemical characteristics, dominant processes, groundwater and surface water interactions, as well as the effect of storm water drainage canals and wastewater inputs.

12.2 Materials and Methods

12.2.1 Study Area

The Tuul River is in central Mongolia, within the Arctic Ocean Basin (Fig. 12.1a). The total catchment area of the Tuul River Basin is 49,774.4 km². The Tuul River is 717 km long and flows through Ulaanbaatar and into the Orkhon River, the main tributary of the Selenge River. The basin is far from the sea and surrounded by mountains. The area is characterized by a semi-arid climate, with short warm summers and long cold winters. About 85–90% of the total precipitation falls during the summer (June–August). In winter, precipitation falls as snow, and the surface of the Tuul River is frozen from mid-November until the end of April, but water still flows under the ice. The maximum average ice depth is 116 cm in mid-February. Tributaries and canal waters were wholly frozen in the winter. The annual average precipitation in Ulaanbaatar is 275 mm, and the yearly average temperature is $-0.4\text{ }^{\circ}\text{C}$, ranging from an average of $-21.6\text{ }^{\circ}\text{C}$ in January $-18.0\text{ }^{\circ}\text{C}$ in July (Fig. 12.1c) (IWMP 2012).

Water sampling and observations were performed in the areas surrounding Ulaanbaatar, which is the capital city of Mongolia; thus, it is politically, economically, and

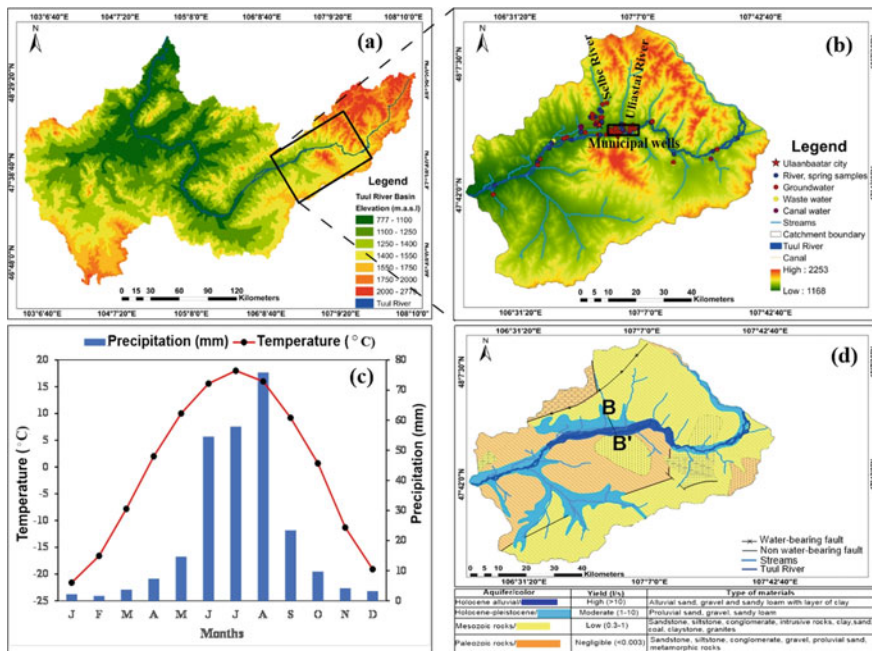


Fig. 12.1 a Map of Tuul river basin, b topography and sampling locations of the study area, c mean annual precipitation and temperature-Ulaanbaatar d geological map (Source Jadambaa N)

environmentally crucial for the nation. The study area covers approximately 5845 km², with elevations varying from 1168 to 2253 m above mean sea level (Fig. 12.1b). The geology of the target area consists mainly of Carboniferous sediments, which are encroached by Jurassic to Triassic granitoid rocks and locally covered by Cretaceous sediments and Neogene and Quaternary deposits (Buyankhishig et al. 2009). Four types of aquifers are distinguished based on water productivity and geological formations (Fig. 12.1d) (IWMP 2012).

12.2.2 Sampling and Analytical Procedures

To understand the seasonal variation of groundwater processes, sampling of groundwater, river water, spring water, and canal water were conducted in the study region of the Tuul River Basin in June 2016 (summer) and in December 2016 (winter). Due to freezing, fewer sampling sites were included in winter. In total, 87 groundwater (GW), 19 Tuul River (TR) samples, six tributary samples, nine spring water samples, five canal water samples (CW), and three wastewater (WW) samples were collected to analyze the stable isotopes and major ions. Electrical conductivity (EC; Twin Cond B173; HORIBA Ltd.), water temperature (Petten Kocher; Nikkyo Technos Co. Ltd.), pH (Twin PH Meter B121; HORIBA Ltd.), dissolved oxygen, and groundwater levels were measured in situ. The sampling site locations were verified using a portable GPS meter (GPSMAP 76S; Garmin Ltd.). All water samples were sealed in 100-mL polyethylene bottles and transported to the laboratory at the University of Tsukuba, Japan, for analysis of stable isotopes of deuterium ($\delta^2\text{H}$) and oxygen 18 ($\delta^{18}\text{O}$) and chemical parameters (cations and anions). Water samples for analysis of major cations and anions were filtered through a 0.2- μm cellulose membrane. The major cations (Ca^{2+} , Mg^{2+} , Na^+ , K^+) and dissolved silica (Si) were analyzed by optical emission spectrometry (Optima 7300DV; Perkin Elmer) with a detection limit of 0.05 ppm for Ca^{2+} , Mg^{2+} , Na^+ , K^+ , and of 0.01 ppm for Si. The anions (Cl^- , NO_3^- , and SO_4^{2-}) were analyzed by ion chromatography (HIC-10A Super; SHIMADZU) with a detection limit of 0.02 ppm for NO_3^- , SO_4^{2-} , and of 0.005 ppm for Cl^- . HCO_3^- was measured via titration with sulfuric acid. As a quality check on the analysis, the charge balance error (CBE $\pm 10\%$) was calculated using the following equation, and the calculated error did not exceed $\pm 10\%$.

$$CBE = \frac{\sum_{cation}(eq) - \sum_{anion}(eq)}{\sum_{cation}(eq) + \sum_{anion}(eq)} * 100 \quad (12.1)$$

The stable isotopes of hydrogen ($\delta^2\text{H}$) and oxygen ($\delta^{18}\text{O}$) were determined by a Cavity Ringdown Spectrometer (L2120i; Picarro), and values were reported as the per mil (‰) deviation from Vienna Standard Mean Ocean Water. The analytical accuracies of $\delta^{18}\text{O}$ and $\delta^2\text{H}$ were 0.1‰ and 1‰, respectively.

12.2.3 Multivariate Statistical Analysis

Principal component analysis (PCA) and hierarchical cluster analysis (HCA) were conducted by using the Statistical Package for Social Sciences (SPSS) software (version-22). Before applying PCA and HCA, the data were screened by charge balance calculations, normality using Skewness and Kurtosis, and by graphical displays (such as histograms and Q-Q plots). The following parameters were used for HCA and PCA: EC, TDS, DO, Na⁺, K⁺, Ca²⁺, Mg²⁺, Cl⁻, SO₄²⁻, HCO₃⁻, NO₃⁻, δ¹⁸O, δ²H, water temperature, and pH. Only pH and dissolved oxygen (DO) parameters were found to be normally distributed. Therefore, prior to the statistical analysis, all other data were log-transformed and standardized according to analytical requirements. The standardization was performed according to their z-score (Woocay and Walton 2008; Davis 1986) as follows:

$$Z_i = \frac{y_i - \bar{y}}{s} \quad (12.2)$$

where Z_i is the standard score of samples i , y_i is the value of sample i , \bar{y} is the mean, and s is the standard deviation. All the variables were standardized, to diminish the effects of differences in measurement units on the data, by making them dimensionless (Davis 1986; Zhou et al. 2007). For the HCA analysis, Ward's linkage method with Squared Euclidean Distance (SED) was used to measure similarity; this approach also yielded the most distinct groupings (Cloutier et al. 2008; Güler et al. 2002):

$$Distance(X, Y) = \sum_{i=1}^n (z_{ij} - z_{kj})^2 \quad (12.3)$$

where z_{ij} and z_{kj} are the z-scores of the medians of the water quality parameters at sites i and k . The SED is the geometric distance in multidimensional space between two sites i and k , based on the difference in the j -th hydrochemical parameter; n is summed across all hydrochemical parameters considered in the HCA (Kumar and Keshari 2009). The levels of similarity were used to build a dendrogram (Davis 1986).

The principal component analysis (PCA) is a method that can reduce the dataset without losing information. PCA was performed on the correlation matrix of standardized data. The same dataset is used for the HCA. According to the Kaiser criterion, the components with eigenvalues greater than one were retained (Cloutier et al. 2008).

12.2.4 Saturation Index

Saturation indexes (SI) of gypsum, calcite and dolomite were calculated for all groundwater samples using PHREEQC computer software according to Parkhurst and Appello (1999). These are common minerals associated with dissolution and precipitation processes in the groundwaters (Deutsch 1997). This approach predicts the subsurface's reactive mineralogy from groundwater data without collecting and analyzing mineral samples (Fisher and Mullican 1997). The saturation index was calculated using the following equation:

$$SI = (IAP/K_t) \quad (12.4)$$

where IAP is the ion activity product, and K_t is the solubility product of the mineral. A negative saturation index ($SI < 0$) indicates undersaturation, which means the dissolution of the mineral phase. A positive saturation index ($SI > 0$) indicates the water that is supersaturated concerning the mineral, indicating that it cannot dissolve more minerals. A neutral index ($SI = 0$) indicates an equilibrium state with the mineral phase.

12.3 Results and Discussion

12.3.1 Chemistry of Groundwater and Surface Water

Summary statistical results of the 15 hydro-chemical variables of all sampling stations (River, tributaries, springs, groundwater, wastewater, and canal water) are given in Tables 12.1 and 12.2. The Tuul River above Ulaanbaatar and floodplain groundwater supply waters have similar characteristics. They exhibit the lowest EC (mean value of 94.27 $\mu\text{s/cm}$ and 117 $\mu\text{s/cm}$, respectively), and possess the lowest individual ion values, indicative of groundwater and surface water interaction. Meanwhile, water chemistry in the downstream sites varied due to mineral weathering and the influence of anthropogenic activities such as wastewater discharges. Water samples from tributaries show higher EC values (mean value of 328.33 $\mu\text{s/cm}$) than Tuul River because of tributaries flowing from ger districts (residential area) which may be more affected by human pollution. Spring water has higher EC and nitrate values, and the lowest temperature and dissolved oxygen concentrations. Non-water supply wells have higher EC (mean value of 498 $\mu\text{s/cm}$) values than river waters and floodplain groundwaters. Finally, canal and wastewaters were found to have the highest EC mean values.

Table 12.1 The summary statistics of all samples in summer season (all elements in mg/l except EC- $\mu\text{s/cm}$, Temp- $^{\circ}\text{C}$, ORP-mV)

Category	EC	TDS	Temp	pH	DO	ORP	HCO ₃	Cl	NO ₃	SO ₄	Ca	Mg	Na	K	Si
<i>Tuul River</i>															
Mean	94.3	44.5	15.1	7.9	5.6	188.4	34.3	4.8	2.9	3.7	8.2	1.2	4.7	1.0	2.8
Standard deviation	55.9	29.7	2.7	0.3	1.2	22.9	15.8	4.0	4.8	3.3	3.6	0.6	4.3	0.6	0.2
Minimum	48	20	12.3	7.5	3.6	151	21.4	2.3	0	1.1	5	0.5	1.9	0.6	2.4
Maximum	193	102	20	8.6	7.3	214	62.2	12.8	14	9.3	15	2.5	12.8	2.1	3.1
<i>Tributaries</i>															
Mean	328.3	156	17.2	8.4	7.0	160.5	113.6	17.4	15.5	19.5	31.1	6.3	15.4	2.0	3.3
Standard deviation	236.5	119.1	1.8	0.3	1.8	16	48.2	21.6	31.3	21.2	18.5	4.7	16.8	1.2	0.8
Minimum	107	52.0	14.8	8.0	5.4	141	54.9	2.4	0	5.1	13	2	3.8	1.1	2.2
Maximum	750	368.0	18.9	8.8	10.1	181	169.6	57.7	79	59.8	62	14.7	47.1	4.2	4.2
<i>Springs</i>															
Mean	974.6	473.6	5.2	7.4	2.9	141.2	203.1	98.8	125.7	103.0	117.5	28.8	38.1	3.6	6.7
Standard deviation	650.7	320.7	4.3	0.4	1.2	56.6	67.3	74.3	132.6	115.4	79.7	26.5	26.6	2.2	3.1
Minimum	193.0	193	2.2	6.9	0.8	47	101.3	4.5	4	10.6	25	4	6.6	1.0	4.2
Maximum	1810	881.0	12.6	7.8	3.7	188	286.7	175.6	272	295.3	233	73	77	6.4	12
<i>Municipal wells</i>															
Mean	117	58	6.7	7.0	5.6	182.2	47.8	6.5	3.6	9.4	13.9	1.8	5.8	1.0	4.3
Standard deviation	120.3	52.6	1.4	0.1	1.4	27.7	21.0	9.3	3.9	19.2	11.2	1.4	6.2	0.6	1.5
Minimum	53	13	4.2	6.8	1.7	146	31.7	2	0	2.3	7.7	1	2.6	0.6	2.8
Maximum	610	278	9.5	7.2	7.7	225	106.1	45	16.9	99.6	60	5	33.6	3.6	8.2

(continued)

Table 12.1 (continued)

Category	EC	TDS	Temp	pH	DO	ORP	HCO ₃	Cl	NO ₃	SO ₄	Ca	Mg	Na	K	Si
<i>Non-municipal wells</i>															
Mean	498	239	4.8	7.4	3.8	154.9	184.7	24.5	35.2	32.0	55.7	11.5	20.7	1.5	6.5
Standard deviation	263.1	143.2	2.4	0.4	1.7	58.8	74	25	41.6	25.1	38.0	6.9	15.3	0.4	1.9
Minimum	139	58	1.3	6.6	0.9	- 17	28	4	0.0	0.0	11.7	3	4.5	0.9	4.2
Maximum	1120	605	8.9	8.0	6.6	204	287.9	88.0	143.3	90.2	148	28	60.8	2.6	13.6
<i>Canals and Wastewater</i>															
Mean	1133	573	17.0	8.0	4.7	85.6	263.3	99.1	104.7	90.4	105.9	23.7	66	6.6	4.5
Standard deviation	420.1	242.3	5.2	0.5	2.6	161	89	55	107.1	50.1	67.5	13.6	22.1	3.6	1.6
Minimum	490	241	7.4	7.1	0.3	- 277	137.3	38.4	0.0	26.4	35	5.4	40	4.1	2.3
Maximum	1690	992.0	22.9	8.5	8.2	176	395	179	266.0	151.3	219	39	91.8	13.8	6.3

Table 12.2 The summary statistics of all samples in winter season (all elements in mg/l except EC- $\mu\text{s}/\text{cm}$, Temp- $^{\circ}\text{C}$, ORP-mV)

Category	EC	TDS	Temp	pH	DO	ORP	HCO ₃	Cl	NO ₃	SO ₄	Ca	Mg	Na	K	Si
<i>Tuul River</i>															
Mean	520.6	252	1.4	7.9	5.8	136.9	141.5	31.6	1.9	22.2	27.7	4.4	33.1	4.7	4.3
Standard deviation	563.1	271.8	1.3	0.5	3.5	60.9	143.7	39.0	3.7	27.1	26.3	3.8	40.5	5.8	1.3
Minimum	91.2	49	0.2	7.0	1.2	82	36.0	2.5	0	1.2	6.4	1.0	3.2	0.4	3.2
Maximum	1230	635	4.3	8.6	9.9	255	344.7	85.2	10.9	61.3	62.5	9.8	88.0	12.6	6.2
<i>Springs</i>															
Mean	966.25	470.8	2.2	7.5	4.7	138	210.8	72.5	102.8	47.3	104.5	19.3	28.2	2.1	6.4
Standard deviation	743.4	386.5	0.9	0.6	1.5	40.8	74.8	68.0	127.2	46.4	85.0	14.1	15.8	1.1	0.8
Minimum	230	113	1.0	7.1	2.9	78	119.6	3.2	4.1	8.8	26.8	4.9	6.8	0.8	5.2
Maximum	2000	1020	3.1	8.4	6.0	166	295.3	156.5	287.7	114.2	225.6	38.7	41.7	3.2	7.0
<i>Municipal wells</i>															
Mean	165.7	74.0	5.3	7.4	5.1	134	54.6	6.0	3.5	8.2	13.4	2.5	6.5	0.8	4.5
Standard deviation	106	50.9	1.3	0.3	1.8	28.6	24.3	7.6	3.4	11.0	8.9	1.6	5.9	0.6	1.0
Minimum	83	38	3.1	7.0	1.9	91	32.3	2.0	0.4	2.2	5.6	0.9	3.3	0.4	3.1
Maximum	500	255	8.9	8.3	10.3	224	124.4	30.1	11.1	54.2	42	6.4	30.5	3.1	7.0
<i>Non-municipal wells</i>															
Mean	613.8	309.3	3.5	7.6	4.5	117	192.1	30.3	47.5	27.9	55.3	15.1	23.1	1.7	6.9
Standard deviation	464.9	247.2	2.2	0.3	2.1	58.3	95.9	44.1	71.4	20.6	38.4	15.2	17.6	2.4	2.1
Minimum	176.4	78	0.2	7.1	1.3	-66	29.9	3.5	0.2	1.5	11.8	3.1	5	0.0	4.4
Maximum	2100	1110	7.7	8.4	10.0	186	387.4	194.4	309.2	75.2	150.5	69.3	63.3	11.0	12.7

12.3.2 Hierarchical Cluster Analysis

Hierarchical cluster analysis (HCA) was used to find the spatial similarity among the sampling sites. All sampling sites were grouped into four statistically different clusters based on physio-chemical and stable isotope characteristics in both seasons (Fig. 12.2 and Table 12.3). The four clusters were differentiated by EC, with the EC organized in the following cluster sequence C1–C2–C4–C3 (Fig. 12.2), representing different rock-water interactions, recharge source, residence time, and anthropogenic activities. The median values of each cluster are presented in Table 12.3 and are clearly differentiated by their chemical and isotope characteristics. The C1–C2 and C4 clusters were characterized as a Ca–HCO₃ type water, while C3 showed Ca-mixed type in summer and Na–HCO₃ type in winter (Fig. 12.3). The Na–HCO₃ type (TR9–11) resulted from contamination by treated municipal wastewater discharges.

In both seasons, water samples from Tuul River upstream and municipal wells were assigned to cluster C1, which has a low concentration in major ions, EC, and NO₃ and is relatively higher in dissolved oxygen and depleted stable isotopes. This result suggests that water sources in these locations were unpolluted, and groundwater may be recharged and have a short residence time, and have low rock-water interaction. Water samples downstream of Tuul River and floodplain areas, tributaries (Uliastai, Selbe, and Dund Rivers), spring (SP1), and two wells (GW35 and GW43) on the southern side were assigned to cluster C2 (Table 12.4). The water samples in the cluster C2 have moderate ion concentrations and compared to cluster C1, are slightly polluted sites. Meanwhile, cluster C3 mainly consisted of different surface water samples, including canal water (CW1–CW5), wastewater (WW1 and WW2), one tributary (DR2), and two spring samples (SP3 and SP5) in summer and TR9, TR10, TR11, and WW2 in winter (Table 12.4). The cluster C3 was characterized by high EC (1220 $\mu\text{s}/\text{cm}$) and nitrate concentration (104.5 mg/L), a wide variation in temperature (2.4–17.2 °C) and stable pH (7.9). Cluster C4 included two springs (SP2 and SP4) and groundwater samples mainly from ger districts to the north of the Tuul River. When compared to cluster C1 and C2, this cluster had enriched stable isotope composition (Fig. 12.5), and high median values of EC (530 and 590 $\mu\text{s}/\text{cm}$), and nitrate (26.2 and 35.5 mg/L) in summer and winter, respectively. This result indicated influences of rock-water interaction such as weathering, dissolution, ion exchange, and anthropogenic pollution on the water quality of the study area. These geochemical characteristics are common in many regions globally (Roy et al. 2020; Arya et al. 2020; Zhang et al. 2020) (Fig. 12.4).

However, comparing the summer and winter results, the EC values increased slightly in winter, and several temporal shifts were observed between clusters (Fig. 12.2b and Table 12.4). For example, municipal wells (GW7, GW10, and GW11) shifted from C1 to C2, and GW40 changed from C4 to C2, indicating less groundwater infiltration in the winter. Similarly, GW7, GW10, GW11, and GW40 shifted cluster groups from summer to winter was caused by decreased dilution, leaching by runoff and rainfall processes increased the EC values. The decreased dilution results from surface water freezing and solid-state precipitation (i.e., snow). Meanwhile,

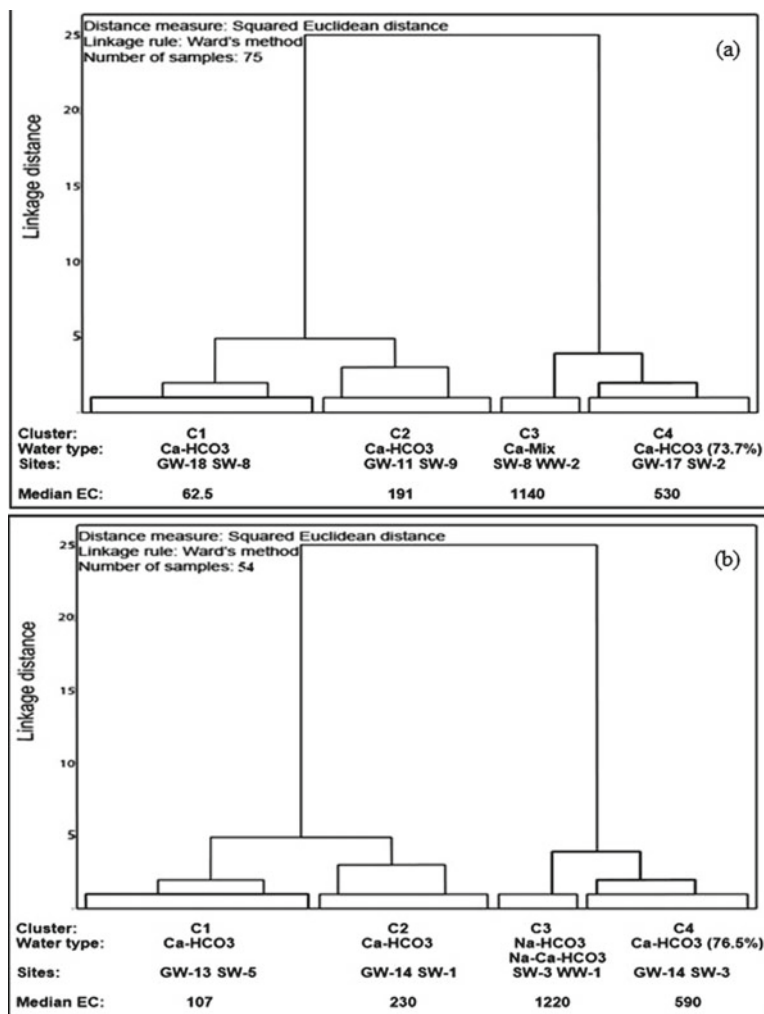


Fig. 12.2 Dendrogram of the cluster analysis using Ward's method in **a** summer and **b** winter

surface water sample results from downstream sites on the Tuul River (TR9, TR10, and TR11) shifted from C2 to C3, and SP3 from C3 to C4, from summer to winter due to anthropogenic activities (Batsaikhan et al. 2020). Because TR9, TR10, and TR11 were located downstream of wastewater discharge points, their EC values increased in winter due to continued wastewater discharge combined with lower dilution by river water. All other sites remained in the same clusters throughout the year, indicating that both the surface and subsurface water samples in the study area do not show a clear seasonal variation in geochemical compositions and stable isotopes.

The HCA also provides a spatial distribution of water geochemistry in the study site. Most samples with low concentrations are in the alluvial aquifers along the river

Table 12.3 Median concentrations of clusters

Parameters	Summer				Winter			
	C1	C2	C3	C4	C1	C2	C3	C4
EC	62.5	191	1140	530	107	230	1220	590
TDS	36	90.5	558.5	252	49	90	607	328
T °C	7.5	7.8	17.2	3.7	4.2	5.3	2.4	2.7
pH	7.0	7.2	7.9	7.6	7.3	7.6	8.0	7.4
DO	5.9	4.7	4.1	3.8	6.0	5.1	1.8	4.2
HCO ₃ ⁻	33.9	61	259.3	203.1	40.0	70.8	334.0	214.1
Cl ⁻	2.8	6.4	96.4	34.4	2.6	4.9	82	34.2
NO ₃ ⁻	1.5	5.5	104.5	26.2	1.2	5.2	0.0	35.3
SO ₄ ²⁻	3.4	9	111.3	36.6	3.6	8.8	56.7	35.7
Ca ²⁺	8.4	17.9	101.7	60.6	8.6	18.5	58.6	66
Mg ²⁺	1.0	3	28.9	12.2	1.6	3.6	8.8	14.6
Na ⁺	3.2	8.1	55.2	21.6	4	6.8	86	24.5
K ⁺	0.8	1.3	4.6	1.64	0.6	0.9	12.4	1.7
SiO ₂	3.1	4.2	4.5	6.3	8.7	11	12.3	14.2
δD	- 126.2	- 112.6	- 96.0	- 98.6	- 114.1	- 110.0	- 109.2	- 98.3
δ ¹⁸ O	- 18.0	- 16.4	- 14.0	- 14.6	- 16.8	- 16.6	- 16	- 14.7

and are grouped into 2 clusters regarding their chemical and isotopic compositions (C1 and C2), which may be related to natural and anthropogenic activities (Fig. 12.5). The C1 cluster is characterized by the natural processes of rainfall recharge and river water infiltration, while the C2 group includes those data exhibiting higher EC values as influenced by mineral weathering. Monitoring sites in the C3 cluster consist of urban storm water runoff canal and wastewater samples with high nitrate concentrations (104.5 mg/L), indicating anthropogenic pollutant sources. Cluster C4 samples have relatively high TDS (252–328 mg/L) and nitrate (26.2–35.3 mg/L) and are mainly distributed on the alluvial-proluvial aquifers of the northern mountainside, indicating the origin of this groundwater is from the northern mountainside and mixed with surface water in floodplain areas. The spatial variation of water geochemistry suggests that hydrogeochemical evolution in the study area is related to hydrogeology and human impacts.

The significant findings of the HCA are: (i) some samples changed cluster from summer to winter, which indicates a seasonal change in the chemical system, especially in the downstream area; (ii) water chemistry in the study area is controlled by rock–water interactions and anthropogenic pollution; (iii) floodplain groundwater and river water were grouped in the same cluster, showing active interaction between these water bodies; and (iv) based on dissolved solids, the HCA distinguished Ca–HCO₃–type water in three clusters depending on the mineral dissolution and pollution inputs (Fig. 12.3).

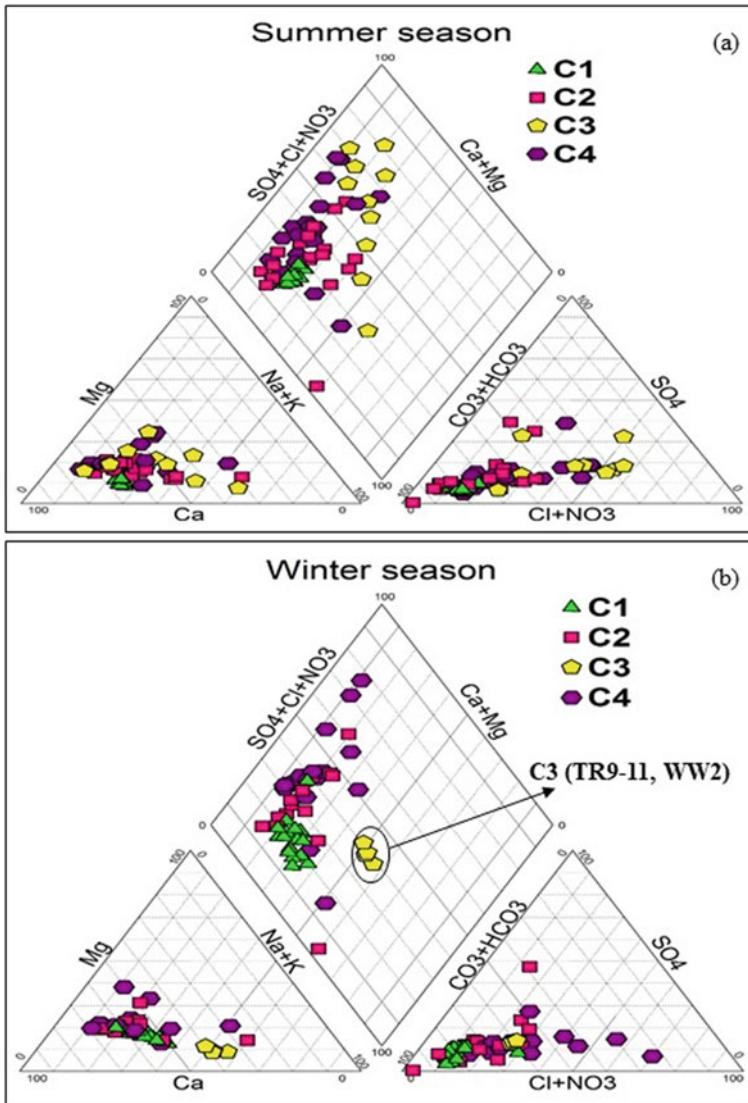


Fig. 12.3 Piper diagram of the collected water samples in the study area in **a** summer and **b** winter

12.3.3 Principal Component Analysis

Correlation analysis was performed between 16 parameters (Tables 12.5 and 12.6) to study hydrochemical relationships (underlining values). In the summer (Table 12.5), electrical conductivity (EC) and TDS have a high positive correlation with HCO_3^- , Cl, NO_3^- , SO_4^{2-} , Ca, Mg, Na, K, and $\delta^2\text{H}$ ($r = 0.6\text{--}1.0$). This shows that minerals in

Table 12.4 Samples of each cluster contained in the dendrogram

Cluster	Samples (summer)	Samples (winter)	Location	Characteristics
C1	GW2, GW5–GW7, GW9–GW22, TR2–TR8	GW2, GW5, GW6, GW9, GW12–GW22, TR2–TR8	East (Municipal wells and Tuul River upstream)	A low concentration in major ions, conductivity, and NO ₃ but relatively higher in dissolved oxygen, and depleted stable isotopes
C2	DR1, TR9–TR11, SR1, SR2, UR1, UR2, GW8, GW25, GW34, GW35, GW37–GW39, GW41–GW43, SP1	GW7, GW10, GW11 , GW25, GW37, GW34, GW35, GW39, GW40 , GW41, GW43, GW42, SP1, GW38, GW8	West (downstream), north-east, south	Moderate ion concentrations and slightly polluted
C3	DR2, SP3, SP5, WW1, WW2, C1–C5	TR9–TR11 , WW2	North-west	Higher EC, temperature, pH and nitrate
C4	GW3, GW4, GW23, GW24, GW26–GW33, GW36, GW40, GW44–GW46, SP2, SP4	GW3, GW4, GW23, GW24, GW26–GW33, GW36, GW44, SP2, SP3, SP4	Mainly north, north-west and east	Enriched stable isotope composition and high median values of EC and nitrate

Bold values indicate shifted values between clusters in 2 seasons

the study area have similar characteristics to the solutes in the water samples and contribute to water mineralization in the study area. Nitrate significantly contributed to conductivity and was highly correlated with major ions (Ca, Mg, Na, SO₄, Cl, HCO₃), indicating pollution inputs. These results are consistent with a previous research finding of high nitrate concentration (> 10 mg/L) in the ger districts due to the lack of sanitary conditions and no centralized wastewater collection and treatment systems (Naranchimeg et al. 2018). Temperature positively correlated with pH, which may be attributed to surface water chemistry, such as rivers, canals, and wastewater. Correlations of pH with other variables was weak or negative; ion concentrations are higher due to the higher aggressiveness of acidic media to soil and host rocks (Négrelet et al. 2003). Silica, HCO₃, and $\delta^2\text{H}$ have positive correlations indicating the weathering of silicate minerals. In the winter (Table 12.4), electrical conductivity (EC) and TDS are highly and positively correlated with HCO₃, Cl, NO₃, SO₄, Ca, Mg, Na, K, SiO₂, $\delta^{18}\text{O}$, and $\delta^2\text{H}$ ($r = 0.6\text{--}1.0$). The contribution of nitrate to EC in winter decreased (from 0.9 to 0.6), indicating reduced dilution from runoff processes due to frozen surface and subsurface. The silica correlated with more parameters than in the results for the summer samples, such as EC, TDS, Ca, Mg, Na, HCO₃, Cl, SO₄, $\delta^2\text{H}$, and $\delta^{18}\text{O}$ ($r = 0.6\text{--}0.7$). This showed the relatively greater influence of natural processes such as rock-water interaction and mineral weathering in winter.

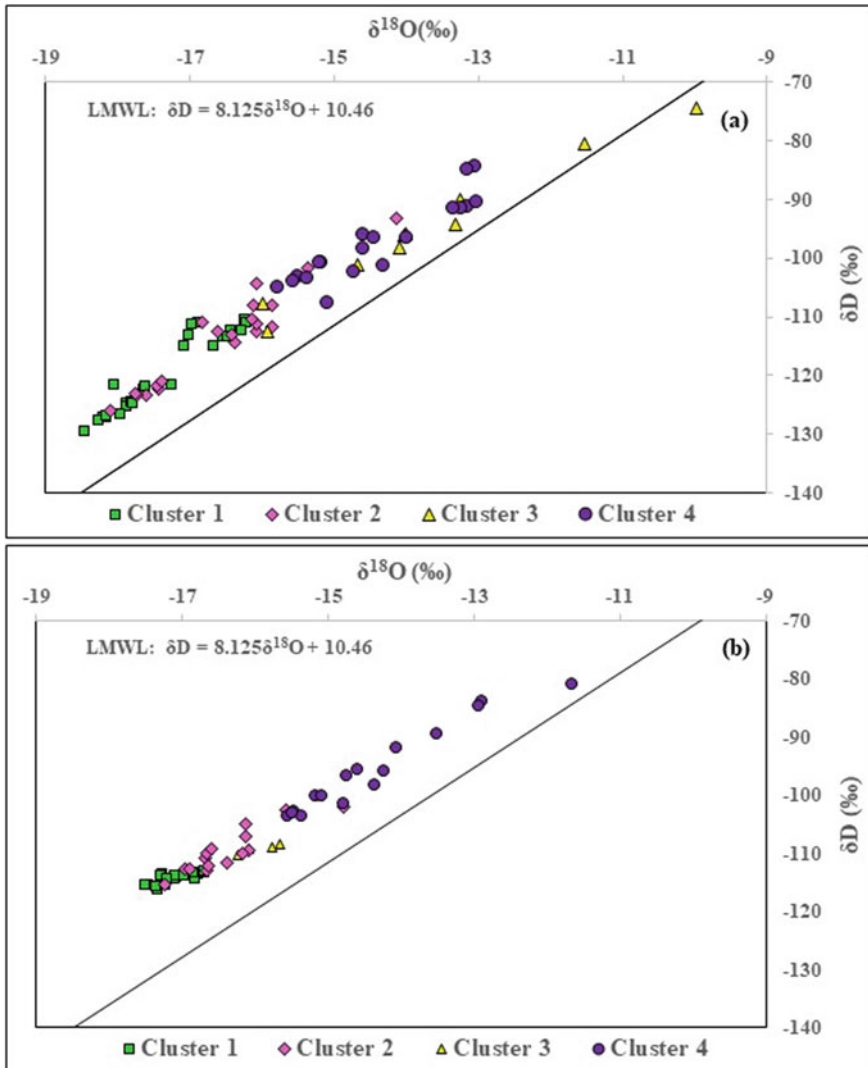


Fig. 12.4 Relationship between $\delta^{18}\text{O}$ and δD in the collected water samples in the study area in **a** summer and **b** winter

Principal component analysis was applied to the log-transformed and standardized data sets. A varimax rotation was conducted to reduce the overlap of original variables over each principal component. The loadings, eigenvalues, explained variance, and cumulative variance are shown in Table 12.7. Four (summer) and three (winter) principal components (PCs) have eigenvalue > 1 , which explained about 86.9% and 83.8% of the total geochemical data variance, respectively (Table 12.7). The factor loadings can be classified as strong, moderate, and weak, corresponding to absolute

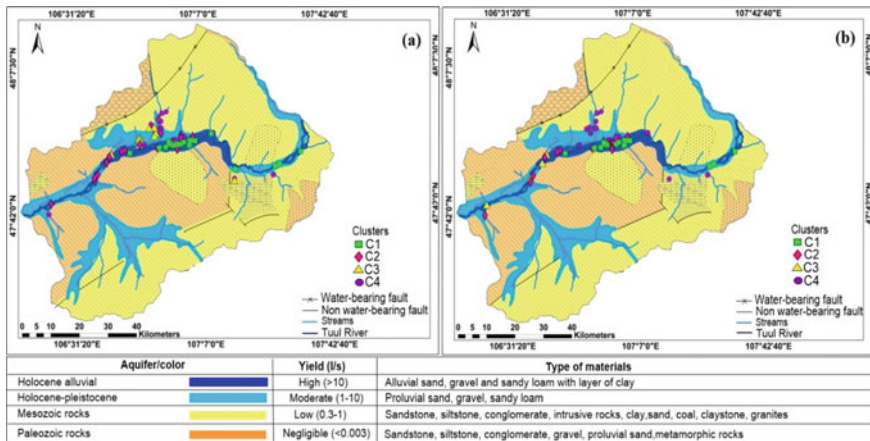


Fig. 12.5 Hydrogeological spatial and temporal distribution of the clusters in **a** summer and **b** winter

loading values of > 0.75, 0.75–0.5, and 0.5–0.3, respectively (Liu et al. 2003). PC1 explains 55.8% of the total variance and strong positive loadings of EC, TDS, Cl, SO₄, NO₃, Ca, and Mg, and moderate positive loadings of HCO₃⁻, Na, and K. It means that water chemistry is controlled by geochemical processes of rock weathering, dissolution, and ion exchange, and anthropogenic activities such as domestic and industrial waste. The highly positive loading of Ca²⁺ and Mg²⁺ coupled with HCO₃⁻ in PC1 indicates that calcite and dolomite dissolution are primary factors influencing the concentration of Ca²⁺ and Mg²⁺ in groundwater (Roy et al. 2020). The identical loading of nitrate in PC1 showed the same pollution sources exist in both seasons since nitrate has no known lithological source (Handa 1988). The source of nitrate is possibly domestic, municipal and industrial discharges (Selvakumar 2017).

PC2 explains 17% of the total variance and strong loading of stable isotopes, in addition to weak positive loading of HCO₃⁻ and SiO₂, which can be identified as regional flow processes with the dissolution of minerals containing these elements. PC3 accounts for 7.8% of the total variance and moderate positive loading of silica and strong negative loading of dissolved oxygen related to silicate weathering of minerals in the water. PC4 represents 6.3% of the total variance, and strong positive loading of temperature and pH, and weak positive loading of Na and K. This principal component describes the physical processes in surface water samples, such as from a river, tributary, canal or wastewater, showing high positive loadings for pH values and temperature. The high loading for pH value may arise from biogenic or organic control of the pH value, which relates to dissolved CO₂ consumed by organisms and aquatic plants (Livingstone 1963).

The number of factors decreased in the winter, and cumulative variance is as low as 84% (Table 12.7). This is because several processes in the study area, such as ion exchange, dilution, leaching by runoff, rainfall and anthropogenic activities, are more active in the summer (Kumar and Keshari 2009). PC1 explains 65% of the

Table 12.5 Correlation coefficients of the 16 physio-chemical parameters in the summer season

	EC	TDS	T °C	pH	DO	HCO ₃	Cl	NO ₃	SO ₄	Ca	Mg	Na	K	SiO ₂	δD	δ ¹⁸ O
EC	1															
TDS	.994	1														
T °C	.092	.084	1													
pH	.289	.263	.636	1												
DO	-.316	-.294	.303	.129	1											
HCO ₃	.836	.821	-.064	.284	-.503	1										
Cl	.946	.945	.129	.215	-.287	.680	1									
NO ₃	.885	.898	.042	.201	-.134	.571	.895	1								
SO ₄	.891	.883	.096	.220	-.139	.595	.856	.842	1							
Ca	.942	.951	-.040	.198	-.294	.745	.917	.933	.817	1						
Mg	.916	.905	.029	.268	-.263	.713	.868	.857	.931	.846	1					
Na	.841	.821	.212	.295	-.295	.815	.781	.580	.727	.646	.735	1				
K	.700	.679	.374	.254	-.276	.630	.711	.450	.562	.504	.528	.844	1			
SiO ₂	.305	.287	-.469	-.298	-.446	.519	.226	.109	.145	.296	.234	.348	.189	1		
δD	.564	.551	-.280	.029	-.280	.646	.445	.406	.424	.545	.484	.478	.351	.506	1	
δ ¹⁸ O	.344	.334	-.467	-.149	-.187	.457	.234	.246	.219	.379	.280	.245	.084	.465	.764	1

Table 12.6 Correlation coefficients of the 16 physio-chemical parameters in the winter season

	EC	TDS	T °C	pH	DO	HCO ₃	Cl	NO ₃	SO ₄	Ca	Mg	Na	K	SiO ₂	δD	δ ¹⁸ O
EC	1															
TDS	.994	1														
T °C	-.290	-.301	1													
pH	.047	.078	-.267	1												
DO	-.515	-.510	-.024	.055	1											
HCO ₃	.939	.946	-.253	.064	-.573	1										
Cl	.956	.956	-.309	-.001	-.500	.857	1									
NO ₃	.575	.579	-.056	-.098	-.083	.493	.549	1								
SO ₄	.883	.879	-.220	-.022	-.433	.778	.886	.612	1							
Ca	.964	.968	-.247	.004	-.462	.920	.926	.726	.903	1						
Mg	.941	.945	-.238	.010	-.438	.908	.884	.746	.841	.972	1					
Na	.924	.924	-.295	.043	-.608	.930	.880	.306	.762	.832	.820	1				
K	.705	.704	-.296	.090	-.469	.600	.750	.028	.636	.576	.511	.750	1			
SiO ₂	.683	.673	.017	-.116	-.362	.730	.583	.433	.560	.685	.715	.692	.313	1		
δD	.772	.779	-.227	.105	-.283	.729	.695	.028	.741	.821	.845	.634	.290	.613	1	
δ ¹⁸ O	.814	.827	-.258	.167	-.320	.766	.749	.734	.753	.854	.878	.677	.326	.596	.965	1

Table 12.7 Loadings of 16 physicochemical variables on 2 rotated components

Variable	Summer				Winter		
	PC1	PC2	PC3	PC4	PC1	PC2	PC3
EC	.906	.241	.281	.186	.689	.699	.127
TDS	.917	.226	.253	.162	.695	.691	.154
Temperature	.059	– .376	– .105	.846	– .120	– .173	– .768
pH	.172	.041	– .129	.839	– .005	– .056	.774
DO	– .139	– .051	– .800	.246	– .086	– .750	.199
HCO ₃ [–]	.571	.460	.551	.213	.640	.698	.079
Cl [–]	.924	.077	.249	.132	.620	.714	.134
NO ₃ [–]	.965	.095	– .045	– .001	.922	– .077	– .088
SO ₄ ^{2–}	.925	.092	.066	.104	.687	.577	.070
Ca ²⁺	.917	.253	.140	– .001	.808	.561	.066
Mg ²⁺	.911	.172	.150	.088	.840	.504	.054
Na ⁺	.639	.207	.512	.394	.468	.838	.114
K ⁺	.502	.027	.553	.482	.076	.871	.246
SiO ₂	.083	.491	.606	– .325	.605	.445	– .248
δD	.345	.837	.202	.012	.895	.267	.193
δ ¹⁸ O	.170	.900	.035	– .196	.900	.220	.137
Eigenvalue	8.920	2.720	1.250	1.000	10.410	1.610	1.370
Explained variance (%)	55.750	17.000	7.790	6.300	65.010	10.090	8.590
Cumulative % of variance	55.750	72.780	80.570	86.870	65.090	75.180	83.770

Bold values represent strong loadings

total variance, with strong loading of $\delta^{18}\text{O}$, $\delta^2\text{H}$, NO_3 , Ca, and Mg, and moderate loadings of EC, TDS, HCO_3 , Cl, SO_4 , and SiO_2 , and weak positive loading of K. The result shows the influence of regional flow and weathering processes, and pollution sources. Group PC2 has a strong positive loading of Na and K, and strong negative loading of dissolved oxygen and positive moderate loadings of EC, TDS, HCO_3 , Cl, SO_4 , Ca, and Mg, and a weak positive loading of SiO_2 . This result shows mainly anthropogenic inputs, especially downstream of the municipal wastewater and stormwater discharges from Ulaanbaatar as exhibited with increasing K, Na, SO_4 , and Cl concentrations. The decreased pH, NO_3 , and DO values in winter water samples in this principal component are related to the oxidation of organic matter in sewage water discharged to the river (Kattan 2006); this interpretation is also clear from the increased loading of EC and TDS. Component PC3 explains 8.6% of the total variance and has positive loading of pH, negative loading of temperature indicating physical processes in surface water, and from the seasonal variation. In both seasons, moderate to strong loading of Na and Cl together in PC1 (summer) and PC2 (winter) indicate the anthropogenic source of these ions.

12.4 Hydrogeochemical Processes

12.4.1 Gibbs Diagram

Gibbs diagrams have been used in hydrochemistry to analyze formation mechanisms (Feth and Gibbs 1971). Two diagrams have been used to evaluate the dominant effects of evaporation, rock weathering, and precipitation on the geochemical evolution of groundwater in arid and semi-arid regions. The diagrams show the weight ratios of $(\text{Na})/(\text{Na} + \text{Ca})$ and $\text{Cl}/(\text{Cl} + \text{HCO}_3)$ against TDS (Gibbs 1970). As seen in Fig. 12.6, all samples plotted in the rock dominance field show that the primary controlling mechanism of the chemical compositions in the study area is the rock weathering process. Most of the samples had lower $\text{Na}/(\text{Na} + \text{Ca})$ ratios, which indicates that carbonate minerals dominate the geology of the study area. The ratio of $\text{Na}/(\text{Na} + \text{Ca})$ and $\text{Cl}/(\text{Cl} + \text{HCO}_3)$ were higher than 0.5 in samples GW39 (C2), SP5, C2, and WW2 (C3), GW4 and SP4 (C4) in summer, and in samples GW39 (C2), WW2 and TR9-11 (C3), GW4 and GW44 (C4) in winter. These clusters have higher TDS values than C1, which indicates that cation exchange processes or anthropogenic activities. The C3 HCA cluster samples had higher ionic ratios and TDS values in both seasons, implying that the evaporation process involves hydrochemistry with anthropogenic activities. Significantly, GW 39 and TR9-11 are located downstream, and are highly affected by wastewater from the wastewater treatment plant (Fig. 12.6). The finding is consistent with the Piper diagram distribution in Fig. 12.3.

12.4.2 Ratios of Major Ions

Many researchers have demonstrated that the relationship between primary ions can give valuable information about the geochemical processes and mechanisms (Zhang et al. 2020; Jalali 2009; Marghade et al. 2012; Canora et al. 2019). The relationship between dissolved species can show the origin of solutes and the processes that produced the observed water compositions (Fisher and Mullican 1997). Accordingly, the dissolution of calcite, dolomite, and gypsum are the dominant processes in the water environment when the plot of $(\text{Ca}^{2+} + \text{Mg}^{2+})$ against $(\text{HCO}_3^- + \text{SO}_4^{2-})$ is close to the 1:1 equiline (Fisher and Mullican 1997; Kumar et al. 2006; Venugopal et al. 2009). The plot of the ratio of major ions also represents ion exchange processes. If the ion exchange is dominant, the points shift to the left side, and if the reverse and the ion exchange process is dominant, then the points change to the right side (Krishnaraj et al. 2011).

As shown in Fig. 12.7a, cluster 1, cluster 2, and most samples from cluster 4 fall on the 1:1 equiline suggesting that groundwater is mainly recharged by surface water or precipitation, and calcium, magnesium, and hydro-carbonate originate from weathering of carbonate rocks (Zhang et al. 2007). In both seasons, GW4 (C4) and

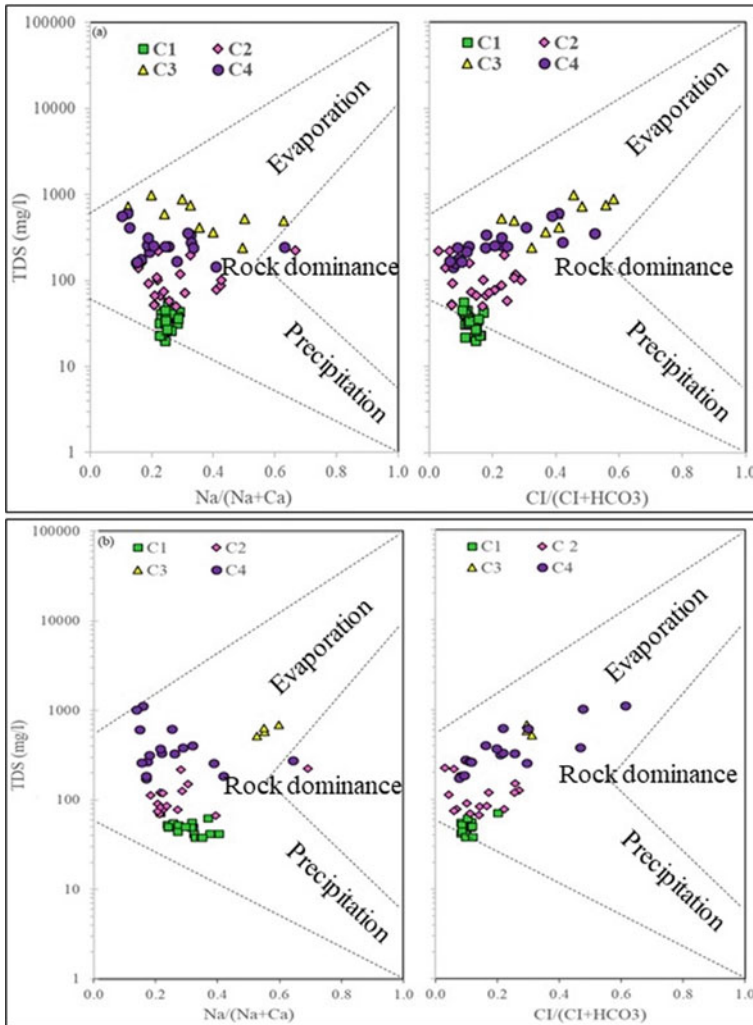


Fig. 12.6 Gibbs diagram of water samples in the study area in **a** summer and **b** winter

GW39 (C2) are plotted above the 1:1 equiline, suggesting a contribution from non-carbonate source or cation exchange processes, such as between $Ca^{2+} + Mg^{2+}$ and $Na^+ + K^+$ (Tiwari and Singh 2014), and silicate weathering, with a possibility of anthropogenic activities. From cluster 4, springs and some groundwater samples located on the north side of the study area fall below the 1:1 equiline, showing some additional sources of cations and are balanced by Cl and NO_3 . Cluster 3 samples lie on both sides of the line, indicating the ion exchange and reverse ion exchange processes. This cluster mainly included samples collected from canal water, wastewater, some springs, and river water downstream, all of which are impacted by anthropogenic

waste discharges For instance, wastewater samples (in both seasons) and downstream samples of Tuul river water after wastewater discharge (in winter) plot above the line, indicating apparent effects of anthropogenic activities from wastewater.

Figure 12.7b indicates that most samples, especially cluster 1 and cluster 2, are close to the carbonate weathering line, suggesting that carbonate weathering occurs in the floodplain of the study area. Cluster 3 is distributed on both sides of the line, indicating ion exchange processes and pollution. Cluster 4 falls below the line, meaning that there are some additional sources to the carbonate weathering, indicating that the ion exchange process is dominant and balanced by some anions, which may be due to anthropogenic inputs as there is a high representation of high nitrate and chloride.

Gypsum dissolution yields Ca^{2+} and SO_4^{2-} in water. A plot of Ca^{2+} and SO_4^{2-} shows that all samples of four clusters fall below the 1:1 line (Fig. 12.7c), indicating that groundwater is in an oversaturated state with respect to calcite and undersaturated concerning gypsum (Tran et al. 2020). The gypsum dissolution process does not contribute in the study area. The enrichment of Ca showed rock-water interaction and dissolution of carbonates and silicate minerals.

The strong correlation between sodium and chloride has often been used in semi-arid regions (Kattan 2006; Sami 1992; Magaritz et al. 1981). The dissolution of halite releases equal concentrations of Na and Cl in water, and the Na/Cl molar ratio will be around one (Hounslow 1995). From Fig. 12.7d, most of the samples from clusters

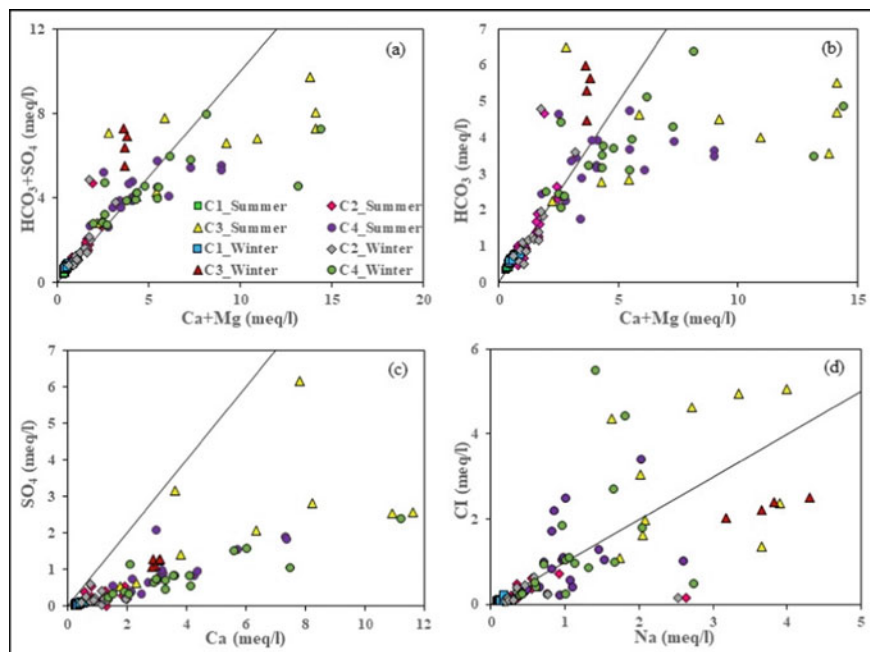


Fig. 12.7 Plots between **a** $\text{HCO}_3 + \text{SO}_4$ and $\text{Ca} + \text{Mg}$, **b** HCO_3 versus $\text{Ca} + \text{Mg}$, **c** SO_4 versus Ca , **d** Cl versus Na

1 and 2 falls around or below the 1:1 line, suggesting the silicate weathering is more significant than halite dissolution. The silicate dissolution can be a probable source of Na because HCO_3^- is the most abundant anion in the study area (Fisher and Mullican 1997). Clusters 3 and 4 have distributed values, and the high chloride and sodium contents may be due to anthropogenic activities such as industrial and municipal waste. Some samples are located above the line, showing that cation exchange of Na for Ca and Mg occurred or that rainwater is a source for Cl. Excess Na in clusters 4 and 3 can be related to silicate weathering and wastewater, respectively, because wastewater samples in cluster 3 have high Na in both seasons. The strong positive correlations between Cl-TDS ($r = 0.91.0$), Na-TDS ($r = 0.8-0.9$), and Na-Cl ($r = 0.8-0.9$) in summer and winter, respectively (Tables 12.2 and 12.3), indicate these ions come from anthropogenic inputs that are relatively increased in wintertime. The interpretations of ionic ratios were consistent with the Piper diagram (Fig. 12.3) and Gibbs plots (Fig. 12.6).

12.4.3 Saturation Index

Saturation indexes (SI) of gypsum, calcite, and dolomite of all groundwater samples were calculated using PHREEQC (Parkhurst and Appello 1999). PHREEQC is useful for finding common minerals in the groundwater environment and their geochemical processes (Deutsch 1997). This approach can predict the reactive mineralogy of the subsurface from groundwater data without collecting and analyzing mineral samples (Fisher and Mullican 1997).

Except for a few samples, most of the samples were undersaturated to these minerals, suggesting that dissolution is yet to reach equilibrium and that solute component concentration is not limited by mineral equilibrium (Fig. 12.8).

12.4.4 Relationship Between PCA and Hydrochemical Characteristics (HCA)

The HCA could help identify similar water samples while PCA classifies similar variables of the samples (Tran et al. 2020; Jiang et al. 2015; Liu et al. 2020; Yang et al. 2020). Therefore, the integration of HCA and PCA can clarify the spatial and temporal processes and main factors affecting the water system and explain pollution sources of each station in the clusters (Razmkhah et al. 2010; Chen et al. 2018; Pervez et al. 2021). Figure 12.9 illustrates the sample scores for the first two factors according to their respective clusters and Stiff diagrams for each cluster based on the median values. This figure shows the water types and processes found in the study area. Clusters C1 and C2 represent low mineral Ca- HCO_3^- type and less polluted water corresponding to a recharge area in the alluvial plain (Figs. 12.3 and 12.5). A negative

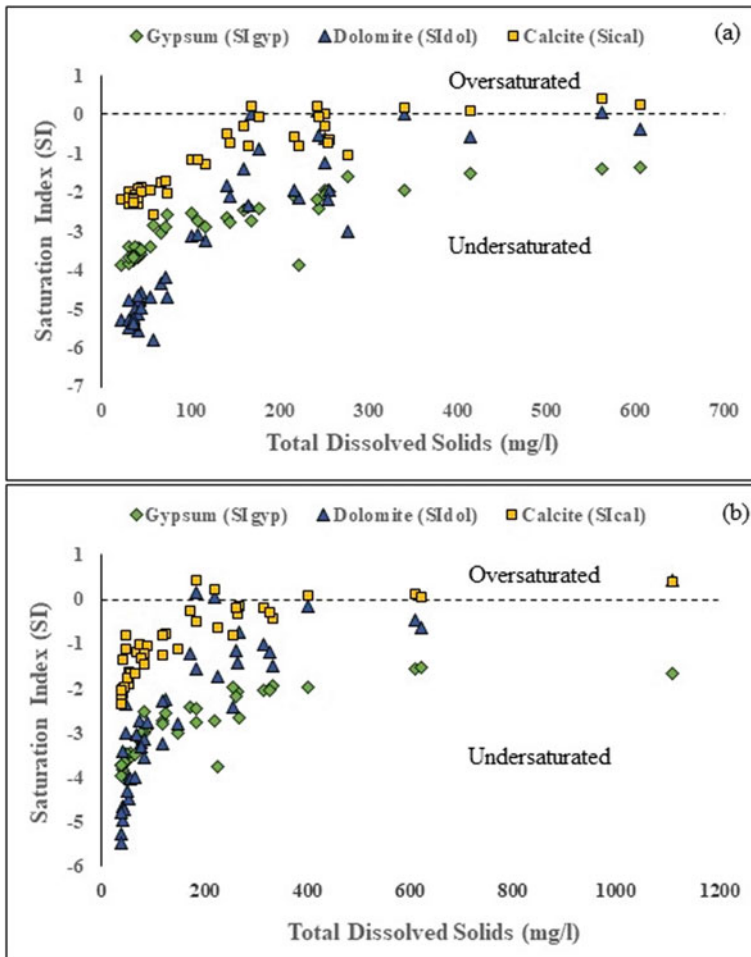


Fig. 12.8 Plot of saturation indices of gypsum, dolomite and calcite against TDS. **a** Summer and **b** winter

high-to-low positive loading of PC2 and a negative loading of PC1 indicates dilution and mixing processes between groundwater and surface water in C1 and C2. In summer, the mixed trend between C1 and C2 samples is caused by several processes functioning in the study area, such as ion exchange, dilution, leaching by runoff, rainfall, and anthropogenic activities. In winter, the number of components decreased, indicating the minor variation in the chemical composition of water samples due to the river freezing and solid-state precipitation, and natural processes more influenced the behavior than the summer season. PC1 indicated mineralized and polluted samples of cluster 3 in summer, and in winter; by PC2 the results from the pollution because C3 samples included two springs, canals, wastewater samples in summer,

and wastewater and Tuul River downstream sites winter. Samples of cluster 4 were more influenced by PC2 (summer) and PC1 (winter), and show regional flow system and mineral weathering, rock-water interactions, and anthropogenic inputs in both seasons. Overall, in the study area, water mineralization is increased from recharge areas with a short resident time to discharge areas with a long resident time, and water chemistry was dominated by the dissolution of mineral weathering processes and influenced by human impacts.

12.5 Conclusions

This study characterized the spatial and temporal geochemical variations in groundwater and surface water interactions in Ulaanbaatar, Mongolia and the main controlling processes, using a multi-tracer approach (hydrochemistry and stable isotope), correlation analysis, and multivariate analysis statistical techniques (HCA and PCA). The main findings of this study are:

- (1) The study identified spatial differences in the water samples analyzed but minimal temporal changes, except in the Tuul River downstream from Ulaanbaatar.
- (2) Ca–HCO₃–type water predominated, and water chemistry in the study area was controlled by rock–water interactions and anthropogenic factors. The downstream sites of Tuul River (TR9, TR10, and TR11) were located below wastewater discharge points and classified as Ca–Na–HCO₃-type water in summer and Na–Ca–HCO₃-type water in winter when sodium became the dominant cation, indicating the effect of wastewater.
- (3) Nitrate was the most significant contributor to conductivity and was highly correlated with major ions (Ca²⁺, Mg²⁺, Na⁺, SO₄²⁻, Cl⁻, HCO₃⁻) indicating pollution inputs, and the correlation decreased in winter (from $r = 0.885$ to 0.575) indicating reduced dilution of runoff processes and infiltrations due to subsurface freezing. Groundwater from a residential area had an especially high level of nitrate due to anthropogenic activities such as pit latrines and septic tank-leach field systems, suggesting that changes in land use and human activities have led to nitrate enrichment.
- (4) The Cluster Analysis indicated a connection between floodplain groundwater and river water and the effect of anthropogenic activities (e.g., canals and wastewater) in addition to infiltration and mineral dissolution.
- (5) Four principal components in summer and three principal components in winter were identified, which explained 86.9 and 83.8% of geochemistry variance. In summer, PC1 represents the pollution and mineral weathering processes and rock-water interactions. PC2 indicates the regional flow system and mineral weathering, PC3 represents the silicate weathering and pollution, and PC4 indicates physical processes. In winter, the number of processes decreased due to the freezing of the river and solid-state precipitation. In winter, PC1 and PC2

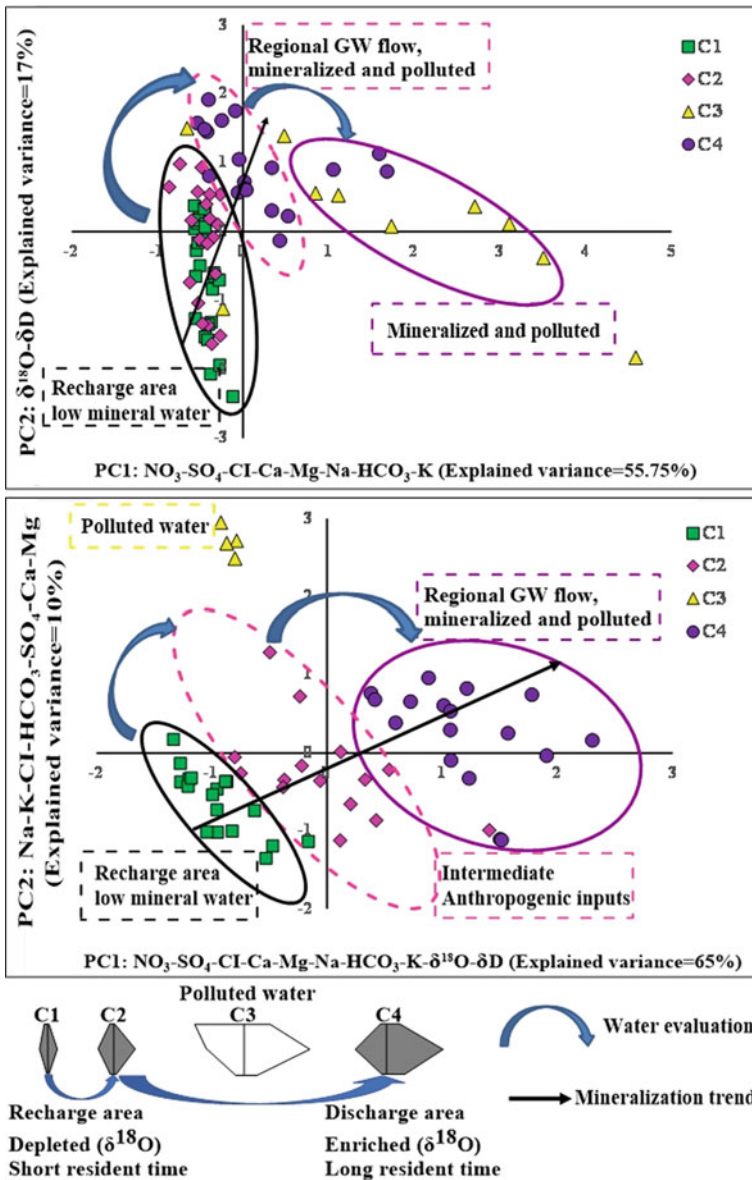


Fig. 12.9 Evaluation of groundwater and surface water hydrochemistry. Plot of the factor scores for PC1 and PC2 with clusters. a Summer, b winter

represent mineral dissolution and anthropogenic inputs, whereas PC3 indicates physical processes. In winter, since the number of components decreased, and the cumulative variance was also lower at 84%.

- (6) The scatter and Gibbs diagrams show that carbonate and silicate weathering and ion exchange are dominant processes controlling the ion content in the study area. Water samples from the area along and near the flood plain were dominated by the carbonate weathering process. Silicate weathering and ion exchange processes governed the water chemistry of samples from the northern mountainside. Some samples have oversaturated calcite values, meaning that these originate from groundwater discharging from an aquifer containing abundant calcite minerals with a long residence time.

This study demonstrates the usefulness of combined approaches in hydrochemistry and data interpretation for understanding spatial/temporal variations in water samples and of pollution sources. The analytical results would also be useful for the design of a future optimal spatial sampling plan. The study offers a reliable method to classify sampling stations in the region, especially along Tuul River.

The study showed the impact of pollution from the ger district on ground and surface waters. Since the area of the ger district, which does not have a sewage system, and continues to grow rapidly, it is recommended that a detailed bacteriological monitoring study be performed to better characterize the distribution of pathogen contaminations and guide new public health policies.

Acknowledgements The authors thank the Japanese Ministry of Education, Culture, Sports, Science, and Technology (MEXT) for providing support under the MEXT Scholarship program. The authors also thank the Geography and Geo-Ecology Institute of the Mongolian Academy of Sciences for their support during the field surveys.

Availability of Data and Materials Available.

Conflict of Interest The authors have no conflicts of interest that are relevant to the content of this article.

References

- Ahamad A et al. (2020) Trace elements contamination in groundwater and associated human health risk in the industrial region of southern Sonbhadra, Uttar Pradesh, India. *Environ Geochem Health*
- Arya S et al (2020) Groundwater vulnerability to pollution in the semi-arid Vattamalaikarai River Basin of south India thorough DRASTIC index evaluation. *Geochemistry* 80(4):125635
- Batdelger O, Julien D (2012) Tuul River Basin, Integrated water resources management assessment report. Water quality and ecology, vol part IV. Ulaanbaatar, Mongolia
- Batsaikhan N et al. (2018) Water resources sustainability of Ulaanbaatar City, Mongolia. *Water* 10(6)
- Batsaikhan B et al. Groundwater contamination assessment in Ulaanbaatar City, Mongolia with combined use of hydrochemical, environmental isotopic, and statistical approaches. *Sci Total Environ* 142790

- Busico G et al (2018) Multivariate statistical analysis to characterize/discriminate between anthropogenic and geogenic trace elements occurrence in the Campania Plain, Southern Italy. *Environ Pollut* 234:260–269
- Buyankhishig N, Aley M, Enkhbayar D (2009) Abstraction influence on alluvial aquifer of the Tuul River, Mongolia in trends and sustainability of groundwater in highly stressed aquifers. IAHS, Hyderabad, India
- Canora F et al (2019) Hydrogeology and hydrogeochemistry of the Lauria Mountains northern sector groundwater resources (Basilicata, Italy). *Geofluids* 2019:7039165
- Cao Z et al (2018) Contamination characteristics of trace metals in dust from different levels of roads of a heavily air-polluted city in north China. *Environ Geochem Health* 40(6):2441–2452
- Cerar S, Mali N (2016) Assessment of presence, origin and seasonal variations of persistent organic pollutants in groundwater by means of passive sampling and multivariate statistical analysis. *J Geochem Explor* 170:78–93
- Chen T et al (2018) Multivariate statistical approaches to identify the major factors governing groundwater quality. *Appl Water Sci* 8(7):215
- Cloutier V et al (2008) Multivariate statistical analysis of geochemical data as indicative of the hydrogeochemical evolution of groundwater in a sedimentary rock aquifer system. *J Hydrol* 353(3):294–313
- Cortes JE et al (2016) Hydrogeochemistry of the formation waters in the San Francisco field, UMV basin, Colombia – A multivariate statistical approach. *J Hydrol* 539:113–124
- Dalai B, Ishiga H (2013) Geochemical evaluation of present-day Tuul River sediments, Ulaanbaatar basin, Mongolia. *Environ Monit Assess* 185(3):2869–2881
- Davis JC (1986) *Statistics and data analysis in geology*. Wiley, New York
- Deutsch WJ (1997) *Groundwater geochemistry: fundamentals and applications to contamination*. CRC, Boca Raton
- Feth JH, Gibbs RJ (1971) Mechanisms controlling world water chemistry: evaporation-crystallization process. *Science* 172(3985):870–872
- Fisher R, Mullican W (1997) Hydrochemical evolution of sodium-sulfate and sodium-chloride groundwater beneath the Northern Chihuahuan Desert, Trans-Pecos, Texas, USA. *Hydrogeol J* 5(2):4–16
- Gao Y et al (2018) Seasonal changes in soil water repellency of different land use types in Inner Mongolia grassland. *Soil Tillage Res* 177:37–44
- Gibbs RJ (1970) Mechanisms controlling world water chemistry. *Science* 170(3962):1088–1090
- Güler C et al (2002) Evaluation of graphical and multivariate statistical methods for classification of water chemistry data. *Hydrogeol J* 10(4):455–474
- Guo H et al (2008) Groundwater geochemistry and its implications for arsenic mobilization in shallow aquifers of the Hetao Basin, Inner Mongolia. *Sci Total Environ* 393(1):131–144
- Handa BK (1988) Content of potassium in groundwater in India. *Fertilizer News* 33(11):15–27
- Hounslow AW (1995) *Water quality data: analysis and interpretation*. CRC Lewis Publ, New York, p 396
- IWMP (2012) *Tuul River Basin Integrated Water Management Plan*. W.v.d.L., Bron J, (ed.) Ministry of Environment and Green Development, Ulaanbaatar, Mongolia, pp 1–259
- Jain CK, Singh S (2019) Best management practices for agricultural nonpoint source pollution: policy interventions and way forward. *World Water Policy* 5(2):207–228
- Jalali M (2009) Geochemistry characterization of groundwater in an agricultural area of Razan, Hamadan, Iran. *Environ Geol* 56(7):1479–1488
- Javzan C et al. (2013) Impact of Ulaanbaatar city's Ger district pollutant sources into groundwater quality. Institute of Geoecology, MAS, Ulaanbaatar
- Jiang Y et al (2015) Principal component analysis and hierarchical cluster analyses of arsenic groundwater geochemistry in the Hetao basin, Inner Mongolia. *Geochemistry* 75(2):197–205
- Kattan Z (2006) Characterization of surface water and groundwater in the Damascus Ghatta basin: hydrochemical and environmental isotopes approaches. *Environ Geol* 51(2):173–201

- Keefe SH et al (2019) Behavior of major and trace elements in a transient surface water/groundwater system following removal of a long-term wastewater treatment facility source. *Sci Total Environ* 668:867–880
- Kourakos G et al. A groundwater nonpoint source pollution modeling framework to evaluate long-term dynamics of pollutant exceedance probabilities in wells and other discharge locations. *Water Resour Res* 48(6)
- Krishnaraj S et al (2011) Use of hydrochemistry and stable isotopes as tools for groundwater evolution and contamination investigations. *Geosciences* 1(1):16–25
- Kumar MRA, Keshari AK (2009) Understanding the extent of interactions between groundwater and surface water through major ion chemistry and multivariate statistical techniques. *Hydrol Process* 23(2):297–310
- Kumar M et al (2006) Identification and evaluation of hydrogeochemical processes in the groundwater environment of Delhi, India. *Environ Geol* 50(7):1025–1039
- Liu C, Lin KH, Kuo YM (2003) Application of factor analysis in the assessment of groundwater quality in a blackfoot disease area in Taiwan. *Sci Total Environ* 313(1):77–89
- Liu S et al (2010) Seasonal and interannual variations in water vapor exchange and surface water balance over a grazed steppe in central Mongolia. *Agric Water Manag* 97(6):857–864
- Liu G et al. (2020) Quantification of water sources in a coastal gold mine through an end-member mixing analysis combining multivariate statistical methods. *Water* 12(2)
- Livingstone DA (1963) Data of geochemistry. In: Professional paper. U.S. geological survey, p G1–G64
- Machiwal D, Jha MK (2015) Identifying sources of groundwater contamination in a hard-rock aquifer system using multivariate statistical analyses and GIS-based geostatistical modeling techniques. *J Hydrol Reg Stud* 4:80–110
- Magaritz M et al (1981) The use of Na/Cl ratios to trace solute sources in a semiarid zone. *Water Resour Res* 17(3):602–608
- Magesh NS et al (2020) Hydrogeochemistry of the deglaciated lacustrine systems in Antarctica: potential impact of marine aerosols and rock-water interactions. *Sci Total Environ* 706:135822
- Marghade D, Malpe DB, Zade AB (2012) Major ion chemistry of shallow groundwater of a fast growing city of Central India. *Environ Monit Assess* 184(4):2405–2418
- Matiatos I (2016) Nitrate source identification in groundwater of multiple land-use areas by combining isotopes and multivariate statistical analysis: a case study of Asopos basin (Central Greece). *Sci Total Environ* 541:802–814
- Matiatos I, Alexopoulos A, Godelitsas A (2014) Multivariate statistical analysis of the hydrogeochemical and isotopic composition of the groundwater resources in northeastern Peloponnesus (Greece). *Sci Total Environ* 476–477:577–590
- Menció A, Folch A, Mas-Pla J (2012) Identifying key parameters to differentiate groundwater flow systems using multifactorial analysis. *J Hydrol* 472–473:301–313
- Naranchimeg B et al (2018) Water resources sustainability of Ulaanbaatar City, Mongolia. *Water* 10(6):750
- Négrel P, Petelet-Giraud E, Barbier J, Gautier E (2003) Surface water–groundwater interactions in an alluvial plain: chemical and isotopic systematics. *J Hydrol* 277(3):248–267
- Nriagu J et al (2012) High levels of uranium in groundwater of Ulaanbaatar, Mongolia. *Sci Total Environ* 414:722–726
- Parkhurst DL, Appello CAJ (1999) User's guide to PHREEQC (ver.2)-A computer program for speciation, batch-reaction, one-dimensional transport, and inverse geochemical calculations. In: U.S. geological survey of water resources investigations report 99-4259, p 310
- Pervez S et al (2021) Sources and health risk assessment of potentially toxic elements in groundwater in the mineral-rich tribal belt of Bastar, Central India. *Groundwater Sustain Dev* 14:100628
- Raiber M et al (2012) Three-dimensional geological modelling and multivariate statistical analysis of water chemistry data to analyse and visualise aquifer structure and groundwater composition in the Wairau Plain, Marlborough District, New Zealand. *J Hydrol* 436–437:13–34

- Razmkhah H, Abrishamchi A, Torkian A (2010) Evaluation of spatial and temporal variation in water quality by pattern recognition techniques: A case study on Jajrood River (Tehran, Iran). *J Environ Manage* 91(4):852–860
- Roy A et al (2020) Geochemical evolution of groundwater in hard-rock aquifers of South India using statistical and modelling techniques. *Hydrol Sci J* 65(6):951–968
- Sakakibara K et al (2017) Spatiotemporal variation of the surface water effect on the groundwater recharge in a low-precipitation region: application of the multi-tracer approach to the Taihang Mountains, North China. *J Hydrol* 545:132–144
- Salifu A et al (2012) Multivariate statistical analysis for fluoride occurrence in groundwater in the Northern region of Ghana. *J Contam Hydrol* 140–141:34–44
- Sami K (1992) Recharge mechanisms and geochemical processes in a semi-arid sedimentary basin, Eastern Cape, South Africa. *J Hydrol* 139(1):27–48
- Selvakumar S, Chandrasekar N, Kumar G (2017) Hydrogeochemical characteristics and groundwater contamination in the rapid urban development areas of Coimbatore, India. *Water Resour Ind* 17:26–33
- Singh CK et al (2017) Multivariate statistical analysis and geochemical modeling for geochemical assessment of groundwater of Delhi, India. *J Geochem Explor* 175:59–71
- Stefania GA et al (2019) Identification of groundwater pollution sources in a landfill site using artificial sweeteners, multivariate analysis and transport modeling. *Waste Manage* 95:116–128
- Taylor RG et al (2013) Ground water and climate change. *Nat Clim Chang* 3(4):322–329
- Tiwari AK, Singh AK (2014) Hydrogeochemical investigation and groundwater quality assessment of Pratapgarh District, Uttar Pradesh. *J Geol Soc India* 83:329–343
- Tran DA et al (2020) Hydrogeochemical characteristics of a multi-layered coastal aquifer system in the Mekong Delta, Vietnam. *Environ Geochem Health* 42(2):661–680
- Trásy B et al (2018) Assessment of the interaction between surface- and groundwater after the diversion of the inner delta of the River Danube (Hungary) using multivariate statistics. *Anthropocene* 22:51–65
- Tsujimura M et al (2007) Stable isotopic and geochemical characteristics of groundwater in Kherlen River basin, a semi-arid region in eastern Mongolia. *J Hydrol* 333(1):47–57
- Tsujimura M et al (2013) Groundwater and surface water interactions in an alluvial plain, Tuul River Basin, Ulaanbaatar, Mongolia. *Sci Cold Arid Reg* 5:126–132
- Venugopal T et al (2009) Environmental impact assessment and seasonal variation study of the groundwater in the vicinity of River Adyar, Chennai, India. *Environ Monit Assess* 149:81–97
- Verhoeven D et al (2018) Water availability as driver of birch mortality in Hustai National Park, Mongolia. *Dendrochronologia* 49:127–133
- Voutsis N et al (2015) Assessing the hydrogeochemistry of groundwaters in ophiolite areas of Euboea Island, Greece, using multivariate statistical methods. *J Geochem Explor* 159:79–92
- Wang P et al (2013) Groundwater recharge and hydrogeochemical evolution in the Ejina Basin, northwest China. *J Hydrol* 476:72–86
- Wang Z-P et al (2018) Dissolved methane in groundwater of domestic wells and its potential emissions in arid and semi-arid regions of Inner Mongolia, China. *Sci Total Environ* 626:1193–1199
- Winter T et al. (1998) Ground water and surface water: a single resource. In: U.S. geological survey circular 1139, USA, p 79
- Woocay A, Walton J (2008) Multivariate analyses of water chemistry: surface and ground water interactions. *Groundwater* 46(3):437–449
- Yang J et al (2020) Using cluster analysis for understanding spatial and temporal patterns and controlling factors of groundwater geochemistry in a regional aquifer. *J Hydrol* 583:124594
- Yang J et al. (2020) Characteristics of non-point source pollution under different land use types. *Sustainability* 12(5)
- Yidana SM et al (2018) Evolutionary analysis of groundwater flow: application of multivariate statistical analysis to hydrochemical data in the Densu Basin, Ghana. *J Afr Earth Sci* 138:167–176

- Zhang G et al (2007) Evolution study of a regional groundwater system using hydrochemistry and stable isotopes in Songnen Plain, northeast China. *Hydrol Process* 21(8):1055–1065
- Zhang H et al (2020) Identification of hydrogeochemical processes and transport paths of a multi-aquifer system in closed mining regions. *J Hydrol* 589:125344
- Zhou F, Liu Y, Guo H (2007) Application of multivariate statistical methods to water quality assessment of the watercourses in northwestern new territories, Hong Kong. *Environ Monit Assess* 132(1):1–13

Chapter 13

Application of Plant Endophytic Microorganisms (*Endophytes*) in the Treatment of Heavy Metal Pollution in Soils



Kieu Bang Tam Nguyen and Thi Hong Thao Phan

Abstract Heavy metal contaminated soils may pose risk and hazards to humans and the ecosystem. Physiochemical approaches have been widely used for remedying polluted soil; however, their large-scale application is difficult due to high cost and side effects. Current research interests are moving towards the application of in situ strategies to reduce costs and to resolve pollution dispersal problems. Phytoremediation is a plant-based, environment-friendly, and cost-effective technology that can potentially be used to remediate contaminated media. However, phytoremediation is with some critical shortcomings, such as phytotoxicity, slower than mechanical method and limited mechanical uptake. Some plant-associated bacteria can overcome these constraints by assisting plants to accumulate higher amount of metal without increasing phytotoxicity. While rhizosphere microorganisms can enhance phytoremediation according to numerous studies, endophytes appear to do so more efficiently by interacting closely with host plants. Endophytes are all microorganisms that inhabit the interior of plant tissues, causing no harm to the host and developing no external structures. In the plant endophyte symbiosis, endophytes receive carbohydrates from plants and improve plant resistant to biotic and abiotic stresses in return. Moreover, recent studies showed that many endophytes are metal resistant, able to degrade organic contaminants and have been successfully used in phytoremediation. This paper focuses on the overview of studies on the ability of endophytes to support plant absorption of heavy metals as an object with potential in environmentally friendly and inexpensive bioremediation.

Keywords Heavy metal · Phytoremediation · Endophytes

K. B. T. Nguyen (✉)

Faculty of Environmental Sciences, University of Science, Vietnam National University, Hanoi, 334 Nguyen Trai, Thanh Xuan, Hanoi 100000, Vietnam

e-mail: tamnkb@hus.edu.vn

T. H. T. Phan

Institute of Biotechnology, Vietnam Academy of Science and Technology, 18 Hoang Quoc Viet Road, Cau Giay, Hanoi 100000, Vietnam

e-mail: pthongthao@ibt.ac.vn

13.1 Introduction

Heavy metals are distinguished by their high relative atomic weight ($> 4 \text{ g/cm}^3$). Some of them, such as zinc (Zn), iron (Fe), or manganese (Mn), are microelements that plants require and absorb through their roots since they are essential to plant survival. These metals, however, can be harmful in excessive doses. Other elements, such as lead (Pb), cobalt (Co), and arsenic (As), have no biological role and are harmful even at low doses; they are categorized as Toxic Heavy Metals (THM) (Rahman and Singh 2019).

Heavy metal pollution is the excessive deposition of hazardous heavy metals in soil as a result of human activity. Lead (Pb), cadmium (Cd), zinc (Zn), mercury (Hg), arsenic (As), silver (Ag), chromium (Cr), copper (Cu), iron (Fe), and platinum group elements are among the heavy metals found in soil. With the expansion of the global economy recently, both the type and concentration of heavy metals in the soil from anthropogenic sources (mining, electroplating and welding, urbanization) (Mishra and Bharagava 2016; Wang and Chen 2009) and the use of metal-based fertilizers and pesticides have gradually increased, resulting in environmental degradation. Heavy metals are extremely dangerous to both the environment and organisms. It can be enhanced via the food chain and finally integrated into living creatures (Sim et al. 2019). Once the soil has been contaminated with heavy metals, it is difficult to be remediated (Bayata 2020).

The main purpose of heavy metal removal is to minimize their negative effects on ecosystems and human health. Numerous remediation techniques for heavy metal contaminated soils have been introduced to cope with this problematic issue, which can be divided into three main groups: physical, chemical and biological. Physical and chemical technologies are often expensive and time-consuming besides the negative environmental impacts due to generating a large quantity of hazardous waste (Sim et al. 2019). On the contrary, phytoremediation is attracting great interest because of its outstanding advantages of being a green technology, environmentally friendly and more economical than traditional methods. Phytoremediation of heavy metal contaminated soil is more effective due to the interaction between plants and plant-associated microorganisms. While rhizobacteria increase plant metal uptake and translocation through various processes, endophytes live inside plant tissues and form a mutualistic relationship with host plant (Sim et al. 2019).

Endophytes support the survivability of their host plants in unfavorable environments, especially in heavily polluted soils. Endophytes residing in such harsh environments are hypothesized to have adapted and evolved to acquire increased tolerance toward the adverse conditions.

In addition to heavy metal tolerance, plant-associated microbes can operate as biocontrol agents against a variety of pathogens and herbivores (Sim et al. 2019), ensure nitrogen fixation and growth regulator production, and contribute to heavy metal tolerance and treatment in plants. The nature of endophytes, their potential in heavy metal removal, and their function in heavy metal uptake by plants utilized in bioremediation will be examined in this paper.

13.2 Endophyte Characteristics

Endophytes were first defined as microorganisms that reside inside plant tissues by Barry in 1866. Then, in 1904, endophytic bacteria were identified in Darnel, Germany. Smith et al. developed the concept of endophytic actinomycetes in 1975 when they isolated *Micromonospora* sp. and discovered that it had a considerable inhibitory impact on the pathogenic fungus *Fusarium oxysporum* in uninfected tomato plant tissues (Shimizu 2011; Zhenhua et al. 2012). Endophytes are non-pathogenic microorganisms that reside inside plants, according to Carroll et al. (Araújo et al. 2008).

Endophytes are microorganisms that invade interior plant tissues without inflicting obvious harm to their hosts (Stepniewska and Kuźniar 2013). Endophytes, according to Wilson and Carroll, are bacteria and fungi that penetrate the tissues of live plants for all or part of their life cycle without causing damage or disease symptoms to the host plant. The most frequently recognized definition is that of Bacon and White, who agree with the aforementioned writers that “endophytes are microorganisms that live inside live tissues of plants and exert no obvious and direct harmful impact on host plants” (Bacon et al. 2000). This definition has a very important implication: because of its asymptomatic nature, the colonization of plant tissues by endophytes suggests a mutualistic relationship between endophytes and host plants.

Endophytes in plants are classified as either obligatory or facultative. The former require particular environmental conditions in the laboratory for successful culture (Waheeda and Shyam 2017). According to some authors, facultative endophytic bacteria may be isolated from surface sterilized plant parts or from plant internal tissues and are not harmful to the host plant. The preceding definitions do not take into account bacteria that are unculturable under laboratory circumstances and have just recently been detected using molecular techniques. As a result, endophytic bacteria might be culturable or unculturable (Araújo et al. 2008).

Each of the 300,000 higher plant species on Earth is a host plant for one or more endophytes, implying that Earth may have a huge endophytic community (Strobel et al. 2004). Endophytes are abundant, yet diverse, in the environment (soil, cultivated areas) (Seghers et al. 2004; Conrath et al. 2006; Hardoim et al. 2008; Singh et al. 2009). Their numbers vary depending on the plant and environmental factors. According to Xu et al., the number of endophytes and their species richness are greater in tropical and subtropical plants than in cold and dry locations, more in fast-growing and perennial plants than in slow-growing and short-term plants, and greater in healthy plants than in polluted plants (Zhenhua et al. 2012).

Endophytic microorganisms are not only asymptomatic, but they can also promote plant growth by producing growth-promoting substances and plant protection agents (Kandpal et al. 2012; Machavariani et al. 2014), protect host plants from biotic or abiotic stresses, and produce a diverse range of bioactive compounds (Waqas et al. 2012). Endophytes, in turn, obtain adequate nutrients from host plants for growth

and survival (Sim et al. 2019). As a result, endophytic microbes are regarded as excellent genetic resources for the development of highly efficient, non-toxic, and environmentally friendly natural products for use in medicine, agriculture, industry, and environmental remediation.

13.3 Mechanisms Employed by Microorganisms to Gain Entry into the Host Plant and Become Endophytes

Endophytic bacteria are thought to originate from the rhizosphere when they have the chance to interact with the host plant (Ali et al. 2014a, b). Thus, endophytes use many mechanisms to gain entry into the host plant, particularly in roots (Santoyo et al. 2016). Typically, this process begins with their concentration in the rhizosphere. They begin to attach to the root surface after successfully colonizing the rhizosphere. This is a critical step in the penetration process. Microorganisms, according to some authors, can adhere to the root surface due to cell surface components such as pili, lipopolysaccharide, or exopolysaccharide etc. Binding sites are usually root tips, where there is a thin cell wall of root apex, or root hairs, or cracks at root emergence sites (Sørensen and Sessitsch 2006), except when endophytes were inoculated on the seeds from the beginning (Truyens et al. 2015).

Microorganisms form microcolonies of hundreds of cells at these sites. Endophytic bacteria have a cellulolytic enzyme system that can hydrolyze the exodermal cell wall, allowing for active penetration. Bacterial cell-wall degrading enzymes are also known to be involved in the elicitation of plant defense pathways, since many proteins involved in defense and repair are biosynthesized to prevent pathogen spread within the plant and are associated with plant cell walls. Endophytic microbes must be able to dodge or dramatically diminish the plant's immune response, which they can achieve by entering from cracks at root emergence sites. This is the case that has been proposed for *Azoacus* and *Burkholderia vietnamiensis* (Malfanova et al. 2013).

Endophytes that pass the exodermal barrier can either remain at the site of entry or move deeper within to colonize the cortex's intercellular space (apoplast). Endophytic microorganisms differ from legume root-nodule bacteria in that they do not generally enter plant cells and cause formation of specific morphological structures. Endophytic microorganisms, on the other hand, can trigger nodule development in some circumstances.

Only a few microbes are able to get through the endodermal barrier and invade the plant's xylem vessels. They may feed on nutrients delivered by the xylem, such as water, ions, and low molecular weight organic compounds including sugars, amino acids, and organic acids. Although the concentration of these nutrients in the xylem is relatively low, it is adequate to support endophyte development. Endophytic microbes may metabolize carbon sources that rhizobacteria do not ordinarily use, such as D-sorbitol, D-galacturonic acid, and L-arabinose, which is one of the most readily

accessible sugars in plant xylem fluid. Thus, the capacity to utilize certain plant metabolites may be required for successful endophytic colonization (Malfanova et al. 2013).

Normally, the concentration of accessible nutrients in the xylem declines along the plant axis. This explains why endophyte variety and population density diminish with distance from the base, and why only few numbers of them reach the plant's upper parts, such as leaves and reproductive organs like flowers, fruits, and seeds. Some microorganisms can enter plants via different pathways, such as stomata on leaves, and become endophytic. They can also invade plants through flowers, fruits, and seeds, but this is more common with pathogens (Malfanova et al. 2013).

Endophytic microbes may have genetic differences from rhizosphere microorganisms in order to colonize interior plant tissues, however no specific group of genes responsible for the endophytic lifestyle has been identified so far (Santoyo et al. 2016). Many authors have recently conducted research on endophytic microbes on various host plants using 16S rDNA sequences to determine their relationships (Glick 2015; Romero et al. 2014; Shi et al. 2014). Ali et al. discovered an array of genes that may play a role in endophytic lifestyle by comparing the genomes of 9 endophytic Proteobacteria species, some of which have been experimentally confirmed to be involved in the colonization of internal plant tissues (Ali et al. 2012).

13.4 The Role of Endophytes in Host Plants

13.4.1 *Production of Plant Growth Promoting Substance*

Endophytic bacteria acquire nutrients from the host plant for survival in a mutualistic relationship (Shimizu 2011), and endophytes can be advantageous to plant development directly (by increasing growth) or indirectly (by inhibiting growth) through disease control. Endophytic microorganisms directly promote growth through supplying nutrients such as dissolved Fe or Mo in the soil (Tokala et al. 2002), nitrogen fixation (Shimizu 2011; Kandpal et al. 2012), either biosynthesis or regulation of growth-promoting substances (also known as growth hormones-phytohormones), especially indole-3-acetic acid (IAA) (Malfanova et al. 2013).

IAA's physiological effects on plants include cell proliferation stimulation, induction of plant chemotaxis (photodynamic), inhibition of lateral shoot development to maintain apical dominance, promotion of fruit growth and seedless fruit production, and inhibition of leaf, flower, and fruit shedding. According to Mohamed Et-Otmani et al., IAA increased the percentage of seed germination and the plant's survival rate in following stages in citrus. IAA and naphthalene acetic acid (NAA) are efficient rooting aids when propagating citrus through cuttings. Bud-grafting success rates are increased by IAA and indolebutyric acid (IBA). To maintain grafted plants in vitro and promote lateral root initiation, 6-benzyladenine (BA) and IAA were added to the basal media (E1-Otmani et al. 2000).

Brick et al. identified and characterized the production of IAA by two types of bacteria, *Pseudomonas* and *Bacillus*, in 1991, and have since expanded their research by studying other strains (Bric et al. 1991). According to some authors, similar to other microorganisms, the production of plant hormones such as IAA in endophytic actinomycetes is one of the mechanisms to promote host plant growth and increase leaf and root dry weight and root length and are considered biological agents in agriculture (Ghodhbane-Gtari et al. 2010; Shutsrirung et al. 2013). Research has found that microorganisms synthesizes IAA from tryptophan (Trp) by deamination, decarboxylation and oxidation and the concentration of IAA biosynthesized by them is dependent on the amount of Trp in the culture medium (Yadav et al. 2010).

Research by P.T.H. Thao et al. showed that, out of 47 endophytic actinomycetes isolated from citrus, 42 strains (88%) were capable of biosynthesizing IAA, two of which (accounting for 4%) produced over 20 $\mu\text{g/ml}$ IAA (Phan et al. 2016).

Endophytic microorganisms, like rhizosphere microorganisms, produce plant growth promoting substances but also have many more complex mechanisms to stimulate plant growth due to their close relationship. Endophytic actinomycetes improve root growth and development by absorbing nutrients, resulting in a larger root surface area and an increase in the number of lateral roots, and therefore increased nutrient uptake for the host plant. *Streptomyces* strains found in the roots have been proven to produce iron-sequestering siderophores and to solubilize inorganic and organic phosphates in order to promote plant health (Shimizu 2011).

Many endophytic microbial strains may produce IAA while also lowering ethylene concentration in plants via the (1-aminocyclopropane-1-carboxylate)-deaminase enzyme (Jaemsaeng et al. 2018; Tiwari et al. 2018). This is significant because high ethylene concentrations can hinder root growth in stressed plants. In addition to producing IAA, several endophytic actinobacterial strains isolated from *Aloe vera*, *Mentha arvensis*, and *Ocimum sanctum* have been shown to solubilize phosphate and produce hydroxamate and catechol (Gangwar et al. 2014) (Fig. 13.1).

Some endophytic bacteria have the ability to promote plant growth through increased availability of mineral elements or tolerance to heavy metals under living conditions. Therefore, when residing in plant tissue, endophytic microorganisms give plants many favorable conditions to help plants grow well (Malfanova et al. 2013).

The relationship between endophytic microorganisms, host plants and the production of bioactive natural products creates an opportunity to find specific preparations with potential applications in plant growth stimulation, fungal diseases control and increasing plant tolerance to adverse environmental conditions.

13.4.2 Disease Control

The primary mechanism of endophytic bacteria in plant disease control is resistance (antibiosis)-the synthesis of antibiotic compounds (Janso and Carter 2010; Kumar and SivaKumar 2011; Taechowisan et al. 2014) and fungal cell wall degrading

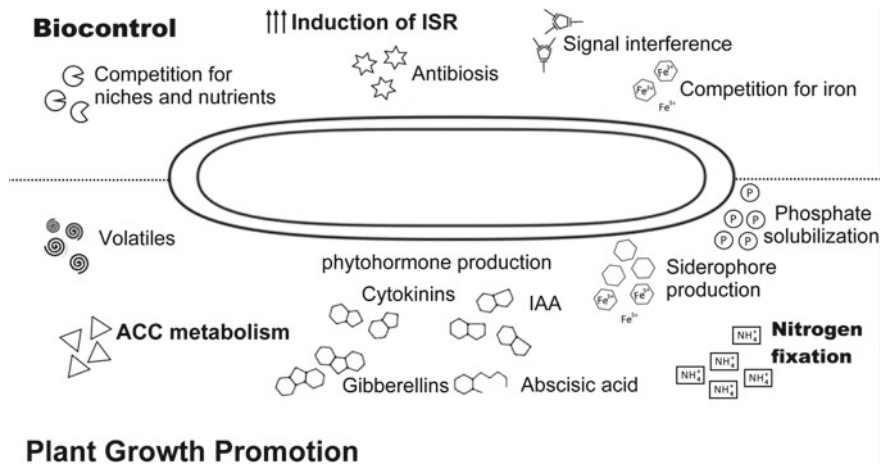


Fig. 13.1 The role of endophytes in host plants (Malfanova 2013)

enzymes (Shimizu 2011), competing for nutrients and habitat, and enhancing host plants' systemic tolerance (Malfanova et al. 2013).

Endophytic microbes colonizing host plants can cause a variety of cell wall modifications, including the buildup of callose, pectin, cellulose, and phenolic compounds, resulting in the creation of a structural barrier at the site of pathogen infection (Mengistu 2020). Furthermore, when attacked by pathogens, plants colonized by endophytic microbes generally have increased biosynthesis of defense proteins such as peroxidase, chitinase, and α -1,3-glucanase, which inhibit pathogen spread. Furthermore, because various antipathogenic compounds may activate the host plant's immune response and even the immune system, many endophytic microbial species frequently adopt a combination of resistance strategies (Shimizu 2011; Priya 2012; Ongena et al. 2007).

Many endophytic actinomycetes have been proved to protect host plants from soil-borne pathogens such as *Aspergillus niger*, *A. flavus*, *Alternaria brassicicola*, *Botrytis cinerea*, *Penicillium digitatum*, *Fusarium oxysporum*, *P. pinophilum*, *Phytophthora dreschlea* and *Colletotrichum fulcatum* (Gangwar et al. 2011). According to Conn et al., seed inoculation of *Streptomyces* sp. EN27 and *Micromonospora* sp. EN43 increased *Arabidopsis thaliana* resistance to bacterial soft rot (caused by *Erwinia carotovora*) and root rot (caused by *F. oxysporum*); activated SA- or jasmonic acid/ethylene synthesis gene expression (Conn et al. 2008). They synthesize secondary metabolites that inhibit some pathogenic fungi such as *A. porri*, *C. musae*, *C. gloeosporioides*, *Curvularia* sp., *Drechslera* sp., *Exserohilum* sp., *F. oxysporum*, *Verticillium* sp. and *Sclerotium rolfsii* (Taechowisan et al. 2013), *A. brassicicola* (Phuakjaiphaeo et al. 2016).

Fungal stem end rot disease of pitaya caused by *Alternaria alternata* is one of the most destructive diseases in Binh Thuan province, Vietnam. The study by Luu

The Anh et al. aimed to assess the antagonistic effects of some endophytic bacteria isolated from the weed plant (*Echinochloa colonum*) against *A. alternata* (Luu et al. 2021).

Pitaya confronts several obstacles in Vietnamese agriculture, including stem end rot disease caused by *A. alternata*. Nineteen endophytic bacteria were isolated from the weed (*E. colonum*). Five of them might suppress the mycelial development of *A. alternata* in distinct ways. Strain EC80 exhibited the strongest inhibition, while a weak inhibition was observed by EC79, EC83, EC90, and EC97. The results also showed that combining EC79 and EC80 significantly improved the reduction of biomass pathogenic fungi. The EC79 and EC80 enhanced seedling biomass in greenhouse studies. As a result, these bacteria have the potential to be highly valuable for agronomic applications and should be investigated further in the near future (Luu et al. 2021).

Streptomyces TQR12-4, isolated from the Ham Yen orange fruits of North-east Vietnam, had high antibacterial activity against 2g-positive bacteria, and 4 phytopathogenic fungi. This strain's crude antibacterial component was rather stable throughout a wide range of pH (3–9) and temperatures (40–100 °C). Separation on silica gel gave five fractions, two of which (X4 and X5) inhibited the growth of fungi at MIC (minimum inhibitory concentration) of 100 and 400 µg/mL, respectively (Hong-Thao et al. 2016).

In the research of Gangwar et al., three medicinal plants, *Aloe vera*, *Mentha arvensis* and *Ocimum sanctum* were explored for endophytic actinomycetes diversity, plant growth promoting and antimicrobial activity (Gangwar et al. 2014). Endophytic actinomycetes were most commonly recovered from roots (70% of all isolates) followed by stems (17.5%) and leaves (12.5%), respectively. *Streptomyces* was the most common genus (60% of all isolates) followed by *Micromonospora* (25%), *Actinopolyspora* (7.5%), and *Saccharopolyspora* (7.5%). The highest numbers of endophytic actinomycetes were isolated from *Ocimum sanctum* (45%). 12 of the 22 isolates tested were able to solubilize phosphate at concentrations ranging from 5.4 to 16.5 mg/100 ml, whereas 16 isolates generated indole-3 acetic acid (IAA) at concentrations ranging from 8.3 to 38.8 g/ml. Nine isolates produced the amount of hydroxamate-type of siderophore ranging between 5.9 and 64.9 µg/ml and only four isolates were able to produce catechol-type of siderophore in the range of 11.2–23.1 µg/ml. Of the nine, interestingly, eight endophytic actinomycetes (88.9%) showed a significant antagonistic activity against one or more phytopathogenic fungi indicating their potential role as plant biocontrol agents.

The roles of endophytes in host plants could be summarized as in Table 13.1:

13.5 Endophytes in Heavy Metal Bioremediation

Endophytes have recently been discovered to have an important role in pollution removal (Gai et al. 2009; Ho et al. 2012; Kim et al. 2012). Endophytes' bioremediation potential was inspired by the use of plants in phytoremediation.

Table 13.1 Plant growth-promoting traits

Plant growth-promoting traits	References
Supplying nutrients such as dissolved Fe or Mo in the soil	Tokala et al. (2002)
Nitrogen fixation	Shimizu (2011), Kandpal et al. (2012)
Biosynthesis or regulation of growth-promoting substances, especially indole-3-acetic acid (IAA)	Malfanova et al. (2013), Bric et al. (1991), Ghodhbane-Gtari et al. (2010), Shutsrirung et al. (2013), Phan et al. (2016)
Produce iron-sequestering siderophores	Shimizu (2011)
Solubilize inorganic and organic phosphates	Shimizu (2011), Gangwar et al. (2014)
Lower ethylene concentration in plants via (1-aminocyclopropane-1-carboxylate)-deaminase	Jaemsaeng et al. (2018), Tiwari et al. (2018)
Produce hydroxamate and catechol	Gangwar et al. (2014)
Disease control	References
Synthesize antibiotic compounds	Janso and Carter (2010), Kumar and SivaKumar (2011), Taechowisan et al. (2014)
Synthesize fungal cell wall degrading enzymes	Shimizu (2011)
Compete for nutrients and habitat with phytopathogens	Malfanova et al. (2013)
Enhance host plants' systemic tolerance	Malfanova et al. (2013)
Cause a variety of cell wall modifications, including the build-up of callose, pectin, cellulose, and phenolic compounds, resulting in the creation of a structural barrier at the site of pathogen infection	Mengistu (2020)

Phytoremediation is a type of biological treatment that uses plants to remove or degrade pollutants. It can be used to clean up soil, sediment, mud as well as surface and groundwater. To absorb nutrients for development, plants employ a variety of absorptive capacities, transport mechanisms, and metabolic reactions. As a result, phytoremediation entails growing plants in polluted environment for the duration of the growing period. The plant roots absorb pollutants from the soil and retain them in the rhizosphere, rendering them harmless by preventing leaching (Gupta et al. 2016).

The term “hyperaccumulator” refers to a group of plants that are distantly related but share the ability to grow on metalliferous soils and accumulate extraordinarily high levels of heavy metals in the aerial organs, far exceeding the levels found in the majority of species, without suffering phytotoxic effects. Hyperaccumulators are distinguished from comparable non-hyperaccumulating taxa by three basic characteristics: a significantly increased rate of heavy metal absorption, a quicker root-to-shoot translocation, and a greater ability to detoxify and sequester heavy metals in leaves. So far, around 450 angiosperm species have been discovered as heavy metal (As, Cd, Co, Cu, Mn, Ni, Pb, Sb, Se, Tl, Zn) hyperaccumulators, accounting for fewer than 0.2% of all known species. However, new reports of this type of plant

continue to emerge, suggesting that numerous unidentified hyperaccumulators may exist in nature (Rascio and Navari-Izzo 2011).

Endophytes are naturally found in plants, and it has been proposed that endophytes in these plants have inherent tolerance and adaptability to contaminants (Fabiana et al. 2020). This “habitat-adapted symbiosis” is thought to provide adaptation and improved tolerance to contaminants on endophytes (Sim et al. 2019). Through overexpression of glutamylcysteine synthetase-glutathione synthetase derived from *Streptococcus thermophiles*, three transgenic lines of sugar beet (*Beta vulgaris* L.) with increased tolerance to different concentrations of cadmium, zinc, and copper were discovered (Chaudhary et al. 2016).

Thus, the development of plants and endophytic microorganisms carrying heavy metal assimilation or absorption genes can be a way to enhance heavy metal tolerance and absorption of hyperaccumulators.

Phytoremediation is seen as a potential strategy for the remediation of heavy metal polluted soils, and the harvested heavy metal-enriched hyperaccumulator biomass should be disposed of properly. Various thermal treatments of hyperaccumulators have recently gotten a lot of interest. Following thermal treatment, the hyperaccumulator was processed to bio-oil, biogas, charcoal, or ash according to the circumstances, and the heavy metals were separated, immobilized, or trapped. Metal ion migration and transformation during thermochemical conversion processes are crucial for the safe disposal and subsequent use of metal ion hyperaccumulators (Cui et al. 2021).

The use of endophytic microorganisms for heavy metals removal has been discovered from a variety plant species. They include cultivated plants such as *Brassica napus* (rapeseed), *Nicotiana tabacum* (cultivated tobacco), *Solanum nigrum* (black nightshade), ornamentals (*Rosa longicuspis*, *Commelina communis*), shrubs (*Acacia decurrens*), and hyperaccumulators (*Phragmites* sp.) (Sheng et al. 2008; Mastretta et al. 2009; Luo et al. 2011; Sim et al. 2016).

Endophytes isolated from these plants are similarly varied, including bacteria (*Pseudomonas fluorescens*, *Stenotrophomonas* sp., *Clostridium aminovalericum*, *Microbacterium* sp., *Flavobacterium* sp., *Bacillus* sp., *Acinetobacter* sp...), actinomycetes and fungi (*Trichoderma asperellum*, *Phomopsis* sp., *Saccharicola bicolor*, *Phoma* sp., *Aspergillus* sp., *Mucor* sp.) (Sim et al. 2019, 2016). Endophytic organisms from both hyperaccumulators and non-hyperaccumulators have been proven in studies to have metal removal capacity.

Various studies have isolated and reported various species of strict aerobic As(III) and anaerobic As(V) detoxin-reducing bacteria from As contaminated sites (Suhadolnik et al. 2017). Bacteria such as *Thermus thermophiles*, *Thermus aquaticus*, *P. arsenitoxidans*, *Crysiogenes arsenates*, *Bacillus arsenic oselenatis*, *Desulfotomaculum auripigmentu*, *Geospirillum barnesi* and *Geospirillum arsenophilus* have the ability to synthesize arsenite oxidase and oxidize As(III) (Pongratz and Heumann 1999). Microorganisms can also decrease As(V) to As(III) via solubilization. Endophytes utilize As(V) as a final electron acceptor for anaerobic respiration in this process. Bacteria that can reduce As(V) include: *Bacillus arsenic*, *Geospirillum arsenophilus*, *Geospirillum barnesi*, *Crysiogenes arsenatis*, *Sulfurospirillum*

barnesii, *Sulfurospirillum arsenophilum*, *Oselenatis* and *Desulfutomaculum auripigmentu* (Vaxevanidou et al. 2012).

Thus, it can be seen that endophytes which belong to groups of fungi, bacteria or actinomycetes are very diverse, present in both cultivated and wild plants, and can be either aerobic or anaerobic... In other words, these are potential objects which are readily available and easy to find in nature, so that they can be applied in combination with plants to clean up soil contaminated with heavy metal.

Endophytes remove heavy metals by two mechanisms: biosorption or bioaccumulation. Biosorption is a chemical and physical interaction that occurs between adsorbents (biosorbents) and pollutants (metal). Metal cations efficiently bind to functional groups of cell walls and membranes to promote efficient biosorption (Khalil et al. 2016). Some microbial strains have been reported to have potential for application in heavy metal absorption. For example, *Trichoderma asperellum* (removes 18 mg/g Zn²⁺, 17.26 mg/g Cu²⁺, 19.24 mg/g Pb²⁺, 19.78 mg/g Cd²⁺, and 16.75 mg/g Cr³⁺ (Sim et al. 2016), *Microsphaeropsis* sp. LSE10 adsorbed a maximum of 247.5 mg/g Cd²⁺ (Chen et al. 2010); and *P. lilacinum* removed Cu²⁺ and Cd²⁺ at 85.4% and 31.43% (El-Gendy et al. 2011).

Bioaccumulation (accumulation) is a process in which metal cations are transported through cell membranes. This is an energy-dependent process that occurs via precipitation, covalent bonding, redox reactions, and crystallization (Wilde and Benemann 1993; Malekzadeh et al. 2002). Metal cations are transported across the cell membrane and further compartmentalized or detoxified during bioaccumulation. Because surviving cells require a period of adaptation to metal stress, bioaccumulation in living cells is substantially slower than biosorption. The amount of metal removed by the former, however, was more than that of the latter (Sim et al. 2016). Deng et al. isolated the endophytic fungal strain *Lasiodiplodia* sp. MXSF31 from the hyperaccumulator *Portulaca olercea* capable of efficiently bioaccumulating Pb²⁺ up to 5.6 × 10⁵ mg kg⁻¹, Cd²⁺ (4.6 × 10⁴ mg kg⁻¹) and Zn²⁺ (7.0 × 10⁴ mg kg⁻¹) (Deng et al. 2014).

The functional groups in the cell walls are primarily responsible for metal removal by endophytes. The peptidoglycan of bacterial endophytes' cell wall is rich in N-acetylglucosamine (NAG) and N-acetylmuramic acid (NAM), which assist in metal binding (Das et al. 2008). Furthermore, metal binding is supported by capsules or slime layers created by certain bacteria, since several functional groups such as sulfate and phosphate are present to chelate and bind metals (Sim et al. 2019). Metal complexation has also been found in fungal endophytes (Dursun et al. 2003).

Endophytes' metal removal efficiency may be increased by providing optimal growth circumstances such as pH, temperature, and metal concentration. The most significant of them is pH, which influences precipitation, the existence of functional groups, and the competition between metal cations and hydroxyl groups (Bayramoglu et al. 2002). The optimal pH for metal removal is between 4 and 8. Because there are more hydrogen ions in acidic environments, hydrogen and metal cations are more competitive in low pH conditions. As a consequence, hydrogen ions attach to functional groups and repel metal ions, resulting in decreased metal bioabsorption. Other factors, such as starting metal concentration, adsorbent dose, and temperature,

are also essential, although their importance is dependent on the kind of endophytic microbes and heavy metals (Sim et al. 2019).

The aforementioned experimental studies have clearly shown the mechanism, conditions and efficiency of removing heavy metals by endophytes, based on which we can grasp a deeper understanding of their optimal conditions for heavy metal remediation as well as opt for those suitable to the characteristics of each type of polluted environment for more efficient bioremediation.

Endophytic plant microorganisms' biological features are also known to influence bioavailability and bio-characteristics that help or facilitate the metabolism of various kinds of inorganic and organic metals by the host plant environment in soil-plant systems (Ahmad et al. 2016; Pantsar-Kallio and Jørgensen 2002). In fact, not only soil microorganisms but endophytic microorganisms are involved in many important biochemical-biological processes that govern the behavior and fate of a metal in the soil-plant system objects (Abbas et al. 2018).

Ma et al. isolated a consortium of endophytes from a grass species growing in lead-contaminated soil at an abandoned mine site in Ballycorus, Co. Dublin, Ireland, and used it in a laboratory experiment with a plant to confirm their role in supporting and stimulating plant growth in heavy metal-contaminated soil (Ma et al. 2016). Overall, plants treated with endophytes germinated and tillered faster and produced more foliar biomass than control plants, demonstrating the importance of endophytes in boosting growth and minimizing the detrimental effects of heavy metals in plants. Furthermore, statistically significant improvements in germination and tillering rate were reported in plant endophytic treated at the highest lead concentrations (800 ppm). This shows that endophytes are especially critical for plant development in the most polluted soils. Although it is uncertain how endophytes enhance growth and toxin tolerance, past research suggests some probable mechanisms. Endophytes appear to limit lead bioavailability, preventing it from entering the plant. Indeed, identical findings were reported in the research by Bibi et al. (Bibi et al. 2018). They cultivated lettuce on cadmium-contaminated soil after inoculating it with a consortium of endophytes. The lettuce's biomass output increased, which was connected with a decrease in accumulated metal in the edible section (the leaf). They claimed that the bacteria might absorb the metal in their membrane and then localize it at the root level.

Many endophytic fungi have been discovered to be resistant to heavy metals and/or capable of decomposing organic contaminants, and endophyte-assisted phytoremediation has been identified as a viable approach for in-situ remediation of polluted soils. Fungi have the biochemical and ecological potential to reduce the risk associated with metals, metalloids, and radionuclides, either by chemical alteration or by affecting chemical bioavailability. Furthermore, fungi with broad mycelial networks are particularly suited for bioremediation processes. The use of filamentous fungus can be an useful approach or a beneficial supplement in situations when bacterial cells fail to develop the mycelia network needed to react with pollutants (Venkateswarlu 2014). According to Deng et al., the Cd, Pb, Zn resistant endophytic fungi *Lasiodiplodia* sp. MXSF31 was isolated from metal accumulating *Portulaca oleracea* and re-isolated from the shoots and roots of inoculated rape (Deng et al. 2014). The endophytic

fungus demonstrated great biosorption and bioaccumulation capabilities of Cd, Pb, and Zn from metal-contaminated solutions and improved rape metal extraction effectiveness in soils polluted with several metals. Endophytic fungi from plants accumulating various metals could be useful microorganism resources for bioremediation of multiple heavy metal polluted water and soils due to their vast host range, endophytic nature, and resistance to multiple metals.

Mesa et al. discovered the potential of indigenous arsenic-tolerant bacteria to enhance arsenic phytoremediation by the autochthonous pseudometallophyte *Betula celtiberica*, the results have showed that: a total of 54 cultivable rhizobacteria and 41 root endophytes, mainly affiliated with the phyla *Proteobacteria*, *Bacteroidetes*, *Firmicutes*, and *Actinobacteria*, were isolated and characterized with respect to several potentially useful features for metal plant accumulation, such as the ability to promote plant growth, metal chelation, and/or mitigation of heavy-metal stress (Mesa et al. 2017).

In the contaminated field, the siderophore and indole-3-acetic acid (IAA) producers of the endophytic bacterial consortium enhanced arsenic accumulation in the leaves and roots of *Betula celtiberica*, whereas the rhizosphere isolate *Ensifer adhaerens* strain 91R mainly promoted plant growth.

Microorganisms and plants have developed a variety of strategies for coping with arsenic, allowing them to resist and metabolize it. These features serve as the foundation for phytoremediation treatments, as well as the understanding that plant-soil bacterial interactions are critical for optimizing arsenic absorption. Endosphere and rhizosphere bacterial populations of the autochthonous *Betula celtiberica* plants growing in arsenic-contaminated soils were studied. Inoculating plants with indigenous bacteria that are As resistant, produce growth factors, and have the ability to convert As(V) to As(III), hence facilitating As detoxification, can increase the effectiveness of As phytoextraction by pseudometallophyte species like *Betula*. Furthermore, the usage of autochthonous plants and indigenous microbes relieved both partners' autoecological requirements, guaranteeing effective plant growth (Xu et al. 2016) (Fig. 13.2).

As(III) has been reported to be 60 times more toxic than As(V) and several hundred times more toxic than methylated arsenic to mammals (Neff 1997). As a result, the use of endophytes in arsenic metabolism is critical for organisms (Fig. 13.3).

To date, different genera of As(III)-oxidizing bacteria and archaea have been reported, including α -, β -, γ -*Proteobacteria*, *Thermus*, green sulfur bacteria, filamentous green non-sulfur bacteria, *Crenarchaeota* and *Euryarchaeota*. Furthermore, some As(III)-oxidizing bacteria use As(III) oxidation as an energy source. Chemolithoautotrophic As(III)-oxidizing bacteria, such as *Rhizobium* sp. NT-26 maintain bacterial growth by using As(III) as an electron donor, oxygen as an electron acceptor, and carbon dioxide-bicarbonate as a carbon source. Moreover, heterotrophic As(III)-oxidizing bacteria, such as *Hydrogenophaga* sp. N14 and *Agrobacterium tumefaciens* GW4, employ As(III) oxidation as an energy resource (Shi et al. 2020).

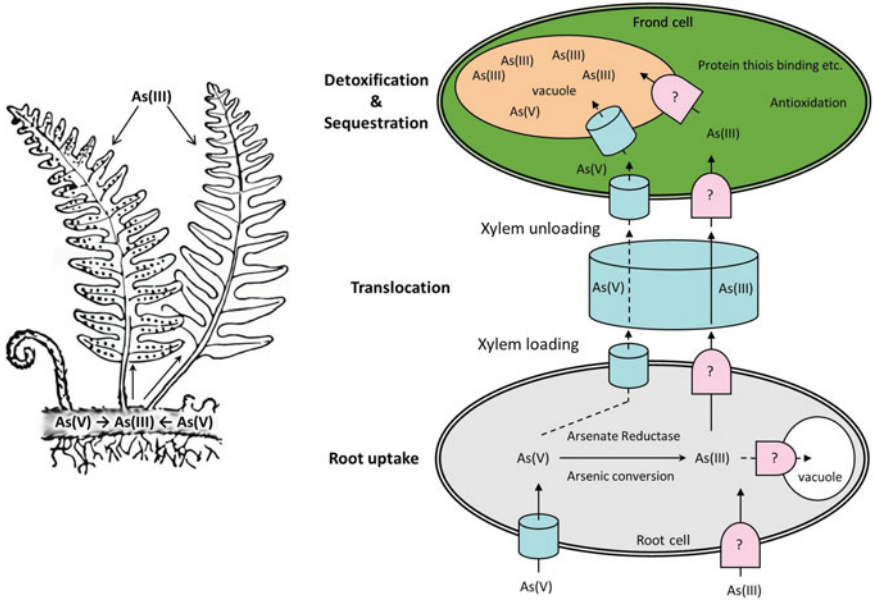


Fig. 13.2 Schematic diagram of arsenic uptake, translocation, detoxification, and sequestration in fern (Xie et al. 2009)

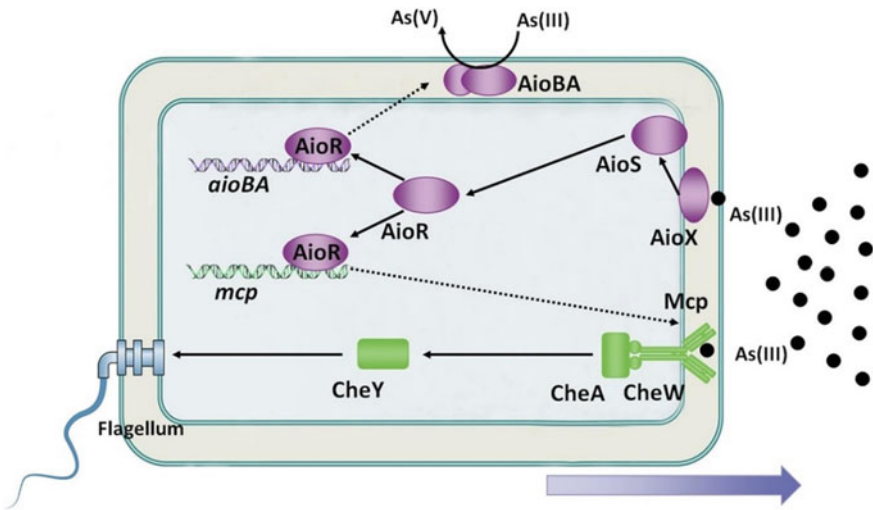


Fig. 13.3 Overview of bacterial As(III) oxidation and chemotaxis (Shi et al. 2020)

While IAA promotes plant growth, siderophores solubilize Fe from soils, allowing plants to absorb more Fe. Many endophytic bacteria found in hyperaccumulators exhibit plant growth promotion (PGP) properties. For example, Luo et al. isolated 30 endophytes from Cd-hyperaccumulator *Solanum nigrum* from a mine tailing, with 70% strains producing IAA at 1.60–122 mg L⁻¹ and 8 strains solubilizing phosphate at 22–400 mg L⁻¹ (Luo et al. 2011). Visioli et al. isolated 5 endophytes from Ni-hyperaccumulator *Noccaea caerulescens* that were capable of producing siderophore (Visioli et al. 2014). Endophytes isolated from *Prettis vitata* (PV) cultivated in clean soils by Zhu et al., on the other hand, demonstrated minimal PGP features (Zhu et al. 2014). It is probable that a plant's PGP ability is connected to its metal resistance. As a result, As-resistant endophytic bacteria from PV cultivated in As-contaminated soils must be isolated and characterized. Aside from PGP features, endophytes have strong tolerance to metal stress, which contributes in the reduction of metal phytotoxicity and the promotion of plant growth (Sessitsch et al. 2013). Endophytes have presumably developed mechanisms to adapt to heavy metal stress since hyperaccumulators have high metal concentrations in their biomass (Idris et al. 2004). For instance, Long et al. found endophyte from *Sedum alfredii* tolerated Zn and Cd while endophytes from hyperaccumulators *Thlaspi goesingense*, *Alyssum bertolonii*, and *Solanum nigrum* exhibited high tolerance to Ni and Cd (Xinxian et al. 2011). However, only one study focused on endophytes from PV growing in a clean soil (Zhu et al. 2014). Soil As pollution is known to influence microbial composition and diversity. Furthermore, endophytes from hyperaccumulators growing in polluted soils are likely to be more metal-tolerant than those from clean soils. Endophytic microbes have the ability to convert As to less toxic forms, allowing them to convert or immobilize As in soil-plant systems (Suhadolnik et al. 2017). Endophytes, or microbial bio-transformations in the host plant, play an essential part in arsenic biochemistry and are critical in risk assessment and remediation research (Anguita et al. 2018). Zhu et al. found that the ability of PV endophytes to reduce AsV and oxidize AsIII was related to their As tolerance (Zhu et al. 2014). Despite this, the study only included a small number of PV endophytes. Furthermore, PV rhizosphere bacteria were studied for As resistance and As transformation; certain rhizobacteria demonstrated a dual function of AsIII oxidation and AsV reduction (Rathinasabapathi et al. 2012). Endophytes linked with PV and their roles in As tolerance and transformation, on the other hand, are poorly understood. The study's goals were to (1) isolate and characterize As-resistant endophytic bacteria from PV cultivated in soil containing 200 mg kg⁻¹ AsV and (2) investigate the relationship between bacterial capability in As resistance and As transformation. The findings of these studies are critical for better understanding As tolerance and transformation mechanisms in As-resistant endophytes, as well as for improving phytoremediation of As-contaminated soils. According to Stazi et al., soil microbes and endophytes in hyperaccumulator plants enhance arsenic bioavailability by assisting in arsenic accumulation, release/conversion to other forms of As that are more mobile or soluble in water (As III) (Abbas et al. 2018). Microorganisms convert arsenic in host plants from one form to another via several processes/mechanisms such as methylation and demethylation (conversion of inorganic form to organic and vice versa) (Pantsar-Kallio and Jørgensen 2002).

Microorganisms have been shown to transform inorganic arsenic to organic arsenic forms (Gadd 1993). Some (demethylated) microorganisms, on the other hand, may convert methylated arsenic to inorganic arsenic via biological methylation (Gao and Baur 1997).

In the study carried out by Xu et al., 43 As-resistant endophytic bacteria from the roots, stems, and leaflets of As hyperaccumulator PV were isolated and characterized (Xu et al. 2016). There was a huge variety, with four phyla and 17 genera, with *Proteobacteria* and *Actinobacteria* dominating. Among endophytes, *Brevundimonas* sp. was the main species in all three PV tissues. PGP characteristics were present in all endophytes. Endophytes from PV roots and stems were more capable of phosphate solubilization than leaflets. Furthermore, all endophytes were resistant to As. Six endophytes in particular grew faster in the presence of 10 mM AsV than the control, most likely due to As-stimulated growth. Endophytes from PV roots were also more resistant to AsV, whilst those from leaflets were more tolerant to AsIII. Bacterial resistance to AsV was shown to be positively associated to their capacity to reduce AsV but not to oxidize AsIII. According to the findings, As-resistant endophytes may promote plant growth in PV, increasing its effectiveness in phytoremediation of As-contaminated locations.

Because pollutants such as heavy metals, polycyclic aromatic hydrocarbons (PAHs), and halogenated hydrocarbons have phytotoxic effects on plants, phytoremediation may be hindered. However, in addition to their ability to promote plant growth, certain endophytes have been demonstrated to produce iron chelators, siderophores, organic acids, and other degrading enzymes, which can change the toxicity of pollutants. Plant-associated bacteria may improve phytoextraction by modifying the solubility, availability, and transport of heavy metals and nutrients via the formation of organic acids and redox changes. Furthermore, the release of low-molecular-mass organic acids by certain endophytes has been demonstrated to promote heavy-metal mobilization (Li et al. 2012).

The efficiency of phytoremediation of metal-contaminated soil is mainly dependent on metal uptake and accumulation in shoots. It has been demonstrated that some heavy-metal-resistant/plant-growth-promoting endophytes can improve metal uptake and accumulation in plants. For example, Ma et al. discovered that inoculating *Alyssum serpyllifolium* with the plant-growth boosting endophytic bacteria *Pseudomonas* sp. A3R3 dramatically enhanced Ni concentration in plant (Ma et al. 2011). Chen et al. (2010) found that four heavy-metal-resistant endophytic bacteria improved Cd accumulation in root, stem, and leaf tissues of *Solanum nigrum* L. growing in three levels of Cd-contaminated soil; they also found that the accumulation capacity changed with the Cd concentration in the soil (Chen et al. 2010). Similarly, Mastretta et al. showed that the inoculation of *Nicotiana tabacum* with Cd-resistant endophyte *Sanguibacter* sp. increased the concentration of Cd in shoot tissues (Mastretta et al. 2009), while Sheng et al. (2008) discovered that the inoculation of *Brassica napus* with Pb-resistant endophytic bacteria increased Pb uptake into the shoot (Sheng et al. 2008).

In Vietnam, soil contaminated with high concentrations of lead and cadmium was investigated and detected in the vicinity of the zinc/lead mining and processing

factory in Tan Long commune, Dong Hy district, Thai Nguyen province. Lead and cadmium concentrations at Tan Long's old solid waste dump from the zinc-lead factory ranged from 1100 to 13,000 mg kg⁻¹ and 11.34 to 61.04 mg kg⁻¹, respectively. Lead and cadmium Soil Pollution Indexes (SPI) were highest in the old solid waste dump region, followed by rice soils. The arsenic pollution of the soil in this area was caused by tin mining and sorting activities in Ha Thuong. Arsenic concentrations in soils were higher than 320 mg kg⁻¹ (dry weight) and up to 3809 mg kg⁻¹ in all evaluated areas (Chu 2011). In our study, 20 fern samples were collected at Nui Phao mine, Thai Nguyen province, Vietnam, where Cd and As concentrations at sampling points were about 0.648 mg kg⁻¹ and ranged from 316 to 1606 mg kg⁻¹, respectively (Tam et al. 2021). 205 strains of endophytic bacteria were isolated from the collected samples, with 73 growing on an LB agar plate containing 5 mM As(III) and 132 growing on an LB agar plate containing 5 mM As(V), distributed in all three parts: stem, root, and leaf. The percentage of endophytic bacterial colonies isolated from the roots was higher than those from branches and leaves (58%, 21% and 21%, respectively). Of the 205 endophytic bacterial isolates, 31 had minimal inhibitory concentrations in the range of 80–320 mM. Among them, strain *Micrococcus luteus* S3.4.1 can be tolerant to the concentration of As (V) up to 320 mM and synthesize high level of IAA (18.72 µg/ml) (Tam et al. 2021).

The experimental evidence presented above have been demonstrated that endophytes possess diverse biological characteristics such as the producing plant growth substances, heavy metal tolerance, reducing toxicity of heavy metals to plants, having wide spectrum of host plants, and degrading organic compounds to supply minerals for plants... This is an advantage of the host-endophyte mutualistic relationship, which can stimulate plant growth, development and tolerance, and thus contribute to promoting the efficiency of heavy metal treatment.

To generalize the content of this section, some of endophytes' traits in heavy metal remediation have been summarized as shown in Table 13.2:

13.6 Conclusions and Future Prospects

The application of endophytic microorganisms in phytoremediation to enhance heavy metal removal efficiency is relatively new but is making rapid progress. Endophytes is clearly a novel group of microorganisms, with great potential in heavy metal removal, the use of which is an environmentally friendly and sustainable approach to bioremediation. Endophytes can be isolated from a variety of hosts, showing high heavy metal tolerance and removal capacity. In the future, introducing endophytic microorganisms with high heavy metal tolerance, absorption and assimilation capacity into polluted areas and host plants used in heavy metal bioremediation to clean the environment might well be possible.

With the presence of endophytic microorganisms, vitality and heavy metal hyper-accumulation capacity of host plants can be enhanced due to better growth, increased resistance to environmental stress, heavy metal transformation and absorption genes

Table 13.2 Endophytes' traits in heavy metal remediation

Heavy metal bioremediation	References
Have metal removal capacity	Sim et al. (2019), Sim et al. (2016)
Reduce As(V) to As(III) and/or oxidize As(III)	Pongratz and Heumann (1999), Vaxevanidou et al. (2012), Abbas et al. (2018), Xu et al. (2016), Shi et al. (2020), Zhu et al. (2014)
Heavy metal absorption	Sim et al. (2016), Chen et al. (2010), El-Gendy et al. (2011), Dursun et al. (2003), Bibi et al. (2018), Mesa et al. (2017)
Bioaccumulating heavy metal	Deng et al. (2014)
Limit heavy metal bioavailability	Ahmad et al. (2016), Pantsar-Kallio and Jørgensen (2002), Ma et al. (2016), Bibi et al. (2018), Venkateswarlu (2014), Li et al. (2012)
Have strong tolerance to metal stress	Venkateswarlu (2014), Sessitsch et al. (2013)
Transform inorganic arsenic to organic arsenic forms and vice versa	Pantsar-Kallio and Jørgensen (2002), Gadd (1993), Gao and Burau (1997)
Promote plant growth	Ma et al. (2016), Mesa et al. (2017), Xu et al. (2016), Visioli et al. (2014), Sessitsch et al. (2013), Li et al. (2012)
Modify solubility, and transport of heavy metals and nutrients via the formation of organic acids and redox changes Release of low-molecular-mass organic acids to promote heavy-metal mobilization	Li et al. (2012)

reducing heavy metal toxicity in cells. In Vietnam, studies on endophytes absorbing heavy metals and supporting host plants in heavy metal absorption are both few in number and small in scale. In the future, the application of endophytes into host plants (heavy metal hyperaccumulators) will be rapidly developed and the interaction mechanism between endophytes and host plants to enhance heavy metal absorption capacity will be further studied, clarified and effectively applied.

Acknowledgements This research is funded by the Vietnam National University, Hanoi (VNU) under Project number QG.20.09

References

- Abbas G, Murtaza B, Bibi I, Shahid M, Niazi NK, Khan MI et al. (2018) Arsenic uptake, toxicity, detoxification, and speciation in plants: physiological, biochemical, and molecular aspects. *Int J Environ Res Public Health* 15
- Ahmad I, Akhtar MJ, Asghar HN, Ghafoor U, Shahid M (2016) differential effects of plant growth-promoting rhizobacteria on maize growth and cadmium uptake. *J Plant Growth Regul* 35:303–315
- Ali S, Charles TC, Glick BR (2012) Delay of flower senescence by bacterial endophytes expressing L-aminocyclopropane-1-carboxylate deaminase. *J Appl Microbiol* 113:1139–1144

- Ali S, Charles TC, Glick BR (2014a) Amelioration of high salinity stress damage by plant growth-promoting bacterial endophytes that contain ACC deaminase. *Plant Physiol Biochem* PPB 80:160–167
- Ali S, Duan J, Charles TC, Glick BR (2014b) A bioinformatics approach to the determination of genes involved in endophytic behavior in *Burkholderia* spp. *J Theor Biol* 343:193–198
- Anguita JM, Rojas C, Pastén PA, Vargas IT (2018) A new aerobic chemolithoautotrophic arsenic oxidizing microorganism isolated from a high Andean watershed. *Biodegradation* 29:59–69
- Araújo W, Lacava P, Andreote F, Azevedo J (2008) Interaction between endophytes and plant host: biotechnological aspects. pp 95–115
- Bacon CW, White J, Stone J (2000) An overview of endophytic microbes: endophytism defined. *Microb Endophytes* 85–117
- Bayata A (2020) Assessment, accumulation, toxicity and importance of heavy metals in agricultural soil and living system—review. *Am J Environ Prot* 9(6):116–119
- Bayramoglu G, Denizli A, Bektas S, Yakup AM (2002) Entrapment of *Lentinus sajor-caju* into Calcium alginate gel beads for removal of Cd(II) ions from aqueous solution: preparation and biosorption kinetics analysis. *Microchem J* 72:63–76
- Bibi S, Hussain A, Hamayun M, Rahman H, Iqbal A, Shah M et al (2018) Bioremediation of hexavalent chromium by endophytic fungi; safe and improved production of *Lactuca sativa* L. *Chemosphere* 211:653–663
- Bric JM, Bostock RM, Silverstone SE (1991) Rapid in situ assay for indoleacetic acid production by bacteria immobilized on a nitrocellulose membrane. *Appl Environ Microbiol* 57:535–538
- Chaudhary K, Jan S, Khan S (2016) Chapter 23-heavy metal ATPase (HMA2, HMA3, and HMA4) genes in hyperaccumulation mechanism of heavy metals. In: Ahmad P (ed) *Plant metal interaction*. Elsevier, pp 545–556
- Chen L, Luo S, Xiao X, Guo H, Chen J, Wan Y et al (2010) Application of plant growth-promoting endophytes (PGPE) isolated from *Solanum nigrum* L. for phytoextraction of Cd-polluted soils. *Appl Soil Ecol* 46:383–389
- Chu H (2011) Survey on heavy metals contaminated soils in Thai Nguyen and Hung Yen provinces in Northern Vietnam. *J Vietnamese Environ* 1
- Conn VM, Walker AR, Franco CM (2008) Endophytic actinobacteria induce defense pathways in *Arabidopsis thaliana*. *Mol Plant Microbe Interact* MPMI 21:208–218
- Conrath U, Beckers GJ, Flors V, García-Agustín P, Jakab G, Mauch F et al (2006) Priming: getting ready for battle. *Mol Plant Microbe Interact* MPMI 19:1062–1071
- Cui X, Zhang J, Wang X, Pan M, Lin Q, Khan KY et al (2021) A review on the thermal treatment of heavy metal hyperaccumulator: fates of heavy metals and generation of products. *J Hazard Mater* 405:123832
- Das N, Vimala R, Karthika P (2008) Biosorption of heavy metals—an overview. *Indian J Biotechnol* 7:159–169
- Deng Z, Zhang R, Shi Y, Hu L, Tan H, Cao L (2014) Characterization of Cd-, Pb-, Zn-resistant endophytic *Lasiodiplodia* sp. MXSF31 from metal accumulating *Portulaca oleracea* and its potential in promoting the growth of rape in metal-contaminated soils. *Environ Sci Pollut Res Int* 21:2346–2357
- Dursun A., Uslu G, Tepe Ö, Cuci Y, Ekiz Hİ (2003) A comparative investigation on the bioaccumulation of heavy metal ions by growing *Rhizopus arrhizus* and *Aspergillus niger*. *Biochem Eng J* 15:87–92
- El-Otmami M, Coggins CW, Agustí M, Lovatt CJ (2000) Plant growth regulators in citriculture: world current uses. *Crit Rev Plant Sci* 19:395–447
- El-Gendy MMA, Hassanein NM, Ibrahim HAEH, El-Baky DH (2011) Evaluation of some fungal endophytes of plant potentiality as low-cost adsorbents for heavy metals uptake from aqueous solution. *Aust J Basic Appl Sci* 5:466–473
- Fabiana T, Francine Falcão de Macedo N, Ana Luisa G, Talita Bernardon M (2020) Endophytes potential use in crop production. Open access peer-reviewed chapter

- Gadd GM (1993) Microbial formation and transformation of organometallic and organometalloid compounds. *FEMS Microbiol Rev* 11:297–316
- Gai CS, Lacava PT, Quecine MC, Auriac MC, Lopes JR, Araújo WL et al (2009) Transmission of Methyllobacterium mesophilicum by *Bucephalagonia xanthophis* for paratransgenic control strategy of citrus variegated chlorosis. *J Microbiol (seoul, Korea)* 47:448–454
- Gangwar M, Dogra S, Sharma N (2011) Antagonistic bioactivity of endophytic actinomycetes isolated from medicinal plants. *J Adv Lab Res Biol* 2:154–157
- Gangwar M, Phutela U, Dogra S, Kharwar R (2014) Diversity and biopotential of endophytic actinomycetes from three medicinal plants in India. *Afr J Microbiol Res* 8:184–191
- Gao S, Bureau RG (1997) Environmental factors affecting rates of Arsenic evolution from and mineralization of Arsenicals in soil. *J Environ Qual* 26:753–763
- Ghodhbane-Gtari F, Essoussi I, Chattaoui M, Chouaia B, Jaouani A, Daffonchio D et al (2010) Isolation and characterization of non-Frankia actinobacteria from root nodules of *Alnus glutinosa*, *Casuarina glauca* and *Elaeagnus angustifolia*. *Symbiosis* 50:51–57
- Glick B (2015) Beneficial plant-bacterial interactions, pp 65–96
- Gupta AK, Joia J, Sood AD, Sood R, Sidhu Y, Kaur G (2016) Microbes as potential tool for remediation of heavy metals: a review. *J Microb Biochem Technol* 8:364–372
- Hardoim PR, van Overbeek LS, Elsas JD (2008) Properties of bacterial endophytes and their proposed role in plant growth. *Trends Microbiol* 16:463–471
- Ho YN, Mathew DC, Hsiao SC, Shih CH, Chien MF, Chiang HM et al (2012) Selection and application of endophytic bacterium *Achromobacter xylosoxidans* strain F3B for improving phytoremediation of phenolic pollutants. *J Hazard Mater* 219–220:43–49
- Hong-Thao PT, Mai-Linh NV, Hong-Lien NT, Van Hieu N (2016) Biological characteristics and antimicrobial activity of Endophytic *Streptomyces* sp. TQR12–4 isolated from *Elite Citrus nobilis* Cultivar Ham Yen of Vietnam. *Int J Microbiol* 2016, 7207818
- Idris R, Trifonova R, Puschenreiter M, Wenzel WW, Sessitsch A (2004) Bacterial communities associated with flowering plants of the Ni hyperaccumulator *Thlaspi goesingense*. *Appl Environ Microbiol* 70:2667–2677
- Jaemsaeng R, Jantasuriyarat C, Thamchaipenet A (2018) Molecular interaction of 1-aminocyclopropane-1-carboxylate deaminase (ACCD)-producing endophytic *Streptomyces* sp. GMKU 336 towards salt-stress resistance of *Oryza sativa* L. cv. KDML105. *Sci Rep* 8, 1950
- Janso JE, Carter GT (2010) Biosynthetic potential of phylogenetically unique endophytic actinomycetes from tropical plants. *Appl Environ Microbiol* 76:4377–4386
- Kandpal KC, Jain DA, Kumar U, Tripathi R, Kumar TS (2012) Isolation and screening of endophytic actinomycetes producing antibacterial compound from *Citrus aurantifolia* Fruit. *Eur J Exp Biol* 2:1733–1737
- Khalil MMH, Abou-Shanab RAI, Salem AE-NM, Omer AM, Aboelazm TA (2016) Biosorption of trivalent chromium using Ca-alginate immobilized and alkali-treated biomass. *J Comput Sci Technol* 5:1–6
- Kim TU, Cho SH, Han JH, Shin YM, Lee HB, Kim SB (2012) Diversity and physiological properties of root endophytic actinobacteria in native herbaceous plants of Korea. *J Microbiol (seoul, Korea)* 50:50–57
- Kumar USA, SivaKumar T (2011) Isolation and screening of endophytic actinomycetes from different parts of *Embllica officinalis*. *Ann Biol Res* 2:423–434
- Li H-Y, Wei D-Q, Shen M, Zhou Z-P (2012) Endophytes and their role in phytoremediation. *Fungal Divers* 54
- Luo SL, Chen L, Chen JL, Xiao X, Xu TY, Wan Y et al (2011) Analysis and characterization of cultivable heavy metal-resistant bacterial endophytes isolated from Cd-hyperaccumulator *Solanum nigrum* L. and their potential use for phytoremediation. *Chemosphere* 85:1130–1138
- Luu TA, Phi QT, Nguyen TTH, Dinh MV, Pham BN, Do QT (2021) Antagonistic activity of endophytic bacteria isolated from weed plant against stem end rot pathogen of pitaya in Vietnam. *Egypt J Biol Pest Control* 31:14

- Ma Y, Rajkumar M, Luo Y, Freitas H (2011) Inoculation of endophytic bacteria on host and non-host plants—effects on plant growth and Ni uptake. *J Hazard Mater* 195:230–237
- Ma Y, Rajkumar M, Zhang C, Freitas H (2016) Beneficial role of bacterial endophytes in heavy metal phytoremediation. *J Environ Manage* 174:14–25
- Machavariani NG, Ivankova TD, Sineva ON, Terekhova LP (2014) Isolation of endophytic actinomycetes from medicinal plants of the Moscow region, Russia. *World Appl Sci J* 30:1599–1604
- Malekzadeh F, Latifi AM, Shahamat M, Levin M, Colwell RR (2002) Effects of selected physical and chemical parameters on uranium uptake by the bacterium *Chryseomonas* MGF-48. *World J Microbiol Biotechnol* 18:599–602
- Malfanova NV (2013) Endophytic bacteria with plant growth promoting and biocontrol abilities. Doctoral thesis, Leiden University
- Malfanova N, Lugtenberg BJJ, Berg G (2013) Bacterial endophytes: who and where, and what are they doing there? In: *Molecular microbial ecology of the rhizosphere*, pp 391–403
- Mastretta C, Taghavi S, van der Lelie D, Mengoni A, Galardi F, Gonnelli C et al (2009) Endophytic bacteria from seeds of *Nicotiana tabacum* can reduce Cd phytotoxicity. *Int J Phytorem* 11:251–267
- Mengistu AA (2020) Endophytes: colonization, behaviour, and their role in defense mechanism. *Int J Microbiol* 6927219–6927219
- Mesa V, Navazas A, González-Gil R, González A, Weyens N, Lauga B et al. (2017) Use of Endophytic and Rhizosphere bacteria to improve phytoremediation of arsenic-contaminated industrial soils by *Autochthonous Betula celtiberica*. *Appl Environ Microbiol* 83
- Mishra S, Bharagava RN (2016) Toxic and genotoxic effects of hexavalent chromium in environment and its bioremediation strategies. *J Environ Sci Health C* 34:1–32
- Neff JM (1997) Ecotoxicology of arsenic in the marine environment. *Environ Toxicol Chem* 16:917–927
- Ongena M, Jourdan E, Adam A, Paquot M, Brans A, Joris B et al (2007) Surfactin and fengycin lipopeptides of *Bacillus subtilis* as elicitors of induced systemic resistance in plants. *Environ Microbiol* 9:1084–1090
- Pantsar-Kallio M, Jørgensen DK (2002) Interactions between metals, microbes and plants: bioremediation of arsenic and lead contaminated soils. Ph.D. thesis, University of Helsinki, Helsinki
- Phan T, ng H, Hong Lien N, Linh N (2016) Biological characteristics and production of plant growth regulator IAA by endophytic streptomyces hebeiensis TQR8–7. *Vietnam J Sci Technol* 54:31–39
- Phuakjaiphaeo C, Chang CI, Ruangwong O, Kunasakdakul K (2016) Isolation and identification of an antifungal compound from endophytic *Streptomyces* sp. CEN26 active against *Alternaria brassicicola*. *Lett Appl Microbiol* 63:38–44
- Pongratz R, Heumann KG (1999) Production of methylated mercury, lead, and cadmium by marine bacteria as a significant natural source for atmospheric heavy metals in polar regions. *Chemosphere* 39:89–102
- Priya M (2012) Endophytic actinomycetes from indian medicinal plants as antagonists to some phytopathogenic fungi. *Open Access Sci Rep* 1:1–5
- Rahman Z, Singh VP (2019) The relative impact of toxic heavy metals (THMs) (arsenic (As), cadmium (Cd), chromium (Cr)(VI), mercury (Hg), and lead (Pb)) on the total environment: an overview. *Environ Monit Assess* 191(7):419
- Rascio N, Navari-Izzo F (2011) Heavy metal hyperaccumulating plants: how and why do they do it? And what makes them so interesting? *Plant Sci* 180:169–181
- Rathinasabapathi B, De Oliveira L, Guilherme L (2012) Bacteria-mediated Arsenic oxidation and reduction in the growth media of Arsenic hyperaccumulator *Pteris vittata*. *Environ Sci Technol* 46:11259–11266
- Romero FM, Marina M, Pieckenstain FL (2014) The communities of tomato (*Solanum lycopersicum* L.) leaf endophytic bacteria, analyzed by 16S-ribosomal RNA gene pyrosequencing. *FEMS Microbiol Lett* 351:187–194

- Santoyo G, Moreno-Hagelsieb G, del Carmen Orozco-Mosqueda M, Glick BR (2016) Plant growth-promoting bacterial endophytes. *Microbiol Res* 183:92–99
- Seghers D, Wittebolle L, Top EM, Verstraete W, Siciliano SD (2004) Impact of agricultural practices on the *Zea mays* L. endophytic community. *Appl Environ Microbiol* 70:1475–1482
- Sessitsch A, Kuffner M, Kidd P, Vangronsveld J, Wenzel WW, Fallmann K et al (2013) The role of plant-associated bacteria in the mobilization and phytoextraction of trace elements in contaminated soils. *Soil Biol Biochem* 60:182–194
- Sheng XF, Xia JJ, Jiang CY, He LY, Qian M (2008) Characterization of heavy metal-resistant endophytic bacteria from rape (*Brassica napus*) roots and their potential in promoting the growth and lead accumulation of rape. *Environ Pollut* 156:1164–1170
- Shi Y, Yang H, Zhang T, Sun J, Lou K (2014) Illumina-based analysis of endophytic bacterial diversity and space-time dynamics in sugar beet on the north slope of Tianshan mountain. *Appl Microbiol Biotechnol* 98:6375–6385
- Shi K, Wang Q, Wang G (2020) Microbial oxidation of arsenite: regulation, chemotaxis, phosphate metabolism and energy generation. *Front Microbiol* 11
- Shimizu M (2011) Endophytic actinomycetes: biocontrol agents and growth promoters. pp 201–220
- Shutsrirung A, Chromkaew Y, Pathom-Aree W, Choonluchanon S, Boonkerd N (2013) Diversity of endophytic actinomycetes in mandarin grown in northern Thailand, their phytohormone production potential and plant growth promoting activity. *Soil Sci Plant Nutr* 59:322–330
- Sim CSF, Tan WS, Ting ASY (2016) Endophytes from Phragmites for metal removal: evaluating their metal tolerance, adaptive tolerance behaviour and biosorption efficacy. *Desalin Water Treat* 57:6959–6966
- Sim C, Chen SH, Ting A (2019) Endophytes: emerging tools for the bioremediation of pollutants
- Singh G, Singh N, Marwaha TS (2009) Crop genotype and a novel symbiotic fungus influences the root endophytic colonization potential of plant growth promoting rhizobacteria. *Physiol Mol Biol Plants Int J Funct Plant Biol* 15:87–92
- Sørensen J, Sessitsch A (2006) Plant-associated bacteria lifestyle and molecular interactions. *Mod Soil Microbiol* 211–236
- Stępniewska Z, Kuźniar A (2013) Endophytic microorganisms-promising applications in bioremediation of greenhouse gases. *Appl Microbiol Biotechnol* 97:9589–9596
- Strobel G, Daisy B, Castillo U, Harper J (2004) Natural products from endophytic microorganisms. *J Nat Prod* 67:257–268
- Suhadolnik MLS, Salgado APC, Scholte LLS, Bleicher L, Costa PS, Reis MP et al (2017) Novel arsenic-transforming bacteria and the diversity of their arsenic-related genes and enzymes arising from arsenic-polluted freshwater sediment. *Sci Rep* 7:11231
- Taechowisan T, Chanaphat S, Ruensamran W, Phutdhawong WS (2013) Antibacterial activity of 1-methyl ester-nigericin from *Streptomyces hygrosopicus* BRM10; an endophyte in *Alpinia galanga*. *J Appl Pharm Sci* 3:104–109
- Taechowisan T, Chanaphat S, Ruensamran W, Phutdhawong WS (2014) Antibacterial activity of new flavonoids from *Streptomyces* sp. BT01; an endophyte in *Boesenbergia rotunda* (L.) mansf. *J Appl Pharm Sci* 4:8–13
- Tam NKB, Linh NT, Truc TT, Linh NVM, Nhung ĐT, Tra LT et al. (2021) Research on some biological characteristics of arsenate resistant endophytic bacteria from ferns. *Vietnam Environ Adm Mag* 51–55
- Tiwari G, Duraivadivel P, Sharma S, Hariprasad P (2018) 1-Aminocyclopropane-1-carboxylic acid deaminase producing beneficial rhizobacteria ameliorate the biomass characters of *Panicum maximum* Jacq. by mitigating drought and salt stress. *Sci Rep* 8, 17513
- Tokala RK, Strap JL, Jung CM, Crawford DL, Salove MH, Deobald LA et al (2002) Novel plant-microbe rhizosphere interaction involving *Streptomyces lydicus* WYEC108 and the pea plant (*Pisum sativum*). *Appl Environ Microbiol* 68:2161–2171
- Truyens S, Weyens N, Cuyper A, Vangronsveld J (2015) Bacterial seed endophytes: genera, vertical transmission and interaction with plants. *Environ Microbiol Rep* 7:40–50

- Vaxevanidou K, Giannikou S, Papassiopi N (2012) Microbial arsenic reduction in polluted and unpolluted soils from Attica, Greece. *J Hazard Mater* 241–242:307–315
- Venkateswarlu D (2014) Role of endophytic fungi in restoration of heavy metal contaminated soils. *Indo Am J Pharm Res* 4:5427–5436
- Visioli G, D'Egidio S, Vamerali T, Mattarozzi M, Sanangelantoni AM (2014) Culturable endophytic bacteria enhance Ni translocation in the hyperaccumulator *Noccaea caerulescens*. *Chemosphere* 117:538–544
- Waheeda K, Shyam KV (2017) Formulation of novel surface sterilization method and culture media for the isolation of endophytic actinomycetes from medicinal plants and its antibacterial activity. *J Plant Pathol Microbiol* 8:399
- Wang J, Chen C (2009) Biosorbents for heavy metals removal and their future. *Biotechnol Adv* 27:195–226
- Waqas M, Khan AL, Kamran M, Hamayun M, Kang SM, Kim YH et al (2012) Endophytic fungi produce gibberellins and indoleacetic acid and promotes host-plant growth during stress. *Molecules* 17:10754–10773
- Wilde EW, Benemann JR (1993) Bioremoval of heavy metals by the use of microalgae. *Biotechnol Adv* 11:781–812
- Xie Q-E, Yan X-L, Liao X, Li X (2009) The arsenic hyperaccumulator fern *Pteris vittata* L. *Environ Sci Technol* 43(22):8488–8495
- Xinxian L, Xuemei C, Yagang C, Wong J, Zebin W, Qitang W (2011) Isolation and characterization endophytic bacteria from hyperaccumulator *Sedum alfredii* Hance and their potential to promote phytoextraction of zinc polluted soil. *World J Microbiol Biotechnol* 27:1197–1207
- Xu J-Y, Han Y-H, Chen Y, Zhu L-J, Ma LQ (2016) Arsenic transformation and plant growth promotion characteristics of As-resistant endophytic bacteria from As-hyperaccumulator *Pteris vittata*. *Chemosphere* 144:1233–1240
- Yadav J, Verma J, Tiwari K (2010) Effect of plant growth promoting Rhizobacteria on seed germination and plant growth Chickpea (*Cicer arietinum* L.) under in vitro conditions. *Biol Forum Int J* 2:15–18
- Zhenhua X, Dongmei G, Xiuli S, Ying X (2012) A review of endophyte and its use and function. In: International conference on environmental engineering and technology advances in biomedical engineering, pp 124–130
- Zhu LJ, Guan DX, Luo J, Rathinasabapathi B, Ma LQ (2014) Characterization of arsenic-resistant endophytic bacteria from hyperaccumulators *Pteris vittata* and *Pteris multifida*. *Chemosphere* 113:9–16

Chapter 14

Evaluation of Density Characterization of Municipal Solid Waste in Southern Part of Vietnam



Hung-T. Vo, Thong-H. Nguyen, Vinh-T. Bui, Ngoc-L. Dang, Phong-T. Le, Hau-T. Le, Linh-T. D. Le, and Thong-V. Pham

Abstract Unit weight of municipal solid waste (MSW) varies notably depending on waste composition, operational conditions, and waste decomposition process. The unit weight of MSW is an essential key parameter in determining acting loadings and construction costs for landfills, specifically evaluating a safety factor and total capacity volume. The improper unit weight could lead to the incorrect conversion between the weight and the volume, thus causing issues in the management and treatment of MSW. This study presents an experimental evaluation of density characterization of MSW in the southern part of Vietnam. To achieve the objective, first, experimental tests of MSW unit weight for three landfills in southern areas of Vietnam are conducted. Then, MSW unit weight for current landfills using measured masses and total waste volume is estimated. The predicted unit weight is compared with pre-published to evidence the correctness of the proposed method. The analyzed result shows that the unit weight of MSW is varied from 5.53 to 15.65 kN/m³ depending on waste compositions, landfilling time, and locations of waste sampling.

Keywords Municipal solid waste · Sanitary landfill · Unit weight · Waste density · Waste management

H.-T. Vo (✉) · H.-T. Le · T.-V. Pham

Technology Center for Water and Environment Research, Floor 7, 224 Dien Bien Phu Street, District 3, Ho Chi Minh city, Vietnam
e-mail: vthung.sdh21@hcmut.edu.vn

H.-T. Vo · T.-H. Nguyen · V.-T. Bui · P.-T. Le · H.-T. Le · L.-T. D. Le

Faculty of Geology and Petroleum Engineering, Ho Chi Minh City University of Technology (HCMUT), 268 Ly Thuong Kiet Street, Dist. 10, Ho Chi Minh City, Vietnam

N.-L. Dang

Urban Infrastructure Faculty, Mien Tay Construction University, Vinh Long, Vietnam

14.1 Introduction

Any residual materials, originating from human activities and industrial works and having no residual value, are defined as waste. The increasing population leads to urbanization levels and consumption of goods, thus resulting in more waste produced (Ding et al. 2021; Alam and Qiao 2020). It is estimated that by 2050 the amount of municipal solid waste (MSW) worldwide will be about 3.40 billion tons a year, which is 1.7 times larger than that produced in 2016 (Kaza et al. 2050). When untreated waste is directly released into the surrounding environment, it could cause risks to lands, water, and even air pollution. The proper disposal of residual waste materials (non-hazardous waste and hazardous waste) makes a significant concern (Richter et al. 2021; Prajapati et al. 2021), especially in megacities.

In Vietnam, rapid urbanization, and population growth lead to increasingly high amounts of waste. The amount of waste in 2015 is estimated to be over 27 million tons. As reported (Katelijjn et al. 2018), the yearly growth rate of MSW is about 8.4% for urban areas and about 5% for rural areas. By 2030, MSW volume in the whole country is predicted to be about 54 million tons.

Among waste treatment methods (Bilgin and Tulun 2015; Lu and Tam 2013; Edalatpour et al. 2018), a landfill is commonly used to dispose of MSW (Moberg et al. 2005; Gopikumar et al. 2021) since it is a simple and cost-effective method. Thousands of landfills are active, closed, and abandoned (Jain et al. 2014) (e.g., nearly 100,000 in the U.S or more than 20,000 in China). In Vietnam, about 60–70% of collected MSW is treated by landfill methods, while the remaining waste is disposed into the surrounding environment or freely transferred to local markets (e.g., construction solid waste). Of the 660 landfills, only 30% of them are classified as sanitary landfills (Jain et al. 2014). As planned by the Vietnam government, by 2025, less than 30% of MSW will be dumped. This is extremely challenging for not only the government and local authorities but also the society due to a large amount of waste.

Designing and operational landfills can be a challenge for engineering since the complex geotechnical properties, and mechanical behavior of MSW causes some issues (i.e., stability of the slope, leachate escape, and settlement (Zeccos 2005)). Among geotechnical properties of MSW, such as waste composition, unit weight, hydraulic conductivity, shear strength, and compressibility, the unit weight is found to be the most essential for landfill design and increasing landfill capacity so far (Breitmeyer et al. 2020; Raviteja et al. 2021). The unit weight helps to decide the layout options in order to ensure the safety factors and environmental safety. The unit weight can differ from one area to others depending on variances such as climate conditions, operational conditions, waste compositions, and testing methods. It leads to the varied values reported in the literature (Raviteja et al. 2021; Zekkos et al. 2006). To ensure structural safety, appropriate values of unit weight of municipal solid waste should be selected based on the changeability of MSW data at a specific landfill site.

Experimental investigations on MSW showed that the changes in unit weight values were from 8 to 21 kN/m³ (Matasović et al. 1998), which was quite dependent on the aging and degradation of MSW. For newly dumped MSW, the unit weight is generally influenced by covering soil layers, the compaction techniques, and waste compositions with weight values of about 9 kN/m³ for dry waste and 16–20 kN/m³ for degraded waste (Kavazanjian et al. 1996). Moreover, the height of the landfill and confinement can also lead to variations in the MSW unit weight (Raviteja et al. 2021; Zekkos et al. 2006).

According to official data from the Ministry of Science, Technology, and Environment, Ministry of Construction, Vietnam (No. 01/2001/TTLT-BKHCNMT-BXD dated 18/01/2001), the unit weight of MSW was varied from 5.2–8.0 kN/m³. The unit waste from Vietnamese guidelines conflicts with examined data from other experimental studies. In addition, the diversity of waste composition for landfills in six cities (i.e., Hanoi, Hai-Phong, Hue, Da-Nang, HCM city, and Bac-Ninh) (Nguyen et al. 2014) from the North to South of Vietnam shows that there exist differences in the receiving process, classification, landfilling, and decomposition. Currently, a rare study has been conducted to determine MSW due to no established standard method. This study presents an experimental evaluation of density characterization of municipal solid waste in the southern part of Vietnam. To achieve the objective, first, an experimental test of MSW unit weight for three landfills in southern areas of Vietnam is conducted. Second, municipal solid waste unit weight for current landfills using mass and total waste volume is estimated. Lastly, by comparing with pre-published to evidence the correctness of the proposed method, some suggestions for waste management in Vietnam are made (Fig. 14.1).

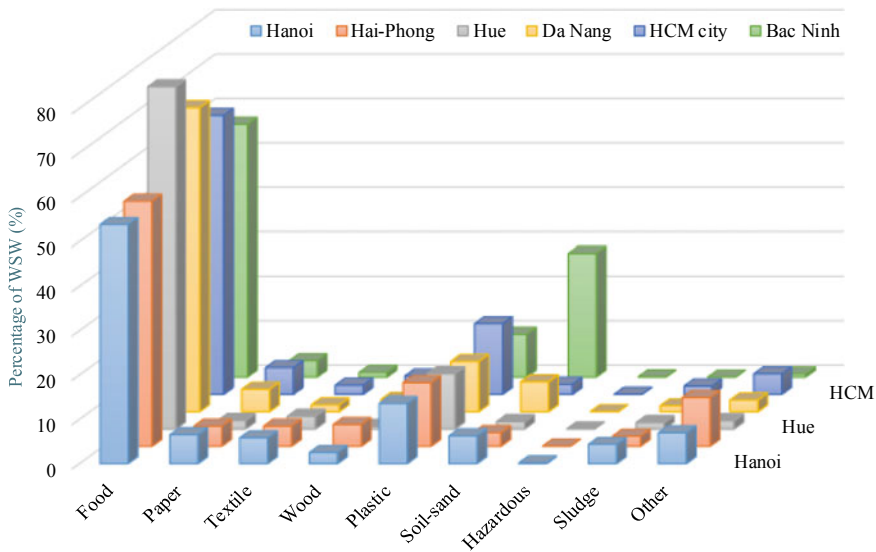


Fig. 14.1 Composition of MSW in some Vietnam landfills

14.2 Materials and Methods

14.2.1 Experimental Test of MSW Unit Weight for Landfills

In actual point of fact, there is no Vietnamese standard method for determining the unit weight of MSW. This part presents some sampling methods proposed to determine the waste unit weight in landfills in the south areas of Vietnam, as shown in Fig. 14.2. Three different landfills under different operating conditions in Vinh-Long city, Nhon-Trach city, and Bau-Can commune were selected to examine unit weight. Specifically, Hoa-Phu landfill located in Vinh-Long city consists of fresh wastes, and Dong-Mu-Rua landfill located in Nho-Trach city is a residual landfill. Meanwhile, a landfill located in Bau-Can commune contains many types of waste (e.g., fresh, old waste, and residual waste). Waste samplings of each landfill were implemented, according to the conditions of each landfill.

14.2.1.1 Tube-Based Sampling of MSW for Unit Weight Estimation

A plastic tube having a diameter of 220 mm and 600 mm in height was used to take actual samples at Dong-Mu-Rua landfill in Nhon-Trach city, as seen in Fig. 14.3. The waste was collected at four different locations (namely M01-M04) in the landfill at the same depth in the landfill (see Fig. 14.3a). The samples were carried out during the unloading of waste from the landfill, which was moved to the waste treatment areas. At the sampling (April 2017), the waste was dumped for several years, with the top layers of the landfill removed. As a result, the waste has been decomposed. Figure 14.3b shows a real image of waste sampling using tubes.

The values of unit weight in this landfill varied from 9.9 kN/m^3 (at M01) to 13.5 kN/m^3 (at M03). Meanwhile, the ones at M02 and M04 were 13.0 kN/m^3 and 14.5 kN/m^3 , respectively. The measured value was consistent with the declared MSW unit weight (Zekkos et al. 2006).



Fig. 14.2 Locations of examined unit wastes of MSW

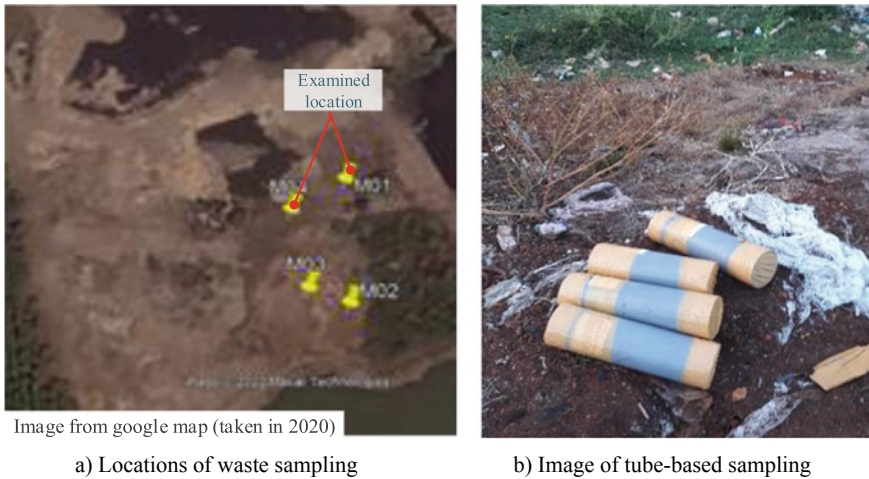


Fig. 14.3 Sampling locations of Dong-Mu-Rua landfill

14.2.1.2 Large Waste Volume-Based Sampling of MSW for Unit Weight Estimation

The method can be applied to landfills with various waste components. A large amount of waste is excavated using an excavator to put into waste containers. The use of waste containers helps to estimate waste volume accurately since it is very hard to keep a stable excavation pit in-site. Then, the waste was weighed, and its volume was measured to compute the unit weight. This method was applied to calculate the unit weight for two landfills, including landfill BCL01 (see Fig. 14.4) and landfill Hvs1 (see Fig. 14.5) in Bau-Can commune (see Fig. 14.2).

For Landfill BCL01, the landfill was covered by soil and HDPE membrane to close the landfill. The waste includes various waste types (new and old waste) received from residual landfills, including from the Dong-Mu-Rua landfill. The samples were

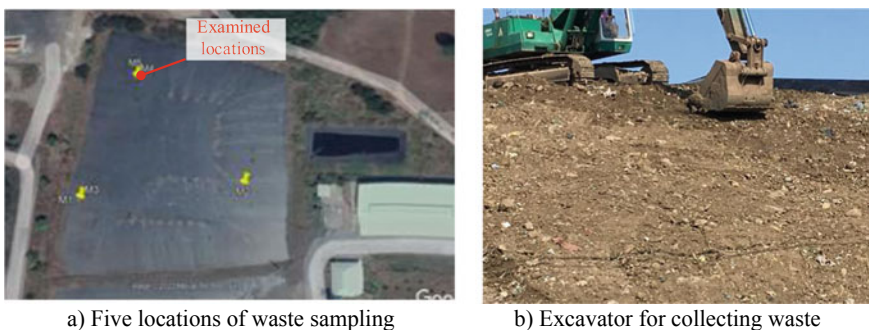


Fig. 14.4 Sampling locations for landfill BCL01 in Bau-Can commune

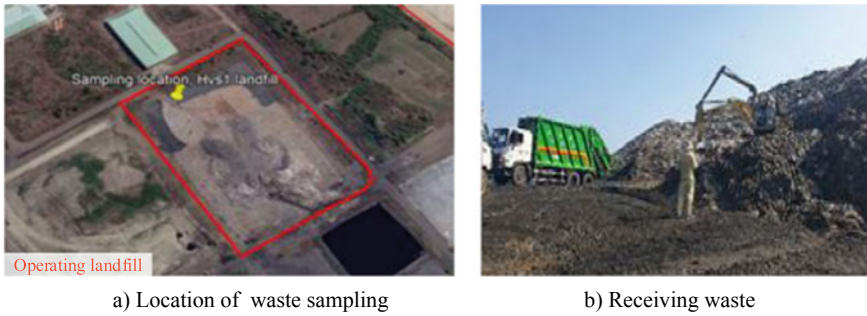


Fig. 14.5 Sampling locations of Bau Can landfill for landfill Hvs1 in Bau-Can commune

taken at a depth of 4–6 m at random locations in the landfill. Figure 14.4a shows five locations (namely M1–M5) for collecting waste in landfill BCL01, and Fig. 14.4b shows an image of the excavator used to get waste put into waste containers. The unit weight was recorded from 12.89 kN/m³ (at M5) to 15.65 kN/m³ (at M1). Meanwhile, the unit weight values at M2, M3, and M4 were 14.24 kN/m³, 13.36 kN/m³, and 13.21 kN/m³, respectively. The measured values at landfill BCL01 are relatively higher than that at Dong-Mu-Rua landfill (9.9 kN/m³ to 13.5 kN/m³) (see Sect. 2.1.1). It could come from the process of transforming old waste, compaction, and different sampling times.

For landfill Hvs1, the landfill is in the operational process, as shown in Fig. 14.5. The location of BCL01 and Hvs1 was close to each other in Bau-Can commune. Waste samples were at one location (see Fig. 14.5a) for different depths from the surface. Totally five samples (namely S1–S5) were collected at an interval of 1 m from the top surface of the landfill. The unit weight corresponding to 1 m depth of waste was 6.04 kN/m³ at S1, 8.87 kN/m³ at S2, 12.17 kN/m³ at S3, 11.34 kN/m³ at S4, 12.88 kN/m³ at S5. The average waste unit weight was about 10.26 kN/m³.

According to Zekkos et al. (2006), the unit weight along with the depth of the landfill could be estimated as follows:

$$\gamma = \gamma + \frac{z}{\alpha_i + \beta_i z} \quad (14.1)$$

where γ_i is the near-surface in-place unit weight (kN/m³), z is the depth (m) weight γ to be estimated, α (m⁴/kN) and β (m³/kN) are modeling parameters.

Table 14.1 shows the comparison of the measured value of the unit weight and estimated ones using Eq. (14.1). In the calculation, $\gamma = 20$ kN/m³ was applied to calculate the coefficient β , and the coefficient α was determined according to the actual unit weight at a depth of 1 m and 5 m. In the table, the γ_{real} represents for measured unit weight at S1–S5 in landfill Hvs1. The result shows a relatively good estimation of unit waste using the empirical equation (Zekkos et al. 2006).

Table 14.1 Comparison of actual unit weight (landfill Hvs1) and estimated one using an empirical equation

z	γ_{real}	α	β	$\gamma_{estimated}$	Difference
m	kN/m ³	m ⁴ /kN	m ³ /kN	kN/m ³	(%)
1	6.04	0.373	0.072	6.04	
2	8.87	0.373	0.072	9.92	- 12%
3	12.17	0.373	0.072	11.14	8%
4	11.34	0.373	0.072	12.11	- 7%
5	12.88	0.373	0.072	12.88	

14.2.1.3 Compressed Waste in Pistons-Based Sampling of MSW for Unit Weight Estimation

Waste collected from households was transported using trucks. The trucks are designed with pistons to introduce pressure 4 kN/m² to compress MSW before dumping in the landfills. The method helps to reduce void and minimize wastewater in MSW before landfilling. The technique was applied to the Hoa-Phu landfill in Vinh Long province, as seen in Fig. 14.6. At first, the waste was sampled on the surface of the landfill at six different locations (namely SL1-SL6), and it was put into the piston with a pressure of 4 kN/m². Then, the waste was weighed to determine the weight, and the actual volume of the piston was also calculated.

The average value of unit weight was about 5.53 kN/m³, with the maximum at SL3 (8.4 kN/m³) and a minimum at SL5 (3.39 kN/m³). Meanwhile, the values of unit weight at other locations were 7.08 kN/m³ for SL1, 6.33 kN/m³ for SL2, 3.73 for SL4 kN/m³, and 4.15 kN/m³ for SL6. The unit value is consistent with the official data (5.2–8.0 kN/m³) by Vietnamese officials (No. 01/2001/TTLT-BKHCNMT-BXD dated 18/01/2001).



Fig. 14.6 Pictures of Hoa Phu landfill in Vinh Long province

14.2.2 Estimation of Municipal Solid Waste Unit Weight for Current Landfill

It is necessary to estimate the unit weight of MSW for checking slope stability or increasing landfill capacity in some cases. As shown in Fig. 14.7, two landfills, namely BCL02 and BCL01A, are located close to each other in the Northwest Complex HCM city. The landfill BCL1A is going to close, and it was equipped with the instrumentation to obtain the necessary parameters for calculating the weight unit. Meanwhile, the landfill BCL2 is planning to increase capacity under rapid MSW in HCM city. The unit weight from BCL1A was used to check the stability (not presented in this study) and to determine the capacity of the BCL2. As zoomed in the figure, the status of the landfill BCL2 before increasing volume capacity (taken in 2013).

To estimate the unit waste, the data for the calculation includes the total amount of received waste, amount of soil cover, amount of rainfall, amount of leachate pumped to treat, and amount of evaporation. The calculation of the unit weight of the current landfill is compared with measured settlement data (bottom ground settlement) and measured pressure at the landfill bottom. The unit weight of MSW is determined using the formula:

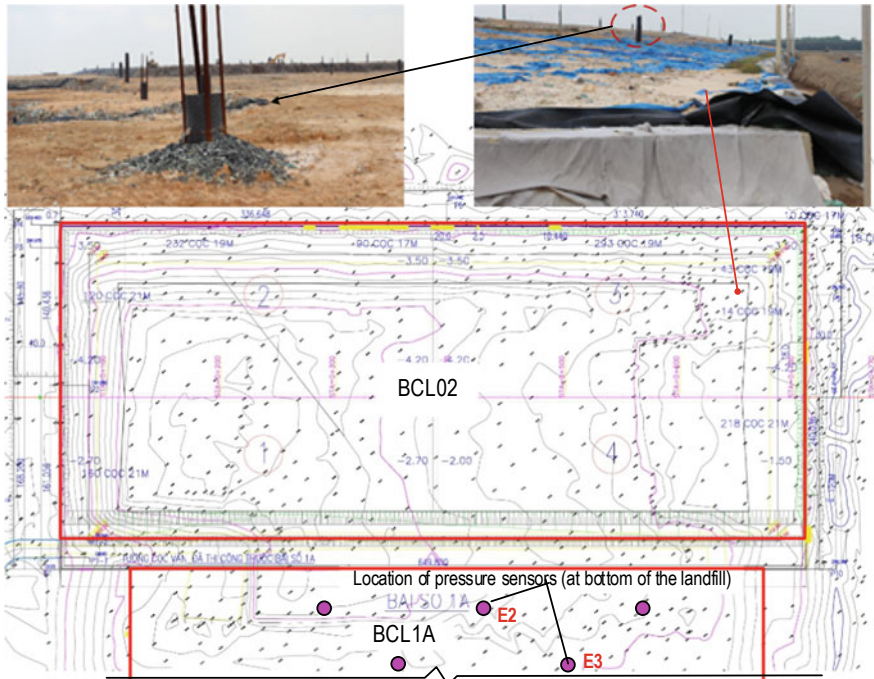


Fig. 14.7 Picture and layout of BCL1A, BCL02 landfill, Northwest complex

$$\gamma_r = \frac{M}{V} \quad (14.2)$$

where γ_r is the unit weight of MSW, M and V are the total weight and total volume of the landfill BCL1A.

The total weight (M) is calculated based on the amount of landfilled waste (M_1 , according to data from weighbridge, decomposition amount (namely M_2 due to biogas generation), covering soil layers (namely M_3), rainfall water weight (namely M_4), leachate weight (namely M_5), and the bottom structure layer weight (namely M_6 , 0.7 m thick and unit weight of 1.8 ton/m³). Total volume (V) is calculated based on geometric volume corresponding to the actual height of landfill (namely V_1), and ground settlement volume due to a load of waste (namely V_2). The details of the calculation process are shown in the following sections.

14.2.2.1 Determining Total Landfill Weight of BCL 1A

Landfill BCL1A received waste 1,186,484 tons in 2007–2008, specifically 613,904 tons in 2007 and 572,580 tons in 2008. In 2009, based on the measured pressure at the bottom of BCL1A (see locations in Fig. 14.7), the remaining waste was about 1,083,450 tons. It meant that the volume of decomposed waste was about 103,034 tons. It was assumed that one-ton waste generated 161.480 m³ CH₄ and 140.631 m³ CO₂, equivalent to 385 kg. The amount of waste lost due to decomposition into biogas (M_2) by 2009 was 39,668 tons.

The volume of covering soil layers with 2 m height of waste covered by 0.2 m covered soil (based on approved project document) was 99,384 m³. For the unit weight of 1.8 tons/m³, the total soil weight (M_3) was 178,891 tons. Table 14.2 shows measured rainfall and evaporation data in 2007, 2008, and 2009 at the landfill. As seen in the table, water entering landfills (M_4) was about 162,547 tons.

For the average amount of leachate pumped for treatment of 400 m³ per day, the weight of M_5 was about 146,000 tons per year. The weight of the bottom layer of the landfill (M_6) was about 122,850 tons, in which landfill has a size of 650 × 150 m.

The total weight (M_1) of the landfill BCL1A was determined using Eq. (14.3). The total weight was estimated at about 1,465,104 tons. The average pressure at the bottom of the landfill was 15.03 tons/m², which was the weight per area of landfill (650 × 150 m).

Table 14.2 Measured rainfall and evaporation within BCL1A landfill area

Year	2007	2008	2009	Sum
Rainfall (tons)	56,886	176,777	193,040	426,704
Evaporation (tons)	29,279	117,439	117,439	264,157
Water entering landfill (tons)	27,607	59,339	75,602	162,547

Table 14.3 Measured pressure at the bottom of landfill BCL1A

Value/date	17/09/2009	11/01/2010
Point E2 (tons/m ²)	11.30	11.15
Point E3 (tons/m ²)	15.96	15.66
Average (tons/m ²)	13.63	13.40
Different from calculation result (%)	10	12

$$M = M1 - M2 + M3 + M4 - M5 + M6 \tag{14.3}$$

Table 14.3 shows the real measured data for the pressure at the bottom of the landfill BCL1A in two years 2009–2010 at two-point E2 and E3 (see marked in Fig. 14.7). The average pressure was about 13.63 tons/m² for data in 2009 and 13.40 tons/m² for data in 2010. Compared with the estimated data (15.03 tons/m²), the differences in calculation and measured data are slightly different. There are some reasons that could cause the differences. First, the calculated bottom pressure is the average waste data in the whole landfill. Second, the measured data represents the pressure at the local measuring points. Third, the amount of evaporation, leachate, and waste decomposition may not be accurately estimated. Last, the changes in geometric parametric parameters of landfills or foundation settlement could also have effects on the estimation result.

14.2.2.2 Determining Total Volume of BCL 1A

Because the landfill was built on soft clay layers (i.e., organic clay mud and bluish-grey), the settlement of the landfill could be large. To determine the volume of the landfill, it is necessary to determine the settlement of the landfill bottom. Twelve locations (namely P1-P12) were picked to measure the settlement of the landfill BCL1A. The measured points P1, P3, P9, and P12 were located at the near edge of the landfill, and the remaining measured points were placed in the middle of the landfill at the bottom. Table 14.4 shows the measured bottom settlement of landfill BCL1A. The average settlement at the edge of the landfill was about 1.28 m (calculated from data at P1, P3, P9, and P12). Meanwhile, the average settlement in the middle of the landfill was about 4.17 m. Overall, the average settlement of the landfill BCL1A was about 3.2 m (Average value was from 12 measured data P1-P12). Meanwhile, the calculation settlement is 2.0–5.1 m.

Table 14.4 Measured bottom settlement for the middle and edge locations of landfill BCL1A

Measured points	P1	P2	P3	P4	P5	P6	P7	P8	P9	P10	P11	P12
Settlement (m)	0.79	3.04	1.28	2.55	5.43	7.98	4.01	3.36	1.65	3.27	3.72	1.4

With the measured elevation of the top of the landfill being + 14.0 m, the volume of the landfill was 964,215 m³ (V1), calculated using the geometric parameters of the landfill. The volume induced by settlement was about 312,000 m³ (V2), which was calculated from 3.2 m by multiplying by the landfill area. The total volume (V) of the landfill, including the settlement, was 1,276,215 m³.

14.2.2.3 Estimation of Unit Weight of MSW for BCL1A

The average unit weight of waste was estimated at about 1.148 tons/m³, calculated using Eq. (14.1). The calculated unit weight from landfill BCL1A was applied to compute the increasing capacity of landfill BCL02. As a result, the capacity of BCL02 increased 30%, from 4.5 million tons to 6.0 million tons. The increasing capacity of landfill BCL02 was conducted from 2013 to 2015. The landfill BCL02 has been successfully operated without any problems, thus evidencing the correctness of the calculation method.

14.3 Discussion on Effects of MSW Unit Weight on Waste Management

From experimental results, it is found that the unit weight of different landfills in the southern provinces of Vietnam was quite different. The unit weight of MSW varied from 6.04 to 15.65 kN/m³ for landfill Hvs1 (Bau-Can commune), 9.9–13.5 kN/m³ for Dong-Mu-Rua residual landfill. Additionally, the unit weight of old waste in some landfills in An Giang province was recorded with an average value of 9.34 kN/m³ (according to No. 4902/SXD-KT&QLXD dated December 31, 2021 by the Department of Construction of An-Giang province). The experimental results in the study were quite consistent with the previous studies (Raviteja et al. 2021; Zekkos et al. 2006). Generally, the MSW from different sources have different values, but the unit weight of compacted waste has a higher value than that of un-compacted one. Moreover, the unit weight of the old waste is higher than that of the new one, and the near-bottom layer waste yields a higher unit weight.

The unit weight of MSW is an important parameter in the calculation of the structure of landfills as well as related waste treatment construction. The changes in unit weight could have an effect on the calculation results. The result of MSW unit weight shows that the unit weight of waste from 5.53 to 15.65 kN/m³, thus leading to difficulties in the selection of unit weight for other works (e.g., landfill design or increasing landfill capacity). On the other hand, the weight and volume of waste are converted through the unit weight. The improper unit weight could lead to the incorrect conversion between the weight and the volume, thus causing some issues in the management and treatment of MSW.

As presented, the official value of the unit weight of waste used in the design landfill (in Vietnam) varied from 5.2 to 8.0 kN/m³. The unit value is only suitable for fresh waste (just collected from households). In fact, the unit weight is changed depending on the nature of decomposition, waste composition, and structure of the waste, as analyzed in Sect. 14.2. Moreover, when a low value of unit weight is applied for landfill design, it will lead to inappropriate design, thus causing a reduction in the volume of received waste or incorrect construction safety calculations.

In terms of waste management, environmental management agencies usually set a specific volume of the landfill that can be received. When the landfill reaches the design volume, it will be closed (according to 02/2022/TT-BTNMT dated January 10, 2022 of the Ministry of Natural Resources and Environment). As analyzed in Sect. 14.2.2, the landfill volume can be influenced by the ground settlement. The settlement can increase landfill capacity, a good point in terms of social efficiency. However, increasing dumped waste can affect construction safety and environmental safety due to damage to the waterproofing layer, the leachate collection system, and the biogas collection system. Another point, the same permit volume is not mean the same total weight of received waste, because the different of unit weight.

Currently, waste management has a significant concern in Vietnam since most landfills are open-type landfills and unsanitary (Katelijon et al. 2018). These landfills are being cleaned up by excavating and transporting to waste treatment companies to ensure the environment. It is known that the calculation of weight volume trickily depends on the unit weight. The inappropriate selection of unit weight leads to incorrect determination of the waste amount, causing disagreements about the amount of waste treatment.

14.4 Concluding Remarks

In this study, the density characterization of municipal solid waste in the southern part of Vietnam was experimentally examined. At first, the experimental test of MSW unit weight for three landfills in southern areas of Vietnam was conducted. Then, the MSW unit weight of current landfills was estimated using measured masses and total waste volume.

Regarding experimental determination of the unit weight of MSW, three methods for waste samplings were implemented, as follows:

- (1) Tube-based sampling can be applied for residual waste partially or fully decomposed.
- (2) Large waste volume-based sampling is applicable to landfills with a variety of waste types (old waste, fresh waste, and non-hazardous industrial waste).
- (3) Compressed waste in pistons-based sampling can be applied to fresh waste or waste on the surface of the landfill.

The result of the study shows that the empirical formula by Zekkos (Zekkos et al. 2006) could be applied to determine values at different depths in the Southern part of Vietnam. Moreover, it suggests that a combination of waste sampling methods should be used to determine on-site unit weight.

Furthermore, this paper presents the method to determine the waste unit weight using real monitoring data from landfill operating progress (e.g., amount of waste received, time, weather conditions). In case of no monitoring data, design data of landfills would be combined with the actual operation data to enable the calculation of weight unit. Depending on the requirement of each project, the distribution of unit weight along with the depth of the landfill can be estimated using monitoring waste properties in a landfill.

Regarding the value of unit weight of waste for waste management issues, the following remarks can be gained from the study, as follows:

- (1) The value of unit weight of MSW is a value that changes over time and the storage space due to changes in the physical and chemical properties of the waste, especially for landfills that receive many types of waste (e.g., porosity, moisture, waste composition, waste chemical component, temperature, pH, and microbial content affecting the decomposition rate of waste). The decomposition of waste leads to a change in the composition of the waste structure and vice versa, so far.
- (2) The value of the unit weight of MSW varied from 5.53 to 15.65 kN/m³. The value is quite different from the reference value announced by the Vietnamese authorities (5.2–8.0 kN/m³). The actual data proved that the unit weight value is about 5.2–8.0 kN/m³ is suitable for the fresh waste.
- (3) The improper unit weight could lead to the incorrect conversion between the weight and the volume. The same permit volume of landfill is not mean the same total weight of received waste because of the difference in the unit weight.
- (4) The calculated and surveyed values in this report were also consistent with the published values of solid waste landfills.
- (5) It is necessary to update the unit weight of waste in the authority document to help the calculation load and landfill design better. Moreover, other MSW parameters, such as internal friction angle, and physicochemical properties overtimes, need to be further considered.

References

- Alam O, Qiao X (2020) An in-depth review on municipal solid waste management, treatment and disposal in Bangladesh. *Sustain Cities Soc* 52
- Bilgin M, Tulun S (2015) Biodrying for municipal solid waste: volume and weight reduction. *Environ Technol* 36:1691–1697
- Breitmeyer RJ, Benson C.H., Edil TB (2020) Effect of changing unit weight and decomposition on unsaturated hydraulics of municipal solid waste in bioreactor landfills. *J Geotech Geoenvironmental Eng* 146

- Ding Y, Zhao J, Liu J-W, Zhou J, Cheng L, Zhao J, Shao Z, Iris Ç, Pan B, Li X, Hu Z-T (2021) A review of china's municipal solid waste (Msw) and comparison with international regions: management and technologies in treatment and resource utilization. *J Cleaner Prod* 293
- Edalatpour MA, Al-E-Hashem SMJM, Karimi B, Bahli B (2018) Investigation on a novel sustainable model for waste management in megacities: a case study in tehran municipality. *Sustain Cities Soc* 36:286–301
- Gopikumar S, Raja S, Robinson YH, Shanmuganathan V, Chang H, Rho S (2021) A method of landfill leachate management using internet of things for sustainable smart city development. *Sustain Cities Soc* 66
- Jain P, Powell JT, Smith JL, Townsend TG, Tolaymat TJES (2014) Technology: life-cycle inventory and impact evaluation of mining municipal solid waste landfills. 48:2920–2927
- Katelijin VDB, Duong CT, Joan MN, Carsten S, Gerard S, Nguyen TKT, Lieu TB, Bui TN (2018) Management assessment of solid and industrial hazardous waste: options and action area to implement the national strategy
- Kavazanjian Jr E, Matasovic N, Stokoe K, Bray J (1996) In Situ shear wave velocity of solid waste from surface wave measurements. In: *Proceedings 2nd international congress on environmental geotechnics*, Osaka, Japan, pp 97–104
- Kaza S, Yao L, Bhada-Tata P, Van Woerden F (2018) *What a waste 2.0: a global snapshot of solid waste management to 2050*. World Bank Publications
- Lu W, Tam VWY (2013) Construction waste management policies and their effectiveness in Hong Kong: a longitudinal review. *Renew Sustain Energy Rev* 23:214–223
- Matasović N, Kavazanjian Jr EJJOG, Engineering G (1998) Cyclic characterization of OII landfill solid waste 124:197–210
- Moberg Å, Finnveden G, Johansson J, Lind P (2005) Life cycle assessment of energy from solid waste—part 2: landfilling compared to other treatment methods. *J Clean Prod* 13:231–240
- Nguyen HH, Heaven S, Banks C (2014) Energy potential from the anaerobic digestion of food waste in municipal solid waste stream of urban areas in Vietnam. *Int J Energy Environ Eng* 5:365–374
- Prajapati KK, Yadav M, Singh RM, Parikh P, Pareek N, Vivekanand V (2021) An overview of municipal solid waste management In Jaipur City, India—current status, challenges and recommendations. *Renew Sustain Energy Rev* 152
- Raviteja K, Basha BMJJOH, Toxic, Waste R (2021) Characterization of variability of unit weight and shear parameters of municipal solid waste. 25:04020077
- Richter A, Ng KTW, Karimi N, Chang W (2021) Developing a novel proximity analysis approach for assessment of waste management cost efficiency in low population density regions. *Sustain Cities Soc* 65
- Zeccos DP (2005) *Evaluation of static and dynamic properties of municipal solid-waste*. University Of California, Berkeley
- Zekkos D, Bray JD, Kavazanjian E, Matasovic N, Rathje EM, Riemer MF, Stokoe KH (2006) Unit weight of municipal solid waste. *J Geotech Geoenvironmental Eng* 132:1250–1261

Chapter 15

Assessment of Lead (Pb) Accumulation in Native Plants Growing on Coal Mine Site in Northeastern Vietnam



Bui Xuan Dung , Truong Ngoc Anh , and Nguyen Thi My Linh 

Abstract Heavy metals are environmental contaminants that are hazardous to soil, water, animals, and human health. Recently, the problem of heavy metal treatment in soil after mining has been studied by many scientists both at laboratory and field. The application of native plants in treating heavy metals (Phytoremediation) in the soil after mining is interesting, appreciated, and highly applicable because of its friendliness to the polluted environment, cost-saving, improving the landscape and environment, and favorable for long-term implementation. The primal objective of this study was to examine the tolerance of native plants to lead (Pb) accumulation in soil. The plant samples and soil samples were taken analyzed for Pb concentration. Research results showed that, all three species of plants had the ability to grow and develop well in the environment with the concentrations of Pb. The average Pb accumulated was the highest in *Lantana camara* at 3.38 mg/kg, followed by *Eleusine indica* and *Aglaonema muntifolium* at 1.67 mg/kg and 1.37 mg/kg, respectively. Based on the enrichment coefficients for stem-leaves and root values, plant was separated into two group including hyperaccumulator (*Aglaonema muntifolium*) and phytostabilizer (*Lantana camara* and *Eleusine indica*). Our study suggested the effectiveness of some native plant species in treating Pb contaminants in soil, this result can be applied in mitigating the effect of heavy metals caused by mining on environmental and human health.

Keywords Heavy metal pollution · Lead (Pb) accumulation · Mining · Native plants · Phytoremediation

B. X. Dung (✉) · T. N. Anh

Department of Environmental Management, Vietnam National University of Forestry, Xuan Mai, Hanoi 13417, Vietnam
e-mail: buixuandungfuv@gmail.com

N. T. M. Linh

Department of Symbiotic Science of Environment and Natural Resources, United Graduate School of Agricultural Science, Tokyo University of Agriculture and Technology, Tokyo 183-8509, Japan

15.1 Introduction

Mine activities have been considered as the main hazardous land uses that lead to the serious consequences on terrestrial ecosystems, particularly because of the long-lasting contamination and risks from heavy metals generated and released into the environment (Hye et al. 2008; Mileusnić et al. 2014). Metals are released from mining sites via activities including mining-milling, ore concentrating, refining processes, and disposal of tailings, and waste rock (Hien et al. 2012). Indeed, the high level of heavy metal derived from the weathering processes of minerals, tailings and waste rock, then concentrated in soil resources and water resources neighboring to mining sites has been reported in many of previous studies (Lee et al. 2001; Israel et al. 2004; Aparajita et al. 2006). The impacts of heavy metal on human health are of concern as the cause of cytotoxicity, mutagenicity, and carcinogenicity (Lim and Schoenung 2010).

In recent decades, the remediation to reduce the concentration of heavy metal in soil and their risks to human health has become a worldwide environmental goal (Sivarajasekar and Baskar 2014). The treatment of heavy metal contaminated soils is complicated and often incomplete because the properties of the soil are changed when associated with heavy metals. Many physio-chemical methods have been selected to treat soil contaminated with heavy metals such as soil washing, concreting, chemical precipitation, thermal desorption, redox, adsorption, incineration, and solidification (Traina et al. 2007; Karthik et al. 2016; Muthusaravanan et al. 2018). Conventional techniques for pollution control can be very effective in solving the contamination, however, on the other hand, these methods have certain disadvantages because of the high cost, high energy consumption, large quantities of wastes that require disposal, and the high potential of contaminants exposure for surrounding residents (Moeller 2005; Vidalli 2005). This situation raises the need for a more eco-friendly and effective approach to rectify polluted soil.

Currently, the method of using plants to treat heavy metals in the soil (Phytoremediation) has been emphasized as an effective and potential strategy for cleaning soil polluted by heavy metals (Edgar et al. 2002). This remediation is outweighed as it provides cheaper, high efficiency, and environmentally acceptable technology for the bioremediation of contaminated soil (Glick 2010; Eslamian 2016). One of the mechanisms of phytoremediation is phytoaccumulation, which is the process of contaminants absorption by plants, the absorbed contaminants then being accumulated in shoots, leaves, and other plant parts (Muthusaravanan et al. 2018; Rashid et al. 2014). This is the best method to be able to remove the pollutant from the soil and then sequester it without destroying the structure and fertility of the soil (Ghosh and Singh 2005). Indeed, numerous of previous studies have focused on the effectiveness of phytoremediation. For instance, (Conesa et al. 2007) reported that *Zygophyllum fabago* can accumulate Pb concentration in soil at 750 mg/kg in the shoots. In another study, (Altinozlu et al. 2012) found that in the polluted area where the soil contains of 2000–3000 mg Ni per kg soil, *Isatis pinnatifida* has the ability to absorb and accumulate Ni contaminant up to 1441 mg/kg in the above-ground plant parts. The

exceptional ability of metal accumulation was also found in *Noccaea caerulescens*, this species can accumulate up to 26,000 mg/kg Zn without any symptom of injuries (Brown et al. 1995).

Despite the current efforts to develop plant base remediation, the selection of suitable plants that can show advanced performance in phytoremediation is still critical and remains certain difficulties (Pan et al. 2019). The adaptation of plant to the environmental conditions of target regions is remaining as the drawback for the success of the phytoremediation strategy (Mahar et al. 2016). Native plants therefore should be an important aspect in treating heavy metal pollution using phytoremediation. Native plant species are often more resistant to changes in their habitat, they perform better in terms of survival, growth, and reproduction compared to exotic species, behind, they are more tolerant to metal pollution in specified soil conditions (Frérot et al. 2006; Yoon et al. 2006; Antosiewicz et al. 2008). Thus, the assessment of native plants that grow naturally around mining and mineral processing areas in treating heavy metal pollution becomes essential.

Vietnam is a developing country, located in Southeast Asia. In recent decades, the rapid industrialization and development of a market for environmental services had led to many issues of environmental protection and sustainable development, among them, the mining waste disposal program became one of the Vietnamese government's strategic priorities (Xuan et al. 2013). Indeed, Vietnam has been ranked as the third-largest mineral producer among Southeast Asian countries (Khoi 2014). The northern part of Vietnam has abundant of Pb and Zinc with a total ore reserve of up to 97 million tons and a lot of metalliferous mines have been established (Tran et al. 2009). Along with the growth of the Vietnamese economy contributed by mining, there are the risks of high contents of heavy metals in waste dumps and soil around mining areas (e.g., Chu Ngoc et al. 2009; Anh et al. 2011; Xuan et al. 2017). Therefore, the monitoring of native plants phytoremediation in soil pollution is needed especially in the vicinity of mining areas in Vietnam. The goal of this study was to examine the tolerance of native plants to lead (Pb) accumulation in soil in northeastern Vietnam. To this end, the concentration of lead in soil at the study site was determined and the ability to absorb and accumulate lead of native plants were examined. Based on the results of this study, we proposed solutions to apply plants in the treatment of lead pollution in soil due to mineral mining.

15.2 Study Site and Method

15.2.1 Study Site

This study was conducted in Vang Danh coal mine, which is located in Uong Bi city, Quang Ninh province, northeastern Vietnam (20° 58' N, 106° 41' E, Fig. 15.1a–c). Vang Danh coal mine is owned by Vang Danh Coal Joint Stock Company—a member of Vietnam National Coal-Mineral Industries Holding Corporation Limited. Vang

Danh is known as the largest underground coal mine in Vietnam's coal industry, the area of the mine site is 2000 ha. The climate is warm and temperate with a mean annual temperature of 22.2 °C and an average annual rainfall of 1600 mm (Son et al. 2019). The rainy season occurs from June to August, accounting for 60% of annual rainfall, while the dry season is usually from November to April. The coal-bearing strata mostly combine of Conglomerate, sandstone, siltstone, claystone, clay-coal, and coal seams (Dung and Quang 2021). The native plant species of the study site mainly belong to Fabaceae, Moraceae, Araceae, Verbenaceae, Poaceae, Polypodiaceae, and Piperaceae. The mining area has been established since 1964. The extent of coal mining has been increased for both open pit and underground mines. Coal mining brings back huge economic benefits, however, the heavy metal pollution in the soil caused by mining activities poses a big threat to the environment and human health (Hai 2007).

15.2.2 Sampling and Analyzing of Soil and Plant Species

Three different areas in the coal mine site were selected for sampling and analysis (Fig. 15.1b). These three areas were located surrounding the mine dump and were covered by a large number of native species. The detailed field survey of soil and native plants was conducted in August/2021.

Soil samples were collected by using the stainless-steel sampler (Diameter: three cm, Height: 20 cm). The samplings were processed following a mixed sampling method (Vietnam Standard 2005). In general, three soil samples including topsoil and subsoil within the top 20 cm were taken, the total amount of each sample was 200 g. The samples then were air-dried, sieved to < two mm, and stored in plastic bags.

The selection of plants for accessing the ability to absorb and accumulate Pb in soil was based on plant coverage of the site as well as plant health. The three most common distributed plant species that grow directly in the coal field of the study area were monitored, including *Aglaonema muntifolium*, *Lantana camara*, and *Eleusine indica* (Fig. 15.1d–f). These plant species associated with soil samples were collected in the same area (Fig. 15.1b). Each plant was divided into three parts, which are root, stem, and leaves. The vegetable samples were stored in plastic bags after being manually washed with tap water and rinsed with deionized water three times to remove dust.

For the chemical analysis, all the soil and plant samples were sent to the Mekong Institute of Science and Technology in Hanoi. The concentration of Pb in soil was determined by flame atomic absorption spectrometry analysis (TCVN 6496:2009). This method is based on atomic absorption spectrometry of elemental concentrations in Aqua Regia sample extracts prepared in accordance with ISO 11466. Used 217.0 nm wavelength is used and the flame type is oxidizing air. Whereas the Atomic absorption spectrometric method was applied to examining Pb concentration in plants after dry ashing (AOAC 999.11). The test portion is dried and then ashed at 450 °C with increasing temperature. Add six M hydrochloric acid solution and evaporate

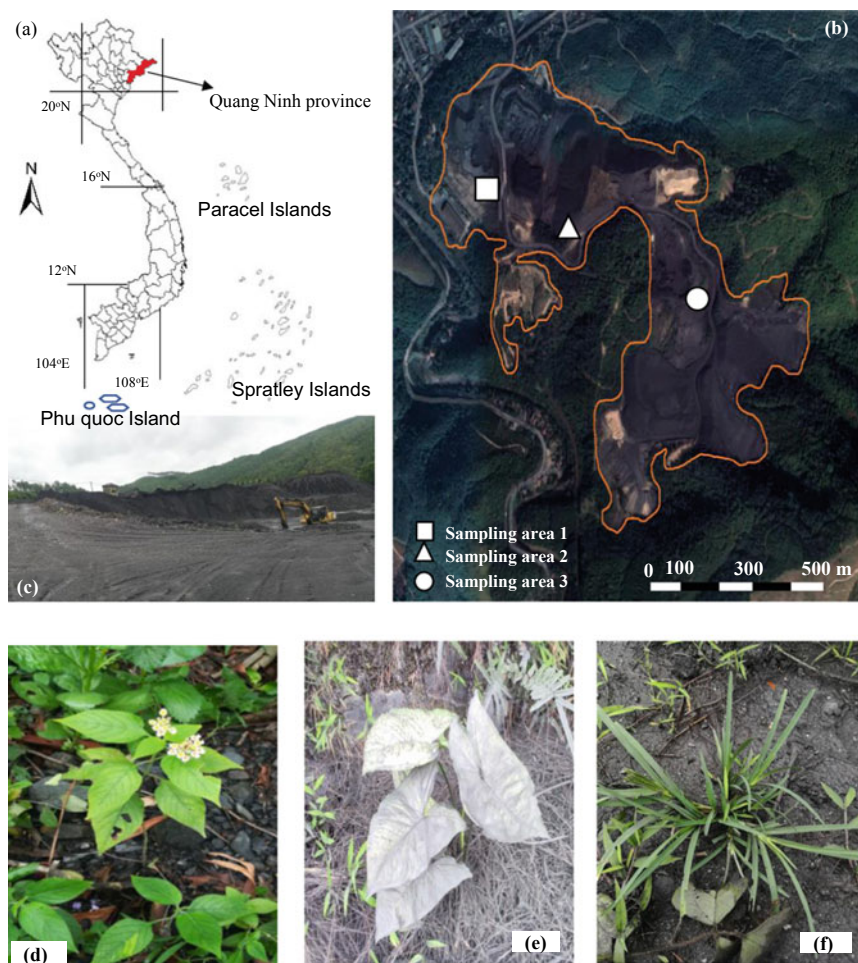


Fig. 15.1 a Location of the study site; b Landsat image the of study site; c photo of the study site; photo of sampling plant species d *Lantana camara*; e *Aglaonema munitifolium*; f *Eleusine indica*

to dryness. The residue was dissolved in 0.1 M nitric acid solution, the analytical samples were determined by flame atomic absorption spectrometry using a graphite furnace.

Bioconcentration factor (BCF), bioaccumulation factor (BAF) and translocation factor (TF) were used in data analyzing (Yoon et al. 2006; Caille et al. 2005; Zu et al. 2005). BCF is calculated as the ratio between the Pb content in the roots with the total Pb content in the original soil, while BAF is calculated by considering Pb concentration in stem-leaves with respect to soil Pb concentrations. The BCF and BAF accumulation coefficient reflects the ability of plants to accumulate Pb

from soil to plants and is used to assess the potential for pollution treatment of plant species (Ghosh and Singh 2005). TF is the ratio between the Pb content in the stem—leaves with the corresponding content in the roots. This index evaluates the ability to transport Pb from the roots to the leaves (Zhang et al. 2002).

Analysis of variance (ANOVA) was performed to determine statistical differences between Pb concentration in soil, plant parts, BCF, BAF, and TF values with a confidence level of 0.95 ($P < 0.05$), using SPSS for Windows, version 20.

15.3 Result and Discussion

15.3.1 Biomass of Plants

The result of fresh biomass of sampling plant species was present in Table 15.1. For all species in three sampling areas, the biomass of stem-leaves was higher compared to that of roots (Table 15.1; Fig. 15.2). The average above-ground biomass of *A. muntifolium* and *L. camara* was comparable at 11 g, whereas there was a slightly different in root biomass of these two species at four and five g, respectively. The lowest biomass was found in *E. indica*, the average biomass of stem-leaves and roots in turn were seven g and two g (Fig. 15.2). Among of three sampling areas, area three had the highest total plant biomass, which was 70% higher than the biomass of area one and 34% higher than the biomass of area two (Table 15.1).

15.3.2 Concentration of Pb in Soil and in Native Plant Species

The mean Pb concentration in soil samples of the study site was 54 ± 18 mg/kg (Table 15.1). Soil Pb concentration in this study was within the Vietnamese standard for Pb concentration in soil (QCVN 03: 2015). There were significant differences among Pb concentrations in three sampling areas with the p -value < 0.05 . The contents of Pb detected in order of smallest to largest were 34.8 mg/kg in area one, 55.7 mg/kg in area two, and 70.8 mg/kg in area three (Table 15.1).

The results of the Pb concentration in plant species grown in coal mine site were presented in Table 15.1. The total concentration of Pb in *L. camara* ranged from 1.62 to 5.26 mg/kg, whereas, in *A. muntifolium* and *E. indica* these values fluctuated from 0.61 to 1.99 mg/kg and 0.86 to 2.84 mg/kg, respectively. In general, the highest concentration of Pb was found in *L. camara*. The concentration of Pb in plants varied among sampling areas, all monitored species in area one contained the lowest amount of Pb, whereas the concentration of Pb in area three was consistently the highest for all sampling plant species (Table 15.1).

Table 15.1 Summary table of plant biomass, Pb concentration in stem-leaves, root and soil, bioaccumulation factor, bioconcentration factor and translocation factor

Area	Pb concentration in soil (mg/kg)	Species	Plant biomass (g)		Pb concentration in plant (mg/kg)			Percentage of Pb accumulated (%)		BAF	BCF	TF
			S + L	R	S + L	R	Total	S + L	R			
1	34.79	<i>A. muntifolium</i>	9.73	3.07	0.35	0.26	0.61	58	42	0.010	0.007	1.35
		<i>L. camara</i>	8.05	3.15	0.76	0.86	1.62	47	53	0.022	0.025	0.87
		<i>E. indica</i>	5.61	2.12	0.17	0.69	0.86	20	80	0.005	0.020	0.25
2	55.68	<i>A. muntifolium</i>	10.90	3.46	0.95	0.56	1.51	63	37	0.017	0.010	1.69
		<i>L. camara</i>	10.56	4.97	1.27	1.99	3.26	39	61	0.023	0.036	0.64
		<i>E. indica</i>	6.96	2.79	0.42	0.88	1.30	32	68	0.008	0.016	0.48
3	70.82	<i>A. muntifolium</i>	12.52	4.63	1.27	0.72	1.99	64	36	0.018	0.010	1.77
		<i>L. camara</i>	14.13	7.26	2.96	2.30	5.26	56	44	0.042	0.032	1.29
		<i>E. indica</i>	7.83	3.89	0.95	1.89	2.84	34	66	0.013	0.027	0.51

S Stem; L Leaves; R Root; BAF bioaccumulation factor; BCF Bioconcentration factor; TF Translocation factor

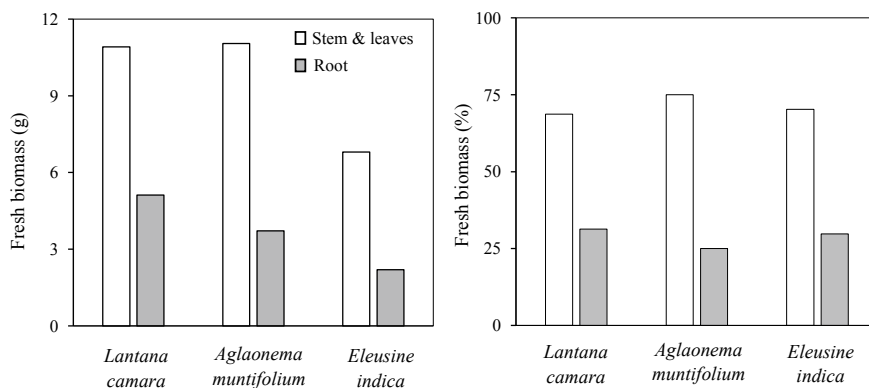


Fig. 15.2 Average biomass and percentage of fresh biomass of stem-leaves and root of the monitored plants

Identifying the tolerance plant that can adapt to local climate and soil condition is essential for soil remediation, thus native plant species have been selected because of their suitability. In this study, none of the visible toxicity symptoms, such as whitish-brown chlorosis, or young leaves deformation were observed in the monitored species. All the studied plants grew normally and exhibited tolerance to Pb contamination. Pb concentrated in the different parts of the plant varied among species (Figs. 15.3 and 15.4). The average concentration of Pb in the stem was the lowest in all species at 0.62 mg/kg in *L. camara*, 0.33 mg/kg in *A. muntifolium* and 0.13 mg/kg in *E. indica* (Fig. 15.3). Pb concentrated in roots was higher than that in the leaves in *L. camara* and *E. indica*. In particular, the average level of Pb in root and leaves of *L. camara* were 1.72 mg/kg and 1.04 mg/kg, respectively. Average root and leaves Pb values of *E. indica* were 1.15 mg/kg and 0.39 mg/kg, respectively. In *A. muntifolium* root and leaves Pb concentrations were similar at 0.51 mg/kg and 0.53 mg/kg, respectively (Fig. 15.3). In general, the concentration of Pb in plants in this study was significantly lower than that in previous studies of (Pan et al. 2019; Nguyen et al. 2009; Petelka et al. 2019), however, results from monitored plants were higher compared to Petelka et al. (2019), suggesting the influence of plant species, the environmental concentrations of heavy metals, and other environmental factors to the concentration of heavy metals in plants.

L. camara and *E. indica* contained the higher amount of Pb in the root parts, which account for 50–70% of the total Pb accumulated. Plants with these characteristics are highlighted to be the potential plant for phytostabilization purposes (Mendez and Maier 2008; Ali et al. 2013). The high concentration of Pb in roots is possibly related to the features of the root system. The study by Pinto et al. (2015) has pointed out that the dense and tough root system is also important for absorbing metals in contaminated soil. *L. camara* and *E. indica* have a notably tough root system, this characteristic can enhance the ability to absorb and accumulate Pb, thus making these species the good candidates for Pb phytostabilization (Pan et al. 2019). In the

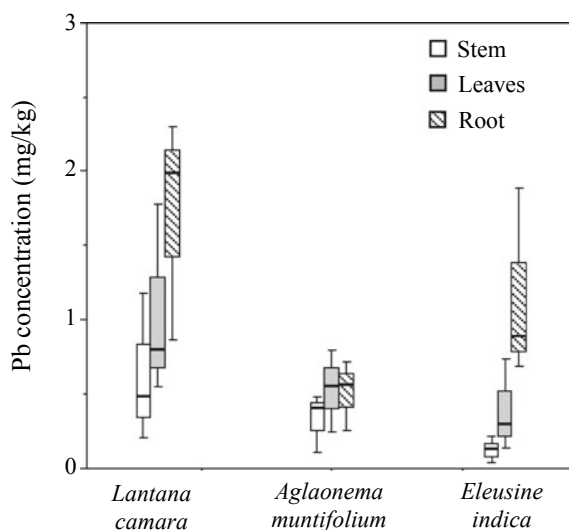


Fig. 15.3 Box-plot results of Pb concentration in stems, leaves and roots of the monitored plants. The length of the box represents the sample interquartile range, the cross bar in the box the sample median, the notch its 95% interval

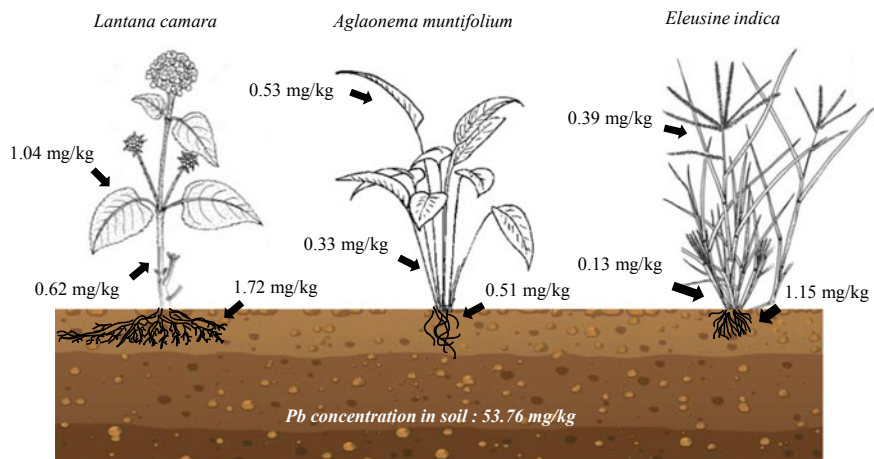


Fig. 15.4 Illustration of Pb concentration in stems, leaves and roots of monitored plants

contrary, *A. muntifolium* exhibited the higher concentration of Pb in the stem-leaves than in the root, suggesting a high transportability for metals from the root to the above-ground parts. Besides the capacity of metal uptake via the xylems, atmospheric deposition of Pb may be another factor that resulted in the high concentrations of stem and leaves (Temmerman et al. 2015).

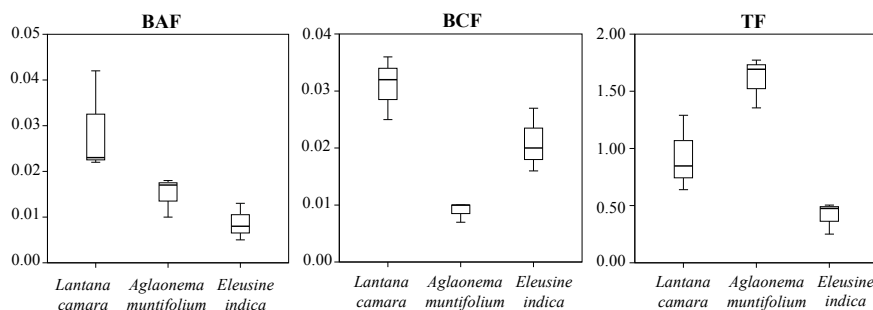


Fig. 15.5 Box-plot results of bioaccumulation factor, bioconcentration factor and translocation factor. The length of the box represents the sample interquartile range, the cross bar in the box the sample median, the notch its 95% interval

15.3.3 The Effectives of Native Plants Remediation in Pb Treatment

The BAF, BCF, and TF are the key factors in evaluating and qualifying the heavy metal hyperaccumulator (Pan et al. 2019), in this study, these factors were used to evaluate the phytoremediation potential of plants.

The BAF values of plants ranged from 0.005 to 0.042 and the accumulation coefficient BCF in the root part varied from 0.007 to 0.036 (Table 15.1; Fig. 15.5). *L. camara* had the highest ability to absorb and accumulate Pb with the average BAF and BCF were 0.029 and 0.031, respectively. The average value of BAF and BCF in *A. muntifolium* in turn were 0.015 and 0.001. *E. indica* had the lowest BAF value among species, which was 0.008 and the BCF value was 0.021 for average (Table 15.1).

The TF value was found to be the highest in *A. muntifolium*, with all the measurement values larger than one, the average TF value for this species was 1.606. TF value was followed by *L. camara* at 0.952 and *E. indica* at 0.410 for average. The significant difference in the TF value of *A. muntifolium* and *E. indica* with p -value < 0.05.

The BAF, BCF, and TF of plant species varied among the sample sites, suggesting the diversity in heavy metal tolerance, absorption and translocation varied with genotypes. These results are possibly explained by the environmental condition and the characteristic of the plant itself. The ability to absorb and accumulate heavy metals in plants depends on many factors, for example, the bioavailability of metal within the rhizosphere (Petelka et al. 2019), the characteristic of the root systems that determine how heavy metals are absorbed and fixed within the root cells (Muthusaravanan et al. 2018), xylem loading capacity and cellular tolerance to toxic metals of the plant (Pan et al. 2019). Plant species that had a BAF, BCF, or TF smaller than one are unsuitable for phytoextraction, which is the withdrawal of heavy metals by the harvestable

parts of roots, stems, and leaves (Kumar et al. 1995; Fitz and Wenzel 2002). Based on the result, none of the studied species is recommended for phytoextraction. TF indicates the efficiency of a plant in translocating heavy metals from roots to aerial parts (Zhang et al. 2002). TF larger than one also indicates that a large portion of Pb was transported from root to stem and leaves then accumulated in the above-ground parts of plants. The low TF value from the plant might relate to the metal toxicity that can damage photosynthetic activity, chlorophyll synthesis, and antioxidant enzymes (Chaabani et al. 2017). When the value of TF is larger than one, the plant is a hyperaccumulator, and if TF is smaller than one, the plant is a phytostabilizer (Yoon et al. 2006). The result of the study indicated that *A. muntifolium* was the hyperaccumulator with a higher concentration of Pb in stem-leaves than in the root part, whereas *L. camara* and *E. indica* were phytostabilizer.

The summary of Pb concentration and translocation of various plant species from other studies was presented in Table 15.2. The amount of Pb content in different plant parts of the three studied species was significantly lower compared to that from some of the previous studies (Pan et al. 2019; Chang et al. 2018), this result was attributable to the 50–1000 times lower in Pb concentration in soil from our study site (Table 15.2). Whereas, the values of bioaccumulation factor, bioconcentration factor, and translocation factor of this study were within the range of previous studies. Most of the plant species contained more metals in their roots than in the above-ground parts and can be classified as phytostabilizer. The ability of the plant to absorb and translocate heavy metals into the plant system is strongly determined by their solubility and complexity (Chaabani et al. 2017; Rungwaa et al. 2013). Pb contaminated in soil being absorbed and uptaken by plants occurs either passively with the water flow taken by roots or actively through the plasma membrane of root epidermal cells (Nouri et al. 2011).

In screening the suitable and effective plant for phytoremediation, besides the characteristics of accumulation or fixation of metals by plants, there are some other botanical features, such as abundance, a high growth rate, and good biomass yields (Ali et al. 2013) that should be considered. In general, *L. camara* and *A. muntifolium* are two species of plants with relatively large biomass, fast growth, and easy cultivation. Especially, *A. muntifolium* is hyperaccumulators, this plant can live well in soils contaminated with heavy metals and accumulate unusually high concentrations of metals in their leaves. Therefore, *L. camara* and *A. muntifolium* might be selected for Pb treatment in coal mine soil. *E. indica* is not a super-accumulator of Pb, however, this species can grow and develop in the mine site and can accumulate Pb, suggesting that it is a potential Pb-processing species in the soil. Behind, with the high amount of Pb content in the root, *E. indica* is an effective material for phytostabilization with a high potential to minimize the concentration of Pb in the soil while reducing the risk of entry into the food chain.

Table 15.2 A review on accumulation of Pb in native plants from mine site

Species	Pb concentration in plant (mg/kg)		Pb concentration in soil (mg/kg)	BAF	BCF	TF	References
	Stem and leaves	Root					
<i>H. incana</i>	9.6–25.4	6.2–11.7	2710.1–2730.9	0.004–0.009	0.002–0.004	1.55–2.16	Chaabani et al. (2017)
<i>D. gnidium</i>	2.9	11.5	1841.6	0.002	0.006	0.25	Chaabani et al. (2017)
<i>A. mauritanien</i>	8.5	9.0	4476.5	0.002	0.002	0.94	Chaabani et al. (2017)
<i>R. alba</i>	4.0	4.5	3383.6	0.001	0.001	0.89	Chaabani et al. (2017)
<i>E. elaterium</i>	6.4	20.8	4476.5	0.001	0.005	0.31	Chaabani et al. (2017)
<i>G. verum</i>	7.9	12.6	3597.1	0.002	0.004	0.62	Chaabani et al. (2017)
<i>J. acutus</i>	2.2	30.1	3873.6	0.001	0.008	0.07	Chaabani et al. (2017)
<i>C. jubata</i>	68.3	665.7	1707.0	0.040	0.390	0.09	Chang et al. (2018)
<i>M. lupulina</i>	102.4	648.7	1707.0	0.060	0.380	0.27	Chang et al. (2018)
<i>F. glyceriantha</i>	85.4	580.4	1707.0	0.050	0.340	0.11	Chang et al. (2018)
<i>L. camara</i>	0.3	na	25.0	0.010	na	na	Petelka et al. (2019)
<i>L. leucocephala</i>	0.2	na	20.0	0.010	na	na	Petelka et al. (2019)
<i>M. purpurea</i>	0.4	na	20.0	0.020	na	na	Petelka et al. (2019)
<i>M. pudica</i>	0.3	na	25.0	0.010	na	na	Petelka et al. (2019)
<i>C. indicum</i>	216.0	133.0	10,800	0.020	0.012	1.60	Pan et al. (2019)
<i>E. ramosissimum</i>	90.0	192.0	1125	0.080	0.171	0.50	Pan et al. (2019)
<i>P. bungeanum</i>	273.0	249.0	568.75	0.480	0.438	1.10	Pan et al. (2019)
<i>E. indica</i>	2798.0	7474.0	46,633.3	0.060	0.160	0.40	Pan et al. (2019)
<i>D. superbus</i>	719.0	406.0	10,271.4	0.070	0.040	1.80	Pan et al. (2019)
<i>P. americana</i>	39.3	45.1	104.8	0.375	0.430	0.87	Xue et al. (2014)

(continued)

Table 15.2 (continued)

Species	Pb concentration in plant (mg/kg)		Pb concentration in soil (mg/kg)	BAF	BCF	TF	References
	Stem and leaves	Root					
<i>C. dactylon</i>	5.2	46.3	104.8	0.049	0.442	0.11	Xue et al. (2014)
<i>A. paniculatus</i>	0.3	3.5	104.8	0.003	0.033	0.09	Xue et al. (2014)
<i>A. subulatus</i>	32.3	6.0	104.8	0.308	0.057	5.38	Xue et al. (2014)
<i>H. indicus</i>	33.0 – 2616.0	67.0 – 3924.0	100.0–10,000.0	0.261–0.330	0.670–0.392	0.49–0.67	Chandra et al. (2005)
<i>P. vittata</i>	68.0	730.5	500.0	0.136	1.461	0.09	Tua et al. (2011)
<i>A. muntifolium</i>	0.35–1.27	0.26–0.72	34.8–70.8	0.010–0.018	0.007–0.010	1.35–1.77	*
<i>L. camara</i>	0.76–2.96	0.86–2.30	34.8–70.8	0.022–0.042	0.025–0.032	0.87–1.29	*
<i>E. indica</i>	0.17–0.95	0.69–1.89	34.8–70.8	0.005–0.013	0.020–0.027	0.25–0.51	*

15.4 Conclusion

The concentration of Pb in soil and dominant native plant species was investigated from Vang Danh coal mine to determine the potential capacity of these plants for phytoremediation. The concentration of Pb in soil samples varied from 35 to 71 mg/kg, and these values were within the Vietnamese standard for Pb concentration in soil. The results indicated that plant native species in the study site could grow intolerance to Pb contaminants. *L. camara* was found to have the highest Pb accumulated at 3.38 mg/kg for average. The concentrations of Pb were lower for *E. indica* and *A. muntifolium* at 1.67 mg/kg and 1.37 mg/kg, respectively. None of the studied species appeared to be suitable for phytoextraction. Based on the monitoring, the plants with high enrichment coefficients but translocation factor smaller than one like *L. camara* and *E. indica* could be appropriate for phytostabilization, while *A. muntifolium*, characterized by the translocation factor larger than one and the small biological absorption coefficient can be considered for the potential application to hyperaccumulation. The phytoremediation potential of native plant species should be investigated further for building better heavy metal remediation practices in the mine site in Vietnam to mitigate the negative impacts of mining on the environment and human health.

References

- Ali H, Khan E, Sajad MA (2013) Phytoremediation of heavy metals—concepts and applications. *Chemosphere* 91(7):869–881
- Altinozlu H, Karagoz A, Polat T, Unver I (2012) Nickel hyperaccumulation by natural plants in Turkish serpentine soils. *Turk J Bot* 36:269–280
- Anh BTK, Kim DD, Van TT, Kien NT, Anh DT (2011) Phytoremediation potential of indigenous plants from Thai Nguyen province, Vietnam. *J Environ Biol* 32:257–262
- Antosiewicz DM, Escudé-Duran C, Wierzbowska E, Skłodowska A (2008) Indigenous plant species with the potential for the phytoremediation of arsenic and metals contaminated soil. *Water Air Soil Pollut* 193(1–4):197–210
- Aparajita B, Joyanto R, Gunnar J, Prosun B, Magnus M (2006) Environmental assessment of abandoned mine tailings in Adak, Vasterbotten district (northern Sweden). *Appl Geochem* 21(10):1760–1780
- Brown SL, Chaney RL, Angle JS, Baker AJM (1995) Zinc and cadmium uptake by hyperaccumulator *Thlaspi caerulescens* and metal tolerant *Silene vulgaris* grown on sludge-amended soils. *Environ Sci Technol* 29(6):1581–1585
- Caille N, Zhao FJ, McGrath SP (2005) Comparison of root absorption translocation and tolerance of arsenic in the hyperaccumulator *Pteris vittata* and the nonhyperaccumulator *Pteris tremula*. *New Phytol* 165:755–761
- Chaabani S, Abdelmalek-Babbou C, Ahmed HB, Chaabani A, Sebei A (2017) Phytoremediation assessment of native plants growing on Pb-Zn mine site in Northern Tunisia. *Environ Earth Sci* 76:585
- Chandra SK, Kamala CT, Chary NS, Balaran V, Garcia G (2005) Potential of *Hemidesmus indicus* for phytoextraction of lead from industrially contaminated soils. *Chemosphere* 58:507–514

- Chang KJ, Gonzales MJ, Ponce O, Ramírez L, León V, Torres A, Corpus M, Loayza-Muro R (2018) Accumulation of heavy metals in native Andean plants: potential tools for soil phytoremediation in Ancash (Peru). *Environ Sci Pollut Res* 25(34):33957–33966
- Chu Ngoc K, Nguyen VN, Nguyen DB, Le TS, Tanaka S, Kang Y (2009) Arsenic and heavy metal concentrations in agricultural soils around tin and tungsten mines in the Dai Tu district, N. Vietnam. *Water Air Soil Pollution* 197:75–89
- Conesa HM, Faz Á, Arnaldos R (2007) Initial studies for the phytostabilization of a mine tailing from the Cartagena-La union mining District (SE Spain). *Chemosphere* 66:38–44
- De Temmerman L, Waegeneers N, Ruttens A, Vandermeiren K (2015) Accumulation of atmospheric deposition of As, Cd and Pb by bush bean plants. *Environ Pollut* 199:83–88
- Dung LT, Quang DH (2021) Field investigation of face spall in moderate strength coal seam at Vang Danh Coal Mine Vietnam. *VNU J Sci Earth Environ Sci* 37(2):107–105
- Edgar VN, Fabián FI, Mario PCJ, Ileana VR (2021) Coupling plant biomass derived from phytoremediation of potential toxic-metal-polluted soils to bioenergy production and high value by-products—a review. *Apply Sci* 11:2982
- Eslamian S (2016) *Urban water reuse handbook*. CRC Press
- Fitz WJ, Wenzel WW (2002) Arsenic transformation in the soil–rhizosphere–plant system, fundamentals and potential application of phytoremediation. *J Biotechnol* 99(3):259–278
- Frérot H, Lefèbvre C, Gruber W, Collin C, Santos AD, Escarré J (2006) Specific Interactions between local metalicolous plants improve the phytostabilization of mine soils. *Plant Soil* 282(1–2):53–65
- Ghosh M, Singh SP (2005) A review on phytoremediation of heavy metals and utilization of its byproducts. *Appl Ecol Environ Res* 3(1):1–18
- Glick BR (2010) Using soil bacteria to facilitate phytoremediation. *Biotechnol Adv* 28:367–374
- Hai TQ (2007) Spatial organization for rational land use and environmental protection in Uong Bi Town by functional sub-areas. *VNU J Sci Earth Sci* 23:88–95
- Hien NTT, Yoneda M, Nakayama A, Matsui Y, Hai HT, Pho NV, Quang NH (2012) Environmental contamination of Arsenic and heavy metals around Cho Dien Lead and Zinc Mine Vietnam. *J Water Environ Technol* 10(3):253–265
- Hye SL, Jin SL, Hyo TC, Manfred S (2008) Heavy metal contamination and health risk assessment in the vicinity of the abandoned Songcheon Au-Ag mine in Korea. *J Geochem Explor* 196:223–230
- Israel R, Letica C, Javier C, Fernando D, Marcos M (2004) Arsenic and heavy metal pollution of soil, water and sediment in a semi-arid climate mining area in Mexico. *Water Air Soil Pollut* 152:129–152
- Karthik V, Saravanan K, Sivarajasekar N, Suriyanarayanan N (2016) Utilization of biomass from *Trichoderma harzianum* for the adsorption of reactive red dye. *Ecol Environ Conserv J* 22:435–440
- Khoi NN (2014) Mineral resources potential of Vietnam and current state of mining activity. *Appl Environ Res* 36(1):37–46
- Kumar PB, Dushenkov V, Motto H, Raskin I (1995) Phytoextraction—the use of plants to remove heavy metals from soils. *Environ Sci Technol* 29(5):1232–1238
- Lee CG, Chon HT, Jung MC (2001) Heavy metal contamination in the vicinity of the Daduk Au-Ag-Pb-Zn mine in Korea. *Appl Geochem* 16:1377–1368
- Lim SR, Schoenung JM (2010) Human health and ecological toxicity potentials due to heavy metal content in waste electronic devices with flat panel displays. *J Hazard Mater* 9:177–251
- Mahar A, Wang P, Ali A, Awasthi MK, Lahori AH, Wang Q, Li R, Zhang Z (2016) Challenges and opportunities in the phytoremediation of heavy metals contaminated soils: a review. *Ecotoxicol Environ Saf* 126:111–121
- Mendez MO, Maier RM (2008) Phytostabilization of mine tailings in arid and semiarid environments—an emerging remediation technology. *Environ Health Perspect* 116(3):278–283
- Mileusić M, Mapani BS, Kamona AF, Ružičić S, Mapaure I, Chimwamurombe PM (2014) Assessment of agricultural soil contamination by potentially toxic metals dispersed from improperly disposed tailings, Kombat mine, Namibia. *J Geochem Explor* 144:409–420
- Moeller DW (2005) *Environmental health*, 3rd edn. Harvard University Press, Cambridge, MA

- Muthusarayanan S, Sivarajasekar N, Vivek JS, Paramasivan T, Naushad M, Prakashmaran J, Gayathri V, Al-Duaij OK (2018) Phytoremediation of heavy metals: mechanisms, methods and enhancements. *Environm Chem Lett* 16:1339–1359
- Nguyen TH, Sakakibara M, Sano S, Hori RS, Sera K (2009) The potential of *eleocharis acicularis* for phytoremediation: case study at an abandoned mine site. *Clean—Soil Air Water* 37(3):203–208
- Nouri J, Lorestani B, Yousefi N, Khorasani N, Hasani AH, Seif F, Cheraghi M (2011) Phytoremediation potential of native plants grown in the vicinity of Ahangaran lead–zinc mine (Hamedan, Iran). *Environ Earth Sci* 62:639–644
- Pan P, Lei M, Qiao P, Zhou G, Wan X, Chen T (2019) Potential of indigenous plant species for phytoremediation of metal(loid)-contaminated soil in the Baoshan mining area. *Environ Sci Pollut Res* 26:23583–23592
- Petelka J, Abraham J, Bockreis A, Deikumah JP, Zerbe S (2019) Soil heavy metal(loid) pollution and phytoremediation potential of native plants on a former gold mine in Ghana. *Water Air Soil Pollut* 230:267
- Pinto AP, Varennes AD, Fonseca R, Teixeira DM (2015) In: Ansari AA et al (eds) *Phytoremediation: management of environmental contaminants phytoremediation of soils contaminated with heavy metals: techniques and strategies*, vol 2015. Springer, pp 133–155
- Rashid A, Mahmood T, Mehmood F, Khalid A, Saba B, Batool A, Riaz A (2014) Phytoaccumulation, competitive adsorption and evaluation of chelators-metal interaction in lettuce plant. *Environ Eng Manag J* 13(10):2583–2592
- Rungwaa S, Arpab G, Sakulasc H, Harakuwed A, Timie D (2013) Phytoremediation-an eco-friendly and sustainable method of heavy metal removal from closed mine environments in Papua New Guinea. *Prog Earth Planet Sci* 6:269–277
- Sivarajasekar N, Baskar R (2014) Adsorption of basic red 9 on activated waste *Gossypium hirsutum* seeds: process modeling, analysis and optimization using statistical design. *J Ind Eng Chem* 20:2699–2709
- Son NP, Anh NT, Hoi NT, Thuy NT (2019) Applying remote sensing images to establish saline soil map: case study in Uong Bi city, Quang Ninh province. *J Geodesy Cartography* 39:28–33
- Traina G, Morselli L, Adorno GP (2007) Electrokinetic remediation of bottom ash from municipal solid waste incinerator. *Electrochim Acta* 52:3380–3385
- Tran AT, Tran TH, Ngo TP, Pham TD, Bui AN, Nguyen VY, Vu VV, Tran QH, Pham NC (2009) Lead-Zinc mineralization in North Vietnam. In: Abstract with programs CD-ROM, 59th annual society of resource geology, June 24–26, Tokyo, Japan
- Tua TV, Kiên NT, Anh DT, Kim DD (2011) Nghiên cứu khả năng chống chịu và hấp thu chì pb, zn của dương xỉ *Pteris vittata* l. *Tạp Chí Khoa Học Và Công Nghệ* 49(4):101–109
- Vidalli M (2005) Bioremediation: an overview. *Pure Appl Chem* 73(7):1167–1172
- Vietnam Standard (2005) Soil quality—sampling. Part 2 guidance on soil sampling technique: TCVN 7538-2:2005
- Xuan PT, Tran TA, Doan TTT, Hoang TTN, Pham TD, Nguyen TL, Nguyen VP (2017) Environmental issues of mining activities in Tay Nguyen. *Vietnam J Earth Sci* 37(2):139–147
- Xuan PT, Phoa NV, Gas'kovab OL, Bortnikova SB (2013) Geochemistry of surface waters in the vicinity of open pit mines at the cay cham deposit, Thai Nguyen Province, Northern Vietnam. *Geochem Int* 51(11):931–938
- Xue L, Liu J, Shi S, Wei Y, Chang E, Gao M, Chen L, Jiang Z (2014) Uptake of heavy metals by native herbaceous plants in an antimony mine (Hunan, China). *Clean: Soil Air Water* 42:81–87
- Yoon J, Cao X, Zhou Q, Ma LQ (2006) Accumulation of Pb, Cu, and Zn in native plants growing on a contaminated Florida site. *Sci Total Environ* 368(2):456–464
- Zhang WH, Cai Y, Tu C, Ma QL (2002) Arsenic speciation and distribution in an arsenic hyperaccumulating plant. *Sci Total Environ* 300(1–3):167–177
- Zu YQ, Li Y, Chen JJ, Chen HY, Qin L, Christian S (2005) Hyperaccumulation of Pb, Zn and Cd in herbaceous plants grown on lead–zinc mining area in Yunnan China. *Environ Int* 31:755–762

Chapter 16

Assessment and Risk Management of Malicious Acts Aimed at Potentially Hazardous Hydrotechnical Constructions



Valery Mitkov

Abstract The following paper presents a methodology developed for risk assessment of terrorist attacks with explosive devices, carried out at potentially hazardous Hydrotechnical constructions and water facilities. Included are scales for determining different parameters such as risk, hazard, likelihood and etc. Examined is a procedure for the study of potentially hazardous constructions and assessment of the damages caused by malicious acts (terrorist attacks) at them.

Keywords Hydrotechnical constructions · Risk management · Hazard · Terrorist attacks · Blast

16.1 Introduction

Currently, Bulgaria is an equal member of EU and NATO and on its territory are built and in function USA military bases. As a result of that, potentially hazardous sites, including Hydrotechnical constructions may become target of terrorist actions from international Islamic groups, like Al Kaida (Mollova 2019b). Similar attacks, at such sites, have already been done in Iraq and Afghanistan and have left disastrous effects on the country's economy (Mollova 2019a).

Taking into consideration that such constructions are very expensive and complicated to build, it can be concluded that in case of terrorist attack with blasting device, the event will cause not only multimillion damages but also human casualties.

To prevent terrorist attacks on Hydrotechnical constructions, it is necessary to have knowledge on the issues of action of blasting devices, locations and methods of their eventual placement, as well as the effects of airblast wave.

V. Mitkov (✉)
University of Mining and Geology, "St. Ivan Rilski", Sofia, Bulgaria
e-mail: valery.mitkov@gmail.com

16.2 Risk Assessment of Hydrotechnical Facilities

Risk can be defined as “possibility of something adverse to happen”, or more precisely this is likelihood, a specific (adverse) event to occur in a specific period of time, under certain conditions (Stoycheva and Shishkov 2019). In other words, risk is a combination of likelihood of certain hazard to emerge and the severity of the consequences of its conduct. In this way risk always consists of two components: likelihood and consequences.

It is necessary to distinguish between some basic concepts that are relevant to risk assessment. While hazard is associated with the potential specifications and characteristics of a phenomenon or process, then risk is related to their likelihood and frequency of conduct and may include many hazards and consequences of their occurrence.

The following approaches can be used for risk assessment:

- Qualitative, i.e. high, medium, low, acceptable, unacceptable, reasonable;
- Semi-quantitative, in this one the basic components of risk - likelihood and consequences are qualitatively defined and combination of them gives pseudo-quantitative risk assessment, which allows comparison of results;
- Quantitative, it is performed by calculation of likelihood (its frequency) of occurrence and its potential consequences.

The summary risk assessment in this paper is based on the so called “Method of the three factors” (Belin and Mollova 2021), and in this case the selected factors, which determine risk of the surveyed construction, are presented in formulae 1:

$$R = H \cdot V \cdot L \quad (16.1)$$

where

R (Risk)—gives a summary risk assessment that a certain construction has to population, environment, buildings and/ or equipments, nearby sites. It may has values from 0.01 to 1000. Depending on the values obtained as a result of these calculations risk degree can be determined (Shishkov and Stoycheva 2019).

H (Hazard)—this factor defines the potential hazard that construction possesses to population, environment, buildings and/or equipments and nearby sites. The hazard identification is carried out mainly on a basis of categorization and classification of the construction under the regulations in the area of application. This factor may reflect other features of the reviewed site, which should be considered in the examination (Penev and Mollova 2020). The accepted values range between 1 and 10.

V (Vulnerability)—This factor includes “Vulnerability” and “Consequences”. It characterizes the influence of the outdoor factors, the interaction between the considered Hydrotechnical construction and other nearby sites. Vulnerability shows the extent to which population, employees, environment, buildings and/or equipments are exposed to the influence of adverse event (several unfavorable events). In relation with the presented data and the possibility for risk assessment, the parameter

“Consequence” can be entirely replaced with “Vulnerability” (Mollova and Penev 2020). This parameter is important in risk assessment and it accepts values between 1 and 100.

L (Likelihood)—reflects the likelihood of an event to occur and lead to risk. Accepted values are from 0.01 to 1.

16.3 Classification of Dam Walls

With regard to grading scale, the values of the parameter “Hazard” for Hydrotechnical constructions and water facilities, depend on the place of the construction in already established national and international classification (Draganov and Pavlov 2012).

Under current regulations in republic of Bulgaria, in the Standards for design of Hydrotechnical constructions from 1985, is regulated the classification of dam walls and Hydrotechnical constructions. According to the consequences of possible demolition and compromise of such buildings and/or equipment they are given risk degrees from I to IV class.

According to classification of International commission of large dams (ICOLD) and depending on summarized parameters of dams and Hydrotechnical constructions, large dam walls are those that meet at least one of the following conditions:

- (a) Structures more than 15 m high, or with more than 5 m of height if it has a storage volume of over 3 million cubic meters;
- (b) Structures with height between 10 and 15 m and complying at least with one of the following conditions:
 - the length of crest not less than 500 m;
 - the capacity of the reservoir not less than 10^6 m³;
 - the maximum flood discharge not less than 2000 m³/s;
- (c) As large dam walls are classified and these that do not have the above characteristics but have the following:
 - have unusual design;
 - have specifically difficult foundations;
 - special methods of construction have been implemented (Balev et al. 2016);

Small dam walls are all dam walls that do not meet any of the conditions mentioned in 2.2.

According to this article the classification of Hydrotechnical constructions and water facilities should be expanded as it follows:

- to the group of Hydrotechnical constructions and water facilities from class I, should be added: dikes along river Danube, downstream of Kamchia river, Varbitsa river, downstream of Maritsa river, bridges and retaining walls in these rivers and Asparouhov’s bridge, port facilities on the Black Sea and river Danube, water

Table 16.1 Grading scale for the parameter H “Hazard” for Hydrotechnical constructions and other water facilities

Large dam walls (ICOLD) and class 1 Hydrotechnical constructions and water facilities	High potential hazard	10–8
Class II Hydrotechnical constructions and water facilities	Significant potential hazard	7–5
Class III Hydrotechnical constructions and water facilities and cascades of dams	Moderate potential hazard	4–3
Class IV Hydrotechnical constructions and water facilities	Limited potential hazard	2–1

intake and water leading facilities to cooler system of Electricity Generating plant, Ovcharitsa river with the pillar of mine Trayanovo North;

- to the group of Hydrotechnical constructions and water facilities from class II, should be added: dikes along Iskar river, Struma river, Mesta river, Tudja river, Arda river, middle stream of Maritsa river, as well as bridges and retaining walls in these rivers;
- to the group of Hydrotechnical constructions and water facilities from class III, should be added: dikes along the upstream of Maritsa river, above Belovo city, all other rivers in Bulgaria, as well as bridges and retaining walls at these rivers, trunk pipelines for local agglomerations, single water intakes, water-using facilities and water supply equipments in urban agglomerations;
- to the group of Hydrotechnical and water facilities from class IV, should be added: derivational canals, major pipelines, water intakes and water-using facilities for individual towns, Hydro power plant facilities and all other Hydrotechnical constructions that do not fall within the above three classifications (Loukanov et al. 2013).

Mitigation and water-using facilities (for different purposes) are classified in the same class of dam walls, whether related to the design of it or not (Pavlov et al. 2016).

Recommended values of the parameter **H “Hazard”** in the grading scale, which has been applied to Hydrotechnical and water facilities can be defined according to Table 16.1.

16.3.1 Likelihood (L)

For each of the analyzed types of hazard should be determined a value of the parameter likelihood of a hazardous event to occur (for example: demolition of a building, loss of base stability, spill of hazardous chemical substances, explosion, flooding and etc.) (Ivanov and Shishkov 2020).

Table 16.2 Assessment of parameter L—“Likelihood”

Very likely: high likelihood of occurrence of hazardous event	1
Possible: it is not unusual malicious act to happen, possibility 50:50	0.6
Unusual to occur but possible: (1 event from 10)	0.3
Less possible: possibility of occurrence of hazardous event is 1 from 100 events	0.1
Less likely: hazardous even hasn't occurred, but it is possible to happen (1 event from 1000)	0.05
Practically impossible: it is not known to has happened (1 event from 10,000)	0.01

The scale of the parameter L according to likelihood of event to happen is presented in Table 16.2.

16.3.2 Vulnerability and Consequences

The overall vulnerability assessment of a particular Hydrotechnical construction is advised to be obtained by procedure of investigation. The vulnerability parameter is an integral characteristic that shows the influence of series of factors reflecting the consequences, technical condition, operation system and other specific conditions.

The normative base for categorization of settlement at the time of this research has not been updated and so in view of the accuracy of the urban risk, it is recommended that vulnerability assessment of the particular construction should refer to one of the risk groups given in Table 16.3 [Engineering—technical rules for civil defense from Decree of Council of Ministries of Bulgaria from 30.12.1988 (unpublished)].

Possible consequences of malicious acts aimed at Hydrotechnical constructions and course of certain emergency are assessed in the following sequence:

Table 16.3 Values of the parameter “Vulnerability”

Risk group for settlement	Settlements very close Hydrotechnical constructions and other water facilities	“Vulnerability” 1–100
1. Essential importance	Sofia, Plovdiv, Varna, Ruse and Bourgas	100
2. First risk group	Cities with population over 100 000 people	80
3. Second risk group	Cities with population over 30 000 people	60
4. Third risk group	Settlements with population over 10 000 people	40
5. Fourth risk group	Settlements with population under 10 000 people	20

- Consequences for people;
- Consequences for environment;
- Property damage.

For the vulnerability of the investigated construction, in terms of natural phenomenon, technogenic factors and terrorist acts, it is necessary to consider the following aspects:

- An event that occurs outside the territory of the investigated construction but it affects it, as well as nearby sites, population in adjacent to the site territories and environment;
- An event that occurs on the territory of a nearby construction and as a result affects the investigated one, population in adjacent to the nearby site territories and environment;
- An event that occurs on the territory of the investigated construction and it affects nearby sites, population in adjacent to the site territories and environment;

The investigation of Potentially Hazardous Construction Sites leads to vulnerability assessment in these aspects (Totev and Pavlov 2020).

Essential for the result of the examination is the determination of effects on people, environment and property damages. Tables 16.4 and 16.5 give examples of the parameter Vulnerability in terms of severity of the consequences for people, environment and property damage. The final values of these parameters are obtained following a detailed survey of the construction under the relevant risks.

At the stage of preliminary expertise the risk assessment is separately determined for each potential hazard.

The results are compared in the limits, shown in Table 16.6.

The risk degree characterizes the site regarding its state, level of operation and its potential hazard. It is essential in determining the necessity of carrying out a detailed assessment and taking appropriate measures for risk reduction (Tondera et al. 2018).

Table 16.4 Consequences for people and environment

Consequences: people and environment	C
Catastrophe: many victims, long term environmental damage of large areas	100
Disaster: death, long-term environmental damage of local area	50
Very serious consequences: long-term disability, long-term environmental damage	25
Serious consequences: temporary damage or illness, adverse environmental impact	15
Considerable consequences: needed are medical cares, there are emissions in environment outside the site territory	5
Noticeably consequences: minor injuries or illness without damages of environment outside the facility	1

Table 16.5 Consequence for property

Consequence: property damages	C
Catastrophe: irreversible damage to constructions and equipment, reconstruction or completely new equipment is needed	100
Disaster: hardly repairable damages to constructions and equipment, it is necessary to stop an essential process for an indefinite period	50
Very serious consequences: repairable damages to constructions and equipment, it is necessary to stop an essential process for definite time	25
Serious consequences: damages to constructions and equipment, it is necessary to stop essential process for some time	15
Considerable consequences: serious damages to construction and equipment, can be repaired when an essential process is interrupted for short time	5
Noticeably consequences: damages to constructions and equipment, can be repaired without interruption of essential process	1

Table 16.6 Risk degree

Risk	Risk degree
> 60	Very high
30–59	High
9–29	Moderate
< 9	Low

16.4 Standard Procedure for Research on Potentially Hazardous Hydrotechnical Constructions

The following paper presents a systematic framework and a standard procedure for examination for research, analyses, assessment and prediction of risks for potentially hazardous sites, in three main stages as shown in Fig. 16.1. Recommended is: Initial stage of identification and two levels of expertise—Preliminary and Detailed. By the expertise of potentially hazardous sites is performed the risk assessment. In the process should be generated measures to reduce risk.

16.5 Consequences of Terrorist Attacks Aimed at Hydrotechnical Constructions and Water Facilities

- In case of destruction of dam wall the consequences for the affected area are: endangered population, water supplies, flooded areas, shaken dike stability, flooded adjacent shores to the reservoir and water flow, damages to companies with continuous manufacturing process, as well as to such with suspended manufacturing process, loss of grain in storage, pesticides, herbicides and etc., damaged

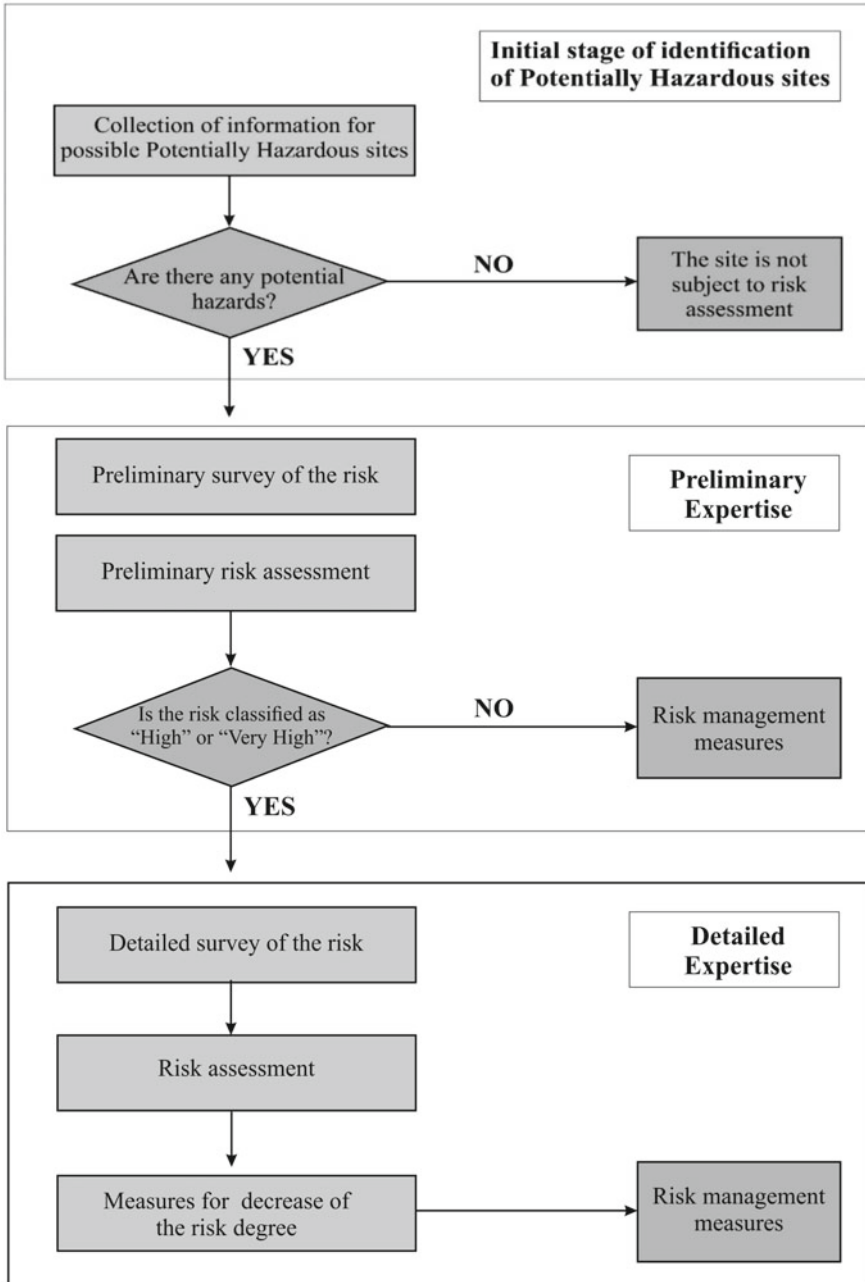


Fig. 16.1 Stages of risk analyses, assessment and prediction

or destroyed equipment which is part of the engineering infrastructure, contaminated water resources, unsuitable to use public buildings and hospitals, sediments effecting on the water-conductivity of river beds, damages on hydromelioration, losses in the agriculture and cultural values;

- In case of destruction of higher situated dam wall the consequences of the affected area are: influence on the stability of lower situated dam wall, spillway facility, adjacent shores to the reservoir and water flow, endangered population, water resources, flooded territories, shaken dike stability', flooded adjacent shores to the reservoir and water flow, damages to companies with continuous manufacturing process, as well as to such with suspended manufacturing process, loss of grain in storage, pesticides, herbicides and etc., damaged or destroyed equipment which is part of the engineering infrastructure, contaminated water resources, unsuitable to use public buildings and hospitals, sediments effecting on the water-conductivity of river beds, damages on hydromelioration, losses in the agriculture and cultural values;
- In case of high wave, which is higher than the suggested one, the consequences for the affected area are: endangered population, water supplies, flooded areas, shaken dike stability, flooded adjacent shores to the reservoir and water flow, damages to companies with continuous manufacturing process, as well as to such with suspended manufacturing process, loss of grain in storage, pesticides, herbicides and etc., damaged or destroyed equipment which is part of the engineering infrastructure, contaminated water resources, unsuitable to use public buildings and hospitals, sediments effecting on the water-conductivity of river beds, damages on hydromelioration, losses in the agriculture and cultural values.

16.6 Correspondence of the Initiatives Against Terrorist Attacks

- Presence of emergency alarm system and announcement to employees and population;
- Presence of emergency action plan (employees, interaction with other units, emergency storage, mechanization, transport, equipment with the necessary' clothing, appliances, tools, communication equipment);
- Presence of an annual plan for preventive action with dates for training in case of emergency event according to the emergency action plan;
- Level of training of operational staff according to the emergency action plan;
- Physical security of Hydrotechnical constructions—this includes security of facilities, employees and presence of alarm system;
- Presence of annual plan in the company, unit, municipality for scheduled repairs, maintenance of equipment, construction and other activities connected with recommendations for increasing the sustainability of Hydrotechnical constructions;

- Programmes of local press and mass media for education and training of the population for adequate action in the event of disasters or emergencies;
- Presence of national programme for development of preliminary risk assessment of floods at certain area (prevention, protection, training);
- Presence of national programme for development of map with areas that are considered to be in danger of flooding (prevention, protection, training).

16.7 General Conclusions and Suggestions

1. This paper presents various possible terrorist actions against Hydrotechnical constructions and water facilities and especially the impact of the blast on soil and rocks, demolition of armored concrete, metal constructions and equipments, and the action of blast wave in air and water and etc.
2. This paper can be used as a basis for a preliminary examination and detailed assessment of the risk, for base for measures to decrease the risk degree and measures for risk management.
3. To minimize the potential danger of terrorist attacks aimed at potentially hazardous Hydrotechnical constructions and water facilities it is necessary to make a preliminary detailed expertise for each big Hydrotechnical construction, which is potential target of terrorist actions. The purpose is to prevent this from happening.

References

- Balev V, Dachev G, Mitev I (2016) Comparative analysis for determination of strength of pressure uniaxial rock samples by comparing laboratory and “In Situ” methods. In: VII International geomechanics conference. Varna, pp.124–127
- Belin V, Mollova Z (2021) Influence of the type of donor charges on the detonation rate of low-sensitivity explosives. *Sustain Dev Mt Territ* 13:112–119
- Draganov L, Pavlov P (2012) Verbesserte Verfahren zur Sanierung von kontaminierten Böden. *Depo Tech* 2012, pp. 775–776. Deponietechnik und Altlasten. Herausgeber Karl E. Lorber F026 Co. Iae, Eigenverlag
- Ivanov N, Shishkov P (2020) Application of non-detonating charges for cautious blasting of concretes. *J Min Geol Sci* 63:53–58
- Loukanov A, Angelov A, Bratkova S, Pavlov P (2013) Leaching of target metals from mining wastewaters by iron nanoparticles in magnetic reactor. In: *Topical Issues of Subsoil Usag*. St. Petersburg State Mining Institute, Russia, pp 233–238
- Mollova Z (2019a) Blast load analysis and effect on building structures. *J Mining Geol Sci* 62:75–81
- Mollova Z (2019b) New insights into the impact of blast wave on the human body. *J Mining Geol Sci* 62:70–75
- Mollova Z, Penev V (2020) Control of blast-induced seismic action generated by technological blastings. *Sustain Extr Process Raw Mater J* 1:64–67

- Pavlov P, Totev L, Tondera D (2016) Folgen des Erzbergbaus und Einwirkungen auf die Umwelt Bulgariens sowie deren regionalen Ökosysteme – Rekultivierung von Bergbaubetrieben. 9th Freiberg Geotechnik-Kolloquium. Technische Universität, Bergakademie Freiberg, pp 81–88
- Penev V, Mollova Z (2020) Design optimization of drilling and blasting operations: a case study on copper ore mining in Asarel. *J Mining Geol Sci* 63:84–88
- Shishkov P, Stoycheva N (2019) Application of long term stored single and double based propellants in advanced blasting methods for dimension stone extraction. In: 22-nd NTREM '2019—international seminar new trends in research of energetic materials. Pardubice, pp 619–629
- Stoycheva N, Shishkov P (2019) Innovative formulations for a new generation of low-speed explosive compositions, designed for blasting in tender conditions and for extraction of rock-cladding materials. *J Min Geol Sci* 62:94–99
- Tondera D, Beier D, Tamaskovics N, Pavlov P, Totev L (2018) Groundwater impact investigation due to installation of a “LWS” silicate gel sealing sole in the water saturated soil zone. *J Min Geol Sci* 61:19–24
- Totev L, Pavlov P (2020) Einsatz des Sprengsystems “Cardox” im Bergbau Bulgariens. Innovation in Non-Blasting Rock Destructuring. In: 3th internationalen Kolloquium zur sprengstofflosen Gesteinsgewinnung. TU Bergakademie, Freiberg, pp 106–110

Chapter 17

3D Numerical Modelling for Hydraulic Characteristics of a Hollow Triangle Breakwater



Tu Le Xuan, Hung Le Manh, Hoang Tran Ba, Thanh Dang Quang,
Vo Quoc Thanh, and Duong Tran Anh 

Abstract The Hollow Triangle Breakwaters (HTBs) is widely constructed in the Vietnamese Mekong Delta (VMD) due to severe coastal erosion in recent years. This study aims at investigating the hydrodynamic performance, wave actions on the HTBs. Three-dimensional numerical modelling using modern MIKE 3 wave flexible mesh (FM) was successfully built for the optimal porosity cases ($P_1 = 22.5\%$; $P_2 = 11.8\%$) to explore the relationships of these hydrodynamic behaviors and wave interaction with the HTBs. This study showed results present of flow pattern, velocity fields, turbulent kinetic energy, vertical eddy viscosity and non-hydrostatic pressure in the HTBs. This can explain the vortex and eddy formations that cause the erosion at the front toe of the breakwater and the negative non-hydrostatic pressure inside the breakwater due to the effect of the baroclinic in the oscillation. These insights highlighted the importance of the numerical model which provided a greater understanding of the impact of the waves than the physical model. The HTBs provide an effective alternative at reducing the impact of waves while also allowing the exchange of sediment and facilitating aquatic species to thrive in the coast side construction in the VMD.

Keywords Hollow triangle breakwaters · Surface porosity · MIKE 3 wave FM · Coastal Mekong delta

T. L. Xuan · H. L. Manh · H. T. Ba
Southern Institute of Water Resources Research, Ho Chi Minh city, Vietnam

T. D. Quang
DHI Vietnam, 4 Nguyen Dinh Chieu, District 1, Ho Chi Minh city, Vietnam

V. Q. Thanh
Can Tho Universtiy, Can Tho city, Vietnam

D. T. Anh (✉)
Laboratory of Environmental Sciences and Climate Change, Institute for Computational Science and Artificial Intelligence, Van Lang University, 69/68 Dang Thuy Tram, Ward 13, Binh Thanh District, Ho Chi Minh City, Vietnam
e-mail: duong.trananh@vlu.edu.vn

Faculty of Environment, Van Lang University, Ho Chi Minh city, Vietnam

17.1 Introduction

The Vietnamese Mekong Delta (VMD) is facing severe erosion along its coast. In fact, this is occurring rapidly in the coastal strip in the last five years, constitutes a significant threat to the coastline in the VMD which consequently leads to a range of impacts including 300–500 ha of lost land attributed to rising water levels every year, infrastructure damage, and mangrove degradation (Anthony et al. 2015). For example, severe coastal erosion in 2018 resulted in 268–744 km of coastline with an erosion rate of 1–40 m/year (Albers et al. 2013; Besset et al. 2019). Consequently, to tackle these issues there have been a range of hard and soft breakwater technologies that have been applied in the region. In which, nearshore vertical wall breakwaters have been used for Vietnamese coastal protection against varying environmental factors (Thorenz 2016) and include semi-circular caisson, perforated-wall caisson, T-fence, hollow triangle and multiple wall breakwaters (Nguyen et al. 2018; Albers 2021; Mai et al. 2019; Xuan et al. 2020a).

The simulation of physical phenomena and hydraulic characteristics through porous and hollow structures is very challenging due to the complex physics of non-ideal flows, sophisticated geometries and the complexity of the fluid dynamic processes with strongly non stationary flows, free boundaries and turbulence. Numerous studies conducted experiments in the laboratory to evaluate wave transmission and hydrodynamic behaviours through the breakwaters without much insight understanding of hydraulic characteristics obtained from three-dimensional modelling (Reis et al. 2008; Koraim and Rageh 2013; Williams et al. 2019). Recently, few studies were focusing primarily on the development of three-dimensional models to investigate the interaction of wave and porous coastal structures (Losada et al. 2008; Jesus et al. 2012; Lara et al. 2012; Gomes et al. 2020). They provide profound understanding of hydrodynamic performance and wave interaction with structures.

The rapid development of numerical and computational capabilities has been able to simulate complicated structures and different hydraulic conditions for coastal construction designs in last decade. Popular CFD models include Flow3D, REEF3D, FLUENT, OpenFOAM[®] and IH-3VOF using volume-averaged Reynolds-Averaged Navier–Stokes and Volume of Fluid method (VOF) to simulate free-surface flows (Jesus et al. 2012; Lara et al. 2012; Fang et al. 2010; Flow Science Inc. 2009; Antonini et al. 2016; Miquel et al. 2018). However, some obstacles have so far hindered wide applications of these models in coastal construction designs. The obtaining robust results with high accuracy require very fine resolution of computational grids that may lead to extensive simulation time and high computational cost for small domain and short computing duration (Dentale et al. 2013; Fitriadhy et al. 2017). Hence, this creates the difficulties to calibrate and validate the 3D model as well as the time-consuming for the simulations of different scenarios. This is only suitable for scientific research and model development while that causes considerable inconvenience in real applications and projects, which does not require very accurate results.

MIKE 3 wave FM was developed by DHI in 2019 and involved three-dimensional incompressible Reynold-averaged Navier–Stokes (RANS) equations using partly Volume of Fluid (VOF) method to simulate porous structures (DHI 2019). This model simplifies the structures by parameterization of the porous breakwater to define different porosity layers that is high suitable for homogeneous or heterogeneous materials, porosity and architectures such as pile-rock, rubble-mound, bamboo fences breakwaters with different amour layers and porosity zones in horizontal and vertical direction and may potentially apply for large domain in coastal area. This software package has a friendly user interface and wide applied not only for researches but also for applications and real projects in many countries. In turn, the objective of this paper is to apply three-dimensional modelling MIKE3 wave FM to analyze the hydrodynamic performance of a HTB breakwater under wave action and this work continues the last study of Xuan et al. (2020a) which proposed new structure of HTB and investigated hydraulic performance and wave transmission by experiment laboratory.

17.2 Laboratory Experiments

17.2.1 Experiment Equipment Setup

The scale of the physical model was decided based on the input hydraulic boundary conditions (i.e. wave size and water depth) and the size constraint of the laboratory channel flume. The laboratory model was set up following Froude's law to ensure that the hydrodynamic conditions and selected scale of the model is $N_L = 1/7$.

The wave flume was 35 m long (effective length), 1.2 m wide and 1.5 m high (see Fig. 17.1a). Additional descriptions of the wave flume set up are detailed in Xuan et al. (2020b). The breakwater consists of two sides with circular holes in four rows with variable diameters that were arranged depending on the different scenarios being tested. The sea and coast sides have a total of 40 holes (i.e. 4 rows \times 10 columns) which have a diameter d_1 (sea side) and diameter d_2 , (coast side). The structure used for the experiment has the following dimensions (see Fig. 17.1b): a height of 47 cm, a crest width of 7 cm, foot width of 53.6 cm and length of 116 cm, and a slope of $\alpha = 66^\circ$.

Wave gauging stations are located in front of and behind the breakwater. Five gauges (WG 1–5) are installed between the wavemaker and the HTB model, WG1 near the wave paddle and four (WG 2–5) near the HTB model to separate incident from reflected waves. HR Wallingford installed all experimental equipment used for the laboratory experiments. Finally, three gauges are placed behind the breakwater (i.e. WG6, 7, 8) which are used to measure the transmitted waves. The locations of the wave gauges in the experiment are shown in a plain view in Fig. 17.1a. To adequately produce the main frequency domain of the desired wave spectra each of the experiments lasted approximately $500 T_p$ (s).

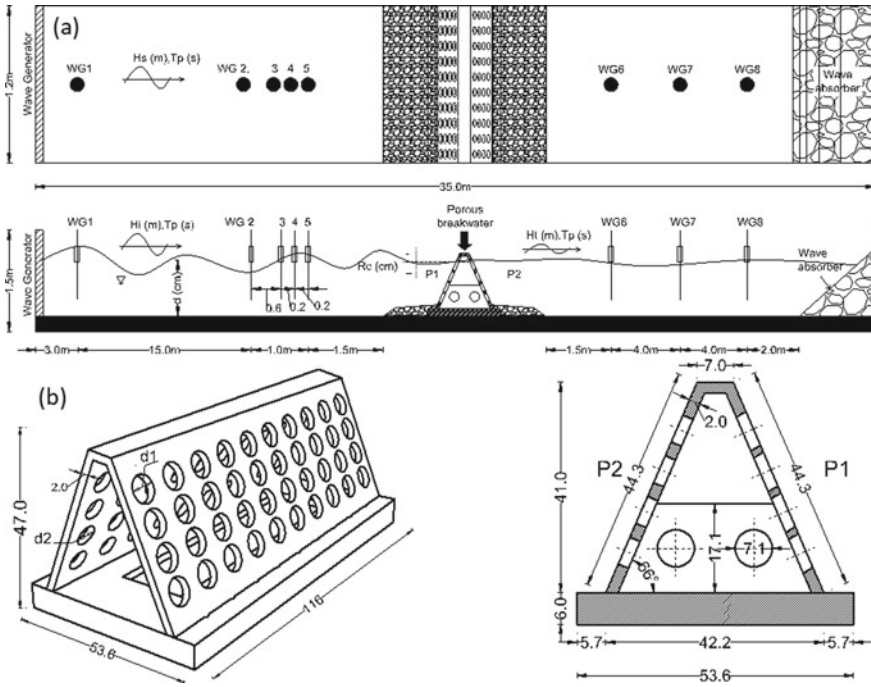


Fig. 17.1 Plain view and side view of the wave flume (a); isometric and cross-sectional view of the HWB structure (b) with dimension in cm. P1 and P2 are percentage of porosity on sea side and coast side, respectively (Xuan et al. 2020a)

17.2.2 Data and Testing Conditions

The KH2 ($P_1 = 22.5\%$; $P_2 = 11.8\%$) configurations were selected for wave transmission testing. Four water depths, $h = 0.33, 0.40, 0.47$ and 0.54 m and 6 sea states were generated with H_{m0} and T_p values given more detail in Xuan et al. (2020a).

17.3 Numerical Model

17.3.1 MIKE 3 Wave Model FM

The MIKE 3 wave model is a computational fluid dynamics numerical solution of the three-dimensional incompressible Reynold-averaged Navier–Stokes (RANS) equations. The model solves the continuity (1) and momentum Eq. (17.2). The spatial discretization is applied using a cell-centered finite volume method. The projection

method is utilized for the non-hydrostatic pressure. The turbulent model is used $k-\varepsilon$ model (DHI 2019). This is the first time DHI developed new module of porous media modelling in 2019 on MIKE 3 wave model FM with advantage of using partly Volume of Fluid (VOF). This highlight feature can effectively simulate the wave transformation for the hollow triangle breakwater in this study. The critical equations governing this model are as follows:

Continuity equation:

$$\frac{\partial u}{\partial x} + \frac{\partial v}{\partial y} + \frac{\partial w}{\partial z} = 0 \quad (17.1)$$

Momentum equation:

$$\frac{\partial u}{\partial t} + \frac{\partial u^2}{\partial x} + \frac{\partial uv}{\partial y} + \frac{\partial wu}{\partial z} = fv - \frac{1}{\rho_0} \frac{\partial q}{\partial x} - g \frac{\partial \eta}{\partial x} + F_u + \frac{\partial}{\partial z} \left(v_t^v \frac{\partial u}{\partial z} \right) \quad (17.2)$$

$$\frac{\partial v}{\partial t} + \frac{\partial uv}{\partial x} + \frac{\partial v^2}{\partial y} + \frac{\partial wv}{\partial z} = -fu - \frac{1}{\rho_0} \frac{\partial q}{\partial y} - g \frac{\partial \eta}{\partial y} + F_v + \frac{\partial}{\partial z} \left(v_t^v \frac{\partial v}{\partial z} \right) \quad (17.3)$$

$$\frac{\partial w}{\partial t} + \frac{\partial uw}{\partial x} + \frac{\partial vw}{\partial y} + \frac{\partial w^2}{\partial z} = -\frac{1}{\rho_0} \frac{\partial q}{\partial y} + F_w + \frac{\partial}{\partial z} \left(v_t^v \frac{\partial w}{\partial z} \right) \quad (17.4)$$

where u , v and w are the velocity components and are all function x , y and z ; t is the time, η is the surface elevation; q is the non-hydrostatic pressure; v_t^v is the vertical eddy viscosity; g is the gravitational acceleration; ρ_0 is the reference density of water.

Total pressure p is equal to non-hydrostatic plus a hydrostatic component

$$p_H = p_A + \rho_0 g (\eta - z) + g \int_z^\eta (p + \rho_0) dz \quad (17.5)$$

The atmospheric pressure (p_A) is assumed to be constant at the free surface.

The turbulence is modelled using an eddy viscosity concept (Rodi 1980, 1984). In the $k-\varepsilon$ model, the eddy viscosity (v_t) is derived from turbulence parameters k and ε .

The non-Darcy flow effects through the porous structure and the porosity are involved in the equations of model by introducing the laminar and turbulent friction terms to calculate losses.

Linear and non-linear resistance forces describe the flow resistance inside the porous structure. These linear and non-linear resistance forces are expressed as:

$$F_i = \rho a u_i + \rho b |u_i| u_i \quad (17.6)$$

where the a and b terms correspond to laminar and turbulent friction loss resistance coefficients. u_i corresponds to the velocity components where the magnitude of the flow velocity is defined by $|u| = \sum_i u_i$.

The a and b terms are determined using the empirical formula developed by Van Gent (1995) and (Liu et al. 1999):

$$a = \alpha \frac{(1-n)^2}{n^3} \frac{\nu}{(d_{50})^2} \quad (17.7)$$

$$b = \beta \left(1 + \frac{7.5}{KC}\right) \frac{(1-n)}{n^2} \frac{1}{d_{50}} \quad (17.8)$$

where n is the porosity, α and β are non-dimensional coefficients, ν is the kinematic viscosity and d_{50} is the grain diameter of the porous materials. The KC coefficient is the Keulegan-Carpenter number which is defined as:

$$KC = \frac{u_m T}{n d_{50}} \quad (17.9)$$

where the u_m term is the maximum oscillating velocity and the T term is the period of the oscillation. In general practice the T term is can be approximated using the characteristic wave period for the simulation.

In the aforementioned momentum equations, the time derivative terms are multiplied by a factor $(1 + C_m)$. C_m is the added mass coefficient to take into account the transient interaction between the grains and the water (Van Gent 1995) proposed C_m as:

$$C_m = \gamma \frac{1-n}{n} \quad (17.10)$$

where $\gamma = 0.34$ is an empirical coefficient.

17.3.2 Grid Mesh and Boundary Conditions

The three-dimensional numerical geometry of the flume and the breakwater was exactly constructed following the dimensions of the physical model in Sect. 17.2.1 with flume 35 m long and 1.2 m wide and 1.5 m height. The total number of elements to discretize the domain was 38,000 and the numbers of faces are 153,920 with total 79,842 nodes. The first grid block (flume) is 0.02 m in size, and the second grid block size including the breakwater is 0.01 m. The detailed information of the mesh and the flume is described in Fig. 17.2. One simulation of the numerical model took 12 h with CPU—Intel 6 × Core. Xeon 6142 @ 2.6 GHz to simulate 1000 irregular waves with 10 min. Note that the time step interval for the model was 0.001 s and the total number of time steps were 3000.

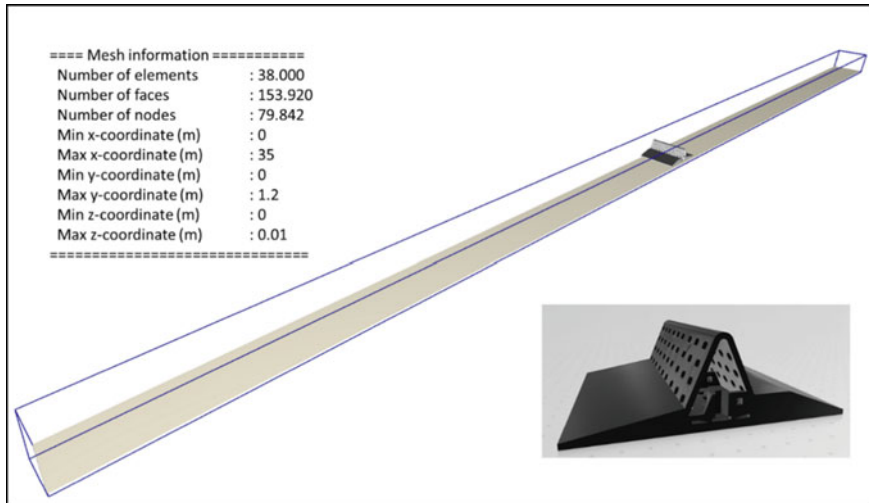


Fig. 17.2 3D numerical model geometry of flume and mesh information

The boundary conditions were setup including the incident waves imposed on the front of breakwater (i.e. at the wave maker) and a sponge for absorption at the rear side of the flume. The irregular incident waves were defined by analysis of wave spectrum from the WG2 to WG5 gauges including frequency and energy with significant wave height $H_{m0} = 0.12$ m and peak wave period $T_p = 1.31$ s.

17.4 Results and Discussion

17.4.1 Calibration and Validation

The model was calibrated and validated by testing with regular waves with $H_s = 0.136$ m and wave period $T_p = 1.31$ s. The porosity was then adjusted while changing three parameters: the turbulence resistance coefficient, the laminar resistance coefficient, and the oscillating period. These values are adjusted based on the references of Ven Gent (1995) and Liu et al. (1999). The breakwater is divided into three zones (i.e. rubble-mound, base and flat-inclined hollow perforations) to define porosity of different parts of porous media as described in Fig. 17.3. A trial-and-error approach was applied to obtain the proper porosity to ensure that the wave spectrum of the incident waves and the waves behind the breakwater were the best-fit for the experiments.

We simulated 1000 irregular waves to ensure the stability of model and to cover a wide range of generated waves from the JONSWAP spectrum. Figure 17.4 shows the calibrated wave spectrum at wave gauge 4 (in front of structure) and wave gauge

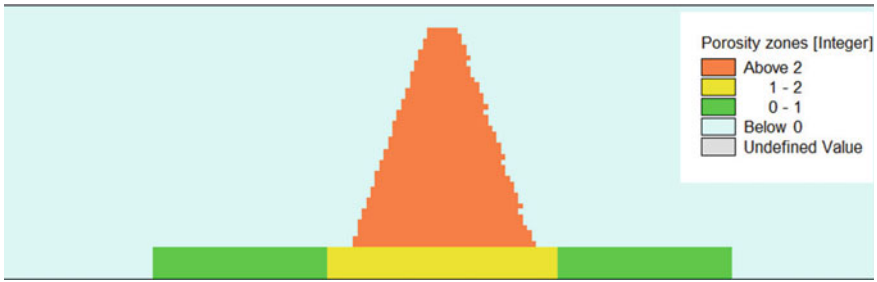


Fig. 17.3 Calibrated porosity distribution of hollow triangle breakwater

6 (behind the structure). The comparison of wave spectrum between experiments and numerical model shows that the energy magnitude and frequency of the model has a good fit with the experimental values, especially for the peak wave period at wave gauge 6 (Fig. 17.4b). The calibrated results with adjustment of porosity are described in Table 17.2.

Figure 17.5 shows the comparison of wave interaction at different stages between the results of numerical and physical models. It can be observed that the processes of wave attacked on the breakwater were captured at four representative stages consisting of (a) wave run-up, (b) onset of overtopping, (c) peak overtopping, and (d)

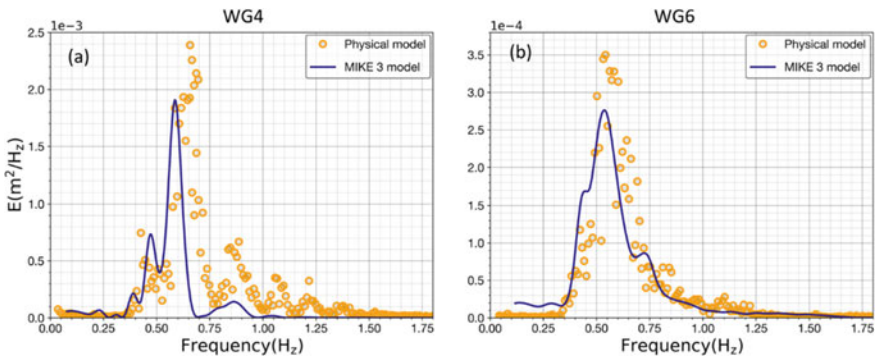


Fig. 17.4 Wave spectrum before (a) and after (b) passing through breakwater after calibration

Table 17.2 The division of the porosity zones and calibrated laminar, turbulent resistance coefficients for breakwater

Zone	Porosity	Laminar resistance coefficient	Turbulent resistance coefficient	Oscillating period (s)
1	0.3	1000	2.8	1.31
2	0.3	1000	2.8	1.31
3	0.4	2000	4.0	1.31

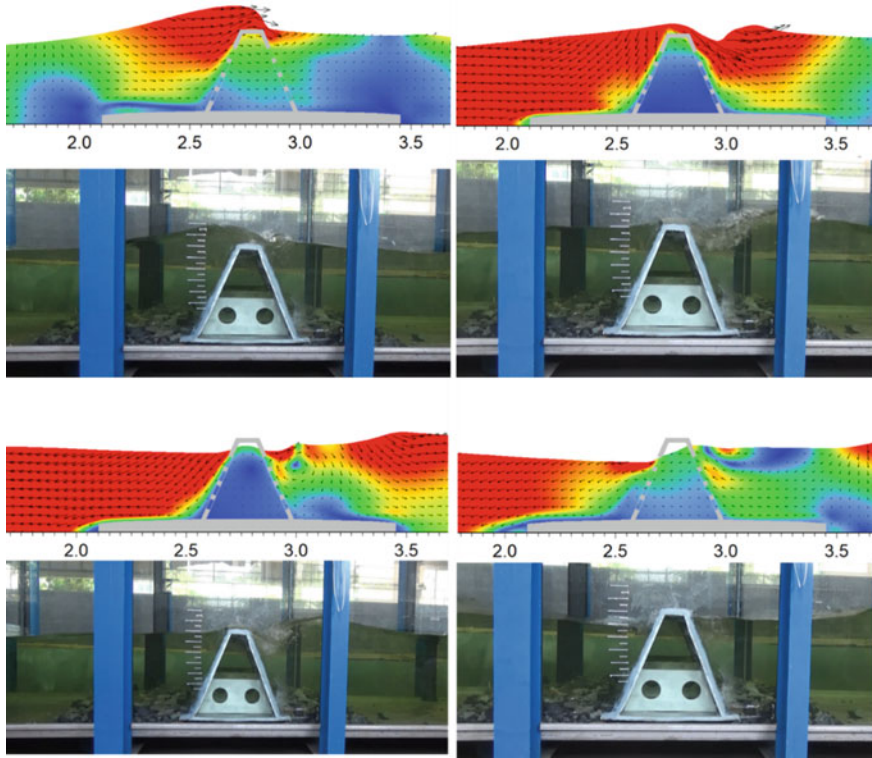


Fig. 17.5 The comparison of wave interaction at different stages between numerical and physical models for calibration

mixing of the overtopped and behind flows which derived from numerical model are similar to the results obtained by physical model. This shows that the MIKE 3 wave FM model has been successfully calibrated and formulated mathematically followed relatively the laws of physics and wave phenomena.

17.4.2 The Evolution of Wave and Velocity Fields Through Structure

The simulations of the MIKE 3 wave FM model were performed for the case of wave height $H_{m0} = 0.12$ m, peak wave period $T_p = 1.31$ s, and corresponding to the porosity of the breakwater of KH2 ($P_1 = 22.5\%$; $P_2 = 11.8\%$). We ran 1000 irregular waves and selected the maximum incident wave attacking the breakwater to present clearly the recognizable variations of wave and velocity fields as described in Figs. 17.6 and 17.7. Due to the large number of time-steps (3000 steps, 0.2 s/step) and the long experimental flume (35 m), we only selected a smaller window size around the

breakwater (i.e. 17.5–22.5 m) to effectively capture the detectable changes in the wave states and velocity fields.

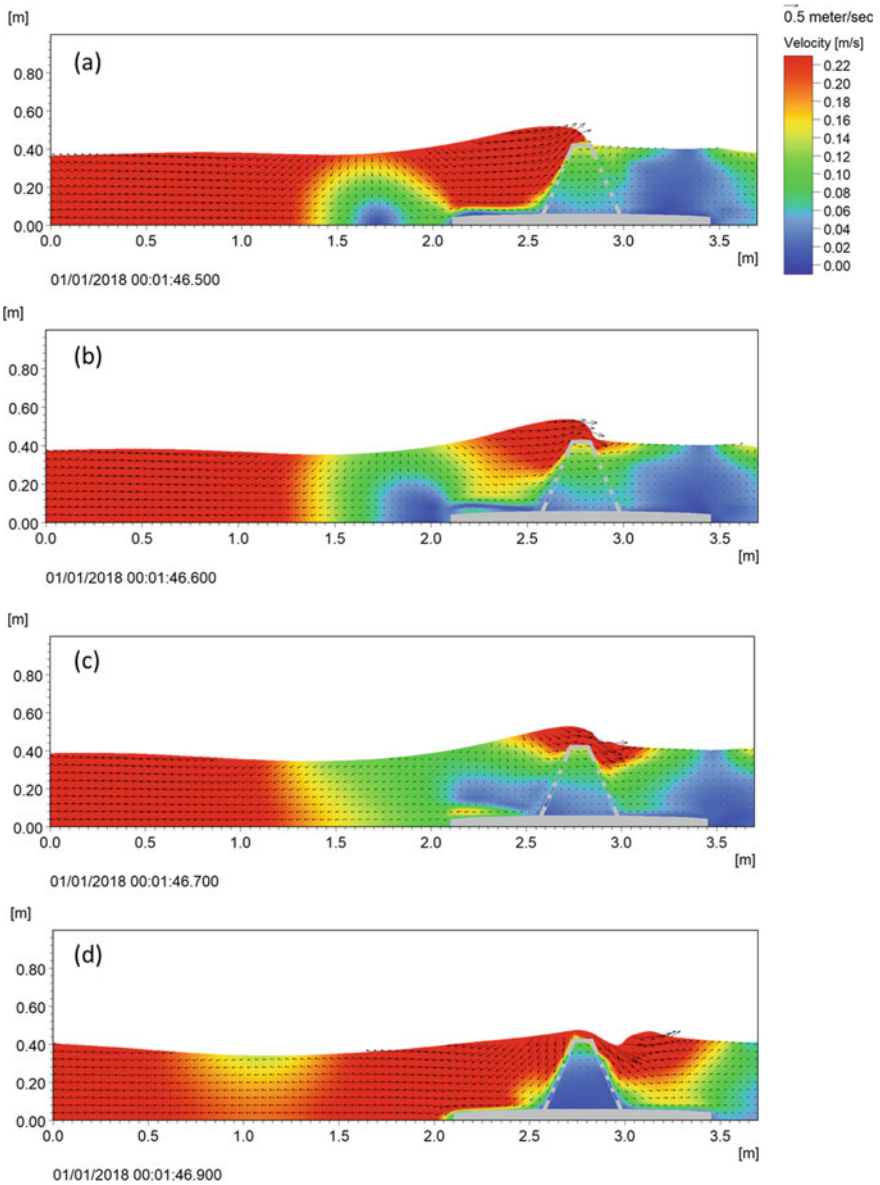


Fig. 17.6 Velocity field in (x, z) direction at $t = 1:46.50$ to $t = 1:46.90$ from time steps 1065 to 1069 with maximum incident wave windows

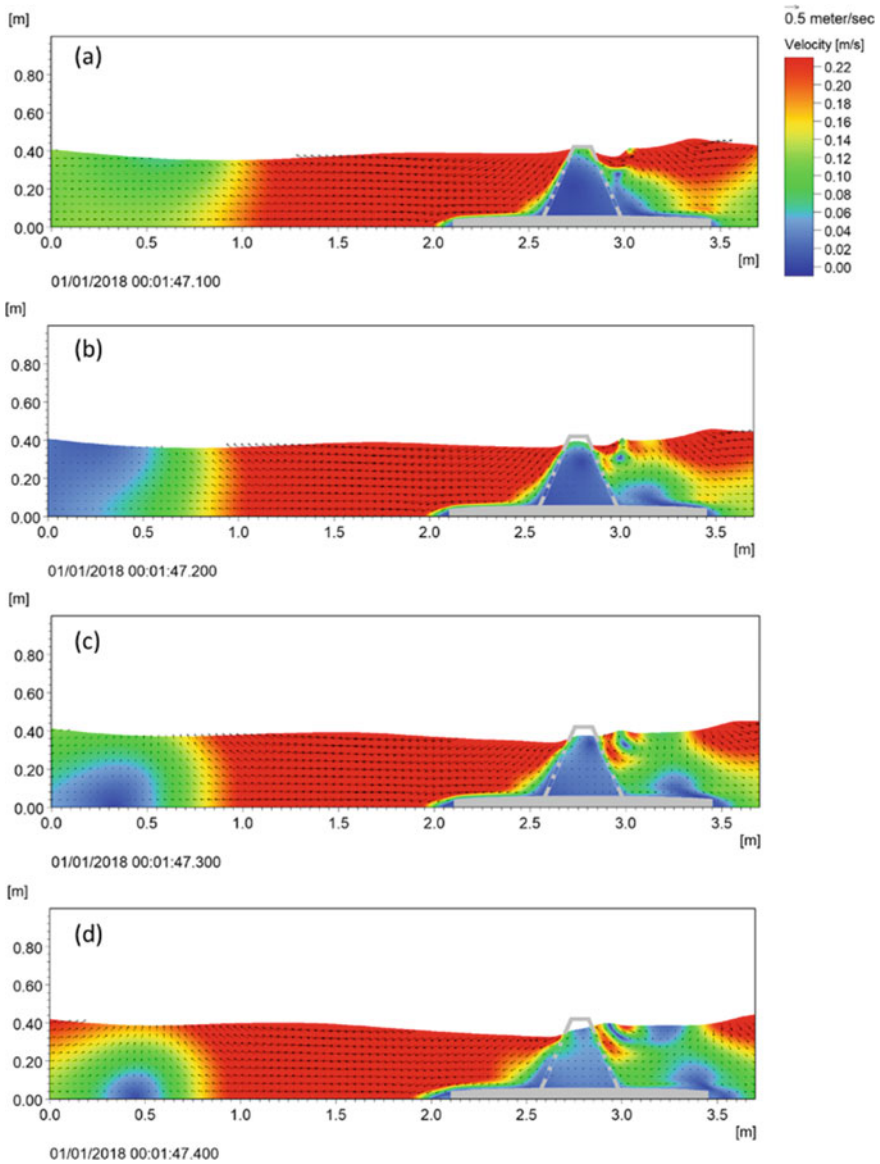


Fig. 17.7 Velocity field in (x, z) direction at $t = 1:47.10$ to $t = 1:47.40$ from time steps 1074 to 1074 with maximum incident wave windows

It can be observed that velocity in front of breakwater has a range of 0.20–0.22 m/s and the wave attacks along the perforated flat-inclined face and then overtops the crest of the structure. The velocity inside the hollow breakwater fluctuates in a range of 0.02–0.12 m/s (Fig. 17.6) and was lower than the velocity in front of breakwater because of the obstruction of the perforated flat-inclined face. The velocity after overtopping the structure is still high (0.18–0.22 m/s) at time step 1065 and reduces rapidly to 0.06–0.12 m/s after an additional 10 time-steps (5 s) due to turbulence and formation of eddies. The clockwise vortex appears near behind the structure due to the interaction of two flows at time step $t = 1:47.2$ s, that is the one from falling overtopping-flow, and the one from reflected flow behind the structure in the flume (Fig. 17.7). It can be seen that the two velocity directions are distinctly opposite behind the breakwater. It is also observed that the surface flow moves to the downstream of the experimental flume and the reverse flow goes back upstream of the experimental flume.

17.4.3 Turbulent Kinetic Energy and Vertical Eddy Viscosity

The turbulent kinetic energy (TKE) and vertical eddy viscosity around the breakwater are subjected to irregular wave propagation and are analyzed at different time-steps in the window of the maximum incident wave. We selected observable windows to present four illustrative stages which include the following: (a) wave run-up, (b) onset of overtopping, (c) peak overtopping, and (d) mixing of the overtopped and behind flows (see Figs. 17.6 and 17.7). In the wave run-up stage, the incident wave attacks and rushes up on the perforated flat-inclined face and starts climbing along the exposed face to the crest, and partially goes through the breakwater via circular holes. The flow reaches on the crest of the breakwater and starts overtopping at stage (b), the forward flow associated with the splashes and squirts begins to overtop over the crest. It is noted that the maximum overtopping rate occurs when a large volume of overtopped water rushes down to the back side of the breakwater at stage (c). At stage (d) the overtopped flow falls into the flow behind the breakwater to create energetic turbulence and formation of eddies and vortices (see Fig. 17.7).

TKE is the average kinetic energy per unit mass and is associated with eddies in turbulent flow. TKE is proportional to the square of its velocity. Figure 17.8 shows the distribution of TKE near the hollow triangle breakwater at four time-steps of 1064, 1066, 1068, 1070 ($t = 1:46.40$ – $1:47.0$ s). When the wave propagates at the crest of breakwater ($t = 1:46.40$ s), the TKE is varies slightly in a range of 0.0035 – 0.009 m^2/s^2 due to insignificant variations of velocity at stage (a). After 10 time-steps, a substantial alteration in velocity makes the turbulent kinetic energy increase on the top of breakwater from 0.0035 to 0.0124 m^2/s^2 and considerably expand to a larger area resulting in the clockwise vortex appearance at time step $t = 1:47.20$ s. Moreover, it can be observed that the largest TKE occurs at two zones including the crest of the breakwater and the rubble-mound in front of the foot of the breakwater. This is because these zones are significantly affected by the considerable variations of

velocity due to the interaction between two different flows and currents. The bed flow forward attacks the breakwater and then reverses direction and the overtopped flow rushes down and is mixed with the flow behind the breakwater resulting in strong turbulence in this area (see Figs. 17.7 and 17.8). Finally, the turbulent kinetic energy shifts from in front of breakwater bed (i.e. offshore) to behind the breakwater surface (i.e. onshore) and then dissipates rapidly due to turbulent energy losses.

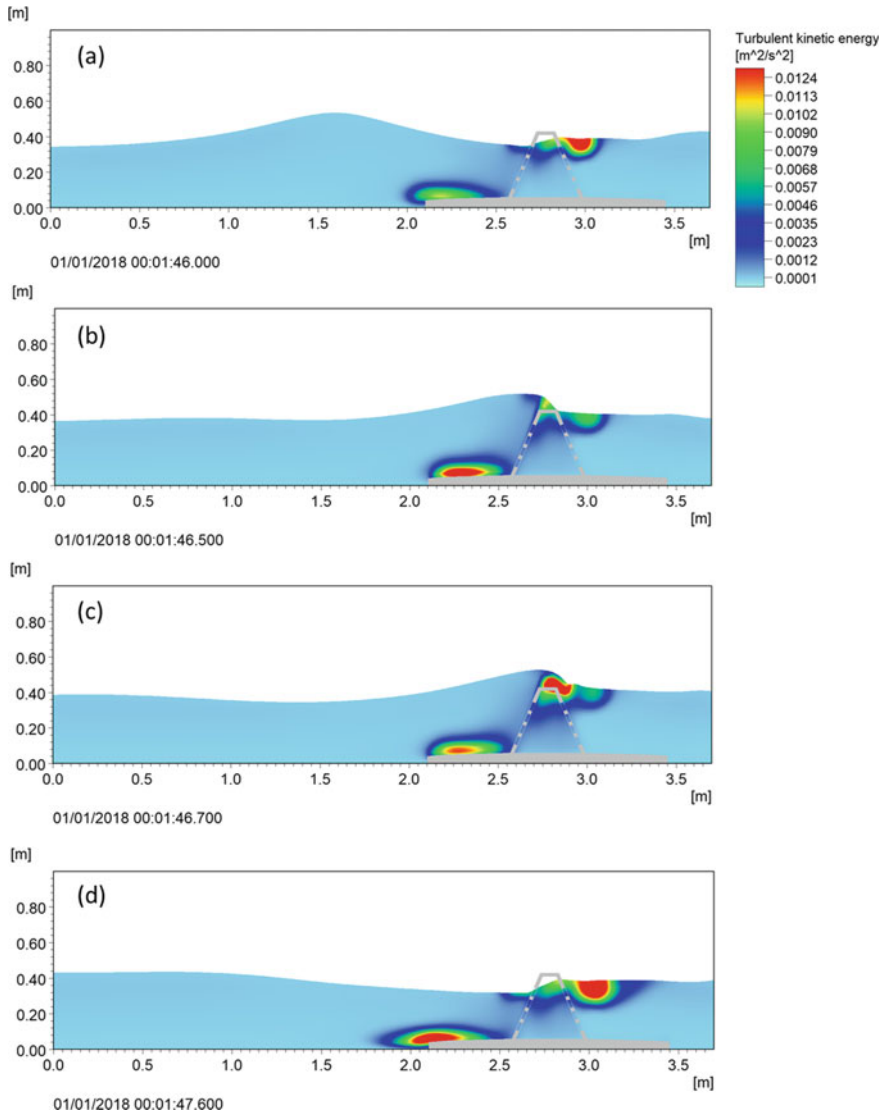


Fig. 17.8 Turbulent kinetic energy at $t = 1:46.40$ s to $t = 1:47.00$ s from time step 1064 to 1070 during with maximum incident wave windows

Figure 17.9 shows the vertical eddy viscosity near the hollow triangle breakwater under irregular waves. Note that this parameter is a function of the local flow conditions rather than representing physical characteristic of the fluid (Blazek 2015). The tendency of vertical eddy viscosity varies similarly to that of turbulent kinetic energy because it assumes that the eddy viscosity has a proportional relationship with the turbulent kinetic energy.

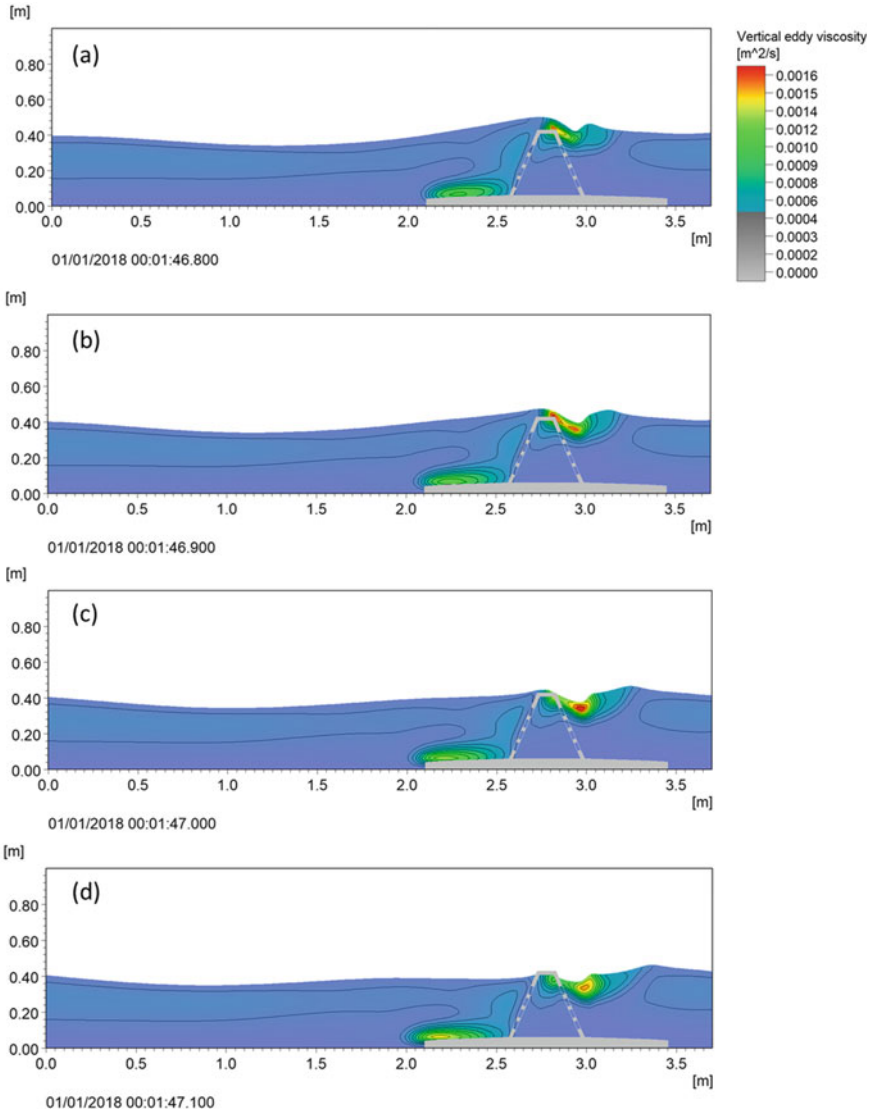


Fig. 17.9 Vertical eddy viscosity at $t = 1:46.80$ to $t = 1:47.10$ from time step 1068 to 1071 during with maximum incident wave windows

17.4.4 *The Non-hydrostatic Pressure on the Structure*

The non-hydrostatic pressure is usually neglected in three-dimensional hydrodynamic models using the Reynolds Averaged Navier–Stokes equation based on hydrostatic assumption to simulate hydraulic regimes in large water resources systems such as river, estuaries and coastal zones (Soulignac et al. 2017; Munar et al. 2018; Cunha et al. 2020). However, this assumption is only valid for large shallow water systems because horizontal length scales are considerable higher than vertical length scales. Moreover, eddy viscosity and acceleration terms in the momentum equations for the vertical velocity components are significantly smaller than the gravitational acceleration term (Pedlosky 1979; Chen 2005). In contrast, the ratio of vertical to horizontal motion scales is not small in the simulation of hydraulic jumps, dam break flows, and storm-surge barriers (Zhou and Stansby 1999). Therefore, to obtain the accuracy of flow and velocity fields during the turbulence and oscillation, the non-hydrostatic pressure component in the MIKE 3 wave FM model has to be fully considered in this case (Cunha et al. 2020; Chen 2005).

Figure 17.10 shows the non-hydrostatic pressure at different time steps from 1:46.40 s to $t = 1:46.90$ s that present clearly the variations of pressure at the aforementioned four stages in Sect. 17.4.2.2. It is an undeniable observation that the hydrodynamic regime inside the hollow triangle breakwater is very complicated due to both forward flow and backward flow. Consideration of non-hydrostatic pressure around the breakwater is critical for design and stability calculations. From Fig. 17.10, it is clear that the non-hydrostatic pressure decreases rapidly from positive (i.e. 80–240 Pa) to negative magnitudes (i.e. -240 to -560 Pa). It can be explained that the non-hydrostatic pressure is significantly influenced by the baroclinic effect in the oscillation (Chen 2005; Stigebrandt 1999). The baroclinic effect is due to the nonalignment of pressure and density gradients, and its result is to induce vorticity production (Batley et al. 1996; May and Kelley 1997; Suanda et al. 2018). Moreover, the flow separation due to circular holes on both sides of the perforated flat-inclined face creates a higher velocity (0.06–0.14 m/s) inside the breakwater (Fig. 17.6a–c), explaining the negative pressure in Fig. 17.9b–d (Berntsen et al. 2009). The forces from the non-hydrostatic pressure gradients acting against the forward flow is in an inverse direction and is represented by the negative magnitudes. From Figs. 17.6 and 17.7, it is noted that there is substantial vertical acceleration due to the significant variations of velocity between the near surface and the lower zones inside the breakwater (Fig. 17.6a–c).

The analysis of non-hydrostatic pressure for different incident wave spectrum and the percentage of porosity in the hollow triangle breakwater is very important to define the weight of the structure and load capacity, and the concrete strength of the structure which is not related to the physical model. This has practical implications in structural design and ensures stability, and efficient operation of the breakwater in the long term.

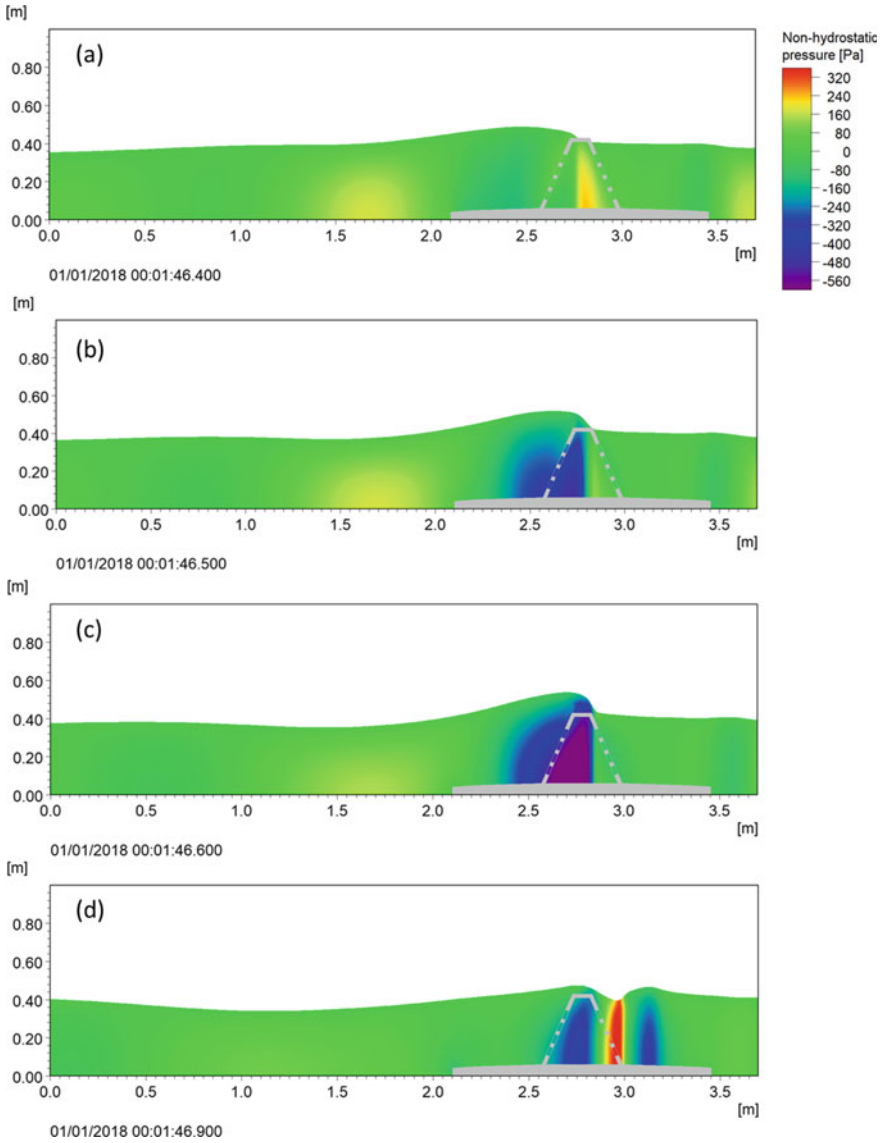


Fig. 17.10 The Non-hydrostatic pressure distribution at different time steps from 1:46.40 s to t = 1:46.90 s

17.5 Conclusion

The key contribution is to improve the understanding of hydrodynamic behaviors and wave action on the HTB including flow patterns, velocity field, turbulent kinetic energy, vertical eddy viscosity, non-hydrostatic pressure which unable to observe

from physical model. This has important implications for design calculation, structural stability and ensuring the function of transmitting waves through the HTB. This study also successfully applied a new numerical model to simulate wave transmission through a hollow triangle breakwater. The incident wave spectrum and the percentage of porosity (KH2) of the hollow triangle breakwater were selected to test with 1000 irregular waves with 3000 time-steps (10 min) running. This numerical modelling is developed an understanding of the undetected aspects of physical modelling at small scale and in very short timeframes. The numerical simulations also provide clear explanation of the complicated mechanism of attacking waves on the breakwater and energy dissipation through the structure. Future works will be conducted with various cases of wave spectrum, different percentages of porosity, and several bed slopes with consideration of fine sediment transport.

Acknowledgements This work was partially supported by the Ministry of Science and Technology (MOST) Vietnam in a national project (No. ĐTĐL.CN-07/17) “Research appropriate solutions and applicable technologies to prevent erosion, stabilize the coastline and estuaries of the Mekong River, from Tien Giang to Soc Trang” and the Southern Institute of Water Resources Research. The authors greatly appreciate the Editor and also deeply thank the three anonymous reviewers for their constructive comments to improve the manuscript.

Declaration of Competing Interest The authors declare that they have no known competing financial interests or personal relationships that could have appeared to influence the work reported in this paper.

References

- Albers T (2018) The T-fence story—application of permeable bamboo fences in the Lower Mekong Delta, Vietnam. <http://coastal-protection-mekongdelta.com/download/Tools/>. Access on 7 May 2021
- Albers T, Schmitt K, Dinh CS (2013) Shoreline management guidelines—coastal protection in the lower Mekong Delta. Published by Deutsche Gesellschaft für Internationale Zusammenarbeit (GIZ) GmbH. ISBN 978-604-59-0630-9. http://coastal-protection-mekongdelta.com/download/library/40.Shoreline-Management-Guidelines_EN.pdf
- Anthony EJ, Brunier G, Besset M, Goichot M, Dussouillez P, Nguyen VL (2015) Linking rapid erosion of the Mekong River delta to human activities. *Sci Rep* 5:1–12
- Antonini A, Lamberti A, Archetti R, Miquel AM (2016) CFD investigations of OXYFLUX device, an innovative wave pump technology for artificial downwelling of surface water. *Appl Ocean Res* 61:16–31
- Batley GA, McIntosh AC, Brindley J (1996) The baroclinic effect in combustion. *Math Comput Model* 24(8):165–176
- Berntsen J, Xing J, Davies AM (2009) Numerical studies of flow over a sill: sensitivity of the non-hydrostatic effects to the grid size. *Ocean Dyn* 59(6):1043
- Besset M, Gratiot N, Anthony EJ, Bouchette F, Goichot M, Marchesiello P (2019) Mangroves and shoreline erosion in the Mekong River delta, Viet Nam. *Estuar Coast Shelf Sci* 226:106263
- Blazek J (2015) *Computational fluid dynamics: principles and applications*, 3rd edon. Butterworth-Heinemann. <https://doi.org/10.1016/C2013-0-19038-1>
- Chen X (2005) A comparison of hydrostatic and nonhydrostatic pressure components in seiche oscillations. *Math Comput Model* 41(8–9):887–902

- Cunha AHF, Fragoso CR, Chalegre CLB, Motta-Marques D (2020) Improvement of non-hydrostatic hydrodynamic solution using a novel free-surface boundary condition. *Water* 12(5):1271
- del Jesus M, Lara JL, Losada IJ (2012) Three-dimensional interaction of waves and porous coastal structures: part I: numerical model formulation. *Coast Eng* 64:57–72
- Dentale F, Donnarumma G, Carratelli EP (2014) Rubble mound breakwater: run-up, reflection and overtopping by numerical 3D simulation. In: *From Sea to shore—meeting the challenges of the Sea: (Coasts, marine structures and breakwaters 2013)*. ICE Publishing, pp 1164–1173
- DHI (2019) MIKE 3 wave model FM hydrodynamic model scientific documentation. https://manuals.mikepoweredbydhi.help/2019/Coast_and_Sea/MIKE_3_Wave_FM_Scientific_Doc.pdf. Access on 10 Apr 2019
- Fang Z, Cheng L, Zhang N (2010) Development of 3-D numerical wave tank and applications on comb-type breakwater. In: *29th International conference on ocean, offshore and arctic engineering (OMAE2010)*. Shanghai, China
- Fitriadhy A, Faiz MA, Abdullah SF (2017) Computational fluid dynamics analysis of cylindrical floating breakwater towards reduction of sediment transport. *J Mech Eng Sci* 11(4):3072–3085
- Flow Science Inc. (2009) Suite Flow 3D. Flow Science Inc., Santa Fe, Mexico
- Gomes A, Pinho JL, Valente T, Antunes do Carmo JS, V Hegde VA (2020) Performance assessment of a semi-circular breakwater through CFD modelling. *J Mar Sci Eng* 8(3):226
- Koraim AS, Rageh OS (2013) Hydrodynamic performance of vertical porous structures under regular waves. *China Ocean Eng* 27(4):451–468
- Lara JL, del Jesus M, Losada IJ (2012) Three-dimensional interaction of waves and porous coastal structures: part II: experimental validation. *Coast Eng* 64:26–46
- Le Xuan T, Ba HT, Le Manh H, Van Do D, Vu HTD, Wright DP, Bui VH, Anh DT (2020a) Hydraulic performance and wave transmission through pile-rock breakwaters. *Ocean Eng* 218:108229
- Le Xuan T, Ba HT, Le Manh H, Van Do D, Nguyen NM, Wright DP, Bui VH, Mai ST, Anh DT (2020b) Hydraulic performance and wave transmission through pile-rock breakwaters. *Ocean Eng* 218:108229
- Liu PLF, Lin P, Chang KA, Sakakiyama T (1999) Numerical modeling of wave interaction with porous structures. *J Waterw Port Coast Ocean Eng* 125(6):322–330
- Losada IJ, Lara JL, Guanche R, Gonzalez-Ondina JM (2008) Numerical analysis of wave overtopping of rubble mound breakwaters. *Coast Eng* 55(1):47–62
- Mai T, Dao T, Ngo A, Mai C (2019) Porosity effects on wave transmission through a bamboo fence. In: *International conference on Asian and Pacific coasts*. Springer, Singapore, pp 1413–1418
- May BD, Kelley DE (1997) Effect of baroclinicity on double-diffusive interleaving. *J Phys Oceanogr* 27(9):1997–2008
- Miquel AM, Kamath A, Alagan Chella M, Archetti R, Bihs H (2018) Analysis of different methods for wave generation and absorption in a CFD-based numerical wave tank. *J Marine Sci Eng* 6(2):73
- Munar AM, Cavalcanti JR, Bravo JM, Fan FM, da Motta-Marques D, Fragoso CR Jr (2018) Coupling large-scale hydrological and hydrodynamic modeling: toward a better comprehension of watershed-shallow lake processes. *J Hydrol* 564:424–441
- Nguyen HH, Pham DH, Nguyen DN, Nguyen TT (2018) Hollow cylinder breakwater for dissipation of wave energy to protect the west coast of Ca Mau Province in Vietnam. In: *Vietnam symposium on advances in offshore engineering*. Springer, Singapore, pp. 599–605
- Pedlosky J (1979) *Geophysical fluid dynamics*. Springer, New York
- Reis MT, Neves MG, Hu K, Ten Voorde M (2008) Numerical and physical modelling of wave overtopping over a porous breakwater. In: *The eighteenth international offshore and polar engineering conference*. International Society of Offshore and Polar Engineers
- Rodi W (1980) Turbulence model and their application in hydraulic a state-of-the-art review. IAHR Publication
- Rodi W (1984) *Turbulence models and their applications in hydraulics*. IAHR, Delft, The Netherlands

- Soullignac F, Vinçon-Leite B, Lemaire BJ, Martins JRS, Bonhomme C, Dubois P, Mezemate Y, Tchiguirinskaia I, Schertzer D, Tassin B (2017) Performance assessment of a 3D hydrodynamic model using high temporal resolution measurements in a shallow urban lake. *J Environ Model Assess* 2017(22):309–322
- Stigebrandt A (1999) Resistance to barotropic tidal flow in straits by baroclinic wave drag. *J Phys Oceanogr* 29:191–197
- Suanda SH, Feddersen F, Spydell MS, Kumar N (2018) The effect of barotropic and baroclinic tides on three-dimensional coastal dispersion. *Geophys Res Lett* 45(20):11–235
- Thorenz F (2016) Strategic advice for coastal protection planning in the southern of Mekong delta (2016)
- Van Gent MRA (1995) Porous flow through rubble mound material. *J Waterway Port Coastal Ocean Eng* 121(3):176–181. ASCE, New York
- Williams HE, Briganti R, Romano A, Dodd N (2019) Experimental analysis of wave overtopping: a new small scale laboratory dataset for the assessment of uncertainty for smooth sloped and vertical coastal structures. *J Mar Sci Eng* 7(7):217
- Zhou JG, Stansby PK (1999) ALES shallow-water flow solver with non-hydrostatic pressure: wave applications. In: *Coastal engineering*, pp 422–432

Chapter 18

The Role of Hydrodynamics in the Development of Mangrove Forests in Can Gio Mangrove Biosphere Reserve (Ho Chi Minh, Vietnam)



**Hoa Tien Le Nguyen, Xuan Dung Tran, Tien Thanh Nguyen,
and Hong Phuoc Vo Luong**

Abstract The Can Gio area once supported natural mangrove forest, but was almost fully destroyed by herbicides during the Second Indochina War. Between 1978 and 1986, the area was reforested with mangroves. In 2000, Can Gio was designated as Vietnam's first biosphere reserve with a total area of 75,740 ha by UNESCO. The aim of research is to study the role of hydrodynamics in the development of mangrove forests in Can Gio. By using remote sensing techniques, the temporal changes of Can Gio vegetation area since 1973 were done and shown how development of Can Gio Mangrove before and after the replantation and up to now. Moreover, the hydrodynamics modelings can prove that hydrodynamics have influenced on the growth of mangrove trees along the coasts and river. Especially, the field experiment for the contribution of river tidal flows to the rehabilitation of mangrove trees after the Durian tropical cyclone in 2006 was done. The results show that thanks to tidal and river dynamics, the seeds of mangroves can be distributed freely and makes the diversity of mangrove species along the coasts and rivers. Wave is the main factor for bank erosion and the deaths for coastal mangrove trees. River flows make the meandering rivers combining with erosion and accumulation processes.

Keywords Can Gio · Mangrove forests · Hydrodynamics · Erosion · Accumulation

18.1 Introduction

Can Gio District (10° 22' 14'' N–10° 40' 09'' N, 106° 46' 12'' E–107° 00' 59'' E) is one of 18 districts of Ho Chi Minh City (HCMC) with an area of 73,361 ha. Can Gio has

H. T. Le Nguyen · X. D. Tran · T. T. Nguyen · H. P. Vo Luong (✉)
Department of Oceanology, Meteorology and Hydrology, Faculty of Physics and Engineering
Physics, University of Science, Ho Chi Minh City, Vietnam
e-mail: vlphuoc@hcmus.edu.vn

Vietnam National University, Ho Chi Minh City, Vietnam

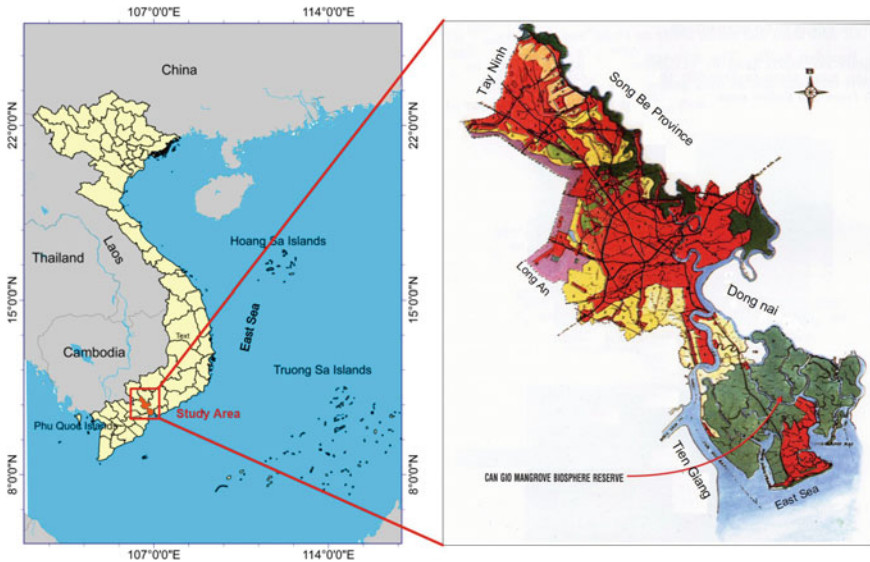


Fig. 18.1 Map locating Can Gio Mangrove Biosphere Reserve in Ho Chi Minh city, South Vietnam (Tuan et al. 2002)

a lot of rivers and channels in the delta and the main waterways leading to the port of HCMC (Nam et al. 1993; Tuan et al. 2002). On 21 January 2000, Can Gio mangrove forest was approved as the Mangrove Biosphere Reserve by MAP/UNESCO and it is also the first Biosphere Reserve in Vietnam. Nowadays, Can gio can be considered as a model for forest protection and management in Vietnam. Beside being the attractive place for tourists, Can Gio is also an idela place for scientific research on geology (Hang and Anh 2003), on biology (Tuan et al. 2002; Hong and San 1993), on natural and social conditions (Nam 1993; Nam and Tuan 2004). There were a lot of studies on the physical processes in Can Gio mangorve forests such as Mazda et al. (2002); Vo Luong and Massel (2006) Horstman et al. (2012); Pavarthy and và Prasad (2017). The aim of research is to study the role of hydrodynamics in the development of mangrove forests in Can Gio. By using remote sensing techniques, the temporal changes of Can Gio vegetation area since 1973 were done and shown how the development of Can Gio Mangrove before and after the replantation and up to now (Fig. 18.1).

18.2 Methodology

Remote sensing analysis was conducted with the dataset of Landsat images collected from 1973 (before the war) to 2021. These images are free to download from the website of the United States Geological Survey (<http://glovis.usgs.gov/>).

The collected results were used based on WAPROMAN (Wave PROpagation in MANgrove forests) model (Vo-Luong and Massel 2008), wave refraction (Vo Luong et al. 2008) and some data analysis from field measurements in 2012 and 2014 in Can Gio mangrove biosphere reserve (HCMC) (Nguyen and Luong 2019).

18.3 Development of Can Gio Mangrove Forest

Before the union of Vietnam (April 30th 1975), Can Gio mangrove forest covered an area of 40 000 ha with high density, tall and big trees (over 25 m tall and 25-40 cm in diameter) (Tuan et al. 2002). From 1964 to 1970, over 665,666 gallons of Agent Orange, 343,385 gallons of Agent White and 49,200 gallons of Agent Blue sprayed in Can Gio mangroves. As a result, most of mangrove trees (over 57%) in the district were died (Nam et al. 1993). In some areas, most of trees of *Rhizophora*, *Sonneratia* and *Bruguiera* were killed. However, tidal oscillation played an important role in restoration of the coastal mangrove areas which were sprayed heavily with herbicides. In the coastal areas with flooded twice daily and once daily, it helps washing out the herbicides for the mangrove trees especially in the lower land (Nam 1993).

In the period of 1978–1987, Ho Chi Minh City Forestry Department has undertaken a vast programme of reforestation. The *Rhizophora aciculate* sp. were chosen to be planted and raised. The species is fast growing tree native to the forest and it is the tree with the highest commercial value (Tuan et al. 2002). However, after some year, there were 50% mangrove deaths. The main causes can be due to tidal oscillation, water levels and hydrodynamic waves in Can Gio (Nam 1993). Especially, high wave prevent the growth of mangrove trees. Furthermore, in mangrove areas, natural succession of mangrove species is determined by various environmental and ecological factors, including soil composition, tidal regimes, geographical location (Vo-Luong and Massel 2008). In particular, the accretion and erosion progress in the coastal areas is influential in determining the distribution of pioneer and successive species (Hong and San 1993). *Avicenia* sp. can be considered the pioneer species growing fast in new muddy flat along the river and the coast. *Rhizophora* grow in stable mud flat and higher land.

Figure 18.2 shows the changes of two mangrove species, *Avicenia* sp. and *Rhizophora* sp. from 1973 to 2021 via remote sensing techniques and field calibration. Obviously, from 1973 to 1978, Can gio almost empty, mainly mud and soil, few *Avicenia* growing along the coast. However, after a vast programme of reforestation, mangrove areas are growing fast, especially for *Rhizophora* sp. Up to now (2021), the mangrove area is increasing every year, especially for *Rhizophora* sp. and *Avicenia* sp.

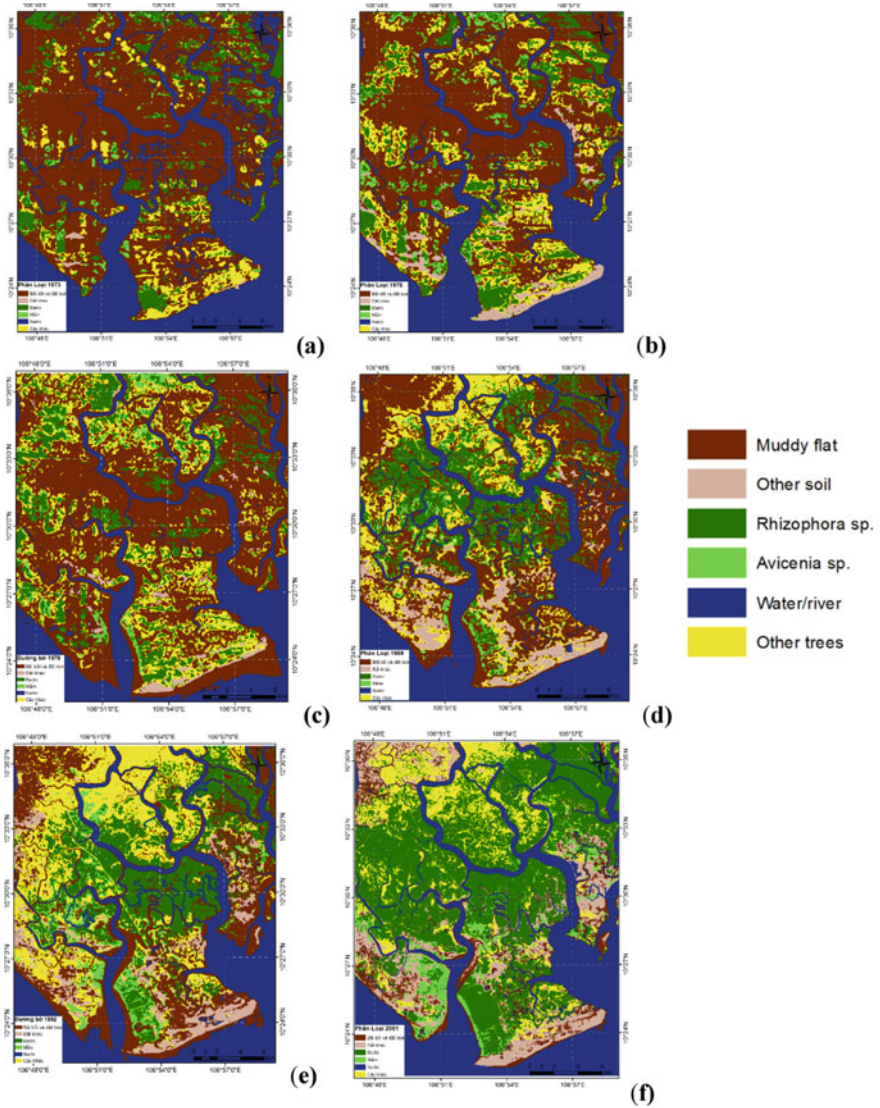


Fig. 18.2 The changes of Mangrove Species in time. **a** 1973, **b** 1975, **c** 1978, **d** 1989, **e** 1992, **f** 2001, **g** 2005, **h** 2009, **i** 2014, **j** 2016, **k** 2018, **l** 2021

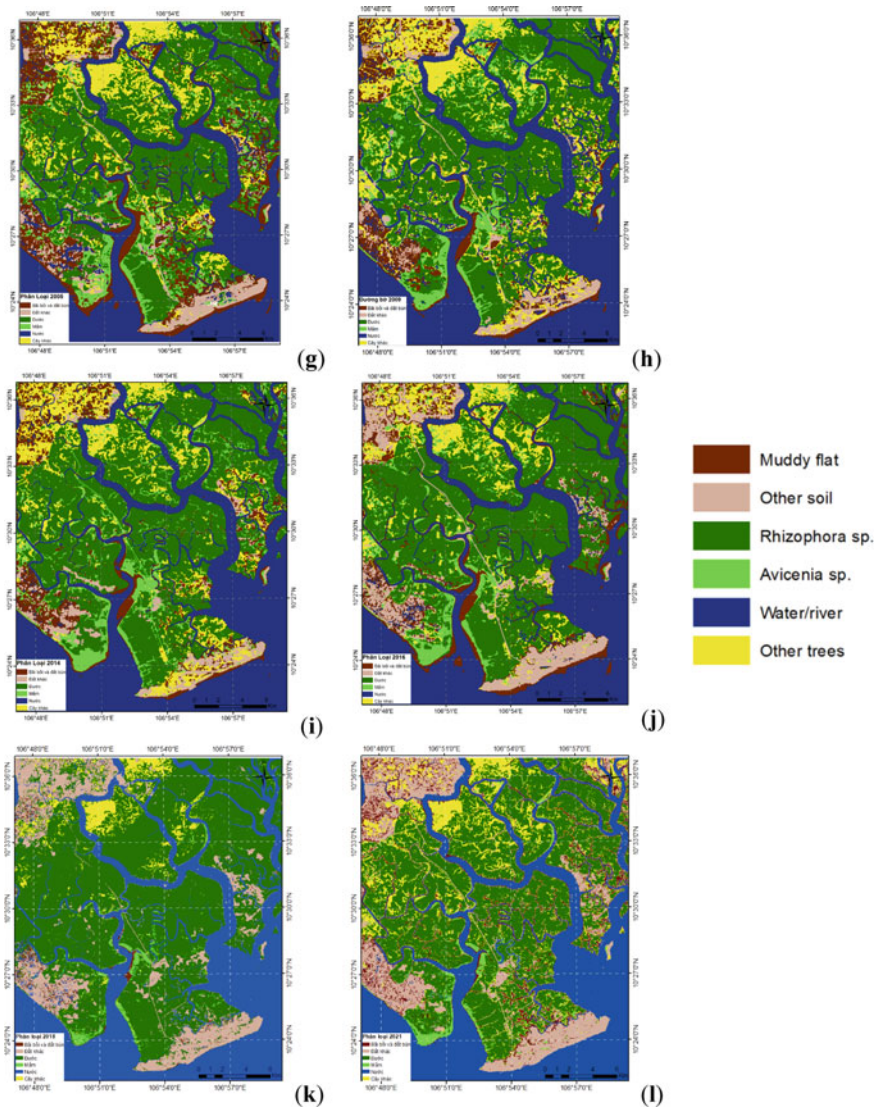


Fig. 18.2 (continued)

18.4 Hydrodynamics Impact on the Development of Can Gio Mangrove

18.4.1 The Role of Mangrove Forest in Sediment Retention

Mangrove forests play an important role in sediment retention and coastal protection. Mangroves not only “occupy” the muddy flats but also “create” new muddy flats, especially *Avicennia* sp. Measured data of Suspended Sediment Concentration (SSC) were made in Can Gio in 2012 and 2014 (Le Nguyen and Vo Luong 2019) shows the changes of SSC in station inside of mangroves depends strongly on wave intensity and tidal currents. Figure 18.3 and Table 18.1 prove obviously that inside of the mangrove, SSC was not only kept but also increased with the wave intensity and tidal currents. These results prove the significant role of mangroves in sediment retention and coastal protection from wave impact. It also confirms the conclusion that mangrove forests are effective barriers to protect coastlines from waves and storms.

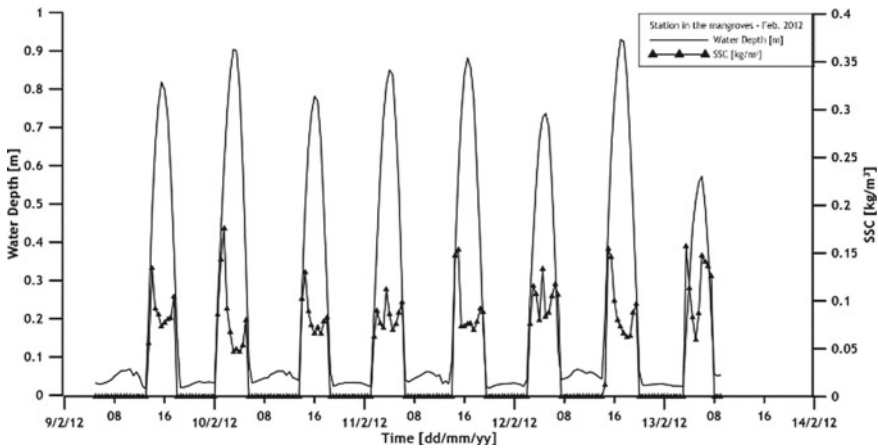


Fig. 18.3 SSCs in the mangrove forest site in Can Gio (Le Nguyen and Vo Luong 2019)

Table 18.1 Calculated suspended sediment rate Q during the flood tides, ebb tides and total Q on one tidal day in the mangrove forest (ST2 station) (Le Nguyen and Vo Luong 2019)

Cases	Station ST2—in the mangrove forest		
	Q_{flood}	Q_{ebb}	Q_{tot}
Case I: strong waves (H_s average = 0.24 m)	$+ 22 \times 10^{-3}$	$- 6 \times 10^{-3}$	$+ 16 \times 10^{-3}$
Case II: weak waves (H_s average = 0.14 m)	$+ 12 \times 10^{-3}$	$- 4 \times 10^{-3}$	$+ 8 \times 10^{-3}$

Note “+ ”: the seaward of Q , “-”: the landward of Q

18.4.1.1 The Rehabilitation of Mangroves After the Storm

During the storm No. 9 Durian on 5th December 2006, Can Gio Mangrove Biosphere Reserve in Ho Chi Minh City “sacrificed” itself for habitants in coastal zones. Five mangrove ha were destroyed and became the “white” area. However, after a short time, it could be recognized that the destroyed area is becoming “green”. The young mangroves are growing up and the mangrove forest is being rehabilitated. The dispersal of seeds by wind and by tidal oscillations can be considered as the main reasons for the rehabilitation. The mangrove seeds by winds could not be scattered far from the mother trees due to the limit wind velocity while the seeds could float and settle anywhere the water level is high enough.

The observations prove that the distribution of seeds depends not only mainly on wind speed but also on tidal water level (Fig. 18.4). Along the creek, the young trees, mainly *Avicennia* sp., are growing up. The topographical height determines the flood possibility of the sites so that it could contribute in the rehabilitation of the mangroves (Vo Luong et al. 2008). The field experiments show that tidal hydrodynamics have strong influence in the rehabilitation of mangroves. The seed distribution depends on the shape of the seeds, the float possibility of seeds, the topographical height and water level as well. *Avicennia* sp. could go through deeper area easier that *Rhizophora* sp. The results also prove that suspended sediment concentration SSC changes to tidal water level.

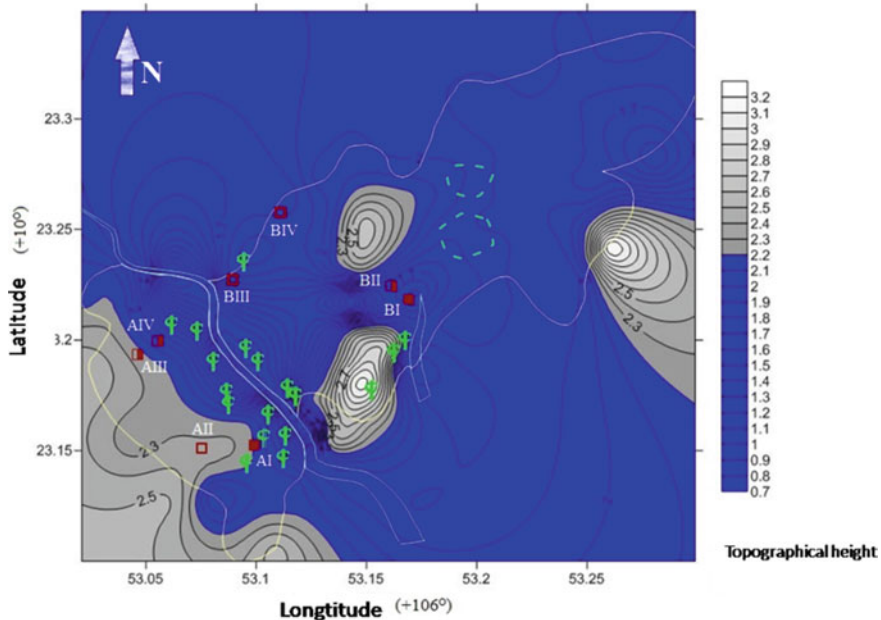


Fig. 18.4 Predicted water level at the study site for high tide (the green sign symbolizes for mangrove seed settlings)

Based on the topographical height, it shows that at the spring tide, the water level is high enough and the observed area is almost flooded, as shown in Fig. 18.4. The results could explain how and why the mangrove seeds could grow and develop in some specific sites which are often inundated.

18.4.2 Relationship of Hydrodynamics and the Development of Can Gio Mangrove Forest

Nowadays, along the creeks and rivers in Can Gio, the mangrove banks are being eroded seriously. Studies from field measurements (Mazda et al. 2002; Vo Luong and Massel 2006) as well as modelling (Vo-Luong and Massel 2008; Vo Luong et al. 2008) prove that mangrove trees contributes the deposition of sediment and dissipates the high wave energy. Furthermore, hydrodynamics of tides and waves are the main causes for sediment transport and erosion processes.

Results from the WAPROMAN model emphasizes that the main reasons of energy dissipation are due to the wave-trunk interaction and due to wave breaking (Vo-Luong and Massel 2008). Figure 18.5. shows the comparison of wave height changes in mangrove forest in different water depths in Can Gio Mangrove Biosphere Reserve, HCMC. Though the studied site can be considered as a less dense forest, the result shows that wave energy decreased very quickly, about 50% of initial wave height in 20 m from mangrove edge. The shallower water gets, the quicker wave energy dissipated. Therefore, Can Gio Mangrove Biosphere Reserve with the total area of 75,740 ha can be considered not only the “green lungs” of HCMC but also the “protective barrier” for the habitants in HCMC. The tropical storm Durian landed in HCMC on 5th December, 2006 is an obvious proof for the safe “protective barrier” for local people.

Figure 18.6 shows that predicted wave field at the Dong Tranh estuary by using the wave refraction model (Vo Luong et al. 2008). It can be seen that high wave field was focused on Nang Hai site, which has been eroded seriously.

18.5 Conclusions

Mangrove forests are classified as a unique and very characteristic system but the most vulnerable ecosystem in the coastal ecosystems. After more than 20 years of rehabilitation and development, Can Gio forest become the largest replanted mangrove areas in Vietnam with a beautiful landscape and diversity of both flora and fauna (Tuan et al. 2002).

Hydrodynamics has also been much contributed to rehabilitation and development of Can Gio forest. The hydrodynamics have great contribution in spreading muddy flat area along the mangrove coastal, reducing the erosion rate, rehabilitating

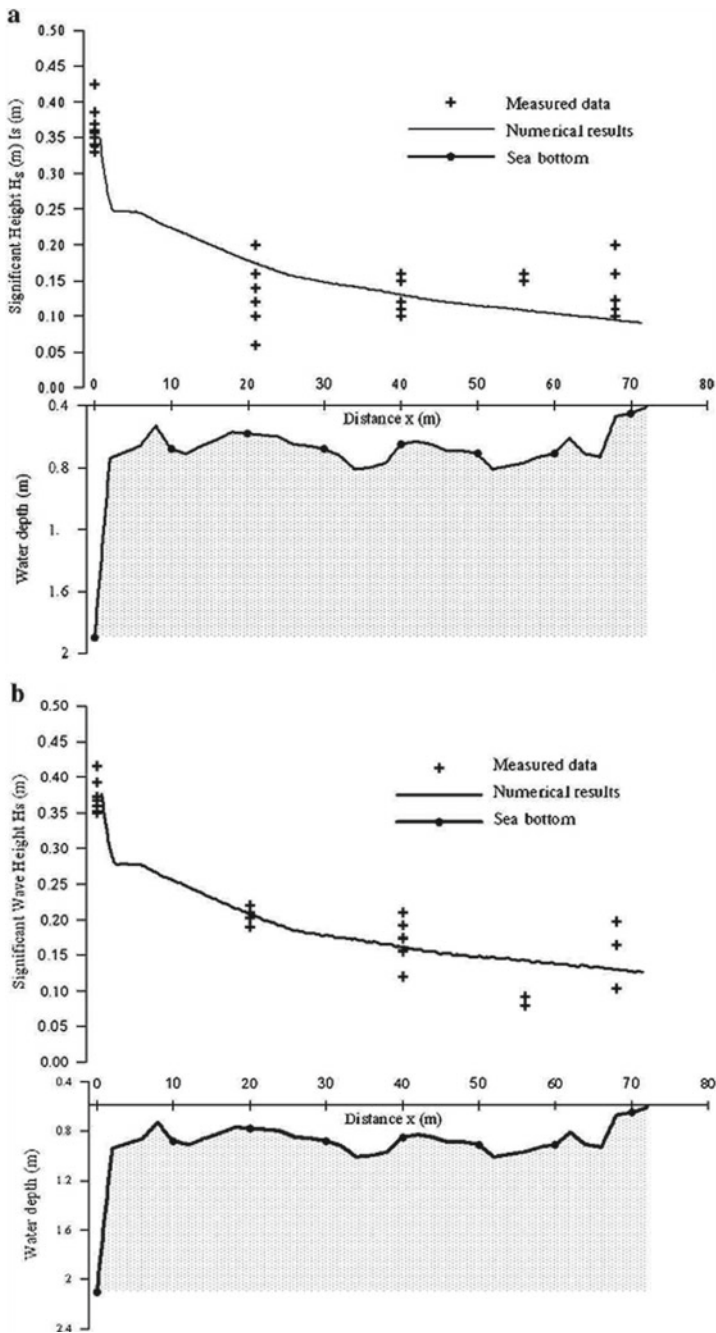


Fig. 18.5 Comparisons of numerical wave height with experimental data for water depths 1.9 m (a) and 2.1 m (b) (Vo-Luong and Massel 2008)

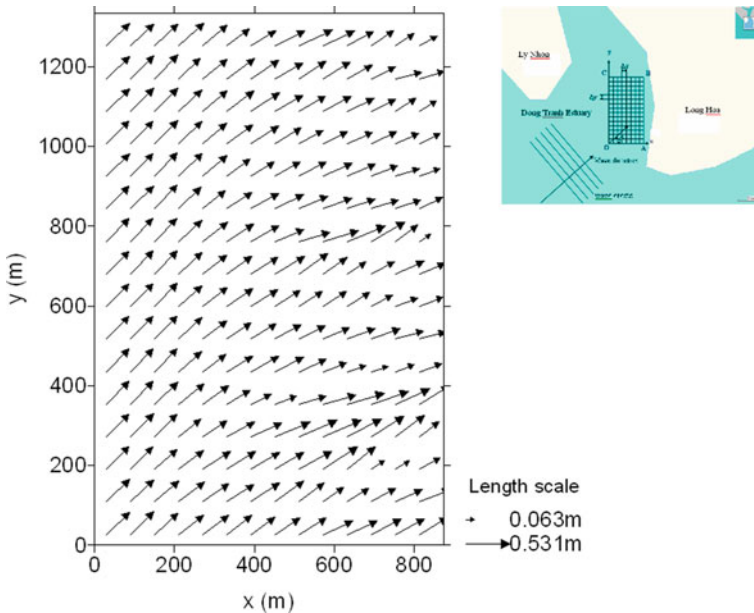


Fig. 18.6 Computed wave field at Dong Tranh estuary in Can Gio (Vo Luong et al. 2008)

the mangroves and protecting the coast from waves and storms. It is very necessary for the further and in-depth studies on hydrodynamics.

References

- Hang HTM, Anh NH (2003) Geoinformatics in environment, monitoring and land-use planning for the wetland—case study of Cangio-Hochiminh City—South Vietnam. *Environ Inf Arch* 1:447–457
- Hong PN, San HT (1993) *Mangroves of Vietnam*. IUCN-The World Conservation Union, Bangkok, Thailand
- Horstman EM, Dohmen-Janssen CM, Narra PMF, van den Berg NJF, Siemerink M, Balke T, Bouma T, Hulscher SJMH (2012) Wave Attenuation in Mangrove forests, Field data obtained in Trang, Thailand. In: Proceedings of 33rd international conference on coastal engineering (ICCE 2012—Santader, Spain), 1–6 July 2012, Coastal Engineering Research Council
- Le Nguyen HT, Vo Luong HP (2019) Erosion and deposition processes from field experiments of hydrodynamics in the coastal mangrove area of Can Gio, Vietnam. *Oceanologia* 61:252—264
- Mazda Y, Magi M, Nanao H, Kogo M, Miyagi T, Kanazawa N, Kobashi D (2002) Coastal erosion due to long-term human impact on mangrove forests. *Wetlands Ecol Manage* 10:1–9
- Nam VN (1993) Rehabilitation and management of mangrove in Can Gio district, Ho Chi Minh city, Viet Nam. In: Asia Pacific symposium on mangrove ecosystem in Hong Kong university of science and technology
- Nam VN, Tuan LD (2004) Status of mangrove biosphere reserve in Can Gio district, Ho Chi Minh city, Viet Nam. Workshop on Methodology, IMAB Project, Hanoi

- Nam VN, My TV, Jensen M (1993) FAO Mangrove for production and protection. A change resource system: case study in Can Gio district, Southern Vietnam. FAO regional wood energy development program in Asia
- Parvathy KG, Bhaskaran PK (2017) Wave Attenuation in presence of mangrove: a sensitivity study for varying bottom slopes. *Int J Ocean Clim Syst* 8(3):126–134
- Tuan LD, Kieu Oanh TT, Thanh CV, Quy ND (2002) Can Gio mangrove biosphere reserve. Agriculture Publisher
- Vo Luong HP, Massel SR (2006) Experiments on wave motion and suspended sediment concentration at Nang Hai, Can Gio mangrove forest, Southern Vietnam. *Oceanologia* 48(1):23–40
- Vo Luong HP, Toan ND, An DT, Hanh TC (2008) Computation of wave field in the Dong Tranh estuary, can Gio by using wave refraction model. *J Geol Ser B* 31–32:164–170
- Vo-Luong HP, Massel SR (2008) Energy dissipation in non-uniform mangrove forests of arbitrary depth. *J Mar Syst* 74(1–2):603–622

Chapter 19

The Method for Delimiting the Maritime Boundary in the Internal Waters of Coastal Provinces of Vietnam (From Binh Thuan Province to Ca Mau Province)



Thi Nguyet Que Phan , Ngoc Lam Hoang, Thi Bao Hoa Dinh, and Van Soat Hoang

Abstract This article presents the results of an analysis of the current management situation and current documents on administrative boundary management, thereby proposing a plan to determine administrative boundaries at sea (internal waters) for the main coastal province of Vietnam (the area from Binh Thuan province to Ca Mau province). The VN2000 national topographic map established, revised, and supplemented by the Ministry of Natural Resources and Environment was used to develop a plan to demarcate maritime boundaries. The research results provide suitable technical solutions for maritime boundary determination, taking into account the morphological characteristics of the coast, the management status, and according to the management documents of the Vietnamese state.

Keywords Administrative boundaries · Maritime boundaries · General direction

T. N. Q. Phan (✉) · N. L. Hoang · V. S. Hoang
Department of Survey, Mapping and Geographic Information of Vietnam, Ministry of Natural Resources and Environment, 2 Dang Thuy Tram, North Tu Liem, Hanoi, Vietnam
e-mail: phannguyetque@gmail.com

T. B. H. Dinh
Faculty of Geography, University of Science, Vietnam National University, 334 Nguyen Trai, Thanh Xuan, Hanoi, Vietnam
e-mail: dinhthibaohoa@hus.edu.vn

19.1 Introduction

Administrative boundaries dossiers show information on the establishment and adjustment of administrative units. The map of administrative boundaries shows administrative boundaries, landmark locations, and characteristics of points on administrative boundaries.

Administrative boundaries, including administrative boundaries on land and at sea (Minister P 2012) in the internal water part, are a content element of geographic background data in state management to serve the tasks of regional, territorial, and other planning tasks.

Land administrative boundary records between localities were made between 1991 and 1994 and continue to be supplemented according to decisions on separation and merger.

The competent authorities have not approved the documents of administrative boundaries at sea, which makes it difficult to manage the relevant localities.

Vietnam has 28 coastal provinces and cities out of a total of 63 provincial administrative units, (https://www.mofa.gov.vn/vi/tt_vietnam/geo/) which are very favorable for economic development while also posing difficulties in managing, protecting, and exploiting economic advantages from the sea and islands.

The extent of maritime space is regulated by the International Convention on the Law of the Sea (Treves 2008), which is concerned with the legal and technical issues of determining maritime boundaries. On November 12, 1982, the Government of the Socialist Republic of Vietnam announced the baseline used to calculate the width of Vietnam's territorial waters (Vietnam 1982). Vietnam declared the sea area inside the baselines and bordering the coast as the internal waters of Vietnam (Vietnam 1977; Assembly 2012).

This article proposes solutions to define maritime boundaries in the internal waters of Vietnam (from Binh Thuan to Ca Mau provinces).

Because surveying and demarcating marine boundaries in the field is not possible, boundary determination will take place at work.

The equidistance method is used to define maritime boundaries for administrative units with opposite or adjacent coastlines.

19.2 Materials and Methodology

19.2.1 Study Areas and Materials

According to the 1982 announcement of the baseline used to calculate the width of Vietnam's territorial sea, provinces ranging from Binh Thuan to Ca Mau are located in the internal water area (Treves 2008; Assembly 2012; Bangert 1992).

The number of landmarks on each administrative boundary line is numbered in the order of non-overlapping components: local names stand for so that there are hyphenations between administrative unit abbreviations in parentheses. The administrative milestone level is abbreviated after the name of the administrative unit in charge of the landmark. T is the provincial level, H is the district level, and X is the commune level.

The typical point is the location in the field where items are easily identifiable. It is chosen for the purpose of identifying and describing administrative borders.

According to Vietnamese legal documents, maritime administrative boundaries continue and are linked to land-based administrative boundaries. The administrative boundary line is determined to respect the current state of local management; to ensure fairness and simplicity in accordance with administrative management conditions.

A fair approach is the most basic way to define boundaries at sea (Ball 1993) (Fig. 19.5).

Using the Coast's General Direction when the coast is replaced by a single general direction line, the median line is perpendicular (Nations 2000). For larger areas, complex coastline shapes can determine the main direction of the coast or of a part of the coastal area. The sea boundary line will be formed by erecting a line perpendicular to the main direction of the coast (Fietta and Cleverly 2016). However, there is frequently disagreement over which part of the shoreline should be used to determine the main direction (Carleton and Schofield 2002).

The boundary between the sea and the opposite coastline will be determined by the median line between the coasts.

Using a compass, draw circles tangent to the shores centers of circles is an equidistance line. The method of using concentric circles is based on the theory that the circle's center is evenly separated from points on its circumference. The boundary line is formed by connecting the points that correspond to the centers of the circles.

Where the coast is too folded, connecting the centers of the circles will result in a boundary line with many segments, which is unsuitable for the description. As a result, it can be simplified by reducing the number of points while keeping the administrative boundaries' main diversion point (Antunes 2002; Macaspac 2002; Organization 1982, 2014; Authority 2001). In this study, the minimum number of points will be proposed to facilitate the description of the demarcation line.

Another way is to swap areas of equal size that are acceptable to the two sides (Carleton and Schofield 2002; Beazley 1994).

The agreement method is a method where two administrative units negotiate and reach an agreement. Old treaties sometimes used meridians (lines of longitude) or parallels (lines of latitude) to define a boundary. The agreement method is the method that takes into account the characteristics of the coast of each region, the agreement related to the current management status of each locality, the habit of living, and the conditions of administrative management. The two administrative units negotiate and agree with each other to choose the appropriate demarcation plan. The demarcation result will be recorded and submitted to the competent authorities for recognition.

19.2.3 Rules for Naming and Numbering Points

Score zero: determine the final boundary point on the mainland, according to administrative boundary records and maps. The symbol of the point is the abbreviation of the relevant provincial-level administrative unit or city. For example, the point (BRVT-TP.HCM) is understood as the final point on the administrative boundary line between the two provinces of Ba Ria–Vung Tau province and Ho Chi Minh City.

Score 1: Determine the intersection point between the land boundary line and the average lowest sea edge over many years. The data is shown on the national topographic map of the VN2000 coordinate system provided by the Vietnam Administration of Seas and Islands; for the estuary or bay section, it will be the dividing point between the part of the river mouth and the bay. The symbol of the point is the abbreviation of the related province, plus the number 1. For example, the point (BRVT-TP.HCM)1 is understood as a point on the administrative boundary line between Ba Ria–Vung Tau province and Ho Chi Minh City that intersects with the average lowest sea edge in many years.

Score 2: Determine the intersection point between the maritime administrative boundary and the baseline. The symbol of the point is the abbreviation of the related province, adding the number 2. For example, the point (BRVT-TP.HCM)2 is understood as a feature point on the administrative boundary line between Ba Ria–Vung Tau province and the city. Ho Chi Minh City intersects with the baseline. Connecting points (BRVT-TP.HCM), (BRVT-TP.HCM) 1, and (BRVT-TP.HCM) 2 are delineated from coast to sea to baseline.

On each segment connecting the points, there may be other characteristic points on the administrative boundary line. The symbols of the points are numbered according to Arabic numerals. For example, 1, 2, 3, 4.

Points identified as river mouth closures or Gulf mouths would be typed in Latin letters. For example, A, B, C.

Points that determine the general direction of the coast are numbered in Roman numerals. For example, I, II.

19.3 Result and Discussion

19.3.1 Result

(a) The study area's maritime administrative boundaries for provinces and cities

From the morphological characteristics of the coastline of the study area, it can be determined that the general direction of the coast is the line connecting two points, I and II. Determine the most protruding position at the point I, located in Sung Trau Cape (also known as Ca Na Cape), on the coast of the Phuoc Diem commune,

Table 19.1 The coordinates of points on the coastal borders of the provinces of Ba Ria–Vung Tau and Binh Thuan are listed below

No	Points	Latitude N	Longitude E
1	I	11° 18' 31.0413"	108° 55' 02.6175"
2	II	8° 38' 15.2767"	105° 06' 15.2912"
3	2 T.9	10° 34' 12.6824"	107° 34' 06.1433"
4	(BT-BRVT)	10° 34' 11.7141"	107° 34' 06.2504"
5	(BT-BRVT)1	10° 34' 04.9234"	107° 34' 11.0810"
6	(BT-BRVT)2	9° 32' 29.2748"	108° 17' 51.7831"

Thuan Nam district, Ninh Thuan province. Point II is located on the coast of Tan An commune, Ngoc Hien district, Ca Mau province.

The plan for determining administrative boundaries at sea is as follows:

The maritime administrative boundary between Ba Ria–Vung Tau province and Binh Thuan province: The landmark 2 T.9 is the provincial level administrative boundary marker in the general direction of the boundary line straight to the shoreline at the point (BT-BRVT). It is the final characteristic point of the mainland administrative boundary line between Binh Thuan province and Ba Ria–Vung Tau province. From the characteristic point (BT-BRVT), it constructs a straight line perpendicular to the general direction of the coast, intersecting with the multi-year average water level at position (BT-BRVT)1; intersecting with the baseline at position (BT-BRVT)2 (Table 19.1).

The maritime boundary between Ba Ria–Vung Tau province and Ho Chi Minh city: Determining the boundary in Cai Mep river. The final point (BRVT-TP.HCM) on the administrative boundary document, point 1 is located at an equidistant distance of $a = 1052$ m from the farthest protruding point of Con Cho mound, Phu Lang islet, and unnamed mound. Point 2 is located at an equidistant distance of $b = 3641.5$ m from the farthest protruding point of Phu Loi islet, Can Gio cape, and Mieu Ba islet. Point 3 is located at a distance of $c = 4791$ m from the farthest protruding point of Ganh Rai cape, Can Gio cape, and the protruding point of the mainland in Ba Ria–Vung Tau province. Point 4 is located equidistant a distance of $d = 4665.5$ m from the farthest protruding point of Da Cai Trang cape, the Ganh Rai cape (Ba Ria–Vung Tau), and, the most protruding point (Ho Chi Minh City) and intersects the midpoint of the Ganh Rai bay closure at the position marked on the map (BRVT-TP.HCM)1. Segment the Ganh Rai bay closure: The segment connects point A located on O Cap cape in Ba Ria–Vung Tau province and point B located near Dong Tranh cape in Ho Chi Minh City. Delimiting the boundary segment outside Ganh Rai bay towards the East Sea: at position (BRVT-TP.HCM)1, it constructs a straight line perpendicular to the general direction of the coast and extends to the baseline at location (BRVT-TP.HCM)2 (Fig. 19.2; Table 19.2).



Fig. 19.2 Characteristic points on the provincial administrative demarcation line between Ba Ria-Vung Tau province and Ho Chi Minh City

Table 19.2 The coordinates of points on the coastal borders of Ba Ria-Vung Tau province and Ho Chi Minh City are listed below

No	Points	Latitude N	Longitude E
9	(BRVT-TP.HCM)	10° 30' 02.2360"	106° 59' 45.3636"
10	1	10° 29' 19.5872"	106° 59' 36.1929"
11	2	10° 26' 22.8961"	106° 59' 58.5451"
12	3	10° 24' 48.7439"	107° 01' 12.8829"
13	4	10° 21' 23.9274"	107° 00' 53.0150"
7	A	10° 19' 15.6903"	107° 04' 54.6466"
8	B	10° 22' 15.1660"	106° 52' 33.8202"
14	(BRVT-TP.HCM)1	10° 20' 45.4820"	106° 58' 44.2732"
15	(BRVT-TP.HCM)2	9° 14' 50.7808"	107° 45' 37.8292"

Table 19.3 The coordinates of points on the coastal borders of Ho Chi Minh City and Tien Giang province are listed below

No	Points	Latitude N	Longitude E
16	(TP.HCM-TG)	10° 21' 59.0560"	106° 48' 43.8746"
8	B	10° 22' 15.1660"	106° 52' 33.8202"
19	C	10° 16' 34.7285"	106° 48' 44.6785"
17	1	10° 19' 24.9663"	106° 50' 39.2095"
20	D	10° 22' 55.8595"	106° 58' 50.8498"
21	E	10° 12' 31.3328"	106° 48' 34.1236"
18	(TP.HCM-TG)1	10° 17' 43.6528"	106° 53' 42.4020"
22	(TP.HCM-TG)2	9° 12' 01.0533"	107° 40' 28.6331"

Administrative boundary at sea between Ho Chi Minh City and Tien Giang province: The section of the provincial administrative boundary between Ho Chi Minh City and Tien Giang province lies on the Soai Rap River, which flows into the Dong Tranh Bay through the Soai Rap estuary. The final point (TP.HCM-TG) on the mainland, next to the boundary line passing through Point No. 1, is the midpoint lying on the road closing Dong Tranh Bay. The section closing Dong Tranh Bay is the section joining point B, located near Dong Tranh cape in Ho Chi Minh City, with point C, located on an Ong Mao dune in Tien Giang province. The boundary continues to the numbered point (TP.HCM-TG) which is the midpoint located on the outer part of the closure of Dong Tranh Bay. The section that closes off Dong Tranh Bay outside is connected at points D and E in Ho Chi Minh City and Tien Giang province, respectively. Determine the boundary segment outside the Dong Tranh Bay towards the East Sea: at location (TP.HCM-TG)1 construct a line perpendicular to the general direction of the coast and extend it to the baseline at location (TP.HCM-TG)2 (Table 19.3).

The maritime boundary between Tien Giang province and Ben Tre province: The section of the provincial administrative boundary between Tien Giang and Ben Tre provinces is located on the Cua Dai River, which flows into the sea through the Cua Dai Mouth. Point (TG-BT) is the mainland's final point. Next, the boundary segment goes to point (TG-BT) 1, which is the midpoint lying on the closed section of Cua Dai Mouth. The section close to Cua Dai Mouth is the section connecting Point E in Tien Giang province and Point F in Ben Tre province. At point (TG-BT)1, construct a line perpendicular to the general direction of the coast and extend it to the baseline at location (TG-BT)2 (Table 19.4).

The maritime boundary between Ben Tre province and Tra Vinh province: The final point (BT-TV) on the provincial administrative boundary line between Ben Tre province and Tra Vinh province, is erecting a line perpendicular to the general direction of the coast, cutting the section closing the mouth of the Co Chien River at the point (BT-TV)1 and extending to the baseline at point (BT-TV)2. The section that closes the mouth of the Co Chien River is the section connecting point G at Con Dam in Ben Tre province and point H in Tra Vinh province (Table 19.5).

Table 19.4 The coordinates of points on the coastal borders of the provinces of Tien Giang and Ben Tre are listed below

No	Points	Latitude N	Longitude E
23	(TG-BT)	10° 11' 28.4415''	106° 45' 26.4803''
21	E	10° 12' 31.3328''	106° 48' 34.1236''
25	F	10° 07' 44.7114''	106° 48' 17.3494''
24	(TG-BT)1	10° 09' 16.6070''	106° 48' 23.6624''
26	(TG-BT)2	9° 12' 01.0533''	107° 40' 28.6331''

Table 19.5 The coordinates of points on the coastal borders of the provinces of Ben Tre and Tra Vinh are listed below

No	Points	Latitude N	Longitude E
27	(BT-TV)	9° 49' 44.6649''	106° 34' 13.7078''
30	G	9° 47' 23.0140''	106° 36' 54.2755''
31	H	9° 44' 43.6034''	106° 33' 50.4972''
28	(BT-TV)1	9° 46' 51.1105''	106° 36' 17.7874''
29	(BT-TV)2	9° 56' 27.9995''	107° 12' 13.1757''

The maritime boundary between Tra Vinh province and Soc Trang province: The point (ST-TV) is located on the border between Tra Vinh and Soc Trang provinces, on the Hau River, which flows into the Dinh An Mouth. The administrative boundary line passing through Point 1 is the midpoint, lying on the inner Dinh An Mouth. The Dinh An closure section connects point K in Tra Vinh province and point L in Soc Trang province. The boundary continues to point (ST-TV)1, which is the midpoint of the outer Dinh An Mouth. The closure section of Dinh An is the section connecting point N in Soc Trang province, located near Con Dung beach, and point M in Tra Vinh province. At point (ST-TV)1, the boundary in a direction perpendicular to the general direction of the coast intersects the baseline at point (ST-TV)2 (Table 19.6).

The maritime boundary between Soc Trang province and Bac Lieu province: The final point (BL-ST) is on the provincial administrative boundary line between Soc Trang province and Bac Lieu province. The boundary continues to go to the south, which is a direction perpendicular to the general coastline, intersecting the average multi-year mean lowest sea level at point (BL-ST)1 and intersecting the baseline at location (BL-ST)2 (Table 19.7).

The maritime boundary between Ca Mau and Bac Lieu provinces: The method involves the conclusion of agreements based on the consensus of the adjacent administrative units. The final point is on the mainland, which is a borderline drawn parallel to the line of longitude or latitude. The People's Committees of Ca Mau and Bac Lieu provinces had an agreement on August 8, 2009, according to which the administrative boundary line at sea goes to the south, parallel to the longitudinal line. The final point (CM-BL) is on the mainland between Bac Lieu province and Ca Mau province. The administrative boundary line at sea intersects with Ganh Hao Mouth at a point

Table 19.6 The coordinates of points on the coastal borders of the provinces of Tra Vinh and Soc Trang are listed below

No	Points	Latitude N	Longitude E
32	(ST-TV)	9° 34' 57.7326"	106° 18' 44.9342"
33	I	9° 31' 24.2044"	106° 20' 59.2875"
34	K	9° 31' 41.1501"	106° 21' 58.7126"
35	L	9° 31' 07.2556"	106° 19' 59.8636"
36	(ST-TV)1	9° 28' 50.0215"	106° 21' 28.0235"
37	N	9° 25' 57.3848"	106° 17' 07.4064"
38	M	9° 31' 42.5937"	106° 25' 48.7088"
39	(ST-TV)2	8° 45' 30.9484"	106° 52' 23.4672"

Table 19.7 The coordinates of points on the coastal borders of the provinces of Soc Trang and Bac Lieu are listed below

No	Points	Latitude N	Longitude E
40	(BL-ST)	9° 14' 43.6829"	105° 49' 31.7607"
41	(BL-ST)1	9° 13' 38.0461"	105° 50' 19.1358"
42	(BL-ST)2	8° 35' 08.2492"	106° 18' 02.8083"

(CM-BL).1 and meets the baseline at point (CM-BL).2. The section closing Ganh Hao Bay is the section connecting Point K in Ca Mau province and Point H in Bac Lieu province (Table 19.8).

(b) The maritime boundary of Con Dao district, Ba Ria–Vung Tau province

* Case 1: the islands of the island district are considered to be valid as the mainland; the furthest locations of the islands in Con Dao district are connected together to limit the scope of the district and find the equidistant line of the distance between the limit line and the multi-year average water level of the coastal provinces.

Table 19.8 The coordinates of points on the coastal borders of the provinces of Bac Lieu and Ca Mau are listed below

No	Points	Latitude N	Longitude E
43	(CM-BL)	9° 01' 02.1167"	105° 24' 58.4996"
46	K	9° 00' 45.4992"	105° 24' 29.7176"
47	H	9° 01' 08.4896"	105° 25' 32.1107"
44	(CM-BL)1	9° 00' 56.1121"	105° 24' 58.4992"
45	(CM-BL)2	8° 27' 34.6937"	105° 24' 58.4415"

The points determining the maritime boundary of the Con Dao district, Ba Ria-Vung Tau province, include: Points (BRVT-BL), 1, 2, and (ST-BRVT-BL) are on the maritime boundary between the provinces of Ba Ria-Vung Tau and Bac Lieu.

The points (ST-BRVT-BL), 1, 2, and (BRVT-TV-ST) are on the maritime boundary between the provinces of Ba Ria-Vung Tau and Soc Trang.

The points (BRVT-TV-ST), 1, 2, 3, and (BRVT-TV) are on the maritime boundary between the provinces of Ba Ria-Vung Tau and Tra Vinh (Table 19.9).

* Case 2: Con Son Island is assigned 6 nautical miles. Determine the general direction of the shoreline, find the limit of 6 nautical miles after having simplified the number of characteristic points, the coordinates of the limited area of Con Son Island include the points: (ST-BRVT)2-1, 1, 2, 3, 4, 5, 6, (ST-BRVT)2-2 (Table 19.10).

Table 19.9 List of coordinates of points in Con Dao district, Ba Ria-Vung Tau province, Case 1

No	Points	Latitude N	Longitude E
1	(BRVT-BL)	8° 30' 03.7498"	105° 42' 19.0427"
2	1	8° 42' 22.8033"	105° 42' 19.6121"
3	2	8° 48' 29.4184"	105° 46' 15.2174"
4	(ST-BRVT-BL)	8° 55' 31.8771"	106° 03' 22.2943"
5	1	8° 57' 12.5667"	106° 07' 27.4852"
6	2	9° 00' 07.0601"	106° 19' 19.4402"
7	(BRVT-TV-ST)	9° 09' 22.3699"	106° 35' 22.5908"
8	1	9° 09' 55.0224"	106° 36' 19.2935"
9	2	9° 10' 15.2588"	106° 48' 26.7746"
10	3	9° 04' 13.7634"	106° 59' 48.9429"
11	(BRVT-TV)	8° 53' 44.5328"	107° 07' 16.8710"

Table 19.10 List of coordinates of con Dao district, Ba Ria-Vung Tau province, Case 2

No	Points	Latitude N	Longitude E
1	(ST-BRVT)2-1	8° 42' 41.4734"	106° 47' 17.1488"
2	1	8° 48' 29.9936"	106° 45' 04.8837"
3	2	8° 50' 22.2114"	106° 42' 20.5639"
4	3	8° 51' 24.6946"	106° 37' 41.0545"
5	4	8° 45' 39.3911"	106° 30' 02.7018"
6	5	8° 43' 40.6028"	106° 28' 15.8641"
7	6	8° 39' 25.8993"	106° 27' 33.6966"
8	(ST-BRVT)2-2	8° 36' 45.5093"	106° 28' 51.8336"

19.3.2 Discussion

Define maritime boundaries to address maritime security issues such as anti-smuggling investigations, handling of accidents at sea, investigating vessels that violate maritime regulations, or resolving disputes among localities over the exploitation of coastal resources.

Maritime boundaries and limits play an important role in determining the rights and responsibilities of sovereign states as well as of local governments. Maritime boundaries aid in determining the scope of organizations' and individuals' rights in the exploitation, use, and management of marine space (Government 2021).

When determining the administrative boundary in the internal waters of the province, the city will be the basis for determining the administrative boundary at the district level, followed by the determination of the commune level within the locality.

For Con Son island district, Ba Ria–Vung Tau is an area with many solutions, in order to implement it, it will need the exchange and unity of the relevant localities. After negotiation and agreement are expressed, the dossier shall be submitted to the competent authorities for approval as prescribed. In case no agreement has been reached, localities will present their local views on the settlement contents as prescribed (Government 2008).

19.4 Conclusion

The results of the analysis of the status of administrative boundaries management and the current documents of the State of Vietnam serve as the basis for determining technical and technological solutions.

The selected boundary determination methods to take into account the general direction of the coast combined with the equidistant method evenly depending on the relevant administrative units with opposite or adjacent coasts. The technical solution is simple, easy to apply, ensuring fairness, easy to convince stakeholders to accept.

The proposed demarcation plans clearly define the scope of administrative boundaries management for provinces and cities in the research area in accordance with the management status, have legal grounds for the sections of boundaries approved by competent authorities; technical solutions for each area are feasible in practice (Figs. 19.3, 19.4 and 19.5).

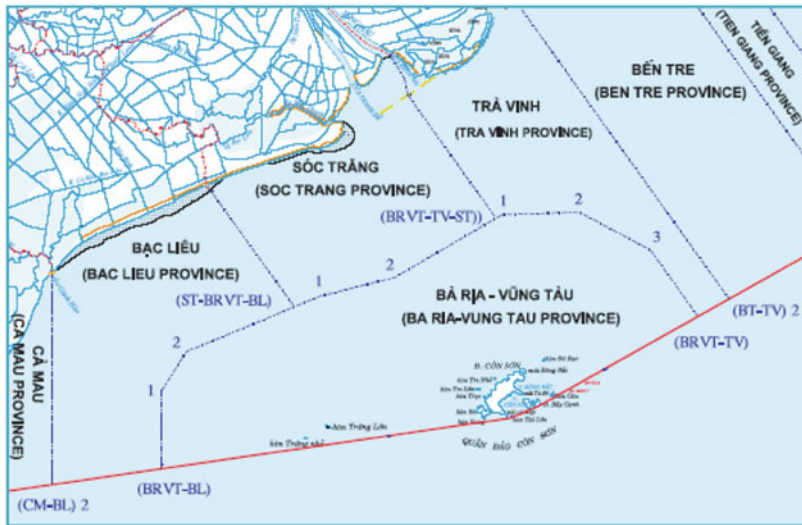


Fig. 19.3 Boundary division by case 1

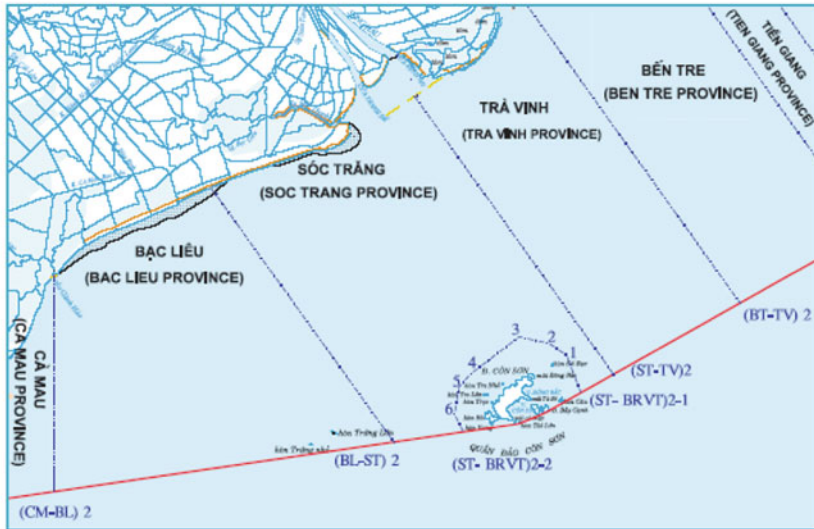


Fig. 19.4 Boundary division by case 2

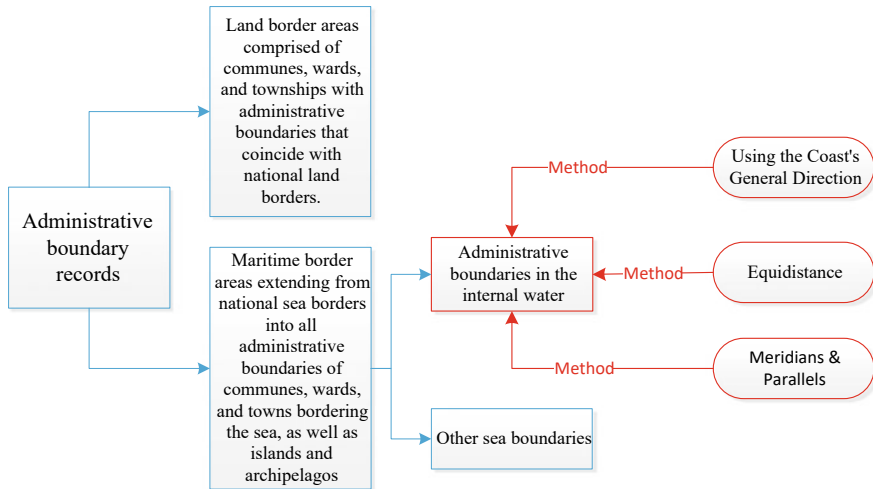


Fig. 19.5 The method of determining the internal water boundary

References

- Antunes NSM (2002) Towards the conceptualization of maritime delimitation: legal and technical aspects of a political process. Department of Law and Department of Geography, vol. Doctor of Philosophy. Durham University, UK
- Assembly TN (2012) Law of the sea of Vietnam. The National Assembly, Vietnam
- Authority NMARI (2001) Guidelines for delineating/delimiting municipal waters. In: Resources DOEAN (ed), vol 2001–17. DENR Administrative Order, Philippine
- Ball WE (1993) Planar median (equidistant) line computations for narrow channels. In: ACSM ASPRS annual convention. American SOC Photogrammetry & Remote Sensing+ AMER Cong ON, pp 1–36
- Bangert K (1992) Internal waters: customary rules of the extension of internal waters. *Nordic J Int Law* 61:43–60
- Beazley P (1994) Technical aspects of maritime boundary delimitation. Ibru, UK
- Carleton C, Schofield CH (2002) Developments in the technical determination of maritime space: delimitation, dispute resolution, geographical information systems and the role of the technical expert. Ibru, UK
- Environment MONR (2014) Circular No. 48/2014/TT-BTNMT provides technical regulations on determining administrative boundary lines, planting boundary markers, and making administrative boundary dossiers at all levels. Ministry of Natural Resources and Environment, VN
- Fietta S, Cleverly R (2016) A practitioner's guide to maritime boundary delimitation. Oxford University Press, UK
- Government (2021) Regulations on the allocation of certain marine areas to organizations and individuals exploiting and using marine resources. Vietnamese Government, Vietnam
- Government (2008) The government's report consults the Standing Committee of the National Assembly on several principles for resolving administrative boundary disputes in some provinces. Government, Vietnam
- https://www.mofa.gov.vn/vi/tt_vietnam/geo/
- Macaspac EA (2002) Delineation of municipal waters. Inf Mapper IX

- Minister P (2012) Decision on the approval of the project. In: Completing and modernizing documents, maps of administrative boundaries and building a database on administrative boundaries. Prime Minister Vietnam
- Nations U (2000) Handbook on the delimitation of maritime boundaries. United Nations Publications, US
- Organization IH (2006) A manual on technical aspects of the United Nations convention on the law of the Sea, 1982. International Hydrographic Bureau, Monaco
- Organization IH (2014) A manual on technical aspects of the United Nations convention on the law of the Sea—1982 (TALOS). International Hydrographic Bureau, Monaco
- Treves T (2008) United Nations Convention on the Law of the sea
- Vietnam SRO (1977) Statement on the territorial Sea, the contiguous zone, the exclusive economic zone, and the continental shelf of Vietnam. In: Legislation N (ed) The Socialist Republic of Vietnam, National legislation—DOALOS/OLA—United Nations
- Vietnam SRO (1982) Statement of 12 November 1982 by the government of the socialist Republic of Viet Nam on the Territorial Sea Baseline of Viet Nam. In: Legislation N (ed) United Nation. The Socialist Republic of Vietnam, National legislation—DOALOS/OLA—United Nations
- Vietnam TNAOTSRO (2003) Law of the national assembly of the socialist republic of Vietnam about national border law. In: Vietnam TNAOTSRO (ed) The National assembly of the socialist Republic of Vietnam, Vietnam

Chapter 20

Assessment of the Status of Supervision and Social Criticism of the Majority of People in the Fields of Land at Quy Nhon City, Binh Dinh Province



Hang Thi Pham , Thuy Le Thi Phan , and Hien Dieu Thi Bui 

Abstract The result shows that in practice, social supervision and criticism have not mobilized public opinions contributions from the people, mainly through the representative mechanism (invitation to meetings, inviting criticism, inviting comments) because the people are still unaware of their right to supervise the land. At the same time, people do not grasp all information related to land use planning, information on compensation, or information on land prices. The current law does not have specific guidelines on how and the process to carry out the counter-arrival and supervision. Notably, only 5% of the survey respondents said that they had contributed ideas about the projects implemented in land use planning, 70.5% of surveyed households suppose dialogue the meeting is only held for small citizens.

Keywords Democracy · Supervision · Social criticism · Quy Nhon

20.1 Introduction

In reality, the mechanism for exercising the people's supervision rights through comments, recommendations, reflections, complaints, and denunciations in the land sector still depends on the level of reception and feedback information from the competent authorities. The reception of people's suggestions has not attracted the attention of officials.

The right to contribute opinions of residents through a referendum in determining compensation land prices; The resettlement support plan; The projects implemented in the land use planning still have certain limitations.

Firstly, Limitations in self-monitoring practice: Many opinions of the people through conferences and group meetings have received little attention and recognition; The work of collecting people's ideas on state management activities on land is not regularly; The content to have comments from the people is not clear,

H. T. Pham (✉) · T. L. T. Phan · H. D. T. Bui
Quy Nhon University, Quy Nhon, Binh Dinh, Vietnam
e-mail: phamthihang@qnu.edu.vn

many people do not understand clearly about the content that needs to review. For example, regarding the content or comments on the implementation of the master plan, the land use plan, 95% of the survey respondents did not understand this issue clearly. Second, there are limitations on the exercise of the right of supervision in the management and use of land through the representative mechanism (the Fatherland Front and political and social organizations) with no connection between users with the Fatherland Front and other political and social organizations. Land users do not know that the Fatherland Front and political and social organizations represent them to exercise social supervision.

It is this practice that limits the role of people in monitoring and social criticism in the field of land management and use. The study “Assessment of the status of supervision and social criticism of the majority of people in the fields of land at Quy Nhon city, Binh Dinh province” is necessary to clarify the actual situation of implementing the monitoring and feedback mechanism.

20.2 Methods

20.2.1 Data Collection

20.2.1.1 Secondary Data Collection

Study the current legal regulations on supervision and social criticism of land management and use. Collecting planning, acquisition, and compensation data of projects implemented in Quy Nhon city from 2014 to 2022. Source from Web, Department of Natural Resources and Environment of Binh Dinh province.

20.2.1.2 Primary Data Collection

To collect information related to the current status of supervision and social criticism in the field of planning, land use planning and compensation, support and resettlement, the authors conducted Interviewing officials and people at five vital projects in the area in Quy Nhon city, period 2014–2022. The authors have selected five research projects based on different project objectives. The selected project is representative of the planning and development of residential areas in inner-city wards (Hung Think Residential project). The need for urban expansion and meeting the accommodation for local people in suburban wards (Quy Nhon Institute of Malaria and Parasitism Residential project, Nguyen Trong Tri Street Residential project). The project serves the purpose of socio-economic development, completing the city’s infrastructure (the project of extending Hoang Van Thu street—one of the central and connecting roads of the city); and representative projects about affecting the livelihoods and lives of

people whose land is acquired (KDC project west of Tran Nhan Tong street—the recovered land area is mainly agricultural land, combined with land live).

Information collected from commune-level People’s Committee officials and people helps the authors to make scientific and objective judgments about the level of approach and practice of monitoring people’s land-use activities.

For officials: Interviewing 16 cadastral officers in 16 communes and wards with works and projects implemented in the period 2014–2019 in Quy Nhon city, Binh Dinh. Including Phuoc My commune and 15 wards (Tran Quang Dieu, Nhon Phu, Ngo May, Thi Nai, Bui Thi Xuan, Ghenh Rang, Quang Trung, Tran Phu, Le Hong Phong, Tran Hung Dao, Dong Da, Nhon). Binh, Ly Thuong Kiet, Nguyen Van Cu, Le Loi).

For people participating in the survey: The sample size was determined based on the Slovin (1984). With an accuracy of $e = 0.1$, the authors have determined that the total number of households to be interviewed is 312, based on the total acquired area of 35.09 ha and 1285 affected households.

$n = N/(1 + N \cdot e^2)$; In which: n: Number of samples to be investigated; N: Total number of individuals;
e: Variance ($e = 0.05-0.1$).

From the above formula, we have a spreadsheet of survey data sample size (n) with 5 specific projects as follows (Table 20.1).

Table 20.1 Number of households interviewed in the projects

Name of project	Project implementation time	Recovered area (ha)	Number of affected households	Number of survey samples (n)
Hung Thinh Residences	2014	10.3	486	84
The East Nguyen Trong Tri Residences, Nhon Binh ward	2016	5.53	50	33
Hoang Van Thu street and branch lines (Area of Ngo May and Le Hong Phong wards)	2015	2.86	499	83
Residential area west of Tran Nhan Tong street	2018	9.8	125	56
Residential Area East of the Institute of Malaria—Parasites—Insects Quy Nhon	2016	6.60	125	56
Total		35.09	1285	312

20.2.2 Methods of Collecting and Analyzing Documents and Data

After collecting survey data, the authors synthesize data using Microsoft Excel and analyze the data to serve as a basis for orienting and exploiting the study and scientific conclusions about the research problem.

For secondary data:

- Qualitative data: Classify and arrange information in order of priority on the importance of information.
- Quantitative data: Entering into the computer-based on Excel software application the data according to the necessary data for the research.

For primary data: Processing matrix, making information tables, conducting synthesis and analysis. Use Excel to enter and standardize data. After the investigation, the data has checked the accuracy of the information obtained. For qualitative data collected from interviews, using Microsoft word to set up a two-dimensional matrix of information types and respondents, leading conclusions on the actual status of social supervision in the land sector can be determined.

20.3 Result

20.3.1 Evaluation of the Practice of Exercising the Right of Social Supervision of People in the Land Sector in Quy Nhon City, Binh Dinh Province

The participation of the people is indispensable in the state management of land (Anh 2014). Monitoring and social criticism demonstrate the participation of the people in state management. In Article 28, Constitution 2013, People have the right to participate in state management, to discuss and recommend with state agencies on village, local and national issues. The State give citizens opportunities to participate in land management; publicity and, transparency in receiving and responding to citizen suggestions.

Supervision activities are implemented by the National Assembly, the National Assembly Standing Committee and agencies of the National Assembly, the National Assembly deputies, and the National Assembly Delegation's Delegation. The supervision role of the people in law-making and implementation activities has also been enacted. Article 199 of the 2013 Land Law stipulates: "Citizens have the right to exercise the right by themselves or through representative organizations to monitor and report violations in land management and use". The right to social supervision is shown through the right to consult the community on specific contents in the land

Table 20.2 Contents of people's exercise of supervision rights

Contents of people's exercise of supervision rights		Yes (%)	No (%)
Land use planning	Making, adjusting land use planning	0	100
	Publication and implementation of master plans and plans on land use	0	100
Compensation, support and resettlement	Compensation plan	0	100
	Support and resettlement plan	0	100
Administrative procedures related to rights and obligations of land users	Processing time for administrative procedures	0	100
	Process of handling administrative procedures	0	100
	Responsibility for handling administrative procedures	0	100

Source Interview survey results 2022

sector such as land price, planning, land use plan, acquisition, compensation, support, resettlement.

There is a difference between the Right to Supervision and Public Consultation. In form, Conferences and seminars are organizational forms in the implementation of the right to supervision and community consultation. In addition, to exercise the right of overseeing, there are three additional forms of complaint, lawsuit, and petition. In the nature, Community consultation to obtain opinions, thoughts, and aspirations of land users for state management activities on land. The right to social supervision, in addition to expressing the content of public consultation, also shows the assessment of land users on state management activities on land through consensus or disagreement expressed in the form of complaints and denunciations).

According to the survey results, people said that they did not know about the right to supervise land-related activities (Planning; Compensation, support, resettlement; Administrative procedures on land). Meanwhile, complaints and petitions are part of social monitoring activities. At the same time, according to the people, the right to supervise state management activities on land is only theoretical because the local people's opinions can be marginalized "No one will listen to my reflection because I'm a common person, the government doesn't pay attention".¹

Table 20.2 shows: 100% of the people who participated in the survey said that they did not exercise the right to supervise all contents related to planning and land use plans (from planning content to planning adjustment using the land). 100% of surveyed households also agreed to write that they did not exercise their right to supervise through compensation, support, and resettlement (from the step of compensation plans, to support and resettlement).

¹ Interviewing households at the land acquisition project of Hoang Van Thu street project, Quy Nhon city, Binh Dinh province.

Table 20.3 Forms of people's supervision in land management

Mode of exercising supervision	Participation rate (%)
Directly (suggestions, recommendations) exercise the right of supervision through local meetings	30.12
Send petitions, settle complaints, and denunciations to agencies that have issued administrative decisions or decisions that do not reach a consensus from the people	50
Send petitions, settle complaints, and denunciations to agencies where officials commit administrative violations in the field of land	15.1
Send petitions, settle complaints, and denunciations to legally recognized representative organizations for these organizations to carry out supervision	4.78

Source Interview survey results 2022

Households participating in the survey do not suppose they have the right to supervise activities of land use administration. They believe that supervision is the duty of departmental inspectors. Citizens are obliged to comply with the regulations issued by the state. In fact, according to law, people can do their right to supervise activities of state management of land through the following forms: comments, recommendations, reflections, complaints, and denunciations report through meetings or send applications to agencies that have issued administrative decisions, or have actions that do not reach a consensus from the people.

The petition is the main form of implementation in land monitoring, management, and use because people are afraid of contacting state agencies and officials, and people still have not had a close connection (Table 20.3).

There are four forms of implementing the citizen's supervision rights in land administration. Directly (suggestions, recommendations) exercise the right of supervision through local meetings made up 30.12%. Send petitions, settle complaints, and denunciations to legally recognized representative organizations for them to do the people right, took a minority, at 4.78%. Send petitions, settling complaints, and denunciations to agencies that have issued administrative decisions or decisions that do not reach a consensus from the people made the lion's share, half of 4 forms of supervision rights in land management.

From the research results shown: The law on land stipulates that citizens have the right to supervise land use and administrative activities. However, in practice, the implementation of the supervisory role of the people is still limited, although the propaganda and dissemination of legal education in the locality have been organized and implemented (Table 20.4).

Table 20.4 illustrates Firstly, people are still not conscious of their right to supervise the land. According to the survey results in 16 communes and wards of Quy Nhon city: 100% of communes wards have built and issued documents to organize the implementation and hold conferences to propagate, disseminate, and educate about the law on the law land law policies related to site clearance, land use planning, and plans, civil law 2015. At the same time, listing the list of administrative procedures

Table 20.4 Propaganda, dissemination and education of the law on land

Propaganda content	Dissemination activities of commune/ward officials		Local people's opinions		
	Yes (%)	No (%)	Join frequently (%)	Join less (%)	No Join (%)
<i>Regulations on master plans and plans on land use</i>					
Rights and obligations of people in the planning area	100	0	3.21	8.01	88.78
The right to access information related to master plans and plans on land use	100	0	0.96	4.81	94.23
Publicize works and projects implemented in the year of the land use plan	100	0	5.77	8.65	85.58
Propagating about the right to participate and contribute opinions of people in master plans and plans on land use	100	0	0.64	3.21	96.15
Rights and obligations of people in the planning area	100	0	3.21	8.01	88.78
<i>Regulations on recovery, compensation, support and resettlement</i>					
Cases of compensation and support when the State recovers land	100	0	1.60	3.85	94.55
Regulations on land allocation for resettlement	100	0	2.24	4.49	93.27
Regulations on policies to support life stabilization and job search when the state recovers land	100	0	2.56	3.21	94.23

Source Interview with commune-level cadastral officers and land users

and legal documents Laws related to people's lives have also been performed in the residential group. However, the propaganda, dissemination, and education of the land law have not received the attention of the people, leading to the situation that people do not understand the basic knowledge about the land legal system band.

According to the results of interviews with 312 land users in 5 research projects: Land users have contributed opinions on land policies and laws, and the ideas of land users are not to be taken as a basis for policy change. At the same time, the level of participation in legal propaganda activities on planning and compensation was only from 3 to 18 people out of 321 interviewees (depending on content), taking a minority from 0.96 to 5.77%. The number of people who do not participate in legal propaganda sessions accounts top of the list, between 88.78 and 96.15%.

The authors believe that local authorities need to implement specific plans to disseminate and educate the people about the law on land. Helping people grasp and better understand the land laws and regulations of the land law. And at the same time, supporting people know their supervisory role in the management and use of land.

Secondly, most people do not grasp all information related to land use planning, compensation, or land prices. People only care about these issues when their land plot is recovered or registered for a land use right certificate. It is noticeable that groups of people living in inner-city wards often learn land law more than in suburban.

Thirdly, although the people's right to supervise is enacted in the 2013 Constitution and the Land Law 2013, these documents do not have specific instructions on how and the process of exercising the supervision rights of the people.

20.3.2 Assessment of the Current Status of Supervision and Social Criticism for Land Use Planning and Planning

Relating to the content of district-level land use planning and plans. According to the provisions of Clause 1, Article 6 of the Law amending and supplementing several Articles of the 37 Laws related to planning in 2018, the collection of comments from agencies, organizations, individuals, and communities on district-level land use planning shall be implemented in the form of holding conferences, directly collecting opinions and publicizing information about the contents of the land use planning on the website of the provincial-level People's Committees and district-level People's Committees. Or display them in public places, distribute questionnaires and interviews, organize conferences, seminars, and other forms following the law on the implementation of democracy in communes, wards, and communes.

Practical implementation of the law in the organization of supervision activities in Quy Nhon shown: Implementing Clause 2, Article 28 of the 2013 Constitution, land management agencies have created conditions for citizens to participate in the state management of land mainly through public announcements of information on land management, organize the collection of people's opinions, receive and respond to

comments. However, the content and process publicity and transparency in receiving and responding to citizens' opinions and recommendations have not been ensured according to regulations. Information deployed at meetings on compensation, support and resettlement has not fully responded to the process of determining compensation land price. Complaint settlement decisions only disclose those decisions that do not recognize the content of the complaint. In cases where the content of complaint settlement with adjustment in compensation and resettlement prices is not publicized on the website and at the headquarters of the People's Committees.

According to the household survey results, 85% of households do not know about consultation conferences, do not know information about planning projects and land use plans implemented, and 10% of surveyors do not know about the consultation meetings. People know but do not participate in consultation conferences. Only 5% of households contributed ideas about the projects implemented in the master plan and plan on land use.

According to Land law, the agency that collects opinions on land use planning is responsible for compiling a general report, absorbing and explaining people's stocks, and finalizing the land use planning before submitting them to the Council. People affected by planning projects are the stakeholders in land use planning. The law needs specific provisions to ensure that people's comments are studied, absorbed, explained, and reported to competent authorities for consideration before appraising, deciding, or approving the planning. The planning agency needs to be responsible for publicizing citizens' contributions and explaining the stocks, ensuring the rights of people affected by the project, and ensuring the principle of fairness, democracy, and publicity in land use planning and planning activities.

Access to information on land use planning has been receiving the attention of the land users. To Land law (Assembly 2013), information on land use planning should be public and transparent. However, according to the surveyed results, only 15% of people know the list of work items that will be done in the year of the land use planning, and 85% of land users do not have access to information. Contents of land use planning have not been publicly on the web portal of the province or city in the study area.

The research also shows the right to supervise and give social criticism on land use planning is not well done since land users do not grasp their rights in land use planning (Table 20.5). Specifically, users do not digest their rights to the area with planning and land use plan. 100% of surveyors do not know the land use rights will not be restricted if issued land use planning without done after three years or there is no decision on adjustment or cancellation.² The updating and adjustment of the

² According to the provisions of Clause 3, Article 49 of the 2013 Land Law, as amended by Clause 1, Article 6 of the Law amending and supplementing several Articles of the 37 Laws related to the 2018 planning, "The land area recorded in the master plan is If the annual land use purpose of the district has been announced to be recovered for project implementation or the land use purpose must be changed, but after 3 years there has been no decision on land recovery or permission to change the land use purpose, then State agencies competent to approve land-use plans must adjust, cancel and announce the adjustment, cancellation of acquisition or change of purpose for the land area stated in the land use plan. In case the state agency competent to approve the land use plan

Table 20.5 Contributing comments related to master plans and plans on land use

Contents of consultation on land use planning and plans	Don't know about consultation meetings	Know there are conferences, but do not participate (%)	Participate in comments (%)
Planning targets, land use plans	85	10	5
Construction projects implemented in the planning period, land use plan	85	10	5

Source Interview survey results 2022

planning have not been carried out on time, leading to the situation that people have to live with “suspended projects³” from 10 to 20 years.

According to the survey results (Table 20.6): In the area with an annual district land use plan, 100% of the people said that they were not allowed to build a new house, not to change the land use purpose, not to plant farming, and only 8% of people interviewed said that they have the right to renovate and repair existing houses and works with the permission of competent state agencies. When land users do not know their rights related to the land plot in the area with land use planning or plan, the right to supervise the implementation of land-related activities will not be exercised or implemented but to no avail.

Regarding the content of public planning and land use plans, 90.4% of the people surveyed said that information about the planning was not made public. This practice does not coincide with the regulations on disclosure of information related to planning in Clause 1, Article 6 of the Law amending and supplementing several Articles of 37 Laws related to planning in 2018. “District-level People’s Committees be responsible for publicizing the district-level land use planning at the agency’s headquarters and on the web portal of the district-level People’s Committee; publicly announce the content of district-level land use planning related to communes, wards, and townships at the headquarters of the commune-level People’s Committee. The public announcement shall be made within 30 days from the date of decision and approval by a competent state agency”. According to Land law, publicity must be done during the planning period. However, the level of public information in the locality is still very limited. It is necessary that the publicity content must be clearly defined in the state management of land. According to the provisions at point c, Clause 1, Article 48 of the 2013 Land Law, as amended by Clause 1, Article 6 of the Law amending and supplementing several articles of 37 Laws related to planning in 2018 “The People’s Committee The district level is responsible for compiling a general report, absorbing and explaining

does not adjust or cancel it or has it adjusted or canceled but fails to announce the adjustment or cancellation, the land user is not restricted in his/her rights according to the law”.

³ The project has been approved, has been included in the annual district land use plan, and has been notified of acquisition. However, the competent state agency has not made any recovery and compensation work.

Table 20.6 Rights of land users in land use master plans

Accessed information on land use master plans and plans	Information has been accessed (%)	This is the first time hearing about this (%)
To continue using the land and to exercise the rights of land users following the law, in case the land use planning has been announced without the district's annual land-use plan	6.4	93.6
To continue to exercise the rights of land users, but not to build new houses, works, or plant perennial crops in case there is an annual land-use plan at the district level	50	50
To renovate and repair existing houses and works in the area where there is an annual land-use plan at the district level but must be permitted by a competent state agency following the law	8.0	92.0
If the land area stated in the district-level annual land-use plan has been announced to be recovered for project implementation, but after 3 years, there is no decision on land recovery, the competent state agency shall approve the plan. Land use must be adjusted, cancelled and must announce the adjustment, cancellation of recovery recorded in the land use plan	0	100
In case the state agency competent to approve the land use plan does not adjust or cancel it or has it adjusted or cancelled but fails to announce the adjustment or cancellation upon the district's annual land-use plan. Has been announced to be recovered for project implementation, but after 03 years, there is no decision on land recovery; the land user is not restricted in terms of land use rights	0	100

(continued)

Table 20.6 (continued)

Accessed information on land use master plans and plans	Information has been accessed (%)	This is the first time hearing about this (%)
Publicize information on land use master plans and plans	9.6	90.4

Source Interview survey results 2022

the people's opinions and finalizing the district-level land use planning plan before submitting it to the District Land Use Planning Appraisal Council". However, up to now, there have been no specific guidelines on how and the implementation process to show the participation, comments, and supervision from the people.

20.3.3 Assessment of the Current Status of Supervision and Social Criticism in Compensation, Support, and Resettlement

Regarding people's right to supervise in compensation, support, and resettlement, the authors have the following observations: The implementation of supervision through the representative mechanism is no connection between land users and the Fatherland Front and political and social organizations in supervision rights. The land users do not know that these are the organizations that exercise their supervisory rights on their behalf. In addition, the Fatherland Front and other political and social organizations have not had activities to propagate, connect and encourage land users to promote their role of supervising land management activities. (Quan 2018) The Fatherland Front needs to play a central role in carrying out monitoring and criticism activities in all areas of society's life, contributing to the promotion of democracy among the people.

The right to supervise in the content of compensation, support and resettlement is done through comments related to the compensation plan. According to the survey results, up to 89.7% of people commented on the contents related to compensation land prices, resettlement land prices, and training and career change support. Some users commented "The price of resettlement land is higher than the price of compensation land. When we moved to the resettlement area, we had no money to pay land use fees, no money to build houses, the poor had to sell their land". According to Land law "The organization compensation coordinate with the People's Committee of the commune to hold a dialogue in case there are still disagreements on compensation, support and resettlement plan". However, surveyed results at five projects in Quy Nhon city, 70.5% users said that: "Dialogue sessions are only held for a small group, not organized a centralized dialogue, it seems that all opinions of the people are ignored".

Local authorities holding meetings in small groups for households who disagree on the compensation plan is not in accordance with current law. According to the provisions at Point a Clause 2, Article 69 of the Land Law 2013: “The organization in charge of compensation and site clearance is responsible for making plans for compensation, support, and resettlement and coordinate with the Committee The commune-level People’s Committees of the places where the recovered land is located shall organize consultations on compensation, support and resettlement plans in the form of direct meetings with people in the area where the land is recovered”. “In charge of compensation and ground clearance are responsible for coordinating with the commune-level People’s Committee of the locality where the recovered land is located to hold a dialogue in case there are still disagreements about the compensation and support plan, resettlement”. Thus, in case of disagreement on compensation plans, a one-time dialogue should be held to avoid group separation and the small settlement of disagreements as the local practice has done.

The survey results at the resettlement sites of 5 research projects show: In the resettlement areas, the project on Tran Nhan Tong street, the project on Le Hong Phong, and Hoang Van Thu streets extend people living in poor conditions there is no address, house number. It is too hard to trade and sell since they do not know how to write a contact address. In the resettlement area of Hoang Van Thu street project, in Nhon Binh ward, Quy Nhon city, in front of the resettlement area are mountains, electricity and roads have not been lit to the resettlement house. In addition, people have to face the situation of snakes crawling into the house. So the resettlement area also contains many problems to be solved. Inadequacies also arise when the complainant or petitioner receives a higher compensation price than the old one, while the executor who relocates first has to pay a low compensation price.

95.5% of the people participating in the survey said: The plan for compensation, support, and resettlement is publicized at the headquarters of the commune-level People’s Committee, the popular living place of the resident (Table 20.7). What households are interested in is on what basis to determine compensation price, and on which basis to determine resettlement land price. The basis for determining compensation, the resettlement plan should be made public to the recoverers before the compensation plan is approved. In this way, users identify the inadequacies related to compensation land prices and compensation plans, from which they can make recommendations and contributions. The authors believe this is the best way to exercise the people’s supervision rights in compensation and resettlement, contributing to balancing the interests of the state, people, and investors.

20.4 Discussion

Although people are consulted in land use planning, acquisition, compensation, support, and resettlement, people do not understand that they will carry out social

Table 20.7 People's supervision rights in compensation, support and resettlement

Content showing the right of supervision in compensation work	Yes (%)	No (%)
To contribute ideas on compensation, support, and resettlement plans in the form of face-to-face meetings	70.5	29.5
The people's comments must be recorded in a record certified by the representative of the commune-level People's Committee, the representative of the Vietnam Fatherland Front Committee at the commune level, and the representatives of the people whose land is recovered	50	50
The organization in charge of compensation and ground clearance is responsible for summarizing written comments, clearly stating the number of agreeing opinions, the number of disagreeing opinions, and the number of other opinions for the method. Compensation, support, and resettlement projects	0	100
The organization in charge of compensation and ground clearance shall coordinate with the People's Committee of the commune where the recovered land is located to hold a dialogue in case there are still disagreements about the compensation and resettlement assistance plan	70.2	29.8
The plan for compensation, support, and resettlement shall be publicized at the headquarters of the commune-level People's Committee, the commonplace of the daily life of the residential area where the recovered land is located	4	98.1

Source Interview survey results 2022

criticism. On the other hand, in some cases, people have contributed to land use planning, acquisition, compensation, support, and resettlement. Still, they do not know that it is exercising their right to protest social argument.

In the context of Vietnam's deeper international integration, the requirement to promote democracy and expand citizens' participation in state management activities is increasingly important and urgent (Anh 2014). The role of people in monitoring land law enforcement activities has been enacted in legal documents. In the state management of land, social criticism not only shows the democratic rights but also the way the citizens supervise the activities of state agencies. However, practice shows that there have not been many studies on social criticism in the contents of state management of land. The research development direction of the authors in the coming time is to study solutions to improve the effectiveness of social criticism in planning, land use planning, land acquisition, compensation, support, and resettlement.

20.5 Conclusion

The right to social supervision is shown through the right to consult the community in the field, planning, land use plan, acquisition, compensation, support, and resettlement. The organization of conferences to propagate and disseminate legal education

on land law policies related to site clearance, planning, and land use plans has not yet attracted the attention of the community because the propaganda content and the form of dissemination are not focused.

Supervision and social criticism serve as a driving force to promote the people's democracy and improve the quality of land use and management (Marshall and Bottomore 1992). The more people actively exercise their right to social supervision in land management, the more effective social criticism will be. However, the law does not have specific regulations on the order and principles of contributing comments to supervision and social criticism, opinions are mainly contributed through the representation mechanism (invitation to meetings, invitations to critique, the invitation to contribute ideas).

To organize and carry out social monitoring and criticism in the best way, the theoretical and legal basis for the role of social supervision and criticism needs to be interesting. Implementation methods in monitoring and social criticism activities in the field of land need to be enacted clearly in the Land Law and its guiding documents. At the same time, the law should specify the roles and responsibilities of organizations that receive supervision and criticism from the people.

The necessary condition for "social criticism" and "social supervision" is to make all management information public and transparent. The sufficient condition is that the relevant state agencies and state officials must be accountable for the criticism and supervision of the people. Thus, the State needs to enact specific laws on publicity and transparency of management information, people's participation, and accountability of agencies and managers (Vo 2015).

Strengthen public and democratic dialogue, and listen to the citizens' legitimate aspirations (Nguyen and Nguyen 2021). At the same time, apply flexibly and appropriately policies to ensure a harmonious settlement of interests between the State and the people in land use planning and planning, recovery, compensation, support, and resettlement. Immigration is a necessity nowadays.

Acknowledgements To complete the research, the authors have received the cooperation and support of agencies and departments in Quy Nhon city. The authors would like to thank the organizations and the individuals who interviewed and assisted the group to wrap up the study.

References

- Anh PT (2014) Guarantee the citizen's right to participate in state management in Vietnam. *Vietnam J Soc Sci* 10(83):49–56
- Assembly N (2018) Land Law 2013. Revised in 2018, National Political Publishing House
- Marshall TH, Bottomore TB (1992) *Citizenship and social class*. Pluto Press, London
- Nguyen TB, Nguyen QG (2021) Study on Citizen participation in local governance in Vietnam. Network of Institutes and Schools of Public Administration in Central and Eastern Europe. NISPAcee J Publ Adm Policy 14:87–109

Quan TTH (2018) Strengthening supervision and social criticism of the Vietnam Fatherland Front in the State administrative management

Vo DH (2015) Current social monitoring and criticism. Reference, Nature.org.vn. http://nature.org.vn/vn/wpcontent/uploads/2015/12/251215_GiamsatvaphanbienXH_GsDangHungVo.pdf

Chapter 21

Assessment of Sustainable Development for Ly Son and Phu Quy Islands Using Sustainable Development Index



Pham Viet Hai, Nguyen Thi Diem Thuy, Phan Thi Thanh Hang,
and Dao Nguyen Khoi

Abstract The objective of this study is to assess the level of sustainable development for the two island districts of Ly Son and Phu Quy using sustainable development index (SDI). The SDI includes 53 indicators representing 17 sustainable development goals (SDGs) for three categorical pillars of sustainable development (society, economy, and environment). The SDI values are estimated based on secondary data and primary data collected from 200 households in the study areas. Results showed that Phu Quy and Ly Son districts had the same level of sustainable development with a standardized value of 0.81. Despite achieving a good level of sustainable development, the two island districts still need some improvements in terms of sex ratio at birth (SDG5), ratios of employment and product in processing and manufacturing industries (SDG12) and forestland area (SDG15). In addition, in order to increase the level of sustainable development, the local managers of Ly Son district should improve policies for poverty reduction (SDG1), and the local managers of Phu Quy district should improve ensuring social security and safety for local people (SDG16). In general, the results obtained from this study demonstrate the appropriateness of the SDI in estimating the level of sustainable development for island districts in Vietnam.

Keywords Indicator approach · Sustainable development · Sustainable development index · Ly Son island · Phu Quy island

P. V. Hai (✉) · N. T. D. Thuy · D. N. Khoi
Faculty of Environment, University of Science, 227 Nguyen Van Cu Street, District 5, Ho Chi Minh City, Vietnam
e-mail: pvhai@hcmus.edu.vn

Vietnam National University Ho Chi Minh City, Linh Trung Ward, Thu Duc District, Ho Chi Minh City, Vietnam

P. T. T. Hang
Institute of Geography, Vietnam Academy of Science and Technology, Hanoi, Vietnam

21.1 Introduction

In 1972, the concept of sustainable development (SD) was first recognized at the United Nations Conference on the Human Environment held in Stockholm. Over time, many definitions of sustainable development have been proposed. However, the concept introduced by the United Nations Conference on Environment and Development (UNCED) in 1987 is the most widely used. According to UNCED, “Sustainable development meets the needs of the present without compromising the ability of future generations to meet their own needs” (World Commission on Environment and Development 1987).

Towards sustainable development, monitoring and evaluating the development process is very important to adjust policies and make appropriate decisions. Therefore, in Chapter 40 of Agenda 21, UNCED had called on countries, international organizations, governments and non-governmental organizations to develop a set of sustainable development indicators (SDI) with the aim of providing a solid basis for decision making (United Nations 1992). In 2001, the United Nations Statistics Division developed a set of indicators to track progress towards the Millennium Development Goals (MDGIs) for all countries by 2015 (United Nations 2000). However, this set of indicators had limitations in terms of structure and feasibility. Therefore, the MDGIs was replaced with the Sustainable Development Goal Indicators (SDGIs) including 232 indicators designed to monitor and evaluate the implementation of 17 goals and 169 targets by 2030 (United Nations 2015).

Following that trend, many sets of sustainable development indicators have been developed with a variety of content as well as application levels, covering from international to local levels. However, the actual application (or actualization) of the set of indicators after being established still had limitations. As a tool to evaluate SD progress for stakeholders to make decisions, the studies only stopped at the stage of building a framework without applying it in practice, leading to these indicators being invalid, as well as the studies having no practical significance. In the previous study on building a set of socio-economic sustainable development indicators for island districts in Vietnam (Hai et al. 2021), we developed an SDI consisting of 52 indicators to assess the level of sustainable development in these localities. In order to generalize the set of indicators for island districts with diverse socio-economic characteristics, it is necessary to have a study that applies the set of indicators simultaneously to different regions. The objective of this study is to evaluate the level of sustainable development for two island districts of Ly Son and Phu Quy using the SDI was developed in the previous study (Hai et al. 2021), which will demonstrate the feasibility of practical application of SDI for other island districts in Vietnam.

21.2 Study Area

The Phu Quy island district is approximately 120 km southeast of Binh Thuan province with an area of about 18 km² (Fig. 1a). Currently, Phu Quy has a population of more than 28,000 people with approximately 15,000 people of working age. Local workers are mainly engaged in fishing and aquaculture. As an island district, Phu Quy's economy is mainly based on fishing, agriculture and tourism. Meanwhile, local industries and services have not yet developed. To orient the socio-economic development, Binh Thuan province has issued Decision no. 1485/2008/QD-UBND on June 3rd, 2008 on the socio-economic planning of Phu Quy district until 2020. Accordingly, this island district is oriented to become a centre of offshore fishing, fisheries logistics and rescue services of the area (People's Committee of Binh Thuan Province 2008).

Meanwhile, Ly Son is a small island district with an area of about 10.32 km², and approximately 28 km northeast of Quang Ngai province (Fig. 1b). With a population of about 22,000 people, Ly Son district is a locality with a population density many times higher than the population density of the whole province. In general, Ly Son district has an abundant labour force with about 63% of the population in working age. Similar to Phu Quy district, Ly Son's economy is mainly based on fishing, agriculture and tourism. Accordingly, the socio-economic development plan of Ly Son district (Decision no. 169/2012/QD-UBND on August 31st, 2012) identified the fishing industry as the key economic sector of the locality. In recent years, Ly Son's tourism industry has also developed rapidly thanks to the natural strengths of the island district (People's Committee of Quang Ngai Province 2020).

21.3 Methodology

21.3.1 Sustainable Development Index (SDI)

In this study, the set of sustainable development indicators (Hai et al. 2021) was used and it was developed based on the United Nations' 17 Sustainable Development Goals (SDGs) to 2030 to measure progress towards achieving these SDGs for island districts in Vietnam. The set of 53 indicators is grouped into sub-dimensions based on the 17 United Nation SDGs, then these SDGs are categorized according to the three dimensions, namely economy, environment, and society (Fig. 21.2). The list of 53 indicators is shown in Table 21.1.

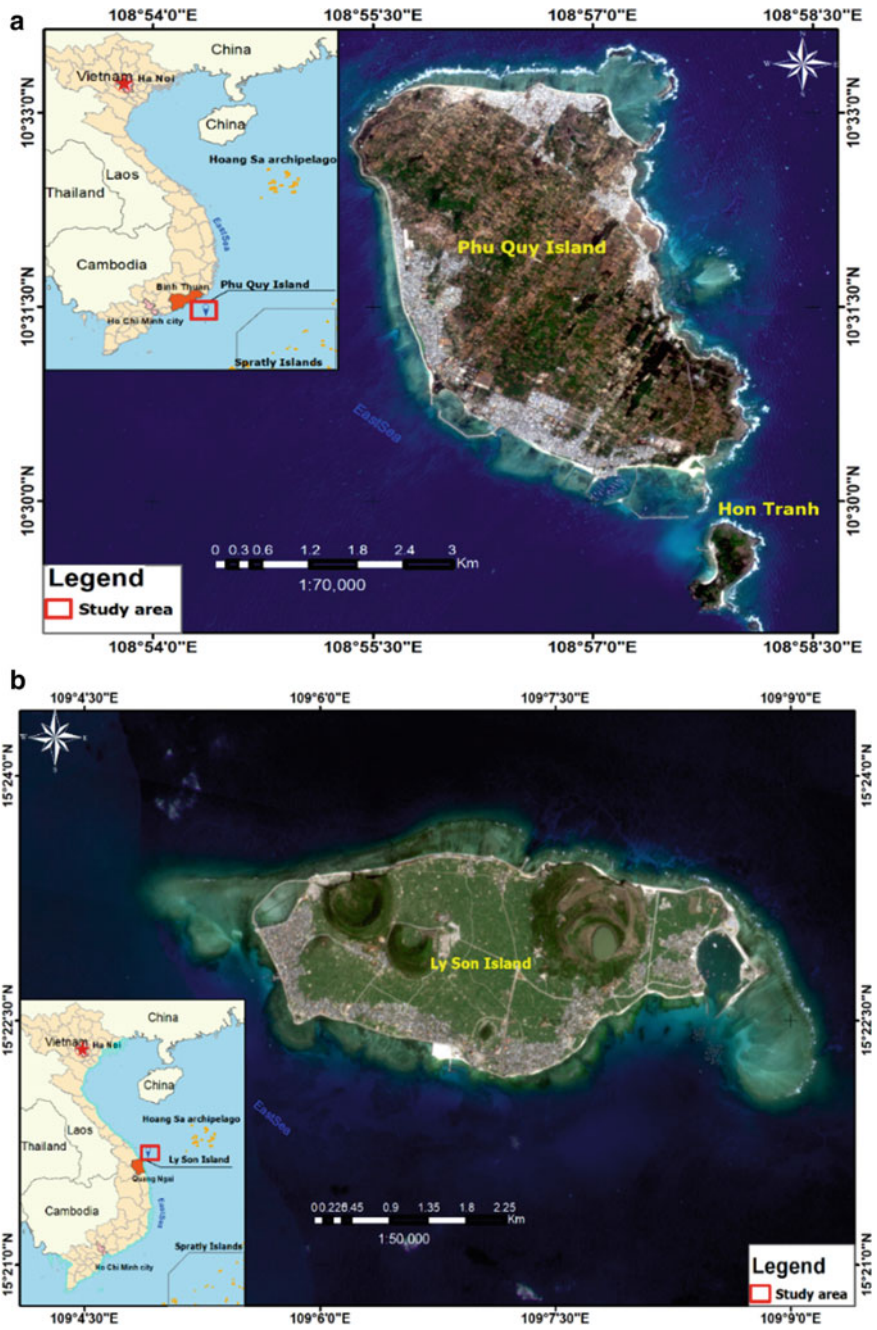


Fig. 21.1 Study area: a Phu Quy district. b Ly Son district

Sustainable Development Index		
Economy	Environment	Society
<ul style="list-style-type: none"> – SDG8: Decent work and economic growth; – SDG9: Industry, innovation and infrastructure; – SDG12: Eesponsible consumption and production; – SDG17: Partnerships 	<ul style="list-style-type: none"> – SDG6: Clean water and sanitation; – SDG7: Affordable and clean energy; – SDG11: Sustainable cities and communities; – SDG13: Climate action; – SDG14: Life in water; – SDG15: Life on land 	<ul style="list-style-type: none"> – SDG1: No poverty – SDG2: Zero hunger – SDG3: Good health – SDG4: Quality education – SDG5: Gender equality – SDG10: Reduce inequalities – SDG16: Peace, justice and strong institutions

Fig. 21.2 Structure of the set of sustainable development indicators for island districts

21.3.2 Standardize the Indicators

The indicators have a variety of calculation methods, as well as reflect different levels of correlation with sustainable development. Therefore, the indicators need to be standardized to the same range of values to facilitate SDI calculation. In this research, the indicators were standardized by the min–max scaling method. Accordingly, the standardized values were calculated as follows:

$$I = \frac{I - I_{\min}}{I_{\max} - I_{\min}} \quad (21.1)$$

where I is the actual value of the indicators, I_{\min} and I_{\max} are the minimum and maximum values reflecting the least and most sustainable levels, respectively.

After standardizing indicators, the values of the sub-dimensions (SDGs) were calculated through the arithmetic average according to formula (21.2). The calculation did not use weights because the indicators are equally important in the integrated sustainability assessment. For dimensions, the values were calculated through averaging the values of the SDGs in each aspect. Similarly, the SDI of the island districts was the average of the values of the three dimensions in each locality.

$$S_j = \frac{\sum_{i=1}^n I_i}{n} \quad (21.2)$$

where n is the number of indicators of each SDG and S_j is the j th-SDG.

After being calculated, the values of the SDGs were shown on radar charts. Based on the calculation results, the research assessed the level of sustainable development and identified the factors that need improvement in the two island districts according to the following hierarchy:

- 0.0 to < 0.2: Very unsustainable
- 0.2 to < 0.4: Unsustainable

Table 21.1 Indicators of the set of sustainable development indicators for island districts

	SDGs	Indicators		Unit	Explanation of indicators relative to SDIs
Environment	SDG6	6.1	Percentage of households supplied with clean water through a centralized water supply system	%	A higher value indicates more sustainable
		6.2	Percentage of households using clean water sources	%	A higher value indicates more sustainable
		6.3	Percentage of households using hygienic toilets	%	A higher value indicates more sustainable
		6.4	Percentage of wastewater is collected and safety treated	%	A higher value indicates more sustainable
	SDG7	7.1	Percentage of households with access to electricity	%	A higher value indicates more sustainable
		7.2	Percentage of renewable energy in gross final electricity consumption	%	A higher value indicates more sustainable
		7.3	Diversification index of electricity source	–	Higher value indicates more sustainable
		7.4	Percentage of households using clean fuel	%	A higher value indicates more sustainable
	SDG11	11.1	Percentage of population living in permanent houses	%	A higher value indicates more sustainable
		11.2	Percentage of solid waste is collected and safety treated	%	A higher value indicates more sustainable
		11.3	Percentage of communes meeting the criteria for new rural standards	%	A higher value indicates more sustainable
	SDG13	13.1	Percentage of households having access to communication media (TV/radio, telephone)	%	A higher value indicates more sustainable

(continued)

Table 21.1 (continued)

	SDGs	Indicators	Unit	Explanation of indicators relative to SDIs	
		13.2	Percentage of population to be disseminated of knowledge on typhoon prevention and mitigation	%	A higher value indicates more sustainable
		13.3	Economic losses due to natural disaster events	Mil. VND	A lower value indicates more sustainable
	SDG14	14.1	Rate of capture fisheries to regional fishery resources	%	Lower value indicates more sustainable
		14.2	Total area of marine protected areas	ha	A higher value indicates more sustainable
		14.3	Number of illegal fishing cases	–	A lower value indicates more sustainable
	SDG15	15.1	Percent change of forest land over the years	%	A lower value indicates more sustainable
		15.2	Percentage of forest cover	%	A higher value indicates more sustainable
Economy	SDG8	8.1	Ratio of revenue budget to total budget	–	A higher value indicates more sustainable
		8.2	Ratio of employment to population	–	A higher value indicates more sustainable
		8.3	Average production value per hectare of agricultural land	Mil. VND/kg	A higher value indicates more sustainable
		8.4	Tourism growth	%	A higher value indicates more sustainable
		8.5	Percentage of unemployment and underemployment	%	A lower value indicates more sustainable

(continued)

Table 21.1 (continued)

	SDGs	Indicators		Unit	Explanation of indicators relative to SDIs
	SDG9	9.1	Rate of waterway passenger transport to total passenger transport	%	A higher value indicates more sustainable
		9.2	Rate of waterway cargo transport to total cargo transport	%	A higher value indicates more sustainable
		9.3	Rate of processed and manufactured industrial products to the total products	%	A higher value indicates more sustainable
		9.4	Rate of employment in processing and manufacturing industries	%	A higher value indicates more sustainable
	SDG16	16.1	Rate of environmental pollution-causing establishments	%	A lower value indicates more sustainable
		16.2	Percentage of agricultural planting area applying safe production processes	%	A higher value indicates more sustainable
Society	SDG1	1.1	Percentage of poor households	%	A lower value indicates more sustainable
		1.2	Percentage of population having social insurance	%	A higher value indicates more sustainable
		1.3	Percentage of population living in households with access to basic living conditions	%	A higher value indicates more sustainable
	SDG2	2.1	Rate of malnutrition in under-5-year-old children	%	A lower value indicates more sustainable
		2.2	Percentage of agricultural land to be applied safety regulations or standards	%	A higher value indicates more sustainable

(continued)

Table 21.1 (continued)

	SDGs	Indicators	Unit	Explanation of indicators relative to SDIs
		2.3	Percentage of population struggling for foods	% A lower value indicates more sustainable
	SDG3	3.1	Annual number of new HIV infections (per 1000 uninfected population)	– A lower value indicates more sustainable
		3.2	Percentage of vaccinated children under 1-year old	% A higher value indicates more sustainable
		3.3	Number of hospital beds (per 10,000 population)	– A higher value indicates more sustainable
		3.4	Number of health workers (per 10,000 population)	– A higher value indicates more sustainable
		3.5	Percentage of communes meeting the criteria for cultural standards	% A higher value indicates more sustainable
	SDG4	4.1	Primary school completion rate	% A higher value indicates more sustainable
		4.2	Percentage of children attending primary school at the right age	% A higher value indicates more sustainable
		4.3	High school completion rate	% A higher value indicates more sustainable
		4.4	Percentage of schools meeting the national standards	% A higher value indicates more sustainable
	SDG5	5.1	Number of child marriage	– A lower value indicates more sustainable
		5.2	Sex ratio at birth	– A value closer to 1 indicates more sustainable
		5.3	Rate of female deputies in the People's Council	% A higher value indicates more sustainable

(continued)

Table 21.1 (continued)

SDGs	Indicators		Unit	Explanation of indicators relative to SDIs
SDG10	10.1	Expenditure growth of households	%	A higher value indicates more sustainable
	10.2	Income growth of households	%	A higher value indicates more sustainable
SDG16	16.1	Percentage of citizen satisfaction with public services	%	A higher value indicates more sustainable
	16.2	Number of family violence incidents	–	A lower value indicates more sustainable
	16.3	Number of crime of social disorder and safety (per 10,000 population)	–	A lower value indicates more sustainable

- 0.4 to < 0.6: Relatively sustainable
- 0.6 to < 0.8: Quite sustainable
- 0.8 to < 1.0: Sustainable.

21.3.3 Data Collection and Processing

The data for the calculating SDI includes primary data and secondary data. Primary data were collected based on questionnaires from 100 households in each island district in October 2019. Secondary data were collected from local regulatory authorities including statistical data sources as well as annual economic, social and environmental reports. These data sources form an important basis in determining the actual value of the indicators. Collected data were analyzed and processed with Microsoft Excel 2013 software.

21.4 Results and Discussion

From the results of the standardization, the SDI value of the SDGs is calculated according to the formula (21.2) and shown in Figs. 21.3, 21.4 and 21.5. The results show that the SDI values of the two island districts are similar and equal to 0.81. This value shows that the level of sustainable development of the two islands is at a good level. However, the difference in the sustainability of the SDGs in the two localities

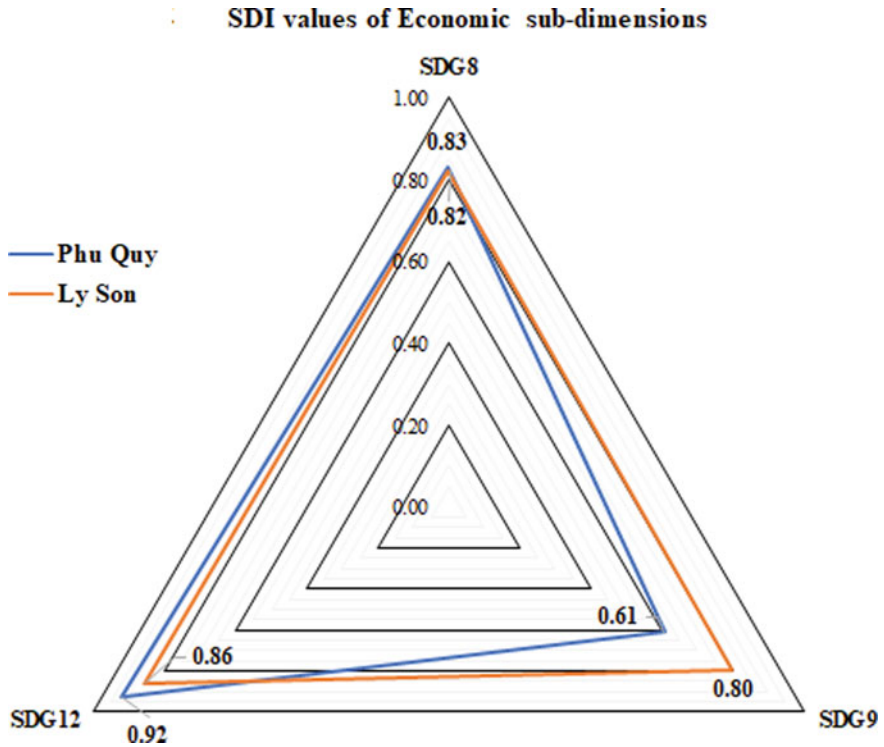


Fig. 21.3 Comparison of SDI values in economic sub-dimensions between Phu Quy and Ly Son

led to the difference in the SDI values of the three dimensions. Specifically, the SDI values of economic, environmental and social components in Phu Quy are 0.79, 0.85 and 0.79 respectively. Meanwhile, Ly Son has a good level of sustainability in the economic and environmental aspects with values of 0.83 and 0.81 respectively, while the social dimension is 0.78.

Regarding the economic aspect, the two island districts are generally similar in level of the sustainability. Accordingly, most of the economic SDGs of Phu Quy and Ly Son have achieved a good level of sustainability. However, for indicators 9.3 and 9.4 on processing and manufacturing industries of SDG9, both island districts have limitations due to rural characteristics. Accordingly, Phu Quy and Ly Son both have a very low percentage of workers participating in the processing and manufacturing industries with 5.5% and 4.6% respectively. The limitations of the workforce and the quality of the labour force are the main reasons why manufacturing products make up a low proportion of Phu Quy’s economy. However, unlike Phu Quy, the development of agriculture, forestry, fishery and tourism-services has contributed to promoting the development of food processing industries in Ly Son district, with a proportion of about 11% of the gross local product. The difference in the proportion of products of the processing and manufacturing industries has led to a clear difference in the

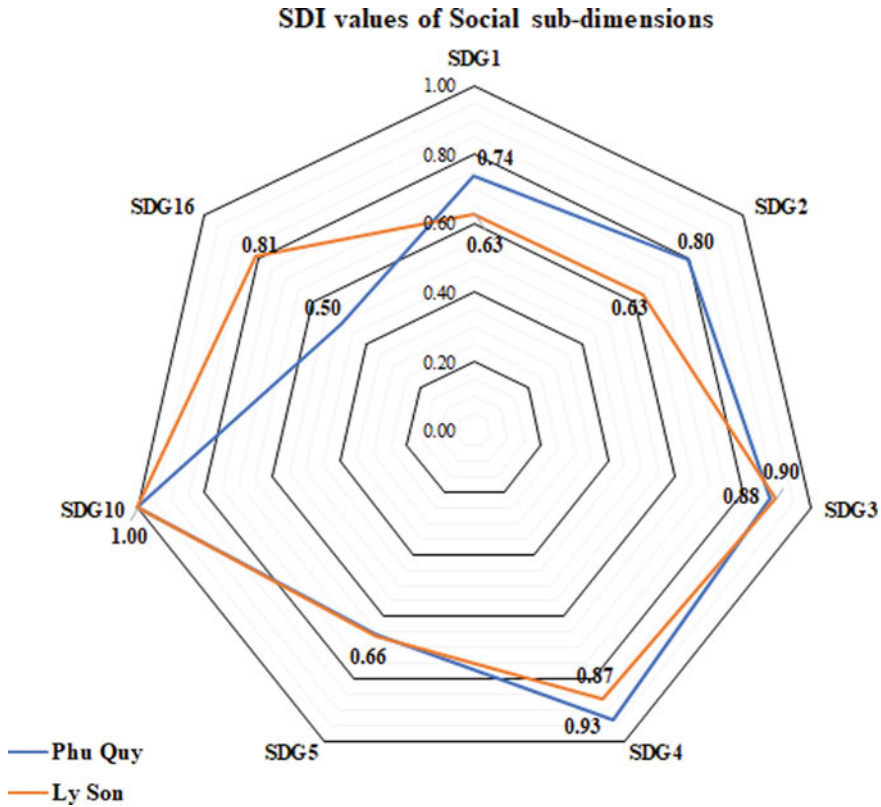


Fig. 21.4 Comparison of SDI values in social sub-dimensions between Phu Quy and Ly Son

value of SDG9 between the two island districts. While Ly Son achieved a good level of SDG9 (0.80), Phu Quy was only at a fairly sustainable level (0.61). Therefore, the overall economy of Ly Son can be assessed as more sustainable than that of Phu Quy.

The social aspect of two island districts Phu Quy and Ly Son are quite sustainable with values of 0.78 and 0.79, respectively. Although there is no difference in the social SDI of the two island districts, the difference in the SDI values of the sub-dimensions shows that the two island districts are facing different social development problems. Specifically, for the goals of hunger eradication and poverty reduction (SDG1, SDG2), Phu Quy district achieves a good level of sustainability, while Ly Son only achieves a relatively sustainable level with the value of both SDGs being 0.63. Accordingly, the poverty rate in Ly Son is still high (8.4%) with most of them being poor in terms of income, along with the frequent re-poor situation, which has caused many difficulties for poverty reduction policies. Besides, hunger eradication is still not guaranteed in Ly Son when more than 14% of children under 5 years old are malnourished. Poverty is one of the main factors affecting access to food. This

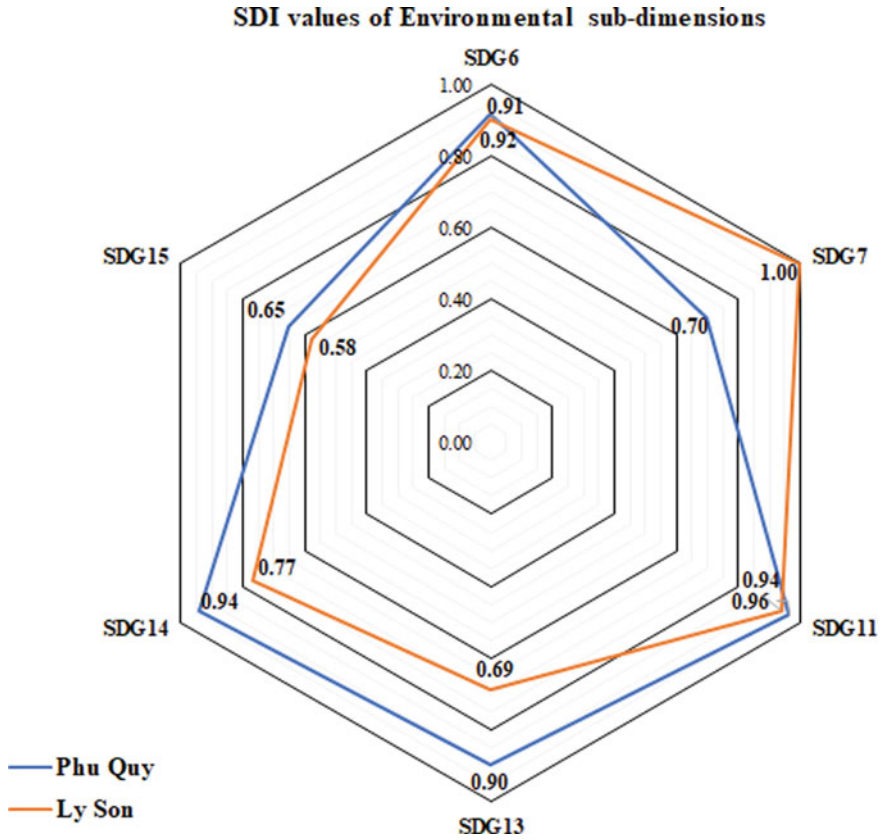


Fig. 21.5 Comparison of SDI values in environmental sub-dimensions between Phu Quy and Ly Son

is shown with the similarity in values of SDG1 and SDG2 of Ly Son district (0.63). Therefore, local authorities need to have integrated poverty reduction and hunger eradication policies to ensure effective improvement of the sustainability of these two SDGs. While Ly Son faces limitations in hunger eradication and poverty reduction, Phu Quy district has great limitations in ensuring security and order. From Fig. 21.4, it can be seen that Phu Quy’s SDG16 has the lowest value in level of sustainability (0.5). The main reason is due to the increasing rate of crime related to security and social order in recent years. In addition, domestic violence is also one of the factors that make Phu Quy has very low sustainability in SDG16. Besides the specific problems of each locality, Phu Quy and Ly Son currently both have limitations on the goal of ensuring gender equality, leading to a low level of sustainability in SDG5 of the two island districts (0.66). The main reason is due to male preference, especially in rural areas such as Phu Quy and Ly Son, which leads to an imbalance in the sex ratio at birth as well as less opportunities for women to participate in social activities. To improve this SDG, local governments need to have policies to propagate to the

community about reducing practices of son preference and undervaluing of girls, as well as increase the role of women in government agencies and the community.

Both Phu Quy and Ly Son island districts have achieved a high level of environmental sustainability with very high SDI values (0.85 and 0.81). However, the biggest environmental issue facing both island districts is the decreasing rate of forest cover. According to the results shown in Fig. 21.5, it can be seen that the goal of sustainable forest protection and development (SDG15) is the sub-dimension with the lowest SDI value in both localities. The cause of forest area decline is mainly due to the increase in demand for residential and agricultural land, especially in island districts with high population density and limited natural area such as Phu Quy and Ly Son. If the local government does not have appropriate solutions to protect and develop forests, the forest area of the two districts will be at risk of decline along with the increase in population in the future. Also, similar to the social dimension, despite having similar levels of sustainability, both island districts have their own local limitations in progress towards the sustainable development goals in the environmental dimension. For Phu Quy district, in addition to SDG15, SDG7 is just quite sustainable due to limitations in the proportion of renewable energy with about 30% of wind power in the total local power output. Therefore, the authority of Phu Quy needs to pay attention to invest in a variety of renewable energy systems (solar, tidal, wind, etc.) besides the existing wind power system to increase the proportion of renewable energy in the total energy consumption. Meanwhile, the authority of Ly Son district needs solutions to improve disaster response and prevention (SDG13) and marine and ocean conservation (SDG14). Accordingly, the percentage of people on the island who are provided with knowledge and prevention of natural disasters is also very low, accounting for only about 43.33% of the surveyed people, leading to SDG13 not achieving a good sustainability level. Therefore, local authorities need to focus on raising people's awareness about climate change and disaster prevention through various forms of communication (i.e., television and newspapers). Besides, although Ly Son marine protected area has been established, illegal fishing is happening frequently which is the main reason why Ly Son's SDG14 does not have a good level of sustainability. To improve the sustainability of SDG14, Ly Son needs to strengthen monitoring of fishing activities in local waters, and coordinate with local people to promptly prevent violations.

21.5 Conclusion

The result from the application of SDI to assess the sustainable development for the island districts of Phu Quy and Ly Son shows that the two island districts currently have a good level of sustainability (0.81). Even so, the two island districts are currently facing many challenges in their progress towards SDGs. In order to improve the level of sustainable development, Phu Quy district needs solutions to increase the proportion of the processing and manufacturing industry; as well as attracting labour resources to participate in this economic sector (SDG9), effectively protecting and

developing forests (SDG15), reducing the sex ratio at birth (SDG5) and reducing the crime rate (SDG16). Similarly, Ly Son needs policies to protect forests, exploit marine resources sustainably (SDG13 and SDG15), reduce the rate of poor households, avoid falling back into poverty (SDG1), ensure food security (SDG2) and increase women's participation in community activities (SDG5) to ensure comprehensive local sustainable development. In addition, the results show the feasibility of SDI to assess the sustainable development of island districts when it is used as a general scale while still being able to highlight specific issues for different localities.

Acknowledgements This research is funded by University of Science, VNU-HCM under grant number T2021-54: "Assessment of sustainable development for the Ly Son and Phu Quy island districts using sustainable development indicators".

References

- Hai PV, Thuy NTD, Hang PTT, Khoi DN (2023) Assessment of sustainable development in Phu Quy island, Binh Thuan Province using sustainable development index. In: Reddy JN, Wang CM, Luong VH, Le AT (eds) ICSCEA 2021. Lecture notes in civil engineering, vol 268. Springer, Singapore. https://doi.org/10.1007/978-981-19-3303-5_7
- People's Committee of Binh Thuan Province (2008) Decision No. 1485/QD-UBND approving the Master plan for socio-economic development of Phu Quy district for the period 2006–2020
- People's Committee of Quang Ngai Province (2012) Decision No. 169/QD-UBND approving the Master plan for socio-economic development of Ly Son district to be strong in economy, solid in defense and security by 2020
- United Nations (1992) Agenda 21. UN, Rio de Janeiro, Brazil
- United Nations (2000) Resolution 55/2 United Nations Millennium declaration. UN, New York
- United Nations (2015) Resolution 70/1 transforming our world: the 2030 Agenda for sustainable development. UN, New York
- World Commission on Environment and Development (1987) Our common future. Oxford University Press, Oxford, UK

Chapter 22

Multi Criteria Decision Analysis (MCDA) Approach to Evaluate the Applicability of Nature Based Solutions (NBS) in Tropical Region: A Field Note from the Asian Institute of Technology (AIT), Thailand



Fahad Ahmed, Ho Huu Loc , Sangam Shrestha , Sutat Weesakul, and Nguyen Hoai Thanh

Abstract Rapid urbanization and population growth have increased around the world's natural water resources more than ever. The changes in land use due to increased urbanization cause impervious surfaces leading to extreme to severe urban flooding and deterioration in water quality. The aforementioned issues can be minimized by employing Nature Based Solutions (NBS). In recent decades, NBS have been adapted for urban drainage in developed countries, mostly having temperate climate while there is a need to develop similar sustainable measures for urban drainage in tropical regions as currently there are no guidelines for their implementation in tropical climate. In this study multi criteria decision analysis (MCDA) approach was utilized to identify the best site for NBS in Asian Institute of Technology (AIT), Thailand. The NBS type used in this study was Bioretention system and the number of alternatives is three. To select one alternative among three Analytical Hierarchy Process (AHP) method was adapted. Ten criteria were determined as suitable, based on different dimensions of sustainability including economic (Design and capital costs), environmental (Stormwater quality indicators), technical (Soil parameters, catchment size, contributing structures and physical restrictions) and

F. Ahmed · H. H. Loc (✉) · S. Shrestha · S. Weesakul
Water Engineering and Management, Asian Institute of Technology (AIT), Klong Luang, Pathum Thani 12120, Thailand
e-mail: hohuuloc@ait.asia

F. Ahmed
Department of Civil Engineering, University of Sargodha, Sargodha 40100, Pakistan

S. Weesakul
Hydro and Agro Informatics Institute (HAI), Khwaeng Thanon Phaya Thai, Khet Ratchathewi, Krung Thep Maha Nakhon, Bangkok 10400, Thailand

N. H. Thanh
AECOM Singapore, 300 Beach Rd, #23-00, The Concourse, Singapore, Singapore

Social (Aesthetics). The results strongly suggested that Site-2 is a suitable alternative having maximum value of overall priority calculated by AHP process. The present study will provide a guideline for deciding the most suitable site for the operation of bioretention system for urban water management in tropical climate. Moreover, the results obtained in this research will be used for further design and execution of NBS project in AIT.

Keywords Nature based solutions · Urban Stormwater · Multi criteria decision analysis · Analytical hierarchy process

22.1 Introduction

There is continuous expansion of urban areas in terms of density and space, as the global population is expected to increase by 66% in 2050 (United Nations 2014). Because of the population growth and urbanization, the pollution in water bodies has risen exponentially (Kabir and Daly 2014). The stormwater runoff has a considerable contribution in water pollution and has been recognized as a non-point source of water pollution (Shrestha et al. 2018). Hence, rapid urbanization along with climate change has caused severe environmental problems as the impervious surfaces allows the precipitation to convert into runoff causing numerous problems related to water quantity and quality (Nontikansak et al. 2022; Brabec et al. 2002; Loc et al. 2020a, b). The conventional measures such as drains, channels, sewers and culverts were utilized initially to control urban floods (Loc et al. 2023; Ahmed et al. 2022; Ebrahimian et al. 2015). Though these measures help in the reduction of ponding and flooding, but they lack sufficient water quality management, preventing the application of stormwater for both non-potable and potable uses (Spahr et al. 2020).

To mitigate aforementioned problems some alternative measures or approaches involving vegetation and soil have been evolved with the aim of improving runoff quality, promoting evapotranspiration, and reducing surface runoff amount (Dagenais et al. 2018). These approaches have wide-ranging adoption in the world particularly in the developed countries or regions under different names and terminologies including LID (low impact development) and best management practice (BMP) in North America (Fletcher et al. 2015), SUDS (sustainable urban drainage system) in the United Kingdom (CIRIA 2015), Water Sensitive Urban Designs (WSUD) in Australia (Water by Design 2014; Loc et al. 2020a, b), Green and Blue Infrastructure in European countries (European Commission 2019), ABC Waters Programme in Singapore (PUB 2018) and Sponge Cities in China (Ren et al. 2017).

Some of the renowned sustainable stormwater management techniques make use of bioretention systems, rain gardens, permeable pavements, vegetated open channels, constructed wetlands and green roofs (Li et al. 2019; Vijayaraghavan 2016; Schmitter et al. 2016). Among them, one of the most used and effective stormwater management techniques is a bioretention system which is being used increasingly around the globe and considered as a useful alternative for treating stormwater runoff

(Davis et al. 2009). The typical configuration of a bioretention system is composed of a storage layer, a planting and packing layer and an aquifer. The bioretention system has been reported for removal of pollutants from stormwater by different processes including filtration, ion exchange, adsorption, microbial transformation and plant absorption (Collins et al. 2010; Falconer et al. 2018).

Multicriteria decision analysis (MCDA) is a decision support tool which is used to systematically evaluate and rank different options according to set of criteria to guide the decision makers to select best suitable alternative and has been used in various (Adem Esmail and Geneletti 2018; Cinelli et al. 2020). MCDA has been used in various fields including selection of appropriate nature-based solution for stormwater (Geronimo et al. 2021), flood risk assessment (Shivaprasad Sharma et al. 2018), evaluation of the most significant flood risk parameters (Dang et al. 2011), flood hazard mapping (Fernández and Lutz 2010) and reduction of flood risk by selecting grey infrastructures (Azibi and Vanderpooten 2003). MCDA has been employed particularly for stormwater management using nature based solutions (NBS) or LIDs by many researchers.

MCDA was performed by Ahammed et al. (2012) to select best LID among three LIDs namely soak-away, leaky-well and infiltration trench under technical, economic and social criteria and found that leaky well was best option among other alternatives. A decision making framework was developed by Gogate et al. (2017) to choose most suitable LID by using economic, environmental, social and technical aspects and employed Analytic hierarchy process (AHP) and technique for order of preference by similarity to ideal solution (TOPSIS) for evaluation. They found that the combination of leaky well and rain garden as the most preferred alternative. An evaluation was done by Li et al. (2017) by using both single and combined LID scenarios and utilized AHP method to determine criteria weights and concluded that the combination of bioretention system and green roof was the most suitable alternative in terms of social and environmental aspects. (Yang and Chui 2018) concluded that bioretention system was more effective for stormwater management than the green roof as the bioretention utilizes lesser area based on different hydro-environmental aspects. (Loc et al. 2017) used four methods of MCDA namely, pair-wise voting, Borda count, range of value and AHP and found that the urban green space is the most suitable type of LID followed by green roof, pervious pavement and rainwater harvesting. Furthermore, (Koc et al. 2021) evaluated seven different LID scenarios considering social, economic, and environmental aspects using AHP-TOPSIS framework and concluded that the combination of bioretention system and green roof was best alternative, while combination of other LID such as Green Roof, bioretention system, permeable pavements and infiltration trench depicted best performance considering economic, social and environmental aspects.

This study intends to evaluate the applicability of NBS (bioretention system) by using MCDA approach particularly the Analytic hierarchy process. The site selection for the application of NBS is a critical process as there is a need to consider many aspects such as environmental, social and economic. In this study different criterion including environmental, technical, economic and social aspects will be considered and used to decide the best alternative among the other alternatives. This is the first

published research using MCDA for site selection of NBS that we are aware of with previous studies focused on using MCDA for other applications, as discussed above.

22.2 Methodology

22.2.1 Study Area

The study area was located in Asian Institute of Technology (AIT), Pathumthani, Thailand with coordinates of 14.0785° N and 100.6140° E. The elevation is approximately 7 m above sea level and the total catchment area is 1.4 Sq.Km which contributes to runoff. The climate is tropical and average high temperature is 35–36 °C. The wet period is from May to September, and the dry period is mostly from November to February while the average annual rainfall is approximately 1301 mm. The atmosphere is humid, with humidity of 60–70% approximately. The drainage of AIT is composed of pipelines, manholes, open channels (canals and ponds) and outlets. The stormwater is drained through the above-mentioned conduits and conveyed to perimeter ponds of AIT through outlets. The average area and volume of perimeter ponds are 97,647 m² and 98,034 m³, respectively. Being a green campus, the pervious area around the AIT campus are substantially larger than impervious areas. The pervious areas are grassy swales, soccer fields whereas the impervious areas mostly consist of roads, buildings, surface pavements and parking lots (Fig. 22.1).

Three potential sites were proposed in this study for MCDA and the location of each site is mentioned below:

- Site-1: In front of the WEM building.
- Site-2: Near Industrial Systems Engineering Department.
- Site-3: Parking near AIT grocery.

The site-wise runoff contributing structures and drainage area are described in Table 22.1.

22.2.2 Data Collection and Site Investigations

Site investigations were performed at three potential sites to obtain data for Multi criteria analysis. Stormwater samples were collected from three sites on three different storm events. Maximum concentration of pollutants was selected among three trials performed. The pollutants considered for the analysis includes Total suspended solids (TSS), Total Nitrogen (TN), Total Phosphorus (TP), Chemical

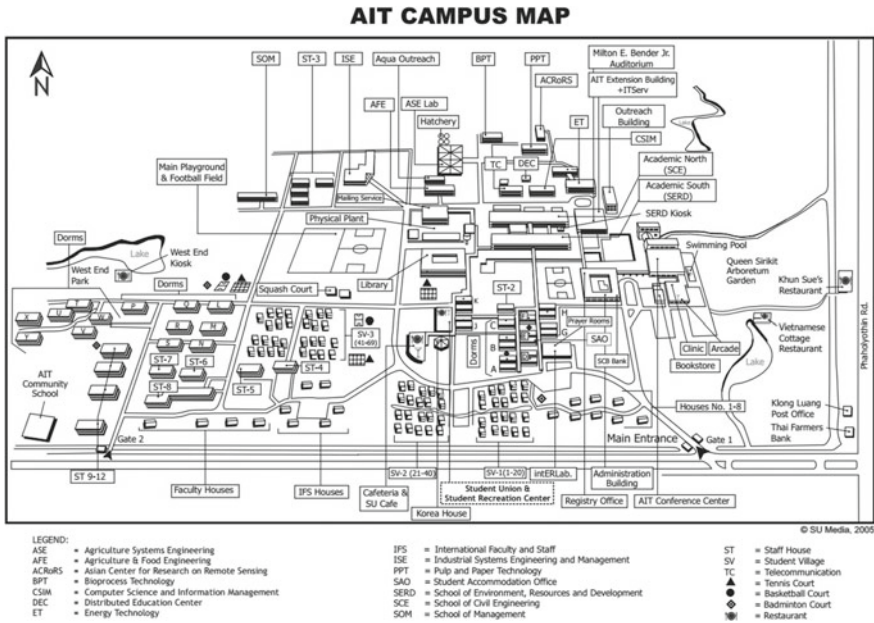


Fig. 22.1 Asian Institute of Technology (AIT) campus map (Source: SU Media, 2005)

Table 22.1 Contributing structures

Site	Runoff contributing structures	Drainage area (m ²)
1	i. Building roof ii. Road	1442
2	Parking lot	1300
3	Parking lot	700

Oxygen demand (COD) and Biochemical Oxygen demand (BOD). For soil properties, samples were obtained from sites and tested in laboratory for Hydraulic conductivity and porosity (Figs. 22.2, 22.3 and 22.4).

The hydraulic conductivity was not included in the analysis because it was revealed after testing that the values for each site were very less as compared to the recommended values (100–300 mm/h), and it is recommended to use engineered soil for soil filter media, therefore, only porosity was included in the analysis. The soil available in AIT can store water but cannot transmit it. Field visits were done to inspect physical restrictions which included trees, roots and wooded areas. The catchment or drainage area was measured by Google Earth and used in the analysis. The estimated cost was obtained by using Low Impact Development costing tool developed by Sustainable Technologies Evaluation Program



Fig. 22.2 Site-1 for NBS. Source Google Earth



Fig. 22.3 Site-2 for NBS. Source Google Earth



Fig. 22.4 Site-3 for NBS. Source Google Earth

(STEP), Toronto, Canada (<https://sustainabletechnologies.ca/home/urban-runoff-green-infrastructure/low-impact-development/bioretention-and-rain-gardens/>). The tool is useful from a comparison standpoint as it features a number of stormwater management practices that can be compared and there are separate costing sheets for bioretention, grass swales, green roof, infiltration chambers, infiltration trench and rainwater harvesting. Cost for each component of bioretention system was obtained by local vendors and used in the analysis. The cost was estimated based on the

Table 22.2 Stormwater quality for different sites

Pollutant	Trial	Rainfall depth (mm)	Site-1	Site-2	Site-3
TSS (mg/l)	1	9.5	9.5	65.33	134.67
TN (mg O ₂ /l)	3	4.1	8.96	15.8	11.59
TP (mg O ₂ /l)	1	9.5	0.15	0.57	0.55
COD (mgN/l)	2	31.8	7.87	78.69	39.34
BOD (mgP/l)	1	9.5	N.D	16.5	14.4

Table 22.3 Data collected by site investigations

Site	Hydraulic conductivity (mm/h)	Porosity (%)	Catchment size (ha)	Area of bioretention system (m ²)	Cost (Thai Baht)
Site-1	0.12	42.3	0.14	100	395,010
Site-2	0.81	44.63	0.13	50	240,474
Site-3	2.05	49.95	0.07	60	271,394

drainage area and area of bioretention system which was calculated according to the available space for construction. The data obtained by site investigations is shown in Tables 22.2 and 22.3.

22.2.3 The Analytic Hierarchy Process (AHP)

The Analytic Hierarchy Process (AHP) (Saaty 2004) has been employed considerably in the literature for multi-criteria analysis in numerous fields due to many advantages (Darko et al. 2019). It has been observed that the procedure required for AHP is simple and can be understood easily as compared to other methods (Zyoud et al. 2016). One more aspect of AHP is Hierarchical representation which eases the understating of problem (Yang et al. 2013; Loc et al. 2015). AHP organizes and analyzes complex decision problems by using mathematics and psychology. AHP consists of three parts including ultimate goal, possible solutions called alternatives and the criteria we will judge the alternatives on. AHP provides a rational framework for a needed decision by quantifying its criteria and alternative options and for relating those elements to the overall goal. At first pairwise comparisons were derived for each criterion with respect to each other using a numerical scale developed by Saaty as shown in Fig. 22.5.

To perform the pairwise comparison a comparison matrix of the criteria involved in the decision was developed. Consistency test is performed to check the consistency of answer and consistency ratio (CR) is obtained. The relative priorities (preferences) were derived for the alternatives with respect to each criterion. Since these priorities are valid only with respect to each specific criterion, they are called local priorities to

Verbal judgment	Numeric value
Extremely important	9
	8
Very Strongly more important	7
	6
Strongly more important	5
	4
Moderately more important	3
	2
Equally important	1

Fig. 22.5 Saaty’s pairwise comparison scale

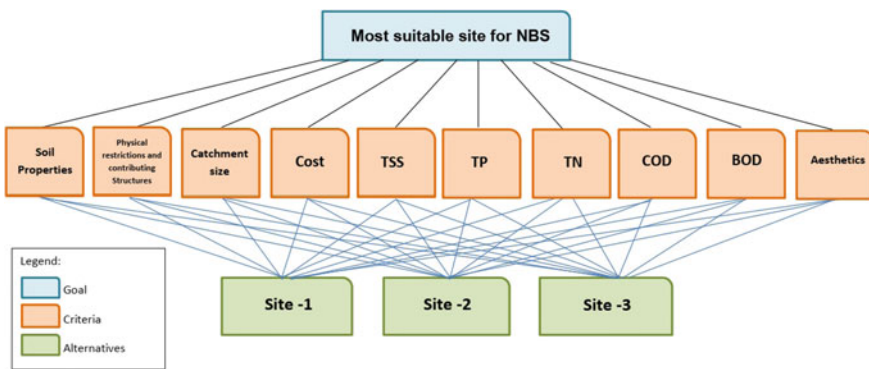


Fig. 22.6 The analytic hierarchy process

differentiate them from the overall priorities to be calculated later. A pairwise comparison (using the numeric scale) of all the alternatives was performed, with respect to each criterion. Overall priority was calculated at the end to rank each alternative according to the calculated priority. The AHP process is depicted in Fig. 22.6.

22.2.4 Criteria for MCDA

For MCDA, ten criteria were decided considering environmental, technical, economic and social aspects. The criteria include Soil properties (Porosity), Physical restrictions and contributing structures, Catchment size, Cost, Stormwater pollutants (TSS, TN, TP, COD, BOD) and Aesthetics. For each criterion priorities were decided according to Table 22.4.

Table 22.4 Priority decision for each criterion

S. No.	Criteria	Priority decision based on
1	Soil properties	Results obtained from field tests
2	Water quality	Water quality tests (Max. values are preferred)
3	Cost	Minimum cost
4	Physical restrictions and contributing structures	Minimum physical restrictions, Max. Contributing structures
5	Catchment size	Maximum Catchment size
6	Aesthetics	Site having good aesthetic will be preferred

Criteria Weights

Weights for each criterion were calculated by using a social survey. A questionnaire was developed and sent to the experts including faculty and alumni of Water Engineering and Management (WEM) at AIT. The experts were asked to give priority for each criterion according to five level likert scale. The weights were calculated from the opinion of 14 experts using a scoring scheme of 5 (Essential) having the highest priority and 1 (Not a priority) being the lowest priority. The summary of the importance of each criterion is given Table 22.5.

Calculation of Local Priorities

A pairwise comparison of all the alternatives was performed, with respect to each criterion to obtain local priority and consistency test was performed to check its consistency. The value of consistency ratio (CR) should not be in excess of 0.1 otherwise the judgments are untrustworthy because they are too close for comfort to randomness and the exercise must be repeated. An example for calculation of local priority and consistency test is given in Table 22.6.

Consistency Test

$$\begin{aligned} \lambda_{max} &= 3.05 & \lambda_{max} &= \text{Principal eigen value} \\ CI &= (\lambda_{max} - n)/(n - 1) \\ CR &= CI/RI \\ n &= 3 \\ RI &= 0.58 \\ CI &= 0.02 \\ CR &= \mathbf{0.04} \end{aligned}$$

The value of consistency ratio (CR) is $0.04 < 0.10$.

Table 22.5 Summary of the importance of each criterion

Criteria	Response of 14 experts for each criteria														Average score
	1	2	3	4	5	6	7	8	9	10	11	12	13	14	
Soil parameters—porosity	5	3	5	5	5	2	4	4	5	3	5	4	3	5	4.14
Physical restrictions and contributing structures	4	2	4	4	2	3	4	3	5	4	4	5	5	3	3.71
Catchment size	5	2	3	3	4	3	5	5	5	3	4	4	5	3	3.86
Cost	5	3	5	3	3	5	5	5	5	3	4	3	4	2	3.93
Total suspended solids	2	3	4	3	4	4	5	4	5	5	4	3	4	2	3.71
Total nitrogen	2	3	3	3	4	4	5	3	4	5	4	4	4	2	3.57
Total phosphorus	2	3	3	3	4	4	5	3	4	5	4	4	4	2	3.57
Chemical oxygen demand	2	3	4	3	4	5	5	4	4	5	3	3	4	2	3.64
Biochemical oxygen demand	2	3	4	3	4	5	5	5	4	5	3	3	4	2	3.71
Aesthetics	4	3	4	3	3	5	5	4	5	3	4	3	3	5	3.86

Table 22.6 Calculation of local priority

Porosity	Site-1	Site-2	Site-3	Priority
Site-1	1	1/3	1/5	0.106
Site-2	3	1	1/3	0.260
Site-3	5	3	1	0.634
Sum	9	4.33	1.53	

The bold values are calculated local priorities for each criteria

22.3 Results and Discussion

The results of criteria weights calculations and overall priority are shown in Tables 22.7 and 22.8 respectively.

It can be seen that the maximum criteria weight is obtained for soil parameters and cost while less importance is given to stormwater quality indicators while equal importance is given to aesthetics and catchment area.

The ranking of each site according to overall priority calculated in Table 22.8 is shown in Table 22.9.

As shown in Table 22.9 the rank 1 is given to site-2 as it has maximum overall priority, hence site-2 is recommended to be used for bioretention system.

22.4 Conclusions and Recommendations

The MCDA is a potential technique which can be used for overcoming and integration of considerable differences between social and technical measurements. Site selection for NBS is a critical process as it requires considering many aspects such as technical, social, economic and environmental, hence a unique and precise technique is required for this purpose. This study demonstrated selection of a potential site for bioretention system in AIT which is a well-known NBS technique. Three sites were considered as potential sites and AHP technique was employed considering different criteria such as soil properties, stormwater quality, cost, catchment size, physical restrictions and aesthetics. It was found that the best possible site for implementation of NBS project is site-2 having overall priority of 0.394. The criteria weights which have maximum contribution are cost and soil properties according to the social survey. Site-2 has minimum cost and good soil properties (porosity) while it has maximum values of stormwater quality indicators. The site has medium aesthetics and physical restrictions, hence it is recommended for the construction of NBS (bioretention system) project. Furthermore, the study provides a guideline for site selection and implementation of NBS project in tropical climate.

Recommendations

The AHP technique is a recommended technique for selection of potential sites for NBS projects and can be used for other types of LIDs such as green roofs etc. It is

Table 22.7 10 × 10 comparison matrix and calculated criteria weights

Suitable site for NBS	Soil parameters	Physical restrictions and contributing structures	Catchment size	Cost	TSS	TN	TP	COD	BOD	Aesthetics	Criteria weight
Soil parameters	1	5	3	3	5	7	7	7	5	3	0.28
Physical restrictions and contributing structures	1/5	1	1/3	1/5	1	5	5	3	1	1/3	0.06
Catchment size	1/3	3	1	1/3	3	5	5	5	3	1	0.12
Cost	1/3	5	3	1	5	7	7	7	5	3	0.22
TSS	1/5	1	1/3	1/5	1	5	5	3	1	1/3	0.06
TN	1/7	1/5	1/5	1/7	1/5	1	1	1/3	1/5	1/5	0.02
TP	1/7	1/5	1/5	1/7	1/5	1	1	1/3	1/5	1/5	0.02
COD	1/7	1/3	1/5	1/7	1/3	3	3	1	1/3	1/5	0.03
BOD	1/5	1	1/3	1/5	1	5	5	3	1	1/3	0.06
Aesthetics	1/3	3	1	1/3	3	5	5	5	3	1	0.12

The bold values are calculated criteria weights for each criteria

Table 22.8 Overall priorities for each site

Aspects	Technical		Economic	Environmental				Social	Overall priority	
	Porosity	Physical restrictions and contributing structures		Cost	TSS	TN	TP			COD
Criteria weights	0.276	0.064	0.219	0.064	0.020	0.020	0.033	0.064	0.120	
Site-1	0.106	0.724	0.074	0.064	0.106	0.091	0.074	0.074	0.644	0.262
Site-2	0.260	0.193	0.643	0.267	0.634	0.455	0.644	0.644	0.282	0.394
Site-3	0.634	0.083	0.283	0.669	0.260	0.455	0.282	0.282	0.074	0.344

The bold values are calculated overall priorities for all three sites

Table 22.9 Ranking of each site

Rank	Priority	Site
Rank-1	0.394	Site-2
Rank-2	0.344	Site-3
Rank-3	0.262	Site-1

also recommended that different aspects or criteria can be used for MCDA other than used in this study.

Acknowledgements The authors thankfully acknowledge and appreciate the support from Environmental Engineering department (EEM) of AIT for providing resources for lab work. The authors also acknowledge Mr. Ky Le Gia of EEM department and Mr. Ruel Francisco of WEM for their support in site investigations.

References

- Adem Esmail B, Geneletti D (2018) Multi-criteria decision analysis for nature conservation: a review of 20 years of applications. *Methods Ecol Evol* 9(1):42–53
- Ahmed F, Loc, HH, Park E, Hassan M, & Joyklad P (2022). Comparison of Different Artificial Intelligence Techniques to Predict Floods in Jhelum River, Pakistan. *Water*, 14(21): 3533.
- Ahmed F, Hewa GA, Argue JR (2012) Applying multi-criteria decision analysis to select WSUD and LID technologies. *Water Sci Technol Water Supply* 12:844–853
- Azibi R, Vanderpooten D (2003) Aggregation of dispersed consequences for constructing criteria: the evaluation of flood risk reduction strategies. *Eur J Oper Res*
- Brabec E, Schulte S, Richards PL (2002) Impervious surfaces and water quality: a review of current literature and its implications for watershed planning. *J Plan Lit* 16:499–524
- Cinelli M et al (2020) How to support the application of multiple criteria decision analysis? Let us start with a comprehensive taxonomy. *Omega (UK)* 96
- CIRIA (2015) The SuDS manual. <https://www.ciria.org>
- Collins KA, Lawrence TJ, Stander EK, Jontos RJ, Kaushal SS, Newcomer TA, Grimm NB, Ekberg MLC (2010) Opportunities and challenges for managing nitrogen in urban stormwater: a review and synthesis. *Ecol Eng* 36:1507–1519
- Dagenais D, Brisson J, Fletcher TD (2018) The role of plants in bioretention systems; does the science underpin current guidance? *Ecol Eng* 120:532–545
- Dang NM, Babel MS, Luong HT (2011) Evaluation of flood risk parameters in the Day River Flood Diversion Area, Red River Delta, Vietnam. *Natural Hazards*
- Darko A, Chan APC, Ameyaw EE, Owusu EK, Parn E, Edwards DJ (2019) Review of application of analytic hierarchy process (AHP) in construction. *Int J Constr Manag* 19:436–452
- Davis AP, Hunt WF, Traver RG, Clar M (2009) Bioretention technology: overview of current practice and future needs. *J Environ Eng* 135(3):109–117
- Ebrahimian A, Ardeshir A, Zahedi Rad I, Ghodsypour SH (2015) Urban stormwater construction method selection using a hybrid multi-criteria approach. *Autom Construct* 58:118–128
- European Commission (2019) Natural capital accounting: overview and progress in the European Union. 6th report. <https://ec.europa.eu>
- Falconer L, Telfer TC, Ross LG (2018) Modelling seasonal nutrient inputs from nonpoint sources across large catchments of importance to aquaculture. *Aquaculture* 495:682–692

- Fernández DS, MA (2010) Lutz: urban flood hazard zoning in Tucumán Province, Argentina, using GIS and multicriteria decision analysis. *Eng Geol*
- Fletcher TD et al (2015) SUDS, LID, BMPs, WSUD and more—the evolution and application of terminology surrounding urban drainage. *Urban Water J* 12(7):525
- Geronimo FK, Reyes NJ, Choi H, Yano K, Kim L (2021) H: Selection of appropriate nature-based solution for stormwater through multi-criteria performance. *Desalin Water Treat* 219:392–398
- Gogate NG, Kalbar PP, Raval PM (2017) Assessment of stormwater management options in urban contexts using multiple attribute decision-making. *J Clean Prod* 142:2046–2059
<https://sustainabletechnologies.ca/home/urban-runoff-green-infrastructure/low-impact-development/bioretenion-and-rain-gardens/>
- Kabir MI, Daly E, Maggi F (2014) A review of ion and metal pollutants in urban green water infrastructures. *Sci Total Environ* 470:695–706
- Koc K, Ekmekcioğlu O, Ozger M (2021) An integrated framework for the comprehensive evaluation of low impact development strategies. *J Environ Manage* 294:113023
- Li J, Deng C, Li Y, Li Y, Song J (2017) Comprehensive benefit evaluation system for low-impact development of urban stormwater management measures. *Water Resour Manag* 31:4745–4758
- Li C, Peng C, Chiang P-C, Cai Y, Wang X, Yang Z (2019) Mechanisms and applications of green infrastructure practices for stormwater control: a review. *J Hydrol* 568:626–637
- Loc HH, Babel MS, Weesakul S, Irvine KN, Duyen PM (2015) Exploratory assessment of SUDS feasibility in Nhieu Loc-Thi Nghe Basin, Ho Chi Minh City, Vietnam. *Br J Environ Clim Change* 5(2):91–103
- Loc HH, Duyen PM, Ballatore TJ et al (2017) Applicability of sustainable urban drainage systems: an evaluation by multi-criteria analysis. *Environ Syst Decis* 37:332–343
- Loc HH, Do QH, Cokro AA, Irvine KN (2020a) Deep neural network analyses of water quality time series associated with water sensitive urban design (WSUD) features. *J Appl Water Eng Res* 8(4):313–332. <https://doi.org/10.1080/23249676.2020.1831976>
- Loc HH, Park E, Chitwatkulsiri D, Lim J, Yun SH, Maneechot L, Phuon DM (2020b) Local rainfall or river overflow? Re-evaluating the cause of the Great 2011 Thailand flood. *J Hydrol* 589:125368
- Loc, Ho Huu, et al. "The Great 2011 Thailand flood disaster revisited: Could it have been mitigated by different dam operations based on better weather forecasts?" *Environmental research* 216 (2023): 114493.
- Nontikansak P, Shrestha S, Shanmugam MS, Loc HH, & Virdis SG (2022). Rainfall extremes under climate change in the Pasak River Basin, Thailand. *Journal of Water and Climate Change*, 13(10): 3729–3746.
- PUB (2018) Active, beautiful, clean waters design guidelines, 4th edn. https://www.pub.gov.sg/Documents/ABC_Waters_Design_Guidelines.pdf
- Ren N, Wang Q, Wang Q, Huang H, Wang X (2017) Upgrading to urban water system 3.0 through sponge city construction. *Front Environ Sci Eng* 11(9). Retrieved from <http://water.epa.gov/infrastructure/greeninfrastructure/index.cfm>
- Saaty TL (2004) Decision making—the analytic hierarchy and network processes (AHP/ANP). *J Syst Sci Syst Eng* 13:1–35
- Schmitter P, Goedbloed A, Galelli S, Babovic V (2016) Effect of catchment-scale green roof deployment on stormwater generation and reuse in a tropical city. *J Water Resour Plann Manag* 142(7):05016002
- Shivaprasad Sharma SV, Roy PS, Chakravarthi V, Srinivasa Rao G (2018) Flood risk assessment using multi-criteria analysis: a case study from Kopili river basin, Assam, India. *Geomat Nat Hazards Risk* 9:79–93
- Shrestha P, Hurley SE, Wemple BC (2018) Effects of different soil media, vegetation, and hydrologic treatments on nutrient and sediment removal in roadside bioretention systems. *Ecol Eng* 112:116–213
- Spahr S, Teixeira M, Sedlak DL, Luthy RG (2020) Hydrophilic trace organic contaminants in urban stormwater: occurrence, toxicological relevance, and the need to enhance green stormwater infrastructure. *Environ Sci Water Res Technol* 6:15–44

- United Nations (2014) World urbanization prospects. United Nations, San Francisco, CA, USA
- Vijayaraghavan K (2016) Green roofs: a critical review on the role of components, benefits. *Limit Trends Renew Sustain Energy Rev* 57:740–752
- Water by Design (2014) Bioretention technical design guidelines
- Yang Y, Chui TFM (2018) Optimizing surface and contributing areas of bioretention cells for stormwater runoff quality and quantity management. *J Environ Manag* 206:1090–1103
- Yang X, Ding J, Hou H (2013) Application of a triangular fuzzy AHP approach for flood risk evaluation and response measures analysis. *Nat Hazards* 68:657–674
- Zyoud SH, Kaufmann LG, Shaheen H, Samhan S, Fuchs-Hanusch D (2016) A framework for water loss management in developing countries under fuzzy environment: integration of Fuzzy AHP with Fuzzy TOPSIS. *Exp Syst Appl* 61:86–105

Chapter 23

Decision Support Tool for Integrated Water Resources Management Based on GIS, Remote Sensing and SWAT Model: A Case Study in the Upper Part of Dong Nai River Basin, Vietnam



Pham Hung, Le Van Trung, and Phu Le Vo 

Abstract Integrated Water Resources Management (IWRM) has been a promising approach to ensure sustainable water resources management. Therein, the management tool is one of the key components for successful IWRM implementation. This paper introduces the IWRM decision support tool for the upper part of the Dong Nai (UPDN) river basin, which plays a pivotal role for the socio-economic development in the Southeast region of Vietnam, through the application of an integrated technology of GIS, remote sensing, and SWAT (Soil and Water Assessment Tool) model. The paper also describes how to calculate water balance and map water resource vulnerability index (VI) for the UPDN as well as its sub-basins. Landsat satellite images and data related to water resources information (quantity and quality) of the basin were collected. The results show that the UPDN basin's water pollution and water vulnerability were at a moderate level of which VI was 0.318. However, there were relative differences of these between sub-basins. The VIs of the sub-basins of Dak Nong, Dak R'Keh, and La Nga rose up 0.4–0.7 as highly vulnerable areas which should be prioritized for sustainable water management actions. These results evidenced that the integrated techniques could be an efficient approach to

P. Hung (✉) · L. Van Trung

Faculty of Environment and Natural Resources, Ho Chi Minh City University of Technology (HCMUT), 268. Ly Thuong Kiet Street, District 10, Ho Chi Minh City, Vietnam
e-mail: hungp@stnmtld.gov.vn

L. Van Trung

e-mail: lvtrung@hcmut.edu.vn

Vietnam National University Ho Chi Minh City, Linh Trung Ward, Thu Duc District, Ho Chi Minh City, Vietnam

P. Hung

Department of Natural Resources and Environment, Lam Dong Province, Dalat, Vietnam

P. L. Vo

Faculty of Environment and Natural Resources, Ho Chi Minh City University of Technology (HCMUT), Vietnam National University Ho Chi Minh (VNU-HCM), Ho Chi Minh City, Vietnam
e-mail: volephu@hcmut.edu.vn

provide useful information on the status of water resources to stakeholders in terms of sustainable basin development and management via IWRM.

Keywords Integrated water resources management (IWRM) · Upper Part of Dong Nai river · GIS · Remote sensing · SWAT model · Vulnerability index

23.1 Introduction

Integrated Water Resources Management (IWRM) should be widely executed to ensure sustainable water resources management (UN 1992; Ako et al. 2010). IWRM was defined as “a process which promotes the coordinated development and management of water, land and related resources in order to maximize the resultant economic and social welfare, paving the way towards sustainable development, in an equitable manner without compromising the sustainability of vital ecosystems” (Global Water Partnership 2000). On over the world, 172 countries counting for nearly 90 percent of the 193 UN member states have carried out IWRM (United Nations Environment Programme 2018). However, the status of IWRM implementation between countries is quite different ranged via key components of the IWRM, including: (i) enabling environment (policy, laws, plans); (ii) institutional frameworks, (iii) management instruments; and (iv) financing. Vietnam, a developing nation locates in Southeast Asia, has a low rank in IWRM implementation with an overall score of 38/100 (i = 47, ii = 35, iii = 36, iv = 34) low (Global Water Partnership 2018). Therefore, in order to improve national IWRM, the Government not only needs to upgrade the institutional framework related to IWRM as well as invest in finance but also enhance management instruments. Therein, management instruments should be prioritized.

According to the Global Water Partnership (GWP) (Global Water Partnership 2021), the management instruments of IWRM include eight main components and Geographic Information Systems (GIS) as well as Decision Support Systems (DSSs) which are the indispensable components of the Modelling and Decision-Making. GIS programs help decision-makers of IWRM visualize the water resources and identify the interactions between multiple water resources and human actions. In addition, remote sensing (RS) enables observation, mapping, monitoring, and assessment of landuse and landcover (LULC) at a large scale of spatial and temporal characteristics (Rogon and Chen 2004). Annually updated LULC is useful for developing socio-economic policies, planning natural resource management, modeling environmental variables, implementing environmental management, and assessing environmental vulnerability and risk (Gomez et al. 2016). RS and GIS technology is a practical tool to estimate spatial and temporal soil erosion in large areas facing land degradation as well as environmental deterioration to assess prior areas for conservation.

On the other hand, understanding the freshwater resource vulnerability and water balance of the river basin plays an important role in effective water resource management. The water balance assessment is a complicated process (Nugroho et al. 2013), this work refers to the balance between incoming water by precipitation and outgoing

water from evapotranspiration, groundwater recharge, and streamflow (Suryatmojoa et al. 2013). The water balance can be easily changed due to climate change, population growth, socio-economic development, and urbanization. To evaluate water balance and to assess the impacts of LULC and climate change assessments on runoff, a great number of hydrological models have been developed and applied, such as AGNPS, MIKE-SHE, WEPP, and EUROSEM. At the sub-catchment or river basin level, hydrological models can simulate water balance elements (run-off, evapotranspiration, and ground water) as well as water quality (sediments, pesticides, and other pollutants). Amongst the hydrological models, SWAT (Soil and Water Assessment Tool) is a well-established model and it has been used successfully in a wide range of environmental conditions and regions (Shi et al. 2011; Gassman et al. 2007). Indeed, SWAT has been a practical model with wide applications (Borah and Bera 2003), as well as a robust, elastic, interdisciplinary tool for simulation of various watershed problems, such as continuous simulations of stream flow, soil erosion, and nutrient/sediment transport (Gassman et al. 2007; Huang and Lo 2015), and evaluation of the simultaneous impacts of climate land use changes on hydrological conditions (Khoury et al. 2015; Mango et al. 2011; Zhu and Li 2014; Schilling et al. 2008).

This paper aims to introduce the incorporation of combining remote sensing, GIS, and the SWAT model as technical tools for IWRM decision support in the upper part of Dong Nai (UPDN) river basin as a case study. This work is to elucidate its existing water resources status, and hence, to identify the most vulnerable freshwater resources at the sub-basin scale. The estimated information of such an assessment will provide managers with adequate options to modify existing policies and to implement measures for the management practices of water resources by the IWRM approach.

23.2 Study Areas and Methods

23.2.1 Study Area

The Dong Nai river basin located in the southeast of Vietnam is the largest national river. The river originates in the Lang Biang plateau with an elevation of over 1500 m above sea level and flows through 10 provinces and HCM City. This land is the dynamic economic development region with more than 60 industrial parks and export processing zones (Ringler and Huy 2004; Vietnam Ministry of Natural Resources and Environment (MONRE) 2006). Water from Dong Nai river is used for many purposes such as supplying domestic water for 19 million people, irrigating for 22,874 km² of agricultural land, operating for more than 15 hydropower plants with a total installed capacity of 2380 MW, and mitigating sea water intrusion the for the estuary delta (Truong et al. 2018). Therefore, this study focuses on the UPDN river basin with an area of 11,036 km² belongs to Lam Dong province accounting for 70% of the entire

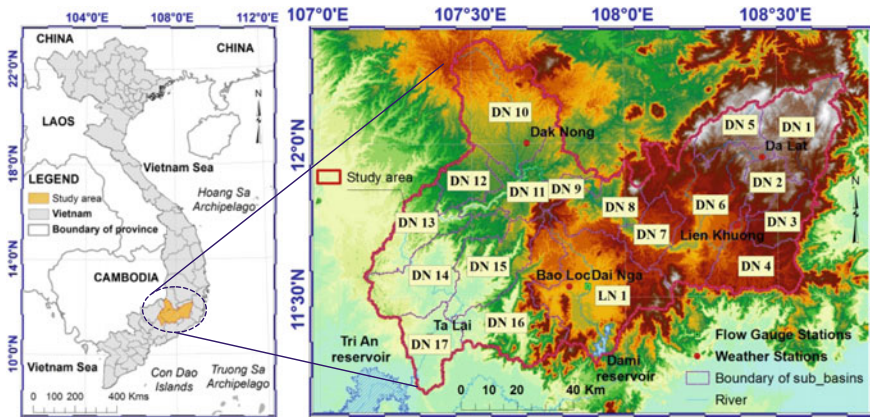


Fig. 23.1 Location of the study area and its digital elevation model (DEM)

basin compared to 18%, 7%, 4%, and 2% of Dak Nong, Dong Nai, Binh Phuoc, and Binh Thuan provinces, respectively. The location of the UPDN river basin is presented in Fig. 23.1.

The UPDN river basin consists of two tributaries and is divided into 18 sub-basins (Jolk et al. 2010). The main tributary, which involves 17 sub-basins from DN1 to DN17, originates in the northern area of Lam Dong province and ends at the Tri An hydropower reservoir. Another tributary that covers only one sub-basin (LN1) sits on the Di Linh plateau and ends at the Da Mi hydropower reservoir. The region has a tropical monsoon climate regime, which is hot and humid throughout the year. There is the rainy season from May to November, and the dry season from December to April of the following year. The average annual rainfall was nearly 2500 mm. The average annual temperature was approximately 22 °C. The annual humidity was about 83% (Lam Dong Statistical Department 2015). Agriculture is the main economic activity providing nearly 50% of the economic value of the region. Coffee is mainly a cropping tree of area counting for 61.3% compared to 15.2% of vegetables, 11.9% of paddies, 9.5% of green tea, and 3.9% of the others (Lam Dong Statistical Department 2019). Overview of the 18 sub-basins of the UPDN river shows as Table 23.1.

23.2.2 Remote Sensing and GIS for Monitoring Land Use Changes

According to the report of Lam Dong Province (People's Committee of Lam Dong Province 2014), the forest area of Lam Dong was 513,529 ha in 2014 and accounted for 52.5% of the provincial area. The report also implies that the area of forest-cover in the UPDN river basin has decreased with the average cover rate falling nearly 8%

Table 23.1 Characteristics of sub-basins of the UPDN river basin

No.	ID	Sub-basin/reservoir	Land use (the largest area % first)	Overall topology	Mean elevation (m)	Area (km ²)
1	DN1	Da Nhim	Forest, perennial crops	Highlands	1500	729
2	DN2	Da Tam	Forest, annual crops	Highlands	1321	227
3	DN3	Don Duong	Forest, annual crops	Highlands	1141	372
4	DN4	Da Quyen	Forest, annual crops	Highlands	978	562
5	DN5	Suoi Vang	Forest, perennial crops	Highlands	1550	314
6	DN6	Da Dang	Forest, industrial crops	Highlands	987	1283
7	DN7	Dong Nai 2	Perennial crops, forest	Highlands	907	332
8	DN8	Dong Nai 3	Forest, perennial crops	Highlands	847	495
9	DN9	Dong Nai 4	Forest, perennial crops	Highlands	714	159
10	DN10	Dak Nong	Perennial crops, forest	Highlands	757	1120
11	DN11	Dong Nai 5	Forest, perennial crops	Highlands	637	592
12	DN12	Dak R' Keh	Perennial crops, forest	Highlands	567	321
13	DN13	Dong Nai 6	Forest, perennial crops	Hill country	372	483
14	DN14	Cat Tien	Forest, perennial crops	Hill country	285	773
15	DN15	Da Teh	Forest, perennial crops	Low mountain	414	630

(continued)

Table 23.1 (continued)

No.	ID	Sub-basin/reservoir	Land use (the largest area % first)	Overall topology	Mean elevation (m)	Area (km ²)
16	DN16	Da Huoai	Forest, perennial crops	Low mountain	592	909
17	DN17	Ta Lai	Perennial crops, forest, rice	Hill country	140	431
18	LN1	La Nga	Perennial crops, forest	High plateau	811	1304

in 10 years. Landsat images of 1994 and 2020 were collected for assessing land use changes in the river basin as well as establish GIS database to create input data in the SWAT model, which is used in order to analyze the impacts on water resources in many manners. Figure 23.2 illustrates the proposed method for monitoring land use changes in the UPDN river basin.

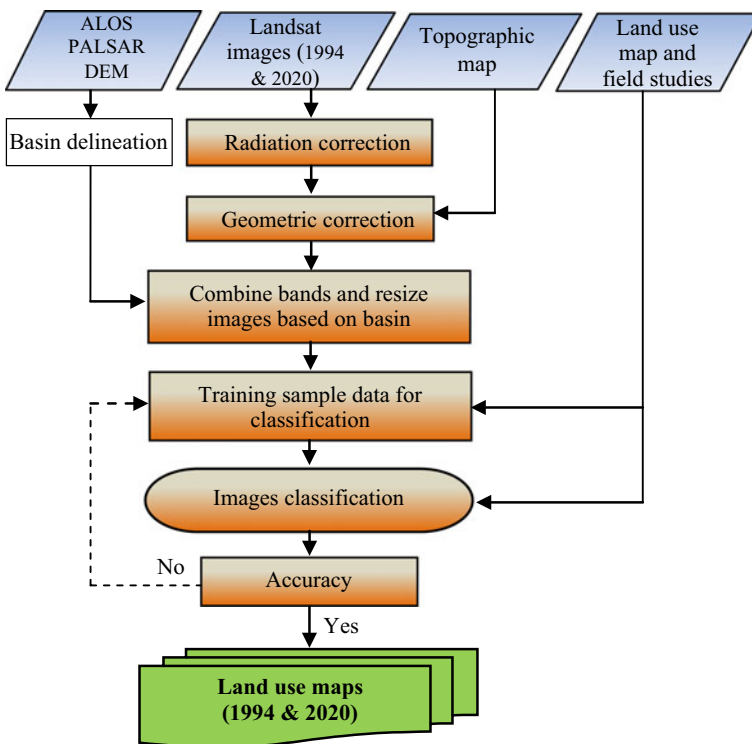


Fig. 23.2 Methodology flowchart for monitoring land use changes

Table 23.2 Land use classes of the study area

Type of land use	Description
(1) Water bodies	Natural (rivers, lakes, etc.) or man-made water bodies (e.g. reservoirs)
Forest (2) <i>Broadleaf evergreen forest</i> (3) <i>Mixed forest</i> (4) <i>Coniferous forest</i>	All forests: evergreen broadleaf forest, coniferous forest (pine), mixed forest (bamboo and broadleaf forests, pine, and broadleaf forest, etc.)
(5) Built-up residential areas	Residential areas, roads and built-up areas
(6) Perennial agriculture	Rubber, coffee, tea, etc.
(7) Annual agriculture and others	Rice fields, soybean, potatoes, etc.

ENVI 4.5 software is used in geometric correction of Landsat-5 TM image (01-07-1994) and Landsat-8 OLI/TIRS image (15-01-2020) based on the topographic map of Lam Dong province in 2010 (scale 1: 100,000). The corrected geometric images were then clipped (subset) to the UPDN watershed. The maximum likelihood classification (MLC) method was applied for Landsat images with the same training sample data, whose regions of interest (ROIs) were categorized into the seven classes (as in Table 23.2) based on field studies and the knowledge about the land use map of the study area. All datasets of the UPDN basin (topographic and thematic maps; training sample; ground truth and statistics data, etc.) were carried out on the basis of GIS data for the purposes of assessing forest land changes by using ArcGIS 10.2 software.

23.2.3 *GIS and Remote Sensing for Soil Erosion Risk Mapping*

The solution for integrating RUSLE, GIS, and RS technology was applied in order to quantitatively assess the risk of spatial and temporal soil erosion in the UPDN river basin. This is a possible potential solution for sustainable management of the basin in the context of climate change. The annual average soil loss map (A) per unit area was computerized using RUSLE (Eq. 23.1 and Fig. 23.3) (Belasri and Lakhouili 2016; Renard et al. 1997; Farhan and Nawaiseh 2016).

$$A = R \times K \times LS \times C \times P \quad (23.1)$$

where, A is the average soil loss ($t \text{ ha}^{-1} \text{ year}^{-1}$); R is the rainfall-runoff erosivity factor ($\text{MJ mm ha}^{-1} \text{ h}^{-1} \text{ year}^{-1}$); K is the soil erodibility factor ($t \text{ ha h ha}^{-1} \text{ MJ}^{-1} \text{ mm}^{-1}$); LS is the slope length–steepness factor; C is the cover-management practice factor; P is the erosion control (conservation support) practices factor.

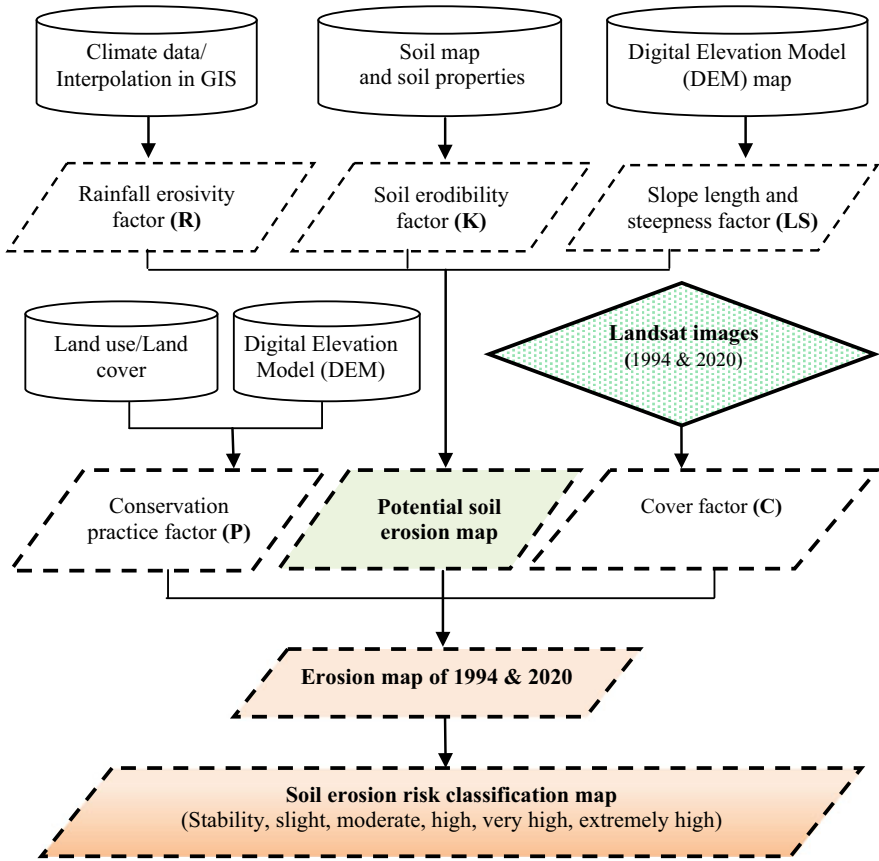


Fig. 23.3 Methodology flowchart for mapping soil erosion

Rainfall erodibility factor (R): this study used the Roose (1975) formula applied for tropical climate countries to calculate the R factor (Roose 1975). The value of R was calculated based on the total of amount annual precipitation.

$$R = (0.5 + 0.05) \times H \tag{23.2}$$

where, H (mm) is the average annual rainfall.

Rainfall datasets of 30 years (1984–2014) collected from Lam Dong Meteorological Department (LMD) were used to calculate the average R-factor. After the calculation of the R-factor ($\text{MJ mm ha}^{-1} \text{ h}^{-1} \text{ year}^{-1}$) for the specific 4 rain-gauge stations (as in Table 23.3), the spatial interpolation techniques available (ordinary Kriging method) in the ArcGIS software were applied to interpolate the rainfall erosivity to generate a raster map for the R-factor.

Table 23.3 Monthly rainfall data with annual average *R*-factor

Station	Elevation (m)	Jan.	Feb.	Mar.	Apr.	May	Jun.	July	Aug.	Sep.	Oct.	Nov.	Dec.	Total	Average <i>R</i>
Dalat	1500	23	24	75	192	200	205	218	179	303	262	123	48	1853	1853
Lien Khuong	1100	15	12	39	156	190	137	220	151	264	285	111	32	1592	1592
Bao Loc	800	60	42	146	218	238	270	386	373	421	354	176	77	2761	2761
Cat Tien	250	23	54	15	267	218	394	700	532	717	484	138	51	3591	3591

Soil erodibility factor (K): this study used the formula proposed by Williams (1995) to determine K based on the grain composition and mean aberrations (Neitsch et al. 2011).

$$K = f_{csand} \times f_{cl-si} \times f_{orgc} \times f_{hisand} \quad (23.3)$$

where f_{csand} is a factor that gives low soil erodibility factors for soils with high coarse-sand contents and high values for soils with little sand. f_{cl-si} is a factor that gives low soil erodibility factors for soils with high clay to silt ratios. f_{orgc} is a factor that reduces soil erodibility for soils with high organic carbon content. f_{hisand} is a factor that reduces soil erodibility for soils with extremely high sand contents.

Topographic factor (LS): the topographic map (1:100,000 scale) in the river basin was used to determine the slope, direction, and flow direction by using analysis tools in GIS. The Bernei mathematical formula was used to generate the slope length (L) and steepness (S) factors in GIS (Demirci and Karaburun 2012; Lu et al. 2004; Wischmeier and Smith 1978).

$$LS = ([\text{Flow accumulation}] \times \text{cellsize}/22, 13)^n \times (\sin \text{slope}/0.0896)^{1.3} \quad (23.4)$$

where Flow Accumulation is the grid layer of flow accumulation expressed as the number of grid cells. Cellsize is the length of a cell side. Slope is the angle of slope in degrees and n is a constant dependent on the value of the slope gradient (S): n = 0.2 if S < 1%; n = 0.3 if 1% < S < 3.5%; n = 0.4 if 3.5 < S < 4.5%; n = 0.5 if S > 5%.

Cover factor (C): this factor (C) has significantly influence the runoff and erosion rates. The factor also plays a important role in reducing water erosion, but it usually changes because of the harvest and the crop (Belasri and Lakhouili 2016). In this study, the C factor and their spatial distribution in the study area were evaluated based on Normalized Difference Vegetation Index (NDVI) from Landsat TM images mentioned above (Demirci and Karaburun 2012; Lu et al. 2004).

$$C = -\exp\left[\alpha\left(\frac{NDVI}{(\beta - NDVI)}\right)\right] \quad (23.5)$$

where, α and β are unitless parameters that determine the shape of the curve relating to NDVI and C factor. The values of 2 and 1 were selected for the parameters α and β , respectively (Belasri and Lakhouili 2016; Prasannakumar et al. 2013; Alexakis et al. 2013). The NDVI was calculated by using Landsat images with the spectral band of the near-infrared (NIR) and Red band such as Eq. (23.6).

$$NDVI = \frac{NIR - Red}{NIR + Red} \quad (23.6)$$

Table 23.4 *P*-factor based on LULC and slope

Land use/land cover (LULC)	Farm planning	
	Land slope (%)	Strip crop <i>P</i> factor
Agriculture	1–2	0.30
	3–8	0.25
	9–12	0.30
	13–16	0.35
	17–20	0.40
	21–25	0.45
	>25	0.60
Bare land, forest and other land	–	1.0

Support practice factor (*P*): this factor is defined as the ratio of soil loss with a specific support practice to the corresponding loss with natural slope culture. The highest value of *P* is 1 if there weren't erosion control practices, and the *P* factor is less than 1 if there were erosion control practices. Table 23.4. shows that each value of *P* was derived from the LULC and slope maps. Therein, ArcGIS was used to reclassify the LULC and slope length maps according to their *P* values.

23.2.4 GIS Database for Water Quality in the UPDN River Basin

The GIS database allows managers to use the functions of GIS in managing, storing, and analyzing all types of spatial and attribute data of the UPDN river basin. The data on 8 physical and chemical parameters of surface water quality at 49 monitoring sites in the UPDN river basin during the period of 2012–2020 were collected from Department of Natural Resources and Environment (DONRE) of Lam Dong province and Dak Nong province. The physico-chemical parameters include DO (mg/L), BOD₅ (mg/L), COD (mg/L), NH₄⁺-N (mg/L), PO₄³⁻-P (mg/L), TSS (mg/L), and pH. Then, the datasets were structured in the ArcGIS 10.2 software program for statistical analysis and database management.

The monitoring program requires the measurement and analysis of a large number of the water quality parameters that performed as Water Quality Index (WQI). The Decision No. 879/QD-TCMT on WQI is used to determine the level of water quality based on 9 parameters, including: DO, BOD₅, COD, NH₄⁺-N, PO₄³⁻-P; TSS, pH, temperature, and total coliforms. In this study, 8 parameters retrieved from the local monitoring program were applied to calculate the WQI, whereas the indicator of coliforms was not included due to inadequate data. Accordingly, WQI is calculated as Eq. (23.7) (Pham 2017; Vietnam Ministry of Natural Resources and Environment 2011; Linh et al. 2016)

$$WQI = \frac{WQI_{pH}}{100} \left[\frac{1}{5} \sum_{a=1}^5 WQI_a \times \frac{1}{2} \sum_{b=1}^2 WQI_b \right]^{1/2} \quad (23.7)$$

where WQI_a (denotation of the sub-index values for the ‘organics’) is calculated through six parameters: DO, BOD₅, COD, NH₄⁺-N, and PO₄³⁻-P; WQI_b (representation of the sub-index values for the ‘particulates’) is calculated with the TSS parameter; WQI_{pH} is calculated with the pH parameter and temperature.

The WQI number ranges from 0 to 100 (as shown in Table 23.10), its values range corresponding to color signifies with higher values indicating better water quality.

23.2.5 SWAT Model for Hydrological Assessment and Water Balance Calculation

SWAT is a physical hydrological model developed by Jeff Arnold for the USDA-Agricultural Research Service (USDA-ARS) that is used to estimate the amount of water in the UPDN river basin under the conditions of climate change coupled with land cover change in 1994, and 2020. SWAT divides a watershed into sub-basins or sub-basins connected by a network of streams and further delineates them into Hydrological Response Units (HRUs). The SWAT model simulates the hydrology of a watershed in two phases. Firstly, the terrestrial phase of the hydrological cycle calculate the quantity of water, nutrients, pesticides, and sediment loads from each HRU and sums up them to the level of sub-basins. Secondly, the routing phase of the hydrological cycle defines the movement of water, sediment, and other non-point sources of pollution through the channel network to an outlet of the watershed (Huang and Lo 2015; Neitsch et al. 2011). The hydrological cycle is simulated in the SWAT model based on the water balance equation (Neitsch et al. 2011):

$$SW_t = SW_0 + \sum_{i=1}^t (R_{day} - Q_{surf} - E_a - w_{seep} - Q_{gw}) \quad (23.8)$$

where SW_t is the final soil water content. SW_0 is the initial soil water content on day i . t is the time (days). R_{day} is the amount of precipitation on day i . Q_{surf} is the amount of surface runoff on day i (mm H₂O). E_a is the amount of evapotranspiration on day i . w_{seep} is the amount of water entering the vadose zone from the soil profile on day i . Q_{gw} is the amount of return flow on day i (all water units are in mm H₂O).

In addition, SWAT model is also used to determine the water balance changes based on climate variations and LULC changes as well as to calculate water resources and water demand in the UPDN river basin. The water demand within a river basin consists of the following components: population demand, agricultural demand, industrial demand, service sector demand, and the minimum flow requirement (ecological water) (Stolpe 2011). Population water demand (domestic water

consumption) mainly includes water use for all residential needs and is usually estimated based on population numbers (urban and rural areas combined), per capita water consumption, and water use efficiency (Xiao-jun et al. 2013). The generalization of the calculation diagram of the water balance components is shown in Fig. 23.4.

In this study, per capita water consumption is estimated according to the Vietnam Construction Standard TCXDVN 33:2006 (Vietnam Ministry of Construction (MOC) 2006). Agricultural water demand includes crop and livestock water demands (FAO 1998; Stolpe 2011; Allen et al. 1998). Industrial water demand is estimated based on the average amount of water needed to produce a given product. Water use for the service sector is defined as the amount of water needed per tourist per day (based on the provincial statistical yearbook). The ecological water requirement

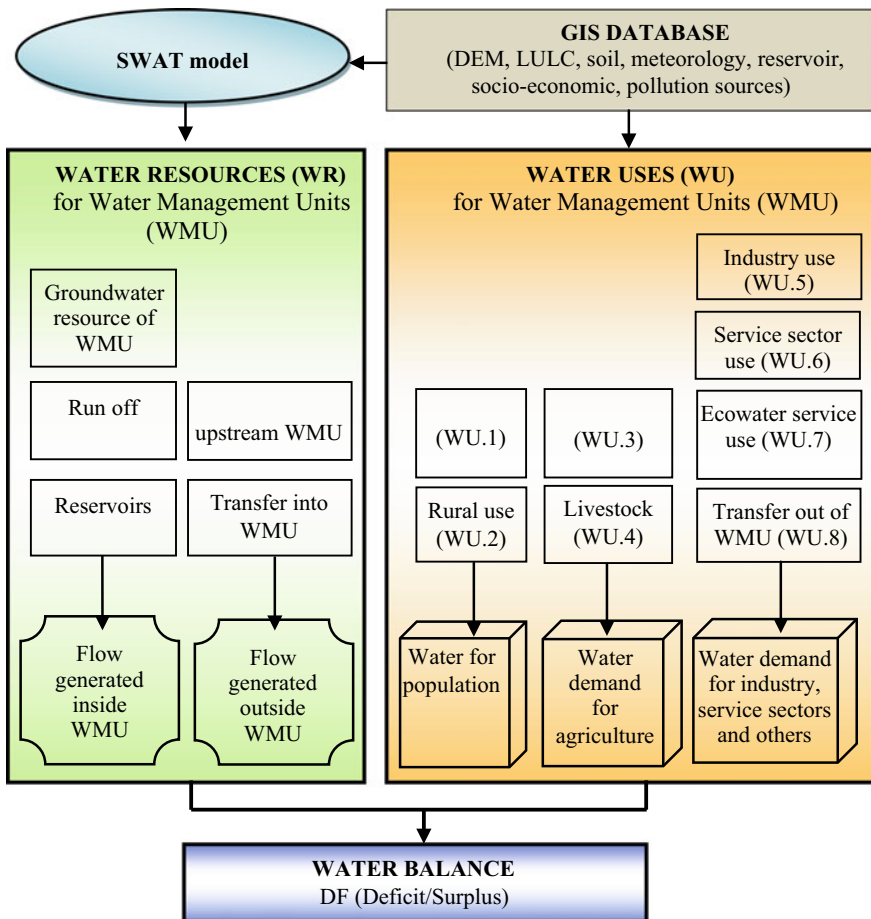


Fig. 23.4 Calculation diagram for the water balance components

is the minimum flow needed to sustain the basic ecological properties of a river. The ecological water requirement in a river basin is defined as the runoff at the Q₉₅ percentile (Vietnam Ministry of Natural Resources and Environment 2017).

23.2.6 GIS, Remote Sensing and SWAT Model for Mapping Freshwater Vulnerability

The implementation method as well as the calculation of all categories and parameters of the VI, which is based on the guideline of UNEP (UNEP 2009), is shown in Fig. 23.5.

The freshwater resources vulnerability index (VI), a guideline developed by United Nations Environment Program (UNEP) and Peking University (UNEP 2009), enables decision makers to make rational and informed selections for sustainable water resources use and management. Therein, the vulnerability index (VI) of the water resources is measured via four elements including resource stresses (RS), development pressure (DP), ecological health (EH), and management capacity (MC). Thus, the VI of water resources is often expressed as:

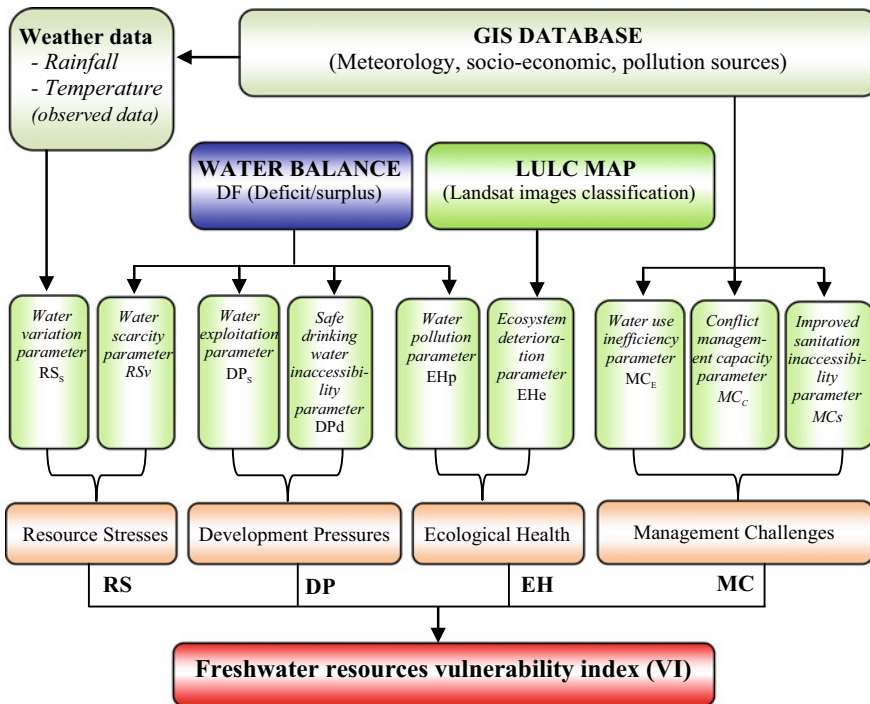


Fig. 23.5 Freshwater resources vulnerability components and indicators

$$VI = f(RS, DP, EH, MC) \quad (23.9)$$

The VI value ranges from zero to one. The sum of the weights for all categories is one, and the sum of the weights for all the parameters for each category is also one (Babel and Wahid 2009). The process of determining the relative weights and how to calculate of all categories and parameters of VI can be applied by some equations in the guideline of UNEP (UNEP 2009; Al-Kalbani et al. 2014). According to UNEP (2009) (UNEP 2009), the vulnerability index is categorized into 4 levels, including low (0.0–0.2), moderate (0.2–0.4), high (0.4–0.7) and severe (0.7–1.0). Each level draws on the state of vulnerability of water resources and respectively suitable policy recommendations.

23.2.7 Dataset

DEM map, soil map, LULC map, weather information, stream-flow, water quality monitoring, and socio-economic statistics were used for the study. The description of the main datasets is shown in Table 23.5.

The SWAT model requires key data including DEM map, soil map, LULC map, weather data, and stream-flow. The DEM map with a 12.5-m resolution could be downloaded from the NASA website: <https://urs.earthdata.nasa.gov/users/new>. The main weather datasets using for the SWAT model consist of rainfall, temperature, wind speed, humidity, and solar radiation. Daily maximum and minimum temperatures and daily rainfall from 1984 to 2014 were collected from 4 weather stations (Da Lat, Lien Khuong, Bao Loc, and Dak Nong). The spatial location of these stations can be seen in Fig. 23.1. The missing data in daily solar radiation, wind speed, and relative humidity were generated automatically by SWAT (Mango et al. 2011; Jha et al. 2007). The SWAT model needs soil property data like the physical properties, available moisture content, texture, hydraulic conductivity, bulk density, chemical composition, and organic carbon content for the different layers of each soil type (Setegn et al. 2010). Soil information was obtained from the 1:100,000 soil map of DONRE Lam Dong province. The LULC maps applying for SWAT were derived from LULC classification results of Landsat images which downloaded from the USGS website: <http://earthexplorer.usgs.gov>. Field survey data, thematic land use map, and Google Earth images were used to create the polygons of training sample data for classification and assess classification accuracy. In which, based on the characteristics of the basin, the study selected 30 sample points/image for each of 7 LULC types distributed in the entire areas. Also, the main datasets to estimate water demand and VIs were mostly based on the Statistical Yearbook of Lam Dong and Dak Nong provinces.

Table 23.5 Properties, sources and purpose of used data

Data	Properties	Sources	Used for
DEM map	Resolution of 12.5 m	Downloaded from the NASA website: https://urs.earthdata.nasa.gov/users/new	SWAT model; RUSLE
Soil map	Resolution of 30 m	Obtained from DONRE of Lam Dong province	SWAT model; RUSLE
LULC map	Resolution of 30 m	Landsat TM/ETM/OLI-TIRS images (1994 and 2020), downloaded from the website: http://earthexplorer.usgs.gov	SWAT model; RUSLE
Weather	4 stations	Obtained from 4 weather stations (Da Lat, Lien Khuong, Bao Loc, and Dak Nong)	SWAT model; RUSLE
Stream-flow	3 gauges	Derived from 3 gauges (Thanh Binh, Dai Nga, and Ta Lai)	SWAT model;
Water quality monitoring	49 sites	Obtained from DONRE of Lam Dong and Dak Nong province	Assessing water quality
Field surveys	30 sample regions	30 sample points/image for each of 7 LULC types from the field surveys	Classification of Landsat images
Socio-economic statistics	Provincial data	Obtained from the Statistical Department (Lam Dong, Dak Nong)	Calculating water balance, VIS

23.3 Results and Discussion

23.3.1 Land Use and Land Cover Change

The accuracy assessment is derived from the error matrices in which overall accuracy, user's and producer's accuracy and Kappa coefficient were used to analyze in 2 cases of the classified images. The overall accuracy of all seven LULC classifications in 1994 and 2020 was very good with 77.7% and 85.5%, as shown in Table 23.6. In cases, the Kappa coefficients were also quite high with values of 0.74 and 0.83. The results show that the highest accuracy was for water bodies (User (%) = 98.26 and 98.64 for 1994 and 2020, respectively). Therefore, the thematic map was used to analyze LULC change trends and use for SWAT model input data.

For the purposes of assessing forest land changes, three natural forest classes were combined (evergreen broadleaf forest, mixed forest, and coniferous forest),

Table 23.6 Summary of classification accuracy for the LULC map in 1994 and 2020

Class name	1994		2020	
	User (%)	Prod. (%)	User (%)	Prod. (%)
Water bodies	98.26	98.64	87.40	90.12
Broadleaf evergreen forest	90.38	57.02	85.94	78.26
Mixed forest	65.54	87.19	89.51	86.71
Coniferous forest	91.42	92.52	89.27	81.85
Built-up residential areas	70.51	81.55	81.17	82.11
Perennial agricultural land	69.03	90.51	77.56	88.44
Annual agricultural land	89.69	79.35	77.78	77.78
Overall accuracy (OA)	77.7%		85.5%	
Kappa	0.74		0.83	

and thematic maps containing five main classes were created. The maps of two periods between 1994 and 2020 were overlaid in order to identify the regions where major changes have occurred in the five LC classes. The area for each type of LULC in the river basin and the cover percentages are summarized in Table 23.7.

The results show that the forest area covered 768,625 ha (69.6%) and 444,039 ha (40.2%) in 1994 and 2020. This means that the area of forest coverage has changed significantly over the last 26 years. In contrast, there was a significant increase in seasonal agricultural land and perennial agricultural land, as shown in Fig. 23.6.

The area of water bodies also increased over the study period measuring 9,110 ha (0.80%) in 1994 compared to 19,299 ha (1.7%) in 2020. This rising fluctuation can be explained by the recent construction of large hydropower plants in the river basin

Table 23.7 LULC changes between 1994 and 2020 in the UPDN river basin

LULC type	1994		2020		Changes (26 years)	
	Area (ha)	(%)	Area (ha)	(%)	Area (ha)	(%)
WATR ^{1*}	9,110	0.8	19,299	1.7	+10,189	+0.9
FOREST	768,625	69.6	444,039	40.2	-324,586	-29.4
• <i>FRSE</i> ²	306,417	27.8	160,504	14.5	-145,913	-13.3
• <i>FRST</i> ³	311,670	28.2	166,884	15.1	-144,786	-13.1
• <i>PINE</i> ⁴	150,537	13.6	116,651	10.6	-33,886	-3.0
URML ⁵	9,423	0.9	36,700	3.3	+27,277	+2.4
AGR ⁶	236,588	21.4	467,734	42.4	+231,146	+21.0
AGRC ⁷	79,820	7.2	135,794	12.3	+55,974	+5.1
Total	1,103,566	100	1,103,566	100		

*The symbols were the abbreviation of SWAT land use codes encrypted from 7 land cover types (1) water bodies, (2) broadleaf evergreen forest, (3) mixed forest, (4) coniferous forest, (5) built-up residential areas, (6) perennial agriculture land, and (7) annual agriculture land, respectively

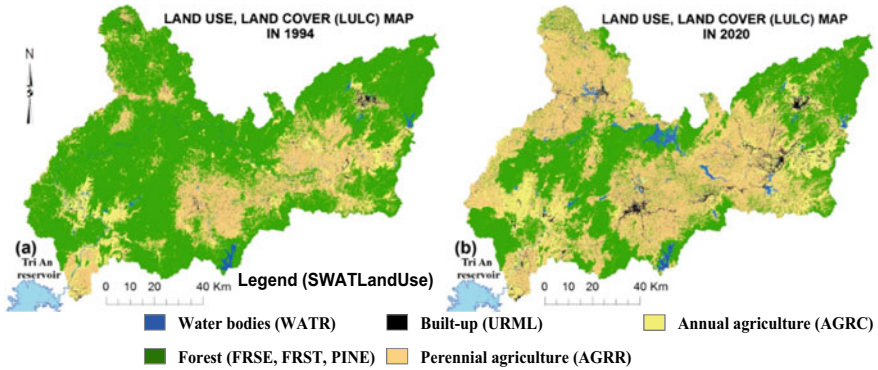


Fig. 23.6 LULC map of 1994 (a), and 2020 (b)

such as: Dai Ninh (300 MW), Da Dang 2 (34 MW), Dong Nai 3 (180 MW), Dong Nai 4 (340 MW), Dong Nai 2 (70 MW) and Dong Nai 5 (150 MW), which came into operation from 2008 to 2014, respectively (Lam Dong Statistical Department 2015; Lam Dong Department of Natural Resources and Environment 2013). Residential coverage was 9423 ha (0.9%) in 1994 and 36,700 ha (3.3%) in 2020. In terms of sub-basins, the Dak Nong (DN10) had the highest deforestation rate with 63.5% (an approximate loss of 71,015 ha), and the Ta Lai (ND17) had the lowest deforestation rate with 7.6% (nearby loss of 3270 ha).

23.3.2 Soil Erosion Risk

The results show that the potential erosion in the basin is very high, whereas the areas of potential erosion greater than 100 tons/ha/year account for 50.48% of the basin's area. The hillside and mountainous areas with an average slope greater than 15° have potential erosion greater than 500 tons/ha/year and these regions should be prioritized for sustainable soil management actions, as presented in Fig. 23.7.

Figure 23.8 depicts an evaluation of the yearly erosion rate between 1994 and 2020 in the UPDN river basin. Statistical calculations of soil erosion were summarized in Table 23.8. The results showed that the level of erosion status in 2020 was higher than in 1994. Therein, the soil erosion rate greater than 10 tons/ha/year in 2020 occupied 509,034 ha (46.12%) compared to in 1994 with 461,077 ha (41.78%) that can be explained by the deforestation in the period 1994–2020, as mentioned above.

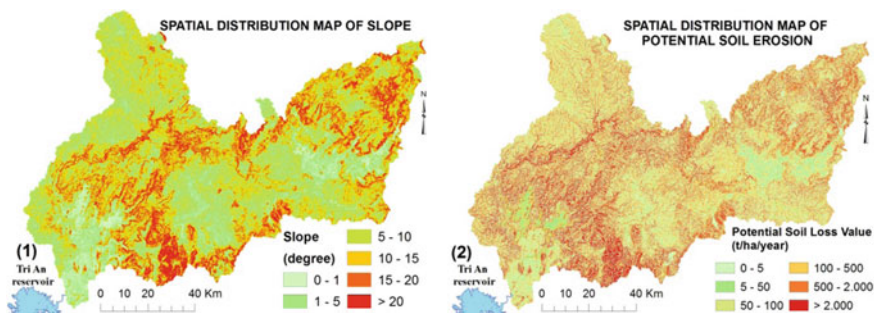


Fig. 23.7 Spatial distribution of slope zones (1) and potential soil loss (2)

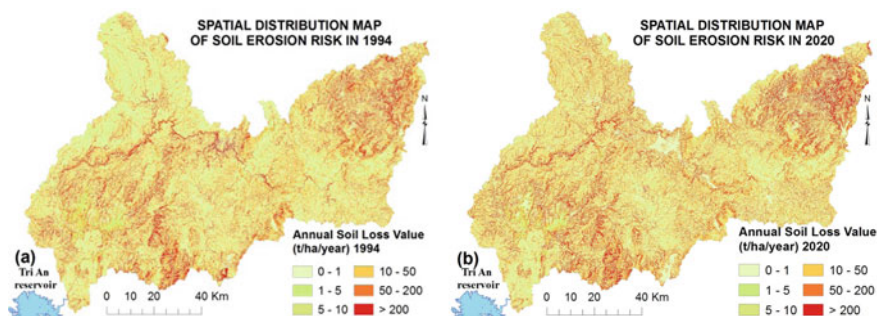


Fig. 23.8 Spatial distribution of soil loss of 1994 (a) and 2020 (b)

Table 23.8 Potential soil erosion and erosion in 1994 and 2020

Erosion risk class	Range (ton ha ⁻¹ year ⁻¹)	Potential soil loss (×10)		1994		2020	
		Area (ha)	Per. (%)	Area (ha)	Per. (%)	Area (ha)	Per. (%)
Stability	0–1	480,206	43.51	492,243	44.60	499,361	45.25
Slight	1–5	33,184	3.01	74,666	6.77	41,656	3.77
Moderate	5.0–10	33,081	3.00	75,580	6.85	53,516	4.85
High	10–50	213,205	19.32	242,681	21.99	245,772	22.27
Very high	50–200	253,015	22.93	155,181	14.06	185,432	16.80
Extremely high	>200	90,875	8.23	63,215	5.73	77,830	7.05
Total		1,103,566	100	1,103,566	100	1,103,566	100

23.3.3 Surface Water Quality Status

In general, the surface water of the river system in the study area was contaminated moderately with total suspended solids (TSS), organic matters (BOD₅, COD), nutrients (NH₄⁺-N, PO₄³⁻-P) by runoff from agricultural fields and untreated wastewater discharged from domestic and industrial activities. In Vietnam, the QCVN 08-MT:2015/BTNMT is currently being used as the national technical regulation on surface water quality (Pham 2017). In the dry season, the numbers of 11.7% of TSS, 23.5% of COD, 19.1% of BOD, 20.1% of NH₄⁺-N, 10.7% of PO₄³⁻-P did not meet the permissible levels. The TSS concentrations in the rainy season were significantly higher than in the dry season. This matches with the capacity of highly potential soil erosion in the river basin, as mentioned above. In a similar way, the value of NH₄⁺-N concentration has highly increased in the rainy seasons compared to the dry seasons. This result is similar to previous studies (Hanh et al. 2010; Canada 2004), which found that the use of fertilizer releasing NH₄⁺-N into the watershed during the rainy season is insignificant (Table 23.9).

The spatial distribution of the WQI water quality index at monitoring sites in the rainy and dry season is shown in Fig. 23.9. Hierarchical cluster analysis (HCA) categorized WQI into 2 main clusters (1-relatively contaminated sites; 2-relatively clean sites). Then, the main clusters were divided into 5 sub-clusters (1a, 1b, 2a, 2b1, 2b2), which were relatively represented for 5 water quality groups (very bad, poor, medium, excellent, and good) in accordance with the ratings of WQI, as in Table 23.10.

Cluster 1a, the so-called excellent water quality sites, most of them in the upstream (H1, H2, H3, H4, L7, L8, N2, N9). *Cluster 1b* is not as clean as cluster 1a, the so-called good water quality sites (L2, L3, L4, L5, Dk2, Dk4, Dk7, N1, N5, D12, T4). *Cluster 2a*, the so-called medium water quality sites, is formed by 11 sites (D2, D11, D13, D15, Dk1, Dk3, Dk6, N3, N6, N8, T1, T3, L6). *Cluster 2b1*, the so-called very bad water quality sites, is formed by 4 sites (D1, D3, D7, L1). *Cluster 2b2* is not as polluted as cluster 2b1, the so-called poor water quality sites, formed by 13 sites (D4, D5, D6, D8, D9, D10, D14, N4, N7, N10, N11, Dk5, T2).

Table 23.9 Percentage of samples that did not meet the permissible level

Parameter	pH (mg/L)	DO (mg/L)	TSS (mg/L)	COD (mg/L)	BOD ₅ (mg/L)	NH ₄ ⁺ -N (mg/L)	PO ₄ ³⁻ -P (mg/L)	T (°C)
Dry (%)	2.6	4.4	11.7	23.5	19.1	20.1	10.7	–
Rain (%)	1.6	3.8	29.5	12.8	16.2	22.2	5.7	–
QCVN*	5.5–9	≥4	<50	<30	<15	<0.9	<0.3	°C

QCVN* National technical regulation on surface water quality, QCVN 08-MT 2015/BTNMT (B1). B1 is the surface water source for irrigation or other purposes. *Dry* dry season; *Rain* rainy season

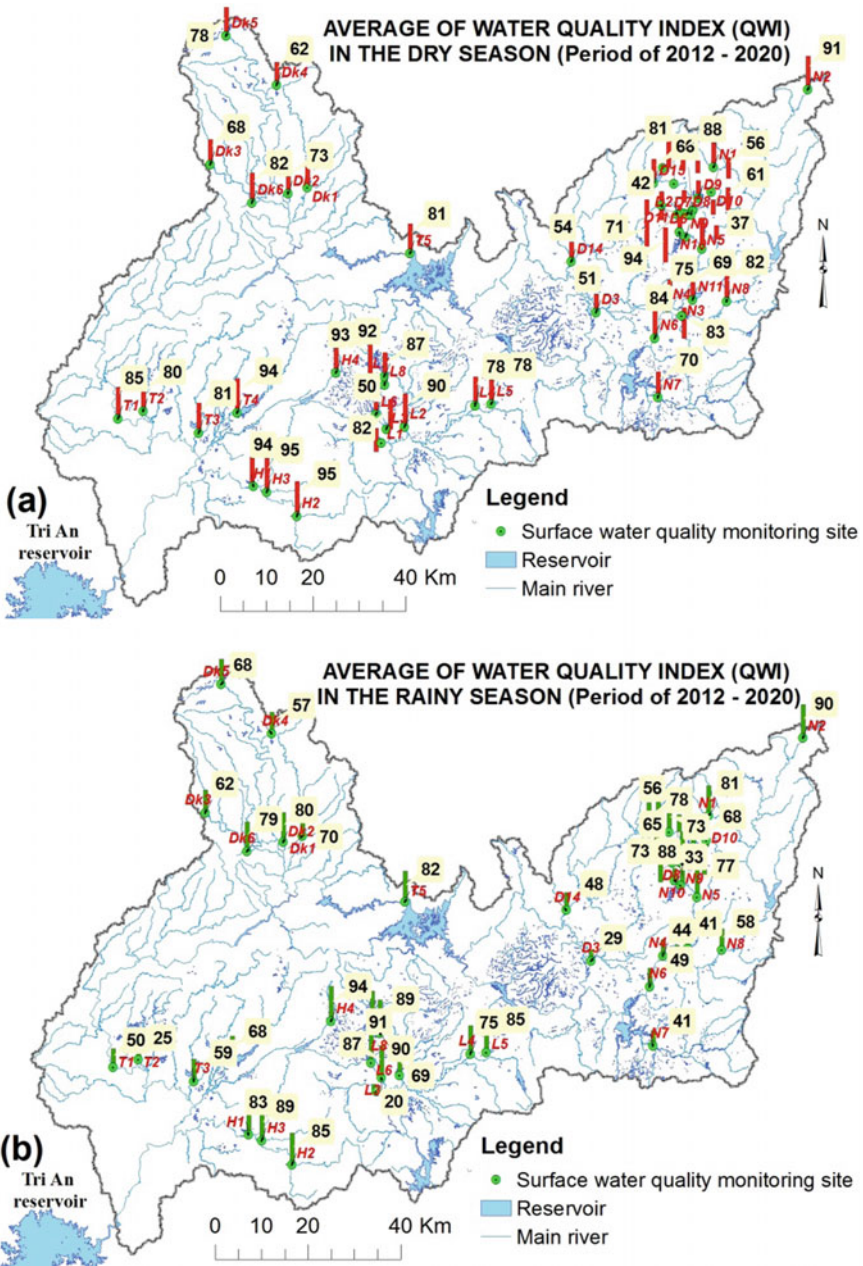


Fig. 23.9 WQI at monitoring sites in the dry (a) and rainy (b) season

Table 23.10 Surface water quality classification based on WQI (2012–2020)

WQI Value/Color	Rating Water Quality	Suitability for water use	Cluster/ No. of sites	Name of sites
91 – 100 (Blue)	Excellent water quality	Used for domestic water supply purposes	1a/8	H1, H2, H3, H4, L7, L8, N2, N9
76 – 90 (Green)	Good water quality	Used for domestic water supply purposes but need appropriate treatment.	1b/11	L2, L3, L4, L5, Dk2, Dk4, Dk7, N1, N5, D12, T4
51 – 75 (Yellow)	Medium water quality	Use for irrigation and other similar purposes.	2a/11	D2, D11, D13, D15, Dk1, Dk3, Dk6, N3, N6, N8, T1, T3, L6
26 – 50 (Orange)	Poor water quality	Use for waterways and other similar purposes.	2b1/13	D4, D5, D6, D8, D9, D10, D14, N4, N7, N10, N11, Dk5, T2
0 – 25 (Red)	Very bad water quality	Water is heavily polluted and needs to recovery	2b2/4	D1, D3, D7, L1

23.3.4 Fresh Water Resources Vulnerability

The calibration and validation of the SWAT model were conducted based on hydrological observation data at three local stream-flow gauge stations, two in the upper stream (Thanh Binh and Dai Nga) and the other in the lower stream (Ta Lai). The graphs of observed and simulated monthly flow are shown in Fig. 23.10. The simulated and observed stream-flow during the calibration period achieved relatively good results with all R^2 , and E_{NS} values were greater than 0.70, so the simulated results of the SWAT model were predicated to be good (Can et al. 2015; Moriasi et al. 2007).

The estimation of the water balance was based on climate and land use variations. In view of the LULC 2020 over the entire basin, total annual water resources were based on simulation results from the SWAT model of DN1 to DN17 and LN1. The spatial distribution of changes in VI of the sub-basins of the UPDN river in 1994 and 2020 is shown in Fig. 23.11.

The water resources vulnerability indices of 1994 and 2020 were evaluated based on using the same data of water resources stress (RS) and management capacity (MC) parameters of 2020. This is to highlight the effects of LULC, climate conditions, and economic status on the basin's water resource vulnerability. The water development pressure (DP) parameter was estimated from total water resources, total water requirements, total population, and water supply coverage. Therein, the total water resources were determined by the SWAT model at the sub-basin level. Total water demand was calculated based on the LULC classification results of Landsat images in collaboration with socio-economic statistics data. The ecological health (EH) parameter, which is affected by natural phenomena and human activities, was measured by water pollution and the ecosystem deterioration indicators. The level of pollution was estimated by the ratio of total wastewater, which is calculated based on the total water demand and total water resources in each sub-basin. The ecosystem

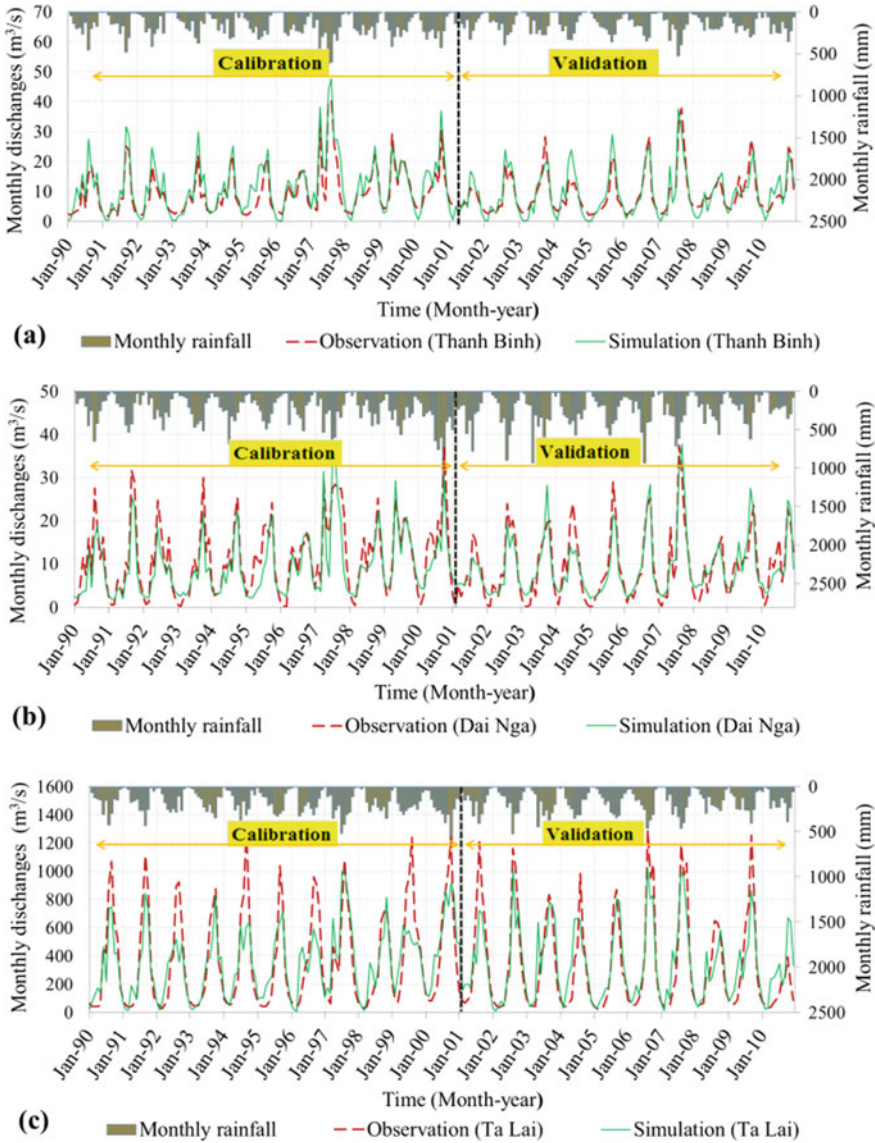


Fig. 23.10 Comparison between simulated and observed monthly streamflow in the calibration and validation period of SWAT model: **a** Thanh Binh; **b** Dai Nga; and **c** Ta Lai gauge

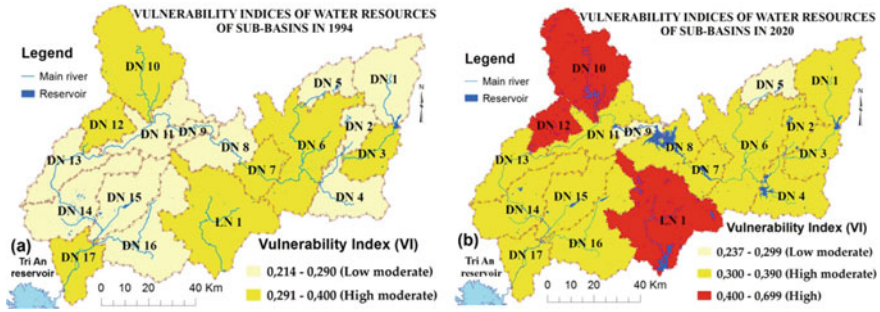


Fig. 23.11 Changes in VI of the sub-basins of the UPDN river in 1994 and 2020

deterioration (EH_c) was determined based on the LULC classification results from the Landsat image. Each VI of each sub-basin in 2020 is presented in Table 23.11.

In the year 2020, the calculated overall vulnerability index (VI) for the entire UPDN basin was 0.318 compared to 0.276 of 1994. This value was the same as the VI of Mekong river in Southeast Asia ($VI = 0.31$) (Babel and Wahid 2009). The level

Table 23.11 Water resources vulnerability index (VI) with various parameters of the sub-basins and the entire UPDN basin in 2020

Sub-basin/ Reservoir name	ID	Resource	Development	Ecological	Management	Overall Score (VI)
		Stress	Pressure	Health	Capacity	
		RSt	DP	EH	MC	VI
Da Nhim	DN1	0.227	0.374	0.076	0.539	0.304
Da Tam	DN2	0.21	0.185	0.283	0.534	0.303
Don Duong	DN3	0.243	0.146	0.337	0.539	0.316
Da Quyen	DN4	0.258	0.344	0.351	0.539	0.373
Suoi Vang	DN5	0.192	0.11	0.112	0.534	0.237
Da Dang	DN6	0.273	0.166	0.427	0.534	0.350
Dong Nai 2	DN7	0.29	0.141	0.431	0.539	0.350
Dong Nai 3	DN8	0.305	0.118	0.171	0.539	0.283
Dong Nai 4	DN9	0.277	0.111	0.125	0.539	0.263
Dak Nong	DN10	0.32	0.331	0.449	0.639	0.435
Dong Nai 5	DN11	0.305	0.089	0.258	0.639	0.323
Dak R'Keh	DN12	0.305	0.31	0.434	0.639	0.422
Dong Nai 6	DN13	0.307	0.154	0.294	0.539	0.324
Cat Tien	DN14	0.307	0.161	0.215	0.539	0.306
Da Teh	DN15	0.305	0.163	0.207	0.521	0.299
Da Huoai	DN16	0.29	0.177	0.267	0.521	0.314
Ta Lai	DN17	0.29	0.118	0.334	0.539	0.320
La Nga	LN1	0.34	0.332	0.411	0.534	0.404
UPDN	-	0.263	0.159	0.296	0.553	0.318

* Notes: Water Stress (RSs); Water Variation (RSv); Water Exploitation (DPs); Safe Drinking Water Inaccessibility (DPd); Water Pollution (EHp); Ecosystem Deterioration (EHe); Water Use Inefficiency (MCE); Improved Sanitation Inaccessibility (MCs); Conflict Management Capacity (MCg); Vulnerability Index (VI).

* Color guide: (0-0.2) Low (0.2-0.4) Moderate (0.4-0.7) High (0.7-1) Severe

of vulnerability of water resources in the UPDN basin was moderate and implied that the basin was generally in good condition for the realization of sustainable water resources management. However, the calculated VI indicators of DN10, DN12, and LN1 were 0.435, 0.422, and 0.404 (in the range of 0.4–0.7), which indicate that the water resources of these sub-basins are highly vulnerable and should be prioritized for sustainable water management actions.

The management capacity (MC) of the UPDN basin was 0.553, and it was approximately equal to the MC of Mekong basin (MC = 0.60) (Babel and Wahid 2009). The vulnerability of water resources in the UPDN basin was mostly contributed by weak management capacity. The reasons for the weaknesses were first due to the wide gap between water use efficiency in the basin and the defined world average, secondly the restrictive capacity of the Dong Nai River Basin Environmental Protection Commission (RBEP) to solve trans-boundary conflicts, and lastly the lack of access to improved sanitation facilities (especially DN10, DN11, and DN12 of Dak Nong province).

23.4 Conclusion

GIS and remote sensing integration were successfully used to establish LULC maps and assess changes in LULC of the UPDN river basin. Over the 26 years, the forest area was approximately reduced to 324,586 ha (29.4%). In terms of sub-basins, the Dak Nong (DN10) and Dak R'Keh (DN12) had the highest deforestation rates. Further, the distribution of soil erosion risks in terms of spatial and temporal scale was also established. Therein, the highly potential erosion regions with greater than 100 tons/ha/year account for 50.48% of the basin's area, and these regions should be prioritized for sustainable soil management actions. For items of water quality, the technology of GIS and WQI effectively supported assessing water quality as well as understanding the spatial and temporal variations in water quality which plays an effective and useful role in communicating information on water quality to citizens and policymakers. According to the results, the surface water of the Dong Nai river was moderately polluted, and the water quality greatly fluctuated between seasonally and spatially (monitoring sites).

The integrating solution of GIS, remote sensing, and SWAT model has been feasibly applied to calculate water balance and computerize the water vulnerability at the basin and sub-basin level based on guidelines prepared by UNEP and Peking University. The VIs for the UPDN river basin were 0.318 and 0.276 in 2020 and 1994, respectively. These values imply that the basin is generally in good condition for the realization of sustainable water resources management. However, calculated VI indicators of the sub-basins DN10, DN12, and LN1 were in the range of 0.4–0.7, which classified as highly vulnerable regions should be prioritized for sustainable water management actions.

Overall, this study demonstrated an effective solution in creating decision support tools for IWRM in the UPDN river basin based on GIS, remote sensing, and SWAT

model. Therein, GIS database is established to develop spatial analysis tools and visualize the information to make decisions on different scales as river basin level or river sub-basin level in implementing IWRM. Remote sensing was used to monitor and assess changes in LULC. The SWAT model was used to assess hydrology, calculate water balance, and map the water resources vulnerability index, which not only provides early warning signals for authorities to mitigate negative impacts, but also assists them in identifying information gaps to increase public awareness about water-related potential threats. Clearly, the study has created a scientific basis to replicate solutions for the similar regions that have lacked the IWRM decision support tools.

Acknowledgements The authors would like to thank you DONRE of Lam Dong and Dak Nong provinces for their support for this study by providing early access to statistical data and reports of local authorities.

We acknowledge the support of time and facilities from Ho Chi Minh City University of Technology (HCMUT), VNU-HCM for this study.

References

- Ako AA, Eyong GET, Nkeng GE (2010) Water resources management and integrated water resources management (IWRM) in Cameroon. *Water Resour Manage* 24:871–888
- Alexakis DD, Hadjimitsis DG, Agapiou A (2013) Integrated use of remote sensing, GIS and precipitation data for the assessment of soil erosion rate in the catchment area of “Yialias” in Cyprus
- Al-Kalbani MS, Price MF, Abahussain A, Ahmed M, O’Higgins T (2014) Vulnerability assessment of environmental and climate change impacts on water resources in Al Jabal Al Akhdar, Sultanate of Oman. *Water* 6:3118–3135
- Allen RG, Pereira LS, Raes D, Smith M (1998) FAO irrigation and drainage paper no. 56, Crop Evapotranspiration (guidelines for computing crop water requirements)
- Babel MS, Wahid SM (2009) Fresh water under threat: South East Asia—vulnerability assessment of freshwater resources to environmental change Mekong River Basin
- Belasri A, Lakhouili A (2016) Estimation of soil erosion risk using the universal soil loss equation (USLE) and geo-information technology in Oued El Makhazine Watershed, Morocco. *J Geogr Inf Syst* 8:98–107
- Borah DK, Bera M (2003) Watershed-scale hydrologic and nonpoint-source pollution models: review of mathematical bases. *Am Soc Agric Eng* 46:1553–1566
- Can T, Xiaoling C, Jianzhong L, Gassman PW, Sabine S, José-Miguel SP (2015) Assessing impacts of different land use scenarios on water budget of Fuhe River, China using SWAT model. *Int J Agric Biol Eng* 8:95–109
- Canada E (2004) Canadian guidance framework for the management of phosphorus in fresh water system. *Ecosyst Health Sci Based Solutions Rep* 1–8
- Demirci A, Karaburun A (2012) Estimation of soil erosion using RUSLE in a GIS framework: a case study in the Buyukcekmece Lake watershed, northwest Turkey. *Environ Earth Sci* 66:903–913
- Farhan Y, Nawaiseh S (2016) Spatial assessment of soil erosion risk using RUSLE and GIS techniques. *Environ Earth Sci* 4649–4669
- Gassman PW, Reyes MR, Green CH, Arnold JG (2007) The soil and water assessment tool: historical development, applications, and future research directions. *Am Soc Agric Biol Eng* 50:1211–1250
- Global Water Partnership (2000) Integrated water resources management global water partnership. Stockholm

- Global Water Partnership (2018) Looking back, looking forward—evaluation of the global water partnership
- Global Water Partnership (2021) Towards a water secure world—IWRM ToolBox. https://www.gwp.org/en/learn/iwrn-toolbox/About_IWRM_ToolBox
- Gomez C, White JC, Michael A (2016) Wulder: optical remotely sensed time series data for land cover classification: a review. *ISPRS J Photogramm Remote Sens* 116:55–72
- Hanh PTM, Kim K-W, Hung NQ, Sthiannopkao S, Ba DT (2010) Anthropogenic influence on surface water quality of the Nhue and Day sub-river systems in Vietnam. *Environ Geochem Health* 32:227–236
- Huang TCC, Lo KFA (2015) Effects of land use change on sediment and water yields in Yang Ming Shan National Park, Taiwan. *Environments* 2:32–42
- Jha MK, Gassman PW, Arnold JG (2007) Water quality modeling for the Raccoon River watershed using SWAT. *Trans ASAE* 50:479–493
- Jolk C, Greassidis S, Jaschinski S, Stolpe H, Zindler B (2010) Planning and decision support tools for the integrated water resources management in Vietnam. *Water* 2:711–725
- Khoury AE, Seidou O, Lapen DR, Que Z, Mohammadian M, Sunohara M, Bahram D (2015) Combined impacts of future climate and land use changes on discharge, nitrogen and phosphorus loads for a Canadian river basin. *J Environ Manage* 151:76–86
- Lam Dong Department of Natural Resources and Environment (2013) Report 456/BC-STNMT dated 11/28/2013 on hydropower development projects in Lam Dong Province
- Lam Dong Statistical Department (2015) Statistical yearbook of Lam Dong province. Lam Dong Statistical Office, Da Lat, Lam Dong, Vietnam
- Lam Dong Statistical Department (2020) Lam Dong statistical yearbook 2019. Lam Dong Statistical Office, Da Lat, Lam Dong, Vietnam
- Linh LTK, Hien LTD, Tat PV (2016) Application GIS for evaluating water quality according to WQI at Tra An reservoir. In: Proceedings of the GIS 2016 application conference. Hue University, Hue, Vietnam, pp 253–260
- Lu D, Li G, Valladares GS, Batistell M (2004) Mapping soil erosion risk in Ronnonia, Brazilian Amazonia: using RUSLE, remote sensing and GIS. *Land Degrad. Develop* 15:499–512
- Mango LM, Melesse AM, McClain ME, Gann D, Setegn SG (2011) Land use and climate change impacts on the hydrology of the upper Mara River Basin, Kenya: results of a modeling study to support better resource management. *Hydro Earth Syst Sci* 15:2245–2258
- Moriassi DN, Arnold JG, Liew MWV, Bingner RL, Harmel RD, Veith TL (2007) Model evaluation guidelines for systematic quantification of accuracy in watershed simulations. *Trans ASABE* 50:885–900
- Neitsch SL, Arnold JG, Kiniry JR, Williams JR (2011) Introduction and history. In: Soil and water assessment tool theoretical documentation version 2009. Texas Water Resources Institute Technical Report No. 406, Texas A&M University System College Station, Texas 77843-2118, pp 6–10
- Nugroho P, Marsono D, Sudira P, Suryatmojo H (2013) Impact of land-use changes on water balance. *Proc Environ Sci* 17:256–262
- People’s Committee of Lam Dong Province (2015) Decision No. 299/QĐ-UBND dated 28/1/2015 on reporting the results of forest investigation of Lam Dong province in 2014
- Pham TL (2017) Comparison between Water Quality Index (WQI) and biological indices, based on planktonic diatom for water quality assessment in the Dong Nai River, Vietnam. *Pollution* 3:311–323
- Prasannakumar V, Vijith H, Abinod S, Geetha N (2013) Estimation of soil erosion risk within a small mountainous sub-watershed in Kerala, India, using Revised Universal Soil Loss Equation (RUSLE) and geo-information technology 3:209–215
- Renard KG, Foster GR, Weesies GA, McCool DK, Yoder DC (1997) Introduction and history. Predicting soil erosion by water: a guide to conservation planning with the revised Universal soil loss equation (RUSLE). The U.S Government Printing Office, Washington, DC 20402-9328, pp 7–11

- Ringler C, Huy NV (2004) Water allocation policies for the Dong Nai river basin in Vietnam: an integrated perspective
- Rogon J, Chen DM (2004) Remote Sensing technology for mapping and monitoring land cover and land use change. *Prog Plan* 61:301–325
- Roose EJ (1975) Use of the universal soil loss equation to predict erosion in West Africa. Prediction and Control Copyright © 1976, Soil Conservation Society of America Ankeny, Iowa
- Schilling KE, Jha MK, Zhang Y-K, Gassman PW, Wolter CF (2008) Impact of land use and land cover change on the water balance of a large agricultural watershed: historical effects and future directions. *Water Resour Res* 44:1–12
- Setegn SG, Srinivasan R, Melesse AM, Dargahi B (2010) SWAT model application and prediction uncertainty analysis in the Lake Tana Basin, Ethiopia. *Hydrol Process* 23:3738–3750
- Shi P, Chen C, Srinivasan R, Zhang X, Cai T, Fang X, Qu S, Chen X, Li Q (2011) Evaluating the SWAT model for hydrological modeling in the Xixian watershed and a comparison with the XAJ model. *Water Resour Manage* 25:2595–2612
- Stolpe H (2011) Planning and decision support tools for integrated water resources management. Ruhr-Universität Bochum Printing Center, Bochum, Germany
- Suryatmojo H, Fujimoto M, Yamakawa Y, Kosugi KI, Mizuyama T (2013) Water balance changes in the tropical rainforest with intensive forest management system. *Int J Sustain Future Hum Secur* 1:56–62
- Truong NCQ, Nguyen HQ, Kondoh A (2018) Land use and land cover changes and their effect on the flow regime in the upstream Dong Nai River Basin, Vietnam. *Water* 10:1–15
- UN (1992) Report on the international conference on water and environment
- UNEP (2009) Methodologies guidelines, vulnerability assessment of freshwater resources to environmental change. United Nations Environment Programme (UNEP), Thailand
- United Nations Environment Programme (2018) Progress on integrated water resources management—global baseline for SDG 6 indicator 6.5.1: degree of IWRM implementation. UN Environment
- Vietnam Ministry of Construction (MOC) (2006) Construction standards TCXDVN 33:2006, water supply—pipe-line networks and facilities-design standards. Ha Noi, Vietnam, pp 1–158
- Vietnam Ministry of Natural Resources and Environment (MONRE) (2006) The state of water environment in 3 river basins of Cau, Nhue—Day and Dong Nai river system
- Vietnam Ministry of Natural Resources and Environment (2011) Decision No. 879/QĐ-TCMT on the guidelines issuance for calculation of Water Quality Index (WQI). Ha Noi, pp 1–8
- Vietnam Ministry of Natural Resources and Environment (2017) Circular 64/2017/TT-BTNMT regulations on determining minimum flows in rivers, streams and downstream of reservoirs and dams. Ha Noi, Vietnam, pp 1–8
- Wischmeier WH, Smith DD (1978) Predicting—rainfall erosion losses. U.S. Government Printing Office, Washington, DC
- Xiao-jun W, Jian-yun Z, Shamsuddin S, Rui-min H, Xing-hui X, Xin-li M (2013) Potential impact of climate change on future water demand in Yulin city, Northwest China. *Mitig Adapt Strateg Glob Change* 20:1–19
- Zhu C, Li Y (2014) Long-term hydrological impacts of land use/land cover change from 1984 to 2010 in the Little River Watershed, Tennessee. *Int Soil Water Conserv Res* 2:11–22

Chapter 24

Spatial–Temporal Changes in Land Surface Temperature Pattern in the Western Edge of the Inner Hanoi City, Vietnam During the 2005–2019 Period



Duc-Loc Nguyen , Tien-Yin Chou , Thanh-Van Hoang , Mei-Hsin Chen, Chun-Tse Wang , and Van-Khue Phan 

Abstract Urbanization is a primary driver that leads to the increase of urban heat, including air temperature and surface temperature. Recently, Hanoi city has been experienced a high urbanization rate, especially at the edge of the inner city. In this study, the surface temperature bands of Landsat-5 and Landsat-8 Collection 2 Level-2 were directly utilized to calculate LST for the study area at the two selected years 2005 and 2019. Furthermore, the spatial–temporal changes in Land Surface Temperature (LST) in the period 2005–2019 were analyzed and the relationships between Normalized Land Surface Temperature (NLST) and the two indices NDVI (Normalized Difference Vegetation Index) and NDBI (Normalized Difference Built-up Index) were clarified. The study results indicated a significant increase in the mean LST and the mean NLST between 2005 and 2019. In fact, the mean LST rose from 33.18 to 38.06 °C and the mean NLST rose from 0.38 to 0.43. Additionally, a negative correlations between NLST and NDVI were explored at correlation coefficients (R) of

D.-L. Nguyen (✉)

Ph.D. Program for Infrastructure Planning and Engineering, College of Construction and Development, Feng Chia University, Taichung 40724, Taiwan
e-mail: st_loc@gis.tw

T.-Y. Chou · T.-V. Hoang · M.-H. Chen · C.-T. Wang
Geographic Information Systems Research Center, Feng Chia University, Taichung 40724, Taiwan
e-mail: jimmy@gis.tw

T.-V. Hoang
e-mail: van@gis.tw

M.-H. Chen
e-mail: ivy@gis.tw

C.-T. Wang
e-mail: james@gis.tw

D.-L. Nguyen · V.-K. Phan
Faculty of Natural Resources and Environment, Vietnam National University of Agriculture, Trau Quy, Gia Lam, Hanoi, Vietnam

−0.69 and −0.77 in 2005 and 2019, respectively. In contrast, a positive relationships between NLST and NDBI were shown at R-value of 0.74 and 0.85. The outcomes revealed the importance of vegetation in urban cooling and forces authorities to implement urban green space planning seriously.

Keywords Land surface temperature (LST) · Normalized land surface temperature (NLST) · Normalized difference vegetation index (NDVI) · Normalized difference built-up index (NDBI) · Spatial–temporal change

24.1 Introduction

The increase in land surface temperature (LST) is one of the consequences of urbanization. Urban expansion due to rapid population growth leads to the conversion of earth covers, mainly from vegetation to impervious surfaces (Daramola et al. 2018; Wu and Murray 2003). Previous studies showed that land surface temperature on water bodies and vegetation is always lower on built-up land (Madanian et al. 2018; Soydan 2020). Hence, urban areas with a high rate of built-up land have higher LST than rural areas (Hua et al. 2020). Higher LST typically much more presence in an urban area than a rural area.

There were numerous researches using satellite images in LST estimation (John et al. 2020; Mustafa et al. 2021; Wu et al. 2019). Retrieval LST from satellite data is more advantageous than that by point-based measurements on the field. Because satellite image-based technique can provide LST information for a continuous large scale. Whereas point-based measurements only provide LST at some points of interest. Owned the vast and continuous data collection from 1982 (Landsat-4) till now (Landsat-8), Landsat satellite images have been the most frequently used for analyzing the spatial–temporal change of LST. Some algorithms that have been utilized for extracting LST from the thermal band of Landsat level-1 data, including Mono Window Algorithm (MWA), Radiative Transfer Equation (RTE) method, Single Channel Algorithm (SCA), and Split Window (Majumder et al. 2021; Sekertekin and Bonafoni 2020). In these methods, land surface emissivity (LSE) is a crucial factor that needs to be carefully considered. The two models that are often used to determine LSE are classification-based emissivity method and NDVI-based emissivity method.

In December 2020, Landsat Collection 2 Level-2 data collection was released by the Department of United States Geological Survey (USGS) (Hemati et al. 2021; Esad et al. 2021). Compared to collection 1, this collection has a lot of improvements, such as the enhancement in the accuracy of GPCs and DEM enhancements, or radiometric calibration improvements (Hemati et al. 2021). Furthermore, it also provides surface reflectance and surface temperature level-2 product that can be directly used for applications. Hence, scientists and researchers nowadays have selected level-2 product to derive LST for their studies (Ferral et al. 2021; Jung et al. 2021; Park and Kim 2021).

Hanoi capital is the second largest and the fastest-growing city in Vietnam. It has over 3300 km² of the area and 47.55% of urbanization rate (Hoang and Fogarassy 2020). Under the rapid urbanization, Hanoi’s meteorological factors must have had significant changes, especially in LST. Therefore, the purposes of this study was: (i) to analyze the spatial–temporal change in LST from 2005 to 2019 in the western edge of Hanoi center where the urbanization has occurred quickly in recent years, (ii) to clarify the relationships between LST and the two indices extracted from Landsat images, including Normalized Difference Vegetation Index (NDVI) and Normalized Difference Built-up Index (NDBI). The study results can be a good reference for planners to release reasonable urban land-use structures.

24.2 Study Site

The study area contains five western districts of Hanoi center, including Ha Dong, Bac Tu Liem, Nam Tu Liem, Hoai Duc, and Dan Phuong (Fig. 24.1). These districts have been experienced rapid population growth. According to Hanoi statistical yearbooks 1999, 2009 and 2019, the total population of the five selected districts in these years is 643,278 people, 959,280 people, and 1,455,200 people respectively (HNSO 2000, 2010, 2020). Thus, the population growth rate in 2009–2019 was 1.7 higher than that in 1999–2009. Along with the population explosion, the process of urbanization has occurred strongly.

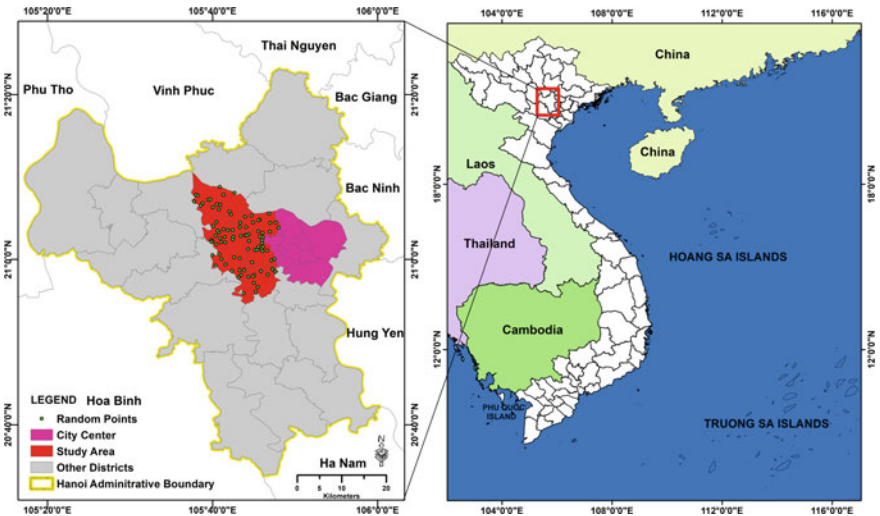


Fig. 24.1 Study area

Table 24.1 Satellite data

Satellite sensor	Path/row	Cloud cover (%)	Date of acquisition	Time of acquisition	Used bands (R, NIR, SWIR, TIR)
LS5	127/045	15	09/10/2005	03:11:27	3, 4, 5, 6
LS8	127/045	0.12	30/09/2019	03:23:46	4, 5, 6, 10

24.3 Data and Methods

24.3.1 Data

In this study, the two level-2 images, Landsat-5 acquired on 09 October 2005 and Landsat-8 acquired on 30 September 2019, were directly downloaded from USGS's website (<https://earthexplorer.usgs.gov/>). The small difference in acquisition time in a day (12 min) and in a year (9 days) is a good condition for comparing of the LSTs between the two selected years. The characteristics of data is presented in Table 24.1.

The products of Landsat-5 and Landsat-8 collection-2 level-2 are distributed on USGS's website after 25–27 days and 15–17 days, respectively (USGS 2021a, b).

24.3.2 Method

Land Surface Temperature (LST)

Land surface temperature retrieved from Landsat Collection 2 Level-2 is calculated by Eq. (24.1).

$$LST(^{\circ}\text{C}) = M \cdot B_{ST} + A - 273.15 \quad (24.1)$$

where, M is the multiplicative rescaling factor and A is the additive rescaling factor. The value of this two factors can be found in meta data file. In fact, these values are 0.00341802 and 149.0, respectively (USGS 2021a, b). B_{ST} is pixel value of surface temperature.

Normalized Land Surface Temperature (NLST)

Although the two chosen images have a slight difference in acquisition time in a day and a year, the comparison of LSTs extracted from them directly is inadequate. Thus, the LSTs should be normalized to the range of 0–1 to eliminate the time imaging effects. Furthermore, it is useful for revealing the difference in the spatial distribution of LSTs in the two times. NLST is determined by Eq. (24.2).

$$NLST_i = \frac{LST_i - LST_{\min}}{LST_{\max} - LST_{\min}} \quad (24.2)$$

In which, $NLST_i$ and LST_i are normalized land surface temperature and land surface temperature of pixel i . LST_{max} and LST_{min} are maximum value and minimum value of LST.

Normalized Difference Vegetation Index (NDVI)

Normalization Difference Vegetation Index (NDVI) is one of the biophysical parameters that has been frequently used in environmental studies (Wani et al. 2021; Dong et al. 2021). It reflects the presence of vegetation on the Earth's surface. This index is extracted based on the different interactions of the sunlight energy in the red band of the near-infrared band. Healthy vegetation almost absorbs red light, whereas near-infrared light is strongly reflected. The lowest NDVI value is -1 and the highest NDVI value is $+1$. The negative value indicates water or snow while the positive value reveals the different vegetation situations. Impervious surfaces and bare soil have an NDVI value of approximately 0 (Chien et al. 2016). NDVI is calculated by Eq. (24.3).

$$NDVI = \frac{NIR - R}{NIR + R} \quad (24.3)$$

With NIR is Near-Infrared band and R is Red band.

Normalized Difference Built-Up Index (NDBI)

Normalization Difference Built-up Index (NDBI) is an indicator that has been frequently used in urbanization studies through remote sensing techniques (Abulibdeh 2021; Zheng et al. 2021). It provides information on impervious surfaces, a major cause of the urban heat island effect. This index is calculated through two bands, Near-Infrared and Short-wave Infrared, by Eq. (24.4). Its value ranges from -1 to $+1$.

$$NDBI = \frac{SWIR - NIR}{SWIR + NIR} \quad (24.4)$$

In which, SWIR stands for Short-wave Infrared band.

Correlation Analysis

The relationship between NLST and the two indices, NDVI and NDBI, was determined using linear regression. The input data for this model was randomly generated using ArcGIS's tool, including 100 random points with the minimum allowed distance of 100 m. In order to avoid the negative effects of water pixels on the NLST-NDVI and NLST-NDBI relationship determination, sample points located on water bodies were eliminated. Thus, the random sample dataset was only 92 samples. The results were represented by 2D scatter plot with the support of R software.

24.4 Results and Discussion

24.4.1 *Spatial–Temporal Changes in Land Surface Temperature*

Under the influence of urbanization, there has been a significant rise in impervious surfaces (Wu et al. 2020), especially in urban areas and rural residential zones. Along with this, the presence of vegetation and water bodies has been decreased considerably (Tania et al. 2021; Wen et al. 2021). Consequently, the LST in residential, industrial, and urban areas has also risen.

The resulting LST maps of 2005 and 2019 are shown in Fig. 24.2a, b. From the overall perspective, this period experienced an increase in LST. The values of maximum LST, minimum LST, and mean LST in 2019 are around 2.5–5 °C higher than those in 2005. In more detail, the mean LST increased 4.88 °C, from 33.18 to 38.06 °C. The maximum LST and minimum LST of the year 2005 were also lower than those of 2019. In fact, these pair values were (45.94 °C, 26.32 °C) and (49.73 °C, 29.08 °C), respectively.

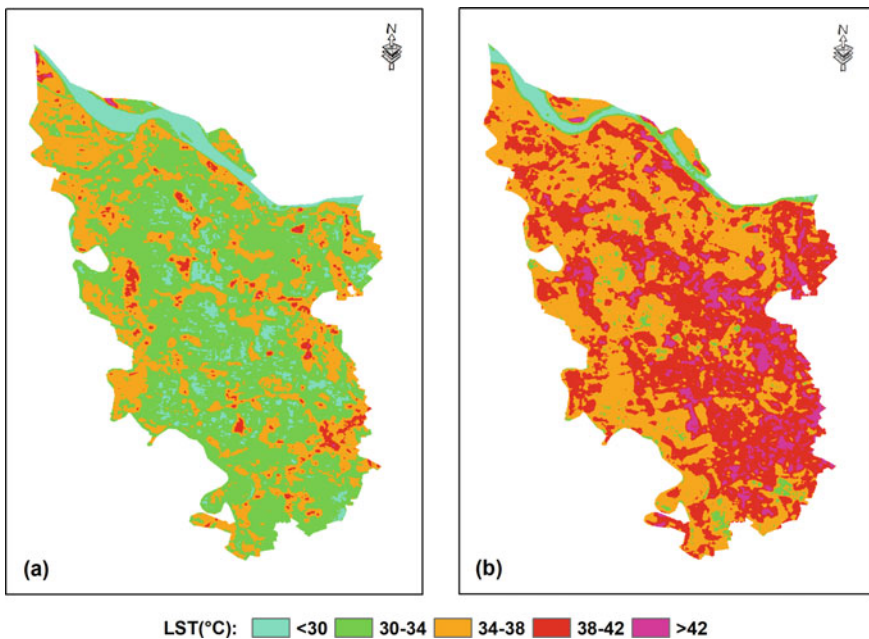


Fig. 24.2 LST maps in 2005 and 2019

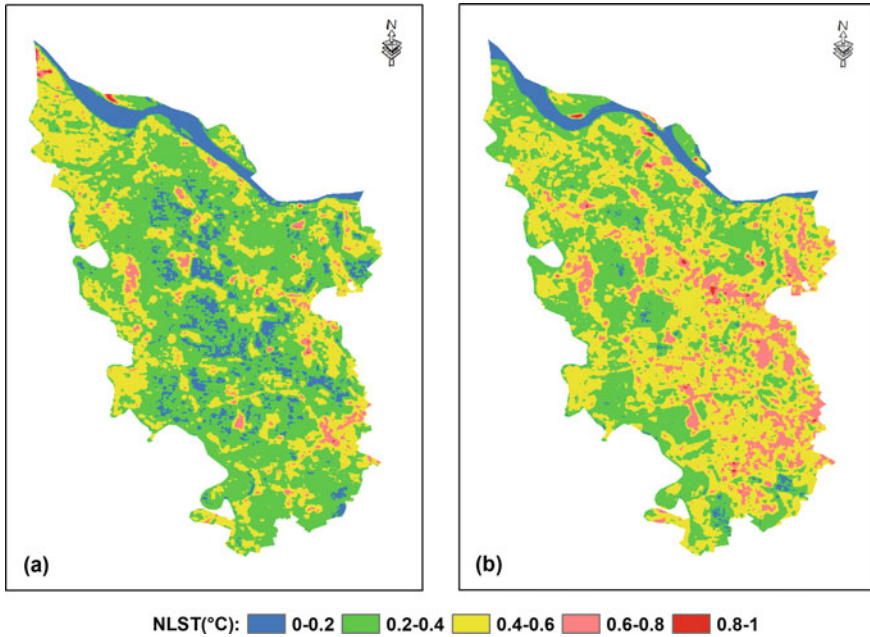


Fig. 24.3 NLST maps in 2005 and 2019

In order to remove the influence of different time imaging and compare more accurately, it is necessary to compare the LSTs in the same range [0, 1] through normalization. In this scale, the mean Normalized Land Surface Temperature increased 0.08, from 0.35 in 2005 to 0.43 in 2019. The NLST maps is represented in Fig. 24.3a, b.

Figure 24.4a represents the percentage area by LST ranges. It reveals a significant change of percentage area between low LST and high LST in this period. The total land area covered by low LST, from 26.3 to 34 °C, declined dramatically from 64% in 2005 to 5.4% in 2019, a massive decline of over ten times. Whereas the total land area covered by higher LST rose from 35.8% in 2005 to 87.8% in 2019, an increasing of over two times. The total land area covered by LST greater than 42 °C in 2005 was approximate 0 while the figure for 2019 was 6.8%. Some points covered by LST greater than 38 °C in 2005 were My Dinh stadium, surrounding area of Ha Dong Post Office, residential areas in Duong Lieu commune (Hoai Duc district), and residential areas in La Phu commune (Hoai Duc district). In 2019, these points were expanded and LST also increased to over 42 °C. At the same year, the land covered by LST greater than 38 was also spread out to other points, for example, residential areas in Co Nhue 1 ward and Co Nhue 2 ward (Bac Tu Liem district), My Dinh 1 ward and My Dinh 2 ward (Nam Tu Liem district), Me Tri ward (Nam Tu Liem district), residential areas along the national highway 32 to Hanoi Industrial University.

Figure 24.4b reveals information on the percentage area by 5 NLST groups (0–0.2, 0.2–0.4, 0.4–0.6, 0.6–0.8, 0.8–1) of the years 2005–2019. It shows the opposite

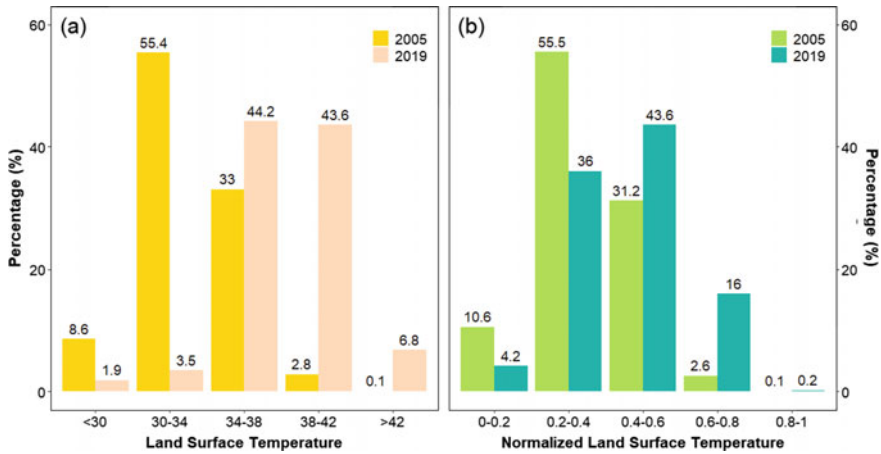


Fig. 24.4 Percentage area of LST and NLST in 2005 and 2019

rate between the two years. In 2005, the percentage area of the low NLST group (0–0.4) was about two times higher than that of the higher NLST group (0.4–0.8). Actually, these figures were 66.1% and 33.8%, respectively. Conversely, these figures for 2019 were 40.2% and 59.6% correspondingly. It means the percentage area of the higher NLST group (0.4–0.8) was almost 1.5 times of the low NLST (0–0.4). In the very high NLST group (0.8–1), the percentage area for both selected years was approximate 0.

24.4.2 Correlation Between NLST-NDVI and NLST-NDBI

NDVI maps are shown in Fig. 24.5a, b. They were extracted based on the Red band and Near-Infrared band of Landsat satellite images. Statistical information of these maps is stored in Table 24.2. The mean NDVI of the year 2005 was found to be 0.21 and it decreased slightly to 0.20 in the year 2019. The minimum NDVI and maximum NDVI were (−0.12, 0.4) for 2005 and (−0.09, 0.5) for 2019. By reading these maps, it is easy to observe that the NDVI value of water bodies, for example the Red River in the north of maps, was less than 0. On the 2019 NDVI map, the number of pixels with low NDVI (0–0.15) is more than that on the 2005 NDVI map. Whereas the number of pixels with higher NDVI (0.15–0.3) on the 2005 NDVI map is more than that on the 2019 NDVI map. Hence, there was a slight decline in the NDVI value between the two years.

NDBI maps are shown in Fig. 24.6a, b. They were extracted from the two bands SWIR and NIR supplied by Landsat images. Statistical information of NDBI maps is portrayed in Table 24.2. Contrary to mean NDVI, mean NDBI was an upward trend in this period, from −0.08 in 2005 to −0.07 in 2019. The number of pixels

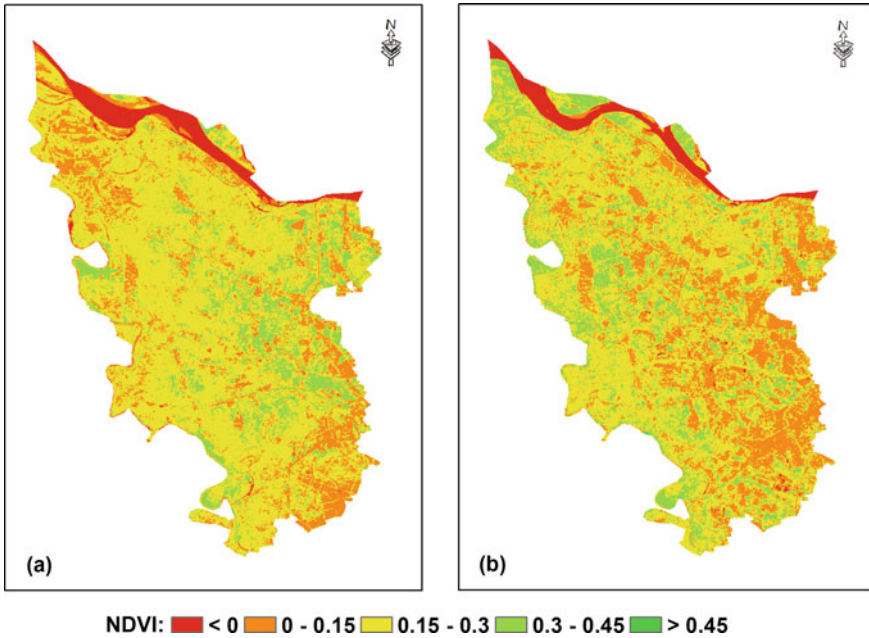


Fig. 24.5 NDVI maps

Table 24.2 Statistical information

Index	Year	Max	Min	Mean	Std. Dev
LST	2005	45.94	26.32	33.18	2.35
	2019	49.73	29.08	38.06	2.81
NLST	2005	1	0	0.35	0.13
	2019	1	0	0.43	0.14
NDVI	2005	0.48	-0.12	0.21	0.09
	2019	0.5	-0.09	0.20	0.09
NDBI	2005	0.61	-0.31	-0.08	0.06
	2019	0.32	-0.33	-0.07	0.07

in the highest NDBI group (>0.05) on the NDBI 2019 map was more than that on the NDBI 2005 map. They were diffusely distributed in the center and the southeast of the study site where currently is rural residential areas or urban residential areas. While the whole center of the 2005 NDBI map was essentially the lowest NDBI group (<-0.15). Therefore, NDBI had increased in this period.

NDVI, the index extracted from remote sensing data, is an indicator that represents the vegetation cover status on the earth’s surface (Yang et al. 1982; Rani et al. 2018). The areas that have high NDVI values mean covered by high vegetation density. To

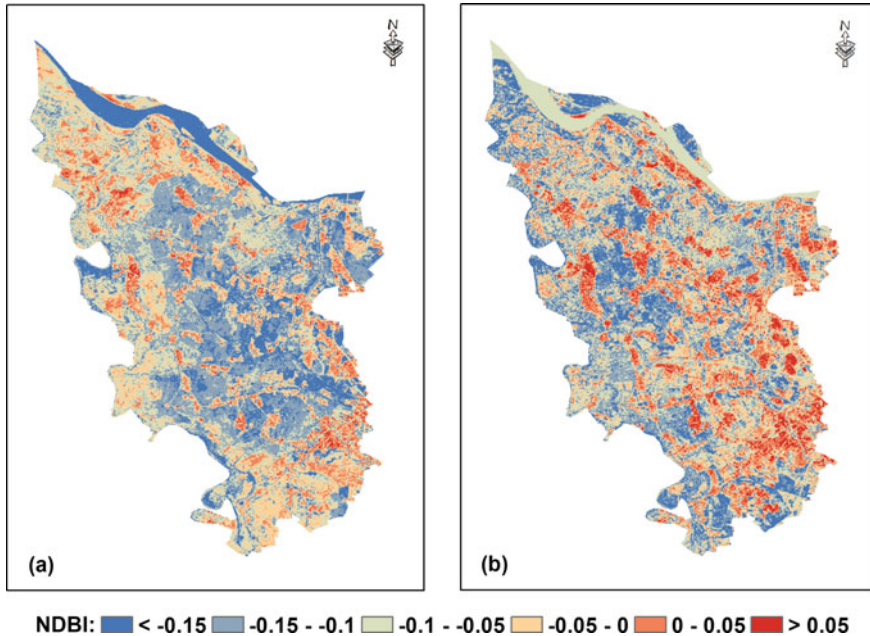


Fig. 24.6 NDBI maps in 2005 and 2019

clarify the importance of vegetation in cooling land surface temperature, this part will analyze the correlations between NLST and NDVI. The relationships between the NLST index and the NDVI index of the years 2005 and 2019 are revealed through scatter plots in Fig. 24.7a, c. One of the most outstanding features is that both regression lines were going down. The coefficient of correlation (R) between NLST and NDVI of the two years 2005 and 2019 were -0.69 and -0.77 . Thus, the regression models ($NLST = -1.36942 * NDVI + 0.68532$) and ($NLST = -1.20825 * NDVI + 0.71315$) were strong fit. These also revealed the inverse relationship between LST and vegetation. High vegetation density areas had low LST, and vice versa. Hence, this finding one more time defines the role of vegetation in cooling the land surface temperature.

NDBI is frequently used in urban studies or surface temperature studies. It helps to highlight urban regions where temperatures are normally higher than rural areas and are usually affected by urban heat island phenomena. The relationships between NLST and NDBI are shown in Fig. 24.7b, d. Inversing NDVI, the correlation between NLST and NDBI was found to be positive with the $R = 0.74$ in 2005 and $R = 0.85$ in 2019. In fact, the regression models were ($NLST = 1.63300 * NDBI + 0.51068$) and ($NLST = 1.44487 * NDBI + 0.54574$) for the year 2005 and 2019, respectively. The strong correlation between NLST and NDBI reveals the strong influence of urbanization on land surface temperature. Land-use planners should particularly consider this issue in new urban planning.

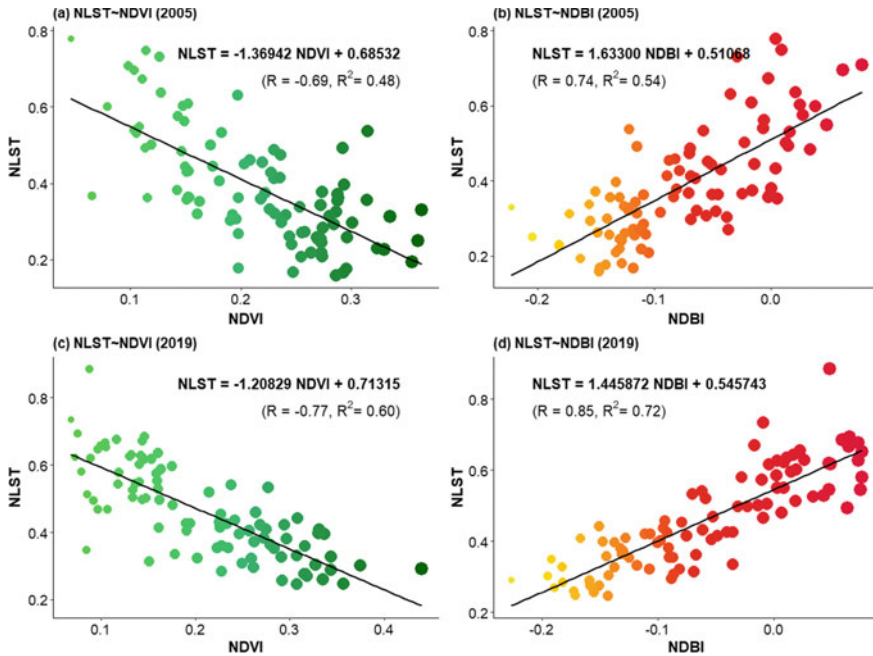


Fig. 24.7 Linear regression models between NLST-NDVI and NLST-NDBI

24.5 Conclusion

In this study, spatial–temporal changes of LST at the western edge of the Hanoi capital were investigated on several indices extracted from remote sensing data, such as LST, NDVI, and NDBI. The period 2005–2019 was experienced an increase in mean LST, from 33.18 °C in 2005 to 38.06 °C in 2019. The percentage of total land area covered by LST less than 34 °C and LST from 34 to 42 °C were significant changes between two years. These figures are 64.0 and 35.8% for 2005, 5.4 and 87.8% for 2019. Several points at the center and the southeast of the study site that their LST greater than 38 in 2005 were expanded in 2019. It is due to the expansion of residential areas in the urbanization at these points.

Statistical analysis indicates strong correlations between NLST and the two biophysical indices NDVI and NDBI with converse trends. The correlations between NLST and NDBI in the two selected years were negative with $R = -0.69$ and $R = -0.77$. Whereas, the correlations between NLST and NDBI in 2005 and 2019 were positive with $R = 0.74$ and $R = 0.85$, respectively. These findings are useful for authorities in land-use orientation in the future.

References

- Abulibdeh A (2021) Analysis of urban heat island characteristics and mitigation strategies for eight arid and semi-arid gulf region cities. *Environ Ear Sci* 80:259
- Chien W-H, Wang T-S, Yeh H-C, Hsieh T-K (2016) Study of NDVI application on turbidity in reservoirs. *J Indian Soc Rem Sens* 44:829–836
- Daramola MT, Eresanya EO, Ishola KA (2018) Assessment of the thermal response of variations in land surface around an urban area. *Model Ear Syst Environ* 4:535–553
- Dong Y, Yin D, Li X, Huang J, Su W, Li X, Wang H (2021) Spatial–temporal evolution of vegetation NDVI in association with climatic, environmental and anthropogenic factors in the Loess Plateau, China during 2000–2015: quantitative analysis based on geographical detector model. *Remote Sens* 13
- Esad M, Md Obaidul H, Julia B (2021) Radiometric performance of Landsat 8 Collection 2 products. *Proc SPIE*
- Ferral A, German A, Beltramone G, Bonansea M, Burgos PM, Carvalho LSD, Michal S, Roque M, Scavuzzo M (2021) Spatio–temporal analysis of water surface temperature in a reservoir and its relation with water quality in a climate change context. In: 2021 IEEE international geoscience and remote sensing symposium IGARSS, pp 76–79
- Hemati M, Hasanlou M, Mahdianpari M, Mohammadimanesh F (2021) A systematic review of landsat data for change detection applications: 50 years of monitoring the earth. *Remote Sens* 13
- HNSO (2000) Hanoi statistical yearbook 1999. Hanoi Statistical Office (HNSO)
- HNSO (2010) Hanoi statistical yearbook 2009. Hanoi Statistical Office (HNSO)
- HNSO (2020) Hanoi statistical yearbook 2019. Hanoi Statistical Office (HNSO)
- Hoang NH, Fogarassy C (2020) Sustainability evaluation of municipal solid waste management system for Hanoi (Vietnam)—why to choose the ‘waste-to-energy’ concept. *Sustainability* 12
- Hua L, Zhang X, Nie Q, Sun F, Tang L (2020) The impacts of the expansion of Urban impervious surfaces on Urban heat islands in a Coastal City in China. *Sustainability* 12
- John J, Bindu G, Srimuruganandam B, Wadhwa A, Rajan P (2020) Land use/land cover and land surface temperature analysis in Wayanad district, India, using satellite imagery. *Ann GIS* 26:343–360
- Jung MC, Dyson K, Alberti M (2021) Urban landscape heterogeneity influences the relationship between tree canopy and land surface temperature. *Urban for Urban Green* 57:126930
- Madanian M, Soffianian AR, Soltani Koupai S, Pourmanafi S, Momeni M (2018) The study of thermal pattern changes using Landsat-derived land surface temperature in the central part of Isfahan province. *Sustain Cities Soc* 39:650–661
- Majumder A, Setia R, Kingra PK, Sembhi H, Singh SP, Pateriya B (2021) Estimation of land surface temperature using different retrieval methods for studying the spatiotemporal variations of surface urban heat and cold islands in Indian Punjab. *Environ Dev Sustain* 23:15921–15942
- Mustafa EK, Liu G, Abd El-Hamid HT, Kaloop MR (2021) Simulation of land use dynamics and impact on land surface temperature using satellite data. *Geo J* 86:1089–1107
- Park S, Kim M (2021) Availability of land surface temperature using landsat 8 OLI/TIRS science products. *Korean J Rem Sens* 37:463–473
- Rani M, Kumar P, Pandey PC, Srivastava PK, Chaudhary BS, Tomar V, Mandal VP (2018) Multi-temporal NDVI and surface temperature analysis for Urban Heat Island inbuilt surrounding of sub-humid region: a case study of two geographical regions. *Rem Sens Appl Soc Environ* 10:163–172
- Sekertekin A, Bonafoni S (2020) Land surface temperature retrieval from landsat 5, 7, and 8 over rural areas: assessment of different retrieval algorithms and emissivity models and toolbox implementation. *Rem Sens* 12
- Soydan O (2020) Effects of landscape composition and patterns on land surface temperature: Urban heat island case study for Nigde, Turkey. *Urban Clim* 34:100688

- Tania AH, Gazi MY, Mia MB (2021) Evaluation of water quantity–quality, floodplain landuse, and land surface temperature (LST) of Turag River in Bangladesh: an integrated approach of geospatial, field, and laboratory analyses. *SN Appl Sci* 3:63
- USGS (2021a) Landsat 4–7 collection 2 (C2) level 2 science product (L2SP) guide. Department of the Interior, Sioux Falls, SD 57198
- USGS (2021b) Landsat 8 collection 2 (C2) level 2 science product (L2SP) guide. Version 3.0
- Wani AA, Bhat AF, Gatoo AA, Zahoor S, Mehraj B, Najam N, Wani QS, Islam MA, Murtaza S, Dervash MA, Joshi PK (2021) Assessing relationship of forest biophysical factors with NDVI for carbon management in key coniferous strata of temperate Himalayas. *Mitig Adapt Strat Glob Change* 26:1
- Wen C, Zhan Q, Zhan D, Zhao H, Yang C (2021) Spatiotemporal evolution of lakes under rapid urbanization: a case study in Wuhan, China. *Water* 13
- Wu C, Murray AT (2003) Estimating impervious surface distribution by spectral mixture analysis. *Remote Sens Environ* 84:493–505
- Wu P, Yin Z, Yang H, Wu Y, Ma X (2019) Reconstructing geostationary satellite land surface temperature imagery based on a multiscale feature connected convolutional neural network. *Rem Sens* 11
- Wu W, Li C, Liu M, Hu Y, Xiu C (2020) Change of impervious surface area and its impacts on urban landscape: an example of Shenyang between 2010 and 2017. *Ecosyst Health Sustain* 6:1767511
- Yang J, Wan Z, Borjigin S, Zhang D, Yan Y, Chen Y, Gu R, Gao Q (2019) Changing trends of NDVI and their responses to climatic variation in different types of grassland in inner Mongolia from 1982 to 2011. *Sustainability* 11
- Zheng Y, Tang L, Wang H (2021) An improved approach for monitoring urban built-up areas by combining NPP-VIIRS nighttime light, NDVI, NDWI, and NDBI. *J Clean Prod* 328:129488

Chapter 25

Salinity Prediction in Coastal Aquifers of the Vietnamese Mekong River Delta Using Innovative Machine Learning Algorithms



Dang An Tran , Ha Nam Thang , Dieu Tien Bui ,
and Vuong Trong Kha 

Abstract Groundwater salinization is a severe issue, causing various problems to human health, agriculture, ecosystems, and infrastructure in many coastal regions across the world. However, this phenomenon is difficult to predict with high accuracy. In this study, we propose and verify a new artificial intelligence approach for predicting groundwater salinity and identifying the main factors of salinization. The coastal aquifers of the Mekong River Delta (Vietnam) were selected to test the new approach. In the proposed approach, Extreme Gradient Boosting (XGB) was used to build a groundwater salinity model, and Genetic Optimization (GO) was employed to optimize the model parameters. Gaussian Processes (GP) and Random Forests (RF) were also used as a benchmark for the model comparison. For this regard, a groundwater salinity database with 215 groundwater samples and 20 driven factors related to hydrology, geology, geography, and anthropogenic activities was prepared. Performance of the models was assessed using Correlation Coefficient (r), Root Mean Square Error (RMSE), Mean Absolute Percentage Error (MAPE), and Mean Absolute Error (MAE). The results show that the proposed GO-XGB model yields high performance both on the training dataset ($r = 0.999$, RMSE = 18.450, MAPE = 2.070, and MAE = 4.864) and the validation dataset ($r = 0.787$, RMSE = 141.042, MAPE = 87.250, and MAE = 74.993). The proposed GO-XGB model

D. A. Tran (✉)

Faculty of Water Resources Engineering, Thuyloi University, 175 Tay Son, Dong Da, Hanoi, Vietnam

e-mail: antd@tlu.edu.vn

H. N. Thang

Faculty of Fisheries, University of Agriculture and Forestry, Hue University, Hue 530000, Vietnam

e-mail: hanamthang@hueuni.edu.vn

D. T. Bui

Department of Business and IT, USN School of Business, Campus Bø (1-324), Bø, Norway
e-mail: dieu.t.bui@usn.no

V. T. Kha

Department of Mine Surveying, Hanoi University of Mining and Geology, Hanoi, Vietnam

performed better predictive result compared to the benchmark, GP, and RF. Among the 20 factors, groundwater level, vertical hydraulic conductivity, lithology, extraction capacity, horizontal hydraulic conductivity, distance to saline sources, and well density are the most important factors to groundwater salinization prediction.

Keywords Groundwater salinization · GO-XGB model · Coastal aquifers · Mekong River Delta · Vietnam

25.1 Introduction

Groundwater is identified as the primary source of water for about two billion people and accounts for 33% of the total water withdrawal worldwide (Famiglietti 2014). It is a crucial freshwater resource for domestic uses, industrial development, and irrigational activities (Mohanty and Rao 2019; Behera et al. 2019; Kaur et al. 2020). However, groundwater resource is highly vulnerable to human activities (Ma et al. 2019a; Brouwer et al. 2018; Graaf et al. 2019) and natural variation (Kagabu et al. 2020; Giambastiani et al. 2018), especially in coastal regions where are facing groundwater overexploitation, seawater intrusion, climate change, and sea-level rise (Ferguson and Gleeson 2012). In such regions, groundwater is likely to increase in salinity due to paleo-seawater intrusion (Delsman et al. 2014), modern seawater intrusion (Han and Currell 2018), leaking brines from oil fields and irrigation activities (Paine 2003). High salt concentrations in groundwater may cause various environmental and health issues. For example, high salinity in irrigated water may cause physiological drought and reduce crop yield (Nishanthiny et al. 2010). High salt in drinking water increases the risk of hypertension (Vineis et al. 2011), coronary heart disease (Park and Kwock 2015), and chronic kidney disease; therefore, assessing groundwater quality, especially the salinization level, is crucial to protect the environment and human health (Melloul and Goldenberg 1997; Guhl et al. 2006; Gallardo and Marui 2007; Carretero et al. 2013; Larsen et al. 2017).

For last several decades, mathematical model has been used widely in prediction of groundwater dynamics and seawater intrusion into coastal aquifers (Lal and Datta 2019; Abdelhamid et al. 2016; Mahmoodzadeh and Karamouz 2019; Stein et al. 2019; Voss and Souza 1987). However, mathematical groundwater modelling requires expert knowledge about the physical characteristics of hydrogeological system, governing process, various types of input data (i.e., topography, soil properties, geology, initial and boundary conditions, hydrological and climate data, etc.) while the accuracy of the model simulation depends on reliable model input parameters (Lal and Datta 2019; Kim and Yang 2018). Meanwhile, machine learning is a data-driven model with little requirement about the physical process, and it could provide an accurate prediction (Sun et al. 2016; Yadav et al. 2018). Therefore, machine learning has been considered as an alternative, i.e., Genetics algorithm (Sreekanth and Datta 2010), artificial neural networks (Banerjee et al. 2011), multi-objective optimization (Javadi et al. 2015), multivariate adaptive regression spline

(Roy Dilip and Datta 2017), support vector regression (Lal and Datta 2019; Isazadeh et al. 2017; Nadiri et al. 2018), ensemble multiadaptive boosting logistic regression (Rizeei et al. 2019), and Gaussian Process Regression (Yadav et al. 2018; Kopsiaftis et al. 2019), and hybrid computational intelligence models (Pham et al. 2019a; Chen et al. 2019). A common conclusion from the above works is that machine learning is a highly flexible tool with the ability to handle complex non-linear relationships between groundwater salinity and influencing factors (Naghibi et al. 2015; Ransom et al. 2017; Sajedi-Hosseini et al. 2018). Nonetheless, no studies have figured out which are the most important factors influencing on groundwater salinity in coastal areas, while the rapid development in the field of computer science has introduced more superior methods.

In spite of many advantages of applying machine learning in predicting environmental issues, this approach has some limitations such as lacking good data, deterministic problems, and misapplication. Especially, the predictive results mainly based on statistical relationship instead of performing directly physical processes like numerical models therefore it requires in-depth understanding between target variable and independent variables to improve reliability and accuracy of the ML models. In this research, therefore, we propose and validate a new artificial intelligence approach, which is based on Extreme Gradient Boosting (XGB) and Genetic Optimization (GO), named as GO-XGB, for predicting groundwater salinity in the coastal aquifers of the Mekong River Delta (Vietnam). To the best of our knowledge, this is the first time that GO-XGB is considered for groundwater salinity modelling. We also compare and discuss the performance of our models and traditional models such as random forests and Gaussian processes to understand if this approach adds value to the field of groundwater salinity prediction. Besides, the role of various influencing factors in aquifer salinization is assessed. The proposed models were tested using groundwater salinity data and its controlling factors in the multi-aquifers in the Mekong Delta, Vietnam.

25.2 Background of the Machine Learning Algorithms Used

In this section, we first review two traditional machine learning models which are already applied to predict groundwater salinity, namely random forests, and Gaussian processes. We then introduce the idea of the combination of Extreme Gradient Boosting and Genetic Optimization to form a new hybrid algorithm. The performance of the two traditional models is then considered as benchmarks to assess our model.

25.2.1 Gaussian Processes

Gaussian processes (GP) are a type of supervised learning for both regression and classification problems (Kopsiaftis et al. 2019; Rasmussen et al. 2003; Hall et al. 2012; Azimi et al. 2018). The principal idea of Gaussian processes is that in the input space $x = [x_1, \dots, x_n]^T$, every point is associated with a random variable, so as the joint distribution of them can be modelled as a multivariate Gaussian and a function (called f) can be modelled using an infinite multivariate Gaussian distribution (Ma et al. 2019b). Similarly, if we have a salinity dataset $M = ([X_i, y_i], i = 1, 2, \dots, m)$ with $X_i \in \mathbb{R}_n$ is a matrix of m input variables with n observation, whereas $y_i \in \mathbb{R}$ is an output variable (Cl^- concentration in groundwater). A GP regression model formulates the relation of the input and output variables as following equation (Rasmussen et al. 2003; Hoa et al. 2019):

$$y(x) = \sum_{i=1}^n \alpha_i K(X_i, X) \quad (25.1)$$

where α_i is the weight and K is the Radial Basis kernel function (RBF) (Eq. 25.2) (Park and Sandberg 1991; Scholkopf et al. 1997).

$$K(X_i, X) = \beta \times e^{-\sum_{i=1}^m \left[\frac{(x_i^m - x_i^m)^2}{2\sigma^2} \right]} \quad (25.2)$$

where β is the scaling factor and σ is the kernel parameter.

The performance of the GP model is dependent on the parameters β and weights α_i and they could be automatically turned and optimized through maximizing the marginal likelihood (Rasmussen et al. 2003).

25.2.2 Random Forests

A random forest (RF) is a method for both classification and regression based on the ensemble of decision trees (Breiman 2001). A decision tree is a top-down tree-like structure, in which each non-leaf node is a test, each branch is an outcome of the test, and each leaf node is a decision. Regression with a single decision tree may result in the problem of overfitting (high variance) and is dependent on the distribution of training sets. A large number of decorrelated decision trees can form a random forest which then can reduce the variance and boost model performance (Criminisi 2011). The procedure developing RFs is as follows: (1) n random subsets (called “bootstrapped subsets”) are sampled from a training dataset based on a random selection of features of the dataset. A subset may contain overlapped data in other

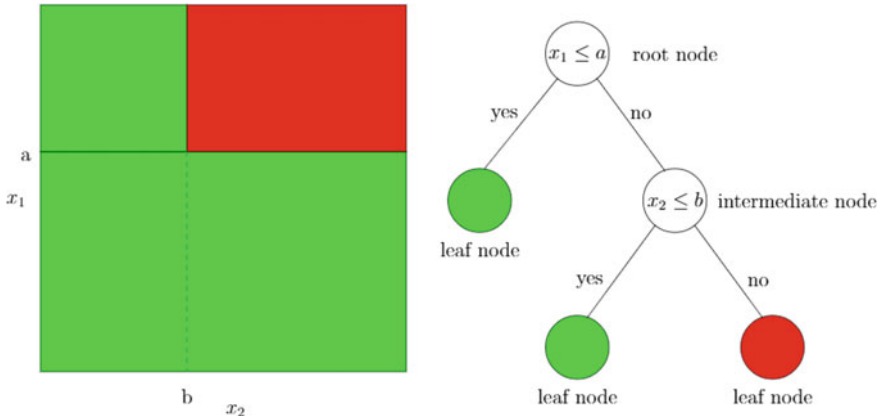


Fig. 25.1 Example of the partitions left and classification tree structure right with two classes coloured in green and red

subsets; (2) n decision trees are built using these n bootstrapped subsets (Fig. 25.1). The number of trees n is decided using either cross-validation or out-of-bag (OOB) error methods. A detailed description of the statistical formulation of RF can be found in Breiman (2001).

25.2.3 Extreme Gradient Boosting

Similar to the random forest, an Extreme Gradient Boosting (XGB) is an ensemble-machine learning algorithm that is based on decision trees (weak learners) (Friedman 2001). However, a boosting model constructs the “forest” of decision trees sequentially, or one decision tree can be constructed based on learning experience inherited from previous trees (Chen and Guestrin 2016; Johnson et al. 2018). The second tree focuses on the cases in which the first tree gives a poor prediction, and this learning process is repeated many times, so as the combination of these trees can better capture the relationship between predictands and predictors. Gradient Boosting is a form of boosting models in which poor prediction cases are assessed if they contribute to minimize the overall lost function (also called the prediction error) (Lim and Chi 2019). A case can be considered as highly valuable if the adding decision tree built for this case can reduce the prediction error significantly while no change in the error implicates a no value case; thus, only useful decision trees are kept. This may give XGB models advantages in complex problems like quantifying saline concentration in groundwater since data measurement in the underground environment may contain many special cases. It is also worth to notice that the learning efficiency of each machine learning algorithm is controlled by its model parameters, and in the case of the XGB model, they include three groups: tree-specific, boosting, and miscellaneous

parameters. Selection of these model parameters is a challenging task and depends on user experience while this process does not always return in an optimum set of parameters. Thus, we propose to use a genetic algorithm to automatically search in parameter spaces to improve the accuracy of numerical forecasts.

25.2.4 Genetic Algorithm

Genetic Algorithm takes the idea from the Darwinian theory of natural selection to evolve solutions by utilizing computer capacity to tune model parameters as an alternative to manual efforts (Forrest 1993). The most crucial concept of GA is the chromosome which consists of model parameters to define a solution (called individual) (Jennings et al. 2019). A certain number of individuals then forms a population. In the lower level, each chromosome consists of some genes which are often denoted as 0 s or 1 s ($X \equiv (x_1, x_2, \dots, x_n), x_k \in [0.0, 1.0] \forall k$). Each individual is evaluated by its fitness value, a result of a fitness function.

The basic operation performed during the training of XGB based model is as following steps: (1) A number of individuals are initialized to form a population, (2) individuals with the best fitness values are selected to generate a mating pool, (3) from the mating pool, either sequential or random selection methods select parents, and (4) several operators called crossover and mutation are then applied to each pair of parents to generate their offspring. This process keeps high-quality individuals to create more individuals, so as it evolves solutions to obtain the desired solutions.

25.3 Study Area and Data

25.3.1 Description of the Study Area

The study area, Soc Trang province, is in the coastal area of the Mekong River Delta. The study area covers an area of 3,312 km² with an elevation ranging from 0.5 to 2.5 m above the mean sea level (Fig. 25.2). The province is bordered by the Hau River (one main branch of the Mekong River) to the Northwest and the Vietnamese East Sea (South China Seas) to the Southwest. Since this area has a dense river system connected to the sea, the hydrological regime in the study area is complex and strongly influenced by the flow regime of the Mekong River and tidal fluctuation.

The study area is in a tropical monsoon climate region with two distinct seasons, the dry season from May to November and the rainy season from December to April (in the following year). The annual average rainfall is about 1772 mm with substantial seasonal variation. About 85% of the annual rainfall occurs during the rainy season. The study area has recognized as one of the most vulnerable regions to climate change and sea-level rise in the world.

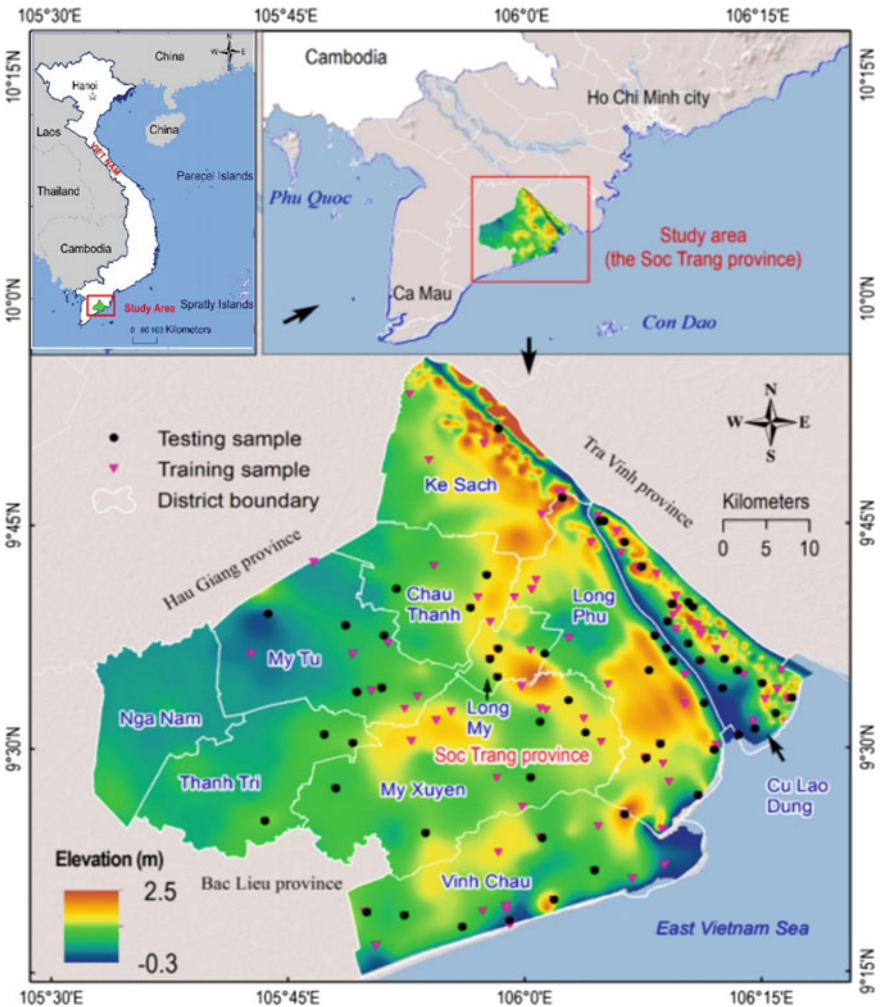


Fig. 25.2 Location of the study area (Soc Trang province), the Vietnamese Mekong River Delta

Soc Trang province has around 1.20 million people in which a majority of the population depends on agriculture for their livelihoods, contributing to 42% of the total GDP in the province (Hoang et al. 2019). Agriculture lands are dominant, accounting for 84.77% (276,690 ha of total area), which includes rice fields (52.98%), fishponds (19.69%), orchards (15.51%), and lands of other vegetable types (6.75%), and other types of land use (Decision No. 108/NQ-CP of the Government 2018).

In the study area, groundwater is used as a dominant source of water for domestic, industrial and agricultural activities, resulting in rapid groundwater level depletion in the irrigated areas (Hoang and Bäumlé 2018; Minderhoud et al. 2017). Groundwater salinization has been identified as one of the significant threats to the groundwater

resource in this region (An et al. 2018). The extent of groundwater salinization in the study area has recently been increased due to the rapid increase in groundwater demand (Minderhoud et al. 2017; Nam et al. 2019).

The hydrogeological setting of the study area is characterized by a multi-layered aquifer system, formed between the Miocene and Holocene epoch (Wagner et al. 2012; Hung et al. 2019). Groundwater in the Pleistocene aquifers is the primary source of drinking water because these aquifers have high yields and good-quality water compared to other aquifers (An et al. 2018). In this study, we focus on assessing the vulnerability and risk of groundwater in the Pleistocene aquifers to salinity.

25.3.2 Data Preparation and Variables Selection

In this research, 215 groundwater samples from the Pleistocene aquifers were collected between 2013 and 2018 during both the rainy and dry seasons. On-site measurements were conducted to obtain physical parameters such as groundwater temperature T ($^{\circ}\text{C}$), pH, dissolved oxygen DO, and electrical conductivity EC using the HANNA portable instruments (Hanna Instruments Inc. 2015). The chloride concentration in groundwater samples was analyzed using Ion Liquid Chromatography (Shimadzu Co. Ltd., Japan) at the University of Tsukuba, Japan.

The accumulation of salinity in groundwater is a complex process because it is controlled by influencing factors (Mahlknecht et al. 2017; Kanagaraj et al. 2018). The selection of influencing factors for groundwater salinization prediction based on the possibilities of saltwater migration into aquifers. In the Pleistocene aquifers, groundwater salinity is originated from (1) downward or upward leakage of paleo-saline water (Khaska et al. 2013; Chatton et al. 2016), (2) halite dissolution in the topsoil layer (Walter et al. 2017; Blasco et al. 2019), (3) seawater intrusion (Han and Currell 2018; Kanagaraj et al. 2018; Werner et al. 2013), and (4) irrigation return flow (Essaid and Caldwell 2017; Lapworth et al. 2017; Malki et al. 2017; Tweed et al. 2018). The downward or upward leakages of paleo-saline water may relate to the formation of aquifers, which is further incorporated into the lithology influencing factor. Furthermore, the thicknesses of aquitards, distance to the hydraulic window, distance to fault, fault density, and vertical hydraulic conductivity could also affect the leaking rate (Elmahdy and Mohamed 2013; Liu et al. 2018). Besides, other geographical variables such as distance from main rivers, distance to the drainage and drainage density are also widely considered as influencing factor to groundwater salinity (Winkel et al. 2008). The halite dissolution process is characterized by salt rock/sediment properties, soil type, and horizontal and vertical hydraulic conductivity. Variables which represent the effect human activities on groundwater salinity in the study area are the groundwater level, extraction capacity, well density, extraction density, and operation time. The severity of seawater intrusion may also depend on the distance to the sea, groundwater level, well density, extraction capacity, extraction density, and horizontal hydraulic conductivity (Lee et al. 2016; Yechieli et al. 2019). The four processes mentioned above interact with each other and result in a

Table 25.1 Influencing factors for prediction of groundwater salinity using machine learning models

No.	Explanatory variables	Coding	Unit	Data type
1	Distance to the sea	DTS	km	Numeric
2	Distance to main river	DTR	km	Numeric
3	Distance to drainage	DTD	km	Numeric
4	Drainage density	DD	m/km	Numeric
5	Distance to hydraulic window	DTW	km	Numeric
6	Distance to fault	DTF	km	Numeric
7	Fault density	FD	m/km	Numeric
8	Distance to saline sources	DTS	km	Numeric
9	Temperature of groundwater	T	°C	Numeric
10	Depth of screen well	DSW	m	Numeric
11	Soil properties	AT	#	Ordinal
12	Horizontal hydraulic conductivity	Kh	m/d	Numeric
13	Vertical hydraulic conductivity	Kv	m/d	Numeric
14	Thickness of aquitard	WA	m	Numeric
15	Operation time (of well)	OTW	year	Numeric
16	Well density	WD	well/km ²	Numeric
17	Discharge density	DCD	m ³ /km ²	Numeric
18	Extraction capacity	EXC	m ³ /d	Numeric
19	Groundwater level	GWL	m.abmsl	Numeric
20	Lithology	LT	#	Ordinal

complex salinization process in the study area (An et al. 2018). Based on the analysis mentioned above, 20 influencing factors were selected for predicting the spatial distribution of salinity in groundwater (Table 25.1).

25.4 The Proposed Methodology for the Prediction of Groundwater Salinity in Coastal Aquifers with Artificial Intelligence Techniques

The modelling framework used in this study is as follows: (1) data pre-processing, (2) feature selection, (3) model parameters, (4) model performance and evaluation, (5) Data post-processing (Fig. 25.3).

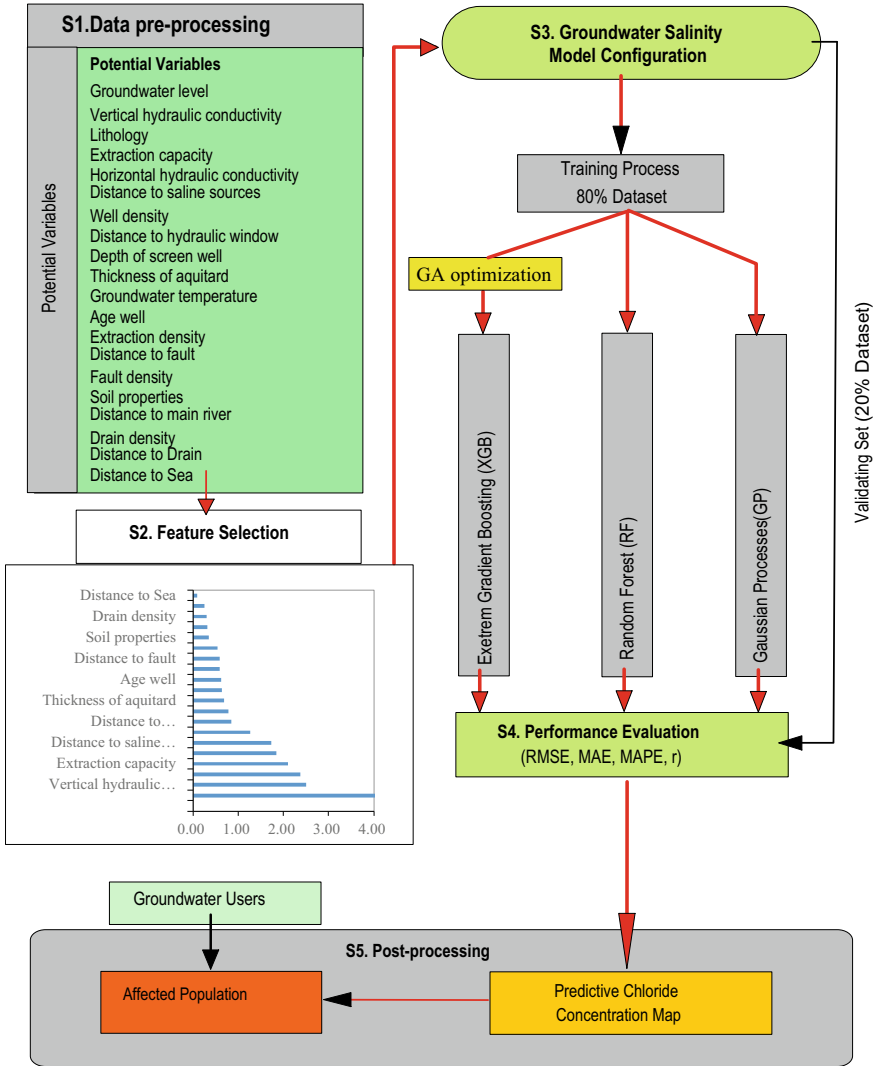


Fig. 25.3 Methodological chart of the present study

25.4.1 Data Pre-processing

Prior to modelling, 215 groundwater samples from middle and lower Pleistocene aquifers were selected, and each sample consists of 20 variables (Table 25.1). The measured Cl^- concentration is assigned as a dependent variable, while the 20 influencing factors are assigned as independent variables. The dataset was then randomly

split to training and testing datasets 80% of the dataset was used for training, and 20% of the dataset was used for testing.

Since the influencing factors for predicting groundwater salinization have significantly different ranges, normalization was used to convert the values of numeric columns into a range from 0 to 1 using the following equation:

$$X_n = \frac{X_i - X_{\max}}{X_{\max} - X_{\min}} \quad (25.3)$$

where X_n and X_i represent the moralized and raw training and testing data; X_{\max} and X_{\min} are the minimum and maximum of the training and testing data.

25.4.2 Feature Selection

As many factors control groundwater salinization processes in coastal aquifers, the selection of influencing factors plays a vital role in reducing time and cost of computation processes and improving the accuracy of prediction results. For several decades, numerous variable selection methods have been applied to identify significant variables before feeding machine learning algorithms to construct predictive models such as filters, wrappers, and embedded techniques (Kohavi and John 1997; Guyon and Elisseeff 2006; Hira and Gillies 2015).

Recently, Random Forests (RF) and its improved algorithms (XGB) have been widely used not only for predicting but also for selecting essential variables as the embedded technique to predictive models (Rodriguez-Galiano et al. 2014; Zeng et al. 2018; Zhao et al. 2019). In this study, the RF algorithm is employed to select input parameters for predicting chloride concentrations in the middle and lower Pleistocene aquifers of the study area. The procedure was followed below steps:

Step 1: Estimation of permutation-based mean squared error (MSE) reduction as Eq. (25.2):

$$MSE_{OOB}^t = \frac{1}{n_{OOB}(t)} \cdot \sum_{i=1}^{n_{OOB}} (y_i - \hat{y}_{i_{OOB},t}) \quad (25.4)$$

where MSE_{OOB} is mean squared error, n_{OOB} is the total of out-of-bag (OOB) samples, y_i is the measure Cl^- concentration in groundwater samples, and $\hat{y}_{i_{OOB},t}$ is the predicted Cl^- concentration of the i -th sample from a decision tree t of OOB samples.

Step 2: Estimation of MSE for permuted input variable x_i using the following equation:

$$MSE_{OOB}^t[x_i \text{ permuted}] = \frac{1}{nOOB(t)} \cdot \sum_{i=1}^{nOOB} (y_i - \hat{y}_{iOOB,t})[x_i \text{ permuted}] \quad (25.5)$$

Step 3: Estimation of variable importance score for variable x_i using the following equation:

$$VI(x_i) = \frac{1}{T_{tree}} \cdot \sum_{t=1}^{T_{tree}} (MSE_{OOB}^t[x_i \text{ permuted}] - MSE_{OOB}^t) \quad (25.6)$$

25.4.3 Model Configuration and Training

The configuration and training for the three machine learning models are conducted using a training dataset (80% of measured data). For the RF model, the tree-net system is built from 1000 trees with a maximum of 4 nodes per tree and the maximal tree depth of 17. For the GP model, the radial basis function (RBF) kernel and $\gamma = 0.014$ are chosen to predict chloride concentrations in groundwater. In the GO-XGB model, each XGB prediction rule is trained with tenfold cross-validation to identify the number of trees (n_{tree}) that minimizes an objective function. The prediction rule is fine-tuned by identifying the optimal combination of hyperparameters that further minimized the objective function for each area. The hyperparameters include the number of base classifiers ($n_{estimators}$), the maximum depth of each tree (max_depth), the learning rate (eta), the number of observations in each leaf node of the tree (min_child_weight), the minimum loss reduction required to partition further a leaf node on a single tree (γ and reg_alpha), the proportion of observed data were used by XGB algorithm to grow each tree (subsample), and the proportion of predictor variables used at each level of tree splitting ($colsample_bytree$). The $n_{estimators}$ is defined as the number of base classifiers and improper setting of $n_{estimators}$ will result in model failure. The $maximum_tree_depth$ was selected appropriately to prevent model complexity. This parameter is crucial in controlling under and over-fitting issues in which too small values of $maximum_tree_depth$ will cause underfitting while too large values will result in overfitting. $Learning_rate$ represents the weight-reduction factor of each base classifier. Min_child_weight represents the weight of the minimum leaf node sample and is used to improve the generalization of the model. The value of γ ranges from 0 to infinite, which represents the minimum loss reduction required to make a further partition on a leaf node of the tree. The γ parameter controls the drop value of the model loss function when the node splits. The $subsample$ controls the proportion of random sampling for each tree, typically between 0.5 and 1. The regularization parameter α (reg_alpha) denotes the L1 regularization term of the weight, which is used to simplify the complexity of the model.

In this study, the XGB algorithm was used to construct the model and optimizes parameters with GA. The details framework is described in Fig. 25.3. The main parameters of the XGB algorithm that need to be optimized are *max_depth*, *learning_rate*, *min_child_weight*, *subsample*, *alpha*, and *gamma*. After adjusting parameters by a genetic optimization function, we found the best value of these parameters *max_depth* = 15, *learning_rate* = 0.153, *min_child_weight* = 1, *subsample* = 1, *alpha* = 0.005, and *gamma* = 0.0015. In addition, *n_estimators* = s1200, *colsample_bytree* = 0.635, and *n_estimators* = 1200 were selected. The decision rule was retrained and applied to the withheld testing data to predict a new series of count observations and evaluate the accuracy of the decision rule based on the optimal values of the hyperparameters and number of trees. The variable importance of each environmental predictor variable was also obtained using the XGB algorithm.

25.4.4 Performance Assessment

The performance criteria used for evaluating model performance depends on the output variables of each model, e.g., categorical or continuous variable (Tien Bui et al. 2016). For evaluating the model with output values is continuous, performance criteria such as the root mean square error (RMSE), the mean absolute percentage error (MAPE), the mean absolute error (MAE), and Pearson's correlation coefficient (*r*) (Pham et al. 2019a) are used. Each performance criteria term indicates specific information regarding predictive performance efficiency (Li et al. 2016). RMSE is a quadratic scoring rule that measures the average magnitude of errors. It gives a relatively high weight to large errors; hence, it is most useful when large errors are undesirable. The Mean Absolute Percentage Error (MAPE) is the average of absolute errors divided by actual observation values. MAE measures the average magnitude of errors in a set of predictions without considering their direction. It is a linear score, implying that all individual differences between predictions and corresponding observed values are weighted equally in the average. The *r* is a measure of the linear correlation between observation and prediction values. RMSE, MAPE, MAE, and *r* are estimated by the equations (Pham et al. 2019b):

$$RMSE = \sqrt{\frac{\sum_{i=1}^n (y_i^{obs} - y_i^{pr})^2}{n}} \quad (25.7)$$

$$MAE = \frac{1}{n} \sum_{i=1}^n (y_i^{obs} - y_i^{pr}) \quad (25.8)$$

$$MAPE = \sum_{i=1}^n \frac{\left| \frac{y_i^{obs} - y_i^{pr}}{y_i^{obs}} \right|}{n} \times 100 \quad (25.9)$$

$$r = \frac{\sum_{i=1}^n (y_i^{obs} - \overline{y_{obs}}) \times (y_i^{pr} - \overline{y_{pr}})}{\sqrt{\sum_{i=1}^n (y_i^{obs} - \overline{y_{obs}})^2} \times \sqrt{\sum_{i=1}^n (y_i^{pr} - \overline{y_{pr}})^2}} \quad (25.10)$$

where y_i^{obs} and y_i^{pr} are measured and predicted Cl^- concentration in observation i , and n is the number of observations. Higher values of r are preferred, i.e. close to 1, means better model performance and regression line fits the data well. Conversely, the lower values of RMSE, MAPE, and MAE values the better model performances.

25.4.5 Generating Groundwater Salinity Map

The results from the three machine learning models are then used to create chloride concentration maps. Prediction maps are constructed with four main steps as follows: (i) interpolating chloride concentrations in groundwater based on prediction results, (ii) reclassifying chloride concentrations based on the drinking water standard from WHO, (iii) estimating the salinity affected area, and (iv) estimating the number of people in each class of salinity affected area. In the first step, the predicted chloride concentrations are interpolated to create maps using the Kriging method by Spatial Analysis Tool in ArcGIS 10.3. In the second step, the interpolated results are reclassified into four main classes, including low ($\text{Cl}^- < 250 \text{ mg/L}$), moderate ($250 \leq \text{Cl}^- \leq 500 \text{ mg/L}$), high ($500 \leq \text{Cl}^- \leq 1000 \text{ mg/L}$), and high ($\text{Cl}^- > 1000 \text{ mg/L}$). In the third step, the salinity affected area for each class of the salinity concentration in groundwater was calculated using geometry functions in ArcGIS 10.3. In the final step, the numbers of people within each salinity affected area was estimated based on the salinity-affected areas and population density.

25.5 Result and Discussion

25.5.1 Feature Selection for the Groundwater Salinity Modelling

The results in Table 25.2 showed the variable importance selection with the permutation based MSE decreased values ranged from 4.03 to 0.69.

In the study area, the top ten most important influencing factors are groundwater level (4.03), vertical hydraulic conductivity (2.50), lithology (2.37), extraction capacity (2.10), horizontal hydraulic conductivity (1.85), distance to saline sources (1.73), well density (1.26), distance to hydraulic windows (0.85), depth of screen wells (0.79), and thickness of aquitards (0.69). The result reveals that groundwater salinization depends not only on hydrogeological features (vertical and horizontal hydraulic conductivities, lithology, paleo-saline sources, hydraulic connection, depth

Table 25.2 Variable importance (permutation based MSE decreased)

No.	Variable	Permutation-based MSE decreased	Number of nodes used	Ranking
1	Groundwater level	4.03	636	1
2	Vertical hydraulic conductivity	2.50	35	2
3	Lithology	2.37	50	3
4	Extraction capacity	2.10	281	4
5	Horizontal hydraulic conductivity	1.85	260	5
6	Distance to saline sources	1.73	379	6
7	Well density	1.26	242	7
8	Distance to hydraulic window	0.85	529	8
9	Depth of screen well	0.79	518	9
10	Thickness of aquitard	0.69	376	10
11	Groundwater temperature	0.64	354	11
12	Age well	0.62	135	12
13	Extraction density	0.59	208	13
14	Distance to fault	0.59	400	14
15	Fault density	0.54	158	15
16	Soil properties	0.35	83	16
17	Distance to main river	0.32	863	17
18	Drain density	0.30	686	18
19	Distance to Drain	0.25	628	19
20	Distance to Sea	0.10	2199	20

of screen well, and thickness of aquitard) but also groundwater extraction practices (groundwater level, extraction capacity, well density). These influencing factors also play an important role in transportation processes of other solutes such as arsenic, fluoride and nitrate in groundwater (Ransom et al. 2017; Winkel et al. 2008; Podgorski et al. 2018). The hydrogeological features influence on moving of saline groundwater from shallow to deeper aquifers (Hung et al. 2019) while groundwater exploitation activities exacerbate groundwater salinization (Hoang and Bäumle 2018; An et al. 2018). The result may also suggest that saline groundwater leaking from upper layers to lower layers is a dominant process, resulting in an increase of chloride concentration in groundwater of the study area. Hydraulically, an increase hydraulic gradient due to groundwater depletion coupled with high vertical hydraulic conductivity, thick aquitard, and high-density gradients cause an increase of vertical flow rate as shown in the following equations (Ma et al. 2015).

$$q_v = -\delta \times K_v \left[\frac{h_{up} - h_{low}}{\Delta L} + \varepsilon \left(\frac{C_{up} + C_{low}}{2} \right) \right] \quad (25.11)$$

$$\delta = \frac{\mu_0}{\mu} = 1 - \xi \times \varepsilon \quad (25.12)$$

where: δ —the ratio of the dynamic viscosity of freshwater to seawater; K_v is a vertical hydraulic conductivity (m d^{-1}); h_{up} and h_{low} denote the freshwater equivalent hydraulic heads at upper and lower layers (m), ΔL is the distance from upper to lower layers (m); μ_0 and μ denote the dynamic viscosity ($\text{kg m}^{-1} \text{d}^{-1}$); ξ is a constant; C_{up} is average observed salinity of pore water in upper aquifers (kg/m^3); C_{low} is observed salinity of pore water in lower aquifers (kg/m^3), and ε is a constant. The similar findings were also observed in other coastal aquifers in the world (Chatton et al. 2016; Cary et al. 2015; Delsman et al. 2014; Larsen et al. 2017), which indicated strong influences of over groundwater exploitation on seawater intrusion in coastal aquifers (Yechieli et al. 2019; Yu and Michael 2019; Han et al. 2015).

The other major influencing factors have permutation based MSE values from 0.64 for groundwater temperature to 0.10 for distance to the sea. It was noted that the distance to the sea had a little score value of 0.10, indicating less contribution to groundwater salinization processes. This result may suggest that direct seawater intrusion from the sea to coastal aquifers of the study is not dominant in the study area.

25.5.2 Model Performance Evaluation and Comparison

In this study, the predictive models for groundwater salinization are built using the training and the testing datasets, drawing upon a total of 215 observation wells and 20 variables. The results of the goodness-of-fit assessment of the three machine learning algorithms-based models including the GO-XGB model, RF model and the GP model for both training and testing steps are shown in Fig. 25.4 and summarized in Tables 25.3 and 25.4, and respectively.

The training model performance (Table 25.3) shows that the GO-XGB model has the lowest value RMSE = 141.042 mg/L, followed by the RF (RMSE = 176.179 mg/L) and GP (RMSE = 176.179 mg/L) models. The similar trend is also observed in MAE and MAPE for the GO-XGB (MAE = 4.864, MAPE = 2.070), RF (MAE = 58.286 mg/L, MAPE = 29.410 mg/L) and GP (MAE = 71.802 mg/L, MAPE = 61.42 mg/L). In contrast, the GO-XGB model has the highest r-value of 0.999 compared to that of RF ($r = 0.786$) and Gaussian Processes ($r = 0.882$).

In the testing step, the results of the predictive models are validated by using the testing dataset consisted of 20% random samples from the original dataset (Fig. 25.4). The testing results show that the GO-XGB model has the highest performance compared to the RF and GP models (Table 25.4). For example, GO-XGB has the best result of $r = 0.787$, followed by the RF model ($r = 0.596$) and the GP model

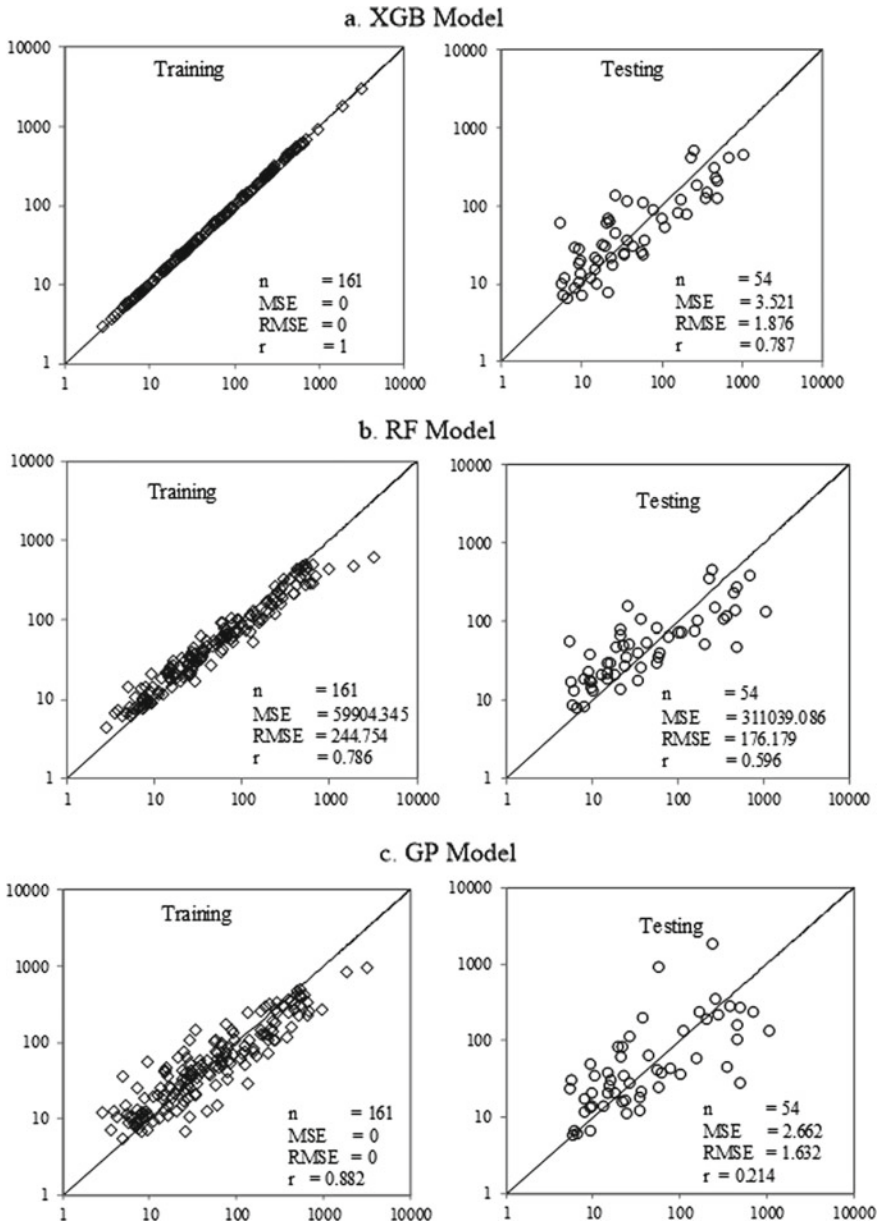


Fig. 25.4 Observed versus predicted chloride concentration for training and test data for **a** GO-XGB, **b** RF, and GP model

Table 25.3 Goodness-of-fit of the ground water salinity models on the training dataset

Statistical metrics	GO-XGB	RF	Gaussian processes
RMSE	18.450	244.754	219.329
MAE	4.864	58.286	71.802
MAPE	2.070	29.410	61.42
r	0.999	0.786	0.882

Table 25.4 Prediction performance of the ground water salinity models using the validation dataset

Statistical metrics	GO-XGB	RF	Gaussian processes
RMSE	141.042	176.179	305.782
MAE	74.993	84.708	127.355
MAPE	87.250	95.780	130.840
r	0.787	0.596	0.214

($r = 0.214$). Similarly, the GO-XGB model shows the lowest values of RMSE = 141.042 mg/L, MAE = 74.993 mg/L, and MAPE = 87.250 mg/L, followed by the RF (RMSE = 176.179 mg/L, MAE = 84.708 mg/L, MAPE = 95.780 mg/L) and GP (RMSE = 305.782 mg/L, MAE = 127.355 mg/L, MAPE = 130.840 mg/L) models.

Overall, the GO-XGB model produces an excellent predictive performance with the highest value of $r = 0.99$ and $r = 0.787$ for training and validation steps among three predictive models. Likewise, this model also has the lowest values of RMSE, MAE, and MAPE compared to the RF and GP models in both training and validation steps.

Although we have considered various influencing factors to provide the accurate prediction of groundwater salinity in a coastal area of the Mekong River Delta, however, the processes of seawater intrusion into fresh aquifers depend not only human activities but also natural variations. Therefore, for broader applicability, these models would be required to include additional influencing factors such as the regional groundwater flow system, tidal fluctuation, climate change, and sea-level rise. Also, the performance of prediction models may have to compare with numerical models and other stochastic models.

25.5.3 Mapping Salt-Groundwater-Affected Area

In general, the average results obtained from the three machine learning models, including the GO-XGB (Fig. 25.5), RF (Fig. 25.6), and the GP models (Fig. 25.7), shows the main salinity-affected region, extending from the My Thanh River to the Central of Soc Trang City. It was noted that the prediction results from GO-XGB model strongly agree with salinity observation in this study (Fig. 25.8) and

previous studies (An et al. 2018). Accordingly, high chloride concentrations which exceed the limited standard for drinking water $Cl^- > 250$ mg/L is predicted in the areas with to paleo-saline sources, high extraction rates, and significant groundwater level depletion. The severely affected areas are the Tran De estuary, the My Thanh river and the central region including Soc Trang city and My Xuyen district where chloride concentrations in wells elevate to 2000 mg/L. Surprisingly, low chloride concentrations ($Cl^- < 250$ mg/L) in groundwater is predicted in coastal areas even if in the production wells located just around 2 km from the sea and at -10.5 m below the mean sea level (m.a.m.sl). Meanwhile, Soc Trang city, which locates far from the sea approximately 40 km, is predicted to have high chloride concentrations in groundwater. This reveals that processes of salinity accumulation in aquifers are very complex, depending not only on natural processes but also human-induced activities.

The spatial distributions of affected areas with moderate and high chloride concentration are relative differences among models. For example, in the GO-XGB model, the affected area is predicted to extend from the coastal line to the central area of the study (Fig. 25.6).

In addition, the profoundly affected area is observed in the substantial groundwater extraction locations. These locations are located close to the paleo-saline groundwater sources coupled, and these areas also have high groundwater extraction rates and significant groundwater level depletion. This indicates that these influencing factors play an essential role in increasing chloride concentrations in groundwater. The similar finding is also in-line with recent studies (Hoang and Bäumle 2019; Tran

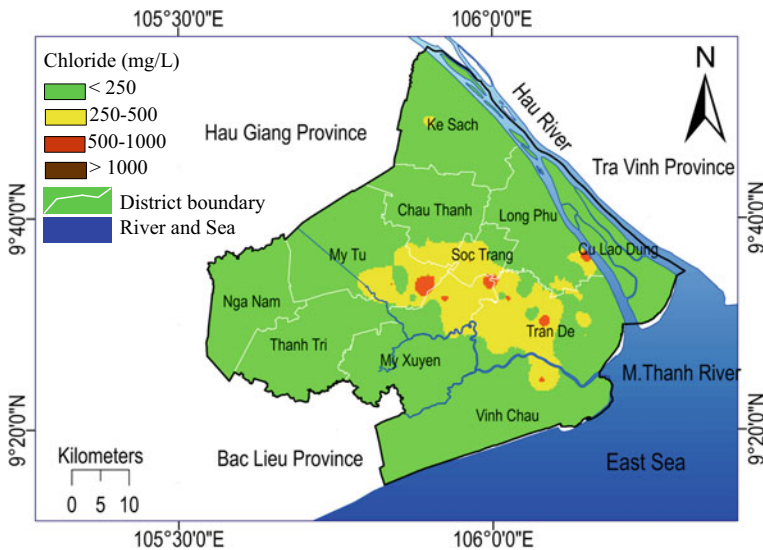


Fig. 25.5 Predicted chloride concentration in groundwater of the study area using GO-XGB model

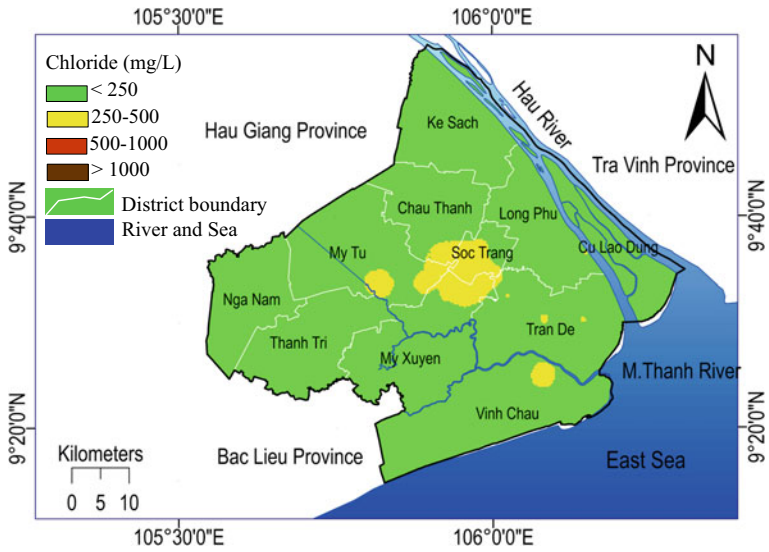


Fig. 25.6 Predicted chloride concentration in groundwater of the study area using RF model

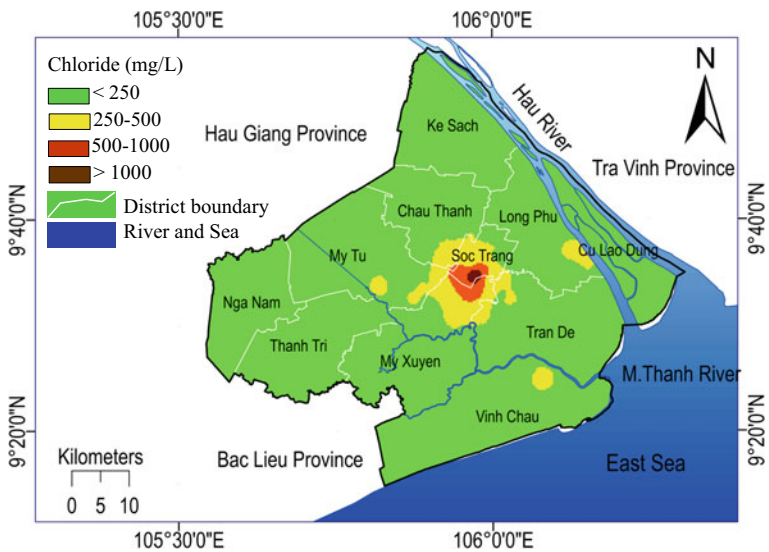


Fig. 25.7 Predicted chloride concentration in groundwater of the study area using GP model

et al. 2019). Conversely, the results from the RF (Fig. 25.6) and the GP models (Fig. 25.7) show that the moderately affected areas are the central area of the study region.

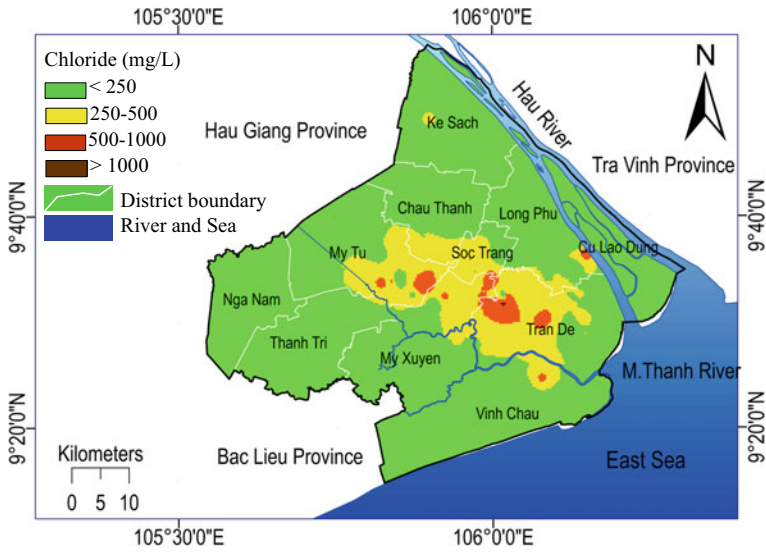


Fig. 25.8 Measured chloride concentration in groundwater of the study area

The three models provide different predictions in the affected area (Table 25.5). The RF model predicted the largest affected area (3118.50 km²) followed by the GP model (3055.35 km²) and GO-XGB (2879.0 km²) with low chloride concentration (Cl⁻ < 250 mg/L). Meanwhile, the largest affected-areas with moderate-high chloride concentration (Cl⁻ = 250–500 mg/L) are observed by the GO-XGB model (433 km²), the GP model (256.65 km²), and the RF model (193.50 km²). Both the GO-XGB model and the GP models predicted the large affected-areas with high (Cl = 500–1000 mg/L) and very chloride concentration (>1000 mg/L) while RF model predicted non-affected areas of high and very high chloride concentration.

25.6 Concluding Remarks

In this study, three advanced machine learning models, including GO-XG, RF, and GP, were employed to predict chloride concentration in groundwater and assess impacts of salinity on water users in a coastal area of the Mekong River Delta, Vietnam. Twenty influencing factors were evaluated using the RF model based on score estimation. The most influenced factors to high salinity are related to both groundwater exploitation (groundwater level depletion, extraction capacity, and well density) and hydrogeological features (vertical hydraulic conductivity lithology, horizontal hydraulic conductivity, distance to the saline source, distance to the hydraulic window, depth of screen well, and thickness of aquitard). This finding confirms

Table 25.5 Predictive results of affected areas (in km²) following four classes of chloride concentration in groundwater

Statistical metrics	Low (Cl < 250 mg/L)	Moderate (250 ≤ Cl ⁻ ≤ 500 mg/L)	High (500 < Cl ⁻ ≤ 1000 mg/L)	Very high (Cl ⁻ > 100 mg/L)	% Affected area
GO-XGB	2879.00	433.00	42.40	0.88	14.0
RF	3118.50	193.50	0	0	6.0
Gaussian processes	3055.35	256.65	34.46	4.86	9.0
Average	3017.62	294.38	25.62	1.91	10.0

previous studies in which groundwater exploitation is one of the most important influencing factors to seawater intrusion in coastal lowland regions.

All three models perform well in predicting the probability of groundwater salinity. However, the GO-XGB model provides the highest accuracy prediction with RMSE = 18.450, MAE = 4.864, MAPE = 2.070, and $r = 0.999$ compared to the GP model (RMSE = 219.329, MAE = 71.329, MAPE = 61.42, and $r = 0.882$) and the RF model (RMSE = 244.754, MAE = 58.286, MAPE = 29.410, and $r = 0.786$). This indicated that GO-XGB model could be a useful tool to predict groundwater salinization in the coastal aquifers.

All three models predicted that approximately 35% of the total population might have to use groundwater with chloride concentration exceeding the WHO drinking water standard ($\text{Cl}^- > 250 \text{ mg/L}$). More seriously, urban areas are close to paleo-saline sources. While the thicknesses of aquitards are thin and groundwater levels deplete quickly, leaking paleo-saline becomes more server and cause groundwater salinization. This is stimulated by the hydraulic connection between aquifers and over groundwater exploitation. Given the rapid increase of water demand, significant groundwater depletion and unpredictable impacts of climate change and sea-level rise, immediate actions must be taken by the water authorities to find a suitable solution to this environmental crisis.

Conflicts of Interest The authors declare no conflict of interest.

References

- Abdelhamid H et al (2016) Simulation of seawater intrusion in the Nile Delta aquifer under the conditions of climate change, vol 47
- An TD et al (2018) Isotopic and hydrogeochemical signatures in evaluating groundwater quality in the Coastal Area of the Mekong Delta, Vietnam. In: Bui DT et al (eds) *Advances and applications in geospatial technology and earth resources: proceedings of the international conference on geo-spatial technologies and earth resources 2017*. Springer International Publishing, Cham, pp 293–314
- Azimi S, Moghaddam MA, Hashemi Monfared SA (2018) Large-scale association analysis of climate drought and decline in groundwater quantity using Gaussian process classification (case study: 609 study area of Iran). *J Environ Health Sci Eng* 16(2):129–145
- Banerjee P et al (2011) Artificial neural network model as a potential alternative for groundwater salinity forecasting. *J Hydrol* 398(3–4):212–220
- Behera AK et al (2019) Identification of seawater intrusion signatures through geochemical evolution of groundwater: a case study based on coastal region of the Mahanadi delta, Bay of Bengal, India. *Nat Hazards* 97(3):1209–1230
- Blasco M, Auqué LF, Gimeno MJ (2019) Geochemical evolution of thermal waters in carbonate—evaporitic systems: the triggering effect of halite dissolution in the dedolomitisation and albitisation processes. *J Hydrol* 570:623–636
- Breiman L (2001) Random forests. *Mach Learn* 45(1):5–32
- Brouwer R et al (2018) Economic valuation of groundwater protection using a groundwater quality ladder based on chemical threshold levels. *Ecol Ind* 88:292–304

- Carretero S et al (2013) Impact of sea-level rise on saltwater intrusion length into the coastal aquifer, Partido de La Costa, Argentina. *Cont Shelf Res* 61–62:62–70
- Cary L et al (2015) Origins and processes of groundwater salinization in the urban coastal aquifers of Recife (Pernambuco, Brazil): a multi-isotope approach. *Sci Total Environ* 530–531:411–429
- Chatton E et al (2016) Glacial recharge, salinisation and anthropogenic contamination in the coastal aquifers of Recife (Brazil). *Sci Total Environ* 569–570:1114–1125
- Chen T, Guestrin C (2016) XGBoost: a scalable tree boosting system. In: Proceedings of the 22nd ACM SIGKDD international conference on knowledge discovery and data mining. ACM, San Francisco, California, USA, pp 785–794
- Chen W et al (2019) Applying population-based evolutionary algorithms and a neuro-fuzzy system for modeling landslide susceptibility. *CATENA* 172:212–231
- Criminisi A (2011) Decision forests: a unified framework for classification, regression, density estimation, manifold learning and semi-supervised learning. *Found Trends Comput Graph Vis* 7(2–3):81–227
- de Graaf IEM et al (2019) Environmental flow limits to global groundwater pumping. *Nature* 574(7776):90–94
- Delsman JR et al (2014) Paleo-modeling of coastal saltwater intrusion during the Holocene: an application to the Netherlands. *Hydrol Earth Syst Sci* 18(10):3891–3905
- Elmahdy SI, Mohamed MM (2013) Influence of geological structures on groundwater accumulation and groundwater salinity in Musandam Peninsula, UAE and Oman. *Geocarto Int* 28(5):453–472
- Essaid HI, Caldwell RR (2017) Evaluating the impact of irrigation on surface water—groundwater interaction and stream temperature in an agricultural watershed. *Sci Total Environ* 599–600:581–596
- Famiglietti JS (2014) The global groundwater crisis. *Nat Clim Chang* 4(11):945–948
- Ferguson G, Gleeson T (2012) Vulnerability of coastal aquifers to groundwater use and climate change. *Nat Clim Chang* 2(5):342–345
- Forrest S (1993) Genetic algorithms: principles of natural selection applied to computation. *Science* 261(5123):872–878
- Friedman JH (2001) Greedy function approximation: a gradient boosting machine. *Ann Stat* 29(5):1189–1232
- Gallardo AH, Marui A (2007) Modeling the dynamics of the freshwater-saltwater interface in response to construction activities at a coastal site. *Int J Environ Sci Technol* 4(3):285–294
- Giambastiani BMS et al (2018) Forest fire effects on groundwater in a coastal aquifer (Ravenna, Italy). *Hydrol Process* 32(15):2377–2389
- Guhl F et al (2006) Geometry and dynamics of the freshwater—seawater interface in a coastal aquifer in southeastern Spain. *Hydrol Sci J* 51(3):543–555
- Guyon I, Elisseeff A (2006) An introduction to feature extraction, in feature extraction. Springer, Berlin, Heidelberg, pp 1–25
- Hall J, Rasmussen C, Maciejowski J (2012) Modelling and control of nonlinear systems using Gaussian processes with partial model information. In: 2012 IEEE 51st IEEE conference on decision and control (CDC)
- Han D, Currell MJ (2018) Delineating multiple salinization processes in a coastal plain aquifer, northern China: hydrochemical and isotopic evidence. *Hydrol Earth Syst Sci* 22(6):3473–3491
- Han D, Post VEA, Song X (2015) Groundwater salinization processes and reversibility of seawater intrusion in coastal carbonate aquifers. *J Hydrol* 531:1067–1080
- Hira ZM, Gillies DF (2015) A review of feature selection and feature extraction methods applied on microarray data. *Adv Bioinform* 2015:1–13
- Hoa PV et al (2019) Soil salinity mapping using SAR Sentinel-1 data and advanced machine learning algorithms: a case study at Ben Tre Province of the Mekong River Delta (Vietnam). *Rem Sens* 11(2):128
- Hoang HT, Bäumle R (2018) Complex hydrochemical characteristics of the middle–upper Pleistocene aquifer in Soc Trang Province, Southern Vietnam. *Environ Geochem Health*

- Hoang HT, Bäuml R (2019) Complex hydrochemical characteristics of the middle-upper Pleistocene aquifer in Soc Trang Province, Southern Vietnam. *Environ Geochem Health* 41(1):325–341
- Hoang LP et al (2019) The Mekong's future flows under multiple drivers: how climate change, hydropower developments and irrigation expansions drive hydrological changes. *Sci Total Environ* 649:601–609
- Isazadeh M, Biazar SM, Ashrafzadeh A (2017) Support vector machines and feed-forward neural networks for spatial modeling of groundwater qualitative parameters. *Environ Earth Sci* 76(17):610–614
- Javadi A et al (2015) Multi-objective optimization of different management scenarios to control seawater intrusion in coastal aquifers. *Water Resour Manage* 29(6):1843–1857
- Jennings PC et al (2019) Genetic algorithms for computational materials discovery accelerated by machine learning. *NPJ Comput Mater* 5(1):46–52
- Johnson NE, Bonczak B, Kontokosta CE (2018) Using a gradient boosting model to improve the performance of low-cost aerosol monitors in a dense, heterogeneous urban environment. *Atmos Environ* 184:9–16
- Kagabu M et al (2020) Describing coseismic groundwater level rise using tank model in volcanic aquifers, Kumamoto, southern Japan. *J Hydrol* 582:124464–14
- Kanagaraj G et al (2018) Hydrogeochemical processes and influence of seawater intrusion in coastal aquifers south of Chennai, Tamil Nadu, India. *Environ Sci Pollut Res* 25(9):8989–9011
- Kaur L et al (2020) Groundwater potential assessment of an alluvial aquifer in Yamuna sub-basin (Panipat region) using remote sensing and GIS techniques in conjunction with analytical hierarchy process (AHP) and catastrophe theory (CT). *Ecol Ind* 110:105850–19
- Khaska M et al (2013) Origin of groundwater salinity (current seawater vs. saline deep water) in a coastal karst aquifer based on Sr and Cl isotopes. Case study of the La Clape massif (southern France). *Appl Geochem* 37:212–227
- Kim IH, Yang J-S (2018) Prioritizing countermeasures for reducing seawater-intrusion area by considering regional characteristics using SEAWAT and a multicriteria decision-making method. *Hydrol Process* 32(25):3741–3757
- Kohavi R, John GH (1997) Wrappers for feature subset selection. *Artif Intell* 97(1):273–324
- Kopsiaftis G et al (2019) Gaussian process regression tuned by Bayesian optimization for seawater intrusion prediction. *Comput Intell Neurosci* 2019:2859429–12
- Lal A, Datta B (2019) Multi-objective groundwater management strategy under uncertainties for sustainable control of saltwater intrusion: Solution for an island country in the South Pacific. *J Environ Manage* 234:115–130
- Lapworth DJ et al (2017) Groundwater quality in the alluvial aquifer system of northwest India: new evidence of the extent of anthropogenic and geogenic contamination. *Sci Total Environ* 599–600:1433–1444
- Larsen F et al (2017) Groundwater salinity influenced by Holocene seawater trapped in incised valleys in the Red River delta plain. *Nat Geosci* 10(5):376–381
- Lee S, Currell M, Cendón DI (2016) Marine water from mid-Holocene sea level highstand trapped in a coastal aquifer: evidence from groundwater isotopes, and environmental significance. *Sci Total Environ* 544:995–1007
- Li Y et al (2016) A fully coupled depth-integrated model for surface water and groundwater flows. *J Hydrol* 542:172–184
- Lim S, Chi S (2019) Xgboost application on bridge management systems for proactive damage estimation. *Adv Eng Inform* 41:100922–14
- Liu Y et al (2018) Geographically weighted temporally correlated logistic regression model. *Sci Rep* 8(1):1417–14
- Ma Q et al (2015) Estimation of seawater–groundwater exchange rate: case study in a tidal flat with a large-scale seepage face (Laizhou Bay, China). *Hydrogeol J* 23(2):265–275
- Ma Y et al (2019a) Characteristics of groundwater pollution in a vegetable cultivation area of typical facility agriculture in a developed city. *Ecol Ind* 105:709–716

- Ma X, Xu F, Chen B (2019b) Interpolation of wind pressures using Gaussian process regression. *J Wind Eng Ind Aerodyn* 188:30–42
- Mahlknecht J et al (2017) Assessing seawater intrusion in an arid coastal aquifer under high anthropogenic influence using major constituents, Sr and B isotopes in groundwater. *Sci Total Environ* 587–588:282–295
- Mahmoodzadeh D, Karamouz M (2019) Seawater intrusion in heterogeneous coastal aquifers under flooding events. *J Hydrol* 568:1118–1130
- Malki M et al (2017) Impact of agricultural practices on groundwater quality in intensive irrigated area of Chtouka-Massa, Morocco. *Sci Total Environ* 574:760–770
- Melloul AJ, Goldenberg LC (1997) Monitoring of seawater intrusion in coastal aquifers: basics and local concerns. *J Environ Manage* 51(1):73–86
- Minderhoud PSJ et al (2017) Impacts of 25 years of groundwater extraction on subsidence in the Mekong delta, Vietnam. *Environ Res Lett* 12(6):064006-13
- Mohanty AK, Rao VVSG (2019) Hydrogeochemical, seawater intrusion and oxygen isotope studies on a coastal region in the Puri District of Odisha, India. *CATENA* 172:558–571
- Nadiri AA et al (2018) Mapping specific vulnerability of multiple confined and unconfined aquifers by using artificial intelligence to learn from multiple DRASTIC frameworks. *J Environ Manage* 227:415–428
- Naghbi SA, Pourghasemi HR, Dixon B (2015) GIS-based groundwater potential mapping using boosted regression tree, classification and regression tree, and random forest machine learning models in Iran. *Environ Monit Assess* 188(1):44–71
- Nam NDG et al (2019) Assessment of groundwater quality and its suitability for domestic and irrigation use in the coastal zone of the Mekong Delta, Vietnam. In: Stewart MA, Coclanis PA (eds) *Water and power: environmental governance and strategies for sustainability in the lower Mekong Basin*. Springer International Publishing, Cham, pp 173–185
- Nishanthiny SC et al (2010) Irrigation water quality based on hydro chemical analysis, Jaffna, Sri Lanka. *Am Eurasian J Agric Environ Sci* 7(1):100–102
- Paine JG (2003) Determining salinization extent, identifying salinity sources, and estimating chloride mass using surface, borehole, and airborne electromagnetic induction methods. *Water Resour Res* 39(3):3–10
- Park J, Kwok CK (2015) Sodium intake and prevalence of hypertension, coronary heart disease, and stroke in Korean adults. *J Ethnic Foods* 2(3):92–96
- Park J, Sandberg IW (1991) Universal approximation using radial-basis-function networks. *Neural Comput* 3(2):246–257
- Pham BT et al (2019a) Hybrid computational intelligence models for groundwater potential mapping. *CATENA* 182:104101–104113
- Pham BT et al (2019b) A novel artificial intelligence approach based on multi-layer perceptron neural network and biogeography-based optimization for predicting coefficient of consolidation of soil. *CATENA* 173:302–311
- Podgorski JE et al (2018) Prediction modeling and mapping of groundwater fluoride contamination throughout India. *Environ Sci Technol* 52(17):9889–9898
- Ransom KM et al (2017) A hybrid machine learning model to predict and visualize nitrate concentration throughout the Central Valley aquifer, California, USA. *Sci Total Environ* 601–602:1160–1172
- Rasmussen CE (2003) Gaussian processes in machine learning. In: Bousquet O, von Luxburg U, Rätsch G (eds) *Advanced lectures on machine learning: ML summer schools 2003*, Canberra, Australia, 2–14, 2003, Tübingen, Germany, 4–16 Aug 2003. Springer, Berlin, Heidelberg, pp 63–71
- Rizeei HM et al (2019) Groundwater aquifer potential modeling using an ensemble multi-adoptive boosting logistic regression technique. *J Hydrol* 579:124172-11
- Rodriguez-Galiano V et al (2014) Predictive modeling of groundwater nitrate pollution using random forest and multisource variables related to intrinsic and specific vulnerability: a case study in an agricultural setting (Southern Spain). *Sci Total Environ* 476–477:189–206

- Roy Dilip K, Datta B (2017) Multivariate adaptive regression spline ensembles for management of multilayered coastal aquifers. *J Hydrol Eng* 22(9):04017031-13
- Sajedi-Hosseini F et al (2018) A novel machine learning-based approach for the risk assessment of nitrate groundwater contamination. *Sci Total Environ* 644:954–962
- Scholkopf B et al (1997) Comparing support vector machines with Gaussian kernels to radial basis function classifiers. *IEEE Trans Signal Process* 45(11):2758–2765
- Sreekanth J, Datta B (2010) Multi-objective management of saltwater intrusion in coastal aquifers using genetic programming and modular neural network based surrogate models. *J Hydrol* 393(3–4):245–256
- Stein S et al (2019) The effect of pumping saline groundwater for desalination on the fresh–saline water interface dynamics. *Water Res* 156:46–57
- Sun Y et al (2016) Technical note: Application of artificial neural networks in groundwater table forecasting—a case study in a Singapore swamp forest. *Hydrol Earth Syst Sci* 20(4):1405–1412
- Tien Bui D et al (2016) Spatial prediction models for shallow landslide hazards: a comparative assessment of the efficacy of support vector machines, artificial neural networks, kernel logistic regression, and logistic model tree. *Landslides* 13(2):361–378
- Tran DA et al (2019) Stable isotope characteristics of water resources in the coastal area of the Vietnamese Mekong Delta. *Isot Environ Health Stud* 55(6):566–587
- Tweed S et al (2018) Impact of irrigated agriculture on groundwater resources in a temperate humid region. *Sci Total Environ* 613–614:1302–1316
- Van Hung P et al (2019) Paleo-hydrogeological reconstruction of the fresh-saline groundwater distribution in the Vietnamese Mekong Delta since the late Pleistocene. *J Hydrol Reg Stud* 23:100594-22
- Vineis P, Chan Q, Khan A (2011) Climate change impacts on water salinity and health. *J Epidemiol Glob Health* 1(1):5–10
- Voss CI, Souza WR (1987) Variable density flow and solute transport simulation of regional aquifers containing a narrow freshwater-saltwater transition zone. *Water Resour Res* 23(10):1851–1866
- Wagner F, Tran VB, Renaud FG (2012) Groundwater resources in the Mekong Delta: availability, utilization and risks. In: Renaud FG, Kuenzer C (eds) *The Mekong delta system: interdisciplinary analyses of a River Delta*. Springer, Netherlands, Dordrecht, pp 201–220
- Walter J et al (2017) The influence of water/rock—water/clay interactions and mixing in the salinization processes of groundwater. *J Hydrol Reg Stud* 13:168–188
- Werner AD et al (2013) Seawater intrusion processes, investigation and management: recent advances and future challenges. *Adv Water Resour* 51:3–26
- Winkel L et al (2008) Predicting groundwater arsenic contamination in Southeast Asia from surface parameters. *Nat Geosci* 1(8):536–542
- Yadav B et al (2018) Data-based modelling approach for variable density flow and solute transport simulation in a coastal aquifer. *Hydrol Sci J* 63(2):210–226
- Yechieli Y et al (2019) Recent seawater intrusion into deep aquifer determined by the radioactive noble-gas isotopes ^{81}Kr and ^{39}Ar . *Earth Planet Sci Lett* 507:21–29
- Yu X, Michael HA (2019) Mechanisms, configuration typology, and vulnerability of pumping-induced seawater intrusion in heterogeneous aquifers. *Adv Water Resour* 128:117–128
- Zeng X et al (2018) Identifying key factors of the seawater intrusion model of Dagou river basin, Jiaozhou Bay. *Environ Res* 165:425–430
- Zhao X et al (2019) Identifying N6-methyladenosine sites using extreme gradient boosting system optimized by particle swarm optimizer. *J Theor Biol* 467:39–47

Chapter 26

Application of Convolution Neural Network for Rapid Flood Mapping Using Sentinel-1 Imagery—A Case Study in Central Region of Vietnam



Hien Phu La and Quan Van Ngo

Abstract Climate change is becoming more and more serious leading to extreme weather events, such as drought, storm, flood, etc. occurring with increasing frequency and unpredictability. In Vietnam, recent historic flood events caused a lot of damage to property and life urgently requested a solution to rapidly map the flood area to help government respond promptly mitigating loss of life. However, floods usually occur when most of the sky is covered with clouds. In such weather condition, satellite radar imagery such as Copernicus Sentinel-1 Synthetic Aperture Radar (SAR) imagery is a valuable data source in flood mapping tasks. This study aims to design a Convolutional Neural Network (CNN) based method which isolates the flooded pixels in freely available Sentinel-1 imagery. The CNN architecture was obtained empirically by modifying the model based on visual inspection on the generated flood masks. The experimental results showed that the pre-trained CNN model provided similar results compared to conventional Google Earth Engine (GEE) based method but significantly reduced the time take to map the flood which allows it to be applied for real-time flood mapping.

Keywords Convolutional neural network · Sentinel-1 imagery · Flood mapping

26.1 Introduction

Flood is a complex weather phenomenon, leaving a lot of heavy loss of property and life in areas directly affected by natural disasters. According to statistics of the Organization for Economic Co-operation and Development (OECD), each year, the world suffers a loss of more than 40 billion USD, affecting approximately 250 million people. The frequency of floods has almost doubled between 2000 and 2009

H. P. La (✉) · Q. Van Ngo
AICOST Team, Thuyloi University, 175 Tay Son, Dong Da, Hanoi, Vietnam
e-mail: laphuhien@tlu.edu.vn

Q. Van Ngo
e-mail: ngovanquan@tlu.edu.vn

compared to the previous decade, and the number of floods between 2010 and 2013 is more than the total number of floods in the 1980s (OECD 2016; Christina 2019). Vietnam is one of the countries with high flood frequency. In recent years, the Mekong River Delta, Central Coastal Delta, and Northern Delta regions have witnessed many historic floods, culminating in the central flood occurring in October and November of 2020. Therefore, timely and accurate mapping and assessment of inundation is urgent not only in Vietnam, but also around the world.

However, floods usually occur when there is a considerable number of clouds in the sky making optic data useless. Therefore, Synthetic Aperture Radar (SAR) imagery is appropriate data set for assessing flood area due to its ability to work independently of day-night and weather conditions. Several algorithms have been proposed to map the flood using SAR data. Among them, thresholding is an efficient and probably the most popular method. It is based on theory that the specular backscattering characteristics of active radar pulses on plain water surfaces and the resultant low signal return. This method is fast and simple, however, it has several drawbacks as it does not consider the spatial context of the image pixels, and strongly depend on the bimodal distribution assumption. Additionally, the algorithm cannot accurately determine flooded area if it is either too small or too large (Landuyt et al. 2019). Another widely used method to map flood is change detection approaches when two-time data of a region are available (Zhao et al. 2019). One of conventional change detection approaches is post-classification comparison between two classified map obtained at two different times. Conventional classification algorithms like Support Vector Machine (SVM) and Neural Network cannot handle the disturbances and distortions existence in the SAR dataset. Whereas, Convolutional Neural Networks (CNN) present an automatic feature extractor connected to a fully connected layer that partition the feature space after removing the uncertainties inherent in the input data. Since flooding can occur in a variety of different environmental settings, the generalizability of many existing methods is highly limited, often requiring the careful intervention of analysts to update parameters and fine-tune results. Such tuning severely limits the speed with which accurate maps can be produced and released for use by disaster response teams (Nemni et al. 2020).

In this paper we attempt to build a pre-trained CNN model, then applied it to rapidly generate flooded map in a portion of Thua Thien Hue province in Vietnam, where heavily affected by consecutive floods in period from September 2020 to October 2020. Additionally, the performance of CNN model for flood mapping was compared to conventional Google Earth Engine (GEE) based method.

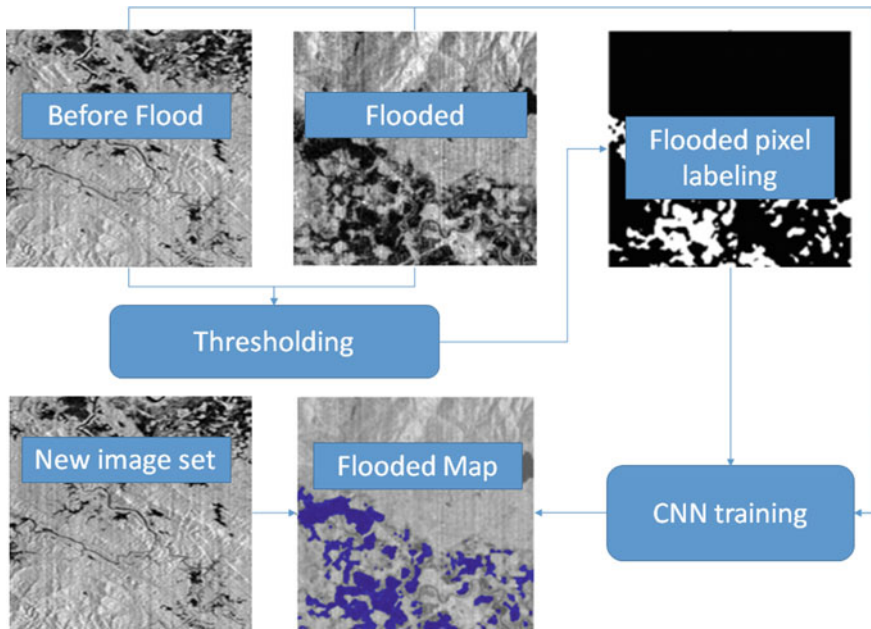


Fig. 26.1 Flowchart of experiment implemented in this research

26.2 Methodology

26.2.1 Workflow

The workflow implemented in this research is illustrated in Fig. 26.1 including three main steps: (1) A set of Sentinel image pairs were processed to get Labeled images containing Flood and Non-Flood pixels based on thresholding method; (2) The labeled images as well as corresponding Sentinel-1 images were used as input data to train CNN model; (3) After training, the CNN model was used to generate flooded map from new Sentinel pair; the flooded map was compared with the map derived from GEE algorithm. The image pair contains one Sentinel image captured before flood and the other captured during flooding.

26.2.2 Data Preprocessing

Normalization and conversion of Sentinel-1 imagery. Since the original Sentinel-1 imagery data type is a double using 8-bytes, but the range of values is small, which can affect the performance of the CNN training. Therefore, the input data was

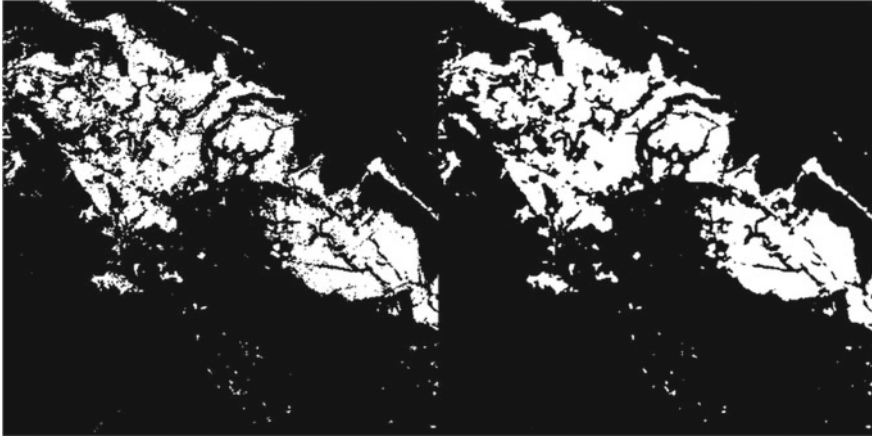


Fig. 26.2 Unprocessed labels (left), post-processed labels (right)

normalized by translating the value and amplifying it by 2 times, and at the same time changing to the uint8 data type taking up 1-bytes to reduce memory usage when learning the model.

Flood pixel labeling and filtering. To train CNN model, it need a labeled dataset which contains images with only flood and non-flood pixels. This dataset was obtained by thresholding on Sentinel-1 imagery pairs covering other areas where flood occurred.

However, the flooded pixel labeling contains noise when detecting flood water with small puddles, these noises can affect the accuracy of the CNN learning model. Therefore, we used a simple algorithm to solve this problem by using 2D Gaussian image filtering (neighborhood smearing), as a results small puddles will be blurred compared to the neighborhood, and the edges of the large ones will not be grainy. The results were illustrated in Fig. 26.2.

Label balancing. In labeled images, there are a large area with no flooded pixels, therefore the labeled data is imbalance. If using this data, the model only needs to classify all pixels as non-flooded to achieve accuracy of 90%. Therefore, to avoid this problem we used following approach: (1) Input image was divided into fixed size squares; (2) Check label balancing, if it is balanced then put it into the model; (3) If it is unbalanced then repeat the Step #1 and #2 until satisfying the balancing threshold.

Criteria to evaluate whether the cropped image having balanced label or not is based on the threshold determined by Eq. (26.1):

$$threshold = Absolute(T_{flooded} - T_{non-flooded}) \quad (26.1)$$

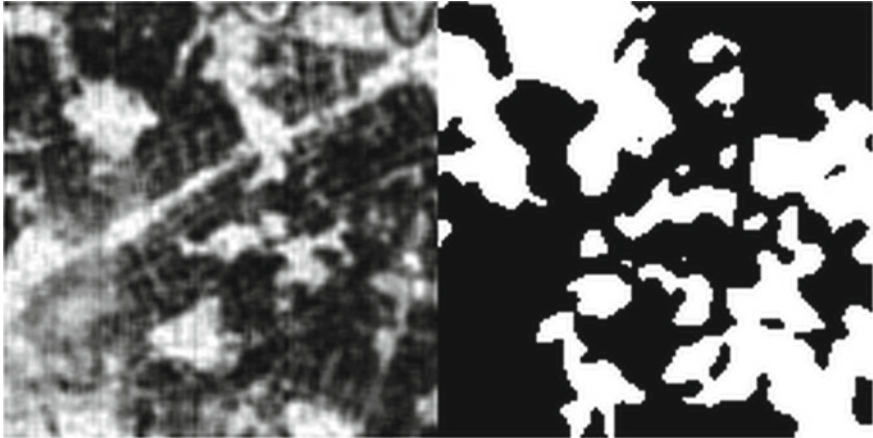


Fig. 26.3 A subset image with balanced label: (left) Sentinel image; (right) corresponding labeled image

where: $T_{flooded}$ is total number of flooded pixels in the sub-image; $T_{non-flooded}$ is total number of non-flooded pixels in the sub-image.

The higher the threshold, the easier it is for the cropped image to be included in the model. In this paper, the threshold value was 0.5, which means that in the worst case 1 class occupied 0.75% of the cropped image and the other class occupied 0.25% of the area (Fig. 26.3).

Generate auxiliary data using Image Data Augmentation (IDA). IDA is a method to generate more imagery data when training a model. It uses simple image processing methods such as translation, rotation, scaling, flipping, random cropping, noise generation, color shift, and degree conversion. contrast. This method is applied when the input data collected is small. In this research, two image processing methods are applied to enhance the imagery are random translation, random rotation and image flip (Shorten and Khoshgoftaar 2019).

26.2.3 Unet Structure of CNN for Flood Mapping

Introduction to Unet. Unet introduced in 2015 is a convolutional neural network architecture for the semantic segmentation of images. Unet can localize and differentiate the feature by per-pixel classification, so input and output are the same size. This architecture is widely used in medicine such as muscle and blood vessel image segmentation; X-ray segmentation of benign cells with cancer (Ronneberger et al. 2015).

The entire architecture does not use a fully connected layer, so it is completely different from the neural network structure for conventional labeling problems. To predict a pixel in the border region of the image, the lost information is extrapolated by symmetric reflection through the network. This layered architecture is important to apply the network to large images, because otherwise the resolution will be limited by the Graphics Processing Unit (GPU) memory.

The Unet architecture include two important block which are Encoder and Decoder. When building a Unet model, there is a top concern that is the encoder depth. The greater the depth, the model explodes with the number of parameters to be calculated, and the length and width of the image are halved, but the number of filters is doubled to be able to extract the features (McGlinchy et al. 2019). Therefore, choosing appropriate the encoder depth can optimize the model's performance.

Encoder block. Unet's Encoder is a set of neural network layers in pairs: the convolutional layer—the activation function layer and finally the pooling layer (e.g. MaxPooling). In addition to the first block of the network, which receives information directly from the input image, the remaining blocks all start with a pooling layer to reduce the dimension of the image. The encoder block is used to reduce the length and width of the image and extract features from the original large image.

Decoder block. The decoder block is also a set of neural network layers. The decoder block, in addition to enhancing the dimensionality of the image, also performs a symmetric connection with the last neuron layers of the encoding to recover the original information of the image lost when pooling is performed. In other words, the decoding block turns the features into image which is classified or predicted label with high accuracy due to the information from the symmetric join.

Unet network architecture diagram. Diagram showed in Fig. 26.4 is the Unet network architecture built for experiment of this research. The Unet network has an encoding depth of 4, this value allows the CNN model to learn and find the imagery features and with this depth value, the model's complexity is also optimal.

Model training and application. The environment used to train the CNN model is Matlab language and toolkit version 2020b running on Microsoft Windows 10; hardware configuration: Intel Core i5-9400 CPU with 6 cores and speed of 2.9 GHz (up to 4.1 GHz), 16 GB RAM, Nvidia GTX 1660 Ti 6 GB GPU.

After training, the CNN model was used to predict flood pixel on new images. In order to predict a large image, the original image is clipped into sub-image which has same size as the trained model. Then the output images are combined to get an output image with the same size as the original satellite image (Fig. 26.5).

26.2.4 Performance Assessment of CNN-Based Method

Because, the flood had occurred a long time ago, its footprint is no longer exist in the ground. Therefore, we cannot have ground truth data for accuracy assessment

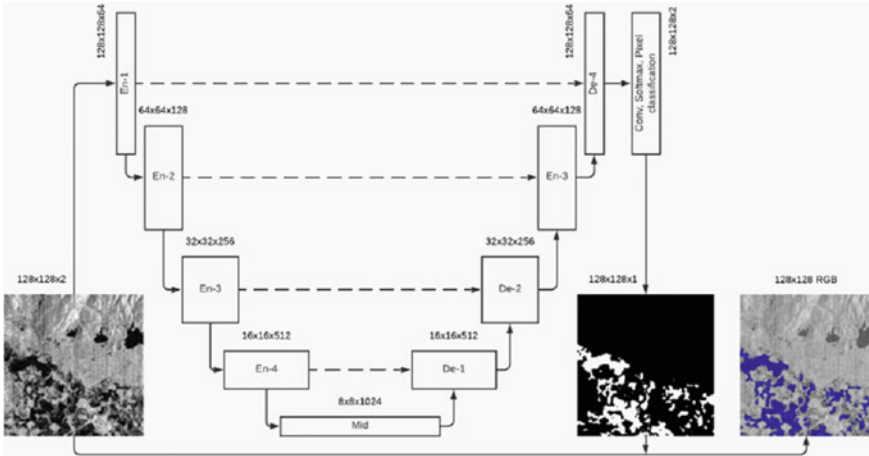


Fig. 26.4 CNN-Unet architecture

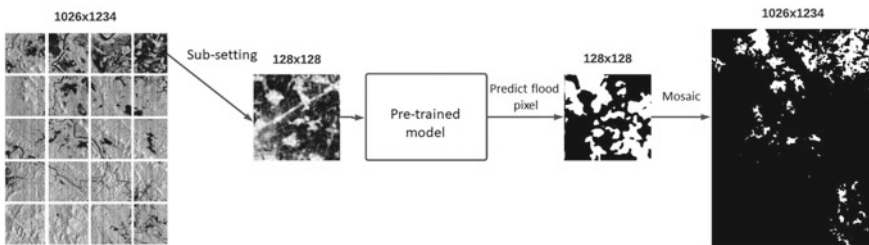


Fig. 26.5 Application of pre-trained model on Sentinel image

of CNN-flood map. Additionally, the purpose of this manuscript is to assess the possibility of using pre-trained CNN for rapid flood mapping which is very useful in early stage of flooding when field data is not available. Meanwhile, the United Nation (UN) has recommended to use GEE for flood mapping using Sentinel-1 SAR data (United Nation 2020). The accuracy of GEE-Flood map has been assessed in many researches such as Faizan and Palanisamy (2021), Kurapati et al. (2020), Kumar et al. (2022) and been proved to be reliable results (Faizan and Palanisamy 2021; Kurapati et al. 2020; Kumar et al. 2022). Therefore, to overcome the lack of ground truth data, we used GEE-based results for assessing CNN-based method’s performance by comparing the time take to generate the flood maps and the match between the two maps.

26.3 Study Area and Materials

26.3.1 Study Area

This research focuses on generating flood map covering a portion of Thua Thien Hue province, a coastal province located in the North Central region of Vietnam. Terrain of Thua Thien Hue has pretty clear hierarchical structure: the west area has mountain terrain stretching from Viet-Laos border to Danang city; whereas, the east and north east areas are river delta and flat land, where was heavily affected by consecutive floods in September–October 2020. Therefore, the experiment of flood mapping was focused on this area. The location of Thua Thien Hue province denoted by red polygon and a sub Sentinel-1 image captured on 10 October 2020 used in the experiment was shown in Fig. 26.6.

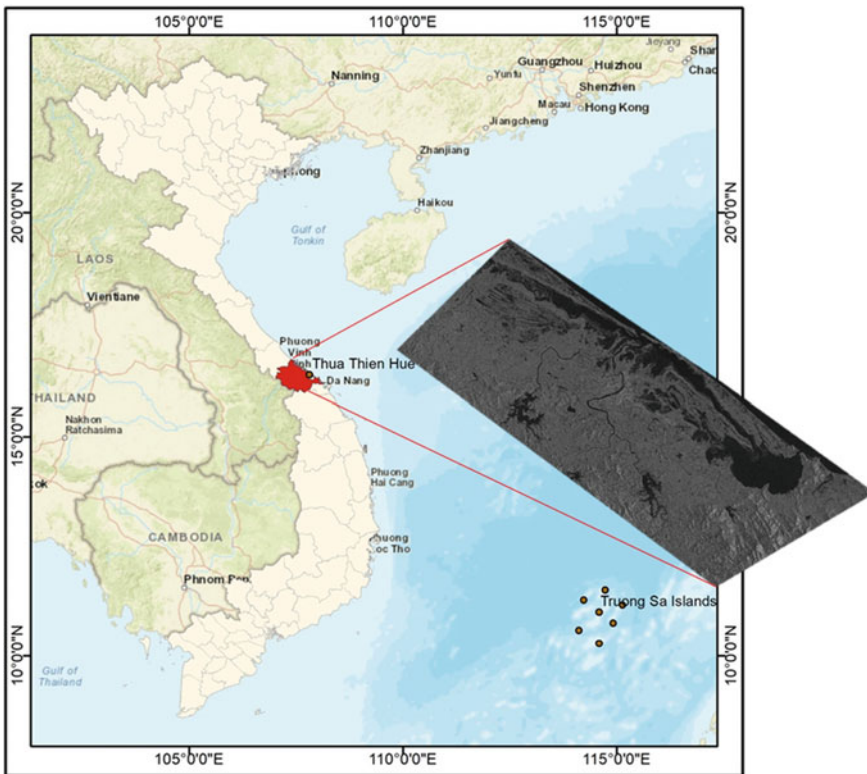


Fig. 26.6 Location of Thua Thien Hue province in Vietnam and a sub Sentinel-1 image captured on 10 October 2020

Table 26.1 Sentinel images used in this research

Data set	Location	Date		Number of image-pair
		Before flood	Flood	
Training	Central area of Ha Tinh City, Ha Tinh	8/8	3/10, 27/10, 8/11	15
	North west area of Ha Tinh City, Ha Tinh	8/8	27/10, 8/11, 20/11	
	Quang Nam Province	3/8	10/10, 28/10, 9/11	
	Quang Ngai Province	3/8	29/10, 15/11, 22/11	
	Quy Nhon City, Binh Dinh	3/8	11/10, 29/10, 10/11	
Validation	North East area of Nghe An Province	6/8	2/11, 8/11	3
	Vinh City, Nghe An	6/8	8/11	
Testing	Huê	8/8	10/10, 29/10, 15/11, 27/11	4

26.3.2 Materials

In order to train the CNN model a set of Sentinel cross-polarization (VH) image-pair were collected by GEE script. These images cover central regions of Vietnam, where affected by consecutive floods in September–October 2020. Fifteen of them were used for training, three ones were used for validation and four images covering a portion of Thua Thien Thue affected by the floods captured on October 10th, October 29th, November 15th and November 27th were used to test the model. The details of data used in this research were listed in Table 26.1.

26.4 Results and Discussion

The CNN training process is illustrated in below graph including the accuracy graph (top) and the error graph (bottom) (Fig. 26.7).

The model took about 15 min to load and normalize the data and almost 40 min to learn. With the error formula used as cross entropy, the precision in terms of the pixel labels, the model quickly increases in accuracy and reduces the error. After running the model training for about 21 epochs, we actively stopped learning, because after studying for the 467th time, the test accuracy of the model was good enough (94.51%) and the model was stable.

At the end of training, the model has a test accuracy of 94.5%, the test error is 0.1095 (bits). The size when saving the CNN model is nearly 62 MB, much lower than the theoretical level (about 120 MB).

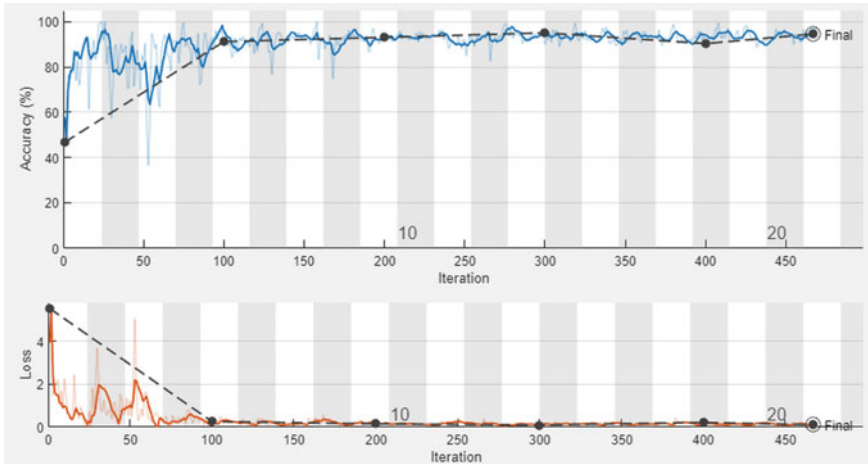


Fig. 26.7 Training process using Matlab tool

After training, the model was used to predict flood area in Thua Thien Hue at four different times: October 10th, October 29th, November 15th and November 27th. In this period, Hue was heavily affected by the floods. The data on this area does not participate in the learning process of the model, but participates in the assessment process. However, the field measured flood map is not available, the test results are compared with the flood image obtained by GEE script. After running the image comparison, the obtained statistics are as Table 26.2. The average overall accuracy and average intersection over union (IOU) is very high, over 98% and 0.9 respectively. It shows that the CNN model has high reliability and accuracy in flood mapping from satellite images.

Figure 26.8 illustrated the Sentinel image superimposed with flood labels (in blue). The image was rotated and cropped to focus on key areas for visual comparison.

As can be seen in the above figure, the detected flood water area is not falsely positive with natural waters, rivers and lakes. However, in land area, there were some misdetections, but mostly noise or small puddles. Large bodies of water are accurately predicted in terms of shape and area. The performance of CNN was also compared to GEE script as Table 26.3. Compared to GEE method, the pre-trained

Table 26.2 Statistics of comparison results

No.	Date	Area of flood region (ha)	Overall accuracy (%)	Average IOU
1	10/10/2020	36,674	98.32	0.9175
2	29/10/2020	29,610	98.51	0.9183
3	15/11/2020	28,116	98.56	0.9019
4	27/11/2020	18,725	99.11	0.8655
Mean			98.625	0.9008

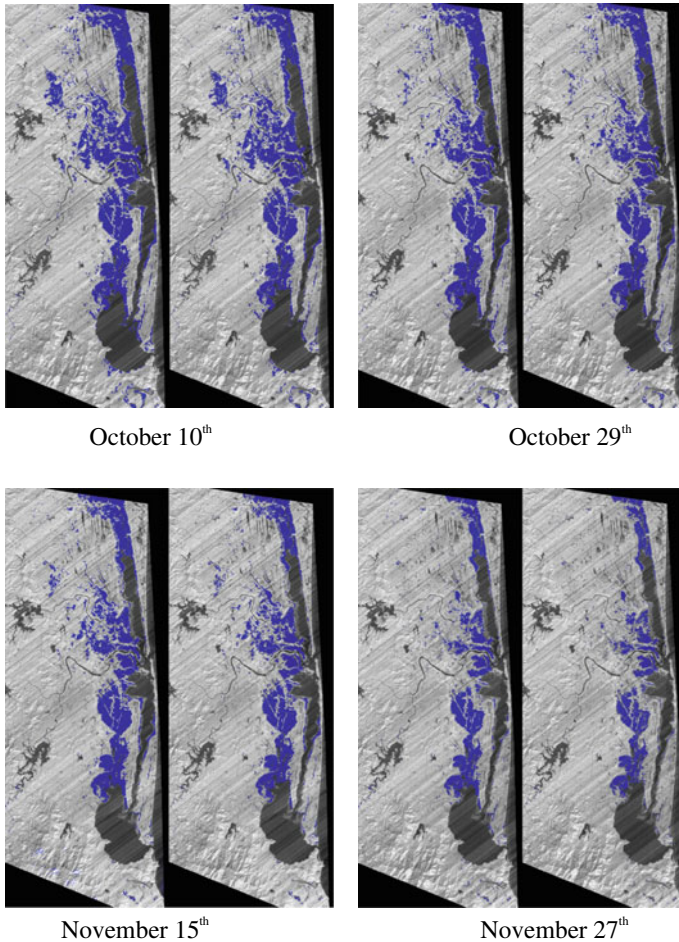


Fig. 26.8 Comparison between CNN-flood map (left) and GEE-flood map (right)

CNN model demonstrates a high performance through which it can completely replace the GEE algorithm and still give almost the same result.

As can be seen in Table 26.3, the prediction time to map the flood was incredibly impressive. It is even much shorter if a more powerful computer is used. With a very

Table 26.3 Comparison between CNN and GEE method for flood mapping

Criteria	GEE	CNN
Training	Not required	105 min using GPU
Mapping 4 flood map covering area of 2800 km ² in Thua Thien Hue	113 min using Google Earth Engine on Chrome Web browser	Approximately 37 s using Matlab

short running time, the model can detect the area affected by flooding in real time. The potential of the model can be applied to the flood warning system, avoiding floods for people and vehicles in the vicinity; in addition, it is also possible to promptly notify the rescue force with a rescue plan; blocking the route divided by floods; provide statistics in the area to assess topography, damage, and localities to take preventive measures in the following year.

Although the number of training satellite images for the model is not much (15 training image pairs, 3 validate image pairs), and they were acquired in a short period of time. Whereas, the specific requirement for deep learning problems is that it requires large amounts of data (e.g. from several thousand images per label) to train. However, by applying the image enhancement method as mentioned in Sect. 26.2, this problem can be solved. As a result, the CNN-Flood maps were almost the same as the GEE-Flood maps.

However, the CNN model is too simple, the Unet network architecture is not deep enough and has many weights to learn features from the image. Even though 385 weight updates have passed, the training accuracy has not improved further and the test accuracy has been destabilized. Therefore, to improve the model accuracy, it is needed to collect more data, add more scenarios in other flood areas in Vietnam or in the world or at different flood times. Additionally, we can increase the depth of the Unet network when solving multi-label, multi-channel image problems because if the model is simple, it may not be able to learn the features from the image.

26.5 Conclusion

The research results show that the CNN model is really useful for flood identification. Comparing to GEE-Flood maps, the highest value of overall accuracy and average IOU is 99.11% and 0.9183, respectively. Meanwhile, the average overall accuracy and average IOU is also very high, over 98% and 0.9 respectively. Additionally, the pre-trained CNN took only 37 s to generate a flood map. It means that using the pre-trained model, we can map the flood areas in real time, as a result the model can be applied to the flood warning system, avoiding floods for people and vehicles in the vicinity. Based on the real time flood map, locality can take timely response measures which can significantly help minimizing damage to people and property.

However, the data used in this research are still locally specific for a short period of time (i.e. October–November 2020) and are not representative of generalized flood data. Additionally, due to the lack of field data, the results were only compared to GEE-Flood maps. Therefore, it is necessary to collect more historical data and ground truth data as well as increasing the network deep to improve the pre-trained model accuracy.

Acknowledgements This research is funded by Thuyloi University.

References

- Christina N (2019) Flood, facts and information. <https://www.nationalgeographic.com/-environment/naturaldisasters/floods/#:-:text=Floods%20cause%20more%20than%20%2440,than%20100%20people%20a%20year>
- Faizan M, Palanisamy G (2021) Mapping of flood areas using Sentinel-1 synthetic aperture radar (SAR) images with Google Earth Engine cloud platform—a case study of Chamoli district, Uttarakhand, India. In: 3rd intercontinental geoinformation days (IGD). Mersin, Turkey, pp 18–21
- Kumar H, Karwariya SK, Kumar R (2022) Google earth engine-based identification of flood extent and flood affected paddy rice fields using Sentinel-2 MSI and Sentinel-1 SAR data in Bihar State, India. *J Indian Soc Rem Sens* 50(5):791–803
- Kurapati PV, Babu A, Rajosarimalala ST, Pyla KR (2020) Flood mapping and damage assessment using sentinel-1 & 2 in Google Earth Engine of Port Berge & Mampikony districts, Sophia region, Madagascar. In: Proceeding of 41st Asian conference on remote sensing (ACRS), pp 1–9
- Landuyt L, Van Wesemael A, Schumann GJP, Hostache R, Verhoest NEC, Van Coillie FMB (2019) Flood mapping based on synthetic aperture radar: an assessment of established approaches. *IEEE Trans Geosci Remote Sens* 57:722739
- McGlinchy J, Johnson B, Muller B, Joseph M, Diaz J (2019) Application of UNet fully convolutional neural network to impervious surface segmentation in urban environment from high resolution satellite imagery. In: IGARSS 2019–2019 IEEE international geoscience and remote sensing symposium, pp 3915–3918
- Nemni E, Bullock J, Belabbes S, Bromley L (2020) Fully convolutional neural network for rapid flood segmentation in synthetic aperture radar imagery. *Remote Sens* 12:2532
- OECD Publishing (2016) Financial management of flood risk. https://read.oecd-ilibrary.org/finance-and-investment/financial-management-of-flood-risk_9789264257689-en#page14
- Ronneberger O, Philipp Fischer P, Brox T (2015) U-Net: convolutional networks for biomedical image segmentation. [arXiv:1505.04597](https://arxiv.org/abs/1505.04597)
- Shorten C, Khoshgoftaar TM (2019) A survey on image data augmentation for deep learning. *J Big Data* 6:60
- United Nation (2020) In detail: recommended practice: flood mapping and damage assessment using Sentinel-1 SAR data in Google Earth Engine. <https://un-spider.org/advisory-support/recommended-practices/recommended-practice-google-earth-engine-flood-mapping/in-detail>
- Zhao M, Ling Q, Li F (2019) An iterative feedback-based change detection algorithm for flood mapping in SAR images. *IEEE Geosci Remote Sens Lett* 16(2):231–235

Chapter 27

WebGIS and Random Forest Model for Assessing the Impact of Landslides in Van Yen District, Yen Bai Province, Vietnam



**Xuan Quang Truong, Nhat Duong Tran, Nguyen Hien Duong Dang,
Thi Hang Do, Quoc Dinh Nguyen, Vasil Yordanov, Maria Antonia Brovelli,
Anh Quan Duong, and Thanh Dong Khuc**

Abstract Van Yen district in Yen Bai province of Vietnam is one of the most affected areas indicating high and very high potential of landslide occurrences. WebGIS technology is useful for dissemination of the geographical information related to landslides. To this aim, this paper provides a landslide information system for Van Yen district of the Yen Bai province. The paper firstly provides a landslide susceptibility

X. Q. Truong
Hanoi University of Natural Resources and Environment, Hanoi, Vietnam
e-mail: txquang@hunre.edu.vn

N. D. Tran (✉) · N. H. D. Dang
University of Science and Technology of Hanoi, Hanoi, Vietnam
e-mail: duongtn.bi9081@st.usth.edu.vn

T. H. Do
Osaka City University, Osaka, Japan

Q. D. Nguyen
Vietnam Institute of Geosciences and Mineral Resources, Hanoi, Vietnam

V. Yordanov · M. A. Brovelli
Department of Civil and Environmental Engineering (DICA), Politecnico di Milano, Piazza
Leonardo da Vinci 32, Milano, Italy
e-mail: vasil.yordanov@polimi.it

M. A. Brovelli
e-mail: maria.brovelli@polimi.it

M. A. Brovelli
Istituto Per Il Rilevamento Elettromagnetico Dell'Ambiente, CNR-IREA, via Bassini 15, Milano,
Italy

A. Q. Duong
Hanoi University of Mining and Geology, Hanoi, Vietnam

T. D. Khuc
Hanoi University of Civil Engineering, Hanoi, Vietnam
e-mail: dongkt@huce.edu.vn

map produced using a Random Forest-based model. Along the process, a landslide inventory from three investigations of 2013, 2017, and landslides along national road 32 and provincial road 163 (collected in November 2021) was considered. Additionally, thirteen factors were used in the model as variables including geological data, DEM (digital elevation model), slope, aspect, plan curvature, profile curvature, stream power index, topographic wetness index, fault network, river network, road network, land use-land cover data, and Sentinel-2 based NDVI (normalized difference vegetation index). The model was validated based on confusion matrix, and gave an excellent accuracy of 91.33%. Finally, WebGIS was created using open-source technologies such as Leaflet, Openlayers, Geoserver, PostgreSQL as the database management system, and PostGIS as it is plugin for spatial database management. WebGIS not only contains information relevant to landslides, but it also combines the landslide susceptibility map with population data in order to assess exposure for warning purposes.

Keywords Landslide · Van Yen district · Random Forest · WebGIS

27.1 Introduction

Landslides are among the most destructive geological hazards that contribute to the history of natural disasters all over the world (Miao et al. 2022). Which brings potential risks to people's lives and assets, also in terms of financial resources to recover the damaged areas and maintain their stability (Habumugisha et al. 2022; Barančoková et al. 2021). Landslides directly impact on the geomorphology as a consequence of active natural factors (geological structure, landforms, climate, etc...), and also artificial factors (human activities) (Qi et al. 2021). In Vietnam, complex terrain and geographical conditions divide the whole country into different climate regions, and each region is affected by several typical natural disasters. Landslides were identified to occur in many regions of Vietnam with severity from light intensity to severe intensity. Additionally, it is known that storms, floods and flash floods are the ones to occur with extreme severities (WCDR 2005). From this point of view, rainfall is considered to be one of the most influencing factors that is the cause of most of landslides (Tien Bui et al. 2012). In the context of this research, focus will be on the northeast mountainous region of Vietnam where flash floods and landslides are the most common hazards that occurred with very high severity according to the recent reports as given in Table 27.1 by FAO in 2012 (FAO 2012) and MONRE in 2017 (MONRE 2017).

For the last four decades, because of the unpredicted impacts of landslides, landslide susceptibility mapping has been a really interesting research topic and has become dominant topic in many articles around the world. Most studies use quantitative statistical methods or model-based methods as tools to generate such maps. Among them, there are methods such as multivariate method (Carrara 1983; Lee and Pradhan 2007; Bui et al. 2011), method using neural networks or fuzzy sets (Tien Bui

Table 27.1 Natural disasters and its occurrence frequency in each region of Vietnam

Disasters	Northwest mountainous region	Northeast mountainous region
Storms	Light	Severe
Flood	Very severe	Very severe
Flash flood and landslide	Very severe	Very severe
Whirlwind	Very severe	Very severe
Drought	Severe	Severe
Inundation	None	None
Forest fire	Very severe	Very severe
Earthquake	Severe	Severe
Failure of water reservoir	Severe	Severe

Source FAO (2012), MONRE (2017)

et al. 2012; Kanungo et al. 2006; Yilmaz 2009); some other studies use method of deterministic models or process models based on the laws of physics to calculate the slope stability, thereby interpolating the landslide susceptibility map of the study area (Montgomery and Dietrich 1994; Claessens et al. 2007). However, recent research works are focusing on random forest algorithm which is an useful tool for mapping and predicting models in the scope of assessing the impacts of natural disasters (Yordanov and Brovelli 2021). Landslide susceptibility modelling using GIS-based approach with the comparisons between artificial intelligence methods that Random Forest gave the best result among all which gives the highest accuracy (Zhao et al. 2022). Zhao et al. (2020), Shahzad et al. (2022), Yu et al. (2022), Chang et al. (2019), together show that Random Forest was presented as a potential algorithm performing good landslide susceptibility maps.

In Vietnam, landslides occurred with high frequency in the northern mountainous region where Van Yen is the one of the districts of the Yen Bai province most affected by landslides. The data used in the landslide susceptibility mapping is generated using GIS tools and plugins in QGIS software. Accordingly, the input data includes historical landslide locations recorded in 2013, 2017, and landslides along national road 32 and provincial road 163 (collected in November 2021); geological map provided by Vietnam Institute of Geosciences and Mineral Resources (VIGMR); digital elevation model; road network, river network, fault network maps, land use-land cover data, and normalized difference vegetation index map (NDVI) derived from Sentinel-2 imagery; and processing-based generations of binary hazard labels, slope, aspect, plan curvature, profile curvature, topographic wetness index, and stream power index. With the plugin import tool in QGIS, a plugin was adopted and imported based on R language and relying on the basic functions of the R ModelMap package (Freeman et al. 2018). The map is validated against the concept of confusion matrix (Kulkarni et al. 2020) to calculate the accuracy and ROC–AUC of the model.

Finally, in order to investigate population exposure for warning purposes, WebGIS was implemented using open-source technologies such as Leaflet, Openlayers,

Geoserver, PostgreSQL as the database management system, and PostGIS as its plugin for spatial database management. WebGIS will be used not only for data visualization and dissemination purpose but it also presents susceptibility map with the population data in order to assess exposure for warning purposes.

27.2 Methodology

27.2.1 Study Area

In this study, Van Yen district of the Yen Bai province is chosen for assessing the impacts of landslides, and to estimate the number of people exposed to landslide hazards. Locating in the moonsoon region of Vietnam, particularly northeast mountainous region, Van Yen district has geographical coordinates from 104°23' E longitude to 104°23' W longitude, and from 21°50'30" to 22°12' N latitude (<https://vanyen.yenbai.gov.vn/gioi-thieu/gioi-thieu-chung>), covers an area of 1389 km² with a total number of people of 129,679 according to the complete results of the 2019 Vietnam population and housing census in 2019 (General Statistics Office of Vietnam 2019).

Van Yen district is also divided into 25 administrative units, of which one town Mau A. The rest units are 24 rural communes, namely An Binh, An Thinh, Chau Que Ha, Chau Que Thuong, Dai Phac, Dai Son, Dong An, Dong Cuong, Lam Giang, Lang Thip, Mau Dong, Mo Vang, Na Hau, Ngoi A, Phong Du Ha, Phong Du Thuong, Quang Minh, Tan Hop, Vien Son, Xuan Ai, Xuan Tam, Yen Hop, Yen Phu, Yen Thai (Fig. 27.1).

Topography in Van Yen is complex, with high hills and high mountains up to nearly 2000 m above sea level, the terrain is strongly divided with flows of the red river. Besides, the climate is tropical hot and humid, thus dividing the whole district into different climate sub-regions. Humidity is usually over 80% and has an average rainfall of 1800 mm per year. With such climate characteristics, the farming types of Van Yen are also very diverse, which includes typical types such as: rice cultivation, cash crops and fruit trees, and cinnamon cultivation (<https://vanyen.yenbai.gov.vn/gioi-thieu/gioi-thieu-chung>).

27.2.2 Data Used

Landslides are predisposed by many environmental factors including natural ones and human-based ones. These factors, can become triggering factors at any time and can simultaneously affect a mass of matter causing it to slide down under the influence of gravity, which is the concept of landslides (Highland and Bobrowsky 2008) that has been mentioned in previous studies (Habumugisha et al. 2022; Dechkamfoo et al.

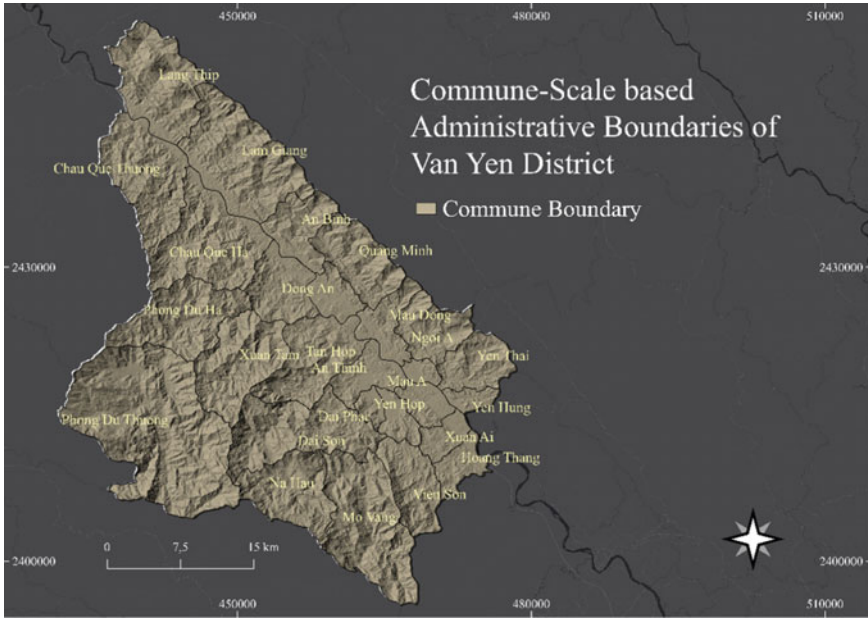


Fig. 27.1 Van Yen district and its administrative divisions

2022; Sharma et al. 2021). For that reason, landslide susceptibility mapping also depends on environmental factors (Rabby et al. 2022; Liu et al. 2022; Harmouzi et al. 2021; Rong et al. 2021). Thirteen environmental factors have been adopted and generated, including geology, digital elevation model, road buffer map from road network, river buffer map from river network, fault buffer map from fault network, normalized difference vegetation index (NDVI), slope, aspect, plan curvature, profile curvature, topographic wetness index, and stream power index.

27.2.2.1 Landslide Inventory

Landslide inventory is an essential factor in assessing the landslide susceptibility of a study area (Bordoni et al. 2020; Du et al. 2020; Zieher et al. 2016). 302 samples of landslides annotated with their natural or human-triggered agents were collected by criteria in the framework of a national project in 2013 and updated again in 2017. This dataset is based on several different evaluation criteria including both fieldwork and satellite image interpretation. Structures in terms of shape, size, chromatogram, identifying features, topographical structure were set out to compare with satellite images, thereby mapping the true landslides.

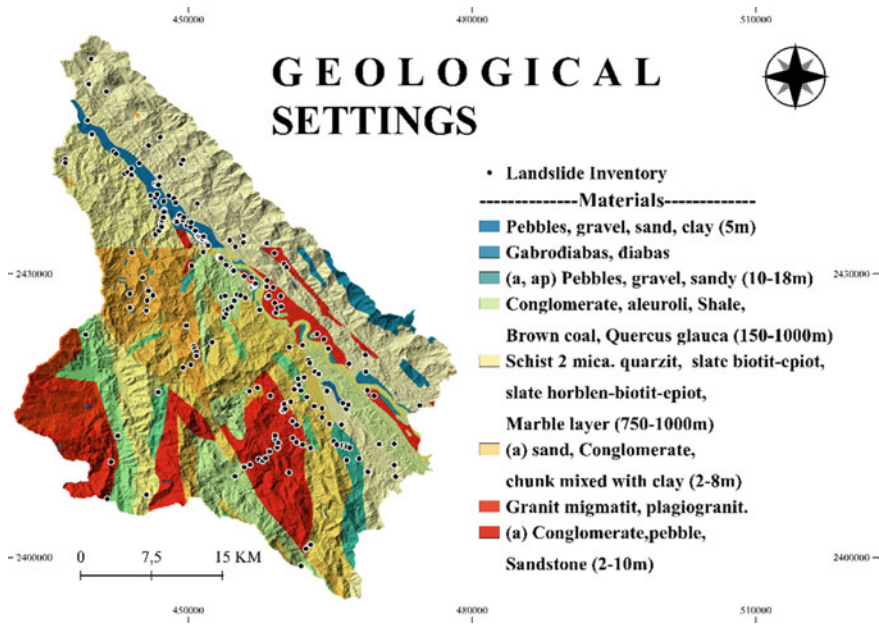


Fig. 27.2 1:200,000-scaled geological settings with the most hazardous materials labeled

27.2.2.2 Geological Settings as Lithology Information

Geological information is one of important factors in landslides studies (D’Amato Avanzi et al. 1996; Cui et al. 1933; Guerriero et al. 2021). Depending on the weathering properties of geological layers, it is possible to estimate the possibility of landslide occurrences in an area. Normally, geological layers that are weathered under the influence of their own weight or by external forces tend to separate and fail, thus causing landslides. Geological information is provided by the Vietnam institute of geosciences and mineral resources at a moderate scale of 1:200,000 (Fig. 27.2). Which also effect on the accuracy of landslide susceptibility model in the study area. In the study area, the most common types are of different stratigraphic forms such as Cha Pha, Da Dinh, Ngoi Thia formations, along with granite minerals and bedrock layers of the form gabbro, gabrodiabas, diabas or quartz-slate. In the areas of limestone, almost no landslides occur.

27.2.2.3 Topographic Factors

In this study, 12.5 m–DEM from alospalsar was used to create landslide susceptibility map. Four variables including slope, aspect, profile curvature, plan curvature (Fig. 27.3) were also calculated based on the 9-parameter-2nd order polynom method introduced by Zevenbergen and Thorne (1987). Specifically, from the original full

quadratic surface equation with 6 parameters (Evans and Chorley 1972), Zevenbergen and Thorne modified it to an equation with 9 parameters including Z_1-Z_9 that defined 9 lagrange polynomials a-i presented in Eq. (27.1):

$$Z = ax^2y^2 + bx^2y + cxy^2 + dx^2 + ey^2 + fxy + gx + hy + i \quad (27.1)$$

Slope is calculated as Eq. (27.2) by the first derivative of the Eq. (27.1) around the center point ($x = y = 0$). Aspect is the maximum-slope direction at the smallest theta angle, and this angle is determined when Eq. (27.3) takes the first derivative and to be solved. Finally, profile curvature, and plan curvature are also determined in Eqs. (27.4) and (27.5):

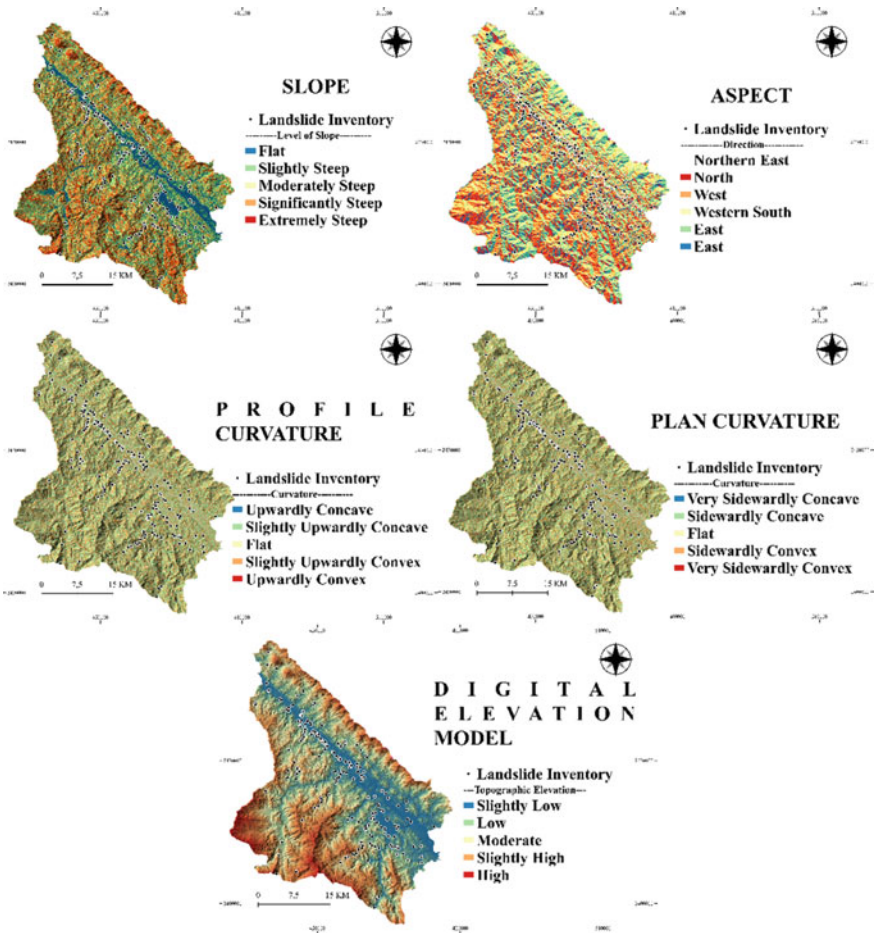


Fig. 27.3 Topographic factors including 5 necessary layers: 12.5 m-digital elevation model (DEM), slope, aspect, plan curvature, and profile curvature

$$\text{Slope} = \frac{\delta z}{\delta s} = g \cos \theta + h \sin \theta. \tag{27.2}$$

$$\text{Aspect} = \theta = \arctan\left(\frac{-H}{-G}\right). \tag{27.3}$$

$$\text{Profilec} = -2(dg^2 + Eh^2 + fgh)(g^2 + H^2). \tag{27.4}$$

$$\text{Planc} = 2(dh^2 + Eg^2 - fgh)(g^2 + H^2). \tag{27.5}$$

27.2.2.4 Hydrological Factors

Topographic Wetness Index (TWI) (Fig. 27.4) was first proposed by Beven and Kirkby (1979), and describes the hydrological characteristics of the topographic soil moisture which also describes the water accumulation tendency of the area, and is defined by:

$$\text{TWI} = \ln\left(\frac{\text{area}}{\tan \theta}\right) \tag{27.6}$$

where the *area* parameter is the specific catchment area or flow accumulation area and the θ parameter is the slope angle. Large contributing drainage areas by low slope will result in high values of TWI. On the other hand, where are steep slopes will be associated with low values of TWI. For small catchment areas, the index has good correlations with the true soil moisture but depends on seasonal changes and topographic condition. In fact, the flat topography will not be considered to be good at estimating the TWI (Western et al. 1999).

Stream power index (SPI) (Fig. 27.4) was introduced by Moore et al. (1991) describes the power of erosion of the water and is defined by:

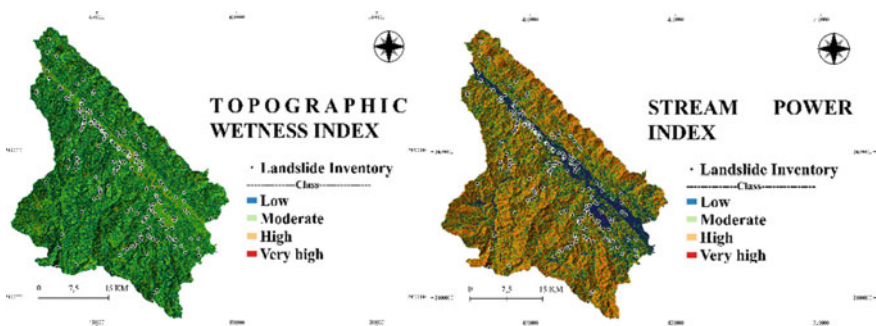


Fig. 27.4 Wetness index of terrain (left) and stream power index (right)

$$\text{SPI} = \text{area} \times \tan \theta \quad (27.7)$$

where the *area* parameter is the specific catchment area or flow accumulation, the same as the *area* parameter used to compute the TWI, and the θ is the same slope angle derived from 12.5 m-DEM.

27.2.2.5 Environmental Factors

In the study area, road network, river network, fault network, NDVI, and land use-land cover data are also included as the environmental factors (Fig. 27.5). The fact that almost all landslides are located close to the transport routes. For the spatial concept, buffers of road network and fault network are 50 m, 100 m, 200 m, 500 m, and greater than 500 m; buffers of river network is greater than 300 m, 200 m, 100 m, 50 m, 25 m, and lower than 25 m; NDVI was divided into 5 classes which are very low, low, medium, high, and very high; land use-land cover data was divided into 7 classes including water, built-up, agriculture, rice terrace, non-forest vegetation, forest, and others. Accordingly, these factors are used as inputs for modelling the landslide susceptibility using the R ModelMap.

27.2.3 Methods

A number of 604 of non-landslides and landslides, which were generated by a setting condition to the slope layer where it is less than 20° or greater than 70° and combined with the landslide inventory points (or called historical landslides) to form a training set including 422 points (70% of the total 604 points) and a testing set including 128 points (30% of total 604 points) to conduct a supervised classification through the R ModelMap package. The landslide inventory points had been made sure that they were grouped with label 1 into two subsets—training1 and testing1, and the same performance was made for non-landslide points with label 0—training0 and testing0. In addition, the training set and testing set were sampled with topographic, hydrological, geological, and environmental factors to form meaningful sets for landslide susceptibility computation and some statistical performances (Fig. 27.6).

In the model, Random Forest did classification for the training set into 50 decision trees with a rate of one decision tree out of ten training samples, according to which 50 classification bags were formed. The main output of this model is the landslide susceptibility map. Each pixel in the map contains the susceptibility index that were normalized by the final process of the model. The principle of forming this susceptibility map is a linear combination of all variables. In particular, each factor was voted for its most hazardous component in the training set to become the decision tree or so-called the weighted factor of the factor. The model takes six factors—road network, river network, fault network, NDVI, land use-land cover data, and geological data for modelling the landslide susceptibility.

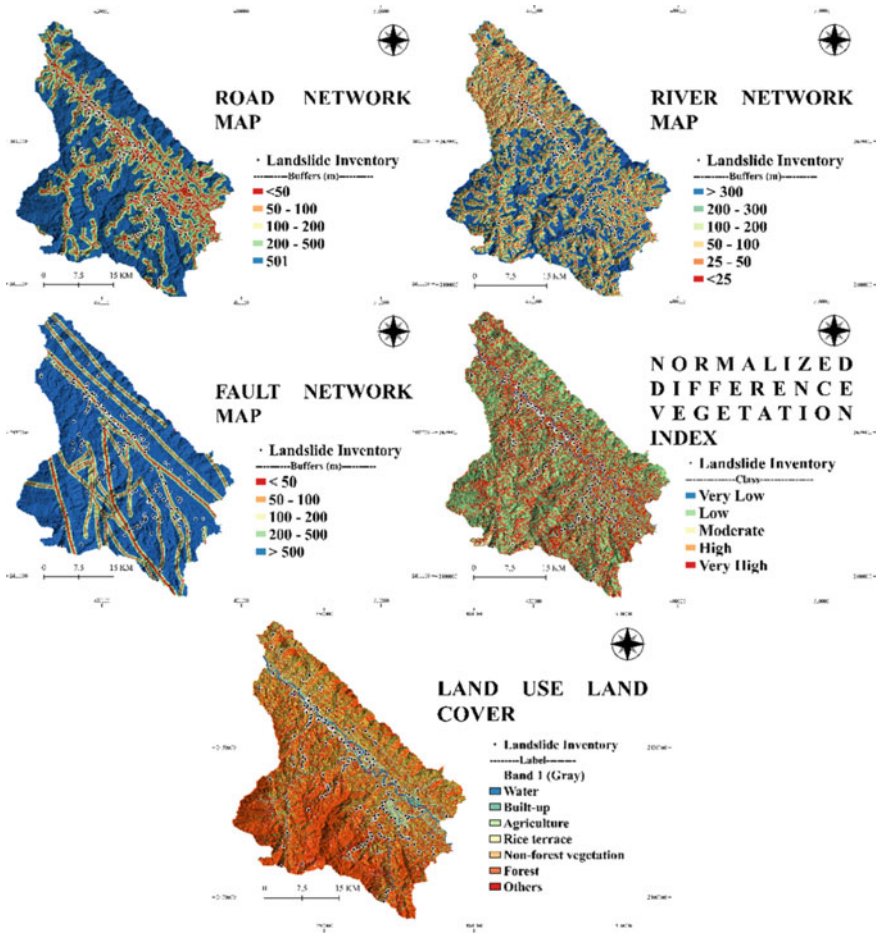


Fig. 27.5 Environmental factors including 5 factors: road network, river network, fault network, normalized difference vegetation index (NDVI), and land use-land cover data

Finally, the testing set is used to validate the model using confusion matrix and compute the accuracy which can be derived from the Eq. (27.8).

$$\text{Accuracy} = \frac{TP + FN}{TP + TN + FP + FN} \tag{27.8}$$

The 2019 census population map of Vietnam was used to calculate population exposed to landslides. Initially, the 100 m-population map censused in 2018 (<https://www.worldpop.org/geodata/summary?id=6449>) was clipped, resampled to 12.5 m, and reprojected to the coordinate reference system of WGS84 48 N. In the end, the population data and the landslide susceptibility model were combined to estimate the population exposed to landslides.

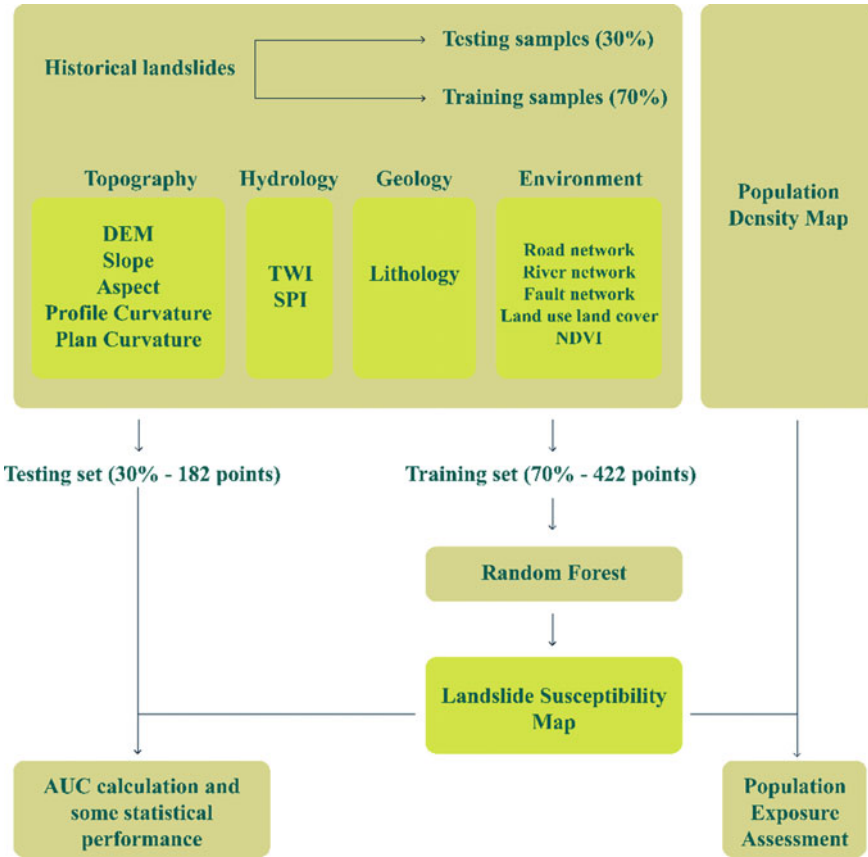


Fig. 27.6 Landslide susceptibility mapping workflow

To assist in visualizing the concept of this paper, a WebGIS was built to convey this information to the social community.

27.3 Results

27.3.1 Landslide Susceptibility Mapping

The accuracy shows that the landslide susceptibility model (Fig. 27.7) was 92% realistic with the high score of the area under the curve (AUC) of 91.33% (Fig. 27.8). To build this susceptibility map, the model used only six predictors out of total 13 ones that are road network, NDVI, land use-land cover data, river network, fault network,

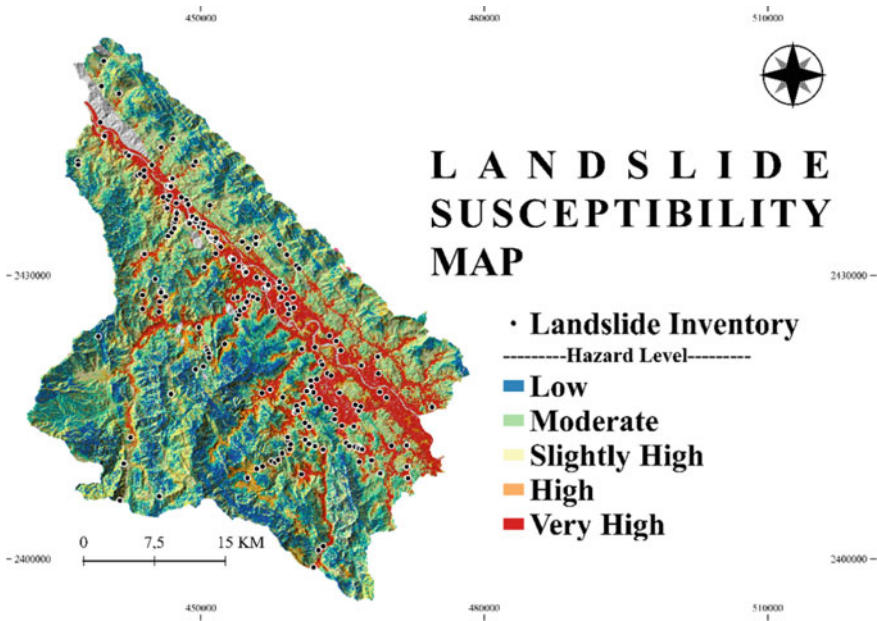


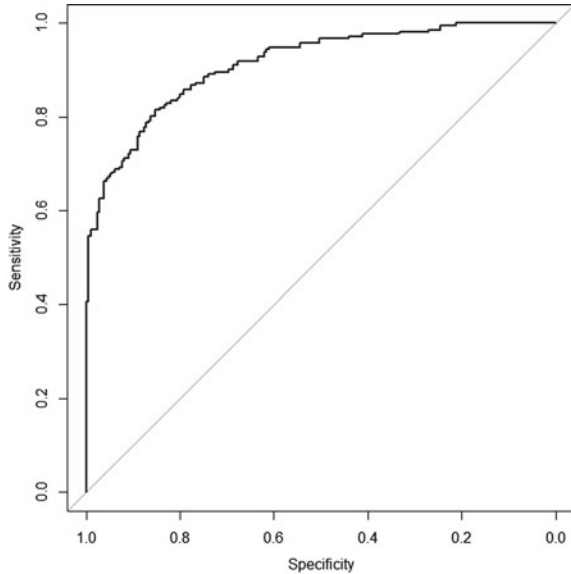
Fig. 27.7 Landslide susceptibility was divided into 5 hazardous areas with low, moderate, slightly high, high, and very high severities. Then, it was reclassified with 4 hazardous areas with low, moderate, high, and very high severities

and geological data. Among these 13 factors, the DEM has the most influence on the accuracy of model but not the road network as expected.

First of all, analyzing the influence of the six predict factors that has the following results:

- Road network: although the frequency of occurrence of routes with buffers less than 50 m on the variable is not much compared to the entire road network, 60% of the landslides appear inside the buffers of 50 m and has more than 80% of probability for landslide occurrence. In the consequent buffers between 50 and 200 m keep also high (70%) probability of landslide.
- Geological data: there were usually pebbles, gravel, sand, clay with 5 m thick and up to 18 m thick; or intrusive rock forms gabrodiabas and diabas; several landslides included sand, clay mixed layers and agglomerates with a thickness of 2–8 m; or pebbles, conglomerates and sandstone with a thickness of 2–10 m. Thus, it shows that landslides often appear in areas with mostly sand and/or pebbles.
- River network, fault network, NDVI, and land use-land cover data: the river network also shows that most landslides occur between 25 and 200 m from streams with a distance of 50 m from faults with confidence to 80%. Where the NDVI is very low from 0 to 0.2, the confidence of the landslide occurrences is nearly 100%. The statistical results also show that built-up areas and agricultural soil were the places that landslides mostly activated. Most notably, although the vegetation

Fig. 27.8 The area under the curve score (ROC–AUC)—91.33% of performance



cover characteristics do not have a great influence on the activation of landslides but a meaningful role, the analysis results show that landslides mostly respond to where have no vegetation cover.

27.3.2 *Population Exposure Assessment*

Population data, acquired from the WorldPop website, is combined with the landslide susceptibility model to estimate the population exposure assessment (Fig. 27.9). The estimation was based on 4 hazard levels including low risk, moderate risk, high risk, and very high risk. Which shows that, nearly 40% of the population could be potentially affected by low-risk areas, and nearly 17% of the population is within very high susceptible areas (Table 27.2).

27.3.3 *WebGIS*

The WebGIS can be summarized as the use case diagram, it shows the main interactions among system and users within the system (Fig. 27.10). Administrator has full authority to manage the overall system, admin can accessed all control management such as lodging management, add/remove map, can manage user contributor, also new landslide points (add, edit, delete) and edit map styles. While the WebGIS users only able to view public services maps and interact with the maps. The overall

Population Exposure Assessment

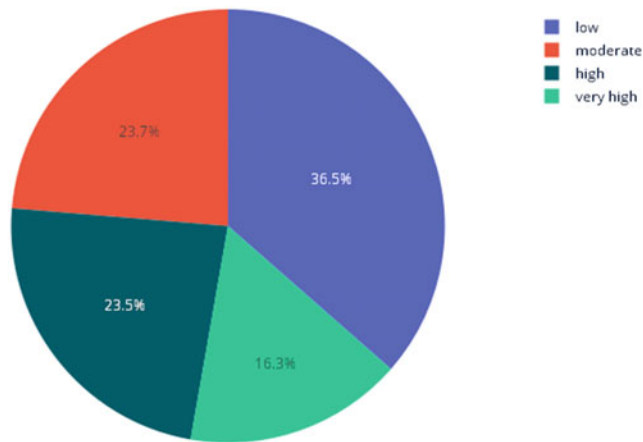


Fig. 27.9 Population exposure assessment depicts the percentage of population exposed to landslides

Table 27.2 Population exposure assessment in each class of hazardous areas

Class	Number of pixels	Areas (km ²)	Relative area (%)	Possibility of people affected (people/km ²)
Low	3,144,884	491.40	36.47	7
Moderate	2,046,912	319.83	23.73	10
High	2,028,910	317.01	23.52	15
Very high	1,403,623	219.32	16.28	30

structure of the system is shown in (Fig. 27.11) The client side of the WebGIS was developed based on Angular with Leaflet library as tools to visualize thirteen environmental factors, landslide inventory, landslide susceptibility map (Fig. 27.12), and population exposed to landslide hazards based on geoweb map services (Fig. 27.13). On the other hand, server side relies on Geoserver and PostgreSQL/PostGIS in order to manage landslide points (including add, edit and remove landslide events), login and manage account for both administrators and users. Population data was extracted from worldpop, converted to polygons and managed in postgis/postgresql. The polygons were classified into 4 classes based on density of population in each pixel value (Fig. 27.13). The Web API in PHP was implemented in order to support client to query total number of population for each polygon. With the map overlay, client can easily identify whether population area is exposed to landslide hazards. In order to implement landslide early warning system purpose, using specific Web API, system can automatically invoke density of population for each classes of susceptibility (Fig. 27.14).

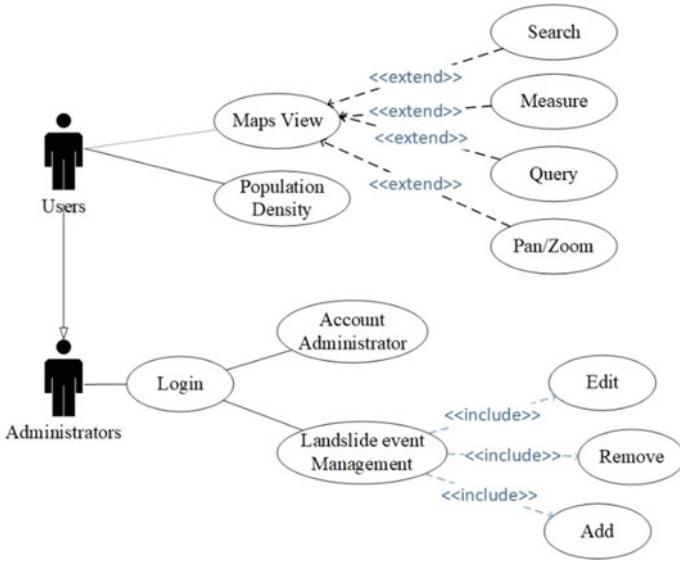
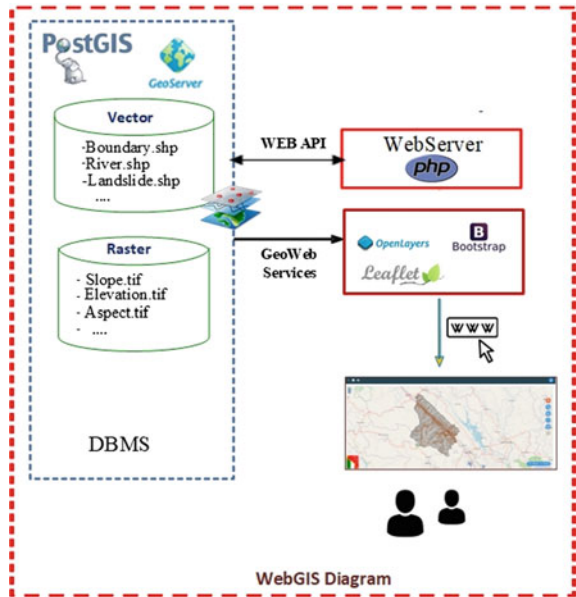


Fig. 27.10 UML use case diagram of the system

Fig. 27.11 The overall system architecture diagram



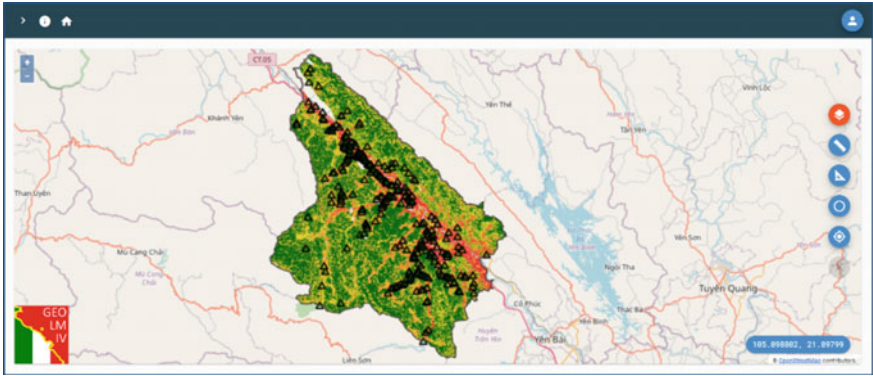


Fig. 27.12 WebGIS deployment

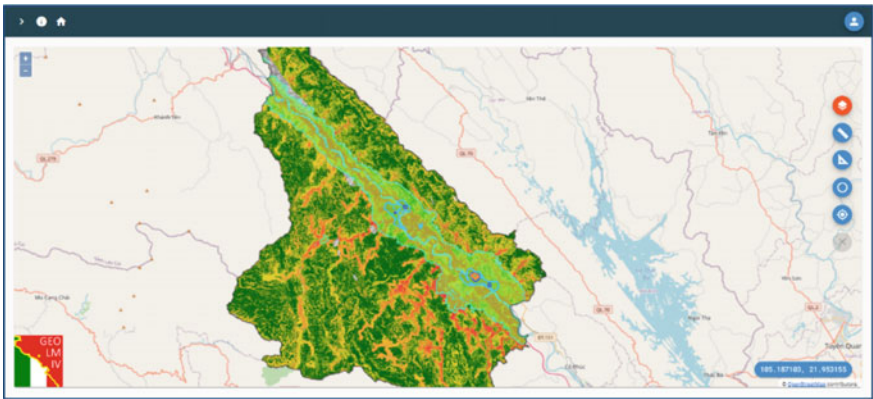


Fig. 27.13 WebGIS shows landslide susceptibility map and population density classes, the population density of mau a town, Van Yen district is presented in the different colored polygons

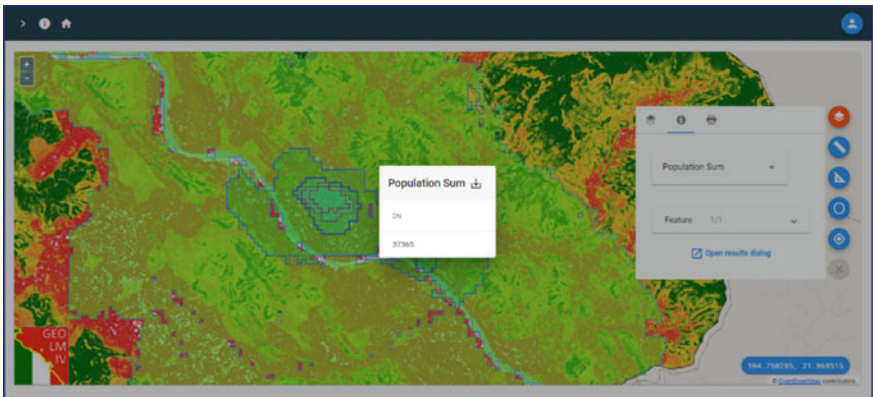


Fig. 27.14 WebGIS presents ability to query total number of population in every polygon

27.4 Discussions and Conclusions

The results of modelling landslide susceptibility using the Random Forest algorithm through the ModelMap show that the potential applicability in practice is completely met with the modeling work, and the results are not only the foundation for other studies but they are also very useful in disaster warning systems for landslides and flash floods in Vietnam.

In the context of this study, thirteen factors were used to explore the insights of landslide hazard with indicated factors of the study, whereby the six out of thirteen factors were used for computing the landslide susceptibility including road network, river network, fault network, NDVI, land use-land cover data, geology. Population density data was used to have an overview of population exposed to the landslide hazards. In short, the statistical result can be understood that the landslides almost caused nearby the transportation routes or roads, they are not far from the river area and fault area. These landslide occurrences had a low vegetation cover, specifically were in the area of agriculture. The geological materials or lithological information contain mainly sand, conglomerate, chunk mixed with clay in the occurrence sites.

The total landslide points including the landslide points of the landslide inventory and the non-landslide points were divided into training set with 422 points and testing set with 192 points. The input for the model is the training set for exploring the factors. Lastly, the overall accuracy of the model is 92% with the performance of the ROC–AUC of 91.33% validated by testing set.

Population is also directly and indirectly affected by natural disasters. Using the landslide susceptibility map, it can be noted that people exposed to landslides in the very high risk areas take up 16%, and nearly 24% in the high risk areas. Although the correlation between different areas of influence is not much different, these numbers estimate a very large group of population that can be affected by possible slope failure.

From the statistical measurements, the DEM, slope, road network, land use-land cover data, and geology play an important role in establishing the landslide susceptibility map. Which means that when the model leaves out the factors, the accuracy of the model will be decreased as the measurement of the Mean Decreased Accuracy (percentage of increasing mean square error) and Mean Decreased Gini of the model. Figure 27.15 shows the reason why these important factors stand out that DEM is the most important factor holding the highest left-out error rate of more than 40%, followed by road network, slope, land use-land cover data, geological factor with 30%, more than 20%, more than 10%, and 10%, respectively.

In summary, the model used in the study is adopted under the scope of a cooperating project that cooperating between Vietnam and Italy named “Geoinformatics and earth observation for landslide monitoring”. For continuous explorations of the model, several scenarios will be conducted to choose the best applicable scenario for real warning systems in Vietnam. The results of the analysis clearly show that landslides in the study area are greatly influenced by topographic elevation along with DEM, slope, road network, land use-land cover data, and geological settings. To

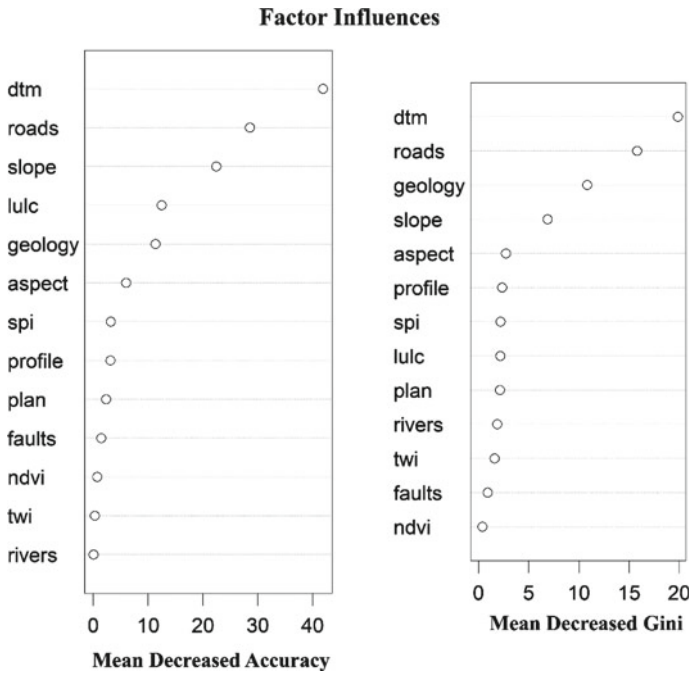


Fig. 27.15 Statistical results show the useful variables and their importances in establishing the landslide susceptibility map

obtain such results with the very high accuracy, the reliability and confidence of the data are also guaranteed under the provision of legitimate organizations. However, this methodology has its limitation. The 0-labeled points (non-landslide points) were derived from the conditional calculation of the slope factor, these points might be misunderstood with the actual natural state the real world. Which means that the derived non-landslide points could be landslide points. Otherwise, these accuracy of this model is just suitable with the proposed scenario from slope, and the two sets of training and testing points. Nevertheless, the 92% accuracy and 91.33% AUC point out the insignificant influence of the derived non-landslide points to the whole model.

Acknowledgements The work is partially funded by the Italian Ministry of Foreign Affairs and International Cooperation within the project “Geoinformatics and Earth Observation for Landslide Monitoring”—CUP D19C21000480001 (Italian side) and partially funded by Ministry of Science and Technology of Vietnam (Vietnamese side) by the bilateral scientific research project between Vietnam and Italy, code: NĐT/IT/21/14.

References

- Barančoková M, Šošovička M, Barančok P, Barančok P (2021) Predictive modelling of landslide susceptibility in the Western Carpathian Flysch Zone. *Land* 10:1370
- Beven KJ, Kirkby MJ (1979) A physically based, variable contributing area model of basin hydrology/un modèle à base physique de zone d'appel variable de l'hydrologie du bassin versant. *Hydrol Sci Bull* 24:43–69
- Bordoni M, Galanti Y, Bartelletti C et al (2020) The influence of the inventory on the determination of the rainfall-induced shallow landslides susceptibility using generalized additive models. *CATENA* 193:104630
- Bui DT, Lofman O, Revhaug I et al (2011) Landslide susceptibility analysis in the Hoa Binh province of Vietnam using statistical index and logistic regression. *Nat Hazards* 59:1413
- Carrara A (1983) Multivariate models for landslide hazard evaluation. *Math Geol* 15:403–426
- Chang KT, Merghadi A, Yunus AP et al (2019) Evaluating scale effects of topographic variables in landslide susceptibility models using GIS-based machine learning techniques. *Sci Rep* 9:12296
- Claessens L, Schoorl JM, Veldkamp A (2007) Modelling the location of shallow landslides and their effects on landscape dynamics in large watersheds: an application for northern New Zealand. *Geomorphology* 87:16–27
- Cui S, Wu H, Pei X et al. (2022) Characterizing the spatial distribution, frequency, geomorphological and geological controls on landslides triggered by the 1933 MW 7.3 diexi earthquake, Sichuan, China. *Geomorphology* 403:108177
- D'Amato Avanzi G, Giannecchini R, Puccinelli A (2004) The influence of the geological and geomorphological settings on shallow landslides. An example in a temperate climate environment: The June 19, 1996 event in northwestern Tuscany (Italy). *Eng Geol* 73:215–228
- Dechkamfoo C, Sitthikankun S, Kridakorn Na Ayutthaya T et al. (2022) Impact of rainfall-induced landslide susceptibility risk on mountain roadside in northern Thailand. *Infrastructures* 7:17
- Du J, Glade T, Woldai T et al (2020) Landslide susceptibility assessment based on an incomplete landslide inventory in the Jilong Valley, Tibet. *Chin Himalayas Eng Geol* 270:105572
- Evans S (1972) General Geomorphometry, Derivatives of Altitude, and Descriptive Statistics. In: Chorley RJ (ed) *Spatial Analysis in Geomorphology*. Methuen and Co., Ltd., London, pp 17–90
- FAO: Strengthening capacities to enhance coordinated and integrated disaster risk reduction actions and adaptation to climate change in agriculture in the northern mountain regions of Vietnam, Baseline Survey of Yen Bai Province (2012)
- Freeman EA, Frescino TS, Moisen GG (2018) ModelMap: an R package for model creation and map production. *R Package Ver* 4–6
- General Introduction to Van Yen District. <https://vanyen.yenbai.gov.vn/gioi-thieu/gioi-thieu-chung>
- General Statistics Office of Vietnam. Completed Results of the 2019 Viet Nam Population and Housing Census. <https://www.gso.gov.vn/wp-content/uploads/2019/12/Ket-qua-toan-bo-Tong-dieu-tra-dan-so-va-nha-o-2019.pdf>
- Guerriero L, Prinzi EP, Calcaterra D et al (2021) Kinematics and geologic control of the deep-seated landslide affecting the historic center of Buonalbergo. *Southern Italy Geomorphology* 394:107961
- Habumugisha JM, Chen N, Rahman M et al (2022) Landslide susceptibility mapping with deep learning algorithms. *Sustainability* 14:1734
- Harmouzi H, Schlögel R, Jurchescu M, Havenith H-B (2021) Landslide susceptibility mapping in the vrancea-buzău seismic region, southeast Romania. *Geosciences* 11:495
- Highland L, Bobrowsky PT (2008) *The landslide handbook: a guide to understanding landslides*, US Geological Survey, Reston, Va
- Kanungo DP, Arora MK, Sarkar S, Gupta RP (2006) A comparative study of conventional, ANN, black box, fuzzy and combined neural and fuzzy weighting procedures for landslide susceptibility zonation in Darjeeling Himalayas. *Eng Geol* 85:347–366
- Kulkarni A, Batarseh FA, Yang R (2020) Foundations of data imbalance and solutions for a data democracy. In: *Data democracy: at the Nexus of artificial intelligence, software development,*

- and knowledge engineering, Academic Press, an imprint of Elsevier, London, San Diego, CA, pp 83–106
- Lee S, Pradhan B (2007) Landslide hazard mapping at Selangor, Malaysia using frequency ratio and logistic regression models. *Landslides* 4:33–41
- Liu R, Yang X, Xu C et al (2022) Comparative study of convolutional neural network and conventional machine learning methods for landslide susceptibility mapping. *Remote Sens* 14:321
- Miao Z, Peng R, Wang W et al (2022) Integrating data modality and statistical learning methods for earthquake-induced landslide susceptibility mapping. *Appl Sci* 12:1760
- MONRE: National disaster risk in Vietnam in the Period 2006–2016 and forecasting and warning system (2017)
- Montgomery DR, Dietrich WE (1994) A physically based model for the topographic control on shallow landsliding. *Water Resour Res* 30:1153–1171
- Moore ID, Grayson RB, Ladson AR (1991) Digital terrain modelling: a review of hydrological, geomorphological, and biological applications. *Hydrol Process* 5:3–30
- Qi T, Zhao Y, Meng X et al (2021) Distribution modeling and factor correlation analysis of landslides in the large fault zone of the western qinling mountains: a machine learning algorithm. *Remote Sens* 13:4990
- Rabby YW, Li Y, Abedin J, Sabrina S (2022) Impact of land use/land cover change on landslide susceptibility in Rangamati Municipality of Rangamati District. *Bangladesh ISPRS Int J Geo Inf* 11:89
- Rong G, Li K, Su Y et al (2021) Comparison of tree-structured Parzen estimator optimization in three typical neural network models for landslide susceptibility assessment. *Remote Sens* 13:4694
- Shahzad N, Ding X, Abbas S (2022) A comparative assessment of machine learning models for landslide susceptibility mapping in the rugged terrain of northern Pakistan. *Appl Sci* 12:2280
- Sharma A, Prakash C, Manivasagam V (2021) Entropy-based hybrid integration of Random Forest and support vector machine for landslide susceptibility analysis. *Geomatics* 1:399–416
- Tien Bui D, Pradhan B, Lofman O et al (2012) Landslide susceptibility mapping at Hoa Binh Province (Vietnam) using an adaptive neuro-fuzzy inference system and GIS. *Comput Geosci* 45:199–211
- Vietnam Population Data, <https://www.worldpop.org/geodata/summary?id=6449>
- WCDR: National Report on Disaster Reduction in Vietnam, 12 (2005)
- Western AW, Grayson RB, Blöschl G et al (1999) Observed spatial organization of soil moisture and its relation to terrain indices. *Water Resour Res* 35:797–810
- Yilmaz I (2009) Landslide susceptibility mapping using frequency ratio, logistic regression, artificial neural networks and their comparison: a case study from kat landslides (Tokat—Turkey). *Comput Geosci* 35:1125–1138
- Yordanov V, Brovelli MA (2021) Application of various strategies and methodologies for landslide susceptibility maps on a basin scale: the case study of Val Tartano. *Italy Appl Geomat* 13:287–309
- Yu L, Zhou C, Wang Y et al (2022) Coupling data-and knowledge-driven methods for landslide susceptibility mapping in human-modified environments: a case study from Wanzhou County, three gorges reservoir area. *China Remote Sens* 14:774
- Zevenbergen LW, Thorne CR (1987) Quantitative analysis of land surface topography. *Earth Surf Proc Land* 12:47–56
- Zhao L, Wu X, Niu R et al (2020) Using the rotation and Random Forest models of ensemble learning to predict landslide susceptibility. *Geomat Nat Haz Risk* 11:1542–1564
- Zhao P, Masoumi Z, Kalantari M et al (2022) A GIS-based landslide susceptibility mapping and variable importance analysis using artificial intelligent training-based methods. *Remote Sens* 14:211
- Zieher T, Perzl F, Rössel M et al (2016) A multi-annual landslide inventory for the assessment of shallow landslide susceptibility—two test cases in Vorarlberg. *Austria Geomorphology* 259:40–54

Chapter 28

Analysis of Riverbank Changes of Go Gia River in Can Gio District in the Period of 2013–2021



Nguyen Phuong Uyen, Pham Thi Loi, Nguyen Thi Diem Thuy,
Nguyen Thi Bay, and Dao Nguyen Khoi

Abstract The objective of this study was to analyze the changes of riverbanks of the Go Gia River in the Can Gio District for the period 2013–2021 using remote sensing and GIS. This study used multi-temporal Landsat satellite images, including nine Landsat 8 OLI/TIRS images in the period 2013–2021 to classify the riverbanks for each time period and to calculate the change rates of river banks. Combination of AWEI (Automated Water Extraction Index) and thresholding method was used to extract the river bank. Results showed that the processes of erosion and accretion intertwined but most of the main riverbanks had erosion trend in the period 2013–2021. Evaluating the riverbank changes using multi-temporal remote sensing data may contributed an important reference to managing and protecting the riverbanks.

Keywords Riverbank change · Landsat imagery · DSAS · AWEI · Go Gia River

28.1 Introduction

The computation of shoreline or river bank is one of foremost parameters in detecting erosion and accretion processes together with the study of morphological dynamics in estuarial and coastal zones (Armenio et al. 2019). This represents an important step in understanding the morpho-dynamic evolution of estuarial and coastal areas. Additionally, policy-makers could do better to reduce risk of coastal and river bank erosion and minimize physical and socio-economic losses.

N. P. Uyen · P. T. Loi · N. T. D. Thuy · D. N. Khoi (✉)
Faculty of Environment, University of Science, Ho Chi Minh City, Vietnam
e-mail: dnkhai@hcmus.edu.vn

N. T. Bay
Faculty of Civil Engineering, University of Technology, Ho Chi Minh City, Vietnam

N. P. Uyen · P. T. Loi · N. T. D. Thuy · N. T. Bay · D. N. Khoi
Vietnam National University, Ho Chi Minh City, Vietnam

There have been numerous efforts to monitor changes of river bank and shoreline, including repeated measurement of cross section profiles, hydro-morphological modeling and remote sensing techniques (Khoi et al. 2020). The repeated measurement of cross section profiles can provide highly accurate topography and morphology, but it is time, labor, and cost consuming. In case of the hydro-morphological modeling, this approach does not always apply for long-term evaluations of river bank change because of large requirements of input data and computational amount (Binh et al. 2020). Amongst the mentioned approaches, remote sensing technology is preferred because this technique could reconstruct the history and evolutionary trajectories of morphological changes with a minimum cost and efforts. Remote sensing allows objective and repeatable assessments to explore a full range of spatial and temporal variations of river systems.

In the remote sensing technology, the popular data utilized for extracting shoreline or river bank are Landsat images by reason of their open access, large coverage, and long period of time (Liu et al. 2017). The Landsat data collected from sensors of Multi-spectral Scanner (MSS), Thematic Mapper (TM), Enhanced Thematic Mapper Plus (ETM +), and Operational Land Imager (OLI)/Thermal Infrared Sensor (TIRS) are useful for the extraction of shoreline or river bank. There are three types of popular methods used to extract water bodies and land using the remotely sensed imagery include spectral banks, classification, and water indices (Jiang et al. 2014). In the midst of them, the water indices have been broadly utilized due to their relatively high degree of accuracy in detecting water bodies and low-cost implementation. There are some popular water indices used to monitoring changes of shoreline and river bank, namely normalized water index (NDWI) (McFeeters 1996), modified normalized difference water index (MNDWI) (Xu 2006), and automated water extraction index (AWEI) (Feyisa et al. 2014). For example, Duru (2017) applied NDWI and MNDWI to monitor shoreline changes along Lake Sapanca in Turkey. Tobón-Marín and Barriga (2020) used three water indices, including NDWI, MNDWI, and AWEI to analyze changes in river banks in eight Colombian rivers.

The objective of this work was to investigate the river bank changes of the Go Gia River in the Can Gio District for the period 2013–2021. Estimation of the riverbank changes may contribute an important reference to manage and protect the riverbanks in the study area.

28.2 Study Area

The study area is Go Gia River in the Can Gio District (Fig. 28.1), which is located between the Long Tau and Thi Vai Rivers, two main transportation waterways to enter seaports in Ho Chi Minh City. This region has a low elevation with an average of approximately 1.5 m above the mean sea level. The climate is tropical monsoon with two different dry and wet seasons (Khoi and Trang 2016). The annual rainfall varies from 1.300 to 1.400 mm. The tidal regime in the study area is an irregular semi-diurnal regime with a meso-tidal range from 2.0 (mean tide) to 4.0 m (spring

tides) (Nguyen and Vo Luong 2019). The highest value of tidal amplitudes appear during October to November and the lowest value happen during April to May.

28.3 Methodology

To investigate the change analysis of river bank along the Go Gia River, the research workflow applied in the present work is illustrated in Fig. 28.2. Firstly, the Landsat 8 OLI/TIRS images for the analysis are selected to be radiometric normalized and atmospheric corrected in the pre-processing. Secondly, the water index (Automated Water Extraction Index (AWEI_{sh})) is utilized to extract the river bank lines. Finally, the river bank change statistics are calculated using Digital Shoreline Analysis System (DSAS) tool.

28.3.1 Data

Operational Land Imager (OLI)/Thermal Infrared Sensor (TIRS) imageries of Landsat sensors were utilized to detect river bank changes (Table 28.1). The Landsat 8 OLI/TIRS data were obtained from the United States Geological Survey (USGS) earth explore website (<http://earthexplorer.usgs.gov/>). To avoid the effect of the cloud and other kinds of atmospheric errors, the Landsat data during the dry-seasonal months from January to April were utilized in the present work. The Landsat data is with the World Geodetic System 1984 (WGS84) datum and projected using the Universal Transverse Mercator (UTM) zone 48 N.

28.3.2 Water Index

This work uses Automated Water Extraction Index (AWEI_{sh}) (Feyisa et al. 2014) as a water index to extract the water bodies and land. The formulation of AWEI_{sh} is written as follows

$$AWEI_{sh} = \rho_{band2} + 2.5 \times \rho_{band3} - 1.5 \times (\rho_{band5} + \rho_{band6}) - 0.25 \times \rho_{band7} \quad (28.1)$$

where ρ represents the reflectance from the Landsat 8 OLI data for Bands 2 (blue), 2 (green), 5 (near-infrared), 6 (SWIR1), and 7 (SWIR2).

To calculate the AWEI_{sh}, the integer values of the Landsat 8 OLI/TIRS satellite imagery need to be converted to the spectral reflectance value. The threshold value of the AWEI_{sh} to separate the water and non-water bodies was obtained on the basis of the manually thresholding method (Feyisa et al. 2014).

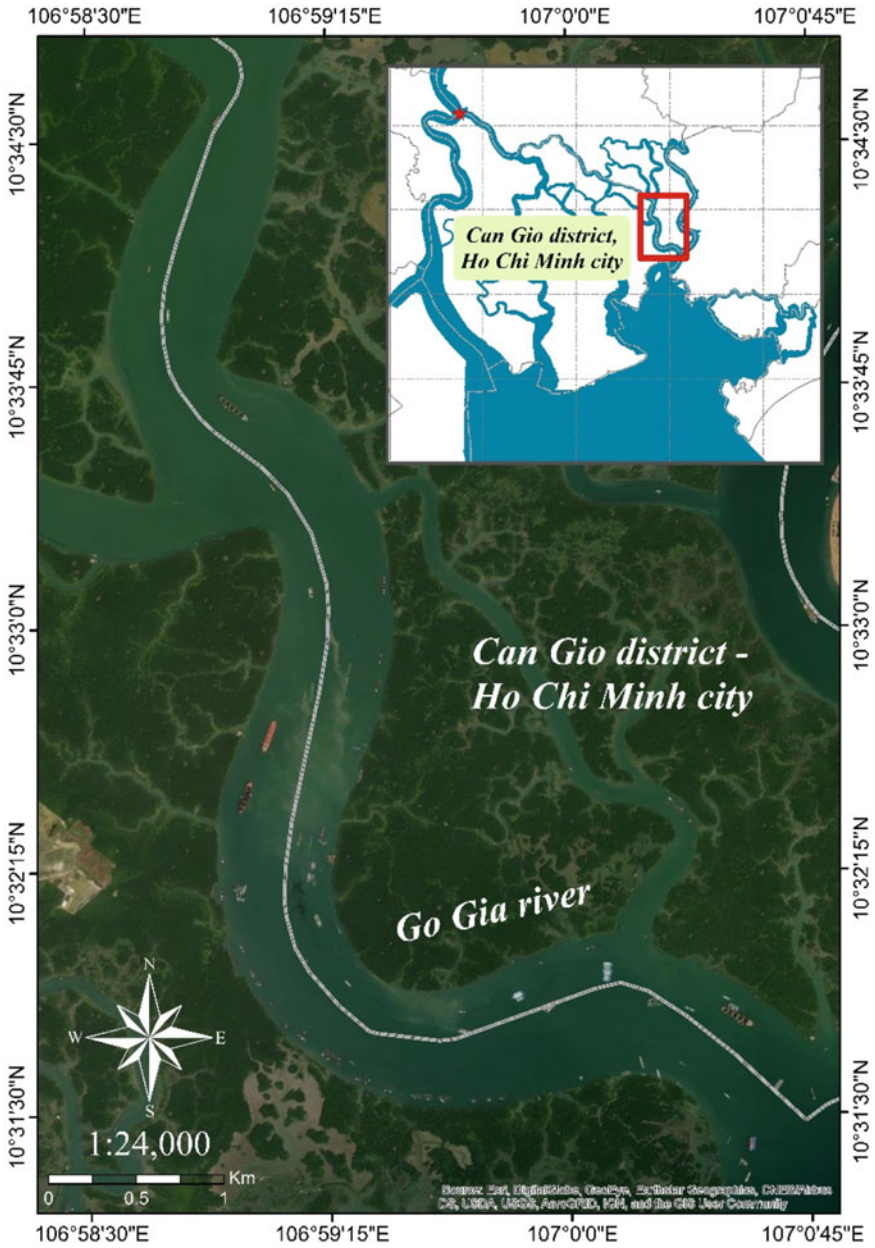


Fig. 28.1 Study area

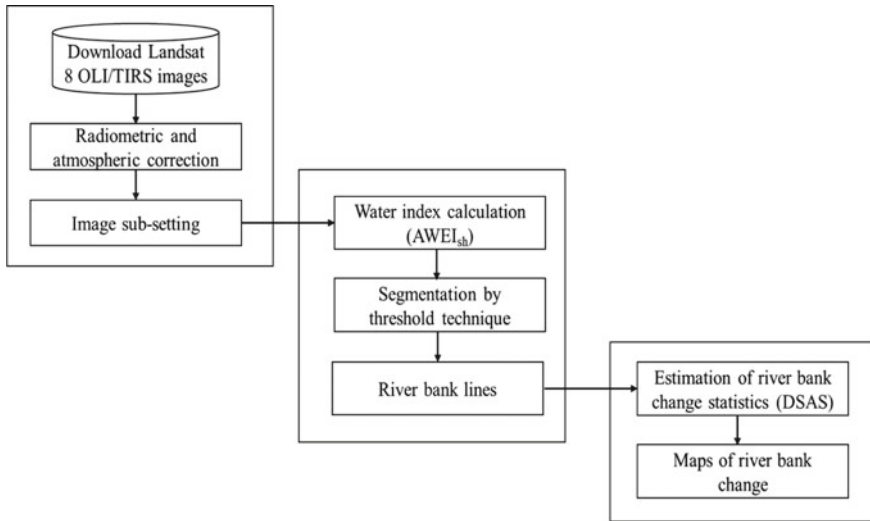


Fig. 28.2 The research workflow used in this work

Table 28.1 Landsat 8 OLI images utilized in the present work

Ord	Path/row	Date	Cloud cover (%)
1	124/053	26/10/2013	15.06
2	124/053	03/03/2014	32.02
3	124/053	02/02/2015	24.04
4	124/053	24/03/2016	24.04
5	124/053	06/01/2017	4.36
6	124/053	14/03/2018	10.12
7	124/053	02/02/2019	2.04
8	124/053	31/01/2020	5.36
9	124/053	06/03/2021	0.01

28.3.3 Digital Shoreline Analysis System (DSAS)

Digital Shoreline Analysis System (DSAS) was utilized to compute change rates (erosion or deposition) along the river. There are three major steps conducted, including (1) determining baselines of river banks, (2) drawing lines at right angles of the baselines, and (3) computing change rates. In the present work, the linear regression rate (LRR), a statistical parameters given in DSAS, was utilized to compute the change rates of river banks based on the extracted riverbank lines in the period 2013–2021. According to the LRR values, the river bank changes are divided into three levels of erosions, including high (<5 m/year), medium (–5 to –1 m/year), and low (–1 to –0.5 m/year); three level of accretion, including low (0.5–1 m/year),

medium (1–5 m/year), and high (>5 m/year); and stable level (–0.5 to 0.5 m/year) (Khoi et al. 2020; Hoan et al. 2014).

28.4 Result and Discussion

The river bank lines were extracted from Landsat 8 OLI/TIRS for the Go Gia River in different years during the period from 2013 to 2021. The results show that the erosion and accretion along the Go Gia River were alternating and the morphological change was characterized by the horizontal direction and slow rate over time (Fig. 28.3). The analysis of river bank change in the period 2013–2021 showed that the river had an average erosion rate of approximately –0.92 m/year and an accretion rate of approximately 0.89 m/year. The left river bank of the Go Gia River appeared some points with high erosion rates of about –8.42 m/year. In general, the trend of erosion prevailed over accretion in the period 2013–2021. Our result is quite similar to the finding of Thuy et al. (2022) which indicated that the main rivers in the Can Gio district had mainly eroded at the rate of 1.7 m/year.

Since 2016, the project of dredging for storm shelters on the Go Gia River have implemented. Figure 28.4 illustrates dredging activities along the river during the period 2016–2020 observed from Google Earth. In order to investigate the effect of this project on the erosion and accretion processes along the Go Gia River, the morphological changes between two periods 2013–2016 and 2017–2021 were considered (Fig. 28.5). In the period 2013–2016, the Go Gia River had mainly accretion process with moderate level and the left river bank had accretion rate of about 2.51 m/year. However, under the effect of dredging project, the left river bank were subjected to erosion at rate of about –1.73 m/year during the period 2017–2021. In general, the erosion process was dominant in the period 2017–2021. It is easy to observe the correlation between river bank erosion and dredging activities (Fig. 28.4). Thuy et al. (2022) indicated that the dredging activities may cause erosion at locations around the dredging areas.

28.5 Conclusion

The present work demonstrated that the integration of remote sensing and GIS technology is useful for studies on long term change of river bank using Landsat 8 OLI/TIRS images with reasonable accuracy. The study shows that average erosion rate along the Go Gia River was –0.92 m/year and accretion rate was 0.89 m/year in the period 2013–2021. Additionally, the Go Gia River was subjected to more erosion in the period 2017–2021 compared to that in 2013–2016. The obtained results may contributed an important reference to managing and protecting the Go Gia River in a sustainable way.

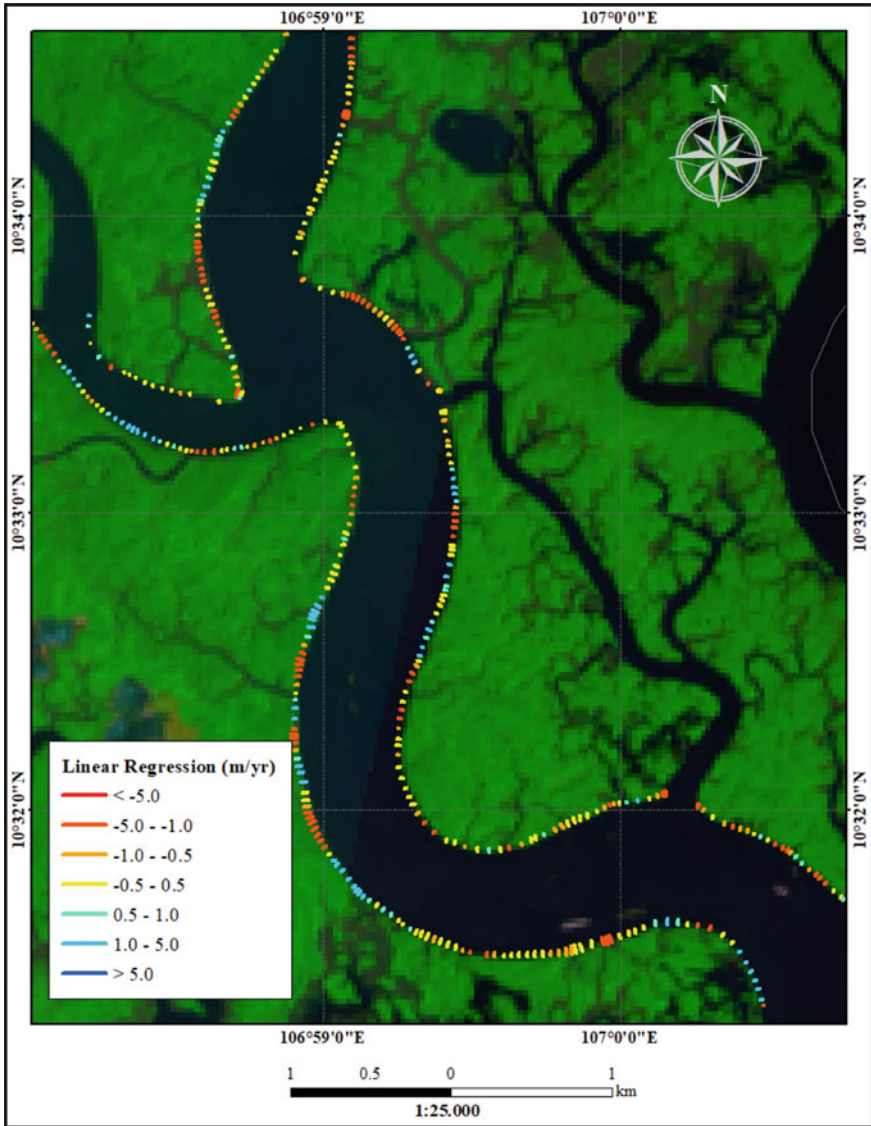


Fig. 28.3 Morphological changes of the Go Gia River in the period 2013–2021

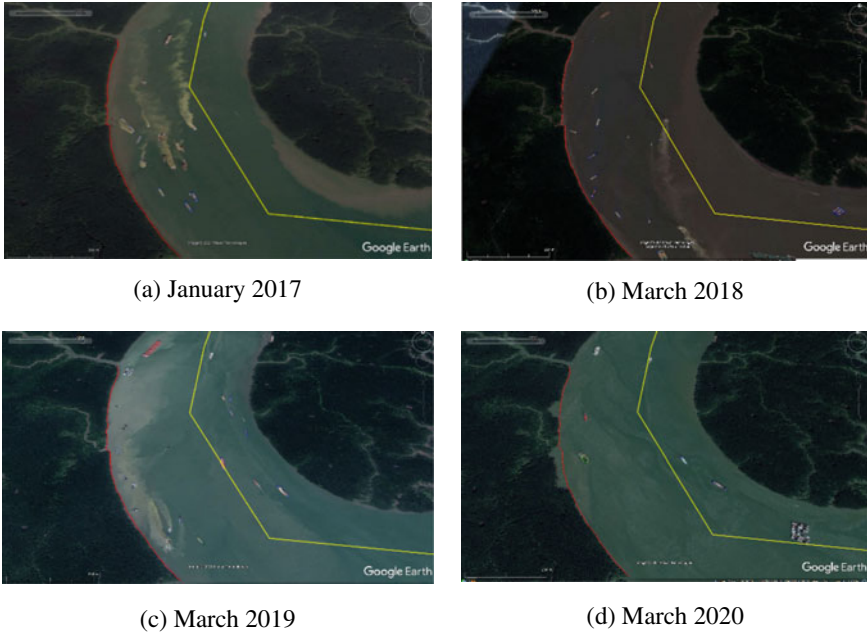


Fig. 28.4 Dredging activities along the Go Gia River during 2016–2020 from google earth images

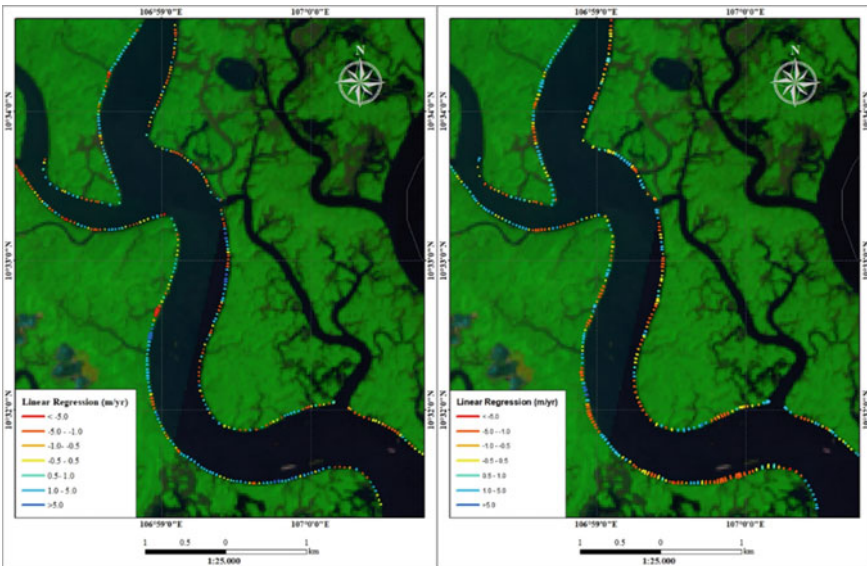


Fig. 28.5 Morphological changes of the Go Gia River in the periods 2013–2016 (left-hand side) and 2017–2021 (right-hand side)

Acknowledgements The research, under the project entitled “Assessing the current situation and causes of Go Gia riverbank erosion in Can Gio district and proposing the prevention solutions”, was supported by the Department of Science and Technology of Ho Chi Minh City under the contract number 112/2020/HD-QPTKHCN.

References

- Armenio E, De Serio F, Mossa M, Petrillo AF (2019) Coastline evolution based on statistical analysis and modeling. *Nat Hazards Earth Syst Earth Syst* 19:1937–1953. <https://doi.org/10.5194/nhess-19-1937-2019>
- Binh DV, Wietlisbach B, Kantoush S, Loc HH, Park E, Cesare G, Cuong DH, Tung NX, Sumi T (2020) A novel method for river bank detection from landsat satellite data: a case study in the Vietnamese Mekong Delta. *Remote Sens* 12:3298
- Duru U (2017) Shoreline change assessment using multi-temporal satellite images: a case study of Lake Sapanca. *NW Turkey Environ Monit Assess* 189:385
- Feyisa GL, Meilby H, Fensholt R, Proud SR (2014) Automated water extraction index: a new technique for surface water mapping using landsat imagery. *Remote Sens Environ* 140:23–35
- Hoan HD, Kiet BNT, Binh CH, Quy PV (2014) Monitoring riverbank erosion in Can Gio Mangroves. *ISME Mangrove Ecosyst Tech Rep* 6:37–41
- Jiang H, Feng M, Zhu Y, Lu N, Huang J, Xiao T (2014) An automated method for extracting rivers and lakes from landsat imagery. *Remote Sens* 6:5067–5089. <https://doi.org/10.3390/rs6065067>
- Khoi DN, Trang HT (2016) Analysis of changes in precipitation and extremes events in Ho Chi Minh City. *Vietnam Proc Eng* 142:229–235
- Khoi DN, Dang TD, Pham LTH, Loi PT, Thuy NTD, Phung NK, Bay NT (2020) Morphological change assessment from intertidal to river-dominated zones using multiple-satellite imagery: a case study of the Vietnamese Mekong Delta. *Reg Stud Mar Sci* 34:101087. <https://doi.org/10.1016/j.rsma.2020.101087>
- Le Nguyen HT, Vo Luong HP (2019) Erosion and deposition processes from field experiments of hydrodynamics in the coastal mangrove area of Can Gio. *Vietnam Oceanologia* 61:252–264. <https://doi.org/10.1016/j.oceano.2018.11.004>
- Liu Y, Wang X, Ling F, Xu S, Wang C (2017) Analysis of coastline extraction from landsat-8 OLI imagery. *Water* 9:816. <https://doi.org/10.3390/w9110816>
- McFeeters SK (1996) The use of the normalized difference water index (NDWI) in the delineation of open water features. *Int J Remote Sens* 17:1425–1432
- Thuy NTD, Khoi DN, Phung BP, Bay NT (2022) Assessing the impact of dredging project on the erosion and accretion processes in the Go Gia River. *Can Gio Vietnam J Hydrometeorology* 737:40–52 [in Vietnamese]
- Tobón-Marín A, Barriga JC (2020) Analysis of changes in rivers planforms using google earth engine. *Int J Remote Sens* 41:8654–8681
- Xu HQ (2006) Modification of normalized difference water index (NDWI) to enhance open water features in remotely sensed imagery. *Int J Remote Sens* 27:3025–3033

Chapter 29

Estimate Petrophysical Properties by Using Machine Learning Methods



Tran Nguyen Thien Tam  and Dinh Hoang Truong Thanh

Abstract The petrophysical properties such as porosity and permeability play the most important role in reservoir characterization. Porosity display the capacity to contain fluids and permeability is fluid movement. These are important properties in reserves estimation and production capacity of oil and gas. Therefore, it is necessary to estimate it exactly. In this study, the authors use traditional methods in petroleum engineering and popular machine learning methods to estimate porosity and permeability via petrophysical data. Research data collected from the Volve field in Norway includes well logging and core logging. Herein, we present the prediction of porosity and permeability using an Artificial neural network (ANN) model, as compared to Least-squares support-vector machines (LSSVM) model and empirical model. The results show that the ANN model could predict porosity and permeability with the highest R^2 (coefficient of determination) of 0.9997 and lowest MSE (mean squared error) of 6.7769. This finding would be helpful in deploying the application of machine learning to estimate the reservoir characteristics.

Keywords Porosity · Permeability · Petrophysical properties · Machine learning · Artificial neural networks (ANN) · Support vector machine (SVM)

Nomenclature

x_i Input value of neuron i
 w_i Input weight

T. N. T. Tam (✉) · D. H. T. Thanh
Faculty of Geology and Petroleum Engineering, Ho Chi Minh City University of Technology (HCMUT), 268 Ly Thuong Kiet Street, District 10 Ho Chi Minh City, Vietnam
e-mail: trantam2512@hcmut.edu.vn

D. H. T. Thanh
e-mail: thanh.dinh1603_99@hcmut.edu.vn

Vietnam National University Ho Chi Minh City (VNU-HCM), Linh Trung Ward, Thu Duc District Ho Chi Minh City, Vietnam

© The Author(s), under exclusive license to Springer Nature Switzerland AG 2023
P. L. Vo et al. (eds.), *Advances in Research on Water Resources and Environmental Systems*, Environmental Science and Engineering,
https://doi.org/10.1007/978-3-031-17808-5_29

f	Transfer function
b	Bias value
GR_{\log}	Gamma value of interest point on the well log
GR_{\min}, GR_{\max}	Maximum and minimum value of gamma on the well log
ϕ	Porosity
K	Permeability
ϕ^*	Porosity from neural network
K^*	Permeability from neural network
ϕ_{\max}, ϕ_{\min}	Maximum and minimum value of porosity in the original dataset [0.2775; 0.01]

29.1 Introduction

Porosity and permeability are two extremely important properties in petroleum engineering. These two properties determine oil and gas reserves and flow capacity of the reservoir. In particular, two properties determine the commerciality of an oil and gas field.

Porosity and permeability values can be determined from the analysis of well logging data and core samples in the laboratory. However, these methods are costly and time consuming. In addition, one uses empirical correlations to get the porosity and permeability calculation equations. However, each study is only true for certain geological conditions, the calculation results are local to each region, not general to the geological conditions of each different region. This leads to errors, and inaccuracies in calculations.

Therefore, finding a new method to determine porosity and permeability is essential. Machine learning methods such as artificial neural networks (ANNs) or support vector machines (SVMs) are the best methods for building nonlinear relationships to determine porosity and permeability quickly and accurate (Ahmadi and Chen 2019).

In this study, a comparison was carried out to find which approach was better among traditional methods in petroleum engineering or machine learning techniques. We also introduced the structure of machine learning models associated with the model building procedure for estimating porosity and permeability.

29.2 Machine Learning Methods

29.2.1 Artificial Neural Networks (ANN)

What Is Artificial Neural Networks? Artificial Neural Networks (ANN), first introduced by McCulloch and Pitts, are a mathematical model that mimics the capabilities

of biological neural structures for the purpose of designing a intelligent information processing system. An artificial neural network is a collection of neurons with a certain structure, neurons are divided into different layers. Usually a neural network has an input layer, one or more hidden layers, and an output layer. A neural network can be represented by numbers. For example, a 3–4–4–1 network is a network with 3 neurons in the input layer, 4 neurons in the first hidden layer, 4 neurons in the second hidden layer, and 1 neuron in the output layer. Between neurons in different layers there are transmission links containing individual weights of each link (Mohaghegh 2000).

Transfer Function. Transfer function has the function of transferring the variable domain of the input variable to another variable domain. Some of the transfer functions used are logistic sigmoid nonlinear function, tangent sigmoid nonlinear function and linear function. Where the logistic nonlinear function sigmoid returns values in the range [0; 1], and the nonlinear tangent function sigmoid returns values in the range [− 1; 1]. Nonlinear functions are often used for pattern recognition and are often used in the hidden layer, while linear functions are often used in prediction problems and are often used in the output layer (Zou et al. 2008).

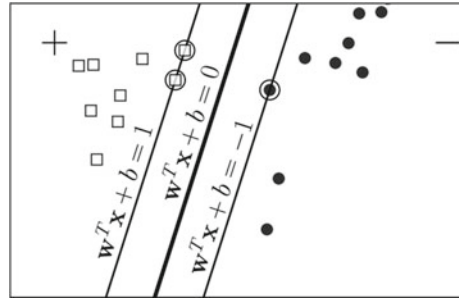
Principle of Artificial Neural Network. An artificial neural network is characterized by three factors that are network structure, network training method and activation (transfer) function. The output value of the neurons is multiplied by their respective association weights and passed to the next neuron as input parameters. The sum of all input values is substituted in the activation function, then the activation function result is the output value of the neuron as the formula:

$$y(x) = f\left(\sum_{i=1}^n w_i x_i + b\right) \quad (29.1)$$

The principle of an artificial neural network is the process of training the network to update the weights. The network training process consists of two stages: the forward propagation phase and the back propagation phase (Zou et al. 2008).

Overfitting. Overfitting is a phenomenon in which an artificial neural network model is built too fit the training data. This phenomenon causes the network's inability to generalize the data, which falsifies the prediction, and the model quality fails to cross validation. Overfitting occurs when the error in training the network is low and the error in testing the network is high. If the model does not have overfitting, the training error and the network test error will be low and stable in the last iterations. In order to avoid overfitting, the network training process needs to perform two parallel actions: error reduction and cross validation. The dataset used to train the network is divided into three parts: training data to adjust the set of weights linking neurons, validation data used for cross validation during network training, and testing data used to check the network (Ying 2019).

Fig. 29.1 The margin that divides two data sets with the equation $w^T x + b = 0$



29.2.2 Support Vector Machines (SVM)

What Is Support Vector Machines (SVM). Support vector machines (SVM) are machine learning algorithms that analyze data for classification and regression problems. This is a supervised learning method that looks at the data and sorts it into one of two categories. SVM outputs a plot of the sorted data with the margins between the two data as far apart as possible.

Figure 29.1 shows the division of two data sets by the margin with the equation $w^T x + b = 0$. The optimization problem of SVM is to find w and b so that the margin reaches the maximum value. This is a quadratic programming problem with the problem of optimizing (minimizing or maximizing) a quadratic objective function with many variables under linear constraints (Madeo et al. 2012).

Least-Squares Support-Vector Machines (LSSVM). Least-squares support-vector machines (LSSVM) are least-squares versions of SVM. In this version one finds the solution by solving a set of linear equations instead of a convex quadratic programming (QP) problem for classical SVMs. The least squares SVM classifier was proposed by Suykens and Vandewalle. LSSVM is a class of kernel-based learning methods (Suykens and Vandewalle 1999).

29.3 Results and Discussion

29.3.1 Dataset

In this study, the author uses the Volve field dataset located at Block 15/9 in the center of the North Sea region, Norway (Field: VOLVE—Norwegian Petroleum. xxxx). The petrophysical data include core logging with 557 data points of porosity and permeability by depth and well logging with 453 data points of DT (sonic), GR (gamma ray), RHOB (formation density), NPHI (neutron porosity) by depth.

29.3.2 Estimate Porosity and Permeability by Traditional Methods

Porosity. First, prepare input data from well logging and core logging. Then, calculate Shale Volume (V_{sh}). To calculate V_{sh} , we need to determine the Gamma Ray Index (IGR) with the input parameter being the gamma value read on the well log.

$$I_{GR} = \frac{GR_{log} - GR_{min}}{GR_{max} - GR_{min}} \tag{29.2}$$

Using the neutron method and the sonic method with correction of the clay volume, we have the results according to Tables 29.1, 29.2 and Fig. 29.2.

Permeability. According to the Tables 29.1, 29.2 and Fig. 29.2, estimating porosity by neutron method is exactly than sonic method. Therefore, we use porosity is estimated by neutron method for estimate permeability by using Wyllie & Rose and Timur methods (Shang et al. 2003). The results are shown in Tables 29.3, 29.4 and Fig. 29.3.

Observing Tables 29.3, 29.4 and Fig. 29.3, the authors found that the permeability is estimated by Wyllie and Rose and Timur method are different from most of the value of core samples. This shows that the two methods for estimate permeability in this case are not reliable.

In addition, the permeability can be estimated from the correlation between permeability and porosity of core logging is shown in Eq. (29.3) and Fig. 29.4.

$$permeability = 0.0278e^{0.4013*porosity} \tag{29.3}$$

From the observation of Table 29.5 and Fig. 29.5, the authors found that the core permeability (K_{core}) and estimated permeability (K_{cal}) values have a large difference.

Table 29.1 The results of porosity is estimated by neutron method

Sample	1	2	...	452	453
Depth (m)	3838.6	3839.4	...	3999.45	3999.7
ϕ -core	0.170	0.128	...	0.209	0.173
ϕ N	0.160	0.137	...	0.158	0.178

Table 29.2 The results of porosity is estimated by sonic method

Sample	1	2	...	452	453
Depth (m)	3838.6	3839.4	...	3999.45	3999.7
ϕ -core	0.170	0.128	...	0.209	0.173
Φ -sonic	0.194	0.145	...	0.194	0.201

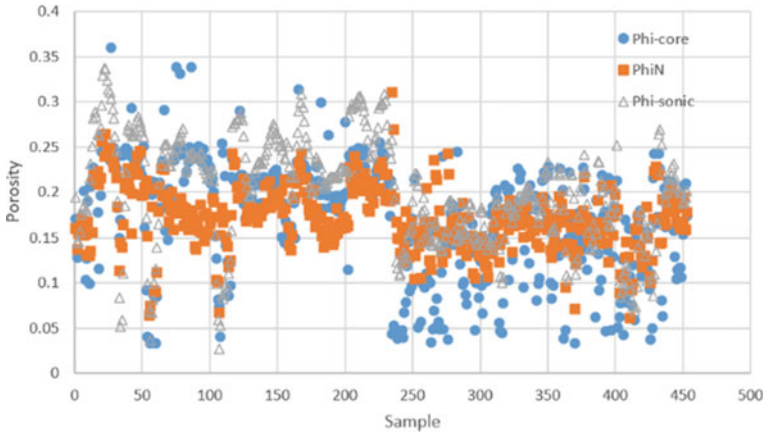


Fig. 29.2 Compare the porosity of core logging and porosity is estimated by neutron and sonic methods

Table 29.3 The results of permeability is estimated by Wyllie and Rose method

Sample	1	2	...	452	453
Depth (m)	3838.6	3839.4	...	3999.45	3999.7
K-core (mD)	13.8	1.02	...	3600	180
K-Wyllie and Rose (mD)	45.89	20.00	...	1.46	3.19

Table 29.4 The results of permeability is estimated by Timur method

Sample	1	2	...	452	453
Depth (m)	3838.6	3839.4	...	3999.45	3999.7
K-core	13.8	1.02	...	3600	180
K-Timur (mD)	119.63	66.31	...	3.86	7.03

29.3.3 Estimate Porosity and Permeability by Machine Learning Methods

Artificial Neural Networks (ANN)

Building an ANN Model to Estimate Porosity and Permeability. For the network to work properly, the authors convert the values of dataset to dimensionless [0; 1]. Dataset include 453 data points. Therein, 353 data points for building an ANN, 100 data points for testing the ANN. 353 data points for building an ANN divide into 3 parts:

- Training data: accounts for 70% (247 data points). These values are used in the training process, the network is adjusted according to the training error.

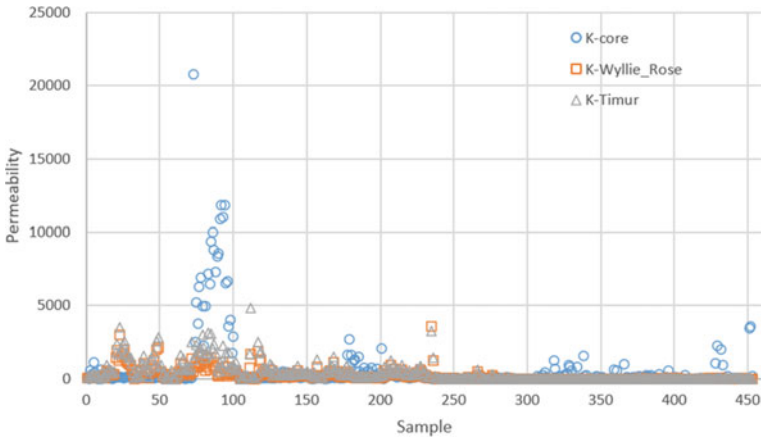


Fig. 29.3 Compare the permeability of core logging and permeability is estimated by Wyllie and Rose and Timur methods

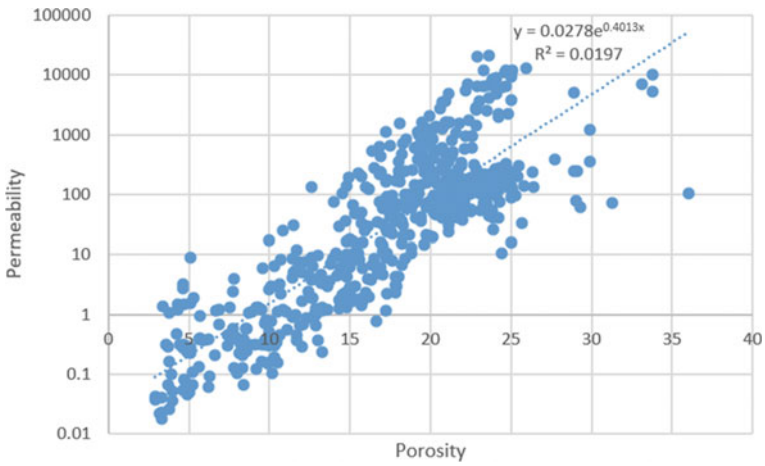


Fig. 29.4 Correlation between permeability and porosity

Table 29.5 The results of permeability is estimated by correlation

Sample	1	2	...	556	557
Depth (m)	3838.6	3839.15	...	3999.7	3999.95
K-core (mD)	13.8	25.2	...	180	850
K-cal (mD)	25.52	2.12	...	28.78	46.59

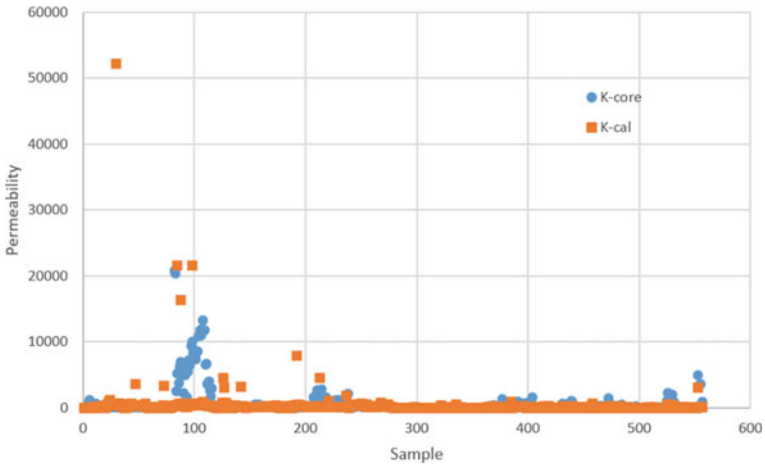


Fig. 29.5 Compare the permeability of core logging and permeability is estimated by correlation

- Validation data: accounts for 15% (53 data points) to check over-fitting of network.
- Testing data: accounts for 15% (53 data points) to test the network’s efficiency.

The neural network training for the best performance is at epoch 11 with Mean Square Error (MSE) = 0.00034899 (Fig. 29.6).

The result of neural network building is shown in Fig. 29.7.

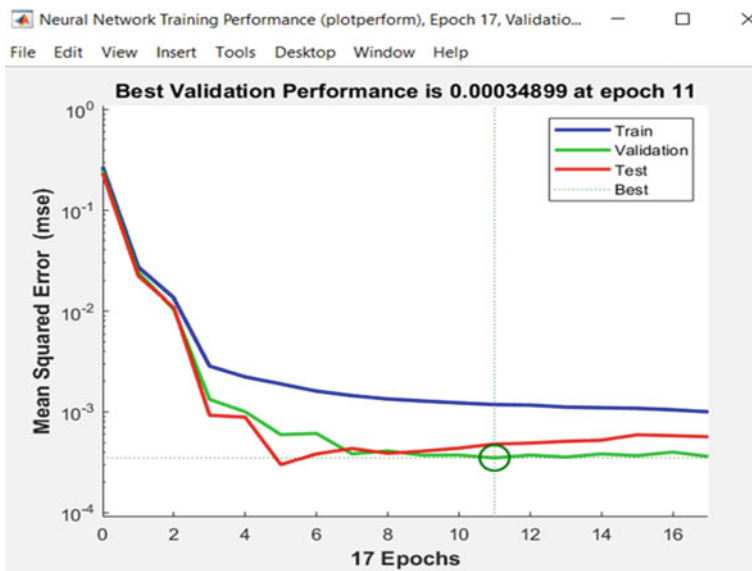


Fig. 29.6 Neural network training performance

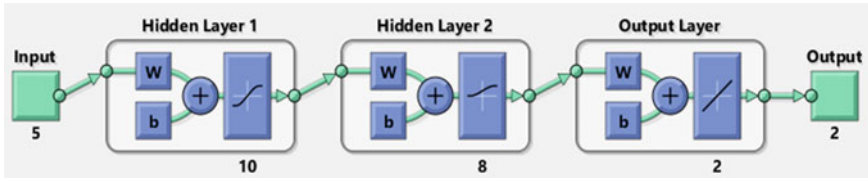


Fig. 29.7 Artificial neural network model for estimating porosity and permeability

According to the network structure 5-10-8-2 as shown in Fig. 29.7, the first hidden layer uses 10 neurons and the transfer function is the sigmoid tangent, the second hidden layer uses 8 neurons and the transfer function is the logistic sigmoid and the output layer uses purelin function.

Using the ANN Model to Estimate Porosity and Permeability. Neural network is used to estimate porosity and permeability from 5 input parameters include Depth, DT, GR, RHOB, NPHI.

Combining the dimensional transformation equation with the weights of the artificial neural network, the porosity and permeability estimation equation as follows:

$$\phi = \phi * .(\phi_{max} - \phi_{min}) + \phi_{min} \tag{29.4}$$

$$K = K * .(K_{max} - K_{min}) + K_{min} \tag{29.5}$$

Least-Squares Support-Vector Machines (LS-SVM)

Building an LS-SVM model to estimate porosity and permeability. From the original dataset (453 value points), we proceed to randomly divide into 2 subsets at the ratio of 80:20%:

- Training data (80%): this is the dataset for building the model.
- Testing data (20%): evaluate the accuracy of the training data.

The results of building the LSSVM model are shown as follows:

- Porosity: The best fit with $RMSE = 0.0064231$ and $R^2 = 0.99$ (Fig. 29.8)
- Permeability: The best fit with $RMSE = 7.9063$ and $R^2 = 0.99$ (Fig. 29.9).

Using the LS-SVM to Estimate Porosity and Permeability. To extract porosity and permeability from the model, Matlab provides the following function:

$$Yfit = c.predictFcn (T)$$

With:

c is the trained model name, here is trainedModel.

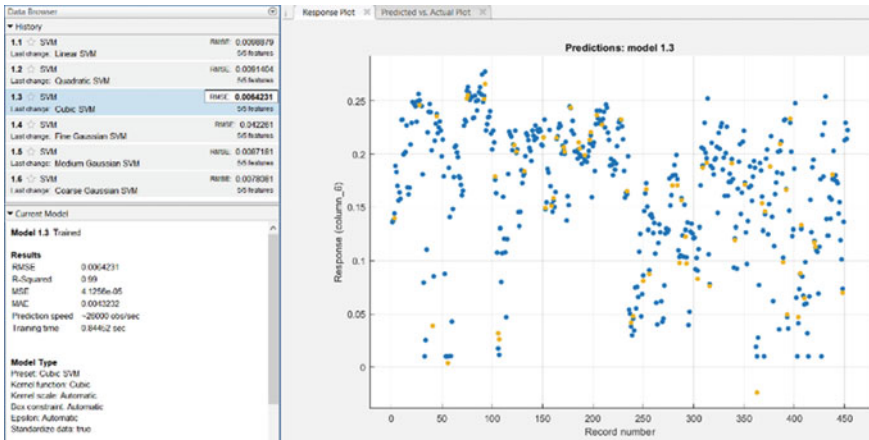


Fig. 29.8 Distribution of the trained model on the porosity dataset

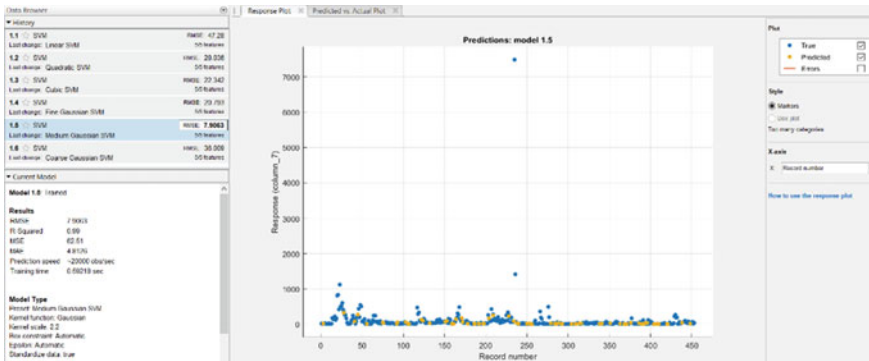


Fig. 29.9 Distribution of the trained model on the permeability dataset

T is the new measurement point with the format of a 5-column matrix of 5 input parameters.

Y_{fit} : will return the predicted porosity and permeability values at the measuring point T .

Enter the code in Command Window:

$$porosity = trainedModel.predictFcn(T_{test})$$

$$permeability = trainedModel.predictFcn(T_{test})$$

Matlab returns the predicted porosity and permeability values at each measurement point and outputs the data to a table.

Table 29.6 Compare error of methods for estimating porosity

No	Method	MSE	RMSE	R ²
1	Neutron	0.002996663	0.054741784	-1.34334913
2	Sonic	0.003560034	0.059666018	0.183129365
3	LLSVM	$1.77908 * 10^{-5}$	0.0042179	0.995478441
4	ANN	$1.26908 * 10^{-5}$	0.0035624	0.996432023

Table 29.7 Compare error of methods for estimating permeability

No	Method	MSE	RMSE	R ²
1	Wyllie and Rose	3,776,046.024	1943.205091	-11.03160734
2	Timur	3,303,967.445	1817.681888	-5.854611846
3	Correlation	10,337,618.26	3215.216674	-0.413731588
4	LLSVM	251.0630506	15.84496925	0.98093591
5	ANN	45.92752224	6.776984746	0.999741476

29.3.4 Compare Results

To evaluate the accuracy of the above methods to estimate porosity and permeability, the authors compares the errors of each method (traditional, LLSVM and ANN) by using statistical parameters include: mean squared error (*MSE*), square root of mean squared error (*RMSE*), coefficient of determination (*R*²).

From the results of Table 29.6, both LLSVM and ANN machine learning methods have high *R*² and low *MSE*. In which, the ANN method has the highest value of *R*² and lowest values of *MSE* and *RMSE*. It can be concluded that both LLSVM and ANN methods can predict porosity accurately than traditional methods and ANN is the most accurate and reliable method in porosity estimation.

From the results of Table 29.7, in general, the traditional methods give high *MSE* and very low *R*², while the LLSVM and ANN methods have high value of *R*² and low values of *MSE* and *RMSE*. In which, the ANN method still has the highest value of *R*² and lowest values of *MSE* and *RMSE*.

Thus, it can be seen that two LLSVM and ANN machine learning methods give accurate results than traditional methods in estimating porosity and permeability. In particular, the artificial neural network method is better than other methods.

29.4 Conclusions

With the estimation and comparison of different methods, the study has shown the great advantages of two machine learning methods, LLSVM and ANN with traditional methods.

ANN model has structure 5-10-8-2 with two hidden layers. The results showed that both the ANN and LSSVM models could be used. Nevertheless, based on the R^2 values of 0.9997 and 0.9809, MSE values of 6.7769 and 15.8849 respectively, the ANN model is a robustness to the LSSVM model. The highest value of R^2 and lowest values of MSE prove that the ANN is best method in this study.

Acknowledgements We would like to thank Ho Chi Minh City University of Technology (HCMUT), VNU-HCM for the support of time and facilities for this study.

References

- Ahmadi MA, Chen Z (2019) Comparison of machine learning methods for estimating permeability and porosity of oil reservoirs via petro-physical logs. *Petroleum* 5:271–284. <https://doi.org/10.1016/j.petlm.2018.06.002>
Field: VOLVE—Norwegian Petroleum
- Madeo RCB, Peres SM, Lima CAM (2012) Overview on support vector machines applied to temporal modeling
- Mohaghegh S, UWV (2000) Virtual-intelligence applications in petroleum engineering : part 1—artificial neural networks 64–71
- Shang BZ, Hamman JG, Chen HL, Caldwell DH (2003) A model to correlate permeability with efficient porosity and irreducible water saturation. In: Proceedings SPE annual technical conference exhibition 2203–2210. <https://doi.org/10.2523/84303-ms>
- Suykens JAK, Vandewalle J (1999) Least squares support vector machines
- Ying X (2019) An overview of overfitting and its solutions. *J Phys Conf Ser* 1168. <https://doi.org/10.1088/1742-6596/1168/2/022022>
- Zou J, Han Y, So SS (2008) Overview of artificial neural networks. *Methods Mol Biol* 458:15–23. https://doi.org/10.1007/978-1-60327-101-1_2

Chapter 30

Mapping Wetland Ecosystems Protection and Restoration Priority Using GIS, Remote Sensing, Landscape Ecology, and Multi-criteria Analysis (Case Study in Dong Thap Muoi)



Phi Son Nguyen , Thanh Thuy Nguyen , Thi Thanh Dinh ,
Thi Hang Vu , Thi Thanh Huong Nguyen , and Lam Le 

Abstract The prioritisation of wetland ecosystems is the essential information contributing to scientific and methodological fundamentals for establishing the National strategy and plan on environment protection and biodiversity conservation for each wetland ecosystem in Vietnam. This paper proposes the method of mapping and ordering the priority of wetland ecosystems protection and restoration based on the application of GIS, remote sensing, landscape ecology approach, and multi-criteria analysis. The primary method consists of 3 phases: (i) Defining the protection and restoration criteria; (ii) Mapping wetland ecosystems and building criteria layers based on GIS, remote sensing, and landscape ecology approach; (iii) Determining the priority of wetland ecosystems using multi-criteria analysis. This method is applied to Dong Thap Muoi—a high biodiversity wetland region composing two Ramsar sites and conservation areas. The data of 14 criteria on capacity, degradation services, and pressures on each wetland ecosystem are synthesised using GIS and remote sensing images. AHP-TOPSIS—a hybrid multi-criteria assessment method prioritises wetland ecosystems’ conservation and restoration. The study indicated that the criteria of the number of endangered and rare species, total species, invasive alien species, and the lost number of endangered, rare animals and plants play a crucial role in prioritising protection and restoration. The results are the wetland ecosystems protection and restoration priority order maps, which support making appropriate

The original version of this chapter was revised. The Author name has been corrected from “Thi Dinh” to “Thi Thanh Dinh”. The correction to this chapter can be found at https://doi.org/10.1007/978-3-031-17808-5_40

P. S. Nguyen · T. T. Nguyen (✉) · T. T. Dinh · T. T. H. Nguyen · L. Le
Vietnam Institute of Geodesy and Cartography, Ministry of Natural Resources and Environment,
Hanoi 100000, Vietnam
e-mail: ntthuydostic@gmail.com

T. H. Vu
Faculty of Geography, VNU University of Science, Hanoi 100000, Vietnam

© The Author(s), under exclusive license to Springer Nature Switzerland AG 2023, 487
corrected publication 2023

P. L. Vo et al. (eds.), *Advances in Research on Water Resources and Environmental Systems*, Environmental Science and Engineering,
https://doi.org/10.1007/978-3-031-17808-5_30

decisions to formulate policies and build conservation strategies and plans in the Dong Thap Muoi region.

Keywords Wetland ecosystem · GIS · Remote sensing · Landscape ecology · Multi-criteria analysis · Priority order · Wetland protection · Restoration

30.1 Introduction

Wetland is among the most valuable environments globally, essential for the survival, reproduction, and biodiversity of animals and plants, where birds, mammals, reptiles, amphibians, fish, and invertebrates are densely gathered and store the vital plant gene sources. The interaction of physical, biological, and chemical elements of the wetlands as part of the “infrastructure nature” of the Earth forms the functions for life, such as water storage, storm shielding, flood mitigation, coastal stability and erosion control, groundwater supply and storage, water purification, nutrients, sediments, and contaminants retention, local climatic condition regulation. Besides that, wetland ecosystems also provide education, entertainment, travel services, and human livelihoods (Ramsar Convention Secretariat 2013a, b; Vietnam Environmental Protection Department 2005).

Having had 12 million ha of wetland (<https://baotainguyenmoitruong.vn/bao-ton-va-su-dung-ben-vung-cac-vung-dat-ngap-nuoc-298871.html>), Vietnam is known as one of the high biodiversity countries in the world with a variety of wetland ecosystem types, species of creatures, and richness of gen source. Economic development and climate change have been making a significant negative impact on wetland ecosystems. Human activities have significantly resulted in the lost and degraded biodiversity lost and degraded, such as mangrove deforestation, forest burning, destructive fishing practices, environmental pollution, overexploitation, and the introduction of invasive species. Besides, such natural disasters as fires, storms, drought, salinisation, cyclones, and epidemics, are also other factors that badly affect the condition and primary natural resources of wetlands (Vietnam Environmental Protection Department 2005; Ministry of Natural Resources and Environment 2021; Nhan 2014). Consideration of great biodiversity potentials, services, and the threats to the wetland ecosystems, it is vital to investigate and evaluate the environmental status, the gen and the species richness, and the degraded natural ecosystem to find possible solutions for restoration, conservation, and wise and resilient usage of Vietnam’s biological resources.

In Vietnam, the contents of planning for environmental protection and biodiversity conservation include: assessing the status and evolution of environmental quality, natural landscape, biodiversity, and climate change effects; defining the objectives, the tasks, and solutions for environmental protection; zoning the environment; conserving nature and biodiversity; and building criteria to determine the critical level and the implement priority order of national projects, (National Assembly of the Socialist Republic of Vietnam 2020; National Assembly of the Socialist Republic

of Vietnam 2017). The decrees detail several articles of the Law on Environmental protection and planning (Government of the Socialist Republic of Vietnam 2019; Government of the Socialist Republic of Vietnam 2022) show that wetland ecosystem is one content of biodiversity conservation planning, which has to evaluate and order the priority for investment and implementation.

By 2030, Vietnam's National strategy on biodiversity (Prime Minister of the Socialist Republic of Vietnam 2022) is conservation with sustainable ecosystem services usage, and biodiversity contributes to developing the social economy, reducing poverty, and improving people's living standards by applying the ecosystem approach to conservation and biodiversity. The National strategy's general target on biodiversity is increasing the area of protected and restored natural ecosystems, keeping the integrity and connection. Besides, the strategy also defines some of the content and critical building the processes and technical guidance for restoring the degraded natural ecosystems, especially wetland ecosystems, coral reefs, and seagrass, and developing the guide of ecosystem services quantification.

Previous studies and projects mainly focused on wetland classification based on water and land cover elements without indicating the different conditions of wetland ecosystems such as forming origin, soil, elevation, climate, hydrology, oceanography (Hai et al. 2015; Phuong and Hoe 2015; Linh et al. 2018; Vietnam Institute and of Geodesy and Cartography 2012; Vietnam Institute and of Geodesy and Cartography 2018; Vietnam Institute and of Geodesy and Cartography 2020; Xuan and Hoa 2015). These are also the essential elements that form in a particular wetland ecosystem.

In Vietnam, the ecological landscape approach has been applied to study the adaptation of some plants to develop the economy and conserve mangrove forests (Nguyen et al. 2015); zone and evaluate the ecological landscape potential for territorial organisation, planning for sustainable development of coastal wetland ecosystem (Hang 2012; Duong 2009) or assess landscape according to ecological-economic approach (Huan 2005). Landscape analysis is also used in the world to research wetlands (Tudor 2014; Environmental Law Institute 2013; Lopez et al. 2013; Malekmohammadi and Jahanishakib 2017); there has not been any proposal on the mapping process of wetland ecosystems based on the ecological landscape approach in all the above papers and books.

The requirements to show that the project or wetland ecosystem needs to be prioritised for protection and restoration are appropriate criteria and assessment methods. Globally, there are a significant number of studies to identify wetlands that need conservation based on assessing the criteria about biodiversity value, role of ecosystem functions and services (Ramsar Convention Secretariat 2013a, b; Mekong River Commission 2017), risks and vulnerabilities (Malekmohammadi and Jahanishakib 2017; Jiang et al. 2017; Sarkar et al. 2016; Malekmohammadi and Rahimi Blouchi 2014). In Vietnam, the papers often focus on the vital status, pressor, and benefits indicators for measuring and monitoring wetland ecosystems

(Nhan 2010, 2014; Lan and Hai 2009)¹; sensitive and degradation assessment criteria for coastal wetland ecosystems (Yet et al. 2010; Hung and Hoe 2014), ... Using the proposed criteria separately in these studies may not have been sufficient; therefore, the combination usage will comprehensively assess priorities for protecting and restoring wetland ecosystems.

The multi-criteria assessment methods are widely used around the world in many fields. The MCA, AHP, F-AHP, TOPSIS, and F-TOPSIS methods are used to assess and choose the solution for waste management, finding the best position for burying waste. The combinations of MCA, ELECTRE, Delphi, DA, F-MAA, F-AHP, TOPSIS, SWOT, ANP, DPSIR and MUPOM are used to assess environmental quality and climate change, sustainability and ecology. Based upon the association of the DPSIR model with DSS, MCA, MCDA, TOPSIS, and CP, combining Delphi and AHP methods, integrated AHP—GIS to evaluate and manage water resources, river basin, reservoir, flood, and hazards. Using ANP, MCA, MCDA, AHP-TOPSIS for land management; assessing crop selection, agricultural risks, and deciding in agriculture (Chan et al. 2019; Hajkovicz and Higgins 2008; Jozaghi et al. 2018; Opricovic and Tzeng 2004; Velasquez and Hester 2013).

In Vietnam, AHP, PCA, PRA, and SAW methods are used to assess land-use sustainability, select crop models, and determine the weight of the component indexes in the green urban index set. PAM, MFA, AHP, and PCA are used to evaluate green growth. Assessment of landscape ecological adaptation is done by using AHP and F-AHP. The selection of locations for the planning of waste burial using AHP, F-AHP GIS (Cuong 2009; Dat et al. 2017; Dinh 2016; Huong 2030; Linh et al. 2017; Luan and Tram 2013) ... However, the multi-criteria analysis method to prioritise wetland ecosystems protection and restoration in Vietnam has not been studied yet.

Remote sensing and GIS have been popularly used to extract, process, and analyse data from multiple sources such as satellite images, geodatabase, topographic maps, elevation data, and LiDAR data... for many applications. The wetland's information on the cover, water quality, landscape degradation, fire risk, and elevation can be captured using remote sensing data. GIS is used to model spatial distribution, character, and attributes of natural, social-economic features by using the algorithm of assign information, overlay, analysis, calculation, interpolation; editing and publishing thematic maps (Linh et al. 2018; Vietnam Institute and of Geodesy and Cartography 2012; Vietnam Institute and of Geodesy and Cartography 2018; Vietnam Institute and of Geodesy and Cartography 2020; Xuan and Hoa 2015; Hang 2012; Kien et al. 2013; Vietnam Environment Administration 2011; Ve et al. 2013; Tin et al. 2011; Phu 2009; Son 2008).² Therefore, remote sensing and GIS are useful

¹ Nhan, H.T.T., Hai, H.T.: Building biodiversity indicators for surveying the wetland ecosystems of Xuan Thuy national park, Nam Dinh province. The 5th National Scientific Conference on Ecology and Biological Resources, pp. 1498–1505. (in Vietnamese).

² Thuy, N.T.: Proposing the process of mapping inland wetlands. In: The 9th National Geography Conference, pp. 1097–1100. (Year) (in Vietnamese).

technologies to extract and build data to prioritise wetland ecosystem protection and restoration.

Dong Thap Muoi stretches over three Long An, Tien Giang, and Dong Thap provinces, with about 700,000 ha of *Melaleuca* forest and water surface. The region is a closed floodplain surrounded by high mounds along the Vietnam-Cambodia border with the storage of over 100 billion m³ of water storage. Dong Thap Muoi is the last place where the flooded cane and reed forest, one of the typical wetland ecosystems, still exists. Dong Thap Muoi has a relatively sizeable flooded area and high biodiversity in Vietnam with two Ramsar sites, namely Tram Chim National Park in Dong Thap and Lang Sen wetland reserve in Long An. In addition, there are Dong Thap Muoi ecological reserve, biodiversity conservation areas such as Xeo Quyt relic site, and Gao Giong eco-tourism area. These places are the habitat of many species of birds, fish, reptiles, and benthic animals, including many endemic and rare species that need to be protected, and several species, that are in danger of extinction. The wetlands in this area face many problems such as drought, saltwater intrusion, forest fires, sea-level rise, the invasion of alien species due to agricultural production and farming activities, aquaculture, industrial development, tourism, and other human factors demands (Vietnam Institute of Geodesy and Cartography 2012). The ongoing conducted studies in the Dong Thap Muoi region mainly focus on solutions to improve the land and the economic efficiency of the rice-growing wetlands, evaluate the potential for tourism development; conservation of ecosystems, wetlands, and adaptation to climate change with no research related to determining the priority level of protection and restoration of wetland ecosystems. Therefore, the study and application of GIS, remote sensing, landscape ecology approach, and multi-criteria analysis for mapping and ordering priority of wetland ecosystems protection and restoration is essential (Fig. 30.1).

30.2 Researching Data and Methodology

30.2.1 Researching Data

This paper used the data below to build the thematic data layer for each protection and restoration assessment criteria. The detail is shown in Table 30.1. Dong Thap Muoi's data is shown in the VN2000 coordinate system.

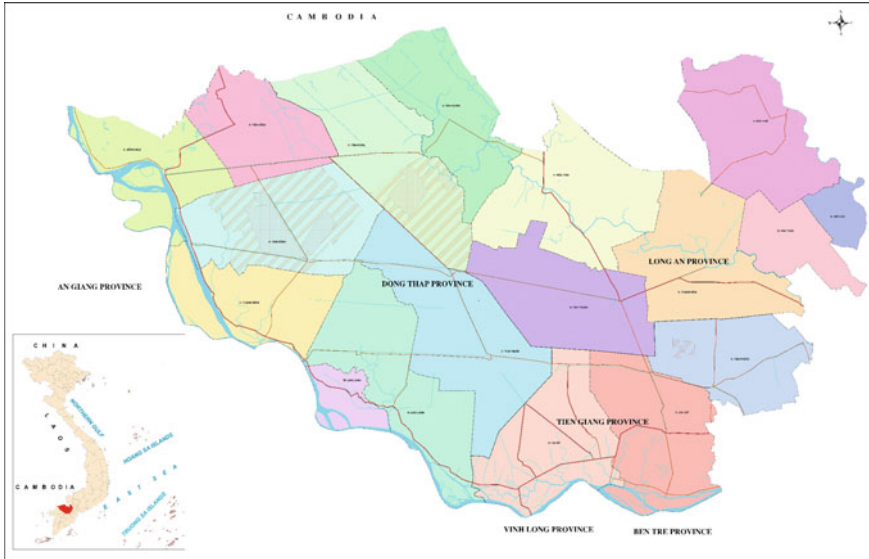


Fig. 30.1 Location of the Dong Thap Muoi (Vietnam Institute and of Geodesy and Cartography 2012)

Table 30.1 Data used for research

Ord	Data	Source
1	Hydrological network	Geodatabase 1:2000 and 1:5000
2	Roads network	Geodatabase 1:2000 and 1:5000
3	Fire points	https://earthdata.nasa.gov/data/near-real-time-data/firms/active-fire-data
4	Water quality	People’s Committees of Dong Thap, Tien Giang, Long An
5	Landsat 7, 8 images	http://earthexplorer.usgs.gov/ LE07_L1TP_125052_20100424_20161215_01, LE07_L1TP_125053_20100424_20161215_01, LC08_L1TP_125052_20181031_20181115_01, LC08_L1TP_125053_20181031_20181115_01
6	Land use map	People’s Committees of Dong Thap, Tien Giang, Long An
7	Biodiversity, invasion species, strategies, planning map ...	Statistical yearbook of Long An, Tien Giang, Dong Thap provinces; Vietnam institute of Geodesy and Cartography; the investigation and survey data, papers and documents ...

30.2.2 Researching Methodology

The mapping and ordering of wetland ecosystem protection and restoration priority shown in Fig. 30.2 include three main phases: (i) Defining the protection and restoration definition criteria; (ii) Mapping wetland ecosystems and building criteria layers; (iii) Ordering the protection and restoration priority of wetland ecosystems.

30.2.2.1 Defining the Wetland Ecosystem Protection and Restoration Priority Criteria

The targets of wetland ecosystem protection and restoration are defined based on the referenced documents and data on natural, socio-economic, and environmental conditions and previous research results or use survey consultation results with people,

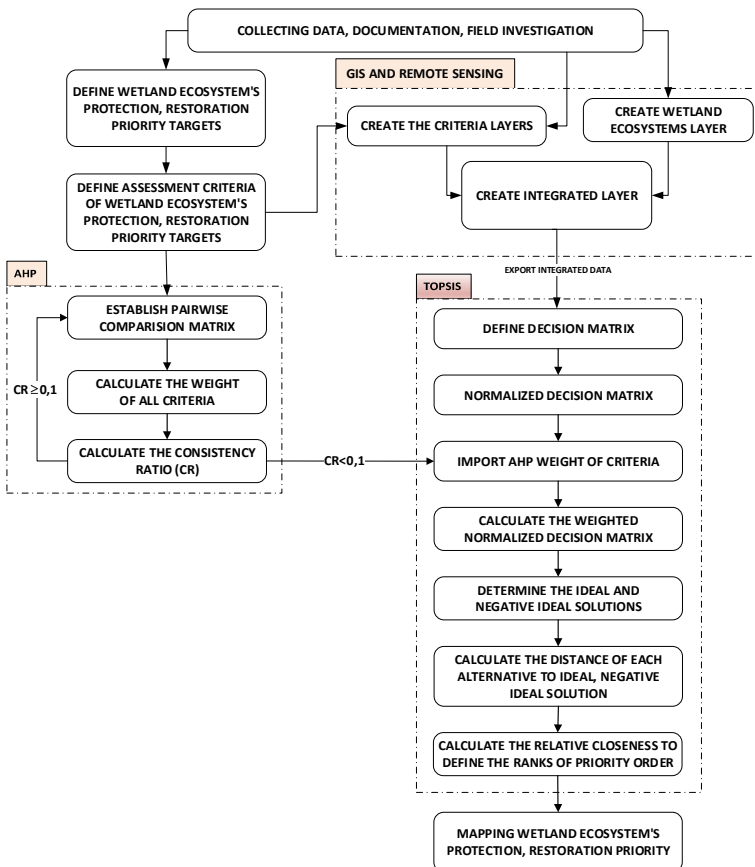


Fig. 30.2 Process of mapping and ordering wetland ecosystem protection, restoration priority

managers, or experts. For each aim, criteria for ordering protection and restoration priority of wetland ecosystems are defined based on ecosystem service values, potential risk pressures, and external factors (natural or man-made hazards).

30.2.2.2 Mapping Wetland Ecosystems and Building Criteria Layers

(a) *Mapping wetland ecosystems*

The wetland ecosystems mapping process is indicated in Fig. 30.3. In this step, the wetland ecosystems map is built using seven thematic landscape ecology data: geology, topography and geomorphology, oceanology and hydrology, bioclimate, soil, vegetation cover, and land use status. These data are created from existing ones or extracted from satellite data and normalised the attribute, boundaries, and topology by GIS. Classifying and numbering landscape types is carried out by overlaying thematic layers. The next step is establishing the wetland ecosystems map based on numbered landscape types using criteria to identify wetland types. The steps as shown in Thuy (2020).

(b) *Building criteria layers*

Using the methods such as collection, statistic, synthesis document, data; field interview, investigation, and survey; measuring, sampling, and analysing samples; modelling; analysing and processing information; and mapping, remote sensing, and GIS to extract and build criteria layers. Area and density

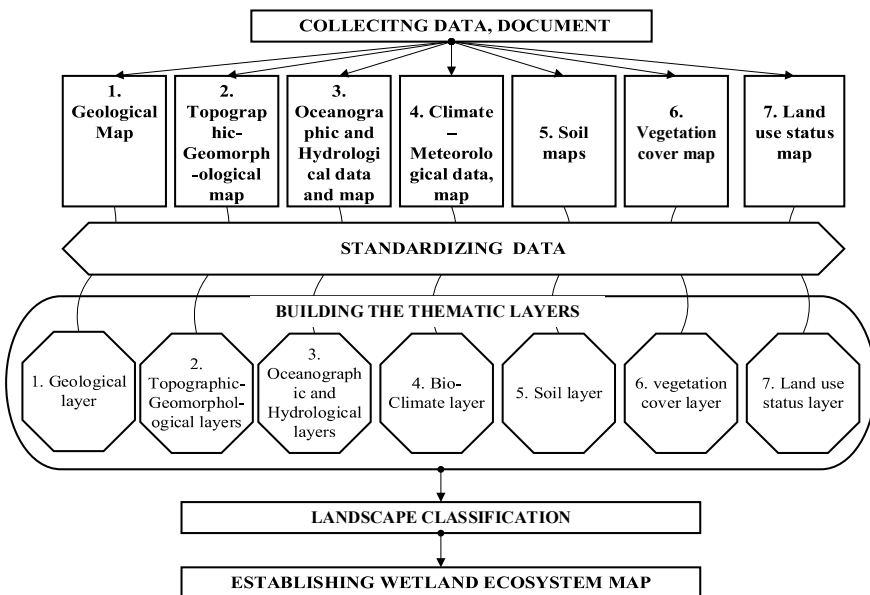


Fig. 30.3 The process of wetland ecosystems mapping

of vegetation, land-use change, surface water quality indicators, land surface temperature, and moisture content are extracted from satellite images combined with field observation data. GIS technology is used to assign and spatialise attributes, overlay, and calculate change; interpolate, re-classify, and construct raster data layers on distance, slope, terrain elevation, temperature, humidity, and precipitation.

The above methods will be chosen depending on the studying regions to collect, extract, model data, and information for the proposed method’s input data.

(c) *Creating the integrated map*

The integrated criteria data layer is done by joining the attribute information according to each criterion into the wetland ecosystem layer (map). This step is performed using data superposition techniques, spatial queries, raster data analysis, and attribute association of GIS tools. The result will be exported to build a decision matrix—input data for assessing and ranking priority levels for the protection and restoration of wetland ecosystems.

30.2.2.3 Ordering the Protection and Restoration Priority of Wetland Ecosystems

Analysing many multi-criteria assessment methods shows that the AHP method provides a solution to determine the weights of the reliable criteria through assessing consistency. This solution eliminates the disadvantage of the TOPSIS in that there is no technique to control the reliability of the input criteria weight set. TOPSIS provides a solution to determine the distances from alternatives to the positive and negative ideal solutions, determining the order of priority and overcoming the weakness of AHP, which is the ranking permutation (Velasquez and Hester 2013; Dat et al. 2017) ... From these characteristics, this paper proposes a combination of AHP and TOPSIS to order the priority of wetland ecosystems.

(a) *Defining the input criteria weight set by using AHP*

AHP method is used to construct the pair-wise comparison matrix, calculate the weighted set of the evaluation criteria, and determine the consistency in assessing the importance of the criteria. The comparisons are made in pairs and aggregated into a pair-wise comparison matrix of n rows and n columns (n is the number of criteria).

The pair-wise comparison matrix is represented by the following formula (Saaty 1980; Phuong and Mai 2018):

$$A = (a_{ij})_{n \times n} = \begin{bmatrix} 1 & a_{12} & \dots & a_{1n} & a_{21} & \vdots & a_{n1} & 1 \\ & & & & & & & \\ & & & & & & & \\ & & & & & & & \\ & & & & & & & \\ \vdots & a_{n2} & \dots & \ddots & \dots & a_{2n} & \vdots & \\ & & & & & & & 1 \end{bmatrix} \tag{30.1}$$

Table 30.2 Table to look up RI values according to the number of criteria (Saaty 1980)

n	1	2	3	4	7	8	9	10	11	12	13	14	15
RI	0	0	0.58	0.9	1.32	1.41	1.45	1.49	1.51	1.48	1.56	1.57	1.59

In which, a_{ij} shows the importance of the i th row criterion compared to the j column criterion. The relative importance of criterion i compared to criterion j is calculated according to the ratio k , whereas criterion j compared to criterion i is $1/k$ thus $a_{ij} = \frac{1}{a_{ji}}$. The level of importance is referenced in Saaty’s pair-wise comparison table (Saaty 1980).

The AHP determines the inconsistency of pair-wise comparisons (expert judgments) through the consistency ratio (CR) according to the following formula (Saaty 1980):

$$CR = \frac{CI}{RI} \tag{30.2}$$

$$CI = \frac{\lambda_{\max} - n}{n - 1} \tag{30.3}$$

where CR is the consistency ratio, CI is the consistency index, and RI is the random consistency index corresponding to the number of criteria (n) provided in Table 30.2.

If $CR < 0.1$, the pair-wise comparison matrix is consistent, so the set of weights is accepted to move on to the next step. Use the AHP method’s weights to calculate, process, and rank the wetland ecosystems that must be prioritised for protection and restoration.

(b) *Ordering the protection and restoration priority of wetland ecosystems*

TOPSIS based on the fundamental premise that the best solution has the shortest distance from each alternative to the positive-ideal solution and the longest distance from each alternative to the negative-ideal one. Alternatives are ranked using an overall index calculated based on the distances from the ideal solutions. The ordering of the protection and restoration priority of wetland ecosystems by TOPSIS contains the below steps (Jozaghi et al. 2018):

Step 1 *Building the decision matrix*

The decision matrix $X = (x_{ij})_{m \times n}$ has the number of rows as the wetland ecosystems to be ranked and the number of columns as the criteria used to calculate the order of protection and restoration priority.

Step 2 *Calculating the normalised decision matrix*

The normalised decision matrix is built to transform the dimensional units into scalar units to compare the criteria values in the matrix $X = (x_{ij})_{m \times n}$. The normalised value r_{ij} is calculated by the following formulas:

$$R = (r_{ij})_{m \times n} = A_1 A_2$$

$$\begin{matrix} \vdots & A_m & (r_{11} & r_{12} & r_{21} & r_{22} & \dots & r_{1n} & \dots & r_{\dots n} & \dots \\ & & \vdots & \dots & \dots & \dots & & \vdots & \dots & \vdots & \dots \\ & & \dots & \dots & \dots & \dots & & \dots & \dots & \dots & \dots \end{matrix} \quad (30.4)$$

where

$$r_{ij} = x_{ij} / \sqrt{\sum_{i=1}^m (x_{ij})^2} \quad (30.5)$$

$$r_{ij} = 1 - (x_{ij} / \sqrt{\sum_{i=1}^m (x_{ij})^2}) \quad (30.6)$$

The formula (30.5) is used to calculate normalised values of the positive (good) criteria, and formula (30.6) is applied for the negative (bad) criteria.

Step 3 *Calculating the weighted normalised decision matrix*

The weighted normalised matrix is calculated by multiplying the value normalised decision matrix r_{ij} by the weight of corresponding criteria (which is calculated by AHP). The weighted normalised value v_{ij} is presented by the formula (30.7):

$$v_{ij} = w_j \times r_{ij} \quad (30.7)$$

where $i = 1, \dots, m; j = 1, \dots, n; m$ is the number of attribute values in each criterion, n is the number of criteria, w_j is the weight of j th criteria.

Step 4 *Calculating the positive and negative ideal solutions*

The positive (A^+) and negative (A^-) ideal solutions are defined by using formula (30.8) and formula (30.9) as:

$$A^+ = [v_1^+, \dots, v_2^+, \dots, v_n^+] \quad (30.8)$$

$$A^- = [v_1^-, \dots, v_{\dots}^-, \dots, \dots, v_n^-] \quad (30.9)$$

where $\{v_j^+ = \{v_{\dots}\}; i = 1, 2, \dots, m; v_j^- = \{v_{ij}\}; i = 1, 2, \dots, m$ if j th criterion is positive.

$\{v_j^+ = \{v_{ij}\}; i = 1, 2, \dots, m; v_j^- = \{v_{\dots j}\}; i = 1, 2, \dots, m$ if j th criterion is negative.

Step 5 *Calculating the distance from each alternative (wetland ecosystem) to the positive and negative ideal solution*

The distance from each alternative to the positive and negative ideal solutions is obtained by applying the Euclidean distance theory. Formulas (30.10) and (30.11) show positive and negative distance calculation processes.

$$S_i^+ = \sqrt{\sum_{j=1}^n (v_{ij} - v_j^+)^2} \quad (30.10)$$

$$S_i^- = \sqrt{\sum_{j=1}^n (v_{ij} - v_j^-)^2} \quad (30.11)$$

Step 6 *Calculating the relative proximity of each alternative (wetland ecosystem) to the positive ideal solution*

The below formula determines the relative closeness of the i th alternative:

$$C_i^+ = S_i^- / (S_i^+ + S_i^-) \quad (30.12)$$

where $0 \leq C_i^+ \leq 1$, $i = 1, 2, \dots, m$

Step 7 *Ordering the protection and restoration priority of wetland ecosystem*

The order of wetland ecosystem protection and restoration priority is based on the relative proximity calculated in the previous step. The wetland ecosystems with a high priority will have higher C_i^+ values and are closer to the ideal positive solution. They are suitable and should be chosen. The orders in this step are assigned to the wetland ecosystem data layer to present the wetland ecosystem protection and restoration priority map.

30.3 Results and Discussion

30.3.1 *Defining Dong Thap Muoi's Wetland Ecosystems Protection and Restoration Criteria*

The selected objectives and criteria for assessing the wetland ecosystems protection and restoration priority of Dong Thap Muoi region are proposed based on synthesising the collected documents, research, and interviewed local people and managers about the natural, social-economic, ecological conditions, master plan, planning, plan. After considering all interviews and available data of Tram Chim National Park (TC), Lang Sen Wetland Reserve (LS), Dong Thap Muoi Ecological Reserve (DTME), Xeo Quyt relic site (XQ), Gao Giong eco-tourism area (GG), Dong Thap Muoi medicinal plant conservation area (DTMM), Tan Lap floating village tourist site, Dong Sen Go Thap ecological area (DSGT), the authors decided to select objectives and criteria that are protecting and restoring the cultural and supporting services. The criteria are listed in Table 30.3.

Table 30.3 Selected criteria for ordering protection and restoration wetland ecosystems priority of Dong Thap Muoi region

No	Name of the criteria	Unit	Sign
A	Protection		
I	Support Services		
<i>1</i>	<i>Biodiversity</i>		
1.1	Total species	Species	BV1
1.2	The number of endangered and rare species	Species	BV2
<i>2</i>	<i>Pressure on biodiversity</i>		
2.1	The number of invasive alien species	Species	BV3
2.2	Water salinity	‰	BV8
2.3	Forest fire sensitivity		BV9
II	Cultural services		
<i>1</i>	<i>Ability to provide tourism and entertainment services</i>		
1.1	The average number of tourists per year	Person	BV10
1.2	Average annual revenue from tourism	Million	BV11
<i>2</i>	<i>Pressure on tourism and entertainment</i>		
2.1	Distance from livestock areas to wetland regions	m	BV4
2.2	Distance from industrial areas to wetland regions	m	BV5
2.3	Distance from residential areas to wetland regions	m	BV6
2.4	Distance from roads to wetland regions	m	BV7
B	Restoration		
I	Support services		
1	Decreased vegetation cover area	ha	PH1
2	The lost number of endangered, rare animals and plants	Individual	PH2
3	Surface water quality		PH3

30.3.2 Creating Wetland Ecosystems Map

The wetland ecosystems map is inherited from previous research (Thuy 2020), which was established using seven thematic landscape ecology data: geology, topography and geomorphology, hydrology, bio-climate, soil, vegetation cover, and land use. The Landsat satellite images were used to correct the vegetation cover and land use layers. The wetland ecosystems map is shown in Fig. 30.4.

30.3.3 Building Criteria Data Layers

The decreased vegetation cover area (PH1) is extracted and calculated using Landsat 7 and 8 imagery on 24/4/2010 and 15/11/2018. All of them are converted from the

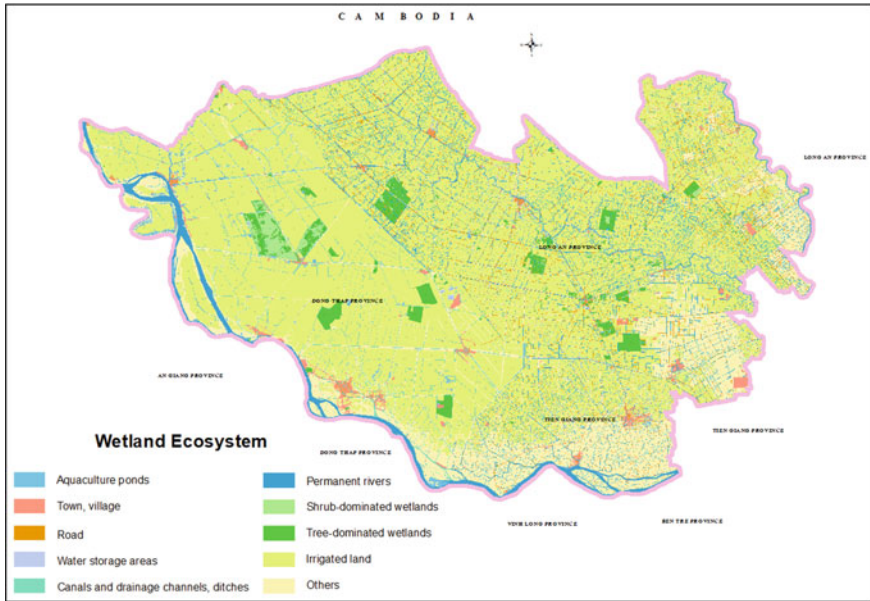


Fig. 30.4 Wetland ecosystems map (Thuy 2020)

WGS-84 coordinate system to the VN2000 coordinate system. Landsat 7 images are filled gaps using the SCP tool of QGIS to fix scan line errors.

The criteria values of BV1, BV2, BV3, and PH2 are collected from papers, projects and field investigations. The livestock, industrial, and residential areas are extracted from the land-use map; the road network is derived from the geodatabase at scales 1:2000 and 1:5000. Using ArcGIS 10.5 Euclidean Distance tool creates distance rasters of BV4, BV5, BV6, and BV7. The water salinity (BV8) layer referenced the data of saltwater intrusion in the state scientific project BDKH.11/16-20 (Nghi et al. 2019).

The forest fire sensitivity (BV9) data layer is an algorithm of density (D), humidity (H), vegetation types (LC); land surface temperature (LST); distances from wetland ecosystems to water sources (WS), residential areas (RA), and roads (RO). The characteristic vegetation and land surface temperature rasters are achieved from satellite images; the water sources (hydrological network) are derived from the geodatabase at scales 1:2000 and 1:5000; the distance rasters are done the same as BV4, BV5, BV6 and BV7. The fire sensitivity can be explained as below:

$$FI = 0.35 \times LC + 0.25 \times LST + 0.05 \times H + 0.11 \times D + 0.15 \times RA + 0.04 \times RO + 0.05 \times WS \quad (30.13)$$

The forest fire sensitivity raster is compared with fire points data and inquired fire information, indicating the suitable fire happening in Dong Thap Muoi region.

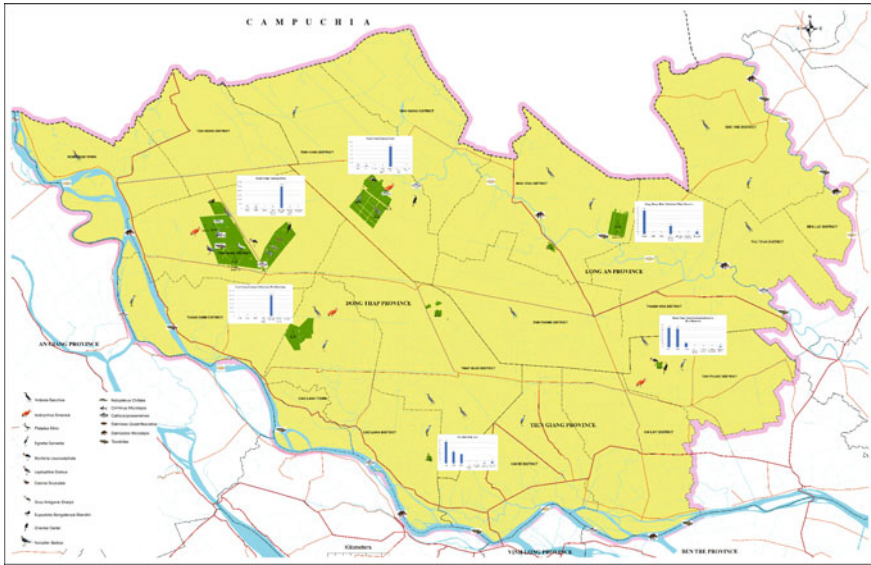


Fig. 30.5 Biodiversity data

The potential provision of tourism and entertainment service is counted through two parameters: the average number of tourists per year (BV10) and the average annual revenue from tourism (BV11). These data are collected, processed, and converted to the current time in 2018.

Surface water quality data (DO, COD, TSS) is defined based on regression Landsat 8 images (Band 1, 2, 3, and 5) and sampled data on 11/2018, in Dong Thap Muoi region.

All criteria layers will be spatialised and assigned to each wetland ecosystem using ArcGIS 10.5 software (Figs. 30.5, 30.6, 30.7, 30.8, 30.9, 30.10, 30.11 and 30.12).

30.3.4 Ordering and Mapping Dong Thap Muoi’s Wetland Ecosystems Protection, Restoration Priority

The assigned data of 14 protection and restoration criteria in the wetland ecosystems map are exported by ArcGIS 10.5 tool to excel format to calculate and rank the priority protection and restoration of wetland ecosystems. The detailed data are shown in Tables 30.4 and 30.5.

This study determined the importance of each pair of all protection and restoration criteria based on surveys and interviews with experts who are managers and

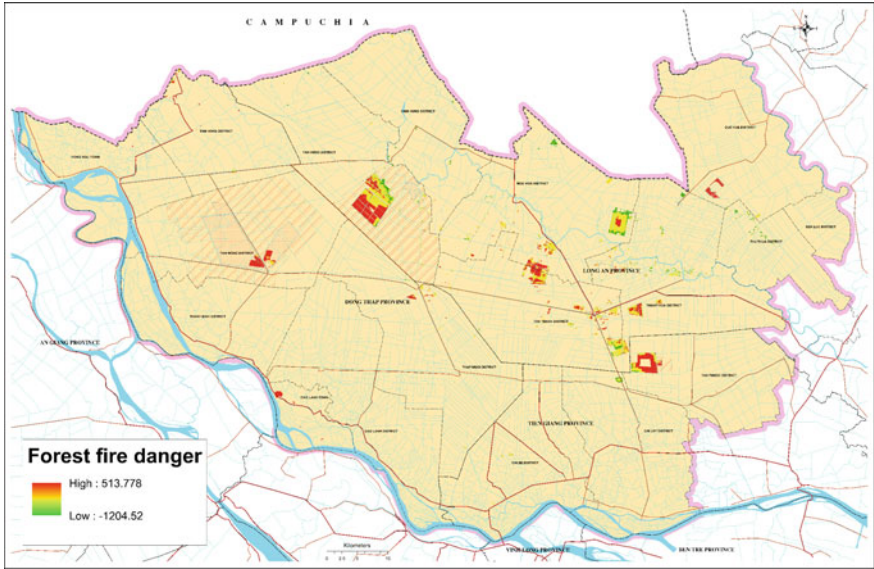


Fig. 30.6 Forest fire sensitivity data

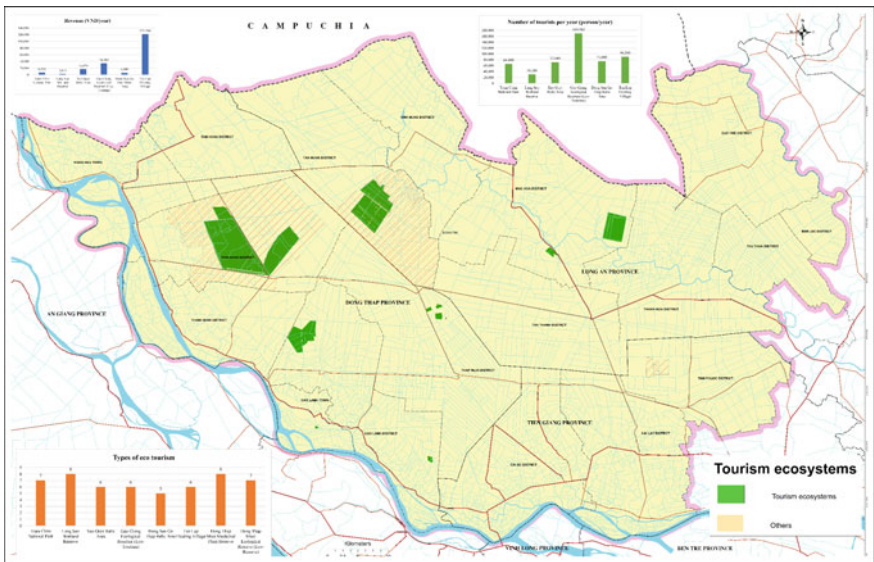


Fig. 30.7 Tourism and entertainment data

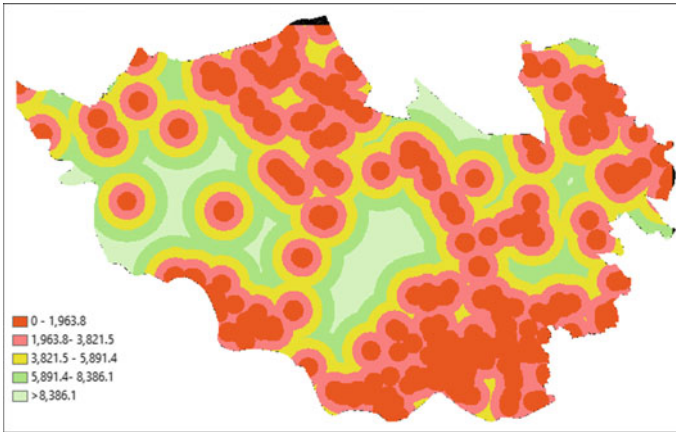


Fig. 30.10 Distance from industrial areas



Fig. 30.11 Distance from roads

The protection and restoration priority orders of 8 wetland ecosystems are computed by the TOPSIS method. The results are respectively shown in Tables 30.8 and 30.9.

The calculated orders are reassigned into the wetland ecosystem layer to establish the wetland ecosystem protection and restoration priority maps. The symbols are expressed in fractions $\frac{8}{S_{Tx-M}}$, in which the numerator (8) is priority order, and the denominator is the ecosystems wetland sign names (Vietnam (Stx)—Ramsar (M)). These maps are shown in Figs. 30.13 and 30.14.

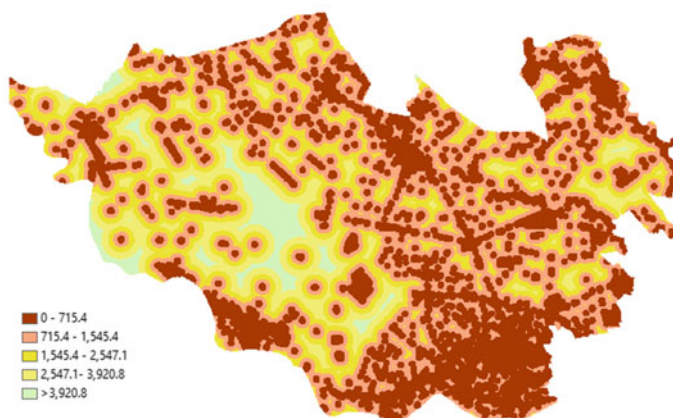


Fig. 30.12 Distance from residential areas

Table 30.4 Detailed criteria data to evaluate the priority of protection

Wetland ecosystem	Criteria										
	BV1	BV2	BV3	BV4	BV5	BV6	BV7	BV8	BV9	BV10	BV11
TC	667	57	12	2280.9	1066.7	937.9	210.9	0	189.1	66,000	6.7
LS	382	20	3	2036.2	1149.6	774.5	127.7	0	38.9	30,200	2.833
DTME	337	8	0	1942.2	1975.6	655.7	163.9	0.25	37.5	0	0
XQ	334	15	6	3037.4	2146.9	313.1	84.6	0	0	72,000	16.92
GG	389	7	0	2870.9	1337.9	1368.7	124.1	0	0	169,582	34.5
DTMM	91	10	0	2361.9	1094.2	810.6	909.4	0	35.0	0	0
TL	0	0	0	2439.7	1174.8	694.7	620.5	0	29.8	90,500	121.5
DSGT	0	0	0	3380.1	1821.1	1812.4	186.7	0	0	75,600	6.3

Table 30.5 Detailed criteria data to evaluate the priority of restoration

Wetland ecosystem	Criteria		
	PH1	PH2	PH3
TC	-383.8	1042	4
LS	0.0	258	5
DTME	0.0	0	4
XQ	-24.3	0	3
GG	0.0	0	5
DTMM	0.0	0	5
TL	0.0	0	4
DSGT	0.0	0	4

Table 30.6 Protection criteria weights

Criteria	BV1	BV2	BV3	BV4	BV5	BV6	BV7	BV8	BV9	BV10	BV11
Weight (AHP)	0.19	0.23	0.14	0.11	0.08	0.08	0.06	0.05	0.03	0.04	0.01

Table 30.7 Restoration criteria weights

Criteria	PH1	PH2	PH3
Weight (AHP)	0.29	0.65	0.06

Table 30.8 Wetland ecosystems protection priority order

Wetland ecosystem	Solution			
	S^+_i	S^-_i	C_{+i}	Rank of protection
TC	0.071	0.268	0.791	1
LS	0.184	0.107	0.366	2
DTME	0.227	0.088	0.289	4
XQ	0.190	0.105	0.356	3
GG	0.230	0.086	0.272	5
DTMM	0.241	0.059	0.196	6
TL	0.274	0.034	0.109	8
DSGT	0.274	0.047	0.147	7

Table 30.9 Wetland ecosystems restoration priority order

Wetland ecosystem	Solution			
	S^+_i	S^-_i	C^+_i	Rank of restoration
TC	0.294	0.630	0.682	1
LS	0.474	0.333	0.413	2
DTME	0.630	0.294	0.318	5
XQ	0.630	0.275	0.304	8
GG	0.630	0.295	0.318	3
DTMM	0.630	0.295	0.318	3
TL	0.630	0.294	0.318	5
DSGT	0.630	0.294	0.318	5

30.3.5 Verifying and Discussing Results

In order to verify the accuracy of the results, the study: (i) Conducts a field investigation as interviews and surveys; (ii) Compares the results with information on planning and existing studies on these rated sites. Collected data for assessing wetland ecosystem protection and restoration priority are shown in Table 30.10.

Table 30.10 Data for assessing wetland ecosystem protection and restoration priority

No	Area	Protection						Restoration			
		Total species	Plant (species)	Bird (species)	Fish (species)	Endangered and rare species	Invasive alien species	Land use change	Sarus crane change	Surface water quality	
1	TC	667	304	230	133	57	12	-383.75	1042	4	
2	LS	382	156	148	78	20	3		258	5	
3	DTME	337	156	147	34	8	-		-	4	
4	XQ	334	170	91	73	15	6	-24.30	-	3	
5	GG	389	326	63	-	7	-		-	5	
6	DTMM	91	91	-	-	10	-			5	

Tram Chim's biodiversity is the richest: (the total number of plants, birds, and fish is 667 species), 57 species are endangered and rare, but some of the invasive alien species are the largest (12). Therefore, the value of diversity and the pressure is also the largest. Tram Chim is also the area that meets 7 out of 9 Ramsar international convention standards on wetlands, recognised as the 2000th Ramsar site in the world, the 4th in Vietnam on May 22, 2012. In addition, Tram Chim also has an eco-tourism function with increasingly diverse forms, attracting a significant number of domestic tourists. In 2018, there were over 66,000 visitors with total revenue of over 6.7 billion VND. Therefore, it indicates that the research results that rank this area at the top regarding protection priority are entirely consistent with reality.

Tram Chim ranked first in the restoration priority because the number of Red-crowned Cranes has decreased from 1052 (in 1988) to 11 individuals (in 2018). The lack of food due to the shrinking and degradation of hemp grass area when the local government allows year-round water storage to prevent forest fires and convert the wetlands using the purpose of *Melaleuca* forest into agricultural land. Satellite data shows an increase in vegetation area of 383.75 ha, which can be explained by the growing area of *Mimosa pigra* trees. Overexploitation and tourism without reinvestment in planting and restoring *Eleocharis ochrostachys* grass is also a reason for the decline of cranes.

Lang Sen Wetland Reserve has the second protection and restoration priority order, consistent with the fact that data was collected, surveyed, interviewed, and extracted from satellite images. In terms of the total number of species, this is the area with the third highest biodiversity after Xeo Quyt relic site (382 compared to 389) but has 20 endangered and rare species, ranked 2nd after Tram Chim; there are three invasive alien species which is lower than 6 in Xeo Quyt. With the priority level of endangered and rare species protection, Lang Sen is appropriate, and this has also been proven when Lang Sen was recognised as the 2227th Ramsar site in the world and the 7th in Vietnam (27/11/2015). The number of Red-crowned Cranes in decline is 258, so a high restoration priority is appropriate.

In comparison with the total number of species, Xeo Quyt is the 5th; however, the number of endangered and rare species ranks the third, and the number of invasive alien species ranks the second. Therefore, the protection priority ranked 3/6 sites is consistent with the logic and criteria importance level. In terms of priority for restoration, Xeo Quyt is at a low priority because this area has the best surface water quality in the ranked areas and the reduced cover area is -24.30 ha (an increase of 24.3 ha compared to 2010).

Results were verified by the overall planning conservation of biodiversity in Dong Thap 2020, including Tram Chim, Gao Gieng, Go Thap, Xeo Quyt are the areas prioritised for conservation (Dong Thap Department of Natural Resources and Environment 2020).

Tables 30.6 and 30.8 show the number of endangered and rare species, total species, the number of invasive alien species, and the distance from livestock areas to wetland regions significantly affect ranking wetland ecosystems protection priority. Tables 30.7 and 30.9 indicate that the loss number of endangered, rare animals and

plants is the most considerable and following is decreased vegetation cover area effect on ordering wetland ecosystems restoration priority.

30.3.6 Solution

For such areas as Tram Chim, Lang Sen, Gao Giong, Dong Thap Muoi ecological reserve, Xeo Quyt, Dong Thap Muoi medicinal plants conservation, it is vital to improve and restore the habitat for grass species, especially for *Eleocharis ochrostachys* grass as this is the primary food source for the Red-Crowned crane. It is recommended to plant and protect the melaleuca forest system as a shelter and breeding ground for water birds. Consider keeping the water to prevent forest fires while maintaining and developing grassland ecosystems to attract birds, especially cranes. Having a suitable management mechanism to avoid converting natural land to agricultural production. Developing a mechanism for sustainable ecological and green economic development, combining conservation with tourism development to bring livelihoods and generate incomes to people, and involve them in protecting wetland ecosystems. In areas invaded by alien species, it is necessary to take measures to destroy and limit their spread and development, especially *Mimosa pigra* trees in Tram Chim. It is essential to further promote people's education through local authorities' propaganda and advocacy of protecting wetland ecosystems with specific policies for protection participants.

For areas with potential for eco-tourism development, such as Tan Lap, Gao Giong, and Xeo Quyt, it is necessary to have solutions to ensure economic development without affecting the ecological habitats of species. There should be a mechanism for reinvesting in improving the living environment, increasing the vegetation cover to attract animals, especially resident birds, to nest, lay, and live.

30.4 Conclusions

Proposing the method of mapping and ordering priority of wetland ecosystems protection and restoration based on the application of GIS, remote sensing, landscape ecology approach, and AHP is the basis for policymaking, environmental protection, and biodiversity conservation planning.

Experimental results show that the application of remote sensing and GIS in establishing, extracting, and modelling input data for assessment, ranking, and mapping protection and restoration of wetland ecosystems is entirely achievable. The results also are valuable in referencing documents and data for Dong Thap Muoi's environmental protection and biodiversity conservation planning.

Besides, the proposed method also has some limitations. It requires having landscape ecological experts and much data to establish the wetland ecosystems map. The input data are often derived from multiple sources, scales and times. Defining

the criteria weights also demands expert and indigenous knowledge. Therefore, this method requires local managers and experts to define the criteria' importance and use many techniques to process and normalise data to the same scale and time.

Acknowledgements This study is within the framework of the project “Application GIS, remote sensing and landscape analysis tools for establishing zoning map of wetland ecosystems protection and restoration prioritisation (Case study in Dong Thap Muoi)”, Vietnam Institute of Geodesy and Cartography, 2017–2020.

References

- Chan HK, Sun X, Chung S-H (2019) When should fuzzy analytic hierarchy process be used instead of analytic hierarchy process? *Decis Support Syst* 125:113114
- Cuong LD (2009) MCA for selecting solid waste burial sites. *J Constr Plann* 37:80–81 (in Vietnamese)
- Dat LQ, Phuong BH, Thu NTP, Anh TTL (2017) Building an integrated multi-criteria decision-making model to select and analyse a group of green suppliers. *VNU J Econ Bus* 33:43–54 (in Vietnamese)
- Dinh LC (2016) An integrated model of GIS and AHP-VIKOR in land adaptation assessment for sustainable land use management. *J Sci Technol Dev* 19:97–104 (in Vietnamese)
- Dong Thap Department of Natural Resources and Environment (2018) Biodiversity conservation planning of Dong Thap to 2020 (in Vietnamese)
- Duong NT (2009) Research on changes in landscape and biodiversity of coastal wetlands in Thai Binh, the orientation of regional use planning for sustainable development, vol Doctor. University of Science, Vietnam National University, Hanoi (in Vietnamese)
- Environmental Law Institute (2013) A handbook for prioritizing wetland and stream restoration and protection using landscape analysis tools. Environmental Law Institute, Washington, D.C.
- Government of the Socialist Republic of Vietnam (2019) Decree No. 37/2019/ND-CP detailing a number of articles of the law on planning, Hanoi (in Vietnamese)
- Government of the Socialist Republic of Vietnam (2022) Decree No. 08/2022/ND-CP detailing a number of articles of the law on environmental protection, Hanoi (in Vietnamese)
- Hai HT, Nhan HTT, Tuan TA (2015) Analysis of changes in space and time of wetland ecosystems in Xuan Thuy national park, Nam Dinh province using remote sensing and GIS techniques. *J Biol* 156–163 (in Vietnamese)
- Hajkowicz S, Higgins A (2008) A comparison of multiple criteria analysis techniques for water resource management. *Eur J Oper Res* 184:255–265
- Hang NTT (2012) Studying landscape structure for the spatial organisation, rational use of resources and environmental protection in Ninh Binh province with the help of remote sensing and GIS technologies, vol Doctor. University of Science, Vietnam National University, Hanoi (in Vietnamese)
- <https://baotainguyenmoitruong.vn/bao-ton-va-su-dung-ben-vung-cac-vung-dat-ngap-nuoc-298871.html>
- Huan NC (2005) Landscape assessment (according to the eco-economic approach). Vietnam National University Publisher, Hanoi (in Vietnamese)
- Hung LV, Hoe ND (2014) Developing a set of criteria to identify key areas of interest in biodiversity conservation planning in Vietnam. *J Biol* 36:189–202 (in Vietnamese)
- Huong BTT (2015) Proposing the grape planning areas to 2030 in Binh Thuan based on the integration of GIS and AHP. *J Geodesy Cartography* 35–39 (in Vietnamese)

- Jiang W, Lv J, Wang C, Chen Z, Liu Y (2017) Marsh wetland degradation risk assessment and change analysis: a case study in the Zoige Plateau, China. *Ecol Ind* 82:316–326
- Jozaghi A, Alizadeh B, Hatami M, Flood I, Khorrami M, Khodaei N, Ghasemi Tousi E (2018) A comparative study of the AHP and TOPSIS techniques for dam site selection using GIS: a case study of Sistan and Baluchestan Province, Iran. *Geosciences* 8
- Kien NV, Thuy NT, Hoa PK, Manh ND, Thinh LC (2013) Proposing the process and symbology of wetland. Vietnam Institute of Geodesy and Cartography (in Vietnamese)
- Lan PTN, Hai HT (2009) Some of the research results on indicators development for assessing the state and progress of the water environment and aquatic ecosystems downstream of the Tra Khuc River. *J Water Resour Environ Eng* 26:14–20 (in Vietnamese)
- Linh NX, Khanh TV, Van HT, Duy NL, Hao VTK (2017) Application of GIS and F-AHP in assessing the rationality of planning location industrial park land in Hung Ha district, Thai Binh province. *J Mar Sci Technol* 166 (in Vietnamese)
- Linh NHK, Ngoc NB, Mai NTH, Bao HN (2018) Building wetland database using remote sensing and GIS technologies in Duy Xuyen district, Quang Nam province. *J Agric Rural Dev* 95–103 (in Vietnamese)
- Lopez R, Lyon J, Lyon L, Lopez D (2013) Wetland landscape characterization: practical tools, methods, and approaches for landscape ecology, 2nd edn
- Luan PH, Tram LTT (2013) Combination of AHP, VIKOR and TOPSIS for selecting construction contractors. *J Constr* 12:84–87 (in Vietnamese)
- Malekmohammadi B, Jahanishakib F (2017) Vulnerability assessment of wetland landscape ecosystem services using driver-pressure-state-impact-response (DPSIR) model. *Ecol Ind* 82:293–303
- Malekmohammadi B, Rahimi Blouchi L (2014) Ecological risk assessment of wetland ecosystems using multi criteria decision making and geographic information system. *Ecol Ind* 41:133–144
- Mekong River Commission (2017) Criteria and process of Wetland site selection for implementation of testing and improvement of WI and WEFASAM (including WBIA). Environmental Management Division
- Ministry of Natural Resources and Environment (2021) Report of state of the national environment for the period 2016–2020. Dan Tri Publisher, Hanoi (in Vietnamese)
- National Assembly of the Socialist Republic of Vietnam (2017) Law on planning. No. 21/2017/QH14, Hanoi (in Vietnamese)
- National Assembly of the Socialist Republic of Vietnam (2020) Law on environmental protection. No. 72/2020/QH14, Hanoi (in Vietnamese)
- Nghi VV, Hai HQ, Nga DTT, Hung BV, Khoi DN, Hien LTT, Lam DT, Dung DD, Huy NV, Hai TX (2019) The national-level project, code CC.11/16–20: research on solutions for planning Dong Thap Muoi region becomes Cuu Long Delta's freshwater storage to adapt to climate change. Southern Institute of Water Resources Planning (in Vietnamese)
- Nguyen PH, Hai TQ, Son LK (2015) Assessment of ecological adaptation for economic development and mangrove conservation in the cape Ca Mau area. *Sci J Vietnam Nat Univ Hanoi: Earth Environ Sci* 4:29–40 (in Vietnamese)
- Nhan HTT (2010) Researching, building a number of parameters, processes for biodiversity observation. Vietnam Environment Administration (in Vietnamese)
- Nhan HTT (2014) Scientific and technological research project: researching scientific and practical foundation for the formulation of biodiversity conservation strategy up to 2020 in line with Vietnam's sustainable development orientation. Biodiversity Conservation Department (in Vietnamese)
- Opricovic S, Tzeng G-H (2004) Compromise solution by MCDM methods: a comparative analysis of VIKOR and TOPSIS. *Eur J Oper Res* 156:445–455
- Phu H (2009) Research on ecological zoning for aquaculture in Dong Thap province for exploitation and sustainable use of natural resources. *J Water Resour Environ Eng* 26:10–16 (in Vietnamese)
- Phuong BT, Hoe VT (2015) Application for remote sensing and GIS in mapping wetland. *J Nat Resour Environ* 24–26 (in Vietnamese)

- Phuong NV, Mai DT (2018) Application of GIS and AHP for establishing the map of key forest fire areas in Dong Hoi city, Quang Binh province. *J Agric Rural Dev* 126–131 (in Vietnamese)
- Prime Minister of the Socialist Republic of Vietnam (2022) Decision No. 149/QĐ-TTg dated January 28, 2022, of the Prime Minister approving the national strategy on biodiversity to 2030, vision to 2050, Hanoi (in Vietnamese)
- Ramsar Convention Secretariat (2013a) The Ramsar convention manual: a guide to the convention on wetlands (Ramsar, Iran, 1971), Gland, Switzerland
- Ramsar Convention Secretariat (2013b) Information sheet on Ramsar wetlands (RIS) 2009–2014 version, Gland, Switzerland
- Saaty TL (1980) The analytic hierarchy process. McGraw-Hill, Inc.
- Sarkar S, Parihar SM, Dutta A (2016) Fuzzy risk assessment modelling of East Kolkata wetland area: a remote sensing and GIS based approach. *Environ Model Softw* 75:105–118
- Son TPH (2008) Report on the scientific and technological research project “Investigation of the current status of distribution of coral reef ecosystems in coastal waters of Khanh Hoa province as a basis for planning protection, restoration and use lasting”. Institute of Oceanography (in Vietnamese)
- Thuy NT (2020) Landscape approach—based wetland ecosystem mapping for Dong Thap Muoi region at 1:100,000 scale. *J Geodesy Cartography* 9–15 (in Vietnamese)
- Tin HC, Phap TT, Tuan NQ (2011) Application of remote sensing and GIS technologies in assessing the status of seagrass beds in wetlands Huong Phong commune, Huong Tra district, Thua Thien Hue province. *Hue Univ J Sci* (in Vietnamese)
- Tudor C (2014) An approach to landscape character assessment. Natural England, England
- Ve ND, Lan TD, Thao NV (2013) Building the distribution of coastal ecosystems in Thanh Hoa province (Project: Building marine natural resources and environmental database of Thanh Hoa province). Institute of Marine Environment and Resources (in Vietnamese)
- Velasquez M, Hester PT (2013) An analysis of multi-criteria decision making methods. *Int J Oper Res* 10:56–66
- Vietnam Environment Administration (2011) Investigating, assessing the situation of planning and coastal wetland use and proposing planning orientations for protecting the environment and preventing disaster. Vietnam Environment Administration (in Vietnamese)
- Vietnam Environmental Protection Department (2005) Overview of the status of Vietnam’s wetland after 15 years of implementing the Ramsar convention, Hanoi, pp 72 (in Vietnamese)
- Vietnam Institute of Geodesy and Cartography (2012) Surveying, measuring and establishing all kinds of maps for zoning for conservation and sustainable development of Dong Thap Muoi wetlands. Vietnam Institute of Geodesy and Cartography (in Vietnamese)
- Vietnam Institute of Geodesy and Cartography (2018) Surveying, measuring and establishing all kinds of maps for zoning for conservation and sustainable development of Ca Mau peninsula. Vietnam Institute of Geodesy and Cartography (in Vietnamese)
- Vietnam Institute of Geodesy and Cartography (2020) Surveying, establishing all kinds of maps to serve the building of a database for management, conservation and sustainable development of wetlands in the Long Xuyen Quadrangle. Vietnam Institute of Geodesy and Cartography (in Vietnamese)
- Xuan NT, Hoa DTB (2015) Assessment of wetland changes for the development of multi-benefit solutions for sustainable use of wetland resources in Quang Yen town, Quang Ninh province with the support of remote sensing and GIS. *J Geodesy Cartography* 24–31 (in Vietnamese)
- Yet NH, Ken LV, Hanh TD, Thu NT, Thung DC, Huong TTL, Quan NV, Tien DD (2010) Assessment of the degradation of coastal ecosystems in Vietnam Nam and propose sustainable management solutions. State-level project KC.09.26/06-10. Vietnam Institute of Science and Technology (in Vietnamese)

Chapter 31

The Study of Extraction Soil Salinity Information from High Resolution Multispectral Remote Sensing Data, Pilot Area in Dong Nai Province, Vietnam



Xuan Huy Chu , Minh Ngoc Nguyen , Ngoc Dat Dinh , Thu Thuy Le , Quang Huy Bui , Thi Lan Pham , Thi Huyen Ai Tong , Van Tiep Trinh, and Van Lap Nguyen

Abstract Soil salinity is one of the causes that directly affect agriculture in many countries and territories around the world. This study establishes a map of saline soils in the area of Long Thanh and Nhon Trach districts, Dong Nai province, using Sentinel-2 data taken in the dry season 2020–2021. The indicators used are Salinity Index, SI and Enhanced Vegetation Index, EVI. The electrical conductivity (EC) data collected at that time was used to build a suitable model for the study area on the basis of correlation with the used indicators. On the basis of correlation calculations of a multiple linear regression model with the determination coefficient of approximately 0.75. At the same time, the March 2021 Sentinel-2 dataset is used to map saline soils as this is when saline soils are most apparent.

Keywords Sentinel-2 · Soil salinity · Dong Nai Province · Multiple linear regression

31.1 Introduction

Soil salinization is a major process of soil fertility degradation that result in the information of salt affected soil (Azabdaftari and Sunar 2016). Soil quality deterioration has become a global problem, especially in coastal areas, where 50% of the world's population is concentrated (FAO 2000) (100 km from the coast to the continental).

X. H. Chu · M. N. Nguyen (✉) · N. D. Dinh · T. T. Le · Q. H. Bui · T. H. A. Tong
Space Technology Institute, Vietnam Academy of Science and Technology, Hanoi, Vietnam
e-mail: nmngoc@sti.vast.vn

M. N. Nguyen · T. L. Pham
Faculty of Geomatics and Land Administration, Hanoi University of Mining and Geology, Hanoi, Vietnam

V. Tiep Trinh · V. Lap Nguyen
Khanh Hung Construction Joint Stock Company, Lang Son, Vietnam

It is also a place strongly affected by one of the phenomena of soil degradation as soil salinity. A large amount of soil salinity is unavailable for cultivation. There are half billion land becomes infertile for crop production and agriculture due to salinity (Douaoui et al. 2006). The soil salinity and loss of soil quality caused declining crop yield (Douaoui et al. 2006). World food security can only be achieved with the development of crops that are salinity tolerant (FAO 2020; Liu and Huete 1995). Saline soil causes serious problems in management and exploitation, significantly affecting the farming ability. The nature and characteristics of saline soils are also very diverse, so it requires a specific approach and research if you want to manage as well as exploit the benefits from saline soil. Therefore, the extending of saline soils should be regularly monitored to ensure updates on their severity, spatial distribution, nature, and trend of widening.

The timely and accurate acquisition of soil salinization information are strongly important role for the prevention and management of land degradation and ecological restoration in arid areas (Rhoades et al. 1999). To detect the occurrence, dynamics, and distribution of salinization, soil salinization monitoring is a basic task (George et al. 2020). The saline soil map is usually established by collecting in situ soil samples and analyzing those samples in the laboratory to determine their solute concentrations or electrical conductivity. However, these methods are often time-consuming, costly, and labor-intensive. Beside, traditional soil salinization monitoring is suitable on large-scale distribution information, and it is difficult to monitor soil salinization on a large scale. Recently, remote sensing data have been widely applied in soil salinization monitoring because of more efficiently and economically rapid tools (Kim-Anh et al. 2020), and accurate of soil salinity mapping is imperative (George et al. 2020). So research on soil salinization mapping using remote sensing data is crucial (Rhoades et al. 1999).

In recent years, satellite remote sensing data have become useful tool to extract soil salinization information. There are many types of satellites providing imagery that is useful information in detecting and monitoring saline soils such as LANDSAT, Sentinel-2, SPOT, IKONOS, EO-1, IRS, Terra-ASTER, ... (Kim-Anh et al. 2020; Khan et al. 2001; Khan and Abbas 2007; Ai et al. 2018; Shirokova et al. 2020). One of them is Sentinel-2 imagery with multiple wavebands and a high spatial resolution of 10 m, which can be met accuracy requirements for small areas. However, there are still few studies using this data to extract saline soil information.

There are many researches that soil salinization mapping using spectral response extracted directly from sensors or after the application of spectral transformations such as principal component analysis (PCA) (Khan et al. 2001; R-Development Core Team 2011), tasseled cap transformation (Khan and Abbas 2007), and spectral indices (Ai et al. 2018). Vegetation has been used as an indirect indicator to predict and map soil salinity. Among the vegetation indices, NDVI, SAVI, and Ratio Vegetation Index (RVI) have been used to establish soil salinity map (Shirokova et al. 2020; Liu et al. 2018). Beside, Lobell et al. (2010) revealed that the Enhanced Vegetation Index (EVI) is a more reliable indicator of soil salinity than the NDVI. Furthermore,

direct salinity indicators, indices such as salinity index (SI) have been developed and commonly used to identify salt-affected areas. The goal of the current study is to test the utility of Sentinel-2 for mapping soil salinity in the Long Thanh, Nhon Trach districts, Dong Nai province, Vietnam.

31.2 Pilot Area and Data

The pilot area is located along the Dong Nai River in the two districts of Long Thanh, Nhon Trach, and a small part of Bien Hoa city, Dong Nai province (Fig. 31.1). This is an area with a lot of rice-growing areas in the province, but also an area with an increasing area of saline soil due to the influence of saline intrusion from the sea along the Dong Nai river up to Bien Hoa city. Here, rice production is quite complicated, in communes strongly affected by saline intrusion such as Phuoc Khanh, Phu Hoi, Phu Dong of Nhon Trach district, there are only one or two rice crops, even in the area. In Phuoc Khanh commune, the cultivated rice areas also have differences in salt-tolerant rice varieties, which are 3-month varieties and 6-month varieties; however, in some communes such as Long Phuoc of Nhon Trach district, due to adequate water supply, there are 3 rice crops a year. The complex crop season makes challenging in monitoring saline soil changes by satellite imagery, especially in small study areas. Imagery data requirements are not only high spatial resolution but also short revisit time to collect information at different times.

Sentinel-2 is a part of the European Commission's Copernicus program, which was designed specifically to deliver a wealth of data and imagery. The satellite supplies imagery in high resolution of 10 m in the visible (Red, Green, Blue), near-infrared (NIR), which ensures the capture of not only vegetation state but also soil salinity information due to NIR band.

The collected data is Sentinel-2 imagery at the beginning and the end of the dry season in the pilot area and close to the time of survey on December 3, 2020, and March 28, 2021, including scenes named: T48PXS, T48PXT, T48PYS (Table 31.1).

The measurement data were collected through the survey at the beginning and the end of the dry season to monitor change the whole season, the first phase was from November 29–30, 2020 with 50 samples (for model generation), and the second phase was from March 22–23, 2021 with 35 samples (for model verification). At each sample, soil salinity was collected using the FieldScout instrument, which is used in agricultural salinity measurement. These samples were all taken based on soil map and land use map in the area (Rhoades et al. 1999; George et al. 2020).

31.3 Methodology

Firstly, Sentinel-2 data was atmosphere corrected to get reflectance data before calculation by formulas listed in Table 31.2:

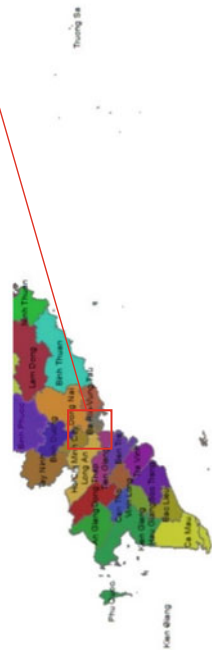


Fig. 31.1 Pilot area location

Table 31.1 Acquisition and sampling date

Imagery date	Sampling date
03/12/2020	29–30/11/2020
28/3/2021	22–23/3/2021

Table 31.2 Used formulas in study

Index	Formula	Ref.
SI1	$SI = \sqrt{B \times R}$	Khan et al. (2001)
SI2	$SI = \sqrt{G \times R}$	Douaoui et al. (2006)
SI3	$SI = \sqrt{G^2 + R^2 + NIR^2}$	Douaoui et al. (2006)
SI4	$SI = \sqrt{G^2 + R^2}$	Douaoui et al. (2006)
SI5	$SI = \frac{B}{R}$	Khan and Abbas (2007)
SI6	$SI = \frac{B-R}{B+R}$	Khan and Abbas (2007)
SI7	$SI = \frac{G \times R}{B}$	Khan and Abbas (2007)
SI8	$SI = \frac{B \times R}{G}$	Khan and Abbas (2007)
SI9	$SI = \frac{NIR \times R}{G}$	Khan and Abbas (2007)
SI10	$SI = \sqrt{G + R}$	Khan and Abbas (2007)
EVI	$EVI = 2.5 \times \frac{NIR-R}{NIR+c_1 \times R-c_2 \times B+L}$	Liu and Huete (1995)

In the EVI formula, $c_1 = 6$; $c_2 = 7.5$; $L = 1$

These indicators were selected according to the relevant literature based on their effectiveness in mapping soil salinity (Douaoui et al. 2006; Liu and Huete 1995; Khan et al. 2001; Khan and Abbas 2007). Therefore, correlation analysis of each index with electrical conductivity values was performed by linear regression method to investigate the best correlation with the salinity of samples (Azabdaftari and Sunar 2016; Kim-Anh et al. 2020; Ai et al. 2018).

The correlation between the electrical conductivity through the samples collected in the field and the calculated value from the spectral bands will be used to find out the relationship between the calculated values from the image and the actual measured value. The selection method is a linear regression method that is widely used in the study of spatial distribution. However, the simple linear regression method could hardly meet the accuracy requirements (Azabdaftari and Sunar 2016; Kim-Anh et al. 2020; Ai et al. 2018), so we chose the multiple linear regression method. In which, using the Bayesian Model Average algorithm (abbreviation is BMA) combines Bayesian Information Criteria (abbreviation is BIC) and Akaike Information Criterion (abbreviation is AIC) to pick the most suitable model. After that, consider the coefficient of determination R^2 between the measured value and the estimated value (R-Development Core Team 2011). The multiple linear regression according to BIC and AIC criteria method is performed on R software.

31.4 Result and Discussion

The following results (Table 31.3) express the estimation models for salinity index using BIC criteria. Model 1 is the best model with BIC = -35,759; R² = 0.616, and Post prob = 0.273 (Douaoui et al. 2006) with the independent variables SI2, SI3, SI4, SI9 (calculated results shown in Fig. 31.2). And the estimation model is:

$$EC_{\text{estimation}} = 11.668 - 697.087 * SI2 - 98.301 * SI3 + 511.201 * SI4 + 86.717 * SI9 \tag{31.1}$$

Similarly for the AIC, we also found the optimal model to estimate the salinity index with the highest correlation with the measured value. The results are shown in the following Table 31.4.

The obtained results also show that with variables SI2, SI3, SI4, SI9, the correlation value of R² is also nearly similar to the BIC information criterion.

After selecting a model to estimate the salinity index from Sentinel-2 image data, we verified the accuracy of the model. The results show that the correlation between the estimated value and the measured value is quite good, with R² ≈ 0.75 (Fig. 31.3).

After the model was verified and achieved good results, the saline soil map was established with salinity levels classified according to Table 31.5 following (FAO 2020; Shirokova et al. 2020):

Table 31.3 The estimation models based on the BMA algorithm with BIC

	p! = 0	EV	SD	Model 1	Model 2	Model 3	Model 4	Model 5
Intercept	100.0	1.359e+01	4.426	11.668	15.791	10.697	11.481	13.803
SI1	7.0	-1.727e+00	30.245					
SI2	59.1	-3.949e+02	397.555	-697.087		-786.402	-714.433	-711.581
SI3	100.0	-8.558e+01	19.244	-98.301	-70.142	-87.427	-100.839	-97.157
SI4	58.4	2.886e+02	294.047	511.201		575.738	528.126	519.378
SI5	6.7	3.388e-02	2.609					-2.580
SI6	6.5	-1.996e-03	3.781					
SI7	7.3	-1.551e-01	9.703					
SI8	6.3	-2.768e-01	7.798				-8.740	
SI9	100.0	7.470e+01	19.779	86.717	57.969	81.739	90.049	84.582
SI10	6.4	-6.325e-02	1.762					
EVI	8.2	-2.483e-01	2.765			-6.504		
nvar				4	2	5	5	5
R ²				0.616	0.548	0.621	0.617	0.617
BIC				-35.759	-34.926	-32.515	-31.856	-31.852
Post prob				0.273	0.180	0.054	0.039	0.039

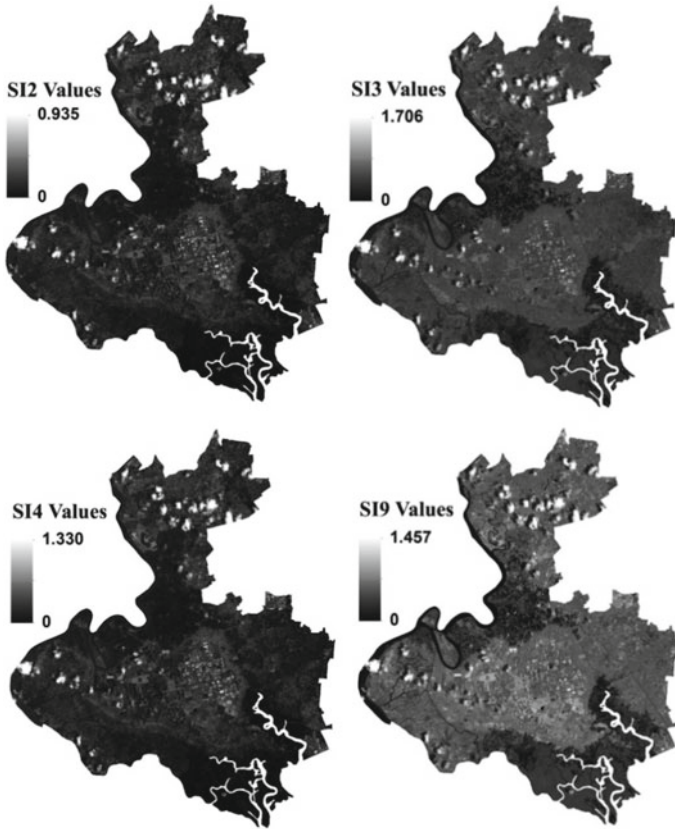


Fig. 31.2 Calculated results of indexes SI2, SI3, SI4, SI9

The pilot area is located in the sub-equatorial monsoon tropical climate, with only two rainy and dry seasons; The soil salinity is highest is at the end of the dry season (around March and April every year), so the images taken on March 28, 2021, is used to establish a map that could reflect the current saline soil situation in the area.

Figure 31.4 shows the soil saline distribution in the study area, the most affected areas are the southern part of the pilot area, in communes such as Phu Huu, Phu Dong of Nhon Trach district, the paddy fields are saline (between 8 and 15 dS/m), so yields are low, there is only one crop per year but there are some areas with high salinity, with a common value of 17–18 dS/m. Besides, Phuoc Khanh commune is a strongly affected area, the soil is saline (common value is about 16–16.5 dS/m) cannot culture, only sedges. However, Vinh Thanh commune, which has relatively large paddy fields, due to its high terrain, is less affected than Phuoc Khanh commune. Going north along the Dong Nai river, the salinity of the soil also decreases gradually so that it is less affected by saline intrusion. Dai Phuoc commune is located on Phu Huu commune, but the soil is much less salty, and the paddy fields is still quite large.

Table 31.4 Selected optimal model based on BMA algorithm with AIC

Residuals					
<i>Min</i>	<i>IQ</i>	<i>Median</i>	<i>3Q</i>	<i>Max</i>	
-14.3467	-1.5275	-0.1436	1.5506	11.8853	
Coefficients					
	<i>Estimate</i>	<i>Std. error</i>	<i>t value</i>	<i>Pr (> t)</i>	**
<i>(Intercept)</i>	11.668	3.428	3.404	0.00133	**
SI2	-697.087	240.789	-2.895	0.00565	***
SI3	-98.301	13.553	-7.253	2.69e-09	**
SI4	511.201	182.095	2.807	0.00715	***
SI9	86.717	13.860	6.257	9.40e-08	
Signif. codes	0 '***' 0.001 '**' 0.01 '*' 0.05 '.' 0.1 ' ' 1				
<i>Residual standard error: 4.795 on 49° of freedom</i>					
<i>Multiple R²: 0.6162, Adjusted R²: 0.5849</i>					
<i>F-statistic: 19.67 on 4 and 49 DF, p-value: 1.039e-09</i>					

Fig. 31.3 Correlation between measurement and estimation from images

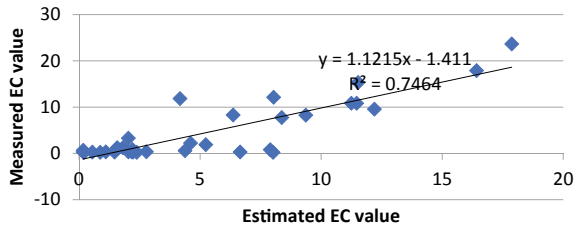


Table 31.5 Soil salinity level classification

No.	Salinity level	EC (dS/m)
1	Non salinity	<4
2	Low salinity	4–8
3	Mid salinity	8–15
4	High salinity	>15

Up to the communes of Long Tan, Phu Hoi of Nhon Trach district, and Tam An of Long Thanh district, the salinity of the soil is quite low, only about 1–2 dS/m, so the paddy fields here is very large, and crops also increase with 2–3 crops/year. To the east of the pilot area, the soil is almost not salty and the water is fully supplied, so the paddy fields are in communes such as Long An in Long Thanh district, Hiep Phuoc and Phuoc Thien in Nhon Trach district can cultivate 3 crops/year.

There are some confusing results in the inland area that is less affected by seawater rising but showing high salinity in Fig. 31.4. The main cause of spectral confusion,

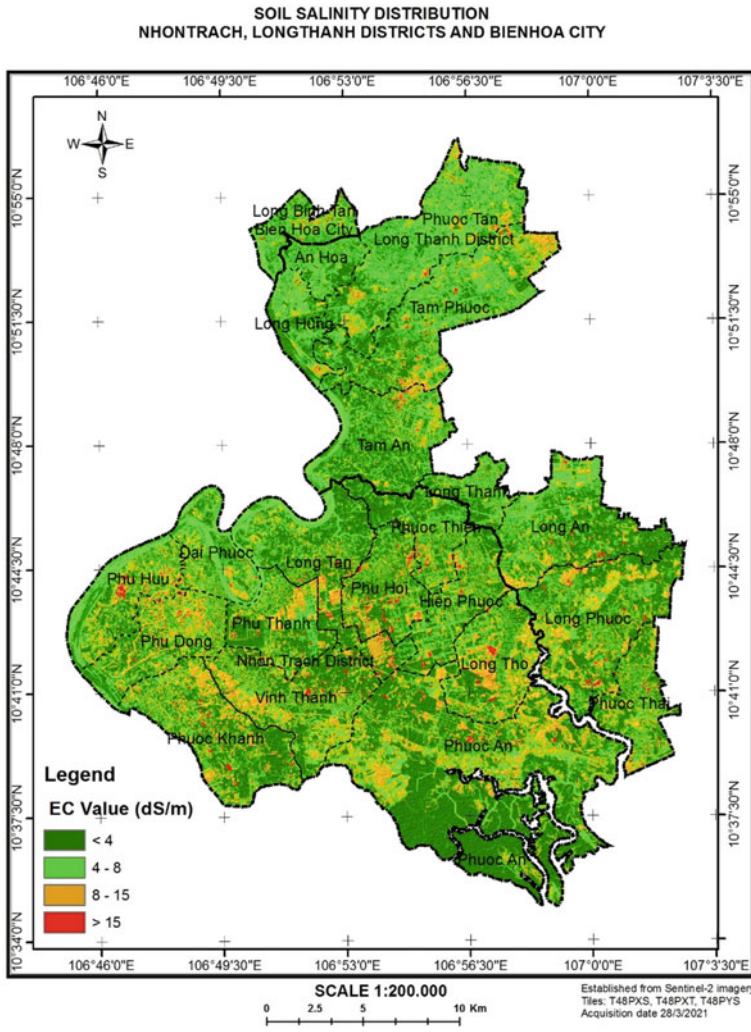


Fig. 31.4 The soil salinity map

on the bare soil, there is the presence of a large amount of sand. Surface brightness due to high sand content determines higher reflectance that makes spectral confusion between the soil saline and sand.

There are many kinds of land use in the pilot area, however, we have only focused on paddy fields, which are most affected by saline soil. Moreover, in some areas the soil has become so saline that it is not possible to culture rice or yields are low, farmers have left it fallow or have begun to change the use purpose to exploit the land more efficiently.

31.5 Conclusions

A model to estimate soil salinity based on a multiple linear regression method using the BMA algorithm combined with BIC and AIC has been developed, it makes the correlation between measurement results and calculated from images is better than simple linear regression. The verification results show that the correlation between the calculated value and the measured value is good (the coefficient of determination is 0.74).

Results of the study have demonstrated the Sentinel-2 ability in terms of extraction soil salinity information, and moreover can be applied to small areas.

Acknowledgements This article was completed with the support of the project “Application of remote sensing technology and GIS to map saline soils in some areas of Dong Nai province”, ID: UDNGDP.04/20-21

References

- Ai TTH, Giang NV, Hanh NC, Thao GTP, Mon D, Hoa P (2018) Study on soil salinity estimation using Sentinel-2 satellite images and EM31-EK2 ground conductivity instrument. *J Sci Nat Sci Technol* 15(11b):71–78
- Azabdaftari A, Sunar F (2016) Soil Salinity Mapping using multitemporal landsat data. In: *The international archives of the photogrammetry, remote sensing and spatial information sciences*, volume XLI-B7, 2016 XXIII ISPRS congress, 12–19 July 2016, Prague, Czech Republic
- Douaoui AEK, Nicolas H, Walter C (2006) Detecting salinity hazards within a semiarid context by means of combining soil and remote-sensing data. *Geoderma* 134(1):217–230
- FAO (2020) Mapping of salt-affected soils—technical specifications and country guidelines. Rome
- George K, Paraskevi L, Anastasia S (2020) Comparison of soil EC values from methods based on 1:1 and 1:5 soil to water ratios and ECe from saturated paste extract based method. *Water* 1010. <https://doi.org/10.3390/w12041010>
- Khan S, Abbas A (2007) Remote sensing based modelling applications in land and water management: using remote sensing for appraisal of irrigated soil salinity. In: *MODSIM 2007. International congress on modelling and simulation*. Modelling and Simulation Society of Australia and New Zealand
- Khan NM, Rastoskuev VV, Shalina EV, Sato Y (2001) Mapping salt-affected soils using remote sensing indicators—a simple approach with the use of GIS IDRISI. In: *22nd Asian conference on remote sensing* 5(9)
- Kim-Anh N, Yuei-An L, Ha-Phuong T, Phi-Phung H, Thanh-Hung N (2020) Soil salinity assessment by using nearinfrared channel and Vegetation Soil Salinity Index derived from Landsat 8 OLI

- data: a case study in the Tra Vinh Province, Mekong Delta, Vietnam. *Prog Earth Planet Sci* 7(1). <https://doi.org/10.1186/s40645-019-0311-0>
- Liu HQ, Huete AR (1995) A feedback based modification of the NDVI to minimize canopy background and atmospheric noise. *IEEE Trans Geosci Remote Sens* 33:457–465
- Liu L, Ji M, Buchroithner M (2018) A case study of the forced invariance approach for soil salinity estimation in vegetation-covered terrain using airborne hyperspectral imagery. *ISPRS Int J Geo-Inf* 7(2)
- Lobell DB et al (2010) Regional-scale assessment of soil salinity in the Red River Valley using multi-year MODIS EVI and NDVI. *J Environ Qual* 39(1):35–41
- R-Development Core Team (2011) A language and environment for statistical computing
- Rhoades JD, Chanduvi F, Lesch S (1999) Soil salinity assessment: methods and interpretation of electrical conductivity measurements. *FAO Irrigation and drainage paper* 57
- Shirokova Y, Forkutsa I, Sharafutdinova N (2020) Use of electrical conductivity instead of soluble salts for soil salinity monitoring in Central Asia. *Irrig Drainage Syst* 14:199–205

Chapter 32

Dynamics and Determinants of Forest Changes Across Mainland Vietnam in the Recent Three Decades



Duong Cao Phan , Ba Thao Vu, Dang An Tran, Vuong Trong Kha, and Kenlo Nishida Nasahara 

Abstract In the recent few decades, Vietnam has experienced a considerable change in land use/land cover (LULC), especially forest land. However, there is not a comprehensive analysis of the dynamics and drivers at the nationwide spatial scale for a long-term period. In this research, we estimate the socioeconomic and biophysical drivers of forest changes at the commune scale. Utilizing our results from the Vietnam-wide annual LULC database available in the Japan Aerospace Exploration Agency (JAXA), we first computed the dynamic changes in forest land from 1990 to 2020. To decide the major drivers of the changes, we conduct a synthesis of case studies working on the analysis of the forest changes in Vietnam at various spatial levels. Subsequently, a machine learning technique was adopted to measure the drivers of the forest changes. Our results indicate that although the forest area has increased from 2005 to 2010, it has undergone a decrease over the full study period. There is a dramatic conversion between forest and agricultural land, especially in the North-West and Central Highlands. This conversion is mainly driven by agricultural expansion/shifting, topographic position index, accessibility/infrastructure,

Duong Cao Phan and Ba Thao Vu these authors contributed equally to this work.

Supplementary Information The online version contains supplementary material available at https://doi.org/10.1007/978-3-031-17808-5_32.

D. C. Phan (✉)

Graduate School of Science and Technology, University of Tsukuba, Tsukuba, Japan
e-mail: Pcduong8088@gmail.com

D. C. Phan · B. T. Vu

Department of Geotechnical Engineering, Hydraulic Construction Institute, Vietnam Academy for Water Resources, Hanoi, Vietnam

D. A. Tran

Faculty of Water Resources Engineering, Thuyloi University, Hanoi, Vietnam

V. T. Kha

Department of Mine Surveying, Hanoi University of Mining and Geology, Hanoi, Vietnam

K. N. Nasahara

Faculty of Life and Environmental Sciences, University of Tsukuba, Tsukuba, Japan

population growth/migration, and distance to systems such as irrigation, drainage, and mining/industry. The identification of the drivers in this study is likely to help enhance the accuracy of the land use/land cover change prediction. These findings provide coherent evidence-based information about the dynamics and drivers of forest changes at the nationwide spatial and decadal temporal scales and thus can support informing land policies in Vietnam.

Keywords Land use land cover change · Forest change and transition · Drivers · Machine learning techniques · Vietnam

32.1 Introduction

A change in land cover refers to the alteration of the biophysical surface of the Earth while land-use changes can be defined as variations in the way of using and managing a specific land area. Due to a direct connection between these two terms, land use/land cover change (LULCC) is generally used in the literature. One of the greatest changes in LULC is forest transition, especially forest degradation and deforestation. The unexpected change of forests impacts adversely on regional climate extremes (Findell et al. 2017), biodiversity (Semenchuk et al. 2022), and ecosystem services (Chung et al. 2021). As a result, proper estimations of forest changes and drivers is a central topic in international discussions and projects such as Paris Agreement and Reducing Emissions from Deforestation and Forest Degradation (REDD+) (Winkler et al. 2021). Long-term monitoring and interpreting of forest changes and drivers at a large scale and a fine spatial level provide evidence-based information for these discussions and projects. This information is also essential to making decisions in informing policy, planning, and managing forest resources.

Despite its importance, the detailed long-term estimation of forest transition is challenging, especially in developing regions, which frequently have a lack of information about the accurate datasets of forests for a long period. Recent evidence suggests that many developing countries are short of professional competence to generate fine spatiotemporal and accurate forest mapping resources (Saah et al. 2019). For example, a careful synthesis of over 200 case studies focusing on forest and agricultural land in South and Southeast Asia shows that although numerous studies have been conducted in certain countries such as India and Indonesia, few studies have been done in the other countries of the regions such as Cambodia, Laos, and Vietnam (Xu et al. 2019).

Vietnam has a major resource of tropical forests, but it has undergone highly dynamic changes over the recent three decades (Goldblatt et al. 2018; Phan et al. 2021a). These changes are expected to adversely influence the long-term balance of ecosystem services (Truong et al. 2018) and climate (Laux et al. 2017). Unfortunately, very few accurate and consistent datasets of forests have been conducted for a long-term period across the country. According to the report of the general statistics office on forest management, available five-year-interval national-scale forest

maps are frequently utilized by local policymakers. These maps are not always meet the requirement of all users and are not frequently published to various institutes, organizations, and analysts. Up to date, some data sources have developed, but their differences, for example, production methods, producers, and input data usage result in inconsistencies in the resultant data products (Saah et al. 2019). Likewise, regional and global products have limitations when they are applied for analyses at a local-level scale. They cannot reflect accurately at a local and a national scale due to their coarse spatial resolution and low accuracy (Phan et al. 2018, 2021b; Hansen et al. 2013). These limitations challenge the effective usage of the existing forest data sets to provide scientific information for decision-makers to inform coherent policies, do long-term strategic planning, and offer corporate management.

Currently, we have first created a database for the Vietnam-wide annual land use/cover data sets (VNLCD) from 1990 to 2020 (Phan et al. 2021a). Although the database does not focus only on forests, it is beneficial for the estimations of forest changes and drivers. First, the accuracy of the forest class is high. The database contains variously different LULC, which allows for measuring the transition between forests and other land types.

Although we have a manuscript talking details about how the database has been conducted (Phan et al. 2021a), we herein summarize the process for a general understanding. Specifically, a state-of-the-art framework was established utilizing various ground-based and satellite-based data sources, including Landsat and Sentinel sensors. The framework contained an automatic training migration model and an optimal approach for post classification optimization. The established approach could address issues such as cloud-contaminated problems by employing the availability of multiple spatiotemporal data, thus improving the accuracy of mapping. The satellite data were separated into wet seasons (May–November) and dry seasons (December to the next April) to identify the changes in LULC phenology, including forest and agriculture. The automatic training migration model offered a practical mode for collecting reference data over the recent three decades. Regarding the land cover classification system (LCCS), we applied the standard land cover scheme, viz. Land Cover Classification System with necessary modifications according to the local biophysical environment and end-users' suggestions in Vietnam. That is, ten land cover types (Fig. 32.4) were decided. Applying a benchmark (Olofsson et al. 2014), the quality of the VNLCD was statistically validated with ground-based reference data derived from extensive field surveys (from 2015 to 2020) and inventory data over the country. Different metrics were provided, including overall accuracy, kappa coefficients, and standard error of the mean. The VNLCD was published on the Japan Aerospace Exploration Agency website.

This paper aims to explore the dynamics and drivers of forest changes across mainland Vietnam. To this end, we first analyze the forest change from 1990 to 2020 over the study area, utilizing the VNLCD. We then conduct a synthesis of the case studies to identify major drivers of the forest changes before deciding the selected major drivers for this study. The remaining main part of the paper is to quantify the drivers using a logistic regression model. This is the first study to undertake a longitudinal analysis of the long-term dynamics and drivers of the forest changes in

Vietnam. It provides an important opportunity to advance the understanding of the pattern, rate, and process of forest changes at a commune level, which can provide insights into informing more coherent policy to enhance the management of forest in Vietnam and expecting to apply in other tropical regions.

32.2 Materials and Methods

32.2.1 Forest

Forests provide with different valuable services such as soil erosion protection and habitat provision for animals and humans. In the field of ecology, various definitions of forests are found. In this study, we adopted the definition of forests provided by the Food and Agriculture Organization of the United Nation (FAO). Herein, forest is defined as “land spanning more than 0.5 ha with trees higher than five meters and a canopy cover of more than 10%, or trees able to reach these thresholds in situ. It does not include land that is predominantly under agricultural or urban land use”. Also, mangrove is not defined as forests in this study.

32.2.2 Forest Diversity and Change Quantification

We first estimated and removed possible errors in the VNLCD. Although the VNLCD had a high level of accuracy, there might be misclassifications due to the effects of different climate situations and changes in plant phenology. The misclassifications would happen a few times in the time-series maps. To eliminate the errors, we created occurrence maps derived from the 1990 to 2020 time-series maps with arbitrary quantiles, including the first quartile, third quartile, and ninetieth percentile. For each land type, we overlaid the occurrence map on the fine-resolution images in Google Earth to identify misclassifications. With a trial-and-error technique, we found that the third quartile was the best threshold to eliminate possible misclassifications. Subsequently, we quantified the dynamics of forestland, including gain, loss, and major conversion from 1990 to 2020. We also estimate the diversity of forest changes by computing the number of changes between forest and non-forest land at a commune scale over the recent three decades (Fig. 32.2).

32.2.3 Hotspot Analyses

Changes in LULC are interests, but the change might not be statistically significant, biasing the estimation of main drivers. To increase the reliability of the estimation, we

employed a hotspot analysis to identify the statistically significant changes. Although several approaches have been established to estimate hotspots, Getis-Ord G_i^a (Ord and Getis 1995) has been practically applied in the geographic research (Ma et al. 2012). Hence, we employed the Getis-Ord G_i^a method to compute z -score and p -value for each area of interest (ROI). An ROI that has a high z -score and a small p -value is a significant hotspot while a coldspot has a low negative z -score and a small p -value. Herein, the ROI that has a z -score greater than three was defined as a hotspot. The hotspot analysis was performed at the commune level known as the ROI. We computed Getis-Ord G_i^a values as follows Eqs. (32.1), (32.2) and (32.3). The Getis-Ord local statistic is given as:

$$G_i^a = \frac{\sum_{j=1}^n w_{i,j} x_j - \bar{X} \sum_{j=1}^n w_{i,j}}{S \sqrt{\frac{n \sum_{j=1}^n w_{i,j}^2 - (\sum_{j=1}^n w_{i,j})^2}{n-1}}} \quad (32.1)$$

$$\bar{X} = \frac{\sum_{j=1}^n x_j}{n} \quad (32.2)$$

$$S = \sqrt{\frac{\sum_{j=1}^n x_j^2}{n} - (\bar{X})^2} \quad (32.3)$$

where G_i^a is Getis-Ord local statistics; x_j is the attribute value for feature j ; $w_{i,j}$ is the spatial weight between feature i and j ; and n is equal to the total number of features.

32.2.4 Case-Study Synthesis

We conducted a review of 47 publications to detect the drivers of spatio-temporal changes in forest land in Vietnam. We used the query expression “TI = (drivers OR drivers OR causes OR dynamics AND land*) AND TS = (Vietnam OR “Viet Nam” AND land*) AND TS = (*fores* OR defor* OR refor* OR degrad*)” to search the publications in Web of Science and Google Scholar databases. Then, we eliminated duplicates before gathering 456 publications in total, of which about 357 publications worked on LULC, including forests. Reading the titles and abstracts of the 357 publications, we eliminated 189 publications, which did not discuss forest topics. Among 168 publications remained, the third-fourth mainly worked on the general LULC and LULCC assessment. Finally, we selected 47 publications, which worked on estimating the drivers of forest changes. After the careful scanning of the full publications, we noted study topics, main drivers, research places, research periods, and approaches applied by the selected publications. If a major driver was noted in the publications, we defined it as a major driver. Otherwise, the mentioned drivers in the publications could be seen as the main drivers. Similar drivers were

merged to generalize the drivers. They are presented in Table A.1 (Supplementary document).

32.2.5 Proxy Data Drivers

The main biophysical and socio-economic drivers (Sect. 32.2.4) were derived from different sources. Most of the data were extracted annually from the General Statistics Office of Vietnam (1990–2020; household surveys). They were originally presented in various formats including vector, tabular, and raster formats with different spatial resolutions. After that, considerable efforts were made to interpret the data before they were used for the coming analysis. Since the data had different spatial resolution, we kept the original spatial resolution and computed mean values at the commune scale. Then, for the time-series data (e.g., climate) we computed mean, rate of change, and standard deviation values over the study period (1990–2020). For the constant data (e.g., elevation and slope) which were insignificantly alter over the study period, we computed mean values in the area of interest. Details about the proxy drivers are presented in Table A.2 (Supplementary document).

32.2.6 Handling the Multicollinearity of the Driver Proxy Data and Modelling Selection

Multicollinearity causes the inaccurate assessment of the regression coefficients. Herein, we first detected the high level of multicollinearity between the driver variables by computing the variance inflation factors (VIF). We then excluded the driver proxy variables which have a high level of multicollinearity or $VIF > 10$ (Supplementary Document: Fig. A.1) (Hsieh et al. 2003). We acknowledged this limitation to reduce the analysis bias of the regression model.

It is noted that even though several models have been established to estimate the drivers of LULCC, there is not the best model. The performance of a model varies according to certain research cases. When a model is selected, it should be considered major factors, including reliability, generalizability, computational cost, and stability (Sun et al. 2022). Recently, a logistic regression model has been commonly applied for identifying the drivers of LULCC, due to its clear understanding and impressive performance (Xu et al. 2019). A logistic regression model, therefore, was applied in this study.

32.3 Results and Discussion

32.3.1 Synthesis of the Case Study

The detailed drivers of the forest gain and loss from the synthesis of 47 case studies are presented in Table A.1 (Supplementary Document). Only eight studies worked on a national scale (including a regional scale covering Vietnam) while the others were conducted at smaller areas from a village to provincial scale. Most studies quantified the drivers utilizing quantitative methods such as logistic regression, multiple correlation analysis, and linear regression whereas ten studies interpret the drivers based on interviews, fieldwork surveys, and historical data. There was a larger number of studies on the drivers of forest loss (deforestation) in comparison to forest gain (reforestation/afforestation). The frequent distribution of the main drivers is presented in Fig. 32.1. They include socioeconomic drivers such as policy and income, and biophysical drivers such as climate and topography. As can be seen from the figure, the socioeconomic drivers were mentioned more frequently than the biophysical drivers (47 against 33, respectively). Regarding the forest loss, frequently mentioned drivers were agricultural expansion/shifting, policy/tenure, and accessibility/infrastructure. Meanwhile, policy/tenure and plantation were the most common drivers of deforestation. The most interesting aspect of this table is that tenure/policy decisions were involved actively in both the forest gain and loss. In contrast, plantation solely contributed to reforestation/afforestation while fuelwood/logging/charcoal, land size, climate, urbanization, etc. were only mentioned in the deforestation studies.

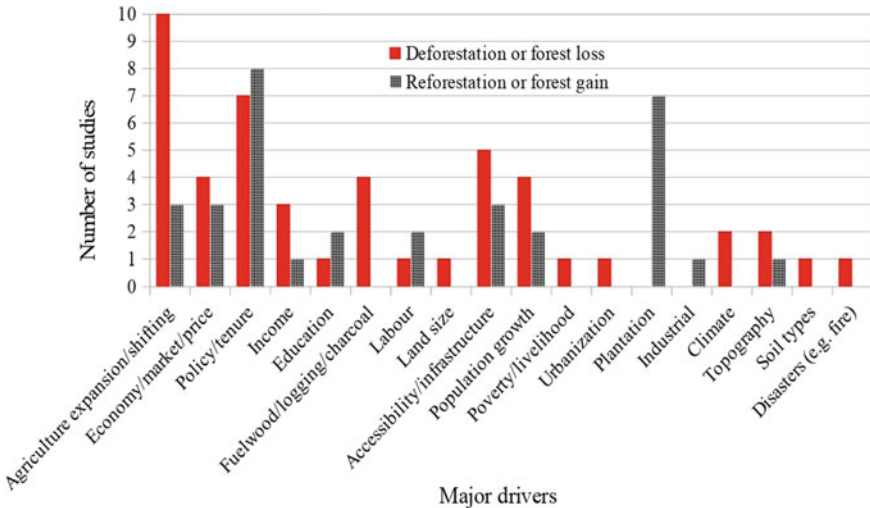


Fig. 32.1 Frequency distribution of the main drivers extracted from the synthesis of case studies in Vietnam. More details about specific drivers can be found in Table A.1 (supplementary document)

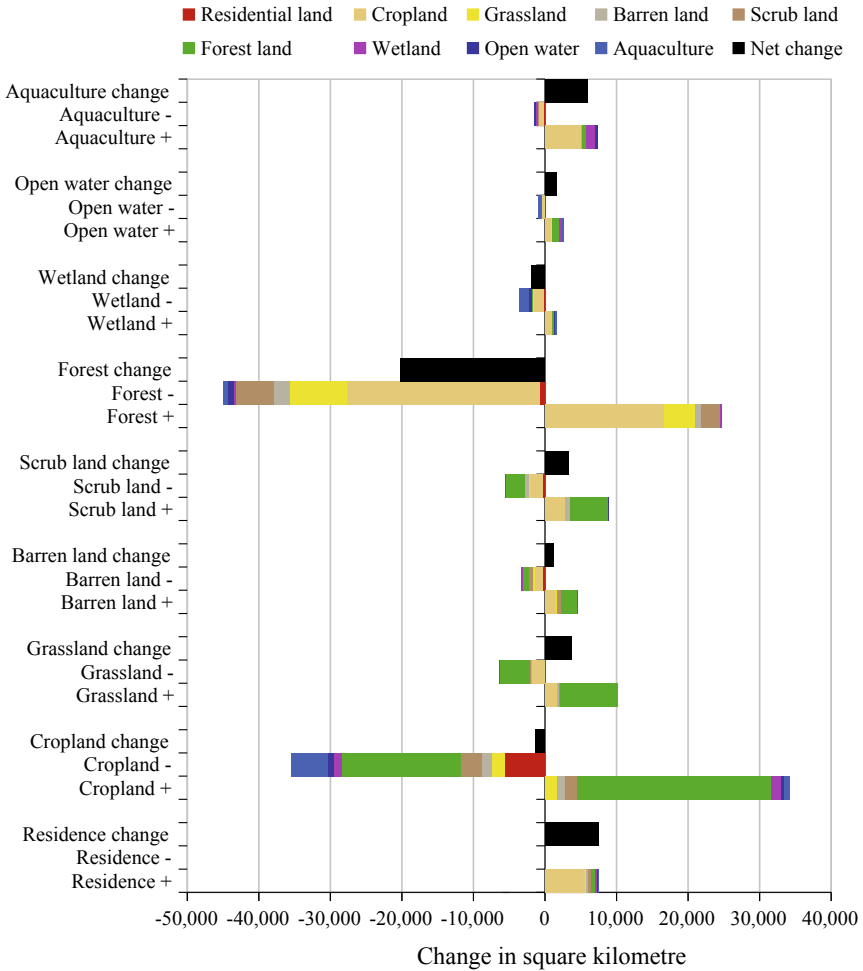


Fig. 32.2 Gross losses, gross gains, and net change in land use/cover at Vietnam-wide scale between 1990 and 2020. Land use/cover types are showed in different colors. Areas are measured in square kilometer. The left represents losses while the right represents gains. Black bars present the net changes (gross gains–gross losses) of different land use/cover types

32.3.2 Land Use/Land Cover and Forest Dynamic Changes

The conversion of different land use/land cover types between 1990 and 2020 is presented in Fig. 32.2. As can be seen from the figure, major LULC changes were forests, residential areas, and aquaculture land. While the residential and aquaculture land experienced increased trends, the area of forest significantly shrank over the study period. This finding was also reported by Hansen et al. (2013) and Leinenkugel et al. (2015). This result is, however, likely contrary to that of Meyfroidt et al.,

Jadin et al., and the report of the Vietnamese Ministry of Agriculture and Rural Development (MARD) who found that the area of forests increased (Meyfroidt and Lambin 2008; Jadin et al. 2013). These differences are due to several rationales. First, Meyfroidt et al. and Jadin et al. only estimated within a shorter period from 1990 to 2010. Over this period, our previous results also showed an increase in forests in Vietnam (Phan et al. 2021a). Second, there was a slight difference in the definition of forests provided by this study and the MARD who did not consider rubber, scattered trees, etc. as forests. These LULC types changed dynamically but were not fully included in the report of forests by the MARD (Hoang et al. 2020). Interestingly, the MARD included certain areas administrated by the forestry division into the forest land although there may be no forests on the land (Van Khuc et al. 2018).

Spatial distributions and dynamics of forests in 1990 and 2020 across mainland Vietnam are presented in Fig. 32.3a and b, respectively. As can be seen from the figures, forests are mainly distributed in the northern and west-center regions that had high altitudes/elevation. It is apparent from Fig. 32.3a and b that very few areas of forests were detected in delta areas, especially the Red River Delta and Vietnamese Mekong Delta/the South. Figure 32.4a and b present apparently the fractional distribution of forest losses and gains at the commune-level scale. Meanwhile, the hotspots and coldspots of forest gains and losses are shown in Fig. 32.4c and d. What stands out in the figures is the most dynamics and losses of forests in the Central Highlands and the North-West. This finding was also reported by Imai et al. (2018) and Kissinger (2020). This result may be explained by several reasons. As can be seen in Fig. 32.2, there is a major conversion between forests and agricultural land. The central Highlands provide for commercial agriculture with reasonable conditions such as adequate precipitation, moderate temperatures, and good soils. In this region, dominant commercial agriculture lands are rubber and coffee, which have significantly expanded between 2005 and 2015 (Kissinger 2020).

32.3.3 *Measurement of the Major Drivers*

Standardized coefficients are used to compare the relative effect of each individual driver variable to the forest change area. Specifically, before running the multiple least squares model, we standardized the driver variables to z-scores. Herein, the coefficients that we obtain from the model are standardized coefficients, which have standard deviations as their units. This means the driver variables can be precisely compared to each other, although they are measured on different units and scales. The higher the absolute value of the coefficient, the stronger the impact. A positive value of the coefficient means that a higher value of a driver variable causes a greater change in the forest area. In contrast, a negative value of the coefficient means a higher value of a driver variable has a lower change in the forest area. Herein, the standardized coefficients are presented in Fig. 32.5.

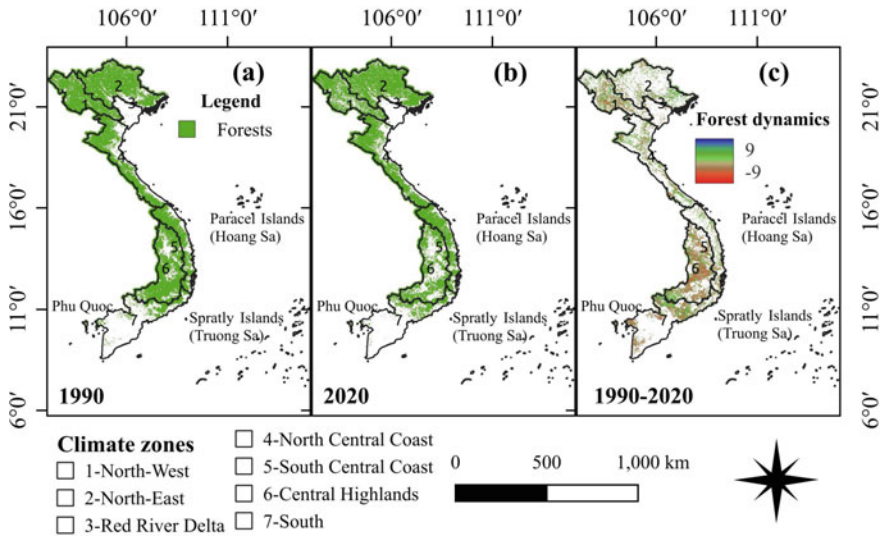


Fig. 32.3 Spatial distribution of forests in mainland Vietnam in 1990 (a), in 2020 (b), and the dynamic change of forests over recent three decades (c). The red color represents a gain while blue color represents a loss over the study period. The data were analyzed using the Vietnam-wide annual land use/cover data sets (Phan et al. 2021b)

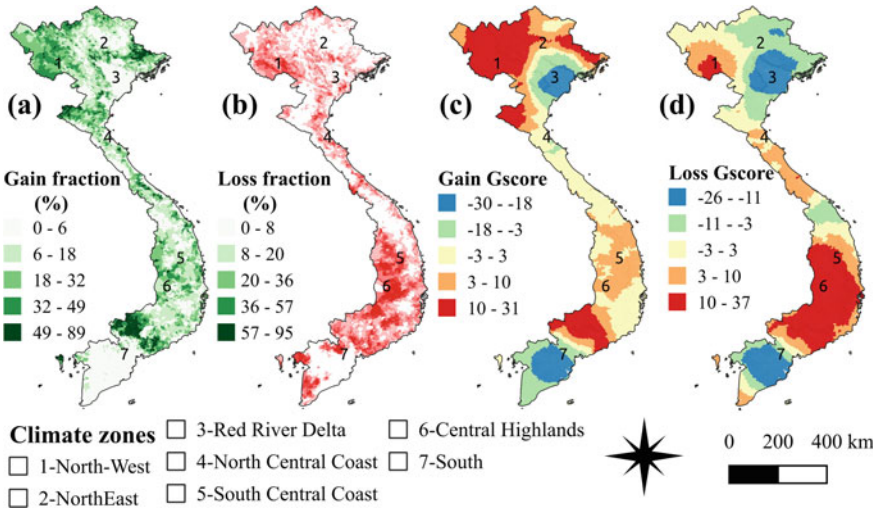


Fig. 32.4 Spatial pattern of forest change in mainland Vietnam between 1990 and 2020. **a** the fraction of forest gain (%) and **b** the fraction of forest loss (%). **c** Presents hotspot analysis of forest gain and **d** shows hotspot analysis of forest loss. Red color represents hot spots while blue color represents cold spots

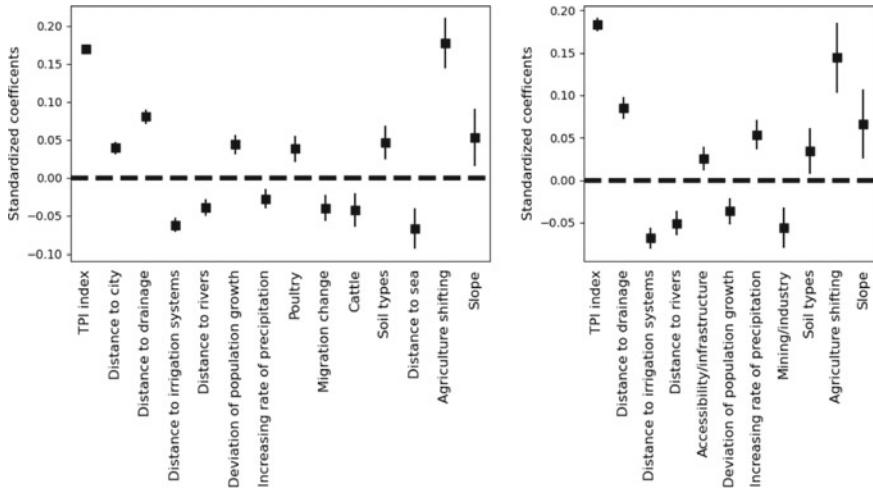


Fig. 32.5 Most prominent drivers of forest changes: forest gain (left) and forest loss (right). Square dots indicate the coefficients while the bars indicate the uncertainties at the 95% confidence interval

Forest gain Fourteen major drivers significantly relate to the forest gain, of which a half is biophysical drivers and the others are socioeconomic drivers (Fig. 32.5a and Table A.3; Supplementary document). Eight major drivers have positive relationships with the forest gain; of which the most important driver is agricultural shifting. This result can be explained by several possible reasons. As can be seen from Fig. 32.2, there is a considerable conversion between forests and agricultural land. In other words, agricultural shifting can significantly cause changes in forest areas. This result also corroborates the findings of a great deal of the previous work on forest transition in Vietnam, which are described in detail in Sect. 32.3.1. For example, Ashraf et al. has identified a net increase of forests in certain areas of Vietnam due to the major shrinkage of agricultural land (Ashraf et al. 2017). What is surprising is that the topographic position index (TPI) and slope positively have substantial impacts on the forest gain, although our synthesis shows few studies that have mentioned these drivers. A possible explanation for this might be that forests are mainly located in mountainous areas that have high values of slope and TPI indexes (Meyfroidt and Lambin 2008; Nguyen 2019). Other positive relationships between the forest gain and the driver variables are distance to the city, distance to drainage, deviation of population growth rate, poultry, and soil types. Among these drivers, the distance to drainage is the strongest factor correlating to the forest gain. This finding was also reported by Nguyen (2019). It seems possible that drainage systems are frequently constructed in flat regions such as cities and densely populated residential areas that are non-forest land (La Rosa and Pappalardo 2020). In terms of negative relationships, there are six major drivers, of which distance to the sea is the most considerable driver. This means forest gains occur in regions close to the sea. This result may be explained by the fact that planting forests are considered an effective solution to prevent natural

hazards and disasters. Several reports have shown that forests are planted in coastal areas for protecting erosion and typhoons (Hai et al. 2020; Nguyen et al. 2017).

Forest loss Standardized coefficients corresponding to forest loss are shown in Fig. 32.5b and Table A.4 (Supplementary document) with seven positive relationships and four negative relationships. The most interesting finding was that the topographic position index (TPI) also has the most positive relationship with forest loss, indicating that forest loss frequently occurs in regions that have high values of the TPI. However, we have not found studies that identify the relationship between deforestation and TPI while slope has been utilized instead (Chi et al. 2013; Meyfroidt 2013). In this study, the slope has a strong positive correlation with forest loss.

It is not surprising that agricultural shifting was found to cause a significant loss of forests. This finding broadly supports the work of other studies in this area linking agricultural expansion/shifting and deforestation (Jadin et al. 2013; Van Khuc et al. 2018; Imai et al. 2018; Muller and Zeller 2002). There are several types of agricultural expansion/shifting. For example, in the Central Highlands (e.g., Dak Lak, Dak Nong, and Binh Phuoc), a large number of forests areas have been converted into coffee and rubber since the 1990s (Meyfroidt et al. 2013). Specifically, Dak Lak has relatively high elevation, fertile soil, and cool weather which offer a suited environment to coffee crops, especially Robusta coffee (Pohlan and Janssens 2010). In contrast, with a lower elevation and a higher temperature, Binh Phuoc offers a favorable condition to rubber plantations (Li and Fox 2012). Also, the quickly growing global demand for coffee and rubber resulted in the expansion of these crops. It is also supported by governmental policy to convert poor forests into coffee and rubber plantations (Meyfroidt et al. 2013; Li and Fox 2012).

Other major positive drivers correlating to forest loss are accessibility/infrastructure and increasing rate of precipitation. These results support evidence from previous observation (Chi et al. 2013; Muller and Zeller 2002; Castella et al. 2005; Sikor 2001). Particularly, Nguyen et al. found that forest loss occurs more frequently in remote access areas, for example, far from roads, drainage, and a densely populated residence (Nguyen 2019). Meanwhile, the positive relationship between deforestation and the increasing rate of precipitation indicates that wetter areas are favorable conditions for forest transition. A possible explanation for this might be that increasing rate of precipitation might introduce extreme climate conditions, such as typhoons and floods, which may reduce forest productivity and degradation, and thus may cause deforestation (Xiaoming et al. 2019; Rutten et al. 2014). Another possible explanation for this is that the major degradation or loss of forests results in changes in precipitation (O'Connor et al. 2021; Baudena et al. 2021; Molina et al. 2019). The literature also reported an increase in extreme climate events, especially in the Central Highlands which is a hot spot of deforestation (Nam et al. 2018, 2019).

Regarding the negative relationships between drivers and forest loss, there are four major drivers, namely distance to irrigation, distance to rivers, deviation of population growth, and mining/industry. It means that the loss of forest frequently happens in regions closer to rivers, irrigation systems, mining/industry zones, and diffusely populated areas. Although these drivers have not been mentioned in our synthesis of

case studies on forest transition in Vietnam, these results match those observed in earlier studies in other regions (Rodriguez-Galiano et al. 2012; Siqueira-Gay et al. 2020).

32.3.4 Limitations and Future Work

The generalisability of these results is subject to certain limitations. First, although we have collected the most essential drivers mentioned in our synthesis of the case studies and added new drivers, we could not quantify some important drivers such as forest management policy/tenure, globalization, disasters, and economy/market/price. These drivers may have profound effect the transition of forests (Meyfroidt and Lambin 2008; Nguyen 2019; Chi et al. 2013; Webb and Honda 2007; Liu et al. 2020). In this study, the data of these drivers are not available at a proper spatiotemporal scale; or some have high multicollinearity, causing difficulties in the precise measurement of the impact of individual drivers; we, therefore, have excluded them from the analysis model. The lack of these drivers might impact our quantitative results. Secondly, the spatiotemporal difference of some collected drivers may cause uncertainties in the analysis of the drivers. Specifically, most of the drivers are derived from the General Statistics Office of Vietnam, which have been calibrated by the office; some are extracted from the WorldClim 2 database (Fick and Hijmans 2017) or the satellite-based information (e.g., the Shuttle Radar Topography Mission) (Farr and Kobrick 2000). These data may have relatively low quality and added further uncertainties in this work. However, the current shortage of the properly available data does not permit us to overcome this limitation. This would be a fruitful area for further work.

32.4 Conclusion

The present research aimed to analyze the changes and drivers of the land use/land cover changes focusing on forests in mainland Vietnam. To our best knowledge, this is the first work on the analysis of inter-annual dynamics of forests at the national scale from 1990 to 2020. Results have shown that Vietnam experiences a considerable change in LULC over the recent three decades. There is a significant transition between forests land and other lands, especially agriculture, grassland, and shrubland. One of the more significant findings to emerge from this research is that the forest change has occurred in differences in space and time. The North-West and Central Highlands are the most dynamic change areas, which are considered hot spots. The study has also shown that although a net gain of forests has been reported in a short period (e.g., 2005–2010), Vietnam has undergone a net loss of forests from 1990 to 2020. The drivers of forest changes are various. Our synthesis of case studies on forest transition has indicated that previous studies mainly focused on socioeconomic

drivers. However, our results show that biophysical drivers also have significantly contributed to forest changes. In general, both biophysical and socioeconomic drivers are highlighted in this study. The development of the economy requires more food and agricultural products, forcing the extensive conversion of forests into other land types if biophysical conditions are reasonable for production. The second major contribution of our synthesis was that it broadens a more general knowledge of the drivers of the forest changes. These findings have significant implications for the understanding of how effectively manage forest resources in Vietnam. They may be of interest to other countries. The identification of socioeconomic and biophysical drivers in this study is likely to help enhance the accuracy of the land use/land cover change prediction.

References

- Ashraf J, Pandey R, de Jong W (2017) Assessment of bio-physical, social and economic drivers for forest transition in Asia-Pacific region. *Forest Policy Econ* 76:35–44
- Baudena M, Tuinenburg OA, Ferdinand PA, Staal A (2021) Effects of land-use change in the Amazon on precipitation are likely underestimated. *Glob Change Biol* 27(21):5580–5587
- Castella JC, Manh PH, Kam SP, Villano L, Tronche NR (2005) Analysis of village accessibility and its impact on land use dynamics in a mountainous province of northern Vietnam. *Appl Geogr* 25(4):308–326
- Chi VK, Rompaey AV, Govers G, Vanacker V, Schmoock B, Hieu N (2013) Land transitions in Northwest Vietnam: an integrated analysis of biophysical and socio cultural factors. *Hum Ecol* 41(1):37–50
- Chung MG, Frank KA, Pokhrel Y, Dietz T, Liu J (2021) Natural infrastructure in sustaining global urban freshwater ecosystem services. *Nat Sustain* 4(12):1068–1075
- Farr TG, Kobrick M (2000) Shuttle radar topography mission produces a wealth of data. *Eos* 81(48):583–585
- Fick SE, Hijmans RJ (2017) WorldClim 2: new 1-km spatial resolution climate surfaces for global land areas. *Int J Climatol* 37(12):4302–4315
- Findell KL, Berg A, Gentine P, Krasting JP, Lintner BR, Malyshev S, Santanello JA, Shevliakova E (2017) The impact of anthropogenic land use and land cover change on regional climate extremes. *Nat Commun* 8(1)
- Goldblatt R, Deininger K, Hanson G (2018) Utilizing publicly available satellite data for urban research: mapping built-up land cover and land use in Ho Chi Minh City, Vietnam. *Dev Eng* 3:83–99
- Hai NT, Dell B, Phuong VT, Harper RJ (2020) Towards a more robust approach for the restoration of mangroves in Vietnam. *Ann For Sci* 77(1)
- Hansen MC, Potapov PV, Moore R, Hancher M, Turubanova SA, Tyukavina A, Thau D, Stehman SV, Goetz SJ, Loveland TR, Kommareddy A, Egorov A, Chini L, Justice CO, Townshend JRG (2013) High-resolution global maps of 21st-century forest cover change. *Science* 342(6160):850–853
- Hoang TT, Truong VT, Hayashi M, Tadono T, Nasahara KN (2020) New JAXA high-resolution land use/land cover map for Vietnam aiming for natural forest and plantation forest monitoring. *Remote Sens* 12(17)
- Hsieh FY, Lavori PW, Cohen HJ, Feussner JR (2003) An overview of variance inflation factors for sample-size calculation. *Eval Health Prof* 26(3):239–257
- Imai N, Furukawa T, Tsujino R, Kitamura S, Yumoto T (2018) Factors affecting forest area change in Southeast Asia during 1980–2010. *PLoS ONE* 13(5)

- Jadin I, Vanacker V, Hoang HTT (2013) Drivers of forest cover dynamics in smallholder farming systems: the case of northwestern Vietnam. *Ambio* 42(3):344–356
- Kissinger G (2020) Policy responses to direct and underlying drivers of deforestation: examining rubber and coffee in the central highlands of Vietnam. *Forests* 11(11)
- La Rosa D, Pappalardo V (2020) Planning for spatial equity—a performance based approach for sustainable urban drainage systems. *Sustain Cities Soc* 53
- Laux P, Nguyen PNB, Cullmann J, Kunstmann H (2017) Impacts of land-use/land-cover change and climate change on the regional climate in the Central Vietnam. In: *Water resources development and management*. Springer Nature, pp 143–151
- Leinenkugel P, Wolters ML, Oppelt N, Kuenzer C (2015) Tree cover and forest cover dynamics in the Mekong Basin from 2001 to 2011. *Remote Sens Environ* 158:376–392
- Li Z, Fox JM (2012) Mapping rubber tree growth in mainland Southeast Asia using time-series MODIS 250 m NDVI and statistical data. *Appl Geogr* 32(2):420–432
- Liu S, Li X, Chen D, Duan Y, Ji H, Zhang L, Chai Q, Hu X (2020) Understanding land use/land cover dynamics and impacts of human activities in the Mekong Delta over the last 40 years. *Global Ecol Conserv* 22
- Ma Z, Zuckerberg B, Porter WF, Zhang L (2012) Use of localized descriptive statistics for exploring the spatial pattern changes of bird species richness at multiple scales. *Appl Geogr* 32(2):185–194
- Meyfroidt P (2013) Environmental cognitions, land change and social-ecological feedbacks: local case studies of forest transition in Vietnam. *Hum Ecol* 41(3):367–392
- Meyfroidt P, Lambin EF (2008) Forest transition in Vietnam and its environmental impacts. *Glob Change Biol* 14(6):1319–1336
- Meyfroidt P, Vu TP, Hoang VA (2013) Trajectories of deforestation, coffee expansion and displacement of shifting cultivation in the Central Highlands of Vietnam. *Global Environ Change* 23(5):1187–1198
- Molina RD, Salazar JF, Martínez JA, Villegas JC, Arias PA (2019) Forest-induced exponential growth of precipitation along climatological wind streamlines over the Amazon. *J Geophys Res: Atmos* 124(5):2589–2599
- Muller D, Zeller M (2002) Land use dynamics in the central highlands of Vietnam: a spatial model combining village survey data with satellite imagery interpretation. *Agric Econ* 27(3):333–354
- Nam DH, Duong PC, Thuan DH, Mai DT, Dung NQ (2018) Assessment of near-term runoff response at a river basin scale in central Vietnam using direct CMIP5 high-resolution model outputs. *Water (Switzerland)* 10(4)
- Nam DH, Hoa TD, Duong PC, Thuan DH, Mai DT (2019) Assessment of flood extremes using downscaled CMIP5 high-resolution ensemble projections of near-term climate for the upper Thu Bon catchment in Vietnam. *Water (Switzerland)* 11(4)
- Nguyen TTH (2019) Drivers of forest change in Hoa Binh, Vietnam in the context of integration and globalization. *Singap J Trop Geogr* 40(3):452–475
- Nguyen TA, Vu DA, Van Vu P, Nguyen TN, Pham TM, Nguyen HTT, Le HT, Nguyen TV, Hoang LK, Vu TD, Nguyen TS, Luong TT, Trinh NP, Hens L (2017) Human ecological effects of tropical storms in the coastal area of Ky Anh (Ha Tinh, Vietnam). *Environ Dev Sustain* 19(2):745–767
- O'Connor JC, Dekker SC, Staal A, Tuinenburg OA, Rebel KT, Santos MJ (2021) Forests buffer against variations in precipitation. *Glob Change Biol* 27(19):4686–4696
- Olofsson P, Foody GM, Herold M, Stehman SV, Woodcock CE, Wulder MA (2014) Good practices for estimating area and assessing accuracy of land change. *Remote Sens Environ* 148:42–57
- Ord JK, Getis A (1995) Local spatial autocorrelation statistics: distributional issues and an application. *Geogr Anal* 27(4):286–306
- Phan DC, Trung TH, Nasahara KN, Tadono T (2018) JAXA high-resolution land use/land cover map for Central Vietnam in 2007 and 2017. *Remote Sens* 10(9)
- Phan DC, Trung TH, Truong VT, Sasagawa T, Vu TPT, Bui DT, Hayashi M, Tadono T, Nasahara KN (2021a) First comprehensive quantification of annual land use/cover from 1990 to 2020 across mainland Vietnam. *Sci Rep* 11(1)

- Phan DC, Trung TH, Truong VT, Nasahara KN (2021b) Ensemble learning updating classifier for accurate land cover assessment in tropical cloudy areas. *Geocarto Int* 1–18
- Pohlan HAJ, Janssens MJJ (2010) Growth and production of coffee. In: *Soils, plant growth and crop production*, vol III
- Rodríguez-Galiano VF, Ghimire B, Rogan J, Chica-Olmo M, Rigol-Sánchez JP (2012) An assessment of the effectiveness of a random forest classifier for land-cover classification. *ISPRS J Photogramm Remote Sens* 67(1):93–104
- Rutten M, Van Dijk M, Van Rooij W, Hilderink H (2014) Land use dynamics, climate change, and food security in Vietnam: a global-to-local modeling approach. *World Dev* 59:29–46
- Saah D, Tenmeson K, Matin M, Uddin K, Cutter P, Poortinga A, Nguyen QH, Patterson M, Johnson G, Markert K, Flores A, Anderson E, Weigel A, Ellenberg WL, Bhargava R, Aekakkararungroj A, Bhandari B, Khanal N, Housman LW, Potapov P, Tyukavina A, Maus P, Ganz D, Clinton N, Chishtie F (2019) Land cover mapping in data scarce environments: challenges and opportunities. *Front Environ Sci* 7
- Semenchuk P, Plutzer C, Kastner T, Matej S, Bidoglio G, Erb KH, Essl F, Haberl H, Wessely J, Krausmann F, Dullinger S (2022) Relative effects of land conversion and land-use intensity on terrestrial vertebrate diversity. *Nat Commun* 13(1):615
- Sikor T (2001) The allocation of forestry land in Vietnam: did it cause the expansion of forests in the northwest? *Forest Policy Econ* 2(1):1–11
- Siqueira-Gay J, Sonter LJ, Sánchez LE (2020) Exploring potential impacts of mining on forest loss and fragmentation within a biodiverse region of Brazil's northeastern Amazon. *Resour Policy* 67
- Sun Z, Sandoval L, Crystal-Ornelas R, Mousavi SM, Wang J, Lin C, Cristea N, Tong D, Carande WH, Ma X, Rao Y, Bednar JA, Tan A, Wang J, Purushotham S, Gill TE, Chastang J, Howard D, Holt B, Gangadagamage C, Zhao P, Rivas P, Chester Z, Orduz J, John A (2022) A review of earth artificial intelligence. *Comput Geosci* 159:105034
- Thiha, Webb EL, Honda K (2007) Biophysical and policy drivers of landscape change in a central Vietnamese district. *Envir Conserv* 34(2):164–172
- Truong NCQ, Nguyen HQ, Kondoh A (2018) Land use and land cover changes and their effect on the flow regime in the upstream Dong Nai River Basin, Vietnam. *Water (Switzerland)* 10(9)
- Van Khuc Q, Tran BQ, Meyfroidt P, Paschke MW (2018) Drivers of deforestation and forest degradation in Vietnam: an exploratory analysis at the national level. *For Policy Econ* 90:128–141
- Winkler K, Fuchs R, Rounsevell M, Herold M (2021) Global land use changes are four times greater than previously estimated. *Nat Commun* 12(1)
- Xu X, Jain AK, Calvin KV (2019) Quantifying the biophysical and socioeconomic drivers of changes in forest and agricultural land in South and Southeast Asia. *Glob Change Biol* 25(6):2137–2151

Chapter 33

Monitoring Mangrove Forest Changes in Vietnam Using Cloud-Based Geospatial Analysis and Multi-temporal Satellite Images



Quang Thang Le  and Si Son Tong 

Abstract This study aims to use cloud computing and Sentinel-2 satellite data to map mangrove forests in Vietnam. To distinguish mangroves from other areas, it is necessary to rely on biological properties: water and vegetation cover. This study develops a method by analyzing the time series of water and vegetation cover in specific areas to determine criteria for accurate mangrove extraction. For more detail, 5 criteria canopy, greenness, $NDVI > 0.6$, $NDVI < 0.2$, and $LSWI > 0.45$ are extracted. These 5 indices are considered to correlate with annual mean NDVI to set thresholds for mangroves. Besides, terrain elevation data is also considered to filter out the mixed vegetation close to mangrove. This approach is applied to coastal areas of Vietnam to produce a mangrove forests map in 2020 using Google Earth Engine. Then 47 mangrove-reference points are used to check the mangrove map with an accuracy of about 85%. Finally, the mangrove map in 2020 is overlaid with the mangrove map in 2011 generated from Landsat images to determine the change of mangroves over 9 years. The results show that after 9 years, 95,000 ha of mangrove was preserved, approximately 120,000 ha disappeared, and approximately 67,000 ha of new forests.

Keywords Mangrove · Canopy · Greenness · NDVI · LSWI · GEE

33.1 Introduction

Vietnam has more than 3000 km of coastline with biodiversity. Mangroves are typical plant species of coastal areas. Large numbers of mangroves in Vietnam, which possess an important role in protecting the environment and reducing the effects of climate change. However, mangrove forests in Vietnam have declined sharply (up to 38%) during the Vietnam War and after that by economic development (Veettit et al. 2019). In order to face the issue of losing mangrove forest, Vietnam has been implementing

Q. T. Le · S. S. Tong (✉)

Space and Applications Department, University of Science and Technology of Hanoi (USTH), Vietnam Academy of Science and Technology (VAST), 18 Hoang Quoc Viet, Cau Giay, Ha Noi, Vietnam

e-mail: tong-si.son@usth.edu.vn

policies in mangrove protection and restoration (Brown and Chu 2012). It is necessary to have up to date and accurate information about the variation of mangrove forest in the whole territory of Vietnam for the purpose of those policies. Mangrove forest maps can be made by field measurement or using remote sensing data. The field measurement to investigate mangrove forests is hard to apply for such a large area as in Vietnam due to the high costs of transporting, traveling, time, and labor consumption. Only remote sensing techniques with the advantages of multi-temporal, multi-spectral, multi spatial resolutions can instantaneously map mangrove forests at regional or global scale.

Previously, there were some studies that used satellite data to map mangrove forests in Vietnam: Mangrove mapping in Hai Phong city (Pham and Yoshino 2013), mangrove forest map in Ca Mau Peninsula (Nguyen et al. 2015) and mangrove forest map all over Vietnam in 2011 (Mangroves of Vietnam 2011). The disadvantages are that 2 out of 3 studies only mapped mangroves for a small region in Vietnam, and all of the above studies utilized Landsat satellite images with 30 m resolution. Therefore, the re-mapping of mangroves all over Vietnam is necessary because, after years, there were many changes affected by economic activities in Vietnam, and new Earth observation satellites provide better quality images.

Google Earth Engine (GEE) is a cloud computation resource to solve the problems of processing spatial data with unlimited input data. Google Earth Engine combines multiple types of satellite imagery, it is simple to access and especially suitable for remote sensing projects. Some previous studies have used the time variation of Landsat and Sentinel data to perform satellite data processes such as cloud detection (Maiersperger et al. 2013), atmospheric correlation (Zhu and Woodcock 2012) using GEE. Chen et al. (2017) applied GEE for time series analysis on Landsat 7/8 and SAR images to map mangroves in China with high accuracy. Their method is based on the phenology analysis of the water and vegetation time series. Data from the spectrum channels on satellite images of a given area were obtained over a period of time to observe the change, from which characteristics were drawn. It is concluded that the GEE is a powerful tool for mapping mangrove methods at regional and global scales with high accuracy. However, the use of GEE to investigate mangrove forests in Vietnam has not been found in the literature. Besides, the parameters, thresholds, and algorithms used to extract mangrove information are not always the same in different areas in the world due to the different mangrove species, environment, climate, etc. The development of a method to extract information on mangrove forests in Vietnam is indispensable.

This study aims to investigate the variation of mangrove forest in Vietnam between 2011 and 2020 using the GEE platform. An algorithm based on the sequence of changes over time on Sentinel-2 images to create a mangrove map is developed for a specific study area such as Vietnam. The map will then be compared with ground reference data and very high-resolution satellite images for validation.

33.2 Study Area

The study area includes the coastal area that extends throughout the coastline of Vietnam within latitudes between 8° 33' N and 21° 32' N. The mangrove forests in Vietnam can be divided into three main areas: The Northern zone from Quang Ninh to Thanh Hoa province, The Central coastal zone between Thanh Hoa to Ba Ria Vung Tau provinces, The Southern zone from Ba Ria Vung Tau to Kien Giang provinces. The Northern zone has medium conditions (alluvium, wind, tides) for mangroves, and mangroves in this area are low (height smaller than 10 m) and sparse. The Central coastal zone lacks alluvial which limits the growth of mangroves, mangroves in the Central coastal zone only exist inside the river mouths and do not appear along the coastline. Mangroves in the Northern and Central coastal zones contain plenty of red mangroves, mangroves apple. The Southern zone has alluvium created by The Mekong River as well as suitable temperature and river flow, mangroves thrive and have large size (up to 20 m high) in Southern Vietnam (Phan 1991). Mangroves in the Southern area comprise numerous White and Blume species (Fig. 33.1).

33.3 Data in Use

33.3.1 Sentinel-2 Data

Sentinel-2 is an Earth observation mission that includes two satellites: Sentinel-2A and Sentinel-2B for acquiring optical imagery at space resolution from 10 to 60 m. Sentinel-2 was developed and used for remote sensing applications such as land monitoring, natural disaster mapping, urban mapping, agriculture management, etc. Two levels of pre-processing Sentinel-2 data are available for end users: Level-1C and Level-2A. Level-1C product receives the reflectance from the top of the atmosphere (TOA). Level-2A products are images of the earth surface after systematically correcting atmospheric effects so called images from the bottom of the atmosphere (BOA). This study used only the Sentinel-2 Level-2A images, the characteristics of Sentinel-2 Level-2A are described in Table 33.1.

This study utilized Sentinel-2 Level 2A images covering Vietnam's coastline. All images are automatically geo-corrected to reduce the effects of topography and standardized to WGS84 Zone 48 N projection. These images are available in GGE as image collections. In this research, we use totally 5135 Sentinel-2 images, taken from May 31, 2019 to May 31, 2020.

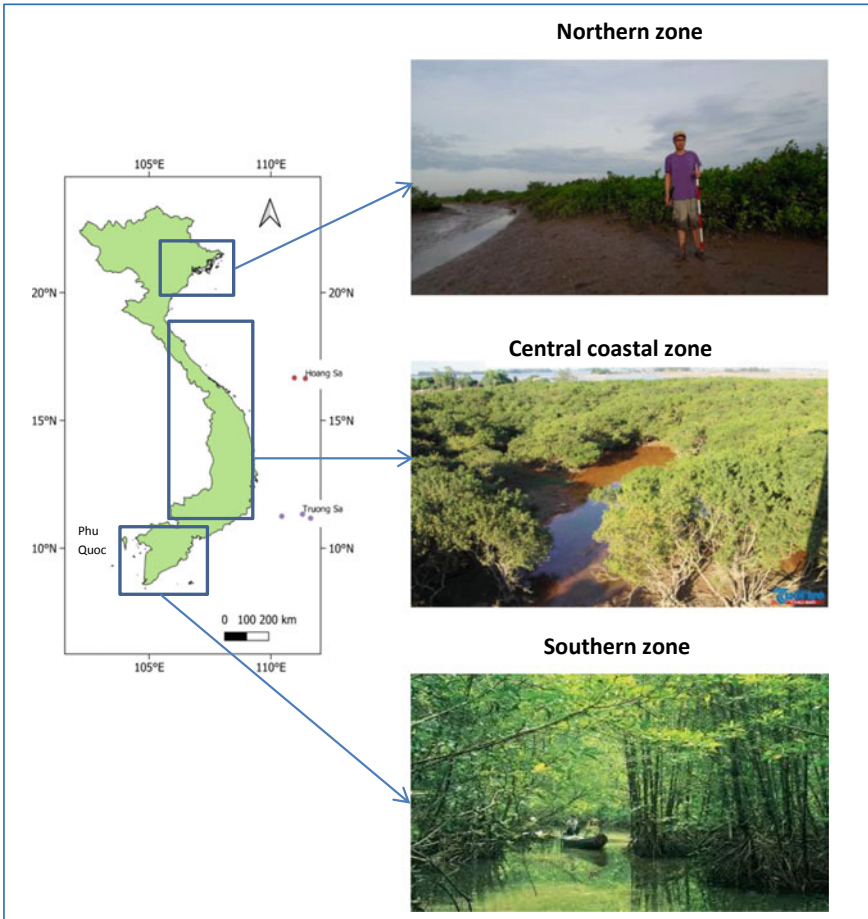


Fig. 33.1 Three mangrove areas in Vietnam from North to South

33.3.2 Vietnam Mangrove Forest Map in 2011

The Vietnam mangrove map was a part of the world mangrove map, data can be downloaded via website (<https://vietnam.opendevlopmentmekong.net/>) (Mangroves of Vietnam 2011). The 2011 mangrove map was built in 2011 based on Landsat 7 ETM+ images acquired in 2011 with a resolution of 30 m but small mangrove patches (900–2700 m²) were difficult to identify (Mangroves of Vietnam 2011). The 2011 Vietnam mangrove map was imported into GGE, mainly used as a reference dataset to validate mangrove positions and compare the results (Fig. 33.2).

Table 33.1 Bands characteristics of Sentinel-2 Level 2A (<https://sentinels.copernicus.eu/>)

Sentinel-2 bands	Central wavelength (nm)	Bandwidth (nm)	Spatial resolution (m)
Band 1—coastal aerosol	442.2	21	60
Band 2—blue	492.1	66	10
Band 3—green	559.0	36	10
Band 4—red	664.9	31	10
Band 5—vegetation red edge	703.8	16	20
Band 6—vegetation red edge	739.1	15	20
Band 7—vegetation red edge	779.7	20	20
Band 8—NIR	832.9	106	10
Band 8A—narrow NIR	864.0	22	20
Band 9—water vapour	943.2	21	60
Band 10—SWIR—cirrus	1376.9	30	60
Band 11—SWIR	1610.4	94	20
Band 12—SWIR	2185.7	185	20

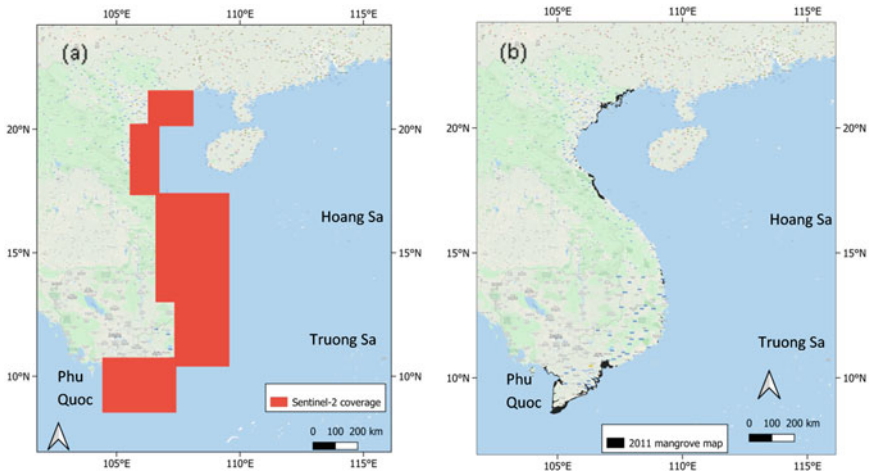


Fig. 33.2 **a** Coverage of Sentinel 2 images and **b** mangrove forest map in 2011 in Vietnam

33.3.3 Elevation Data

Shuttle Radar Topography Mission (SRTM) digital elevation data represents the elevation of land surface within the range of latitude from 56° S to 60° N. The SRTM

data is provided by NASA JPL with resolution 30 m and can be imported directly in GGE. In this study, the elevation model is used to filter out mangrove segments errors classified in high elevation areas.

33.3.4 Sample Points and Mangrove Boundary for Algorithm Development

In total, 398 points were collected throughout Vietnam for sampling, identifying characteristic features, thereby setting thresholds to differentiate mangrove forests and other land covers. Points were collected based on mangroves and non-mangroves areas. To determine the exact points representing mangroves and non-mangroves areas, we used very high-resolution satellite images acquired in 2019 and 2020 in Google Earth service and some ground points (6 points in the Xuan Thuy national park). We used 47 points included 6 ground points for the accuracy assessment of the results.

Besides, a boundary for mangroves is constructed based on a 15 km-distance from coastline because mangroves usually do not appear further than 15 km seaward from the coastline (Chen et al. 2017). The boundary of mangrove is relatively determined on very high resolution satellite images in the Google Earth service. The boundary is used to remove the inland that does not contain mangroves (Fig. 33.3).

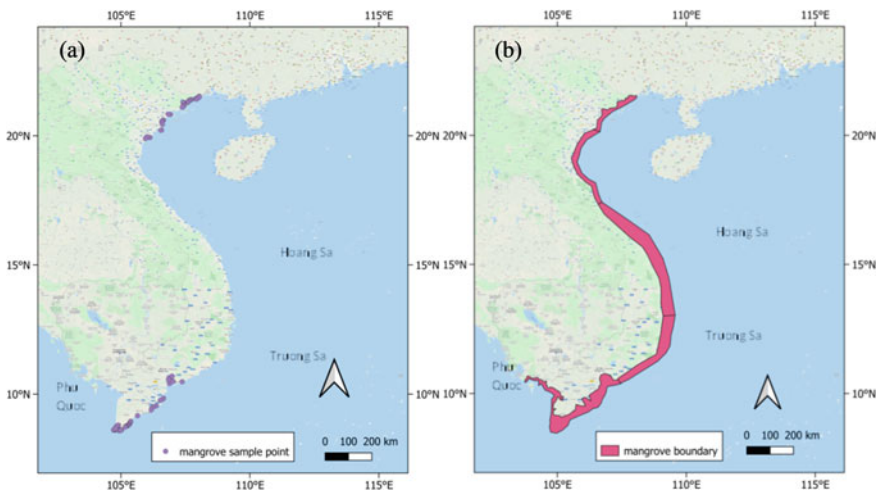


Fig. 33.3 a Sample points of mangrove forests and b the boundary for mapping mangrove forests

33.4 Method

33.4.1 Vegetation and Water Index

Three indices including the Normalized Difference Vegetation Index (NDVI) (Tucker 1979), the Land Surface Water Index (LSWI) (Gao 1996; Xiao 2004), and the Enhanced Vegetation Index (EVI) (Huete et al. 2002) are calculated by the equations below:

$$\text{NDVI} = \frac{B8 - B4}{B8 + B4} \quad (33.1)$$

$$\text{LSWI} = \frac{B8 - B11}{B8 + B11} \quad (33.2)$$

$$\text{EVI} = \frac{2.5 \times (B8 - B4)}{B8 + 6 \times B4 - 7.5 \times B2 + 1} \quad (33.3)$$

where B8, B4, B11, B2 are near infrared band (NIR: 0.842 μm wavelength), red (0.665 μm wavelength), short wave infrared (SWIR1: 1.61 μm wavelength) and blue band (0.49 μm wavelength) respectively of the Sentinel-2 data (Table 33.1).

33.4.2 Discriminating Mangroves and Other Land Covers

33.4.2.1 Characteristics of Mangroves

To map mangrove forests, it is important to distinguish between mangroves and non-mangroves. Mangrove forests have a prominent feature that they possess high vegetation cover and high surface water index. Besides, the mangrove forests appear in low elevation (at sea level). Those characteristics are the keynotes to determine mangroves due to the evergreen species and usually submerged in seawater.

In this study, the relations of mangrove forests with other land covers are divided into five pairs: (1) mangroves with low vegetated area (cities, ponds, river, etc.); (2) mangroves with low water area (normal forest, sand, whistling pine tree, etc.); (3) mangroves and agricultural land (rice crops); (4) mangroves with high water forests (such as *Casuarina equisetifolia* forests); (5) mangroves with hilly and mountain forests. The criteria indices and algorithm are developed to discriminate mangrove forest from the other land covers in each pair.

33.4.2.2 Criteria Used to Determine Mangrove

Sentinel-2 time series show the change of NDVI, LSWI, EVI over one year of the period 2019–2020. The first four relation pairs in the previous part can be solved by analyzing the phenology of mangrove based on the variation of NDVI, LSWI, and EVI. By comparing phenology of mangrove areas and non-mangrove areas at sample points, the necessary criteria is determined for differentiating mangrove forests. In this study, 5 criteria indices are drawn: greenness, canopy, $NDVI > 0.6$, $NDVI < 0.2$, $LSWI > 0.45$ to distinguish mangrove. Besides, with hilly and mountain forests, SRTM data can limit the elevation because mangrove is low compared to sea level.

33.4.3 Method Flow Chart

The flow chart in Fig. 33.4 briefly describes the steps in the method to determine mangroves. Firstly, 3 indexes NDVI, LSWI, EVI are calculated from Sentinel-2 data. Then time series analysis of NDVI, LSWI, and EVI produces 5 criteria: Greenness, Canopy, $NDVI > 0.6$, $NDVI < 0.2$, and $LSWI > 0.45$. The frequencies of the 5 criteria are computed and set thresholds for the mangrove forests. Those thresholds combined with the elevation threshold are used to build the algorithm applied to the Sentinel-2 image for extracting the mangrove forests.

33.5 Results and Discussions

33.5.1 Criteria Indexes

33.5.1.1 Greenness and Canopy

This study uses two criteria introduced from Chen et al. (2017): Greenness and Canopy. The greenness index represents evergreen trees, the canopy index is specific to high leaf areas (Chen et al. 2017). Greenness is the condition that $LSWI > 0$ and $EVI > 0.2$ are applied to tropical regions of America, Africa, and Asia (Xiao et al. 2009). Canopy condition $NDVI > 0.3$ and $LSWI > 0.3$ based on results from Chen et al. (2017) for mangrove in China. However, in statistical processes from the sample points of mangrove forests in Vietnam, it is shown that the majority of NDVI and LSWI values over one year also produce canopy conditions $NDVI > 0.3$ and $LSWI > 0.3$ (Figs. 33.5 and 33.6). The canopy and greenness indexes are suitable to remove areas with low vegetation and low water cover.

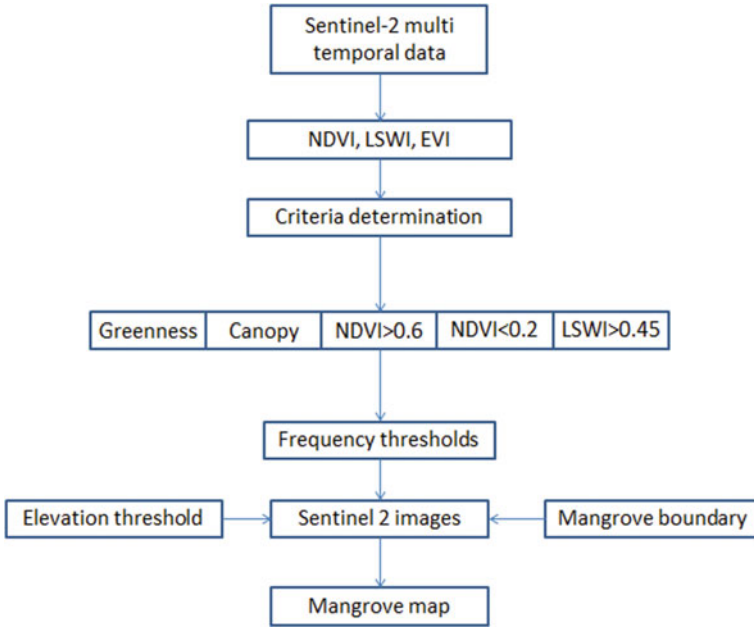


Fig. 33.4 Method flow chart

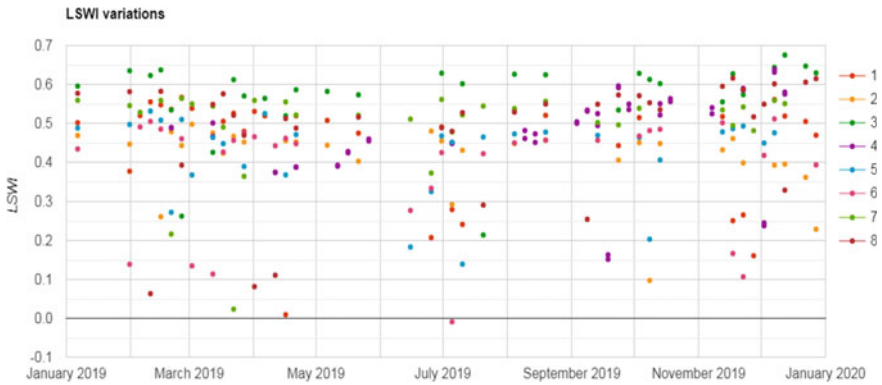


Fig. 33.5 Analyzing LSWI time series of 8 mangrove sample points within one year indicates that most of the LSWI values are higher than 0

33.5.1.2 Three Criteria Indices NDVI > 0.6, NDVI < 0.2, LSWI > 0.45

Based on NDVI and LSWI time series analysis applied on mangrove and non-mangrove areas, three criteria were also added: LSWI > 0.45, NDVI < 0.2, and NDVI > 0.6. Criterion LSWI > 0.45 is due to the fact that water in mangrove areas is always higher than other normal plant areas, especially plants located inland (rice field,

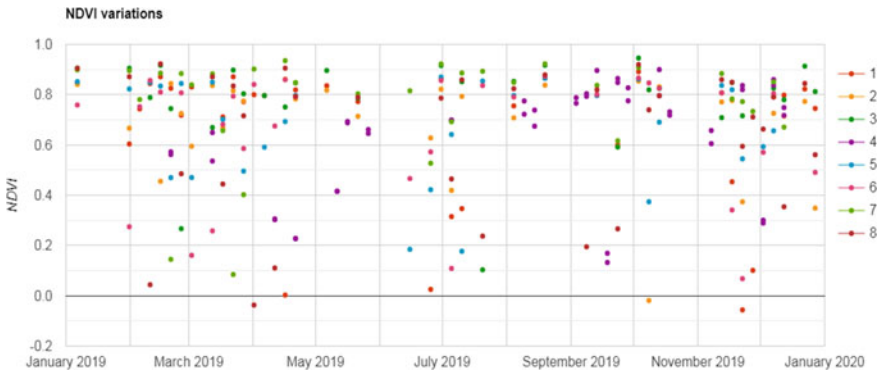


Fig. 33.6 Analyzing NDVI time series of 8 mangrove sample points within one year show most of the NDVI values are higher than 0.3

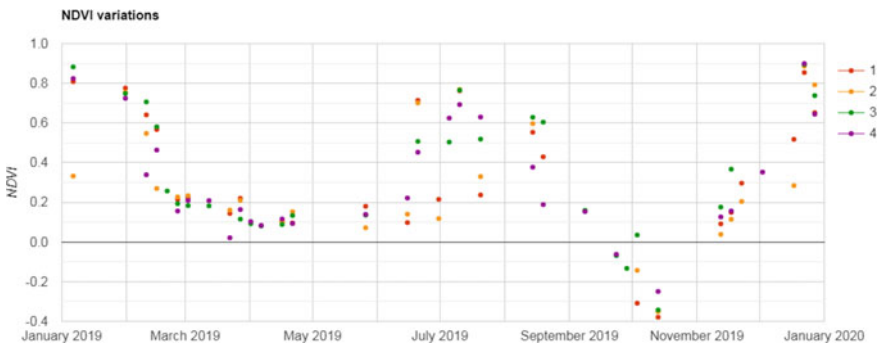


Fig. 33.7 Analyzing NDVI time series within one year of 4 rice field sample points, NDVI values lower than 0.2 especially in April, May, and November (after harvest)

Casuarina equisetifolia forest). The reason is that mangroves are often submerged in seawater, so they have better water indexes. The criterion $NDVI < 0.2$ is used to distinguish mangroves from annual agriculture crops. For short-term crops (such as rice), there are times of the year after harvest, vegetation covers are very low (NDVI usually smaller than 0.2), therefore $NDVI < 0.2$ was set as the separation threshold. Criterion $NDVI > 0.6$ was added to the study, as several NDVI statistics of mangrove areas show that plenty of NDVI values in time series higher than 0.6 because mangroves are evergreen over year (Figs. 33.7 and 33.8).

33.5.1.3 Summary Table

Summarize of five criteria canopy, greenness, $NDVI > 0.6$, $NDVI < 0.2$, $LSWI > 0.45$ is listed in Table 33.2.

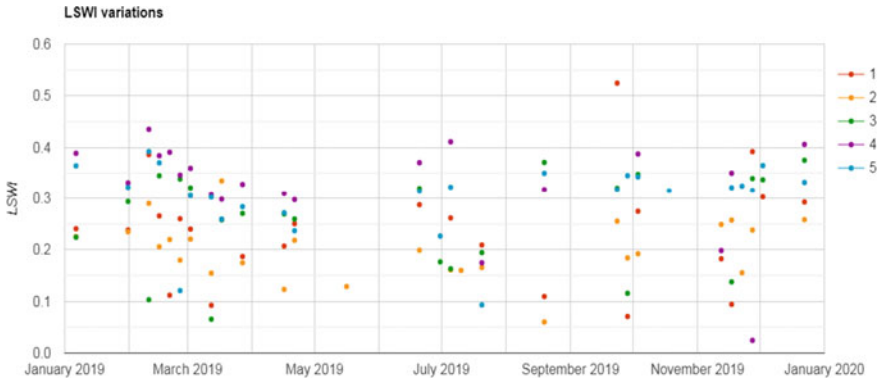


Fig. 33.8 Analyzing LSWI time series within one year of 5 *Casuarina equisetifolia* sample points, LSWI values are mostly lower than 0.45

Table 33.2 Criteria summary table

Number	Criteria	Conditions
1	Canopy	NDVI > 0.3 and LSWI > 0.3
2	Greenness	LSWI > 0 and EVI > 0.2
3	NDVI > 0.6	NDVI > 0.6
4	NDVI < 0.2	NDVI < 0.2
5	LSWI > 0.45	LSWI > 0.45

33.5.2 Developed Algorithm for Mangrove Extraction

33.5.2.1 Cloud Removing

The effect of clouds can be eliminated in Sentinel-2 images by the cloud band named QA60. This band uses different values for the amount of cloud on each pixel. When the band value is lower than 1024, it means that there is nearly no cloud on this pixel. Therefore, a threshold for cloud is the QA60 value smaller than 1024 was applied on Sentinel-2 image collection to reduce the dates in the time series (for each pixel, not the whole image) that cannot be analyzed by the influence of clouds.

33.5.2.2 Frequencies of Greenness and Canopy

The first condition of the Canopy is determined based on NDVI and LSWI higher than 0.3.

$$\text{Canopy} = \begin{cases} 1 & \text{if NDVI} > 0.3 \text{ and LSWI} > 0.3 \\ 0 & \text{other values} \end{cases} \quad (33.4)$$

Frequency of canopy can be calculated as follow:

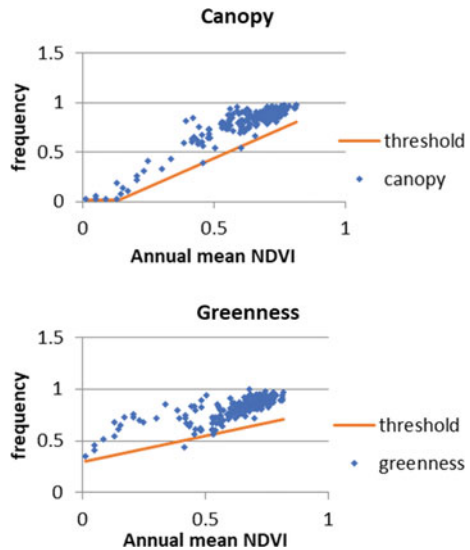
$$F_{canopy} = \frac{\sum N_{canopy}}{\sum N_{total} - \sum N_{cloud}} \tag{33.5}$$

where F_{canopy} is frequency of canopy index with scale from 0 to 1. For each pixel in image, with time series within one year (from May 31, 2019, to May 31, 2020), $\sum N_{canopy}$ is the number of observation counts that satisfy the canopy condition ($NDVI > 0.3$ and $LSWI > 0.3$). $\sum N_{total}$ is the total number of obtained observations. $\sum N_{cloud}$ is the number of observations affected by clouds. Besides, the annual mean NDVI needs to be calculated because it represents mangrove forest density (Jensen 1991). Frequencies of canopy and greenness can be assumed that they have correlation with mean NDVI (Chen et al. 2017). In total, 209 mangrove sample points were taken to calculate frequencies of canopy, greenness, and then the frequencies were plotted on the diagrams associated with its annual mean NDVI (Fig. 33.9). From the diagrams, thresholds are set up based on the lowest frequency values corresponding to the annual mean NDVI and the regression lines. The frequency threshold is constructed by first-order linear lines so that most of the blue points representing mangroves are above thresholds. The thresholds of canopy and greenness are highlighted with yellow lines in Fig. 33.9.

The formulas used to construct the threshold are rewritten as inequality equations. These equations below describe the yellow lines on the diagrams:

$$F_{canopy}(x) = \begin{cases} 1.15x - 0.14 & NDVI > 0.138 \\ 0.02 & NDVI \leq 0.138 \end{cases} \tag{33.6}$$

Fig. 33.9 Thresholds of canopy frequency and greenness frequency



$$F_{\text{greenness}}(x) \geq 0.5x + 0.29 \quad \text{for all cases} \quad (33.7)$$

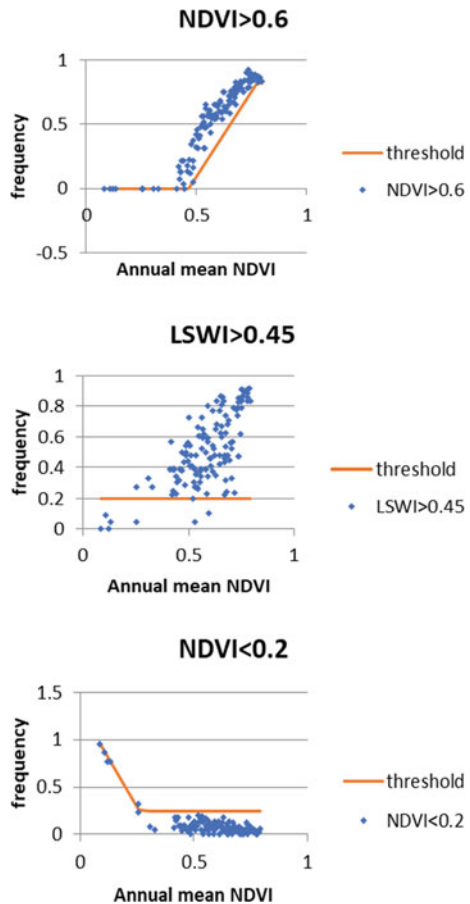
where x is the mean NDVI.

33.5.2.3 Frequencies of Three Indices NDVI > 0.6, NDVI < 0.2 and LSWI > 0.45

We used 125 sampling points taken within one year. The frequencies of three criteria NDVI > 0.6, NDVI < 0.2 and LSWI > 0.45 are calculated similarly with frequency F_{canopy} in the previous part. Data are plotted on the diagram and set the thresholds (Fig. 33.10).

The threshold formulas are also given:

Fig. 33.10 Thresholds of NDVI > 0.6, LSWI > 0.45 and NDVI < 0.2 frequencies



$$F_{\text{NDVI}>0.6}(x) \geq \begin{cases} 0 & \text{NDVI} < 0.467 \\ 2.64x - 1.23 & 0.467 \leq \text{NDVI} \leq 0.77 \\ 0.82 & 0.77 < \text{NDVI} \end{cases} \quad (33.8)$$

$$\text{FLSWI} > 0.45(x) \geq 0.2 \quad \text{for all cases} \quad (33.9)$$

$$F_{\text{NDVI}<0.2}(x) \geq \begin{cases} -4.13x + 1.31 & \text{NDVI} \leq 0.267 \\ 0.24 & \text{NDVI} > 0.267 \end{cases} \quad (33.10)$$

where x is annual mean NDVI.

33.5.2.4 Distinguish Between Mangroves and *Casuarina Equisetifolia* Forests

Phenology analysis according to NDVI, LSWI of *Casuarina equisetifolia* and mangrove forests to separate these two types is difficult because phenology based on NDVI, LSWI of the *Casuarina equisetifolia* and mangrove forests show great similarities. However, in some areas of *Casuarina equisetifolia* forest during the analysis of canopy frequency, it is interesting to note that the difference between canopy frequency and correspond NDVI mean value is always lower 0.09, when comparing to mangrove forests, this difference is usually higher than 0.09 especially when NDVI is higher than 0.59, so an additional threshold is included:

$$F_{\text{canopy}}(x) \geq x + 0.09 \quad \text{if NDVI} \geq 0.59 \quad (33.11)$$

where x is annual mean NDVI.

33.5.2.5 Elevation Threshold

To separate mangroves and forests on hills and mountains, an additional condition is the elevation limitation. Mangroves have relatively low elevations compared to hills and mountains. By statistics from sample points, mangroves enter a range of -4 m to 20 m above sea level. On the SRTM elevation map, the limitation is given:

$$-4\text{m} < y < 20\text{m} \quad (33.12)$$

where y is the elevation of mangrove.

33.5.3 Mangrove Forest Map of Vietnam in 2020

Applying all 7 thresholds from (33.6) to (33.12) to Sentinel-2 image collection that contains coastline in Vietnam, in the time between May 31, 2019, and May 31, 2020, to generate the mangrove map. The calculations and processing are performed on Google Earth Engine. The 2020 mangrove map is exported as digital maps (TIFF file) with the red color shown for mangroves, while white color is defined as not mangroves. From the map obtained, the results show that in Northern Vietnam, mangroves mostly concentrate in the coastal area. Mangroves in Central Vietnam are small in number and scattered, making it difficult to observe on maps. Mangroves are most abundant in Southern Vietnam, distributed mainly in the two regions of Ca Mau Peninsula and Can Gio (Ho Chi Minh city).

From the results, 47 points were selected for validation of the accuracy of the mangrove map. Those 47 points are chosen based on high-resolution satellite images (Google satellite maps) and ground reference data to make sure they are in mangrove areas. The results checked that 42/47 points were recognized as mangroves, accounting for approximately 85% (Fig. 33.11).

33.5.4 Mangrove Forest Changes

The mangrove forest map generated in 2011 using Landsat data is overlaid the mangrove forest map in 2020 using Sentinel 2. The changes show that after 9 years, 95,000 ha of mangroves were preserved, approximately 120,000 ha of forests have disappeared, and approximately 67,000 ha of new forests.

The decrease of mangroves can be explained by several reasons. The first is due to errors in mapping methods in the 2011 map, for example in Xuan Thuy National Park, many patches of whistling pine trees and mudflats along with mangrove forests also appear in the map. Especially in Central Vietnam, mangroves appear in a large area in the 2011 mangrove map, which is inaccurate in reality. Secondly, due to the transition from mangroves to economic sectors such as aquaculture, this can be seen in mangrove forests near major cities in Central and South Vietnam. The third reason is that the mangroves are also reducing sharply in the Southern Coastal Area because of erosion (Veettil et al. 2019).

Besides, the number of additional mangrove forests can be explained by three main reasons. The first reason is the amount of additional forests from mangrove conservation and development activities. The second reason is the number of mangroves that grow after 9 years. Finally, errors in methods did not display all mangrove forests in the 2011 map (Fig. 33.12).

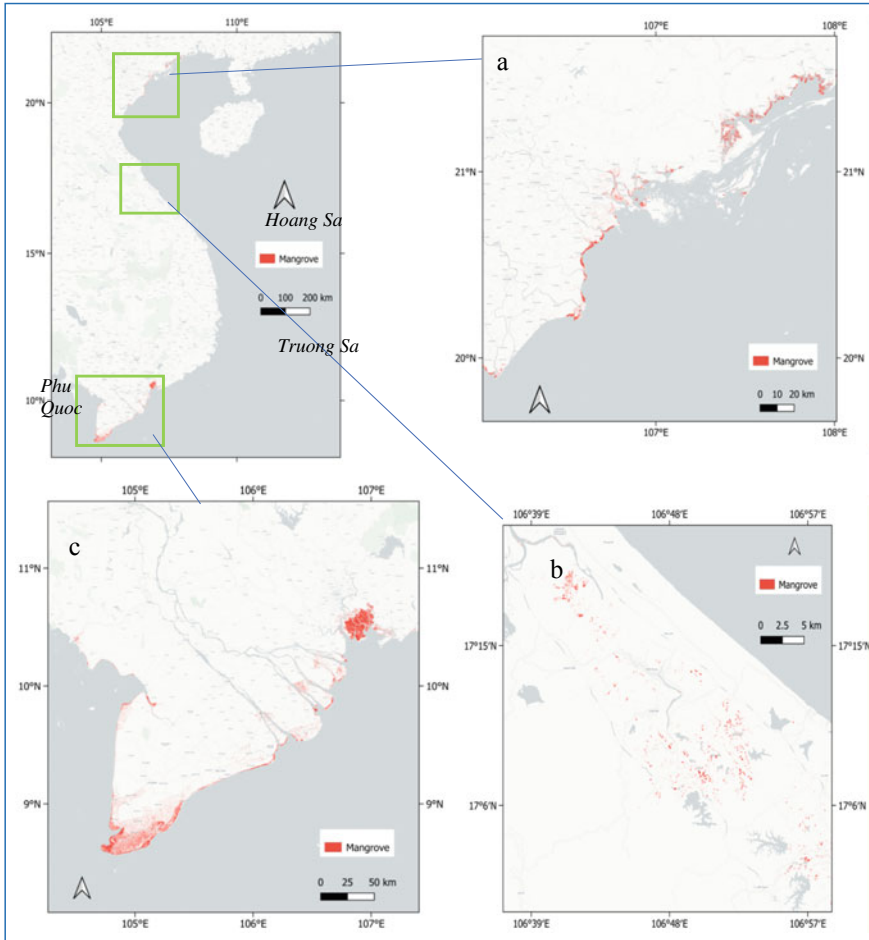


Fig. 33.11 Mangrove forest map in Vietnam, **a** Northern Vietnam, **b** Central Vietnam, **c** Southern Vietnam

33.6 Conclusion

Mangrove maps give good quality with a high density of concentrated mangroves such as coastal areas in Tonkin Gulf and Mekong Delta. Mangroves are well displayed on the map. Land covers have low water or vegetation can easily be removed by the algorithm. The SRTM digital map also performed efficiently in order to detach mangroves and mountain forests. However, non-mangrove areas still appear on the map. Compared with the 2011 map, the 2020 map has eliminated many areas that are not mangroves such as whistling pine trees and mudflats along rivers.

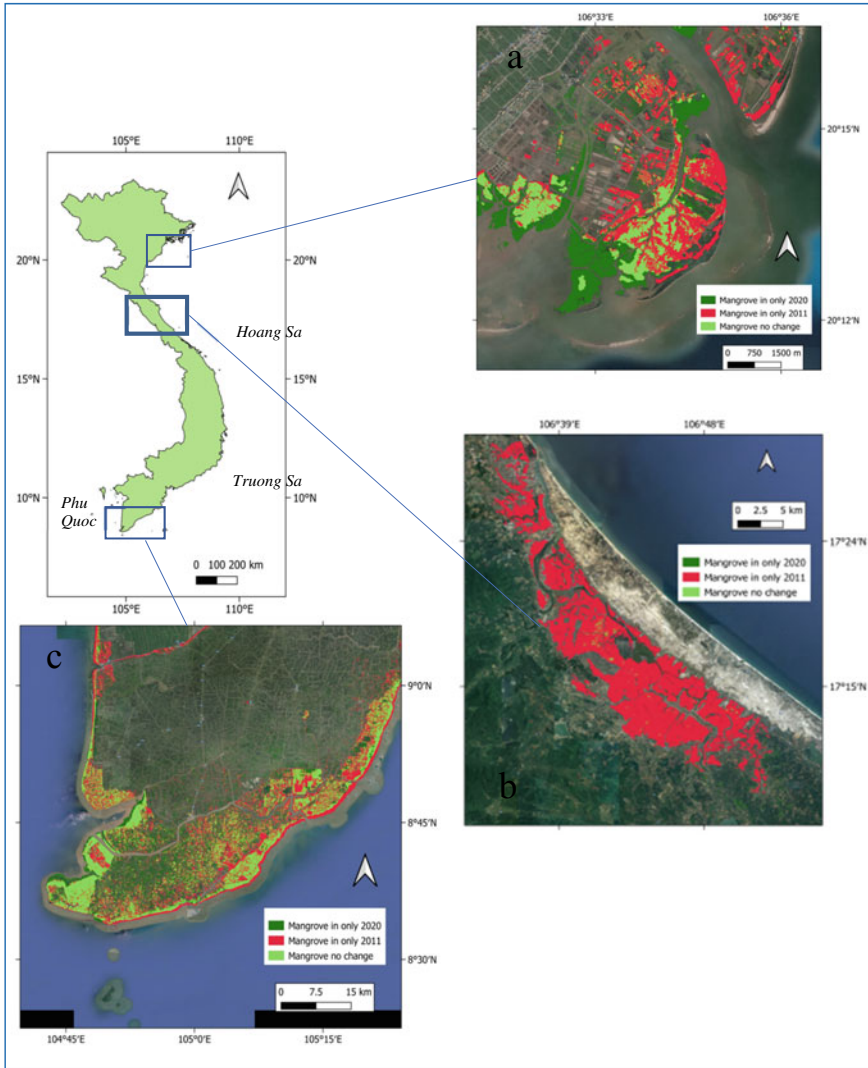


Fig. 33.12 **a** Errors by mudflats and whistling pine trees in Xuan Thuy National Park, **b** large mangrove areas appeared in North Central Vietnam is inaccurate by errors in mapping methods of 2011 map, **c** mangroves declined along the South coast of Vietnam after 9 years due to erosion and the increase of aquaculture

The mangrove map with a resolution of 10 m gives results with high accuracy of over 85%, which can be used in mangrove management and conservation in Vietnam. In addition, the 2020 map also shows that besides the increase in mangrove forest areas due to conservation activities, mangroves in Vietnam are still decreasing for many reasons, but mainly due to economic development activities and climate

change. Overall, the method using in this study based on the cloud computing and multi temporal satellite data is efficient solution for the investigation of mangrove forest not only in Vietnam but also in a global scale.

Acknowledgements This study is supported by Institutional S&T Project 2020–2022 “Coupling Radar remote sensing and Unmanned aerial vehicle techniques to monitor the changes of mangrove forest” No. USTH.SA.01/20-22.

References

- Brown S, Chu C (2012) Restoration of coastal mangrove forest in Vietnam. In: Technical report of the conservation and development of the Kien Giang biosphere reserve project
- Chen B, Xiao X, Li X, Pan L, Doughty R, Ma J (2017) A mangrove forest map of China in 2015: analysis of time series Landsat 7/8 and Sentinel-1A imagery in Google Earth Engine cloud computing platform. *ISPRS J Photogram Remote Sens* 131:104–120
- Gao B (1996) NDWI-A normalized difference water index for remote sensing of vegetation liquid water from space. *Remote Sens Environ* 58(3):257–266
- Huete A, Didan K, Miura T, Rodriguez E, Gao X, Ferreira L (2002) Overview of the radiometric and biophysical performance of the MODIS vegetation indices. *Remote Sens Environ* 83(1–2):195–213
- Jensen J (1991) The long perspective. In: *Environmental concerns*, pp 13–21
- Maiersperger T, Scaramuzza P, Leigh L, Shrestha S, Gallo K, Jenkerson C, Dwyer J (2013) Characterizing LEDAPS surface reflectance products by comparisons with AERONET, field spectrometer, and MODIS data. *Remote Sens Environ* 136:1–13
- Mangroves of Vietnam in 2011. <https://data.vietnam.opendevlopmentmekong.net/vi/dataset/grater-mekong-subregion-distribution-of-mangroves-thailand-cambodia-vietnam-and-myanmar/resource/7a48395b-0c51-4c6a-9b5a-37a32b126a7c>
- Nguyen TS, Chen CF, Chang NB, Chen CR, Chang LY, Thanh BX (2015) Mangrove mapping and change detection in Ca Mau Peninsula, Vietnam, using Landsat data and object-based image analysis. Selected topics in applied earth observations and remote sensing. *IEEE J Sel Top Appl Earth Observations Remote Sens* 8:503–510. <https://doi.org/10.1109/JSTARS.2014.2360691>
- Pham TD, Yoshino K (2013) Mangrove mapping and change detection using multi-temporal Landsat imagery in Hai Phong city, Vietnam
- Phan NH (1991) Mangrove forests in Vietnam, Hanoi University of Science. PhD thesis
- Tucker C (1979) Red and photographic infrared linear combinations for monitoring vegetation. *Remote Sens Environ* 8(2):127–150
- Veettil B, Ward R, Quang N, Trang N, Giang T (2019) Mangroves of Vietnam: historical development, current state of research and future threats. *Estuar Coast Shelf Sci* 218:212–236
- Xiao X (2004) Modeling gross primary production of temperate deciduous broadleaf forest using satellite images and climate data. *Remote Sens Environ* 91(2):256–270
- Xiao X, Biradar C, Czarnecki C, Alabi T, Keller M (2009) A simple algorithm for large-scale mapping of evergreen forests in tropical America, Africa and Asia. *Remote Sens* 1(3):355–374
- Zhu Z, Woodcock C (2012) Object-based cloud and cloud shadow detection in Landsat imagery. *Remote Sens Environ* 118:83–94

Chapter 34

Analysis and Assessment of the Relationship Between Chlorophyll and Hydrodynamic Factors in Cu Lao Dung (Soc Trang)



Pham Vu Phuong Trang and Vo Luong Hong Phuoc

Abstract Nowadays, scientists have used chlorophyll (CHL) to study primary productivity and assess water quality. There are many environmental factors that affect the concentration of CHL in water. Especially in estuaries, the complex dynamics greatly affect to the CHL. However up to now, the current research on “the influence of hydrodynamics on CHL distribution” is rare and limited especially in Viet Nam. Particularly, the studies from the measured data have not been synchronized due to its complication as well as its implementation expense. Therefore, the study can be considered as the pioneer on assessment of the relationship between chlorophyll (CHL) and hydrodynamic factors (tide, wave and flow) from the measured data in two monsoons (the Southwest and Northeast monsoons) in September 2014 and March 2015 at Cu Lao Dung offshore station (Soc Trang, Viet Nam). Data statistics, SPSS model and Matlab programming are used and applied to data process and analyze data. The results show that tide has an influence on the CHL concentration on the surface over time, especially, the CHL concentration gets highest at the low tide. The medium wave (wave height < 0.45 m) is the most suitable for phytoplankton growth (highest CHL concentration is 12.42 $\mu\text{g/l}$). However, the study could not find out the clear relationship between flow and CHL. The flow is influenced by many complex factors such as tides, waves, riverine flows or longshore currents. The study not only gives the high scientific significance on relationship between chlorophyll and hydrodynamic factors in Cu Lao Dung (Soc Trang province) but also has the real, actual application for any research institutions related

P. V. P. Trang · V. L. H. Phuoc (✉)

Department of Oceanology, Meteorology and Hydrology, Faculty of Physics and Engineering
Physics, University of Science, Ho Chi Minh City, Vietnam
e-mail: vlphuoc@hcmus.edu.vn

P. V. P. Trang

e-mail: phamtrang2183@gmail.com

Vietnam National University, Ho Chi Minh City, Vietnam

P. V. P. Trang

Institute of Coastal and Offshore Engineering, Ho Chi Minh City, Vietnam

to biology, environmental ecology and especially in the sustainable management of estuarine ecosystems.

Keywords Chlorophyll · Hydrodynamic factors · Tide · Wave · Flow · Phytoplankton · Cu Lao Dung (Soc Trang)

34.1 Introduction

Phytoplankton are known as primary producers of the ocean, the organisms that form the base of the food chain that directly synthesizes organic matter through the process of photosynthesis. The major constituent of phytoplankton is chlorophyll (CHL), and CHL is widely used as a measure of biomass for phytoplankton. Today, scientists use CHL to study primary production productivity and assess water quality. However, phytoplankton is a suspended species, using nutrients (nitrogen, phosphorus, iron...) directly from water and barely able to move actively, hence their growth and distribution depends generally on environmental factors. Environmental factors affecting CHL in water are mainly physical factors such as: temperature, DO, suspended sediment (characterized by turbidity), light, pH... and dynamic factors: tides, waves, currents..., in addition to many other biological, chemical and human factors. There are many studies on relationship between CHL and physical factors: “Wind-driven changes of surface current, temperature, and chlorophyll observed by satellites north of New Guinea” of Radenac et al. (2016), “The variability of chlorophyll-a and its relationship with dynamic factors in the basin of the South China Sea” of Yu et al. (2019). However, the studies of relationship between CHL and hydrodynamics are not popular. Mainly studies focused on the relationship between CHL and tides, such as: Mallin et al. (1999) studied the influence of tidal variation on the concentration of water quality parameters: CHL concentration and Fecal Coliform bacteria at locations in New Hanover County, North Carolina, USA; Blauw et al. (2012) analyzed the variability of coastal phytoplankton concentrations in relation to the tidal cycle, based on 9-year data with resolution from 12 to 30 min are automatically measured south of the North Sea, Fagherazzi et al. (2014) have studied the spatial relationships between tidal currents, sedimentary characteristics, CHL in sand bars and shoals in Plum Island Sound, Massachusetts, USA.

The studies on the effects of waves and currents on CHL concentration are very limited. Especially in Vietnam, the relationship between CHL and hydrodynamics factors has not been studied yet.

The aim of the study is to evaluate and analyze the relationship between the CHL concentration and the dynamic factors according to the two seasons of the SW and NE monsoon at the offshore station of Cu Lao Dung (Soc Trang).

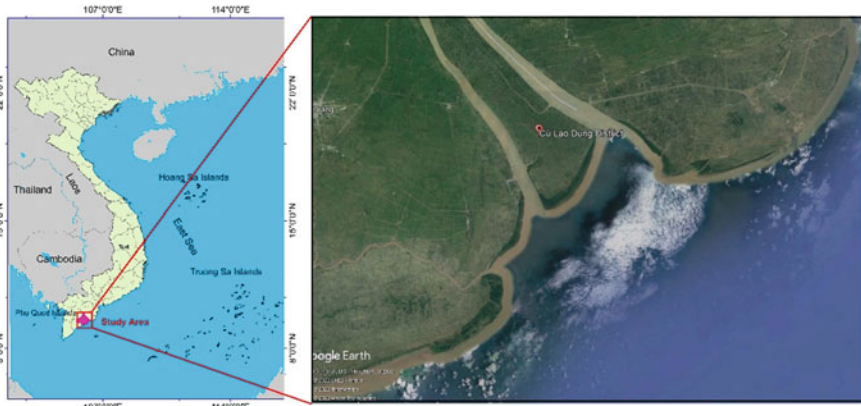


Fig. 34.1 The location of Cu Lao Dung and mooring station in September 2014 and March 2015

34.2 Research Method

34.2.1 Research Area

Cu Lao Dung is an islet at the end of Hau River between two big mouths of river: Dinh An and Tran De—two of main gateways to the East Sea. Cu Lao Dung has 17 km of coastline and more than 16,000 ha of coastal alluvial area.¹ The eastern and northern boundary are bordered by Dinh An; the western boundary borders by Tran De and the south boundary borders by the East Sea. All three sides are surrounded by river water and sea water.

The study site called ST0 station is located in $106^{\circ} 17' 28.0''$ E, $9^{\circ} 28' 15.0''$ N, more than 5 km from Cu Lao Dung islet to the Southeast, (Fig. 34.1). The study site is influent strongly on estuary and tidal regime.

The average flow velocity is from 0.137 to 0.144 m/s.² The average tidal current velocity is 0.11–0.12 m/s in both seasons in the southwest of the mudflat and 0.04 m/s in both seasons in the northeast of the mudflat (Fricke et al. 2017).

The measuring station is located in an area with a tidal regime of mixed semi-diurnal tides. The high tide period lasts about 6 h and the low tide period is about 6 h 45 min to 7 h. In the month, there is there is two spring tide and two neap tide.

¹ People's Committee of Cu Lao Dung District – Soc Trang Province, <https://culaodung.soctrang.gov.vn/>

² Soc Trang provincial department of science and technology, <https://sokhcn.soctrang.gov.vn/>
<https://culaodung.soctrang.gov.vn/>

34.2.2 *Data Origin*

The data in the study were measured in two surveys at Cu Lao Dung (Soc Trang) under the Vietnam-United States cooperation project (2014–2016) between Department of Oceanography, Meteorology and Hydrology and University of Washington: Hydrodynamics and sediments flux through the Cu Lao Dung mangrove forest, from September 19, 2014 to October 5, 2014 (during the SW monsoon season) and from March 2, 2015 to March 16, 2015 (during the NE monsoon season). Specific information about the meter, measurement parameters and measurement time of the elements are shown in Table 34.1.

34.2.3 *Data Processing*

Tide data. Using Matlab programming language, synthesize data and calculate average values of factors: physical factor (temperature, DO, turbidity, CHL) and hydrodynamics (water level, wave height and current speed) at the time intervals of 5, 4, 3, 2, 1 h from the tidal peak, respectively, in the two cases of high tide and low tide to assess the relationship between tides and the CHL.

Wave data. In order to find the correlation between the concentration of CHL and waves, a seasonal analysis and wave height were performed. Wave height at the measuring station during the survey period ranged from 0.01 to 0.84 m, classified into 3 levels as shown in Table 34.2.

Flow data. In order to assess the concentration of CHL transport, the flow is classified according to inshore currents (inflows) and flows from rivers (outflows). North direction is 0° , so inflow direction: from 0 to 45° and from 225 to 360° , outflow direction: from 45 to 225° . The program to filter data according to the flow direction is implemented on the basis of the Matlab programming language.

Calculate correlation and compare averages. The results of calculating the correlation coefficient Pearson r and the significance level p will be performed using the statistical tool SPSS 16.0 in the case of two-tailed test to analyze the relationship between CHL and the dynamics factors. In addition, to evaluate the change of factors according to the two monsoon seasons, mean comparison using Independent Samples T-Test method on the statistical tool SPSS 16.0 (Polar Engineering and Consulting).

Table 34.1 Parameters and measurement time of measuring devices

Factor	Instrument	Instrument setting	Measurement time	
			SW monsoon season	NE monsoon season
Temperature, DO, turbidity, chlorophyll	CTD	Burst: 60 min Depth: 0.1 m	22:00 September 21, 2014–07:00 October 4, 2014	19:00 March 3, 2015–09:00 March 15, 2015
Tide, wave height	Valeport MIDAS DWR 27,111	Rate: 4 Hz Burst: 30 min Wave burst: 2048 Tide burst: 60 s	04:00 September 21, 2014–12:30 October 5, 2014	10:00 March 3, 2015–09:00 March 17, 2015
Flow	ADCP FlowQuest 600	Bin length: 0.5 m Ensemble interval: 1800 s Ping interval: 4 s No. of ping: 1024	19:00 September 21, 2014–18:00 September 30, 2014	10:00 March 3, 2015–10:00 March 15, 2015

Table 34.2 Classification of waves type according to wave height

Wave type	Wave height
Small-wave	<0.1 m
Medium-wave	In the range of 0.1–0.45 m
High-wave	>0.45 m

34.3 Results and Discussions

34.3.1 In the SW Monsoon Season

Tide. The concentration of CHL and tide has average correlation and inverse ratio with coefficient $r = -0.55$. The concentration of CHL gradually lowers towards the tidal peak, the concentration at the tidal peak ranges from 2 to 5 $\mu\text{g/l}$. At the time near the tidal foot, the CHL concentration reached a value higher than 8 $\mu\text{g/l}$. The difference between the low tide at the low tide and at the high tide in a tidal cycle is quite large, about 6.5 $\mu\text{g/l}$.

During high tide, the average concentration of CHL gradually decreased from 8.29 to 3.65 $\mu\text{g/l}$; At low tide, this value increases gradually from 2.52 to 8.33 $\mu\text{g/l}$ (Fig. 34.2). During the period of the SW monsoon season, the CHL concentration has a great dependence on tidal fluctuations. The lower the water level, the higher the amount of suspended sediment, providing a large amount of nutrients for phytoplankton development. As a result, the CHL concentration in the water increases.

Wave. The SW monsoon season is divided into two phases including the medium-wave period and the small wave period.

Compared with the small wave period, the concentration of CHL in the medium-wave period has a huge dispersion (IQR: 4.56 > 1.95). The minimum value does not have a big difference, however, the maximum CHL concentration in the medium-wave period can reach a value of 11.55 $\mu\text{g/l}$ much larger than the small wave period, 5.56 $\mu\text{g/l}$. The mean and median values also have a difference between the 2 periods, the medium-wave period, these values are higher than the other period (with average value: 5.39 > 3.00 $\mu\text{g/l}$, median value: 4.58 > 2.56 $\mu\text{g/l}$).

The average wave height provides just enough energy to create disturbances in the water column at the measuring station, and that brings a large of amounts of nutrient-filled sediments from the bottom to the upper and upper aquifers. At the surface layer with a large light source and abundant nutrients is a suitable environment for the growth of phytoplankton that increasing the CHL concentration. In contrast, when the wave height is low, the small waves energy cannot create disturbance, the amount of nutrients and suspended sediments are deposited, reducing the amount of nutrients at the surface, the phytoplankton is poorly developed, leading to low concentration of CHL. Therefore, in the SW monsoon, the CHL concentration in the small wave period is lower than in the medium-wave period.

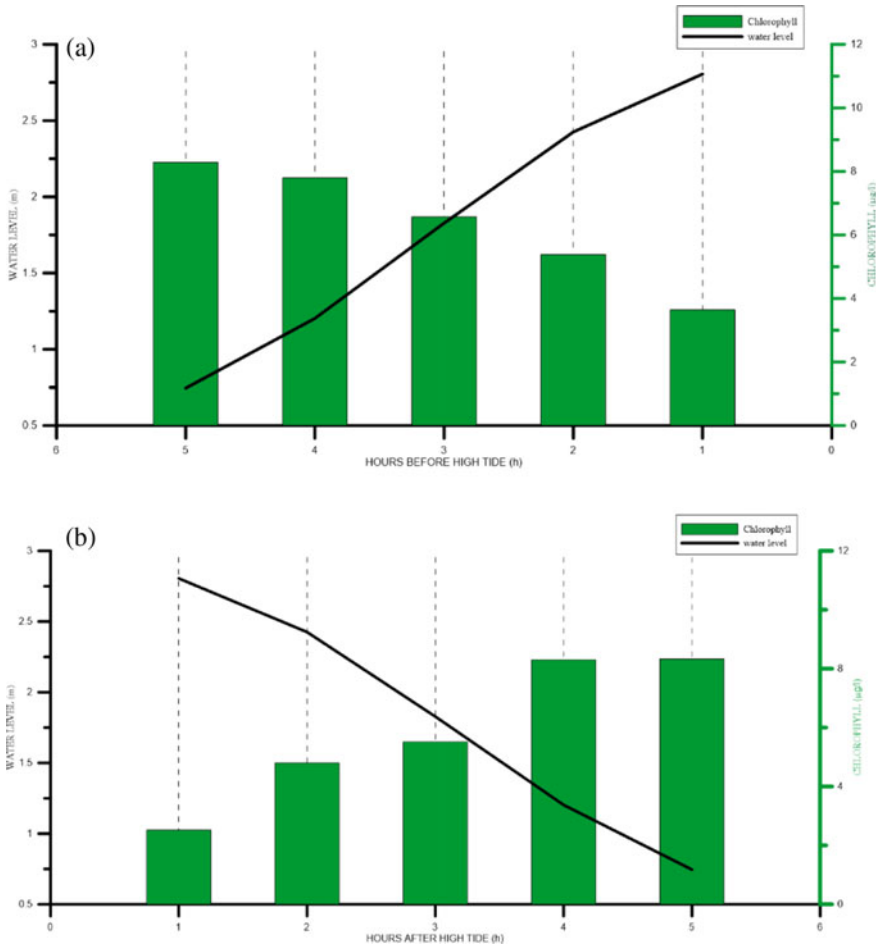


Fig. 34.2 Average value of factors at each time **a** at high tide and **b** at low tide in the SW monsoon season

Flow. The inflow and outflow velocities do not have a significant difference on all statistical values, the strongest inlet velocity (0.59 m/s) is equivalent to the strongest outlet velocity (0.56 m/s).

The inflow CHL concentration is larger than the output CHL concentration on all statistical values. The average CHL concentration when the inflow was 5 µg/l was larger than the average CHL concentration at the outflow (3.8 µg/l). In the SW monsoon season, wave dynamics are not too strong (wave height < 0.4 m). Therefore, the coastal environment is relatively stable and rich in nutrients suitable for the development of phytoplankton, increasing the coastal CHL concentration. This amount of CHL concentration is carried by the flow into the estuary, increasing the CHL concentration at the measuring station (Table 34.3).

Table 34.3 Statistical values of CHL concentration according to two wave periods in the SW monsoon season

	CHL_small wave	CHL_medium-wave
Minimum	1.62	1.85
Maxima	5.56	11.55
Average	3.00	5.39
Medium	2.56	4.58
IQR	1.95	4.56

34.3.2 In the NE Monsoon Season

Tide. The concentration of CHL and tide has a weak correlation and is inversely proportional to the coefficient $r = -0.14$. The CHL concentration gradually lowers towards the tidal peak, however, the difference between the CHL concentration at the high tide and the low tide in a tidal cycle is not too large, only about $3 \mu\text{g/l}$.

The average CHL concentration in the NE monsoon season does not show a great dependence on the average tidal level fluctuations. The average CHL concentration is about $6.50\text{--}8.77 \mu\text{g/l}$ at high tide, and about $5.18\text{--}7.07 \mu\text{g/l}$ at low tide.

Wave. The NE monsoon season is divided into two phases as shown in Table 34.4, including the medium-wave period and the high wave period.

Statistical values of CHL concentration by average wave phase and high wave phase are summarized on Table 34.4, it is found that:

- The CHL concentration in the medium-wave period and the high wave period has almost the same dispersion (IQR: $2.76\text{--}3.05$).
- The minimum value has not much difference, however, the maximum CHL concentration in the medium wave period can reach a value of $12.42 \mu\text{g/l}$ larger than the high wave period, $8.39 \mu\text{g/l}$.

In the NE monsoon season, high wave (wave height up to 0.85 m) make the coastal environment unstable, suspended sediments, and scattered nutrients. Therefore, phytoplankton cannot thrive, so the coastal CHL concentration is not high affecting the amount of CHL concentration taken into the estuary by the flow. At

Table 34.4 Statistical values of CHL concentration according to two wave periods in the NE monsoon season

	CHL_medium-wave	CHL_high wave
Minimum	2.29	1.66
Maximum	12.42	8.39
Average	7.86	4.54
Medium	7.79	4.39
IQR	2.76	3.05

the same time, high wave creates a large source of energy when entering the shore, supporting the outflow to carry large amounts of nutrients and CHL concentration (Fig. 34.3).

Flow. Under the random impact of waves, the relationship between flow and CHL concentration becomes more complicated. Specifically, when considering the flow velocities and CHL concentration in the inflow and outflow directions. The statistical values of the inlet velocity are much higher than the outlet velocity (except for the

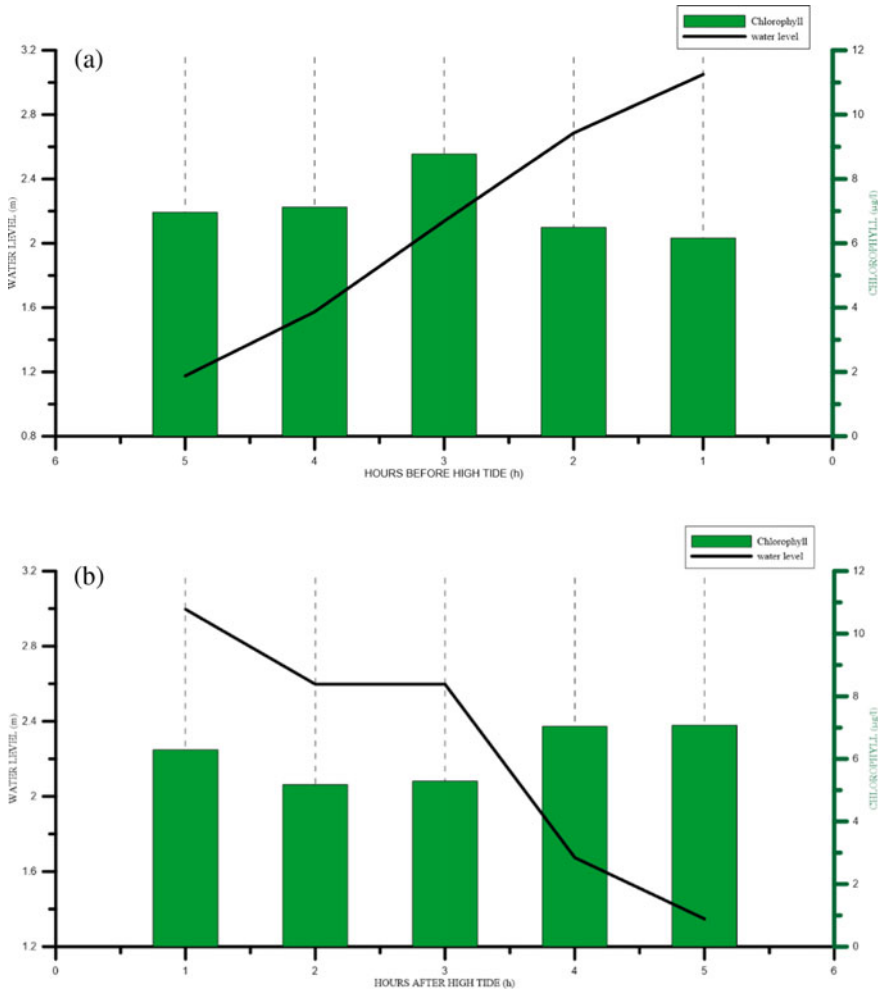


Fig. 34.3 Average values of the factors at each time **a** at high tide and **b** at low tide in the NE monsoon season

smallest value, which is almost the same ~ 0.05 m/s). Meanwhile, the CHL concentration when the outflow (in the range from 3.7 to 7.8 $\mu\text{g/l}$ and the average value is 5.9 $\mu\text{g/l}$) was higher when the inflow (in the range of 3–6.5 $\mu\text{g/l}$ and the average value is 5 $\mu\text{g/l}$).

34.4 Conclusions

- In the SW monsoon season, there is a strong correlation and inverse ratio with the tidal level. In the NE monsoon season, when stronger-wave period has a strong impact on the CHL concentration, the correlation between the CHL concentration and tides is reduced.
- For three wave periods, in the medium-wave period (wave height < 0.45 m), the CHL concentration reaches the highest value (up to 12.42 $\mu\text{g/l}$), the medium-wave period is the appropriate condition for the development of surface phytoplankton. In the period of high wave (wave height < 0.84 m), the CHL concentration has the highest value ~ 8.39 $\mu\text{g/l}$, phytoplankton can still develop when the waves are strong but not as strong as in the medium-wave period. In the period of small wave (wave height < 0.1 m), the CHL concentration is very low (the highest value is less than 5.56 $\mu\text{g/l}$), small wave are not suitable for the development of phytoplankton at the surface.
- Current consists of three components: tidal current, other factor is current and wave current. These three factors affect the lineage, making the relationship between the line and the CHL concentration not clearly shown. In the SW monsoon season: CHL concentration from coastal sources predominates; in the NE monsoon season: CHL concentration is supplied mainly from mudflats and mangroves.

Limitation

Estuaries are dynamic environments in which is strongly influenced by dynamic factors from both the sea and the river. In this study, we focus on examining the relationship of CHL concentration with the action of wave, tidal currents and coastal currents. The influence of river discharge on CHL concentration has not mentioned in this research.

Due to the lack of measured data, this study focus on the correlation of surface CHL concentration with those dynamic factors has mentioned above. The influence of dynamic factors on CHL concentration by depth (vertical profile) has not been considered.

Further Study

With the current data, we could develop the empirical models for simulating and forecasting the change of CHL concentration over time under the influence of the dynamic factors within the study area and its vicinity.

In addition, the combination of survey data of CHL concentration with analyzing it through multi-time remote sensed images will help the prediction of the change in CHL concentration become more accuracy and sensitivity in the research area. This result is the premise for studies in biological processes in the research area in the future.

Acknowledgements The authors would like to express the sincere thanks to Office of Navy Research (ONR, USA) for field dataset.

References

- Blauw AN et al (2012) Dancing with the tides: fluctuations of coastal phytoplankton orchestrated by different oscillatory modes of the tidal cycle. *PLoS ONE* 7(11):e49319
- Fagherazzi S et al (2014) The relationships among hydrodynamics, sediment distribution, and chlorophyll in a mesotidal estuary. *Estuar Coast Shelf Sci* 144:54–64
- Fricke AT et al (2017) Asymmetric progradation of a coastal mangrove forest controlled by combined fluvial and marine influence, Cù Lao Dung, Vietnam. *Cont Shelf Res* 147:78–90
- Mallin MA et al (1999) Tidal stage variability of fecal coliform and chlorophyll a concentration in coastal creeks. *Mar Pollut Bull* 38(5):414–422
- Radenac M-H et al (2016) Wind-driven changes of surface current, temperature, and chlorophyll observed by satellites north of New Guinea. *J Geophys Res: Oceans* 121:2231–2252
- Yu Y et al (2019) The variability of chlorophyll-a and its relationship with dynamic factors in the basin of the South China Sea. *J Mar Syst* 200

Chapter 35

Flash Flood Hazard Mapping Based on Analytic Hierarchy Process for a Complex Terrain: A Case Study of Chu Lai Peninsula, Vietnam



Thi Lan Pham , Si Son Tong , and Viet Nghia Nguyen 

Abstract Flooding prediction for a large scale area has been popularly carried out, nevertheless flood hazard assessment for a small, complex terrain for planning industrial constructions needs more detailed studies. This study aims to: (1) determine forcing factors and their roles in the flood hazard using the Analytic Hierarchy Process (AHP), and (2) generate the flood hazard map using spatial analysis in Chu Lai peninsular, Vietnam. The study shows that 6 important forcing factors on flood hazard include drainage density, infiltration rate, soil saturation, elevation, slope, and land cover. The factor which most impacts on the flood hazard is the elevation with the detected weight of 0.438. The infiltration rate plays the least importance with a weight of 0.066. Consequently, a flood hazard map is generated with 5 levels very low, low, medium, high, and very high hazard of flood. The very high hazard occupies 7.16% area of the peninsula focusing on the regions covered by concrete surface, permanent and temporal water cover, bare soil, and very low slope from 0° to 8°. The map provides critical information to make a plan for one of the most important industrial complexes in the center of Vietnam.

Keywords AHP · Flood hazard · Chu Lai

T. L. Pham · V. N. Nguyen
Hanoi University of Mining and Geology, Hanoi, Vietnam
e-mail: phamthilan@humg.edu.vn

V. N. Nguyen
e-mail: nguyenvietnghia@humg.edu.vn

S. S. Tong (✉)
Space and Applications Department, University of Science and Technology of Hanoi (USTH),
Vietnam Academy of Science and Technology (VAST), 18 Hoang Quoc Viet, Cau Giay, Ha Noi,
Vietnam
e-mail: tong-si.son@usth.edu.vn

35.1 Introduction

Floods are the most frequent type of natural events. Flood events occur every year worldwide. Vietnam is one of the countries that has suffered strongly from negative effects because of a flood. There are about 196 million people in more than 90 countries that are exposed to catastrophic flooding (Karki et al. 2011). Recently, floods in Vietnam occur regularly with severe consequences such as great loss of life, property, and facilities Infrastructure. The Chu Lai peninsula, Vietnam is located in Nui Thanh district, Quang Nam province. Its geographical setting and geomorphologic and climatological conditions make it prone to several types of natural disasters such as floods, landslides, and wind storms. Among these, floods have been identified as the most frequent natural disaster that savages the economic and social activities of the affected areas. Therefore, it is necessary to establish a flood hazard map to ensure healthy and sustainable economic development, and flood hazard assessment has become worldwide one of the hot issues in the field of natural science and technology (Zou et al. 2013). The mapping can be linked to formulating policies for disaster reduction. It is also an advantage for the community and decision-makers to prepare and implement effective measures (Elkhrachy 2015). Climate change projections for 2030 indicate that the number of people exposed to flooding will increase [source: (Parsian et al. 2021)]. There are different approaches to establish flood hazard maps, including geomorphological, historic, and remote sensing (Díez-Herrero et al. 2009). To select an appropriate method, the availability of relevant data is the most critical element. Remote sensing data can be an adaptive data source (Koem and Tantanee 2020). Remote sensing methods are usually more effective for flood hazard mapping because remote sensing data are acquired frequently with various spatial resolutions and cost-effective. However, the acquisition of aerial photographs or satellite images is limited by weather conditions. Therefore, the image of unmanned aerial vehicles (UAV) is becoming increasingly popular due its flexibility (Karamuz et al. 2020). The UAV image is used to extract land cover, elevation and slope. The flood hazard information is determined by appropriate and sufficient criteria. Several studies determined the flood hazard mapping using multi-criteria analysis (Koem and Tantanee 2020; Hoque et al. 2019; Bathrellos et al. 2016; Nguyen et al. 2021). Analytical Hierarchy Process (AHP) is one of the most useful approaches of MCA in the field of flood hazard evaluation (Koem and Tantanee 2020). Impact factor layers are analyzed in the AHP environment that provides weighting and ranking with the guidance of experts and users (Fernandez et al. 2015). However, AHP has been proposed to apply for flood hazard mapping at the region level. In previous research, it was difficult to find a detailed flood hazard mapping in a small complex terrain. This study aims to evaluate a multi-criteria-integrated approach to establish detailed flood hazard mapping using AHP incorporating information produced from UAV images and spatial analysis integrating GIS. This study proposes the integrated AHP and spatial analysis encompassed six parameters in the flash flood hazard assessment: drainage density, infiltration rate, soil saturation, elevation, slope, and land cover.

35.2 Study Area

The survey area belongs to Tam Quang commune, Nui Thanh district, which is located to the South of Quang Nam province. The North borders Ky Ha port, and the South borders Chu Lai airport, the West borders the center of Nui Thanh District, and the East borders the East Sea (Fig. 35.1).

In general, Tam Quang commune has hilly terrain along the coast. The area is flat and low, with stable sand dunes; a part of the delta is deposited by rivers on the sand. This region is located to the east of the Truong Giang River. Sandy soil occupies the largest area in the soil composition of this area. Also, this area has many sedimentary rocks protruding from the sea surface from 10 to 12 m in the commune such as the islands of Ngang, Hon Dua, and Ban Than.

In the survey area, the average annual temperature in the coastal plain ranges from 25.5 to 26 °C. The yearly average wind speed in the coastal plain is 1.3–1.6 m/s. The highest wind speed reaches 34 m/s in the dry season and 25 m/s in the rainy season.

Storms that occur in the area are usually formed from the South China Sea, moving into the area slowly, and the wind speed is low due to the high mountains of the Truong Son mountain range. High winds, and typhoons focus on low-lying areas, which is also the cause of flooding in downstream areas. In upstream areas, floods appear and withdraw very quickly, and flash floods often occur during the rainy season. In Quang Nam province, the rainy season usually takes place from late September to



Fig. 35.1 Location of the survey area

December, the dry season is from January to August every year. In particular, there are two months in the dry season that often have heavy rains, which are May and June every year.

The river system in the study area includes Tuc river, An Tan river, and Trau river. These rivers originate from the west, the northwest. They flow to the east and reach into the sea through An Hoa and Lo estuaries. All rivers have small basins, from 50 to 100 km², with significant slopes, from 20 to 40 km in length, and the water flow varies with the seasons. The amount of water in the rivers is abundant in the rainy season from September to December and drought in the dry season from February to August. Some rivers are prevented from being upstream to make reservoirs such as Phu Ninh Lake on the Tam River. Ky and Thai Xuan lake on Trau River, of which Phu Ninh Lake is a major irrigation project of Vietnam, responsible for irrigating 20,000 ha of rice in coastal districts south of the Thu Bon River as well as supplying domestic water to Tam Ky and surrounding areas. The downstream river has wetland ecosystems in Tam Quang, Tam Anh Nam, Tam Anh Bac, Tam Hoa, Tam Giang, Tam Hai, and Tam Tien communes. No rivers are flowing through the study area. But numerous small streams and trenches flow from the center of the study area to the east and west of the survey area.

35.3 Data and Methodology

35.3.1 Data

The assessment of the flash flood hazard required the data of dynamic criteria, including UAV image, soil (rate of soil permeability and saturation of soil), hydrology (drainage density) and terrain (elevation and slope). We used data from various sources for creating spatial criterion layers using geospatial techniques. The list of data used for flood hazard assessment is shown in Table 35.1.

Table 35.1 List of data used in flash flood hazard assessment of Chu Lai peninsula

No	Name of data	Date	Type (format)	Sources
1	Drainage system	2019	Shape file	Blue whale project, PVE company
2	Watersheds	2019	Shape file	Blue whale project, PVE company
4	UAV image	30/11/2019	Tiff file	Blue whale project, PVE company
5	Soil permeability	30/11/2019	Text file	Blue whale project, PVE company
6	National ground control points	30/11/2019	Text file	Field observation

The WGS 1984 UTM with the coordinate system of zone 48 was projected for all impact factor maps in this paper. The UAV image was used to extract land cover and create a digital elevation model (DEM). Field measurement data, UAV orthoimages, and DSM produced by UAV images are used to produce the land cover map. Field measurement provides information about land cover classes existing on the field, the samples for the classification. Moreover, field data gives the global view and the ideas to construct the theme of the land cover map as well. The extremely high-resolution orthoimage acquired by the UAV technique is the good condition to determine accurately the edges of land cover classes. The DSM simulates the elevation of all objects such as the rooftop of houses, tree canopy. Elevation information from the DSM is used to recognize the difference between objects related to relative height as high trees and lower trees, dense shrubs, and grass. DEM was used to build slope and elevation map spatial analysis methods in GIS. The data of soil is provided by the Blue whale project, PVE company with 63 locations of infiltration rate and 26 positions of soil saturation. The spatial analysis method was used to establish soil permeability and saturation map. Finally, the hydrology system is interpolated to create drainage density.

35.3.2 Methodology

Methodology for flood hazard mapping hazards can be seen in Fig. 35.2. There are four main steps in this process such as the data collection of impact factors, natural break classification, process AHP and building flood hazard map.

35.3.2.1 Impact Factors of Flood Hazard in Chu Lai Peninsula, Nui Thanh District, Quang Nam Province, Vietnam

The definition of the impact factor of a flood potential is crucial. There are many factors that contribute to flood hazard, but the study focuses on the criteria of physical geography hazard. The impact factor of flood potential includes two conditions: (1) prerequisites including precipitation reaches the maximum that it causes flow strongly. (2) Sufficient conditions such as topography, geomorphology, watershed, pedology, land cover, the drainage system, and soil permeability.

The selection of factors affecting flood hazard depends hazard on the study area. According to Dung et al. (2021a), there are six group of the criteria leading to the formation of a flood, namely (1) criteria related to hydrological and orographic characters; (2) factors related to the geomorphologic character; (3) parameters related to the meteorological character; (4) elements related to cover characters; (5) factors related to soil characteristics; (6) variables related to infrastructure and socio-economic characters (Dung et al. 2021a). Most studies used expert methods or Delphi

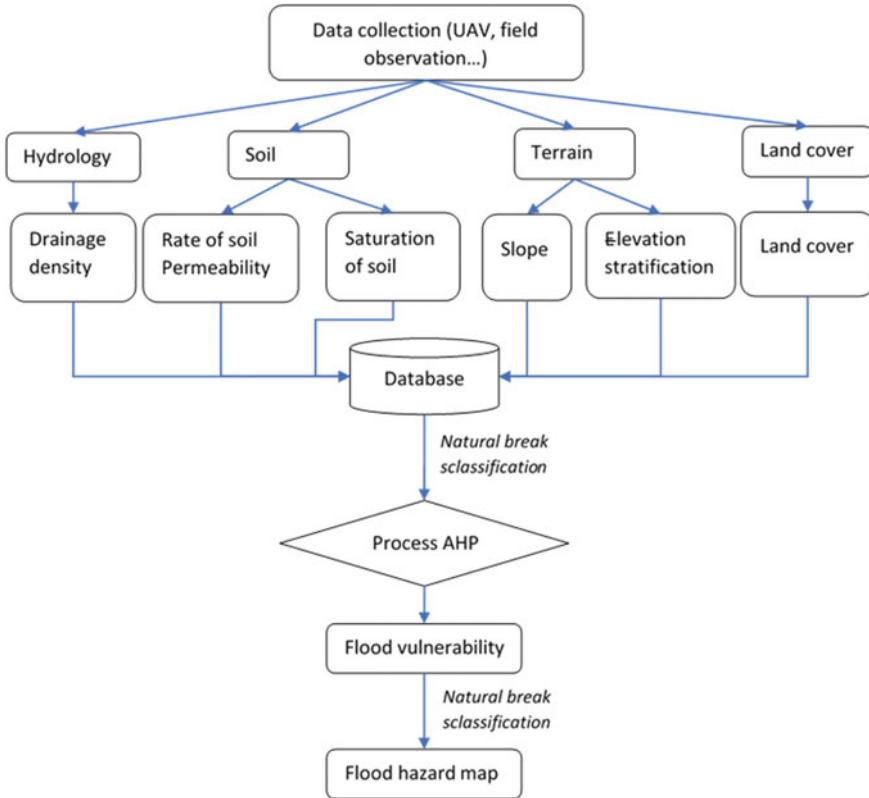


Fig. 35.2 Flowchart of the methodology

methods to determine criteria affecting flood formation (Dung and Tuyet 2021; Dung et al. 2020). However, impact factors are used widely including slope, precipitation, land cover, drainage, stream density, and soil permeability (Nguyen et al. 2021; Dung et al. 2021b).

Chu Lai peninsula located in Nui Thanh district, Quang Nam. The peninsula covers an area of 340 ha and distributes the same amount of precipitation. Thus when determining potential flood, we will not care about precipitation.

In conclusion, there are six impact factors for flood hazard in the Chu Lai peninsula including elevation stratification, slope, land cover, drainage density, infiltrate rate of the soil, and saturation of the soil.

35.3.2.2 Classification of Factors Affecting Flood in Chu Lai Peninsula, Nui Thanh District, Quang Nam Province, Vietnam

In this study, impact factors classification comprises six parameters: Drainage density (Dd), Rate of soil permeability (Ps), Saturation of soil (Sa), Slope (SI), Elevation stratification (EI) and Land cover (Lc). These parameters have been manipulated in GIS using natural break classification with five risk levels namely very low, low, medium, high and very high risk zones of flood. The physical parameters are assigned values 1, 3, 5, 7, and 9 respectively as rating scores. The rating scores have been used in the calculation of the relative significance of each criterion as a pairwise matrix comparison to produce corresponding weighting factors (w).

1. The classification of land cover affecting to flood hazard

The ability to influence flood hazards of land use and land cover will vary for different geographic areas.

According to Tehrany, rain-water on bare land will be stronger than on agricultural land and plantation forest. In the Residence area, urban areas with impervious surveys will have more intense flow than the regions covered by vegetation and woodland (Tehrany et al. 2013). This indicates that the hazard of flooding will be higher in vacant areas and residential areas than in areas covered with vegetation, forests or agricultural land.

This conclusion was also proved in the study (Tehrany et al. 2013) with the frequency (frequency) (FR) floods in the non-vegetated bare land areas being the maximum and the dense areas with FR value will be the minimum. In many studies, the authors have classified the hazard of affecting land cover on flood hazard in ascending or descending order based on the above analysis.

In Yasooj, Iran, Rahmati said that the most vulnerable land to floods is the river zone, the second is residential land and roads, followed by vacant land, agricultural land, and finally forest land at hazard (Rahmati et al. 2016). The influence of land cover on flood hazard in the Kassandra Peninsula, Greece was divided into three levels according to influence from low to high in the following order: forest land, shrubs, and grasslands, agricultural land. And vacant land (Stefanidis and Stathis 2013). According to Sekac, Jana and Pal, the influence of land cover on the hazard of flooding decreases gradually in the order of water surface land, bare land, construction land, agricultural land, open forest, dense forest (Sekac et al. 2015).

Detail the ability to affect the flood hazard of land use and overlay factors in a study (Elkhrachy 2015), the author assessed that the water surface is most at hazard of flooding, followed by wet soil, urban land, industrial parkland, agricultural land, land with sparse vegetative cover, grassland and finally forest land. Besides the land cover, the type of forest and its quality also affect the potential flood. According to Ngo Dinh Que, forest cover in the basin is an important indicator to manage water resources in the basin in a rational and sustainable manner. When the forest cover is low, the water regulation capacity of the forest in the basin is poor, so in the rainy

season, the water flow in the river basins will be large and concentrated so it is easy to cause floods (Que 2011).

Thus, the water regulation capacity of multi-storey, high coverage forest (rich and medium forests) is better than that of planted forests, bamboo forests and natural forests with low coverage, low canopy floors (poor forest). In addition, because the permeability under the forest canopy is often higher than the condition covered by shrubs, the possibility of generating groundwater flow is much lower than that of the shrub (Dung 2016). It means that the forested area is less likely to be flooded than the area covered by shrubs. The greater the level of the impact on flood hazards is the lower the capacity to retain water and protect the land of different land cover/land use types. According to the above statements, the land covers affecting flood potential are stratified into 5 levels and they are assigned with values 1, 3, 5, 7, 9 as seen in Table 35.2 and Fig. 35.3.

2. The classification of slope effecting to flood hazard

It is necessary to classify the slope according to the level that affects the hazard of flooding. Some flood hazard studies show that it depends on the largest and smallest slope in the study area. These studies stratified the slope into an equal interval as 3°, 5°, 9°, 18° (Saini and Kaushik 2012; Schultz 1995; Ouma and Tateishi 2014). Besides, the slope is lower the hazard of flood is higher (Moglen et al. 1998; Kazakis et al. 2015). The slope was separated into 5 levels:

- Flat area (<3°)
- Low slope (3°–8°)
- Medium slope (8°–15°)
- High slope (15°–25°)
- Steep slope (>25°).

The classification of slope is suitable for the geographic characteristics of the study area. Thus, with 5-level sloped terrain in the study area, the area with the lowest slope is considered to have the lowest flood hazard, and vice versa, the region with the highest slope will have the highest flood hazard (Van Hoan et al. 2019; Costache et al. 2021; Shawaqfah 2020). It means that the more flood hazard increases, the

Table 35.2 Hierarchy of land cover effecting to flood hazard

No	Land cover	Mark	Level of flood hazard
1	Dense shrubs, Acacia trees	1	Very low
2	Eucalyptus trees, coniferous trees, spare shrubs, grass	3	Low
3	Resident area, construction, cemetery	5	Medium
4	Bare land, concrete surface, roads, laterite holes	7	High
5	Temporal water, permanent water, sandy area	9	Very high

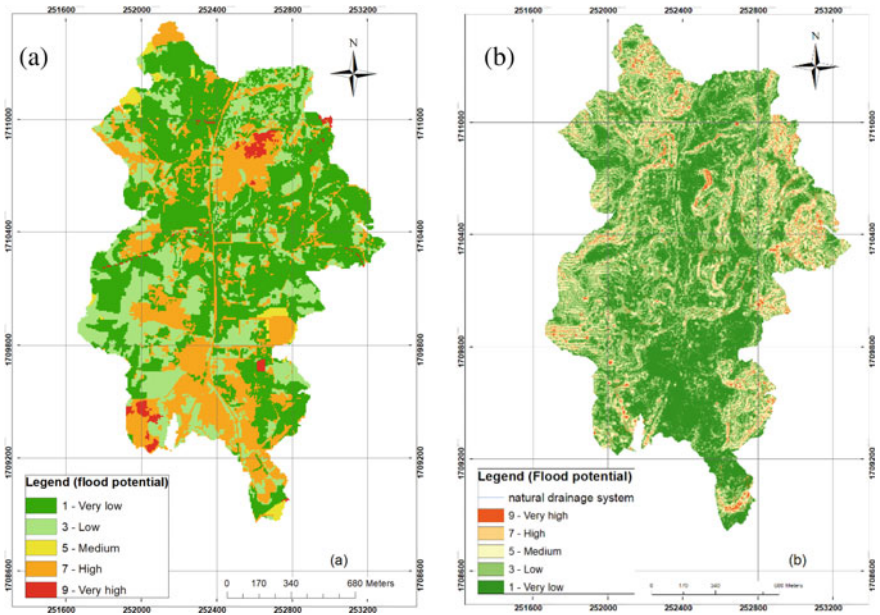


Fig. 35.3 Map of land cover (a) and slope (b) effecting to flood hazard

more slope rises, and the score corresponding to the level of influence will vary from 1 to 9 as shown in Table 35.3 and Fig. 35.3.

Using Digital Terrain Model—DTM (DTM is provided by Contractor) and spatial analysis methods to do slope interpolation. The resolution of the DEM determines the accuracy and detail of the slope map. However, because ArcGIS software interpolates and assigns the range of slope values automatically, the values of the slope thresholds do not match the standard slope scale. Therefore, in order to classify the gradients in accordance with the requirements, it is necessary to reclassify with the Reclassify tool.

Table 35.3 Hierarchy of slope effecting to flood hazard

No	Slope	Mark	Level of flood hazard
1	>25°	1	Very high
2	15°–25°	3	High
3	8°–15°	5	Medium
4	3°–8°	7	Low
5	<3°	9	Very low

Table 35.4 Hierarchy of elevation stratification affecting to flood hazard

No	Elevation stratification (m)	Mark	Level of flood hazard
1	37–52.54	1	Very low
2	28–37	3	Low
3	25–28	5	Medium
4	15–25	7	High
5	–0.5–15	9	Very high

3. The classification of elevation stratification affecting to flood hazard

Elevation stratification has a significant impact on environmental modeling. Several studies have also been done to demonstrate the effect of the DTM characteristics in hydrological studies.

There are seven methods to reclassify DTM: manual interval, defined interval, equal interval, quantile, natural breaks, geometrical interval and standard deviation. These methods were tested for creating the DTM of the study area. The natural breaks method is used for this work because its result well represents the distribution of topographic stratifications. The Digital Terrain Model (DTM) of the study area is reclassified to five levels which show the level of flood hazard in the following Table 35.4 and Fig. 35.4.

4. The classification of drainage density affecting to flood hazard

The drainage density relates to the runoff and the gathering water potential as well. The natural breaks method was used to create the hierarchy of drainage density affecting flood hazard because it produces the most appropriate results compared to other methods. The levels of flood hazard caused by drainage density are shown in Table 35.5. Figure 35.4 illustrates the effect of drainage density on flood potential. The drainage density is calculated for each pixel with the size of 1 m². In regulation, the higher the value of drainage density is, the amount of water simultaneously gathering in the area of pixel size is. Thus, the floods tend to occur in the area with higher drainage density. In this case, the flood develops in a gradual ponding or build-up of water in low-lying, flood-prone areas as well as creeks and streams.

5. The classification of Soil (soil permeability rate and soil saturation) effecting to flood hazard

Soil permeability data can provide an early warning of soil degradation, flood hazard, and erosion. In this study, we use two parameters of soil to assess flood-prone areas such as infiltrate rate and saturation. The higher the permeability of a soil layer, the faster water can infiltrate through and avoid flooding. In addition, the higher the saturation of the soil, the lower the flood potentialis. The rest area is equally divided into four particle-size classes (Clay; Clay Loam; Loam and Sandy Loam)

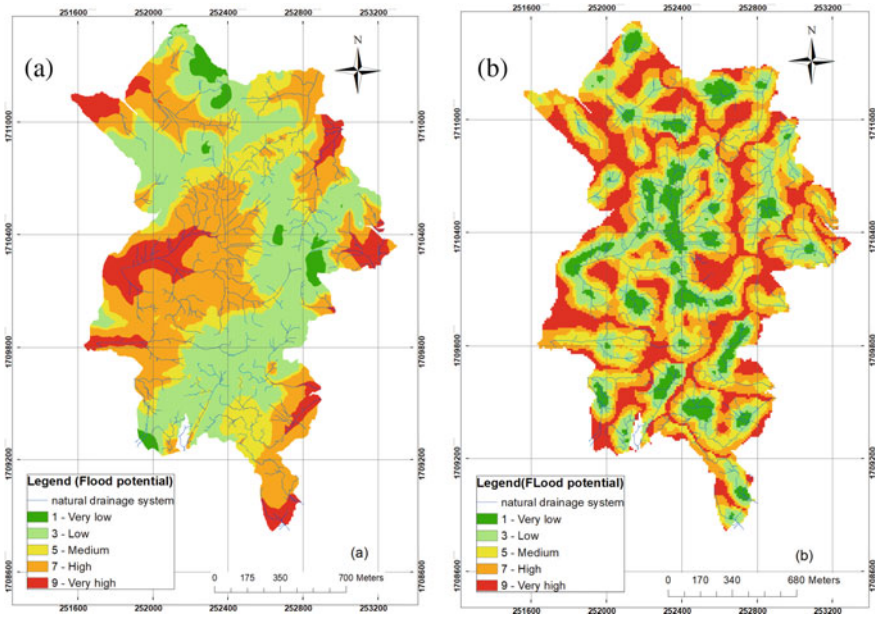


Fig. 35.4 Map of elevation (a) and drainage density (b) affecting flood hazard

Table 35.5 Hierarchy of drainage density affecting flood hazard

No	Drainage density (m/ha)	Mark	Level of flood hazard
1	0.031–0.065	1	Very high
2	0.021–0.031	3	High
3	0.013–0.021	5	Medium
4	0.004–0.013	7	Low
5	0–0.004	9	Very low

with infiltration rate varies from 0.2 to 2.5 cm/h (source: Report on the results of soil permeability and infiltration rate). Table 35.6 shows the hierarchy of infiltrating rate and saturation affecting flood hazard. The hierarchy of infiltrating rate is based on the regulation that the higher particle size is the lower level of the flood potentialis (Table 35.6). The soil saturation tends to affect the flood potential in the linear negative trend thus the equal interval separation method is used to build the hierarchy of soil saturation (Table 35.6) (Fig. 35.5b).

Table 35.6 Hierarchy of infiltrating rate and saturation of soil affecting to flood hazard

No	Permeability rate (distribution of infiltration rates for certain particle-size classes)	Saturation	Mark	Level of flood hazard
1	Sand	75.08–93.86	1	Very low
2	Loam	56.31–75.08	3	Low
3	Sandy loam	37.54–56.31	5	Medium
4	Clay loam	18.77–37.54	7	High
5	Clay	0–18.77	9	Very high

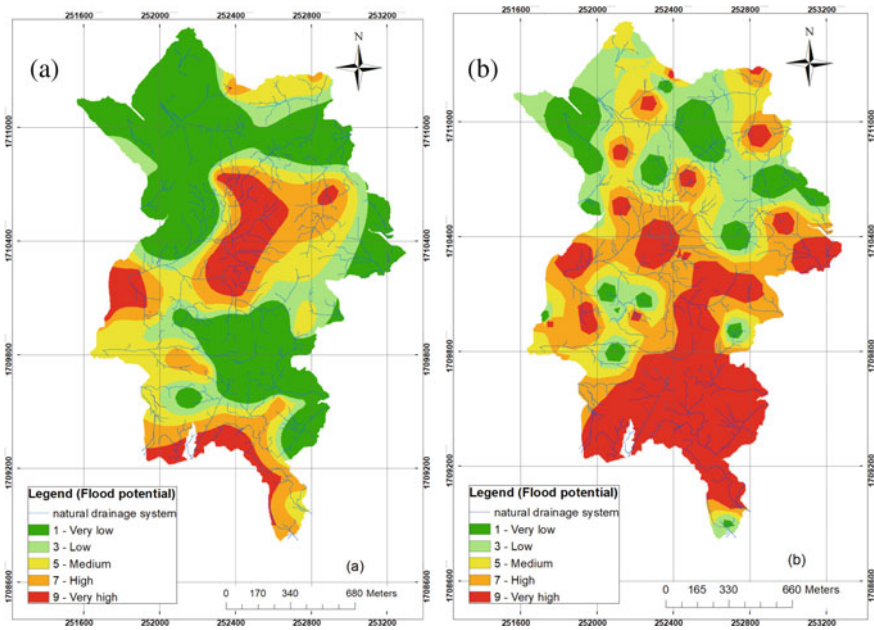


Fig. 35.5 Map of infiltrating rate (a) and saturation rate (b) of soil affecting flood hazard

35.3.2.3 Analytical Hierarchy Process (AHP)

Flood hazard is formed and developed by the impact of many factors, this section refers to six factors that the author assessed as the main factors. With the use of AHP, the study was able to obtain a relative significance of the relevant factors after the pairwise-comparison matrix have been constructed. Impact factors of flood hazard have different roles, so a quantitative assessment of the importance of the influencing factors is necessary. This paper assesses with the determination of weights, based on statistical results analysis of architectural components or based on the knowledge of experts.

Table 35.7 The scores of a pairwise comparison matrix (Saaty 1980)

Scale	Meaning
1	Equally more important (EQ)
3	Moderately important—Weakly more important (WK)
5	Important—Strongly more important (ST)
7	Very strongly more important (VS)
9	Extremely important—Absolutely more important (AB)

Table 35.8 Pairwise comparison matrix

	Land cover	Slope	Elevation	Drainage density	Permeability rate	Saturation
Land cover	1	1/7	1/7	7	9	9
Slope	7	1	1/7	1	1/3	1/3
Elevation	7	7	1	7	9	9
Drainage density	1/7	1	1/7	1	5	1/3
Permeability rate	1/9	3	1/9	1/5	1	1
Saturation	1/9	3	1/9	3	1	1

For each criterion, a pairwise comparison matrix is created. The scores to be used in the matrix are based on the Saaty scale (1980) as shown Table 35.7:

The pairwise comparison matrix is shown in Table 35.8 using a 6 × 6 matrix, where diagonal elements are equal to 1. The values of each row are compared with each column to define the relative importance to obtain a rating score. For example, Table 35.2 shows that elevation is significantly more important than slope and therefore assigned the value 7. Row describes the importance of slope. Therefore, the row has the inverse value of the pairwise comparison (1/7).

The consistency of the created eigenvector matrix for AHP needs to be evaluated. The required level of consistency is evaluated using the following index:

The consistency index (CI) is calculated using Eq. (35.1) where calculated $\lambda_{max} = 6.57$.

$$CI = \frac{Y_{max} - n}{n - 1} \tag{35.1}$$

where: the number of parameters (n = 6)

Y_{max} the maximum Eigenvalue

$$C.I. = 0.114;$$

Table 35.9 Weights of factors

Evaluation items	Weights
Land cover	0.19
Slope	0.16
Elevation	0.44
Drainage density	0.06
Rate of soil permeability	0.07
Saturation of soil	0.08

We then determine the consistency ratio (CR) by the formula:

$$CR = \frac{CI}{RI} \quad (35.2)$$

where

- CR the consistency ratio
- CI the consistency index
- RI random index (1.7).

Eventually, the calculated consistency ratio is 0.07 that is lower than the threshold of 0.1, the weights' consistency is affirmed and the weights are acceptable (Table 35.9).

35.4 Results

After developing the impact criteria maps, and determining the weight of the factors affecting the flood, building maps of flood hazard zoning by spatial analysis method in the GIS environment. It is the integration of the component maps (map of impact criteria) based on the general equation for calculating the hazard score according to the hierarchical point of each element and the weight of each specific element. Determination of potential flooding in the Chu Lai peninsula was calculated using the Map Algebra in ArcGIS

$$Y = 0.19 * Lc + 0.16 * Sl + 0.44 * El + 0.06 * Dd + 0.07 * Ps + 0.08 * Sa \quad (35.3)$$

where

- Lc Land cover
- Sl Slope
- El Elevation
- Dd Drainage density

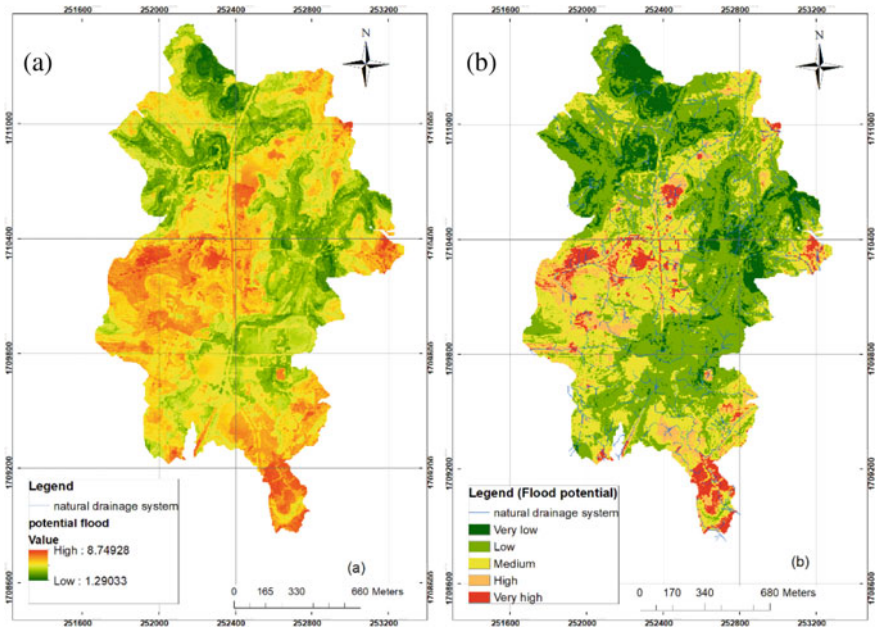


Fig. 35.6 Map of flood hazard (non-stratification) (a) and map of flood hazard stratification in Chu Lai peninsula (b)

- Ps Rate of soil permeability
- Sa Saturation of soil.

The flowing Fig. 35.6 shows the value of flood potential in the Chu Lai peninsula. Assessment flood-prone needs to classify the flood potential into five classes. In this study, there was a significant leap between the frequency of very low potential value and the frequency of the very high potential value. Thus we use the natural breaks classification method to reclassify the flood potential as shown in Table 35.10. Besides, Fig. 35.6 illustrates the flood potential in Chu Lai Peninsula, Nui Thanh, Quang Nam.

Figure 35.6 shows that the flood potential is predominated by low and medium potential classes. The low flood potential ranged 3.6–5.08 covers 34.68% of the whole

Table 35.10 Stratification of the flood potential area

Number	Mark of potential flood	Class	%
1	0–3.60	Very low	13.88
2	3.60–5.08	Low	34.68
3	5.08–5.97	Medium	27.83
4	5.97–6.77	High	16.45
5	6.77–9.0	Very high	7.164

area (Table 35.10). Four other classes medium, high, very low, and very high flood potential occupy 27.83%, 16.45%, 13.88% and 7.16%, respectively. These numbers indicate that most of the Chu Lai peninsula area has a low vulnerability to floods. Flood events are concentrated in certain areas only. The very high and high potential floods have small area where distribute land covers composing of spare shrubs, residents, concrete surface, bare land, laterite holes, eucalyptus trees, temporal water and permanent water. The area with very low and low slope, high drainage density, and the low elevation of less than 15 m are also available for high flood potential. The area of the medium flood potential is relatively large. The vegetation of these areas is spare shrubs, dense shrubs, concrete surface, bare land, acacia trees, and eucalyptus trees. In addition, the areas have medium slope and elevation. Besides, most of the study area is very low and low flood potential where are covered by spare shrubs, dense shrubs, bare land, and acacia trees.

In sum, the flood potential strongly depends on the elevation (0.437991 affecting weight), the land cover and the slope with the affecting weight of 0.192821 and 0.158047, respectively. Whereas, the drainage density, infiltration rate and saturation of soil insignificantly affect the flood-prone.

35.5 Conclusions

This study presents a multi-criteria-incorporated approach of spatial flood hazard mapping using UAV images, spatial analysis and field data at a detailed scale. The UAV was used to extract land cover and DEM. Geospatial techniques were used to map all selected criteria under each component of hazard flood. The AHP model was applied to integrate multi-criteria in a spatial decision-making process. The Chu Lai peninsular, Vietnam was used for examining the suitability of the method.

A detailed scale study integrated with multi-criteria evaluation is required to achieve accurate and detailed flood hazard information. However, collecting spatial data at the detail scale is highly challenging. The AHP was a useful model for weighting the selected multi-criteria and spatial decision-making process. This paper presented a framework for the overall spatial flood hazard assessment that integrates six impact factors. The generated information from this study could be applied by planners and administrators to develop effective flood effect mitigation strategies.

Acknowledgements We would like to express our thanks to the internal Blue whale project, funded by Petro Vietnam Engineering Company.

References

- Bathrellos GD, Karymbalis E, Skilodimou HD, Gaki-Papanastassiou K, Baltas EA (2016) Urban flood hazard assessment in the basin of Athens Metropolitan city, Greece. *Environ Earth Sci* 75
- Costache R, Arabameri A, Blaschke T, Pham QB, Pham BT, Pandey M, Arora A, Linh NTT, Costache I (2021) Flash-flood potential mapping using deep learning, alternating decision trees and data provided by remote sensing sensors. *Sensors (Basel)* 21
- Díez-Herrero A, Huerta LL, Isidro ML (2009) A handbook on flood hazard mapping methodologies, vol 2. *Geological Hazards/Geotechnics*
- Dung BX (2016) Soil infiltration characteristics of different landuse types at Luotmountain, Xuan Mai, Ha Noi. *Forest Sci Technol J* 4:47–58
- Dung NB, Tuyet MD (2021) Assessment of flood influence criteria in the Lam river basin using a combined delphi-AHP method. *Sustain Dev Mt Territ* 3:387–396
- Dung NB, Minh DT, Long NQ, Ha LTT (2020) Weights of factors contributing to flood formation in the Lam River Basin, Vietnam. *J Southwest Jiaotong Univ* 55
- Dung NB, Long NQ, Goyal R, An DT, Minh DT (2021a) The role of factors affecting flood hazard zoning using analytical hierarchy process: a review. *Earth Syst Environ*
- Dung NB, Long NQ, An DT, Minh DT (2021b) Multi-geospatial flood hazard modelling for a large and complex river basin with data sparsity: a case study of the Lam River Basin, Vietnam. *Earth Syst Environ*
- Elkhrachy I (2015) Flash flood hazard mapping using satellite images and GIS tools: a case study of Najran City, Kingdom of Saudi Arabia (KSA). *Egypt J Remote Sens Space Sci* 18:261–278
- Fernandez P, Mourato S, Moreira M (2015) Social vulnerability assessment of flood risk using GIS-based multicriteria decision analysis. A case study of Vila Nova de Gaia (Portugal). *Geomatics, Nat Hazards Risk* 7:1367–1389
- Hoque MA, Tasfia S, Ahmed N, Pradhan B (2019) Assessing spatial flood vulnerability at Kalapara Upazila in Bangladesh using an analytic hierarchy process. *Sensors (Basel)* 19
- Karamuz E, Romanowicz RJ, Doroszkiewicz J (2020) The use of unmanned aerial vehicles in flood hazard assessment. *J Flood Risk Manage* 13
- Karki S, Shrestha A, Bhattarai M, Thapa S (2011) GIS based flood hazard mapping and vulnerability assessment due to climate change: a case study from Kankai Watershed. *Eastern Nepal*
- Kazakis N, Kougiyas I, Patsialis T (2015) Assessment of flood hazard areas at a regional scale using an index-based approach and analytical hierarchy process: application in Rhodope-Evros region. *Greece Sci Total Environ* 538:555–563
- Koem C, Tantane S (2020) Flash flood hazard mapping based on AHP with GIS and satellite information in Kampong Speu Province, Cambodia. *Int J Disaster Resilience Built Environ* 12:457–470
- Moglen GE, Eltahir EAB, Bras RL (1998) On the sensitivity of drainage density to climate change. *Water Resour Res* 34:855–862
- Nguyen BD, Nguyen QN, Pham TL, Le TL, Dang TM (2021) Evaluation and validation of flood hazard zoning using analytical hierarchy process and GIS: a case study of Lam River basin (Vietnam). *Vestnik SPbSU. Earth Sci* 66
- Ouma Y, Tateishi R (2014) Urban flood vulnerability and risk mapping using integrated multi-parametric AHP and GIS: methodological overview and case study assessment. *Water* 6:1515–1545
- Parsian S, Amani M, Moghimi A, Ghorbanian A, Mahdavi S (2021) Flood hazard mapping using fuzzy logic, analytical hierarchy process, and multi-source geospatial datasets. *Remote Sens* 13
- Que ND (2011) Impacts of forests on flows and erosion in drainage basins in the Middle and Central highlands in Vietnam. In: *Proceedings of the forestry science and technology conference for sustainable forest development and climate change*, pp 355–361 (in Vietnamese)
- Rahmati O, Zeinivand H, Besharat M (2016) Flood hazard zoning in Yasooj region, Iran, using GIS and multi-criteria decision analysis. *Geomatics, Nat Hazards Risk* 1000–1017
- Saaty TL (1980) *The analytic hierachy process*. McGrawHill, New York

- Saini SS, Kaushik SP (2012) Risk and vulnerability assessment of flood hazard in part of Ghaggar Basin: a case study of Guhla block, Kaithal, Haryana, India. *Int J Geomatics Geosci* 3:42–54
- Schultz GA (1995) Changes on flood characteristics due to land use changes in river basin. In: U.S.-Italy research workshop on the hydrometeorology, impacts, and management of extreme floods, Perugia, Italy
- Sekac T, Jana SK, Pal DK (2015) A remote sensing and GIS approach to assessing multiple environmental factors leading to delineation of flood hazard risk zone in the Busu River Catchment, Morobe Province, Papua New Guinea. *Melanesian J Geomatics Property Stud* 1:40–55
- Shawaqfah M (2020) Mapping flash flood potential and risk level using GIS techniques and the flash flood potential index (FFPI) in Amman Zarqa Basin of Jordan. *Jordanian J Eng Chem Ind (JJECI)* 3:81–90
- Stefanidis S, Stathis D (2013) Assessment of flood hazard based on natural and anthropogenic factors using analytic hierarchy process (AHP). *Nat Hazards* 68:569–585
- Tehrany MS, Pradhan B, Jebur MN (2013) Spatial prediction of flood susceptible areas using rule based decision tree (DT) and a novel ensemble bivariate and multivariate statistical models in GIS. *J Hydrol* 504:69–79
- Van Hoan K, Nguyen HT, Thuy NP, Thanh NH (2019) Application GIS and remote sensing to map flash flood in Son La province. *HNUE J Sci* 64:120–132
- Zou Q, Zhou J, Zhou C, Song L, Guo J (2013) Comprehensive flood risk assessment based on set pair analysis-variable fuzzy sets model and fuzzy AHP. *Stoch Environ Res Risk Assess* 525–546

Chapter 36

A Comparative Flood Susceptibility Assessment in a Norwegian Coastal City Using Feature Selection Methods and Machine Learning Algorithms



Lam Van Nguyen , Dieu Tien Bui , and Razak Seidu 

Abstract Identification of significant input factors plays a crucial role in optimizing the predictive model performance of floods. A good predictive model is a model that can predict the outcome with the best accuracy but using the least input parameters. In this study, the Bayesian Model Averaging (BMA) method was applied instead of the traditional stepwise regression method for determining flood-conditioning factors. In general, the BMA method had higher accuracy than the stepwise regression method. Fourteen flood conditioning factors were used to compare feature selection capacity using the LR and BMA methods, including altitude, slope, aspect, curvature, normalized difference vegetation index (NDVI), normalized difference snow index (NDSI), rainfall, stream power index (SPI), topographic wetness index (TWI), modified normalized difference water index (MNDWI), distance from rivers (DFR), soil types, land cover, and geology. By applying the BMA method, the input parameters were reduced from 14 to 4 (altitude, slope, rainfall, and NDVI) but the accuracy of predicted models was maintained. This research applied three machine learning algorithms namely Logistic Regression (LR), Naïve Bayes (NB), and Support Vector Machine (SVM) using the above significant flood-conditioning factors to produce flood susceptibility maps for the coastal city of Ålesund, Norway. A total of 182 flood events were used to develop and evaluate the machine learning models, and

L. Van Nguyen (✉) · R. Seidu

Smart Water and Environmental Engineering Group, Department of Ocean Operations and Civil Engineering, Faculty of Engineering, Norwegian University of Science and Technology, N-6025 Ålesund, Norway

e-mail: Lam.V.Nguyen@ntnu.no

R. Seidu

e-mail: rased@ntnu.no

L. Van Nguyen

Department of Geodesy, Faculty of Geomatics and Land Administration, Hanoi University of Mining and Geology, 18 Vien Street, Duc Thang, Bac Tu Liem, Hanoi 100000, Vietnam

D. T. Bui

GIS Group, Department of Business and IT, University of South-Eastern Norway, Gullbringvegen 36, 3800 Bø in Telemark, Norway

e-mail: Dieu.T.Bui@usn.no

the accuracy and performance of predicted models were tested by employing the area under the curve (AUC) and some statistical indices. Among the input factors, altitude and rainfall in Ålesund were the most important factors that significantly influenced flood events. The studied results indicated that SVM (AUC = 1.0) was the best algorithm for building flood susceptibility in Ålesund, followed by the NB (AUC = 0.996) and LR (AUC = 0.984) algorithms, respectively.

Keywords Flood risk assessment · Logistic regression · Naïve Bayes · Support vector machine · Bayesian model averaging · Machine learning · Ålesund · Norway

36.1 Introduction

In recent years, extreme weather events such as floods, droughts, hurricanes, earthquakes, tsunamis, El Niño and La Niña episodes, etc., have appeared with a higher frequency (Vojtek and Vojteková 2019; Gizaw and Gan 2017; Kjeldsen 2010) and have been seen as an obvious consequence of climate change and global warming (Wang et al. 2019; Mukherjee et al. 2018; Dinan 2017; Usman 2016; Shao et al. 2019; Hu and Fedorov 2017; Lian et al. 2018). Among these natural disasters, floods have been one of the most extreme hazards (Wang et al. 2019; Bui et al. 2019a; Costache et al. 2020). Flood has been implicated in significant damages to infrastructure and properties, destruction of natural ecosystems, environmental pollution, and loss of lives (Wang et al. 2019; Sahana et al. 2020; Pham et al. 2020; Chen et al. 2020; Youssef and Hegab 2019; Paul et al. 2019; Nguyen et al. 2022). For example, an amount of agricultural and residential areas near the main rivers were seriously destroyed (Weydahl 1996); several million NOK were lost and many people were dead or the homeless situation to flooding in 1789, 1860, and 1995 in Norway (Rauken and Kelman 2010; Næss et al. 2005). To mitigate the impacts of floods, there is a need for robust tools for early flood warnings. Flood risk mapping can play a crucial role in early flood warning systems to help determine the most vulnerable areas of flooding (Vojtek and Vojteková 2019), and for the development of optimal flood mitigation strategies concerning land use planning, and infrastructure development (Zhao et al. 2019; Rahman et al. 2019; Liuzzo et al. 2019).

Flood susceptibility maps can be developed using either physically based methods, statistical and data-driven methods, or machine learning (ML) methods (Wang et al. 2019; Dodangeh et al. 2020). Physically-based methods combine a suite of hydrological and hydrodynamic models to identify flood-prone areas (Wang et al. 2019; Zhao et al. 2019). However, Tang et al. (2020) showed that hydrodynamic models are time-consuming and require complex data inputs while hydrological models significantly depend on the drainage pipe network data. Moreover, these models also require an abundance of computational resources (Zhao et al. 2019) and have a very complex construction (Wang et al. 2019). These requirements limit the application of these models. A combination of some statistical and data-driven methods (i.e., such as

analytical hierarchy process (AHP) (Dano et al. 2019; Nguyen et al. 2020), frequency ratio (FR), or weights-of-evidence) and Geographic Information System (GIS) was widely applied for flood-susceptibility assessment. However, these approaches exist some drawbacks such as uncertainties due to ambiguous judgments, depending on sample size or experts' knowledge (Zhao et al. 2019; Dodangeh et al. 2020).

The reliability and accuracy of the flood susceptibility maps mainly depend on the quality of input factors and used ML models (Bui et al. 2012a). Remote Sensing (RS) data is widely used for natural hazard studies because of its significant role in the disaster management cycle (Joyce et al. 2009). Therefore, various factors of this type of study were extracted from RS data in previous studies (Bui et al. 2018a). In this study, RS data (satellite images) were used to compute hydrology-related factors [e.g., normalized difference snow index (NDSI) and modified normalized difference water index (MNDWI)] and a physical-related factor [e.g., normalized difference vegetation index (NDVI)]. These input factors were processed using GIS.

In recent years, ML approaches have been used for flood susceptibility assessments because they can handle complex nonlinear problems without statistical assumptions (Wang et al. 2019) and have good compatibility with Remote Sensing (RS) and GIS (Bui et al. 2019a). ML algorithms can accept many different types of data including continuous, categorical, discrete, dichotomous, or a mix of any of these (Bui et al. 2011). Its outcomes are flexible, for example, the linear regression algorithm can return the continuous values, or the logistic regression algorithm gives multiple categorical variables. Many ML algorithms have been applied for studying flood risks such as Logistic Regression (LR) (Mind'je et al. 2019), Decision Tree (DT) (Chen et al. 2020), Support Vector Machine (SVM) (Costache 2019; Choubin et al. 2019), Naïve Bayes (NB) (Khosravi et al. 2019), Artificial Neural Networks (Falah et al. 2019), Random Forest (Zhao et al. 2018; Wang et al. 2018), Analytical Hierarchy Process (Vojtek and Vojteková 2019; Youssef and Hegab 2019; Talha et al. 2019), hybrid methods (Wang et al. 2019; Bui et al. 2018b), semi-supervised ML (Zhao et al. 2019) or integrated algorithms (Costache et al. 2020; Rahman et al. 2019; Bui et al. 2019b, c). Because flood characteristics highly depend on flood-conditioning factors, the accuracy and reliability of flood susceptibility maps are significantly influenced by the input factors and ML algorithms used. Various methods were developed in the literature to select significant features for ML models (Li et al. 2020; Tang and Zhang 2020; Yan and Zhang 2015). However, the different feature selection algorithms produce different results depending on particular datasets and case studies. Therefore, determining sensitive factors for a particular case study plays a vital role in developing predictive models. These factors not only increase the prediction performance of the model but also reduce time and expense (e.g., reducing field measurements, eliminating redundant variables, etc.). The sensitive factors can be obtained by using the effective feature selection algorithm. As a result, finding a useful feature selection method is critical. The main objective of this study is to compare the performance of the traditional stepwise regression method widely used in flood risk assessment (Bui et al. 2011; Ranganathan et al. 2017; Abraham et al. 2017; Chun et al. 2016; Nazarpour et al. 2016; Zhang 2016; Wang et al. 2016; Gu

et al. 2017), and the Bayesian Model Averaging (BMA) method for choosing the critical flood-conditioning factors for flood susceptibility in Ålesund, Norway.

36.2 Materials and Methods

36.2.1 The Study Area

The study area is Ålesund which is a coastal municipality of Møre and Romsdal County in Norway (Fig. 36.1). It is located between longitudes 6° 05' E and 6° 42' E and latitudes 62° 25' N and 62° 32' E with an area and population of 633.6 km² and 66,148, respectively in 2019 (<https://www.ssb.no/kommunefakta/>). Ålesund's climate is a heavily moderated oceanic type with mild winters. Because Ålesund is surrounded by the ocean, it is significantly affected by changes in climate, especially sea-level rise and rainfall (Simpson et al. 2100). The average annual rainfall of the city is approximately 123 mm (<https://www.weather-atlas.com/en/norway/alesund-climate#rainfall>).

The topography of Ålesund city gradually increases from the central area to the western and eastern areas. Two mountainous regions have altitudes of 300 m and 500 in the West and East, respectively. The central area has an altitude range from 0 to 100 m.

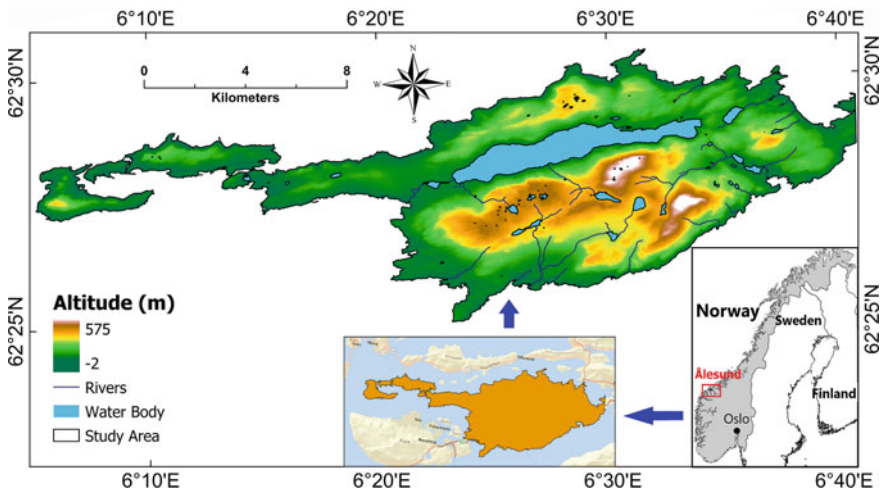


Fig. 36.1 The location of the study area

36.2.2 Flood Susceptibility Assessment Framework

The development of the flood susceptibility assessment framework for the study area involved the following interlinked steps: (1) Data collection and pre-processing; (2) Dividing the flood and non-flood database into training and testing data sets; (3) Building ML models using three different ML algorithms; (4) Validating models' performance and accuracy; (5) Generating flood susceptibility map. This procedure was shown in Fig. 36.2. The different components of the methodological framework are presented in the subsequent sections.

36.2.2.1 Flood Inventory Maps

The accuracy and reliability of flood susceptibility maps depend largely on comprehensive historical flood data (flood inventory) (Bui et al. 2019a; Pham et al. 2020; Paul et al. 2019; Choubin et al. 2019). In this study, a total of 182 flood locations in Ålesund were randomly generated from flood zones provided by the Norwegian Water Resources and Energy Directorate (NVE) (Fig. 36.3a).

Studies have shown that choosing an equal number of flood and non-flood locations can reduce uncertainties and bias caused by unequal proportions in flood susceptibility mapping (Bui et al. 2011, 2012b). Babyak (Babyak 2004) showed that to avoid overfitting, the number of observations should be 10 times more than the number of independent variables. For the model development, a total of 364 flood and non-flood locations were randomly selected from the flood inventory map and divided into training (70%) and testing (30%) data sets. Specifically, 254 flood and non-flood locations were used for building and constructing (training) the model, and 110 of

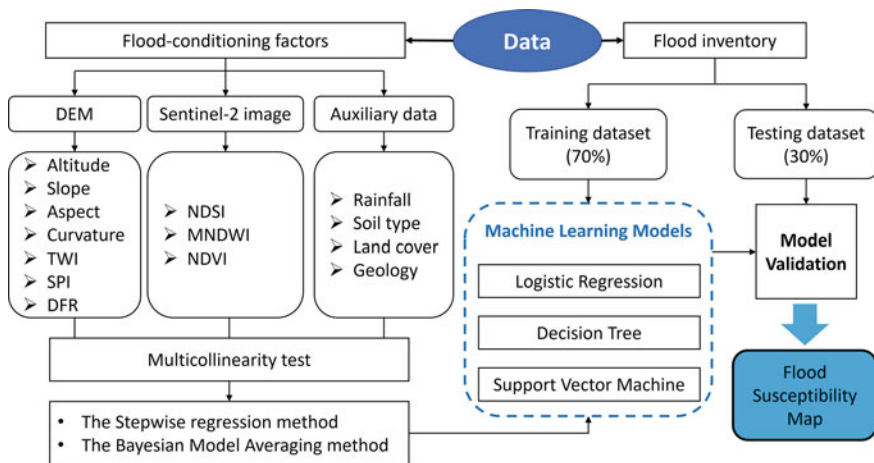


Fig. 36.2 The flowchart for establishing a flood susceptibility assessment in the study

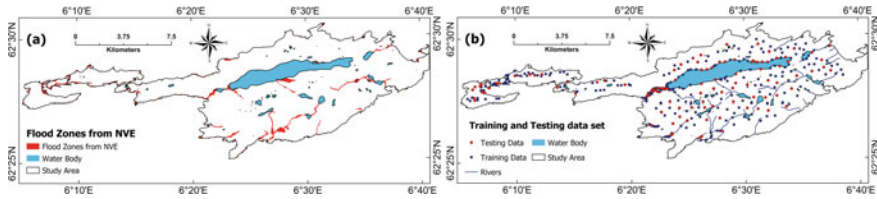


Fig. 36.3 **a** The flood zones obtained from NVE and **b** data for developing and validating machine learning models

the flood and non-flood locations were used for testing and validating the model (Fig. 36.3b).

36.2.2.2 Flood Conditioning Factors

Flood is caused by a myriad of geographically specific conditioning factors. Accurate data on these conditioning factors are critical for the accuracy and reliability of flood susceptibility mapping (Sahana and Patel 2019). There is currently no universal guideline for selecting flood-conditioning factors for flood susceptibility mapping (Dodangeh et al. 2020). The flood-conditioning factors, to a large extent, vary from one location to another depending on the physical attributes and socio-economic characteristics of the area. Therefore, the selection of flood-conditioning factors for flood susceptibility maps in this study was based on the literature, specific site context, field investigations, and experts' knowledge (Chen et al. 2020; Zhao et al. 2019; Sahana and Patel 2019). In this study, a total of 14 flood-conditioning factors were considered. These were: (1) altitude, (2) slope, (3) aspect, (4) curvature, (5) normalized difference vegetation index (NDVI), (6) normalized difference snow index (NDSI), (7) rainfall, (8) stream power index (SPI), (9) topographic wetness index (TWI), (10) modified normalized difference water index (MNDWI), (11) distance from rivers (DFR), (12) soil types, (13) land cover, and (14) geology. These conditioning factors are further categorized into (a) topography-related factors; (b) hydrology-related factors, and (c) physical-related factors.

The Sentinel-2 images used in this study were obtained in the same period as getting the flood inventory map to ensure data consistency. The images downloaded from the website of Copernicus Open Access Hub (<https://scihub.copernicus.eu/>) with the spatial resolution of the data is $10\text{ m} \times 10\text{ m}$ and no cloud cover over the study area (i.e., cloud cover of 4.8% mainly focuses on the ocean). As the Level 1C products, the used Sentinel-2 images have been processed the geometric and radiometric corrections (<https://sentinels.copernicus.eu/web/sentinel/technical-guides/sentinel-2-msi/level-1c/product-formatting>). After that, the downloaded images were used to create a land cover map using supervised classification

in ArcGIS Pro software. More specifically, a Google satellite image was put over the Sentinel-2 image to identify classification sample regions (e.g., forest areas, roads, residential areas, etc.,). Samples of different land cover types were taken and assigned specific values, and different bands of the Sentinel-2 image (depending on the specific purpose) were overlapped. Finally, the object-based classification was applied to cluster areas in the image into different objects based on given samples.

(a) *Topography-related factors*

The topography of an area plays a significant role in flood incidence. It is generally known that low altitude areas are more prone to floods than high altitude areas. Therefore, the topography of an area and its derivative factors have to be accounted for in flood susceptibility mapping (Fernández and Lutz 2010). In this study, a DEM with a spatial resolution of 10 m × 10 m obtained from the Norwegian Mapping Authority (Kartverket) was used to produce slope (Fig. 36.4a), aspect (Fig. 36.4b), and curvature (Fig. 36.4c) maps using ArcGIS Pro software. The altitude, slope, and curvature were introduced into the model as continuous variables, while aspect was introduced as a categorical variable with 9 classes in the models.

(b) *Hydrology-related factors*

The hydrology-related factors are the topographic wetness index (TWI), stream power index (SPI), rainfall, distance from rivers (DFR), the normalized difference snow index (NDSI), and the normalized difference water index (NDWI).

TWI measures the effect of topography on runoff flow direction and accumulation at any location in the catchment and stream power index (SPI) is a measure of the erosive ability of water runoff (Bui et al. 2019a). They were calculated using the following equations (Bui et al. 2019a):

$$TWI = \ln\left(\frac{\alpha}{\tan \beta}\right) \quad (36.1)$$

$$SPI = \alpha \times \tan \beta \quad (36.2)$$

where α is the specific area of the catchment in meters with a slope angle of β (Bui et al. 2019a; Khosravi et al. 2019). The values of TWI and SPI are shown in (Fig. 36.4d) and (Fig. 36.4e), respectively.

Rainfall data were obtained from annual average precipitation from 1900 to 2019 at 11 weather stations inside and outside of the study area, provided by the Norwegian Climate Service Center. The Inverse Distance Weighting (IDW) method was used to interpolate rainfall values in the study area (Fig. 36.4f).

DFR has a significant effect on the distribution and magnitude of floods (Bui et al. 2019a). The river network in this study was provided by the Norwegian Mapping Authority and divided into five classes: 0–500, 500–1000, 1000–1500, 1500–2000, and >2000 m (Fig. 36.4g).

NDSI is an important flood-conditioning factor for areas impacted by snow such as the study area (Fig. 36.4h). Flood events happen with a higher frequency when

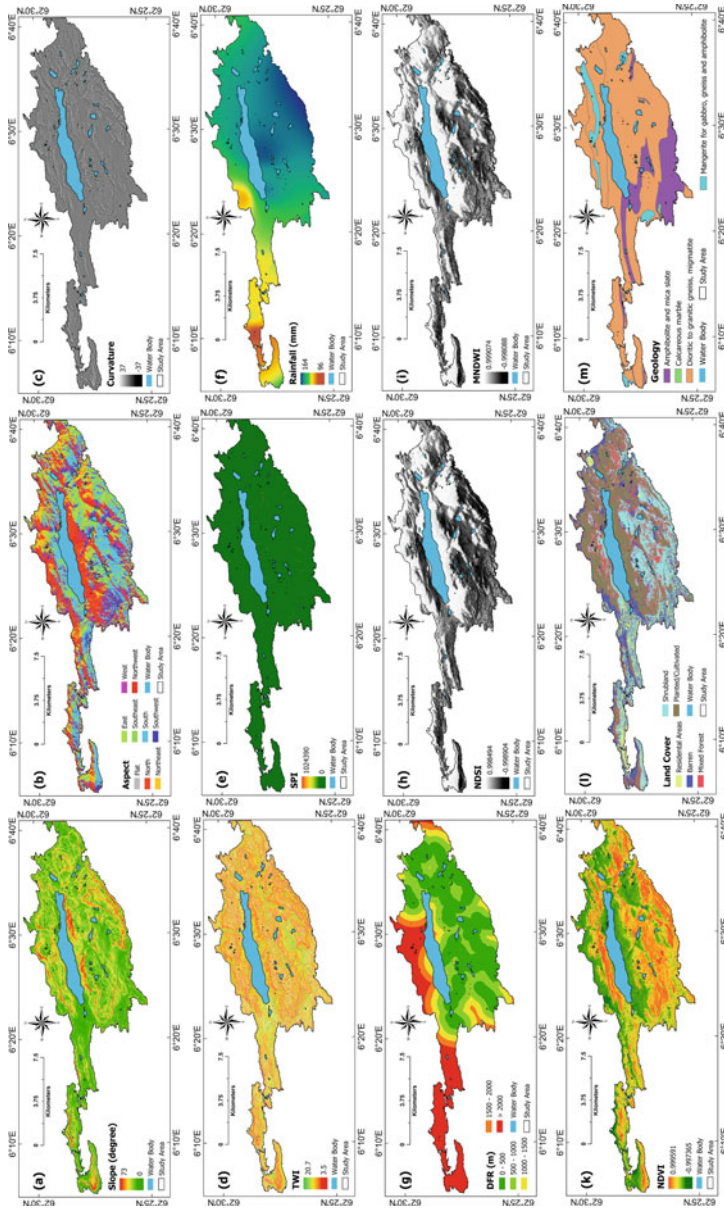
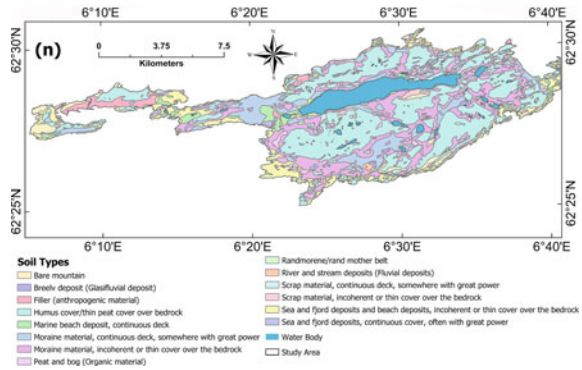


Fig. 36.4 Maps of flood-conditioning factor: **a** slope; **b** aspect; **c** curvature; **d** topographic wetness index (TWI); **e** stream power index (SPI); **f** rainfall (mm); **g** distance from rivers; **h** normalized difference snow index (NDSI); **i** modified normalized difference water index (MNDWI); **k** normalized difference vegetation index (NDVI); **l** land cover; **m** geology; and **n** soil type

Fig. 36.4 (continued)



heavy rainfall is combined with snow melting resulting from increased temperatures (Musselman et al. 2018; Sui and Koehler 2001). Kulkarni, et al. (2002) showed that NDSI reflects different characteristics of snow on the earth’s surface. In this study, the NDSI values were prepared from the Sentinel-2 image (September 08th, 2019) and calculated using the following equation (Kulkarni et al. 2002):

$$NDSI = \frac{Green - SWIR}{Green + SWIR} \tag{36.3}$$

where Green and SWIR are the spectral reflectance observations in the green and the shortwave infrared bands of the electromagnetic spectrum, respectively. With Sentinel-2 image, Green and SWIR correspond to Band 3 and Band 11, respectively.

The normalized difference water index (NDWI) is very sensitive to water (Paul et al. 2019) and it is used to classify water, vegetation, and soil (Xu 2006). However, this index is significantly influenced by noise from built-up areas and has been replaced by the modified normalized difference water index (MNDWI) (Sahana and Patel 2019; Xu 2006; Du et al. 2016). In this study, the MNDWI (Fig. 36.4i) was calculated from the Sentinel-2 image (September 08th, 2019) using the following equation:

$$MNDWI = \frac{Green - MIR}{Green + MIR} \tag{36.4}$$

where MIR is the spectral reflectance observations in the middle infrared band of the electromagnetic spectrum corresponding to Band 12 of the Sentinel-2 image.

(c) *Physical-related factors*

NDVI is an index of vegetation cover on the earth’s surface and is an important factor in flood events (Mind’je et al. 2019; Khosravi et al. 2019), NDVI values are between -1 and +1. The NDVI values for the study area (Fig. 36.4k) were computed based on the Sentinel-2 image using the following equation:

$$NDVI = \frac{NIR - RED}{NIR + RED} \quad (36.5)$$

where NIR and RED are the spectral reflectance observations in the near-infrared and red bands of the electromagnetic spectrum, respectively. In the Sentinel-2 image, NIR and RED correspond to Band 8 and Band 4 of the Sentinel-2 image, respectively.

Land cover affects flood events by mediating factors such as soil infiltration rate, evapotranspiration, or surface runoff, and has been considered an important factor in flood susceptibility mapping (Paul et al. 2019; Rahman et al. 2019). In this study, a land cover map for the study area was prepared using Sentinel-2 image in combination with supervised classification. This resulted in 5 classes of landcover for the study area (Fig. 36.4l).

Bui et al. (2019a) showed that the geological characteristics of an area play a vital role in determining flood susceptibility. In this study, a geology map of the study area was provided by the Norwegian Mapping Authority and divided into 4 classes (Fig. 36.4m).

The soil type in an area affects runoff generation, flood processes, and flood events (Sahana and Patel 2019). Information on the soil types of the study area was obtained from the Norwegian Mapping Authority showing 14 classes of soil (Fig. 36.4n).

Finally, all these factors were resampled to the same spatial resolution and transformed into a grid spatial database using GIS before running ML models.

36.2.3 Flood Susceptibility Modeling Techniques

36.2.3.1 Multicollinearity Problem

Identification of a multicollinearity problem is necessary for the logistic regression (LR) to the correlation of independent variables (Bui et al. 2019a, 2011). In the multicollinearity analysis, tolerance (TOL) and variance inflation factor (VIF) were used to check multicollinearity. The values ≥ 0.2 for TOL and ≤ 5 for VIF were recommended (Bui et al. 2011), in some special situations, a value of 0.1 for TOL and 10 for VIF are considered acceptable (Tang et al. 2020; Bui et al. 2011; Al-Juaidi et al. 2018).

36.2.3.2 Feature Selection Methods

The forward and backward are used for selecting significant variables in regression models based on some statistical tests such as Wald chi-square, t-test, or significant correlation (Bui et al. 2019a; Zeng et al. 2020). The forward selection and backward elimination were implemented using Statistical Package for the Social Sciences (SPSS) version 26.

Bayesian Model Averaging (BMA) method uses multiple models to predict the probability of the event (Sun et al. 2019). This method incorporates uncertainty in the estimation of parameters and prediction by averaging over many different competing models. The BMA method has been efficiently applied to linear regression, generalized linear models, Cox regression models, and discrete graphical models to improve model prediction performance (Fang et al. 2016). The R software was employed for running the BMA model.

In this study, significant flood-conditioning factors are determined using the forward, backward, and BMA methods. These factors, after that, are entered into different ML algorithms. The AUC values and statistical indices are used to assess algorithms' performance.

36.2.3.3 Machine Learning Algorithms

(a) Logistic Regression Algorithm

Logistic Regression (LR) is classified into the supervised ML algorithms and used for predicting the probability of the presence or absence of an event based on the relationship between the dependent and independent variables (Bui et al. 2011; Phong et al. 2019). LR algorithm is especially suitable for classification problems because the dependent variables are binary and independent values can be continuous, categorical, or both. Additionally, input data used for the LR algorithm do not need to have a normal distribution (Rahman et al. 2019; Bui et al. 2011).

The relationship between the probability of presence or absence of flood events using the LR algorithm is given by the following equation:

$$\ln\left(\frac{p}{1-p}\right) = \frac{z}{1+e^{-z}} \quad (36.6)$$

where p is the probability of flood or non-flood event, which has values from 0 to 1; z is a linear function of the dependent variables, which has values from $-\infty$ to $+\infty$ and was calculated as follows:

$$z = a_0 + a_1x_1 + a_2x_2 + \dots + a_nx_n \quad (36.7)$$

where a_0 is the intercept of the z function, $x_i (i = 1, 2, \dots, n)$ are the flood-conditioning factors, n is the number of flood-conditioning factors, and a_i are the coefficients of the x_i variable.

(b) Naïve Bayes Algorithm

Naïve Bayes (NB) is a classification algorithm that belongs to the simple Bayes' theory that determines the relationship between flood-conditioning factors and flood events based on the assumption that these factors are completely independent of the

output class (Bui et al. 2012b). This algorithm does not: (1) require the complex structures, (2) significantly depend on noise irrelevant attributes, and (3) need artificial parameters requirements (Tang et al. 2020; Bui et al. 2012b).

Assume that the output class c (is flood or non-flood), x_i ($i = 1, 2, \dots, n$) are the flood-conditioning factors, n is the number of flood-conditioning factors. The classification probability using NB classifier based on the highest posterior probability is as follows:

$$P_{NB} = \underset{c \in \{flood, non-flood\}}{\operatorname{argmax}} P(c) \prod_{i=1}^k P(x_i|c) \tag{36.8}$$

where $P(c)$ is the classification probability of flood-conditioning factors into class c . $P(x_i|c)$ is the conditional probability of an attribute x_i , which is calculated using: Gaussian Naïve Bayes (GNB), Multinomial Naïve Bayes (MNB), or Bernoulli Naïve Bayes (BNB) as follows:

$$P_{GNB}(x_i|c) = \frac{1}{\sqrt{2\pi}\sigma^2} e^{-\frac{(x_i-\mu)^2}{2\sigma^2}} \tag{36.9}$$

$$P_{MNB}(x_i|c) = \frac{N_i}{\sum_{i=1}^k N_i} \tag{36.10}$$

$$P_{BNB}(x_i|c) = P(i|c)^{x_i} [1 - P(i|c)^{1-x_i}] \tag{36.11}$$

where σ is the standard deviation and μ is the mean of x_i , N_i and $P(i|c)$ are the number and probability of occurrence of the i th factor in the output class c , respectively. GNB is normally used for models with variables that are continuous and large enough (Jahromi and Taheri 2017) while MNB and BNB are used for text classification (Jiang et al. 2016; Singh et al. 2019).

(c) *Support Vector Machine Algorithm*

Support Vector Machine (SVM) is a supervised learning algorithm and is widely used for flood susceptibility mapping (Sahana et al. 2020; Zhao et al. 2019; Choubin et al. 2019; Sachdeva et al. 2017; Tehrany et al. 2015). It creates an optimal separating hyperplane, which is determined by maximizing the distance classification in a given labeled training data set, to classify new examples (Bui et al. 2018a). The SVM formulates a high-dimensional feature space from the original input space based on a nonlinear transformation (Bui et al. 2012b; Phong et al. 2019).

The form of separating hyperplane can be defined as follows (Camps-Valls et al. 2004):

$$\begin{cases} y_i (\mathbf{w} \cdot \boldsymbol{\phi}^T(x_i) + \mathbf{b}) \geq 1 - \xi_i \\ \xi_i \geq 0, \quad i = 1, 2, \dots, n \end{cases} \tag{36.12}$$

where n is the training dataset, $x_i \in \mathbb{R}^n$, $y_i \in \mathbb{R}$, x , and y are vectors that contain flood-conditioning factors and output (including flood or non-flood), respectively; w and b are coefficient vector and bias of the hyperplane in the feature space, respectively; ϕ is the non-linear mapping function, and ξ_i are positive slack variables.

Because the coefficient vector w is in the high-dimensional feature space, an optimal hyperplane can be solved through its Lagrangian dual problem (Camps-Valls et al. 2004; Samui 2008):

$$\begin{cases} \text{Maximising} : \sum_{i=1}^n \alpha_i - \frac{1}{2} \sum_{i=1}^n \sum_{j=1}^n \alpha_i \alpha_j y_i y_j \phi(x_i) \cdot \phi(x_j) \\ \sum_{i=1}^n \alpha_i y_i = 0, \quad 0 \leq \alpha_i \leq C, \quad \forall i = 1, 2, \dots, n \end{cases} \quad (36.13)$$

where auxiliary variables α_i are Lagrange multipliers, and C is the regularization parameter.

The decision function used for the classification is presented as follows (Camps-Valls et al. 2004):

$$f(x) = \text{sign} \left(\sum_{i=1}^n \alpha_i y_i K(x_i, x) + b \right) \quad (36.14)$$

where $K(x, x_i)$ is kernel function which can be linear SVM (LN-SVM), (polynomial SVM (PL-SVM), radial basis function SVM (RBF-SVM), or sigmoid SVM (SIG-SVM) according to the following equations (Bui et al. 2012b; Suykens and Vandewalle 1999):

$$K_{\text{LN-SVM}}(x, x_i) = x^T x_i \quad (36.15)$$

$$K_{\text{PL-SVM}}(x, x_i) = (\gamma x^T x_i + 1)^d \quad (36.16)$$

$$K_{\text{RBF-SVM}}(x, x_i) = e^{-\gamma \|x - x_i\|^2} \quad (36.17)$$

$$K_{\text{SIG-SVM}}(x, x_i) = \tanh(\gamma x^T x_i + r) \quad (36.18)$$

where d is the degree of polynomial kernel function ($d > 0$), γ is the kernel width, and r is the coefficient in kernel projection. Optimizing the parameters C , γ , d , and r will lead to optimizing the kernel function and therefore improve the predicted SVM performance. These parameters can be determined by using the cross-validation technique combined with the grid-search method (Bui et al. 2012b; Liu and Yang 2013).

36.2.3.4 Performance Validation of Machine Learning Algorithms

The ML algorithms use the training data to build models. The performance of these models is validated using the testing data. A testing result with a higher accuracy reflects a good model. The predicted models are completely worthless and have no scientific significance without validation (Bui et al. 2012c). In this study, the efficiency of the models was assessed using the receiver operating characteristic (ROC) curve. The success rate of the model was validated by using the area under the curve (AUC). In addition, other statistical indices such as sensitivity, specificity, accuracy, kappa, and root mean square error (RMSE) on the testing data set were used for validating the models' performance. Table 36.1 shows the range of AUC (0.5–1.0) and their assessment degrees (Zeng et al. 2020).

36.3 Result

36.3.1 Multicollinearity of Flood Conditioning Factors

Results of the multicollinearity analysis of the flood-conditioning factors were shown in Table 36.2. As shown in Table 36.2, the TOL values for NDSI and MNDWI were less than 0.1 and were therefore eliminated from the modeling process. The remaining 12 flood-conditioning factors were used in developing the models for the flood susceptibility maps.

36.3.2 Determination of Flood-Conditioning Factors for Models

The optimal models determined using the stepwise linear regression and BMA methods were presented in Table 36.3. The BMA method resulted in 14 different optimal models for flood prediction and the best 5 models were chosen in this study (Fig. 36.5). Based on the BMA method, the best-performing model (BMA1) had a posterior probability of 40.9%. There was one best performing model each for the

Table 36.1 The assessment degree of AUC values (Zeng et al. 2020)

AUC range	Assessment degree
0.5–0.7	Poor predictive ability
0.7–0.8	Moderate predictive ability
0.8–0.9	Good moderate predictive ability
0.9–1.0	Excellent predictive ability

Table 36.2 The TOL and VIF values for independent variables

No	Independent variables	TOL	VIF	No	Independent variables	TOL	VIF
1	Altitude	0.512	1.953	8	MNDWI	0.077	12.931
2	Slope	0.583	1.715	9	NDVI	0.183	5.471
3	Curvature	0.810	1.235	10	Aspect	0.907	1.103
4	TWI	0.767	1.304	11	DFR	0.540	1.851
5	SPI	0.833	1.200	12	Soil type	0.701	1.427
6	Rainfall	0.441	2.268	13	Land cover	0.623	1.605
7	NDSI	0.049	20.564	14	Geology	0.853	1.173

Table 36.3 Comparison of significant factors received from the stepwise and BMA methods

Method		Factors for optimal models	Post-probability (%)
Stepwise regression	Forward	Altitude, rainfall, soil type, and geology	–
	Backward	Altitude, SPI, rainfall, aspect, DFR, and soil type	–
Bayesian Model Averaging	BMA1	Altitude, slope, rainfall, and NDVI	40.9
	BMA2	Altitude, slope, SPI, rainfall, and NDVI	6.9
	BMA3	Altitude, slope, rainfall, NDVI, and geology	6.3
	BMA4	Altitude, slope, rainfall, NDVI, and landcover	6.0
	BMA5	Altitude, rainfall, NDVI, and landcover	5.7

forward or backward stepwise linear regression method. The results in Table 36.3 also showed that altitude and rainfall were the most important determinants of flood events in the study area as they appeared in all the best-performing models.

In Fig. 36.5, the blue color showed that the regression coefficients had a negative relation with flood events while the red color presented a positive relationship. The results in Fig. 36.5 showed that, in 5 models, altitude, rainfall, NDVI, and slope were the most significant flood-conditioning variables on flooding events; SPI, land-cover, and geology had less influence on the flood; and the remaining factors (curvature, TWI, aspect, distance from rivers, and soil type) did not affect flooding events.

The eight flood-conditioning factors set included a full dataset with 12 variables, one dataset obtained from forward and backward methods (called LR-FR and LR-BR respectively), and five datasets obtained from the BMA method (BMA1, BMA2, BMA3, BMA4, and BMA5) were used to develop and validate three different ML models in Sect. 3.3.

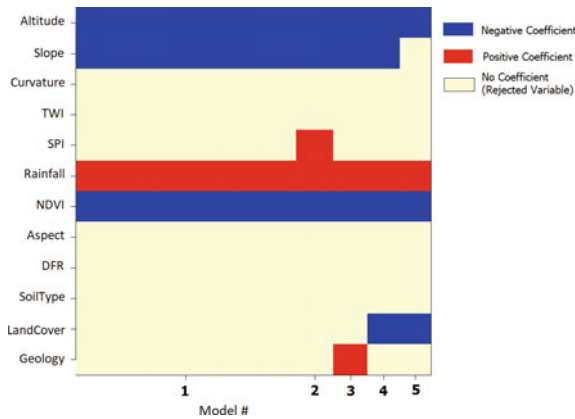


Fig. 36.5 The optimal 5 models proposed by the BMA method

36.3.3 Model Validation

36.3.3.1 Validation of Logistic Regression Model

The accuracy and performance of the LR models are presented in Table 36.4 and Fig. 36.6. All obtained LR models had high accuracy, and it is not significantly different between eight data sets in the training phase (with all the AUC values >0.9) (Fig. 36.6a). However, results in Fig. 36.6b showed that in the validating phase, the model with the full data set did not have the best accuracy and performance although it accounted for the largest number of flood-conditioning factors. The data set obtained from the backward method was the worst model. The models BMA1, BMA2, and BMA3 had equal classification accuracy on the testing dataset. In general, models based on the BMA method had slightly higher classification accuracy and performance than the LR stepwise models.

Table 36.4 Some statistical indices of the logistic regression model on the testing data set

Model	No. variables	Sensitivity (%)	Specificity (%)	Accuracy (%)	Kappa	RMSE
Full dataset	12	91.2	94.3	92.7	0.86	0.27
LR-FR	4	98.1	94.7	96.4	0.93	0.18
LR-BR	6	89.7	94.2	91.8	0.84	0.29
BMA1	4	94.6	96.3	95.5	0.91	0.18
BMA2	5	98.1	96.4	97.3	0.95	0.17
BMA3	5	94.5	94.5	94.5	0.89	0.19
BMA4	5	98.1	93.1	95.5	0.91	0.20
BMA5	4	98.1	93.1	95.5	0.91	0.21

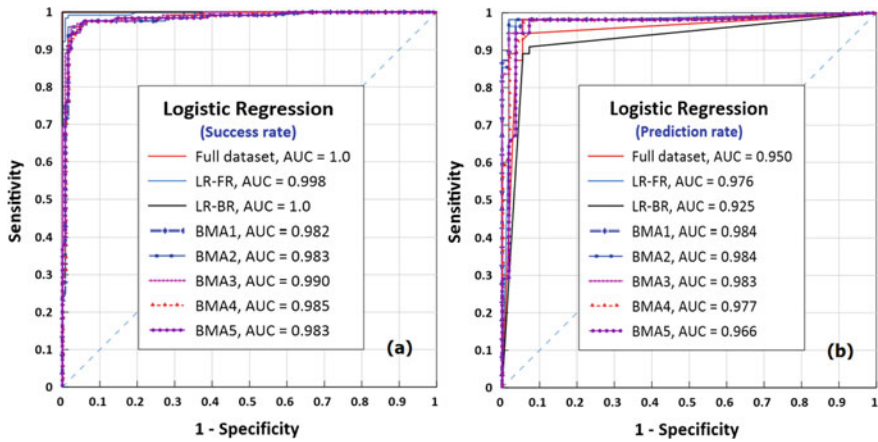


Fig. 36.6 Logistic regression model validation using a success rate and b prediction rate

Although the BMA2, BMA3, and BMA4 models had the same number of (5) flood-conditioning factors, the BMA2 model had the best accuracy and performance, followed by the model BMA3 and BMA4, respectively. This showed that the SPI conditioning factor was an important predictor of floods than geology or land cover (Table 36.3). This result revealed land cover had less effect on flood events than geology. Similarly, the BMA1 model (RMSE = 0.18) was better than the BMA5 model (RMSE = 0.21) on the testing dataset, indicating that slope was a more important predictor of a flood than the landcover. Although the BMA1 model had slightly less classified accuracy than the BMA2 model, the posterior probability of this model was significantly higher than the BMA2 model (40.9% and 6.9% for BMA1 and BMA2 models, respectively). The BMA2 model was therefore selected for building a flood susceptibility map for the study area.

36.3.3.2 Validation of Naïve Bayes Model

Table 36.5 and Fig. 36.7 presents the classification accuracy and performance of the NB models. In the NB model, the stepwise regression models had higher accuracy than the full and the BMA 4 models. The full model with the largest flood-conditioning factors was the worst in the prediction phase. The full data set could develop a high accuracy model in the training phase (Fig. 36.7a) but it had the lowest accuracy in the testing phase (Fig. 36.7b). The remaining data sets had high accuracy in both the training and testing phases.

The AUC values also showed that the NB models have higher accuracy than the LR models. Among these models, the forward regression and BMA2 models had the same AUC value (AUC = 0.996) and were the best model, followed by the remaining BMA models, and the full model was the worst (AUC = 0.984) (Fig. 36.7b). Although having the same AUC value, the BMA2 model reached higher classification accuracy

Table 36.5 Some statistical indices of the Naïve Bayes model on the testing data set

Model	No. variables	Sensitivity (%)	Specificity (%)	Accuracy (%)	Kappa	RMSE
Full dataset	12	85.5	95.8	90.0	0.80	0.27
LR-FR	4	91.5	98.0	94.5	0.89	0.20
LR-BR	6	91.5	98.0	94.5	0.89	0.22
BMA1	4	96.4	98.1	97.3	0.95	0.16
BMA2	5	93.2	100.0	96.4	0.93	0.16
BMA3	5	91.7	100.0	95.5	0.91	0.17
BMA4	5	91.4	96.2	93.6	0.87	0.20
BMA5	4	98.1	96.4	97.3	0.95	0.18

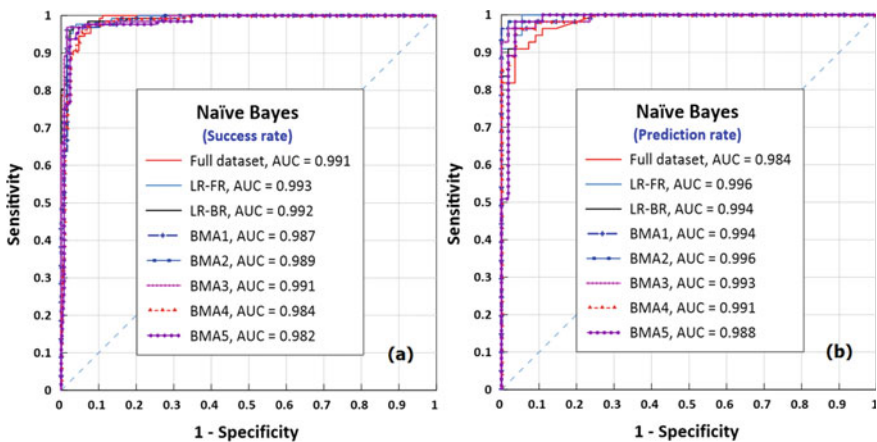


Fig. 36.7 Naïve Bayes model validation using **a** success rate and **b** prediction rate

than the forward regression model. Therefore, the BMA2 model was used for the flood susceptibility mapping.

36.3.3.3 Validation of Support Vector Machine Model

The results of the SVM models are shown in Table 36.6 and Fig. 36.8. In general, the performance and predictive accuracy of SVM models were significantly better than LR and NB models in both the training and testing phases (Fig. 36.8). Table 36.6 showed that the BMA2 model had the least classification accuracy, followed by the model with a full dataset and the backward regression model. The 4 remaining BMA and the forward regression models had the same classification accuracy. The AUC values on the testing set for the SVM in Fig. 36.8b showed that the backward regression model was the worst (AUC = 0.968 and RMSE = 0.22), while the forward regression, BMA1, BMA3, BMA4, and BMA5 had the same AUC values (AUC =

Table 36.6 Some statistical indices of the support vector machine model on the testing data set

Model	No. variables	Sensitivity (%)	Specificity (%)	Accuracy (%)	Kappa	RMSE
Full dataset	12	98.1	94.7	96.4	0.93	0.18
LR-FR	4	98.2	100.0	99.1	0.98	0.09
LR-BR	6	96.4	96.4	96.4	0.93	0.22
BMA1	4	98.2	100.0	99.1	0.98	0.09
BMA2	5	98.1	93.1	95.5	0.91	0.18
BMA3	5	98.2	100.0	99.1	0.98	0.09
BMA4	5	98.2	100.0	99.1	0.98	0.09
BMA5	4	98.2	100.0	99.1	0.98	0.09

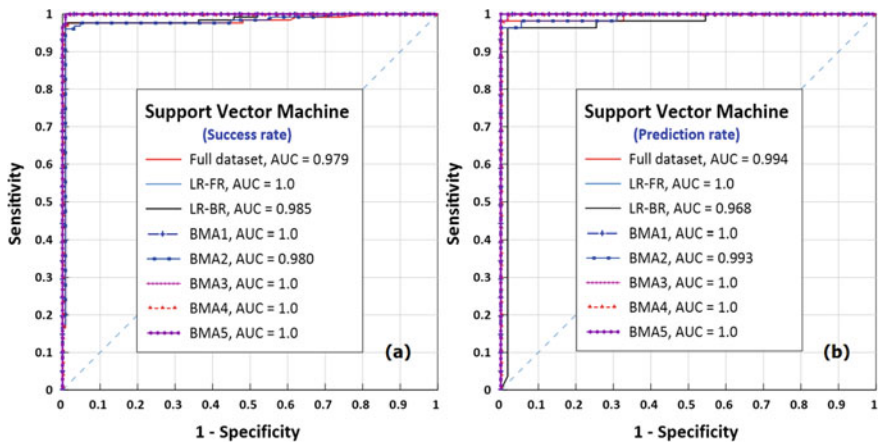


Fig. 36.8 Support vector machine model validation using **a** success rate and **b** prediction rate

1.0) and were the best performing models. Among the best SVM models, the BMA1 required the least flood-conditioning factors; therefore, this model was chosen for the flood susceptibility mapping.

36.3.4 Building Flood Susceptibility Map

From the aforementioned analyses, the models developed by employing the SVM algorithm had more stable accuracy and performance than the LR and NB algorithms. In this study, the input parameters corresponding to the best accurate models were chosen for building flood susceptibility maps for the Ålesund area. Specifically, the BMA2 model with 5 conditioning factors (altitude, slope, SPI, rainfall, and NDVI) was used for the LR and NB algorithms whereas the BMA1 with 4 conditioning

factors (altitude, slope, rainfall, and NDVI) was used for the SVM to conduct the flood susceptibility mapping.

The entire study area was converted to pixels of 10 m × 10 m and the significant flood-conditioning factors of the three ML models were used to build three separated flood susceptibility maps. In this study, the natural breaks (Jenks) method, which is an optimal method for classifying geographic data (North 2009; Khamis et al. 2018; Chen et al. 2013), was used to divide the flood susceptibility probabilities into five classes (No/Very Low, Low, Moderate, High, and Very High) in ArcGIS Pro software. The flood susceptibility maps are shown in Fig. 36.9.

36.4 Discussion

Several ML algorithms have been efficiently applied to study and produce flood susceptibility maps. The different algorithms have pros and cons and require different input data. Moreover, the flood is a consequence of a combination of many flood-conditioning factors, some of them are more important than others (Chen et al. 2020; Khosravi et al. 2019). Therefore, identification of the significant input factors for producing flood susceptibility maps is very important. If the optimal input factors are determined correctly, the model will get the highest accuracy and quality with the least required input data. In this study, the results showed that full models with all more conditioning factors had lower accuracy and performance than models with limited conditioning factors. It also presented the important role of significant flood conditioning factors in developing statistical models and machine learning models as well.

The results in this study presented the BMA method was more effective than the conventional forward and backward regression methods in determining significant flood-conditioning factors, especially in the regression models. For instance, the LR models using the BMA algorithm ($AUC \geq 0.966$) produce higher prediction performance compared to the LR-BR ($AUC \geq 0.925$) (Fig. 36.6b). Similarly, for the SVM models in Fig. 36.8b, the AUC values of all models using the BMA as the feature selection algorithm were higher than the forward and backward regression algorithms ($AUC \geq 0.993$ for the BMA and $AUC \geq 0.968$ for the LR-BR algorithms). For the ML models, the significant flood-conditioning factors had no significantly decisive role in the predictive accuracy of the model. Moreover, while the conventional forward or backward methods gave only one significant flood-conditioning factor, the BMA method gave many significant flood-conditioning datasets thereby allowing more flexibility for model selection and implementation.

Based on the forward, backward, and BMA methods, altitude and rainfall were the most important determinants of flood events in the study area. These factors appeared in all the flood-conditioning datasets (Table 36.3). This is sensible because flood events more frequently occur as a result of heavy rains (Kay et al. 2006; Guhathakurta et al. 2011). Tehrany et al. (2015) showed that the areas with low altitude and slope would be more vulnerable than other areas. Altitude had been seen

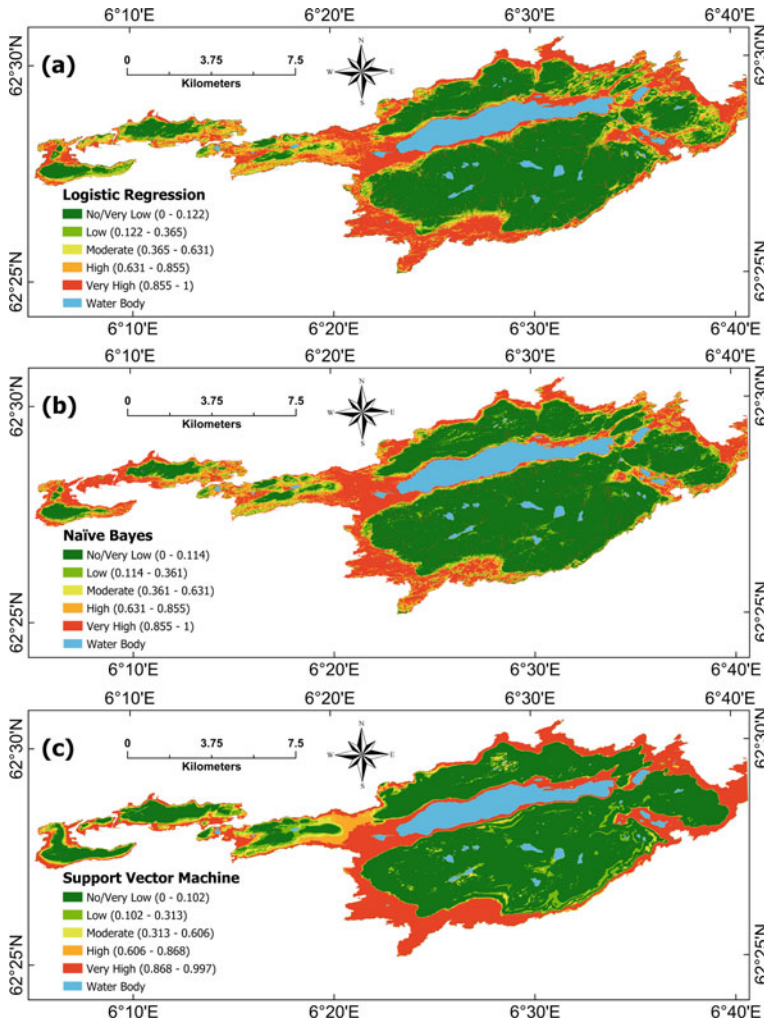


Fig. 36.9 Flood susceptibility maps of the models: **a** logistic regression, **b** Naïve Bayes, and **c** support vector machine

as the most flood conditioning factor that affected flood events using ML techniques in the work of Tehrany et al. (2019). Rainfall data (even in a short-term period) was seen as an important source for forecasting flash-flood (Toth et al. 2000). Several studies focused on studying rainfall as one of the most popular factors related to the flood phenomenon (Ulbrich et al. 2003; Norbiato et al. 2008; Nayak et al. 2005). Digital elevation models were used as the main data source for determining or doing research on flood events in many previous studies (Sande et al. 2012; Zwenzner and Voigt 2009; Ettritch et al. 2018; Manfreda et al. 2011). Flood conditioning factors such as curvature and TWI least affected flood susceptibility in the study area.

The significant dataset obtained from the BMA method seems to be more efficient when used in the LR algorithm (Fig. 36.6). However, there was an insignificant difference between the BMA and the forward and backward methods in SVM models (Fig. 36.7 and Fig. 36.8). This is because the LR models depend significantly on the input parameters, while the ML models, are flexible and can account for various types of input data (Bui et al. 2012a; Lv and Tang 2011). The conclusion of the SVM model has higher accuracy than statistical models in creating a flood susceptibility map is suitable with many previous studies (Sahana et al. 2020; Choubin et al. 2019; Tehrany et al. 2019, 2014).

There is no significant difference between AUC values in NB and SVM algorithms in both the training and testing phases (Figs. 36.7 and 36.8). These results are sensible because many historical studies showed that the difference in classification accuracy between ML algorithms was marginal (Tehrany et al. 2019). For example, several studies showed the DT model had more effective prediction capabilities than the SVM model (Hong et al. 2015; Singh et al. 2009), otherwise, the SVM model had marginally higher predictive capacity than DT or NB model (Bui et al. 2012b; Pradhan 2013).

36.5 Conclusion

In this study, we proposed the using BMA method instead of the traditional stepwise regression method to identify the significant flood-conditioning factors for producing flood susceptibility maps in Ålesund, Norway. Three different ML algorithms namely LR, NB, and SVM were applied to conduct flood susceptibility maps. The flood database including 182 floods were used to generate and validate the models' accuracy and performance employing ROC, AUC, and some statistical indices.

The spatial database included 14 flood-conditioning factors that were considered to develop a predictive model. Tolerance and variance inflation factor methods used for checking the multicollinearity problem, NDSI, and MNDWI revealed no influence on flood occurrence in the study area and were eliminated from the model. The remaining 12 flood-conditioning factors (altitude, slope, curvature, TWI, SPI, rainfall, NDVI, aspect, distance from the river, soil type, land cover, and geology) were used.

The stepwise regression and BMA methods were employed for identifying significant flood-conditioning factors. The predictive models' performance was validated on the testing dataset using some statistical indices and AUC values. The validation analysis showed that the BMA models had higher accuracy than the traditional stepwise regression, especially for the LR model. With ML models such as NB or SVM, changing significant input parameters had no significant influence on the final predictive models' ability in the study area.

The AUC showed that the SVM was the best predictive model in terms of accuracy, followed by the NB and LR models, respectively. However, the reliability

and accuracy of flood susceptibility maps are not only depending on the significant input parameter but also influence the ML algorithms used. Therefore, several new ML algorithms such as hybrid algorithms or optimization techniques should be implemented to improve the map's quality.

Acknowledgements The authors would like to thank the Norwegian Mapping Authority, the Norwegian Climate Service Center, the Norwegian Water Resources and Energy Directorate, the Weather Atlas, and the Mapping Authority for providing data for this research. This research was funded by the Smart Water Project, the grant number is 90392200 financed by Ålesund Municipality and Norwegian University of Science and Technology (NTNU), Norway.

References

- Abraham S, Raisee M, Ghorbaniasl G, Contino F, Lacor C (2017) A robust and efficient stepwise regression method for building sparse polynomial chaos expansions. *J Comput Phys* 332:461–474
- Al-Juaidi AEM, Nassar AM, Al-Juaidi OEM (2018) Evaluation of flood susceptibility mapping using logistic regression and GIS conditioning factors. *Arab J Geosci* 11:765
- Babyak M (2004) What you see may not be what you get: a brief, nontechnical introduction to overfitting in regression-type models. *Psychosom Med* 66:411–421
- Bui DT, Lofman O, Revhaug I, Dick O (2011) Landslide susceptibility analysis in the Hoa Binh province of Vietnam using statistical index and logistic regression. *Nat Hazards* 59:1413
- Bui DT, Pradhan B, Lofman O, Revhaug I, Dick OB (2012a) Landslide susceptibility assessment in the Hoa Binh province of Vietnam: a comparison of the Levenberg–Marquardt and Bayesian regularized neural networks. *Geomorphology* 171–172:12–29
- Bui DT, Pradhan B, Lofman O, Revhaug I (2012b) Landslide susceptibility assessment in Vietnam using support vector machines, decision tree, and Naïve Bayes models. *Math Probl Eng* 2012:974638
- Bui DT, Pradhan B, Lofman O, Revhaug I, Dick OB (2012c) Spatial prediction of landslide hazards in Hoa Binh province (Vietnam): a comparative assessment of the efficacy of evidential belief functions and fuzzy logic models. *CATENA* 96:28–40
- Bui DT, Shahabi H, Shirzadi A, Chapi K, Alizadeh M, Chen W, Mohammadi A, Ahmad BB, Panahi M, Hong H, Tian Y (2018a) Landslide detection and susceptibility mapping by AIRSAR data using support vector machine and index of entropy models in Cameron highlands, Malaysia. *Remote Sens* 10:1527
- Bui DT, Khosravi K, Li S, Shahabi H, Panahi M, Singh VP, Chapi K, Shirzadi A, Panahi S, Chen W, Bin Ahmad B (2018b) New hybrids of ANFIS with several optimization algorithms for flood susceptibility modeling. *Water* 10:1210
- Bui DT, Khosravi K, Shahabi H, Daggupati P, Adamowski JF, Melesse AM, Thai Pham B, Pourghasemi HR, Mahmoudi M, Bahrami S, Pradhan B, Shirzadi A, Chapi K, Lee S (2019a) Flood spatial modeling in Northern Iran using remote sensing and GIS: a comparison between evidential belief functions and its ensemble with a multivariate logistic regression model. *Remote Sens* 11:1589
- Bui DT, Tsangaratos P, Ngo P-TT, Pham TD, Pham BT (2019b) Flash flood susceptibility modeling using an optimized fuzzy rule based feature selection technique and tree based ensemble methods. *Sci Total Environ* 668:1038–1054
- Bui DT, Ngo P-TT, Pham TD, Jaafari A, Minh NQ, Hoa PV, Samui P (2019c) A novel hybrid approach based on a swarm intelligence optimized extreme learning machine for flash flood susceptibility mapping. *CATENA* 179:184–196

- Camps-Valls G, Martín-Guerrero JD, Rojo-Álvarez JL, Soria-Olivas E (2004) Fuzzy sigmoid kernel for support vector classifiers. *Neurocomputing* 62:501–506
- Chen W, Li Y, Xue W, Shahabi H, Li S, Hong H, Wang X, Bian H, Zhang S, Pradhan B, Ahmad BB (2020) Modeling flood susceptibility using data-driven approaches of naïve Bayes tree, alternating decision tree, and random forest methods. *Sci Total Environ* 701:134979
- Chen J, Yang S, Li H, Zhang B, Lv J (2013) Research on geographical environment unit division based on the method of natural breaks (JENKS). *ISPRS—Int Arch Photogramm Remote Sens Spatial Inf Sci* 47–50
- Choubin B, Moradi E, Golshan M, Adamowski J, Sajedi-Hosseini F, Mosavi A (2019) An ensemble prediction of flood susceptibility using multivariate discriminant analysis, classification and regression trees, and support vector machines. *Sci Total Environ* 651:2087–2096
- Chun Y, Griffith DA, Lee M, Sinha P (2016) Eigenvector selection with stepwise regression techniques to construct eigenvector spatial filters. *J Geogr Syst* 18:67–85
- Costache R (2019) Flood susceptibility assessment by using bivariate statistics and machine learning models—a useful tool for flood risk management. *Water Resour Manage* 33:3239–3256
- Costache R, Pham BQ, Sharifi E, Linh TN, Abba SI, Vojtek M, Vojteková J, Nhi TP, Khoi ND (2020) Flash-flood susceptibility assessment using multi-criteria decision making and machine learning supported by remote sensing and GIS techniques. *Remote Sens* 12
- Dano LU, Balogun A-L, Matori A-N, Wan Yusouf K, Abubakar RI, Said Mohamed AM, Aina AY, Pradhan B (2019) Flood susceptibility mapping using GIS-based analytic network process: a case study of Perlis, Malaysia. *Water* 11
- Dinan T (2017) Projected increases in hurricane damage in the United States: the role of climate change and coastal development. *Ecol Econ* 138:186–198
- Dodangeh E, Choubin B, Egidir AN, Nabipour N, Panahi M, Shamsheerband S, Mosavi A (2020) Integrated machine learning methods with resampling algorithms for flood susceptibility prediction. *Sci Total Environ* 705:135983
- Du Y, Zhang Y, Ling F, Wang Q, Li W, Li X (2016) Water bodies' mapping from Sentinel-2 imagery with modified normalized difference water index at 10-m spatial resolution produced by sharpening the SWIR band. *Remote Sens* 8
- Ettrich G, Hardy A, Bojang L, Cross D, Bunting P, Brewer P (2018) Enhancing digital elevation models for hydraulic modelling using flood frequency detection. *Remote Sens Environ* 217:506–522
- Falah F, Rahmati O, Rostami M, Ahmadisharaf E, Daliakopoulos IN, Pourghasemi HR (2019) 14—artificial neural networks for flood susceptibility mapping in data-scarce urban areas. In: Pourghasemi HR, Gokceoglu C (eds) *Spatial modeling in GIS and R for earth and environmental sciences*. Elsevier, pp 323–336
- Fang X, Li R, Kan H, Bottai M, Fang F, Cao Y (2016) Bayesian model averaging method for evaluating associations between air pollution and respiratory mortality: a time-series study. *BMJ Open* 6:e011487
- Fernández DS, Lutz MA (2010) Urban flood hazard zoning in Tucumán Province, Argentina, using GIS and multicriteria decision analysis. *Eng Geol* 111:90–98
- Gizaw MS, Gan TY (2017) Impact of climate change and El Niño episodes on droughts in sub-Saharan Africa. *Clim Dyn* 49:665–682
- Gu Y, Bao Z, Lin Y, Qin Z, Lu J, Wang H (2017) The porosity and permeability prediction methods for carbonate reservoirs with extremely limited logging data: stepwise regression versus N-way analysis of variance. *J Nat Gas Sci Eng* 42:99–119
- Guhathakurta P, Sreejith OP, Menon PA (2011) Impact of climate change on extreme rainfall events and flood risk in India. *J Earth Syst Sci* 120:359–373
- Hong H, Pradhan B, Xu C, Bui DT (2015) Spatial prediction of landslide hazard at the Yihuang area (China) using two-class kernel logistic regression, alternating decision tree and support vector machines. *CATENA* 133:266–281
- <https://sentinels.copernicus.eu/web/sentinel/technical-guides/sentinel-2-msi/level-1c/product-for-matting>

- <https://www.ssb.no/kommunefakta/>
<https://www.weather-atlas.com/en/norway/alesund-climate#rainfall>
- Hu S, Fedorov AV (2017) The extreme El Niño of 2015–2016 and the end of global warming hiatus. *Geophys Res Lett* 44:3816–3824
- Jahromi A, Taheri M (2017) A non-parametric mixture of Gaussian naive Bayes classifiers based on local independent features
- Jiang L, Wang S, Li C, Zhang L (2016) Structure extended multinomial naive Bayes. *Inf Sci* 329:346–356
- Joyce KE, Belliss SE, Samsonov SV, McNeill SJ, Glassey PJ (2009) A review of the status of satellite remote sensing and image processing techniques for mapping natural hazards and disasters. *Prog Phys Geogr* 33:183–207
- Kay, A.L., Jones, R.G., Reynard, N.S.: RCM rainfall for UK flood frequency estimation. II. Climate change results. *Journal of Hydrology* 318, 163–172 (2006)
- Khamis N, Sin TC, Hock GC (2018) Segmentation of residential customer load profile in peninsular Malaysia using Jenks natural breaks. In: *IEEE 7th international conference on power and energy (PECon)*, pp 128–131
- Khosravi K, Shahabi H, Pham BT, Adamowski J, Shirzadi A, Pradhan B, Dou J, Ly H-B, Gróf G, Ho HL, Hong H, Chapi K, Prakash I (2019) A comparative assessment of flood susceptibility modeling using multi-criteria decision-making analysis and machine learning methods. *J Hydrol* 573:311–323
- Kjeldsen T (2010) Modelling the impact of urbanization on flood frequency relationships in the UK. *Hydrol Res* 41
- Kulkarni AV, Srinivasulu J, Manjul SS, Mathur P (2002) Field based spectral reflectance studies to develop NDSI method for snow cover monitoring. *J Indian Soc Remote Sens* 30:73–80
- Li X, Chen W, Zhang Q, Wu L (2020) Building auto-encoder intrusion detection system based on random forest feature selection. *Comput Secur* 95:101851
- Lian T, Chen D, Ying J, Huang P, Tang Y (2018) Tropical Pacific trends under global warming: El Niño-like or La Niña-like? *Natl Sci Rev* 5:810–812
- Liu X, Yang C (2013) A kernel spectral angle mapper algorithm for remote sensing image classification. In: *6th international congress on image and signal processing (CISP)*, pp 814–818
- Liuzzo L, Sammartano V, Freni G (2019) Comparison between different distributed methods for flood susceptibility mapping. *Water Resour Manage* 33:3155–3173
- Lv H, Tang H (2011) Machine learning methods and their application research. In: *2nd international symposium on intelligence information processing and trusted computing*, pp 108–110
- Manfreda S, Leo MD, Sole A (2011) Detection of flood-prone areas using digital elevation models. *J Hydrol Eng* 16:781–790
- Mind'je R, Li L, Amanambu AC, Nahayo L, Nsengiyumva JB, Gasirabo A, Mindje M (2019) Flood susceptibility modeling and hazard perception in Rwanda. *Int J Disaster Risk Reduction* 38:101211
- Mukherjee S, Mishra A, Trenberth KE (2018) Climate change and drought: a perspective on drought indices. *Curr Clim Change Rep* 4:145–163
- Musselman KN, Lehner F, Ikeda K, Clark MP, Prein AF, Liu C, Barlage M, Rasmussen R (2018) Projected increases and shifts in rain-on-snow flood risk over western North America. *Nat Clim Chang* 8:808–812
- Næss LO, Bang G, Eriksen S, Vevatne J (2005) Institutional adaptation to climate change: flood responses at the municipal level in Norway. *Glob Environ Chang* 15:125–138
- Nayak PC, Sudheer KP, Ramasastri KS (2005) Fuzzy computing based rainfall–runoff model for real time flood forecasting. *Hydrol Process* 19:955–968
- Nazarpour A, Paydar GR, Carranza EJM (2016) Stepwise regression for recognition of geochemical anomalies: case study in Takab area, NW Iran. *J Geochem Explor* 168:150–162
- Nguyen LV, Bui DT, Seidu R (2020) Identification of sensitive factors for placement of flood monitoring sensors in wastewater/stormwater network using GIS-based fuzzy analytical hierarchy process: a case of study in Ålesund, Norway. Springer International Publishing, pp 79–97

- Nguyen LV, Tornyeviadzi HM, Bui DT, Seidu R (2022) Predicting discharges in sewer pipes using an integrated long short-term memory and entropy A-TOPSIS modeling framework. *Water* 14:300
- Norbiato D, Borga M, Degli Esposti S, Gaume E, Anquetin S (2008) Flash flood warning based on rainfall thresholds and soil moisture conditions: an assessment for gauged and ungauged basins. *J Hydrol* 362:274–290
- North MA (2009) A method for implementing a statistically significant number of data classes in the Jenks algorithm. In: Sixth international conference on fuzzy systems and knowledge discovery, pp 35–38
- Paul GC, Saha S, Hembram TK (2019) Application of the GIS-based probabilistic models for mapping the flood susceptibility in Bansloi sub-basin of Ganga-Bhagirathi River and their comparison. *Remote Sens Earth Syst Sci* 2:120–146
- Pham BT, Avand M, Janizadeh S, Phong TV, Al-Ansari N, Ho LS, Das S, Le HV, Amini A, Bozchaloei SK, Jafari F, Prakash I (2020) GIS based hybrid computational approaches for flash flood susceptibility assessment. *Water* 12:683
- Phong TV, Phan TT, Prakash I, Singh SK, Shirzadi A, Chapi K, Ly H-B, Ho LS, Quoc NK, Pham BT (2019) Landslide susceptibility modeling using different artificial intelligence methods: a case study at Muong Lay district, Vietnam. *Geocarto Int* 1–24
- Pradhan B (2013) A comparative study on the predictive ability of the decision tree, support vector machine and neuro-fuzzy models in landslide susceptibility mapping using GIS. *Comput Geosci* 51:350–365
- Rahman M, Ningsheng C, Islam MM, Dewan A, Iqbal J, Washakh RMA, Shufeng T (2019) Flood susceptibility assessment in Bangladesh using machine learning and multi-criteria decision analysis. *Earth Syst Environ* 3:585–601
- Ranganathan P, Pramesh CS, Aggarwal R (2017) Common pitfalls in statistical analysis: logistic regression. *Perspect Clin Res* 8:148–151
- Rauken T, Kelman I (2010) River flood vulnerability in Norway through the pressure and release model. *J Flood Risk Manage* 3:314–322
- Sachdeva S, Bhatia T, Verma AK (2017) Flood susceptibility mapping using GIS-based support vector machine and particle swarm optimization: a case study in Uttarakhand (India). In: 8th international conference on computing, communication and networking technologies (ICCCNT), pp 1–7
- Sahana M, Patel PP (2019) A comparison of frequency ratio and fuzzy logic models for flood susceptibility assessment of the lower Kosi River Basin in India. *Environ Earth Sci* 78:289
- Sahana M, Rehman S, Sajjad H, Hong H (2020) Exploring effectiveness of frequency ratio and support vector machine models in storm surge flood susceptibility assessment: a study of Sundarban biosphere reserve, India. *CATENA* 189:104450
- Samui P (2008) Slope stability analysis: a support vector machine approach. *Environ Geol* 56:255
- Shao K, Liu W, Gao Y, Ning Y (2019) The influence of climate change on tsunami-like solitary wave inundation over fringing reefs. *J Integr Environ Sci* 16:71–88
- Simpson M, Øie Nilsen JE, Ravndal O, Breili K, Sande H, Kierulf H, Steffen H, Jansen E, Carson M, Vestol O (2016) Sea level change for Norway: past and present observations and projections to 2100. In: EGU general assembly conference abstracts, pp EPSC2016–17729
- Singh Y, Kaur A, Malhotra R (2009) Comparative analysis of regression and machine learning methods for predicting fault proneness models. *IJCAT* 35:183–193
- Singh G, Kumar B, Gaur L, Tyagi A (2019) Comparison between multinomial and Bernoulli Naïve Bayes for text classification. In: International conference on automation, computational and technology management (ICACTM), pp 593–596
- Sui J, Koehler G (2001) Rain-on-snow induced flood events in Southern Germany. *J Hydrol* 252:205–220
- Sun H, Yang Y, Wu R, Gui D, Xue J, Liu Y, Yan D (2019) Improving estimation of cropland evapotranspiration by the Bayesian model averaging method with surface energy balance models. *Atmosphere* 10


- Suykens JAK, Vandewalle J (1999) Least squares support vector machine classifiers. *Neural Process Lett* 9:293–300
- Talha S, Maanan M, Atika H, Rhinane H (2019) Prediction of flash flood susceptibility using fuzzy analytical hierarchy process (fahp) algorithms and Gis: a study case of guelmim region in Southwestern of morocco. *ISPRS—Int Arch Photogrammetry, Remote Sens Spat Inf Sci* 42W1:407–414
- Tang R, Zhang X (2020) CART decision tree combined with Boruta feature selection for medical data classification. In: 5th IEEE international conference on big data analytics (ICBDA), pp 80–84
- Tang X, Li J, Liu M, Liu W, Hong H (2020) Flood susceptibility assessment based on a novel random Naïve Bayes method: a comparison between different factor discretization methods. *CATENA* 190:104536
- Tehrany MS, Lee M-J, Pradhan B, Jebur MN, Lee S (2014) Flood susceptibility mapping using integrated bivariate and multivariate statistical models. *Environ Earth Sci* 72:4001–4015
- Tehrany MS, Pradhan B, Mansor S, Ahmad N (2015) Flood susceptibility assessment using GIS-based support vector machine model with different kernel types. *CATENA* 125:91–101
- Tehrany MS, Jones S, Shabani F (2019) Identifying the essential flood conditioning factors for flood prone area mapping using machine learning techniques. *CATENA* 175:174–192
- Toth E, Brath A, Montanari A (2000) Comparison of short-term rainfall prediction models for real-time flood forecasting. *J Hydrol* 239:132–147
- Ulbrich U, Brücher T, Fink AH, Leckebusch GC, Krüger A, Pinto JG (2003) The central European floods of August 2002: part 1—rainfall periods and flood development. *Weather* 58:371–377
- Usman M (2016) A study on the enhancing earthquake frequency in northern Pakistan: is the climate change responsible? *Nat Hazards* 82:921–931
- Van de Sande B, Lansens J, Hoyng C (2012) Sensitivity of coastal flood risk assessments to digital elevation models. *Water* 4:568–579
- Vojtek M, Vojteková J (2019) Flood susceptibility mapping on a national scale in Slovakia using the analytical hierarchy process. *Water* 11
- Wang M, Wright J, Brownlee A, Buswell R (2016) A comparison of approaches to stepwise regression on variables sensitivities in building simulation and analysis. *Energy Build* 127:313–326
- Wang P, Bai X, Wu X, Yu H, Hao Y, Hu XB (2018) GIS-based random forest weight for rainfall-induced landslide susceptibility assessment at a humid region in Southern China. *Water* 10
- Wang Y, Hong H, Chen W, Li S, Pamučar D, Gigović L, Drobňak S, Bui DT, Duan H (2019) A hybrid GIS multi-criteria decision-making method for flood susceptibility mapping at Shangyou, China. *Remote Sens* 11:62
- Weydahl DJ (1996) Flood monitoring in Norway using ERS-1 SAR images. In: *IGARSS'96. International geoscience and remote sensing symposium*, pp 151–153 vol 151
- Xu H (2006) Modification of normalised difference water index (NDWI) to enhance open water features in remotely sensed imagery. *Int J Remote Sens* 27:3025–3033
- Yan K, Zhang D (2015) Feature selection and analysis on correlated gas sensor data with recursive feature elimination. *Sens Actuators, B Chem* 212:353–363
- Youssef AM, Hegab MA (2019) Flood-hazard assessment modeling using multicriteria analysis and GIS: a case study—Ras Gharib Area, Egypt. In: Pourghasemi HR, Gokceoglu C (eds) *Spatial modeling in GIS and R for earth and environmental sciences*. Elsevier, pp 229–257
- Zeng Z, Lan J, Hamidi AR, Zou S (2020) Integrating internet media into urban flooding susceptibility assessment: a case study in China. *Cities* 101:102697
- Zhang Z (2016) Variable selection with stepwise and best subset approaches. *Ann Transl Med* 4:136–136
- Zhao G, Pang B, Xu Z, Yue J, Tu T (2018) Mapping flood susceptibility in mountainous areas on a national scale in China. *Sci Total Environ* 615:1133–1142
- Zhao G, Pang B, Xu Z, Peng D, Xu L (2019) Assessment of urban flood susceptibility using semi-supervised machine learning model. *Sci Total Environ* 659:940–949

Zwenzner H, Voigt S (2009) Improved estimation of flood parameters by combining space based SAR data with very high resolution digital elevation data. *Hydrol Earth Syst Sci* 13:567–576

Chapter 37

Application of Fuzzy and Geospatial Analysis for Identifying Water Pollution Zone in the Can Gio Coastal Mangrove Biosphere Reserve Area



Son V. Lam, Phong V. Nguyen, Kien T. Ta, Chau P. T. Nguyen, Hoa T. Le, and Phu L. Vo 

Abstract Can Gio Mangrove Forest (CGMF), the World Biosphere Reserve Area, is located in Can Gio coastal district in the Southeastern area of Ho Chi Minh City. Aquaculture cultivation practices is one of the main livelihood activities the Can Gio coastal zone in which aquacultural sector plays a main contributor to the local economic development. However, surface waterbodies have been exacerbated due to intensive aquaculture practices over the past decade. The purpose of this paper is to identify surface water pollution zones in order to facilitate the local management practices of water resources. In this study, water quality zones were identified by using Fuzzy Comprehensive Evaluation (FCE) technique and geospatial analysis. Thirty-five (35) water samples were collected from aquaculture farms. The results indicated that the quality of surface water sources is being deteriorated by wastewater generated from aquaculture cultivation activities. Further, water quality zones were classified from non-pollution (level 1) to moderate pollution (level 3) according to FCE algorithm calculation based on different groups of monitoring water quality parameters as regulated by decision 1460/QD-TCMT of the Vietnam Environmental Protection Agency. These results are useful to assist local authorities in identifying water pollution areas (zones) influenced by aquaculture activities. More importantly,

S. V. Lam (✉) · P. V. Nguyen · K. T. Ta
HUTECH Institute of Applied Sciences, HUTECH University, Ho Chi Minh City, Vietnam
e-mail: lv.son@hutech.edu.vn

S. V. Lam · C. P. T. Nguyen · H. T. Le
Faculty of Geography, University of Social Sciences and Humanities—VNU HCM, Ho Chi Minh City, Vietnam

P. L. Vo
Faculty of Environment and Natural Resources, Ho Chi Minh City University of Technology (HCMUT), 268 Ly Thuong Kiet street, District 10, Ho Chi Minh City, Vietnam
e-mail: volephu@hcmut.edu.vn

Vietnam National University Ho Chi Minh City, Linh Trung Ward, Thu Duc District, Ho Chi Minh City, Vietnam

this finding is an implication for planners and managers at the top level of management to put aquaculture planning in place in Can Gio for the long-run management practices of coastal water resources towards sustainable livelihood activities.

Keywords Can Gio coastal zone · Aquaculture cultivation activities · Fuzzy comprehensive evaluation · Water quality · Water pollution zone

37.1 Introduction

In parallel with the urbanisation and industrialisation, the fast socio-economic development has posed considerable impacts on environmental components, in which the most affected sector is water resources (Tuan et al. 2017; Vinh 2014). Many river basins are being seriously contaminated due to a great deal of pollutants generated from socio-economic activities that caused the deterioration of environments and resources such as the degradation of water quality, decline of biodiversity, and depletion of groundwater resources, etc. (Vinh 2014).

Can Gio, a coastal district, is located in southeastern of Ho Chi Minh City, and comprises can Thanh town and 6 communes, including: Binh Khanh, An Thoi Dong, Ly Nhon, Tan Thon Hiep, Long Hoa, and Thanh An (UNESCO/MAB 2000; Nam et al. 2014; Tuan and Kuenzer 2012). Can Gio is a resources hub for the development of local livelihoods, including onshore-offshore fishing, aquaculture cultivation (shrimp, crab, fish, and other aquatic products), salt-works, forest guarding, farming, livestock, and tourism services (Lan 2016; Pho 2016).¹ However, these livelihood activities have had adverse impacts on the environment and natural resources of Can Gio Mangrove Forest (CGMF). In fact, the variation of climate conditions such as increasing temperature, heavy rains, abnormal tropical storms, saltwater intrusion, and high level of river water had resulted in a profound loss of livelihood activities (Tuan and Dung 2015). In addition, changes in natural and man-made resources for socio-economic development have placed constraints and disturbance on local livelihood activities. Infrastructure development projects on transportation network, Binh Khanh bridge (connecting Nha Be district—Can Gio district), Can Gio urban reclamation development, etc. have posed profound effects on local livelihood activities which are still far from expectation. Therefore, enhancing management practices and zoning surface water quality in Can Gio is a decisive task which not only for environmental management, but also for sustainable water resources utilisation and planning in the Can Gio Mangrove Forest.

Presently, the assessment of water quality and classification of water quality zones are carried out mainly using WQI and comparing with QCVN 08-MT:2015/BTNMT (Hung 2017). However, this approach to water quality assessment relies on monitored water quality indicators which were merely desultory and temporal (depending

¹ Clough, B.: Continuing the journey amongst mangroves ISME Mangrove Educational Book Series No 1 International Society for Mangrove Ecosystems (ISME) Okinawa Japan and International Tropical Timber Organization (ITTO) Yokohama, Japan.

on sites and time of monitoring practices), and thus, this probably results in inadequate and improper determination of water quality status (Hung 2017). In order to surmount this hurdle, Fuzzy Comprehensive Evaluation (FCE) technique was deployed based on fuzzy logic to overcome the reality of environmental issues by “translating” the information of natural factors into mathematical formula. Basically, the meanings of the same context are combined such as severe pollution, heavy pollution, moderate pollution, lightly pollution, and non-pollution or types of pollution 1, 2, 3, 4, and 5. Accordingly, the FCE technique is applied for translating these meanings into mathematical values and expressing the ultimate results in forms of understandable ways to state what kind of water quality is (Ly 2019). It can be certainly said that “fuzzy” logic is a superset of traditional logic which was used to identify the real value between “completely true” and “completely wrong”. In other ways, the FCE technique helps to process or to omit some multivariates, uncertain, and incoherent monitoring data, and therefore, it is able to create logical, transparent, and reliable information (Hung 2017; Ly 2019; Tran et al. 2014).

The purpose of this study is to assess water quality and classify water pollution zone in the coastal aquaculture cultivation area of Can Gio district by using FCE algorithm based on the Decision 1460/QĐ-TCMT. The results of water quality zoning will be an effective support tool for the management practice and the utilisation of surface water resources for the sustainable development of aquaculture livelihoods in Can Gio district.

37.2 Study Area and Methods

37.2.1 Study Area

The study area is Can Gio coastal district, Ho Chi Minh City, Vietnam. The location of study area is shown in Fig. 37.1, in which aquaculture cultivation activities (shrimp farming, crab, fish, and other aquatic products) are the majority of local livelihoods.

37.2.2 Methods

37.2.2.1 Water Sampling and Analysis

A total of 35 surface water samples at receiving water bodies of wastewater discharging from aquaculture cultivation activities (shrimp, crab, fish, and other aquatic products) were surveyed and collected. Water samples were collected in the dry and rainy seasons of 2020. Water sampling and storing were conducted in accordance with TCVN 6631-1:2011 and transported to the lab at HUTECH within 24 h (Table 37.1).

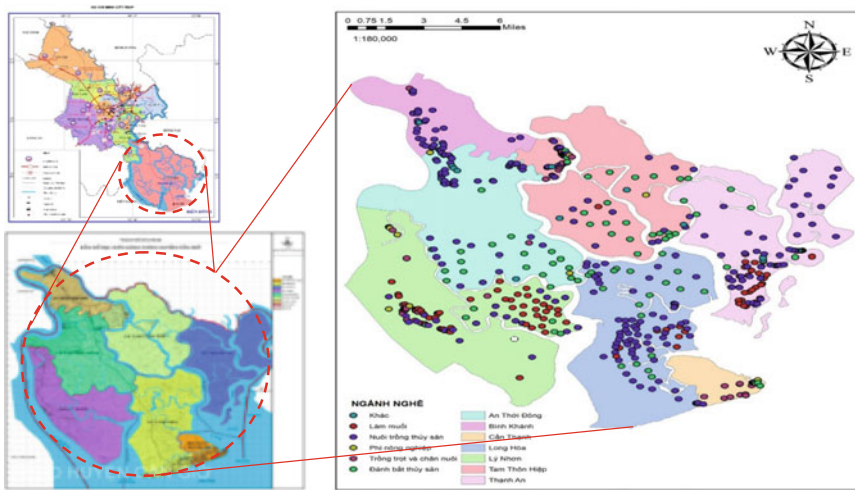


Fig. 37.1 Map of coastal areas with surface water of Can Gio district

The quality of surface water was compared with QCVN 02–19:2014/BNNPTNT—National Technical Regulation on Brackish Water Shrimp Culture Farm—Conditions for Veterinary Hygiene, Environmental Protection and Food Safety and QVCN 08-MT:2015/BTNMT—National Technical Regulation on Surface Water Quality.

37.2.2.2 Fuzzy Comprehensive Evaluation (FCE) Technique

According to Decision 1460/QĐ-TCMT on technical guidelines for calculation of water quality in Vietnam (so-called VN_WQI), parameters of water quality are divided into five groups, including: Group I—pH; Group II—pesticides; Group III—heavy metals; Group IV—organic matter and nutrients; and Group V—microbiology (QĐ-TCMT 2019). The VN_WQI can be built when having 03/05 groups of parameters are suitable to the characteristics of a specific study area. Son et al. (2021) claimed that aquaculture cultivation is a lion share of local livelihood activities, accounting for 52%, and is responsible for the poor quality of coastal waters in Can Gio. Accordingly, organic matter, nutrients, and microorganisms are the main source of pollutants. Therefore, the parameters used for water quality assessment consist of Group I (pH), Group IV (organic matter and nutrients), and Group V (microorganisms). Furthermore, the application of fuzzy algorithm (FCE technique) for classifying pollution level (type) based on 3 above-mentioned groups of water quality parameters from 35 collected surface water samples is consistent with the regulation of Decision 1460/QĐ-TCMT.

Practically, steps to perform a water quality classification by using FCE technique as described in Fig. 37.2.

Table 37.1 Analysis methods for water quality

Parameter	Analysis method/protocol	Permissible limits (B1)	Measurement and analysis instruments
pH	TCVN 6492:2011 Water quality—pH	5.5–9	Model seven compact S220-K
DO (mg/L)	TCVN 7324:2004 Water quality—DO measurement, electrode probe	4	Model Oxi 7310
BOD ₅ (mg/L)	TCVN 6001-2:2008 Water quality—non-dilution protocol	15	Model Oxi 7310
		50	
COD (mg/L)	TCVN 6491:1999 Water quality—COD analysis	30	Elox portable meter
		150	
NH ₄ ⁺ -N (mg/L)	TCVN 6179-1:1996 Water quality—spectrometer	0.9	AmmoniTor
		10	
NO ₃ ⁻ -N (mg/L)	TCVN 6180:1996 Water quality—UV Vis	10	UV Vis 730
NO ₂ ⁻ -N (mg/L)	TCVN 6178:1996 Water quality—UV Vis	0.05	UV Vis 730
PO ₄ ³⁻ -P (mg/L)	TCVN 6202:2008 Water quality—UV Vis (amoni molipdate)	0.3	UV Vis 730
Total P	TCVN 6202:2008 Water quality—UV Vis (amoni molipdate)	6	UV Vis 730
TOC (mg/L)	TCVN 6634:2000 Water quality—TOC	4 (A1)	TOC Ultra
Coliform (MPN)	TCVN 6187-2:1996 Water quality—most probable number	7500	Most probable number
		5000	

37.2.2.3 GIS Technique and Geostatistical Analysis

GIS techniques coupled with ArcGIS 10.4 software were applied for building models. In addition, group data of information on natural conditions, environmental information on inland and coastal areas collected from government agencies, departments, and institutes were processed and analyzed by using geostatistical analysis (an integrated tool on GIS). The results of FCE calculation are deployed for overlaying and mapping water pollution classification. Finally, the classification map of water quality in the coastal zone of Can Gio was constructed (Fig. 37.3).

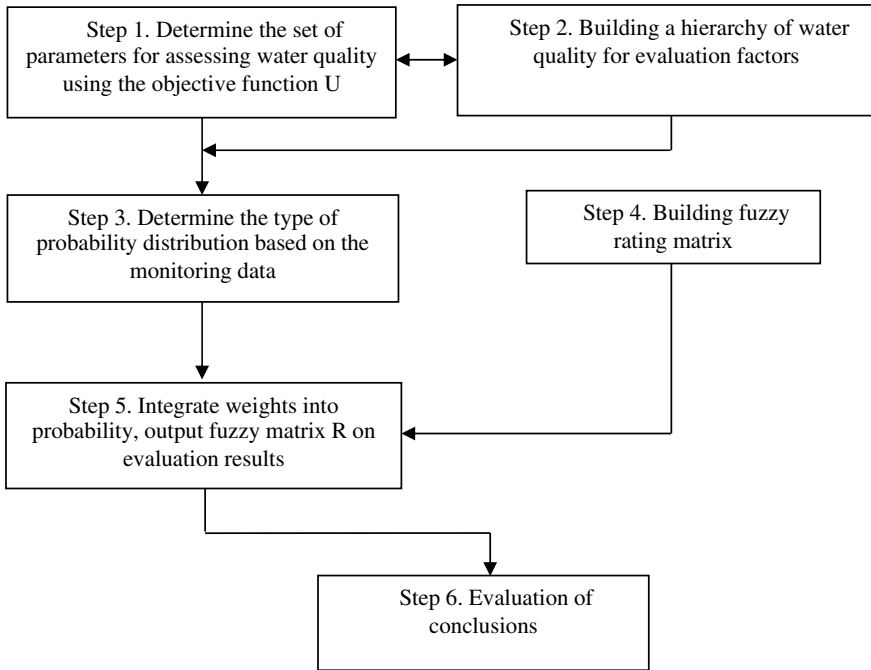
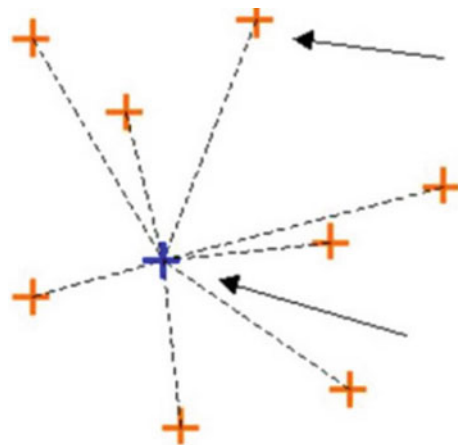


Fig. 37.2 Steps of hierarchical evaluation by using fuzzy algorithm (Tran et al. 2014)

Fig. 37.3 Inverse distance weighting method (IDW)



Further, the inverse distance weighting method—a geostatistical analysis techniques—was used to determine the value of unknown points by averaging the distance weights of the values of the points. Known values in the neighborhood of each pixel (Watson and Philip 1985). The further points which are far away from the point

to be calculated have little influence on the calculated value, the closer points, the greater weight. Therefore, it is possible to interpolate the spatial distribution of pollution levels according to FCE at monitoring points based on calculated water quality index by using Fuzzy algorithm to mapping zones of water pollution in Can Gio district. The IDW weighted interpolation formula is expressed as follows:

$$z(x) = \frac{\sum_i w_i z_i}{\sum_i w_i}$$

whereas W_i the weights depend on the distance. Interpolation calculations were performed by using ArcGIS 10.7. software.

37.3 Results and Discussion

37.3.1 *Current Status of Coastal Water Quality in the Can Gio District*

According to Economic Department of Can Gio District People's Committee (2019), the total value of seafood production in the period 2015–2019 reached 7109 billion VND, a growth rate of 19%/year, corresponding to the total production of aquaculture and marine products are 134,322 tons (average 26,864 tons/year) (Department Economy 2021; Department of Statistics 2018). The ratio of income and profit from the main livelihoods of aquaculture activities is relatively high. Households' income comes from various livelihood activities such as shrimp farming (prawn and white leg shrimp), fish, crab, mollusk farming (clams, oysters, oysters) which occupy the planned area of 5035 ha. Son et al. (2021) indicated that the impact of livelihood activities on water environment was identified at medium level. However, the impact of aquaculture cultivation practices on the quality of water environment ranges from the level of medium to minor impact (from 3 to 4) compared to other livelihood activities. Water quality at receiving waterbodies was assessed by 35 water samples collected at locations of wastewater discharged from aquaculture activities is shown in Figs. 37.4 and 37.5 (Son et al. 2021).

The results showed that the contents of DO, BOD₅, COD, NH₄⁺-N, NO₃⁻-N, NO₂⁻-N, from most of water samples meet the allowable levels of surface water quality—QCVN 08-MT:2015/BTNMT (Class B1) and the quality of shrimp farming water—QCVN 02-19:2014/BNNPTNT (see Figs. 37.4 and 37.5). However, the concentration of total organic carbon (TOC) at the same sampling sites exceeds permissible limits of QCVN 08-MT:2015/BTNMT (>4 mg/L) (Fig. 37.4). The content of P-PO₄³⁻ at sampling site NM34 is the highest (0.45 mg/l) exceeding the permitted level of QCVN 08-MT:2015/BTNMT (with (PO₄³⁻-P < 0.3 mg/L) (Fig. 37.5). The contents of NH₄⁺-N, NO₃⁻-N, NO₂⁻-N meet the allowable

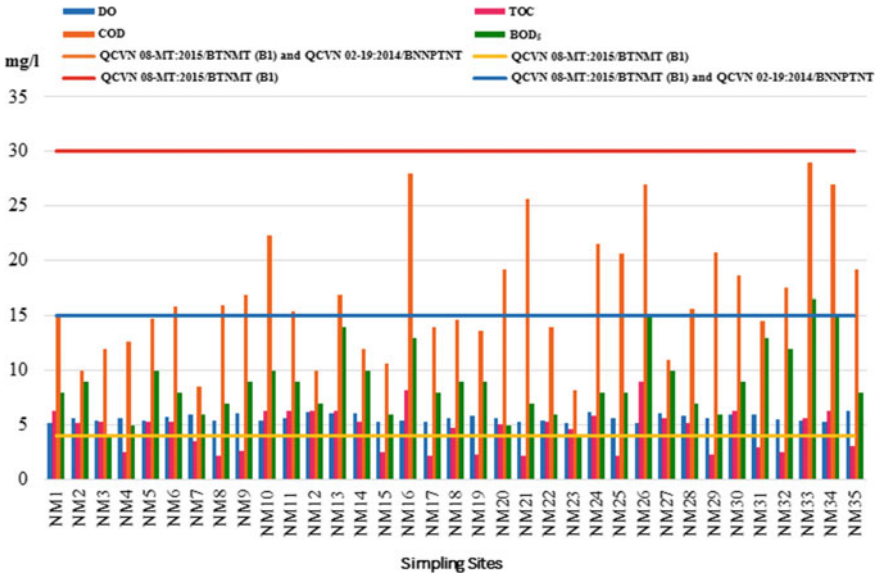


Fig. 37.4 The content of DO, BOD₅, COD và TOC from surface water at receiving waterbodies

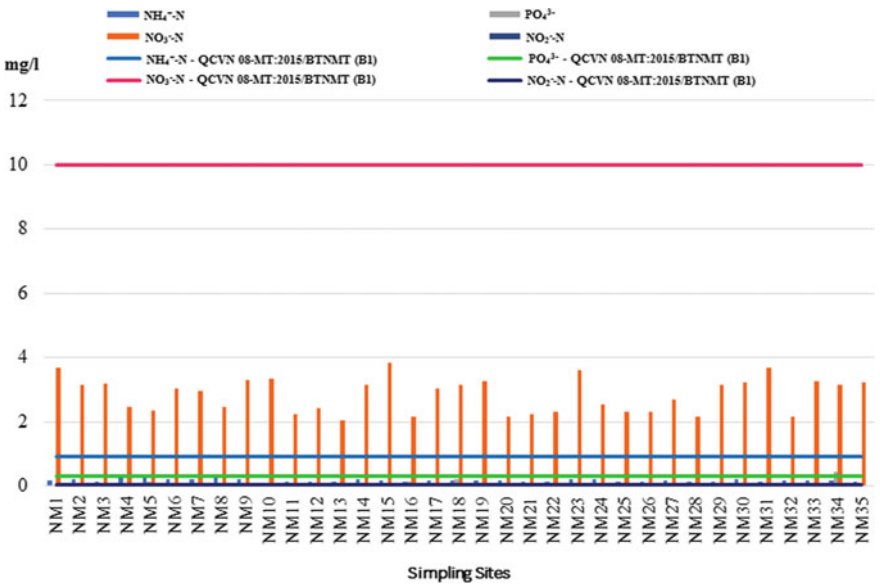


Fig. 37.5 The content of NH₄⁺-N, PO₄³⁻-P, NO₃⁻-N và NO₂⁻-N from surface water at receiving waterbodies of aquaculture cultivation practice

levels of surface water quality QCVN 08-MT:2015/BTNMT (Fig. 37.5). However, aquaculture activities are posing negative impacts on the water environment.

37.3.2 The Quality of Surface Water in Can Gio Coastal Area Using FCE

Based on the steps of performing hierarchical evaluation according to the Fuzzy algorithm and grading parameters based on Decision 1460/QĐ-TCMT, water quality was evaluated by FCE through the following 8 steps:

- Step 1 Statistically remove some parameters that are not suitable for WQI. From Table 37.2, select and remove some unsuitable parameters for the calculation process. There are 10 factors participating in water quality selected to be included in the assessment model, including: pH, DO, BOD₅, COD, TOC, NH₄⁺-N, NO₃⁻-N, NO₂⁻-N, PO₄³⁻-P, Coliform (Fig. 37.6).
- Step 2 Calculate DO % saturation. The DO parameter is calculated according to the interval so it will be converted according to formula (37.1)

$$DO_{\text{saturation}} = A / (14.652 - 0.41022.T + 0.007991.(T)^2 - 0.00007774.(T)^3) \times 100. \tag{37.1}$$

wherein, *A* is the DO value; *T* is the water temperature at the time of monitoring (°C) (Fig. 37.7)

- Step 3 Calculate the case of multiple thresholds. For pH and DO, there will be 3 threshold levels (high, middle, and low), for the remaining parameters,

Table 37.2 Calculation of multiple thresholds

Parameter	High	Middle	Low
pH	9	7	5.5
DO	158.3	100	20
COD		51	
BOD ₅		20	
NH ₄ ⁺ -N		1.42	
PO ₄ ³⁻ -P		1.02	
Coliform		7000	
NO ₃ ⁻ -N		9.4	
NO ₂ -N		0.02	
TOC		20	

Sample Code	Commune	Coordinates X	Parameter	Unit	Sampling batch 1	Sample Code	Parameter	Unit	Sampling batch 1	Sample Code	Parameter	High	Middle	Low
NM1	Binh Khanh	10°38'09.8"N, 106°48'20.3"E	pH	-	6.47	NM1	pH	-	6.47	NM1	pH	9	7	5.5
			DO	mg/l	5.21		DO	mg/l	69.5235322		DO	158.333	100	20
			COD	mg/l	15.9		COD	mg/l	15.9		COD	51		
			BOD5	mg/l	8		BOD5	mg/l	8		BOD5	20		
			NH ₄ -N	mg/l	0.184		NH ₄ -N	mg/l	0.184		NH ₄ -N	1.42		
			PO ₄ -P	mg/l	0.01		PO ₄ -P	mg/l	0.15		PO ₄ -P	1.02		
			Coliform	MBN	1700		Coliform	MBN	1,700		Coliform	7000		
			NO ₂ -N	mg/l	3.67		NO ₂ -N	mg/l	3.67		NO ₂ -N	9.4		
			NO ₃ -N	mg/l	0.012		NO ₃ -N	mg/l	0.02		NO ₃ -N	0.02		
			TOC	mg/l	6.35		TOC	mg/l	10		TOC	20		
			Nhait đô	oC	29.6									
			NM2	Binh Khanh	10°37'43.2"N, 106°47'11.4"E		pH	-	6.47		NM2	pH	-	6.47
DO	mg/l	5.64				DO	mg/l	71.7939932	DO	158.333		100	20	
COD	mg/l	10.0				COD	mg/l	10.0	COD	51				
BOD5	mg/l	9				BOD5	mg/l	9	BOD5	20				
NH ₄ -N	mg/l	0.21				NH ₄ -N	mg/l	0.21	NH ₄ -N	1.42				
PO ₄ -P	mg/l	0.07				PO ₄ -P	mg/l	0.07	PO ₄ -P	1.02				
Coliform	MBN	2400				Coliform	MBN	2400	Coliform	7000				
NO ₂ -N	mg/l	3.15				NO ₂ -N	mg/l	3.15	NO ₂ -N	9.4				
NO ₃ -N	mg/l	0.026				NO ₃ -N	mg/l	0.026	NO ₃ -N	0.02				
TOC	mg/l	5.19				TOC	mg/l	5.19	TOC	20				
Nhait đô	oC	27.1												

Fig. 37.6 Statistics of some suitable parameters for WQI

Sample Code	Commune	Coordinates X	Parameter	Unit	Sampling batch 1	Sample Code	Parameter	Unit	Sampling batch 1	Sample Code	Parameter	High	Middle	Low
NM1	Binh Khanh	10°38'09.8"N, 106°48'20.3"E	pH	-	6.47	NM1	pH	-	6.47	NM1	pH	9	7	5.5
			DO	mg/l	5.21		DO	mg/l	69.5235322		DO	158.333	100	20
			COD	mg/l	15.9		COD	mg/l	15.9		COD	51		
			BOD5	mg/l	8		BOD5	mg/l	8		BOD5	20		
			NH ₄ -N	mg/l	0.184		NH ₄ -N	mg/l	0.184		NH ₄ -N	1.42		
			PO ₄ -P	mg/l	0.01		PO ₄ -P	mg/l	0.15		PO ₄ -P	1.02		
			Coliform	MBN	1700		Coliform	MBN	1,700		Coliform	7000		
			NO ₂ -N	mg/l	3.67		NO ₂ -N	mg/l	3.67		NO ₂ -N	9.4		
			NO ₃ -N	mg/l	0.012		NO ₃ -N	mg/l	0.02		NO ₃ -N	0.02		
			TOC	mg/l	6.35		TOC	mg/l	10		TOC	20		
			Nhait đô	oC	29.6									
			NM2	Binh Khanh	10°37'43.2"N, 106°47'11.4"E		pH	-	6.47		NM2	pH	-	6.47
DO	mg/l	5.64				DO	mg/l	71.7939932	DO	158.333		100	20	
COD	mg/l	10.0				COD	mg/l	10.0	COD	51				
BOD5	mg/l	9				BOD5	mg/l	9	BOD5	20				
NH ₄ -N	mg/l	0.21				NH ₄ -N	mg/l	0.21	NH ₄ -N	1.42				
PO ₄ -P	mg/l	0.07				PO ₄ -P	mg/l	0.07	PO ₄ -P	1.02				
Coliform	MBN	2400				Coliform	MBN	2400	Coliform	7000				
NO ₂ -N	mg/l	3.15				NO ₂ -N	mg/l	3.15	NO ₂ -N	9.4				
NO ₃ -N	mg/l	0.026				NO ₃ -N	mg/l	0.026	NO ₃ -N	0.02				
TOC	mg/l	5.19				TOC	mg/l	5.19	TOC	20				
Nhait đô	oC	27.1												

Fig. 37.7 Calculation of DO % saturation

only the middle threshold level will be calculated by the average sum of the hierarchy (I + II + II + IV + V)/5 (Fig. 37.8).

Step 4 Calculate C_i/S_i flexible weighting for all parameters. For the pH and DO values, they are calculated as formula (37.2):

$$IF(B < 4.5, (Z)/B, IF(AND(B > 4.5, B < 9.5), B/Y, IF(B \geq 9.5, B/X))) \tag{37.2}$$

If $B < 4.5$, then the weighted value is the low threshold; if $4.5 < B < 9$, then the weighted value is the middle threshold, otherwise if $B \geq 9.5$ then the weighted value is the high threshold.

=(75+88+112+125)/4

Sample Code	Parameter	Unit	Sampling batch 1	Sample Code	Parameter	High	Middle	Low	Sample Code	Parameter	Sampling batch 1	Sample Code	Parameter	Sampling batch 1
NM1	pH	-	6.47	NM1	pH	9	7	5.5	NM1	pH	0.92	NM1	pH	0.20
	DO	mg/l	69.5235322		DO	158.333	100	20		DO	0.70		DO	0.15
	COD	mg/l	15.0		COD	51	20			COD	0.29		COD	0.06
	BOD ₅	mg/l	8		BOD ₅	20				BOD ₅	0.40		BOD ₅	0.08
	NH ₄ ⁺ -N	mg/l	0.184		NH ₄ ⁺ -N	1.42				NH ₄ ⁺ -N	0.13		NH ₄ ⁺ -N	0.03
	PO ₄ ³⁻ -P	mg/l	0.15		PO ₄ ³⁻ -P	1.02				PO ₄ ³⁻ -P	0.15		PO ₄ ³⁻ -P	0.03
	Coliform	MBN	1,700		Coliform	7000				Coliform	0.24		Coliform	0.05
	NO ₃ ⁻ -N	mg/l	3.67		NO ₃ ⁻ -N	9.4				NO ₃ ⁻ -N	0.39		NO ₃ ⁻ -N	0.08
	NO ₂ ⁻ -N	mg/l	0.02		NO ₂ ⁻ -N	0.02				NO ₂ ⁻ -N	1.00		NO ₂ ⁻ -N	0.21
	TOC	mg/l	10		TOC	20				TOC	0.50		TOC	0.11
								4.72						1.00
NM2	pH	-	6.47	NM2	pH	9	7	5.5	NM2	pH	0.92	NM2	pH	0.19
	DO	mg/l	71.7939932		DO	158.333	100	20		DO	0.72		DO	0.15
	COD	mg/l	10.0		COD	51				COD	0.20		COD	0.04
	BOD ₅	mg/l	9		BOD ₅	20				BOD ₅	0.45		BOD ₅	0.09
	NH ₄ ⁺ -N	mg/l	0.21		NH ₄ ⁺ -N	1.42				NH ₄ ⁺ -N	0.15		NH ₄ ⁺ -N	0.03
	PO ₄ ³⁻ -P	mg/l	0.07		PO ₄ ³⁻ -P	1.02				PO ₄ ³⁻ -P	0.07		PO ₄ ³⁻ -P	0.01
	Coliform	MBN	2400		Coliform	7000				Coliform	0.34		Coliform	0.07
	NO ₃ ⁻ -N	mg/l	3.15		NO ₃ ⁻ -N	9.4				NO ₃ ⁻ -N	0.34		NO ₃ ⁻ -N	0.07
	NO ₂ ⁻ -N	mg/l	0.026		NO ₂ ⁻ -N	0.02				NO ₂ ⁻ -N	1.30		NO ₂ ⁻ -N	0.27
	TOC	mg/l	5.19		TOC	20				TOC	0.26		TOC	0.05
								4.74						1.00

Fig. 37.8 Calculation of multiple thresholds

For BOD₅, COD, TOC, NH₄⁺-N, NO₃⁻-N, NO₂⁻-N, PO₄³⁻-P, Coliform parameters, they are calculated as formula (37.3):

$$B/Y \tag{37.3}$$

whereas B is the calculated parameter value from DO % saturation; X is the high threshold; Y is the middle threshold; Z is the low threshold (Fig. 37.9).

Step 5 Normalize the weights for the parameters participating in the evaluation as formula (37.4):

$$C/W \tag{37.4}$$

=IF(L7<20,(R7)/L7,IF(AND(L7>20,L7<=200),L7/Q7,IF(L7>200,L7/P7)))

Sample Code	Parameter	High	Middle	Low	Sample Code	Parameter	Sampling batch 1	Sample Code	Parameter	Sampling batch 1	Sample Code	Parameter	Unit	Non-polluted 1	Lightly-polluted 1	
NM1	pH	9	7	5.5	NM1	pH	0.92	NM1	pH	0.20	NM1	pH	-	0.94	0.06	
	DO	158.333	100	20		DO	0.70		DO	0.15		DO	mg/l	0.00	0.78	
	COD	51				COD	0.29		COD	0.06		COD	mg/l	0.00	1.00	
	BOD ₅	20				BOD ₅	0.40		BOD ₅	0.08		BOD ₅	mg/l	0.00	0.78	
	NH ₄ ⁺ -N	1.42				NH ₄ ⁺ -N	0.13		NH ₄ ⁺ -N	0.03		NH ₄ ⁺ -N	mg/l	1.00	0.00	
	PO ₄ ³⁻ -P	1.02				PO ₄ ³⁻ -P	0.15		PO ₄ ³⁻ -P	0.15		PO ₄ ³⁻ -P	mg/l	0.50	0.50	
	Coliform	7000				Coliform	0.24		Coliform	0.05		Coliform	MBN	1.00	0.00	
	NO ₃ ⁻ -N	9.4				NO ₃ ⁻ -N	0.39		NO ₃ ⁻ -N	0.08		NO ₃ ⁻ -N	mg/l	0.44	0.56	
	NO ₂ ⁻ -N	0.02				NO ₂ ⁻ -N	1.00		NO ₂ ⁻ -N	0.21		NO ₂ ⁻ -N	mg/l	1.00	0.00	
	TOC	20				TOC	0.50		TOC	0.11		TOC	mg/l	0.00	0.56	
							4.72									
NM2	pH	9	7	5.5	NM2	pH	0.92	NM2	pH	0.19	NM2	pH	-	0.94	0.06	
	DO	158.333	100	20		DO	0.72		DO	0.15		DO	mg/l	0.00	0.87	
	COD	51				COD	0.20		COD	0.04		COD	mg/l	1.00	0.00	
	BOD ₅	20				BOD ₅	0.45		BOD ₅	0.09		BOD ₅	mg/l	0.00	0.67	
	NH ₄ ⁺ -N	1.42				NH ₄ ⁺ -N	0.15		NH ₄ ⁺ -N	0.03		NH ₄ ⁺ -N	mg/l	1.00	0.00	
	PO ₄ ³⁻ -P	1.02				PO ₄ ³⁻ -P	0.07		PO ₄ ³⁻ -P	0.01		PO ₄ ³⁻ -P	mg/l	1.00	0.00	
	Coliform	7000				Coliform	0.34		Coliform	0.07		Coliform	MBN	1.00	0.00	
	NO ₃ ⁻ -N	9.4				NO ₃ ⁻ -N	0.34		NO ₃ ⁻ -N	0.07		NO ₃ ⁻ -N	mg/l	0.62	0.38	
	NO ₂ ⁻ -N	0.02				NO ₂ ⁻ -N	1.30		NO ₂ ⁻ -N	0.27		NO ₂ ⁻ -N	mg/l	1.00	0.00	
	TOC	20				TOC	0.26		TOC	0.05		TOC	mg/l	0.41	0.60	
							4.74									

Fig. 37.9 Calculation of C_i/S_i flexible weighting for all parameters

Sample Code	Parameter	Sampling batch I	Sample Code	Parameter	Sampling batch I	Sample Code	Parameter	Unit	Non-polluted I	Lightly polluted II	Moderately polluted III	Heavy polluted IV	Severely polluted V	Sum	
NM1	pH	0.92	NM1	pH	0.20	NM1	pH	-	0.94	0.06	0.00	0.00	0.00	1.00	
	DO	0.70		DO	0.15		DO	mg/l	0.00	0.78	0.22	0.00	0.00	0.00	1.00
	COD	0.29		COD	0.06		COD	mg/l	0.00	1.00	0.00	0.00	0.00	0.00	1.00
	BOD5	0.40		BOD5	0.08		BOD5	mg/l	0.00	0.78	0.22	0.00	0.00	0.00	1.00
	NH ₄ -N	0.13		NH ₄ -N	0.03		NH ₄ -N	mg/l	1.00	0.00	0.00	0.00	0.00	0.00	1.00
	PO ₄ -P	0.15		PO ₄ -P	0.03		PO ₄ -P	mg/l	0.50	0.50	0.00	0.00	0.00	0.00	1.00
	Coliform	0.24		Coliform	0.05		Coliform	MBN	1.00	0.00	0.00	0.00	0.00	0.00	1.00
	NO ₃ -N	0.39		NO ₃ -N	0.08		NO ₃ -N	mg/l	0.44	0.56	0.00	0.00	0.00	0.00	1.00
	NO ₂ -N	1.00		NO ₂ -N	0.21		NO ₂ -N	mg/l	1.00	0.00	0.00	0.00	0.00	0.00	1.00
	TOC	0.50		TOC	0.11		TOC	mg/l	0.00	0.56	0.44	0.00	0.00	0.00	1.00
		4.73			1.00										
NM2	pH	0.92	NM2	pH	0.19	NM2	pH	-	0.94	0.06	0.00	0.00	0.00	1.00	
	DO	0.72		DO	0.15		DO	mg/l	0.00	0.87	0.13	0.00	0.00	0.00	1.00
	COD	0.20		COD	0.04		COD	mg/l	1.00	0.00	0.00	0.00	0.00	0.00	1.00
	BOD5	0.45		BOD5	0.09		BOD5	mg/l	0.00	0.67	0.33	0.00	0.00	0.00	1.00
	NH ₄ -N	0.15		NH ₄ -N	0.03		NH ₄ -N	mg/l	1.00	0.00	0.00	0.00	0.00	0.00	1.00
	PO ₄ -P	0.07		PO ₄ -P	0.01		PO ₄ -P	mg/l	1.00	0.00	0.00	0.00	0.00	0.00	1.00
	Coliform	0.34		Coliform	0.07		Coliform	MBN	1.00	0.00	0.00	0.00	0.00	0.00	1.00
	NO ₃ -N	0.34		NO ₃ -N	0.07		NO ₃ -N	mg/l	0.62	0.38	0.00	0.00	0.00	0.00	1.00
	NO ₂ -N	1.30		NO ₂ -N	0.27		NO ₂ -N	mg/l	1.00	0.00	0.00	0.00	0.00	0.00	1.00
	TOC	0.26		TOC	0.05		TOC	mg/l	0.41	0.60	0.00	0.00	0.00	0.00	1.00
		4.74			1.00										

Fig. 37.10 Normalizing weights for the parameters of evaluation

wherein C is the C_i/S_i value of each parameter; W is the sum of the weights. The sum of the normalized weights for all parameters with a value of 1.00 is correct (Fig. 37.10).

Step 6 Calculate the membership function value for each parameter.

For a membership function with a hierarchical level I (non-polluted) is calculated as formula (37.5) below:

$$\begin{aligned}
 \text{Hierarchical level I} &= \text{IF}(\text{AND}(B \geq 6.5, B \leq 7.5), 1, \\
 &\text{IF}(\text{AND}(B > 6, B < 6.5), (6 - B)/(66.5), \\
 &\text{IF}(\text{AND}(B > 7.5, B < 8), (8 - B)/(8 - 7.5), 0))) \quad (37.5)
 \end{aligned}$$

If $(6.5 \leq B \leq 7.5)$ then give the value 1, if $(6 < B < 6.5)$ give the value $((6 - B)/(6 - 6.5))$, if $(7.5 < B < 8)$ then give value $((8 - B)/(8 - 7.5))$, the remaining conditions give value 0.

For a membership function with a hierarchical level II (lightly polluted)—III (moderately polluted)—IV (heavy polluted) is calculated as formula (37.6):

$$\begin{aligned}
 \text{Hierarchical level II} &= \text{IF}(\text{AND}(B \geq 6, B \leq 6.5), (B - 6.5)/(6 - 6.5), \\
 &\text{IF}(\text{AND}(B > 5, B < 6), (5 - B)/(5 - 6), \\
 &\text{IF}(\text{AND}(B > 7.5, B \leq 8), (B - 7.5)/(8 - 7.5), \\
 &\text{IF}(\text{AND}(B > 8, B < 9), (9 - B)/(9 - 8), 0))) \quad (37.6)
 \end{aligned}$$

If $(6 \leq B \leq 6.5)$ give the value $((B - 6.5)/(6 - 6.5))$, if $(5 < B < 6)$ give the value $((5 - B)/(5 - 6))$, if $(7.5 < B \leq 8)$ give the value $((B - 7.5)/(8 - 7.5))$, if $(8 < B < 9)$ give the value $((9 - B)/(9 - 8))$, the remaining conditions give value 0.

$$\begin{aligned} \text{Hierarchical level III} = & \text{IF}(\text{AND}(B \geq 5, B < 6), (B - 6)/(5 - 6), \\ & \text{IF}(\text{AND}(B > 4.5, B < 5), (4.5 - B)/(4.5 - 5), \\ & \text{IF}(\text{AND}(B > 8, B \leq 9), (B - 8)/(9 - 8), \\ & \text{IF}(\text{AND}(B > 9, B < 9.5), (9.5 - B)/(9.5 - 9), 0)) \end{aligned} \tag{37.7}$$

If $(5 \leq B < 6.5)$ give the value $((B - 6)/(5 - 6))$, if $(4.5 < B < 5)$ give the value $((4.5 - B)/(4.5 - 5))$, if $(8 < B \leq 9)$ give the value $((B - 8)/(9 - 8))$, if $(9 < B < 9.5)$ give the value $((9.5 - B)/(9.5 - 9))$, the remaining conditions give value 0.

$$\begin{aligned} \text{Hierarchical level IV} = & \text{IF}(\text{AND}(B \geq 4.5, B < 5), (B - 5)/(4.5 - 5), \\ & \text{IF}(\text{AND}(B > 9, B < 9.5), (B - 9)/(9.5 - 9), 0) \end{aligned} \tag{37.8}$$

If $(4.5 \leq B < 5)$ give the value $((B - 5)/(4.5 - 5))$, if $(9 < B < 9.5)$ give the value $((B - 9)/(9.5 - 9))$, the remaining conditions give value 0.

For a membership function with a hierarchical structure V (severely polluted) is calculated according to formula (37.9):

$$\text{Hierarchical level V} = \text{IF}(B < 4.5, 1, \text{IF}(B > 9.5, 1, 0)) \tag{37.9}$$

If $(B < 4.5)$ then give the value 1, if $(B > 9.5)$ then give the value 1, the remaining conditions give value 0. The sum of membership function values with a hierarchy of each parameter in order will give a value of 1.00 which is correct (Fig. 37.11).

$=\text{IF}(\text{AND}(L6 \geq 6.5, L6 < 7.5), 1, \text{IF}(\text{AND}(L6 > 6, L6 < 8), (6 - L6)/(6 - 6.5), \text{IF}(\text{AND}(L6 > 7.5, L6 < 8), (8 - L6)/(8 - 7.5), 0)))$

Sample Code	Parameter	Sampling batch I	Sample Code	Parameter	Unit	Non-polluted I	Lightly polluted II	Moderately polluted III	Heavy polluted IV	Severely polluted V	Sum	Sample Code	Non-polluted I	Lightly polluted II	Moderately polluted III	Heavy polluted IV	Severely polluted V	
NM1	pH	0.20	NM1	pH	-	0.94	0.06	0.00	0.00	0.00	1.00	NM1	0.18	0.01	0.00	0.00	0.00	
	DO	0.15		DO	mg/l	0.00	0.78	0.22	0.00	0.00	1.00		0.00	0.11	0.03	0.00	0.00	0.00
	COD	0.06		COD	mg/l	0.00	1.00	0.00	0.00	0.00	1.00		0.00	0.06	0.00	0.00	0.00	0.00
	BOD5	0.08		BOD5	mg/l	0.00	0.78	0.22	0.00	0.00	1.00		0.00	0.07	0.02	0.00	0.00	0.00
	NH ₄ -N	0.03		NH ₄ -N	mg/l	1.00	0.00	0.00	0.00	0.00	0.00		1.00	0.03	0.00	0.00	0.00	0.00
	PO ₄ -P	0.03		PO ₄ -P	mg/l	0.50	0.50	0.00	0.00	0.00	0.00		1.00	0.02	0.02	0.00	0.00	0.00
	Coliform	0.05		Coliform	MBN	1.00	0.00	0.00	0.00	0.00	0.00		1.00	0.05	0.00	0.00	0.00	0.00
	NO ₃ -N	0.08		NO ₃ -N	mg/l	0.44	0.56	0.00	0.00	0.00	0.00		1.00	0.04	0.05	0.00	0.00	0.00
	NO ₂ -N	0.21		NO ₂ -N	mg/l	1.00	0.00	0.00	0.00	0.00	0.00		1.00	0.21	0.00	0.00	0.00	0.00
	TOC	0.11		TOC	mg/l	0.00	0.56	0.44	0.00	0.00	0.00		1.00	0.00	0.06	0.05	0.00	0.00
		1.00																
NM2	pH	0.19	NM2	pH	-	0.94	0.06	0.00	0.00	0.00	1.00	NM2	0.18	0.01	0.00	0.00	0.00	
	DO	0.15		DO	mg/l	0.00	0.87	0.13	0.00	0.00	1.00		0.00	0.13	0.02	0.00	0.00	
	COD	0.04		COD	mg/l	1.00	0.00	0.00	0.00	0.00	1.00		0.04	0.00	0.00	0.00	0.00	
	BOD5	0.09		BOD5	mg/l	0.00	0.67	0.33	0.00	0.00	1.00		0.00	0.06	0.03	0.00	0.00	
	NH ₄ -N	0.03		NH ₄ -N	mg/l	1.00	0.00	0.00	0.00	0.00	1.00		0.03	0.00	0.00	0.00	0.00	
	PO ₄ -P	0.01		PO ₄ -P	mg/l	1.00	0.00	0.00	0.00	0.00	1.00		0.01	0.00	0.00	0.00	0.00	
	Coliform	0.07		Coliform	MBN	1.00	0.00	0.00	0.00	0.00	1.00		0.07	0.00	0.00	0.00	0.00	
	NO ₃ -N	0.07		NO ₃ -N	mg/l	0.62	0.38	0.00	0.00	0.00	1.00		0.04	0.03	0.00	0.00	0.00	
	NO ₂ -N	0.27		NO ₂ -N	mg/l	1.00	0.00	0.00	0.00	0.00	1.00		0.27	0.00	0.00	0.00	0.00	
	TOC	0.05		TOC	mg/l	0.41	0.60	0.00	0.00	0.00	1.00		0.02	0.03	0.00	0.00	0.00	
		1.00			eC													

Fig. 37.11 Calculate the membership function value for each parameter

Step 7 Multiply the membership function matrix by the weight vector, which is calculated according to formula (37.10):

$$\text{BoR} = \text{D.V} \tag{37.10}$$

whereas D is the normalized value from the weighted normalization calculation of parameters; V is the value of each parameter of hierarchical {I, II, III, IV, V}. The sum of the values of the parameters by hierarchical and the sum of the values of the five hierarchies will have a value of 1.00 which is correct (Fig. 37.12).

Step 8 Conclusion of hierarchical pollution level.

To conclude that the sampling point belongs to which hierarchical level of pollution, it is calculated as formula (37.11)

$$\text{IF}((\text{E1} = \text{MAX}(\text{F})), \$\text{U1}, \text{IF}((\text{E2} = \text{MAX}(\text{F})), \$\text{U2}, \text{IF}((\text{E3} = \text{MAX}(\text{F})), \$\text{U3}, \text{IF}((\text{E4} = \text{MAX}(\text{F})), \$\text{U4}, \text{IF}((\text{E5} = \text{MAX}(\text{F})), \$\text{U5})))))) \tag{37.11}$$

If (E1 = MAX(F)) then give the value of non-polluted—I, if (E2 = MAX(F)) then give the value of lightly polluted—II, if (E3 = MAX(F)) then give the value of moderately polluted—III, if (E4 = MAX(F)) then give the value of heavy polluted—IV, if (E5 = MAX(F)) then give the value of severely polluted—V.

The max probability is calculated as formula (37.12)

$$\text{IF}((\text{E1} = \text{MAX}(\text{F})), \text{E1}, \text{IF}((\text{E2} = \text{MAX}(\text{F})), \text{E2}, \text{IF}((\text{E3} = \text{MAX}(\text{F})), \text{E3}, \text{IF}((\text{E4} = \text{MAX}(\text{F})), \text{E4}, \text{IF}((\text{E5} = \text{MAX}(\text{F})), \text{E5}))))))$$

Sample Code	Parameters	Unit	Non-polluted I	Lightly polluted II	Moderately polluted III	Heavy polluted IV	Severely polluted V	Sum	Sample Code	Non-polluted I	Lightly polluted II	Moderately polluted III	Heavy polluted IV	Severely polluted V	Conclusion
NM1	pH	-	0.94	0.06	0.00	0.00	0.00	1.00	NM1	0.18	0.01	0.00	0.00	0.00	Non-polluted I
	DO	mg/l	0.00	0.78	0.22	0.00	0.00	1.00		0.00	0.11	0.03	0.00	0.00	
	COD	mg/l	0.00	1.00	0.00	0.00	0.00	1.00		0.00	0.06	0.00	0.00	0.00	
	BOD5	mg/l	0.00	0.78	0.22	0.00	0.00	1.00		0.00	0.07	0.02	0.00	0.00	
	NH4-N	mg/l	1.00	0.00	0.00	0.00	0.00	1.00		0.03	0.00	0.00	0.00	0.00	
	PO4-P	mg/l	0.50	0.50	0.00	0.00	0.00	1.00		0.02	0.02	0.00	0.00	0.00	
	Coliform	MBN/l	1.00	0.00	0.00	0.00	0.00	1.00		0.05	0.00	0.00	0.00	0.00	
	NO1	mg/l	0.44	0.56	0.00	0.00	0.00	1.00		0.04	0.05	0.00	0.00	0.00	
	NO2	mg/l	1.00	0.00	0.00	0.00	0.00	1.00		0.21	0.00	0.00	0.00	0.00	
	TOC	mg/l	0.00	0.56	0.44	0.00	0.00	1.00		0.00	0.06	0.03	0.00	0.00	
NM2	pH	-	0.94	0.06	0.00	0.00	0.00	1.00	NM2	0.18	0.01	0.00	0.00	0.00	Non-polluted I
	DO	mg/l	0.00	0.87	0.13	0.00	0.00	1.00		0.00	0.13	0.02	0.00	0.00	
	COD	mg/l	1.00	0.00	0.00	0.00	0.00	1.00		0.04	0.00	0.00	0.00	0.00	
	BOD5	mg/l	0.00	0.87	0.13	0.00	0.00	1.00		0.00	0.06	0.03	0.00	0.00	
	NH4-N	mg/l	1.00	0.00	0.00	0.00	0.00	1.00		0.03	0.00	0.00	0.00	0.00	
	PO4-P	mg/l	1.00	0.00	0.00	0.00	0.00	1.00		0.01	0.00	0.00	0.00	0.00	
	Coliform	MBN/l	1.00	0.00	0.00	0.00	0.00	1.00		0.07	0.00	0.00	0.00	0.00	
	NO1	mg/l	0.62	0.38	0.00	0.00	0.00	1.00		0.04	0.03	0.00	0.00	0.00	
	NO2	mg/l	1.00	0.00	0.00	0.00	0.00	1.00		0.27	0.00	0.00	0.00	0.00	
	TOC	mg/l	0.41	0.60	0.00	0.00	0.00	1.00		0.02	0.03	0.00	0.00	0.00	
ΣC									0.68	0.27	0.05	0.00	0.00	1.00	

Fig. 37.12 Multiply the membership function matrix by the weight vector

$$\text{IF}((E5 = \text{MAX}(F), E5)))) \tag{37.12}$$

If (E1 = MAX(F)) give the value E1, if (E2 = MAX(F)) give the value E2, if (E3 = MAX(F)) give the value E3, if (E4 = MAX(E)) give the value E4, if (E5 = MAX(F)) give the value E5.

Wherein *E1, E2, E3, E4, E5* is the value of each parameter of hierarchical {I, II, III, IV, V}; *F* is the total value of E1 + E2 + E3 + E4 + E5; *U1, U2, U3, U4, U5* is the value corresponding to the hierarchical level of pollution.

In order to conclude hierarchical level of pollution of monitoring site, it is calculated as formula (37.13):

$$\text{IF}((S = \$U1), 1, \text{IF}((S = \$U2), 2, \text{IF}((S = \$U3), 3, \text{IF}((S = \$U4), 4, \text{IF}((S = \$U5), 5)))))) \tag{37.13}$$

If (S = \$U1) then give the value 1, if (S = \$U2) then give the value 2, if (S = \$U3) then give the value 3, if (S = \$U4) then give the value 4, if (S = \$U5) then give the value 5.

Whereas *S* is the result of the calculated value of pollution hierarchy (Fig. 37.13).

In order to ultimate conclusion for each sampling point (including results from 2 monitoring seasons), it is necessary to calculate the overall average in different ways as follows Table 37.3:

The final conclusion of water pollution hierarchy is calculated by formula (37.14)

$$\begin{aligned} &\text{IF}(P < 1.5, \$U1, \text{IF}(\text{AND}(P > 1.5, P < 2.5), \$U2, \\ &\text{IF}(\text{AND}(P \geq 2.5, P < 3.5), \$U3, \\ &\text{IF}(\text{AND}(P \geq 3.5, P < 4.5), \$U4, \text{IF}(P > 4.5, \$U5)))))) \end{aligned} \tag{37.14}$$

=IF((AM16=MAX(AM16:AQ16)), \$AM54, IF((AN16=MAX(AM16:AQ16)), \$AN54, IF((AO16=MAX(AM16:AQ16)), \$AO54, IF((AP16=MAX(AM16:AQ16)), \$AP54, IF((AQ16=MAX(AM16:AQ16)), \$AQ54))))))																		
AK	AL	AM	AN	AO	AP	AQ	AR	AS	AT	AU	AV	AW	AX	AY	AZ	BA	Form	
Sample Code	Non-polluted I	Slightly polluted II	Moderately polluted III	Heavy polluted IV	Severely polluted V				Conclusion	The max probability	The pollutant hierarchy							
NM1	0.18	0.01	0.00	0.00	0.00				NM1	Non-polluted I	0.53	I						
	0.00	0.11	0.03	0.00	0.00													
	0.00	0.06	0.00	0.00	0.00													
	0.00	0.07	0.02	0.00	0.00													
	0.03	0.00	0.00	0.00	0.00													
	0.02	0.02	0.00	0.00	0.00													
	0.05	0.00	0.00	0.00	0.00													
	0.04	0.05	0.00	0.00	0.00													
	0.21	0.00	0.00	0.00	0.00													
	0.00	0.06	0.03	0.00	0.00													
NM2	0.53	0.38	0.10	0.00	0.00	1.00				NM2	Non-polluted I	0.68	I					
	0.18	0.01	0.00	0.00	0.00													
	0.00	0.13	0.02	0.00	0.00													
	0.04	0.00	0.00	0.00	0.00													
	0.00	0.06	0.03	0.00	0.00													
	0.03	0.00	0.00	0.00	0.00													
	0.01	0.00	0.00	0.00	0.00													
	0.07	0.00	0.00	0.00	0.00													
	0.04	0.03	0.00	0.00	0.00													
	0.27	0.00	0.00	0.00	0.00													

Fig. 37.13 Conclusion of pollution hierarchy

Table 37.3 Calculation of overall average in different ways

Overall average calculation	Average value for 2 measurements
Trimmean	=TRIMMEAN((R),10%)
Average	=AVERAGE(R)
Geomean	=GEOMEAN(R)
Median	=MEDIAN(R)
Overall average	=AVERAGE(Q)

If ($P < 1.5$) then give the value of non-polluted (Level I), if ($1.5 < P < 2.5$) then give the value of lightly polluted (Level II), if ($2.5 \leq P < 3.5$) then give the value of moderately polluted (Level III), if ($3.5 \leq P < 4$) corresponding to value of heavy polluted (Level IV), if ($P > 4.5$) corresponding to value of severely polluted (Level V).

Whereas R is the total value of 2 monitoring periods of the pollution hierarchy conclusion; Q is the average sum of (Trimmean + Average + Geomean + Median); P is the overall average of pollution hierarchy conclusion (Fig. 37.14).

According to the above-mentioned steps, the calculation result of the pollution hierarchy of Can Gio coastal waters in 2020 is presented in the following Table 37.4.

Water quality in aquaculture areas ranges from non-polluted to moderately polluted in which 18 monitoring points are classified as level 1 (non-polluted), 13 points are level 2 (lightly polluted), and 4 sampling points are ranked as level 3 (moderate polluted). Considering the spatial distribution, three (03) communes are likely to be considered affected by wastewater from aquaculture activities, including Tam Thon Thiep, An Thoi Dong, and Ly Nhon. Particularly, three sampling points in Ly Nhon commune are moderately polluted with pollution hierarchical level III.

NM1				NM19			
	Calculate the overall average in many ways	The total value of 2 monitoring	Conclusion		Calculate the overall average in many ways	The total value of 2 monitoring	Conclusion
General conclusion	TRIMMEAN	1	Non-polluted I	General conclusion	TRIMMEAN	1	Non-polluted I
	Average	1	Non-polluted I		Average	1	Non-polluted I
	Geomean	1	Non-polluted I		Geomean	1	Non-polluted I
	Median	1	Non-polluted I		Median	1	Non-polluted I
	General conclusion	1	Non-polluted I		General conclusion	1	Non-polluted I
NM2				NM20			
	Calculate the overall average in many ways	The total value of 2 monitoring	Conclusion		Calculate the overall average in many ways	The total value of 2 monitoring	Conclusion
General conclusion	TRIMMEAN	1	Non-polluted I	General conclusion	TRIMMEAN	2	Lightly polluted II
	Average	1	Non-polluted I		Average	2	Lightly polluted II
	Geomean	1	Non-polluted I		Geomean	2	Lightly polluted II
	Median	1	Non-polluted I		Median	2	Lightly polluted II
	General conclusion	1	Non-polluted I		General conclusion	2	Lightly polluted II
NM3				NM21			
	Calculate the overall average in many ways	The total value of 2 monitoring	Conclusion		Calculate the overall average in many ways	The total value of 2 monitoring	Conclusion
General conclusion	TRIMMEAN	1	Non-polluted I	General conclusion	TRIMMEAN	1	Non-polluted I
	Average	1	Non-polluted I		Average	1	Non-polluted I
	Geomean	1	Non-polluted I		Geomean	1	Non-polluted I
	Median	1	Non-polluted I		Median	1	Non-polluted I
	General conclusion	1	Non-polluted I		General conclusion	1	Non-polluted I

Fig. 37.14 The pollution hierarchy conclusion

Table 37.4 Results of pollution hierarchy calculated by using FCE technique

Sample code	Coordinates	Commune	FCE calculation	Conclusion
NM1	10° 38' 09.8" N; 106° 48' 20.5" E	Binh Khanh	1	Non-polluted—I
NM2	10° 37' 43.2" N; 106° 47' 11.4" E	Binh Khanh	1	Non-polluted—I
NM3	10° 37' 34.5" N; 106° 47' 40.5" E	Binh Khanh	1	Non-polluted—I
NM4	10° 37' 08.4" N; 106° 47' 20.4" E	Binh Khanh	1	Non-polluted—I
NM5	10° 37' 12.8" N; 106° 48' 35.9" E	Binh Khanh	2	Lightly polluted—II
NM6	10° 36' 20.0" N; 106° 49' 09.7" E	Binh Khanh	1	Non-polluted—I
NM7	10° 35' 04.5" N; 106° 49' 22.5" E	An Thoi Dong	1	Non-polluted—I
NM8	10° 35' 03.2" N; 106° 48' 23.6" E	An Thoi Dong	2	Lightly polluted—II
NM9	10° 35' 29.0" N; 106° 47' 57.6" E	An Thoi Dong	1	Non-polluted—I
NM10	10° 37' 06.8" N; 106° 50' 49.4" E	Tam Thon Hiep	2	Lightly polluted—II
NM11	10° 37' 07.0" N; 106° 51' 05.9" E	Tam Thon Hiep	1	Non-polluted—I
NM12	10° 36' 26.3" N; 106° 51' 42.9" E	Tam Thon Hiep	2	Lightly polluted—II
NM13	10° 36' 08.1" N; 106° 51' 27.1" E	Tam Thon Hiep	1	Non-polluted—I
NM14	10° 36' 23.0" N; 106° 51' 14.4" E	Tam Thon Hiep	2	Lightly polluted—II
NM15	10° 35' 15.8" N; 106° 50' 29.4" E	Tam Thon Hiep	1	Non-polluted—I
NM16	10° 35' 14.5" N; 106° 50' 08.8" E	An Thoi Dong	3	Moderately polluted—III
NM17	10° 35' 03.9" N; 106° 49' 42.4" E	An Thoi Dong	1	Non-polluted—I
NM18	10° 33' 51.8" N; 106° 48' 38.1" E	An Thoi Dong	2	Lightly polluted—II
NM19	10° 23' 50.8" N; 106° 54' 26.2" E	Long Hoa	1	Non-polluted—I
NM20	10° 27' 46.0" N; 106° 46' 24.6" E	Ly Nhon	2	Lightly polluted—II
NM21	10° 28' 07.3" N; 106° 46' 05.7" E	Ly Nhon	1	Non-polluted—I

(continued)

Table 37.4 (continued)

Sample code	Coordinates	Commune	FCE calculation	Conclusion
NM22	10° 28' 46.9" N; 106° 45' 42.6" E	Ly Nhon	2	Lightly polluted—II
NM23	10° 27' 48.3" N; 106° 46' 49.8" E	Ly Nhon	1	Non-polluted—I
NM24	10° 28' 40.8" N; 106° 46' 27.2" E	Ly Nhon	1	Non-polluted—I
NM25	10° 28' 51.6" N; 106° 46' 08.7" E	Ly Nhon	2	Lightly polluted—II
NM26	10° 29' 14.8" N; 106° 45' 57.6" E	Ly Nhon	3	Moderately polluted—III
NM27	10° 29' 33.3" N; 106° 45' 45.0" E	Ly Nhon	1	Non-polluted—I
NM28	10° 30' 10.0" N; 106° 45' 47.5" E	Ly Nhon	1	Non-polluted—I
NM29	10° 30' 09.8" N; 106° 45' 47.4" E	Ly Nhon	2	Lightly polluted—II
NM30	10° 30' 53.0" N; 106° 45' 54.4" E	Ly Nhon	2	Lightly polluted—II
NM31	10° 31' 22.9" N; 106° 46' 32.9" E	Ly Nhon	2	Lightly polluted—II
NM32	10° 31' 02.1" N; 106° 46' 32.7" E	Ly Nhon	2	Lightly polluted—II
NM33	10° 32' 27.0" N; 106° 45' 42.1" E	Ly Nhon	3	Moderately polluted—III
NM34	10° 33' 22.3" N; 106° 45' 31.1" E	Ly Nhon	3	Moderately polluted—III
NM35	10° 33' 06.3" N; 106° 46' 31.4" E	An Thoi Dong	1	Non-polluted—I

37.3.3 Identification of Water Pollution Zone in Can Gio

FCE analysis is used to comprehensively assess water quality through sampling points to determine pollution hierarchies based on suitable selected parameters. The FCE results showed that nutrients and organic matter generated by aquaculture activities are the main potential factors affecting water quality in the study area. Therefore, the inverse distance weighting (IDW) method is used to interpolate the sampling points according to the pollution hierarchies. The interpolation results of IDW enabled to identify the current spatial distribution of polluted areas in the coastal zone of Can Gio district as shown in Table 37.5 and Fig. 37.15 with 3 levels: non-pollution (0.00–0.29); lightly pollution (0.29–0.45); and moderately pollution (0.45–0.61). Importantly, the FCE calculation and analysis showed that non-pollution zones are riverine areas of Soai Rap River, Long Tau River, and surface water bodies

in the coastal area. Further, the FCE analysis of water quality parameters are also homogenous between sampling points. Most of the monitored parameters are below the allowable limits of QCVN 08-MT:2015/BTNMT.

The lightly polluted areas [with low IDW weights (0.29–0.45)] are agricultural and aquaculture areas, where the exchange of water flow is small and slower than in the river and coastal areas. In addition, the spatial distribution of regions with numerical values of the average IDW weights (0.45–0.61) is located in the hinterland where water exchange and flow velocities are slow. This results in an increase in sedimentation and higher accumulation of pollutants than other areas. It can be concluded that water quality is generally stable, meanwhile the water quality of surrounding aquaculture areas is poor and worse than other areas. Organic matter and non-biodegradable pollutants are the main cause of water pollution.

Table 37.5 Score of the IDW weight according to FCE analysis

Range	Score	Area (ha)
Non-pollution	0.00–0.29	4421.12
Lightly pollution	0.29–0.45	18,307.71
Moderately pollution	0.45–0.61	47,717.54

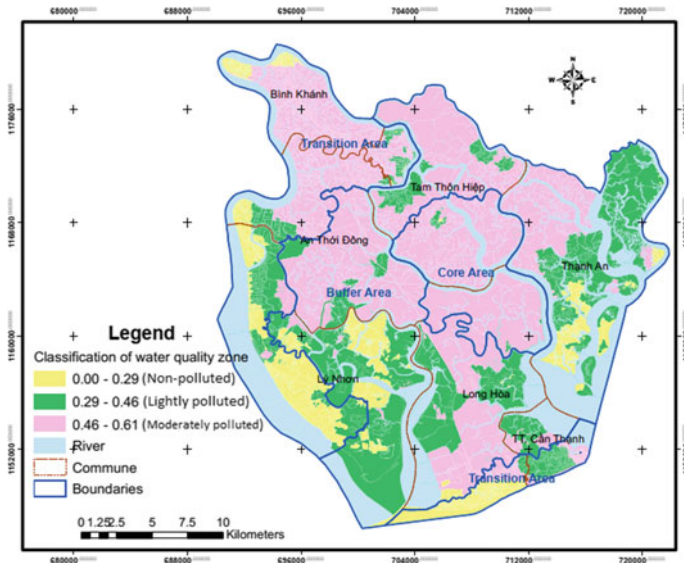


Fig. 37.15 Classification of water quality zone according to pollution hierarchical level in the study area

37.4 Conclusion

The quality of surface water in the Can Gio district is being affected by aquaculture cultivation practices—the majority of the local livelihood activities. Water quality of receiving bodies is deteriorated by wastewater discharged from aquaculture cultivation activities in which the concentration of phosphate ($\text{PO}_4^{3-}\text{-P}$), total organic carbon (TOC) and total Coliform exceeds the allowable limits for aquaculture cultivation. Households treat input water to suit farming practices upon the type of aquaculture cultivation activities (shrimp, fish, crabs, and other aquatic products). In addition to the massive development of aquaculture activities in terms of scale and density, the lack of planning on farming areas has placed constraints on the sustainable development of aquaculture cultivation activities.

The identification of water pollution zones is an important task to the management practices of local authorities in planning aquaculture activities for sustainable livelihoods in the Can Gio district. Therefore, the quality of surface water sources in and surrounding aquaculture areas was classified by different pollution hierarchical level using FCE technique. Accordingly, water quality in aquaculture areas ranges from non-polluted to moderately polluted with 18 monitoring points were classified as level 1 (non-polluted), 13 points are level 2 (lightly polluted), 4 sampling points are ranked as level 3 (moderate polluted). Spatially distribution, three (03) out of five (05) communes are likely to be considered affected by wastewater from aquaculture activities, including Tam Thon Thiep, An Thoi Dong, and Ly Nhon. Particularly, three sampling points in Ly Nhon commune are moderately polluted with pollution hierarchical level III. This unveils that surface water sources in the coastal zone of Can Gio would be further exacerbated by the boom development of aquaculture cultivation activities in association with coastal urbanisation in recent years. More importantly, this finding is useful to local authorities, planners, and managers at the top level of management to put aquaculture planning in place.

References

- Decision No. 1460/QĐ-TCMT dated April 12, 2019, of the Vietnam environment administration on technical guidelines for calculation and publication of Vietnam's water quality index (2019)
- Department Economy—Can gio District: report on agriculture in the period 2016–2020 (2021)
- Department of Statistics—Can Gio District: statistical book 2013–2017 (2018)
- Hung BV (2017) Assessing coastal water quality in Ninh Thuan province by using fuzzy comprehensive evaluation. *J Hydrol Sci Technol* 41:111–119
- Lan NTP (2016) Livelihood activities in Can Gio, Ho Chi Minh City: an interaction of political and market factors (in Vietnamese). *Sci Technol Dev J* 19(X3):95–113
- Ly CD (2019) Lecture notes on decision-making systems—part I: foundations of managerial decision-making
- Nam VN, Sinh LV, Miyagi T, Baba S, Chan TH (2014) An overview of Can Gio district and mangrove biosphere reserve. ISME Mangrove Ecosystem Technical Report No.6

- Pho NDH (2016) A theoretical approach to sustainable DFID livelihood framework for the study on livelihoods of Ma ethnic in Cat Tien National Park (in Vietnamese). *J Sci Dev—Dong Nai Univ* 2:101–112
- Son LV, Phong NV, Kien TT, Chau NTP, Hoa LT, Phu VL (2021) Impacts of livelihood activities on the environment and natural resources of Can Gio Mangrove Forest, Ho Chi Minh City. *IOP Conf Ser: Earth Environ Sci* 964:1–16
- Tran LHB, Ly CD, Than NH (2014) Comparing the results of water quality assessment by fuzzy comprehensive evaluation method and the water quality index: a case study in Dong Nai river (in Vietnamese). *Sci Technol Dev J* 17(M1):40–49
- Tuan VV, Dung LC (2015) Driving factors affecting livelihood outcomes of farm households in the Mekong Delta (in Vietnamese). *Sci J—Can Tho Univ* 38:120–129
- Tuan VQ, Kuenzer C (2012) Can Gio mangrove biosphere reserve evaluation. Final report of UNESCO/MAB Project implemented by the Vietnam MAB National Committee
- Tuan DH, Mung VT, Cuong DM (2017) Evaluation of water quality of a Blue Lake at An Son commune, Thuy Nguyen district, Hai Phong city by water quality index (WQI), trophic state index (TSI) and heavy metal pollution index (HPI) (in Vietnamese). *J Sci Hanoi National Univ: Earth Environ Sci* 33(1S):45–54
- UNESCO/MAB valuation of the mangrove ecosystem in Can Gio mangrove biosphere reserve Vietnam Hanoi Vietnam (2000)
- Vinh NQ (2014) Mapping water quality of Lam river, Nghe An. Thesis (Master), University of Science, National University Ha Noi
- Watson DF, Philip GM (1985) A refinement of inverse distance weighted interpolation. *Geoprocessing* 2:315–327

Chapter 38

Closed Chain System for Plastic Wastes Model Toward Circular Economy, Case Study in Co to, Quang Ninh, Vietnam



Hung Son Pham, Thi Minh Hang Tran, Manh Dat Ngo,
Thi Hoang Hao Phan, Anh Hung Pham, Dinh Tuan Vu, Le Anh Tuan,
Thien Cuong Tran, and Thi Thuy Pham

Abstract The market of plastics has increased by 23% in 7 years (from 2008 to 2015) due to their versatile properties and cheap production. Combating the menace of plastic waste pollution has become a global environmental challenge and the plastic waste disposal is a major obstacle for waste management and recycling all over the world. In Vietnam, It is a common practice to see a large number of waste plastic products not collected in waste bins for further processing, recovery and standard disposal via recycling centers, incinerators or landfills, rather, they are carelessly scattered or discarded into regions that are inaccessible for waste collection and hence terminating the possibility of recovery/recycling. The usual practices include plastic bottles and containers being thrown on the ground, thrust out of vehicles, hipped around narrow passages or blown away by wind which litter the surroundings and subsequently pollute the immediate ecosystem. This paper therefore seeks to the appropriated closed chain system for plastic wastes toward to circular economy in Vietnam, the special case model was applied in Co To district with the participation of community, social organizations, local authorities and 02 collected vendors to collect, reuse and recycle from plastic waste. The model has contributed to improve the tourism environment, reduce the plastic waste disposal and change the inhabitant's awareness and consumption habits.

Keywords Plastic waste · Closed chain system · Circular economy

H. S. Pham · T. M. H. Tran · A. H. Pham · D. T. Vu · L. A. Tuan · T. C. Tran · T. T. Pham (✉)
Faculty of Environmental Sciences, University of Science, Vietnam National University, 334
Nguyen Trai, Thanh Xuan, Hanoi, Vietnam
e-mail: phamthithuy@hus.edu.vn

M. D. Ngo · T. H. H. Phan
Quang Ninh Department of Natural Resource and Environment, Km8, Hong Ha, Ha Long, Quang
Ninh, Vietnam

38.1 Introduction

Plastic plays a very important role in the fast-paced life today. This common polymer product is very important to all aspect of social. With the development of chemical engineering technique, many convenient and useful product was come to the human life, and plastic is one of outstanding invention. Plastics are made from petroleum by-products, most common sourced from natural gas-producing countries at very affordable prices. Plastic waste management and recycling capabilities will be far exceeded in next two decades with the enormous increase of plastic production which was foreseen to double at that time (Plastics Europe 2018). Because plastic is a product of the oil industry, as the industry grows, so does the plastic production. The plastics industry explains that this increase in production is driven by an increase in demand for disposable plastics, such as soft drinks and packaging, and that this market is particularly flourishing in developing countries. This means that most plastics produced are planned to be exported to developing countries, where waste management services may not be properly equipped for disposal. Nowadays, plastic waste was existing in every part of environment, ocean, earth, soil, ... With approximate 730,000 tons of plastic waste discharged to the ocean annually and a lot of other mismanaged plastic waste, Vietnam which ranked number 15 in the list of countries (and dependencies) by population took a 4th position on the list of countries which discharge the largest amount of plastic (Ghisellini et al. 2016). On both land and sea, plastic waste damage the environment and cause the harmful consequence to the life and health of animal and aquatic species, as well as human health. In Vietnam, in 1990, the average amount of plastic consumption in Vietnam was 3.8 kg/person/year, after 10 years (2019), the amount of plastic consumption has increased more than 10 times in comparison to 1990 and reached 41 kg/person/year (Le et al. 2019) The most common single-use plastics are caps—plastic bottles, food wrappers, plastic bags, straws, etc. Plastic waste when released into the environment not only affects the landscape and cause environmental pollution, but also have great effects on animals and humans, for example, about 267 marine species have been entangled or eaten by microplastics in the sea (Kühn and Franeker 2020; Moore 2008); about 1 million seabirds, 100,000 marine mammals sea turtles and countless fish species die from plastic waste each year (Susanti et al. 2020). The marine debris is being considered as one of the most remarkable environment pollutants. People dispose enough plastic waste to surround the Earth four times each year, particularly oceans suffer more than 8 million tons, but just only 27% of them are processed and recycled, this number for Vietnam is just 10% (Thuy 2019). However, the government and other social organizations in Vietnam have taken actions to improve the recycling efficiency of plastic waste over the years. For example: (1) waste sorting, (2) turning plastic into energy for industrial companies, (3) study into application of waste plastic in construction and environmental treatment.

Currently, the circular economy and economic and technical (technological) solutions were proposed to move away from the traditional way of managing the economy

in a linear (Linearity Economy), for example, from the “cradle” (exploitation, production, consumption) straight to the “grave” (burial) to a way of managing the economy in a “circular” (revolving) style through reuse, recycling all waste generated before returning to the environment (burial). Hence, this paper aimed to set up the general closed chain system for plastic wastes management which includes stakeholders, achieved activities and measurable factors aspects of sustainability. This model was applied in Co To with the participation of community, social organizations, local authorities and 02 collected vendors to collect, reuse, recycle and recover energy from plastic waste. The goal of the model will be expressed in 03 factors: (i) improve the living environment, (ii) reduce the plastic waste disposal and (iii) the inhabitant’s awareness, consumption and disposal of plastic wastes.

38.2 Closed Chain System for Plastic Waste Management

38.2.1 Research Hypothesis

- Based on the actual situation of plastic waste generation, plastic waste management system and polluted generation from plastic waste, the needs reduce and recycle plastic waste for living conditions improvement are achieved.
- Plastic wastes are mostly collected together with domestic solid waste and other wastes without being sorted, so the efficiency of recycling plastic waste is almost non-existent. From there, the adequate closed chain system for plastic waste management including management, collection, treatment and reduction from supply to consumption and collection, recycling and reuse need to be conducted.
- Model-based approach to using environmentally friendly green products, reducing and moving towards no use of single-use plastic products. From there, provide policy, technology and management solutions as well as specific implementation plans to replace single-use plastic products with environmentally friendly green products such as products made from starch, paper, wood, ...

38.2.2 Design Closed Chain System for Plastic Waste Management Model

The closed chain system for plastic waste management model comprises types of economic and social development which protect and enhance the natural environment and social equity. Hence, general model of plastic waste management, which offers a comprehensive theoretical framework integrating of approach, stakeholders, achieved activities and measurable factors aspects of sustainability. The model exhibits the underlying ethical principles, broad goals and measurable objectives.

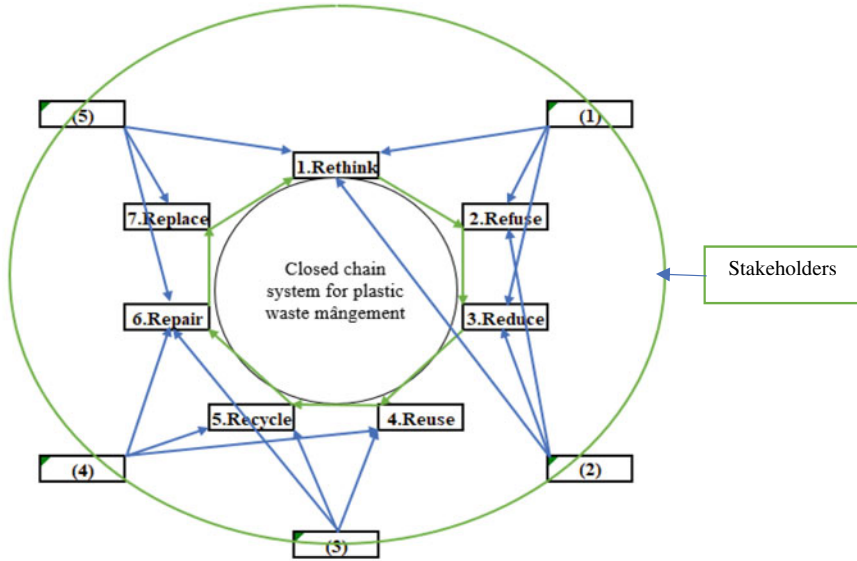


Fig. 38.1 Plastic waste management model toward circular economy. Local communities, (2) tourists, (3) local management agencies, (4) collection-recycle-treatment enterprise, (5) plastic wastes vendor

The closed chain system for plastic waste management model was built based on a product lifecycle-based approach that integrates reduction, reuse and recycling activities in the production process, exchange and consumption. The plastic waste management model was shown in Fig. 38.1.

The principle of closed chain system for plastic waste management model was based on 7Rs approach, as following:

Rethink: Change public awareness on using, selection and disposal of plastic wastes by understanding the impact of plastic wastes on environment and human health;

Refuse: Refuse plastic products which are not recyclable or reusable;

Reduce: Reduce the demand of using plastic products to reduce the plastic waste disposal, especially single-use plastic products;

Reuse: Reuse to prolong the life cycle of plastic products before replacing.

Recycle: Recycle discarded plastic products into other useful products.

Repair: Repair to reuse plastic products to prolong life, reduce waste, and save costs.

Replace: Replace non-biodegradable plastic products by other friendly environment and reusable products such as from craft paper, fabric, etc.

Based the 7Rs approach, the achieved activities were defined to reach the goals of the model (i) improve the living environment, (ii) reduce the plastic waste disposal and (iii) the inhabitant's awareness, consumption and disposal of plastic wastes; as follows: (1) Public awareness activities for Rethink, Refuse and Reduce such as: design leaflets and propaganda materials on impact of plastic waste to environment and human health and information on non-biodegradable plastics, organize the workshop for guidance plastic waste collection classification and simple solution for recycle, reuse, repair the plastic waste, introduce the successful case study on utilization of plastic wastes; (2) Design and finding friendly environmental and reusable products for Refuse and Replace; (3) Classification and collection activities for Reuse, Recycle such as: sorting directly as sources in households; (4) Provide the potential chances to use plastic waste as resources and raw materials for Recycle and Repair; (5) Provide the solutions to modify plastic wastes into useful products for Recycle and Repair; (6) Provide regulation and policy to support collection—classification—treatment activities for Refuse, Reduce, Reuse.

Base on the 7Rs approach and achieved activities above, the 5 groups of stakeholders who decided the successful of model, were defined as given: (1) Local communities: were the key stakeholders that will join in the Rethink, Refuse and Reduce approach; their active participation will effectively give more successful chances of the model; (2) Tourists: were also join in the model in Rethink, Refuse and Reduce approach; (3) Local management agencies: were join in the model by supported policy and management, will join in Reuse, Recycle and Repair approach, the appropriated policy, regulation also decided the successful chances of the model; (4) Collection—recycle—treatment enterprises: were join in the model in Reuse, Recycle and Repair approach; the use the plastic waste as their products materials will reduce the plastic waste disposal and achieved benefits from the waste; (5) Plastic vendors: were join in this model by changing their selling products to friendly environment products, and will join in Rethink, Replace and Repair approach.

The inputs of closed chain system for plastic waste management model were current status conditions in case study such as: (1) the generation, collection, recycle and treatment of plastic waste, (2) the infrastructure conditions for collection, recycle and treatment of plastic waste, (3) social and economic conditions, (4) public awareness. From these inputs, the activities and stakeholders should be designed to reach the goals model. After applying designed activities in case study, the effective of the closed chain system for plastic waste management model were measured by factors: (i) percentage of plastic waste reused, (ii) percentage of plastic waste recycle, (iii) number of inhabitants use reusable products instead of plastic products, (iv) number of social enterprises joining in recycle activities.

38.3 Applied Closed Chain System for Plastic Waste Management Model in Co To District, Quang Ninh Province, Vietnam

38.3.1 Methodologies

38.3.1.1 Case Study

Quang Ninh is a coastal province in the Northeast region of Vietnam, one of the key areas in the socio-economic development strategy of the Gulf of Tonkin. Statistics of the Department of Natural Resources and Environment showed that the total amount of domestic solid waste generated in the province is more than 1200 tons/day, of which plastic waste accounts for a very large proportion, an average of about 13.5% (Department of Natural Resources and Environment 2020).

Co To is an island district located in the East of Quang Ninh province with an area of 47.5 km² including Dong Tien, Thanh Lan and Co To town with about 6768 people. Co To is considered as a tourist “paradise” with dozens of pristine beaches such as Van Chay, Hong Van, and Vung Tien.... However, the solid waste, plastic bottles, and plastic bags are not properly collected in Co To island district, causing landscape and biodiversity deterioration, and adversely affecting human health and living conditions in the island. According to statistics in 2020, the total amount of plastic wastes generated about 2.8 tons/day, equivalent to 1012 tons/year, of which 89.9 tons/year equivalent to about 8.9% of plastic wastes were not collected (Department of Natural Resources and Environment 2021).

Co To island district was selected for testing closed chain system for plastic wastes pilot toward to circular economy, following by three main reasons:

1. Co To is an island district, hence, the pilot applied had higher reliability in comparison with other areas due to its isolation.
2. The spearhead of economic development of Co To island district is based on tourism; moreover, Co To sea is part of the Co To—Tran Island Marine Protected Area with high biodiversity.
3. Solid waste treatment in Co To district is mainly buried and dumping, accounting for about 80%. Therefore, the closed chain system for plastic wastes will has the important meaning on improving the living conditions and utilization the plastic waste, toward to circular economy.

38.3.1.2 Data Acquisition

Collecting information through questionnaires, 200 questionnaires were used to survey and interview households and tourists related to the plastic supply vendors; plastic management agencies, collection and treatment plastic wastes vendors in Co To district. The content of the questionnaire focused on the following issues:

- People's awareness on the problem of plastic waste pollution.
- Awareness of the utilization plastic waste toward circular economy.
- People's understanding of Vietnam's policies and action plans to reduce plastic waste.
- Channel to receive information about plastic waste.
- Should CONTINUE or BANN the use of single-use plastic products?
- Willing to change the habit of using single-use plastic products.

Field investigation and survey were carried out by interview the plastic supply vendors (composition, quantity and type); end users (the life cycle of using plastic products, plastic waste generation); collection, treatment and recycling of plastic waste; plastic waste disposal to the sea, ... in Co To district.

38.3.1.3 Stakeholders

- Local communities included inhabitants in Thanh Lan commune, Dong Tien commune and Co To town including farmers, scrap collectors, traders and tourists, trading at markets, supermarkets and commercial centers in Co To town, fishermen, boat owners...
- Tourists: During survey time, there were no international tourists, only domestic tourists because of affecting of Covid-19 epidemic.
- Local management agencies: Including staff of the Department of Natural Resources and Environment; People's Committee of Co To district, People's Committee of Co To town and People's Committee of 2 communes Dong Tien and Thanh Lan and social organizations such as youth union, women's union.
- Enterprises related to collect, recycle and treat plastic waste, including: Co To Urban Environment Joint Stock Company (the current waste collection enterprise in Co To district); SEIDO Import-Export and Production Co., Ltd (plastic waste collection and recycle enterprise); Ha Long Cement Joint Stock Company (plastic waste collection and other scraps as input materials for the factory's clinker production process).
- Plastic product vendors.

38.3.2 Surveyed the Input of Closed Chain System for Plastic Waste Management Model in Co To District, Quang Ninh Province, Vietnam

38.3.2.1 Surveyed the Community Behavior on Recycle Collection, Transportation and Treatment of Plastic Wastes

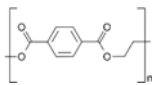
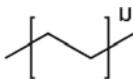
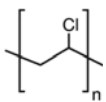
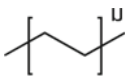
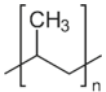
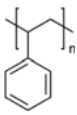
Plastic plays a very important role in the fast-paced life today. This common polymer product is very important to all aspect of social. With the development of chemical

engineering technique, many convenient and useful product was come to the human life, and plastic is one of outstanding invention. Plastics are made from petroleum by-products, most common sourced from natural gas-producing countries at very affordable prices. The plastic type was associated with the number based on the SPI (Society of Plastics Industry) code to identify what they were made from (Table 38.1).

The results of the field investigation and survey in 2021 in Co To district showed that the volume of solid waste generation were about 17 tons/day. In which, the proportion of plastic waste in domestic waste accounts for about 12.5% with 06 main types of plastic: Poly ethylene terephthalate (PET), High density polyethylene (HDPE), Polyvinyl chloride (PVC), Low density polyethylene (LDPE), Polypropylene (PP) and Polystyrene (PS).

The diagram of collection, transportation and treatment of plastic waste in the district was given in Fig. 38.2, with the collection rate reaching 98%. The collected plastic wastes were treated by incinerator and dumping site. In the district, 01 incinerator with a capacity of 7 tons/day (EST-100S incinerator) is treated plastic wastes in Dong Tien commune and Co To town. Especially in Thanh Lan commune, the temporary burial is main treatment method (Fig. 38.3).

Table 38.1 SPI resin identification codes

SPI code	Polymer	Structure	Uses
1	Poly(ethylene terephthalate) (PET)		Soda bottles, water bottles, medicine jars, and salad dressing bottles
2	High density polyethylene (HDPE)		Soap bottles, detergent and bleach containers, and trash bags
3	Polyvinyl chloride (PVC)		Plumbing pipes, cables, and fencing
4	Low density polyethylene (LDPE)		Cling wrap, sandwich bags, and grocery bags
5	Polypropylene (PP)		Reusable food containers, prescription bottles, and bottle caps
6	Polystyrene (PS)		Plastic utensils, packaging peanuts, and styrofoam

CO TO DISTRICT

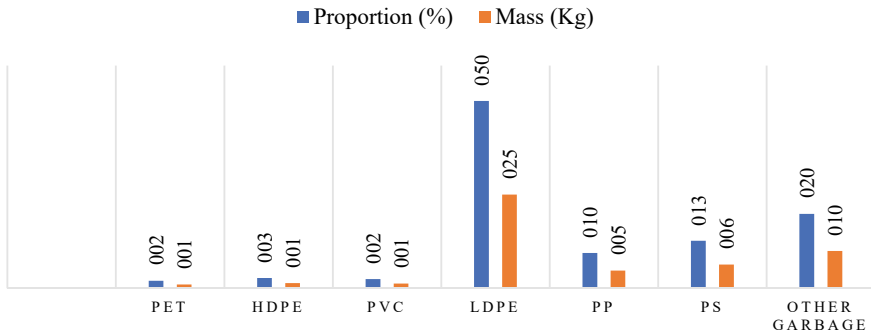


Fig. 38.2 Composition of plastic waste in Co To district

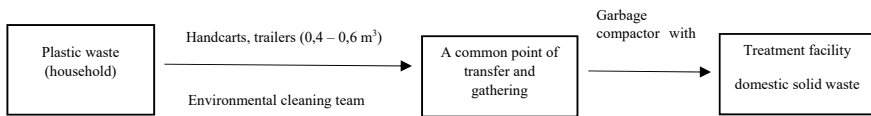


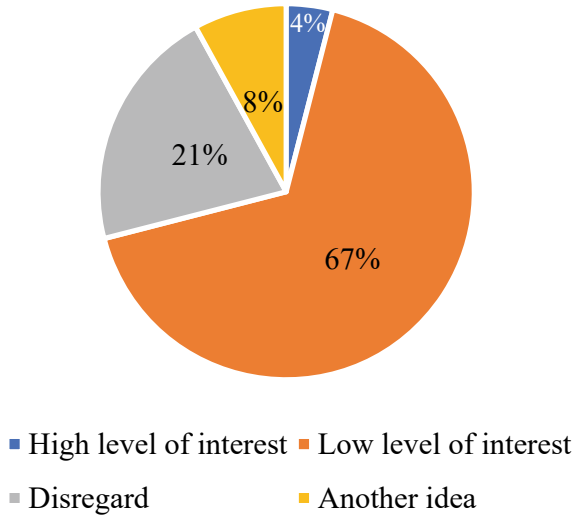
Fig. 38.3 Diagram of collection, transportation and treatment of plastic wastes in Co To district

Although the plastic wastes collection rate reaches 98%, whatever the treatment of domestic waste in general and plastic waste in particular still faces many difficulties due to the unsatisfactory infrastructure, low costs for collection, transportation and treatment. In addition, the promoting the 5R model and developing sustainable tourism without plastic wastes were not implemented. The classification, recycling and reuse of plastic wastes were carried out at the individual and household scale without specific policies and sanctions.

38.3.2.2 Surveyed Public Awareness Related on Plastic Wastes

Survey results, assessing people’s awareness of plastic waste based on 200 sociological survey questionnaires, showed that Co To inhabitants were aware that the plastic wastes were harmful effects on the environment and health, human and biological health as well as policies and plans on reducing plastic waste and single-use plastic products. Inhabitants knew the information mainly through such as radio and television. Most of inhabitant supported to ban the single-use plastic products and were basically ready to use more environmentally alternatives. 67% of inhabitants were aware of the local plastic wastes pollution, but the level of concern is very low, only 4% (Fig. 38.4).

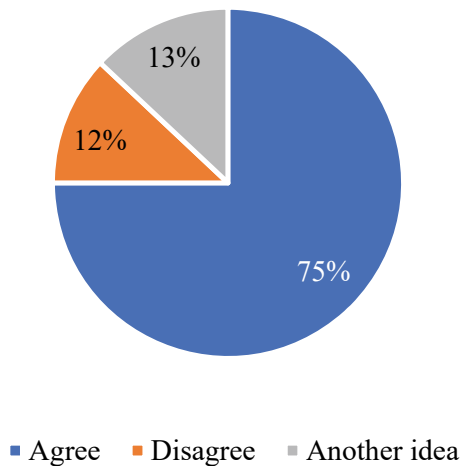
Fig. 38.4 Public perception of plastic waste pollution



Impact assessment of plastic wastes on the environment resulted as following: 75% of respondents agree that plastic waste is a serious environmental pollution, only 12% disagree, and 13% have different opinions (Fig. 38.5).

Perception of impact assessment of plastic wastes in living environment resulted as following: 50% said plastic wastes were cause of the environmental landscape deterioration and 41% said plastic wastes affected organisms and only 4% said that plastic wastes affected the environment to human health and 5% said plastic wastes were cause of drainage blockage. It can be seen that most of inhabitants do not know the harmful effects of plastic waste on human health, especially the harmful of micro-plastic (Fig. 38.6).

Fig. 38.5 Impact assessment of the plastic wastes on the environment



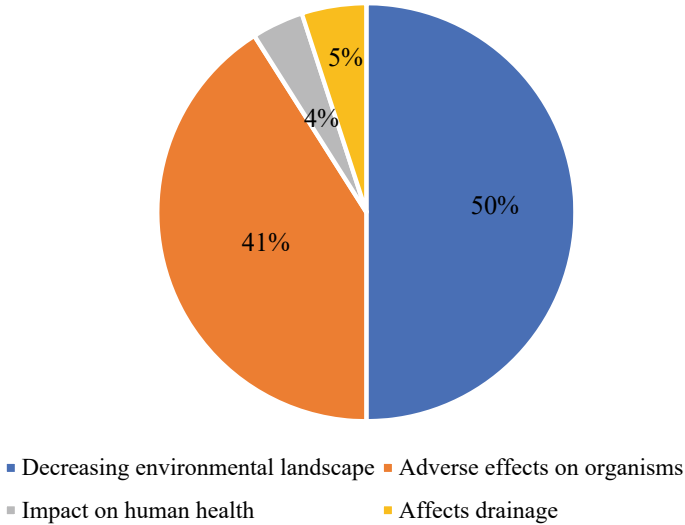


Fig. 38.6 Impact assessment of plastic waste in living environment

People’s understanding of Vietnam’s policies and action plans to reduce plastic waste resulted as given: 37% inhabitants were aware and interested in information about Vietnam’s policies and action plans to reduce plastic waste; 29% inhabitants knew but have little interest and 23% do not know about these issues. This shows that the locality needs to propagate more about policies and plans on reducing plastic waste (Fig. 38.7).

The channel to receive information on plastic waste survey resulted as given: about 80% inhabitants knew plastic waste through radio and television, and only about 6% inhabitants knew through posters, newspapers, online newspapers and 7% inhabitants were through direct communication launched by the neighborhood group and environmental programs. Thus, the form of propaganda through important information channels (Television station, radio station, newspaper...) still has the largest role that needs to be further promoted and maintained (Fig. 38.8).

Should CONTINUE or BANN the use of single-use plastic products such as plastic bags, cups, cups, food foam boxes, plastic straws.... Most inhabitants realized the harmful effects of single use plastic waste disposal with 76% agreeing and wanting to use these products (Fig. 38.9).

Ready to change the habit of using single-use plastic products survey results showed that 51% inhabitants were ready to change the habit of using single-use plastic products and 42% inhabitants were not ready but will be prepared to change in the future (Fig. 38.10).

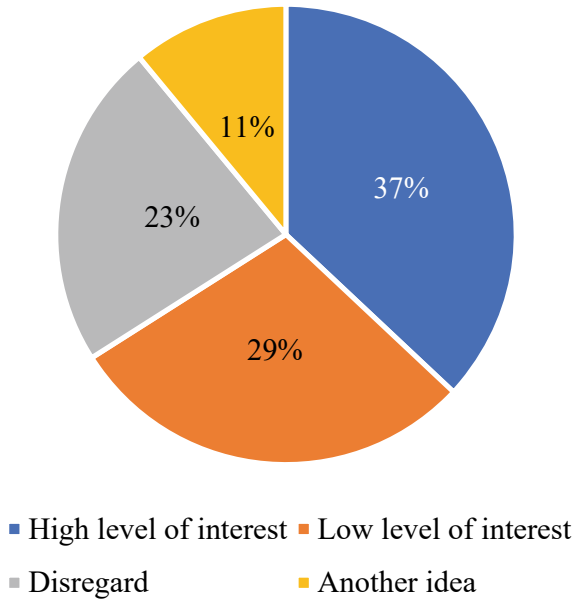


Fig. 38.7 Understanding Vietnam’s policies and action plans to reduce plastic wastes

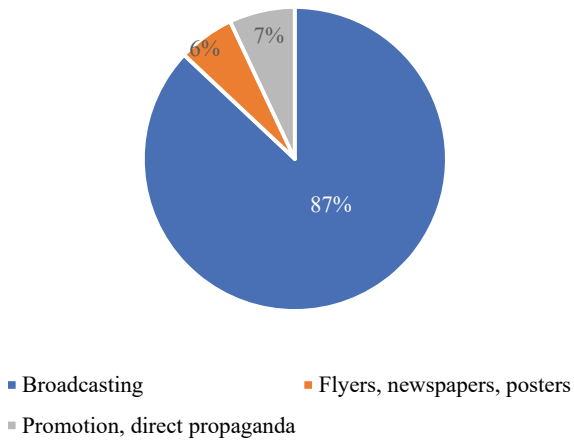


Fig. 38.8 Community outreach channels on plastic waste

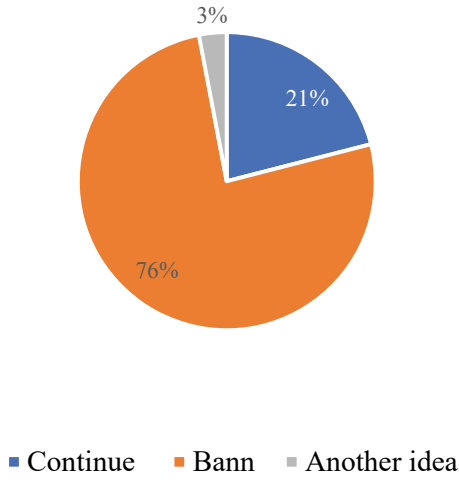


Fig. 38.9 Public opinion on using single-use plastic products

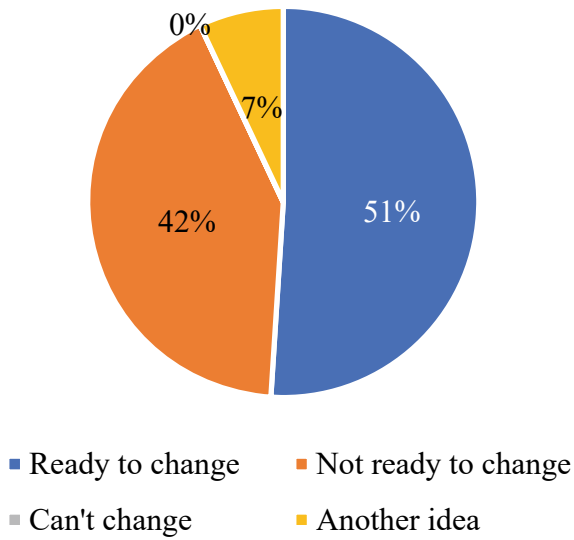


Fig. 38.10 Willing to change the habit of using single-use plastic products

38.3.3 Activities

38.3.3.1 Designed Activities

Due to the current condition, the designed activities for closed chain plastic management in Co To district, Quang Ninh province, Vietnam were given, as following

- Develop leaflets and propaganda materials to guide the people of Co To district on the collection and classification of plastic waste at the source;
- Design and choose friendly environment products to replace single-use or non-decomposition plastic products;
- Set up, guide and train local garbage collection teams to collect and classify plastic.
- Set up and design a plastic waste sorting container.

38.3.3.2 Achieved Activities

- Distributing leaflets, documents and instructing people in Co To district to collect and classify plastic waste at arising sources (Figs. 38.11 and 38.12).



Fig. 38.11 Leaflets and documents guiding the collection and classification of plastic waste

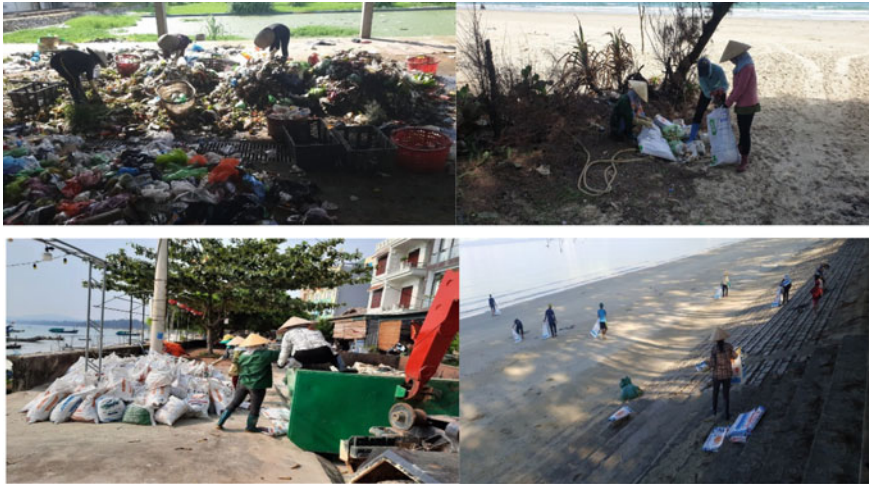


Fig. 38.12 People collect and sort plastic waste at several sources

- Reuse discarded plastic products into decorative model products with economic value (Fig. 38.13).
- Plastic waste recycling: The volume of plastic wastes which collected, sorted, treated and recycled from the pilot, were 3293 kg with the participation of the inhabitants, social organizations, and local authorities in the area. 02 enterprises: SEIDO Import–Export and Production Company Limited and Ha Long Cement Joint Stock Company are provide the service on treatment, recycling and reuse plastic wastes (Fig. 38.14).
- Replace disposable, hard-to-decompose plastic products with environmentally friendly products: plastic bags with cloth bags; plastic bottles, plastic cups with glass bottles; plastic straws with bamboo straws (Fig. 38.15).



Fig. 38.13 Reusing plastic bags and plastic bottles into decorative models



Fig. 38.14 Plastic waste collection and transportation by enterprises



Fig. 38.15 Alternative products are designed with a logo with a message to change the consumption habits of plastic products for the community

38.3.4 *Measured Factors of the Model*

The results which achieved after three months running were given:

- 02 types of leaflets and propaganda materials were developed with 3000 printed-version leaflets and propaganda materials to guide the people of Co To district on the collection and classification of plastic waste at the source.
- 03 friendly environment products to replace single-use or non-decomposition plastic products were chosen and applied such as: 1500 cloth bags, 1500 500 ml glass water bottles, 20,000 bamboo straws.
- 15 persons in local garbage collection teams were guided and trained to collect and classify plastic, such as: 6 persons in Co To town, 5 persons in Thanh Lan commune and 4 persons Dong Tien commune.
- 02 private enterprises joined in collection-classification and reusing plastic wastes, such as: (1) SEIDO Import–Export and Production Co., Ltd. is a unit that imports

and purchases plastic scrap as input materials for the production of plastic products; (2) Ha Long Cement Joint Stock Company is a unit that collects plastic waste and other scraps to use as input materials for the factory's clinker production process.

- 82% plastic wastes were collected and 100% plastic wastes were reused.

The circular economy model of plastic waste management in Co To district has brought certain effects, contributing to improving the environmental landscape, reducing pressure on waste treatment, changing awareness and consumption habits for the people.

38.3.5 *Lessoned Learnt*

- The main key point for successful closed chain system pilot in plastic waste management is the actively participation from all levels of the Party Committee, local authorities, local social organizations and especially the participation of the local community.
- The collection and classification of plastic waste from domestic solid wastes need to be supported by national and local policy.
- The utilization of plastic wastes should have clearly policy that will attract the participation of enterprises used plastic waste as their product materials.
- It is necessary to propagate and raise awareness for inhabitants to change their habits and behaviors of using non-degradable plastic bags and disposable plastic products.
- It is necessary to study and come up with products to replace plastic products such as plastic bags and disposable plastic products because of being convenient and low-cost.

38.4 Recommendation

38.4.1 *Building a Link Mechanism Between Vendors of Environmentally Products to Replace Single-Use Plastic Products*

- There are preferential sanctions to attract suppliers of environmentally products to replace disposable plastic products.
- Create a mechanism to encourage tourism, restaurant and service businesses to use environmentally products from potential suppliers.
- Build a public-private partnership (3P) mechanism to promote the commitment to provide environmentally products, ensure sufficient supply and have a wide and easily accessible distribution network.

- Develop an environment product distribution system, at least 01 store to introduce products to a market/commercial center/communal/ward/neighborhood (can take advantage of the same system of convenient supermarkets Circle K, Vinmart + ...).
- There should be a mechanism to support taxes and production inputs for units producing disposable plastic products to contribute to lowering product costs corresponding to disposable plastic products very common in daily life.

38.4.2 Building a Linkage Mechanism Between Inhabitants, Private Waste Collectors and Transporting, Recycling, and Reusing Plastic Waste Enterprises

- Establish the cooperation network of classification, collection and recycling plastic waste including households, collection—transportation and recycling enterprises.
- Build up the reward system such as: voucher, gifts... for participating in sorting and classifying garbage.
- Local government should play the role of catalyzing and managing the cooperation mechanism between stakeholders, ensuring the commitment and cooperation of the stakeholders.

38.4.3 Develop Supported Regulations on Collection, Transportation and Utilization of Plastic Waste

- Supported regulations in terms of transportation, treatment and recycling costs of plastic wastes should be clearly developed.
- Stakeholders involved in the closed chain system: classification → collection → recycling is prioritized in local support policies, recognized and rewarded.
- Develop communication programs by example, good practice to honor typical households and individuals participating in the network of classification, collection and recycling.

38.5 Conclusion

The study has built up a model of plastic waste management toward circular economy model with specific criteria and implementation steps. This pilot applied in Co To district initially brought certain effects, contributing to improving the tourism environment for the island district, reducing the pressure on waste treatment, changing the perception and habits of the island consumption habits for the people.

Acknowledgements The authors thank to Quang Ninh Department of Natural Resource and Environment, Co To People's Committee for your supports during implementing model's activities in Co To district.

References

- Department of Natural Resources and Environment (2021) Report on investigating, surveying, making plans on reducing plastic waste emissions, using reduction plans, supplying non-biodegradable plastic products, using a times, collect, treat, reuse plastic waste
- Department of Natural Resources and Environment (2020) Report on domestic solid waste management in Quang Ninh province
- Ghisellini P, Cialani C, Ulgiati S (2016) A review on circular economy the expected transition to a balanced interplay of environmental and economic systems. *J Clean Prod* 114:11–32
- Kühn S, Van Franeker JA (2020) Quantitative overview of marine debris ingested by marine megafauna. *Mar Pollut Bull* 151:110858
- Le THO, Tran TLA, Nguyen TPL (2019) Plastic waste generation in Vietnam and management and treatment measures towards minimization of plastic waste to the ocean. In: International workshop Marine plastic pollution in Vietnam: current situation and solutions, Hanoi 29-30/11/2019, pp 322–330
- Moore CJ (2008) Synthetic polymers in the marine environment: a rapidly increasing, long-term threat. *Environ Res* 108(2):131–139
- Plastics Europe (2018) Annual review 2017–2018. *Plastic Ann Rev* 15
- Susanti NKY, Mardiasuti A, Wardiatno Y (2020) Microplastics and the impact of plastic on wildlife: a literature review. *IOP Conf Ser: Earth Environ Sci* 528:012013
- Thuy PT (2019) Evaluation of ion exchange material from sulfonated polystyrene waste synthesized for removal Cr^{3+} from aqueous solution by column experiment. *J Sci Technol Civ Eng (STCE)—NUCE* 13:92–100

Chapter 39

Evaluation of the Possibility of Application of Porous Asphalt Concrete Containing Steel Slag to Road Construction



Van Long Nguyen, Duc Sy Nguyen, Thi Hanh Nguyen, and Thuy-Linh Le

Abstract The fast speed of urbanization has led to an increasingly scarce supply of construction materials while the increasing volume of construction and industrial waste has adversely affected of the environment in Vietnam. To solve these two issues, the study uses steel slag aggregate to produce the porous asphalt concrete (PAC). The experiments show that PAC containing steel slag aggregate can be used as a foundation for high quality pavement layers or road surface layers.

Keyword Steel slag · Porous asphalt concrete · Waste materials · Mechanical properties of materials · Aggregate

39.1 Background

The rapid development of infrastructure construction has resulted in a massive increase in material demand in Vietnam. However, the government has strictly limited raw material extraction, exacerbating the shortage of construction materials. As a result, it is critical to find alternative material sources to replace traditional construction materials.

There are many steel factories in Vietnam. During steelmaking processes, most steel slag is discharged into the environment with 10–20% of the steel billets in volume. In fact, 07 steel factories in Ba Ria-Vung Tau province's Phu My Industrial Park discharged approximately 0.29 million tons of steel slag per year (Du 2017).

V. L. Nguyen
Ho Chi Minh City University of Transport, Ho Chi Minh City, Vietnam

D. S. Nguyen (✉) · T.-L. Le
University of Technology and Education—The University of Danang, Danang, Vietnam
e-mail: ndsy@ute.udn.vn

T. H. Nguyen
Colleges of Transportation Ho Chi Minh City, Ho Chi Minh City, Vietnam

Based on previous studies (Ta 2014; Tran 2011; Das et al. 2012; Manso et al. 2004; Patel 2008), this study aims to evaluate the ability of PAC to construct road surfaces using steel slag aggregate. It addresses the scarcity of construction materials and utilizes waste materials to protect the environment (<http://www.asa-inc.org.au/knowledge/technical-literature/technical-guides>; Rohde et al. 1819; Aiban 2005).

39.2 Research Information

39.2.1 Steel Slag

In this study, steel slag are provided by Green Material—Ba Ria Vung Tau Co., Ltd. The chemical compositions and hazardous components of the steel slag are analyzed at the Institute of Chemical Technology.

After sampling the steel slags, the study conducts experiments on mechanical properties and determines the particle size distribution. They meet the Vietnamese standards for aggregates in asphalt concrete mixtures, allowing the study to evaluate the ability of steel slag aggregate to produce PAC.

39.2.1.1 The Particle Size Distribution of Steel Slag

The particle size distribution of unclassified steel slag samples does not meet the requirements for the road foundation layers. For example, the tested steel slag has a lower proportion of fine particles (<0.425 mm) than was required (Nguyen 2014; Pasetto and Baldo 2007; Hisyamudin and Yokoyama 2012; Yi et al. 2012). However, if the material requirements for various purposes are determined in advance, it is possible to determine aggregate grading requirements. Then, steel slag is classified into different sizes before mixing according to the predetermined grades, the particle sizes and the aggregate grading requirements. As a result, the particle size distribution issue of steel slag can be easily solved (Yi et al. 2012; Qasrawi 2014).

After sampling, the authors conduct the experiments to determine the parameters of the particle size distribution based on TCVN 7572-2: 2006, and the mechanics. The experimental results are shown in Table 39.1.

39.2.1.2 The Mechanical and Physical Properties of Steel Slag

The mechanical and physical properties of steel slag taken at Green Material Company are shown in Table 39.2.

Table 39.2 shows that the values of the properties of steel slag are much higher than gravel. Therefore, steel slag is much heavier and denser than gravel. The steel slag has better durability and mechanical properties than the gravel.

Table 39.1 Result of determining the particle size distribution of steel slag

Sieve size (mm)	Mass %							
	Steel slag size of 19 mm × 25 mm		Steel slag size of 9.5 mm × 19 mm		Steel slag size of 4.75 mm × 9.5 mm		Steel slag size of 0.6 mm × 2.36 mm	
	Accumulate on sieve	Sieving	Accumulate on sieve	Sieving	Accumulate on sieve	Sieving	Accumulate on sieve	Sieving
25	0.0	100.0	0.0	100.0	0.0	100.0	0.0	100.0
19	54.4	45.6	0.0	100.0	0.0	100.0	0.0	100.0
9.5	88.7	11.3	9.8	90.2	0.0	100.0	0.0	100.0
4.75	96.1	3.9	89.2	10.8	12.7	87.3	0.0	100.0
2.36	97.4	2.6	95.2	4.8	55.2	44.8	46.7	53.3
0.600	100.0	0.0	100.0	0.0	100.0	0.0	100.0	0.0

Table 39.2 The mechanical and physical properties of steel slag

No	Experimental targets	Value	Unit
1	Specific weight	3.50	g/cm ³
2	Volumetric mass at dry state	3.24	g/cm ³
3	Volumetric mass at saturation state	3.32	g/cm ³
4	Water absorption	2.07	%
5	Volumetric mass at porous state	1826	Kg/m ³
6	Porosity	46.86	%
7	Content of dust, mud, clay	0.95	%
8	Impact wear	20.8	%
9	Flat and elongated particles content	0.74	%
10	Optimal humidity	3.47	%
11	Volumetric swelling	0	%
12	California bearing ratio	90.68	%
13	Elastic modulus	230.7	MPa

The Los Angeles (L.A.) abrasion test is determined according to TCVN 7572-12-2006. The experimental results are shown in Table 39.3.

The steel slag specifications shown in Table 39.3 meet the requirements of TCVN 8819-2011.

Table 39.3 Experimental results of the L.A. abrasion

Grain size (mm)	Initial samples weight (g)	Samples weight after rotation (g)	L.A. abrasion (%)	TCVN8819: 2011 standards
12.5–19	2500	3719	25.62	≤28
9.5–12.5	5000			

Table 39.4 Aggregate gradation for PAC

Grain size (mm)	TCVN8819: 2011 standards (%)	By design (%)
25.0	100/100	–
19.0	90/100	95
9.5	40/70	55
4.8	15/39	27
2.4	2/18	10
0.6	0/10	5

39.2.2 The Aggregate Grading Design for PAC Using Steel Slag Aggregate

The porous asphalt concrete containing steel slag in this study is designed according to the Marshall method (TCVN 8820-2011). The aggregate is the steel slag taken from Green Material Co., Ltd., in Ba Ria-Vung Tau Province. The asphalt used in this research is Shell 60/70. They meet the requirements of TCVN 8819-2011 (TCVN 2011). The mineral powder used in the study is the Hoclim mineral powder taken from the mixing station of BMT company.

39.2.2.1 Determine Gradations of the Hollow Cylindrical Asphalt Using Steel Slag Aggregate

The study chose the average gradations in the allowed standards according to TCVN 8819–2011. It is the middle value in the gradation curve shown in Fig. 39.2. Compact PAC mixture design Table 39.4 and Fig. 39.1.

After determining the gradation design, the next step is mixing and casting cylindrical samples with different asphalt contents, such as 4.1, 4.3, 4.5, 4.7 and 4.9%. They allow this study to determine the optimal asphalt content of PAC containing steel slag aggregate.

39.2.2.2 Determination of Optimum Asphalt Content of the PAC Mixture Using Steel Slag

According to the experimental results with different asphalt contents (4.1, 4.3, 4.5, 4.7 and 4.9%), the optimal asphalt content is 4.3% by total weight of mixture.

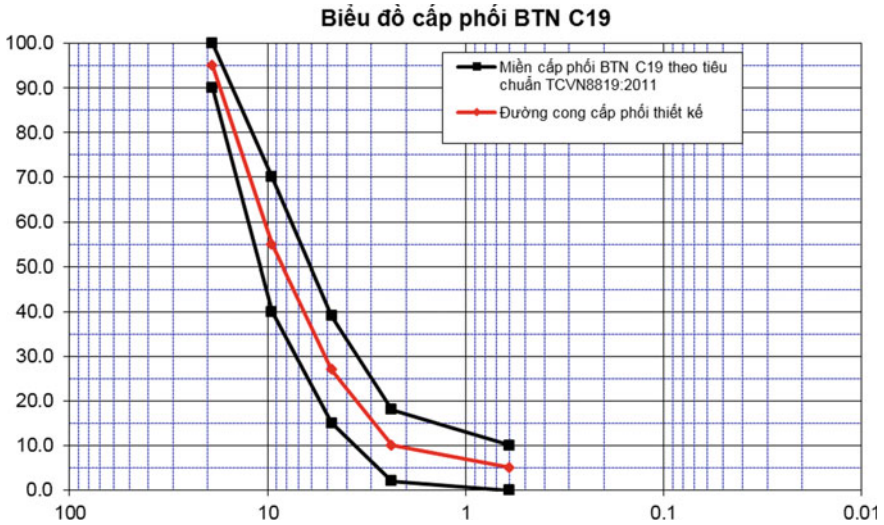


Fig. 39.1 Gradation curve PAC



Fig. 39.2 Compact PAC mixture design

39.3 Experimental Study Mechanical and Physical Properties of PAC with 4,3% Steel Slag

39.3.1 Compact PAC Mixture Design and Create Test Sample

The study conducts 7 PAC groups (each group has 3 cylindrical samples) based on the designed gradation shown in Fig. 39.2. Compact PAC mixture design Table 39.5.

Table 39.5 Compositions of PAC

Material	Slag 19 × 25	Slag 9.5 × 19	Slag 4.75 × 9.5	Slag 2.36 × 4.75	Slag 0.6 × 2.36	Mineral powder	Asphalt	Sum
Aggregate percentage by mass	5	40	28	17	5	5	4.49	104.49
Percent mixture by mass	4.79	38.3	26.8	16.3	4.8	4.8	4.30	95.22
Mass (kg)	47.85	382.8	268.0	162.7	47.9	47.9	43.00	952.15

They are used to determine the mechanical and physical criteria of the mixture by the Marshall method based on TCVN 8820-2011 standards (Fig. 39.2).

In order to make the PAC samples following the Marshall requirements, such as homogeneity, asphalt cover and compaction, it is necessary to make some modifications in mixing temperature and mixing time. Due to the porous surface and large volume of steel slag, it is necessary to increase the drying temperature and the mixing time to ensure that the asphalt can encapsulate steel slag particles well (Du 2017). The study' results indicate some ideal conditions (1) drying asphalt at 155 °C, (2) heating steel slag aggregate at 170 °C, (3) mixing time is between 60 and 80 s.

The experiment was conducted in 2 stages:

- Phase 1: the experiment includes a total of 15 samples (5 groups) based on the Marshall method. After molding, the samples are cooled completely to the room temperature before removing the sample from the mold. After cleaning, the samples are weighed and measured to determine height and volume. Then, they are submerged in a thermostatic flask at 60 °C and leave it for 40 min.
- Phase 2: After obtaining the results of the above experiments, the study conducts two other sample groups to evaluate the remaining stability of PAC containing steel slag aggregate after soaking the samples in 24 h at 60 °C.

39.3.2 Evaluate Experimental Results Determine the Mechanical and Physical Properties of the PAC Using Steel Slag

The experimental results determine the mechanical and physical properties of the PAC groups using steel slag aggregate shown in Tables 39.6 and 39.7.

The experimental results in Tables 39.6 and 39.7 show that the technical specifications of the PAC groups containing steel slag aggregate completely meet the requirements of TCVN 8819-2011.

Table 39.6 Experimental results of the PAC samples with optimal asphalt content with 4.3%

Group	% Asphalt in PAC19 mixture	Mass of sample	The highest proportion	Hollow		Aggregate porosity (%)	Marshall stability soaked at 60 °C			Marshall plasticity index (mm)
				In PAC (%)	Occupancy (%)		The destructive compression (kN)	Calibration factor	Stability (kN)	
1	4.3	2.68	3.031	11.52	52.42	24.2	9.62	1.008	9.69	2.72
2	4.3	2.69	3.031	11.39	52.75	24.1	9.65	0.986	9.51	2.74
3	4.3	2.68	3.031	11.52	52.42	24.2	9.51	0.970	9.22	2.73
4	4.3	2.69	3.031	11.10	53.48	23.8	9.53	1.015	9.66	2.72
5	4.3	2.68	3.031	11.48	52.51	24.2	9.61	0.990	9.52	2.73
TCVN 8819-2011										
				7/12	-	-			≥5.5	2/4

Table 39.7 Experimental results to verify the technical specifications corresponding to the optimum asphalt content of the PAC 19

Sample	% Asphalt in PAC19 mixture	Mass of sample	The highest proportion	Hollow		Aggregate porosity (%)	Marshall stability soaked at 60 °C			Marshall plasticity index (mm)
				In PAC (%)	Occupancy (%)		The destructive compression (kN)	Calibration factor	Stability (kN)	
The sample is soaked in water at 60 °C for 40 min										
1	4.3	2.68	3.031	11.53	46.22	21.43	9.59	0.972	9.32	2.75
The sample is soaked in water at 60 °C for 24 h										
2	4.3	2.68	3.031	11.48	46.32	21.39	8.11	0.990	8.03	
Stability remaining for 24 h compared to the original stability:										
According to TCVN 8819-2011 standards, stability remaining for 24 h										
≥65%										

39.4 Conclusion

The above results draw some conclusions. First, the steel slag samples obtained from Green Material Co., Ltd. fully meet the technical requirements to produce asphalt concrete in accordance with TCVN 8819-2011. Second, PAC can be used to create the foundation layer for high-grade roads as well as road surface layers in urban areas. It contributes to solve the scarcity of gravel. Third, the ideal conditions for producing PAC with uniform steel slag aggregate are as follows: (1) the steel slag aggregate is heated to 175 °C, (2) the asphalt is heated to 155 °C and more, (3) the mixing time is from 60 to 80 s.

References

- Aiban SA (2005) Utilization of steel slag aggregate for road bases. *J Test Eval* 34(1):1–11
- Australasian Slag Association A guide to the use of iron and steel slag in roads. Available at <http://www.asa-inc.org.au/knowledge/technical-literature/technical-guides>
- Das B, Prakash S, Reddy P, Misra V (2012) An overview of utilization of slag and sludge from steel industries. *Resour Conserv Recycl* 50(1):40–57
- Du NV (2017) Study on the possibility of using steel slag aggregate to produce hot asphalt concrete in the southern region of Vietnam
- Hisyamudin MN, Yokoyama AKARS (2012) Dissolution behavior of hazardous materials from EAF slag in water with wet grinding method. In: *The international conference on civil and environmental engineering sustainability*, Johor Bahru, Malaysia (2012)
- Manso JM, Gonzalez JJ, Polanco JA (2004) Electric arc furnace slag in concrete. *J Mater Civ Eng* 16(6):639–645
- Nguyen QH (2014) Research on recycling slag from steel mills to use as materials for road foundations
- Pasetto M, Baldo N (2007) The use of EAF steel slag in bituminous mixes for flexible pavements: a numerical and experimental analysis
- Patel JP (2008) Broader use of steel slag aggregates in concrete. Master Thesis, Cleveland State University
- Qasrawi H (2014) The use of steel slag aggregate to enhance the mechanical properties of recycled aggregate concrete and retain the environment. *Constr Build Mater* 54:298–304
- Rohde L, Nunez WP, Ceratti JAP (2003) Electric arc furnace steel slag, transportation research record 1819. Transportation Research Board, Washington, D.C., pp 201–207
- Ta TH (2014) Research on the application of steel slag to replace crushed stone aggregates of asphalt concrete components in road construction. University of Communications and Transport
- TCVN 8819-2011 (2011) National standard: hot asphalt concrete pavement—construction and acceptance requirements
- Tran HB (2011) Research on using slag particles from steel mills in Ba Ria-Vung Tau province as a mineral additive for cement concrete in road construction
- Yi H, Xu G, Cheng H, Wang J, Wan Y, Chen H (2012) An overview of utilization of steel slag. *Procedia Environ Sci* 16:791–801

Correction to: Mapping Wetland Ecosystems Protection and Restoration Priority Using GIS, Remote Sensing, Landscape Ecology, and Multi-criteria Analysis (Case Study in Dong Thap Muoi)



Phi Son Nguyen , Thanh Thuy Nguyen , Thi Thanh Dinh ,
Thi Hang Vu , Thi Thanh Huong Nguyen , and Lam Le 

Correction to:
**Chapter 30 in: P. L. Vo et al. (eds.), *Advances in Research on Water Resources and Environmental Systems, Environmental Science and Engineering*,
https://doi.org/10.1007/978-3-031-17808-5_30**

In the original version of the book, the following belated correction have been incorporated: The author name “Thi Dinh” has been changed to “Thi Thanh Dinh” in the Chapter 30. The chapter and book have been updated with the change.

The updated original version of this chapter can be found at
https://doi.org/10.1007/978-3-031-17808-5_30